BOOK of ABSTRACTS

1Mth International School and Conference on Optoelectronics, Photonics, Engineering and Nanostructures

May, МП-МТ, 202П Saint-Petersburg, Russia

Copyright © by 2024 National Research University Higher School of Economics - St. Petersburg and individual contributors. All rights reserved. No parts of this electronic publication may be multiple copied, stored in a retrieval system or

transmitted in any form or by any means, electronic, mechanical, photocopying, recording or otherwise, without the written permission of the publisher. Single photocopies of single articles may be made for private study or research.

11 th International School and Conference “Saint Petersburg OPEN 2024” on

Optoelectronics, Photonics, Engineering and Nanostructures carries on the tradition of annual conferences and schools organized at St Petersburg Academic University for students, PhD students and young scientists. More detailed information on the School and Conference is presented on https://spb.hse.ru/spbopen/ The Book of Abstracts includes abstracts of contributed works accepted for presentation at the Conference. The volume was composed by HSE University - St. Petersburg from electronic files submitted by the authors. Only minor technical corrections were made by the composers.

Chief Editor: A. E. Zhukov Published by HSE University - St. Petersburg, Soyuza Pechatnikov 16, 190121, St Petersburg, Printed in Russian Federation

Head of Program Committee

Alexey E. Zhukov corr. member of the RAS, HSE University, Russia

Program Committee

Andrey A. Lipovskii (Peter the Great St.Petersburg Polytechnic University, Russia) George E. Cirlin (Alferov University, Russia)

Valentina V. Zhurikhina (Peter the Great St.Petersburg Polytechnic University, Russia) Natalia V. Kryzhanovskaya (HSE University- St.Petersburg)

Head of Organizing Committee

Alexey E. Zhukov (HSE University- St.Petersburg)

Organizing Committee

Mikhail V. Maximov (Ioffe Institute, Alferov University, Russia)

Andrey A. Lipovskii (Peter the Great St.Petersburg Polytechnic University, Russia)

Valentina V. Zhurikhina (Peter the Great St.Petersburg Polytechnic University, Russia)

Vladimir V. Korenev (Alferov University, Russia)

Eduard I. Moiseev (HSE University- St.Petersburg)

Anastasia Baryshnikova (HSE University- St.Petersburg)

Conference Schedule

May 14, 2024 (Tuesday)

15:00–16:00 **Pre-registration**
(Higher School of Economics – St. Petersburg, site on Kantemirovskaya 3)

15:00–**Round table "Physics and technology of III-V structures for micro- and nanolasers" the presented scientific results were prepared based on materials from the "Mirror Laboratories" project of the HSE University and Southern Federal University.**

May 15, 2024 (Wednesday)

09:00–10:00 **On-site registration (Higher School of Economics – St. Petersburg, site on Kantemirovskaya 3)**

10:00–10:10 **Opening ceremony**
Alexey Zhukov *(Higher School of Economics – St. Petersburg, Russia)*

10:10–10:40 **Vortex laser beams and their application in signal transmission - online**
Victor Soifer *(Samara University, RAS, Russia)*

10:40–11:10 **Halide perovskite microlasers**
Anatoly Pushkarev *(ITMO University – St. Petersburg, Russia)*

11:10–11:40 **Plasmon structures in silicon integrated photonic**
Vladimir Drachev *(SKOLTECH, Russia)*

11:40–12:00 **Coffee Break**

12:00–12:30 **Carbon nanostructures. Discovery at the tip of a pen and applications in electronics**
Alexander Vul *(Ioffe Institute, Russia)*

12:30–13.00 **Race for high speed data communication. Pathway to 200 Gb/s VCSELs**
Vitaly Shchukin *(VI Systems, Germany)*

13.00–13:30 **Elevator speech session I**
(Young scientists explain key idea of their posters in 1 minute presentation using 1-2 slides)

13:30-15:00 **Lunch**

15:00–16:30 **Poster Session I**

1. Nanophotonics, Spectroscopy, Microcavities, Optics, Plasmonics, Spintronics, Electro- and Magnetooptics
2. Nanobiotechnology, Biophysics and Biophotonics
3. Electric, Magnetic and Microwave Devices

16:30–17:00 **Coffee Break**

17:00–18:00 **Poster Session I**

1. Nanophotonics, Spectroscopy, Microcavities, Optics, Plasmonics, Spintronics, Electro- and Magnetooptics
2. Nanobiotechnology, Biophysics and Biophotonics
3. Electric, Magnetic and Microwave Devices

May 16, 2024 (Thursday)

09:00–10:00 **On-site registration**

10:00–10:30 **Energy flux balance in conservative mediums and fields**

Anton Krivtsov *(Peter the Great St. Petersburg Polytechnic University, Russia)*

10:30–11:00 **III-Nitride Technologies, Lasers and transistors**

Evgeny Lutsenko *(B.I.Stepanov Institute of Physics, Belarus)*

11:00–11:30 **Application of photoelectron spectroscopy methods for the electronic and magnetic structure studies of 2D materials - online**

Yuriy Dedkov *(Shanghai University, China)*

11:30–12:00 **Coffee Break**

12:00–12:30 **The mystery of blinking quantum dots**

Pavel Frantsuzov *(Voevodsky Institute of Chemical Kinetics and Combustion Siberian Branch of the Russian Academy of Sciences, Russia)*

12:30–13:00 **Neuromorphic information processing using quantum dot lasers**

Evgeny Viktorov (*ITMO University – St. Petersburg, Russia*)

13.00-13.15 - **Presentations by sponsors**

13.15–13.30 **Elevator speech session II**

(young scientists explain key idea of their posters in 1 minute presentation using 1-2 slides)

13:30–15:00 **Lunch**

15:00–16.30 **Poster Session II**

4. Lasers, solar cells and other optoelectronic devices
5. Crystal growth and structural properties of semiconductor materials and nanostructures
6. Other Aspects of Nanotechnology

16:30–17:00 **Coffee Break**

17:00–18:00 **Poster Session II**

4. Lasers, solar cells and other optoelectronic devices
5. Crystal growth and structural properties of semiconductor materials and nanostructures

6. Other Aspects of Nanotechnology

18:00–18:30 **Closing remarks and award ceremony**
Alexey Zhukov *(Higher School of Economics – St. Petersburg, Russia)*

18.30-**Round table "Design, fabrication and study of wide-bandgap III-N heterostructures and high quality resonator microlasers" in the framework of HSE Academic Cooperation project on the current agenda of the joint project between the International Laboratory of Quantum Optoelectronics (HSE - St. Petersburg) and the Center for Wide-Bandgap Nano- and Microelectronics (B. I. Stepanov Institute of Physics of the NAS of Belarus)**

May 17, 2024 (Friday)

The whole day **Departure, free time**
Optional: Guided tour at the Int. Lab. of Quantum Optoelectronics, HSE – St Petersburg (11.00-12.00)

1. Nanophotonics, Spectroscopy, Microcavities, Optics, Plasmonics, Spintronics, Electro- and MagnetoopticsNanophotonics, Spectroscopy, Microcavities, Optics, Plasmonics, Spintronics, Electro- and Magnetooptics

May 15, 2024

15:30 - 18:00 Poster Session I

1-1	Алхалаби	Хадиль	Нет	Университет ИТМО	Strengthening irradiated areas of photo-thermo-refractive glass with silver nanoparticles.
1-2	Аринушкина	Ксения	Геннадьевна	Санкт-Петербургский государственный университет телекоммуникаций им. проф. М. А. Бонч-Бруевича	Overview of fiber optic communications in railway transport
1-3	Бабухин	Данила	Валерьевич	Физический институт имени П. Н. Лебедева РАН	Efficiency analysis of generative adversarial networks for single pixel imaging
1-4	Баитова	Валерия	Александровна	НИУ ВШЭ	Evolution of luminescent properties of single perovskite nanocrystals CsPbBr3 in the photodegradation process
1-5	Башегурова	Елена	Александровна	Санкт-Петербургский государственный университет	Study of areas of dimentional quantization in GaAs/AlGaAs quantum dots
1-6	Бондарева	Полина	Игоревна	НИУ ВШЭ МИЭМ им. А.Н. Тихонова	The development of graphene-based terahertz bolometers using the noise-thermometry method
1-7	Бородина	Любовь	Николаевна	Международный научно-образовательный центр физики наноструктур, Университет ИТМО	Fluorescence recovery and holographic grating relaxation studies of photoinduced changes in diffusivity
1-8	Бразовский	Глеб	Русланович	СПБГУТ	Experimental investigation of the fiber-optic sensor for solution concentration
1-9	Вакорина	Дарья	Владимировна	СПБГУТ	Express kidney monitoring method for early detection of kidney damage
1-10	Грибовская	Ольга	Сергеевна	СПбГЭТУ	The use of Raman and laser-induced breakdown spectroscopy for the study of iron-containing inks
1-11	Дерий	Илья	Александрович	Университет ИТМО	Optical Spintronics
1-12	Ересько	Родион	Павлович	СПБАУ РАН им. Ж. И. Алферова	Development of directional coupler based on gallium phosphide nanowires for integrated nanophotonics
1-13	Ершов	Александр	Александрович	Санкт-Петербургский государственный электротехнический университет "ЛЭТИ"	Influence of the annealing on the optical properties of silicon nitride waveguides with various thicknesses

				им. В.И. Ульянова (Ленина)	
1-14	Завьялова	Есения	Сергеевна	СПБАУ РАН им. Ж. И. Алферова	Peculiarities of the local electromagnetic field distribution in Non-van-der-Vaals InGaS3 thin layers slot waveguides
1-15	Иванов	Федор	Леонтьевич	Московский Государственный Университет имени М.В. Ломоносова	Application of properties of neuromorphic optoelectronic sensors in machine vision tasks
1-16	Игнатьева	Ирина	Олеговна	Южный федеральный университет	Optical properties of the CuO–ZnO thin films
1-17	Ильин	Матвей	Евгеньевич	Санкт-Петербургский государственный электротехнический университет «ЛЭТИ» имени В. И. Ульянова (Ленина)	Features of the reduced graphene oxides: spectral and conductive properties
1-18	Кадинская	Светлана	Алексеевна	СПбАУ РАН им. Ж.И. Алферова	Random lasing in hydrothermal ZnO structures
1-19	Кан	Геннадий	Радионович	СПбАУ РАН им. Ж.И. Алферова	Ion exchange for obtaining second-order nonlinearity in glass
1-20	Карамышева	Софья	Павловна	Университет ИТМО	The influence of chiral ligands on the optical properties of AgBiS2 nanocrystals
1-21	Кашапов	Артем	Ильясович	Самарский университет/Институт систем обработки изображений	Metal–dielectric resonator integrated in an asymmetric slab wavegude for spatiotemporal optical vortex generation
1-22	Кириченко	Данил	Владимирович	Лаборатория эпитаксиальных технологий ЮФУ	Study of the photoluminescence properties of subcritical InAs/GaAs quantum dots formed onto structured substrates
1-23	Клименко	Дарина	Игоревна	Университет ИТМО	Two-dimensional PbSe/PbS near-infrared heterostructures with perovskite passivated surface
1-24	Лебедева	Елизавета	Сергеевна	Московский Педагогический Государственный Университет, Лаборатория квантовых детекторов.	Spatial light modulator based on rotating disk for single-pixel imaging in IR-range
1-25	Лунёв	Андрей	Юрьевич	Санкт-Петербургский государственный электротехнический университет «ЛЭТИ»	Numerical analysis of dispersive wave generation in glass whispering gallery mode resonators doped with plasmonic CuS nanoparticles
1-26	Марасанов	Дмитрий	Вячеславович	Университет ИТМО	Spectral and photocatalytic properties of Ag-AgCl nanostructures formed on surface of silicate glass by ion exchange
1-27	Масталиева	Виктория	Анатольевна	СПбАУ РАН им. Ж.И. Алферова	Nonlinear optical phenomena in mesoporous SiO2 and Si/SiO2 nanoparticles
1-28	Машинский	Константин	Викторович	Саратовский филиал Института радиотехники и	Terahertz lasing in a metal groove with population inverted graphene

				электроники им. В.А. Котельникова РАН	
1-29	Меньшиков	Евгений	Владимирович	Университет ИТМО	Laser imprinting of large-scale phase patterns in GST using a spatial light modulator
1-30	Михайлова	Анна	Владимировна	ФИЦ ХФ РАН	Spectrocopic markers in raman spectra for the analysis of wood bases of antique icons
1-31	Мурзагалина	Софья	Маратовна	МФТИ	The research and analysis of nonlinear optical phenomena in silicon slot waveguide structures
1-32	Новосёлов	Артём	Кириллович	Московский физико-технический институт (МФТИ)	The effect of electrode diameter on the composition of zinc aluminate particles obtained in a gas discharge.
1-33	Нуралдин	Мессан	Салех	МФТИ	Synthesis of aluminum nanoparticles using spark discharge for applications in ultraviolet plasmonics
1-34	Осколкова	Татьяна	Олеговна	Университет ИТМО	Spectrally-resolved photoluminescence decay kinetics of size-selected AgInS2 quantum dots
1-35	Паньков	Анатолий	Сергеевич	Пермский государственный национальный исследовательский университет	Microlenses at the ends of optical fibers that preserve radiation polarization
1-36	Папылев	Денис	Сергеевич	Университет ИТМО	Study of planar microcavity structure with In0.63Ga0.37As quantum dots and Al0.2Ga0.8As/Al0.9Ga0.1As mirrors
1-37	Пашина	Олеся	Игоревна	Университет ИТМО	Surface Plasmon-Polariton excitation in GaAs films via optically-induced diffraction grating
1-38	Песняков	Владислав	Викторович	Университет ИТМО	Photocatalytic properties of Ag-AgBr nanostructures formed by ion-exchange in photo-thermo-refractive glass for water-dye degradation
1-39	Пешкичева	Людмила	Евгеньевна	ФГУП «РФЯЦ-ВНИИТФ им. Академ. Е.И. Забабахина”	Cleaning of miniaturized lenses integrated on optical fibers
1-40	Пленингер	Максимилиан	-	Южный Федеральный Университет	Simulation of an all-optical logical comparator based on a GaAs photonic crystal operating at a wavelength of 1.3 μm
1-41	Поповский	Никита	Игоревич	Санкт-Петербургский государственный университет телекоммуникаций им. Проф. М.А. Бонч-Бруевича	Features of the implementation of optical superchannels in flexible optical networks
1-42	Проводин	Даниил	Сергеевич	Санкт-Петербургский политехнический университет Петра Великого	A new method of managing the discretization of the scale in a differential mobile refractometer
1-43	Рабош	Екатерина	Владимировна	Университет ИТМО	Confocal microscopy of a display hologram
1-44	Розенблит	Алина	Дмитриевна	Университет ИТМО	Topological edge states supported by two-dimensional square-lattice arrays of bianisotropic dielectric resonators

1-45	Ружевич	Максим	Станиславович	Университет ИТМО	Photoluminescence of self-induced InAs nanowires diluted with nitrogen
1-46	Савельев	Дмитрий	Андреевич	Самарский национальный исследовательский университет им. Академика С.П. Королева	The investigation of optical needle formation by subwavelength optical elements using high-performance computer systems
1-47	Санатулина	Арина	Фяридовна	Московский физико-технический институт (национальный исследовательский университет)	Influence of gas flow rate and heating on the dimensional properties of platinum particles synthesized in a gas discharge
1-48	Соломонов	Никита	Александрович	СпбАУ им. Ж.И.Алферова	Luminescence enhancement in inelastic tunnelling of electrons by changing the geometry of the tunnelling contact
1-49	Солонович	Никита	Евгеньевич	НИТУ МИСИС	Investigation of the characteristics of the metaatom field in the high-frequency range.
1-50	Станчик	Алёна	Викторовна	ГО "Научно-практический центр Национальной академии наук Беларуси по материаловедению"	Quantum size effect in cadmium sulphide films after plasma treatment
1-51	Степаненков	Григорий	Викторович	СПбГУТ им. проф. М. А. Бонч-Бруевича	Features of express control of three-component mixture of volatile hydrocarbon media in visible light
1-52	Табиева	Арина	Вадимовна	Университет ИТМО	Modeling the dynamics and properties of the compressed state of light in a phase modulator.
1-53	Фетисенкова	Ксения	Алексеевна	Московский физико-технический институт (Физтех)	E-beam resist AR-N 7520 in the formation of the photonic structures
1-54	Филиппов	Иван	Алексеевич	ФГБОУ ВО «Пензенский государственный университет»	Hierarchical self-assembly of SiO2-SnO2 nano- and microstructures in combined sol-gel systems
1-55	Фомин	Алексей	Андреевич	Лаборатория Оптики спина имени И.Н. Уральцева, Санкт-Петербургский государственный университет	Optically driven spin-alignment precession in cesium vapor
1-56	Фунтикова	Анастасия	Сергеевна	Санкт-Петербургский политехнический университет им. Петра Великого	Numerical study of the optical mode structure of GaP nanowires
1-57	Чередникова	Арина	Алексеевна	ИТМО	Design of an optical fiber based sensor for temperature-sensitive measurements
1-58	Чиглинцев	Эмиль	Олегович	МФТИ	Organic kainate single crystals as a broadband

					THz source for Yb laser
1-59	Шеин	Кирилл		МИЭМ НИУ ВШЭ/МПГУ	Towards the realization of NbSe2 NIR photodetectors integrated on a silicon nitride waveguide.
1-60	Ячук	Владимир	Аркадиевич	НИУ "Московский энергетический институт"	Improvement of the technique for describing the scattering of photoelectrons in a solid
1-61	Мельниченко	Иван	Алексеевич	СПбАУ РАН им. Ж.И. Алферова	Study of mode leakage into substrate in microdisk lasers
1-62	Реутов	Алексей	Алексеевич	Физический институт имени П. Н. Лебедева РАН	
1-63	Давыдов	Роман	Вадимович	СПбАУ РАН им. Ж.И. Алферова	Features of monitoring the state of liquid flow by nuclear magnetic resonance using the modulation technique to record the NMR signal
1-64	Матвеева	Милена	Вадимовна	Университет ИТМО	Investigation of entangled states of a three-mode electro-optical modulator
1-65	Малохатко	Софья	Владиимировна	ИНЭП ЮФУ	Determination of metasurface structure dimensions by plasma chemical etching for metalens application
1-66	Масютин	Дмитрий	Алексеевич	СПбАУ РАН им. Ж.И. Алферова	The effect of rapid thermal annealing on the optical properties of structures with InGaPAS/InGaAs Quantum dots

2. Nanobiotechnology, Biophysics and BiophotonicsNanobiotechnology, Biophysics and Biophotonics

May 15, 2023

15:30 - 18:00 Poster Session I

2-1	Андреев	Владислав	Сергеевич	НИУ ВШЭ/МПГУ	Superconducting Single Photon Detector with multimode fiber coupling for PLIM\FLIM applications
2-2	Антипенко	Владимир	Викторович	ФГБОУ ВО "Пензенский государственный университет"	Automated bioimpedance measurement system for body composition studies
2-3	Артамонова	Дарья	Александровна	Санкт-Петербургский Государственный Университет	Formation of compact DNA structures with nanoparticles
2-4	Бабаев	Кирилл	Владимирович	Санкт-Петербургский	Development of hardware and software

				политехнический университет Петра Великого	complex for assessment of the functional state of the microvasculature
2-5	Бойцова	Наталья	Андреевна	Санкт-Петербургский национальный исследовательский Академический университет имени Ж. И. Алфёрова Российской академии наук	NELM - multi-algoritmh software for analysis of high resolution bioimpedance spectra
2-6	Вакорина	Дарья	Владимировна	СПБГУТ	Express kidney monitoring method for early detection of kidney damage
2-7	Винокуров	Егор	Константинович	Федеральное государственное автономное образовательное учреждение высшего образования «Санкт-Петербургский политехнический университет Петра Великого»	Integrated application of Calcium Imaging and electrophysiological recording of neuronal activity in vivo
2-8	Власов	Александр	Андреевич	ФГБОУ ВО «МПГУ»	Dorsal skinfold chamber adaptation for optimal microscopy studies
2-9	Демидов	Юрий	Андреевич	НИУ ВШЭ в Санкт-Петербурге	Structure and properties of small gold clusters labeled by actinium
2-10	Денисова	Елена	Артемовна	Институт аналитического приборостроения Российской академии наук	Application of the convolutional neural network AlexNet in the problem of classification of electrocardiosignals obtained by ultra-high resolution electrocardiography method
2-11	Дубина	Филипп	Михайлович	СПбАУ РАН им. Ж.И. Алферова	Microlithography Technology Using BioLaboratory Equipment for Multielectrode Arrays Fabrication
2-12	Душина	Анастасия	Олеговна	НИЯУ МИФИ	Conditions of AgNPs/flavin mononucleotide complex formation as a tool to tune optical properties of this complex
2-13	Жесткая	Екатерина	Алексеевна	Санкт-Петербургский государственный университет телекоммуникаций имени профессора М. А. Бонч-Бруевича	Express diagnostics of human health using laser radiation absorption signals
2-14	Заневская	Мария	Юрьевна	Государственный университет аэрокосмического приборостроения	Investigation of tissue respiration functions by optical methods
2-15	Исаева	Юлия	Александровна	Институт синтетических полимерных	Nanoparticles based on organic donor-acceptor compounds for biomedicine

				материалов им. Н.С. Ениколопова РАН	
2-16	Левин	Алексей	Игоревич	ФГБОУ ВО "Пензенский государственный университет"	Options for implementing electrical impedance tomography for diagnostics blood clots and bruises
2-17	Мсукар	Сухайр	-	Санкт-Петербургский политехнический университет Петра Великого	A sensor for monitoring pulse wave parameters for express diagnostics of human cardiovascular system
2-18	Нефедьев	Николай	Алексеевич	Алферовский университет	Improving Compliance of Brain MRI Studies with the Atlas using a Modified TransMorph Neural Network
2-19	Никитин	Данила	Александрович	Санкт-Петербургский Государственный Университет	Iron mediated DNA-catechin complexes
2-20	Романова	Вероника	Вячеславовна	Институт аналитического приборостроения Российской Академии наук	Methodology of potentiometric microbiological testing as applied to the comparative evaluation of antibiotic properties of essential oils (Методика потенциометрического микробиологического тестирования применительно к сравнительной оценке антибиотических свойств эфирных масел)
2-21	Ронишенко	Богдан	Вячеславович	Институт физико-органической химии Национальной академии наук Беларуси	N-arylated DABCOnium salts for thiol and selenol sensing
2-22	Рябкин	Дмитрий	Игоревич	Первый Московский государственный медицинский университет имени И. М. Сеченова	Laser welding of biological tissues using galvanoscanner and focused laser radiation transport
2-23	Сосновицкая	Злата	Филипповна	Академический университет им. Алферова	Survival rate, viability and transfection of eukaryotic cells on GaP and GaAs nanowires.
2-24	Степанов	Максим	Евгеньевич	Московский государственный педагогический университет	Intravital microscopy: dorsal skinfold chamber model.
2-25	Сучков	Максим	Юрьевич	РНИМУ им. Н. И. Пирогова	Modified natural polymers with bioactive additives for restoration of critical bone defect
2-26	Сучкова	Виктория	Викторовна	Первый Московский государственный медицинский университет имени И. М. Сеченова	Investigation of solder based on nanoparticles with metallic properties for laser reconstruction of blood vessels
2-27	Сырчина	Мария	Сергеевна	ФИЦ ХФ РАН им. Н.Н. Семёнова	Fluorescent cell imaging with femtosecond laser pulses-produced protein nanoaggregates
2-28	Федотова	Елизавета	Владиславовна	СПбГУ	Structure of bovine serum albumin in solution

					and films as revealed from vibrational spectroscopy
2-29	Харламова	Анастасия	Александровна	Лаборатория диагностики углеродных материалов и спиново-оптических явлений в широкозонных полупроводниках Северного (Арктического) федерального университета	Scattering of ultrashort laser pulses on pseudoknots RNA
2-30	Шеховцов	Николай	Викторович	Санкт-Петербургский государственный университет	Pteridines Sensors Based on Amino Acids-Stabilized Gold Nanoclusters
2-31	Шрам	Полина	Петровна	ФГБОУ ВО «МПГУ»	Antibacterial properties of riboflavin under photodynamic exposure in a culture of fluorescent bacteria E. Coli.
2-32	Порфирьева	Елена	Витальевна	Санкт-Петербургский политехнический университет Петра Великого	A new technique for determining calibration coefficients in the esCCO method
2-33	Лямина	Юлия	Владимировна	СПбАУ РАН/ИАП РАН	Methodology of Mass Spectrometric Quality Control and Toxicosafety of Dairy Products

3. Electric, Magnetic and Microwave Devices

May 15, 2024

15:30 - 18:00 Poster Session I

3-1	Афанасьев	Никита	Сергеевич	Санкт-Петербургский политехнический университет Петра Великого	Voltage controlled generator for multifunctional radar station
3-2	Барыкин	Дмитрий	Артемович	СПбАУ РАН им. Ж.И. Алфёрова	Tunnel effect investigation in GaN/Si heterostructure
3-3	Белозеров	Игорь	Александрович	Ярославский Филиал (ЯФ ФТИАН РАН) Федерального государственного бюджетного учреждения науки Физико-технологического института Российской	A compact MEMS switch for advanced radar systems

				академии наук	
3-4	Бурмистров	Олег	Ильич	Университет ИТМО	Wireless power transfer in MRI with a detuned birdcage coil
3-5	Бурцев	Владимир	Денисович	МФТИ, Физтех	Mobius strip inspired design of a multiband dipole-like circularly polarized antenna
3-6	Ведь	Михаил	Владиславович	НИФТИ ННГУ	Control of the functional characteristics of spin light-emitting diodes InGaAs/GaAs/Al2O3/CoPt
3-7	Гусс	Людмила	Евгеньевна	ФГУП "РФЯЦ - ВНИИТФ им. академ. Е.И. Забабахина"	Manufacturing of C-Cu-C laser targets
3-8	Емельянов	Никита	Сергеевич	Пензенский государственный университет	Structure of a software -hardware complex for the study of ferroelectrics
3-9	Ершова	Маргарита	Игоревна	МПГУ (Московский педагогический государственный университет)	A mmWave dielectric antenna with symmetric beam compatible with PCB machinery
3-10	Исупова	Екатерина	Васильевна	Санкт-Петербургский политехнический университет Петра Великого	System of the temperature controller for the rubidium frequency standard
3-11	Клименко	Дарья	Юрьевна	Санкт-Петербургский политехнический университет Петра Великого	New stripline linear sensor design for industrial applications
3-12	Климова	Софья	Андреевна	Санкт-Петербургский политехнический университет Петра Великого	Analysis of the trajectory of a symmetrical spinning top in the Earth's magnetic field
3-13	Кожевников	Василий	Юрьевич	Институт сильноточной электроники СО РАН	The role of ectons in the vacuum breakdown process
3-14	Кожуховский	Алексей	Константинович	Московский Педагогический Государственный Университет, Институт Физики Технологий и Информационных Систем, Кафедра Общей и Экспериментальной Физики, Лаборатория Квантовых Детекторов	Terahertz integrated H-plane bend: simulation and experimental investigation
3-15	Козловская	Екатерина	Андреевна	Национальный исследовательский университет «МИЭТ»	Field plates design optimization to increase breakdown voltage of GaN HEMT
3-16	Морозов	Матвей	Олегович	ЯРГУ им. П.Г. Демидова / ЯФ ФТИАН им. К.А. Валиева РАН	Combined resistive-capacitive MEMS switch for advanced communication systems
3-17	Назаров	Натанил	Михайлович	МГТУ им. Н.Э. Баумана/МФТИ, Физтех	Development of a Ku-band phased array antenna for satellite communication
3-18	Никитин	Константин	Германович	Национальный	Research of thin Ti/Al films resistivity and

				исследовательский университет «МИЭТ»	transparency change after thermal treatment to determine the possibility of solid solution formation and decrease of the ohmic contacts formation temperature
3-19	Патарашвили	Антон	Николаевич	Московский Физико-Технический Институт (Национальный Исследовательский Университет)	Effect of the electrostatic focusing lens voltage on structures size in 3D printing by charged Au nanoparticles.
3-20	Попов	Александр	Александрович	Санкт-Петербургский политехнический университет Петра Великого	A 100 MHZ signal conversion device with low phase noise
3-21	Разакова	Анита	Анваровна	МПГУ	Subterahertz circularly polarized 1k-pixel reflective surface for 6G applications
3-22	Рожкова	Полина	Вадимовна	Московский Педагогический Государственный Университет	Polyethylene-on-quartz platform for subterahertz reconfigurable reflective surfaces
3-24	Седов	Артём	Павлович	РТУ МИРЭА/ МФТИ, Физтех	Surface roughness modeling for extremely high frequency applications
3-25	Селиверстов	Сергей	Валерьевич	Московский педагогический государственный университет	Transmittance of TE and TM radiation modes in a dielectric THz integrated waveguide
3-27	Трактирщиков	Виктор	Сергеевич	Национальный исследовательский университет «МИЭТ»/АО «НПП «ЭСТО»	Research of the dependence of the clamping force of a silicon wafer by ESC on the holding time
3-28	Шавшин	Артём	Владимирович	Санкт-Петербургский государственный университет телекоммуникаций им. проф. М. А. Бонч-Бруевича	Increasing frequency stability of atomic frequency standards by organizing a group frequency standard
3-29	Шлепаков	Павел	Сергеевич	ЯФ ФТИАН им. К.А. Валиева РАН	A fast and strong microactuator powered by explosion of a hydrogen-oxygen mixture
3-30	Яковлев	Никита	Николаевич	Национальный исследовательский томский государственный университет	Electroconductive properties of Pt/(100) β-Ga2O3 Schottky barrier diode based on Czochralski grown crystal
3-31	Mahmoodpoor	Abolfazl	-	ITMO university	All-electronic memristor based on charge carrier confinement in bulk semiconductor of metal-semiconductor-metal structure
3-32	Pilipenko	Kirill	Sergeevich	Bryansk State Technical University	Radiation behaviour study of linear voltage regulator
3-33	Pilipenko	Kirill	Sergeevich	Bryansk State Technical University	Method for increasing of the voltage regulator radiation hardness
3-34	Афанасьев	Никита	Сергеевич	Санкт-Петербургский	Voltage controlled generator for

				политехнический университет Петра Великого	multifunctional radar station
3-35	Сидорова	Светлана	Владимировна	МГТУ им. Н.Э. Баумана	Technological aspects of island thin films usage in sensors for various purposes
3-36	Сидорова	Светлана	Владимировна	МГТУ им. Н.Э. Баумана	Technological aspects of increasing capacitor capacitance method
3-37	Валов	Антон	Петрович	СПбГУТ, АО "Обуховский завод"	Development of an excitation signal generation system for a rubidium frequency standard

4. Lasers, solar cells and other optoelectronic devices

May 16, 2024

15:30 - 18:00 Poster Session II

4-1	Андреев	Владислав	Сергеевич	НИУ ВШЭ/МПГУ	Superconducting Single Photon Detector with multimode fiber coupling for PLIM\FLIM applications
4-2	Попов	Максим	Андреевич	МФТИ	Millifluidic polyol synthesis of Ag nanowires and microplotter printing of transparent conductive films
4-3	Бобров	Михаил	Александрович	ФТИ им А.Ф.Иоффе	Relative intensity noise of 89X nm-range single-mode vertical-cavity surface-emitting lasers
4-4	Болтанский	Матвей	Вячеславович	«Qrate»	Influence of optical feedback on a signal of a semiconductor laser
4-5	Вячеславова	Екатерина	Александровна	СПбАУ РАН им. Ж.И. Алферова	Gallium phosphide/black silicon heterojunction solar cells
4-6	Григоренко	Илья	Николаевич	Университет ИТМО / ФТИ им. А.Ф. Иоффе РАН	Lateral mod modification of Fabry-Perot semiconductor laser by focused ion beam
4-7	Дашков	Александр	Сергеевич	Алферовской университет, СПбГЭТУ "ЛЭТИ"	Optimization of Mid-Infrared Quantum Cascade Detectors
4-8	Дедков	Евгений	Андреевич	МФТИ (Московский физико-технический институт)	Security of BB84-like protocol on coherent states with different intensities
4-9	Дуплинский	Алексей	Валерьевич	НИУ ВШЭ / КуСпэйс Технологии	Polarization extinction ratio conversion due to pointing system impact in satellite quantum key distribution
4-10	Дэн	Юаньбяо	-	Санкт-Петербургский политехнический университет Петра Великого	Photovoltaic potential in the Subarctic region
4-11	Ершов	Евгений	Васильевич	ФГУП "РФЯЦ-ВНИИТФ им. академика Е.И. Забабахина"	Heterostructure design features for 975 nm high-power laser diodes.
4-12	Журба	Данила	Владимирович	Университет ИТМО (аспирант)/ Университет "ЛЭТИ" (инженер)	3D laser cleaning as a novel approach to artworks conservation

4-13	Иванов	Антон	Евгеньевич	СПбГЭТУ "ЛЭТИ" им. В.И. Ульянова (Ленина) / НТЦ микроэлектроники РАН	Competing processes affecting the properties of nitride MQWs of LEDs
4-14	Иванов	Владимир	Сергеевич	Университет ИТМО	Development of Semitransparent Perovskite Solar Cells with double electron transport layer and modified top electrode
4-15	Игнатьев	Андрей	Николаевич	ФГУП «РФЯЦ – ВНИИТФ им. академ. Е.И. Забабахина»	Fast axis collimation lens misalignment influence on the fiber coupling efficiency of high-power laser diode module
4-16	Исупов	Александр	Ильич	СПбГУТ	Modeling the broadband measuring source using the optical fiber nonlinear properties
4-17	Кенесбай	Рамазан	-	Санкт-Петербургский национальный исследовательский Академический университет Российской академии наук	Suppressed phase segregation in CsPbBr2I based PeLEC
4-18	Костромин	Никита	Андреевич	Санкт-Петербургский Политехнический Университет Петра Великого	Numerical optimization of semiconductor waveguide structures
4-19	Кудряшов	Игорь	Сергеевич	МФТИ/QRATE	"Quantum state preparation with optical injection: Issue of intersymbol interference"
4-20	Лавриненко	Валерий	Витальевич	СПбГЭТУ "ЛЭТИ"	Investigation of microfluidic topology formation with the use of IR pulse laser
4-21	Любчак	Анастасия	Николаевна	НИУ ВШЭ МИЭМ	Research and development of terahertz photodetectors based on graphene integrated on a dielectric waveguide
4-22	Огородников	Егор		Университет ИТМО	Antisolvent modification by carbon nanodots to enhance the performance of FACsPbI3 solar cells
4-23	Неелова	Ангелина	Дмитриевна	СПбГЭТУ "ЛЭТИ"	A study of laser cleaning of paper with fat-containing contaminations
4-24	Новикова	Кристина	Николаевна	СПбАУ РАН им. Ж.И. Алферова;	Nano-sized red LEDs based on GaPNAs nanowires synthesized on silicon substrate
4-25	Пиронин	Ольга	Алексеевна	Санкт-Петербургский государственный электротехнический университет «ЛЭТИ» им. В.И. Ульянова (Ленина)	Studying the color characteristics of painting materials using spectrophotometry
4-26	Подойлов	Игорь	Олегович	Северный (Арктический) федеральный университет	Development of an experimental device for measuring the internal stresses of single crystal diamond plates
4-27	Поздняков	Артём	Андреевич	Санкт-Петербургский государственный университет телекоммуникаций им. проф. М.А. Бонч-	Experimental study of the broadband optical source with hybrid amplification

				Бруевича	
4-28	Пылаев	Вадим	Евгеньевич	СПбГУТ им. проф. М. А. Бонч-Бруевича	Экспериментальное исследование использования в системах мониторинга оптических кабелей с волокнами разных типов
4-29	Рудавин	Никита	Владимирович	НИУ ВШЭ	Calibration of the parameters of the polarization controller for polarization control algorithms
4-30	Рюпина	Анна	Сергеевна	НИУ ВШЭ	Study of the Influence of the Surface Density of In(Ga)As/GaAs Quantum Dots on the Microdisk Laser Characteristics
4-31	Саенко	Александр	Викторович	Южный федеральный университет	Development of a device for automated measurement photovoltaic characteristics of solar cells
4-32	Самарцев	Илья	Владимирович	Нижегородский государственный университет им. Н.И. Лобачевского	InGaAs metamorphic diode for 1550 nm wavelength grown on GaAs substrate by MOCVD
4-33	Синицкая	Олеся	Алексеевна	Алферовский университет	GaN based ultraviolet narrowband photodetectors
4-34	Соколов	Никита	Михайлович	Санкт-Петербургский Государственный Электротехнический Университет "ЛЭТИ"	Identification of unreadable marginalia by means of hyperspectral imaging: case study of the Ostrog Bible from the Library of the Academy of Sciences and the Russian National Library
4-35	Сыч	Денис	Васильевич	Физический институт им. П.Н. Лебедева, РАН	Combining compressed sampling and neural networks for single-pixel imaging
4-36	Тойкка	Андрей	Сергеевич	СПбГЭТУ "ЛЭТИ"	Surfaces modifications in functional layers for Liquid Crystal devices
4-37	Тойкка	Андрей	Сергеевич	Академический университет им. Ж.И. Алферова	Red light emitting diode based on CsPbBr2I perovskite
4-38	Толкач	Никита	Михайлович	Национальный Исследовательский университет «МИЭТ», Москва, Зеленоград	Stability of photovoltaic performance of solar cells sensitized with dye based on thieno[3,2-b]indole / 2,2'-bithiophene
4-39	Фролов	Илья	Владимирович	Ульяновский филиал Института радиотехники и электроники им. В.А.Котельникова Российской академии наук	Threshold current of separate spectral components of the emission spectrum of InGaN LEDs
4-40	Цымбалов	Александр	Вячеславович	Национальный исследовательский Томский государственный университет	Influence of the Substrate Type on the Photoelectric Characteristics of Ga2O3/GaAs Structures
4-41	Чернев	Игорь	Михайлович	Институт автоматики и процессов управления Дальневосточного	Mg2Si contact layer for narrowband Si detector with 1045 nm peak photoresponse

				отделения Российской академии наук	
4-42	Шавшин	Артём	Владимирович	Санкт-Петербургский государственный университет телекоммуникаций им. проф. М. А. Бонч-Бруевича	Development of a space debris recognition system based on artificial intelligence
4-43	Ярчук	Эрнст	Янович	СПбГЭТУ "ЛЭТИ" им. В.И. Ульянова (Ленина)	Influence of light incidence angle on silicon solar cells performance with different texturing
4-44	Мерзлинкин	Виталий	Евгеньевич	НИТУ МИСиС	Ground receiving station with superconducting single photon detector in the laser communication system with the satellite «Impulse-1»
4-45	Мысь	Дмитрий	Александрович	Санкт-Петербургский политехнический университет Петра Великого	Лазерный локатор для подводного обнаружения объектов

5. Crystal growth and structural properties of semiconductor materials and nanostructures

May 16, 2024

15:30 - 18:00 Poster Session II

5-1	Балаган	Семён	Анатольевич	ИАПУ ДВО РАН	The quest for direct band beta iron disilicide: collaboration of theoretical and experimental approaches
5-2	Балаган	Семён	Анатольевич	ИАПУ ДВО РАН	Effect of diameter on lattice thermal conductivity of a-FeSi2 and e-FeSi nanowires
5-3	Баранцев	Олег	Вячеславович	Alferov Federal State Budgetary Institution of Higher Education and Science Saint Petersburg National Research Academic University of the Russian Academy of Sciences	Influence of the doping level in the absorption layer of InGaAs/InP 2.5 um photodetectors on their electrical properties
5-4	Белов	Ярослав	Дмитриевич	Физико-технический институт имени К.А. Валиева	Formation of nanocones on the surface of Pb0.4Sn0.6Te films during ion-plasma treatment with argon ions with an energy of 140 eV
5-5	Бобков	Антон	Алексеевич	ООО "НТ МДТ"	Non-resonant vibrational scanning probe microscopy techniques for studying nanomaterials

5-6	Ефимова	Арина	Александровна	Университет ИТМО	Optically active nanocomposites based on CsPbBr3 nanocrystals and chiral carbon dots
5-7	Воробьев	Максим	Геннадьевич	Институт Проблем Машиноведения РАН	Study of evolution of SiC/Si hybrid structures by RHEED and Owens-Wendt methods
5-8	Вторыгин	Георгий	Эдуардович	СПбАУ РАН им. Ж.И. Алфёрова	Investigation of properties of periodic multilayer BP/Si nanoheterostructures grown by PECVD
5-9	Гридчин	Владислав	Олегович	СПбАУ РАН им. Ж.И. Алфёрова	MBE Growth of InGaN Nanowires: Influence of the III/V Flux Ratio on the Structural and Optical Properties
5-10	Грушевский	Егор	Алексеевич	ЯФ ФТИАН им. К.А. Валиева РАН	The method of obtaining Ni and Co nanowires in porous anodic alumina matrices
5-11	Гуляева	Ирина	Александровна	Южный федеральный университет	Surface and electrical properties of La-SnO2 thin films
5-12	Духан	Денис	Дмитриевич	Лаборатория эпитаксиальных технологий ИНЭП ЮФУ	Ab initio study of In adsorption on AlxGa1-xAs substrates during first stages of droplet epitaxy
5-13	Ерёменко	Михаил	Михайлович	Южный Федеральный Университет	Combined approach of patterning on SiO2/Si substrate using ion beam and chemical wet etching
5-14	Жуков	Михаил	Валерьевич	ИАП РАН	Technique for characterizing a nanocapillary probe: aperture and mechanical stability measuring
5-15	Журина	Ангелина	Евгеньевна	Пензенский государственный университет	Study of the electrophysical properties of BaTiO3 films formed in the process of micro-arc oxidation
5-16	Здоровейщев	Даниил	Антонович	Федеральное государственное автономное образовательное учреждение высшего образования «Национальный исследовательский Нижегородский государственный университет им. Н.И. Лобачевского»	Influence of isovalent Bismuth on the properties of Gallium Arsenide
5-17	Зинченко	Тимур	Олегович	ФГБОУ ВО "Пензенский государственный университет"	Model of the relationship between the parameters of smart glasses based on fundamental physical and chemical laws
5-18	Исаева	Юлия	Александровна	Институт синтетических полимерных материалов им. Н.С. Ениколопова РАН	Nanoparticles based on organic donor-acceptor compounds for biomedicine
5-19	Карамышева	Софья	Павловна	Университет ИТМО	The influence of chiral ligands on the optical properties of AgBiS2 nanocrystals
5-20	Карташова	Анастасия	Максимовна	Саратовский национальный исследовательский	Laser-stimulated tin-induced crystallization of silicon on flexible nonwoven substrates

				государственный университет имени Н. Г. Чернышевского.	
5-21	Ким	Ксения	Борисовна	ВГУИТ	Depoaition of Copper and Gold onto porous silicon
5-22	Козюменко	Константин	Алексеевич	Южный федеральный Университет	Formation of transparent memristor structures based on ZnO using RF magnetron sputtering
5-23	Кошевая	Екатерина	Дмитриевна	ФГБУ ГНЦ ФМБЦ им. А.И. Бурназяна ФМБА России	Stokes and Anti-Stokes Luminescent Rare-Earth-Doped Tantalum Oxide Nanoparticles
5-24	Кукенов	Олжас	Игоревич	Томский Государственный университет	1x2 and 2x1 superstructures changes during the growth of Ge on Si(100)
5-25	Кулешова	Алина	Олеговна	Университет ИТМО	Droplet microfluidic synthesis of HKUST-1 metal-organic frameworks
5-26	Лахина	Екатерина	Александровна	Южный федеральный университет	Influence of annealing conditions on the characteristics of nanoholes formed by focused ion beams on the GaAs(111) surface
5-27	Лебедева	Эльгина	Маратовна	Институт органической и физической химии им. А.Е. Арбузова ФИЦ Казанский научный центр РАН	Thin-film zinc oxide as a sensitive element of a conductometric NO2 sensor
5-28	Лендяшова	Вера	Вадимовна	Академический университет им. Ж.И. Алфёрова	MBE growth and optical properties of InAs QD heterostructures on Si
5-29	Максимова	Алина	Андреевна	СПбГЭТУ "ЛЭТИ"	Influence of in-situ plasma treatment during PE-ALD of GaN on growth rate and morphology
5-30	Насиров	Павел	Денисович	ФГБОУ ВО "Университет "Дуна"	Modified highly fluorescent carbon dots for immunochemical application
5-31	Низамеева	Гулия	Ривалевна	Институт органической и физической химии им. А.Е. Арбузова ФИЦ Казанский научный центр РАН	Registration of the sensor response based on a network of oriented nickel oxide fibers to nitrogen dioxide using impedance spectroscopy
5-32	Паршин	Богдан	Александрович	Московский Государственный Технический Университет им. Н.Э. Баумана.	Investigation of the effect of functional sublayers on the characteristics of deposited diamond-like carbon coatings
5-33	Песняков	Владислав	Викторович	Университет ИТМО	Quantum efficiency of water photocatalytic decomposition by Ag-Ag2S nanostructures
5-34	Поздеев	Вячеслав	Алексеевич	СПбАУ РАН / ЛЭТИ	Study of the effect of surfactants on surface tension of PEDOT:PSS aqueous solution
5-35	Портнова	Ксения	Александровна	Университет ИТМО	Structural engineering of bactericidal Mn-doped ZnO-ZrO2 nanocomposites as effective photogenerators of reactive oxygen species
5-36	Ратова	Анастасия	Дмитриевна	НИУ ИТМО	Investigation of the luminescent properties

					of glasses activated by CsPbBr3 perovskite nanocrystals and europium ions
5-37	Решетов	Илья	Валентинович	Алферовский университет	Formation of silver nanoparticles in glass by vacuum thermal poling
5-38	Сидоров	Евгений	Александрович	Государственный университет "Дубна"	Study of the fluorescent properties of boron nitride quantum dots depending on functionalizing ligands
5-39	Старникова	Александра	Павловна	Южный федеральный университет	Gas sensing properties of TiO2-SnO2 nanocrystalline thin films for NO2 sensing
5-40	Старникова	Александра	Павловна	Южный федеральный университет	Study of the electrical properties of ZnO nanorods under the influence of controlled intensity UV radiation
5-41	Степченко	Артем	Дмитриевич	Южно-Российский государственный политехнический университет (НПИ) имени М. И. Платова	Влияние скорости изменения температуры на термомиграцию жидких включений в кремнии
5-42	Субботин	Евгений	Юрьевич	ИАПУ ДВО РАН	The features of Mg2Si growth by ultra-fast reactive epitaxy on porous Si(100) surface
5-43	Трошкина	Наталья	Николаевна	Государственный университет "Дубна"	Creation of portable sensors based on quantum dots of different composition for determination of heavy metal ions.
5-44	Фаттахов	Илья	Сергеевич	ЯФ ФТИАН им. К.А.Валиева	Obtaining chiral metasurfaces from SiO2 target by oblique angle deposition
5-45	Фетисенкова	Ксения	Алексеевна	Московский физико-технический институт (Физтех)	E-beam resist AR-N 7520 in the formation of the photonic structures
5-46	Филиппов	Иван	Алексеевич	ФГБОУ ВО "Пензенский государственный университет"	Hierarchical self-assembly of SiO2-SnO2 nano- and microstructures in combined sol-gel systems
5-47	Чернев	Игорь	Михайлович	Институт автоматики и процессов управления Дальневосточного отделения Российской академии наук	CoSi ultrathin films on Si(111) substrate: comparison of the stage’s formation in ultra-high vacuum and during annealing in argon
5-48	Черненко	Наталия	Евгеньевна	Лаборатория эпитаксиальных технологий ЮФУ	Quantum dots formation by InGaAs decomposition onto a patterned GaAs surface
5-49	Шандыба	Никита	Андреевич	Институт нанотехнологий, электроники и приборостроения Южного федерального университета / Лаборатория эпитаксиальных технологий ЮФУ	Control of properties and geometric characteristics of selectively formed GaAs nanowires within the FIB treatment area on Si(111)
5-50	Шепелева	Анастасия	Эдуардовна	АО "НИИЭМП"	Study of the sodium iodide influence on the selectivity of thin-film gas-sensitive structures
5-51	Шкапина	Алена	Сергеевна	Национальный	Химический состав и электрические

				исследовательский Нижегородский государственный университет имени Н. И. Лобачевского	свойства систем на основе Si-Fe
5-52	Шубина	Ксения	Юрьевна	СПбАУ РАН им. Ж. И. Алферова	Study of GaPN(As) layers grown by molecular beam epitaxy on silicon substrates
5-53	Шугабаев	Талгат	Маратович	Академический университет им. Ж.И. Алферова РАН	Influence of the wet-chemical treatment on the optical properties of core-shell InGaN nanowires
5-54	Boudjemila	Linda	Linda	СПбПУ	Evaluation of c-Si/CsPbBr3 solar cells: afors-het thickness simulation and analysis of optoelectrical properties
5-55	Кочетков	Федор	Михайлович	Академический университет им. Ж.И. Алферова РАН	Эластичный электрод на основе текстурированных одностенных углеродных нанотрубок для гибкой электроники

6. Other Aspects of Nanotechnology

May 16, 2024

15:30 - 18:00 Poster Session II

6-1	Агафонов	Дмитрий	Вячеславович	Научно-исследовательский институт электронно-механических приборов	Rapidly varying and static pressure sensor
6-2	Багров	Александр	Романович	Самарский национальный исследовательский университет имени академика С.П. Королева	Thermal entanglement in three-qubit Tavis-Cummings model with many-photon transitions
6-3	Бастракова	Марина	Валерьевна	Нижегородский государственный университет им. Н.И. Лобачевского	Optimization of superconducting adiabatic neural network implementing boolean function
6-4	Василевская	Юлия	Олеговна	Национальный исследовательский университет	Percolation dynamics in the memristive system of Ag nanoparticles coated by HfOx layers

				"Московский институт электронной техники" (МИЭТ)	
6-5	Водяшкин	Андрей	Алексеевич	МГТУ им. Н.Э. Баумана	Green synthesis of titanium nanoparticles suitable for creating transparent electrodes
6-6	Волик	Артем	Владиславович	ФГБОУ ВО "Пензенский государственный университет"	Digital signal processing in the process of measuring parameters of magnetic materials
6-7	Гайна	Анна	Алексеевна	Санкт-Петербургский политехнический университет Петра Великого	Modeling of the scanning track formation in the selective laser melting process of 316L steel
6-8	Голубков	Павел	Евгеньевич	ФГБОУ ВО "Пензенский государственный университет"	Determination of the equivalent electric circuit parameters of a galvanic cell in the micro-arc oxidation process
6-9	Еуров	Даниил	Александрович	ФТИ им. А.Ф. Иоффе	Formation of mesoporous silica coating on cores with different surface properties
6-10	Исокжанов	Шахбоз	Шокиржон угли	Московский физико-технический институт	Silicon/graphite nanocomposite for lithium-ion battery anode
6-11	Козловский	Александр	Валерьевич	ФГБОУ ВО "СГУ имени Н.Г. Чернышевского"	Investigation of electrical characteristics of semiconductor film structures obtained on a flexible substrate
6-12	Кондратьев	Валерий	Михайлович	Алфёровский университет	Towards Nanowire-Based Multi-Environment Alkali and Acid Sensing
6-13	Лагуткина	Александра	Андреевна	Московский физико-технический институт	Development of solid-state composite cathode material for solid-state lithium-ion batteries based on lithium ferrophosphate LiFePO4
6-14	Максов	Андрей	Анатольевич	ФГБОУ ВО "Пензенский государственный университет"	Methods and instruments for measuring surface morphology and mechanical parameters of oxide coatings
6-15	Морозова	Екатерина	Владимировна	ФГБОУ ВО Ульяновский государственный университет	Study of thermal and electrical conductivity properties of grain boundaries in metals and semiconductors with bcc and fcc crystal lattices
6-16	Никитин	Константин	Германович	Национальный исследовательский университет «МИЭТ»	Research of thin Ti/Al films resistivity and transparency change after thermal treatment to determine the possibility of solid solution formation and decrease of the ohmic contacts formation temperature
6-17	Николаева	Александра	Владиславовна	СПбАУ им. Ж. И. Алфёрова РАН	Pressure and temperature sensing via ZnO-PDMS based membrane for wearable electronic applications
6-18	Новичков	Максим	Дмитриевич	ФГБОУ ВО	Nanostructured bimetallic PtNi catalyst for

				"Пензенский государственный университет"	electrochemical systems with solid polymer electrolyte
6-19	Першин	Николай	Алексеевич	МФТИ	The mechanism of filtering of nanoscale aerosols with renewable electret filters
6-20	Поздеев	Вячеслав	Алексеевич	СПбАУ РАН / ЛЭТИ	Study of the effect of surfactants on surface tension of PEDOT:PSS aqueous solution
6-21	Хомленко	Дмитрий	Николаевич	Институт нанотехнологий, электроники и приборостроения, Южный Федеральный Университет	Study of the influence of ambient temperature on the magnitude of the piezoelectric strain coefficient of nitrogen-doped carbon nanotubes for the creation of nanopiezotronics devices
6-22	Ромашкин	Алексей	Валентинович	Национальный исследовательский университет «МИЭТ»	Change in the carbon nanotube thin layer refractive index after water and ammonia molecules adsorption
6-23	Соболева	Ольга	Игоревна	Институт нанотехнологий, электроники и приборостроения, Южный федеральный университет	Study of the influence of ambient humidity on the magnitude of the piezoelectric strain coefficient of nitrogen-doped carbon nanotubes for the creation of strain sensors
6-24	Тимкаева	Диана	Абдулхаковна	Ульяновский государственный университет	Transport properties of quasi-fractal in-plane heterostructures of graphene and hexagonal boron nitride
6-25	Храмов	Артем	Петрович	Ярославский Филиал Федерального государственного бюджетного учреждения науки Физико-технологического института имени К.А. Валиева Российской академии наук	Evolution of crystalline phases of P(VDF-TeFE) films filled with nanographite in various aprotic solvents
6-26	Шиповская	Анна	Борисовна	Саратовский национальный исследовательский государственный университет имени Н.Г. Чернышевского	Supramolecular ordering of thin glycerohydrogel plates of chitosan L- and D-aspartate
6-27	Лаздин	Илья	Александрович	Академический университет им. Ж.И. Алферова РАН	Resistive microelectromechanical gas sensor for detection of low concentrations of Hydrogen Sulfide

6-28	Шарапов	Андрей	Анатольевич	МФТИ	Hybrid model of photolithography physicochemical processes for estimation of optical losses in waveguides
6-29	Лепаев	Алекссандр	Николаевич	Чебоксарский институт (филиал) Московского политехнического университета	Chemical activity of dispersed particles of potassium compounds in the flame of a pyrotechnic composition
6-30	Малохатко	Софья	Владимировна	ЮФУ	Research the effect of internal mechanical stresses in a multilayer structure on displacement for various designs of MEMS membranesResearch the effect of internal mechanical stresses in a multilayer structure on displacement for various designs of MEMS membranes

Conference materials
UDC 535.55
DOI: https://doi.org/10.18721/JPM.

Strengthening irradiated areas of photo-thermo-refractive glass with silver nanoparticles

Alhalabi H. [1]✉**, Marasanov D. V.** [1]
[1] ITMO University, Saint Petersburg, Russia
✉ hadeelalhalabi98@mail.com

Abstract. Photo-Thermo-Refractive (PTR) glass, a versatile material highly sought after in today's photonics market, holds significant promise as a medium for holography, luminescence, ion exchange, and laser applications. Its potential for crafting advanced photonics elements and devices is noteworthy. The adoption of ion exchange technology exhibits potential in elevating the mechanical, thermal, and optical attributes of PTR glass, enabling the fabrication of holographic optical elements suitable for robust laser systems, such as ultra-narrow band spectral filters and laser beam combiners. This study delves into the effects of UV exposure and heat treatment on the refractive index profile of Na+/K+ ion-exchanged layers and the microhardness of glass surfaces. Through varied UV dosages, alterations in refractive index profiles and microhardness were examined. Results suggest that heightened irradiation dosage impacts the depth of ion exchange layers, enhancing birefringence and subsequently increasing compressive stress within the glass. This phenomenon fortifies recorded Bragg gratings, hinting at potential advancements in the durability and functionality of optical components.

Keywords. Photo-Thermo-Refractive glass, Ion-Exchange, Volume Bragg grating.

Introduction

Currently, photo-thermo-refractive glasses are a photosensitive material for recording Bragg gratings in glass volumes [1]. The presence of NaF crystals around silver nanoparticles leads to a decrease in the refractive index of the irradiated region of the PTR glass, which makes it possible to write Bragg gratings [2]. At the same time, for the practical application of Bragg gratings in glass, the presence of a hardened surface will be an advantage. It is known that glass can be strengthened using ion exchange technology, which involves the exchange of cations at the glass-molten salt interface. When cations with very different ion radius are exchanged, mechanical stresses arise, anisotropy of the refractive index occurs, and, therefore, strengthening of the material occurs [3].

Materials and methods

The primary objective is to analyze changes in the refractive index profile and microhardness of irradiated and heat-treated PTR glasses following Na^+/K^+ Ion-Exchange.

Three samples of original PTR glasses are prepared, two of which are irradiated with a He-Cd laser (325 nm) at doses of 1 J/cm^2 and 2 J/cm^2. Subsequently, the irradiated samples undergo heat treatment at 505 °C for 10 hours. All three samples are subjected to Na^+/K^+ Ion-Exchange at 365 °C for 5 hours. The diffusion of potassium ions into the glass surface layers results in an increased refractive index and the formation of gradient waveguide layers. The effective refractive index of the diffusion layers is measured using waveguide spectroscopy with a prismatic system for inputting radiation from a helium-neon laser (λ = 0.63 μm) for both TE and TM polarizations [4]. The refractive indices of waveguide modes are calculated by the inverse Wenzel-Kramers-Brillouin method from the measured effective refractive indices [5].

Results and discussion

The thickness of the diffusion layer is estimated based on the calculated refractive index profiles, with the birefringence value σ calculated from the difference in refractive index for both polarizations. The birefringence value was 0.0016, 0.0024, 0.0034 on the surface of the ion exchange layer for glasses after irradiation with 0 J/cm^2, 1 J/cm^2, 2 J/cm^2 dose, respectively. Which indicates that the increase in the irradiating dose affects the depth of the ion exchange layer which leads to an increase in compressive stress in the glass, thereby strengthening the recorded Bragg grating in the future.

Conclusion

This research contributes valuable insights into the optimization of PTR glass for advanced optical applications.

REFERENCES

1. **Nikonorov, N. V., Panysheva, E. I., Tunimanova, I. V., & Chukharev, A. V.** (2001). Influence of glass composition on the refractive index change upon photothermoinduced crystallization. Glass physics and chemistry, 27, 241-249.

2. **Lumeau, J., Glebova, L., Golubkov, V., Zanotto, E. D., & Glebov, L. B.** (2009). Origin of crystallization-induced refractive index changes in photo-thermo-refractive glass. Optical materials, 32(1), 139-146.

3. **Gy, R.** (2008). Ion exchange for glass strengthening. Materials Science and Engineering: B, 149 (2), 159-165.

4. **Ulrich, R., & Torge, R.** (1973). Measurement of thin film parameters with a prism coupler. Applied Optics, 12(12), 2901-2908.

5. **White, J. M., & Heidrich, P. F.** (1976). Optical waveguide refractive index profiles determined from measurement of mode indices: a simple analysis. Applied optics, 15(1), 151-155.

Overview of fiber optic communications in railway transport

K. G. Arinushkina[1,2]✉, A. S. Adadurov[2], I. Yu. Savelev[2]
[1] The Bonch-Bruevich Saint Petersburg State University of Telecommunications, Saint Petersburg, Russia;
[2] VNIIZhT-ENGINEERING LLC, Saint Petersburg, Russia
✉k-arinushkina@mail.ru

Abstract. To monitor the technical condition and dimensional parameters of railway tunnels, technical solutions are used based on well-known diagnostic methods and techniques: laser scanning and photogrammetry, accelerometers, acoustic emission, magnetic sensors, strain gauges, inclinometers. However, these approaches do not fully meet the requirements for inexpensive, stable, long-term and high-precision monitoring of the performance of modern railway infrastructure. In addition, every year in the area where the railway track is located and when trains move directly, the amount of interference of various kinds increases. This has an extremely negative impact on various control and monitoring equipment, especially if they operate on radio engineering principles. The electromagnetic compatibility of the equipment is disrupted, which leads to malfunctions.

Currently, a variety of track circuits are used as sensors, the main disadvantages of which are the high consumption of copper cable, as well as the need to operate in large volume modes. Defects in the cable network in such a train control system cause a large number of failures. Moreover, when train speeds exceed 200 km/h, especially when they move in the opposite direction on parallel tracks, some schemes begin to work incorrectly. The noted problems require a new approach to solving these problems, especially on congested railway junctions. The development of new control systems based on fiber-optic communication lines is the most promising option for solving this problem for the Russian Federation, which has the longest railway network.

Keywords: Fiber-optic communication line, remote control, rolling stock, train traffic safety, capacity, artificial intelligence.

Introduction

Fiber-optic communication lines have been laid in the area where the railway tracks are located. These lines in the classic version are resistant to various types of interference along their entire length. One cable can accommodate more than 1,500 channels with unidirectional transmission over single-mode fiber. In this case, stable transmission of information will be ensured over distances of up to 300 km with a laser radiation power of 7-8 mW. It is proposed to place fiber optic sensors along the entire line (one for each channel). This will make it possible to obtain information about changes in the nature of the train's movement due to emerging defects, determine its position at a distance, etc [1].

Materials and Methods

At the moment, the error in the results of the algorithm for measuring the exact length of the train at control points is 94 cases, which is 17 % of the cases of the total number of trains passed. These cases are observed mainly when calculating the length of trains with more than 30 cars or at a very low train departure speed. Train tracking accuracy is 2-20 m.

The developed system, unlike the previous ones, does not require track circuits (Fig. 1). At the same time, the system can monitor the integrity of rail threads, identify certain track defects, count the number of rolling stock axles, recognize the slightest movements of various objects along the track and, in general, allows one to abandon a significant number of floor-mounted devices currently used [2].

Results and Discussion

The OTDR uses a fiber optic link as the sensing medium to provide real-time monitoring of critical connections between data centers. Thanks to a range of up to 100 km and a distance

between sensors of 2 m, the reflectometer can receive information about changes in the nature of train movement as a result of emerging defects, as well as determine its position at a distance.

Monitoring of railway crossings, monitoring of energy cables, detection of natural hazards, broken overhead contact line, detection of rail defects, detection of wheel defects, detection of unauthorized entry and theft, fire detection in tunnels and stations, warning of track workers - all these are opportunities for expanding the functionality of the system.

The ability to detect periodic impacts moving along the tracks at train speed is a clear indication that these impacts are caused by wheel defects. Additionally, by analyzing data at a specific location, we can see both the frequency and signal level associated with each impact, allowing us to classify the severity of a wheel defect [3].

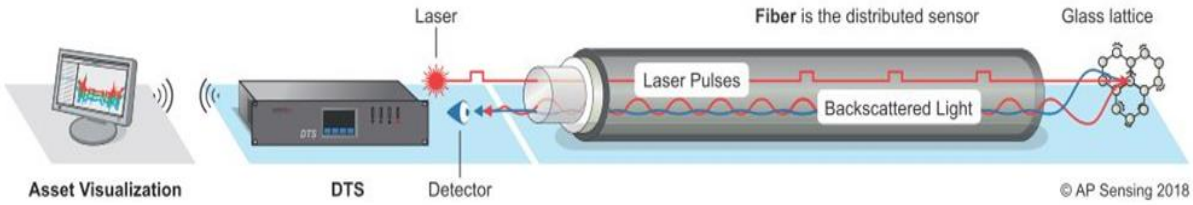


Fig. 1. Schematic structure of the FOS system with glass fiber as a sensing element.

On average, one monitoring site of approximately 80 km transmits 4 terabytes (TB) of data per day. To address the problem of increasing data volumes, a number of machine learning techniques are proposed, increasing the benefits of improved data accuracy and reducing the time to commission new devices. In addition to supervised machine learning techniques, another priority is the use of adaptive classification algorithms, which use target search techniques to dynamically and continuously adjust each channel along the fiber according to estimates of background noise levels. This makes it possible to capture data around the clock every day.

Conclusion

The article will use a new method for constructing a fiber-optic system control system to monitor the movement of trains, as well as the condition of the transport route and rolling stock. This new method and technologies for its implementation are being developed taking into account the high length of railways in the Russian Federation, as well as the need to increase train speeds to reduce costs for the delivery of various goods.

In addition, the new fiber-optic system will increase the set of data on train movement and others by at least an order of magnitude. For this reason, problems arise in the form of efficient processing and classification of large volumes of data of interest.

The artificial intelligence system can process massive amounts of real-time data from across the country and can alert maintenance crews to abnormal situations within 40 minutes with 95 percent accuracy.

REFERENCES

1. **Yan H., Zhao X., Wünnemann B., Chen M., Xiao D.** A method for predicting the subgrade uplift intensity along a high-speed railway track in red-bed areas in China, Bulletin of Engineering Geology and the Environment. 82(8) (2023) 303.

2. Etnisa Haqiqi, Mokhammad & Barruna, Elang & Yayienda, Nibras & Ajiesastra, Raden & Apriono, Catur. (2021). Optical Fiber Communication Design and Analysis for A Railway Line. 180-184. 10.1109/ICRAMET53537.2021.9650501.

3. Nikolaev D., Chetiy V., Dudkin V. Determining the location of an object during environmental monitoring in conditions of limited possibilities for the use of satellite positioning, IOP Conference Series: Earth and Environmental Science. 578(1) (2020) 012052.

EFFICIENCY ANALYSIS OF GENERATIVE ADVERSARIAL NETWORKS FOR SINGLE PIXEL IMAGING

D. V. Babukhin [1]✉, **A. A. Reutov** [1], **D. V. Sych** [1]

[1] P.N. Lebedev Physical Institute, Russian Academy of Sciences, Moscow, Russia;

✉dv.babukhin@gmail.com

Abstract. The single-pixel camera provides a prospective tool for imaging beyond conventional pixel-matrix-based devices. In recent years, neural networks have become a part of single-pixel imaging as a method to computationally restore an image from intensity measurements. Generative adversarial networks (GAN) are particularly well suited to the task, but the most optimal architecture of such networks is unknown. Here we provide a comparison between two popular architectures of generative adversarial networks in the context of single-pixel imaging. We demonstrate that a least squares network acquires a slightly better quality of image restoration than a deep convolution network.

Keywords: Single pixel imaging, neural networks, image restoration.

Funding: This study was funded by RSF grant number 23-22-00381.

Introduction

Single-pixel imaging emerged as a result of the mathematical development of approaches to image restoration [1]. The central problem of single-pixel imaging is the computational generation of an image from intensity measurements acquired via measuring a camera with a single light detector. These intensity data combined with specific light patterns – masks, responsible for spatial modulation of light, illuminating the object – allow the generation of an object image. While in theory an almost perfect image of an object can be generated (provided enough intensity measurements), in practice device imperfections and limited intensity data make the problem of image generation complicated. In the last years, a conventional method for image generation [1] was challenged via the use of neural networks [2] and in particular, generative adversarial networks [3]. However, the optimal type of network to solve a problem is unknown. Here we provide a comparison of image restoration for two common architectures of generative adversarial networks.

Materials and Methods

We train two generative adversarial networks – a least squares GAN [4] and a deep convolution GAN [5] – on simulated intensity measurements of the MNIST dataset, processed with a single-pixel camera. We calculate two efficiency metrics – a peak signal-to-noise ratio (PSNR) and a structural similarity index measure (SSIM) for images restored from a hold-out test dataset for two trained neural networks.

Results and Discussion

We provide the results of our simulations in Fig. 1. Here, we demonstrate the dependency of PSNR and SSIM on the sampling rate – a ratio between a number of spatial patterns M, used to modulate the light, and the number of pixels N in the restored image. The sampling rate characterizes the time required to gather intensity data, and the value of the sampling rate influences the quality of the computationally generated image. The desiderata of single-pixel imaging algorithms is to make the sampling rate as low as possible (to work in regime $M << N$). From Fig. 1, we can see that, for chosen sampling rates, a trained least squares generative adversarial network provides better image restoration quality than a deep convolution generative adversarial network. We conclude that, in ideal devices or in the regime of negligible device noises, a least squares generative adversarial network can be a better choice for single-pixel imaging.

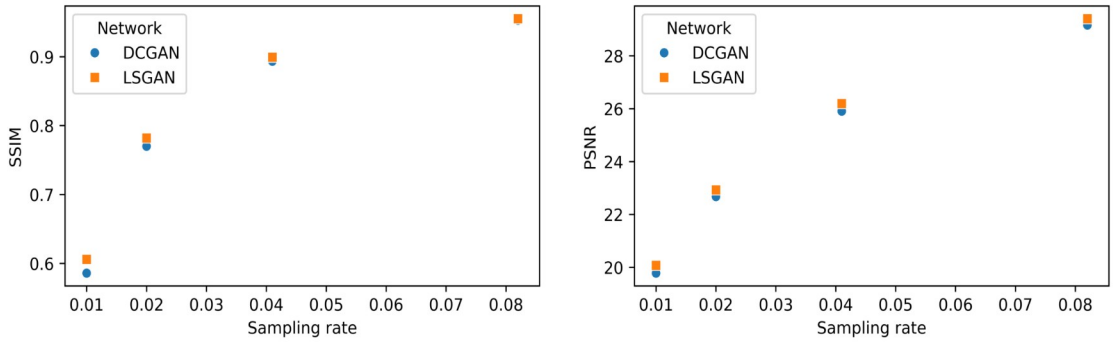


Fig. 1. Dependencies of SSIM (left) and PSNR (right) on sampling date. LSGAN stands for least squares generative adversarial network and DCGAN stands for deep convolution generative adversarial network.

Conclusion

In this work, we compared the efficiencies of two types of generative adversarial networks in the problem of image restoration in single-pixel imaging. We found that least squares generative adversarial networks provide a better quality of restored images than deep convolution generative adversarial networks for various sampling rates. Our work is aimed at advancing the development of computational tools for single-pixel imaging.

REFERENCES

1. **M. F. Duarte, M. A. Davenport, D. Takhar, J. N. Laska, T. Sun, K. F. Kelly, R. G. Baraniuk**, Single-Pixel Imaging via Compressive Sampling, IEEE Signal Processing Magazine 25, 83 (2008)

2. **C. F. Higham, R. Murray-Smith, M. J. Padgett, M. P. Edgar**, Deep learning for real-time single-pixel video, Scientific Reports 8 (2018).

3. **M. Zhao, F. Li, F. Huo, Z. Tian,** Generative adversarial network-based single-pixel imaging, Soc for Inf Disp 30 8 (2022)

4. **X. Mao, et al.,** Least Squares Generative Adversarial Networks, IEEE International Conference on Computer Vision (ICCV), Venice, Italy, pp. 2813-2821. (2017)

5. **A. Radford, L. Metz, S. Chintala**, Unsupervised Representation Learning with Deep Convolutional Generative Adversarial Networks, arXiv:1511.06434, (2015)

Evolution of luminescent properties of single perovskite nanocrystals $CsPbBr_3$ in the photodegradation process

V.A. Baitova[1*], M. A. Kniazeva[1,2,3], A.O. Tarasevich[1,2,3], A.V. Naumov[2,3], A.G. Son[4], S.A. Kozyukhin[4], I. Yu. Eremchev[2,3]

[1] *Higher School of Economics — National Research University 105066, Russia, Moscow, Staraya Basmannaya Str., 21/4*

[2] *Institute of Spectroscopy of the Russian Academy of Sciences 108840, Russia, Moscow, Troitsk, Fizicheskaya Str., 5*

[3] *Moscow Pedagogical State University 119435, Russia, Moscow, Malaya Pirogovskaya Str., 29/7*

[4] *N. S. Kurnakov Institute of General and Inorganic Chemistry.*

**email: vabaitova@edu.hse.ru*

Abstract. Here we study luminescence blinking of single nanocrystals $CsPbBr_3$ by time-correlated single photon counting. The technique for separation of the different blinking mechanisms based on the analysis of exciton and biexciton recombination rates and second-order cross-correlation function is used. The transition due to photoinduced degradation process from only trapping blinking mechanism to a mixed type (charging and trapping) was discovered.

Key words: semiconductor nanocrystals, perovskites, luminescence blinking.

Introduction

Perovskite nanocrystals show great potential in a range of applications due to their unique optical and electrical properties. However, perovskite nanocrystals have limitations because of low stability with its sensitivity to ambient parameters. At single perovskite nanocrystals two undesirable effects can be observed [1]: photodegradation and luminescence blinking. The first manifest itself as slow wavelength blue-shift due to size change [2], the second is a stochastic evolution of luminescence intensity. Currently, there are two main models describing the blinking in nanosized semiconductor crystals: based on the trapping [3] and charging mechanisms [4]. Meanwhile, the photodegradation process provides a unique opportunity to study the evolution of single nanocrystal (NC) photophysical properties under continuous change of its size. In particular, evolution of blinking luminescence can be studied.

Materials and Methods

Investigations with single NC (luminescence peak at ~518 nm, with sizes from 25-29 nm) were done by using a unique luminescence microscope-spectrometer, allowing to analyze signals from single emitters in the single-photon counting mode. Nanocrystals were excited at a wavelength of 400 nm by a pulsed laser source. Blinking dynamics, the second-order cross-correlation function $g^2(t)$ (antibunching $g^2(0)$), and luminescence lifetime (exciton τ^x_{fl} and biexciton τ^{xx}_{fl}) were measured with two single photon detectors in a Hanbury-Brown and Twiss scheme. The ratio of radiative recombination rates of exciton to biexciton states k^r_{xx}/k^r_x for the different emitter states in the blinking process (bright, dim) and for different time moments of the photoinduced degradation process were used to determine the dominant blinking mechanism in a particular NC [5].

Results and Discussion

Decrease in the effective size due to photodegradation result in decrease in luminescence intensity (see fig 1a.) and shift of luminescence spectra to the blue region (fig. 1b) [2]. At the beginning of the measurement (when the crystal is large ~25 nm and photoinduced degradation neglected) the blinking luminescence caused only by trapping mechanism (fig.1c). It is due to Auger processes are weak and not able to quench luminescence in trion (charged state of nanocrystal). The ratio is k^r_{xx}/k^r_x =4.1. The decrease in the effective size of the nanocrystal

during photodegradation leads to increasing of Auger processes rates, and, consequently, to possibility of charging mechanism in blinking. For the example in Fig. 1.d the ratio k^r_{xx}/k^r_x = 3.03, which correspond to charging blinking mechanism.

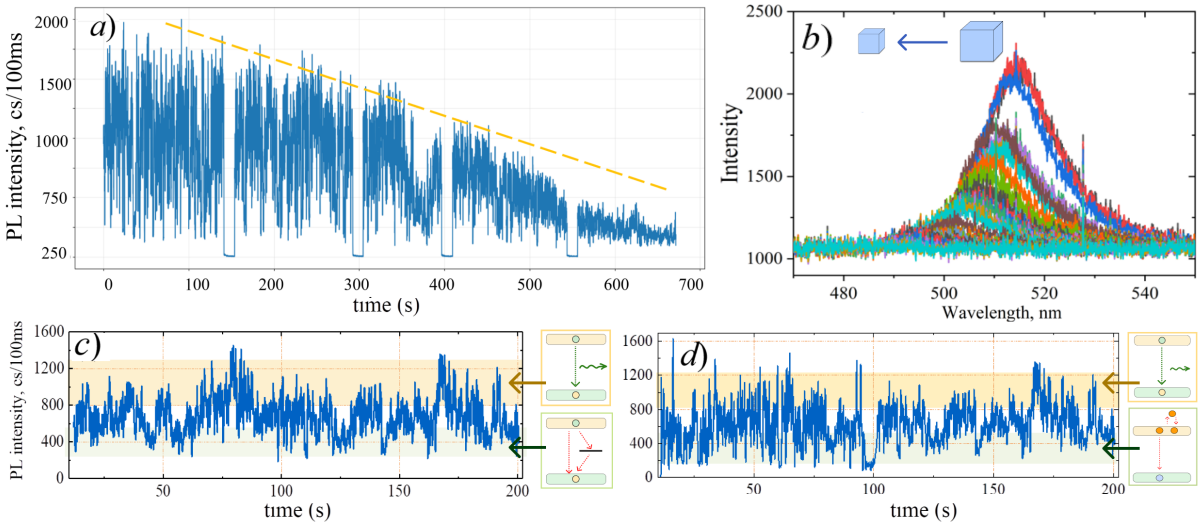


Fig 1. a) Fluorescence track $CsPbBr_3$ nanocrystal. Power density of excitation radiation is 0.6 W/ cm^2.The orange dashed line shows the general trend of luminescence intensity drop in the photodegradation process. b) Spectra measured at different moments. The excitation power density is 7.5 W/cm^2. The exposure time for each spectrum is 60 s. Luminescence blinking corresponding to the c) beginning of the measurement (λ_{lum} =518 nm) and d) the end (λ_{lum}~500 nm) of measurement.

Conclusion

The photodegradation in single $CsPbBr_3$ perovskite crystals is studied by luminescence microscopy and time-correlated single photon counting. The dynamics of luminescence blinking under quasi-continuous nanocrystal size change is discussed. Method based on the estimation of the ratio of the radiative recombination rates of the biexiton and exciton $k^{xx}{}_r/k^x{}_r$ to determine the mechanisms of luminescence blinking was used. Transition from a single trap blinking mechanism to a charge mechanism occurrence during photodegradation is observed. It was associated with the increasing role of Auger processes in the reduction of the nanocrystal size.

References

[1] Park, Y. S.; Guo, S.; Makarov, N. S.; Klimov, V. I. ACS Nano 2015, 9 (10), 10386–10393.

[2] Darmawan, Y. A.; Yamauchi, M.; Masuo, S. J. Phys. Chem. C 2020, 124 (34), 18770–18776.

[3] P. A. Frantsuzov, S. Volkan-Kacso, and B. Janko. Phys. Rev. Lett.. 103. 207402 (2009).

[4] A.L. Efros and M. Rosen,.Phys. Rev. Lett.. 78. 1110 (1997).

[5]V. A. Baitova, M. A. Knyazeva, I. A. Mukanov, A. O. Tarasevich, A. V. Naumov, A. G. Son, S. A. Kozyukhin, and I. Yu. Eremchev. JETP Letters. Vol. 118. No. 8. pp. 560–567(2023)

Study of areas of dimentional quantization in GaAs/AlGaAs quantum dots

E. A. Basheguro va [1✉], **E. I. Deribina** [1], **Yu. V. Kapitonov**[1]
[1] St Petersburg University, Saint-Petersburg, Russia;
✉e.basheguro va@spbu.ru

Abstract. In this work GaAs/AlGaAs semiconductor with quantum dots (QDs) was studied using its photoluminescence (PL) spectroscopy. Such pair of materials was used due to the close values of lattice constant of barrier and dot materials, which leads to low level of strain inside the sample. Growth of the heterostructure is carried out by the droplet epitaxy – this method gives possibility to control various parameters of sample: density of quantum dots (QD), volume of the dot. The PL spectrum of the sample containing such QDs exhibits several emission bands associated with different quantization regions within the semiconductor. In other works, a hypothesis was proposed that the observed emission bands are related to QDs inside the nanohole and smaller quantum-sized objects, formed at the boundary of the nanohole. This assumption can be verified by a detailed examination of the micro-PL spectrum of the sample. For achieving most full information about samples, several experiments have been carried out: single QD PL and microPL (μPL) measurements, μPL depending on coordinates on sample and PL depending on temperature of sample. Analysis of spatial dependency of PL spectra was used to distinguish signals origin from different quantum-sized structures.

Keywords: quantum dots, quantum wells, photoluminescence, semiconductors, GaAs/AlGaAs, quantum heterostructures.

Funding: this work was supported by the Ministry of Science and Higher Education of the Russian Federation (Megagrant no. 075-15-2022-1112).

Introduction

Studying structures based on GaAs/AlGaAs is of interest because the lattice constant values of the material of the dot and its barrier are similar, leading to low internal stress in the sample. Low-temperature PL spectra contains several resonances related to different quantum-sized structures. In the magneto-PL study [1] a hypothesis was proposed that the observed emission bands are related to nanohole-filled droplet epitaxy (NFDE) QDs, and an additional QD formed at the boundary of the nanoholes. The main aim of our work was to determine which part of the sample structure corresponds to certain parts of the spectrum, as well as how these objects are interacting in the semiconductor, and in particular, check the assumption from work [1].

Materials and Methods

A sample T874 containing sparsely located dots was grown according to recipe described in [1]. The sample was grown using the NFDE method in our laboratory, which allows for control of the growth process, resulting in samples with precisely defined parameters. To obtain PL spectra, a green laser at 532 nm was focused on the sample by the 10x microlens, and for study of μPL spectra 50x microlens was used. The temperature was maintained at 4 K using a closed-cycle helium cryostat Montana. A spectrometer equipped with a CCD-camera was used to obtain spectra. The micrometre stage moved by the stepper motor was used to record the spatial dependency of the PL spectra with micrometre resolution.

Results and Discussion

After conducting all the experiments, it can be said which peaks belong to which structure on the photoluminescence graph of sample T874 (Fig. 1, a).

The PL emission spectrum revealed the following bands (from lower energy to higher): emission from carbon contamination in GaAs:C (E = 1,493 eV), emission from the three-dimensional GaAs layer (E = 1,515 eV), bands related to QDs A (E = 1,56 eV), QDs B1 (E = 1,61 eV), and QDs B2 (E = 1,65 eV), heavy-hole excitons in the quantum well (QW) (E = 1,700 eV), and emission from recombining excitons in the three-dimensional $Al_{0.38}Ga_{0.62}As$ layer (E = 1,98

eV). The emission bands of all three QDs consist of individual peaks, as observed in the micro-PL spectrum analysis of the sample.

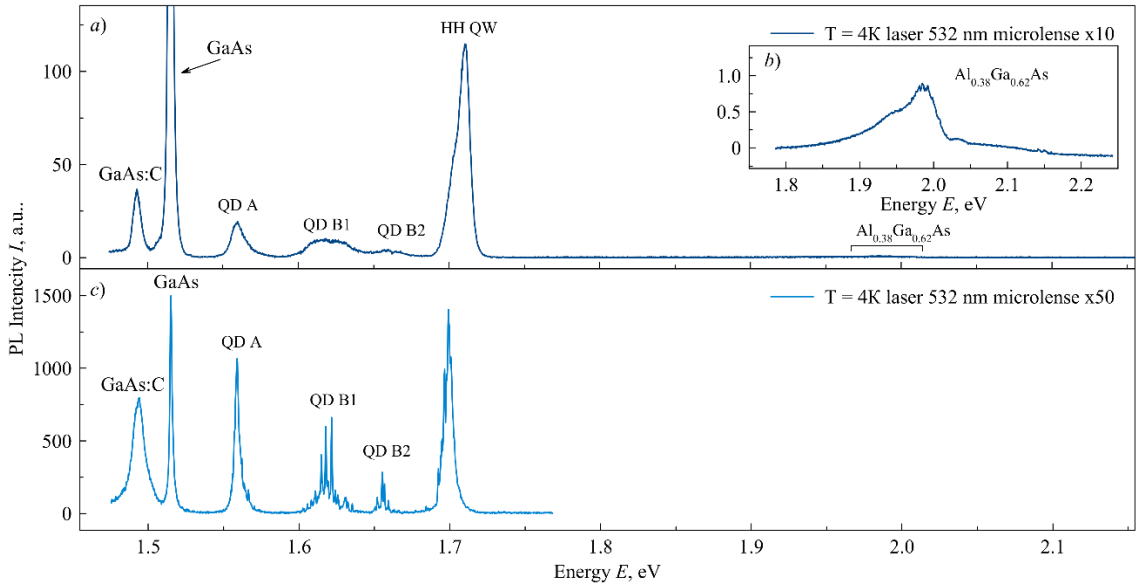


Fig. 1. PL emission spectrum of GaAs/AlGaAs semiconductor with NFDE QDs, T = 4 K, laser 532 nm, 10x microlense (*a*); PL band from recombining excitons in the three-dimensional $Al_{0.38}Ga_{0.62}As$ layer (*b*); μPL emission spectrum of single QD, T = 4 K, laser 532 nm, 50x microlense (*c*)

After scanning the sample along the x-axis crystal direction with a laser spot (diameter 1 μm), the spatial derivative for the micro-PL map was calculated, showing that the emission from the three QD ensembles is anticorrelated with the emission from the QW, while each of the QD ensembles correlates with the other two ensembles.

Conclusion

As a result, the nature of the PL emission bands in the GaAs/AlGaAs semiconductor with QDs was determined. The analysis conducted indicated a region of separation between the QW and QDs, resulting in an anticorrelation of emission from these nanostructures. The lowest energy emitting QDs A were identified as filled with GaAs nanoholes. QDs B1 and QDs B2 are smaller quantum-sized structures inside or at the boundary of the nanohole.

Acknowledgments

This work was carried out on the equipment of the SPbU Resource Center "Nanophotonics".

REFERENCES

1. **Ulhaq A., Duan Q., Zallo E., Ding F., Schmidt O. G., Tartakovskii A. I., Skolnick M. S., and Chekhovich E. A.**, Vanishing electron g factor and long-lived nuclear spin polarization in weakly strained nanohole-filled GaAs/AlGaAs quantum dots, Phys. Rev. B 93, 165306.

The development of graphene-based terahertz bolometers using the noise-thermometry method

I. A. Gayduchenko [1,2] ✉, K. V. Shein[1,2,] P. I. Bondareva,[1,2], A. N. Lyubchak[1,2,] R. I. Izmailov[2,3], E. M. Baeva [1,2] and G. N. Goltsman [1,2]

[1]Moscow Pedagogical State University, Moscow, 119435, Russia;
[2] National Research University Higher School of Economics, Moscow, 101000, Russia;
[3] National Research Nuclear University MEPhI (Moscow Engineering Physics Institute), Moscow, 115409, Russia;
✉ igaiduchenko@hse.ru

Abstract. The paper investigates a new approach for the development of graphene-based terahertz bolometers using the noise thermometry method. Graphene, due to its record low electron heat capacity and weak electron-phonon coupling at low temperatures, is considered as a promising material for creating terahertz bolometers on hot electrons. The main obstacle to the development of such devices is the weak dependence of graphene resistance on temperature. Here we are trying to solve this problem by directly measuring the electron temperature in graphene using noise thermometry. Our first data demonstrate a strong heating of the graphene electronic system under the influence of direct current (up to 10 K at a current of 500 nA). An analysis of the results shows that the internal electrical sensitivity of the devices under study is 100,000 V/W, which allows them to be considered as the basis for creating sensitive terahertz detectors.

Keywords: graphene, THz detectors, bolometers, noise thermometry.
Funding: The research was supported by RSF (project No. 23-72-00014).

Introduction

Currently, the terahertz (THz) range of the electromagnetic spectrum is of great interest due to a wide range of potential applications: medical diagnostics, non-destructive testing, security systems and data transmission [1]. These and many other applications require fast and sensitive THz detectors that can be easily combined into matrices. In this paper, we explore a new approach to the creation of graphene-based terahertz bolometers using the noise thermometry method [2]. Graphene is a unique material for recording radiation in the terahertz range due to its record-low electron heat capacity and weak electron-phonon coupling. This leads to a strong heating of the graphene electronic system under the action of terahertz radiation. The main problem in the implementation of graphene terahertz detectors arises from the weak dependence of graphene resistance on temperature [3]. In this paper, we try to solve this problem by measuring the spectral noise density in graphene devices [2]. The measured thermal noise directly depends on the temperature of the electrons in graphene and can be used as a detector signal, as well as a probe for measuring the electronic temperature when heated by terahertz radiation. Our first experimental data demonstrate the possibility of detecting sub-terahertz radiation by this method in a wide temperature range from 3.5 K to 300 K. The obtained data can be used to optimize existing graphene terahertz detectors and develop new ones.

Results and Discussion

Our samples are field-effect transistor devices in which graphene serves as a conduction channel. There is also a gate electrode that controls the concentration of charge carriers in the device. We have manufactured two types of devices: those based on graphene synthesized using chemical vapor deposition (CVD), which is the most industrially viable method for producing graphene, and those based on split graphene encapsulated in hBN, a method for obtaining the highest-quality graphene.

The transport properties of the manufactured devices were characterized. The field mobility of the CVD graphene-based device was 1500 $cm^2V^{-1}s^{-1}$, which is typical for graphene on a Si02 substrate. According to the data obtained, it can be said that the devices are manufactured on high-quality CVD graphene. The field mobility estimates for devices based on encapsulated graphene, obtained from the dependence of the resistance of manufactured structures on the concentration of charge carriers, gives from 10000 $cm^2V^{-1}s^{-1}$ at 300 K to 100,000 $cm^2V^{-1}s^{-1}$ at 4.2 K, which corresponds to the best graphene samples known from the literature.

The temperature of the electronic system of graphene encapsulated in boron nitride was measured depending on the concentration of charge carriers and scattered power. For this purpose, the method of noise thermometry was used -precision measurement of current/voltage fluctuations through a sample in the white noise region. Assuming that the main source of noise in the system is the thermal noise of the sample or calibration load, it is possible to calibrate the circuit based on theoretical predictions of the Nyquist noise spectral density and determine the electronic temperature of the sample. The measurements were carried out in a closed-cycle cryostat cooled to 4.2 K. A detailed description of the experimental technique is presented in [4].

Based on measurements of the dependence of the differential resistance and spectral density of noise on the current through the sample, the dependence of the temperature of the graphene electron gas on the value of the transmitted current was determined.

The obtained data demonstrate that at a low concentration of charge carriers, electrons heat up sharply with an increase in the modulus of the transmitted current. According to the results of the experiment, the maximum temperature of the electron gas was about 18 K with a current strength of 30 μA. It can be seen that at a low concentration of charge carriers, the electrons heat up asymmetrically, the reason for this is also the differences in the materials of the contacts.

Conclusion

The electronic temperature was measured in graphene samples encapsulated in boron nitride at a cryostat temperature of 4.2 K. An analysis of the results shows that the internal electrical sensitivity of the devices under study is 100,000 V/W, which allows them to be considered as the basis for creating sensitive terahertz detectors.

Acknowledgments

The research was supported by RSF (project No. 23-72-00014).

REFERENCES

1.**Alfred Leitenstorfer** et al.// J. Phys. D: Appl. Phys. 2023. V. 56. P. 223001.

2.**Fong, Kin Chung, and K. C. Schwab**. // Physical Review X. 2012. V. 2.3. P. 031006.

3.**Du X.** et al. //Graphene and 2D Materials. 2014. V. 1. N. 1.

4.**Baeva, Elmira M.**, et al. // Physical Review Applied. 2021. V. 15.5. P. 054014

Fluorescence recovery and holographic grating relaxation studies of photoinduced changes in diffusivity

L. N. Borodina [1✉], **A. V. Veniaminov** [1]
[1] ITMO University, St.Petersburg, Russia
✉ lnborodina@itmo.ru

Abstract. Comparative studies of diffusivity provide a cross-check of fluorescence recovery after photobleaching and holographic grating relaxation techniques and prove their applicability to revealing photoinduced changes in diffusivity. The two optical techniques utilizing the implementation and monitoring of photoinduced spatial heterogeneity in an object of study are shown to be capable of providing information on the properties of both intact and phototransformed species.

Keywords: fluorescence recovery after photobleaching, holographic grating relaxation, confocal microscopy, diffusion, complementary gratings

Funding: This research was funded by the RPMA grant of School of Physics and Engineering of ITMO University.

Introduction

Multiple applications of nanophotonics, sensorics, and biomedicine provide a tremendously increasing demand for knowledge on various sophisticated properties of luminescent nanoparticles and nanostructures. The information about sizes of luminescent nanoparticles, their distribution, changes under the influence of light and other factors is of considerable interest, along with spectral characteristics.

Materials and Methods

We apply two approaches to study diffusion, using imprinting a photoinduced optical inhomogeneity in an object and monitoring its evolution caused by diffusion. One of the approaches consists in exposing a narrow strip of a sample with a focused laser beam, tracking the subsequent change in the spatial distribution of luminescence intensity in its transverse direction and extracting the diffusion coefficient, and then the particle size from the rate of change in its width [1]. The technique was implemented using the LSM 710 confocal laser scanning microscope (Carl Zeiss).

Another technique, referred to as the holographic grating relaxation method [2], involves exposing an object with an interference field and observing the diffraction of light on the resulting optical grating, the efficiency of which varies due to a decrease in concentration modulation, hence the refractive index, caused mainly by diffusion. The diffusion coefficient is determined from the dependence of the grating relaxation rate on the spatial period.

Results and Discussion

We have found that instead of the usual Gaussian luminescence intensity profile, in some experiments using the florescence recovery technique its shape appears more complicated (as in Fig. 1), which can supposedly be interpreted as a manifestation of the diffusion of two forms of particles, by analogy with the complementary grating effect in holographic grating relaxation technique.

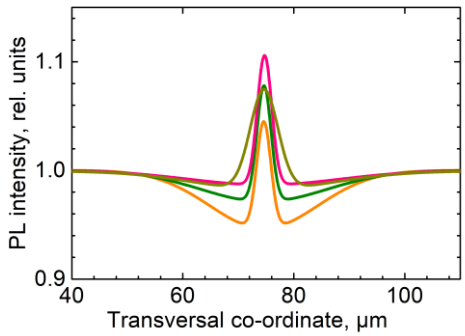


Fig. 1. Exemplary sequence of transversal fluorescence intensity profiles recorded in 3 to 4000 seconds after exposure, whose evolution is due to diffusion of initial and phototransformed molecules

To verify this assumption, a comparative study of camphoroquinone molecular diffusion in a viscous low molecular weight melt was fulfilled using the luminescence recovery and the holographic grating relaxation techniques. The nonmonotonic kinetics of grating relaxation with two characteristic times has encouraged us to consider the diffusion of two species. The coincidence, within the error bars, of the diffusion data obtained by the two methods confirms the new possibilities of the luminescence method in the study of phototransformations and allows us to interpret the unusual patterns of luminescence as evidencing for the changes in hydrodynamic sizes.

Conclusion

The method of fluorescence recovery after photobleaching, based on monitoring of changes in the photoinduced spatial inhomogeneity of luminescence, provides valuable information about the optical and diffusion properties of both the initial and phototransformed species, similar to the holographic relaxation; a comparative diffusivity study by these two techniques proves the agreement between them.

Acknowledgments

The authors are grateful to Dr. Vladimir Borisov for his valuable thoughts and recommendations, and Irina Arefina and Ilia Vovk of ITMO University for sharing their experience and knowledge in luminescence of carbon dots and the theory of physics of nanostructures.

REFERENCES

1. **Braeckmans K., Remaut K., Vandenbroucke R. E., Lucas B., De Smedt S. C., Demeester J.** Line FRAP with the confocal laser scanning microscope for diffusion measurements in small regions of 3-D samples, Biophysical journal. 92(6) (2007) 2172-2183.

2. **Schärtl W.** Forced Rayleigh Scattering – Principles and Application (Self Diffusion of Spherical Nanoparticles and Copolymer Micelles) Ed. by Borsali R., Pecora R., Soft Matter Characterization, Springer, 2008.

Experimental investigation of the fiber-optic sensor for solution concentration

G. R. Brazovskii[1]✉, **A. I. Isupov**[1], **E. I. Andreeva**
[1] The Bonch-Bruevich Saint Petersburg State University of Telecommunications, Saint-Petersburg, Russian Federation;
✉gl-hl@inbox.ru

Abstract. The design of the sensor device – a solution concentration sensor on the polymer optical fiber (POF) is proposed. The results of an experimental study of this sensor device for determining the concentration of an alcohol-containing solution in the range from 0 to 96% are presented. The linearity of the sensor response, determined by the level of excess loss, from the refractive index of the solution, has been empirically confirmed. Using the light emitting diodes (LEDs) with wavelengths 430, 525 and 630 nm, the possibility of the spectral multiplexing of such sensors into the single system is shown.

Keywords: POF, polymer optic fiber, WDM, wavelength-division multiplexing, optical fiber, sensor, bend, loss.

Introduction

Recently, there has been an increased interest in monitoring environmental safety. Fiber-optic sensor systems can occupy an important place in this segment. Their advantages are the possibility of remote monitoring. If necessary, the power supply and processing of the received information can be removed from the observation point at a great distance.

Systems based on polymer fiber attract attention by the availability of the components included in their composition, ease of maintenance, and low cost in the case of mass production.

One of the potentially applicable sensors is U-shaped sensor.

Results and Discussion

The experimental study was carried out using a polymer fiber of class A4a in accordance with GOST R IEC 60793-2-40.

The block diagram of the measuring unit is shown in Fig. 1.

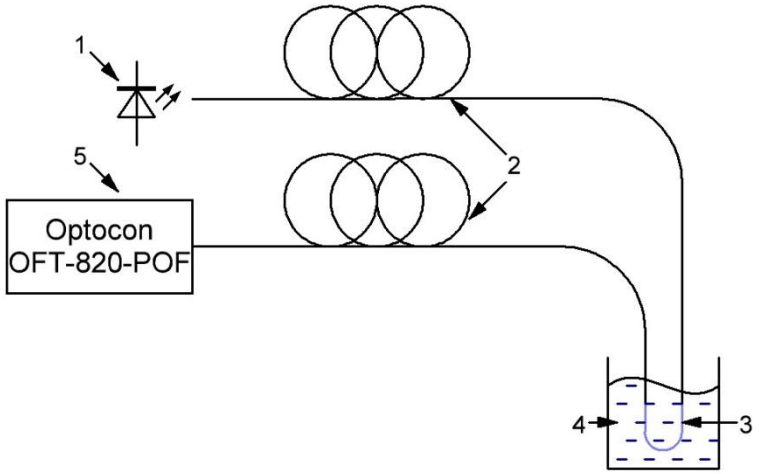


Fig. 1. Scheme of the experimental setup: 1 – LED with wavelengths of 430, 525 or 630 nm, 2 – POF, 3 – U-shaped sensor element, 4 – the tested liquid solution, 5 – Optocon OFT-820-POF power meter.

Signal from LEDs (1) at wavelengths of 430, 525 or 630 nm was alternately injected into a 50 m long main POF (2) coupled to the sensor. The sensor element (3) was immersed in liquid solutions (4) with different concentrations of the controlled substance, with different values of refractive indices. Optocon OFT-820-POF was used as the power meter. The reference value P_o

was taken as the power at the output of the sensor immersed in distilled water. The measurement result $\Delta\alpha$ was taken as the reference value of the optical output power level P_s when the sensor element was immersed in testing solution. The dependences of the increment of the insertion loss $\Delta\alpha$ from the value of the refractive index n of the solution for the different wavelengths used in the experiment are shown in Fig. 2.

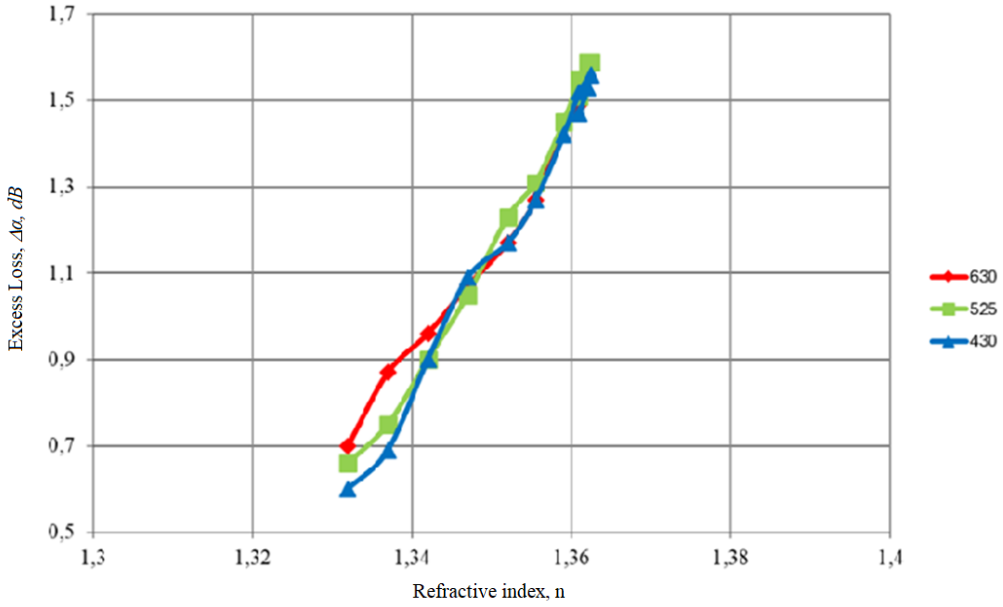


Fig. 2. The dependence of the increment of the level of excess loss $\Delta\alpha$ on the value of the solution refractive index n.

As can be seen from the results of the experimental study, the dependence of the insertion losses on the solution refractive index for concentrations from 10 to 96% is linear. Considering the experimental error, the dependences $\Delta\alpha(n)$ for different wavelengths can be considered identical.

Conclusion

Therefore, a fully fiber-optic sensor is presented, suitable for remote monitoring of the concentration of an aqueous solution based on a change in the refractive index.

The linearity of the dependence of the insertion losses on the concentration of the solution in the entire range from 0 to 96% is demonstrated.

The possibility of carrying out measurements at different wavelengths is shown, which proves the prospect of using WDM in such a sensor system and expands the scope of its application.

REFERENCES

1. Ziemann O., Krauser J., Zamzow P. E., Daum W., POF Handbook: Optical Short Range Transmission Systems / Springer Berlin – Heidelberg: Springer Berlin, 2008. – 884 c. – ISBN 978-3-540-76628-5

2. David J., Dante A., Allil R., Matias I., Del Villar I., Werneck M., Effect of Metal Oxide Layers on the Performance of Polymer Optical Fiber-based Hydrogen Sulfide Sensors, 2023 International Conference on Optical MEMS and Nanophotonics (OMN) and SBFoton International Optics and Photonics Conference (SBFoton IOPC), (2023) 1-2, 10.1109/OMN/SBFotonIOPC58971.2023.10230937.

3. Lopes R., Pinto P., David J., Dante A., Macrae A., Allil R., Werneck M., Development of an Immunocapture-Based Polymeric Optical Fiber Sensor for Bacterial Detection in Water. Polymers., (2024) 16. 861. 10.3390/polym16060861.

Express kidney monitoring method for early detection of kidney damage

D. V. Vakorina [1]✉, G. V. Stepanenkov[1] and V. V. Davydov[1, 2]

[1]The Bonch-Bruevich Saint Petersburg State University of Telecommunications, Saint Petersburg, Russia.

[2]Peter the Great Saint-Petersburg Polytechnic University, Saint Petersburg, Russia

✉cementary.ley@gmail.com

Abstract. The necessity of determining kidney damage at an early stage using fast and reliable express methods was substantiated. A method based on refractometric measurements of refractive index at three wavelengths with grading of refractive indices to the values of three basic parameters (osmolarity, amount of solids, density) was proposed for express analysis of kidney damage control. Additionally, the sizes of protein compounds were investigated and their sizes were also graded to refractive indices. The advantages of using the refractometer design at three wavelengths over other methods were noted. The peculiarities of measuring the refractive index of biological liquids on the example of urine are established. The results of the study of various samples and their analysis are presented. The comparison of the obtained results with the results of measurements in clinical diagnostics is carried out.

Keywords: kidney damage, laser radiation, wavelength, refractive index, express control, health condition.

Introduction

In the modern world kidney disease after cardiovascular diseases comes second place in people as the main cause of death. The Russian Federation is not an exception. Factors that now in the world affect the increase in the number of cases of kidney disease with the formation of stones of various sizes in them in people are quite a lot. They begin with the environment, improper nutrition due to overload at work, high levels of stress and others. Many people do not notice the beginning of kidney damage and stone formation at the primary stage of the disease. A person at this time can feel good and be able to work, temporarily arising malaise people associate with other causes. Studies conducted by doctors have shown that the earlier the kidney lesion is detected, the more effective and successful will be the course of treatment. The probability of recovery of almost all kidney functions increases with the stage at which kidney damage is detected (early stage is the highest probability). In this situation, rapid, affordable and reliable methods of rapid monitoring of kidney damage detection, especially at an early stage, are essential.

Rapid Diagnostic Methods and Problems

Currently, various methods of express control have been developed. The most widely used of the most accessible are test strips, urometer, urine analyzer. Various studies have shown that these methods do not allow you to detect the disease at an early stage. Only in the clinic can be reliably done. In my work, a new and affordable method of diagnosing kidney disease at an early stage is proposed, which is related to express control of urine based on refractometric measurements, which are highly accurate (the error of measuring the refractive index of urine is $5*10^{-5}$).

I have analyzed various studies related to the detection of early-stage renal damage. The results showed that at this stage of the disease, the greatest changes occur in the following three urine parameters (osmolarity - O_s, the presence (N_b concentration) of solids in it and the size of protein compounds - D_b, as well as (urine density ρ_m)). It is proposed to relate changes in the values of these three or four parameters to changes in the refractive index of urine. For this purpose, it is necessary to realize measurements of the refractive index of urine at three wavelengths: λ_1 = 436.4 nm, λ_2 = 589.3 nm, λ_3 = 657.2 nm (standard composition of wavelengths for a wave refractometer, the principle of operation of which is based on total internal reflection). To use the four parameters, it is necessary to perform measurements at four wavelengths.

And perform graduations of the change of O_s, N_b, D_b and ρ_m values from the change of refractive index values $n_{\lambda 1}$, $n_{\lambda 2}$, $n_{\lambda 3}$ and $n_{\lambda 4}$ in urine samples at different temperatures T (unknown in further three-four components, three-four equations (graduations) for each length of laser radiation (eventually 9-12 graduation curves). The reliability of the results increases with

increasing number of measurements at different wavelengths. Therefore, in the new refractometer design developed in the future it will be necessary to use another wavelength λ_4 = 505.3 nm (green radiation). The reliability of the measurements will increase further.

In the initial stages of preparation for the study, the creation of model solutions was proposed, an important aspect of which is to analyze the biophysical properties of samples with known composition. With the help of model solutions, theoretical indices of kidney condition determination will be established, so samples were prepared to consider 3 different cases: 1. A healthy person, 2. A person with diabetes mellitus and onset of kidney disease, 3. A person with critical stage of kidney disease. For further refractometer measurements, urine samples were collected from people whose health conditions reflected the prepared model solutions. The results of the study of two groups of people for kidney damage were presented. In the first group, a volunteer with healthy kidneys undergoing medical examination (Pavlova). In the second group the rest of the experimental participants (Ivanov and Kendev) with profound changes in kidneys. The data are summarized in Table 1.

Table 1: Basic urine parameters in people with different states of kidney disease.

Sample	Refractive index at 3 values of λ			Urine Osmotic Pressure	Urine Specific Gravity	Urine Total Solids
	436,4 nm	589,3 nm	657,2 nm	mOsm/l	g/ml	% vol
Ivanov	1,349653	1,342072	1,340126	1047	1,0263	5,94
Pavlova	1,351017	1,343340	1,341395	1184	1,0300	6,73
Kendev	1,347952	1,340456	1,338511	872	1,0215	4,91
sample №1	1,344454	1,337078	1,335164	504	1,0112	2,72
sample №2	1,345145	1,337816	1,335920	584	1,0135	3,20
sample №3	1,342265	1,335003	1,333116	276	1,0047	1,34

Conclusion

As a result of the analysis, a number of human urine parameters have been determined that can be used for early detection of kidney diseases during express urine control. A new express method of human urine control based on refractometric measurements of refractive index nm at different wavelengths was developed. The comparison of the obtained data on the change of total solids, specific gravity (density), osmolarity and size of proteins from the measured refractive index values with the data of model solutions of human urine simulating kidney lesions of different stages was carried out. Coincidence of the results within the measurement error was obtained.

REFERENCES

1. **R. Davydov, A. Zaitceva, D. Isakova, and M. Mazing,** "New Methodology of Human Health Express Diagnostics Based on Pulse Wave Measurements and Occlusion Test," Journal of Personalized Medicine, vol. 13(3), pp. 443, March 2023.
2. **N. M. Grebenikova, V. V. Davydov, and K. J. Smirnov,** "Features of optical signals processing for monitoring the state of the flowing liquid medium with a refractometer," *Journal of Physics: Conference Series*, vol. 1368(2), pp. 022057, September 2019.
3. **V. Davydov, I. Gureeva, R. Davydov, and V. Dudkin,** "Flowing Refractometer for Feed Water State Control in the Second Loop of Nuclear Reactor," Energies, vol. 15(2), pp. 457, March 2022.

The use of Raman and laser-induced breakdown spectroscopy for the study of iron-containing inks

O. S. Gribovskaya[1]✉, **N. A. Sharkova**[1], **A. V. Vasilieva**[1]

[1] Saint-Petersburg State Electrotechnical University «LETI», Saint-Petersburg, Russia

✉osgribovskaya@stud.etu.ru

Abstract. The paper considers development of the method of determining elemental composition of iron-containing inks by combination of Raman and laser-induced breakdown spectroscopy (LIBS). A sample of iron-gall ink on a paper substrate was made for the studies. Raman and LIBS spectra were obtained and compared with several databases to determine the elements contained in the sample. The results showed that combination of Raman spectroscopy and LIBS could solve the problem of iron-containing components identification for paper artifacts.

Keywords: iron gall ink, Raman spectroscopy, laser-induced breakdown spectroscopy, LIBS, chemical composition study.

Introduction

Iron gall ink – one of the earliest materials used by humans for writing, which is made from iron salts (most commonly from vitriol) and a mixture of organic colorants and tannins. Comparing with inks, containing copper salts as a base, iron gall inks can eventually cause damage to paper [1], which is a significant obstacle to preserving paper manuscripts and ancient books. In order to address the issue of detecting iron and other chemical elements within ink, it becomes necessary to develop techniques for its detection in various ways.

One of the modern methods for study chemical composition of different materials is Raman spectroscopy. Despite the fact that Raman spectroscopy is a highly effective, non-invasive technique, working with inks can be challenging [2]. This may be due to the complex nature of inks and the presence of fluorescent additives that can hinder the detection of weaker band intensities [3, 4]. That is why it is necessary to create an investigation technique for inks, which includes some alternative methods of identification.

Laser-induced breakdown spectroscopy (LIBS) technique, unlike many others, can detect the presence of specific elements in a material's composition. The method is not completely nondestructive, but it does allow for measurements with minimal damage to the surface of the sample [5]. Thus, in this work chemical composition of model ink sample is studied with Raman spectroscopy and LIBS to create a technique for paper artifacts investigation.

Materials and Methods

The model sample was created in a cellulose paper, where the inks, made by hot infusion of gall nuts, iron vitriol, cherry resin and drinking water were put with the brush.

For this work a Raman Confocal microscope Confotec MR350 (SOL instruments Ltd., Germany) with 785 and 850 nm working wavelength and 1 micron laser spot was used. The detector had special cooling system to increase temperature up to -30° C. In order to avoid the thermal heating of the paper by laser and the destruction of the sample, the ND filter (absorber) was installed either. The sample was placed on the working surface, then it was pressed with a weight to avoid fluctuations. Spectral range for Raman spectra detection was from 99 cm^{-1} to 1734 cm^{-1}.

For the study, LIBS setup (Onteko, USA) was employed. A pulsed (single-pulse, two-pulse and three-pulse modes are available) Nd:YAG nanosecond laser with spot size up to 30 microns operated at a wavelength of 1064 nm with a maximum pulse energy of 28 mJ. USB4000 spectrometer (Ocean Insight, USA) operated in the spectral range of 200–1100 nm with optical resolution ranging from 0.1–10 nm and an integration time ranging from 3.8 milliseconds to 10 seconds. Additionally, part of the setup included the following software programs: OceanView (a specialized spectrometer software), and LIBS Identification Software for processing the acquired

spectra. The sample was placed at 7 cm from the laser outlet. A two-pulse laser mode with pulse energy of 5 mJ was used for measurements.

In both cases, for Raman and LIBS, measurements of paper uncoated with ink and paper covered with ink were carried out, when subtracting the first measurement from the second, a spectra of pure ink were obtained.

Results and Discussion

Analysis of Raman spectrum showed no peaks of iron-containing components, however clear peaks corresponding to glucose and fructose, as well as peaks corresponding to tannin, were detected in the spectrum, making possible the identification of cherry resin (1400 cm^{-1}) and gall nuts (550 cm^{-1}).

The obtained LIBS spectrum was compared with the National Institute of Standards and Technology (NIST) database [6]. Peaks corresponding to iron at wavelengths of 274.7, 357.8, 374.1, 382.4, 385.6 and 393 nm, as well as sodium at 589 nm, were detected in the spectrum. After reviewing relevant literature [7, 8, 9], it was determined that the spectral data obtained from LIBS method agrees with reference data, indicating that the method can detect iron and sodium in various compounds.

Conclusion

The problem of iron-containing components identification in Raman spectroscopy could be explained by alternative prohibition rule. This study showed that inclusion of LIBS method during the ink investigation allows neglecting this problem. The Raman spectroscopy was suitable for identifying organic components of inks such as gall nuts and cherry resin, while LIBS peaks indicated the presence of iron and sodium. Sodium could be referring to contaminations or hand marks. In both spectral measurements no paper destroy was observed. Combination of Raman and LIBS methods could be effective technique for paper artifacts diagnostics.

REFERENCES

1. **Hidalgo D., R.J., R. Córdoba, P. Nabais,** et al. New insights into iron-gall inks through the use of historically accurate reconstructions. Herit Sci 6, 63 (2018)
2. **Cicconi F., Lazic V., Palucci A., Assis A. C. A., Romolo F. S. ,** Forensic analysis of commercial inks by Laser-Induced Breakdown Spectroscopy (LIBS). Sensors, 20 (2020)
3. **Edwards H. G. M.**, in Raman Spectroscopy in Archaeology and Art History: Volume 2, ed. P. Vandenabeele and H. Edwards, The Royal Society of Chemistry, 2018, pp. 1-15.
4. **Lee A. S., Mahon P. J., Creagh D. C.** Raman analysis of iron gall inks on parchment. Vibrational Spectroscopy, 41(2), 170–175, (2006).
5. **Goltz D. M.** A Review of Instrumental Approaches for Studying Historical Inks. Analytical Letters, 45(4), 314–329, (2012).
6. NIST LIBS Database. URL: https://physics.nist.gov/PhysRefData/ASD/LIBS/libs-form.html. Accessed: 25.03.2024.
7. LIBS Info: Fe Analysis. URL: https://libs-info.com/element/Fe/. Accessed: 25.03.2024.
8. **Nasrullah I., Kurnia L., F. and M. Ramli** Study on Emission Spectral Lines of Iron, Fe in Laser-Induced Breakdown Spectroscopy (LIBS) on Soil Samples // Journal of Physics: Conference Series. - 2015. - №846.
9. **Usmawanda T.N., Ramli M., Idris N.** Emission Spectral Profile of Salt in Laser-Induced Breakdown Spectroscopy (LIBS) on River Clamshell Sample // Journal of Physics: Conference Series. - 2018. - №1116.

Optical Spintronics

I. Deriy[1,2], **D. Kornovan**[1], **A. Bogdanov**[1,2]✉

[1] School of Physics and Engineering, ITMO University, Lomonosova st. 9, Saint-Petersburg, 197101, Russia

[2] Qingdao Innovation and Development Center, Harbin Engineering University, Sansha road 1777, Qingdao, 266000, Shandong China

✉a.bogdanov@metalab.ifmo.ru

Abstract: In this work, we present the concept of optical spintronics, which uses optical spin rather than electromagnetic energy to transfer information. We show that transfer of optical spin is possible without energy transfer, and present an optical spin diode - a device that support non-reciprocal propagation of optical spin currents.

Keywords: Optical spin angular momentum, optical chirality, optical spin diode

Modern electronics are finding it difficult to satisfy the increasing demands on the computing power and bandwidth of information devices. The answer to the question of improving the above-mentioned characteristics is photonics, which is many times superior to electronics in terms of information transfer speed and energy efficiency. Unfortunately, creating photonic devices such as a diode or transistor requires the use of nonlinear materials, breaking of electromagnetic reciprocity, or other tricks that complicate the process of large-scale production.

However, information transfer is not always associated with particle transfer. An example is spintronics: a field of electronics in which information is transferred via spin currents while the electrons themselves may remain in place. As a vectorial field, electromagnetic fields, carry spin angular momentum (SAM) $\mathbf{S}$, which satisfies continuity equation [1]

$$\nabla \cdot \mathrm{J} = \frac{\partial}{\partial t}\mathbf{S}, \tag{1}$$

where J is the SAM flux density to which we will refer as to *optical spin current*. For monochromatic electromagnetic field, time averaged values of $\mathbf{S}$ and J are [1, 2]

$$\langle \mathbf{S} \rangle = \frac{1}{16\pi\omega}\Im\left[\mathbf{E}^* \times \mathbf{E} + \mathbf{H}^* \times \mathbf{H}\right], \quad \langle \mathrm{J} \rangle = \frac{\omega}{8\pi c}\Im\left[\hat{\mathbb{1}}\left(\mathbf{E}\cdot\mathbf{H}^*\right) - \mathbf{E}\otimes\mathbf{H}^* - \mathbf{H}^*\otimes\mathbf{E}\right] \tag{2}$$

For a plane electromagnetic wave with electric field

$$\mathbf{E}\left(\mathbf{r},t\right) = a_0\left(\mathbf{e}_x + \sigma i\mathbf{e}_y\right)e^{i\beta kz}, \tag{3}$$

where $k = \omega/c$,$\sigma = \pm 1$, $\beta = \pm 1$, and a_0 is the complex amplitude, nonzero components of Poynting vector, SAM, and optical spin current are

$$\langle P_z \rangle \sim \beta\left|a_0\right|^2, \quad \langle S_z \rangle \sim \sigma\left|a_0\right|^2, \quad \langle J_{zz} \rangle \sim \sigma\beta\left|a_0\right|^2. \tag{4}$$

Therefore, two contrapropagating waves with same amplitude but opposite SAM will have zero energy flux but nonzero SAM slux (see Fig. 1.a). Indeed, let us consider following field configuration

$$\mathbf{E}\left(\mathbf{r}\right) = a_+\mathbf{e}_0\, e^{ikz} + a_-\mathbf{e}_0^*\, e^{-ikz}, \tag{5}$$

where $\mathbf{e}_0 = \left[1,\ i\ ,0\right]^{\mathrm{T}}/\sqrt{2}$, and $a_\pm$ are complex amplitudes. Calculation of energy flux and optical spin current gives

$$\langle P_z \rangle \sim \left|a_+\right|^2 - \left|a_-\right|^2, \quad \langle J_{zz} \rangle \sim \left|a_+\right|^2 + \left|a_-\right|^2. \tag{6}$$

Thus, when $|a_+| = |a_-|$ such field configuration allows transfer of optical spin without transfer of energy.

However, both electromagnetic energy and spin can propagate in everry direction in freespace. A natural question arises: is it possible to create a device in which the optical spin current can flow only in one direction? The answer is yes. Consider four-port network presented on Fig. 1.b, with each channel having following elecrtic field

$$\mathbf{E}^a_{j,\pm}(\mathbf{r}) = a_{j,\pm}(\mathbf{e}_x \pm i\mathbf{e}_y)\, e^{i\beta_j kz}, \quad \mathbf{E}^b_{j,\pm}(\mathbf{r}) = b_{j,\pm}(\mathbf{e}_x \pm i\mathbf{e}_y)\, e^{-i\beta_j kz}, \tag{7}$$

where index $j = 1, 2$ encodes halfspace to the left ($j = 1,\ z < 0$) and to the right ($j = 2,\ z > 0$) of the structure, $\beta_1 = -\beta_2 = 1$, and scattering matrix

$$\begin{bmatrix} b_{1+} \\ b_{2+} \\ b_{1-} \\ b_{2-} \end{bmatrix} = \begin{bmatrix} 0 & 1 & 0 & 0 \\ 1 & 0 & 0 & 0 \\ 0 & 0 & 0 & 1 \\ 0 & 0 & 1 & 0 \end{bmatrix} \begin{bmatrix} a_{1+} \\ a_{1-} \\ a_{2+} \\ a_{2-} \end{bmatrix}. \tag{8}$$

Only waves with positive SAM are allowed to travel in positive direction, and only waves with negative SAM are allowed to travel in negative direction. Thus optical spin current is able to flow only in positive direction in such a network, what makes it an *optical spin isolator*. While an isolator is an idealized device, in real life it is possible to create an *optical spin diode* using chiral materials. In chiral media, waves with different handedness have different refractive index. Consider plane electromagnetic wave, incidend on a chiral slab (see Fig.1c). By selecting the material parameters and the angle of incidence of the wave in such a way that the waves of one handedness pass through the slab, while the waves of the other handedness experience total internal reflection on the slab, it is possible to achieve the spin optical diode regimes. Energy flux and spin current for transmitted wave is presented in Fig.1c. One can see three different regimes. When, for one of the polarizations, the normal component of the wave vector becomes imaginary inside the chiral slab, then the structure becomes an optical spin diode.

In conclusion we have introduced the concept of optical spintronics, in which information is transferred via optical spin currents. We also proposed an optical spin diode and its implementation based on chiral materials.

This work was supported by Russian Science Foundation (Project No. 23-72-10059). I.D. acknowledges the Foundation for the Advancement of Theoretical Physics and Mathematics "BASIS" for support.

References

[1] Yoshito Y Tanaka, Ryoma Fukuhara, Tsutomu Shimura, et al. Continuity equation for spin angular momentum in relation to optical chirality. *Physical Review A*, 102(2):023531, 2020.

[2] Konstantin Y Bliokh, Aleksandr Y Bekshaev, and Franco Nori. Optical momentum, spin, and angular momentum in dispersive media. *Physical review letters*, 119(7):073901, 2017.

Development of directional coupler based on gallium phosphide nanowires for integrated nanophotonics

R. P. Eresko [1✉], **A. Kuznetsov** [1,2], **A. D. Bolshakov**[1,2,3]
[1]Alferov University, Saint Petersburg, Russia;
[2]Moscow Institute of Physics and Technology, Dolgoprudny, Russia;
[3]Erevan State University, Erevan, Armenia
✉rodioneresko@gmail.com

Abstract. In this work, a GaP nanowires (NWs) based nanostructure - directional coupler is under consideration. The dependence of the spectral characteristics of the structure depending on its geometrical parameters, such as NW diameter, length of the coupling zone, and distance (gap) between NWs in the coupling zone, is investigated using numerical simulations. Considered nanostructure can claim to be a basis component of photonic integrated circuits.

Keywords: gallium phosphide, nanowires, directional coupler, numerical simulations
Funding: A.K. thanks the Ministry of Science and Higher Education of the Russian Federation (agreement 075-03-2023-106, project FSMG-2021-0005).

Introduction

Optical integrated circuits can serve as an alternative to silicon electronics. Their most notable advantages - higher data transfer speeds and the absence of joule heating make full optical photonics a promising platform for classical and quantum computing. Nowadays, some of the most popular optical circuits are silicon-based optical circuits, but they cannot achieve the desired performance due to the lower packing density of the elements compared to electronic circuits. To reduce the size of optical components, it's necessary to move towards materials that can expand the possibilities in the context of creating passive and active elements by utilizing shorter wavelength spectral range. GaP nanowires are a good candidate for such applications due to high structure perfection, large aspect ratio, and the possibility of synthesis on mismatched substrates [1]. Also, GaP is transparent in almost the entire visible and IR range, and has a high refractive index, that opens up new ways in developing optical components. Together with the advantages of the synthesis technology – molecular beam epitaxy (MBE), GaP NWs become an ideal candidate for the realization of basis elements of optical circuits - directional couplers (DCs). Investigation of the propagating electromagnetic waves in two coupled hexagonal waveguides hasn't ever been under consideration that makes the obtained data especially important for the development of a large number of different devices.

Materials and Methods

In this work, the propagation of electromagnetic waves along two coupled waveguides were investigated using finite difference time domain (FDTD) method (see Fig. 1). The influence of geometrical parameters on its spectral characteristics was considered. In accordance with the NWs structure [l], they were represented as equilateral hexagonal prisms. DCs consisted of the NWs of different diameter (150, 200, 250 nm), different gaps (50, 100, 150, 200 nm), different coupling length (5, 10, 15 μm) were considered. The numerical simulations were performed with absorbing boundary condition (PML), which allow to absorb incident light with minimum reflection. An inhomogeneous grid with a step of 7 nm was utilized. The so-called ports were used as the source, which can simultaneously act as a mode source and field monitor. Transmission spectra were obtained in the wavelength range of 500 to 1100 nm.

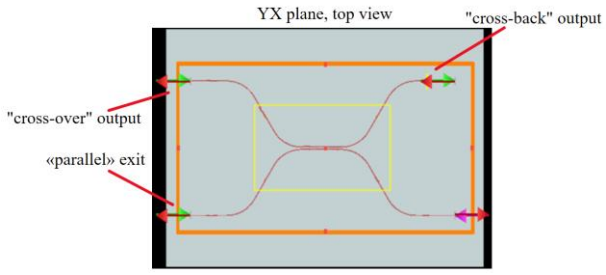


Fig. 1. Schematic of the model geometry for the numerical simulation

Results and Discussion

On the Fourier images of the electric field intensity distribution, an energy transition from one NW to another is observed (see Fig. 2 (*a*)). The number of energy transition cycles is also influenced by the GaP NW diameter: the GaP NW diameter increases, so we observe a decrease in the number of transition cycles. Transmittance spectrum also demonstrates a cyclic pattern of energy transition between the DCs shoulders depending on a wavelength. For the shorter wavelength we observe peaks broadening due to stronger field localization in each NW. To increase the bandwith we can use broader gaps and thicker NWs but in this case we have a red-shift of the operating wavelength. Increasing the coupling length from 5 up to 15 microns increase a number of transitions so making it 50 microns or longer allows us to achieve the power division 50:50 regime in a very broad spectral range.

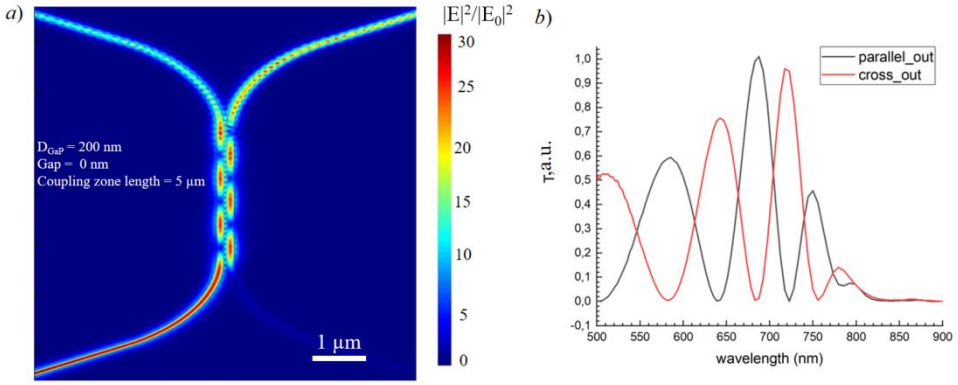


Fig. 2. Fourier image of the electric field distribution at a wavelength of 790 nm (*a*) and the transmission spectra (*b*)

Conclusion

We've demonstrated how we can control output signal in submicron directional coupler made of two single GaP NWs. Gap broadening affect the operating wavelength (red shift) and also decrease the number of transition cycles. Increasing the NW diameter we shift the transmission spectra to the longer wavelength range by making the modes confinement higher which hinder them to couple to the another shoulder. Increase of the coupling length multiply the number of peaks in transmission spectrum so if we have 50-100 microns coupling length it's possible to achieve 50:50 power division in a very wide spectrum range which will be limited by GaP absorption and NWs diameter for longer wavelength range. The results indicate the possibility of using such a structure as a basic passive element in integrated nanophotonics.

Acknowledgments

A.K. thanks the Ministry of Science and Higher Education of the Russian Federation (agreement 075-03-2023-106, project FSMG-2021-0005).

REFERENCES

1. **Bolshakov, Alexey D., et al.**, Single GaP nanowire nonlinear characterization with the aid of an optical trap, Nanoscale 14.3 (2022): 993-1000.

Influence of the annealing on the optical properties of silicon nitride waveguides with various thicknesses

A. A. Ershov [1✉], **K. N. Chekmesov** [1], **A. A. Nikitin** [1], **S. N. Abolmasov** [2,3], **E. I. Terukov** [1,2,3], **A. V. Eskov** [1], **A. A. Semenov** [4], **A. B. Ustinov** [1]

[1] Saint Petersburg Electrotechnical University "LETI", St Petersburg, Russia;
[2] Scientific and Technical Center of Thin Film Technologies in Energy LLC, St. Petersburg, Russia;
[3] Ioffe Institute, St. Petersburg, Russia;
✉ aaershov@etu.ru

Abstract. Silicon nitride (SiN_x) is a promising material for photonic integrated circuits. In this work the losses, coupling coefficient and group index of SiN_x waveguides are studied before and after the thermal annealing. It is shown that before annealing SiN_x waveguides demonstrate weak dependence of the propagation losses versus frequency in the frequency range from 185 THz to 190 THz. In this frequency range the losses are about 4-5 dB/cm. Starting from 190 THz the propagation losses grow up reaching 12 dB/cm at 196 THz. The thermal annealing at 600 °C for 30 min. in vacuum leads to the decrease of the losses down to 4 dB/cm at the whole frequency range from 185 THz to 196 THz. This indicates the destruction of Si-H and N-H complexes remaining after plasma-enhanced chemical vapor deposition.

Keywords: photonic integrated circuits, optical waveguides, silicon nitride, annealing.

Funding: The work was carried out with the support of Ministry of Education and Science of Russian Federation (project no. 075-01438-22-07, grant FSEE-2022-0017).

Introduction

Nowadays silicon nitride (SiN_x) is one of the promising materials for photonic integrated circuits (PICs). Due to low propagation losses, the absence of two-photon absorption, high Kerr nonlinearity and potential compatibility with CMOS technology it is possible to create linear and nonlinear PICs that find applications in optics and microwave photonics [1 – 7]. Currently, the most accessible and cheapest method for silicon nitride films production is plasma-enhanced chemical vapor deposition (PECVD). The absorption on Si-H and N-H complexes limits the applications of PECVD technology. The thermal annealing paves the way to destroy these complexes and to reduce the losses [8]. Thus, the aim of this work is to study the influence of annealing on the optical properties of a SiN_x PICs.

Materials and Methods

The PICs under investigation are made of silicon nitride films with thicknesses of 400 nm and 700 nm. All films are deposited using the PECVD technology. The waveguide structures are obtained by the electron beam lithography. The width of the waveguides is chosen to be 900 nm in order to ensure a quasi-single-mode operation. The experimental chips include a directional coupler, a set of various straight waveguides, and a ring resonator with radius of 1 mm. The ring resonator coupled with two straight waveguides. The gap between the straight waveguide and the ring is 500 nm. The waveguide properties of these structures are experimentally obtained according to the extraction method [9] before as well as after a thermal annealing. The chips are annealed at the temperature of 600 °C for 30 minutes in a vacuum. The transfer functions of elements are analyzed with high definition component analyzer – Aragon in the frequency range from 185 THz to 196 THz (wavelength form 1529.6 nm to 1620.5 nm).

Results and Discussion

The losses of the SiN_x waveguides are obtained by the extraction method in the frequency range from 185 THz to 196 THz. It was found that before annealing SiN_x waveguides demonstrate the propagation losses of 4-5 dB/cm at frequencies below 190 THz. Starting from 190 THz the losses rise with the frequency up to 12 dB/cm. Also it was shown that the SiN_x waveguides with

the cross sections of 900×400 nm^2 и 900×700 nm^2 demonstrate the group index of 1.773 and 1.869, respectively. After annealing at 600 °C for 30 min. in vacuum, the losses decreased down to 4 dB/cm at the whole frequency range from 185 THz to 196 THz. It is also shown that the group index of both waveguides increases by 2.6 %. It can be explained by the destruction of the Si-H and N-H complexes remaining after PECVD. For the verification obtained frequency dependences of the propagation losses, coupling coefficient and group index are used for calculation the theoretical transfer functions of ring resonators, that demonstrate a good agreement with the experimental data.

Conclusion

The propagation losses, coupling coefficient, and group index of SiN_x waveguides are studied before and after the thermal annealing. It is found that the thermal annealing at 600 °C for 30 min. in vacuum leads to the decrease of losses in the frequency range from 185 THz to 196 THz. This indicates the destruction of Si-H and N-H complexes remaining after plasma-enhanced chemical vapor deposition.

Acknowledgments

The work was carried out with the support of Ministry of Education and Science of Russian Federation (project no. 075-01438-22-07, grant FSEE-2022-0017).

REFERENCES

1. **Ji X., Roberts S., Corato-Zanarella M., Lipson M.**, Methods to achieve ultra-high quality factor silicon nitride resonators, APL Photonics. 6 (7) (2021) 071101.

2. **Liu J., Huang G., Wang R. N., He J., Raja A. S., Liu T., Engelsen N. J., Kippenberg T. J.,** High-yield, wafer-scale fabrication of ultralow-loss, dispersion-engineered silicon nitride photonic circuits, Nature communications. 12 (1) (2021) 2236.

3. **El Dirani H., Youssef L., Petit-Etienne C., Kerdiles S., Grosse P., Monat C., Pargon E., Sciancalepore C.**, Ultralow-loss tightly confining Si3N4 waveguides and high-Q microresonators, Optics express. 27 (21) (2019) 30726–30740.

4. **Brasch V., Chen Q. F., Schiller S., Kippenberg T.J.**, Radiation hardness of high-Q silicon nitride microresonators for space compatible integrated optics, Optics express. 22 (25) (2014) 30786–30794.

5. **Marpaung, D., Yao, J., Capmany, J.**, Integrated microwave photonics, Nature photonics. 13 (2) (2019) 80–90.

6. **Blumenthal D. J., Heideman R., Geuzebroek D., Leinse A., Roeloffzen C.,** Silicon nitride in silicon photonics, Proceedings of the IEEE. 106 (12) (2018) 2209–2231.

7. **Kippenberg T. J., Gaeta A. L., Lipson M., Gorodetsky M. L.**, Dissipative Kerr solitons in optical microresonators, Science. 361 (6402) (2018) eaan8083.

8. **Ay F., Aydinli A.**, Comparative investigation of hydrogen bonding in silicon based PECVD grown dielectrics for optical waveguides, Optical materials. 26 (1) (2004) 33–46.

9. **Ershov A. A., Eremeev A. I., Nikitin A. A., Ustinov A. B.**, Extraction of the optical properties of waveguides through the characterization of silicon-on-insulator integrated circuits, Microwave and Optical Technology Letters 65 (8) (2023) 2451-2455.

Peculiarities of the local electromagnetic field distribution in Non-van-der-Vaals $InGaS_3$ thin layers slot waveguides

E. S. Zavyalova, [1]✉, **A. Kuznetsov** [1,2], **A. D. Bolshakov**[1,2,3]
[1]Alferov University, Saint Petersburg, Russia;
[2]Moscow Institute of Physics and Technology, Dolgoprudny, Russia;
[3]Erevan State University, Erevan, Armenia
✉ladieseniya@gmail.com

Abstract. $InGaS_3$ thin layers are promising nanostrures in the field of nanophotonics owing to the broad bandgap, sufficiently high refractive index and the simplicity of fabrication. Here we numerically investigate a system based on $InGaS_3$ waveguides, standing side by side. We demonstrate the localization of the electromagnetic field inside the gap between two waveguides and obtain the refractive indices and losses for the slot waveguide modes at a wavelength of 505 nm. Transmittance spectra of considered configurations of different geometrical parameters were obtained The waveguiding cut-off related to the absorption inside the material and the delocalization of the electromagnetic field was determined. The obtained results open the possibility for fabrication of novel photonic devices based on $InGaS_3$ thin layers.

Keywords: $InGaS_3$, slot waveguide, transmittance, thin layer, numerical simulations

Funding: This work is supported by the Russian Science Foundation (grant № 24-22-20064).

Introduction

Nowadays, the research of new materials for the development of new element and component basis of integrated nanophotonics is important. One of the main task of integrated photonics is to increase the surface packing density of the functional elements, which can be achieved using an optically dense material, operating in the range of shorter wavelengths, for example in visible. Also, the material should be technologically versatile in the context of circuits fabrication technology.

$InGaS_3$ is a semiconductor with a large bandgap (2,73 eV) and high refractive index (< 2,5) [1]. It is a novel layered material with hexagonal symmetry of the crystal lattice, however, it is non-van-der-Waals: the bonds between the layers are covalent, but in the plane of the layer they are distributed inhomogeneously and their density per unit area is rather small, which makes it quite easily to separate the layers from each other by various methods [1]. From the optics point of view, it is extremely promising in the context of developing passive elements of integrated optical circuits. By the example of other layered materials (MoS_2, $MoSe_2$, WS_2, WSe_2, etc.) the possibility of separating thin layers of a given thickness and transferring them onto different substrates has been demonstrated [2]. The layered structure of the material allows the exfoliation method to separate the layers with monolayer accuracy, which will allow to integrate $InGaS_3$ into the processes of planar technology and control the geometry of elements precisely.

Materials and Methods

In this work, we study two different configurations of the $InGaS_3$ slot waveguides by numerical simulation methods, namely finite difference frequency domain (FDFD) and finite difference time domain (FDTD) in Ansys Lumerical software (see Fig. 1 for schematic). An inhomogeneous grid was modeled with a minimum grid step of 1.5 nm in the case of the FDFD solver and 7 nm of the FDTD solver. The absorbing boundary conditions were chosen in order to obtain a minimum reflection of the incident light. The optical constants used were taken from the work [1]. The systems with the following geometry and parameters were investigated: two square waveguides with a 5 μm long, standing side by side, placed on SiO_2 substrate. The square side varied from 100 to 250 nm with step of 50 nm. The gap between two $InGaS_3$ waveguides varied from 10 to 100 nm by the same step. For the second configuration with an extra layer of the material between waveguides, the thickness of the unetched layer was 10, 20 and 50 nm. The

waveguides properties of the considered system were studied at a wavelength of 505 nm. A model mode source was used to obtain the transmittance spectra in the range of 400 to 800 nm.

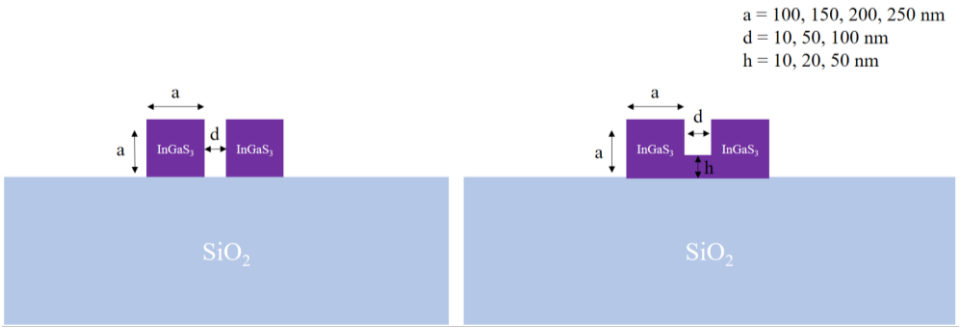


Fig. 1. Schematic of the model geometry for the numerical simulation

Results and Discussion

Numerical simulation has demonstrated effective localization of the electromagnetic field inside the gap between two waveguides due to the high difference in refractive indices of $InGaS_3$ and air (see Fig. 2) and interaction of the both waveguides modes. The slot guided mode exists only in specific range of waveguides dimensions: for smaller waveguides it's easier for electric field to interact due to the waveguides eigenmodes worse localization but for the thicker waveguides localization increases and slot mode is suppressed due to the shortening of the electric field evanescent tails. Adding extra layer of $InGaS_3$ to the slot region can shift the field maximum along the y-axis but it causes the mode leakage from the slot to the $InGaS_3$. From the obtained transmission spectra, it was determined that with an increase in the dimension of the waveguides, the mode inside the gap is delocalized due to less interaction of the electromagnetic field tails.

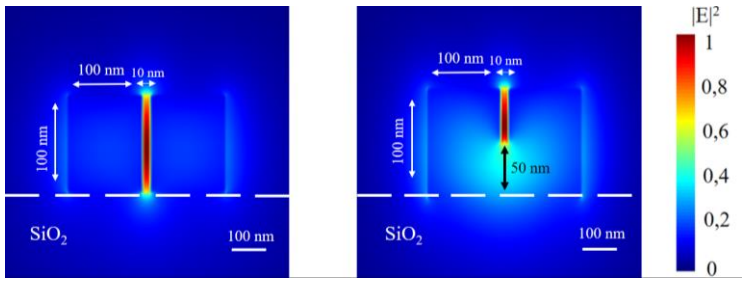


Fig. 2. Electric field distribution for two different slot waveguides configurations

Conclusion

We investigated the waveguide properties of the slot waveguides based on a novel layered non-van-der-Waals material. It was obtained, that 1) localization of the electromagnetic field between two waveguides increases due to waveguide dimension and gap decreasing; 2) the effective refractive index of the fundamental mode grows up with the increase of the waveguide dimension and the thickness of the unetched layer, and with the decrease of the gap between $InGaS_3$ waveguides. The results indicate that the slot waveguides based on $InGaS_3$ can be used as a passive element in integrated nanophotonics.

Acknowledgments

This work is supported by the Russian Science Foundation (grant № 24-22-20064).

REFERENCES

1. **Toksumakov, Adilet N., et al.,** High-refractive index and mechanically cleavable non-van der Waals InGaS3, npj 2D Materials and Applications 6.1 (2022): 85.
2. **Huo, Chengxue, et al.,** 2D materials via liquid exfoliation: a review on fabrication and applications, Science bulletin 60.23 (2015): 1994-2008.

Application of properties of neuromorphic optoelectronic sensors in machine vision tasks

Ivanov Fedor [1]✉, **Krasnikov Victor**[1], **Chizhov Artem**[1], **Koratushova Daria**[1], **Artem Chetvertuchin**[1], **Grunin Andrey**[1], **Fedyanin Andrey**[1]

[1]Lomonosov Moscow State University, Moscow 119991, Russia;

✉ivanov.fed@list.ru

Abstract. In recent years, machine vision systems have become more and more widespread. However, due to fundamental limitations of the Von Neumann architecture[1], such electronic systems consume a large amount of power and are not compact. One of the approaches to overcome these difficulties is intrasensory image preprocessing[2], as well as the use of memory properties and nonlinearity characteristic of optical neuromorphic transistors.

Keywords: Optoelectronic transistors, machine vision, artificial intelligence, neuromorphic computing, metal oxide nanocrystallites

Funding: This study was funded by A.Grunin, grant number: 02/01-2022/ФФ-ЛИАБ

Introduction

In recent years, neuromorphic artificial optoelectronic synapses[3] have received much attention, potentially being considered as basic elements of SNN[4]. In our work, we propose another possible application of optical transistors. Due to their memory properties and internal computation ability, they can preprocess visual information, avoiding excessive memory access to the computing device and outperforming standard sensors in energy efficiency.

Materials and Methods

In this work, artificial optoelectronic synapses based on zinc oxide nanocrystallites were used. Such devices are able to memorize the information about the illumination, translating it into an analog signal.

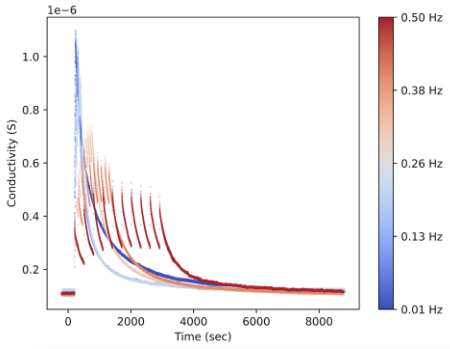


Fig. 1. Graph of dependence of conductivity of structures on illumination frequency

Results and Discussion

Based on the obtained illumination properties of neuromorphic synapses, a mathematical model capable of simulating the operation of an array of sensors, each pixel of which represents an artificial optoelectronic synapse, was created.

Imulations of the neuromorphic sensor operation were performed (Fig. 2). Object is directly opposite the sensor and there are no stray highlights.

The first line of Fig. 2 shows the motion of the circle. All other lines show the response of the sensor, assuming that the circle moves at different speeds. Near each line is written the time, which shows how many seconds the circle stands still before moving one cell.

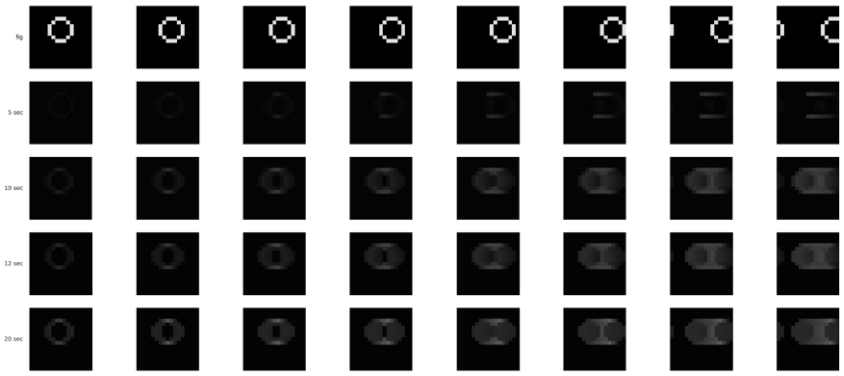


Fig. 2. Results of simulation of array response to lap movements with different speeds

To demonstrate this fact, a dataset of images of a circle moving in different directions was compiled. Gaussian noise was added to the image to simulate spurious illumination and noise. Then the CNN[5] was successfully trained(Fig. 3) on this dataset and despite the noise showed good accuracy and learning speed. Training accuracy was counted as the ratio of correct predictions to the total number of predictions.

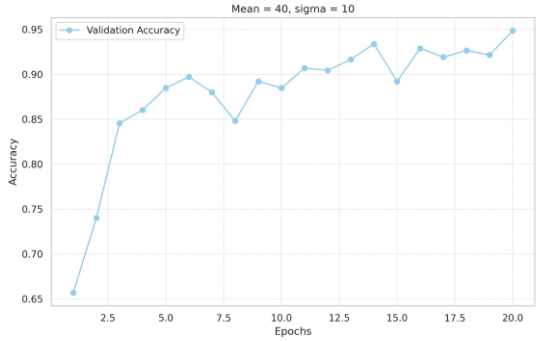


Fig. 3. Dependence of training accuracy on the number of training epochs

Conclusion

In this way, efficient preprocessing for machine vision tasks has been demonstrated to improve the energy efficiency and compactness of computing systems.

REFERENCES

1. **J. R. Powell**, "The Quantum Limit to Moore's Law,"in Proceedings of the IEEE, vol. 96, no. 8, pp. 1247-1248, Aug. 2008, doi: 10.1109/JPROC.2008.925411.

2. **Landau L. D., Liefshitz E. M.**, Theoretical physics, Vol. 3, Quantum mechanics, Nauka, Moscow, 1989.

3. **Wang Y.** et al. Photonic synapses based on inorganic perovskite quantum dots for neuromorphic computing //Advanced materials. – 2018. – Т. 30. – No. 38. – С. 1802883.

4. **Wei Y.** et al. Study of Spiking Neural Network-Based Regressor on Applications in Digital Predistortion for Power Amplifiers //2023 6th International Conference on Advanced Communication Technologies and Networking (CommNet). – IEEE, 2023. – С. 1-7.

5. **LeCun Y., Bengio Y., Hinton G.** Deep learning //nature. – 2015. – Т. 521. – №. 7553. – С. 436-444.

Optical properties of the CuO–ZnO thin films

I. O. Ignatieva[1]✉, A.P. Starnikova[2], V. V. Petrov[2], E M Bayan[1]

[1]Department of Chemistry, Southern Federal University, Rostov-on-Don, 344090, Russia,

[2]Institute of Nanotechnologies, Electronics, and Equipment Engineering, Southern Federal University, Taganrog, 347922, Russia

✉ iignateva@sfedu.ru

Abstract. The optical properties of CuO–ZnO composite thin films are studied. CuO–ZnO films with different atomic Cu:Zn ratios (1:99, 3:97, 5:95, 10:90) were fabricated on quartz glass substrates by solid-phase pyrolysis. The XRD method established that the prepared films are nanocomposite. It was found that transmittance is more than 84% for all materials in the range from 400 to 1000 nm.

Keywords: zinc oxide copper oxide, composite, thin films, optical properties.

Funding: The work was supported by Grant 4L/22-04-PISH carried out at the Southern Federal University.

Introduction

It is known that p-n heterojunctions based on semiconductors made of transition metal oxides are used to create promising materials as optical and optoelectronic devices, photocatalysts, sensors, and solar cells. The combination of n-type ZnO with p-type CuO makes it possible to create promising optical and photovoltaic devices [1]. In this work, CuO–ZnO thin films were synthesized by a new method of solid-phase pyrolysis [2] and the phase composition, optical properties of CuO–ZnO composite thin films were investigated.

Materials and Methods

Zinc (II) acetate dihydrate $Zn(CH_3COO)_2 \cdot 2H_2O$, copper (II) acetate dihydrate $Cu(CH_3COO)_2\ 2H_2O$ and organic acid $C_{19}H_{29}COOH$ were used to produce thin CuO-ZnO films by solid-phase pyrolysis. The synthesis method consists of two stages. During the first stage, an intermediate product, which is a mixture of organic salts of zinc and copper, was obtained. During the second stage, a solution of the resulting product in an organic solvent was applied to preliminarily prepared quartz glass substrates. The quartz glass substrates with intermediate product were calcined for two hours at 600°C for composite thin films synthesis.

The phase composition of the obtained materials was studied by X-ray diffraction using ARLX'TRA, Thermo ARL diffractometer, Cu-Kα radiation, $\lambda = 0.15406$ nm.

Optical properties of obtained thin films were studied using an optical transmittance spectrum obtained on a UV-1100 spectrophotometer in the wavelength range of 300-1000 nm.

Results and discussion

Based on the results of the X-ray diffraction, it was established that the materials are two-phase, which is confirmed by the presence of peaks characteristic of wurtzite ZnO and tenorite CuO. It was determined that the intensity of the peaks of zinc oxide is much more pronounced than the peaks of copper oxide, which appear as the CuO content increases.

Figure 1 shows the optical transmission spectrum of CuO-ZnO materials with a different atomic Cu:Zn ratios (1:99, 3:97, 5:95, 10:90).

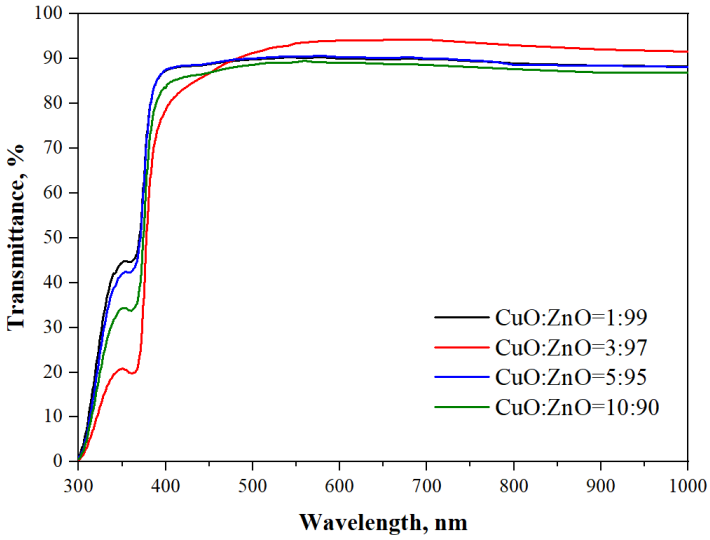


Figure 1. Optical transmittance spectra of CuO-ZnO films of various composition.

Studies have shown that the obtained CuO-ZnO thin films are optically transparent in the range from 400 to 1000 nm with a transmittance of more than 84% for all materials. It was established that CuO-ZnO thin film with an atomic ratio Cu:Zn=3:97 has the least transmittance in the visible light range, and the highest transmittance in the UV light range of 94%.

Conclusion

Thus, in this work, CuO-ZnO thin films were synthesized by a new method of solid-phase pyrolysis, in which the phase composition and the optical properties were investigated. It was defined that the obtained thin film materials are optically transparent in the visible light range, transmittance is more than 84%. CuO-ZnO thin films can be used in the creation of the optical and optoelectronic devices, such that light emitting devices and UV photodetectors.

REFERENCES

1. **Yatskiv R., Tiagulskyi S., Grym J., Vaniš J., Bašinová N., Horak P., ... & Vrňata M.**, Optical and electrical characterization of CuO/ZnO heterojunctions, Thin Solid Films. 693 137656 (2020).

2. **Petrov, V. V., Sysoev, V. V., Ignatieva, I. O., Gulyaeva, I. A., Volkova, M. G., Ivanishcheva, A. P., Khubezhov, S.A., Varzarev Y. N. Bayan, E. M.**, Nanocomposite Co_3O_4-ZnO thin films for photoconductivity sensors. Sensors. 23(12) 5617 (2023).

Features of the reduced graphene oxides: spectral and conductive properties

M.E. Ilin [1,2✉], **A.S. Toikka** [1,2], **N.V. Kamanina**[1,2,3]

[1]Saint Petersburg Electrotechnical University "LETI", Russia;

[2] Department of Advanced Development, Petersburg Nuclear Physics Institute, National Research Center "Kurchatov Institute", Russia

[3]Lab for Photophysics of Nanostructured Materials and Devices, Joint Stock Company Scientific and Production Corporation S.I. Vavilov State Optical Institute;

✉ilin_matwei@mail.com

Abstract.

This article compares the spectral properties of the reduced graphene oxide films with different thickness values obtained using spin-coating method on a glass substrate. Increasing the layer thickness leads to a decrease in the film resistance and light transmittance, so a compromise between the conductivity and light transmittance is required to use such films as the translucent contacts. For samples with different number of the layers the transmittance in the IR range of the unpolarized light incident perpendicular to the surface and reflected at an angle of 45 degrees was measured. Using this data the absorption for each sample was achieved and extended area of the application is proposed.

Keywords: graphene oxide, spin coating, IR spectral range, surface features, resistivity

Funding: This research has been partially supported by the Russian Science Foundation, grant number 328 24-23-00021

Introduction

Graphene oxide (GO), first obtained by Oxford scientist Benjamin Brodie in 1859 [1] is an affordable and promising material for the implementation in modern optoelectronics. It can be presented in both dielectric and conductor states. Standard graphene oxide is a solution of the graphene layers with the oxide-containing groups [2]. It has high light transmittance, relatively small edge angle of the flow and high resistivity of GOhm or more. Reduced graphene oxide is obtained by heating the sample to the temperatures of 170 degrees Celsius and above [2] or by other methods of the local energy transfer. Thus, during heated, the decrease is observed in the number of the oxide-containing bonds that increase the forbidden zone and reduce the conductivity of the structure [3]. As graphene oxide is reduced, its light transmission deteriorates and its conductivity increases.

Due to importance of finding compromise between conductivity and transmittance, this work compares the near- and mid-IR ranges spectrums of the GO samples with different thickness and hence – obtained resistance.

Materials and Methods

The graphene oxide used in this work is an original modification of the Hammers-Offeman method manufactured by NanoTechCentre Ltd (Tambov, Russia). Samples with the following values of the free surface energy (FSE) were used as the glass substrates: dispersive component $\gamma_s(d)$ = 45.8-48.3 mJ/m^2, polar component $\gamma_s(p)$ = 10.7-11.0 mJ/m^2.

Thin graphene oxide films on the glass substrates using spin-coating method at the speed of 4300 rpm multiple times was formatted. After one cycle of coating (one layer), the sample was exposed to the heat at 230 degrees Celsius and the resistance of the film was measured. It is known that the resistance of a film decreases with the film thickness increasing. Four samples with different number of layers were prepared.

To obtain the transmittance and reflection data the FTIR-spectrometer FSM-1202 was used. Transmittance in the IR range of unpolarized light with the wavelength of 1000-2400 nm incident perpendicular to the surface and reflected at an angle of 45 degrees was measured.

Results and Discussion

The results of the transmittance and reflection spectrometry are shown on figure 1. As was expected, the average transmittance on entire range decreases by about 10%; the reflection increases by 3-6% with increasing thickness on 10 nm.

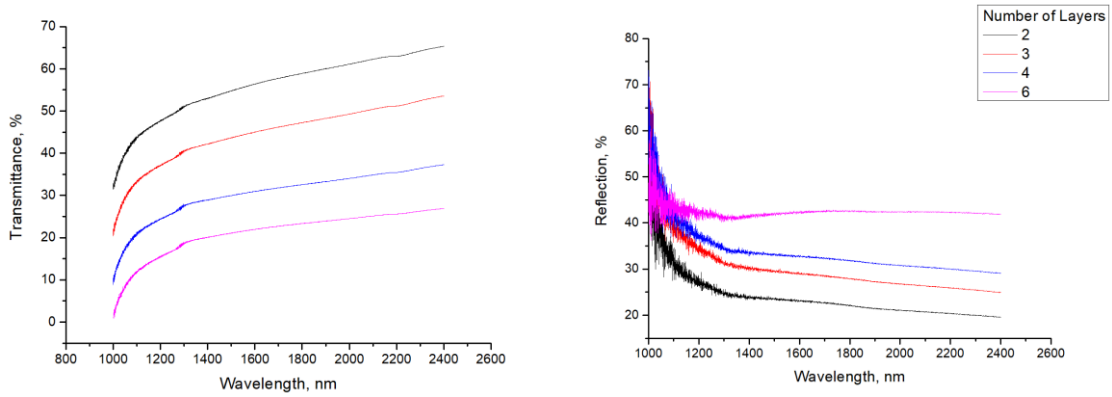


Fig.1. Transmittance and Reflection of RGO samples with different number of layers

Obtained absorption is shown on figure 2. The minimal average value of absorption is 21% with 2 layers. Each layer ads about 5-7% to that value.

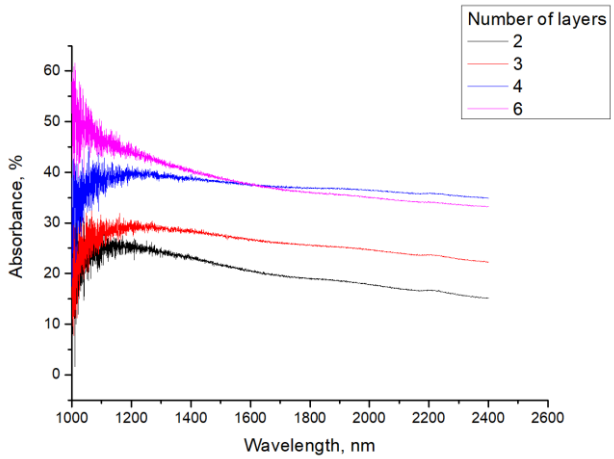


Fig2. Absorption of RGO samples with different number of layers

The results presented can extend the area of the application of the reduced graphene oxide, for example, in the optical limiting process use. This is very important to protect the human eyes and technical devices from high laser irradiations. Also with achieving compromise between transmittance and resistance, it can be possible to integrate reduced graphene oxide films in liquid crystal (LC) schemes. Orienting layers that being used in classical LC displays have a limitation on the electrical consumption due it material properties. With reduced oxide thin contact films removing orienting layer in classical liquid crystal schemes lower values of the voltage falling on RGO layer can be achieved.

Conclusion

In this work, the experimental dependences of the transmittance and reflectance of the RGO films with different number of the layers and thickness in the infrared (1000-2400 nm) ranges were measured. Based on the obtained data, the absorption distribution for each sample was found. As a result, the samples have similar dependences. With the layer thickness increasing, the transmittance (about 10%), and reflection (3-6%) decreases and the light absorption (5-7%) increases. Transmittance has a positive dispersion dependence on the wavelength. For the reflection and absorption spectra that dependence is negative.

REFERENCES

1. **Loh, K. P., Bao, Q., Eda, G., Chhowalla, M.** (2010). Graphene oxide as a chemically tunable platform for optical applications. Nature Chemistry, 2(12), 1015–1024**.**

2. **Schöche, S., Hong, N., Khorasaninejad, M., Ambrosio, A. et.al** (2017). Optical properties of graphene oxide and reduced graphene oxide determined by spectroscopic ellipsometry. Applied Surface Science, 421, 778–782.

3. **Nasehnia, F., Mohammadpour Lima, S., Seifi, M., & Mehran, E.** (2016). First principles study on optical response of graphene oxides: From reduced graphene oxide to the fully oxidized surface. Computational Materials Science, 114, 112–120.

Random lasing in hydrothermal ZnO structures

S. A. Kadinskaya[1,2]✉, V. M. Kondratev[1,2], A. V. Nikolaeva[1], I. Kh. Akopyan[3], A. Yu. Serov[3], M. E. Labzovskaya[3], S. V. Mikushev[3], B. V. Novikov[3], I. V. Shtrom[3,4], A. D. Bolshakov[1,2,3,5]

[1] Alferov University, St. Petersburg, Russia
[2] Moscow Institute of Physics and Technology, Dolgoprudny, Russia
[3] Saint Petersburg State University, St. Petersburg, Russia
[4] IAI RAS, St. Petersburg, Russia
[5] Yerevan State University, Yerevan, Armenia
✉skadinskaya@bk.ru

Abstract. We demonstrate optically pumped lasing in ZnO grown via hydrothermal method. This study suggests the effective use of zinc oxide as a basis for a light-emitting device.

Keywords: zinc oxide, hydrothermal, photoluminescence

Funding: Ministry of Science and Higher Education of the Russian Federation: agreement 075-03-2023-106, project FSMG-2021-0005; Grant FSRM-2023-0009.

Research project of St. Petersburg State University: № 95446496, № 95440344.

Introduction

Zinc oxide (ZnO) is one of the promising materials for development of UV emitters due to the band gap (3.37 eV at room temperature) and high exciton binding energy (60 meV) [1]. In addition, ZnO is inexpensive, relatively abundant, chemically stable, easily synthesized, and non-toxic. Although a wide variety of ZnO-based light-emitting devices (LEDs) have been developed so far, their performance, light-emitting ability, and production technology are still below expectations.

Synthesis

Hydrothermal synthesis is a method of growing various materials and compounds, based on the use of physical and chemical processes that take place in aqueous solutions at slightly elevated temperatures often used to obtain ZnO nanostructures [2].

In our work, silicon substrates Si (111) are used for the hydrothermal synthesis of ZnO nanostructures since this material is known to be the most often used in nanoelectronics. Zinc acetate is used as a seed layer material. The growth solution consists of equimolar aqueous solutions of $Zn(NO_3)_2$ and hexamethylenetetramine (HMTA).

Results

The samples were placed in a closed-cycle helium cryostat (Janis Research Company, USA). The sample temperature was about 10 K. The PL was excited by a He-Cd laser (λ = 325 nm, excitation power W = 50 kW·cm^{-2}) and by an ultraviolet solid-state laser LCM-DTL-374QT (λ = 355 nm). The excitation power of this laser was varied in the range from 1 to 800 kW·cm^{-2}. The threshold generation value was 95 kW·cm^{-2}.

Upon excitation and recording of luminescence, narrow lines in the spectral region $\lambda \simeq 373$–376 nm are observed in the PL spectra (Fig. 1). A cluster of disoriented zinc oxide crystals forms a closed circuit that acts as a resonator, which leads to the formation of narrow lines in the photoluminescence spectra. The spectral position of these lines indicates that laser generation probably occurs in the P band region of the exciton–exciton interaction [3].

Laser generation is observed at different points of the sample (Fig.1), which indicates the good quality of the synthesized structures.

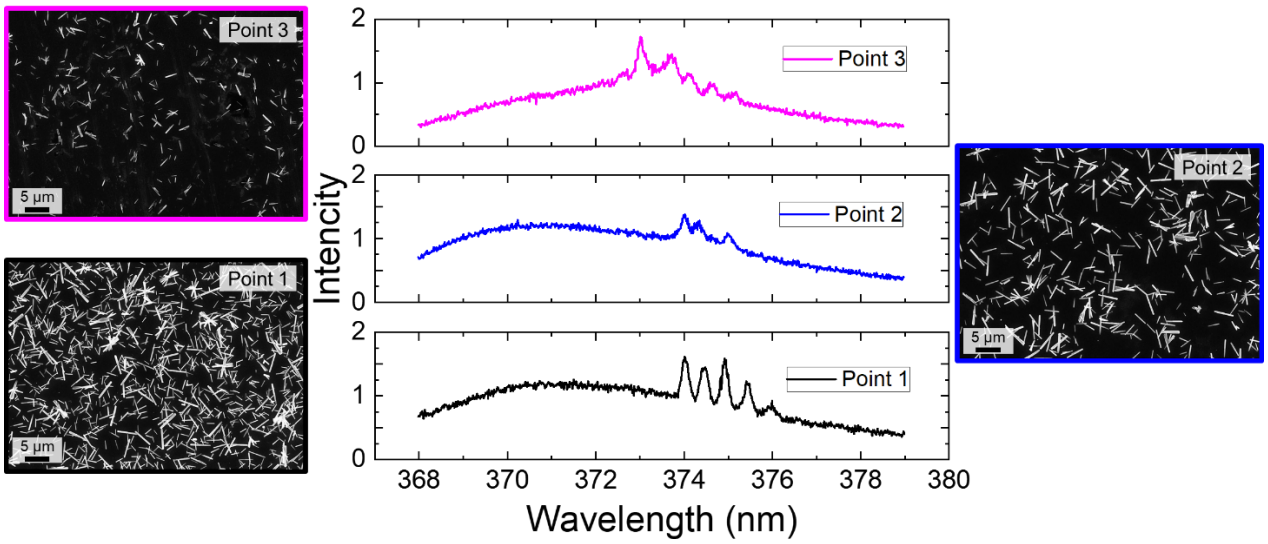


Fig. 1. Photoluminescence spectra and SEM images taken at different points of the synthesized sample.

Conclusion

The results show that a simple hydrothermal synthesis method is promising for fabricate efficient light-emitting devices based on ZnO.

Acknowledgments

S.A.K. acknowledge financial support of the synthesis from the Ministry of Science and Higher Education of the Russian Federation (FSRM-2023-0009). V.M.K acknowledges financial support of the microscopic studies by the Ministry of Science and Higher Education of the Russian Federation (agreement 075-03-2023-106, project FSMG-2021-0005). A.D.B. acknowledges Saint Petersburg State University for a research project № 95446496. I.V.Sh. acknowledges Saint Petersburg State University for a research project № 95440344.

REFERENCES

1. **Özgür Ü., Alivov Ya. I., Liu C., Teke A., Reshchikov M. A., Doğan S., Avrutin V., Cho S-J and Morkoç H.,** A comprehensive review of ZnO materials and devices, Journal of Applied Physics 98 (2005) 041301.

2. **Xu H. Y., Wang H., Zhang Y. C., He W. L., Zhu M. K., Wang B., Yan H.,** Hydrothermal synthesis of zinc oxide powders with controllable morphology, Ceramics International 30(1) (2004) 93-97.

3. **Klingshirn C., Fallert J., Zhou H., Sartor J., Thiele C., MaierFlaig F., Schneider D., Kalt H.,** 65 years of ZnO research – old and very recent results, Phys. Status Solidi B 6 (2010) 1424.

Ion exchange for obtaining second-order nonlinearity in glass

G. Kan [1,2]✉, I.V. Reshetov [1,2], A.N. Terpitskiy [1], S.A. Scherbak [1,2]

[1] Alferov University, Khlopina 8/3, St. Petersburg, Russia

[2] Peter the Great St. Petersburg Polytechnic University, Polytechnicheskaya 29, St. Petersburg, Russia

✉kan@spbau.ru

Abstract. We demonstrate that the use of a simple and well-known technique of ion exchange in glass makes it possible to create structures capable of accumulating nonequilibrium electric charge. Electric field generated by this charge causes the appearance of the second-order optical nonlinearity in the initially isotropic glass. The charge and discharge of the formed ion-exchange structure are manifested in the dynamics of current flowing through the glass and the generation of the second harmonic of laser radiation. This approach opens up previously unexplored possibilities for creating, tailoring and controlling second harmonic generation in glasses.

Keywords: ion-exchange, Maxwell-Wagner effect, EFISH, second harmonic generation.

Funding: The study was funded by the Ministry of Science and Higher Education of Russian Federation, project FSRM-2023-0009.

Introduction

The functionality of initially isotropic glasses can be expanded for nonlinear optics applications via inducing the second-order optical nonlinearity (SON) initially forbidden by the central symmetry of glasses. SON can be provided by thermal poling (TP) which is the application of a DC voltage to a heated glass [1] followed by cooling the glass under the voltage. TP leads to the accumulation of nonequilibrium charge in the glass, which electric field mixed with the third-order nonlinearity presenting is responsible for the second optical harmonic generation (SHG) in the glass [2]. However, applying a DC voltage even at room temperature to the interface of media differing in dielectric constant and conductivity also leads to the accumulation of a charge, and this is known as the Maxwell-Wagner (M-W) effect [3]. Electric field generated by this charge allows in isotropic media a phenomenon known as EFISH (Electric-Field Induced Second-Harmonic) [4] similarly to the SHG in thermally poled glasses.

Ion exchange (IE) can also be used to create a conductivity difference in a glass by formation gradient profile of diffusion, and subsequent DC voltage application should also lead to M-W charge accumulation, the EFISH effect and the SHG, respectively. So, the aim of this article is to test and characterize SHG in ion-exchanged glasses.

Materials and Methods

In this study, we used soda-lime glass slides. The samples were subjected to IE at 365 °C for 8 hours in molten KNO_3 salt. After IE, potassium and sodium concentration profiles along the sample cut were characterized with EDX spectroscopy. We measured current flowing through the specimen while applying 1300 V DC to it (charging current) and after the voltage was turn off (discharging current) using picoammeter. We used transparent ITO electrodes for simultaneous optical experiments. Particularly, we measured temporal behavior of the second harmonic (SH) signal generated by the specimen under 1.064 μm laser radiation. Details of the optical setup can be found elsewhere [5].

Results and Discussion

First, the sodium and potassium concentration distribution in IE glass was investigated. Normalized concentration profiles are presented in Fig. 1a. One can see that the sum of the concentrations is about constant which shows that K^+ occupied the places if Na^+ ions after the IE. The estimated penetration depth of potassium ions is ~5 μm. There is a noticeable incomplete sodium replacement at the surface, which is probably due to the conditions of the IE, and this requires more detailed study. The resulting structure was then assessed for the possibility of nonequilibrium charge accumulation. For this, the temporal dependence of current was measured

(Fig. 1b), which showed that the time required to charge the sample was about 30 minutes. Afterwards, the contacts were short-circuited and the discharge curve was recorded, discharging time being similarly ~30 minutes. The dynamics of the second harmonic intensity also made possible estimating the saturation SH decay time as 30 minutes (Fig. 1c). Besides, we compared the SH signal level from the sample with one from TP soda-lime glasses and found these levels very close. After short-circuiting the sides of the sample, the SH intensity decreased, but the behavior of these decrease differed from expected. This phenomenon still needs to be studied.

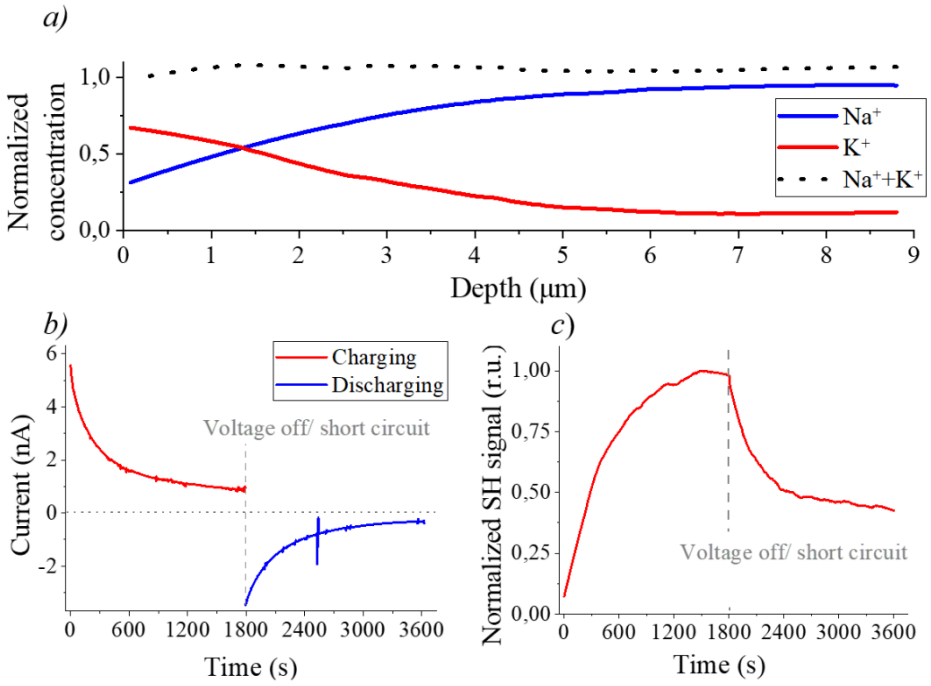


Fig. 1. Concentration profiles, obtained by EDX spectroscopy measurements (*a*), Charging current under applied voltage and discharging current with short circuit after (*b*), SH dynamics under applied voltage and with short circuit after (*c*).

Conclusion

We have demonstrated for the first time a method for producing SON in glass using IE. Fundamentally, this opens up the possibility of controlling the amplitude characteristics of SH and relaxation processes in various ways (for example, by varying the IE parameters, using glass annealing, different types of ions).

Acknowledgments

The authors thank V.P. Kaasik for the assistance in the second harmonic measurements. The study was supported by the Ministry of Science and Higher Education of Russian Federation, project FSRM-2023-0009.

REFERENCES

1. **Myers, R.A.; Mukherjee, N.; Brueck, S.R.J.** Large second-order nonlinearity in poled fused silica. Opt. Lett. 1991, 16, 1732, doi:10.1364/OL.16.001732.
2. **Kazansky, P.G.; Russel, P.S.J.** Thermally poled glass: frozen-in electric field or oriented dipoles? Opt. Commun. 1994, 110, 611–614.
3. **Wagner, K.W.** Erklärung der dielektrischen nachwirkungsvorgänge auf grund maxwellscher vorstellungen. Arch. für Elektrotechnik 1914, 2, 371–387.
4. **Guillet de Chatellus, H.; Freysz, E.** Measurement of the third-order susceptibility of glasses by EFISH of femtosecond pulses. Opt. Express 2001, 9, 586, doi:10.1364/oe.9.000586.
5. **Reshetov, I. V; Zhurikhina, V. V; Lipovskii, A.A.; Scherbak, S.A.** Second harmonic generation by surface of poled glasses: modeling and measurement of Maker fringes. St. Petersbg. State Polytech. Univ. Journal. Phys. Math. 2021, 14, 95.

The influence of chiral ligands on the optical properties of $AgBiS_2$ nanocrystals

S. P. Karamysheva [1✉], **E. V. Ushakova** [1,2], **S. A. Cherevkov** [1]
[1] ITMO University, Saint-Petersburg, Russia;
[2] City University of Hong Kong, Hong Kong SAR, China
✉spkaramysheva@itmo.ru

Abstract. Currently, semiconductor nanocrystals are considered as a promising material for use in many fields, especially for the fabrication of photodetectors, solar cells, and displays. Among them, there is a special subclass of biocompatible and eco-friendly ones – nanocrystals of a ternary composition based on silver, indium or bismuth, and sulfur. The optical and electrical properties of such structures are considered special, which is why they have found wide application in many fields. It can be controlled by changing their shape, size, and making surface modifications. Thus, in this work, a synthesis method of nanostructures of ternary compounds based on silver, bismuth, and sulfur with chiral molecules was developed, and the influence of chiral molecules on their spectral characteristics was studied. A study of the electronic structure of the synthesized nanocrystal-chiral ligand systems using circular dichroism and magnetic circular dichroism spectroscopy together with their morphological properties was provided. The developed nanomaterial is promising for use as an active material in chiral photodetectors.

Keywords: nanocrystals, ternary compounds, chirality, circular dichroism, magnetic circular dichroism, atomic force microscopy

Funding: This study was funded by the Federal Academic Leadership Program "Priority 2030".

Introduction

Nowadays, semiconductor nanocrystals (NCs) are considered as a material for various current tasks in photovoltaics, sensorics, and other industries due to their unique optical and electrical properties. To expand their applications in biomedicine and in connection with concern for the environment, classical NCs based on mercury, cadmium, and tellurium are gradually being replaced by NCs of ternary compounds of the composition I-V-VI_2 and I-III-VI_2. Such nanomaterials have properties that can be controlled by changing their shape [1] and composition [2], their synthesis route, or surface functionalization [3]. Thus, in this work the $AgBiS_2$ NCs synthesis method was developed, and the influence of chiral ligands (CLs) on the $AgBiS_2$ NCs spectral characteristics was examined.

Materials and Methods

The synthesis of $AgBiS_2$ NCs was based on the method reported in [4] with some modifications using several types of CLs: L-Cysteine (L-Cys), L-Phenylglycine (L-PhG), L-Tryptophane (L-Try), and L-Glutathione (L-Glu). Reference samples that did not contain CLs were also prepared by this method. Instead of CLs, thioglycolic acid (TGA) was used in the synthesis.

The morphology of the obtained NCs was studied by atomic force microscopy (AFM) using a Solver PRO-M atomic force microscope with a Smena measuring module (NT-MDT, Russia). The absorption properties of the obtained samples were studied using a UV-3600 spectrophotometer (Shimadzu, Japan). The circular dichroism (CD) and magnetic circular dichroism (MCD) spectra were recorded on a JASCO J-1500 spectrometer.

Results and Discussion

A protocol for the synthesis of $AgBiS_2$ NCs-CLs nanostructures was developed and presented in Figure 1. Four L-CLs types were used here (see Materials and Methods).

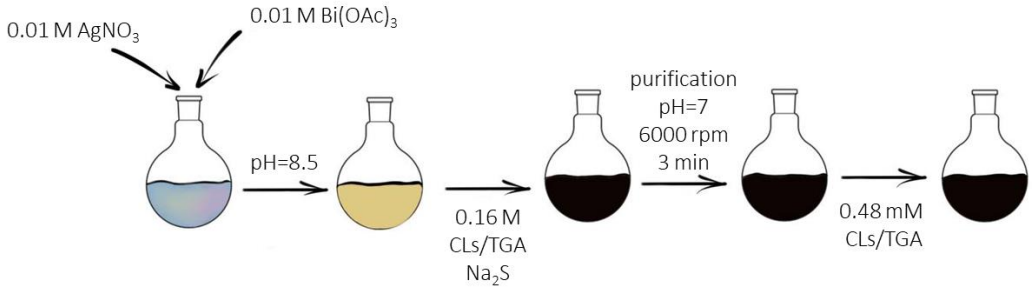


Fig. 1. Scheme of syntheses of $AgBiS_2$ NCs-CLs nanostructures

These performed reactions showed that the presence of an SH-group in the chiral molecule is necessary for the formation of NCs, otherwise aggregation of nanoparticles occurs at the stage of adding CLs with the formation of large flakes. That is why, as a result of the reaction with L-Try and L-PhG, the previously described effect occurred. Analysis of NCs using AFM showed that their average size does not exceed 25±1 nm. CD and MCD spectra of NCs with L-Cys or L-Glu did not coincide with the reference spectra of free L-Cys and L-Glu molecules. In the case of a NCs with L-Cys, when a magnetic field is applied, the absorption spectrum at the first optical transition (~325 nm) does not change, but at the second transition (~250 nm), the optical density is decreased twice while CD and MCD spectra coincide. For NCs with L-Glu, the magnetic field influences the optical density at first and second optical transitions similarly as for the NCs with L-Cys. At the same time, Zeeman splitting obviously occurs and the spectrum changes sign depending on the sign of the magnetic field. The first derivatives of the absorption spectra are different from both CD and MCD spectra for both NCs samples.

Conclusion

In this study, $AgBiS_2$ NCs with two types of chiral molecules (L-Cys and L-Glu) were synthesized. The study of the electronic structure of NCs using the of CD and MCD spectroscopy made it possible to study the nature of the broadband absorption of such nanostructures in more detail, as well as to consider in detail the influence of chiral ligands on the excitonic transitions of $AgBiS_2$ NCs. Taking into account high optical density in a wide spectral range, developed NCs are promising for the fabrication of photodetectors.

Acknowledgments

The authors express their gratitude to the ITMO University Core Facility Center “Nanotechnologies”. The authors thank the Federal Academic Leadership Program “Priority 2030” for financial support.

REFERENCES

1. Dai H. et al. A paper-based photoelectrochemical aptsensor using near-infrared light-responsive $AgBiS_2$ nanoflowers as probes for the detection of Staphylococcus aureus in pork // Talanta. Elsevier B.V. – 2024. – Vol. 266.
2. Martín-Rodríguez R., Geitenbeek R., Meijerink A. Incorporation and luminescence of Yb3+ in CdSe nanocrystals // J Am Chem Soc. – 2013. – Vol. 135. – № 37. – P. 13668–13671.
3. Kuznetsova V. et al. Ligand-induced chirality and optical activity in semiconductor nanocrystals: Theory and applications // Nanophotonics. De Gruyter Open Ltd. – 2020. – Vol. 10. – № 2. – P. 797–824.
4. Branzi L. et al. Chiral non-stoichiometric ternary silver indium sulfide quantum dots: investigation on the chirality transfer by cysteine // Nanoscale. Royal Society of Chemistry. – 2022. – Vol. 14. – № 33. – P. 12174–12182.

Metal–dielectric resonator integrated in an asymmetric slab wavegude for spatiotemporal optical vortex generation

A. I. Kashapov [1,2]✉, **E. A. Bezus** [1,2], **D. A. Bykov** [1,2], **L. L. Doskolovich** [1,2]

[1] Image Processing Systems Institute, National Research Centre "Kurchatov Institute", 151 Molodogvardeyskaya st., Samara, 443001, Russia

[2] Samara National Research University, 34 Moskovskoe shosse, Samara, 443086, Russia

✉kashapov.ai@ssau.ru

Abstract. We theoretically and numerically demonstrate an efficient approach for generating a spatiotemporal optical vortex (STOV) beam in an asymmetric dielectric slab waveguide. We consider a metal-dielectric structure consisting of several metal strips "buried" in the waveguide core layer. The presented rigorous numerical simulation results are in good agreement with the developed theoretical model.

Keywords: spatiotemporal optical vortex, integrated optics, asymmetric dielectric slab waveguide, spatiotemporal differentiation.

Funding: This work was funded by the Russian Science Foundation (project 24-12-00028).

Introduction

An optical vortex (OV) beam is a special type of monochromatic optical beams possessing a zero in the field amplitude and a screw-type phase dislocation. Recently, a new class of OV beams has been discovered in optics, referred to as spatiotemporal optical vortex (STOV) beams [1]. In contrast to the conventional OV beams, STOV beams are essentially polychromatic and carry orbital angular momentum, which is orthogonal to the beam propagation direction. STOV beams have many important potential applications including optical trapping, super resolution microscopy, and free-space telecommunications, among others.

Results and Discussion

As an integrated nanophotonic element intended for the generation of an STOV in the waveguide layer, we propose to use a "three-strip" metal-dielectric structure consisting of three gold (Au) strips "buried" in the waveguide (Fig. 1). We theoretically studied the transfer function of the structure and obtained that generating a spatiotemporal optical vortex requires the difference between the arguments of the complex coefficients at the "spatial" and "temporal" linear terms of the transfer function of the structure to equal $\pi / 2$.

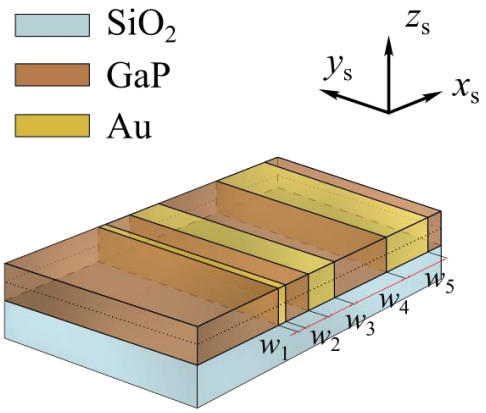


Fig. 1. Geometry of the considered integrated structure consisting of several metal strips "buried" in the core layer of an asymmetric dielectric slab waveguide

We consider a 100 nm thick gallium phosphide (GaP) waveguide layer sandwiched between air and silicon dioxide (SiO2) cladding (see Fig. 1). Using a specially developed optimization algorithm which involved multiple solution of the "direct" diffraction problem (simulation of the diffraction of TE-polarized incident modes on the structure), which was carried using an in-house implementation of the aperiodic Fourier modal method adapted to the solution of the problems of integrated optics [2], we obtained the following structure satisfying the STOV generation conditions at the angle of incidence $\theta = 65°$ and the free-space wavelength $\lambda = 630$ nm: $w_1 = 25.1$ nm, $w_2 = 53.2$ nm, $w_3 = 64$ nm, $w_4 = 222$ nm, and $w_5 = 125$ nm (see Fig. 1).

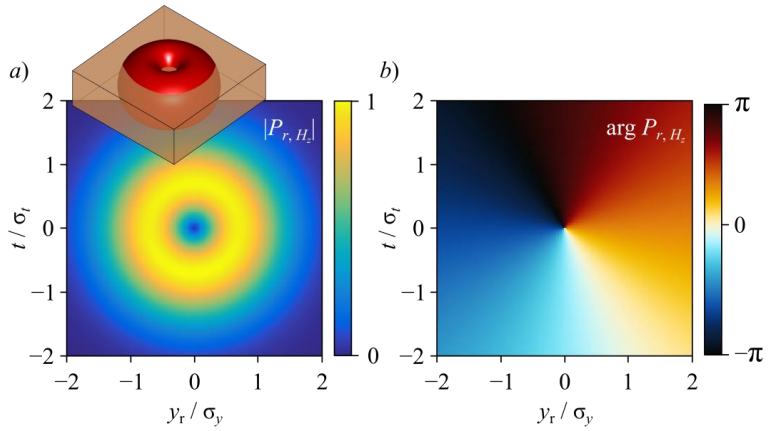


Fig. 2. Amplitude (absolute value) (*a*) and phase (argument) (*b*) of the numerically calculated envelope of the H_z component of the reflected optical pulse

Figures 2(*a*) and 2(*b*) show the absolute value and phase of the numerically calculated envelope of the H_z component of the reflected pulse at the central plane of the waveguide core layer (at $z_c = 0$) for an incident optical pulse described by a Gaussian function ($\sim exp[-t^2/\sigma_t^2 - y^2/\sigma_y^2]$, where $\sigma_t = 2.8$ ps and $\sigma_y = 14$ μm). From these figures, it is evident that the reflected optical signal indeed contains a spatiotemporal optical vortex. The inset to Fig. 2(*a*) shows the three-dimensional envelope of the reflected pulse in the coordinates associated with the reflected optical pulse at the 10^{-3} level. The numerically calculated and model envelopes (not shown here for the sake of brevity) are in a good agreement: the normalized root-mean-square deviation between them amounts to only 0.49%.

Conclusion

We investigated theoretically and demonstrated numerically the generation of an STOV beam in an asymmetric dielectric slab waveguide. In the proposed integrated geometry, the generation of an STOV beam is performed upon reflection of a spatiotemporal optical pulse with a Gaussian envelope propagating in the asymmetric waveguide from a metal-dielectric structure consisting of several metal strips "buried" in the waveguide core layer. The rigorous numerical simulation results of the designed three-strip metal-dielectric structure fully confirmed the obtained theoretical results and demonstrated the generation of an STOV in the slab waveguide.

REFERENCES

1. **Wan C., Chong A., Zhan Q.**, Optical spatiotemporal vortices, eLight. 3 (2023) 11.

2. **Silberstein E., Lalanne P., Hugonin J.-P., Cao Q.**, Use of grating theories in integrated optics, J. Opt. Soc. Am. A. 18 (2001) 2865–2875.

Study of the photoluminescence properties of subcritical InAs/GaAs quantum dots formed onto structured substrates

D. V. Kirichenko[1]✉, I. S. Makhov[2], S. V. Balakirev[1], N. V. Kryzhanovskaya[2], M. S. Solodovnik[1]

[1] Laboratory of Epitaxial Technologies, Southern Federal University, Taganrog, Russia
[2] International Laboratory of Quantum Optoelectronics, HSE University, St. Petersburg, Russia
✉dankir@sfedu.ru

Abstract. In this work we study the optical properties of InAs quantum dots grown on the GaAs(001) nanostructured surfaces at sub-critical thickness of deposition. For substrate nanostructuring we used technique based on two-stage thermal desorption of native GaAs oxide under molecular arsenic flux. The results of experimental studies showed the possibility of quantum dots formation on structured surfaces at equivalent deposition thicknesses in the range of 0.5-1.5 ML. In this case, quantum dots are formed predominantly in nanoholes on the surface and are high inhomogeneous in size. At the same time measurements by photoluminescence spectroscopy showed broad (900 – 1100 nm) emission spectrum for quantum dot only for sample with 1.5 ML of InAs. We hypothesize that at smaller thicknesses, the formed quantum dots become smaller than the minimum acceptable sizes due to segregation effects during overgrowth. The use of a structured surface also makes it possible to suppress the wetting layer formation – in the photoluminescence spectra there are only lines of platelets, apparently formed on morphological inhomogeneities outside the holes.

Keywords: native oxide, quantum dots, A3B5, molecular beam epitaxy, nanopatterning

Funding: This work was supported by the Russian Science Foundation Grant No. 22-79-10251 and by the Ministry of Science and Higher Education of the Russian Federation Grant No. FENW-2022-0034 at the Southern Federal University.

Introduction

The production of low-density quantum dots (QD) is becoming increasingly popular since they underlie the sources of single and entangled photons that act as the elemental basis for quantum communications and computing. One of the directions for obtaining low density quantum dots is the use of preliminary structuring of the growth surface with subsequent deposition of the quantum dot material. In this case, the nanoholes formed on the surface subsequently act as nucleation centers for self-organizing nanostructures. Today, surface structuring methods have a number of limitations that affect the optical qualities of subsequently formed quantum structures, mainly due to contamination of the growth surface. In this work we experimentally demonstrate the possibility of obtaining relatively low-density self-organizing InAs/GaAs quantum dots obtained on the GaAs(001) nanostructured surfaces at sub-critical thickness of deposition with an emission range of up to 1100 nm.

Materials and Methods

For experimental studies, we used GaAs(001) substrates with a pre-grown GaAs/AlGaAs structure, on the surface of which native oxide film was then formed in air. To form nano-sized holes, we used technique based on two-stage thermal desorption of native GaAs oxide under molecular arsenic flux. Control of oxide removal was carried out in-situ using an integrated RHEED system. At the next stage, an InAs layer with an equivalent thickness in the range of 0.5 – 1.5 ML was deposited. To study the optical properties, a GaAs/AlGaAs heterostructure was grown on top of the structures prepared in this way. Uncapped structures were analyzed using scanning electron and atomic force microscopy. The optical properties were analyzed using photoluminescence spectroscopy.

Results and Discussion

SEM- and AFM-analysis of the surface of the uncapped samples showed that for all samples deposited material accumulates in the nano-sized holes formed at the nanopatterning stage, thereby

forming an array of inhomogeneous QDs. In this case, decreasing the amount of InAs from 1.5 ML to 1.0 ML leads to a pronounced decrease in their size. And it was found that the structures do not assemble into obvious 3D objects after deposition of 0.5 ML. However, according to AFM data, a decrease in the hole depth was observed, which indicates their filling with deposited material and the localization of nanostructures within them. However, relevant assessment of the size of such structures is difficult using AFM or SEM.

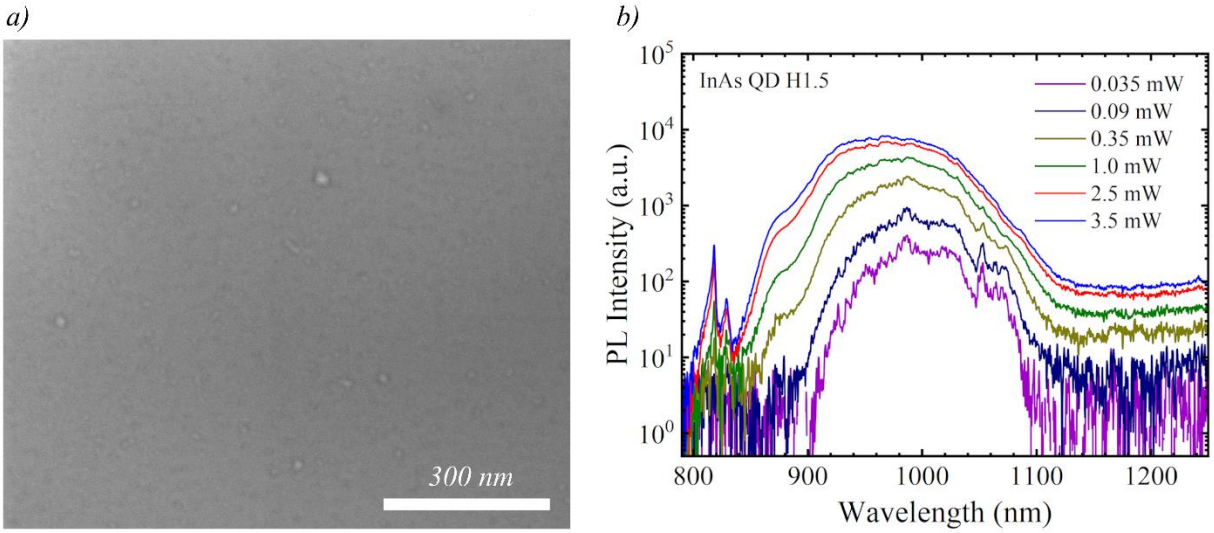


Fig.1 – SEM images of a structured GaAs surface after deposition of 1.5 ML of InAs (a), PL spectra for the same sample at different excitation power (b)

Figure 1b shows the photoluminescence spectra at different excitation powers for a sample with 1.5 ML of InAs. It is noticeable that the spectrum contains a broad band in the wavelength range of 870 – 1100 nm, which can be associated with In(Ga)As nanostructures. Analysis of the PL spectra of this sample shows that with increasing excitation power, in addition to the QD peaks (900 – 1100 nm), a low-intensity short-wavelength shoulder (850 – 900 nm) appears in the spectrum. We associate this feature with the emission of so-called platelets – two-dimensional structures formed on morphological inhomogeneities in the spaces between the hole with QDs. In addition, there is no peak of the wetting layer in the spectrum, which indicates the suppression of its formation during deposition on a structured surface.

On samples with smaller thicknesses (1.0 and 0.5 ML), the PL spectra do not have any features characteristic of QD. This may be due to the fact that during the overgrowth process, part of the QD material segregates, which leads to a decrease in their effective size below the limit at which an electronic level exists in a quantum-sized system.

Conclusion

Thus, studies have been carried out on the formation and optical properties of subcritical InAs/GaAs quantum dots on structured substrates. The possibility of obtaining subcritical QDs of low density, emitting in the range of 900 – 1100 nm, has been demonstrated. The results obtained can be used to develop a technological process for the formation of low-density InAs QDs in the O- and, in the future, C-bands without a wetting layer.

Two-dimensional PbSe/PbS near-infrared heterostructures with perovskite passivated surface

D.I. Klimenko [1✉], **A.A. Babaev** [1], **I.D. Skurlov** [1], **S.A. Cherevkov** [1]
[1] ITMO University, Saint-Petersburg, Russia
✉ohiko27@gmail.com

Abstract. In this work, the influence of passivation by lead-halide perovskite $CsPbX_3$ (X = Br, I, Cl) on optical, luminescent, structural and morphological properties of semiconductor two-dimensional quantum PbSe/PbS heterostructures of core/shell and core/wings types emitting in the near-infrared region is investigated. It is shown that passivation of the two-dimensional quantum structures surface leads to an improvement of their crystallinity expressed as a decrease in the full width at half maximum (FWHM) of the PbSe band in the Raman spectra of the nanoplatelets (NPls); in addition, the build-up of the perovskite shell reduces the number of trap states, which leads to a decrease in the radiation-free relaxation constant and an increase in the mean lifetime of photoluminescence, while increasing the quantum yield of luminescence. Thus, this work provides important information on how to improve the passivation of IR heterostructures by coating with an inorganic perovskite ligand for photovoltaic or other optoelectronic applications.

Keywords: nanoplatelets, perovskite, passivation, heterostructures

Funding: This study was funded by the Russian Science Foundation, Project No. 21-73-10131.

Introduction

Semiconductor quantum two-dimensional nanocrystals and heterostructures based on them with optical transitions in the near-infrared region are a promising class of nanostructures used in various optoelectronic and photonic devices. In the last decade, progress in their synthesis techniques and optical properties was made, but they are still inferior to their analogues in the visible range, which necessitates an in-depth methods study for obtaining this type of structures and studying their fundamental properties. This work discusses the results of optimization of structural and optical properties of two-dimensional PbSe/PbS heterostructures of core/shell and core/wing types by passivation of their surface with inorganic perovskite $CsPbX_3$ (X = Br, I, Cl).

Materials and Methods

The two-dimensional PbSe/PbS heterostructures of core/shell and core/wing types were obtained by cation exchange from initial CdSe/CdS heterostructures [1 - 3]. Passivation of the surface of PbSe/PbS heterostructures by inorganic perovskite $CsPbX_3$ (X = Br, I, Cl) was carried out by oleic acid replacement and subsequent phase transition, which occurred in the process of mixing a nonpolar solvent, toluene, containing PbSe/PbS NPls with a polar solvent, dimethylformamide (DMF), containing perovskite ink precursors. To investigate the properties of the samples, a series of films were deposited on the substrates by spin-coating and annealing in an inert atmosphere.

The absorption spectra of the samples were measured on a UV-Probe 3600 spectrophotometer (Shimadzu); the photoluminescence (PL) signal under excitation by a 633 nm laser was passed through an Acton SP2150i monochromator and recorded using an InGaAs/InP avalanche single-photon diode (Micro Photon Devices). To evaluate the luminescence attenuation kinetics, a complex consisting of a high-speed current amplifier FEMTO (Messtechnik) with a Tektronix TDS2022B oscilloscope (Beaverton) was used for excitation using a 532 nm Nd:YAG laser. The size and shape of the obtained two-dimensional heterostructures were controlled by scanning electron microscopy (SEM) using MERLIN (Carl Zeiss and investigated by Solver PRO-M (NT-MDT) atomic force microscopy (AFM). The chemical composition of the nanostructures was determined by energy dispersive X-ray spectroscopy (EDX) and IR spectroscopy. The films of two-dimensional nanoplatelets passivated with inorganic perovskite were also investigated by Raman spectrometer InVia (Renishaw).

Results and Discussion

NPls films passivated with bromine and chlorine perovskites, in accordance with the AFM and SEM images, have the worst uniformity, many cracks and other defects with high roughness values. The obtained iodine films are characterized by a porous structure, which is formed by individual nanoplatelets with maximum sizes reaching few microns. At the same time, studies of the photoluminescence (PL) signal distribution at different points of the film showed a deviation of the PL signal of 5%, which allows that the NPls have a uniform distribution within the film. Thus, iodine passivation was found to be the most suitable for the formation of thin films.

The Raman spectra indicates an improvement in the crystallinity of obtained heterostructures, because the passivation by perovskite leads to a decrease in the half-width of the characteristic peak corresponding to the LO-phonon of PbSe. EDX analysis of the elemental composition of films showed that the difference in the I to Br ratios in the two types of structures is probably due to differences in the cation exchange process of the initial NPls.

As a result of comparison of the PL spectra of perovskite-passivated films of both types of NPLs, it was revealed that in the case of iodine-containing perovskites, the shift of PL maxima compared to untreated NPLs is minimal and amounts to 26 nm. The use of chlorine-containing perovskites leads to broadening of the spectrum and its red shift. When NPls are treated with bromine-containing perovskite, in the case of the core/shell structure there is a slight shift to lower energies and an increase in the intensity of the PL signal, while in the case of the core/wings structure there is a more significant red shift and a decrease in the PL intensity compared to the iodine-containing analogue.

The build-up of iodine perovskite shell leads to the enhancement of the PL signal intensity and the increase of the relative quantum yield: for NPls of the core/shell type by 2.3 times, for the core/wings heterostructure by 2.7 times. However, perovskite passivation leads to an increase in the FWHM of PL band in the case of the core/shell structure by 10 meV and in the case of the core/wings NPls by 40 meV.

It was shown that the perovskite shell contributes to an increase in the mean lifetime of the photoexcited state, which is explained by a decrease in the excitation-free relaxation constant of the excited state because of a decrease in the number of trap states by passivation of surface defects.

Conclusion

Passivation by $CsPbI_3$ perovskite improves the optical properties of two-dimensional heterostructures, as well as the morphology of formed thin films based on them. In addition, the obtained films of core/shell heterostructures with perovskite matrix retain the spectral properties of the original film during long-term storage in atmospheric conditions.

Acknowledgments

This work was supported by the Russian Science Foundation, Project No. 21-73-10131.

REFERENCES

1. **Skurlov, I., Sokolova, A., Galle, T., Cherevkov, S., Ushakova, E., Baranov, A., Lesnyak, V., Litvin, A.** Temperature-Dependent Photoluminescent Properties of PbSe Nanoplatelets, Nanomaterials, Vol 10 (12) (2020) 2570.

2. **Kelestemur, Y., Guzelturk, B., Erdem, O., Olutas, M., Gungor, K., Demir, H. V.** Platelet-in-Box Colloidal Quantum Wells: CdSe/CdS@ CdS Core/Crown@ Shell Heteronanoplatelets, Advanced Functional Materials, Vol 26 (21) (2016) 3570-3579.

3. **Prudnikau, A., Chuvilin, A., Artemyev, M.** CdSe–CdS nanoheteroplatelets with efficient photoexcitation of central CdSe region through epitaxially grown CdS wings, Journal of the American Chemical Society, Vol 135 (39) (2013) 14476-14479.

SPATIAL LIGHT MODULATOR BASED ON ROTATING DISK FOR SINGLE-PIXEL IMAGING IN IR-RANGE

E. S. Lebedeva [1, 2] ✉, **M. S. Elezov** [3], **G.N. Goltsman**[1, 3]

[1]Department of Physics, Moscow State Pedagogical University, Moscow, 119992, Russia;
[2] National University of Science and Technology MISiS, Moscow, 119049, Russia
[3] National Research University Higher School of Economics, Moscow, 101000, Russia
✉ narniyall02@gmail.com

Abstract. A single-pixel camera is an innovative technology for obtaining a single-photon image using a radiation source, a spatial light modulator (SLM) and a single-photon detector. The main advantage of this type of camera is the ability to work with a wide range of radiation sources, single-photon sensitivity. Most types of SLM are suitable for working with the visible range, so it is necessary to create an SLM for working in the IR range. In this paper, we will describe an experiment of obtaining a single-photon image in the IR range with SLM based on the Nipkow disk.

Keywords: Single Pixel Imaging (SPI), Spatial Light Modulator (SLM), Superconductive Single Photon Detector (SSPD), disk, IR-range.

Introduction

The basis of any method of obtaining an image is the illumination of an object by a radiation source and the further transformation of the received optical signal into an image of the object. Digital cameras use a semiconductor photomatrix, consisting of photodiodes that convert optical signals into digital, while the spectrum of radiation sources is relatively narrow. Single-pixel imaging offers another way - the use of a Spatial Light Modulator (SLM) – the device, that turns the initial radiation into the series of the spatial spots [1, 2]. In this case images are produced by splitting the beam that illuminates the imaged object into sequences of binary patterns of different intensities, which are recorded by the single detector.

There are many types of the SLMs – Digital Micromirror Devices (DMDs), Light Emitting Diodes (LEDs), Liquid Crystal Devices (LCDs). But these SLMs has low speed of frame getting. To increase speed there is on more type of SLM. It is a rotating disk [3] with a mask of holes based on the Nipkow disk - a rotating circular plate who's spirally arranged holes sequentially scan the source beam. This type of SLM allows to get high speed frame getting, detect infrared photons.

In our work such SLM was developed and tested at 1550 nm - images of small metal object in the infrared range were obtained.

Experimental setup

The experimental setup consists of 4 main elements: a laser radiation source, electrical motor with rotating disk, an imaged object and a SSPD and two fiber collimators. Radiation source is 1550 nm laser. Leaving the source, the beam goes to the collimator through the fiber, then falls orthogonally on the SLM. The disc with the mask of holes were designed in the program, and cut out of cardboard covered with foil. The diameter of the disc is 105 mm, the size of the holes is 0.1 mm, the diameter of the beam is 3.3 mm, so a total of 33 holes were cut so that they could all scan the entire beam. The speed of rotation of the disk is controlled by the applied voltage. Rotating frequency was 64 Hz.

To determine the beginning of the first line in time, a synchronization system was used - a diode and a photodiode arranged so that the disk rotates between them. A special hole was cut on the disk so that when the diode shone through it, the first line was scanned. The signal from the photodiode went to the pulse generator, and from it to the counter.

Passing through the disk, the beam splits into a sequence of spots that illuminate the object and then goes to the output collimator, then goes through the fiber and get detected by the SSPD. For each recorded photon, the detector generates an electric pulse, which is registered by a time converted single photon counter (TCSPC). It outputs the dependencies of the received counts per second on the measurement time for each line. This numerical data is processed by a Python program, it converts the numbers into pixels of appropriate intensity according to the black-and-white scale and places them under each other, forming an image.

Results

Radiation source was IR-ranged, beam was round-shaped, its size was 3.3 mm, so imaged object's size was comparable with beam diameter. To simplify data processing in further experiments, firstly laser image without any object was pictured. Obtained result (fig 1(a)) is 33x516 pixels picture of the complete white spot.

Then small metallic object was placed between rotating disk and collimator – rectangular screwdriver tip (fig.1(b)). Screwdriver tip was fixed horizontally. Comparing its picture with the beam profile, it can be noticed, that screwdriver tip leaves rectangular dark spot right in the middle of the picture (fig.1 (c)).



Fig. 1. Results. a) Beam profile picture; b) Screwdriver tip; c) Picture of the tip

Conclusion

A single-pixel camera with a rotating disk as an SLM was designed and tested experimentally. Images of metal object in 1550 nm radiation were obtained. This proves the high efficiency of such cameras, which is very important for their further use, for example, for the study of cells of living biological tissues [4].

REFERENCES

1. **Edgar M.P., Gibson G.M., Padgett M.J.,** Principles and prospects for single-pixel imaging, Nature Photon. 13 (2019) 13–20.

2. **Duarte M. F. et al.**, Single-pixel imaging via compressive sampling, IEEE Signal Processing Magazine. 25 (2008) 83–91

3. **Hahamovich E., Monin S., Hazan Y., Rosenthal A.,** Single pixel imaging at megahertz switching rates via cyclic Hadamard mask, Nature Communications. 12 (2021) 4516.

4. **Studer V., Bobin J., Chahid M., Mousavi S.H., Candes E., Dahan M.,** Compressive fluorescence microscopy for biological and hyperspectral imaging, Proceeding of National Academy of Sciences. 109 (2012) E1679–E1687.

Numerical analysis of dispersive wave generation in glass whispering gallery mode resonators doped with plasmonic CuS nanoparticles

A. Y. Lunev [1✉], **E. A. Mikharev** [1], **A. I. Sidorov** [1,2], **P. A. Kostin** [1]

[1] Saint-Petersburg State Electrotechnical University «LETI», Saint-Petersburg, Russian Federation

[2] ITMO University, Saint-Petersburg, Russian Federation

✉ayulunyov@stud.etu.ru

Abstract. In this work, we study numerically the influence of plasmonic CuS nanoparticles on the optical properties of silicate glass and on the dynamics of generation of frequency combs in microcavities based on it. The optical properties of the composite under study were calculated using the effective medium theory in the Maxwell Garnett approximation. The Lugiato-Lefever model was used as a model to describe the dynamics of generation of frequency combs. In all cases the dispersion around the pump frequency shows parabolic behavior and is anomalous. The position of generated dispersive wave changes from 230 THz to 245 THz with increase in NP diameter. The free spectral range of the comb is equal to 218.8 GHz. Spectral width and dispersive wave position of the comb can be controlled by doping the WGM resonator material with plasmonic CuS NPs of different size.

Keywords: whispering gallery mode resonators, plasmonic nanoparticles, Kerr frequency comb, dispersive wave

Introduction

The unique characteristics of whispering gallery mode (WGM) resonators, such as extremely high quality factor and small mode volume, make them attractive for a wide range of applications, including sensors, lasers and, in particular, the generation of optical frequency combs[1]. Recent studies have focused on controlling dispersive waves in Kerr combs by manipulating the geometry of the WGM resonator, doping the resonator material and the pump wavelength. Some semiconductor nanoparticles, like their metal counterparts, exhibit localized surface plasmon resonance (LSPR) [2]. The position of the LSPR peak in these nanoparticles can be finely adjusted by varying the doping level or the size of the nanoparticle. By doping the base material of a WGM resonator with plasmonic semiconductor nanoparticles (NP), its refractive index and thereby the integrated dispersion of the microcavity can be precisely controlled. The purpose of this work is to numerically study the effect of plasmonic CuS nanoparticles on the generation of Kerr frequency combs in a spherical WGM cavity.

Materials and Methods

The optical properties of the composite under study were calculated using the effective medium theory in the Maxwell-Garnett approximation [3]. The finite element method was used to calculate the resonant modes and integral dispersion of WGM resonator [4]. Lugiato-Lefever model was used to describe the generation of frequency combs [5].

Results and Discussion

Fig. 1 shows the calculated integrated dispersion of the resonator around the pump wavelength of 1550 nm for different composites. In all cases the dispersion around the pump frequency shows parabolic behavior and is anomalous [4]. The position of the zero dispersion point in high frequency part changes with varying NP size.

Fig 2. shows the simulated frequency comb spectra for different NP size. The position of generated dispersive wave changes from 230 THz to 245 THz with increase in NP diameter. The free spectral range of the comb is equal to 218.8 GHz. It changes slightly with varying NP size due to the fact that NPs affect mainly the higher order dispersion components.

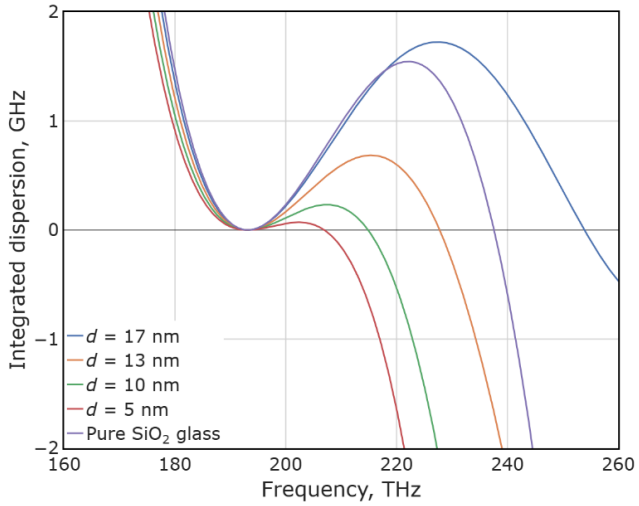


Fig. 1. Simulated integrated dispersion of the WGM resonator of radius 150 um for composite with different NP diameter *d*

a) *b*)

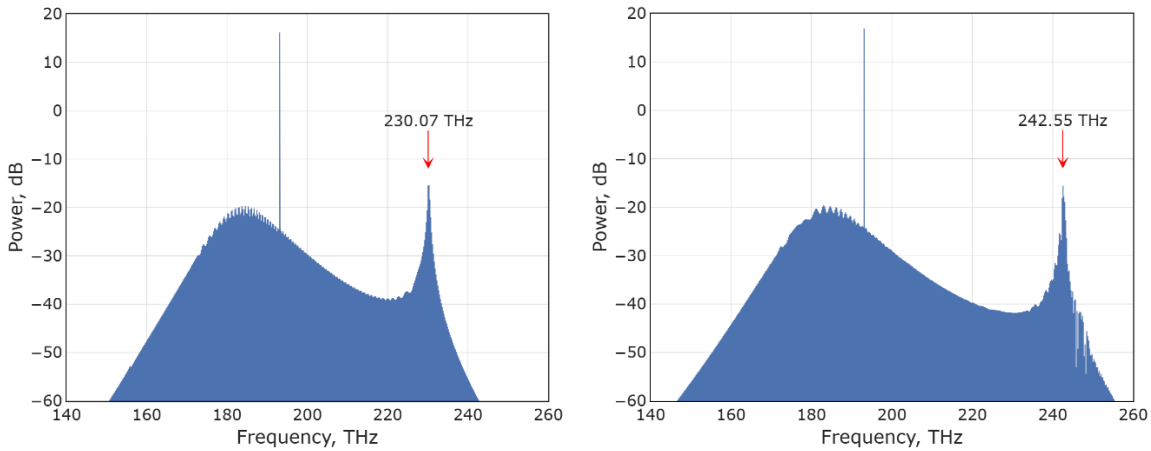


Fig. 2. Simulated spectra of frequency combs for composites with NP of diameter 17 nm(*a*) and 13 nm (*b*)

Conclusion

The results of frequency comb simulation show that the spectral width and dispersive wave position of the comb can be controlled by doping the WGM resonator material with plasmonic CuS NPs of different size. The free spectral range of the comb lines remains constant as the NPs affect mainly the higher order dispersion.

REFERENCES

1. **Ward J., Benson O.,** WGM microresonators: sensing, lasing and fundamental optics with microspheres, Laser & Photonics Reviews. 5 (4) (2011) 553–570.

2. **Kriegel I., Scotognella F., Manna L.**, Plasmonic doped semiconductor nanocrystals: Properties, fabrication, applications and perspectives, Physics Reports. 674 (2017) 1–52.

3. **Sipe J. E., Boyd R. W.**, Nonlinear susceptibility of composite optical materials in the Maxwell Garnett model Physical Review A. 46(3) (1992) 1614.

4. **Fujii S., Tanabe T.** Dispersion engineering and measurement of whispering gallery mode microresonator for Kerr frequency comb generation. Nanophotonics. 9 (5) (2020) 1087–1104.

5. **Lugiato L. A., Prati F., Gorodetsky M. L., Kippenberg T. J.**, From the Lugiato–Lefever equation to microresonator-based soliton Kerr frequency combs. Philosophical Transactions of the Royal Society A: Mathematical, Physical and Engineering Sciences. 376 (2135) (2018) 20180113.

Spectral and photocatalytic properties of Ag-AgCl nanostructures formed on surface of silicate glass by ion exchange

D. V. Marasanov [1]✉, **I. N. Litunovskiy** [1], **V. V. Pesnyakov** [1], **Y. M. Sgibnev** [1], **N. V. Nikonorov** [1]

[1] ITMO University, Saint Petersburg, Russia;

✉dvmarasanov@itmo.ru

Abstract. In this work, the effectiveness of Ag-AgCl nanocrystals on the surface of silicate glass as a photocatalyst, as well as its spectral properties, is studied. The degradation value of an aqueous solution of methyl orange dye increased from 80 to 92% with increasing chlorine concentration in the photocatalyst with Ag-AgCl nanostructures.

Keywords: ion exchange, nanostructures, nanocrystals, silver, absorption, photocatalysis.

Funding: This study was funded by Russian Science Foundation grant № 20-19-00559.

Introduction

Currently, photocatalysts are being actively developed and used in various fields of science, technology and medicine. However, the quantum efficiency of modern photocatalysts is relatively low. This is mainly due to recombination processes between electrons in the conduction band and holes in the valence band, which arise under the influence of light. One of the most promising methods for suppressing recombination processes is the creation of noble metal nanoparticles in the photocatalyst matrix, which act as electron “suppressors”.

Since the presence of nanoparticles on the glass surface is important for photocatalytic applications, a promising tool for introducing silver into the glass composition is the ion exchange method. Ion exchange is the simplest and most effective way to create a layer on the surface of a substance with ions of another substance.

The photocatalytic properties of Ag-AgBr and Ag-AgCl structures were previously studied in [1, 2]. Thus, according to [2], a photocatalyst with Ag-AgBr particles is capable of decomposing more than 80% of methyl orange dye in 2 minutes under solar radiation. However, the properties of Ag-AgCl photocatalyst based on sodium silicate glass have not yet been studied.

The aim of this paper is study of the spectral and photocatalytic properties of a photocatalyst with Ag-AgCl nanostructures in layers of sodium silicate glass formed by ion-exchange.

Materials and Methods

The photocatalyst was created based on a matrix of sodium silicate glass $Na_2O{-}ZnO{-}Al_2O_3{-}SiO_2{-}F$ doped with CeO_2, Sb_2O_3, Cl. The Cl concentration in the glass was 0.5 and 1 mol. %. The 1 mm thick sample was carefully ground and polished.

The next step was to perform ion exchange on the sample in the $AgNO_3/NaNO_3$ melt (5 mol.%/95 mol.%, respectively). Ion exchange was carried out at 320℃ for 15 minutes.

The last stage of sample preparation was additional heat treatment of the sample above the glass transition temperature. The treatment temperature was 500℃ for 3 hours. After each stage, absorption spectra were measured.

The photocatalytic properties of the sample were then measured by measuring the absorption properties of an aqueous solution of methyl orange dye before and after irradiation. Its initial concentration was about 1 mg/100 ml of water.

The solution together with the photocatalyst was subjected to broadband irradiation every 5 minutes. After each period, the absorption spectrum of the solution was measured. All spectra were measured using a Perkin-Elmer lambda 650 spectrophotometer.

Results and Discussion

After heat treatment (blue graph), the resulting Ag-AgCl nanocrystals were absorbed. The position of this absorption peak (450 and 470 nm) of silver nanoparticles is slightly shifted to longer wavelengths relative to the spectrum of glass without chlorine from [3]. The displacement itself increases with increasing chlorine concentration and is caused by the growth of AgCl/NaCl shells around silver particles (**Figure 1**).

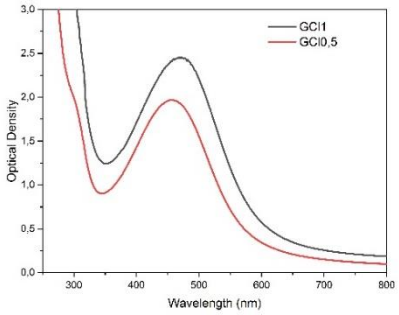


Fig. 1. Absorption of Ag-AgCl nanostructures in ion exchange layers of silicate glass with 0.5 and 1 mol. % chlorine concentration

Figure 2 shows the dependence of the value of degradation of an aqueous solution of methyl orange dye on the chlorine concentration. The amount of degradation of an aqueous solution of methyl orange dye was calculated from the ratio of the dye absorption amplitude after irradiation to the dye absorption amplitude before irradiation. The amount of degradation of an aqueous solution of methyl orange dye increased with increasing chlorine concentration and amounted to 80 and 92%, respectively. The reason for the increase in the C/C_0 value is the formation of hot electrons on the surface of the sample due to the transfer of these charge carriers from silver chloride to silver nanoparticles, which enhance the effect of destruction of the dye molecule with increasing chlorine concentration.

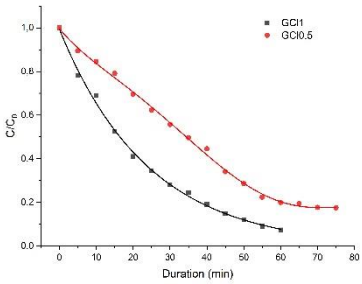


Fig. 2. The dependence of the value of degradation of an aqueous solution of methyl orange dye on the chlorine concentration

Conclusion

The work assessed the photocatalytic degradation of an aqueous solution of methyl orange dye in the presence of a photocatalyst with Ag-AgCl nanostructures on the surface of silicate glass formed by the ion exchange method. It was shown that with increasing concentration of Ag-AgCl nanostructures, the C/C_0 ratio increases from 80% to 92%, associated with photocatalytic degradation of the dye.

REFERENCES

1. **Kuai, L., Geng, B., Chen, X., Zhao, Y., Luo, Y.** Facile subsequently light-induced route to highly efficient and stable sunlight-driven Ag− AgBr plasmonic photocatalyst, Langmuir. 26(24) (2010) 18723-18727.

2. **Han, L., Wang, P., Zhu, C., Zhai, Y., Dong, S.** Facile solvothermal synthesis of cube-like Ag@ AgCl: a highly efficient visible light photocatalyst, Nanoscale. 3(7) (2011) 2931-2935.

3. **Marasanov, D. V., Sgibnev, Y. M., Nikonorov, N. V.** The Influence of Chlorides on the Spectral Properties of Ion-Exchange Layers of Photo-Thermo-Refractive Glass, Optics and Spectroscopy. 130(6) (2022) 402-408.

Nonlinear optical phenomena in mesoporous SiO_2 and Si/SiO_2 nanoparticles

Mastalieva V.[1,2✉], Neplokh V.[1,3], Aybush A.[4], Stovpiaga E.[2], Eurov D.[2], Vinnichenko M.[3], Karaulov D.[3], Kirillenko D.[2], Golubev V.[2], Smirnov A.[2], Makarov S.[5], Kurdyukov D.[2], Mukhin I.[1,3,5]

[1] Saint Petersburg National Research Academic University, Saint Petersburg, Russia;

[2] Ioffe Institute, Saint Petersburg, Russia;

[3] Peter the Great St.Petersburg Polytechnic University, Saint Petersburg, Russia;

[4] N.N.Semenov Federal Research Center for Chemical Physics, Moscow, Russia;

[5] Qingdao Innovation and Development Center, Qiungdao, China

✉ strindberg76@mail.ru

Abstract. In this work we study the optical response of mesoporous SiO_2 and Si/SiO_2 nanoparticles considering different fabrication and post-synthesis treatment processes. We show that thermal annealing of mesoporous Si/SiO_2 nanoparticles transforms the Si phase from amorphous to crystalline and enhances the second harmonic generation response.

Keywords: second harmonic generation, silicon, nanostructures, mesoporous nanoparticles, IR visualiser

Funding: This work was supported by the Russian Science Foundation № 23-79-00018

Introduction

For efficient second harmonic generation (SHG) in bulk silicon, special conditions are required. This paper proposes the use of mesoporous nanoparticles with SiO_2 framework filled with Si phase, which may find applications in the nanophotonic field as a replacement for electronic modulators with optical modulators ones as in the [1-3]. The advantage of using dielectric resonant structures is due to the fact that modulators are based on waveguides wrapped with two-dimensional materials much larger than the wavelength [4]. The various Si/SiO_2 and SiO_2 mesoporous nanoparticles were used to compare the performance of SHG pump. Annealing of Si improves the nonlinear characteristics of the nanoparticles. The heat-treated Si/SiO_2 nanoparticles exhibit broadband photoluminescence under fs-laser excitation. The results obtained confirm the efficiency of mesoporous Si/SiO_2 nanoparticles for second harmonic generation [5].

Results and Discussion

Spherical mesoporous SiO_2 and Si/SiO2 nanoparticles were synthesized according to [6]. The optical studies were carried out using a confocal laser-scanning microscope setup (LSM-980, Zeiss, Germany). Femtosecond laser pulses (Discovery-NX, Coherent, USA) with a repetition rate of 80 MHz, duration of 150 fs, and pulse wavelength range of 800-1020 nm were delivered through the external acousto-optic modulator port of the LSM. The spectral characteristics of the nonlinear response were obtained in the range of 900-980 nm.

SHG-to-pump curves for the obtained particles are shown in Fig. 1. The slope of 2.3 is in agreement with data reported in the literature, and the strong signal indicates an efficient SHG process that is related to the presence of OH^- groups (Figure 1) [7]. Note, that the SiO_2 NPs with high hydroxy-groups content did not demonstrate significant changes of SH intensity due to the fs-laser annealing, indicating thermal stability of OH^- group-related SHG in SiO_2 NPs. It is

experimentally revealed that the mesoporous SiO_2 framework in Si/SiO_2 nanoparticles not only stabilizes the Si material, but also influences the SHG signal. The observed wide-range optical response of Si/SiO_2 nanoparticles makes them promising for visualization of IR radiation.

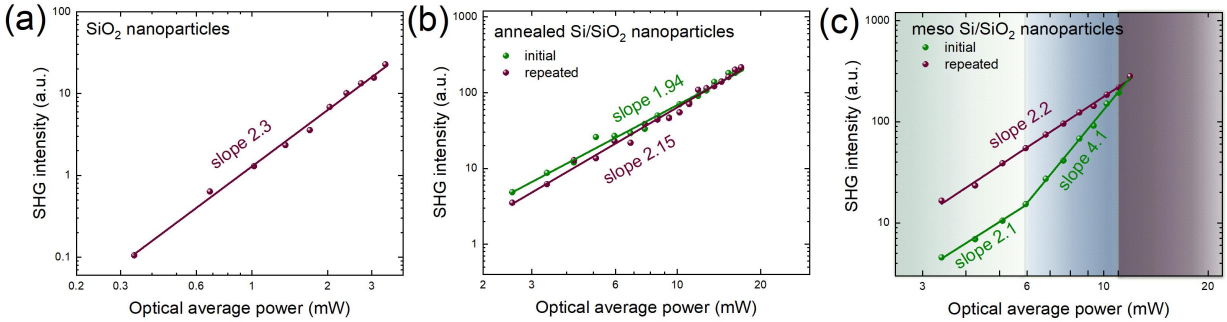


Fig. 1. SHG-to-pump curves for a) reference SiO_2 NPs, b) thermally annealed and c) as-synthesized meso Si/SiO_2 NPs. For b) and c) the green curves correspond to initial measurements, purple curves - to the repeated measurements. The colored areas in c) present follows: green area - normal SHG response, blue area - an increased slope on SHG response, purple area - irreversible sample damage

Conclusion

Thus, mesoporous SiO_2 framework of the Si/SiO_2 nanoparticles stabilizes the Si material and also the SiO_2:OH^- material influences the observed second harmonic signal. The proposed mesoporous Si/SiO_2 nanoparticles can be considered as a promising structure for applications in different fields.

REFERENCES

1. **Maestre, D., Palais, O., Barakel, D., Pasquinelli, M., Alfonso, C., Gourbilleau, F., ... & Irace, A.** (2010). Structural and optoelectronical characterization of Si–SiO_2/SiO_2 multilayers with applications in all Si tandem solar cells. Journal of Applied Physics, 107(6).

2. **Chen, T. P., & Ding, L.** (2010). Optical and optoelectronic properties of silicon nanocrystals embedded in SiO_2 matrix. Nanostructured Thin Films and Coatings: Functional Properties, Zhang, S.(Ed.), 113-165.

3. **Hirschman, K. D., Tsybeskov, L., Duttagupta, S. P., & Fauchet, P.** (1996). Silicon-based visible light-emitting devices integrated into microelectronic circuits. Nature, 384(6607), 338-341.

4. **Li, W., Chen, B., Meng, C., Fang, W., Xiao, Y., Li, X., ... & Shen, Y. R.** (2014). Ultrafast all-optical graphene modulator. Nano letters, 14(2), 955-959.

5. **Wei, J., Wirth, A., Downer, M. C., & Mendoza, B. S.** (2011). Second-harmonic and linear optical spectroscopic study of silicon nanocrystals embedded in SiO 2. Physical Review B, 84(16), 165316.

6. **Kurdyukov, D. A., Eurov, D. A., Shmakov, S. V., Kirilenko, D. A., Kukushkina, J. A., Smirnov, A. N., ... & Golubev, V. G.** (2019). Fabrication of doxorubicin-loaded monodisperse spherical micro-mesoporous silicon particles for enhanced inhibition of cancer cell proliferation. Microporous and Mesoporous Materials, 281, 1-8.

7. **Vandalon, V.** Second-Harmonic Generation: Spectroscopic Phase and Intensity Study of the Si (100) Interface with SiO.

Terahertz lasing in a metal groove with population inverted graphene

K. V. Mashinsky, V. V. Popov, M. Yu. Morozov✉
Kotel'nikov Institute of Radio Engineering and Electronics (Saratov Branch), Saratov, Russia
✉mikhail.yu.morozov@gmail.com

Abstract. Terahertz amplification and lasing regimes in a metal groove with population inverted (active) graphene are studied theoretically. Terahertz amplification and lasing arise at the Fabry-Perot resonance in the graphene substrate in vicinity of the cut-off frequency of the metal groove.

Keywords: terahertz, lasing, graphene, inversion, metal groove, Fabry-Perot resonance.

Funding: This study was financially supported by the Russian Science Foundation through grant number 24-22-00114.

Introduction

Elaboration of new concepts of terahertz (THz) lasers is one of the vibrant trends in modern THz photonics. Terahertz laser based on optically pumped graphene was proposed in [1]. A concept of THz laser based on stimulated generation of plasmons in a planar array of graphene nanocavities was reported in [2]. A graphene-based THz surface emitting laser with diffusion pumping was proposed in [3].

In this paper, we theoretically study the THz amplification and lasing in a metal groove with active (population inverted) graphene. The structure under consideration is schematically shown in Fig.1*a*. Graphene is deposited on a dielectric substrate with dielectric constant ε_s and thickness d, which is placed on the bottom of rectangular metal groove of width L and infinite depth. We assume that the lowest-order TE mode (having non-zero field components E_x, H_y, H_z) incident normally upon graphene reflects from the structure being amplified when interacting with the active graphene.

Method

Solving the Maxwell equations with conventional electromagnetic boundary conditions in the graphene plane and on metal boundaries of the groove, we arrive at the following relation for the power reflection coefficient of the incident TE wave:

$$R = \left| \frac{Y_{\text{ch}} - Y_{\text{load}}}{Y_{\text{ch}} + Y_{\text{load}}} \right|^2, \tag{1}$$

where Y_{ch} and Y_{load} are the characteristic admittance of the lowest-order incident TE mode of the hollow parallel-plate metal waveguide above graphene and the admittance of the terminal load (including graphene and dielectric substrate), respectively. These admittances are defined as

$$Y_{\text{ch}} = \frac{k_{ya}}{\omega\mu_0}, \quad Y_{\text{load}} = \sigma(\omega) + \frac{k_{ys}\,\text{cth}\left(ik_{ys}d\right)}{\omega\mu_0}, \tag{2}$$

where ω and μ_0 are the angular frequency and magnetic constant, respectively, $\sigma(\omega)$ denotes the dynamic conductivity of active graphene [4], and

$$k_{ya} = \sqrt{\left(\frac{\omega}{c}\right)^2 - k_z^2}, \quad k_{ys} = \sqrt{\varepsilon_s\left(\frac{\omega}{c}\right)^2 - k_z^2} \tag{3}$$

are the normal-to-graphene-plane components of the wavevector of TE mode in the parallel-plate metal waveguide above graphene and in the substrate, respectively, with c being the speed of light, and $k_z = \pi/L$ (for the lowest-order TE mode).

Results and Discussion

In Fig. 1*b*, we present the reflection spectrum of the incident wave in dependence on frequency and the groove width for the substrate thickness $d = 7.7$ μm (corresponding to the Fabry-Perot resonance in the substrate), the quasi-Fermi energy value 27 meV, the mean free time of the charge carriers in graphene 1 ps, and charge carriers temperature 300 K. The frequency region below the cut-off frequency of the incident lowest-order TE mode of parallel-plate metal waveguide, $f_c = c/2L$, is shown in grey color. One can see the reflection resonance near the cut-off frequency. Increase of the groove width L leads to the increase of k_{ys}, which, enhances the electrical width of the substrate and, hence, decreases the frequency of the Fabry-Perot resonance in the substrate. Amplification of the incident wave considerably enhances at the Fabry-Perot resonance in the substrate in vicinity of the cut-off frequency of the parallel-plate metal waveguide above graphene, reaching the infinite value at certain parameter values, which corresponds to THz lasing (see the inset in Fig. 1*b*). Terahertz lasing develops for a relatively small quasi-Fermi energy values which may be useful for low threshold lasing regime.

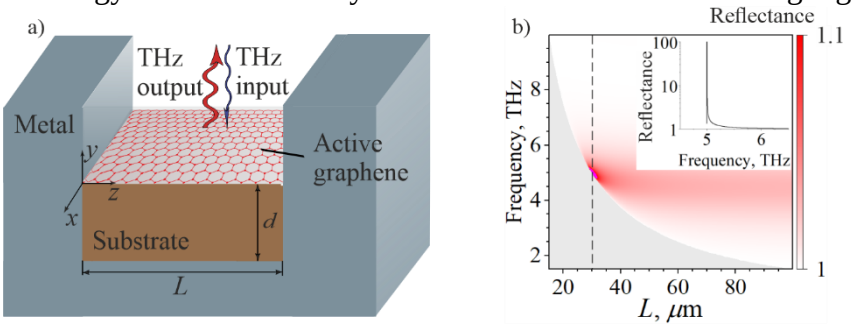


Fig. 1. a) The structure under consideration. b) Reflection spectrum in dependence on frequency and the groove width. The region below the cut-off frequency is marked by grey color. The inset represents the section of the raster map for L = 30 μm shown by vertical dashed straight line.

Conclusion

Terahertz amplification and lasing regimes in a metal groove with the population inverted (active) graphene are studied theoretically. Terahertz lasing develops at the Fabry-Perot resonance in graphene substrate in vicinity of the cut-off frequency of the parallel-plate metal waveguide above graphene.

REFERENCES

1. **V. Ya. Aleshkin, A. A. Dubinov, V. Ryzhii**, Terahertz laser based on optically pumped graphene: model and feasibility of realization, JETP Letters 89 (2009) 63–67.
2. **V. V. Popov, O. V. Polischuk, A. R. Davoyan, V. Ryzhii, T. Otsuji, M. S. Shur**, Plasmonic terahertz lasing in an array of graphene nanocavities, Phys. Rev. B 86 (2012) 195437.
3. **A. R. Davoyan, M. Yu. Morozov, V. V. Popov, A. Satou, T. Otsuji**, Graphene surface emitting terahertz laser: Diffusion pumping concept, Appl. Phys. Lett. 103 (2013) 251102.
4. **A. A. Dubinov, V. Ya. Aleshkin, V. Mitin, T. Otsuji, V. Ryzhii**, Terahertz surface plasmons in optically pumped graphene structures, J. Phys.: Condens. Matter 23 (2011) 145302.

Laser imprinting of large-scale phase patterns in GST using a spatial light modulator

E. V. Menshikov [1,2,3]✉, **P. I. Lazarenko** [2], **D. Y. Terekhov** [2], **A. Y. Kokhanovskiy** [1]

[1] School of Physics and Engineering, ITMO University, St. Petersburg 197101, Russia

[2] National Research University of Electronic Technology, Zelenograd 124498, Russia

[3] Department of Information Engineering, University of Brescia, Brescia 25123, Italy

✉evgenii.menshikov@metalab.ifmo.ru

Abstract. One of the promising materials enabling tuning in photonic devices is the class of chalcogenide optical phase-change materials (PCMs), such as $Ge_2Sb_2Te_5$ (GST). These materials exhibit stable amorphous and crystalline phase states at normal conditions, while offering quick (ns-) optical response and prominent optical contrast, which can be induced by fs-laser stimuli. Direct laser patterning of phase distribution of thin PCM films is usually realized through a point-by-point approach, where the phase state is locally switched. Although this technique is straightforward, it significantly limits the potential switching speeds. In this work, we study laser-induced phase transition in GST films using a spatial light modulator. We demonstrate that this approach enables fast and reversible patterning of large-scale areas of the material.

Keywords: phase-change materials, GST, laser imprinting, spatial light modulator.

Funding: The study was funded by the grant of the Russian Science Foundation No. 20-79-10322.

Introduction

Phase change materials enable variety of applications for tunable photonics, due to combination of such properties as nonvolatality, ns-switching speeds and large refractive index contrast (Δn up to 2 units) [1]. Direct laser writing applied for PCMs has shown its richness, as recently demonstrated for the direct imprinting and rewriting of photonic integrated circuits (PICs) without additional fabrication processes [2]. This technique can be further advanced by combining with a spatial light modulator (SLM), which has been successfully applied for precision phase modulation in holographic displays, optical tweezers and lithography [3]. Possibility of using a SLM for the crystallization of thick (1 um) GSST films was demonstrated earlier [4]. In this work we focus on applications for integrated devices, studying the laser-induced phase transition in 20 nm thick GST films deposited on top of a silicon nitride guiding layer. We show that the SLM enables large-scale – up to tens of microns – reversible crystallization and reamorphization of the PCM and demonstrate the possibility of multilevel crystallization using fs-laser irradiation.

Materials and Methods

Amorphous GST films with a thickness of 20 nm were deposited using a DC magnetron sputtering system on a thermally oxidized silicon wafers with a 450 nm thick stoichiometric low pressure chemical vapor deposited (LPCVD) silicon nitride (Si_3N_4) layer. The pressure of Ar ions during the GST deposition process was 4 mTorr, the sputtering power was 25 W.

Figure 1a shows a schematic of the optical setup. For laser sources, we utilized a Yb:KGW femtosecond laser system PHAROS, which operates at 1030 nm with a pulse duration of 290 fs, and a continuous wave (CW) laser that works at 1064 nm. Light modulation was realized with a reflective phase-only SLM Holoeye Pluto-2. The laser beam was focused on the sample with a Zeiss A-Plan 60× objective when using the CW laser source and through a 10× Mitutoyo M Plan Apo NIR objective with the fs-laser. Phase masks for the SLM were calculated using Fidoc algorithm [5].

Results and Discussion

We find out that CW laser irradiation enables the formation of binary patterns (grating couplers), consisting either of fully crystallized or amorphous areas (see Fig. 1b). This can be attributed to the continuous stimulation of the material, causing stationary heating and subsequent full crystallization in the intensity maxima. Irradiation of the film with fs-pulses induce temporal

heating of the film. With relatively small pulse amplitude, insufficient for single-pulse full crystallization, multi-pulse exposure can result in gradual modificaton with intermediate values of GST refractive index, which appear as a grayscale image in visible light (see Fig. 1c) [6].

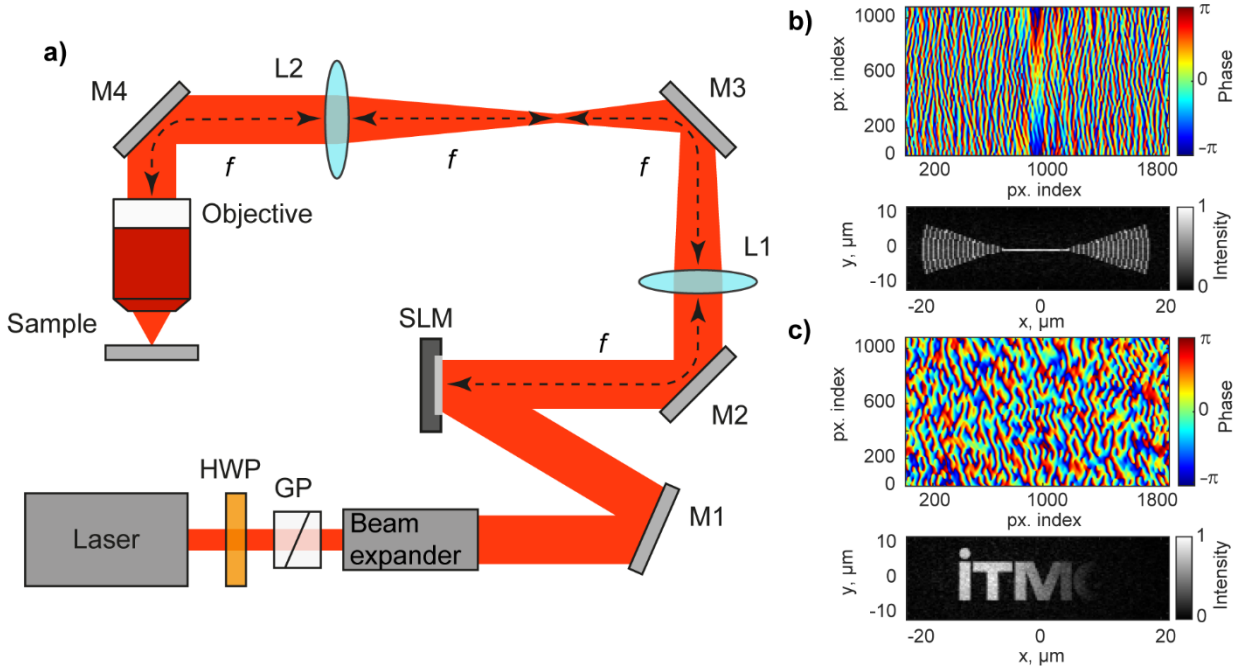


Fig. 1. Large-scale GST laser patterning. *a*) schematic of the optical setup; here HWP – half-wave plate, SLM – spatial light modulator, GP – Glan polarizer, M – mirror, L – lens; dashed lines denote distance between the optical elements equal to the focal length of lenses. b) and c) phase masks on SLM reconstructed with Fidoc algorithm and intensity distributions in focal plane of the objective.

Conclusion

In this work we have explored large-scale phase modification in a thin GST film integrated with a silicon nitride planar waveguide, using a spatial light modulator. We have demonstrated the formation of binary and gradient phase patterns induced by CW and fs-laser irradiation. We find out that fs-pulses enable multilevel phase modulation and its single-shot erasing. The proposed method of large-scale phase modification opens the way for fast direct laser imprinting in PCMs for tunable PICs or grayscale imaging and holography.

Acknowledgments

The samples were fabricated with contributions from the research laboratory “Materials and devices for active photonics”, MIET.

REFERENCES

1. **Zheng, Chunqi, et al.** "Enabling active nanotechnologies by phase transition: From electronics, photonics to thermotics." Chemical Reviews 122.19 (2022): 15450-15500.
2. **Wu, Changming, et al.** "Freeform direct-write and rewritable photonic integrated circuits in phase-change thin films." Science Advances 10.1 (2024): eadk1361.
3. **Yang, Yiqian, Andrew Forbes, and Liangcai Cao.** "A review of liquid crystal spatial light modulators: devices and applications." Opto-Electronic Science 2.8 (2023): 230026-1.
4. **Driggers, Megan, and Clara Rivero-Baleine.** "Investigation of the crystallization behavior of laser-irradiated EXTREME pattern by Raman spectroscopy." International Journal of Applied Glass Science 11.3 (2020): 415-420.
5. **Pi, Dapu, Juan Liu, and Yongtian Wang.** "Review of computer-generated hologram algorithms for color dynamic holographic three-dimensional display." Light: Science & Applications 11.1 (2022): 231.
6. **Kunkel, Tatyana, et al.** "Crystallization of GST225 thin film induced by a single femtosecond laser pulse: Experimental and theoretical study." Materials Science in Semiconductor Processing 139 (2022): 106350.

Spectrocopic markers in raman spectra for the analysis of wood bases of antique icons

Mikhailova A.V.[1,2], Dobryakov A.L.[1,2], Astafiev A.A. . [1,2], Nadtochenko V.A.[1,2]

[1]N.N. Semenov Federal Research Center of Chemical Physics,
Russian Academy of Sciences, Kosygina 4, Moscow, Russia

[2]Moscow Institute of Physics and Technology,
Institutsky per., 9 Dolgoprudny, Moscow region, Russia.

✉ann_mikhailova@mail.ru

Abstract. A methodology was developed for determining spectroscopic markers characterizing the state of wood material, which underlies cultural heritage objects. A standardized and controlled approach for background removal in Raman spectra is proposed on the example of antique icons. This approach makes it possible to determine the ratio of intensities in the Raman spectra of antique icons to determine the parameters characterizing the degree of crystallinity/amorphousness and degradation of cultural heritage samples.

Keywords: Raman spectroscopy, baseline, cultural heritage.

Introduction

Identification of the composition and characterization of the state of wood material is an urgent and demanded task for cultural heritage sites. Fourier transform infrared spectroscopy (FTIR) and micro-Raman spectroscopy are non-destructive techniques widely used to analyze the wood base of antique icons [1]. Raman spectroscopy of cultural heritage requires robust data processing approaches to accurately compare spectra with minimal errors [2-3]. The complexity of the problem is explained by the fact that the probability of Raman scattering of light is several orders of magnitude lower compared to elastic light scattering and fluorescence. Thus reliable background removal in Raman spectra is a time-consuming but at the same time important step in determining the relative intensities of specific lines in Raman spectra [2-3].

Materials and methods

Micro-Raman scattering measurements were made at room temperature using a Bruker spectrometer (OPUS software) with a 785 nm laser line with a spectral resolution of 9.18 cm^{-1}. The laser power was 50 mW, the objective lens was 10x 0.3NA, the exposure time and number of accumulations were 5s and 20, respectively. For each icon, 20-35 spectra were obtained. Infrared absorption spectra were collected using a Bruker Lumos II FTIR microscope-spectrometer in ATR mode with an average of 1000 scans.

The objects of the study were ancient icons: "St. Nicholas in Height, Below the Discovery of His Relics" (author unknown), "Vasily the Holy Fool and Artemy of Verkola" (author unknown), Our Lady "Joy of All Who Sorrow" (author unknown), "Savior in Strength" (author unknown), "Savior in Strength" (author – Dionysius), "Xenia of St. Petersburg" (author – F.I. Sorokin), modern dried linden.

Results and discussion

The analysis of samples may depend on the way the experimental data are processed. In this regard, the background subtraction in the Raman spectra of the samples was compared in several ways. The first one is to subtract the background using the OPUS software installed with the Bruker Raman spectrometer.

The following variants were made in the MATLAB programming language. The second option was to subtract a polynomial of a given degree (polynomial approximation). The experimental data above the approximation are replaced by the polynomial values [2-3]. Then this approximation is continued a specified number of times. As a result of this procedure, a smooth background is determined, which is subtracted from the experimental data to obtain Raman spectra (Fig. 1). The next option was to subtract the background using the moving average method. A certain number of points in the window for smoothing are selected. After that, the resulting spectrum is smoothed again a specified number of times to obtain a smooth background. In addition, other methods for determining a smooth background were developed, in particular using neural networks.

The main idea is to find a smooth background, obtained in a uniform manner, to determine the relative intensities of specific lines in the Raman spectra of antique icons (Fig. 2). The ratios of the obtained intensities were used to determine spectroscopic markers that determine the parameters of the wood bases of antique icons. These markers characterize the degree of crystallinity/amorphousness and degradation of cultural heritage samples [4-5]. In this regard, the accuracy of determining the position of the spectrum peaks plays a significant role (Fig. 3).

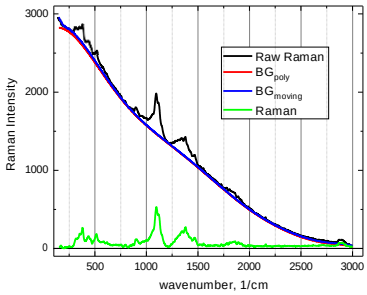


Figure 1. Subtraction of the background from the Raman spectrum of cellulose using the polynomial approximation method and the moving average method.

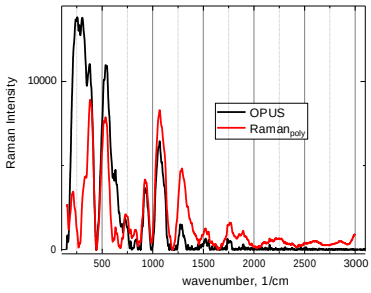


Figure 2. Comparison of Raman spectra for the icon of the Mother of God “Joy of All Who Sorrow” obtained using standard OPUS software and the moving average method.

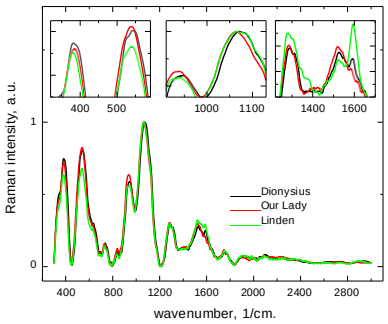


Figure 3. Spectral markers that determine the condition of the wood base of ancient icons.

Also, the age marker of the difference between the icons can be the water content (degree of drying), determined by IR spectroscopy.

Conclusion

Different options of subtraction of the baseline for Raman spectra are proposed in order to find spectroscopic markers characterizing the state of the wood bases of antique icons. The main advantage of the presented methods of background removal is that the process of determining the background is controlled and can be performed uniformly for all antique icons under study. Accordingly, it becomes possible to reliably identify markers to determine the status of cultural heritage samples [1,4,5].

Acknowledgements

The work was carried out within the framework of the joint program between the State Tretyakov Gallery, and the Moscow Institute of Physics and Technology, and the Federal Research Center of Chemical Physics of the Russian Academy of Sciences.

References:

1. **Boukir A., Mehyaoui I., Fellak S., Asia L., Doumenq P.**, The effect of the natural degradation process on the cellulose structure of Moroccan hardwood fiber: a survey on spectroscopy and structural properties, Mediterranean Journal of Chemistry. 8(3) (2019)179-190.

2. **Sheehy G., Picot F., Dallaire F., Ember K., Nguyen T., Petrecca K.,** Open-sourced Raman spectroscopy data processing package implementing a baseline removal algorithm validated from multiple datasets acquired in human tissue and biofluids, Journal of Biomedical Optics. 28(2023) 1–20.

3. **He S., Zhang W., Liu L., Huang Y., He J., Xie W., Wu P., Du C.,** Baseline correction for Raman spectra using an improved asymmetric least squares method, Anal. Methods. 6(2014) 4402-4407.

4. **Agarwal U. P., Reiner R. S., Ralph S. A.,** Cellulose I crystallinity determination using FT–Raman spectroscopy: univariate and multivariate methods, Cellulose. 7(2010) 721-733.

5. **Lionetto F., Del Sole R., Cannoletta D., Vasapollo G., Maffezzoli A.**, Monitoring Wood Degradation during Weathering by Cellulose Crystallinity, Materials. 5(10) (2012) 1910-1922.

Study of the optical properties of silicate glass with silver for use in sensors.

E. A. Mikharev [1]✉, A. Y. Lunev[1] , A. N. Sidorov[1,2] , P. A. Kostin [1]

[1] Department of Photonics, Faculty of Electronics, St. Petersburg Electrotechnical University "LETI", St. Petersburg, Russia;

[2]ITMO University, Saint Petersburg, Russia

✉eamikharev@stud.etu.ru

Abstract. This study investigates spherical microresonators containing molecular silver clusters for sensing applications. Silver is introduced into glass through a low-temperature ion exchange process with silver nitrate and sodium nitrate, creating unique optical properties. This study examines luminescence in the visible range (400–600 nm) upon excitation with long-wavelength UV light (360–410 nm), offering potential for sensing applications. Based on the results of a study of optical characteristics, the formation of Ag_3 molecular clusters in glass was confirmed. For I_{exc} = 370-390 nm, luminescence in the spectral range 450-700 nm is determined mainly by the Ag_2 and Ag_4 MCs, and in the spectral range 550-650 nm - by the Ag_3 MCs. The peak at 616 nm can be attributed to the silver trimer. Therefore, it can be concluded that after ion exchange, most of the silver is present in the form of silver ions, which do not contribute to the luminescence.

Keywords: microspheres; silver molecular clusters; microresonators; luminescence; sensor technologies.

Funding: This research received no external funding

Introduction

The study focuses on a new material for use in WGM sensors. We were particularly intrigued by silicate glass microspheres filled with ions and neutral Molecular Clusters (MCs) of silver. Such glasses demonstrate a high quantum yield of luminescence in the visible spectrum and also exhibit resistance to degradation, which is important for use in sensors [1]. One of the challenges faced by such sensors is the need for direct coupling between the WGM resonator and external optics, such as a tapered optical fiber or bus waveguide, to achieve phase-matched evanescent coupling [2]. An alternative route involves WGM sensors with optically active resonators [3], facilitating UV excitation using LEDs and remote sensing via free-space optics.

Materials and Methods

To obtain glasses with molecular silver clusters, the Low-Temperature Ion Exchange (LTIE) method was used. Its simplicity allows silver ions to be concentrated near the glass surface. Despite more than half a century of research into glasses filled with Ag+ ions and silver ions produced by Ion Exchange (IE), their full potential remains largely untapped.

Ion exchange took place in a molten mixture of silver nitrate ($AgNO_3$) and sodium nitrate ($NaNO_3$) salts at 330 °C for 15 minutes. To study the properties of the resulting glasses in one crucible, glass plates of identical composition with a thickness of 0.17 mm were also subjected to the same process.

The study of the optical properties of the obtained samples included both absorption measurements and measurements of luminescence spectra. For all luminescence measurements, the integration time was 0.1 s.

Results and Discussion

In soda-silicate glass, silver initially exists in the form of Ag+ ions. Structural defects in glass may contain unbalanced negative charges arising from various sources, such as lattice defects or additional ions forming negatively charged regions. When electronic defects coexist near these structural defects, Ag+ ions upon heating are easily reduced to neutral silver atoms Ag0, releasing

electrons. These Ag0 atoms can combine into molecular clusters, potentially consisting of multiple silver atoms, each with distinctive optical and electronic characteristics.

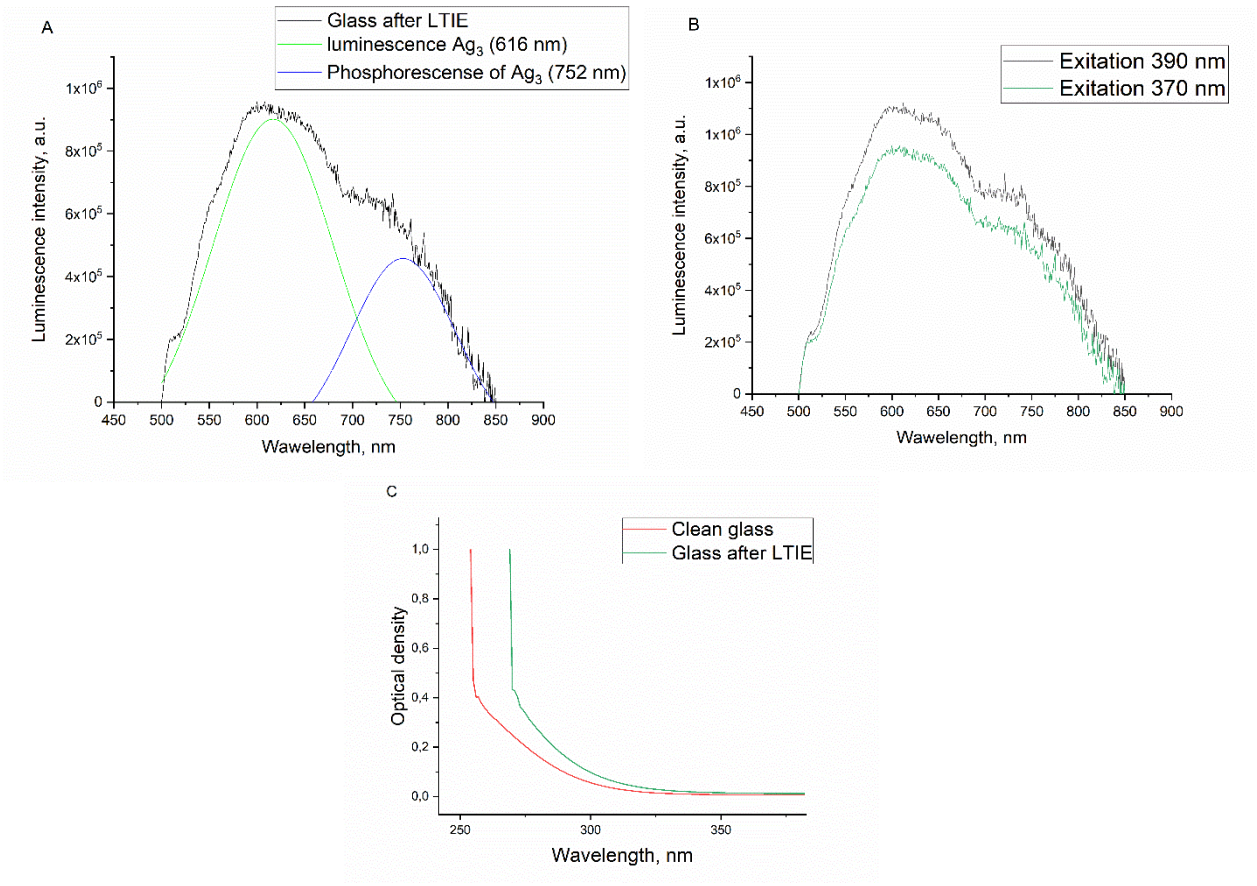


Fig. 1. (a) Sample luminescence peaks; (b) luminescence spectrum at excitation wavelengths of 390 and 370 nm. (c) optical density of produced glass.

Figure 1(a) shows the resulting luminescence spectrum of the sample at an excitation wavelength of 370 nm. The spectrum shows a peak of luminescence [4] and phosphorescence [5] of Ag_3 molecular clusters. Absorbance spectrum shows a shift of the main absorption line by 15 nm.

Conclusion

Luminescence measurements demonstrated a broad emission band in the visible spectrum, especially in the 500–900 nm range, confirming the formation of Ag_3 MCs during the LTIE process. Such glass containing silver MCs can be used as a material for active spherical microresonators.

REFERENCES

1. **Demichev, I.A.; Ignat'ev, A.I.; Nikonorov, N.V.; Sgibnev, E.M.; Sidorov, A.I.; Khrushcheva, T.A.; Shakhverdov, T.A.** Specific features of the luminescence of silicate glasses with silver introduced by ion exchange. Opt. Spectrosc. 2014, 116, 587–592.

2. **Wienhold, T.; Kraemmer, S.; Wondimu, S.F.; Siegle, T.; Bog, U.; Weinzierl, U.; Schmidt, S.; Becker, H.; Kalt, H.; Mappes, T.; et al.** All-polymer photonic sensing platform based on whispering-gallery mode microgoblet lasers. Lab Chip 2015, 15, 3800–3806.

3. **Hanumegowda, N.M.; White, I.M.; Oveys, H.; Fan, X.** Label-free protease sensors based on optical microsphere resonators. Sens. Lett. 2005, 3, 315–319.

4. **S. Fedrigo, W. Harbich, J. Buttet**; Optical response of Ag_2, Ag_3, Au_2, and Au_3 in argon matrices. *J. Chem. Phys.* 15 October 1993; 99 (8): 5712–5717.

5. **Mironov, L.Y.; Marasanov, D.V.; Sannikova, M.D.; Zyryanova, K.S.; Slobozhaninov, A.A.; Kolesnikov, I.E.** Formation and Photophysical Properties of Silver Clusters in Bulk of Photo-Thermo-Refractive Glass. *Ceramics* 2023, *6*, 1546-1558.

The research and analysis of nonlinear optical phenomena in silicon slot waveguide structures

S. M. Murzagalina [1,2✉], **M. Y. Barabanenkov** [1,2,3]

[1] JSC « Molecular Electronics Research Institute», Moscow, Russia

[2] Moscow Institute of Physics and Technology, Dolgoprudny, Russia

[3] The Institute of Microelectronics Technology and High-Purity Materials of the Russian Academy of Sciences, Moscow, Russia

✉murzagalina.sm@phystech.edu

Abstract. This work is devoted to the study and computational modeling of nonlinear phenomena in silicon slot waveguide structures. The developed model is analyzed using computational methods such as the finite element method (FEM), the finite difference method in the time domain (FDTD) and the singular perturbation technique (SPT), as well as optimization of the geometric parameters of the device using a genetic algorithm and machine learning methods.

Keywords: nonlinearity, doped polymers, slot waveguides, genetic algorithm

Introduction

The silicon technological foundation has the great potential in conjunction with electronics, photonics and quantum technologies. It has opportunities in performing as solution for growing demands in such applications as data processing and telecommunications industry. Using the linear optical phenomena significant quantity of devices have been implemented on the SOI platform, for example optical buffers, interconnections [1] and sensors.

The second and third-order nonlinearities provide optical power losses, but in same time nonlinear optical effects may lead to new applications such as multiplexing and modulating signals. Therefore, researchers come across with the new challenge – to create the device with minimal losses and best functional characteristics.

Materials and Methods

The second-order nonlinearity in silicon remains absent due to the centrosymmetric crystal structure, while the third-order nonlinearity is sufficiently low, and it is accompanied by the effect of two-photon absorption (TPA) and TPA-induced absorption of free carriers. To overcome these limitations, various materials were analyzed, including silicon-organics hybrids (SOH), which also has strong second and third-order nonlinearities [2]. The propagation of optical mode in waveguide structures is influenced by both the properties of silicon and SOH materials [3].

Currently, the model of slot waveguide with nonlinear properties is under development. It consists of silicon strips with a high refractive index and a nanoscale gap with a low refractive index, which formed between them as shown in Fig. 1. The unique advantage of the slot waveguide structure is that the electromagnetic field is concentrated inside the slot, as shown in Fig.2, thus nonlinearity in the silicon material becomes less significant, and the nonlinear response is

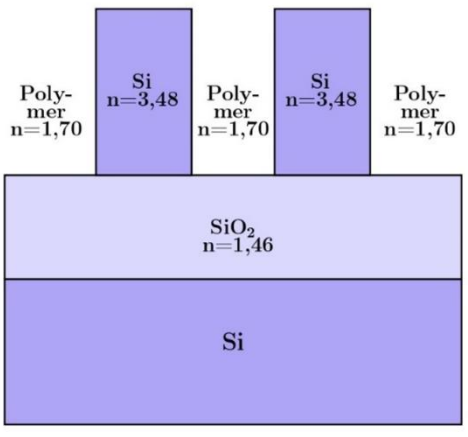


Fig. 1. Planar overview of waveguide parameters

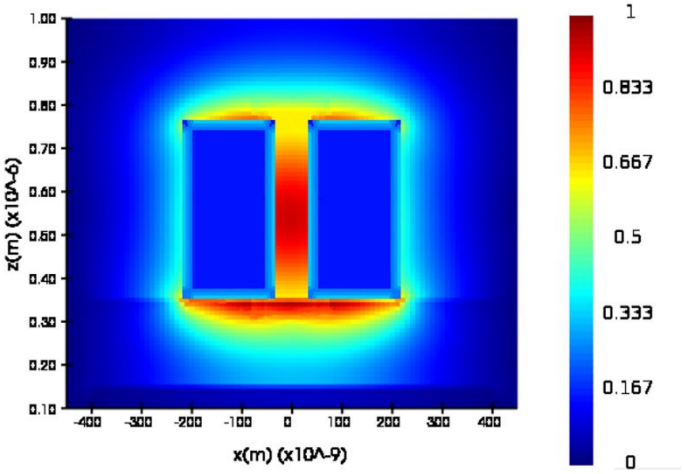


Fig. 2. Mode profile

determined by the material deposited between the silicon strip waveguides. This configuration is capable of providing new applications, such as optical waveguide commutation, fully optical switching and sensor technologies due to the advantages such as high efficiency and integration with new CMOS-compatible materials.

Organic compounds or doped polymers can be embedded to fill the gap in the structure of a slot waveguide, demonstrating the second- and third-order nonlinear response. In this research, the polymer OrmoCore was selected. Such polymer-coated structures provide great potential for high-speed electro-optical modulators and optical data processing devices [4].

The nonlinear phase shift was caused in the slot waveguide by the nonlinear optical Kerr effect. The analysis of this structure is carried out using software for modeling based on the finite element method (FEM) and the finite difference method in the time domain (FDTD). In order to minimize optical losses, it was decided to optimize the geometric parameters of the model using machine learning methods. An analytical approach to obtain the parameters of a slot waveguide with nonlinear characteristics using the singular perturbation technique (SPT) is also considered. SPT is used to study the behavior of waveguides with spatial perturbation [5] and weak second- and third-order nonlinearities, leading to solutions with sufficiently high accuracy [6].

Results and Discussion

In the conducted research, silicon-organic hybrids materials were analyzed. The modeling of the structure was carried out during which the distribution of fields in the structure was revealed depending on the characteristics of the source and the geometric parameters of the slot waveguide. A value for the minimum effective area of nonlinear interaction was also obtained, which is crucial in order to improve the characteristics of waveguides by optimizing geometric parameters, increasing FOM of the device.

Furthermore, an optimization model based on a genetic algorithm has been developed [7] in order to reduce the losses of optical signal power by varying the geometric parameters of the structure and determining their combination to achieve maximum efficiency.

Thus, computational modeling in the conducted research allows us to analyze the nature of optical mode propagation in the structure of a slot waveguide and propose an optimal geometry to improve the nonlinear response with minimal power losses.

REFERENCES

1. **Valeev A.S., Krasnikov G.Y**. Manufacturing technology of intracrystal and intercrystal interconnections of modern ASIC// Microelectronics. 2015. vol. 44. No. 3. pp. 180-201

2. **Leuthold J. [et al.]**, "Silicon Organic Hybrid Technology—A Platform for Practical Nonlinear Optics," in Proceedings of the IEEE, vol. 97, no. 7, pp. 1304-1316, July 2009, doi: 10.1109/JPROC.2009.2016849.

3. **Lipson M. [et al.]**, "Guiding, modulating, and emitting light on Silicon-challenges and opportunities," in Journal of Lightwave Technology, vol. 23, no. 12, pp. 4222-4238, Dec. 2005, doi: 10.1109/JLT.2005.858225.

4. **Palmer R. [et al]**, Low power Mach–Zehnder modulator in silicon-organic hybrid technology //IEEE Photonics Technology Letters. – 2013. – Т. 25. – №. 13. – С. 1226-1229.

5. **Nayfeh A.H., Asfar O.R.** Parallel-plate waveguide with sinusoidally perturbed boundaries //Journal of Applied Physics. – 1974. – Т. 45. – №. 11. – С. 4797-4800.

6. **Yokota M. [et al.]**, Guided transverse-magnetic waves supported by a weakly nonlinear slab waveguide //JOSA B. – 1993. – Т. 10. – №. 6. – С. 1096-1101.

7. **Koza J.R.** Genetic programming as a means for programming computers by natural selection. Stat Comput 4, 87–112 (1994). https://doi.org/10.1007/BF00175355

The effect of electrode diameter on the composition of zinc aluminate particles obtained in a gas discharge.

A.K. Novoselov✉, A.F. Sanatulina, O.V.Vershinina, A.A.Lizunova

Moscow Institute of Physics and Technology, Dolgoprudny, Russia

✉novoselov.ak@phystech.edu

Abstract. In this work, we investigated the change of the size and elemental composition of zinc aluminate nanoparticles synthesized in a gas discharge in the dependence on the geometric dimensions of cylindrical electrodes. We used electrodes made of aluminum with different surface areas as a cathode, and a zinc electrode as an anode. It was found that diameter of primary particle varies from 12.8 nm to 18.6 nm. A range of sizes of aerosol nanoparticle agglomerates and the mass ratio of zinc to aluminum are well approximated by an increasing linear functions of erosion surface of aluminum electrode.

Keywords: nanoparticles, zinc aluminate, size measurement, gas discharge, TEM

Funding: This work was financially supported by the Russian Science Foundation (project № 22-19-00311, https://rscf.ru/en/project/22-19-00311/).

Introduction

In modern times, the task of creating new sources of visible and ultraviolet radiation is urgent. Such sources are a cathodoluminescent source, which is a vacuum tube with an electron gun and a fluorescent screen, as well as a solid-state fluorescent light source. The most important component of such radiation sources is the cathodoluminophore, which converts the energy of accelerated electrons into visible or ultraviolet radiation. One of these substances is zinc aluminate [1]. There are several ways to obtain its nanoparticles. One of them is a gas discharge [2], which was used to synthesize particles in this work. This study aims to investigate the sizes of nanoparticles obtained at different electrode sizes, which will allow in the future to obtain particles of the required size.

Materials and Methods

The synthesis was carried out on an installation consisting of a gas discharge chamber and a gas path [2]. A capacitor 107 nF was used for discharge, a voltage of 1.5 kV and a current value of 60 mA were set on the generator, which made it possible to achieve a discharge frequency of 500 Hz. Pure Ar 4.8 with a flow rate of 600 ml/min was used as the carrier gas, in which self-passivation of the obtained particles was carried out for 20 hours after synthesis.

Studies of the crystal structure, particle sizes and elemental composition of nanoparticles, were carried out using transmission electron microscopy (TEM) JEM-2100 (JEOL, Ltd., Tokyo, Japan) with energy dispersive X-ray analysis Oxford X-MaxN, data on the particle size distribution of agglomerates were obtained using the aerosol spectrometer TSI SMPS 3936.

Results and Discussion

Based on the images obtained on the TEM (fig. 1*a*), a primary particle size distribution was obtained for each surface area of the electrodes. It was found that the particle sizes range from 12.8 ± 0.2 nm to 18.6 ± 0.5 nm regardless of the size of the aluminum electrode. To determine the elemental composition of the particles obtained, spectra obtained by energy dispersion analysis on TEM were taken (fig. 1*b*), from which the mass fraction of each element of the mixture of nanoparticles was calculated. The minimum value of the ratio of the mass fraction of zinc to aluminum is 2.5 with an aluminum electrode area of 37,7 mm^2 and increases to 20 when the area is 188,5 mm^2 (fig. 1*c*). The size distribution of agglomerates of particles obtained during synthesis

using an aerosol spectrometer was also determined. A range of sizes of nanoparticle agglomerates was obtained: from 88 ± 2 nm to 139 ± 1 nm and is described by an increasing linear function (fig. 1*d*).

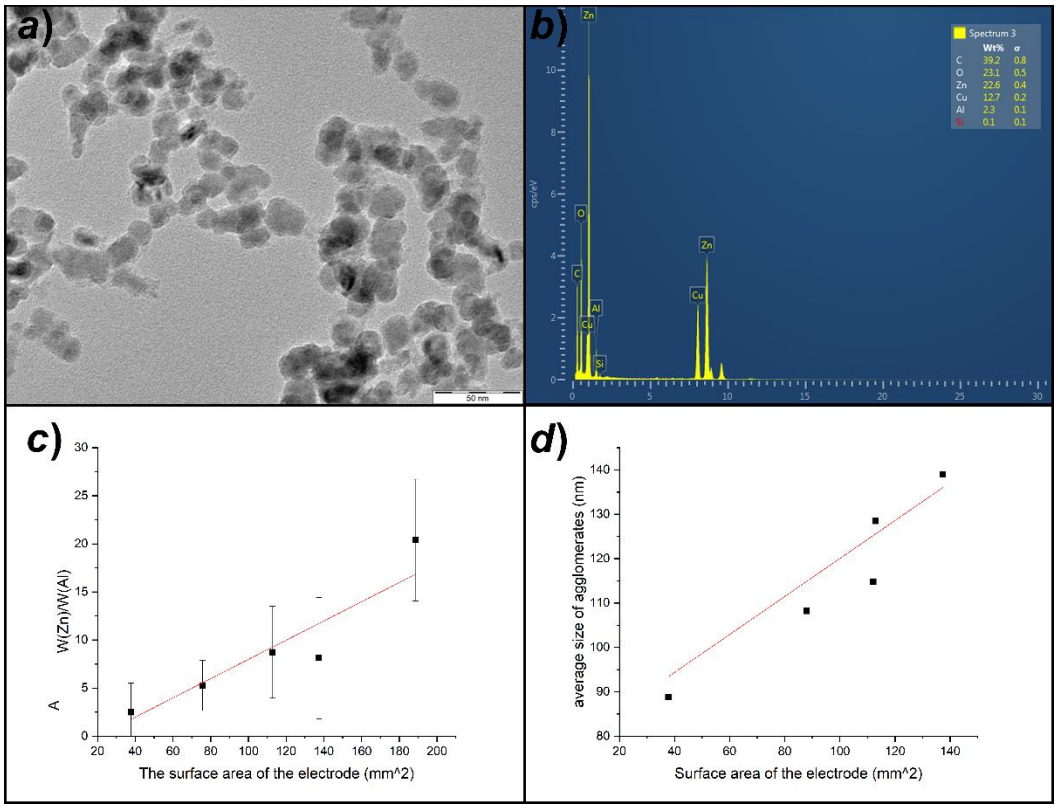


Fig. 1. Characterization of nanoparticle: typical TEM image of primary nanoparticles in an agglomerate the particle image obtained on the TEM *(a)*; EDX spectrum of an agglomerate *(b)*; The dependence of the ratio of the mass fractions of zinc and aluminum on the surface area of the aluminum electrode *(c)*; The dependence of the size of agglomerates on the surface area of the aluminum electrode *(d)*

Conclusion

It was found that the sizes of nanoparticles obtained during synthesis vary from 13 nm to 19 nm regardless the erosion surface of aluminum electrode. At the same time, there is a linear dependence of the size of the aerosol agglomerates on the surface area of the aluminum electrode. The sizes of agglomerates increase from 88 nm to 139 nm and the ratio of the mass fraction of zinc to the mass fraction of aluminum enlarges from 7 to 20 when the erosion surface grows from 37,7 mm^2 to 188,5 mm^2.

Acknowledgments

This work was financially supported by the Russian Science Foundation (project № 22-19-00311, https://rscf.ru/en/project/22-19-00311/).

REFERENCES

1.**V. V. Bakhmetyev, B. B. Malygin, N. S. Podsypanina** [et al.]. Synthesis and investigation of the properties of phosphors for cathodoluminescent sources of ultraviolet radiation// Innovative materials and technologies in design. 2017. P. 53–64.

2. **Ivanov, V. V., Efimov, A. A., Mylnikov, D. A.** [et al.]. High-efficiency synthesis of nanoparticles in a repetitive multigap spark discharge generator// Technical Physics Letters. 2016. V. 42(8). P. 876–878. DOI: 10.1134/S106378501608023X.

Synthesis of aluminum nanoparticles using spark discharge for applications in ultraviolet plasmonics

Messan Nouraldeen [1✉], **N. R. Shestakov** [1], **O.V. Vershinina** [1], **V. V. Ivanov** [1,2]
[1] Moscow Institute of Physics and Technology, Dolgoprudny, Russia;
[2] Lebedev Physical Institute, Russian Academy of Sciences, Moscow, Russia
✉messannouraldeen@phystech.edu

Abstract. This work demonstrates synthesis Al metal nanoparticles with plasmon resonance in the ultraviolet region by the spark discharge method in an argon atmosphere. The resulting primary particles have an Al metal core and a natural oxide shell and size in range from 5 to 50 nm. Importantly, these nanoparticle ensembles show wide extinction peaks, with the highest point between 250 and 480 nm wavelength. The position of the peak can be varied by synthesis parameters. During our research, we employed laser radiation at a wavelength of 355 nm, with pulse energies reaching up to 350 μJ and pulse repetition rates of up to 2000 Hz. We observed that the sintering process of nanoparticles exhibited a dynamic change in size, which correlated with the energy of the laser pulses. This dependence was illustrated by an S-shaped shrinkage curve. By subjecting the initial agglomerates to a series of impacting laser pulses, we successfully achieved complete sintering, resulting in the transformation of the agglomerates into spherical nanoparticles.

Keywords: aluminum nanoparticles, nanoparticles sintering, laser sintering, plasmon resonance.

Funding: The research is supported by the Ministry of Science and Higher Education of the Russian Federation (Goszadaniye) №075-03-2024-107 project No. FSMG-2022-0034.

Introduction

Al nanoparticles are interesting due to their light absorption properties in the UV range, which has applications in light harvesting using solar cells, as well as enhancing light absorption in thin silicon solar cells. The reason behind this property is that Al nanoparticles are capable of absorbing light as a result of their interaction with conduction electrons and surface plasmon resonance, making them effective light absorbers. In addition, Al nanoparticles with different sizes have different optical properties. Al nanoparticles that are small in size will act as excellent UV absorbers, while for bigger particles, this would be the role of an optical scatterer. There is active research in this area, and emerging applications of plasmonics are still being identified through ongoing research and development activities.

Materials and Methods

The spark discharge method was used to obtain Al nanoparticles [1]. Synthesis was carried out in argon of purity 6.0 at pressure of 1,2 atm and flow of 50 mL/min with the following conditions: capacitor of 107 nF, pulse repetition rate of 500 Hz and discharge voltage of 2 kV. Pairs of hollow aluminum cylinders with an outer diameter of 4 mm and an inner diameter of 2 mm were used as consumable electrodes in the setup. To conduct studies of the interaction of optical radiation with aerosol nanoparticles a specially designed laser modification cell was used, which made it possible to combine the aerosol flow with optical radiation along its length. The construction of laser modulation cell is described in [2]. The agglomerates size distribution in the flow was measured using a TSI SMPS 3936 Aerosol spectrometer. The impact on aerosol Al NPs was studied by nanosecond pulsed laser (CNI AO-355A) with wavelength of 355 nm, pulse repetition rate in the range of 0,2 to 10 kHz with a step of 100 Hz, pulse width of 15 ns and pulse energy in the range of up to 350 μJ. Aerosol HEPA filter were installed in the cell to collect NPs after the cell and deposited particles on it for 30 minutes, with laser frequencies 200, 1500 and 2000 Hz. Absorption spectra of nanoparticles in isopropanol solution were obtained using a JASCO V–770 spectrophotometer.

Results and Discussion

The change in mean diameter of the agglomerates with varying 355 nm laser energy due to sintering shows a size reduction from ~460 to ~290 nm (Fig. 1).

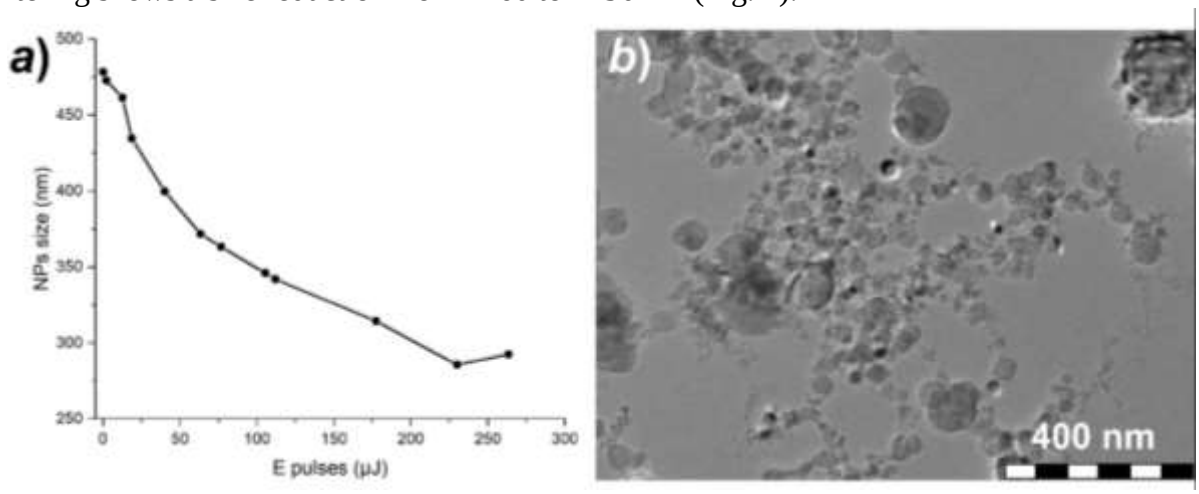


Fig. 1. Dependence of the average particle diameter of the agglomerates on the laser power (*a*), TEM image of typical particles (*b*) at laser pulse frequency of 1500 Hz and a gas flow of 50 mL/min.

From the obtained TEM images, we collected statistics on the diameters of the modified spherical NPs, processing an average of 500 pieces, and rounding them as spheres, and the sizes of the spherical nanoparticles correlate correctly with increasing gas flow rate. Most of the particles in all samples are characterized by sizes in the range from 5 to 50 nm. For samples interacting with the ultraviolet laser, the range increases from 5 to about 100 nm with some single particles with sizes of up to 140 nm.

According to spectrophotometry data, it has been proven that the absorption of aluminum after laser sintering is characterized by pronounced plasmonic absorption peaks in the ultraviolet region at position 218 nm.

Conclusion

We demonstrated that using the gas discharge method Al nanoparticles with plasmon resonance in the ultraviolet region can be produced. The results correspond with studies using thermal modification in which Al nanoparticles have weakly pronounced plasmonic peaks at 275 nm. The appearance of the second peak is caused by presence of large particles. Due to the spectral dependences of the absorption regions of NPs with an increase in the NP diameter, the maximum shifts to the long-wavelength region of the spectrum and expands.

REFERENCES

1. **Efimov A., Arsenov P., Borisov V., Buchnev A., Lizunova A., Kornyushin D., Tikhonov S., Musaev A., Urazov M., Shcherbakov M., Spirin D., Ivanov V.**, Synthesis of Nanoparticles by Spark Discharge as a Facile and Versatile Technique of Preparing Highly Conductive Pt Nano-Ink for Printed Electronics, Nanomaterials. 11 (1) (2021) 234.

2. **Khabarov K., Nouraldeen M., Tikhonov S., Lizunova A., Efimov A., Ivanov V.**, Modification of Aerosol Gold Nanoparticles by Nanosecond Pulsed-Periodic Laser Radiation, Nanomaterials. 11 (10) (2021) 2701.

Spectrally-resolved photoluminescence decay kinetics of size-selected $AgInS_2$ quantum dots

T. O. Oskolkova [1]✉, **A. Dubavik** [1], **A. O. Orlova** [1]
[1] ITMO University, Saint-Petersburg, Russia
✉to.oskolkova@itmo.ru

Abstract. In recent years, ternary $AgInS_2$ quantum dots (QDs) have attracted considerable interest due to their non-toxicity and remarkable optical properties, such as a direct bandgap, high photoluminescence quantum yield in the visible and near-infrared regions, and long photoluminescence lifetimes. However, there is still limited information available on the size-dependent photoluminescence properties of $AgInS_2$ QDs, which could provide more insights into the mechanisms of their emission. In this work, a detailed spectrally- and time-resolved photoluminescence study of size-selected $AgInS_2$ QDs has been performed using time-correlated single photon counting based photoluminescence spectroscopy equipped with a set of bandpass filters. It has been shown that $AgInS_2$ QDs exhibit a strong dependence of the photoluminescence lifetime on the emission wavelength, which is not observed for conventional binary chalcogenide QDs. Furthermore, the nature of this dependence varies for different-sized QDs. The obtained results support the applicability of the radiative recombination of donor-acceptor pairs model to describe the emission mechanisms in $AgInS_2$ QDs.

Keywords: colloidal nanocrystals, ternary quantum dots, photoluminescence decay
Funding: This study was funded by the Ministry of Education and Science of the Russian Federation, State assignment, Passport 2019-1080 (Goszadanie 2019-1080).

Introduction

Recently, ternary I–III–VI quantum dots (QDs), including $AgInS_2$, have gained much attention as a less toxic alternative to conventional binary II–VI and IV–VI nanocrystals [1]. Due to their low toxicity and large extinction coefficient in the visible to near-infrared wavelength range, $AgInS_2$ QDs have become particularly promising for applications in solar light energy conversion systems [2]. In addition, such nanocrystals exhibit high photoluminescence quantum yield and tunable spectrally broad emission extending to the 600-800 nm optical window, making them suitable probes for bioimaging and biolabeling [3]. However, many intriguing features of ternary $AgInS_2$ QDs, as well as the nature of their photoluminescence, remain unclear, leading to an increasing interest in the photophysical studies of these nanocrystals. In this work, a detailed analysis of the size-dependent photoluminescence decay kinetics of $AgInS_2$ QDs is performed, leading to a better understanding of the mechanisms behind the emission of such nanocrystals.

Materials and Methods

Colloidal $AgInS_2$ QDs capped with glutathione were synthesized according to a previously published procedure [1]. To obtain different size fractions of QDs, the stock solution was centrifuged at 6000 rpm for 3 min with the addition of ethanol. The photoluminescence spectra of the samples were measured using the Cary Eclipse fluorescence spectrophotometer (Varian, Australia). The photoluminescence decay kinetics of QDs was studied by time-correlated single photon counting based fluorescence microscopy (PicoQuant, Germany). Bandpass filters with a full width at half maximum of 10 nm were used to selectively detect the emission in a wavelength range corresponding to the photoluminescence spectrum of $AgInS_2$ QDs.

Results and Discussion

As a result of the size fractionation, a series of samples with different-sized colloidal $AgInS_2$ QDs was obtained. The maximum of the photoluminescence spectrum for the samples ranges from 617 nm (fraction 1) to 547 nm (fraction 5). Each sample exhibits a typical for ternary I–III–VI QDs broad photoluminescence spectrum with a full width at half maximum of about 100 nm. It should be noted that there is still no established theory explaining the origin of the broad photoluminescence spectrum of ternary $AgInS_2$ QDs. The photoluminescence of $AgInS_2$ QDs is

commonly attributed to either the radiative recombination of donor-acceptor pairs, the self-trapped exciton model, or the recombination of a localized hole with a conduction band electron [1]. To gain further insight, the size-selected $AgInS_2$ QDs were investigated using the time-resolved photoluminescence spectroscopy. As shown in Figure 1a, the photoluminescence decay for larger-sized QDs (fraction 1) is slower than that for the smaller-sized QDs (fraction 5).

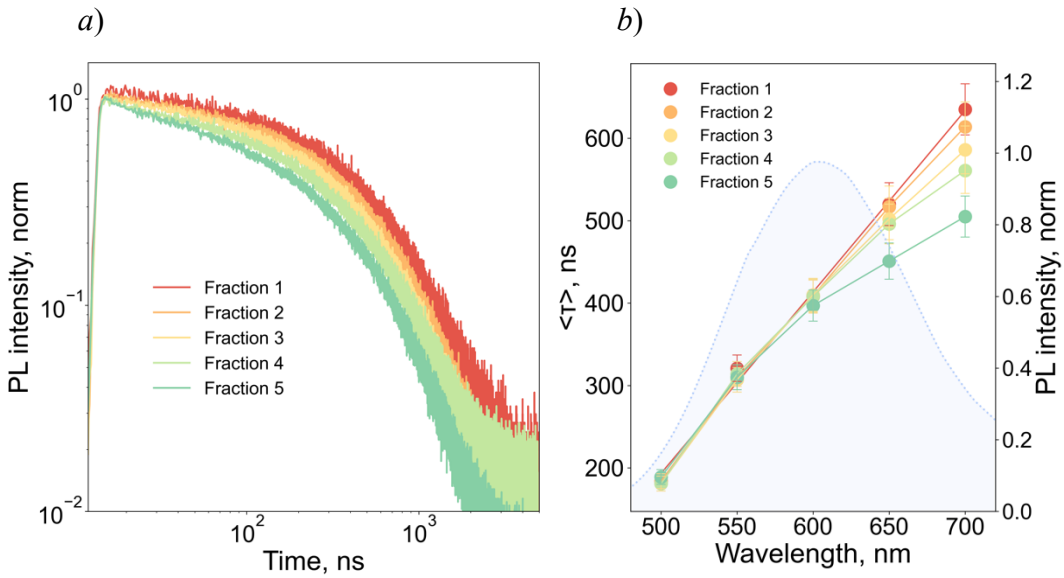


Fig. 1. (*a*) Photoluminescence (PL) decay curves of different size fractions of $AgInS_2$ QDs; (*b*) the dependence of the average photoluminescence lifetime on the emission wavelength for different size fractions of $AgInS_2$ QDs. At the background the photoluminescence spectrum of $AgInS_2$ QDs is presented

It has been shown that the average photoluminescence lifetime of QDs has a spectral dependence and increases with increasing the emission wavelength. The obtained dependence can be well approximated by a linear function for fraction 1 with QDs of the largest size, while decreasing the nanocrystal diameter leads to a deviation of the dependence from linearity in the region of lower energies (Figure 1b). It is interesting to note that conventional binary chalcogenide QDs, such as CdSe or CdTe, on the contrary, have a constant lifetime value over the whole emission wavelength range, suggesting a different emission mechanism for ternary QDs. The obtained results can be explained using the model of donor-acceptor pair recombination, according to which a higher probability of radiative recombination between closer electron-hole pairs is observed.

Conclusion

In summary, in this work the strong dependence of the photoluminescence lifetime on the emission wavelength for ternary size-selected $AgInS_2$ QDs has been demonstrated. The obtained results support the model of radiative recombination of donor-acceptor pairs as a mechanism to explain the emission of $AgInS_2$ QDs.

REFERENCES

1. **Stroyuk O., Weigert F., Raevskaya A., Spranger F., Wurth C. Resch-Genger U., Gaponik N., Zahn D.R.T.,** Inherently broadband photoluminescence in Ag–In–S/ZnS quantum dots observed in ensemble and single-particle studies, The Journal of Physical Chemistry C. 123(4) (2019) 2632–2641.

2. **Kobosko S. M., Jara D. H., Kamat P. V.,** AgInS2–ZnS quantum dots: Excited state interactions with TiO2 and photovoltaic performance, ACS Applied Materials & Interfaces. 9(39) (2017) 33379–33388.

3. **Hashemkhani M., Loizidou M., MacRobert A. J., Yagci Acar H.,** One-step aqueous synthesis of anionic and cationic AgInS2 quantum dots and their utility in improving the efficacy of ALA-based photodynamic therapy, Inorganic Chemistry. 61(6) (2022) 2846–2863.

Hybrid state of the Fabry-Perot and Tamm plasmon-polariton modes in structures with different plasmonic layers

S. V. Osmanov [1]✉, **T. V. Mikhailova** [1]

[1] V.I. Vernadsky Crimean Federal University, Simferopol 295007, Russia;

✉osmanovfti1@mail.ru

(Please provide an institutional email address available)

Abstract. The paper presents the investigation of magneto-photonic crystals (MPCs) with different metal layers for the formation of hybrid state of the Fabry-Perot and Tamm plasmon-polariton (TPP) modes. It was demonstrated that the enhancement of Faraday effect and the transmission coefficient of such structures depend on the metal and symmetry of MPC.

Keywords: Tamm plasmon-polariton, magneto-photonic crystals.

Funding: The work was supported by the Russian Science Foundation (Project No. 19-72-20154, https://rscf.ru/project/19-72-20154/).

Introduction

As is known, solid films of bismuth-substituted iron garnets have magneto-optical (MO) properties. By creating one-dimensional MPCs based on iron garnets, we can achieve enhanced MO effects due to the presence of resonant Fabry-Perot and Tamm plasmon polariton (TPP) modes [1]. In the presence of two modes at the same time, it is possible to select the parameters of the layers so that their resonant wavelengths coincide, forming a hybrid state.

It was previously shown that the amplification factor of the Faraday effect in such structures can be varied by changing the thickness of the "buffer" layer adjacent to the gold layer [2]. Here it is shown that by changing the number of pairs and symmetry of Bragg mirrors relative to the cavity layer, it is possible to influence the bound state of the modes, thereby regulating the splitting of resonances. Additionally, the properties of structures depending on the type of metal layer are investigated.

In general, structures can be described by the formula:

$GGG/[TiO_2/SiO_2]^{m1}/D1/[SiO_2/TiO_2]^{m2}/D2/Me$, (1)

where GGG – substrate of gadolinium gallium garnet, $[TiO_2/SiO_2]^{m1}$ и $[SiO_2/TiO_2]^{m2}$ – Bragg mirrors made of layers of titanium and silicon dioxide, *m1* и *m2* – the number of pairs of layers in Bragg mirrors, Me – metal layer (Au, Ag, Cu), D1 и D2 – the layers through which Fabry-Perot and TPP modes are formed, respectively; D1 – double-layer film $Gd_3Sc_2Ga_3O_{12}/Bi_{2,8}Y_{0,2}Fe_5O_{12}$, D2 – SiO_2 buffer layer.

Materials and Methods

The calculations were carried out using the 4·4 transfer matrix method, which uses the approach of Berreman et al. [3] to form transfer matrices of layers and the entire structure. The thickness of the D1 layer was selected to create the Fabry-Perot mode in the center of photonic band gap (PBG) in the vicinity of 700 nm. The thickness of D2 set respectively to resonant wavelength of the TPP.

Results and Discussion

First of all, the thicknesses of the D2 layer were calculated, at which the resonant wavelengths of the Fabry-Perot and TPP modes had to be combined. But in reality they do not combine, but are pushed apart by a certain amount Δ due to the fact that the electromagnetic field of the light wave is localized simultaneously in two different parts of the structure at the resonant wavelengths of Fabry-Perot and TPP. At the same time, the two modes are in a coupled state, as

their characteristics become similar. The thickness of the D2 layer was 206, 209 and 208 nm for Au, Ag and Cu, respectively.

Figure 1 shows that the transmission coefficient and amplification of the Faraday effect at resonant wavelengths of modes are the highest for the Ag metal.

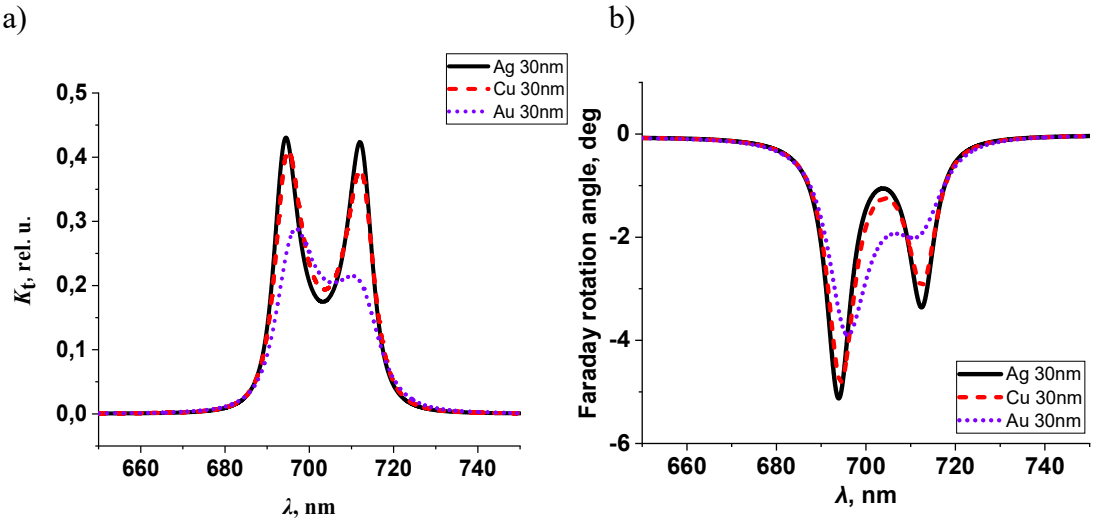


Fig. 1. The transmission coefficient (a) and the angle of Faraday rotation (b) of the MPC (1) with a different metal layer.

Hybrid state investigation have also been carried out for structures with asymmetric Bragg mirrors. It is shown that by changing the number of pairs of mirrors, it is possible to achieve a change in the hybrid state. In the structure $m1 = 2$ and $m2 = 6$, the resonances are not separated due to the weakening of the Fabry-Perot mode. In the structure $m1 = 6$ and $m2 = 2$, Δ becomes larger due to the stronger influence of the separation of the localization of the electromagnetic field when modes occur.

Conclusion

For the configuration of the MPC structure with the hybrid state of the Fabry-Perot and TPP modes, the parameters, on which the Q-factor of the modes depends, are determined.

REFERENCES

1. Magnetophotonics: From Theory to Applications (Springer-Verlag, Berlin, Heidelberg, 2013).

2. **T. Mikhailova, S. Tomilin, S. Lyashko, M. Kozhaev, A. Shaposhnikov, A. Karavainikov, V. Berzhansky, V. Belotelov**, Opt. Mater. Express. 12, 685 (2022).

3. **N. C. Passler, A. Paarmann,** J. Opt. Soc. Am. B, 34, 2128 (2017).

4. **A. M. Grishin, S. Khartsev,** JETP Letters, 109, 83 (2019).

Microlenses at the ends of optical fibers that preserve radiation polarization

A. S. Pankov[1]✉, R.S. Ponomarev[1]

[1] Perm State University, integrated photonics laboratory, Perm 614990, Russia;

✉lab.photon.psu@gmail.com

Abstract. The paper describes a method for creating microlenses based on Panda fibers, while maintaining the radiation polarization. It also presents methods for measuring the key characteristics of these lenses: focal length, mode field diameter (MFD), polarization attenuation coefficient.

Keywords: lensed fiber, polarization attenuation coefficient, mode field diameter.

Funding: This study was funded by «The development of the element base for photonic systems in telecommunications and sensing applications» (grant number [FSNF-2024-0001]).

Introduction

One of the main challenges in integrated optics is the issue of the inextricable connection between optical fibers (OF) and waveguides in a photonic integrated circuit (PIC), which has a characteristic diameter comparable to the wavelength of the guided light [1]. The use of OF with a core diameter of approximately 9 micrometers to dock with PIC with waveguide dimensions of approximately 1,5-2 micrometers results in an increase in optical signal loss. An effective solution to minimizing optical losses when connecting these optical elements is the use of lensed tapered fiber (LTF) with a focal spot size of approximately 2 micrometers. LTF - optical components, which are a fiber-optic guide, on the end of which a microlens is formed [2].

Materials and Methods

For the manufacture of microlenses at the ends of the OF, fiber was used while maintaining the polarization of radiation. The Fujikura FSM-100 welding machine was used to create microlenses. Microlensing occurs in several stages. At the first stage, by continuously exposing the OF to an electric arc, it is softened and stretched until the desired tightness with the required parameters is achieved. Then, in the absence of an electrical arc, the OF breaks in the narrowest area of the constriction. As a result of the breakage, two segments of OF with conical tips are obtained. Additionally, the resulting cones are melted using an electrical arc. The fused section of the optical fiber, under the influence of surface tension forces, forms a symmetrical, convex surface. As a result, a conical lens is created at the end of the fiber.

Polarization-preserving microlenses have the following characteristics: focal length, MFD and polarization attenuation coefficient. The focal length and MFD were measured using the Fabry-Perot method and far-field infrared camera methods, respectively. The polarization attenuation coefficient of a microlens is the numerical difference between the value of this coefficient at the entrance of the lensed fiber and its value at the exit of the lens [3].

Results and Discussion

This paper presents a method for manufacturing and measuring the key parameters of microlenses, with a focal spot size of 2 micrometers. The proposed method makes it possible to obtain lenses with radiation polarization at the output up to 40 dB and a polarization drop in the lens of no more than 3 dB.

REFERENCES

1. **Jung Y., Brambilla G. and Richardson D. J.,** Polarization-maintaining optical microfiber, Opt. Lett. 35(12) (2010) 2034–2036.
2. **Lin C.-H., Lei S.-C. [et al.],** Micro-hyperboloid lensed fibers for efficient coupling from laser chips, Optics Express. 25 (20) (2017) 24480-24485.
3. **Pankov A.S., Zhukov L.O., Ponomarev R.S.,** Measurement of key characteristics of a lensed optical fiber, A special issue of Photon Express Science. 6 (2023) 494-495.

Study of planar microcavity structure with $In_{0.63}Ga_{0.37}As$ quantum dots and $Al_{0.2}Ga_{0.8}As/Al_{0.9}Ga_{0.1}As$ mirrors

A. V. Babichev [1]✉, D. S. Papylev [2], S. D. Komarov [3], N. V. Kryzhanovskaya [3], S. A. Blokhin [1], A. G. Gladyshev [2], L. Ya. Karachinsky [2], I.I. Novikov [2], A.Yu. Egorov [2]

[1] Ioffe Institute, Saint Petersburg, Russia;
[2] ITMO University, Saint Petersburg, Russia;
[3] HSE University, Saint Petersburg, Russia

✉ a.babichev@mail.ioffe.ru

Abstract. The planar microcavity structure based on non-absorbing (at the exciting laser wavelength) $Al_{0.2}Ga_{0.8}As/Al_{0.9}Ga_{0.1}As$ mirrors was fully fabricated by molecular-beam epitaxy. Usage of $In_{0.63}Ga_{0.37}As$ quantum dots reveals room temperature emission close to 1110 nm with emission bandwidth of about 80 meV. The determined spectral mismatch between gain region maxima and microcavity reflectance dip position was about 115 meV at 290 K. The shift of the reflectance dip position along the whole planar microcavity structure was less than 15 meV. The determined by defect inspection root mean square roughness was less than 1.3 nm for studied 8 μm thick planar microcavity structure.

Keywords: molecular-beam epitaxy, planar microcavity, gallium arsenide, InGaAs, Stransky-Krastanow growth mode.

Funding: The authors from Ioffe Institute acknowledge support in part by the grant of the Russian Science Foundation No. 22-19-00221, https://rscf.ru/project/22-19-00221/ for the structure design, MBE epitaxy and the study of photoluminescence spectra.

Introduction

The realization of optical reservoir computing (RC) based on micropillar lasers with optical pumping requires a high spectral uniformity in lasers array and low threshold excitation powers of lasers. Previously, about 190 μeV spectral uniformity for 8×8 micropillar arrays and low threshold excitation power (about 1 mW for 5 μm diameter pillar) were reported for microcavities with absorbing (at the exciting laser wavelength) $GaAs/Al_{0.9}Ga_{0.1}As$ mirrors [1]. The gain to cavity detuning, GCD (spectral mismatch between gain region maxima and microcavity reflectance dip position) determines the threshold excitation power versus temperature behavior.

This paper devoted to studies of the optical characteristics of planar microcavity structure with InGaAs/GaAs quantum dots (QDs) and non-absorbing $Al_{0.2}Ga_{0.8}As/Al_{0.9}Ga_{0.1}As$ mirrors.

Materials and Methods

The microcavity as well as QDs test heterostructure were grown by molecular-beam epitaxy (MBE). The one lambda thick microcavity was formed by non-absorbing (at 700–820 nm range of exciting laser wavelength) bottom and top mirrors consisted of 30 and 20 pairs of $Al_{0.2}Ga_{0.8}As/Al_{0.9}Ga_{0.1}As$. The gain region was positioned in E-field maxima and consisted of three-stacked QDs layers divided by 20 nm thick GaAs barriers. The QDs were formed from $In_{0.63}Ga_{0.37}As$ layer by the Stransky-Krastanow growth mode. The thickness of $In_{0.63}Ga_{0.37}As$ layer was equaled to 2.6 monolayers. In addition, the QDs test structure was also grown and included the same three-stacked QDs layers that were applied as the gain region of microcavity structure [2].

The photoluminescence (PL) temperature studies were inferred in the 77–290 K temperature range. The optical pumping of QDs test heterostructure was provided by a Nd:YAG laser (with 532 nm wavelength excitation) with low CW excitation power density (54 mW/cm^2) aimed to compare with previously published results for structure grown by metal-organic chemical vapor deposition, MOCVD [3]. The reflection spectrum maps of the planar microcavity structure were analyzed by a VerteX PM2000 mapper system (Nanometrics Inc.). Surfscan defect inspection system (KLA Tencor Corp.) was used to measure the normal (with sizes in the range of 0.6–10 $μm^2$) and oval (with sizes in the range of 10–250 $μm^2$) defects distribution over the entire substrate surface.

Results and Discussion

The inhomogeneous broadening determined at 77 K temperature was about 99 meV (cf. Fig. 1). Temperature rise reveals to fall of the PL spectrum full width at half maximum (FWHM), with minimum value coincided to 180 K about 60 meV. Room temperature (at 290 K) value of inhomogeneous broadening was 83 meV that is close to the previously mentioned value for MOCVD-grown single layer QDs (~80 meV [3]). Peak position of PL spectrum measured at 77 K was close to 1030 nm. Rise the temperature to 290 K yields to shift the emission position of ground state to 1110 nm. This value is just above the previously mentioned for MOCVD structure (1014 nm [3]), due to the difference in QDs composition. To clarify the GCD the high-resolution reflectance spectrum was measured. The dip position of reflectance spectrum was located at 993 nm that results GCD about 117 nm (~114 meV). Previously, the PL peak and reflectance dip position was 1100 nm and 1050 nm, respectively that yields GCD of about 50 nm (~54 meV) [3]. By FWHM of the reflectance spectra the quality-factor of planar microcavity structure was determined and equals ~1450. Aimed to clarify the spectral inhomogeneity of reflectance dip position over the whole wafer surface the map of reflectance spectra was measured. The shift of the reflectance dip position along radius was about 7 meV that is about 4 times less than for MOCVD-grown 2-inch wafer of planar microcavity structure [1]. The defects distribution over the entire substrate surface was also analyzed. As a result, the density of normal and oval defects was 179 and 194 per cm^2, respectively. The average haze values were 412 and 388 ppm for normal and oval defects. As a result, the estimated root mean square (RMS) roughness of the surface was less than 1.3 nm.

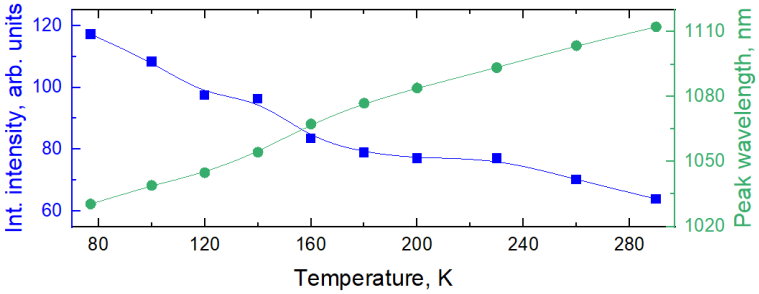


Fig. 1. Integrated intensity (left Y axis) and peak position of PL spectra (right Y axis) versus temperature behaviors for test structure with $In_{0.63}Ga_{0.37}As$ QDs.

Conclusion

One lambda length cavity with $Al_{0.2}Ga_{0.8}As/Al_{0.9}Ga_{0.1}As$ mirrors was fabricated by MBE. $In_{0.63}Ga_{0.37}As$ quantum dots were embedded in the cavity center as the gain region. The estimated from reflectance measurements quality-factor of this planar cavity based on 30 and 20 pairs of $Al_{0.2}Ga_{0.8}As/Al_{0.9}Ga_{0.1}As$ was about 1500. The evaluated zero gain to cavity detuning was located close to 230 K temperature. The small shift of reflectance dip position along radius position reveals about perspective of MBE-grown micropillar structure usage for fabrication of micropillars laser array with ultra-high spectral homogeneity.

REFERENCES

1. **Heuser T., Grose J., Holzinger S., Sommer M. M., Reitzenstein S.** Development of highly homogenous quantum dot micropillar arrays for optical reservoir computing, IEEE J. Sel. Top. Quantum Electron. 26 (1) (2020) 1–9.

2. **Babichev A. V., Komarov S. D., Tkach J. S., Kryzhanovskaya N. V., Nadtochiy A. M., Blokhin A. A., Blokhin S. A., Nevedomskiy V. N., Maleev N. A., Gladyshev A. G., Karachinsky L. Ya., Novikov I. I.** (2022, October). Comparative analysis of InGaAs/GaAs quantum dots produced by various epitaxial techniques. In: Proceedings of the 2022 International Conference on Electrical Engineering and Photonics (EExPolytech), St. Petersburg, Russian, 20–21 October 2022; IEEE. 2022. 253–256.

3. **Kamiński B., Zielińska A., Musiał A., Shih C. W., Limame I., Rodt S., Reitzenstein S., Sęk G.** Optical characteristics of cavity structures with $Al_{0.2}Ga_{0.8}As/Al_{0.9}Ga_{0.1}As$ distributed Bragg reflectors and $In_{0.37}Ga_{0.63}As$ quantum dots as the active region. arXiv preprint arXiv:2305.04938 (2023). Available online: https://doi.org/10.48550/arXiv.2305.04938

Surface Plasmon-Polariton excitation in GaAs films via optically-induced diffraction grating

O. Pashina[1,2], O. Sergaeva[2], A.Seredin[1], C. De Angelis[2], M. Petrov [1*,✉]

[1] ITMO University, School of Physics and Technology, Kronverkskiy Pr., 49, 197101, St. Petersburg, Russia

[2] University of Brescia, Department of Information Engineering, Via Branze 38, 25123, Brescia, Italy

[✉]m.petrov@metalab.ifmo.ru

Abstract: We introduce a theoretical model describing femtosecond optically induced processes in a GaAs film. The model is used to study the evolution of permittivity under illumination by two plane waves. Resulting periodic interference pattern induces diffraction grating that enables the excitation of a surface plasmon polariton at the film-substrate interface.

Keywords: Thermonanophotonics, ultrafast optical processes, plasmonics

Introduction

Rapid advancements in dielectric and semiconductor nanophotonics lead to the growing interest in studying the ultrafast optically induced effects in semiconductor nanostructures. These effects arise from the generation of nonequilibrium carriers in semiconductors, leading to a significant modulation of their properties. This can open the way to ultrafast control of semiconductor systems under the influence of pulsed radiation what makes such systems a very promising platform for the creation of optically modulated photonic devices [1].

Materials and Methods

In this project, we study nonequilibrium processes inside a nanoscale GaAs film with a height of $h = 300$ nm lying on an Ag substrate and exposed to a 100-femtosecond plane wave pulse with a Gaussian time profile. In particular, we focus on the generation of nonequilibrium charge carriers due to the optically induced interband transitions and subsequent heating of the semiconductor by a laser pulse.

We use two-temperature model (eTTM), which describes the temperature dynamics of electrons $T_e(\mathbf{r}, t)$ and phonons $T_{ph}(\mathbf{r}, t)$, as well as the time evolution of concentrations of non-thermalized $N_{\mathrm{e}}^{\mathrm{NT}}(\mathbf{r}, t)$ and thermalized $N_{\mathrm{e}}^{\mathrm{T}}(\mathbf{r}, t)$ electrons and the energy of non-thermalized ones $\mathcal{U}_{\mathrm{e}}^{\mathrm{NT}}(\mathbf{r}, t)$. Our approach involves solving a self-consistent system of differential equations with time resolution, describing the dynamics of the above characteristics, taking into account the distribution of the electromagnetic field inside the film. This model considers the thermalization of conduction electrons, diffusion, relaxation processes, and electron-phonon scattering. Heat source is given by the following relation

$$Q_{\mathrm{Ne}}(\mathbf{r}, t) = \frac{1}{2}\omega \mathrm{Im}[\varepsilon]\varepsilon_0 |\mathbf{E}(\mathbf{r})|^2 \cdot \mathrm{GP}(t)/\hbar\omega, \quad \mathrm{GP}(t) = \exp(-4 \cdot \ln 2 \cdot (t - t_0)^2/\tau_p^2), \quad (1)$$

where $t_0 = 1$ ps represents the peak time of the pulse, and $\tau_p = 100$ fs is the pulse duration. One can see that $Q_{\mathrm{Ne}}(\mathbf{r}, t)$ is a function of permittivity. However, the dielectric constant itself undergoes changes over time

$$\varepsilon = (n_0 + \Delta n_{\mathrm{bf}})^2 + \Delta\varepsilon_{\mathrm{Dr}}. \quad (2)$$

Here n_0 is the linear complex refractive index of the medium, Δn_{bf} is the complex-valued change of refractive index due to the band-filling [2], and $\Delta\varepsilon_{\mathrm{Dr}}$ is the complex-valued change of permittivity due to the generation of nonequilibrium electrons, which can be calculated using Drude model [3].

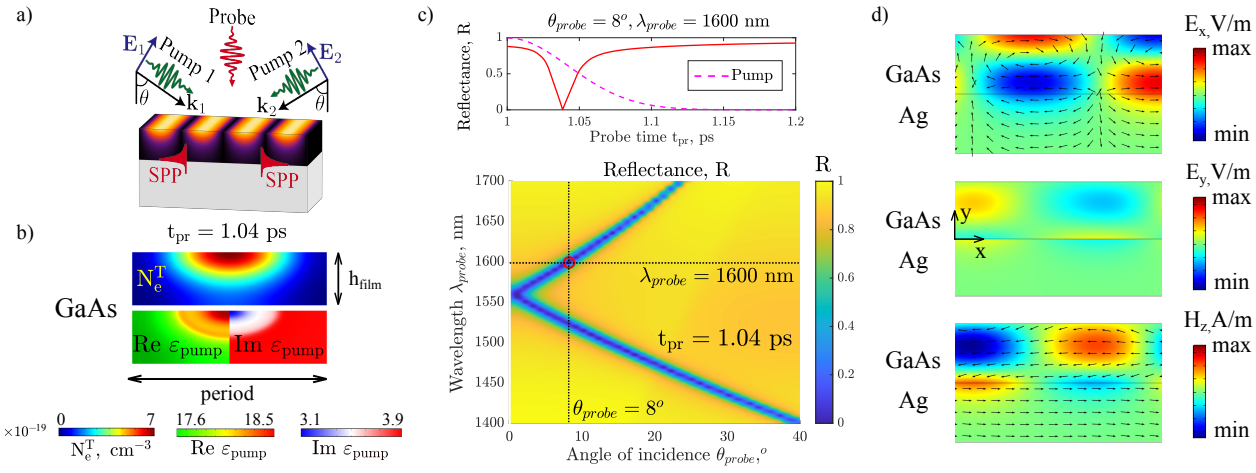


Figure 1: a) Schematic representation of the system. b) Optically transient diffraction grating. c) Reflectance map for the probe as a function of wavelength and angle of incidence. The upper graph demonstrates the evolution of reflectance for specific values of λ and θ. d) Electric and magnetic field distribution close to the interface between Ag and GaAs, illustrating surface plasmon-polariton excitation. The arrows on the upper panel demonstrate the electric field direction, and on the lower one the energy flux.

Results

We apply our model to study the ultrafast excitation of surface plasmon polaritons (SPP). We irradiated the film by two plane waves with $\lambda_{pump} = 500$ nm, incident at opposite angles (see Fig. 1a), which interference induced a change in the permittivity of the film (see Fig. 1b). The period of the diffraction grating is $p = 1100$ nm and equal to the distance between peaks of the interference pattern, which is determined by the angle of pump α_{pump} incidence. We set $\alpha_{\text{pump}} \approx 13^\circ$ using the formula $\alpha_{\text{pump}} = \arcsin\left(\frac{\lambda_{pump}}{2p}\right)$. This diffraction grating allowed to satisfy the momentum conservation law and excite SPP at the film-substrate interface using probe field. The reflection of probe as a function of the angle of incidence and wavelength of the probe (Fig. 1c) shows dip corresponding to the SPP excitation at a time delay of $t_{\text{pr}} = 1.04$ ps. Additionally, Fig. 1d illustrates the field distribution near the interface of semiconductor and metal materials, indicating the propagation of SPP.

Discussion and conclusions

In conclusion, we developed a theoretical model that describes the ultrafast optically induced processes in semiconductors and utilized this model to excite surface plasmon polaritons on a femtosecond timescale based on optically induced transient diffraction grating. Finally, we believe that our model demonstrates great promise for a wide range of applications in optically-adjusted photonic ultrafast devices.

Acknowledgments

This work was supported by Russian Science Foundation 22-12-00204.

References

[1] Yonatan Sivan and Marat Spector. Ultrafast dynamics of optically induced heat gratings in metals. *ACS Photonics*, 7(5):1271–1279, 2020.

[2] Brian Bennett, Richard Soref, and Jesus Alamo. Carrier-induced change in refractive index of InP, GaAs and InGaAsP. *Quantum Electronics, IEEE Journal of*, 26:113–122, February 1990.

[3] K. Sokolowski-Tinten and D. von der Linde. Generation of dense electron-hole plasmas in silicon. *Phys. Rev. B*, 61(4):2643–2650, Jan 2000.

Quantum efficiency of water photocatalytic decomposition by Ag-Ag_2S nanostructures

V. V. Pesnyakov [1]✉, A. I. Sidorov [1], N. V. Nikonorov [1]
[1] ITMO University, Saint-Petersburg, Russia
✉ vvpesnyakov@itmo.ru

Abstract. In this paper quantum efficiency of Ag-Ag_2S nanostructures is studied. Results reveal the increase in quantum efficiency of studied structures by two times in comparison with the Cu substrate. At the same time Ag_2S structures does not exhibit any increase of quantum efficiency after applying 3 V to the structure.

Keywords: photocatalysis, silver nanostructures, semiconductor nanoparticles

Introduction

Photocatalysis is an effective method for converting solar energy, offering an approach to solving energy and environmental problems. Under the influence of sunlight, a multi-stage reaction occurs to produce gaseous forms of oxygen and hydrogen, which can additionally be used in industry or as fuel. There are many catalytic materials that are known today [1]. In this paper Ag and Ag_2S nanostructures' photocatalytic quantum efficiency was studied.

Materials and Methods

In this research nanoporous silver layers were synthesized by a substitution reaction on cuprum substrates from an aqueous solution of copper sulfate (3,75 g/l) and consist of micro- and nanodendrites. To study photoelectrochemical catalysis, samples were placed in an aqueous solution of $NaNO_3$ and irradiated with a fiber source of UV-visible radiation with a voltage of 0.5 - 5 V applied to the photocatalytic cell through a 1 kOhm ballast resistor. Quantum efficiency was determined by the formula [2]: $\eta = N_e/N_{ph}$, where $N_e = I_{ph}\hbar\omega$, $N_{ph} = P_{Abs}e$, N_e – number of photoelectrons, N_{ph} – number of absorbed photons, I_{ph} – photocurrent, P_{Abs} – absorbed radiation power, ω – radiation frequency.

Results and Discussion

Quantum efficiency dependency of the applied voltage is presented in figure 1. Even pure cuprum substrate exhibit quantum efficiency 0,04% at the applied 5V to the photocatalytic sell. However, Ag_2S structures do not show higher quantum efficiency then the pure Ag up until 3V and equal to the Ag at 4-5V.

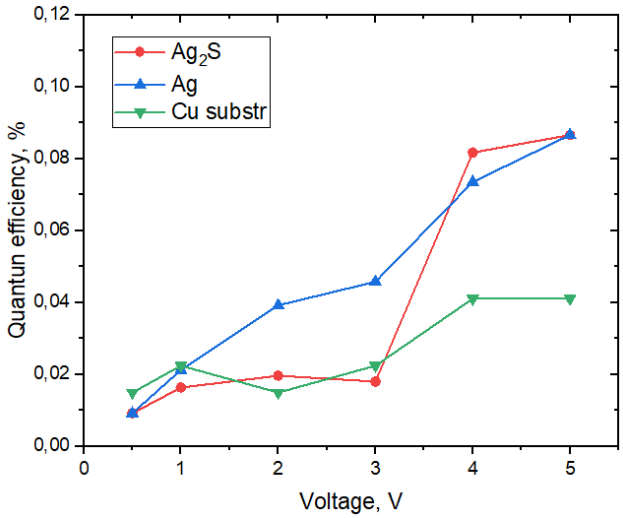


Fig. 1. Quantum efficiency of the studied structures to the applied voltage

Conclusion

Photocatalytic quantum efficiency of Ag and Ag_2S nanostructures were studied. Ag nanoporous layer exhibit twice higher quantum efficiency then the pure cupper substrate when 5V is applied to the sell. However, Ag_2S structures do not show much higher quantum efficiency then the pure Ag.

The research was supported by the Russian Science Foundation grant No. 20-19-00559.

REFERENCES

1. **Takanabe, Kazuhiro.** Photocatalytic water splitting: quantitative approaches toward photocatalyst by design., Acs Catalysis 7.11 (2017): 8006-8022.

2. **Jiao, Yang, et al.** Synthesis of three-dimensional honeycomb-like Au nanoporous films by laser induced modification and its application for surface enhanced Raman spectroscopy. Optical Materials Express 7.5 (2017): 1557-1564.

Cleaning of miniaturized lenses integrated on optical fibers

V.N. Gornov, Peshkicheva L.E. , Yu.Yu. Smirnov, V.V. Stavitskiy
FSUE «RFNC – VNIITF named after Academ. E.I. Zababakhin»
E-mail: dep5@vniitf.ru (for Peshkicheva L.E.)

Abstract. The paper presents method of cleaning miniaturized lenses integrated on optical fibers. The first step is "Wet cleaning" with ultrasonic agitation in ethanol or other solvent. If it is not effective, "Wet-to-dry" method will be used. Examination with a microscope before and after cleaning is important microlense cleaning.
Key words: lenses, optical fibers, lensed optical fiber, optical coatings, cleaning

Introduction

Lenses and optical fibers are the key components of optical systems and are used to change the parameters of the transmitted radiation, light focusing, collimation, coupling to a light source, beam tailoring, and also for imaging and trapping applications. In the last years, technological solutions based on creation of miniaturized lenses integrated on optical fibers have appeared [1-2].

Materials and Methods

Their size ranges from 1 mm to several microns. Functional properties of fiber-integrated lenses can be changed by deposition of optical coating. Clean of such a small surface area is an important step in manufacturing of coating lens integrated on optical fibers. The quality of the coating, i.e. surface morphology, imperfections and adhesion of the coating, changes in spectral characteristics, etc., depends on the cleaning stage.

Generally, the nature of contaminants is unknown, therefore several cleaning steps may be necessary. The cleaning technology combines two methods – "wet cleaning" and "wet-to-dry" [3]. A schematic diagram of cleaning is shown in Figure 1.

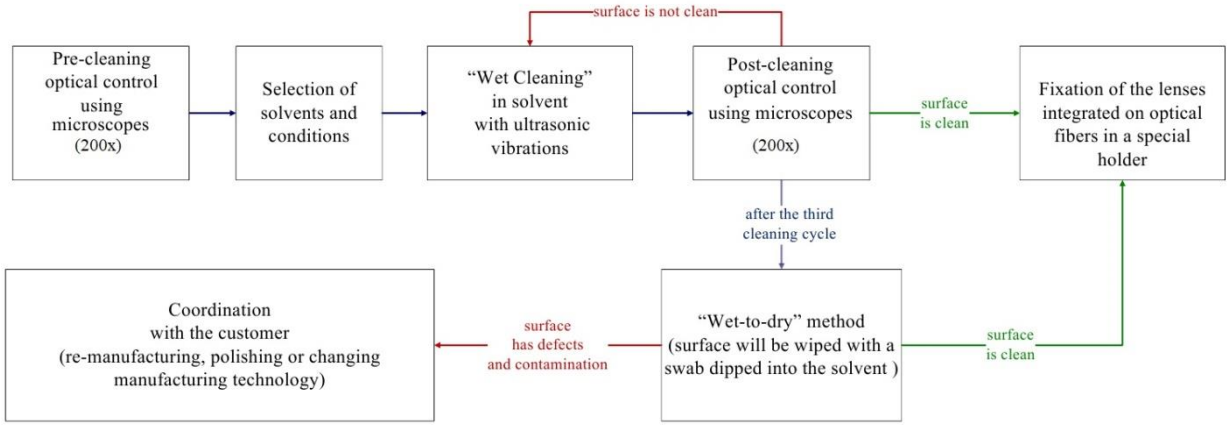


Figure 1. Schematic diagram of the cleaning technology for lenses integrated on optical fibers

Wet cleaning is combined with ultrasonic agitation to increase efficiency of removing different types of contaminants. Ultrasound frequency ranges from 20 kHz to 44 kHz. Ethanol is often used for wet cleaning. It is less volatile than petroleum ether and is not oxidized like isopropyl alcohol to acetone. Lenses integrated on optical fibers by laser welding are cleaned at room temperature. Removing contaminants from optical cement and wax-resin-forming substances needs heating. Drying with high purity argon removes the excessive solvent. If the fiber doesn't pass a visual inspection the process will be repeated. A large number of cleaning cycles can affect the protective coating or weld point of the lens, causing the lens to detach from the fiber. Therefore, if the lens size and shape allows, its surface will be wiped with a swab dipped into the solvent after the third cleaning cycle. If the quality of cleaning is not good enough, a decision is made about the need for re-sealing, polishing or changing the

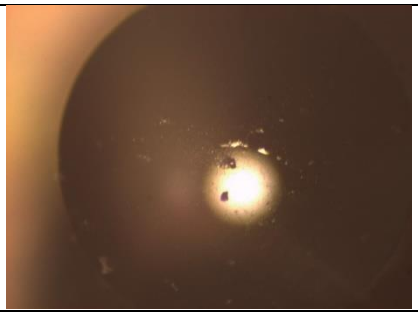
manufacturing technology.

Results and Discussion

Examination with a microscope before and after cleaning allows determining the type of contamination and assures the cleaning technique will provide an expected cleaning result. We use a microscope with 200x magnification equipped with a camera. The cleaning results are presented in Table 1.

Table 1

Example for optical control «before» and «after» cleaning

No	Description	Optical control	
		Pre-cleaning	Post-cleaning
1	Lense integrated on optical fibers made by drawing		
2	Lense integrated on optical fibers made with optical cement		

Conclusion

It is important to understand that cleaning is a careful process that requires an individual approach to every single product. When manufacturing a fiber light guide with a lens is embedded onto the fiber end, it is important to ensure a sufficient quantity of products accounting for rejection, and to carry out quality control at each stage of manufacturing to minimize contamination.

Reference:

1. **Wen S-B., Sundaram V.M., McBride D., Yang Y.** Low-cost, high-precision micro-lensed optical fiber providing deep-micrometer to deep-nanometer-level light focusing, Optics Letters. Vol. 41, No.8 (2016) 1793 – 1796 DOI: 10.1364/OL.41.001793.
2. **Kozhevnikov V.S., Ponomarev R.S., Shmyrova A.I.** The Technology for Manufacturing a Lensed Optical Fiber Using Optical Resin, Instruments and Experimental Techniques No. 6 (2022), 68–77. DOI: 10.31857/S0032816222050263.
3. **Forrest Ed.J., Blair P.** The need for a single cleaning standard for OEM and OSP fiber optic connections, Proc. of SPIE. Vol. 7234 (2009) 72340I-1(9). DOI:10.1117/12.804618.

Simulation of an all-optical logical comparator based on a GaAs photonic crystal operating at a wavelength of 1.3 μm

M. Pleninger✉, S. V. Balakirev, M. S. Solodovnik
Laboratory of Epitaxial Technologies, Southern Federal University, Taganrog 347922, Russia
✉pleninger@sfedu.ru

Abstract. We present the results of the simulation of a compact all-optical logical comparator based on a GaAs photonic crystal operating at a wavelength of 1.3 μm. The influence of the photonic crystal geometrical parameters on the characteristics of an optical comparator are investigated. Dependences of the ratio of signal intensity (electric field strength) at the inputs and outputs of the comparator allowed us to establish that an optimum diameter of the photonic crystal pillars and a period between them are 150 and 600 nm, respectively.

Keywords: photonic crystal, logical comparator, GaAs.

Funding: This work was funded by the Ministry of Science and Higher Education of the Russian Federation; the state task in the field of scientific activity No. FENW-2022-0034.

Introduction

Photonic crystals are a promising engineered dielectric material with a photonic band gap which provides the opportunity to manipulate the propagation of the electromagnetic field. They are widely used in moder optical devices, such as optical sensors and light modulators. In particular, an important area of research on photonic crystals is the development of logical elements of photonic integrated circuits based on them.

In this work, the distribution of electric field is simulated in an all-optical logic comparator based on a GaAs pillar photonic crystal operating at a wavelength of 1.3 μm. This wavelength is in the range of the second transparency window of the optical fiber and has zero dispersion.

Model Description

The study was carried out for a 2D photonic crystal with a hexagonal lattice of cylindrical GaAs pillars, which is of particular interest for the maximum reflection of radiation with a frequency belonging to the photonic band gap. The diameter of the pillars (*d*) and their spacing (*a*) varied in the range 130–160 and 450–750 nm, respectively. Two rows of pillars were removed from the structure, so that missing rows intersected at the center of the photonic crystal, creating two waveguides of the logical comparator. Five pillars with reduced diameters of 83 (one pillar) and 62 nm (four pillars) were added to the waveguide path.

Results and Discussion

A photonic crystal comparator has two input and two output channels. When radiation is input through both channels, the light propagating through the waveguides should be almost completely attenuated when it reaches the waveguide intersection. If radiation is input only through the first channel, or through the second channel, the light should propagate through the waveguide with a minimal loss.

Figure 1 visualizes the distribution of the electric field strength depending on the pillar diameter and spacing. Figures 1*a-c* and 1*d-f* show the operation of the comparator with 1 and 2 working channels, respectively. The pillar diameter and spacing in Figures 1*a*,*d* is 150 and 500 nm, respectively. In this case, the comparator works incorrectly, because the radiation does not pass through the waveguides and attenuates at the center of the photonic crystal.

Figures 1*b*,*e* demonstrate the operation of the comparator with a pillar diameter of 130 nm and a period of 600 nm. With two open channels, the radiation is not attenuated at the point of intersection of the waveguides, which is a violation of the comparator model operation (Figure 1*e*). In Figures 1*c*,*f*, the pillar diameter is 150 nm and the period is 600 nm. One can see that when the only channel is open, the radiation propagates along the waveguide with small losses. With two open channels, the radiation is attenuated at the point of intersection of the two waveguides. In this case, the comparator model works correctly.

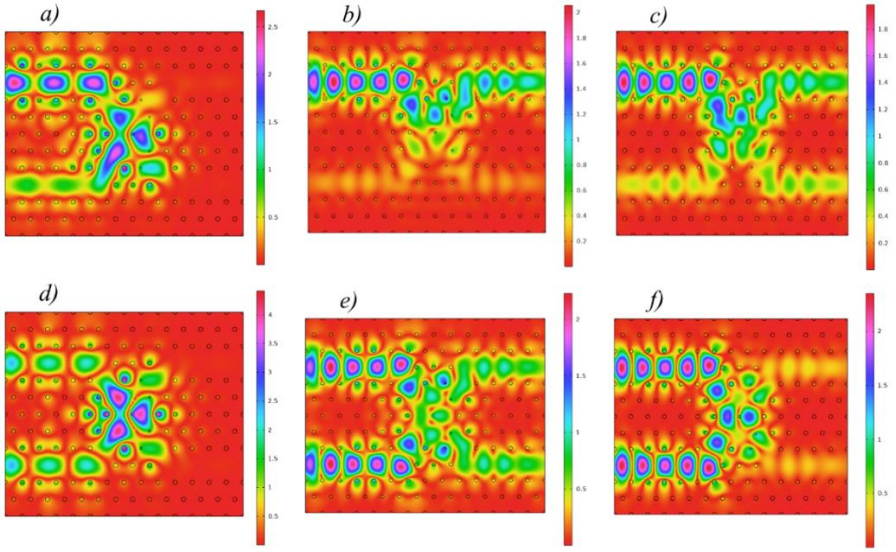


Fig. 1. Distribution of the electric field strength (color bar, V/m) in the logical comparator with one (*a*-*c*) and two (*d*-*f*) open channels: *a*,*d*) *d*=150 nm, *a*=500 nm; *b*,*e*) *d*=130 nm, *a*=600 nm; *c*,*f*) *d*=150 nm, *a*=600 nm.

For better visualization, a ratio of the signal intensities (electric field strengths) at the input and the output of the comparator were plotted against the diameter of GaAs pillars (Figure 2*a*) and their spacing (Figure 2*b*). A red curve in Figure 2 indicates the output/input (O/I) signal ratio in the case of one open channel. The value of this ratio should be as high as possible to provide low attenuation of the signal. The blue curve indicates the O/I signal ratio in the case of two open channels. In contrast, this value should be as small as possible to provide the signal attenuation at the intersection of the two waveguides. Therefore, the difference between these two values (black curve) should be high to achieve the optimal comparator performance.

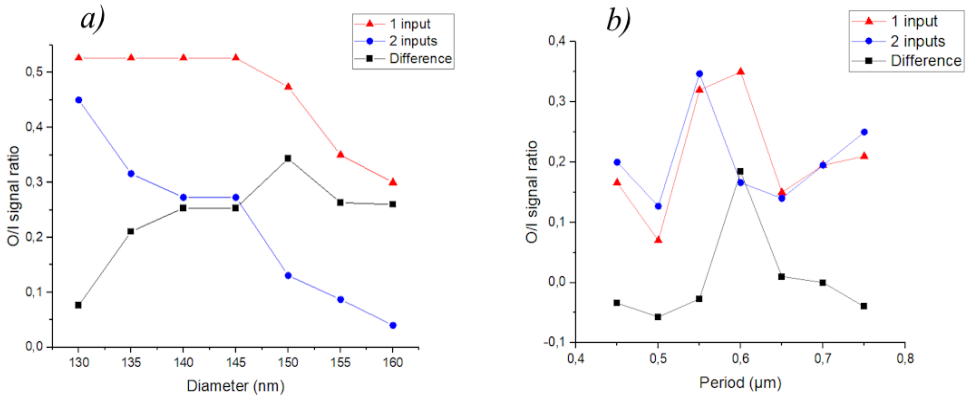


Fig. 2. Dependence of the output/input (O/I) signal intensity ratios on the diameter of GaAs pillars (*a*) and their spacing (*b*).

As can be seen in Figure 2*a*, the maximum value of the difference between the O/I signal intensity ratios is achieved at a pillar diameter of 150 nm. Similarly, the optimal distance between GaAs pillars was found to be 600 nm (Figure 2*b*).

Conclusion

Thus, an all-optical logic comparator based on a GaAs photonic crystal operating at a wavelength of 1.3 μm was simulated in this paper. It was found that the optimal diameter of GaAs pillars for the propagation of radiation with a wavelength of 1.3 μm is 150 nm, and the period is 600 nm. The main advantages of this comparator are its compactness and good output/input characteristics.

Features of the implementation of optical superchannels in flexible optical networks

N. I. Popovskiy[1]
[1] The Bonch-Bruevich Saint Petersburg State University of Telecommunications,
Saint Petersburg, Russia;
nikitanikita24@mail.ru

Abstract. This article discusses the actual problems of using fiber-optic communication systems for efficient data transmission over long distances. Special attention is paid to the concept of optical super channels, combining several optical channels to increase transmission capacity and range. The article discusses the theoretical and practical aspects of the implementation of optical superchannels, including methods for the formation of multichannel signals, the use of optical precompensation of nonlinear effects and dispersion, as well as technologies for multiplexing orthogonal subcarrier channels. The article examines the prospects for the development of flexible optical networks in order to increase productivity and optimize the use of resources in modern telecommunications networks.

Keywords: flexible optical networks, fiber-optic transmission system, dense wavelength division multiplexing, orthogonal frequency division multiplexing, transceiver

Introduction

On existing transport networks built using OTN/DWDM technology, a fixed standardized frequency grid (Fixed Grid) with increments of 50 or 100 GHz is most often used for optical channels (Fig. 1). The simplest equipment is used to organize such a communication line, however, this approach has a number of limitations. The use of Flex Grid technology makes it possible to increase the level of spectral efficiency and throughput of the DWDM system. In the case of organizing an optical channel with a speed of 1 Tbit/s using 10 streams of 100 Gbit/s of the QPSK modulation format and using a standard 50 GHz WDM wave grid with polarization interleaving with partial overlap of the spectra of neighboring signals, the required frequency band will be 500 GHz [1].

Increasing the channel speed while maintaining a single carrier encounters the problem of drastically reducing the transmission range without regeneration. The need to build additional reinforcement points leads to an increase in the cost of communication systems. The optimal solution to preserve the transmission range and increase the channel speed is the use of multiple carrier frequencies in one combined channel, which is commonly called a superchannel.

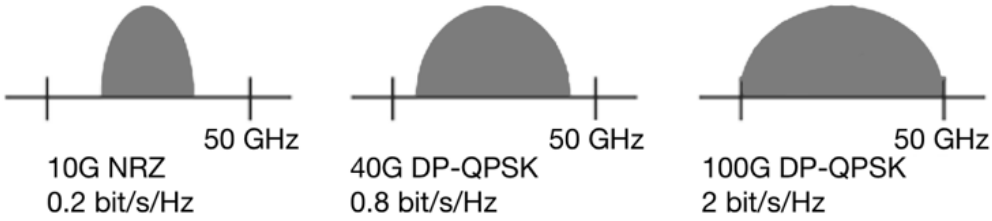


Fig. 1. The frequency band occupied by channels with different speeds

The method of implementing optical superchannels

The scientific novelty in this work lies in the use of exclusively optical elements for the implementation of orthogonal frequency multiplexing. The process involves converting 10 optical client channels, each of which operates at a speed of 10 Gbit/s, into electrical signals. Subsequently, a multichannel group signal is generated in the optical domain by combining signals from various optical subcarrier channels.

A lattice based on an array of waveguides can be used as a demultiplexer for the optical OFDM signal, since it provides both the conversion of a serial signal into a parallel one and the optical Fourier transform in one complex. Since the inverse Fourier transform is topologically identical to the Fourier transform, AWG can also be used as an OFDM signal multiplexer in a transmitter.

In the electronic implementation of optical OFDM transmitters, the process includes QAM modulators for reverse Fourier transform and subsequent conversion from parallel to serial. These modulators convert phase-modulated input signals into a temporary waveform, which is a superposition of subcarrier channel signals. Subsequently, this signal is modulated by an optical carrier using a sophisticated optical modulator. Figure 2 illustrates the optical embodiment of this concept based on AWGR (Arrayed Waveguide Grating Router). The design of this transmitter is based on three layers of plates. The input splitter divides the signal into four copies, each of which is modulated by its own optical modulator, with its own client signal.

The inverse Fourier transform is implemented using a second layer consisting of a plate separator, a phase shift and a combinator. The optical signal passing through it causes a series of phase shifts, where each shift depends on a specific input waveguide (m) and an associated output waveguide (n). Using different delays for different channels, the third level, consisting of a splitter, combines the output signals from the second level. Each input pulse is converted into a sequence of eight output pulses, where each output pulse is a phase-weighted combination of output signals from all modulators.

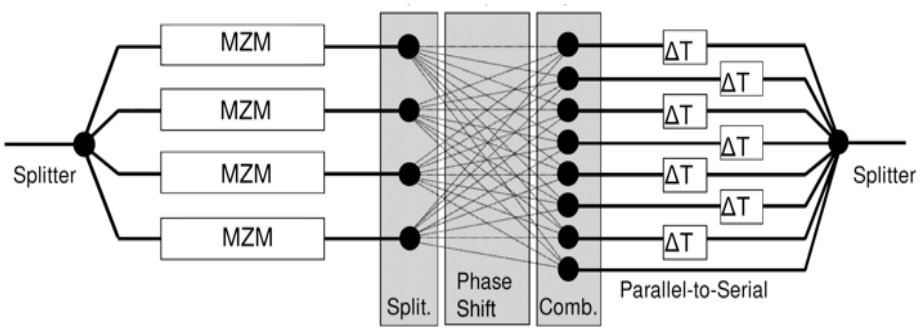


Fig. 2. AWGR block Diagram for an optical OFDM transmitter with four subcarriers

Optical subcarriers come from a single laser radiation source and are modulated by information-carrying client signals using Mach-Zender modulators using lithium niobate (LiNbO3) technology. After modulation, these signals are transmitted via AWGR, which facilitates the OFDM modulation process. The multiplexed signal travels through a 100-kilometer fiber-optic communication channel, reaching both the receiver and the spectroanalyzer.

Results and Discussion

The results of the study showed that the quality of the received signal depends on the bandwidth of the AWGR. As the bandwidth increases, the BER decreases, and therefore the number of correctly received bits decreases.

Conclusion

The studied transmitter circuit uses OFDM to multiplex multiple optical signals, which is a remarkable distinguishing characteristic. OFDM offers significant advantages in terms of high bandwidth and spectrum efficiency. An additional distinguishing feature is the potential design of a transmitter using techniques that integrate all optical elements — such as lasers, modulators, waveguides and gratings — into a single integrated circuit.

REFERENCES

1. **Listvin V.N., Treschikov V.N.** DWDM Systems: Scientific edition. Publishing House "Nauka". 2017. p. 300.

2. **Popovsky N.I., Davydov V.V., Rud V.Yu.** Features of the construction of fiber-optic communication lines with orthogonal frequency division of channels, Scientific and technical bulletin of SPbGPU: Physico-mathematical sciences. 15(3.2) (2022) 178-183.

3. **Speransky V.S., Abramov S.V., Klintsov O.I.** Combination of subscriber code separation and OFDM in fiber data transmission, T-Comm: Telecommunications and Transport. 13(3) (2019) 32-35.

A new method of managing the discretization of the scale in a differential mobile refractometer

D. S. Provodin [1]✉, **M. A. Yakusheva**[2]
Peter the Great St. Petersburg Polytechnic University, St. Petersburg, Russia;
✉provodindanya@gmail.com

Abstract. The necessity of developing a new method for managing the discretization of the scale in a mobile differential refractometer has been justified. The implementation of this method is necessary to expand the functional capabilities of the developed mobile differential refractometer (providing a measurement mode of the refractive index of a liquid medium ranging from 1.23 to 2.63 with an error of 0.0001). All existing liquid media and their mixtures worldwide fall within this measurement range. When using other models of compact and mobile refractometers for express control, such a measurement range of n cannot be provided. Within the range of change of n from 1.23 to 2.63, a new management method has been implemented, which ensured a measurement error of 0.0001. Studies of various media have been conducted, confirming the adequacy of our development.

Keywords: refraction, liquid, refractive index, Anderson cuvette, laser radiation, photodiode array, measurement error.

Introduction

In the modern world, there are numerous fields of human activity that require continuous real-time quality control of liquid media, as the number of different negative factors that affect the quality of liquids and products made with their use is constantly increasing. Currently, there are many different mobile refractometers for express control of liquid media [1]. All of these devices have limitations on the type of liquid measured and the measurement accuracy. One of the most promising solutions to these challenges is the use of a differential refractometer, which allows for measurements of the refractive index of liquid media in the range from 1.23 to 2.63. The problem associated with measuring n using this device lies in achieving an error of 0.0001 throughout the entire range. To address this, a new measurement methodology is being developed in our work.

A new methodology for managing the discretization of the scale using the Anderson differential cuvette

Figure 1 shows the structural diagram of the refractometer with an Anderson cuvette and the path of the laser beam. The refractive index value of the measured liquid is determined by the displacement of the laser beam axis [2].

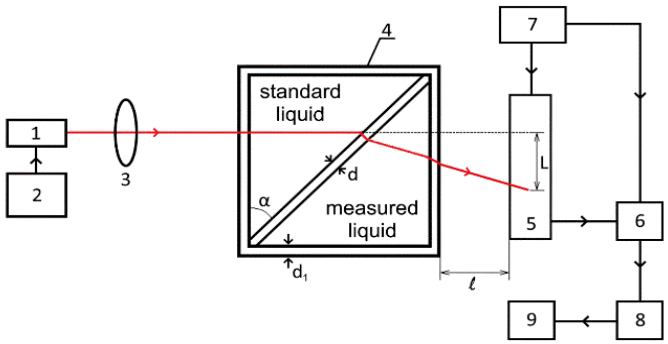


Fig. 1. Block diagram of a laboratory model of a differential refractometer: 1 – laser radiation source; 2 – laser power supply; 3 – macrolens installed at the end of the laser cavity; 4 – Anderson differential cuvette; 5 – photodiode array; 6 – ADC; 7 – multifunctional power supply; 8 – processing device; 9 – laptop.

To register the position of the laser beam axis in the design of the refractometer, a photodiode linear array with 2048 sensors (pixels) is used. This allows for the control of refractive index changes in the range from 1.230 to 2.630 with a step of 0.001 at the initial measurement stage

(with a sensor margin of 600 at the edges of the linear array). This construction ensures the required nm measurement range with a 20% margin, meeting modern requirements. Such arrangement of the laser beam axis registration scheme allows measurements refractive index of measured liquid n_m to start from sensor 310, significantly reducing edge effects compared to the previous use of 1024 sensors in the photodiode linear array 2. In reference [2], the processes of laser beam refraction and various conditions for its reception on the sensors of the photodiode linear array 5 are also detailed, leading to the relationship for determining L.

To obtain a reliable value in accordance with express control requirements, the refractive index of the liquid medium must be measured with an accuracy of 0.0001. To achieve this, a new methodology for changing the scale discretization in a mobile refractometer without altering the linear array construction and laser beam registration principle has been developed. For the measured value of nm, a new Anderson cuvette design and a new standard liquid (new value refractive index of standard liquid n_s) should be selected so that a change of 0.0001 in n_m corresponds to a displacement of one sensor on the photodiode linear array. Previously, the value of n_m was determined up to the third decimal place (for example, n_m = 1.455). After this replacement, the n_m measurement range will be from 1.4050 to 1.5050 with a step of 0.0001 (measurement error of 0.0001). Figure 2 shows the measurement results using the new methodology.

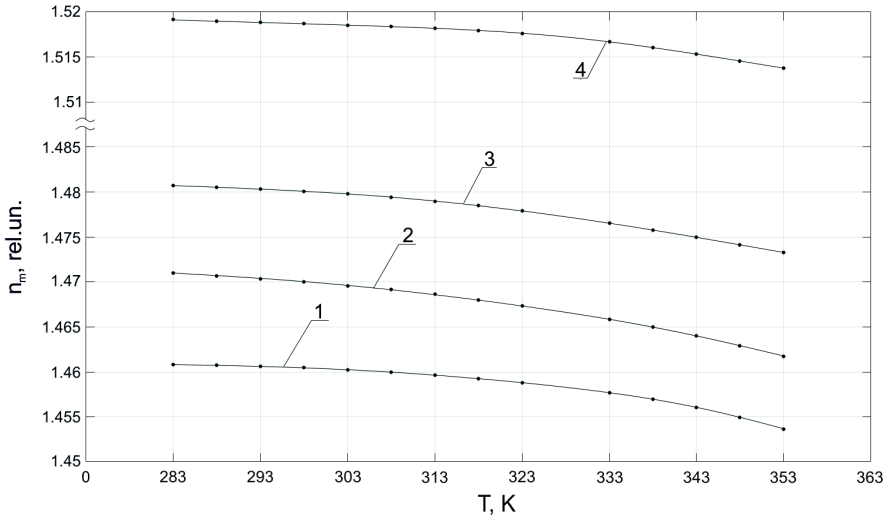


Рис. 2. The dependence of the refractive index n_m of edible oils from the temperature T. Charts 1, 2, 3, 4 correspond to the following oils: olive, sunflower, castor, cedar.

Conclusion

The results obtained showed that our developed new methodology ensures reliable monitoring of liquid media in the measurement range from 1.23 to 2.63. Experimental studies were conducted on various types of vegetable and motor oils, gasoline, sulfur hydrocarbons, and bromonaphthalene. A distinctive feature of the differential refractometer is the ability to use the Anderson cuvette with a sealed lid for measurement, which is crucial when working with volatile and hazardous liquid media. Currently, there are no industrial analogs to this refractometer.

REFERENCES

1. **Guo W., Li, R., Yu, L., Chen, J., Xia, M., Li, W., Yang, K.** Self-referenced technology for refractive index measurement under mechanical vibration and temperature fluctuation, Applied Optics. 58 (7) (2019) 1862–1867.

2. **Provodin D.S., Borodaenko V.I**., Optical method for express control of the state of liquids, Proceeding of VIII International Conference on Information Technology and Nanotechnology (ITNT). Samara, Russian Federation, 23-25 April 2022, Vol. 21992029 (2022), 217-222.

Confocal microscopy of a display hologram

L. N. Borodina[1], **E. V. Rabosh** [1✉], **N. V. Petrov**[1,2], **A. V. Veniaminov**[1]
[1] ITMO University, St. Petersburg, Russia
[2] Harbin Engineering University, Shandong, China
✉rabosh.ev@itmo.ru

Abstract. The expansion confocal laser scanning microscopy was applied for the first time to visualize the subdiffraction-limit internal architecture of display holograms recorded in Slavich silver-halide emulsions. The holograms got enhanced in size due to swelling of the emulsion in a viscous liquid that also served as an immersion medium in high-aperture microscopy. The images were obtained using 3D-scanning in reflection mode. Due to the expansion, the reflection hologram's spatial period is extracted from beyond the diffraction limit and the architecture of the hologram is visualized. Along with the main periodical structure originating from the recorded interference pattern, granularity supposedly caused by scattered light can be observed in the microscopic images.

Keywords: display holography, volume reflection hologram, confocal laser scanning microscopy, expansion microscopy, silver-halide materials.

Funding: This research was funded by the RPMA grant of School of Physics and Engineering of ITMO University.

Introduction

Display holography enables preservation of cultural heritage objects in the form of their most precise optical copies. At the same time, a number of art holograms have been recognized as objects of cultural heritage. Valuable holograms were found to deteriorate, be destroyed under exposure to light, humidity, and the need for their timely examination, monitoring of their health and their proper storage and display conditions has been realized. Therefore, the study of the fine structure of the display hologram is an urgent task.

Despite extremely high spatial resolution characteristic of electron and probe microscopies, they are capable of visualizing only the surface structure of a hologram, but not its volume, therefore they appear insufficient for the studies of three-dimensional display holograms. The optical approach might be the most straightforward, but the diffraction limit makes the structure of reflection-type holograms with typical spatial periods of 130-170 nm hardly accessible.

Diffraction limitations can be overcome by using a new promising approach based on physical expansion (swelling) of the hologram microstructure. The approach developed and applied in the present study originates from the recently invented technique based on physical stretching the object [1,2], which has been applied so far only to biological objects, up to our knowledge.

Materials and Methods

The reflection-type display holograms of the test objects (a flat mirror and a metal sphere) were recorded in high-resolution PFG-03M silver-halide plates (Slavich, RF) in Denisyuk's geometry using an expanded and collimated beam of a 200 mW DPSS laser, undergone the photochemical treatment prescribed by the manufacturer.

As previously noted, the spatial periods of volumetric reflection-type holograms are too small for their direct observation by optical methods. Therefore, an experimental approach has been developed to study their structure, which is implemented by means of confocal laser scanning microscopy. The method is based on the volumetric expansion accompanied by an increase in the spatial period of the hologram due to swelling of the gelatine-based emulsion in various penetrating liquids such as an immersion oil.

The morphology of the hologram was studied at various stages of swelling using a confocal laser scanning microscope LSM 710 (Zeiss, Germany) by constructing a 3D image of the structure from individual optical slices recorded in the reflected light of a 405 nm diode laser.

Results and Discussion

3D images, optical slices and surface profiles of the holograms were obtained, demonstrating changes in the periodicity of its reflective structure resulting from swelling. Figure 1 shows a 3D image of the microstructure of a reflection-type hologram swollen in an immersion oil, obtained using an LSM 710 laser scanning microscope with a 40x/1.3 lens. The colors in the image correspond to the axial coordinate. The physical size of the hologram has been increased due to swelling, thus making it possible to observe the otherwise inaccessible small-period structure. The image shows non-planar isophase surfaces. This eliminates possible doubts about scanning artifacts as the source of the observed volumetric periodic structure.

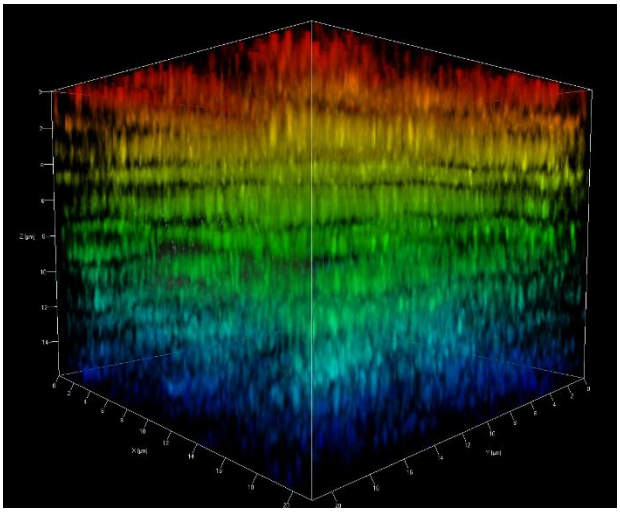


Fig. 1. 3D image of a swollen (bleached) display hologram obtained using LSM710 confocal laser scanning microscope (Zeiss) in reflected light of 405 nm laser. The artificial colors are encoded by depth

Along with the main periodical structure originating from the recorded interference pattern, granularity supposedly caused by scattered light can be observed in the microscopic images.

Conclusion

We show that the small-scale periodic structure of a volumetric hologram can be revealed and studied using laser scanning microscopy assisted by expansion. Along with the main periodical structure originating from the recorded interference pattern, certain granularity supposedly caused by scattered light can be observed in the microscopic images. The approach being developed and used is expected to be applied to monitoring the structure of volume holograms recorded in various high-resolution media.

Acknowledgments

The authors are grateful to Dr. Vladimir Borisov for his valuable thoughts and recommendations.

REFERENCES

1. **Wen Gang, Leen V., Rohand T., Sauer M., Hofkens J.**, Current Progress in Expansion Microscopy: Chemical Strategies and Applications, Chem. Rev., 123 (2023) 3299−3323.
2. **Halpern A.R., Alas G.C. M., Chozinski T.J., Paredez A.R., Vaughan J.C**. Hybrid Structured Illumination Expansion Microscopy Reveals Microbial Cytoskeleton Organization, ACS Nano, 11 (2017) 12677−12686.

Topological edge states supported by two-dimensional square-lattice arrays of bianisotropic dielectric resonators

A. D. Rozenblit [1]✉, **G. D. Kurganov** [1], **N. A. Olekhno** [1], **D. V. Zhirihin** [1]

[1] ITMO University, Saint Petersburg, Russia

✉alina.rozenblit@metalab.ifmo.ru

Abstract. To implement photonic topological insulators, it is essentially to consider symmetry properties of a system as a whole and physical features of individual resonators. Here, we propose a new model of two-dimensional (2D) structure which is composed of centimeter-scale bianisotropic dielectric resonators placed in the nodes of a square lattice and supports topological edge states at microwave frequencies.

The simulation results for a finite structure demonstrate the emergence of in-gap topological edge states at the interface between the domains with oppositely oriented bianisotropic resonators. We numerically demonstrate spin-momentum locking for these modes, and, moreover, the emergence of such edge states at the boundary between the structure and free space, which is unusual for photonic topological insulators. The resilience of the observed states is confirmed by studying the system with double-bend interface and geometrical imperfections.

Keywords: topological edge states, bianisotropy, dielectric resonators, radiophysics

Funding: This study was funded by Russian Science Foundation (project 321258).

Introduction

Topological edge states possess fascinating physical properties like unidirectional wave propagation and robustness to the geometrical imperfections and backscattering [1]. Such states have been observed with the help of diverse experimental platforms including optical [2] and microwave [3] systems.

Materials composed of dielectric resonant particles represent one of the common platforms for realization of photonic topological insulators due to their low losses in comparison with metallic structures [4]. Previously it was shown that the bianisotropy of individual resonators reached by breaking their geometrical symmetry leads to the bandgap opening [5].

In the present work, we consider a two-dimensional (2D) square lattice of dielectric bianisotropic resonators. Even though hexagonal 2D [6] and 3D [7] topological insulators composed of bianisotropic resonators are well studied, the case of the 2D square-lattice systems has not been addressed yet.

Materials and Methods

The proposed system represents a 2D array of dielectric bianisotropic resonators placed in the nodes of a simple square lattice having the period a = 37.1 mm, while a single resonator is implemented as two attached cylinders with the diameters d_1 = 29.1 mm and d_2 = 22 mm, and the heights h_1 = 9 mm and h_2 = 3 mm, respectively, Fig. 1(a). The permittivity of the resonators is ε = 39. We construct the numerical model of such resonators using CST Microwave Studio 2022 software package. To study the model, we first consider a unite cell under Floquet periodic boundary conditions which correspond to the infinite array of such bianisotropic resonators. Next, we extract magnetic response of the finite structure to the linearly and circularly polarized sources to demonstrate topologically protected states at the linear and double-bend domain walls, as well as at the boundary between the array and free space.

Results and Discussion

The results of numerical simulations of the dispersion diagram for the infinite array of dielectric bianisotropic resonators is shown in Fig. 1(b) and demonstrates the bandgap opening in the range from 2.43 GHz to 2.53 GHz at M-point of the Brillouin zone.

The numerically simulated magnetic field profiles at the frequency f = 2.47 GHz demonstrate the presence of topological edge states along the interface in case of linearly polarized excitation,

Fig. 1(c). The topological state is also observed with the same excitation at the boundary between the array of resonators and free space at f = 2.47 GHz, Fig. 1(d).

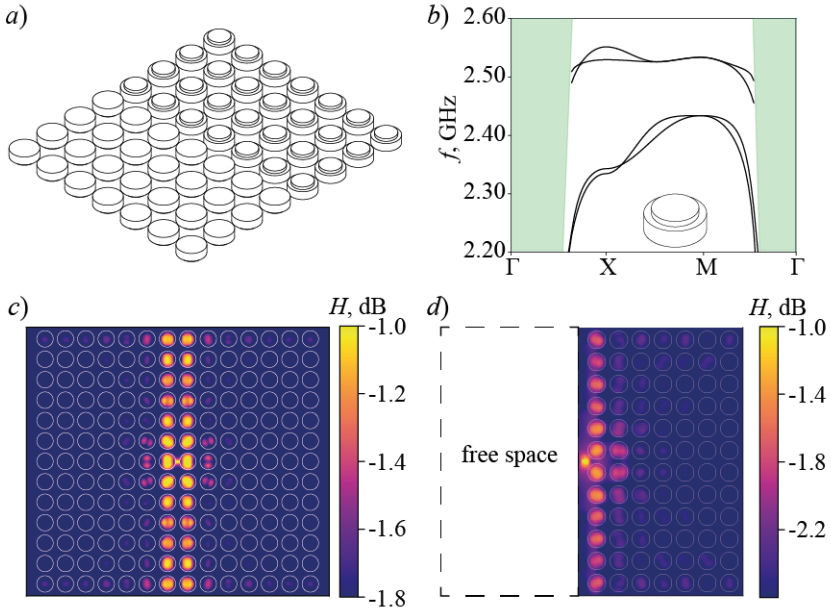


Fig. 1. (a) Schematic model of the considered system. (b) The dispersion diagram for the infinite array of bianisotropic resonators. Green shaded area shows the light cone. (c,d) *H*-field profiles at the frequency f = 2.47 GHz for the two domains and single domain configurations, respectively. White circles show the edges of resonators.

Conclusion

To conclude, we propose a 2D model having square lattice symmetry and supporting topological edge states resulting from the bianisotropy of individual resonators. We perform numerical simulations of such a system implemented as an array of dielectric centimeter-scale resonators working at GHz frequencies and feasible for further experimental realization. The results demonstrate the emergence of topological edge states, their spin-momentum locking for circularly polarized excitation, and their robust propagation both for domain walls and a boundary between the photonic topological insulator and free space.

Acknowledgments

The work is supported by Russian Science Foundation (project 321258).

REFERENCES

1. **Silveirinha M. G.**, Bulk-edge correspondence for topological photonic continua, Physical Review B. 94(20) (2016) 205105.
2. **On M. B., et al.**, Programmable integrated photonics for topological Hamiltonians, Nature Communications. 15.1 (2024) 629.
3. **Li Y., et al.**, Topological LC-circuits based on microstrips and observation of electromagnetic modes with orbital angular momentum, Nature Communications. 9.1 (2018) 4598.
4. **Kurganov G. D., et al.**, Temperature control of electromagnetic topological edge states, Applied Physics Letters. 120.23 (2022).
5. **Alaee R., et al.**, All-dielectric reciprocal bianisotropic nanoparticles, Physical Review B. 92.24 (2015) 245130.
6. **Slobozhanyuk, A., et al.**, Near-field imaging of spin-locked edge states in all-dielectric topological metasurfaces, Applied Physics Letters 114.3 (2019).
7. **Slobozhanyuk A. et al.**, Three-dimensional all-dielectric photonic topological insulator, Nature Photonics 11.2 (2017) 130-136.

Photoluminescence of self-induced InAs nanowires diluted with nitrogen

M. S. Ruzhevich [1✉], **K. D. Mynbaev** [1,2], **N. L. Bazhenov** [2], **A. K. Kaveev**[2], **V. V. Fedorov** [3], **I. S. Mukhin** [3]

[1] ITMO University, Saint-Petersburg, Russia;
[2] Ioffe Institute, Saint-Petersburg, Russia;
[3] Alferov University, Saint-Petersburg, Russia;
✉max.ruzhevich@niuitmo.ru

Abstract. Photoluminescence of self-induced nanowires consisting of pure InAs and of InAs diluted with nitrogen was studied in the 4.2–300 K temperature range. The presence of the cubic sphalerite and hexagonal wurtzite crystal structure modifications was established. A decrease in the band gap of both crystalline phases due to the introduction of nitrogen has been revealed.

Keywords: InAs, nanowires, photoluminescence, crystal structure.

Introduction

InAs is a compound of the A_3B_5 group, characterized by a direct band gap and high electron mobility, and is widely used in infrared (IR) optoelectronics. The bulk material has a cubic crystal lattice of the sphalerite (zinc blende) type with a band gap E_g of the order of ~0.35 eV at 300 K. Recently, interest has been growing in low-dimensional structures based on InAs, in particular in nanowires (NWs). The transition to NW geometry provides an efficient method for electrical and optical confinement, which can improve the efficiency of InAs-based optoelectronic devices. InAs NWs can be used to create highly efficient photodetectors and emitters in the mid-IR spectral region (λ=3-6 μm) [1-3]. However, the growth of low-dimensional InAs structures allows a formation not only of a cubic, but also of a hexagonal wurtzite-type lattice [4], with E_g being about ~0.4 eV at 300 K. In this work, we studied the influence of the morphology and crystal structure modifications on the InAs photoluminescence (PL) spectra. In addition, we used the PL method to study the nitrogen dilution in NWs, replacing the As in InAs partly, and reducing optical E_g via affecting the material electronic structure through the interaction between localized N levels and the InAs band states similar to the GaAsN case [5].

Materials and Methods

Epitaxial NW arrays (120-150 nm in diameter and 1-2.5 μm in height) made of pure InAs and InAs diluted with nitrogen were grown by molecular beam epitaxy on Si(111) substrates using the method described in Ref. [6]. The NW formation occurs in a self-induced mode at the pinhole defects formed in the SiO_x layer at high temperature annealing, without the use of third-party catalysts. According to scanning electron microscopy (SEM) measurements, besides of NWs, additional parasitic islands were formed on the SiO_x surface outside of the pinhole defects due to the tendency of nitrogen to react with SiO_x.

PL spectra were recorded using pulsed semiconductor laser excitation with the 1.03 μm emission wavelength, the 1 kHz frequency, and the 2 μs pulse duration in the 4.2–300 K temperature range. A cooled InSb photodiode was used as a detector.

Results and Discussion

Structural properties of the NWs were studied with use of X-ray diffractometry with reciprocal space mapping (XRD-RSM) and transmission electron microscopy (TEM). The results obtained show the wurtzite structure domination in the In(As,N) NWs.

The PL spectra of the NWs recorded at the T=4.2 K temperature contained two peaks with energies close to ~413 meV and ~454 meV for a pure InAs sample and ~400 meV and ~443 meV for the sample diluted with nitrogen, respectively. The full-widths at half maxima (FWHM) of high-energy (HE) peaks were about 37 meV for the pure InAs sample and about 45 meV for the sample diluted with nitrogen. For the low-energy (LE) peaks, the FWHMs were about 38

meV and about 29 meV, respectively. The temperature increase to 274 K results in change of the HE peak FWHM values close to 85 meV for the pure InAs sample and to 51 meV for the sample diluted with nitrogen. Comparison of PL and XRD-RSM measurements show that the high-intensity HE peaks correspond to the NWs having the wurtzite-type crystal structure, while the less intense LE peak referred to the parasitic islands having a sphalerite-type structure. For InAs NWs diluted with nitrogen, a shift of the PL spectrum to longer wavelengths relative to that of the pure InAs sample by the value close to 11 meV was observed.

The character of the LE peak position dependence on temperature is similar to that for the previously studied dependency for the bulk InAs. The LE peaks were observed up to the temperatures of about 125 K for the pure InAs sample and up to about 50 K for the sample with diluted nitrogen. There is no pronounced dependence of the HE peak position on a temperature in the range up to about 50 K. With a further temperature increase, the experimental dependence approached the $E_g(T)$ dependence for InAs.

Conclusion

We present the results of studying the PL of self-induced NWs consisting of pure InAs and InAs diluted with nitrogen. It was found that the nitrogen introduction in the InAs NWs leads to the PL response red shift of about 11 meV. Based on XRD-RSM measurements, we observed pronounced contribution of both the InAs NWs with the wurtzite crystal structure and parasitic islands with the sphalerite-type structure in the PL spectra.

Acknowledgement

This work was financially supported by the Russian Scientific Foundation (RSF project 22-19-00494) for NW epitaxial growth. Structural characterization was financially supported by the Ministry of Science and Higher Education of the Russian Federation (FSEG-2023-0016).

REFERENCES

1. **Wang Z., Liu L., Zhong Z., Li X., Chen Y., Zhang J., Shi W., Zhang W., Wang J., Chu J., Huang H.**, Regulating the bipolar response of InAs nanowire photodetector and waveguide integration, Appl. Phys. Lett. 124 (10) (2024) 101102.

2. **Xu T., Wang H., Chen X., Luo M., Zhang L., Wang Y., Chen F., Shan C., Yu C.**, Recent progress on infrared photodetectors based on InAs and InAsSb nanowires, Nanotechnology 31 (2020) 294004.

3. **Sonner M., Treu J., Saller K., Riedl H., Finley J., Koblmüller G.**, Carrier concentration dependent photoluminescence properties of Si-doped InAs nanowires, Appl. Phys. Lett. 112 (9) (2018) 091904.

4. **Dick K.A., Thelander C., Samuelson L., Caroff P.**, Crystal phase engineering in single InAs nanowires, Nano Letters 10(9) (2010) 3494-3499.

5. **Wu J., Shan W., Walukiewicz W.**, Band anticrossing in highly mismatched III-V semiconductor alloys, Semicond. Sci. Technol. 17(8) (2002) 860-869.

6. **Fedorov V., Vinnichenko M., Ustimenko R., Kirilenko D., Pirogov E., Pavlov A., Polozkov R., Sharov V., Kaveev A., Miniv D., Dvoretckaia L., Firsov D., Mozharov A., Mukhin I.** Non-Uniformly Strained Core–Shell InAs/InP Nanowires for Mid-Infrared Photonic Applications, ACS Applied Nano Materials. 6 (7) (2023) 5460–5468.

The investigation of optical needle formation by subwavelength optical elements using high-performance computer systems

D. A. Savelyev [1,2]✉

[1] Samara National Research University, Samara, Russia;

[2] Image Processing Systems Institute, NRC "Kurchatov Institute" Samara, Russia

✉savelev.da.2@ssau.ru

Abstract. The optical vortex diffraction on subwavelength optical elements with a standard and GRIN substrate using the finite difference time domain method was simulated in this paper. The possibility of increasing the light needle for input radiation with azimuthal and radial polarization was shown using a GRIN substrate and a subwavelength element with zones alternating in height.

Keywords: optical vortices, GRIN, subwavelength ring gratings, FDTD.

Funding: This research was funded by the Russian Science Foundation (project No. 24-22-00044), https://rscf.ru/en/project/24-22-00044/.

Introduction

Optical vortices are known for their use in various applications [1–3], among which are optical manipulation, sensing, optical information transmission, and sharp focusing [2, 4]. Some optical structures can be used to generate optical vortices such as spiral phase plates [5], metasurfaces, and ring gratings [1, 4]. The ring gratings and diffraction axicons in various combinations are also used to obtain optical needles with a large depth of focus [4, 6].

Also currently well known is the use of materials with a gradient refractive index (GRadient Index, GRIN) to control the propagation of light, solve problems of optical communication, and light collimation [4, 7].

Thus, the study of optical vortex diffraction on subwavelength ring gratings with variable relief heights with a standard and GRIN substrate was carried out in this paper to form an elongated focal segment (light needle).

Materials and Methods

The numerical simulations (3D) in this paper were carried out using the finite difference time domain (FDTD) method on an 850 Gflop computing cluster. This following modeling parameters were considered: the wavelength λ of the input radiation was equal to 0.532 μm, space step – $\lambda/30$, time step – $\lambda/(60c)$, where c is the speed of light. The size of the three-dimensional computational domain is 15.8λ. The computational region was surrounded on all sides by an absorbing layer PML of size 1.12λ. The Meep software package was used for numerical modeling [8]. Optical vortices of the first order (Laguerre - Gauss mode (1,0), σ = 1.5 μm) with radial and azimuthal polarization were considered as input radiation.

The variable-height ring gratings with a standard substrate (refractive index n = 1.47) and a GRIN substrate were considered. The refractive index of GRIN substrate was varied uniformly from the maximum refractive index in the center (n = 2.7) to the minimum refractive index at the edges (n = 1.47). The GRIN substrate consisted of rings of the same width.

The refractive index of the relief was n = 1.47. The relief height of the elements h was chosen based on the phase jump π radians, respectively, for n = 1.47 the base height h was $1.06\,\lambda\,(\pi)$. Next, the height of the odd (h_1) and even (h_2) relief zones of the elements was varied, also based on the phase jump π radians.

Results and Discussion

The results of numerical simulation of the consideration laser radiation are shown in figure 1 (*a* – standard substrate, other cases – GRIN substrate). The length of the light segment was estimated by the full length by the half maximum of the radiation intensity (DOF), similarly to the

assessment of the focal spot on the optical axis - by the full width at half maximum (FWHM) of the intensity.

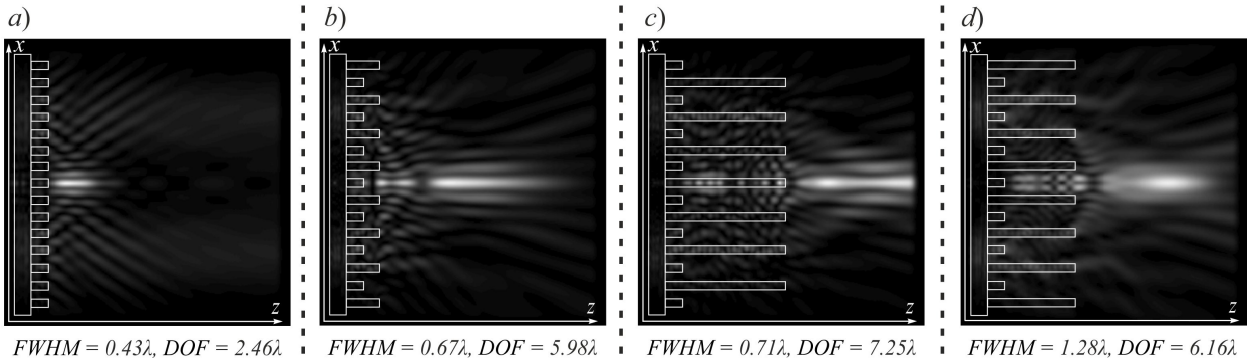


Fig. 1. The two-dimensional diffraction pattern (xz plane) of an optical vortex on ring gratings (total intensity), with azimuthal polarization and relief height h = 1.06λ (a), h_1 = 1.06λ, h_2 = 2.13λ (b), h_1 = 7.45λ, h_2 = 1.06λ (c), radial polarization and relief height h_1 = 1.06λ, h_2 = 5.32λ (*d*)

A diffraction axicon with a height of h = 1.06λ with a standard substrate acted as a basic optical element for comparison. Increasing the height of the relief, as well as the use of a GRIN substrate, made it possible to increase the length of the light needle, for azimuthal polarization, the size of the light needle was DOF = 7.25λ, which is 2.94 times longer than in the case of the basic optical element. It should also be noted that the formation of a long light segment (DOF = 6.16λ) is observed for an element with alternating zones for a GRIN substrate with radial polarization. An increase in the size of the light segments is accompanied by an increase in the size of the focal spots.

Conclusion

The diffraction of first-order optical vortices with azimuthal and radial polarization on subwavelength ring gratings of variable height with a standard substrate and a GRIN substrate using the FDTD method was simulated in this paper. The maximum light needle on the optical axis (DOF = 7.25λ) was obtained for an element with alternating zones (h_1 = 7.45λ, h_2 = 1.06λ) with azimuthal polarization of input radiation.

REFERENCES

1. **Shen Y., Wang X., Xie Z., Min C., Fu X., Liu Q., Gong M., Yuan X.**, Optical vortices 30 years on: OAM manipulation from topological charge to multiple singularities, Light: Science & Applications. 8 (1) (2019) 1–29.

2. **Dong M., Zhao C., Cai Y., Yang Y.**, Partially coherent vortex beams: Fundamentals and applications, Science China Physics, Mechanics & Astronomy. 64 (2) (2021) 224201.

3. **Khonina S. N.**, Vortex beams with high-order cylindrical polarization: features of focal distributions, Applied Physics B. 125 (6) (2019) 100.

4. **Savelyev D. A., Karpeev S. V.**, Development of 3D Microstructures for the Formation of a Set of Optical Traps on the Optical Axis, Photonics. 10 (2) (2023) 117.

5. **Lightman S., Hurvitz G., Gvishi R., Arie A.**, Miniature wide-spectrum mode sorter for vortex beams produced by 3D laser printing, Optica. 4(6) (2017) 605–610.

6. **Shi C., Xu Z., Nie Z., Xia Z., Dong B., Liu J.**, Sub-wavelength longitudinally polarized optical needle arrays generated with tightly focused radially polarized Gaussian beam. Optics communications. 505 (2022), 127506.

7. **Richardson K. A., Kang M., Sisken L., Yadav A., Novak S., Lepicard A., Martin I., Francois-Saint-Cyr H., Schwarz C. M., Mayer T. S., Rivero-Baleine C., Yee A. J., Mingareev I.**, Advances in infrared gradient refractive index (GRIN) materials: a review, Optical Engineering. 59 (11) (2020), 112602.

8. **Srivastava P. R., Majumdar A., Menon R., Swartzlander G. A.**, High forward thrust metasurface beam-riding sail, Optics Express. 32(2) (2024) 1756–1763.

Influence of gas flow rate and heating on the dimensional properties of platinum particles synthesized in a gas discharge

A. F. Sanatulina✉, A. K. Novoselov, O. V. Vershinina, E.I. Kameneva, D. Malo, A. A. Lizunova

Moscow Institute of Physics and Technology, Dolgoprudny, Russia

✉sanatulina.af@phystech.edu

Abstract. This study was devoted to investigating the influence of various gas flows rates on the size properties of platinum nanoparticles (Pt NPs) synthesized by a gas discharge method with additional heat treatment at 985 °C in a gas flow, as well as studying the optical and morphology properties of Pt plasmonic structures formed by dry aerosol printing using from the obtained nanoparticles. The results confirmed that heat treatment in tube furnace and varying a gas flow rate can be employed to alter the morphology and size of Pt NPs from 5 to 145 nm. A relationship between the sizes of nanoparticles processed in the tube furnace and the magnitude of the working gas flow was established. Absorption spectra of Pt thin films produced by dry aerosol printing, and their thickness which are necessary for further researches of plasmonic properties of obtained nanostructures was determined.

Keywords: Platinum nanoparticles (Pt NPs), spark discharge, tube furnace, plasmonic structures, absorption spectra.

Funding: This work was financially supported by the Russian Science Foundation (project № 22-19-00311, https://rscf.ru/en/project/22-19-00311/).

Introduction

Currently, there are numerous methods for synthesizing plasmonic nanostructures used in photonics, electronics, biomedicine, and microscopy [1]. Pt NPs exhibit plasmonic properties in the ultraviolet region, making it crucial to study their characteristics. The cleanest method for obtaining such particles is a gas discharge method [2]. This study examines the size and optical characteristics of Pt NPs synthesized through gas discharge with additional thermal treatment, depending on the gas flow, as well as the properties of platinum films created using the dry aerosol printing method on glass substrates.

Methods and materials

Platinum nanoparticles were synthesized in a pulsed-periodic gas discharge using electric erosion of platinum electrodes in an argon atmosphere with a chemical purity of 6.0 at an excess pressure of 0.6 atm. To achieve this, a voltage of 1.5 kV was applied between the electrodes, with a current of 30 mA, a generation frequency of 500 Hz, and a capacitor capacity of 40 nF. The particles obtained were transported along the gas path and then subjected to modification in a tube furnace heated to 985°C. The synthesis was carried out at various gas flows (ranging from 50 to 1000 ml/min) using platinum electrodes in the form of cylinders with outer and inner diameters of 8 mm and 6 mm, respectively, containing pure material at 99.9999% purity. The aerosol printing of nanostructures was performed on a gas-discharge particle synthesis setup combined with a nozzle for printing in a gas flow of 100 ml/min using quartz glass. The morphology of the nanoparticles was examined using a transmission electron microscope (TEM) Jeol JEM 2100 (200 kV). The absorption spectra of film plasmon nanostructures were analyzed using a JASCO V–770 spectrophotometer. The morphology of platinum plasmonic nanostructures was studied using a scanning electron microscope (SEM) JSM 7001F (JEOL).

Results and discussion

According to the data from the transmission electron microscopy (TEM) in Fig. 1*a*, primary nanoparticles with sizes around 5 nm were synthesized at a gas flow rate of 100 ml/min. Passing through a tube furnace at 985°C in the same gas flow resulted in the transformation of agglomerate morphology into platinum nanoparticles with a size of 93 ± 5 nm, as shown in Fig. 1*b*. Fig. 1*c* shows that as the gas flow rate increases, the average particle size decreases. This dependence of the average particle size on the gas flow is described by a function inversely proportional to the gas flow. In the SEM images, (Fig. 1*d* and Fig. 1*e*) it can be seen that the printed particles form agglomerates, while the thermally modified particles align into lines of individual platinum particles during printing. Additionally, films printed at a flow rate of 100 ml/min, with and without thermal treatment in the tube furnace, have different film thicknesses: 4.7 ± 2.7 nm based on NP without modification and 26.2 ± 5.6 nm with thermal modification. The absorption spectra of platinum plasmon nanostructures are shown in Fig. 1*f*.

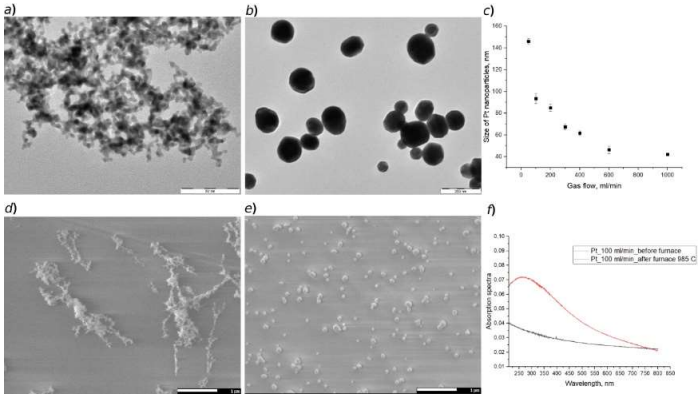


Fig. 1. Size analysis of Pt NPs: TEM image of Pt NPs for a gas flow of 100 ml/min: agglomerates produced without modification (*a*); after thermal treatment (*b*), then a graph of the dependence of the average size of Pt NPs after passing through a tube furnace heated to a temperature of 985 °C on the gas flow (*c*), study of Pt plasmon nanostructures formed using nanoparticles produced at a gas flow of 100 ml/min: SEV image of a Pt film prepared by NPs without modification (*d*); after thermal modification (*e*), the absorption spectra of Pt plasmon nanostructures (*f*)

Conclusion

During the research, it was found that thermal treatment in a tube furnace heated to 985 ° C, the largest NPs (145 ± 2 nm) are formed at a flow rate of 50 ml/min. Plasmon film nanostructures based on obtained NPs using dry aerosol printing were formed. The optical properties of Pt nanostructures showed an absorption peak in ultraviolet range between 240 and 300 nm.

Acknowledgments

The research was financially supported by the Russian Science Foundation project № 22-19-00311, https://rscf.ru/en/project/22-19-00311/.

REFERENCES

1. **Kruis F.E., Fissan H., Peled A.,** Synthesis of Nanoparticles in the Gas Phase for Electronic, Optical and Magnetic Applications - a review, Journal of Aerosol Science. 29 (5-6) (1998) 511–535.

2. **Efimov A. A., Arsenov P. V., Borisov V. I., Buchnev A. I., Lizunova A. A., Kornyushin D. V., Tikhonov S. S., Musaev A. G., Urazov M. N., Shcherbakov M. I., Spirin D. V., Ivanov V. V.,** Synthesis of nanoparticles by spark discharge as a facile and versatile technique of preparing highly conductive Pt nano-ink for printed electronics, Nanomaterials. 11 (1) (2021) 234.

Luminescence enhancement in inelastic tunnelling of electrons by changing the geometry of the tunnelling contact

N. A. Solomonov [1,2✉], **D. V. Lebedev** [1,3], **K. N. Novikova** [1,2], **S. V. Fedina** [1,2], **N. V. Vaulin** [1], **L. N. Dvoretskaya** [1], **A. V. Arhipov** [2], **A. O. Golubok** [3], **I. S. Mukhin** [1,2]

[1] Alferov University, Saint Petersburg, Russia;

[2] Peter the Great St.Petersburg Polytechnic University, Saint Petersburg, Russia;

[3]Institute for Analytical Instrumentation of the Russian Academy of Sciences, Saint Petersburg, Russia;

✉solomonov.nik@gmail.com

Abstract: We have experimentally investigated the light emission resulting from inelastic electron tunneling in the transition with hemispherical gold nanoantennas (d=400 nm, h=300 nm) created by direct fs-laser ablation and a tungsten scanning microscope probe. We found two characteristic modes of luminescence: standard - increased signal is observed in the region of nanoantennas at tunneling currents below 2.25 nA and inverted-anomalous, where the gold surface is mainly luminescent, while dark spots are observed on the antennas on the contrary. In the inverted-anomalous mode we observe record signal values of $4 \cdot 10^4$ photons per second. We attribute the anomalous effect to the realization of a conditionality for resonant tunneling of electrons with excitation of optical states.

Keywords: golden nanoantenna, femtosecond laser printing, nanoscale on-chip light sourse, luminescence from tunnel junction, inelastic tunneling of electrons, resonant electron tunneling, scanning tunneling microscope.

Funding: The work was supported by the Russian Science Foundation (grant № 21-79-10346).

Introduction

One of the main challenges on the way to the design and successful realization of full-fledged optoelectronic integrated chips is the development of a nanoscale on-chip photon source whose emission can be excited and controlled by electrical signals and which is compatible with current semiconductor technologies.

A promising option for the realization of a nanoscale light source that meets all of the above requirements is the use of tunneling contact between two metal surfaces distant from each other by a subnanometer distance (metal-insulator-metal (MIM)). In the process of inelastic tunneling through the MIM, part of the electron energy can be used up to create a photon, but the probability of such a process is extremely small $\sim 10^{-5}$-10^{-6}, which does not allow the use of simple planar MIM photon sources in practice. However, as shown in our previous work [1], by modifying one of the electrodes of a MIM structure using point femtosecond laser ablation and creating gold hollow nanoantennas on its surface, the external quantum efficiency (EQE – photon ratio per number of tunneled electrons) for the regions above the nanoantennas can be increased by an order of magnitude compared to the planar surface, but the EQE still remains at uncompetitively low values. The aim of this work is to further improve the EQE in a MIM structure with gold nanoantennas by optimizing the geometrical and energetic parameters of the tunnel gap and investigating the photon emission phenomena resulting from inelastic tunneling.

Materials and Methods

The initial sample is a 50 nm gold film deposited on an optically smooth glass substrate by electron beam evaporation without additional adhesive layers. Rows of nanoantennas with a period from 1 to 1.5 μm and a diameter of 400 nm were printed on the gold film by femtosecond laser ablation [2]. The nanocontact with the sample is formed using a tungsten etched probe in an ultrahigh vacuum tunneling microscope (Omicron UHV VT AFM/STM) and can be precisely modified during measurements. Spatial maps of tunnel contact luminescence (STM-L) were recorded using an external data acquisition system based on a single-photon counter with a spectral

range of 400-900 nm, and the counter readings were synchronized with the STM microscope [3]. The optimum tunnel contact parameters were searched for at a fixed bias voltage of 2.7 V (one of the characteristic luminescence peaks of the structures on tunnel VACs) and tunnel currents in the range of 100-5000 pA by repeatedly recording STM-L distributions. In Figure 1, two STM-L images were selected from a series of experimental data, showing two characteristic results of the search for optimal parameters, the standard luminescence mode - Fig. 1 (a, b, c), the anomalous mode - Fig. 1 (d, e, f)

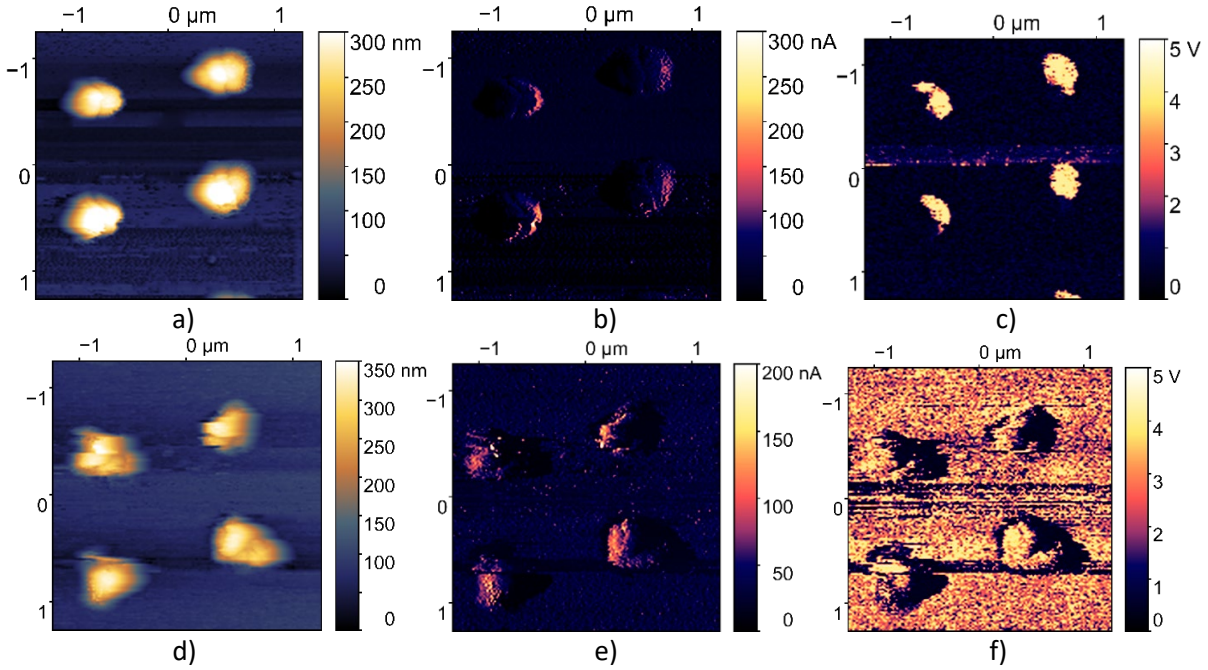


Fig.1 Synchronized recording of topography and tunnel luminescence (STM-L technique): a, d) - STM topography of nanoantennas, b), e) - map of tunnel currents, c), f) - map of tunnel luminescence (STM-L).

Results and Discussion

In the whole investigated range of tunnel contact parameters, two modes can be distinguished: the first, the mode of standard luminescence, consists in a smooth increase of the signal on the STM-L map when the tunnel current is increased to ~2.25 nA (increasing current = probe coming closer to the surface). Further increase of the current leads to a sharp change of the picture to an anomalous one, the luminescence signal sharply increases over the whole surface area on the STM-L map by about 5 times in amplitude from $5 \cdot 10^3$ photons per second to more than $4 \cdot 10^4$ photons per second, while above the nanoantenna zone, on the contrary, an area of weak luminescence is observed. When the currents are reduced back to 2nA or when 3nA is exceeded, the glow mode is switched back to normal.

Conclusion

The fact of such a sharp change in the luminescence pattern and increase in the luminescence intensity, respectively, EQE, may indicate the manifestation of resonant tunneling of electrons with excitation of optical states or the manifestation of other effects. Electron tunneling processes occurring in the anomalous luminescence regime require further deeper investigations.

REFERENCES

1. **Lebedev D. V., et al.,** Indirect Detection of the Light Emission in the Local Tunnel Junction." physica status solidi (RRL)–Rapid Research Letters 14.3 (2020): 1900607.

2. **Pavlov, D. V., et al.,** Laser-induced surface relief nanocrowns as a manifestation of nanoscale Rayleigh-Plateau hydrodynamic instability, Applied Surface Science. 511 (2020): 145463.

3. **Lebedev D. V., Solomonov N. A.**, Femtosecond Laser-Printed Gold Nanoantennas for Electrically Driven and Bias-Tuned Nanoscale Light Sources Operating in Visible and Infrared Spectral Ranges, The Journal of Physical Chemistry Letters 14.22 (2023): 5134-5140.

Investigation of the characteristics of the metaatom field in the high-frequency range.

N. E. Solonovich [1]✉
[1] NUST MISIS, Moscow, Russia;
✉ m2209649@edu.misis.ru

Abstract

The resonant interaction of electromagnetic radiation with a two-level quantum system has recently aroused increased interest in connection with the development of quantum information technologies. Particular importance is attached to the problem of increasing the retention time of the coherence of the qubit. Electro-wave experiments in the high-frequency range with such quantum systems make it possible to obtain information that is of interest to a wide range of physical objects. One of the possible ways to influence the quantum mechanical system is the use of high-quality metamaterials. Obtaining a high-Q resonance is possible when a bound state in a continuum (BIC) occurs in the system.

In the work, a system consisting of a meta-atom in a cylindrical waveguide was modeled. A bound state in the continuum was obtained in the system. A multipole analysis of the field in the system was performed. The resonance of the electromagnetic field arising from interaction with the simulated meta-atom was estimated. The change in the contribution of multipole moments of the field of different order was investigated when changing the geometric parameters of the system. Potentially, a system with a bound state in a continuum can extend the lifetime of a quantum state due to high Q-factor.

Bound states in a continuum

Bound states in a continuum (BIC) are non-radiating states that occur in certain physical systems. The concept of Bound States in the Continuum was first introduced by John von Neumann and Eugene Wigner in 1929. In essence, it involves a particle within a continuum band of energy being confined within bounded regions, creating the Bound State. These states were first described in quantum mechanics but were later obtained in photonics, hydrodynamics and acoustics. These states are eigenmodes that in a certain limit of some parameter space cannot couple to any radiation channel [1]. In the absence of material losses, BICs have infinite lifetimes and zero linewidths. Since the mid-2010s, the study of potential applications of BIC has become a growing trend in research. Achieving BICs will be of great interest for the realization of cavities with arbitrarily high Q-factor and for applications such as lasing and detecton [2].

In practice, such states can be obtained by changing the symmetry of the system [3].

In this work, we model the scheme of the high-Q resonator using bound states in the continuum concept.

The model consists of a metaatom located on a silicon substrate in a cylindrical waveguide with two coaxial ports. Copper was chosen as the material for the waveguide and wires, aluminum was chosen as the material for the metaatom.

Electromagnetic response of the system, including spatial distribution of the induced currents required in formulas for multipoles, was modeled using 3D Maxwell's equations solver of the Comsol Multiphysics simulation package. As a result of calculations, the dependencies of the S-parameter for the system were obtained (Fig.1.). A change in the distance from the center of the waveguide to the metaatom leads to the appearance of a resonance which indicates the possibility of BIC.

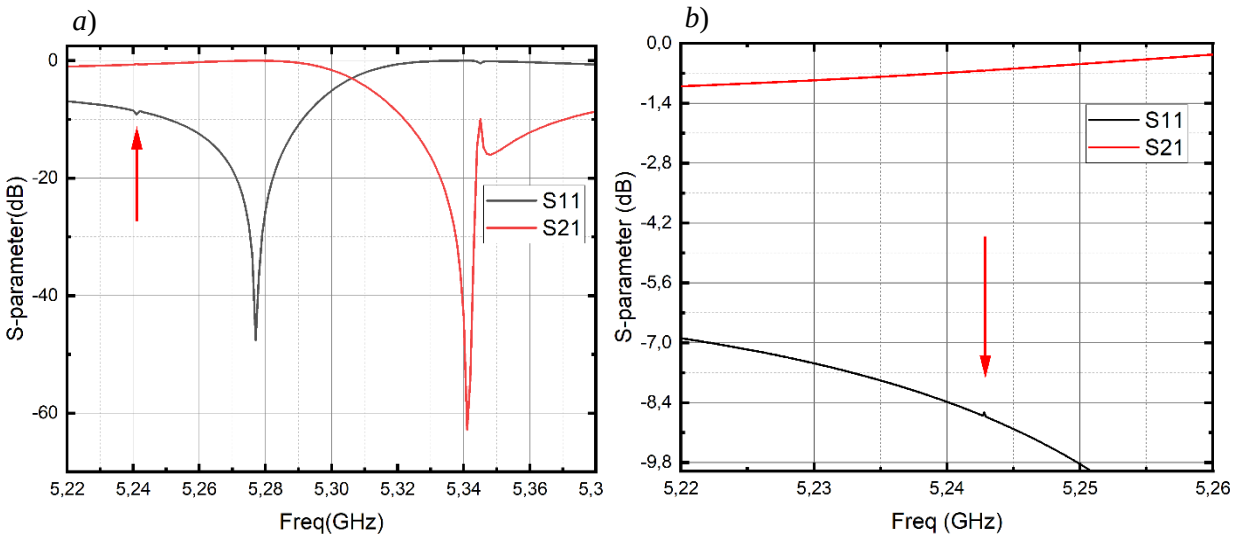


Fig. 1. The dependence of the s parameter on the frequency of incident radiation. Panel (a) shows a wider graph showing two resonances occurring in the system. Panel (b) shows the first resonance, more clearly. Both dependences were obtained when the meta-atom was removed from the center of the waveguide at a distance of 3 mm. The red arrows indicate the resonance resulting from BIC.

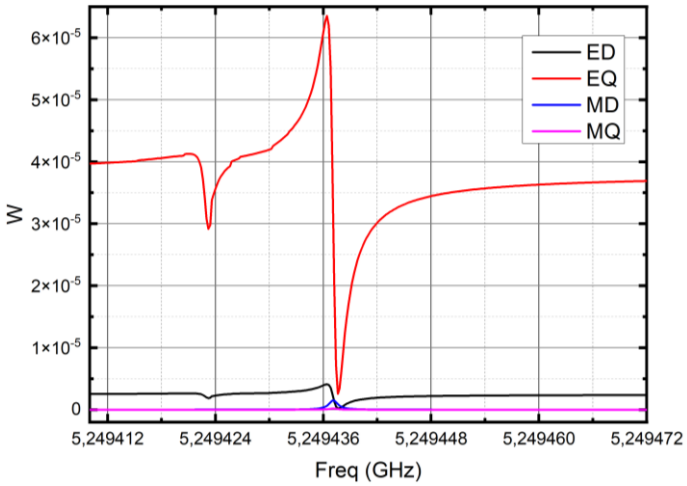


Fig. 2. Contributions of multipoles of various orders to the metaatom field. It can be seen that the electric quadrupole prevails in the resonance region.

Multipole analysis

To study the resonance, the multipole decomposition method was chosen [4]. Multipole moments of the electromagnetic field in long-wavelength approximation (ED, MD, EQ, MQ) can be defined by the following formulas [5].

$$P_\alpha = -\frac{1}{i\omega}\left\{\int d^3\mathbf{r}\mathbf{J}_\alpha^\omega + \frac{k^2}{10}\int d^3\,\mathbf{r}[(\mathbf{r}\cdot\mathbf{J}_\omega)r_\alpha - 2r^2\mathbf{J}_\alpha^\omega]\right\} \quad (1)$$

$$m_\alpha = \frac{1}{2}\int d^3\mathbf{r}(\mathbf{r}\times\mathbf{J}_\omega)_\alpha \quad (2)$$

$$Q_{\alpha\beta}^e = \frac{1}{i\omega}\left\{\int d^3\boldsymbol{r}\left[3\left(r_\beta J_\alpha^\omega + r_\alpha J_\beta^\omega\right) - 2(\boldsymbol{r}\cdot\boldsymbol{J}_\omega)\delta_{\alpha\beta}\right] + \right. \quad (3)$$

$$\left. + \frac{k^2}{14}\int d^3\,\mathbf{r}\left[4r_\alpha r_\beta(\boldsymbol{r}\cdot\boldsymbol{J}_\omega) - 5r^2\left(r_\alpha J_\beta + r_\beta J_\alpha\right) + 2r^2(\boldsymbol{r}\cdot\boldsymbol{J}_\omega)\delta_{\alpha\beta}\right]\right\}$$

$$Q_{\alpha\beta}^m = \int d^3\boldsymbol{r}\{r_\alpha(\boldsymbol{r}\times\boldsymbol{J}_\omega)_\beta + r_\beta(\boldsymbol{r}\times\boldsymbol{J}_\omega)_\alpha\} \quad (4)$$

Where $\boldsymbol{J}_{\omega}(\boldsymbol{r}) = i\omega\epsilon_0(\epsilon_r - 1)E_r(\boldsymbol{r})$ is induce electric current density ($E_r(\boldsymbol{r})$ – the electric field distribution, ϵ_0 – relative permittivity of free space and ϵ_r – relative permittivity of the material).

The the contributions of multipoles of various orders to the metaatom field calculated in the model can be seen on the fig.2.

Conclusion

High Q resonators are a critical component for ultra-narrow linewidth lasers, frequency stabilization, precision spectroscopy, quantum communication and computation. Integration in a photonic waveguide platform is key to reducing cost, size, power and sensitivity to environmental disturbances. One of the options for creating such materials is to obtain Bound States in a Continuum.

In this work, using the example of a metaatom system in a waveguide, a bound state in a continuum was obtained. The parameters of the resonance arising in the system were investigated. In the future, it is planned to use a quantum system with two states (qubit) as a metaatom and investigate the lifetime of the quantum state.

REFERENCES

1. **C. W. Hsu, et al**, "Bound states in the continuum," Nat. Rev. Mater. 1, 16048 (2016).
2. **S. Han, et al**, "All-dielectric active photonics driven by bound states in the continuum," arXiv:1803.01992 (2018).
3. **Kirill Koshelev, Sergey Lepeshov, Mingkai Liu, Andrey Bogdanov, Yuri Kivshar,** "Asymmetric Metasurfaces with High-Q Resonances" Phys. Rev. Lett. 121, 193903 (2018)
4. **Jackson J.D**., Classical electrodynamics, Mir, Moscow (1965)
5. **Rasoul Alaee, Carsten Rockstuhl, I. Fernandez-Corbaton,** "An electromagnetic multipole expansion beyond the long-wavelength approximation", V. 407, P. 17-21 (2018)

Quantum size effect in cadmium sulphide films after plasma treatment

A.V. Stanchik[1,2]✉, K.P. Buskis[1], V.F. Gremenok[1,2],
A.V. Kabyliatski[1], V. V. Khoroshko[2], S. P. Zimin[3,4], I. I. Amirov[3]
[1] Scientific-Practical Materials Research Centre of the National Academy of Sciences of Belarus, Minsk, Belarus
[2] Belarussian State University of Informatics and Radioelectronics, Minsk, Belarus
[3] Yaroslavl Branch of the Valiev Institute of Physics and Technology, Russian Academy of Sciences, Yaroslavl, Russia
[4] P.G. Demidov Yaroslavl State University, Yaroslavl, Russia
✉stanchik@physics.by

Abstract. In this work, the optical properties of nanocrystalline CdS films in the initial state and after ion-plasma treatment have been studied. The chemical bath deposition technique was used to prepare CdS films with thickness 90–115 nm on glass substrates. The ion-plasma treatment was carried out in argon plasma in a high-density low-pressure radio frequency inductively coupled plasma reactor at an argon ion energy of 25 eV for 20–50 s. The results showed that the sizes of coherent scattering regions during plasma treatment decreased for a series of studied samples from 8.2–10.0 nm to 6.3–7.7 nm. This led to the appearance of changes in the transmission and reflection spectra, to an increase in the band gap energy of the for nanocrystalline CdS films from 2.53–2.78 eV to 2.95–3.11 eV.

Keywords: Cadmium sulphide, thin films, chemical bath deposition, plasma treatment, transmission spectra, band gap energy.

Funding: This study was funded by the Belarusian Republican Foundation for Fundamental Research grant number T23RNFM-029. This work supported by the Ministry of Higher Education and Science of the Russian Federation was performed in the framework of the state task of the Yaroslavl Branch of K. A. Valiev Institute of Physics and Technology, Russian Academy of Sciences (FFNN-2022-0017).

Introduction

Cadmium sulphide (CdS) is an important semiconductor of II-VI group with a band gap of 2.42 eV at 300 K, which has potential application in nanoelectronic and optoelectronic systems. An actual direction of CdS research in recent years is the formation and study of nanostructured materials with controllable properties. One of the effective methods of nanostructuring is the method of ion-plasma treatment [1]. The aim of this work was to study the effect of plasma treatment on the optical characteristics of nanocrystalline CdS films for further application in various devices.

Materials and Methods

In our experiments the chemical bath deposition technique was used to prepare CdS films (90–115 nm). The resulting solution in the bath used for CdS preparation, composed of 90 ml deionized water, 30 ml NH_4OH (wt 25%), 40 ml 0.0096M $CdSO_4$ as a source of cadmium and 40 ml 0.8M $CS(NH_2)_2$ as a source of sulphide. The deposition is performed at a bath temperature of 50, 60, and 70 °C onto pre-cleaned glass substrates. For different cycles, deposition time was set at 5, 10, 15, and 20 min. The ion-plasma treatment was carried out in argon plasma in a high-density low-pressure radio frequency inductively coupled plasma reactor at an argon ion energy of 25 eV for 20–50 s [2]. Surface morphological properties and cross section were analyzed using an H-800 scanning electron micro-scope (Hitachi, Japan) with a resolution of 0.2 nm. The elemental composition was obtained using energy-dispersive X-ray spectroscopy (EDS) on AZtecLive Advanced with Ultim Max 40 (Oxford Instruments). The structural properties of films were studied by using Ultima IV x-ray diffractometer (Rigaku) in grazing incidence X-ray diffraction geometry at 1 degree of incident x-rays with CuK_α radiation source (λ = 1.5418 Å)

scanned in the range of 10° to 80°. The transmission and specular reflection spectra of the films were obtained using Photon RT (Essent Optics) spectrophotometer in the wavelength range of 300–2500 nm with spectral resolution better than 4 nm using unpolarized light at room temperature.

Results and Discussion

Composition of the deposited CdS thin films on glass substrate is Sulphur 42.5–50.0% at. and Cadmium 50.0–57.5% at. The presence of a broad X-ray diffraction peak is an indication of nanocrystalline nature of the CdS thin films in initial state and after ion bombardment. It was found that ion-plasma treatment results in modification of structural parameters of nanocrystalline CdS films. In the process of ion sputtering, a decrease in film thickness, the appearance of new nanostructures on the surface, and a decrease in the size of coherent scattering regions (crystallite sizes) are observed. The sizes of coherent scattering regions during plasma treatment decreased for a series of studied samples from 8.2–10.0 nm to 6.3–7.7 nm. Such changes lead to changes in the optical properties of the films, which is shown on the example of one of the samples in Fig. 1. Based on the analysis of the transmission spectra, the values of the band gap energy were determined. An increase in the band gap energy from 2.53–2.78 to 2.95–3.11 eV was observed for all samples.

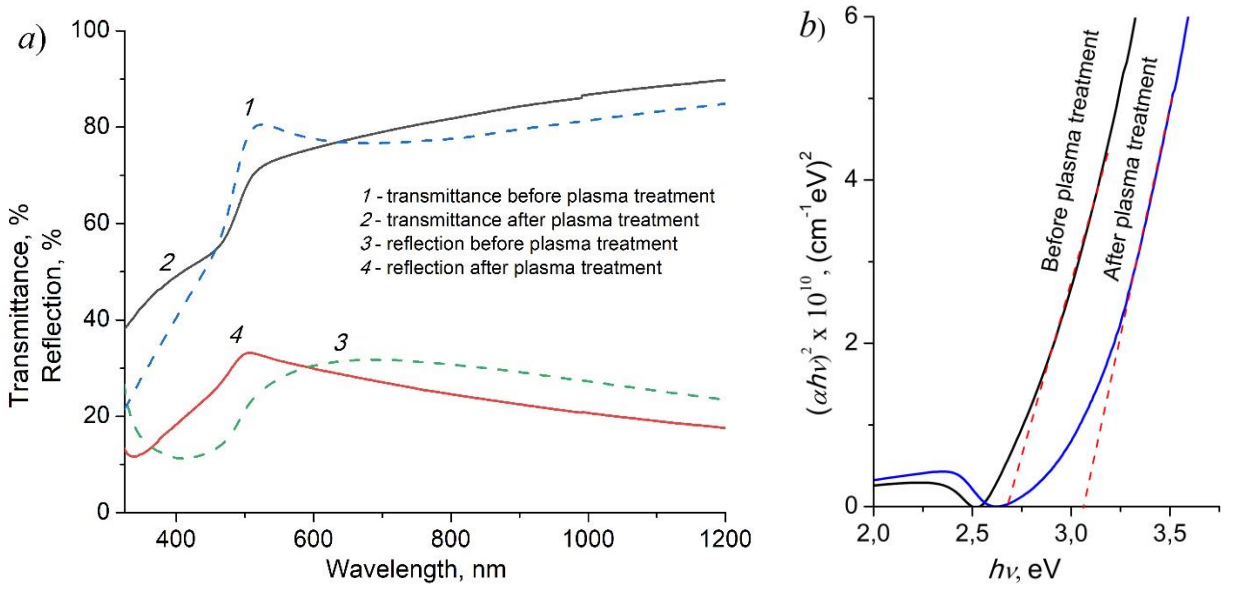


Fig. 1. Reflection and transmission spectra for CdS film before and after plasma treatment (*a*). Tauc plots and band gap values evaluation for as prepared and after plasma treatment CdS (*b*).

Conclusion

The results of this work showed that ion-plasma treatment of nanocrystalline films of cadmium sulphide with 90–115 nm thickness promotes the formation of nanostructures of smaller sizes, which provides an increase in the band gap energy due to the realization of quantum size effects [3]. The report compares the obtained data with literature data and analyzes the physical reasons for the changes in the structural parameters of films during ion-plasma treatment.

REFERENCES

1. **Levchenko I., Ostrikov K.,** Nanostructures of various dimensionalities from plasma and neutral fluxes, J. Phys. D: Appl. Phys. 40 (8) (2007) 2308.

2. **Zimin S., Gorlachev E., Amirov I.,** Inductively Coupled Plasma Sputtering: Structure of IV-VI Semiconductors. In Encyclopedia of Plasma Technology, 1st ed.; Shohet, J.L.; CRC Press, New York, USA (2017) 679–691.

3. **Brus L.,** Electronic wave functions in semiconductor clusters: experiment and theory, J. Phys. Chem. 90 (12) (1986) 2555–2560.

Features of express control of three-component mixture of volatile hydrocarbon media in visible light

G. V. Stepanenkov[1]✉, D. V. Vakorina[1] and V. V. Davydov[1, 2]

[1]The Bonch-Bruevich Saint Petersburg State University of Telecommunications, Saint Petersburg, Russia.

[2] Peter the Great Saint-Petersburg Polytechnic University, Saint Petersburg, Russia

✉ 261199g@gmail.ru

Abstract. The necessity to improve the method of express control of hydrocarbon media and their mixtures, especially volatile ones, is substantiated. The problems arising at controlling the state of a mixture of three components of volatile hydrocarbon media using the refraction phenomenon are noted. Problems arising in the study and analysis of the mixture are noted. The use of this method allows to determine the composition and percentage content of components in hydrocarbon mixtures of three components. The results of calculations are presented.

Keywords: hydrocarbon medium, mixture, refraction, express control, refractive index, visible light, light-shadow boundary, concentration, measurement error.

Introduction

As a basis for the ongoing study, we took the already performed experience with the use of a medium consisting of two components [1]. The necessity of this study is due to the occurrence of situations in which the determination of the concentration factor F1 and F2 when solving equation (1) is impossible [2]. This means that the mixture under study consists of three media.

$$n_m = n_t = n_b = F_1 n_m^t + F_2 n_m^b \quad (1)$$

Measurement methodology

If the solution (1) with respect to coefficients F_1 and F_2 does not exist due to violation of physical laws (there are three or more media in the mixture). In this case, equation (1) must be transformed into the following form (for three media):

$$n_m = n_t = n_b = F_1 n_m^t + F_2 n_m^b + F_3 n_3 \quad (2)$$

There is no unambiguous solution of equation (2) with respect to the coefficients F_1, F_2, F_3 and the chosen value of n_3 for three known values (n_t, n_m^t, n_m^b). There will be a large number of variations on the coefficients F_1, F_2, F_3 given the choice of the real refractive index n3 of the third medium. For example, it makes no sense to mix diesel fuel with gasoline (the media are different in color (gasoline is pale yellow, diesel fuel is the color of brewed tea)). This can be seen very well visually. Therefore, after obtaining F_1, F_2, F_3 values, it is necessary to analyze the obtained data. Reject those results that contradict logic and real life. For example, a mixture of gasoline Ai-95, Ai-92 and alcohol (methanol) in the proportion of 0.4:0.3:0.3 was obtained. This cannot happen in reality, no one will do it on purpose (the car most likely will not start). From the real results of solution (2) there will still remain a sufficiently large number of variants (each of these variants can occur with different probability). In these variants we know the composition of the mixture and their weight coefficients. To unambiguously determine the coefficients and the third component in the mixture, we have developed the following technique based on the weight ratio. For its realization it is necessary to weigh a sample of the investigated mixture with the volume V_m = 100 ml before measuring the refractive indices. The resulting M_m is the mass of the 100 ml mixture. In case of express control on the premises, it is most likely that a 10 ml mixture will have to be weighed, if possible, it is better to weigh 100 ml. The following proportion is made up:

$$M_m = V_m (\rho_1 F_1 + \rho_2 F_2 + \rho_3 F_3) \quad (3)$$

where ρ_1, ρ_2 and ρ_3 are the values of densities of the two media we determined in the sample and one assumed (taking into account the temperature).

Fulfillment of relation (3) allows unambiguously establish the true values of F_1, F_2, F_3, as well as the name of the third medium. Therefore, when using this technique in express control it is necessary to have measuring vessels of 10 and 100 ml and scales with measurement error of 0.1 g or less to solve this problem. It should be noted that the question of the influence of the measurement error Mm on the choice of an unambiguous solution of equation (3) should be investigated separately.

Table 1. Values of densities ρ of liquid media used as fuel at T = 278 K.

Type of fuel	Average value of density ρ by fuel kg/l	Type of fuel	Average value of density ρ by fuel kg/l
Gasoline A-76 unleaded	0,730	Fuel RT	0,778
Normal 80 unleaded	0,730	Aviation kerosene TS	0,780
A-80 leaded	0,730	AI-98 unleaded	0,780
AI-95 unleaded	0,750	Kerosene	0,810
Straight jet kerosene	0,755	Fuel T1	0,819
AI-92 unleaded	0,760	Diesel fuel	0,840
Aviation kerosene TS-2	0,766	Lighting kerosene	0,840
AI-96 unleaded	0,770	Biodiesel	0,870

Analysis of the data on densities ρ from Table 1 showed that only two media can be located between gasoline grades Ai-80 and Ai-92. These are Ai-95 gasoline and straight-run aviation kerosene (PAK). The calculation of gasoline and kerosene densities for temperature T1 = 300 K was performed. The following results for the densities were obtained:

ρ (AI-80) = 0.7254 ± 0.0008 kg/L
ρ (AI-92) = 0.7562 ± 0.0008 kg/L
ρ (AI-95) = 0.7467 ± 0.0008 kg/L
ρ (SJT) = 0.7483 ± 0.0008 kg/l.

The calculation results were compared with the data obtained by measuring the densities of the above media using a DMA 35 EX pycnometer with a measurement error of 0.0007 kg/L at temperature T1 = 299.9 ± 0.1 K. The following results were obtained:

ρ (AI-80) = 0.7253 ± 0.0007 kg/L
ρ (AI-92) = 0.7561 ± 0.0007 kg/L
ρ (AI-95) = 0.7466 ± 0.0007 kg/L
ρ (SJT) = 0.7482 ± 0.0007 kg/l.

As a result of calculations and measurements, the values coincided within the error limits. These values can be used to solve the equation.

Solving the refraction equation (2) for two possible variants of the third mixture (AI-95 or PAK), we obtain a large number of coefficients F1, F2 and F3. Some of them do not correspond to reality and are therefore excluded from further consideration. The probability of occurrence of such events is close to zero. In addition, when excluding the set of F1, F2, and F3 coefficients from consideration, the measured mass of the studied mixture Mm was taken into account.

REFERENCES

1. **G. V. Stepanenkov, D. V. Vakorina**. Peculiarities of express control of volatile hydrocarbon media and their mixtures in visible light, UZFF, MSU (2023), no. 4
2. **Grebenikova N. M., Smirnov K. J., Rud V. Yu., Artemiev V. V.** Features of monitoring the state of the liquid medium by refractometer. Journal of Physics: Conference Series, 2018, V. 1135(1), pp. 012055.

Conference materials
UDC 535.14
DOI: https://doi.org/10.18721/JPM.

Modeling the dynamics and properties of the compressed state of light in a phase modulator.

A. V. Tabieva [1]✉, **A. I. Trifavov, G.V.Tushavin** [1]
[1] ITMO University, St. Petersburg, Russian Federation
✉tabieva.arina@itmo.ru

Abstract. Generation of a compressed multimode state and analysis of statistical characteristics of a given subset of spectral components of a quantum optical signal at the output of a phase modulator

Keywords: phase modulator, multimode quantum optical signal, SU(1,1) algebra, squeezed state of light

Introduction

Research on the processes of transforming the spectral and statistical properties of multimode quantum-optical signals is of great practical importance due to the use of such signals in quantum communication and cryptography systems. This transformation is mainly implemented in phase modulators. A semi-classical model of a phase modulator was proposed and studied in the paper [1], within which the process of modulating an optical signal in a fully quantum state can be described. A nonlinear crystal placed between two parallel metallic electrodes was used as an electro-optic modulator. There are several issues related to quantizing the model of a phase modulator. The direct quantization of the classical model leads to a non-unitary evolution operator: in the classical model, the amplitudes of frequency modes are determined by Bessel functions, which decrease with increasing mode index difference. Due to the fact that the modulated frequency exceeds the modulating frequency by several orders of magnitude, the problem of negative frequencies does not arise in practice.

Materials and Methods

In this work we consider the dynamics of a photon-compressed states of a single-tone signal arriving at the input of the electro-optical modulator and analyze the statistical characteristics of the ensemble of modes at the output of the device. The compressed state is expressed by squares of the mode operators of this signal. The dynamics of the mode operators of the compressed state are expressed by Wigner functions. The beam splitter model allows the output signal to be decomposed into a sum of orthogonal modes. Using their coherent representation, their reduced density matrix is computed.

Results and Discussion

1. Within the framework of the semiclassical model of a phase modulator, the statistical properties of the collective state of a subset of frequency modes at the output of the modulator have been studied.

2. For a given subset of frequency modes of a phase-modulated single-frequency signal in a compressed state, a reduced density matrix is obtained.

3. It is shown that when modulating the state of a single-tone signal compressed by the number of photons, a signal is formed at the output of the modulator, whose frequency modes are in an entangled state.

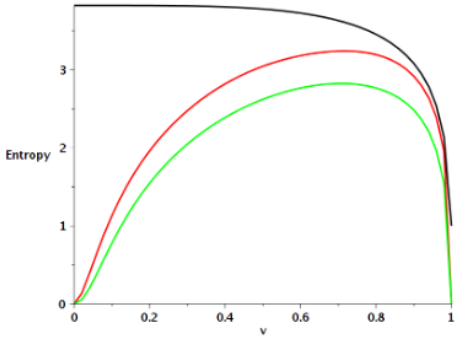


Fig. 1. Dependence of entropy on the parameter v at the compression parameter η =0.2 and comparison with the logarithm of purity log2P.

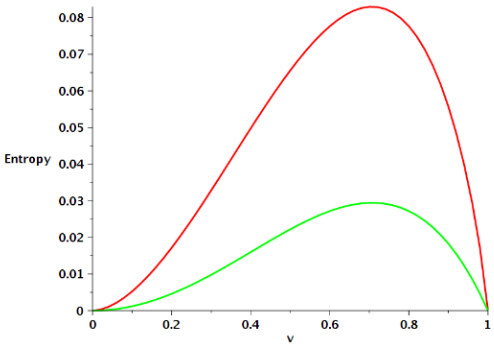


Fig. 2. Dependence of entropy on the parameter v at the compression parameter η = 0.99, comparison with the logarithm of purity log2P and the upper bound.

Conclusion

As a result of the work, an analytical expression was obtained for the reduced density matrix of a selected subset of frequency modes. It has been shown that the collective state of all modes is mixed up and has a significant resource to use when transmitting information. We assessed such characteristics as the degree of entanglement, state purity and quantum entropy.

REFERENCES

1. **G.P. Miroshnichenko**, et al., JOSA B, -2017, 34 (7), 061177-14–772.

2. **Capmany, J., Fernandez-Pousa,** C. R., Laser Photonics Rev., -2011, Vol. 5(6), pp. 7503.

3. **Tushavin G.V., Zaitseva E.V., Trifanov A.I.** Ladder operators approach to representation classification problem for Jordan–Schwinger image of su(2) algebra. Nanosystems: Phys. Chem. Math., 2022, 13 (3), 299–307.

E-beam resist AR-N 7520 in the formation of the photonic structures

K. A. Fetisenkova[1,2]✉, A.E. Melnikov [2], A.V. Miakonkikh[2], A.E. Rogozhin[2], A.A. Tatarintsev[2]

[1]Moscow Institute of Physics and Technology, Moscow, Russia;
[2] Valiev Institute of Physics and Technology of RAS, Moscow, Russia
✉fetisenkova.ka@phystech.edu

Abstract. The study of plasma resistance of the AR-N 7520 was carried out. The selectivity of the reactive ion etching (RIE) of silicon through the mask of negative electron resist AR-N7520 also was investigated. The dependence for selectivity was obtained at different fractions of SF_6 in the feeding gas and at the different values of bias voltage. A high etching selectivity of 8 ± 1.8 was obtained for the etching process. The dependence of the resist line height on the exposure dose is presented. The optimal value for the line exposure dose was found to be 8200 pC/cm.

Keywords: electron-beam lithography; etching kinetic; novolak; reactive-ion etching, waveguide

Funding: This study was supported by Program no. FFNN-2022-0021 of the Ministry of Science and Higher Education of Russia for Valiev Institute of Physics and Technology of RAS.

Introduction

The study of the e-beam resist properties, optimization of the electron beam lithography (EBL) parameters, and the etching process are important for nanoelectronics and photonics because the resolution of EBL is defined by the properties of e-beam resist and by processes during development and exposure [1-3].

The negative e-beam resist AR-N 7520 belongs to the novolaks and has high contrast and high plasma etching resistance [4, 5]. The study of EBL and RIE processes with AR-N 7520 will enable a technology for forming silicon waveguides and other photonic nanostructures with lower sidewall roughness and different aspect ratios.

Materials and Methods

A p-type silicon (100) wafers were pretreated in n-methylpyrrolidone and acetone. To promote adhesion, the silicon wafer was held in hexamethyldisilazane (HMDS) vapor at 85 °C for 10 minutes. The AR-N7520 with a concentration of 7.3% (PGMEA, 1-methoxy-2-propanol acetate) was spin-coated onto the surface using an SM-180 centrifuge (SAWATEC AG, Switzerland) at a centrifuge speed of 3000 rpm. The thickness of the resist layer was measured using a spectral ellipsometer M-2000X (J.A. Woollam Co., Inc., USA) and amounted to 100 ± 1nm. The exposure was carried out on a Raith-150 e-beam lithograph (Raith, Inc., USA) with the e-beam energy of 30 keV, the beam current was 150 pA. The pattern of lines of 1 mm in length was formed. The line exposure dose ranged from 4000 to 16000 pC/cm with a step of 200 pC/cm. Development was performed in 25% tetramethylammonium hydroxide (TMAH) solution for 50 s at 21°C.

RIE was performed on a Dual PlasmaLab 100 (Oxford Instruments Plasma Technology, UK) using an inductively coupled plasma (ICP) of the SF_6/C_4F_8 feeding gas. The wafers were segmented to obtain a set of samples with identical patterns of lines (60 lines per sample). Variation of the SF_6 fraction in feeding gas in the range of 15% – 25% was investigated at 125 V DC bias. The effect of DC bias voltage on the etching process was studied in the range of 80 V – 150 V at a constant fraction of SF_6 in feeding gas 22%. The etching process time was 30 s.

Images of the pattern of lines after etching and the thickness of the AR-N 7520 resist before and after the etching process, and the depth of silicon etching were obtained using a scanning electron microscope (SEM) Ultra 55 (Carl Zeiss AG, Germany).

The selectivity of the silicon RIE through the AR-N7520 mask was calculated as the ratio of the Si etching depth to the decrease in the height resist line during the etching process:

$$S = \frac{d_{Si}}{d_o - d} \quad (1)$$

where d_{Si} is the depth of silicon etching, d_0 is the height of the resist line before etching and d is the height of the resist line after etching. The etching rate was calculated as the ratio of the etching depth to the etching time for each line.

Results and Discussion

To optimize the silicon RIE through the AR-N 7520 mask influence of the SF_6 fraction in the feeding gas (15%, 18%, and 25%) was studied. Figure 1 shows the dependence of the silicon etching rate, resist etching rate, and selectivity for the RIE at different SF_6 fractions in the feeding gas and constant bias voltage of 125 V.

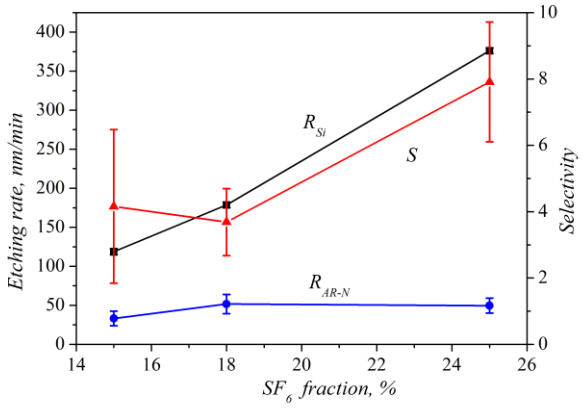


Fig. 1. Dependence of silicon etching rate (R_{Si}), etching rate of AR-N 7520 resist (R_{AR-N}), and selectivity (S) on the SF_6 fraction in the feeding gas

The resist etching rate remains almost constant with an increasing fraction of SF_6 in the feeding gas, and the etching selectivity of silicon to the AR-N 7520 increases.

Conclusion

The process with a fraction of SF_6 in the feeding gas equal to 25% and a bias voltage of 125 V provides an etching selectivity of 8.0 ± 1.8. Selectivity does not depend on the exposure dose, at dose values over 4000 pC/cm.

Acknowledgments

The investigation was supported by Program no. FFNN-2022-0021 of the Ministry of Science and Higher Education of Russia for Valiev Institute of Physics and Technology of RAS.

REFERENCES

1. **Gao J., Zhang S., Cui X., Cong X., Guo X., Hu R., Wang S., Chen J., Li Y., Yang G.** Effective Optimization Strategy for Electron Beam Lithography of Molecular Glass Negative Photoresist, Advanced Materials Interfaces. 10(20) (2023) 2300194.

2. **Nedeljkovic M., Khokhar A. Z., Hu Y., Chen X., Penades J. S., Stankovic S., Chong H. M. H., Thomson D. J., Gardes F. Y., Reed G. T., Mashanovich G. Z.** Silicon photonic devices and platforms for the mid-infrared, Optical Materials Express. 3(9) (2013) 1205–1214.

3. **Gangnaik A. S., Georgiev Y. M., Holmes J. D.** New generation electron beam resists: a review, Chemistry of Materials. 29(5) (2017) 1898–1917.

4. **Grigorescu A. E., Hagen C. W.** Resists for sub-20-nm electron beam lithography with a focus on HSQ: state of the art, Nanotechnology. 20(29) (2009) 292001.

5. **Borzenko T., Fries P., Schmidt G., Molenkamp L. W., Schirmer M.** A process for the fabrication of large areas of high resolution, high aspect ratio silicon structures using a negative tone Novolak based e-beam resist, Microelectronic engineering. 86(4-6) (2009) 726–729.

Hierarchical self-assembly of SiO_2-SnO_2 nano- and microstructures in combined sol-gel systems

I. A. Filippov[1], **N.D. Yakushova**[1], **A. A. Karmanov**[1✉], **I. A. Gubich**[2], **I.A. Pronin**[1]

[1]Penza State University, Penza, Russia;

[2]NIIFI, Penza, Russia

✉starosta07km1@mail.com

Abstract. Using the IR spectroscopy method, studies were carried out on the processes of hierarchical self-assembly of SiO_2-SnO_2 nano- and microstructures in combined sol-gel systems obtained by mixing film-forming sols with different maturation times, which meets the goals and objectives of nanostructural engineering. Characteristic absorption peaks were identified that correspond to the process of hydrolytic polycondensation and carry information about the process of self-assembly in the analyzed systems.

Keywords: nanostructure engineering, hierarchical self-assembly, sol-gel technology, spectroscopic investigation.

Funding: The study was supported by a grant from the Russian Science Foundation № 23-79-01280, https://rscf.ru/project/23-79-01280/

Introduction

In recent years, wide-bandgap semiconductor metal oxides such as ZnO, SnO_2, TiO_2, In_2O_3, etc. have attracted increasing interest. First of all, this is due to the wide scope of their practical application, including, among other things, solving gas sensory problems [1]. At the same time, it is becoming increasingly important to develop new methods and approaches to nanostructure engineering that make it possible to control the properties of these materials both through macro-level influences and by controlling the process of their synthesis at the earliest stages. For example, it is known that varying the maturation time of a film-forming sol leads to a new type of micro- and nanostructure of the metal oxide material [2]

Materials and Methods

Combined sol-gel SiO_2-SnO_2 systems were prepared within the framework of nanostructure engineering methods and approaches, which were first proposed to control the process of hierarchical self-assembly of zinc oxide nano- and microstructures [3]. The main idea is to mix film-forming sols with different maturation times in a given volume ratio (1:1, 2:1, 1:2). As part of this study, an analysis of a two-component SiO_2-SnO_2 system with a mass fraction of tin dioxide of 80 wt% was carried out.

The qualitative composition of film-forming sols, as well as the processes of hierarchical self-assembly, were studied by IR spectroscopy on an IR-Fourier spectrometer FSM 1201 (Infraspek LLC, Russia) within the framework of the method of multiple attenuation of total internal reflection using a MVTIR36 ZnSe cell.

Results and Discussion

Figure 1 shows the IR spectra of combined sol-gel systems SiO_2-SnO_2 with a maturation time of 1 hour (sample no. 1) and 24 hours (sample no. 5), respectively, as well as IR spectra of sols obtained by mixing samples no. 1 and no. 5 in a volume ratio of 2:1 (sample no. 2), 1:1 (sample no. 3) and 1:2 (sample no. 4), respectively. Analysis of the presented IR spectra shows that mixing film-forming sols with different maturation times does not lead to the emergence of new characteristic vibrational modes. This allows us to conclude that new chemical bonds are not formed, and there is no noticeable change in the qualitative composition of combined sol-gel systems when mixing sols with different maturation times.

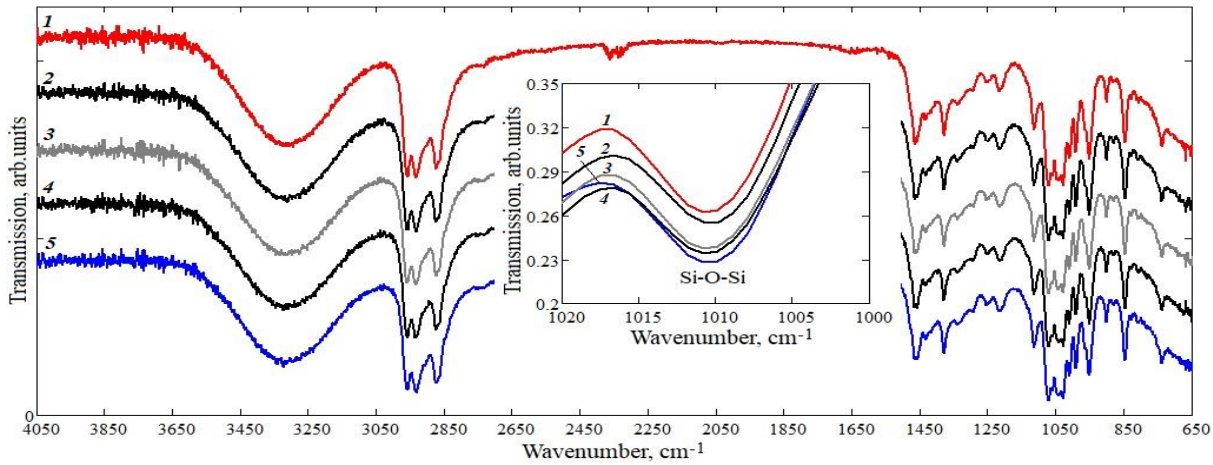


Fig. 1.

IR transmission spectra of combined sol-gel systems with different maturation times: 1 – 1 hour, 2 – 1 hour + 24 hours in a volume ratio of 2:1, 3 – 1 hour + 24 hours in a volume ratio of 1:1, 4 – 1 hour+24 hours in a volumetric ratio of 1:2, 5 – 24 hours

To analyze self-assembly processes occurring in the considered combined sol-gel systems, the most informative is the absorption peak with a maximum of 1010 cm-1 (inset in Fig. 1), which corresponds to the results of previous studies [4]. This vibrational mode corresponds to symmetrical stretching vibrations of Si-O-Si and a decrease in transmission with increasing maturation time of film-forming sols corresponds to the process of hydrolytic polycondensation, the consequence of which is the hierarchical self-assembly of nano- and microstructures of SiO_2-SnO_2, which have a fractal nature [5].

Conclusion

Thus, this study shows that infrared spectroscopy is a promising method for studying the hierarchical self-assembly of SiO_2-SnO_2 nano- and microstructures in combined sol-gel systems. It has been established that the mixing of sols with different maturation times affects the intensity of the characteristic peaks and absorption bands corresponding to the process of hydrolytic polycondensation.

REFERENCES

1. **Ben Arbia M., Helal H., Comini E**. Recent Advances in Low-Dimensional Metal Oxides via Sol-Gel Method for Gas Detection, Nanomaterials. 4(14) (2024) 359.

2. **Xiong L., Li J., Ye F., Wang H., Guo Y., Ming X., Chen Q., Zhang S., Xie R., Chen Z., Lv Y., Hu G., He Y., Fang G.** Bifunctional SnO_2 colloid offers no annealing time effect compact layer and mesoporous scaffold for efficient perovskite solar cells, Advanced Functional Materials 36 (31) (2024) 2103949.

3. **Karmanov A. A., Sukhov I. V., Yakushova N. D., Igoshina S. E., Pronin I. A.** Hierarchical Self-Assembly of Nano- and Microstructures of Zinc Oxide in Combined Sol-Gel Systems, Nano- i mikrosistemnaya tekhnika. 2 (26) (2024) 96-103.

4. **Pronin I. A., Averin I. A., Yakushova N. D., Karmanov A.A., Moshnikov V.A., Ham M.-H., Cho B.K., Korotcenkov G.** Structural features of silica coating obtained from sol cooled to the temperature of liquid nitrogen, Arabian Journal for Science and Engineering. 10 (42) (2017) 4299-4305.

5. **Hasmy A., Primera J., Woignier T.** Cluster–cluster aggregation with mobile impurities, Journal of Sol-Gel Science and Technology. 1 (90) (2019) 87-94.

Optically driven spin-alignment precession in cesium vapor

A. A. Fomin[1]✉
[1]Spin Optics Laboratory, St. Petersburg State University, St. Petersburg, Russia
St031702@student.spbu.ru

Abstract. The effect of optical spin precession is now often used as the basis for numerous experiments in fundamental physics and for various applied applications. In this work, we study a less popular version of light-induced spin-alignment precession. It does not assume coherent precession of the magnetization of the spin system and is excited by linearly polarized light, in contrast to the standard case. Experiments carried out on the D2 line of cesium vapor show that the magnitude of the spin-alignment optical precession signal in cells without a buffer gas is quite close to the magnitude of the classical spin-orientation precession signal. If there is a buffer gas inside the cell, the magnitude of the spin-alignment precession signal is greatly reduced. The discovered effect is associated with spin mixing of excited states of cesium atoms in the optical pumping cycle.

Keywords: magneto-optical effect, spin dynamics, spin relaxation, optical absorption spectroscopy.

Funding: This study was funded by Russian Science Foundation grant number 21-72-10021.

Introduction

Optical orientation, developed by Kastler [1], is based on the transfer of angular momentum from circularly polarized light to the spin system. An interesting effect of optical orientation is observed when exposed to a transverse magnetic field, which causes precession of light-induced angular momentum around the direction of the field [2]. Under these conditions, optical orientation can be achieved using the light beam modulated at the precession frequency.

There is another spin-alignment effect induced by linearly polarized light, which manifests itself as linear anisotropy of the paramagnet [3]. If the selected direction of the optical perturbation and the direction of the magnetic field applied to the sample do not coincide, then the orientation axis of the spin system in the magnetic field should precess around the field. This causes oscillations in the linear anisotropy of the medium. Analogous to optical precession of spin-orientation, modulated linearly polarized light can excite precession of spin- alignment under resonant conditions.

Collisions of atoms with the cell walls are very destructive for the spin polarization. This effect can be strongly suppressed by adding a buffer gas [4] or by using paraffin coated cells [5]. Next, an experimental study of spin-alignment precession induced in cesium vapor by resonant linearly polarized light will be presented. The specific polarization properties of the effect will be considered, and the optimal conditions for observing it at the fundamental harmonic of the Larmor frequency will be described. In addition, a comparison will be made of the effect of the buffer gas on optically induced spin-alignment and spin-orientation precession.

Materials and Methods

A diode laser with an external resonator, tunable in the range of the D2 line of cesium, was used as a light source. The output laser radiation was divided into pump beams and a probe beam. The pump beam, intensity modulated with a frequency of 27 MHz, was directed to a cell with cesium vapor. The modulation depth of the pump beam intensity was about 10%. A linearly polarized probe beam passed through the cesium cell in the opposite direction and hit the photodetector. In this work, we ignored the possible influence of Doppler-free geometry on the spectral behavior of optical precession.

A cell with cesium heated to approximately 60°C was placed in a magnetic field directed across the propagation of the light beam and modulated in magnitude with a frequency of approximately 30 Hz. The output signal from the photodetector was selectively amplified at the

pump intensity modulation frequency and fed to the input of an oscilloscope, the sweep of which was synchronized with the magnetic field modulation. The signal arose at the scanning point where the light modulation frequency coincided with the Larmor precession frequency. The measurements were carried out with linear or circular polarization of both the pump and probe beams passing through the cesium cell. Accordingly, the detected signals in these two cases were due to optically driven precession of spin-alignment or spin-orientation. Three cylindrical cells with cesium with an internal diameter of 20 mm and a length of 20 mm and different buffer gas contents with pressures of 0, 2 and 10 Torr were used.

The wavelength of the laser was tuned approximately to the center of the long-wavelength component of the D2 line, where the magnitude of the signal was the greatest.

Results and Discussion

The first experiments were carried out on the vacuum cell. The polarizations of the pump and probe beams in these experiments were identical and either circular or linear with the same azimuths of the polarization plane. It was found that the signal of spin-alignment precession was largest around $\theta = 45^{\circ}$ and nearly vanished at $\theta = 0^{\circ}$ and 90°. For this reason, all measurements with optically driven spin-alignment precession was performed at $\theta = 45^{\circ}$. The magnitudes of the spin-alignment and spin-orientation signals, under these conditions, were nearly equal.

The measurements performed on the cells with buffer gas show that the effect of the buffer gas on the resonant precession signal is significantly different for the spin-alignment and spin-orientation precession and the equivalence of these two methods is violated. The signals of optically driven spin-alignment and spin-orientation precession were obtained in the Voigt geometry with linearly and circularly polarized light, respectively. In the presence of buffer gas, the optical resonance of the spin-alignment precession practically vanishes, while the spin-orientation precession signal changes its sign, but remains the same in magnitude.

The discovered effect of suppression of precession of optically induced spin-alignment in the presence of a buffer gas is explained by spin mixing in the excited state.

Conclusions

Experimental results show that the signal of the spin-alignment precession driven by the linearly polarized light at the Larmor frequency, in vacuum cells, is practically equal in magnitude to that of the spin-orientation precession.

The optically driven spin alignment has proven to be sensitive to collisions with rare-gas atoms, which are commonly used to maintain spin orientation. It is believed that this effect can be explained by the fact that the linearly polarized light does not cause the depopulation-type pumping due to equality of the excitation probabilities, for an unresolved hyperfine structure of the excited state. It is important that the creation of alignment in a cell with gas by means of nonequilibrium population of levels from the excited state is excluded due to the complete destruction of alignment in the excited state. In the vacuum cell, the alignment arises due to population of the ground-state sublevels through transfer of the alignment from the excited state.

Acknowledgments

The author appreciates the Saint Petersburg State University for the samples provided with the support of research grant No. 95442589.

REFERENCES

1. **A. Kastler**, J. Phys. Radium 11, 255 (1950).
2. **W. E. Bell, A. L. Bloom**, Phys. Rev. Lett. 6, 280 (1961).
3. **W. Happer**, Rev. Mod. Phys. 44, 169 (1972).
4. **J. Brossel, J. Margerie, A. Kastler**, Compt. Rend. 241, 865 (1955).
5. **M. A. Bouchiat**, J. Phys. (Paris) 24, 379 (1963).

Numerical study of the optical mode structure of GaP nanowires

A. S. Funtikova [1,2]✉, A. M. Mozharov [1,2], V.V.Fedorov [1,2], V.A.Sharov [1,3], I. S. Mukhin [1,2]

[1] Alferov University, Saint-Petersburg, Russia;

[2] Saint-Petersburg Polytechnic University, Saint-Petersburg, Russia;

[3] Ioffe Institute, Saint-Petersburg, Russia

✉ n.fn@mail.com

Abstract. Optical integrated circuits are a promising direction in the development of electronic devices due to the necessity to process large amounts of information and transmit it at high speed. Circuits based on nanowires (NWs) and quantum dots make it possible to achieve the required size limits and process large amounts of information at high speed. However, the silicon photon devices are limited by their low refractive index and narrow bandgap, limiting their use to the infrared spectrum. In contrast, III-V, particularly GaP nanowires have high crystallinity, can be compatible with silicon technologies, and provide high refractive index and transparency in the visible and IR ranges. This makes them especially attractive for applications in optical integrated circuits where high performance and efficiency are required. It is important to mention, that usual indirect band gap GaP can be made direct with As or N doping, it is interesting for photonic integrated circuit's devices construction. The simulation results showed that as the length of a nanowire structure increases, the radiation intensity at its output rises, which is associated with the effect of light amplification due to the occurrence of Fabry–Perot resonances. High order optical modes were also detected. Quality factor analysis shows growth in its values with the increase in structures' diameters.

Keywords: nanowires, gallium phosphide, Fabry-Perot resonance, waveguide modes, refractive index.

Funding: This study was funded by the Ministry of Science and Higher Education grant number FSEG-2024-0017.

Introduction

Nowadays electronic integrated circuits strive to reach their fundamental limits. Increase in the amount of information and requirements for the speed of its transmission needs new technological and conceptual solutions for integrated circuits. One of the promising development directions are optical integrated circuits. To obtain necessary size limits, one must use nanostructures, such as nanowires, quantum wires, quantum dots, etc. Such devices can be made with well-known silicon technology, but silicon photonic devices has an amount of significant shortcomings, for example, narrow band gap ($E_{g,\,Si}$ = 1.12 eV, T = 300K), which lead to huge optical loses and make it reasonable to use only in infrared part of the spectrum.

Other perspective structures are III-V nanowires. They demonstrate high crystallinity and can be grown on Si substrate, so, can be compatible with silicon technology [1]. High refractive index [2] and transparency in wide visible and infrared range [3], thus, small optical losses in this part of the spectrum, make GaP structures very promising for use in photonic integrated circuits. In general, gallium phosphide has indirect band gap, but it is possible to make it direct with As and N doping [4], which make them interesting not only for passive circuits' elements, but also active, such as lasers, light-emitting diodes, waveguides and nanoantennas.

In this work numerical study of the resonant Fabry-Perot modes and refractive index of GaP NWs was obtained in dependence on diameter, length of the structure and wavelength of the lightsource.

Materials and Methods

In our study COMSOL Multiphysics was used to simulate the necessary phenomenon. Structure has 35 nm mesh size for all geometries and configurations to except the calculation inaccuracies. The MUMPS (multifrontal massively parallel sparse direct solver) was used to

obtain the solutions. Also we use parametric sweeps to change diameter and length of the structure to analyze all necessary configurations. To get rid of any interference phenomena, a perfect matched layer (PML) on external boundaries was used. Refractive and extinction indexes for GaP, used for our calculations, were taken from [5]. Outer shell is declared as air with refractive index $n = 1$.

Results and Discussion

During the modeling process, it was discovered that as the NW length increases, the radiation intensity at the output of the structure rises, which is associated with light amplification due to Fabry-Perot resonances. Fundamental mode demonstrates localization near the center of NW for small diameter structures. In thick nanowires high order optical modes can be detected. Some parameter configurations can lead to the appearance of the unusual high quality factor modes of higher orders. In addition, as the diameter of the structure increases, the quality factor of the mode inside the structure, which directly depends on the rise in the refractive index values, grows.

Conclusion

We have demonstrated numerical study of the GaP nanowires with different geometry configurations, which can fully describe the modal structure of these objects. The results of this modeling can be used for further study of the optical properties of such structures, as well as the growth of NWs with known characteristics for integration into photonic circuits as waveguides, optical splitters, nanoantennas, etc. with high efficiency indexes in compare with similar silicon devices.

Acknowledgments

The work was supported by the Ministry of Science and Higher Education (state assignment grant FSEG-2024-0017).

REFERENCES

1. **Zhang, G.; Tateno, K.; Sogawa, T.; Nakano, H.** Growth and characterization of GaP nanowires on Si substrate. Journal of Applied Physics, 2008, 103 (1), 014301–.

2. **D. Khmelevskaia; D. I. Markina; V. V. Fedorov; G. A. Ermolaev; A. V. Arsenin; V. S. Volkov; A. S. Goltaev; Yu. M. Zadiranov; I. A. Tzibizov; A. P. Pushkarev; A. K. Samusev; A. A. Shcherbakov; P. A. Belov; I. S. Mukhin; S. V. Makarov**. Directly grown crystalline gallium phosphide on sapphire for nonlinear all-dielectric nanophotonics. Applied Physics Letters, 2021, 118 (20), 201101 –.

3. **Parsons, D. F.; Coleman, P. D.** Far Infrared Optical Constants of Gallium Phosphide. Appl. Opt. 1971, 10, 1683–1685.

4. **Geisz, J.F.; Friedman, D.J.; Kurtz, S.** [IEEE Conference Record of the Twenty-Ninth IEEE Photovoltaic Specialists Conference 2002 - New Orleans, LA, USA (19-24 May 2002)] Conference Record of the Twenty-Ninth IEEE Photovoltaic Specialists Conference, 2002. - GaNPAs solar cells lattice-matched to GaP. , 2002, (0), 864–867.

5. **Adachi, S.** Optical dispersion relations for GaP, GaAs, GaSb, InP, InAs, InSb, $Al_xGa_{1-x}As$, and $In_{1-x}Ga_xAs_yP_{1-y}$. Journal of Applied Physics, 1989, 66 (12), 6030–6040.

Design of an optical fiber based sensor for temperature-sensitive measurements

A.A. Cherednikova[1]✉, D.O. Gagarinova[1], V. Labuntsov[1], K. A. Tomyshev[2], A. Yu. Kokhanovskiy[1], L.I. Fatkhutdinova[1]✉

[1] Department of Physics and Engineering, ITMO University, 191002 St. Petersburg, Russia
[2] Kotelnikov Institute of Radio Engineering and Electronics RAS, 125009 Moscow, Russia
✉a.cherednikova@metalab.ifmo.ru, l.fatkhutdinova@metalab.ifmo.ru

Abstract. In this study, the effect of temperature stabilization on the sensitivity of a sensor based on surface plasmon resonance was investigated. The sensing element of the sensor is a single-mode optical fiber with tilted Bragg grating coated with 5 nm of chromium and 45 nm of gold. The sensitivity of the sensor was determined by serial measurements of calibration solutions with different refractive index. Temperature stabilization was applied to avoid environmental influence. The suggested approach made it possible to record a change in the refractive index of the investigated liquid within 2×10^{-5} RIU.

Keywords: Surface plasmon resonance, microfluidics, sensors
Funding: This research was supported by the Russian Science Foundation (Project 21-72-30018, https://rscf.ru/en/project/21-72-30018/).

Introduction

Sensors based on surface plasmon resonance (SPR) are an important tool in modern scientific and industrial fields, providing high sensitivity in measurements. There are a variety of types of SPR sensors, including sensors based on optical fiber that are highly sensitive [1]. The use of optical fibers makes it possible to integrate them into microfluidic chips, which expands the functionality of sensors [2, 3]. However, the optical fibers are strongly susceptible to temperature changes [4, 5]. It can affect the changes in refractive index and have a significant impact on the results of the study. So, ambient temperature stabilization becomes a critical aspect when using optical fiber sensors to ensure proper performance and reliable results. Therefore, for the effective use of SPR sensors based on optical fiber, it is necessary to take measures to stabilize the ambient temperature. This will ensure reliability of measurements, increase accuracy and improve the quality of data obtained.

Materials and Methods

The experimental setup consists of a microfluidic chip made of polydimethyloxane (PDMS) with a 300μL cavity where the analyzed liquid enters. Inside the chip there is a sample of single-mode (SM) optical fiber with a sensing element – tilted Bragg grating and metal coating: the first layer – 5 nm of chromium, the second – 45 nm of gold.

Temperature stabilization is provided by proportional-integral-derivative (PID) controller – Peltier element controlled by voltage source through temperature transducer. The used design allows to maintain the ambient temperature in the chip and reduce the influence of temperature drift on the results of the experiment. Temperature stabilization was maintained at 27℃. The temperature eliminates the influence of the environment on the experiment.

To determine the sensitivity of the sensor, 6 NaCl solutions were prepared: the refractive index for each solution ranged from 1.3352 to 1.3353 refractive index unit (RIU) with a step $\Delta n = 2 \times 10^{-5}$ RIU. Five measurements were taken for each solution and then the average SPR wavelength for each refractive index was calculated.

Results and Discussion

The use of the PID controller eliminated temperature fluctuations from 0.18℃ to 0.02℃. After conducting a series of experiments, it was concluded that temperature change on 1℃ causes SPR wavelength shift on 0.11 nm. Thus, maintaining a constant temperature allows the value of

the SPR wavelength to be estimated with an accuracy of 0.02 × 0.11=0.0022 nm. As a result of the data processing, the SPR wavelengths for each calibration solution were calculated. The calculated dependence of the refractive index on the SPR wavelength (Fig. 1) is shown that with an increase in the refractive index the value of the SPR wavelength moves to the red-wave spectral region. Moreover, the sensitivity of the temperature-stabilized optical fiber sensor was calculated, which is equal to S = 1465 nm/RIU.

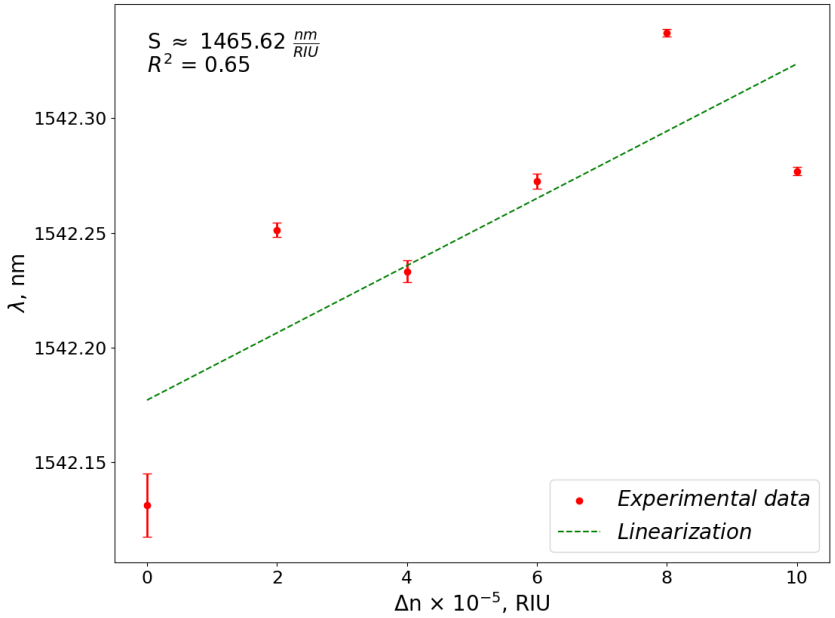


Fig. 1. Dependence of refractive index on SPR-wavelength, S – sensor sensitivity, R^2 – determination coefficient

Conclusion

The way to enhance the results of temperature-sensitive measurements can be obtained by stabilizing the ambient temperature of SPR sensors based on optical fiber. The calculated sensitivity of the sensor was S = 1465 nm/RIU. In comparison with a similar study [6] which has no temperature stabilization integrated, S^* = 566 nm/RIU. S is more than twice as high as S^*.

REFERENCES

1. Klantsataya, E., Jia, P., Ebendorff-Heidepriem, H., Monro, T. M., & François, A. (2016). Plasmonic fiber optic refractometric sensors: From conventional architectures to recent design trends. Sensors, 17(1), 12.
2. Zhao, Y., Hu, X. G., Hu, S., & Peng, Y. (2020). Applications of fiber-optic biochemical sensor in microfluidic chips: A review. Biosensors and Bioelectronics, 166, 112447.
3. Parker, H.E., Sengupta, S., Harish, A.V. et al. A Lab-in-a-Fiber optofluidic device using droplet microfluidics and laser-induced fluorescence for virus detection. Scientific Reports 12, 3539 (2022).
4. Koresawa, H., Seki, K., Nishimoto, K. et al. Real-time hybrid angular-interrogation surface plasmon resonance sensor in the near-infrared region for wide dynamic range refractive index sensing. Scientific Reports 13, 15655 (2023).
5. Caucheteur, C., Guo, T., Liu, F., Guan, B. O., & Albert, J. (2016). Ultrasensitive plasmonic sensing in air using optical fiber spectral combs. Nature communications, 7(1), 13371.
6. Manuylovich, E., Tomyshev, K., & Butov, O. V. (2019). Method for determining the plasmon resonance wavelength in fiber sensors based on tilted fiber Bragg gratings. Sensors, 19(19), 4245.

Organic kainate single crystals as a broadband THz source for spectroscopy

E. O. Chiglintsev [1,2]✉, K.A. Brekhov [2,3], A.I. Chernov[1,2], Pavel Ginzburg[4]

[1]Center for Photonics and 2D Materials, Moscow Institute of Physics and Technology (MIPT), Dolgoprudny, Russia;

[2]Russian Quantum Center, Skolkovo, Moscow region, Russia;

[3]Department of Nanoelectronics, MIREA - Russian Technological University, Moscow, Russia

[4]Department of Physical Electronics, Tel Aviv University, Ramat Aviv, Tel Aviv69978, Israel

✉chiglintsev.eo@phystech.edu

Abstract. Organic crystals have recently attracted attention of researchers for their ability of efficient nonlinear frequency generation. This work focuses on investigation of organic kainite single crystals for time-domain terahertz (TD-THz) spectroscopy. We have obtained a broadband THz signal from kainite crystals, with a bandwidth of approximately up to 8 THz. To pump the crystal, we used an Yb laser with the wavelength of 1030 nm in a THz time-domain spectrometer setup. The generated THz spectrum of the kainite crystal was compared to that of another well-known organic crystal, BNA. These results could be applied to explore optical properties of materials in the THz range.

Keywords: broadband terahertz generation, organic crystal, time-domain spectroscopy.

Introduction

Exploration of nonlinear optical (NLO) properties of materials have started from the first laser source invention [1]. Since then, the development and engineering of materials with large second order nonlinearity coefficient has attracted enormous research attention [2]. While nonlinear crystal as ZnTe, lithium niobate, GaP are widespread in use for second harmonic generation (SHG) and THz generation, organic crystals with strong nonlinearity have recently been produced [3]. In addition to strong nonlinearities for optical use, organic crystal should possess low linear absorption, stability to environment conditions, high optical damage threshold and fabrication reproducibility. Effective frequency doubling, terahertz generation, electro-optical modulation, and high-speed integrated optics have all been demonstrated in recent years using crystals and polymer layers, such as DAST [4], OH1 [5], and BNA [6]. Moreover, studies of the conductivity of single-walled nanotubes of different geometry in the THz frequency range generated using an organic nonlinear BNA crystal were demonstrated [7]. However, increased bandwidth and ability to operate at 1030 nm have been still lacking.

As known from the previous work [8], kainate organic crystal possess all needed properties for its use in SH and THz generation applications. Although, an efficient SHG and broadband THz generation were demonstrated for various pump laser wavelengths except of 1030 nm. In this work we qualitatively characterized THz generation of kainite crystal and compare it with BNA organic crystal for Yb laser wavelength.

Results

We pumped kainate crystal with pulsed Yb laser at the wavelength 1030 nm with energy density approximately 0.05 J/cm2 and repetition rate 500 Hz. To increase THz signal, we rotated and moved kainate crystal, monitoring voltage peak at defined delay line point, which provided maximum overlapping pump and probe signals, in lock-in device inbuilt oscilloscope. We measured 14 ps length of THz pulse several times to obtain high enough resolution and signal-to-noise ratio in spectrum.

To estimate the kainate spectrum we compare it with that of another organic BNA crystal, which THz spectrum is well-studied. The BNA crystal has typically a THz radiation span from 0.2 to 2.5 THz [9]. In the performed measurements we obtained the BNA THz spectrum ranging from 0.2 to 2 THz (Fig.1, red curve). Black curve in Fig.1 shows the obtained THz spectrum using the kainate organic crystal. It has been observed that the terahertz kainite spectrum exhibits a lower maximum amplitude value but a broader terahertz bandwidth, which ranges from 0.2 to 8 terahertz, as demonstrated in previous studies [8].

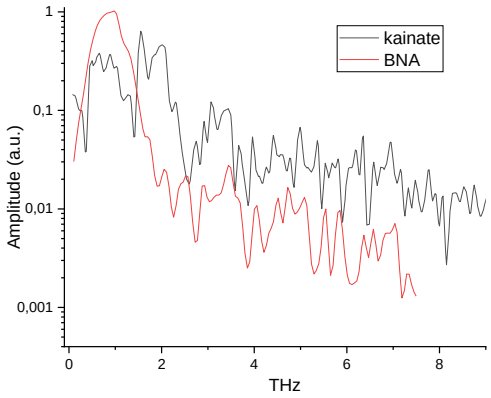


Fig. 1. THz spectra for kainate (black curve) and BNA (red curve) organic crystals.

Conclusion

In this work we demonstrated application of the kainate organic crystal for a broadband THz high-field spectroscopy with Yb laser used as a pump source. In the follow-up work we plan to carry a detailed characterization of kainate crystals for the THz generation depending on thickness and excitation power.

References

1. **Bloembergen, N.; Pershan, P. S.** Light Waves at the Boundary of Nonlinear Media. Phys. Rev. 1962, 128, 606– 622, DOI: 10.1103/PhysRev.128.606. There is no corresponding record for this reference.

2. **Mutailipu, M.; Li, F.; Jin, C.; Yang, Z.; Poeppelmeier, K. R.; Pan, S.** Strong Nonlinearity Induced by Coaxial Alignment of Polar Chain and Dense [BO3] Units in CaZn2(BO3)2. Angew. Chem., Int. Ed. 2022, 61, 1– 6, DOI: 10.1002/anie.202202096

3. **Venkataramudu, U.; Sahoo, C.; Leelashree, S.; Venkatesh, M.; Ganesh, D.; Naraharisetty, S. R. G.; Chaudhary, A. K.; Srinath, S.; Chandrasekar, R.** Terahertz Radiation and Second-Harmonic Generation from a Single-Component Polar Organic Ferroelectric Crystal. J. Mater. Chem. C 2018, 6, 9330– 9335, DOI: 10.1039/c8tc02638f

4. **Ginzburg, P.; Krasavin, A. V.; Wurtz, G. A.; Zayats, A. V.** Nonperturbative Hydrodynamic Model for Multiple Harmonics Generation in Metallic Nanostructures. ACS Photonics 2015, 2, 8– 13, DOI: 10.1021/ph500362y

5. **Hunziker, C.; Kwon, S.-J.; Figi, H.; Juvalta, F.; Kwon, O.-P.; Jazbinsek, M.; Günter, P.** Configurationally Locked, Phenolic Polyene Organic Crystal 2-{3-(4-Hydroxystyryl)-5,5-Dimethylcyclohex-2-Enylidene}malononitrile: Linear and Nonlinear Optical Properties. J. Opt. Soc. Am. B 2008, 25, 1678, DOI: 10.1364/josab.25.001678

6. **Jazbinsek, M.; Puc, U.; Abina, A.; Zidansek, A.** Organic Crystals for THz Photonics. Appl. Sci. 2019, 9, 882 DOI: 10.3390/app9050882

7. **Burdanova M.G., Chiglintsev E.O., Paukov M.I., Mishra P., Brekhov K.A., Arsenin A.V., Volkov V., Chernov A.I.**, High-field terahertz time-domain spectroscopy of single-walled carbon nanotubes, St. Petersburg State Polytechnical University Journal. Physics and Mathematics. 16 (1.3) (2023) 108–111. DOI: https://doi.org/10.18721/JPM.161.318

8. **Hani Barhum, Cormac McDonnell, Tmiron Alon, Raheel Hammad, Mohammed Attrash, Tal Ellenbogen, and Pavel Ginzburg** ACS Applied Materials & Interfaces 2023 15 (6), 8590-8600 DOI: 10.1021/acsami.2c18454

9. **Mostafa Shalaby, Carlo Vicario, Karunanithi Thirupugalmani, Srinivasan Brahadeeswaran, and Christoph P. Hauri**, "Intense THz source based on BNA organic crystal pumped at Ti:sapphire wavelength," Opt. Lett. 41, 1777-1780 (2016)

Towards the realization of $NbSe_2$ NIR photodetectors integrated on a silicon nitride waveguide.

A. N. Lyubchak[1,2,✉], E. Zharkova[3], I. A. Gayduchenko [1,2], K. V. Shein[1,2],Bondareva P.I.[1,2], D.A. Bandurin[3] and G. N. Goltsman [1,2]

✉anlyubchak@miem.hse.ru

[1]Moscow Pedagogical State University, Moscow, 119435, Russia;
[2] National Research University Higher School of Economics, Moscow, 101000, Russia;
[3]Programmable Functional Materials Lab, Brain and Consciousness Research Center, Moscow, Russian Federation, 121205

Abstract. Photonic integrated circuits (PIC) represent a promising platform for applications in the field of quantum technologies, such as quantum computing and cryptography. One of the key components for these applications is detectors based on thin superconducting films. Nevertheless, fabricating thin superconducting detectors atop a waveguide utilizing conventional materials acquired through magnetron sputtering presents a multifaceted and cost-intensive technological challenge. As alternative approach in this study, we present the concept of an on-chip superconducting detector based on two-dimensional superconductor $NbSe_2$, obtained through mechanical exfoliation. The advantage of this approach lies in the ease of device integration onto the waveguide and the possibility to create a detector with a thickness of just one atomic layer.

Keywords: 2D materials, PIC, superconducting electronics, superconductors.
Funding: The research was supported by RSF (project No. 21-72-10117).

Introduction

Currently, there is a rapid development of quantum technologies in the fields of quantum computing, simulators, and cryptography [1]. Similar to modern nanoelectronics, quantum technologies also exhibit a trend towards miniaturization and maximum integration of technologies onto a single chip. Photonics integrated circuits serve as a convenient and functional platform for such applications, where quantum computations and cryptographic protocols are already being implemented [2]. One of the key components of such circuits are superconducting photodetectors, which boast excellent characteristics in sensitivity, signal-to-noise ratio, low noise levels, and high speed. Despite the successful demonstration of superconducting detectors as an important part of modern quantum technologies, integrating them onto waveguides in the form of thin superconducting films of the same quality as for planar structures remains a technologically challenging task. On the other hand, there is a trend towards integrating two-dimensional van der Waals structures onto waveguides [3] due to their ease of integration, thickness down to a single atomic layer, and the ability to create heterostructures with programmable characteristics. A promising material for creating superconducting detectors on waveguides is niobium diselenide ($NbSe_2$), which retains its superconducting properties down to a single atomic layer and has already demonstrated sensitivity as a detector in the terahertz [4] and NIR [5] ranges. In this work, we demonstrate the integration of the hBN/$NbSe_2$/hBN structure onto a waveguide. The results of our modeling and sample resistance will help optimize the geometry of this material and the optical scheme for creating superconducting single-photon detectors and bolometers on a chip.

Materials and Methods

In order to enhance the absorption of the hBN/$NbSe_2$/hBN flake stack for electromagnetic radiation, we conducted simulations of the width of a waveguide made of Si_3N_4. The simulations were performed using the finite element method (FEM), implemented in the COMSOL Multiphysics software. The waveguide width ranged from 0.5 μm to 4 μm. From the obtained

simulation results, the parameters of the waveguide were determined: the waveguide etch depth was 225 nm, and the waveguide width was 2.5 μm. We observed an increase in the effective absorption coefficient for $NbSe_2$ with a thickness of 12.7 nm in the structure with hBN thickness of 20 nm from 0.0145 dB/μm to 0.0685 dB/μm.

The photonic integrated circuit was implemented in the form of a O - ring resonator to enhance the absorption of electromagnetic radiation. The waveguide was fabricated from Si_3N_4, and detailed fabrication technology is described in [5]. To obtain a 2D crystal of niobium diselenide ($NbSe_2$), exfoliation was performed on PDMS. The assembly of the three-layer hBN/$NbSe_2$/hBN structure was carried out on polycarbonate (PC) on PDMS using a transfer machine at a vacuum table temperature of 90°C. The transfer process was monitored using a microscope. The mask made of PMMA/MMA resist was created for the contact area using e-beam litography, followed by plasma etching of the upper hBN flake. Subsequently, small aluminum contacts with a thickness of 190 nm was fabricated. The next step involved photolithography and deposition of larger gold contacts with a thickness of 150 nm. Further details on the fabrication process of the heterostructure and contacts are described in [4]. Two terminal resistances of this device is R_{2pt} = 3700 Ohm.

Conclusion

The hBN/$NbSe_2$/hBN heterostructure integrated with an optical waveguide was fabricated. Modeling of the TE mode and the absorption coefficient was simulated as a function of the waveguide width. The results of this modeling were considered in the fabrication of the waveguide to enhance the absorption coefficient of the optical mode. The resistance of the fabricated structure is 3.7 kΩ, which is an acceptable value for such devices. The obtained technological route will enable the creation of thin superconducting heterostructures for a wide range of applications.

Acknowledgments

The research was supported by RSF (project No. 21-72-10117).

REFERENCES

1. **Antonio Acín et al**., New J. Phys., 20 080201 (2018)
2. **Galan Moody et al.,** 2022 Roadmap on integrated quantum photonics 2022 J. Phys. Photonics, 4 (2022) 012501.
3. **Ramakrishnan, R.K., Mishra, A., Kumar, P. et al.** Integrated multi-mode waveguide devices for quantum communication. J Opt (2023).
4. **Meng, Y., Feng, J., Han, S.** ***et al.*** Photonic van der Waals integration from 2D materials to 3D nanomembranes. Nat Rev Mater, **8** (2023) 498–517 .
5. **K. Shein, E. Zharkova, D. Bandurin, I. Gayduchenko et al** Nano Letters **,** *24* (7) (2024) 2282-2288.
6. **G. J. Orchin et al**., Appl. Phys. Lett. 114 (25) (2019).
7. **Komrakova et al**., Hybrid Silicon Nitride Photonic Integrated Circuits Covered by Single Walled Carbon Nanotube Films, Nanomaterials ,13 (2023).

Improvement of the technique for describing the scattering of photoelectrons in a solid

V. A. Iachuk [1✉], **A. V. Lubenchenco** [1], **D. A. Ivanov** [1], **O.I. Lubenchenco** [1]
[1] NRU «Moscow Power Engineering Institute», Moscow, Russian Federation
✉dr.yachuk@mail.ru

Abstract. The development of nanoelectronics requires more and more accurate methods for determining the physical parameters of devices. For example, in hot electron bolometer mixers (HEB), it is necessary to control the thickness of the oxide layer, which affects the characteristics of the device. This can be done using X-ray photoelectron spectroscopy (XPS). In this paper, a method is proposed for describing the emission of photoelectrons that have experienced multiple inelastic scattering in the volume of the sample under study, taking into account the dependence of the scattering cross section on depth. Using this technique, it is possible to simulate the photoelectronic spectrum and, using the inverse problem method, determine the parameters of the studied layers, such as thickness, structural and phase composition. It is necessary to take into account the dependence of the scattering parameters on the depth. The difference in electron density near the surface and in the volume has a strong effect on the energy spectrum of the emitted electrons, which in turn affects the accuracy of determining the parameters.

Keywords: XPS, inelastic scattering, Monte-Carlo, scattering cross section.

Introduction

Ultra-thin films are widely used in devices such as HEB, which are used as high-frequency radiation detectors [1]. For such a device to work, it is necessary to create a fairly homogeneous NbN layer. Additionally, it is crucial for HEBs to control the thickness of the oxide layer formed during atmospheric oxidation, which should not exceed 2 nanometers. If the oxide layer is thicker, the performance of the device may degrade. Therefore, it is vital to accurately determine the film properties. We can mention memristors, which also consist of layers of thin films besieged on top of each other [2]. In which it is also necessary to know the structural and phase composition, since this will determine their properties, for example, conductivity. XPS is great for obtaining the necessary data on the composition of the film. Having obtained the spectrum of electron energy losses using XPS, it is possible, solving the inverse problem, to determine both the thickness of the studied layers and their composition. To solve the inverse problem, it is necessary to calculate a spectrum that well describes the experimental one. This spectrum is calculated by using the transmission function, which is dependent on the method used to describe energy loss during scattering. The aim of the work was to improve the methodology for calculating the energy loss spectrum of photoelectron taking into account surface effects.

In this work proposes a method for describing photoelectron scattering in a multilayer target. This technique is based on considering the dependence of various scattering parameters on depth, such as the scattering cross section, free inelastic path length, and others. The dependence of the scattering cross-section on the depth must be taken into account, since the cross-section in the surface layer is very different from the cross-section in the volume of the layer [3]. This is due to the difference in electron density [4]. Failure to take into account surface effects leads to an incorrect result of analyzing the parameters of thin films.

Materials and Methods

To build a computational model, the equation of electron flux transfer through a multilayer film was solved. The target model consisted of the multilayer film each layer of which consisted

of a volumetric and a surface (at the interface of the layers) part. In this way, the problem of electron scattering in an inhomogeneous medium was solved. For each layer, the scattering cross-section was calculated, taking into account surface effects related to energy losses due to excitation of plasma oscillations. Using these cross-sections, the transmission function was computed by using a matrix exponential. The transmission function for the surface layer was derived using the formula:

$$T_S = e^{-SEP(E-X_s)}, \quad (1)$$

where $SEP = \frac{d_s}{\lambda_s \cdot cos\theta}$, λ_s is the length inelastic mean free pass, d_s is the layer thickness, E is a scalar unit matrix, X_S is the Toeplitz matrix which contains a scattering cross section.

The transmission function of the entire layer was obtained by convolving the transmission functions of the bulk and surface components [5].

The simulated spectrum was compared to the experimental one and then the inverse problem was solved to determine the parameters of the studied objects, such as the thickness of layers and their phase composition.

The inelastic scattering cross section was constructed using cross-section stitching. A thickness-dependent cross section [6] was used in the range from 0 to 200 eV and a model cross section was used from 200 to 1000 eV, since the electron density was considered constant in the volume of the layer. The calculation based on the proposed model was compared with both the experimental spectrum and the Monte Carlo calculation.

Results and Discussion

This work proposes a method for describing and calculating the scattering of photoelectrons in multilayer inhomogeneous targets. The technique utilizes particle scattering parameters that depend on depth, allowing for the consideration of differences in scattering parameters within the layers of a single material. By using this technique, a photoelectron spectrum can be constructed, and then the inverse problem approach can be used to perform structural and phase analyses, as well as determine the thicknesses of the layers.

Conclusion

In this paper a technique for describing the scattering of photoelectrons is proposed, using which it is possible to calculate the parameters of the objects under study, for example, the thickness of thin films, to conduct phase and structural analysis.

REFERENCES

1. **Meledin D., Pavolotsky A., Desmaris V.** et. al. IEEE Transactions on Microwave Theory and Techniques 57 (2009) 89–98.
2. **Vourkas I., Sirakoulis G. C.** Memristor-based nanoelectronic computing circuits and architectures. – Berlin : Springer, Vol 19 (2016)
3. **Chen Y. F.** Surface science, Vol. 519 (1-2) (2002) 115-124.
4. **Shard A. G.**, Practical guides for x-ray photoelectron spectroscopy: Quantitative XPS. Journal of Vacuum Science & Technology A, Vol. 38 (4) (2020).
5. **Lubenchenko A.V.**, et al. XPS study of multilayer multicomponent films. Applied Surface Science, Vol. 427 (2018) 711-721.
6. **Li Y. C.** et al. Surface science. Vol. 589 (1-3) (2005) 67-76.

Study of mode leakage into substrate in microdisk lasers

I.A. Melnichenko [1,2]✉, **E.I. Moiseev** [1], **K.A. Ivanov**[1], **N.V. Kryzhanovskaya**[1], **A. Vainilovich**[3], **A.E. Zhukov**[1]

[1] HSE University, St. Petersburg, Russia

[2] Alferov University, St. Petersburg, Russia

[3] Institute of Physics of the NAS of Belarus, Minsk, Belarus

✉imelnichenko@hse.ru

Abstract. The propagation of whispering gallery modes of an injection disk microresonator based on InGaAs/GaAs quantum well-dots into a GaAs substrate has been investigated. For a 50 μm diameter GaAs-based microlaser, the mode leakage into the substrate turns out to be quite significant, which is confirmed by both experimental and modeling data.

Keywords: InGaAs quantum well-dots, whispering gallery mode microlasers, mode leakage

Funding: This study was supported by the Russian Science Foundation (grant # 22-72-10002, https://rscf.ru/en/project/22-72-10002/) in part of mode leakage modeling. Support of optical measurements from the Basic Research Program of the National Research University Higher School of Economics is gratefully acknowledged.

Introduction

Microlasers based on whispering gallery modes (WGMs) are promising light emitters for photonic integrated circuits [1]. WGM microlasers with InGaAs/GaAs quantum dots (QDs) formed by the Stransky-Krastanov (SK) mechanism exhibit low threshold currents, good thermal stability, and high modulation rates. It has recently been shown [2] that dense (~$5*10^{11}$ cm^{-2}) arrays of InGaAs QDs formed on GaAs not by the SK mechanism allows to improve the characteristics of microdisk lasers, for example, to increase the power emitted into free space (up to 18 mW in a 31-μm-diameter microlaser). When examining the far-field patterns of such microlasers, azimuthal modulation of the emission intensity is observed, which should reflect the spatial distribution of the mode inside the laser. We found that the number of maxima is much smaller than expected for a first-order radial WGM confined to the periphery of the resonator (144 maxima instead of about 600) [3]. This implies that the generation occurs on a higher radial order WGM located deeper inside the resonator. To investigate this discrepancy, we analyzed the leakage of the microdisk laser mode into the substrate and the magnitude of this type of losses was determined.

Materials and Methods

The epitaxial structure was prepared by MOVPE epitaxy on a 6°-disoriented GaAs substrate. The sample consisted of five InGaAs QWD layers in the center of a ~800 nm thick GaAs matrix bounded by 1.5 μm thick n- and p-$Al_{0.4}Ga_{0.6}As$barrier layers [3]. Using photolithography and dry etching, microdisks with a diameter of 50 μm were formed on the surface of the epitaxial structure. To investigate the mode spreading, the sample was cut so that the substrate cut was in close proximity to the mounted and welded microdisk under study (not more than 5 μm).

The study of the intensity distribution of the electromagnetic field flowing from the laser into the substrate was carried out using the technique of fiber near-field microscopy. For this purpose, a room temperature NT-MDT Integra Spectra microscope-based fiber probe head was used, which is a Nufern 980-HP single-mode optical fiber attached to a fork-shaped quartz resonator. The end of the fiber is tapered by chemical etching and coated with a layer of aluminum (70nm) with a formed aperture of 100 nm at the end. The signal from the fiber probe was transfered into a Sol Instruments MS5204i monochromator and detection was performed using a cooled InGaAs CCD array. Also, to simulate the processes of WGM spreading, a numerical model of the disk was developed in the COMSOL Multiphysics environment using the finite element method.

Results and Discussion

The Figure 1 below shows the electroluminescence (EL) spectrum obtained by near-field fiber microscopy from the GaAs substrate under the microdisk laser and maps of the EL intensity

distribution for the cliff of the GaAs substrate under the microdisk laser. In the investigated wavelength range, two WGMs were identified, the radiation leakage of which was localized under the periphery of the microdisk laser at wavelengths 1082.8 nm and 1099.1 nm. The EL intensity modulations obtained on the maps depend on the thickness of the GaAs substrate layer in which the leakage radiation propagates.

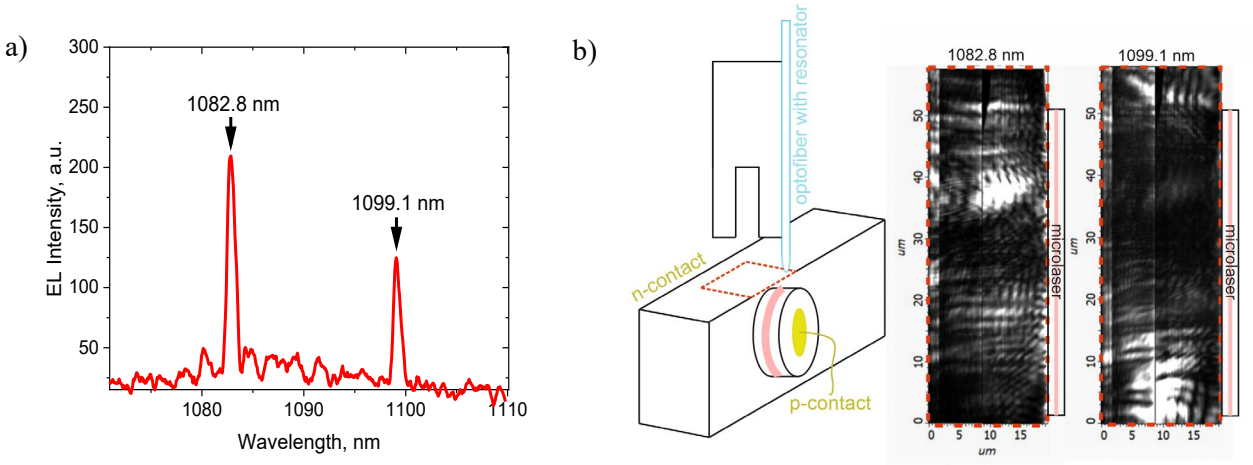


Figure 1. a) EL spectrum obtained by near-field fiber acquisition from the substrate under the microdisk. b) Schematic of the near-field fiber microscopy experiment and electroluminescence intensity distribution maps of the 1082.8 and 1099.1 nm modes.

The amount of mode leakage into the GaAs substrate was calculated as the ratio of the field intensity maxima in the GaAs substrate to the intensity maximum in the microdisk waveguide. For the experimental data, this value was approximately ~10^{-4} for the 1082.8 nm mode wavelength, while the theoretical simulations show a maximum amount of mode leakage ~10^{-5} for the third radial order mode. It was also observed that for different WGMs, the propagation in the GaAs substrate occurs at different angles, and from the theoretical simulation results it can be assumed that the smaller the mode Q-factor, the larger will be the angle to the GaAs substrate surface at which the WGM scatters.

Conclusion

It is shown that for microdisk lasers based on InGaAs/GaAs QWDs the mode leakage into the substrate is quite significant for modes with high radial number, which is confirmed by both experimental and modeling data. The results obtained indicate the necessity to take into account WGMs leakage in to substrate.

Acknowledgments

This study was supported by the Russian Science Foundation (grant # 22-72-10002, https://rscf.ru/en/project/22-72-10002/) in part of mode leakage modeling. Support of optical measurements from the Basic Research Program of the National Research University Higher School of Economics is gratefully acknowledged.

REFERENCES

1. **Yang, S., Wang, Y., & Sun, H.** (2015). Advances and prospects for whispering gallery mode microcavities. Advanced Optical Materials, 3(9), 1136-1162.

2. **Moiseev, E., Kryzhanovskaya, N., Maximov, M., Zubov, F., Nadtochiy, A., Kulagina, M., ... & Zhukov, A.** (2018). Highly efficient injection microdisk lasers based on quantum well-dots. Optics Letters, 43(19), 4554-4557.

3. **Moiseev, E. I., Kryzhanovskaya, N. V., Zubov, F. I., Nahorny, A. V., Urmanov, B. D., Fominykh, N. A., ... & Zhukov, A. E.** (2022). Investigation of far-field patterns of semiconductor microlasers with an active region based on InGaAs/GaAs quantum well-dots. Scientific and Technical Vedomosti of St. Petersburg State Polytechnic University. Physical and Mathematical Sciences, 15(S3. 2), 25-30.

CONVOLUTIONAL NEURAL NETWORKS FOR IMAGE-FREE CLASSIFICATION VIA SINGLE-PIXEL IMAGING

A. A. Reutov [1]✉, **D. V. Babukhin** [1], **D. V. Sych** [1]

[1] P.N. Lebedev Physical Institute, Russian Academy of Sciences, Moscow, Russia;
✉aleksey.reutov@phystech.edu

Abstract. The technology of single-pixel imaging extends visualization capabilities beyond pixel-matrix-based devices. One of possible applications for this technology is fast classification of objects without the need for reconstruction of an image. The single-pixel camera gathers light statistics and then a computational algorithm – such as a neural network – decides on what is the object been illuminated. Here, we train a convolutional neural network on simulated data from single-pixel camera and demonstrate effectiveness of classification images of handwritten digits.

Keywords: Single pixel imaging, convolutional neural networks, image-free classification.

Funding: This study was funded by RSF grant number 23-22-00381.

Introduction

Single-pixel imaging is a technique for image acquisition via illuminating an object with structured light and obtain an image via computational restoration [1]. This technique provides imaging capabilities beyond visible wavelengths and thus perspective for making specific devices. Another possible application of single-pixel imaging is image-free object classification [2]. Gathering structured light via single-pixel camera and processing the raw data without image acquisition allows fast detection and classification of objects in the range of single-pixel imaging applicability. In last years, neural networks were shown to be a convenient tool for computational processing of single-pixel-gathered data [3,4]. Here we investigate on capability of convolutional neural networks to classify handwritten digits, processed with a single-pixel camera.

Materials and Methods

We trained a convolutional neural network on handwritten digits dataset MNIST. For every digit, we simulated a process of structured illumination with M=64 spatial patterns, thus generating 64 intensity measurements. For an image with N=784 pixels, our setup corresponds to approximately 8% sampling rate. We used a dataset of 60000 images, where a neural network was trained on 48000 images, and 12000 images were used to calculate classification accuracy.

Results and Discussion

We provide the results of our simulation in Fig. 1. Here, we can see that after 30 epochs of training – full learning iterations through training dataset – our network classifies digits, based on intensity measurements only, with the best accuracy 94.1%. We also see that value of neural network loss – a characteristic of the learning process – has gradually decreased, which demonstrates a correct learning process.

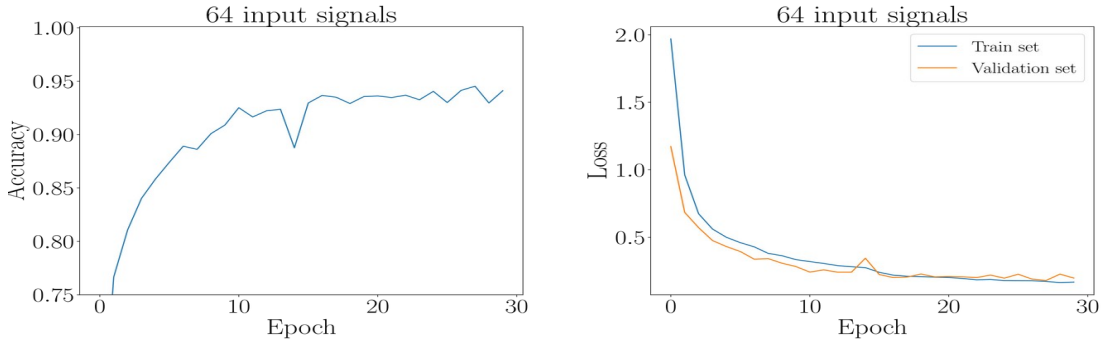


Fig. 1. Dependencies of classification accuracy (left) and neural network loss (right) on training epoch.

Conclusion

In this work, we trained a convolutional neural network to classify objects, using intensity measurements from a single pixel camera and without image acquisition. Our network demonstrated a high classification accuracy, thus serving as an efficient tool in single-pixel framework. We further plan to investigate on image-free classification in the presence of device imperfections.

REFERENCES

1. **M. F. Duarte, M. A. Davenport, D. Takhar, J. N. Laska, T. Sun, K. F. Kelly, R. G. Baraniuk**, Single-Pixel Imaging via Compressive Sampling, IEEE Signal Processing Magazine 25, 83 (2008)

2. **Sadao Ota et al.,** Ghost cytometry, Science, 360, 6394 1246-1251 (2018)

3. **C. F. Higham, R. Murray-Smith, M. J. Padgett, M. P. Edgar**, Deep learning for real-time single-pixel video, Scientific Reports 8, 2369 (2018)

4. **Z, Zhang, X. Li, S. Zheng, M. Yao, G. Zheng, and J, Zhong**. Image-free classification of fast-moving objects using “learned” structured illumination and single-pixel detection. Optics Express, 28(9):13269 (2020)

Features of monitoring the state of liquid flow by nuclear magnetic resonance using the modulation technique to record the NMR signal

A. A. Goldberg[1], I. D. Kochetov[1], R. V. Davydov[1, 2, 3]✉

[1]Peter the Great Saint-Petersburg Polytechnic University, Saint Petersburg, Russia;

[2]Alferov University, Saint Petersburg, Russia;

[3]The Bonch-Bruevich Saint Petersburg State University of Telecommunications, Saint Petersburg, Russia;

✉ davydovroman@outlook.com

Abstract. The features of determining the longitudinal T_1 relaxation time in NMR relaxometer designs for monitoring the state of the condensed medium in the current state are considered. Compared to other methods, the advantages of using the modulation technique for recording the NMR signal are substantiated. It has been experimentally proven that the resulting relationship from the Bloch equations using approximations to determine T_1 from the results of two measurements of NMR signal amplitudes at different modulation frequencies has several application limitations that create problems when monitoring the state of the current environment. Various cases of recording an NMR signal are considered, and the limits of applicability of the relationship for determining T_1 are established.

Keywords: nuclear magnetic resonance, state monitoring, flow, relaxation times, modulation frequency.

Introduction

The modulation technique occupies a special place among the methods of recording a nuclear magnetic resonance (NMR) signal [1]. This is because the modulation technique can be used to record NMR signals from both flowing and stationary condensed matter. In some cases, for example, when monitoring the parameters of a flowing liquid with a rapid change in flow rate, it is possible to obtain the necessary data with an error of less than 1% only using the modulation technique for recording the NMR signal [2]. It is recorded as non-periodic damped oscillations ("wiggles"). Therefore, to determine the state of the medium under study, the values of the longitudinal T_1 and transverse T_2 relaxation times are used, which is one of the features of monitoring the state of the medium compared with other NMR methods. These relaxation times are measured using NMR signals that are recorded at the resonant frequency of protons (^{1}H). This is because protons have the greatest sensitivity to the NMR method and are contained in 99.8% of liquid media and their mixtures [2]. One of the problems with using the modulation technique is the lack of a universal method for measuring T_1 in the current environment. This leads to several limitations and features in T_1 measurements that will be established due to our research.

NMR signal registration using the modulation technique for flowing liquid

Figure 1 shows a block diagram of the NMR flowmeter-relaxometer design. Figure 2 shows the recorded NMR signals from the current medium. The time T_2 is determined from the envelope's decay constructed from the tops of the peaks. The inhomogeneity of the magnetic field is considered in the area where the registration coil is located [1]. However, some problems arise with the measurement of T_1 using the developed relationship:

$$M = M_0 [1 – (1 – \exp (–\tau / T_1)) / (1 + \exp (–\tau / T_1))] \quad (1)$$

where $\tau = 1/ f_m$. Here f_m is the modulation frequency of the H_0 field (Fig. 1).

To determine T_1, two values τ_2 and τ_1 are used, and then the time itself is determined from the relationship between the NMR signals. The technique of such measurements was considered in more detail for various flows of current media.

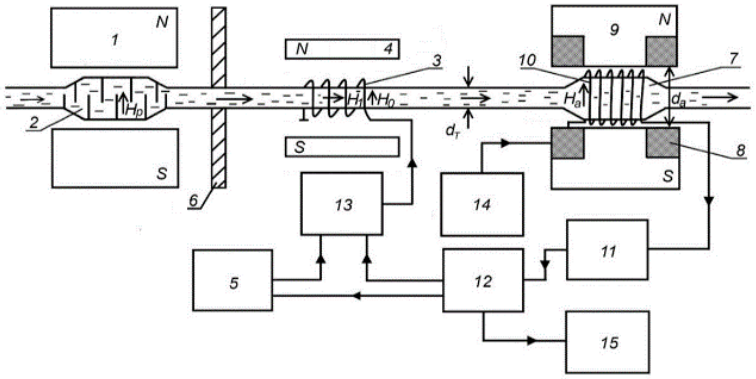


Fig. 1. Block diagram of an NMR flowmeter-relaxometer: 1 – polarizer magnet, 2 – polarizer vessel, 3 – nutation coil, 4 – permanent magnet, 5 – radio frequency generator, 6 – magnetic screen, 7 – analyzer vessel, 8 – modulation coils, 9 – magnet analyzer, 10 – NMR signal recording coil, 11 – autodyne detector, 12 – control and processing circuit, 13 – electronic key, 14 – radio frequency generator, 15 – oscilloscope.

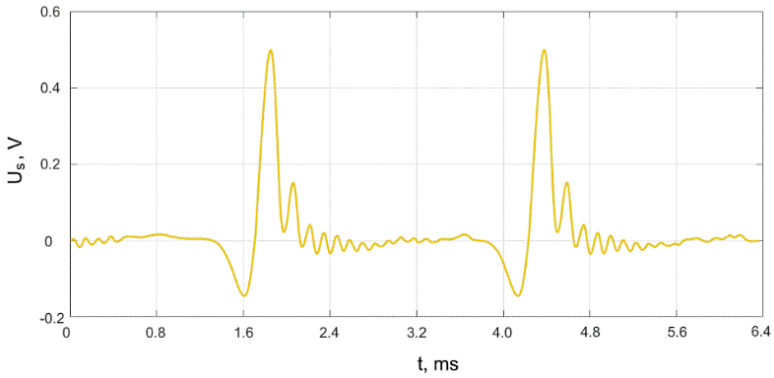


Fig. 2. The recorded NMR signal registered from tap water using a modulation technique.

Results and Discussion

As a result of the research, it was found that the most significant feature that arises when determining T_1 is associated with the residence time of the magnetized liquid in the recording coil at the moment of exposure to the modulation field when recording the NMR signal. Considering the fact that the speed of the current medium can change by an order of magnitude or more, this circumstance plays a key role in many T_1 measurements. The second feature is associated with changes in the fluid flow temperature. In stationary studies, the T value of the condensed medium is adjusted within the required range. In the current environment, especially in cooling systems, changes in T can be significant and challenging to control. As a result of research, it was found that the relationship between τ_1 and τ_2 (the inverse value of the field modulation frequency) should correspond to the following inequality $\tau_2/\tau_1 \geq 5$.

Conclusion

It should also be noted that in addition to a certain limit of applicability of the method for obtaining the T_1 value from relation (1) using two recorded NMR signals, the dependence of the change in the difference between the amplitudes of the recorded NMR signals with two changes in the modulation frequency f_m (corresponding τ_1 and τ_2) has been established. This difference depends on the resonance frequency of the nuclei at which NMR signals from the condensed medium are recorded.

REFERENCES

1. **Leshe A.** Nuclear induction. Veb Deustscher Verlag Der Wissenschaften Berlin, 1963.
2. **Davydov V.V., Myazin N.S., Davydov R.V.** Multiphase NMR Flowmeter-Relaxometer for Controlling the State and Rapidly Changing Flow Rates of Oil Mixtures. Measurement Techniques. 65(6) (2022) 444-452.

Investigation of entangled states of a three-mode electro-optical modulator

M. V. Matveeva [1]✉, **A. I. Trifanov** [1,2]
[1, 2] ITMO University, Saint-Petersburg, Russia
✉mvmatveeva@itmo.ru

Abstract. The problem of studying the dynamic properties and algebraic invariants of the model of phase modulation of light by microwave radiation is considered. The energy levels of the system are described by the eigenvalues of the Hamiltonian, the generators of which have a nontrivial internal structure. The dynamics of states is studied in Fock space. Invariant Hamiltonian spaces are associated with irreducible representations of the su(2) algebra, within which the Hamiltonian matrix is partitioned into finite blocks. The dynamics of states and various characteristics of the system are studied and the problem of visualizing the obtained data is solved, the complexity of which is primarily related to the dimension of the problem.

Keywords: Phase modulator, Hamiltonian, entangled states, ladder operators.

Introduction

In 2017, an algebraically solvable model of electro-optical modulation of light by a microwave field based on the linear electro-optic effect (Pockels effect) was presented [1]. To describe the intermodal interaction of light, the corresponding operators were obtained by the Jordan-Schwinger mapping [2] of generators of the matrix algebra su(2). It was shown that, assuming a high intensity of modulating microwave radiation, the model is reduced to a semiclassical one and the dynamic problem turns out to be exactly solvable. However, when the number of interacting optical modes is greater than three, the irreducible representations of the su(2) algebra associated with invariant spaces turn out to be degenerate—the classification generated by the su(2) algebra is incomplete. To solve this problem, in 2022, a method of ladder operators was proposed for the Casimir operator of the image of the algebra su(2) [3]. The resulting algebra of ladder operators generates the spectrum and eigenvectors of the Casimir operator.

Materials and Methods

In this work, the possibility of generating entangled two-photon states is investigated. Acting on the vacuum vector with ladder operators, we find ourselves in an invariant subspace associated with an irreducible representation of the algebra su(2) of dimension five, containing the states $|200\rangle$, $|110\rangle$, $\sqrt{\frac{2}{3}}|020\rangle + \frac{1}{\sqrt{3}}|101\rangle$, $|011\rangle$, $|002\rangle$.

We consider the Hamiltonian of the phase modulator, which has the form:

$$H = \omega m_{opt} N + \omega J_z + \gamma \cdot (J_+ e^{-i\varphi} + J_- e^{i\varphi}). \quad (1)$$

Next, having constructed the matrix of the Hamiltonian V in the basis of the subspace of the irreducible representation

$$V = \begin{pmatrix} 0 & 2^{i\phi} & 0 & 0 & 0 \\ 2^{-i\phi} & 0 & \sqrt{6}^{i\phi} & 0 & 0 \\ 0 & \sqrt{6}^{-i\phi} & 0 & \sqrt{6}^{i\phi} & 0 \\ 0 & 0 & \sqrt{6}^{-i\phi} & 0 & 2^{i\phi} \\ 0 & 0 & 0 & 2^{-i\phi} & 0 \end{pmatrix}. \quad (2)$$

we have determined the spectrum and eigenvectors corresponding to stationary states.

Results and Discussion

Each eigenvector can be expressed in terms of a Fock basis. We use the stationary states of the Hamiltonian to construct the model evolution operator. By acting on the initial state $|020\rangle$, we find the dependence of the probability amplitudes of the components of the Fock vector on time.

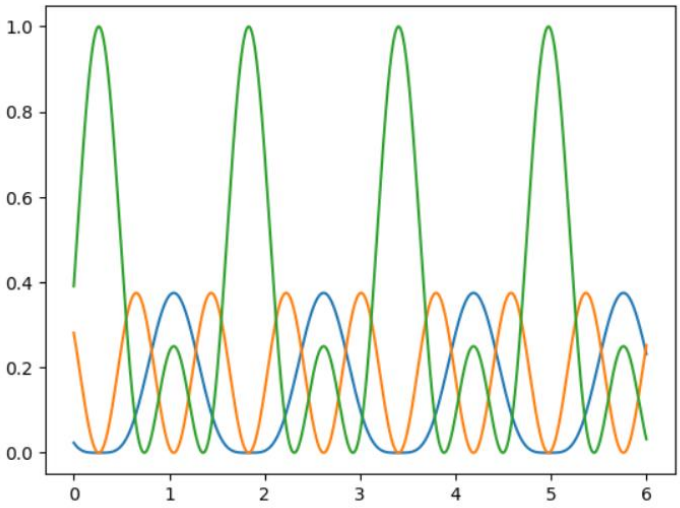


Fig. 1. Probability amplitudes of state |020> in dynamics.

From the graph in Fig. 1 it follows that in the process of evolution quantum multimode states of the form can arise

$$\alpha|200\rangle + \beta|020\rangle + \alpha^*|002\rangle \quad (3)$$

In which the states $|011\rangle$ и $|110\rangle$. At the same time, we have determined a point in time at which the component $|020\rangle$ is absent in expression (3).

Conclusion

In this work, we showed the possibility of the emergence of two-photon entangled states in the process of phase modulation of light.

REFERENCES

1. **Miroshnichenko G. P., Kiselev A. D., Trifanov A. I., Gleim A. V.,** Journal of the Optical Society of America B. 2017. No 34(6). P. 1177-1183.
2. **Biedenharn L. C., Louck J.D**,, Angular momentum in quantum physics, Cambridge univerisity press, London, 1984.
3. **Tushavin G. V., Trifanov A. I., Zaitseva E. V.,** Nanosystems: Physics, Chemistry, Mathematics. 2022. No 13 (3). P. 299-307.
4. **Trifanov A. I., Miroshnichenko G. P.,** Nanosystems: Physics, Chemistry, Mathematics. 2013. No 4(5). P. 635-647.

THE AUTHORS

MATVEEVA Milena V.
mvmatveeva@itmo.ru

TRIFANOV Alexander I.
alextrifanov@itmo.ru

Determination of metasurface structure dimensions by plasma chemical etching for metalens application

E .Yu. Gusev[1]✉, S. P. Avdeev[1], S. V. Malokhatko[1], V. V. Polyakov[1], S. Wang[2], L. Han[2], W. Zhang[2,3], O. A. Ageev[1,4]

[1] Institute of Nanotechnology, Electronics and Electronic Equipment Engineering, Southern Federal University, Taganrog, Russia;

[2] Laser Institute, Qilu University of Technology (Shandong Academy of Sciences), Jinan, China;

[3] School of Optoelectronic Engineering, Qilu University of Technology (Shandong Academy of Sciences), Jinan, China;

[4] Research and Educational Center "Nanotechnologies", Southern Federal University, Taganrog, Russia

✉eyugusev@sfedu.ru

Abstract. In present paper critical dimensions of plasma etched silicon on silicon oxide structures are discussed in terms of mask topology simulation and metasurface-like structure fabrication. Geometric parameters of the metasurface topology were experimentally studied using data of etching patterns in capacitive plasma. Corresponding conditions are determined.

Keywords: metasurface structure, simulation, plasma chemical deposition, etching.

Introduction

The creation of metalenses based on the silicon-silicon oxide structure is a promising direction of research in the field of optics. Lenses based on metamaterials such as silica-silicon oxide are innovative optical devices that can change the properties of light and have unique optical characteristics. The creation of lenses based on metamaterials is a hot topic. Metamaterials make it possible to create lenses with unusual optical properties. Lenses based on metamaterials can be more compact and lightweight compared to traditional optical systems. Metamaterials allow easily change the optical properties of lenses, making them flexible and adaptable to different conditions and tasks. In addition, metamaterial-based lenses can be integrated into micro- and nanodevices such as microphotonics, optical chips and sensors, opening new prospects for the development of compact and efficient optical systems [1]. Along with this, the creation of metalenses on a membrane structure formed on silicon on isolator wafers is a promising direction of research in the field of optics. The use of such a structure provides high mechanical strength, which allows its use under conditions of increased mechanical loads. It has good thermal stability, which allows it to be worked at high temperatures without degradation of its properties. Such substrates are easily integrated into semiconductor device fabrication processes, making it a convenient material for use in a variety of technologies. The key operations that determine resolution are lithography and subsequent etching. The aim is to study metasurface structure formation modes by plasma etching.

Modeling, experiment and results

Previously, a solid mask (metal, silicon oxide) was formed on the Si/SiOx structures using deposition (magnetron, plasma-chemical) and contact lithography [2]. Mask topology was calculated using simulation data [3]. Silicon etching was carried out to the full depth of the silicon layer in capacitive plasma. The geometric parameters of the etching figures were controlled by scanning electron microscopy, atomic force microscopy, and contact profilometry.

The critical parameters of the topology at which preference should be given to etching in inductively coupled plasma instead of capacitive plasma and corresponding conditions are determined.

The obtained results will be useful in the development and creation of metalenses and related metasurface device structures.

Acknowledgments

The results were obtained using infrastructure and equipment of the Research and Education Centre «Nanotechnologies» of Southern Federal University and Laser Institute, Qilu University of Technology (Shandong Academy of Sciences).

REFERENCES

1. **Zou X., Zheng G., Yuan Q., Zang W., Chen R., Li T., Li L., Wang S., Wang Z., Zhu S.**, Imaging based on metalenses, PhotoniX. 1 (1) (2020) 2.

2. **Gusev E. Yu., Avdeev S. P., Polyakov V. V., Ren X., Chen D., Han L., Zhang W., Ageev O. A.**, Investigation of Structure Formation Modes for Metasurfaces and Confocal Optical Systems, Physics of the Solid State. 65 (12) (2023) 2081–2084.

3. **Gusev E. Yu., Avdeev S. P., Malokhatko S. V., Klimin V. S., Polyakov V. V., Wang S., Ren X., Chen D., Han L., Wang Z., Zhang W., Ageev O. A.**, Silicon-on-Silicon Oxide Metalens: Design and Fabrication Aspects, Springer Proceedings in Materials. 41 (2024) 56–67.

THE EFFECT OF RAPID THERMAL ANNEALING ON THE OPTICAL PROPERTIES OF STRUCTURES WITH INGAPAS/INGAAS QUANTUM DOTS

D. A. Masyutin[1]✉, **N. V. Kryzhanovskaya**[2], **A.S. Dragunova**[2], **I. S. Makhov**[2], **A. V. Uvarov**[1], **V. V. Andryushkin**[3], **A. G. Gladyshev**[3], **L. Ya. Karachinsky**[3], **D. S. Papylev**[3], **A. E. Zhukov**[2]

[1] Alferov University, Saint Petersburg, Russia;

[2] HSE University, Saint Petersburg, Russia

[3]ITMO University, Saint Petersburg, Russia

masyutind2002@gmail.ru

Abstract. In this paper, we present the study of the effects of matrix composition and rapid thermal annealing on the photoluminescence properties of the structures with InGaPAs/InGaAs quantum dots. The photoluminescence spectra of the structures with quantum dots annealed at various temperatures measured in a wide range of temperatures and pumping powers were investigated. It is shown that annealing temperature of 620 C is optimal and allows to increase the integrated photoluminescence intensity of the structures up to 4 times without a short-wavelength shift of the emission line due to quantum dots decomposition.

Keywords: annealing, quantum dots, molecular beam epitaxy, photoluminescence

Funding: Support from the Basic Research Program of the National Research University Higher School of Economics is gratefully acknowledged. Growth of the structures with InGaPAs quantum dots was supported by Ministry of Science and Higher Education of the Russian Federation, research project no. 2019-1442 (project reference number FSER-2020-0013).

Introduction

Currently, the development of quantum-dimensional heterostructures for optical data transmission is a crucial task of optoelectronics. Structures with arrays of high-density quantum dots can be used to develop powerful radiation sources, since high gain values can be achieved in such arrays. Typically, semiconductor quantum dots are obtained through the effect of self-organization that occurs during the epitaxy process. Recently a novel technique to realize high-density InGaPAs/InGaAs quantum dots replacing of the fifth group elements using molecular beam epitaxy (MBE) was proposed [1]. As it known thermal annealing can reduce the number of defects in the structures, which improves their optical properties [2]. In this paper, we studied the effect of rapid thermal annealing (RTA) on the optical properties of the InGaPAs/InGaAs quantum dots.

Materials and Methods

Heterostructures №1, №2, №3 for experiments were grown by MBE on GaAs "epi-ready" substrates. The heterostructure №1 consisted of a 100-nm thick GaAs buffer layer and a 200-nm GaAs active layer, which was surrounded by 100-nm thick AlGaAs barriers. A 5-nm thick GaAs layer was also deposited above the upper AlGaAs barrier to prevent its oxidation. The 2 nm thick InGaP layer was formed at the center of the GaAs active layer. After that, the InGaP layer was kept in the As flux for 5 minutes. This process is necessary to replace the P atoms in the InGaP layer with As atoms, followed by the formation of InGaPAs QDs. Heterostructure №2 has an additional 5-nm thick $In_{0.17}Ga_{0.83}As$ layer grown on top of the InGaPAs quantum dots, while №3 has additional $In_{0.17}Ga_{0.83}As$ layers below and above the InGaPAs QDs.

RTA of the structures was made using the Jipelec Jetfirst RTA 100 installation. Annealing was carried out at temperatures of 580°C, 600 °C and 620°C. Photoluminescence (PL) spectroscopy was used to investigate the optical properties of heterostructures. The sample was placed in optical closed cycle cryostat, the temperature in which varied from 5 K to 300 K. A continuous-wave solid-state laser operating at a wavelength of 527 nm was used for non-resonant interband excitation of the samples. The laser beam was focused onto the sample surface using a 5x objective and system of mirrors, creating a spot with a diameter of 10 micrometers. The

pumping intensity was 114 W/cm^2. The near-infrared radiation emitted by the samples was collected using the same objective setup. Photoluminescence spectra were measured in the near-infrared spectral range using an Andor Shamrock 500i grating monochromator and a thermoelectrically cooled InGaAs CCD matrix.

Results and Discussion

Photoluminescence spectra of the samples measured at room temperature before and after annealing at optimal temperature 620 C are presented in Fig. 1. PL spectra of the samples contain several emission bands. PL band with an intensity maximum located near 870 nm for all samples is associated with radiative recombination in GaAs epilayers and substrate of the structures. Wide emission bands located near 1043 nm, 1098 nm and 1103 nm are associated with the emission from InGaPAs QDs of the structures #1, #2 and #3, respectively. Luminescence peak located near 980 nm presented in the PL spectra of the structures #2 and #3 is related to the emission from InGaAs epilayer grown above the InGaPAs QDs, whereas luminescence peak located near 930 nm is presented for the structure #3 only and is related to the emission from InGaAs epilayer located below QDs. RTA of the structures results in increase of the emission intensity of all the structures up to 4 times, which we associate with decrease in the number of defects during the annealing process. Annealing also lead to slight redshift of the QD related PL band peak position by 5-10 nm, that can be attributed to material intermixing.

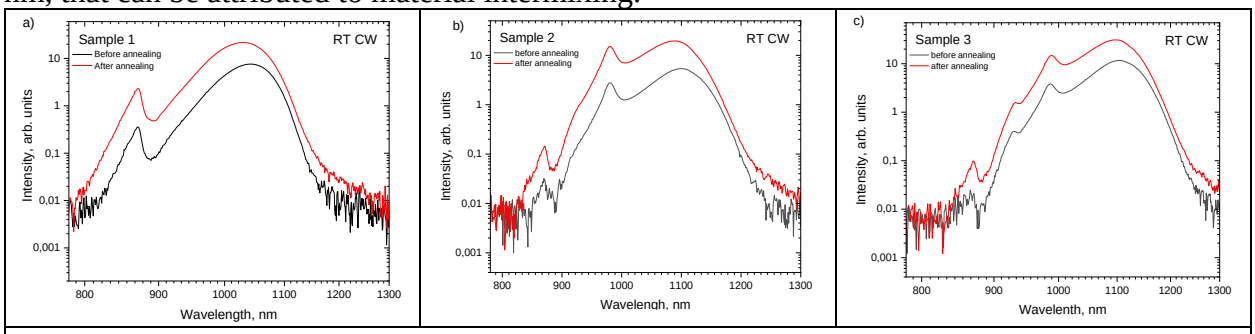


Fig. 1. PL spectra of heterostructures #1 (a), #2 (b) and #3(c) before (black) and after (red) annealing at 620 C measured at room temperature

Conclusion

The PL spectra of the InGaPAs QDs exhibited peaks in the range of 980 to 1104 nm at room temperature, without the annealing. After RTA, there is red shift in the PL intensity of the QDs: 14 nm in №1, 10 nm in №2, and 5 nm in №3. During the annealing process the number of defects in the structure were reduced. As a result, non-radiative recombination decreased. Therefore, we observed an intensity growth up to 4 times for all the samples after annealing.

Acknowledgments

The work was carried out on the equipment of the large-scale research facility No. 2087168 “Complex Optoelectronic Stand”

REFERENCES

1. **Gladyshev A.G., Babichev A.V., Andryushkin V.V. et al.**, Studying the Optical and Structural Properties of Three-Dimensional InGaP(As) Islands Formed by Substitution of Elements of the Fifth Group, Technical Physics. 65 (12) (2020) 2047-2050.
2. **Sobolev M.M., Kochnev I.V, Lantratov V.M. et al.**, Thermal annealing of defects in InGaAs/GaAs heterostructures with three-dimensional islands, Semiconductors. 34 (2) (2000) 195–204.

SUPERCONDUCTING SINGLE PHOTON DETECTOR WITH MULTIMODE FIBER COUPLING FOR PLIM\FLIM APPLICATIONS

V. Andreev[1,4,6]✉, P. Morozov[2,6], M. Yakovleva[5], A. Kostyukov[5], G. Goltsman[1,4]

[1] National Research University Higher School of Economics, 20,Myasnitskaya ulitsa, Moscow, 101000, Russia;

[2]LLC SCONTEL, 11kA,Derbenevskaya Naberezhnaya, Moscow, Russia;

[3]Privolzhskiy Research Medical University, 10\1,Sq. Minina and Pozharskogo, Nizhny Novgorod, 603005, Russia

[4]Moscow Pedagogical State University, 1\1,Malaya Pirogovskaya Street, Moscow,119991, Russia

[5]N.M. Emanuel Institute of Biochemical Physics RAS, 4,Kosygina Street, Moscow,119334, Russia

[6]LLC «SCONTEL»,11kA, Derbenevskaya Naberezhnaya,Moscow,115114, Russia

✉vsandreev@hse.ru

Abstract. In this paper we presents system for direct time-resolved measurement of luminescence coupled with multimode optical fiber large area superconducting single photon detector (SSPD) for visible and near-infrared range applications. SSPDs positively outperform other types of single-photon detectors and may be the best solution for many applications. But the sensitive area of which is rather small and well suited to be coupled to a single-mode optical fiber. Research shows that large area SSPD coupled with multimode fiber can be fabricated. This detectors was coupled with the phosphorescence\fluorescence lifetime imaging microscopy (PLIM\FLIM) system. This detectors works well in visible range and also could have high efficiency in near infrared range. This provides wide range of applications in luminescence measurement. For the test object we used lipofuscin granulas, as well researched object. As excitation laser we used Becker&Hickl BDL-473-SMC picosecond diode laser with wavelength of 473 nm.

Keywords: SNSPD, luminescence, imaging, microscopy, lifetime.

Funding: This study was funded by Russian Science Foundation grant number 23-72-00014.

Introduction

This paper presents system for direct time-resolved measurement of luminescence coupled with multimode optical fiber large area SSPD for visible and near-infrared range applications. Modern FLIM\PLIM research mostly provides data for visible wavelength range. There are growing request for system that can also work in near-infrared range. Superconducting single photon detectors (SSPDs) positively outperform other types of single-photon detectors and may be the best solution for many applications. But the sensitive area of which is rather small and well suited to be coupled to a single-mode optical fiber. Research shows that large area SSPD coupled with multimode fiber can be fabricated [1].

Materials and Methods

Therefore, we provide FLIM\PLIM system with large area SSPD coupled with multimode fiber. For FLIM\PLIM we use TCSPC Becker&Hickl [2] laser scanning system with confocal microscope Zeiss Axio Observer.A1 with optical scanning system. It is well suited for visible range applications and uses hybrid detector for photon counting for standard system.

Optical scanning system was modified by us to use multimode fiber for single photon counting for also visible and near infrared applications with low noise, therefore high signal to noise ratio measurements.

Results and Discussion

One of the promising applications of the FLIM method in medicine is the detection of fundus autofluorescence, the source of which is lipofuscin granules in retinal pigment epithelium cells.

We provide measurement of lipofuscin fluorescence lifetimes and intensity imaging and data in visible range. Excitation laser was Becker&Hickl BDL-473-SMC picosecond diode laser with wavelength of 473 nm wich is near with lipofuscin absorbance peak. At the fiber was put 500 lp filter to cut unwanted radiation to pass thru to the detector. The data obtained is shown at Figure 1, 512x512 pixels images each contained fluorescence decay data. The fit procedure was made with each pixel, the quality of the fit is described by X^2 with is close to 1 at all valuable points.

All data is consistent with the previously obtained data [3].

a) *b*)

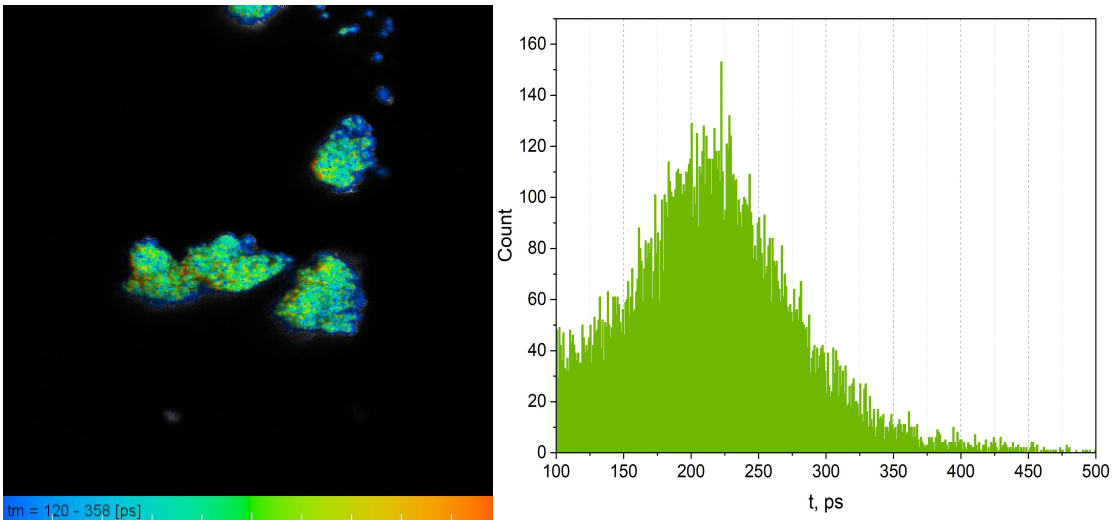


Fig. 1. Fluorescence lifetime of the lipofuscin, (*a*) FLIM image, (*b*) average lifetime histogram.

Conclusion

All data obtained is corresponding to the previously obtained data. The usage of SNSPD opens measurement in the near infra-red range. The properties of the SNSPD in NIR are well known to public. Potentially this approach could be used for detecting singlet oxygen luminescence, its luminescence photons at 1270 nm. [4] Also this is complicated by the very low quantum yield in different solutions.

REFERENCES

1. **Moshkova, M., Morozov, P., Divochiy, A., Vakhtomin, Y., & Smirnov, K.** (2019, December). Large active area superconducting single photon detector. In Journal of Physics: Conference Series (Vol. 1410, No. 1, p. 012139). IOP Publishing.

2. Becker&Hickl. URL: https://www.becker-hickl.com/

3. **Yakovleva, M. A., Radchenko, A. S., Feldman, T. B., Kostyukov, A. A., Arbukhanova, P. M., Borzenok, S. A., ... & Ostrovsky, M. A. (2020).** Fluorescence characteristics of lipofuscin fluorophores from human retinal pigment epithelium. Photochemical & Photobiological Sciences, 19, 920-930.

4. **Krasnovsky Jr, A. A.** (1998). Singlet molecular oxygen in photobiochemical systems: IR phosphorescence studies. Membrane & cell biology, 12(5), 665-690.

Automated bioimpedance measurement system for body composition studies

V. V. Antipenko✉, E. A. Pecherskaya, D. V. Yakushov, D.V. Artamonov, O.V. Karpanin, J.V. Shepeleva

[1]Department of Information and measuring equipment and metrology, Penza State University, Penza 440026, Russia;

✉v.antipenko7@yandex.ru

Abstract. Bioimpedance diagnostic systems play a significant role in modern medicine. These systems provide valuable information about body composition and key physiological parameters. Bioimpedance analysis has the advantage of being able to test non-invasively, and accuracy and availability continue to improve every year. However, it is important to note that although these analyzers have become more widely available, problems with metrology and interpretation of results still exist. In this work, the performance of the developed automated bioimpedance measurement system for studying body composition was tested with a reduced impedance measurement error of up to ±5% and an increase in the information content of the human body composition, thanks to the expansion of the impedance frequency range measurement from 0.3 kHz to 2 MHz..

Keywords: bioimpedance, system, circuit, model, object.

Introduction

Automated bioimpedance measurement systems being developed offer a simple and rapid method for assessing body composition by measuring physiological parameters that are important indicators of physical health [1]. These systems have advantages over analogues in terms of technical and economic indicators, they are portable and do not require specialized training for use. To carry out measurements, the system uses a weak electric current of a given frequency, perceiving the body's reaction as a potential difference, and then processes the received data taking into account the gender, height, weight, and age of the patient to determine a set of physiological parameters [2].

This work uses a developed automated system for measuring bioimpedance, with improved metrological indicators (impedance measurement error up to ±5%) and increased information content about the human body composition, thanks to the expansion of the impedance frequency range measurement from 0.3 kHz to 2 MHz [3].

Bioimpedance measurement and results analysis

Calibration was performed using a 910 Ohm resistor. After calibration, a table of complex coefficients was obtained for each of 13 frequencies in the range from 300 Hz to 2 MHz. Next, using the obtained complex coefficients, the known resistance of a calibration resistor with a nominal value of 910 Ohms is measured. The final frequency response is presented in Figure 1 (*a*).

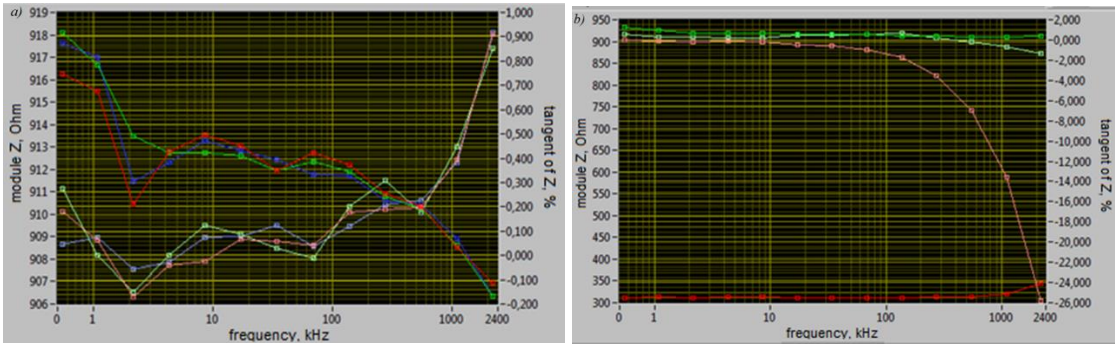


Fig. 1. Frequency response R = 910 Ohm, after calibration using a 910 Ohm resistor (*a*) and Frequency response R = 300 Ohm and R = 910 Ohm, after calibration with a 910 Ohm resistor (*b*)

On the left y-axis is the complex resistance module in Ohm units. Along the ordinate on the right - the tangent of the phase shift angle $tg(\varphi)$, expressed as a percentage. The frequency in Hz

is indicated on the abscissa axis. The axis has a logarithmic scale. Bright red, blue and green colors indicate the impedance module *Z*; pale colors - phase shift tangent. The graph shows that the maximum absolute resistance deviation ΔR = 8 Ohms. The maximum relative deviation is δ = 0.87%. In turn, the maximum absolute deviation $\Delta tg\varphi$ = - 0.9%.

Next, using the previously obtained calibration table, the resistance of a 300 Ohm resistor is measured. The resulting frequency response is plotted in Figure 1 (*b*). Based on the graph, it can be seen that the maximum absolute difference in resistance ΔR = 45 Ohms. The maximum relative error is δ = 13.1%. In turn, the maximum absolute difference is $\Delta tg\varphi$ = 26%.

Next, the measurements are processed. The resulting spectral characteristic is visualized using a Bode diagram, that is, through the dependence of the complex impedance module and the tangent of the phase angle on frequency, however, to facilitate perception and subsequent study of the obtained results, it is necessary to convert this diagram into the Nyquist format. Based on the listed data, the parameters of the equivalent and mathematical models must be determined [4]. In accordance with the measurement protocol, a graph of the frequency dependence of the impedance is plotted (Figure 2 (*a*)).

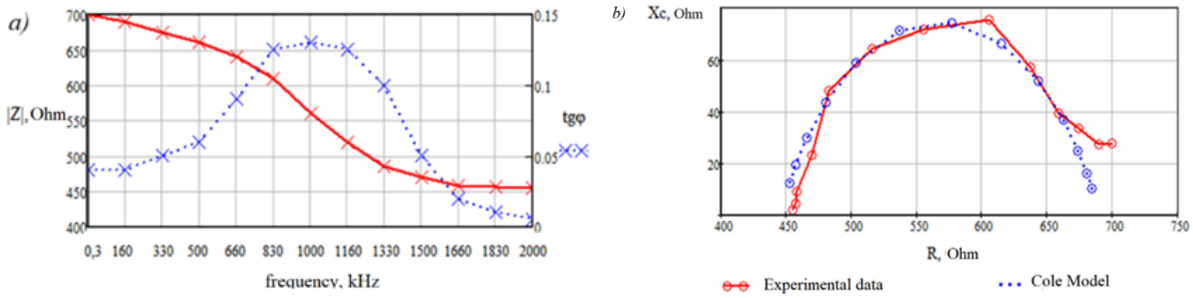


Fig. 2. Experimental frequency dependence of impedance (*a*) and Cole Model (*b*)

Using formula (1), the Cole model is calculated.

$$\bar{Z} = R_\infty + \frac{R_0 - R_\infty}{1+(J\cdot\omega\cdot\tau_z)^\alpha} \quad (1)$$

where R_∞ is the resistance at an infinitely high frequency, R_0 is the resistance at zero frequency, α is a dimensionless parameter, τ_z is the time constant, ω is the circular frequency. We take α = 0.7, ω = 40 Hz R_∞ = 445 Ohm, R_0 = 690 Ohm, τ_z = 3.98 ms. Figure 2 (*b*) shows a plot of the resulting Cole model.

Therefore, we can conclude that measuring different resistances of objects using the same calibration parameters leads to inaccuracy. The more the measured resistance deviates from the calibration value, the lower the measurement accuracy.

Conclusion

By means of the proposed innovative automated bioimpedance analysis system, a study of the body structure on the object was carried out. Fluctuations of the random error are minimized by carrying out numerous measurements followed by mathematical processing of the data. Subjective errors are eliminated due to the automated measurement process.

REFERENCES

1. **D. Dutra, P. Bertemes-Filho,** Extracting parasite effects of electrical bioimpedance measurements, J. Electr. Bioimp., vol. 9, pp. 115-122, 2018

2. **Qin E.S., Mindy M.J. and Chen W.F.,** Diagnostic accuracy of bioimpedance spectroscopy in patients with lymphedema: A retrospective cohort analysis, Journal of Plastic, Reconstructive & Aesthetic Surgery (2018) 71, 1041–1050

3. **Antipenko V.V., Pecherskaya E.A., Tuzova D.E., Yakushov D.V., Artamonov D.V.,** Development of an automated system for measuring bioimpedance for the study of body composition, St. Petersburg State Polytechnical University Journal. Physics and Mathematics. 16 (3.2) (2023) 294–300.

4. **Sindeeva L.V., Kazakova G.N.**, Anthropometry and bioimpedansometry: parallels and divergences // Medical Sciences. No. 9 2013, pp. 476-480

Formation of compact DNA structures with nanoparticles

D. A. Artamonova[1]✉, V. M. Bakulev[1], T. N. Nekrasova[2], N. A. Kasyanenko[1]

[1]St. Petersburg State University, St. Petersburg, Russia
[2]IMC of RAS, St. Petersburg, Russia
✉st077204@student.spbu.ru

Abstract. The aim of this work was to form multicomponent structures containing high molecular weight DNA in compact form, various nanoparticles, and a fluorescent dye. and a compacting agent. The enhancement of a fluorescence of EtBr dye was observed in the systems with nanoparticles. The effect depends on the order of the addition of the components to DNA solutions. The possibility of DNA packaging induced by its interaction with cationic polymers was also discussed. We have used one or two types of nanoparticles pre-reduced on polymers. The estimation of the hydrodynamic radius of multicomponent compact structures with gold and silver NPs has been obtained by the method of dynamic light scattering.

Keywords: DNA, packaging, silver nanoparticles, photodynamic therapy.

Introduction

Titanium dioxide TiO_2 has been widely studied as a promising photocatalyst in various applications. At the same time, several lanthanide complexes, for example, samarium, have shown anticancer effects on tumor cells. Samarium-containing compounds have also been used in osteoblastic metastases radiotherapy. These agents are also the effective drugs in the treatment of bone marrow cancer. Samarium (Sm) nanoparticles have therapeutic and diagnostic applications. They also have anti-bacterial properties. Nanoparticles for drug delivery in the therapy of Crohn's disease can be used [1].

The usage of noble metal nanoparticles in multicomponent structures improves some properties of different systems. Nanoparticles of noble metals have a plasmon resonance in the visible region. TiO_2 and TiO_2 nanoparticles with Sm do not have absorption at wavelength >500 nm. The application of nanoparticles in systems containing DNA and polymers must penetrate into cells. Such structures should be packaging before the usage. DNA packaging can be induced by special agents. The formation of systems with the inclusion of fluorescent dyes and different nanoparticles can lead in some case to the effect of enhancement of the fluorescence. Usually, it is true for the dye bound to the DNA molecule. The development of the effective multicomponent structures is a promising tool for such applications like the detection of cancer during resection operations [2] and the photodynamic therapy.

Materials and Methods

A commercial preparation of high molecular mass calf thymus DNA from Sigma Aldrich was used in the work. Synthetic polymers MAG-DMAEM with incorporated silver nanoparticles and PDMAEM with incorporated TiO_2 and TiO_2-Sm nanoparticles were synthesized at IMC of RAS. EtBr, which was dissolved in deionized water, was used as a fluorescent dye. Salts $NaAuCl_4$ and $AgNO_3$ as sources of gold and silver ions were applied. Sodium borohydride from "Vekton" was used as a reducing agent.

Results and Discussion

The experimental results obtained with low-gradient viscometry showed that all polycationic polymers used in this work induce DNA packaging in solutions of low ionic strength at charge ratio N/P=0.8 (a charge ratio is a ratio of the molar concentrations of polymer and DNA ionogenic groups). Some differences in the dependences of relative viscosity of DNA solutions with polymers on the concentration of added polymer (MAG-DMAEM or MAG-DMAEM-Ag0) are explained by the difference in the electrostatic interactions due to the presence of nanoparticles.

Pre-reduction of gold nanoparticles on DNA followed by the DNA condensation induced by MAG-DMAEM-Ag0 was done. The viscosity drop was observed in this case.

According to the results of spectroscopy in the UV and visible regions, an increase in optical density of solutions with increasing N/P was observed. We can explain this result by the scattering of DNA solutions with nanoparticles. This is also true when PDMAEM-TiO2 or PDMAEM-TiO2-Sm are added to the DNA solutions. For solutions with MAG-DMAEM-Ag0, the plasmon resonance peak of silver nanoparticles was observed in the visible region around 400 nm.

The fluorescence enhancement effect was observed in the systems with EtBr and nanoparticles. The cationic polymer (MAG-DMAEM-Ag0 or PDMAEM-TiO_2) and fluorescent dye were added to DNA solution in different order. The enhancement was observed only at low N/P values, when the dye was added to the solution with DNA-polymer complexes. Indeed, in the case of DNA packaging the intercalation sites on DNA are not open for the ethidium bromide. When we use two types of nanoparticles (Ag and Au), the fluorescence emission was hindered by scattering.

A key step in the study of multicomponent systems is the estimation of their size. The results of dynamic light scattering method (Fig.1) show that the structures (DNA-AuNPs)+(MAG-DMAEM-AgNPs) have a hydrodynamic radius of about 90-100 nm, which can penetrate through the cell membranes.

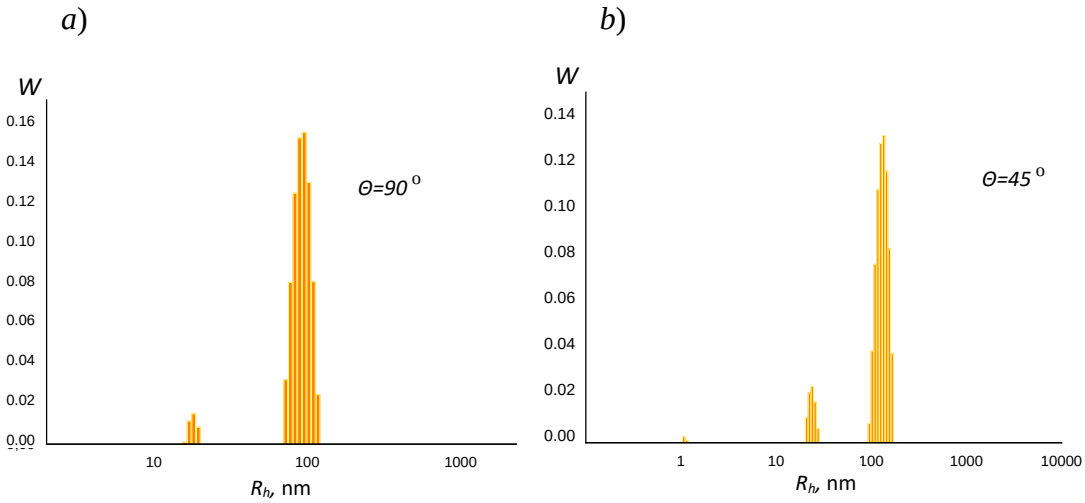


Fig.1. Size distribution of particles in DNA solutions in 0.005 M $NaNO_3$ with AuNPs and MAG-DMAEM-AgNPs from DLS data at scattering angles of 90° (a) and 45° (b)

Conclusion

In this work, the possibility of the creation of the compact structures containing high-molecular-weight DNA, fluorescent dye, nanoparticles can be form. The packaging of such structures induced by cationic polymers allows them to avoid a cleavage by nucleases during the way to the target cells. The choice of components influencing the effect of fluorescence amplification contributes to the application of such structures in photodynamic therapy.

REFERENCES

1. **Ghodrati, Zahra, and Adeleh Divsalar.** "Biological properties, therapeutic and diagnostic applications of Samarium and Samarium nanoparticles." (2020): fa20-fa38.

2. **Kanehira, Koki, et al.** "Fluorescence enhancement effect of TiO2 nanoparticles and application for photodynamic diagnosis." International Journal of Molecular Sciences 20.15 (2019): 3698.

Development of hardware and software complex for assessment of the functional state of the microvasculature

K. V. Babaev[1], **M. S. Mazing**[2]✉, **A. Yu. Zaitceva**[2]

[1] Peter the Great Saint Petersburg Polytechnic University, Saint Petersburg, Russia;

[2] Institute for Analytical Instrumentation, Russian Academy of Sciences, St. Petersburg, Russia

✉mazmari@mail.ru

Abstract. A portable optical hardware and software system designed to assess microcirculation parameters at different depths of biological tissues has been developed and investigated. Preliminary experimental studies confirmed the effectiveness of the developed system. The hardware-software complex can be used both for diagnostics of microcirculatory disorders and as a means of monitoring after surgical interventions.

Keywords. Microcirculation, non-invasive spectrophotometry, biological tissue, optical radiation.

Funding. The study was supported by a grant from the Russian Science Foundation (project No. 24-21-00404).

Introduction

Disturbances of microcirculation in tissues play a key role in the pathogenesis of complications of various diseases [1]. The microcirculation system is a complex structure that provides the processes of metabolism of various substances between blood and tissues. At present, one of the promising directions for noninvasive diagnostics of blood supply and the state of biological tissues is the use of optical noninvasive technologies that allow to determine and analyze the differences in optical properties of biological tissues and, based on this, to draw conclusions about the peculiarities of the biological environment and the processes occurring in it. At the same time, recent successes in the field of research of non-invasive means of optical diagnostics make this area even more promising for research in clinical conditions [2,3].

The aim of this work is to develop and create a portable hardware-software complex for assessing the functional state of the microcirculation system with the possibility of recording the parameters of the microcirculatory channel at different depths of biological tissue.

Materials and Methods

The developed optical system is based on the method of non-invasive optical spectrometry The physical principle of this method consists in the difference of optical absorption properties of different derivative forms of hemoglobin protein. The sensor unit of the hardware-software complex is represented by a multichannel analyzer of optical spectra, operating in the visible and near-IR ranges, and is implemented in the mode of measurement "on reflection" for registration of backscattered in biological tissues radiation emitted on their surface by optical radiation sources. To measure microcirculation parameters at different depths, the system was designed in two configurations with different separation of sources and photodetectors in each device. The principle of operation of the system with different «source-detector» distance is presented in Figure 1.

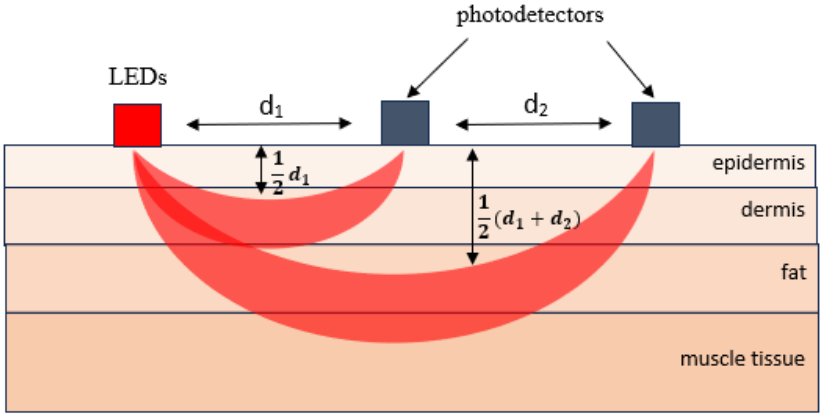


Fig. 1. The principle of operation of the system with different «source-detector» distance

As shown in figure 1, the diagnostic volume and the depth with which the microcirculation parameters are recorded depend on the distance between the radiation source and detector in the system, with light in tissues traveling along a banana-shaped path, and the penetration depth is approximately equal to half of the source-detector distance [4,5].

The measurements recorded by the system are transmitted to the computing unit via Bluetooth connection for further analysis. In addition, the system has a built-in rechargeable battery that allows the device to be used autonomously for up to 7 hours.

Results and Discussion

In the course of preliminary experimental studies, in which test subjects participated, the efficiency and operability of the developed hardware-software complex was confirmed. The results of experimental studies allowed to demonstrate the advantages of the multichannel system, the main of which is the possibility of simultaneous registration of a number of diagnostic parameters. The analysis of the obtained spectral response using the modified Bouguer-Lambert-Beer law allows to obtain information about the degree of tissue oxygen saturation and the general level of blood filling of the microcirculatory channel. The possibility of measuring microcirculation at different depths of biological tissue significantly expands the prospects in the field of biomedical diagnostics.

Conclusion

The results of the studies show the prospects of using the developed portable hardware and software complex for functional assessment of microcirculatory-tissue systems. The device can be used both for diagnostics of microcirculatory disorders and as a monitoring system after surgical interventions.

REFERENCES

1. de Keijzer I. N. et al. What is new in microcirculation and tissue oxygenation monitoring? //Journal of Clinical Monitoring and Computing. – 2022. – Т. 36. – №. 2. – С. 291-299.

2. Messina A., De Backer D., Cecconi M. Assessment of the Macro-and Microcirculation //Management of Dysregulated Immune Response in the Critically Ill. – Cham: Springer International Publishing, 2023. – С. 151-167.

3. Vasudevan V., Unni S. N. Skin microcirculatory responses: A potential marker for early diabetic neuropathy assessment using a low-cost portable diffuse optical spectrometry device //Journal of Biophotonics. – 2024. – Т. 17. – №. 3. – С. e202300335.

4. Scheeren T. W. L., Schober P., Schwarte L. A. Monitoring tissue oxygenation by near infrared spectroscopy (NIRS): background and current applications //Journal of clinical monitoring and computing. – 2012. – Т. 26. – С. 279-287.

5. Cohen D. J. F. Monte-Carlo Simulations of Near-infrared Light Propagation in the Adult Human Head. – 2019.

NELM – Multi-Purpose Software For Analysis Of High Resolution Bioimpedance Spectra

N A Boitcova, P M Dubina, A A Abelit, and D D Stupin
Alferov University, Khlopina 8/3, 194021 St. Petersburg, Russia
natab2002@yandex.ru, anna.abelit@gmail.com, Stu87@ya.ru

Abstract. Currently, bioimpedance spectroscopy (BIS) has become a powerful tool in practical medicine and experimental biology, despite the fact that in general it uses primitive raw data analysis methods, which is due to the lack of modern software for analyzing BIS data. At the same time, advanced data processing methods make it possible to expand the scope of BIS and the quality of information obtained with its help. Following this line in the current study, we developed the NELM software package for extensive BIS data analysis, including multi-algorithm complex nonlinear least squares fitting, and demonstrated the advantages of its use over standard interpretation of raw spectra.
Keywords: Impedance spectroscopy, metal electrolyte cell contact, CNLS, multielectrode array.
Funding: The study was supported by the Ministry of Education and Science of the Russian Federation (Project FSRM-2024-0001).

Introduction

Today, bio-impedance spectroscopy (BIS) has not only firmly entered the arsenal of experimental methods in biology and medicine, but has also become one of the most widely used tools for creating bioelectronic sensors [1-3]. At the same time, despite the increasing popularity of BIS, direct analysis methods are usually used to analyze the data obtained with its help (for example, Cell Index measurement [1]), which, due to the nonlinear nature of the impedance relative to frequency may not fully reflect those phenomena that occur in biological samples. Such a discrepancy between the wide spreading of BIS and the primitiveness of the data processing used for it can be explained by the lack of effective software that would allow, in a reasonable computer time, to compare impedance spectra with theoretical models or equivalent circuits using, for example, the nonlinear complex least squares method [4], and to investigate in this indirect manner various physical, chemical and biological effects in living systems. This problem is especially actual when analyzing spectra obtained with high frequency and time resolutions, that is, when processing highly informative data. In this paper we present the BIS multipurpose MatLab and GNU Octave based package called NELM, which allows to solve this problem.

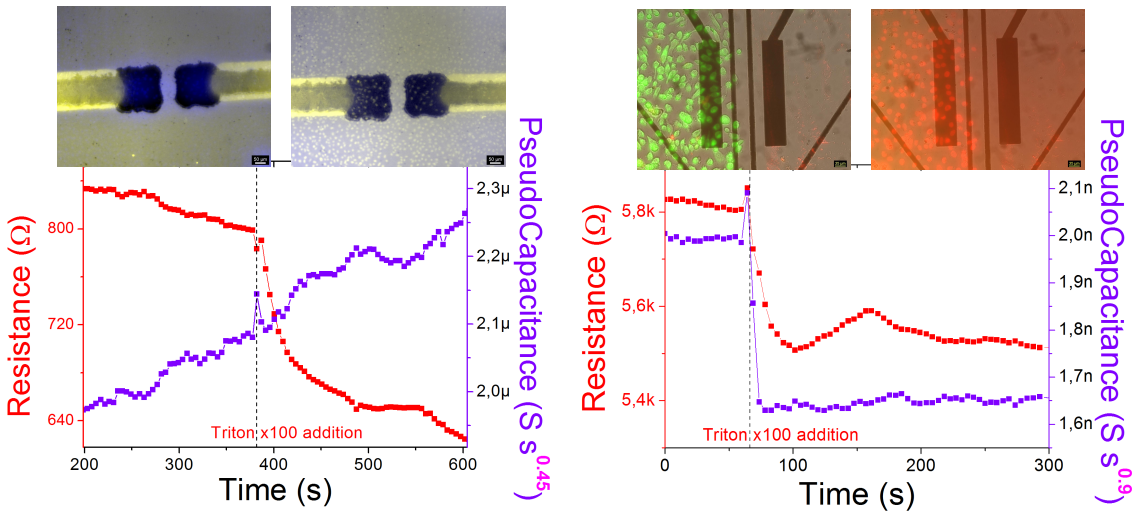


Fig. 1 The NELM fitting result of the application of Triton X100 solution on the electrical properties of the metal electrode contact (MEC). (a) Home-made MEA, (b) commercial MEA. From the data obtained it is clearly seen that the addition of a Triton X100 solution leads to a rapid exponential drop in the resistance of the MEC contact, however for homemade MEA pseudocapacitance stays intact, which is due to the high-porous structure of the electrode surface (CPE exponent equal 0.45). On the contrary, the pseudocapacitance of the commercial MEA varies significantly, which is due to its flat surface relative to the homemade sample (CPE exponent 0.9).

Materials and methods

The proposed software is written for MATLAB package and the freeware GNU OCTAVE. Since it is intended mainly to compare experimental spectra with theoretical ones, it uses more than 10 approximation algorithms (Nelder-Mead, Levenberg-Marquardt, Gauss-Newton, homotopy, etc.) and their combinations. To reduce computation time, NELM can be executed in parallel mode, including cloud computing. For approbation of our software, we have used homemade biocompatible Sn multielectrode array (MEA, 200×200 μm^2), 60StimMEA200/30-Ti MEA (MultiChannels Systems, Germany) multielectrode array and HeLa cells. As a model stimuli were used Triton X100 solution (detergent agent, Biolot, Russia). During the experiment, cells were seeded on multielectrode arrays, and then for their optical investigation was used Leica DM 4000 B microscope (Leica, Germany), homemade dye ABDS (green pseudocolor) and Hoechst (blue pseudocolor) dye (Sigma Aldrich, USA) dyes for living cells visualization and propidium iodide dye (red or yellow pseudocolor, Sigma Aldrich, USA) for dead cells visualization respectively. The impedance spectra we collected ones in 0.5 s with 2 Hz resolution in the band 10 Hz – 40 kHz using apparatus from Ref. [5].

Results and discussion

As a result, as seen on the Fig. 1, we were able to analyze the process of dying of HeLa cells on the microelectrodes under the influence of a Triton X100 solution. It can be seen that cell death for both MEAs leads to a rapid drop in MEC resistance, but the pseudocapacitance changes only for the commercial MEA, which has a flatter surface (CPE exponent value of 0.9) than our homemade MEA (CPE exponent is 0.45). Thus, by using NELM, we not only can study electrocytological effects, but we can also suggest an optimal strategy for using MEA, namely: commercial MEA is useful for multi-parameter cell studies but requires a CNLS approach, while homemade MEA is useful for studying purely resistive effects with using a simple Cell Index measurement.

Conclusion

In this work, we created and tested NELM software based on the MATLAB application package, which allows us to solve the problem of processing highly informative data thanks to the use of parallel computing technology. This computational technology allows us to simultaneously study physicochemical phenomena, that occur in the MEC contact and separate them by their nature. This development opens up new prospects in biosensor engineering, healthcare research, and practical cytology.

Acknowledgements

Author express their gratitude Knyazev N.A., Kornev A.A., Kazantsev V.B., Blinova M.I, Kraevskaya A.A, Fedorova I.S., Yakovleva L.E. and Dubina M.V. for comprehensive assistance and support.

REFERENCES

1. **Stupin, Daniil D., Ekaterina A. Kuzina, Anna A. Abelit, Anton K. Emelyanov, Dmitrii M. Nikolaev, Mikhail N. Ryazantsev, Sergei V. Koniakhin, and Michael V. Dubina**, Bioimpedance spectroscopy: basics and applications, ACS Biomaterials Science & Engineering 7, no. 6 (2021): 1962-1986.

2. **Liu, Qingjun, Chunsheng Wu, Hua Cai, Ning Hu, Jun Zhou, and Ping Wang**, Cell-based biosensors and their application in biomedicine, Chemical reviews 114, no. 12 (2014): 6423-6461.

3. **Jiang, Wen G.**, ed., Electric cell-substrate impedance sensing and cancer metastasis, Vol. 17. Springer Science & Business Media, 2012.

4. **Macdonald, J. Ross, J. Schoonman, and A. P. Lehnen**, Applicability and power of complex nonlinear least squares for the analysis of impedance and admittance data, Journal of Electroanalytical Chemistry and Interfacial Electrochemistry 131 (1982): 77-95.

5. **Stupin, Daniil D. and Koniakhin, Sergei V. and Verlov, Nikolay A. and Dubina, Michael V.**, Adaptive Filtering to Enhance Noise Immunity of Impedance and Admittance Spectroscopy: Comparison with Fourier Transformation, Vol.7, 2017.

Express kidney monitoring method for early detection of kidney damage

D. V. Vakorina [1]✉, G. V. Stepanenkov[1] and V. V. Davydov[1, 2]

[1]The Bonch-Bruevich Saint Petersburg State University of Telecommunications, Saint Petersburg, Russia.

[2]Peter the Great Saint-Petersburg Polytechnic University, Saint Petersburg, Russia

✉cementary.ley@gmail.com

Abstract. The necessity of determining kidney damage at an early stage using fast and reliable express methods was substantiated. A method based on refractometric measurements of refractive index at three wavelengths with grading of refractive indices to the values of three basic parameters (osmolarity, amount of solids, density) was proposed for express analysis of kidney damage control. Additionally, the sizes of protein compounds were investigated and their sizes were also graded to refractive indices. The advantages of using the refractometer design at three wavelengths over other methods were noted. The peculiarities of measuring the refractive index of biological liquids on the example of urine are established. The results of the study of various samples and their analysis are presented. The comparison of the obtained results with the results of measurements in clinical diagnostics is carried out.

Keywords: kidney damage, laser radiation, wavelength, refractive index, express control, health condition.

Introduction

In the modern world kidney disease after cardiovascular diseases comes second place in people as the main cause of death. The Russian Federation is not an exception. Factors that now in the world affect the increase in the number of cases of kidney disease with the formation of stones of various sizes in them in people are quite a lot. They begin with the environment, improper nutrition due to overload at work, high levels of stress and others. Many people do not notice the beginning of kidney damage and stone formation at the primary stage of the disease. A person at this time can feel good and be able to work, temporarily arising malaise people associate with other causes. Studies conducted by doctors have shown that the earlier the kidney lesion is detected, the more effective and successful will be the course of treatment. The probability of recovery of almost all kidney functions increases with the stage at which kidney damage is detected (early stage is the highest probability). In this situation, rapid, affordable and reliable methods of rapid monitoring of kidney damage detection, especially at an early stage, are essential.

Rapid Diagnostic Methods and Problems

Currently, various methods of express control have been developed. The most widely used of the most accessible are test strips, urometer, urine analyzer. Various studies have shown that these methods do not allow you to detect the disease at an early stage. Only in the clinic can be reliably done. In my work, a new and affordable method of diagnosing kidney disease at an early stage is proposed, which is related to express control of urine based on refractometric measurements, which are highly accurate (the error of measuring the refractive index of urine is $5*10^{-5}$).

I have analyzed various studies related to the detection of early-stage renal damage. The results showed that at this stage of the disease, the greatest changes occur in the following three urine parameters (osmolarity - O_s, the presence (N_b concentration) of solids in it and the size of protein compounds - D_b, as well as (urine density ρ_m)). It is proposed to relate changes in the values of these three or four parameters to changes in the refractive index of urine. For this purpose, it is necessary to realize measurements of the refractive index of urine at three wavelengths: λ_1 = 436.4 nm, λ_2 = 589.3 nm, λ_3 = 657.2 nm (standard composition of wavelengths for a wave refractometer, the principle of operation of which is based on total internal reflection). To use the four parameters, it is necessary to perform measurements at four wavelengths.

And perform graduations of the change of O_s, N_b, D_b and ρ_m values from the change of refractive index values $n_{\lambda 1}$, $n_{\lambda 2}$, $n_{\lambda 3}$ and $n_{\lambda 4}$ in urine samples at different temperatures T (unknown in further three-four components, three-four equations (graduations) for each length of laser radiation (eventually 9-12 graduation curves). The reliability of the results increases with

increasing number of measurements at different wavelengths. Therefore, in the new refractometer design developed in the future it will be necessary to use another wavelength λ_4 = 505.3 nm (green radiation). The reliability of the measurements will increase further.

In the initial stages of preparation for the study, the creation of model solutions was proposed, an important aspect of which is to analyze the biophysical properties of samples with known composition. With the help of model solutions, theoretical indices of kidney condition determination will be established, so samples were prepared to consider 3 different cases: 1. A healthy person, 2. A person with diabetes mellitus and onset of kidney disease, 3. A person with critical stage of kidney disease. For further refractometer measurements, urine samples were collected from people whose health conditions reflected the prepared model solutions. The results of the study of two groups of people for kidney damage were presented. In the first group, a volunteer with healthy kidneys undergoing medical examination (Pavlova). In the second group the rest of the experimental participants (Ivanov and Kendev) with profound changes in kidneys. The data are summarized in Table 1.

Table 1: Basic urine parameters in people with different states of kidney disease.

Sample	Refractive index at 3 values of λ			Urine Osmotic Pressure	Urine Specific Gravity	Urine Total Solids
	436,4 nm	589,3 nm	657,2 nm	mOsm/l	g/ml	% vol
Ivanov	1,349653	1,342072	1,340126	1047	1,0263	5,94
Pavlova	1,351017	1,343340	1,341395	1184	1,0300	6,73
Kendev	1,347952	1,340456	1,338511	872	1,0215	4,91
sample №1	1,344454	1,337078	1,335164	504	1,0112	2,72
sample №2	1,345145	1,337816	1,335920	584	1,0135	3,20
sample №3	1,342265	1,335003	1,333116	276	1,0047	1,34

Conclusion

As a result of the analysis, a number of human urine parameters have been determined that can be used for early detection of kidney diseases during express urine control. A new express method of human urine control based on refractometric measurements of refractive index nm at different wavelengths was developed. The comparison of the obtained data on the change of total solids, specific gravity (density), osmolarity and size of proteins from the measured refractive index values with the data of model solutions of human urine simulating kidney lesions of different stages was carried out. Coincidence of the results within the measurement error was obtained.

REFERENCES

1. **R. Davydov, A. Zaitceva, D. Isakova, and M. Mazing,** "New Methodology of Human Health Express Diagnostics Based on Pulse Wave Measurements and Occlusion Test," Journal of Personalized Medicine, vol. 13(3), pp. 443, March 2023.
2. **N. M. Grebenikova, V. V. Davydov, and K. J. Smirnov,** "Features of optical signals processing for monitoring the state of the flowing liquid medium with a refractometer," *Journal of Physics: Conference Series*, vol. 1368(2), pp. 022057, September 2019.
3. **V. Davydov, I. Gureeva, R. Davydov, and V. Dudkin,** "Flowing Refractometer for Feed Water State Control in the Second Loop of Nuclear Reactor," Energies, vol. 15(2), pp. 457, March 2022.

INTEGRATED APPLICATION OF CALCIUM IMAGING AND ELECTROPHYSIOLOGICAL RECORDING OF NEURONAL ACTIVITY *IN VIVO*

E. K. Vinokurov [1✉], **A. I. Erofeev** [1✉], **O. L. Vlasova** [1], **I. B. Bezprozvanny**[1,2]

[1] Peter the Great St. Petersburg Polytechnic University, St. Petersburg, Russian Federation;

[2] University of Texas Southwestern Medical Center, Dallas, United States of America

✉eg.vinokurov@yandex.ru, alexandr.erofeew@spbstu.ru

Abstract. The exploration and understanding of brain function principles, both from a fundamental and applied perspective, stand as a paramount domain within contemporary scientific inquiry. In this field, special attention is paid to *in vivo* techniques that are essential for the lifetime observation of dynamics in complex neural networks that play an important role in the implementation of highly organized brain functions and are involved in shaping both mental and physical human experience. Despite advancements garnered through *in vitro* and *ex vivo* approaches, a considerable knowledge gap persists, primarily due to the inherent limitations of these methods. Consequently, *in vivo* examination of brain functionality is increasingly recognized as a pivotal challenge within neurobiology and neurodegenerative disease research, underscoring the demand for intricate approaches to decipher the intricacies of neural interplay.

Keywords: microelectrode, Wireless Electrophysiology System, miniscope.

Funding: This study was funded by the Russian Science Foundation grant number 22-75-00028 (A.I.E.).

Introduction

In the context of current neurobiological research, the detailed recording of neuronal activity using *in vivo* electrophysiological experiments as well as lifetime calcium imaging is of particular interest. These investigations, encompassing the study of neuronal interconnections to the evaluation of local field potentials, are crucial for deepening our comprehension of cognitive, sensory, and motor processes. Furthermore, they hold significant potential in the research of neurodegenerative conditions like Alzheimer's disease by enabling the observation of neural dynamics alterations in animal models. Such methodologies not only shed light on the pathophysiological mechanisms of these disorders but also pave the path toward identifying new therapeutic avenues. In our research, we have integrated lifetime calcium imaging techniques via a single-photon miniature fluorescence microscope (miniscope) with wireless electrophysiological recordings of neuronal activity.

Contemporary sensors, like GCaMP, which produce fluorescence upon variations in calcium ion levels [1], serve to render neuronal activity observable in living organisms. Termed calcium imaging, this technique facilitates the observation of extensive neuronal populations within freely ambulatory lab animals. Nevertheless, the capacity to record action potentials is constrained by the temporal responsiveness of the calcium sensor, indicating that *in vivo* calcium imaging cannot fully capture the entire neuronal network. Incorporating electrophysiological measurements into this methodology presents a strategy to overcome this restriction, offering a more comprehensive insight into neuronal behavior.

Results and Discussion

Conducting electrophysiological research in living organisms necessitates the utilization of sophisticated apparatus, encompassing electrode arrays and systems for data collection. Leaders in the industry present proprietary systems that are straightforward to use but come with elevated prices and components that lack flexibility. Alternatively, open-source options provide economical and modifiable solutions. Previously, our team developed a 32-channel open-source electrophysiology system including a wireless (2.4 GHz radio channel) wearable module and base charging station for data management, as well as a visualization application [2]. Subsequently, an enhanced iteration of this cordless technology was created, enabling a direct linkage to computers

via Bluetooth 5.4 [3]. This version integrates data processing capabilities within a microchip mounted on a singular printed circuit board, facilitating reductions in both production expenses and energy demands. Concurrently, this iteration is characterized by a diminished weight of 0.95 grams and extended operational duration. Moreover, it features a variable sampling rate ranging from 62 to 1000 Hz.

To realize the study, a microelectrode combined with a gradient lens designed for calcium imaging was also developed. This microelectrode is a three-layer rectangular structure consisting of a polyimide film and thermoformed contact-conducting gold tracks. On one side of the film there are 12 open conductive contacts for registering local field potentials, and on the other side there is a similar number of conductive tracks for connecting a connector that transmits data to the processing board of the wireless complex.

For this work, wild-type mice of the B6SJL line were taken, and at the age of 5 months they were injected with GCaMP6f sensor virus. After 3 weeks, implantation of a gradient lens combined with a microelectrode was performed. After another 3 weeks, a method combination experiment was performed. Calcium imaging was performed using a miniscope (Fig 1B), and neuronal activity was simultaneously recorded using a wireless electrophysiological complex (Fig. 1A).

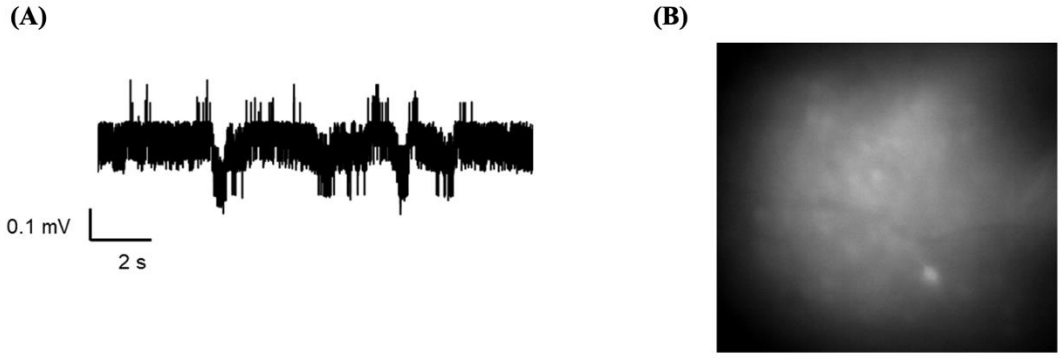


Fig. 1. (A) Example of unfiltered recording of local field potentials at a sampling rate of 1000 Hz. (B) GCaMP6f fluorescence during the experiment

Conclusion

The aim of our further work will be to analyze the activity of hippocampal neurons on the basis of miniature fluorescence microscopy data and parallel registration of local field potentials in laboratory mice of wild type and with a model of Alzheimer's disease (5xFAD line) when assessing conditioned reflex freezing. This approach will allow us to investigate neurodegenerative disorders at the level of neural networks.

Acknowledgments

We are grateful to Anastasia Bolshakova for administrative assistance and to members of Laboratory of Molecular Neurodegeneration.

REFERENCES

1. **Erofeev A., Vinokurov E., Vlasova O., and Bezprozvanny I.,** GCaMP, a Family of SingleFluorophore Genetically Encoded Calcium Indicators, Journal of Evolutionary Biochemistry and Physiology. 59, No. 4 (2023) 1195–1214.
2. **Erofeev A., Kazakov D., Makarevich N., Bolshakova A., Gerasimov E., Nekrasov A., Kazakin A., Komarevtsev I., Bolsunovskaja M., Bezprozvanny I.,** An Open-Source Wireless Electrophysiological Complex for In Vivo Recording Neuronal Activity in the Rodent's Brain, Sensors 21 (2021) 7189.
3. **Erofeev A., Antifeev I., Vinokurov E., Bezprozvanny I. and Vlasova O.,** An Open-Source Wireless Electrophysiology System for In Vivo Neuronal Activity Recording in the Rodent Brain: 2.0, Sensors 23 (2023) 9735.

Dorsal skinfold chamber adaptation for optimal microscopy studies

A. A. Vlasov [1✉], **M. E. Stepanov** [1], **P. A. Demina** [1,2,3], **R. A. Akasov** [1,2,3], **G. Babayeva** [4], **A. N. Generalova** [1,2,3], **E. V. Khaydukov** [1,2,3]

[1] Moscow State Pedagogical University, Moscow, Russia;

[2] FSRC «Crystallography and Photonics» RAS, Moscow, Russia

[3] Shemyakin-Ovchinnikov Institute of Bioorganic Chemistry RAS, Moscow, Russia

[4] Research Institute of Molecular and Cellular Medicine, RUDN University, Moscow, Russia

✉aa.vlasov@mpgu.su

Abstract. Dorsal skinfold chamber is a method of intravital microscopy that allows to conduct research on number of topics including inflammation and angiogenesis processes in rodent species. It is a very promising model for long-term preclinical studies of cancer therapy and biocompatible materials. However dorsal skinfold chamber has some limitations, such as early contamination and inflammation. In this work we tried to avoid those limitations by modifying dorsal skinfold chamber with siloxane covered glass.

Keywords: intravital microscopy, dorsal skinfold chamber.

Funding: The study was prepared as part of the work on the topic «Laser technologies for biomedical applications» (№ 122122600055-2) under the state order of the Ministry of Education of the Russian Federation.

Introduction

The dorsal skinfold chamber is a model for intravital microscopy that has been broadly used for inflammation [1], microcirculation, ischaemia, tissue transplantation [2] and tumor growth [3] research. While other models used for intravital microscopy allow these studies for a short period of time, dorsal skinfold chamber can be used for longer observation period of 3-4 weeks.

The chamber consists of 2 identical parts made of titan [4] or polymer [5], each part has orifices for sutures and 10-15 mm cover glass. The preparation method for dorsal skinfold depends on the purpose of research, the most common way of preparation was described in [6]. Briefly, it includes steps of hair removal with subsequent skin layers (epidermis, dermis and subcutaneous tissue) resection in order to expose underlying muscle and it's blood vessels.

After the preparation of dorsal chamber is done it can be exploited to study the process of interest using transillumination microscopy or epi-illumination fluorescence microscopy. Transillumination microscopy allows analysis of vessel diameter and functional vessel density, while fluorescence microscopy is used for studying distinct cellular or molecular aspects.

Here we report our first experience of using dorsal skinfold chamber model. Several issues appeared, one of them being the possibility of early contamination and inflammation of dorsal chamber space, which leads to subsequent granulation of the tissue leading in tern to decreased resolution due to the light scattering. Also, we have found that this method is very sensitive to surgery conditions and completeness of the operation, which depends on surgeon experience, leading in some cases to low resolution because of residual subcutaneous adipose tissue. Here we discuss the abovementioned issues and suggest some solutions.

Materials and Methods

To study the issues three BALB/c mice 8 weeks old were used. For anesthesia, animals were injected with 20-40 mg/kg xylazine intramuscularly and 5-10 mg/kg Zoletil intraperitoneally. Then the fur was removed from the dorsal area using trimmer and a line was drawn along the mouse's spine. A standard set of surgical instruments and USP 5 Daclon thread were used for the operation. After this self-engineered polycarbonate chamber was implanted. Skin was removed using forceps and scalpel. Then different combination of windows was used as cover glass:

1) both sides covered with glass coated with siloxane;

2) one side (without skin) was covered with glass, and other side with siloxane-glass;
3) both sides covered with glass.

Two days after operation mice were examined using the fluorescent microscope Motic AE31E. White Halogen illumination (Koehler setup) was used to perform brightfield studies, in some cases we've used bandpass filters to restrict the spectral range Detected with Raptor Photonics Camera (digital FALCON EMCCD FA285-CL). In each case the objectives were lifted using special spacers to compensate for the lifting of the DSC window above the height of microscope table.

Results and Discussion

Brightfield studies has shown that covering glass with siloxane can reduce apparent inflammation level and tissue granulation, especially when siloxane-covered glass remains only on intact skin side. It can be explained by the reduction of the gap between exposed muscle and cover glass with simultaneous contribution in sealing of the chamber space.

Surgical operation was adapted to gain better resolution by choosing appropriate resection depth (controlling subcutaneous tissue remains).

Conclusion

In present work dorsal skinfold chamber was adapted by modifying the cover glass with siloxane layer. The post-operation area was shown to contain no granulation signs soon after operation which can be explained by decrease of inflammation level. Additional studies based on gathered experience are now planned to be done to improve the process of dorsal skinfold chamber preparation.

REFERENCES

1. **Hillgruber C, Steingräber AK, Pöppelmann B, Denis CV, Ware J, Vestweber D, Nieswandt B, Schneider SW, Goerge T.** Blocking von Willebrand factor for treatment of cutaneous inflammation. J Invest Dermatol. 2014 Jan;134(1):77-86. doi: 10.1038/jid.2013.292. Epub 2013 Jun 28. PMID: 23812299.
2. **Später T, Menger MM, Nickels RM, Menger MD, Laschke MW**. Macrophages promote network formation and maturation of transplanted adipose tissue-derived microvascular fragments. J Tissue Eng. 2020 Apr 9;11:2041731420911816. doi: 10.1177/2041731420911816. PMID: 32313616; PMCID: PMC7153185.
3. **Seynhaeve ALB, Ten Hagen TLM**. Intravital Microscopy of Tumor-associated Vasculature Using Advanced Dorsal Skinfold Window Chambers on Transgenic Fluorescent Mice. J Vis Exp. 2018 Jan 19;(131):55115. doi: 10.3791/55115. PMID: 29443052; PMCID: PMC5908657.
4. **Laschke MW, Menger MD**. The dorsal skinfold chamber: A versatile tool for preclinical research in tissue engineering and regenerative medicine. Eur Cell Mater. 2016 Sep 20;32:202-15. doi: 10.22203/eCM.v032a13. PMID: 27646143.
5. **Xie W, Lorenz M, Poosch F, Palme R, Zechner D, Vollmar B, Grambow E, Strüder D**. 3D-printed lightweight dorsal skin fold chambers from PEEK reduce chamber-related animal distress. Sci Rep. 2022 Jul 8;12(1):11599. doi: 10.1038/s41598-022-13924-5. PMID: 35803979; PMCID: PMC9270450.

Structure and properties of small gold clusters labeled by actinium

Yu.A. Demidov[✉]
St. Petersburg School of Physics, Mathematics, and Computer Science,
HSE University, St. Petersburg, Russia
[✉]iurii.demidov@gmail.com

Abstract. Theoretical calculations show that the Ac_2Au_6 cluster has highly symmetrical D6h structures with the Ac-Ac axis equatorially coordinated by the Au6 ring. The unusually short Ac-Ac bond length in $Ac_2@Au_6$ suggests that the Au6 ring may serve as a bridging ligand to facilitate multiple binding in transition metal dimers via delocalized σ bonding. This may be useful in the development of new radiopharmaceuticals.

Keywords: Actinium-225, labeled gold clusters, relativistic density functional theory.

Funding: The research was supported by the Russian Science Foundation Grant No. 21-42-04411.

Introduction

Actinium-225 as the alpha-particle-emitter is of considerable interest for radioimmunotherapy applications. Ac-labeled biomolecules are unparalleled cytotoxicity when targeted to cancer and their relative lack of toxicity towards normal tissue. Broad application of ^{225}At in radiotherapy will require its attachment to disease-targeting carrier molecules. The nature and stability of Ac attachment in compounds with biomolecules is the focus recent experimental investigations (see e.g. Ref. [1] for review). In particular, actinium can be conjugated with biomolecules using gold nanoparticles [2].

The use of Ac-labeled small gold clusters for targeted radiotherapy is attractive as they can distribute and localize to diseased areas very rapidly, matching the pharmacokinetics of the targeting agent with the short half-life of ^{225}Ac. Due to the quantities required by standard spectroscopic tools, they are unsuitable to obtain structural information on actinium compounds; “direct” identification of these compounds is therefore practically impossible. Molecular modeling is thus of crucial interest to help in identifying actinium species.

Methods of Calculations

Relativistic effects can be as important as the electron correlation and can largely influence the properties of actinium compounds. The information on the bonding type is essential to sharpen up our chemical intuition on the actinium chemistry, that is, on the reactivity and the properties of its basic chemical forms. Computational studies are thus particularly indicated to guide the design of new labeled molecules for nuclear medicine.

The neutral Au6 cluster consists of a triangular situated atoms. Whereas Au6− cluster form ring. We here call attention to systems, where an Ac atoms, is put inside a coinage gold ring.

The calculations were performed within the two-component shape-consistent small-core pseudopotential model and employed the non-collinear version of relativistic density functional theory to treat electronic correlations [3].

Results and Discussion

The optimized structure for the global minima of $Ac_2@Au_6$ cluster at the RDFT/ PBE0 level is shown in Fig. 1. The $Ac_2@Au_6$ possess D_{6h} symmetry featuring an Au_6 ring building around the Ac – Ac axis. The Ac – Ac bond length in $Ac_2@Au_6$ cluster is 3.49 Å. This value is much shorter than the calculated bond length of 3.71 Å in gaseous Ac_2 molecule. Thus, the Au6 ring acts as a bridging ligand and provides a new strategy to facilitate stronger multiple bonding in early actinide dimers.

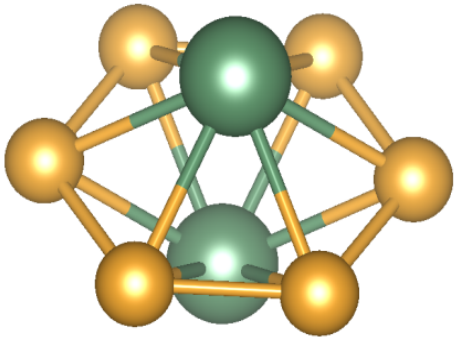


Fig. 1. The optimized structures for the global minimum D_{6h} $Ac_2@Au_6$ at the PBE0/RDFT level

Conclusion

In summary, we report the observation of highly symmetric $Ac_2@Au_6$ molecular wheels, in which an extremely short Ac - Ac bond length is coordinated equatorially by an Au_6 ring and stabilized by σ aromaticity. The energy gap between its highest occupied (HOMO) and lowest unoccupied molecular orbitals (LUMO) equal 0.33 eV. The Au_6 ring acts as a novel bridging ligand, providing a new strategy to facilitate stronger multiple bonding in early actinide dimers. A whole class of $M_2@Au_6$ type molecular wheels containing a strengthened M – M multiple bond may be possible.

Acknowledgments

We thank Prof. C. van Wüllen for providing the relativistic DFT code. The work is partially supported by RSF grant № 21-42-04411.

REFERENCES

1. **Thiele N. A., Wilson J. J.**, Actinium-225 for targeted α therapy: coordination chemistry and current chelation approaches, Cancer biotherapy & radiopharmaceuticals, Vol. 33, P. 336-348 (2018).

2. **McLaughlin M. F. et al.**, Gold coated lanthanide phosphate nanoparticles for targeted alpha generator radiotherapy, PLoS One, V. 8, P. e54531 (2013).

3. **van Wüllen C.**, A quasirelativistic two-component density functional and Hartree-Fock program, Zeitschrift für Physikalische Chemie, V. 224, P. 413 – 426 (2010).

Application of the convolutional neural network AlexNet in the problem of classification of electrocardiosignals obtained by ultra-high resolution electrocardiography method

K. V. Zaichenko[1], **A. S. Afanasenko**[1,2], **E. A. Denisova**[1✉], **D. O. Sevakov**[1,2]

[1] Institute for analytical instrumentation Russian academy of sciences, Saint-Petersburg, Russia;
[2] Saint-Petersburg State University of Aerospace Instrumentation, Saint-Petersburg, Russia
✉tiranderel@yandex.ru

Abstract. Coronary heart disease is the most common cause of death in humans. However, existing electrocardiography (ECG) methods do not allow to obtain all information about the stages of pathology development due to insufficient broadband. In this regard, a new author's technique of ultra-high resolution electrocardiography (UHR ECG) is being developed to identify pathological changes in the cardiovascular system in the areas of processing electrocardiosignals (ECS), which are considered artifacts. However, the expansion of the amplitude and frequency range leads to the fact that many standard methods of ECS analysis are ineffective when applied to UHR ECS. This article demonstrates the effectiveness of using the fifteen-layer convolutional neural network (CNN) AlexNet in the task of classifying ECS obtained by the UHR ECS method. A large-scale set of labeled ECG recordings for clinical and prognostic studies obtained by the ECG UHR method from Vistar series experimental rats during experiments on modeling acute myocardial ischemia was used for training and testing of CNN.

Keywords: Electrocardiogram, convolutional neural network, classifying, ultra-high resolution electrocardiography, AlexNet, Keras, coronary heart disease, ishemia.

Funding: The work has been supported by Education and Science Ministry of Russian Federation, State task No. 075-01157-23-00, project No. FZZM-2023-0011.

Introduction

Coronary heart disease (CHD) is the most common cause of death in humans [1]. Existing electrocardiography (ECG) methods do not allow to obtain all information about the stages of pathology development due to insufficient broadband. In this regard, a new author's technique of ultra-high resolution electrocardiography (UHR ECG) is being developed to identify pathological changes in the cardiovascular system in the areas of processing electrocardiosignals (ECS), which are considered artifacts [2]. However, the expansion of the amplitude and frequency range of ECG registration leads to the fact that many standard methods of ECG analysis are ineffective when applied to UHR ECS. Neural networks have the potential to solve the problem of classification of UHR ECG. This article demonstrates the effectiveness of using the fifteen-layer convolutional neural network (CNN) AlexNet in the task of classifying ECS obtained by the UHR ECG method [3]. The Keras high-level API was used to build and train a neural network. For the training and testing of CNN, a large-scale set of ECG recordings with labeling for clinical and prognostic studies obtained by the UHR ECG method from experimental rats of the Vistar series during experiments on modeling acute myocardial ischemia at the Institute of Experimental Medicine of the Almazov National Research Medical University was used [3].

Materials and Methods

The aim of the training was to classify the morphology of the UHR ECS fragment as characteristic of the stabilization, ischemia, or reperfusion stage. The task was also complicated by the fact that the dataset contains fragments of records corresponding to the transitional stages between the various stages of the experiment. To train and test the model, a dataset consisting of 20 ECG recordings was collected. The total duration of the recordings was 22 hours and 13 minutes. The data were obtained during experiments on experimental animals (rats), that is, the heart rate is 420 beats per minute [4]. To evaluate the effectiveness of the developed model, three datasets were prepared, the first of which contains records of UHR ECS obtained from the low-frequency (LF) channel of signal registration, the second from the high-frequency (HF) channel, and the third is a set of spectra of signal fragments from the HF-channel. According to the study [2], it is the change in the shape of the spectrum of the signal from the HF-channel that is a marker

of the onset of CHD. The dataset was divided into training and test samples. The training sample contains 98% of the data. The test sample consists of the remaining 2% of the dataset, and it was used to set up hyperparameters. As a preprocessing, the UHR ECS records were filtered according to the algorithm described in [5]. In addition, each signal was divided into sections with a duration of 1 second (6250 samples).

Results and Discussion

The values of the accuracy and loss parameters for the training and test samples are shown in Table 1, where *Lf* is the dataset consisting of fragments of the signals from the LF-channel, *Hf* is the dataset consisting of fragments of the signals from the HF-channel, *Hz* is the dataset consisting of spectrums of fragments of the signals from the HF-channel.

Table 1

Parameters for evaluating the effectiveness of the model.

Type of dataset	loss	accuracy	test_loss	test_accuracy
Lf	0.1257	0.9524	0.1822	0.9373
Hf	0.0667	0.9781	0.1703	0.9583
Hz	0.1257	0.9592	0.2211	0.9340

The prediction of CNN AlexNet, trained on a dataset containing the UHR ECS from the HF-signal registration channel, is the most accurate. In addition, when using the AlexNet model to classify the UHR ECG, it is possible to determine the onset of ischemia on average 45 seconds earlier than the doctor will do. However, the use of a dataset containing spectra of signal fragments from the HF-channel of the UHR ECS registration makes it possible to determine the onset of ischemia 10 seconds earlier than when training CNN on data from the LF-channel. The results obtained confirm the hypothesis described in [2].

Conclusion

The use of CNN makes it possible to detect ECG abnormalities characteristic of CHD much earlier than a cardiologist can do. At the same time, using the UHRECG method allows you to do this on average 10 seconds earlier than using the standard ECG method. CNN can analyze large amounts of data and identify pathological changes that could go unnoticed during visual analysis. However, the introduction of neural networks into medical practice requires careful validation and ensuring their safety and reliability, since any error in diagnosis can have serious consequences for the patient.

REFERENCES

1. World Health Organization. URL: https://www.who.int/news-room/fact-sheets/detail/the-top-10-causes-of-death.html. Accessed March 25, 2024.

2. **Zaichenko K.V., Kordyukova A.A., Logachev E.P., Luchkova M.N**., Application of Radar Techniques of Signal Processing for Ultra-High Resolution Electrocardiography. Biomedical Engineering. 2019. Vol. 55(1), pp. 31–35.

3. **Aarthy S.T., Mazher Iqbal J.L.,** Modified parametric-based AlexNet structure to classify ECG signals for cardiovascular diseases. Measurement: Sensors. 2023. Vol. 27 (2023) 100816.

4. **Zaichenko K.V., Zhmyleva A.A., Khrapov S.O., Logachev E.P., Gurevich B.S.,** Application of modern technologies in new ultra-high resolution electrocardiography method. IEEE Xplore library. 2020, pp. 0004–0007.

5. **Zaichenko K.V., Afanasenko A.S., Kordyukova A.A., Denisova E.A., Sevakov D.O.,** Development of an algorithm for preprocessing ultra-high resolution electrocardiosignals. St. Petersburg Polytechnic University Journal. Physics and Mathematics. 2023. Vol. 16. No. 3.2, pp. 307–311.

MICROLITHOGRAPHY TECHNOLOGY USING BIOLABORATORY EQUIPMENT FOR MULTIELECTRODE ARRAYS FABRICATION

P. M. Dubina, N. A. Boitsova, A. A. Abelit, and D. D. Stupin
Alferov University, Khlopina 8/3, 194021 St. Petersburg, Russia
filipp.dubina@gmail.com, Stu87@ya.ru

Abstract. Nowadays, a significant scientific efforts in the field of bioelectronics focuse on integrating cells with electronic components to develop biosensors and bioelectronic devices, which hold promise for addressing critical issues in healthcare, biology, and biosensing. For stimulating progress in this area in this paper we have introduce a microlithography technology – a pivotal process for fabricating bioelectronic devices – that exclusively relies on standard equipment found in biological laboratories and commercially available in electronic-components stores reagents. Using our technology, we have successfully fabricated microstructures with resolutions ranging from 10 to 100 μm and based on them 100 μ-bioelectrodes sufficient for applications such as bioimpedance detection or vision prosthetic implants.
Keywords: lithography, bioelectrodes, confocal microscopy.
Funding: The study was supported by the Ministry of Education and Science of the Russian Federation (Project FSRM-2024-0001).

Introduction

The pivotal stage in microelectronic manufacturing, especially concerning bioelectronic devices, revolves around structuring patterns with specific topologies on a substrate [1]. Photolithography stands out as a prevalent technique for addressing this challenge [2]. However, conventional lithography apparatuses are often costly and unsuitable for deployment within bio-laboratory environments. In contemporary bio-laboratories, the integration of a fluorescent microscope featuring a UV-pumping lamp and motorized stage has become ubiquitous. Remarkably, these instruments have minimal technical distinctions from scanning lithographers. Furthermore, they are often complete with supplementary hardware for precisely positioning samples and software for automating sample manipulations and adjusting lighting parameters. Consequently, they offer a viable platform for conducting lithography processes directly within bio-application laboratories [3]. Using this concept, we have introduced a novel paradigm for repurposing a fluorescence microscope into a lithographer machine for fabricating bioelectronic devices.

Materials and methods

As an apparatus for providing lithography, we have used the Zeiss Observer.Z1 confocal microscope (Zeiss, Germany) equipped with a metal halide illuminator HXP 120 (LEj JENA GmbH, Germany) and motorized XY stage. Thin film deposition was improved by pre-dissolving it in ethanol in a mass ratio of 1:1.7 and spin coating it for two minutes on copper-coated textolite sheets 12x24mm. The defects were never possible to fully eliminate, but this technique allowed us to significantly reduce the film thickness from several hundred to almost 10 μm. The lithographic pattern of the bioelectrodes was obtained moving sample relative UV-beam using microscope motorized stage. Further the sample was baked at a temperature of 100°C degrees and then non-exposured resist was soluted by sodium carbonate aqueous solution (1.6 mg/ml), after which the copper was etched from the sample with a 20% aqueous solution of ferric chloride. For providing biocompatibility the resulting electrodes profile was subjected to electrolysis in a aqueous solution of tin chloride ($SnCl_2$, 50 mg/ml, Sigma Aldrich, USA). The conductive tracks of the electrodes were additionally insulated with AQUA MER ME720 resist, similar to the fabrication of the bioelectrode pattern.

Results and Discussion

The obtained results are presented in Fig. 1. As can be seen, the proposed technology allows us to create 2D-electrodic arrays with resolution from 10 to 100 μm, which satisfies the requirements for electrodes in bioelectronic devices in studies of single cells and their populations and in prosthetic care [1,4].

Conclusion

In this research, we have developed a technology that allows micro-bioelectrodes fabrication using readily available equipment suitable for biology laboratories. Our results show that the use of modern confocal microscopes allows us to create microstructures with resolution down to 10 μm while maintaining a cost-effective approach. This highlights the potential of our method to advance the development of bioelectronic devices and expand their use in various fields of life, science, and industry. We expect that the results of our research will catalyze advances in bioelectronics, helping to solve pressing problems in health care, ecology, pharmacology, and cell research.

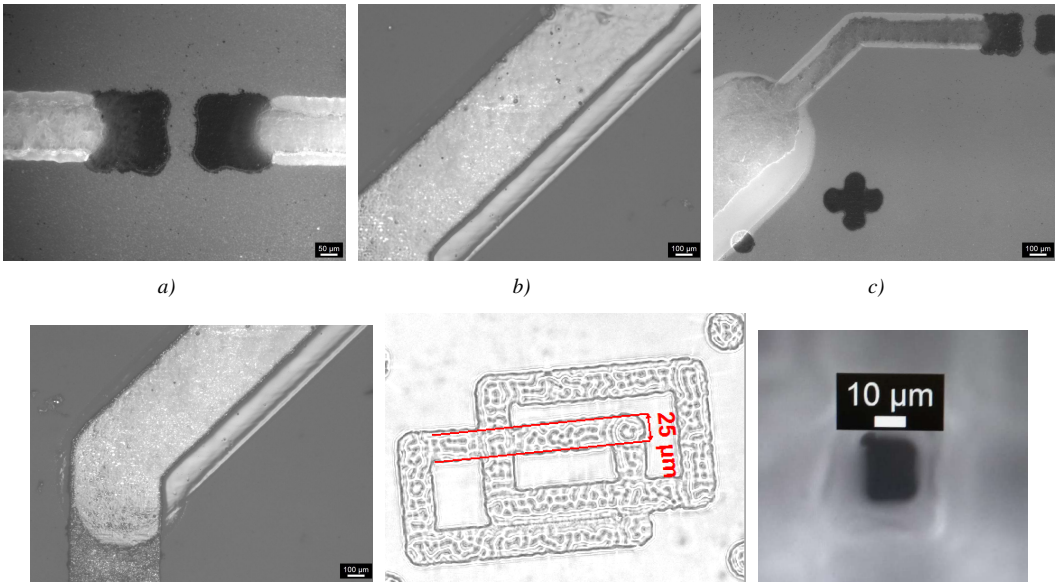


Fig. 1. Resulting structures and resolution tests. (a) Electrode pads, (b) Conductive path, (c) Conductive paths along the transition to the external electronics attachment and indicator (cross) for the exposure-control software for mask alignment; (d) End of the conductive path with dielectric coat and beginning of the conductive track to external electronics; (e) Path resolution test; (f) Single pit resolution test.

Acknowledgements

Author express their gratitude Lihachev A.I., Kotlyar K.P., and Dubina M.V. for comprehensive assistance and support.

REFERENCES

1. **Stupin D. Daniil, Ekaterina A. Kuzina, Anna A. Abelit, Anton K. Emelyanov, Dmitrii M. Nikolaev, Mikhail N. Ryazantsev, Sergei V. Koniakhin, and Michael V. Dubina**, Bioimpedance spectroscopy: basics and applications, ACS Biomaterials Science & Engineering 7, no. 6 (2021): 1962-1986.

2. **Moreau, Wayne M.**, Semiconductor lithography: principles, practices, and materials. Springer Science & Business Media, 2012.

3. **Leigh, Steven Y., Aashay Tattu, Joseph SB Mitchell, and Emilia Entcheva**, M^3: Microscope-based maskless micropatterning with dry film photoresist, Biomedical microdevices 13 (2011): 375-381.

4. **Neroev V. V., Astakhov Yu S., Lobanova M. M., Stupin D. D., Verlov N. A., Ryazantsev M. N., Zaitseva O. V., Bogdanov A. A., Vasilyev V. N., and Dubina M. V.**, Artificial vision: advances, topical issues, and prospects, Russian Ophthalmological Journal 11, no. 3 (2018): 3-27.

Conditions of AgNPs/flavin mononucleotide complex formation as a tool to tune optical properties of this complex

A.O. Dushina[1,2✉], **M.E. Stepanov**[3], **A.I. Arzhanov**[3,4], **E. V. Khaydukov**[2,3,5], **A. N. Generalova**[1,2]

[1] National Research Nuclear University MEPhI, Moscow, Russia;
[2] Russian Academy of Sciences, Shemyakin-Ovchinnikov Institute of Bioorganic Chemistry, Moscow, Russia;
[3] Moscow State Pedagogical University, Moscow, Russia;
[4] Lebedev Physical Institute of the Russian Academy of Sciences, Branch in Troitsk, Moscow, Russia;
[5] Russian Academy of Sciences, Institute of Photonic Technologies "Crystallography and Photonics", Moscow, Russia
✉dushina02@gmail.com

Abstract. Instead of using antibiotics, antimicrobial photodynamic therapy can be employed as a non-resistance-inducing approach to inactivate microorganisms. Flavin mononucleotide (FMN), a derivative of vitamin B2, exhibits photosensitizing properties, enabling the generation of reactive oxygen species to target and disrupt biomolecules. Its inherent low photostability predisposes it to photodegradation upon light exposure. The integration of silver nanoparticles, recognized for their antibacterial characteristics, has the potential to amplify the antimicrobial efficacy of FMN and influence its photodegradation kinetics. This study introduces the advancement of a method aimed at regulating the photodegradation of FMN due to formation of FMN-silver nanoparticles complexes.

Keywords: flavin mononucleotide, silver nanoparticles, photodegradation, optical properties

Funding: The study was prepared as part of the work on the topic «Laser technologies for biomedical applications» (№ 122122600055-2) under the state order of the Ministry of Education of the Russian Federation.

Introduction

A promising non-antibiotic alternative is antimicrobial photodynamic therapy based on generating reactive oxygen species (ROS) upon irradiation of a photosensitizer. The ROS effectively disrupt biomolecules, leading to microbial death [1]. Recent studies demonstrate the successful use of FMN (a derivative of vitamin B2), which in the triplet state (after irradiation) is a strong oxidizing agent and can also act as a photosensitizer capable of generating singlet oxygen [2, 3]. However, FMN is sensitive to light, and stability depends on many factors, including irradiation wavelength, as well as the presence of other components in the system [4]. Silver nanoparticles (AgNPs), known for their antibacterial characteristics, can enhance the antimicrobial effectiveness of FMN and influence its optical properties by the formation of an AgNPs/FMN complex [6]. The creation of complex that combine the antibacterial activity of silver nanoparticles and the phototoxicity of FMN, as well as prolonging their effect, is an urgent task.

Materials and Methods

Chemicals. Silver nitrate «Serva», Germany; Riboflavin-mononucleotide ampoule, JSC Pharmstandard-UfaVITA, 10 mg/ml; Sodium citrate «Helicon», MSU, Russia; Sodium Borohydride «Serva», Germany; Polyvinylpyrrolidone (PVP) «Merck», Germany. **Equipment.** «Evolution 200» spectrophotometer, Thermo Scientific (USA); LED device "Polyronic" (Russia); 90plus Particle Size Analyzer, Brookhaven (USA); SmartEngine^{TM} spectrometer, Oto Photonics (Taiwan). **Methods.** To prepare a colloidal solution of cAgNPs by slow reducing, a solution of sodium citrate (10 ml, 0.5 mg/ml) was added dropwise to a solution of silver nitrite (50 ml, 0.4 mg/ml) with constant stirring and heating in a water bath to 70–80°C for 4–6 hours. To prepare a

colloidal solution of bAgNPs by rapid reducing, a solution of silver nitrite (5 ml, 0.2 mg/ml) was added dropwise to a solution of sodium borohydride (15 ml, 0.1 mg/ml) with constant stirring in a cold water bath. To stabilize the nanoparticles, PVP solution (50 μl, 3 mg/ml) or FMN (2 μl, 10 mg/ml) were added dropwise to the AgNPs solution.

Results and Discussion

The hydrodynamic diameters of cAgNPs and bAgNPs were 30 and 20 nm, respectively. In contrast to cAgNPs, the colloidal stability of bAgNPs was low and required the stabilizer utilization. The FMN and PVP made the dispersion homogenous, avoiding the large aggregate sedimentation. The acquired absorption spectra of NPs demonstrated the peak with higher intensity for bAgNPs than for cAgNPs at wavelength 395 nm and 425 nm, respectively. It is worth noting that the FMN addition led to appearance the second maximum at 550 nm on the spectrum of bAgNPs, probably indicating the formation of bAgNPs/FMN aggregates, which were not observed in the case of cAgNPs. Irradiation at specific wavelengths (365 nm/450 nm) caused an increase in the localized surface plasmon resonance (LSPR) peak for cAgNPs, with minimal change for bAgNPs. Addition of FMN to cAgNPs/bAgNPs and subsequent 365 nm diode irradiation resulted in disappearance of FMN peaks at 378 nm and 445 nm, producing a peak at 550 nm, indicating potential AgNPs/FMN complex formation. Irradiating FMN and cAgNPs with a 450 nm diode increased and broadened the absorption peak. When FMN with PVP-stabilized bAgNPs was irradiated at 450 nm, no peak formed at 550 nm; however, for FMN-stabilized bAgNPs, a peak was formed, possibly due to reduced distances between FMN and AgNPs. Additionally, the yellow AgNPs solution with FMN turned brown upon irradiation, signifying potential FMN and AgNPs complex formation.

Using a custom device that allows real-time measurement of fluorescence intensity during light irradiation, it was found that in the case of the AgNPs/FMN complex, the FMN photoproduct peaks at a wavelength of 478 nm were not detected upon irradiation. The photodegradation time of FMN in the presence of cAgNPs increases by 1.5-2 times compared to a pure FMN solution, while the photodegradation time of FMN in the presence of bAgNPs decreases by 1.2-1.5 times, which may be due to the different distance between FMN molecules and the surface of the NPs.

Conclusion

The formation of a complex between FMN and silver nanoparticles can be monitored by changes in optical properties, in particular by the formation of an additional absorption peak at a wavelength of 550 nm. The process of complex formation, as well as the time of FMN photodegradation, is influenced by both the irradiation wavelength and the type of silver nanoparticles.

REFERENCES

1. **Youf R., Müller M., Balasini A., Thétiot F., Müller M. et al.**, Antimicrobial photodynamic therapy: Latest developments with a focus on combinatory strategies, Pharmaceutics. 13 (12) (2021) 1995.

2. **Insińska-Rak M., Sikorski M., Wolnicka-Glubisz A.**, Riboflavin and Its Derivates as Potential Photosensitizers in the Photodynamic Treatment of Skin Cancers, Cells. 12 (18) (2023) 2304.

3. **Buchovec I., Vyčaitė E., Badokas K., Sužiedelienė E., Bagdonas S**., Application of antimicrobial photodynamic therapy for inactivation of *Acinetobacter baumannii* biofilms, International Journal of Molecular Sciences. 24 (1) (2022) 722.

4. **Sheraz M.A., Kazi S. H., Ahmed S., Anwar Z., Ahmad I.**, Photo, thermal and chemical degradation of riboflavin, Beilstein Journal of organic chemistry 10 (1) (2014) 1999–2012.

5. **Rivas Aiello M.B., Romero J.J., Bertolotti S.G., Gonzalez M.C., Mártire D.O.,** Effect of silver nanoparticles on the photophysics of riboflavin: consequences on the ROS generation, The Journal of Physical Chemistry C. 120 (38) (2016) 21967–21975.

Express diagnostics of human health using laser radiation absorption signals

E. A. Zhestkay[1], **S. Msokar**[2,3], **D. D. Isakova**[1]
[1]The Bonch-Bruevich Saint Petersburg State University of Telecommunications, Saint Petersburg, Russia;
[2] Higher Institute for Applied Sciences and Technology, Damascus, Syria;
[3]Peter the Great Saint-Petersburg Polytechnic University, Saint Petersburg, Russia;
katy.zhestkay@gmail.com

Abstract The necessity of using pulse oximetry based on the laser radiation absorption signal for diagnosing the state of human health is substantiated. A new design of a sensor for recording a pulse wave and a new technique for its processing are proposed. New results were obtained when recording a pulse wave using a new sensor (the third peak, which had not previously been observed). Deviations in the functioning of the patient's cardiovascular system were identified using new information that was previously unavailable.

Keywords: express diagnostics, non-invasive measurements, laser radiation, pulse wave, signal.

Introduction

Regular express diagnostics of a person's health status is one of the most important factors in identifying various diseases at an early stage and their timely treatment [1]. Particularly important here is control the state of the cardiovascular system. One of the most common methods is pulse oximetry, the advantage of which is its non-invasive measurements, since is its non-invasive measurements [2]. One of the shortcomings in the design of pulse oximeters is the presence in their design of an analog-to-digital converter (ADC), the transfer function of which distorts information in the structure of the pulse wave, individual for each person, which cannot be restored by further processing [3]. This prompted us to develop a new method for recording and processing the pulse wave. It is based on recording the absorption signal of laser radiation in the far peripheral zone using a line of CCDs with horizontal charge transfer (an ADC is not required in this design).

Results and Discussion

The CCD line and the technology for its placement in the optical sensor were developed in such a way that the principle of recording the laser radiation absorption signal (Fig. 1) in the far peripheral zone does not fundamentally change when using it, compared to the conventional use of a CCD matrix in an optical sensor. A during using the CCD line, the functions of the pulse oximeter (pulse detection and percentage of hemoglobin oxygen saturation) are preserved.

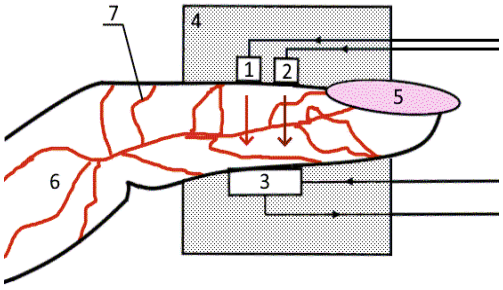


Figure 1. Block diagram of registration of a laser radiation absorption signal: 1 – semiconductor laser diode at λ = 660 nm, 2 – semiconductor laser diode at λ = 940 nm, 3 – CCD line, 4 – sensor body, 5 – nail, 6 – finger, 7 – blood vessels.

In figure 2 shows, as an example, two pulse wave signals recorded from one patient for 3 minutes using two different optical sensors (with a CCD matrix and a CCD array). Using a sensor

with a CCD array, it was possible to identify an additional (third peak) in the pulse wave signal when examining a patient several minutes after the first examination with a sensor with a CCD array.

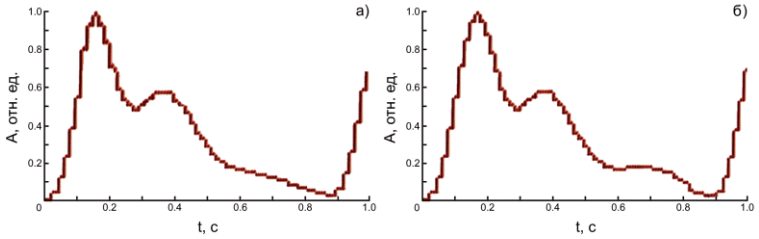


Figure 2 (a, b). Dependence of the ratio of the amplitudes of the recorded pulse wave signal for various devices for recording laser radiation in the design of the optical sensor: a) – CCD matrix, b) – CCD array.

To monitor negative changes in the functioning of the cardiovascular system, the pulse wave signal is processed. By dividing the period of the pulse wave into parts: rise, fall and the vicinity of the maxima, the signal is converted and visualized on graphs using developed mathematical functions. An example of such results is shown in Fig. 3 and 4. The obtained processing results allow us to establish that the use of a new system for recording the absorption signal of laser radiation with a higher signal-to-noise ratio introduces changes into the structure of the histograms when considering the first and second maximum, helping to identify changes.

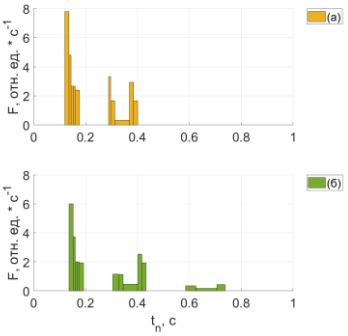


Figure 3 Results of processing the maxima of one period of the pulse wave: graph (a) corresponds to its registration using a CCD matrix, graph (b) – CCD rulers.

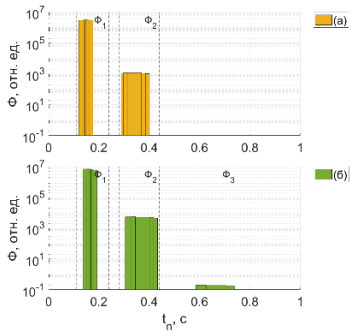


Figure 4 Results of processing the rising edges of one period of the pulse wave: graph (a) corresponds to its registration using a CCD matrix, graph (b) – CCD rulers.

Conclusion

The obtained results of experimental studies showed the effectiveness of the developed design and methodology for processing the pulse wave signal. Clinical results of the patient's examination confirmed the identified abnormalities in the functioning of the cardiovascular system.

References

1. **Bergis B., Harrois, A., Duranteau J.** Microcirculation: Physiological Background. In Advanced Hemodynamic Monitoring: Basics and New Horizons, Eds.; Springer: Cham, Switzerland, 2021; pp. 173–180.
2. **Rosic, T.; Petrina, N.; Baysari M.; Ritchie A.; Poon, S.K. Patient** and clinician use characteristics and perceptions of pulse oximeter use: A scoping review. International Journal of Medical Informatics. 162(2022) 104735.
3. **Fine, J.; Branan, K.L.; Rodriguez, A.J.; Boonya-ananta, T.; Ajmal; Ramella-Roman, J.C.; McShane, M.J.; Coté, G.L.** Sources of Inaccuracy in Photoplethysmography for Continuous Cardiovascular Monitoring. Biosensors. 11(2022) 126.

Investigation of tissue respiration functions by optical methods

Zanevskaya M.Yu.[1,2]✉, Mazing M. S.[2], Antifeev I. E.[2], Zaitseva A.Yu.[2]

[1] State University of Aerospace Instrumentation, St. Petersburg, Russia;

[2] Institute of Analytical Instrumentation, Russian Academy of Sciences, St. Petersburg, Russia

✉mnevskaya1@gmail.com

Annotation. A hardware-software complex was developed in order to perform remote monitoring of the functional state of a person. In order to find correlation between the data obtained by the developed device and the data obtained with the help of medical equipment, an experimental study was carried out with the participation of subjects who were offered physical load.

Keywords. Functional status, hardware-software complex, optical radiation.

Funding. The study was supported by a grant from the Russian Science Foundation (project No. 24-21-00404)**.**

Introduction

Currently, extensive efforts are being made to research and develop intelligent wearable systems for human health monitoring, which will help to improve the quality of medical services [1, 2]. Any physical activity is accompanied by energy expenditure, part of which is produced in aerobic mode due to oxidation of proteins, fats and carbohydrates. As a result of oxidative reactions, oxygen (O_2) is absorbed and carbon dioxide (CO_2) is released [3]. It has been found that an increase in the rate of CO_2 release is observed in parallel with a decrease in the rate of oxygen consumption, which means that tissue respiration functions are impaired [4]. Thus, remote monitoring of tissue respiration functions will help to track the functional state of the human body.

Materials and Methods

A hardware-software complex (HSC) was developed, including two modules: optoelectronic and information. The optoelectronic module is represented by a wearable sensor of backscattered radiation of visible and near-infrared wavelength ranges. The information module transmitted the received values of backscattered radiation intensity to a personal computer via a wireless personal network, with further processing and analysis of the transmitted data set [5].

An experimental study was conducted with the participation of seven subjects. Each of them was offered physical exercise. Throughout the entire cycle of physical exercise, the above-described hardware-software complex, realized as wearable sensors, and exhaled air sensors were recorded on the subject.

The purpose of the study was to search for correlations between the values of backscattered radiation intensity and the subject's functional state indicator, such as the rate of carbon dioxide excretion.

Results and Discussion

As a result of the experimental study, the time dependences of the volume of released CO_2 were obtained. The dependence for a typical subject is presented in Figure 1.

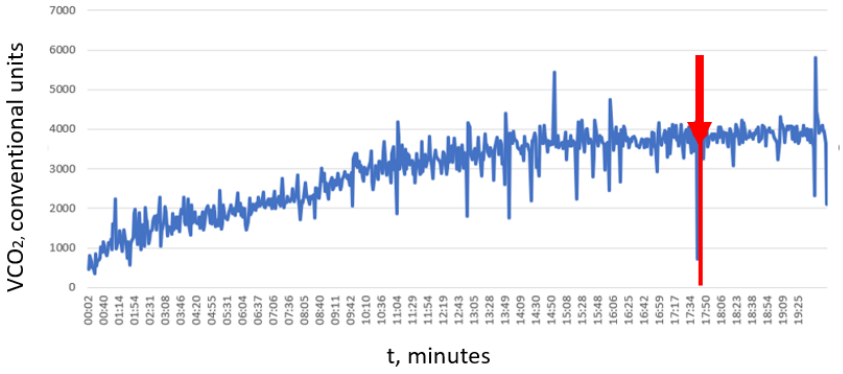


Fig. 1. Time dependence of the volume of extracted CO_2 obtained using exhaled air sensors

On the graph, among the gradual increase in the rate of CO_2 release, the onset of a "plateau" can be traced starting at 17 minutes, 48 seconds of the study. This plateau indicates the limiting rate of CO_2 release, which corresponds to the violation of tissue respiration functions.

The data obtained by the hardware-software complex represented the time dependence of the intensity of backscattered radiation from the forearm of the subject (Figure 2).

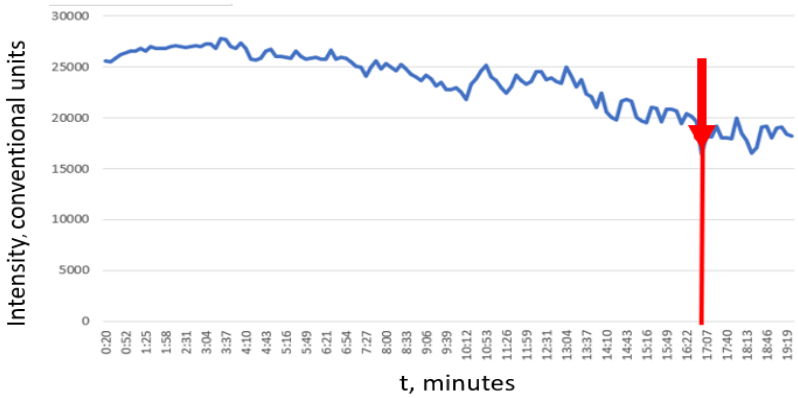


Fig. 2. Time dependence of the intensity of backscattered radiation at a wavelength of 530 nm obtained with the help of the hardware-software complex

The graph shows a gradual decrease in the intensity of backscattered radiation, also followed by a plateau at 17 minutes into the study.

Conclusions

The dependencies obtained during the experimental study revealed a correlation. When using exhaled air sensors detecting CO_2 and the developed AIC in general cases, plateau areas were recorded starting from the 17th minute of the experimental study. Thus, this indicates the ability to track the violation of tissue respiration functions by means of the developed hardware-software complex.

REFERENCES

1. **Chan M**. et al. Smart wearable systems: Current status and future challenges //Artificial intelligence in medicine. – 2012. – Т. 56. – №. 3. – С. 137-156.

2. **Lymberis A.** Smart wearable systems for personalised health management: Current R&D and future challenges //Proceedings of the 25th annual International conference of the IEEE engineering in medicine and biology society (IEEE cat. No. 03CH37439). – IEEE, 2003. – Т. 4. – С. 3716-3719.

3. **Simbirtsev G. C.** Regulatory effect of carbon dioxide on oxygen consumption in endurance athletes in the light of mathematical analysis of aerobic oxidation energy production //Sports Medicine: Science and Practice. - 2019. - Т. 9. - №. 3. - С. 12-24.

4. **Grishin O. V. et al**. Increase in CO 2 excretion rate at rest during short-term hypoxia in healthy subjects // Human Physiology. - 2011. - Т. 37. - №. 5. - С. 77-83.

5. **Zaitseva A. Y., Avdyushenko S. A., Mazing M. S.** Information-measuring systems of non-invasive biomonitoring. - 2023.

Nanoparticles based on organic donor-acceptor compounds for biomedicine

Yu.A. Isaeva [1]✉, A.N. Efremov [1,2], I.V. Dyadishchev [2], D.O. Balakirev [1], R.A. Akasov [3], Yu.N. Luponosov [1]

[1] Enikolopov Institute of Synthetic Polymer Materials, Russia, Moscow;

[2] Lomonosov Moscow State University, Russia, Moscow;

[3] I.M. Sechenov First Moscow State Medical University of the Ministry of Health of the Russian Federation, Russia, Moscow

✉yu.isaeva@ispm.ru

Abstract. This work presents the synthesis of organic donor-acceptor (D-A) molecules based on triphenylamine (TPA) with various donor and acceptor moieties. The relationship between their molecular structure and properties was investigated to optimize their effectiveness in phototherapy and improve the specificity of their effects on cancer cells. Additionally, aqueous dispersions of nanoparticles 50–300 nm in size based on these compounds were prepared and studied with and without amphiphilic polymer matrices. The study demonstrated the potential of the acquired materials for cancer photodynamic therapy due to their high toxicity towards cancer cells (IC50<0.02 mmol and PI>50), generation of reactive oxygen species (ROS), effective light absorption, and photoluminescence in the red spectral range.

Keywords: donor-acceptor small molecules, photodynamic therapy, nanophotosensitizer

Funding: The work was carried out with financial support from the Ministry of Science and Higher Education of the Russian Federation (FFSM-2021-0005) and was prepared as part of the work on the topic «Laser technologies for biomedical applications» (№ 122122600055-2) under the state order of the Ministry of Education of the Russian Federation.

Introduction

Phototherapy, which includes photodynamic and photothermal therapy, is a promising cancer treatment due to its simplicity, high efficacy, and minimal drug resistance. A significant advancement in this field is phototheranostics, which combines diagnostics and therapy through light excitation. However, current materials have drawbacks, including low efficiency and complex synthesis, as well as insufficient specificity in delivering therapeutic agents to tumour sites. The aim of our study was to create photosensitizers using modern approaches. We utilized donor-acceptor organic compounds, which are known in organic electronics and photonics and are gaining interest in biomedical technologies due to their ability to interact with tumors with low toxicity and high biocompatibility. Our synthesis focused on organic D-A molecules with triphenylamine as an electron-donating fragment and various electron-withdrawing groups. We also prepared and analysed aqueous dispersions of nanoparticles based on these molecules, known for their ability to target tumour cells. Incorporating polymer nanocarriers with organic photosensitizers enhances stability and biocompatibility, promising improved properties and effective delivery to tumor sites for clinical use.

Materials and Methods

Organic dyes were synthesized using a range of organic synthesis reactions, such as bromination reactions, cross-coupling conditions, and the Knoevenagel reaction. The resulting molecules were purified using standard organic chemistry methods, including vacuum distillation, column chromatography, and recrystallization. The compounds' purity and structure were confirmed using modern physicochemical methods. Optical absorption spectroscopy and cyclic voltammetry were used to determine the compounds' optical properties and band gap values. Nanoparticles were obtained using a nanoprecipitation method, which relies on a rapid change in solvent polarity. The cytotoxicity of the resulting nanoparticles was assessed in vitro using the standard MTT test on cancer cell cultures SKBR3 (human breast cancer cell line) and MCF7 (estrogen-dependent breast cancer cells). Photodynamic activity was studied using green light with a wavelength of 530 nm.

Results and Discussion

A series of D-A molecules based on TPA were synthesized in this work (Fig. 1a). The relationship between the molecular structure and properties of these compounds was studied to optimize their effectiveness in phototherapy and influence selectivity and specificity towards cancer cells. The study investigated the influence of structure on the optical and electrochemical properties, phase behavior, and thermal stability of resulting compounds. Nanoparticle dispersions were obtained from synthesized organic photosensitizers and in combination with amphiphilic polymer matrices. The study also investigated the effect of polymer encapsulation on the size, stability, and cytotoxicity of the resulting nanoparticle dispersions. Among the synthesized substances, TTInd showed the most promise with a half-maximal inhibitory concentration (IC50) of 0.02 mmol and a phototoxicity index (PI) of 50 (Fig. 1b). When encapsulated in polyethylene glycol–polylactic acid (PEG–PLA) block copolymer, its IC50 values were <0.02 mmol and PI >50. Fluorescence images were obtained using a Leica TCS SPE confocal laser scanning microscope and ROS generation in cells was investigated with the fluorescent compound dichlorodihydrofluorescein diacetate (DCFDA).

a) *b*)

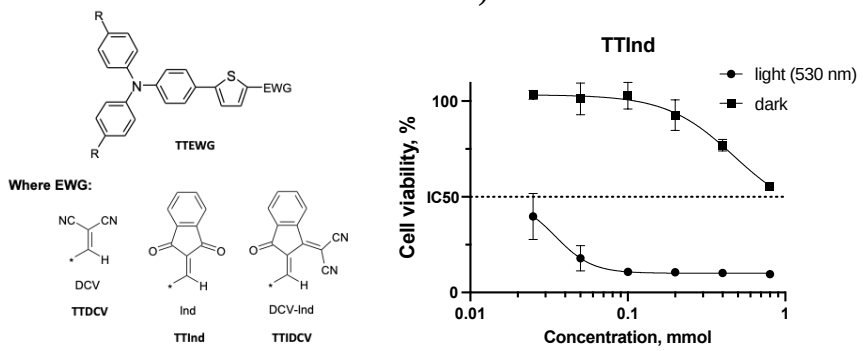


Fig. 1. Chemical structures of D-A molecules *(a)*, viability of SKBR3 cells after addition of different concentrations of NPs in the absence or presence of laser irradiation (530 nm) *(b)*.

Conclusion

Thus, various organic D-A molecules were synthesized, and nanoparticles based on them were obtained with or without polymer encapsulation. The properties of these nanoparticles were studied to optimize their effectiveness in phototherapy and enhance their specificity in targeting cancer cells. Encapsulation in an amphiphilic polymer improved photodynamic properties in some cases. The study showed promising properties for photodynamic theranostics, with effective light absorption and high toxicity towards cancer cells.

Acknowledgments

The biological experiments were caried out as part of the work on the topic «Laser technologies for biomedical applications» (№ 122122600055-2) under the state order of the Ministry of Education of the Russian Federation.

REFERENCES

1. **Paek S., Qin P., Lee Y., Cho K.-T., Gao P., Grancini G**., **Oveisi E., Gratia P., Rakstys K., Al-Muhtaseb S., Ludwig C., Ko J., Nazeeruddin M. K.,** Dopant-Free Hole-Transporting Materials for Stable and Efficient Perovskite Solar Cells, Adv. Mater. 29 (2017) 1606555.

2. **Justin Thomas K. R., Lin J., Velusamy M., Tao Y.-T., Chuen C.-H.**, Color Tuning in Benzo[1,2,5]thiadiazole-Based Small Molecules by Amino Conjugation/Deconjugation: Bright Red-Light-Emitting Diodes, Adv. Funct. Mater. 14 (2004) 83–90

3. **Lu B., Huang Y., Zhang Z., Quan H., Yao Y.,** Organic conjugated small molecules with donor–acceptor structures: design and application in the phototherapy of tumors, Materials Chemistry Frontiers. 6 (20) (2022) 2968-2993.

Options for implementing electrical impedance tomography for diagnostics blood clots and bruises

A. I. Levin [1]✉, **E. A. Pecherskaya** [1], **J. V. Shepeleva**[1]
[1] Department of Information and measuring equipment and metrology, Penza State University, Penza 440026, Russia
✉levin.alescha2013@yandex.ru

Abstract. The use of electrical impedance tomography for the diagnosis of blood clots, bruises and veins or arteries blockage is considered. The advantages of electrical impedance tomography compared to other similar methods are substantiated. Physical principles are presented, implementation options for the electrical impedance tomography method are systematized; the basics of the clinical application of this diagnostic method including the capabilities of both classical and portable installation options are outlined.

Keywords: Electrical impedance tomography, impedance, finite element method, visualization, clots.

Introduction

The electrical impedance tomography (EIT) method is based on the application of electric current or voltage through electrodes that are located on the body of the person being examined. Thus, this method allows you to visualize the impedance distribution of human tissues based on the potential differences between the electrodes and the electrical currents flowing through the electrodes [1].

The electrical impedance tomography method has a number of advantages compared to other similar diagnostic methods, such as computed tomography, magnetic resonance imaging, and ultrasound. The EIT positive functional characteristics include the fact that the method has high resolution and is non-invasive [2]. In addition, the method is also promising in terms of technical and economic indicators, since it is characterized by low cost, the small weight and overall dimensions of the equipment allow it to be portable, which opens up prospects for real-time monitoring. Technical limitations of the EIT method are associated with the inability to reconstruct the image slice by slice, since a change in conductivity anywhere in the region affects the measurement results in various areas, and not just for a specific slice [3]. The possibility of developing wearable portable devices based on EIT has recently given impetus to the development of this technology, which may represent a unique portable imaging technique.

Options for implementing EIT in practice

EIT with time-stretched measurements is useful for monitoring changing physiological phenomena (for example, 24-hour monitoring after surgery), but it is only applicable in special cases where changes occur over time, such as ventilation and perfusion. In contrast, EIT with a varying frequency of the current or voltage probing signal influences various tissue impedance characteristics, allowing image reconstruction if it is necessary to make measurements in a shorter time frame. Various modifications of the EIT imaging method are summarized in Table 1.

When implementing a method based on impedance measurement, single measurements, which are used to restore the distribution of absolute impedance across the tissues of the human body are performed. Despite its theoretical applicability, in clinical applications unknown boundary geometry, uncertainty in electrodes position, and other sources of systematic errors

make image reconstruction unreliable. Possible directions for solving this drawback are widely discussed in a number of scientific papers [2 - 3].

Table 1

Modifications of the electrical impedance tomography method

Modification of the EIT method	Measured parameter	Area of application
Method based on impedance measurement	Bioimpedance	Computer modeling of tissues bioimpedance distribution
Method based on measuring dynamically changing impedance	Time dependence of bioimpedance	Study of the processes dynamics occurring in the body
A method based on measuring impedance with a changing frequency of the measuring signal	Frequency dependence of bioimpedance	Identification of various types of biological tissues

There are two possible approaches to implementing electrical impedance tomography in practice:

- EIT in voltage mode consists of applying a given voltage to biological tissues through electrodes and measuring induced currents;

- EIT in current mode means supplying specified values of electric currents and measuring voltages generated on the human body surface.

The so-called trigonometric modification of the method of arranging electrodes is based on the supply of electric current to all electrodes simultaneously. In this case, the electrical voltage is measured relatively to the reference electrode. The specified implementation of the method involves performing multiple independent measurements, due to a significant reduction in the random component of the measurement error is achieved.

Conclusions

The electrical impedance tomography problem, which reconstructs the impedance distribution based on the structure of the applied current and the measured voltages at the electrodes, is called the inverse problem, and its solution is extremely difficult due to nonlinearity. Compared to X-ray computed tomography, where photon trajectories are straight lines, in EIT the current is determined by the impedance distribution within the object, and thus image reconstruction is a highly non-local and mathematically incorrect problem.

To increase the EIT modeling accuracy, it is necessary to take into account the anatomically realistic geometry of the body, heterogeneity, filling of living tissues with blood and other fluids, and the flow rate of fluids in the body.

REFERENCES

1. **Ke, XY., Hou, W., Huang, Q. et al.** Advances in electrical impedance tomography-based brain imaging. Military Med Res 9, 10 (2022). https://doi.org/10.1186/s40779-022-00370-7.

2. **Shi Y, Yang Z, Xie F, Ren S and Xu S.** The Research Progress of Electrical Impedance Tomography for Lung Monitoring. Front. Bioeng. Biotechnol (2021). 9:726652. doi: 10.3389/fbioe.2021.726652.

3. **Cappellini I, Campiglia L, Zamidei L, Consales G.**, Electrical Impedance Tomography (EIT) to Optimize Ventilatory Management in Critically Ill Patients: A Report of Two Cases. Anesthesia Research. 2024; 1(1):3-7. https://doi.org/10.3390/anesthres1010002.

A sensor for monitoring pulse wave parameters for express diagnostics of human cardiovascular system

S. Msokar[1, 2]✉, D.D. Isakova[3]

[1] Higher Institute for Applied Sciences and Technology, Damascus, Syria;

[2]Peter the Great Saint-Petersburg Polytechnic University, Saint Petersburg, Russia;

[3]The Bonch-Bruevich Saint Petersburg State University of Telecommunications, Saint Petersburg, Russia;

✉souhair.msokar@gmail.com

Abstract. A new design of an optical sensor has been developed using a CCD array with horizontal charge transfer to record the pulse wave signal. It allows you to obtain new information compared to previously used methods. A new technique has been developed to study changes in the shape of the pulse wave. Results of the functioning of the cardiovascular system were obtained and confirmed using certified medical equipment.

Keywords: express diagnostics, cardiovascular system, blood, CCD array, laser radiation, pulse wave, signal processing.

Introduction

Transmission pulse oximetry, which registers the pulse wave in the far peripheral zone, has become widespread to monitor the functioning of the human cardiovascular system. Analysis of the pulse wave shape [1] and its computer modeling and assessment of the pulse wave propagation speed [2] can help identify diseases and track negative changes in a person's health.

Various methods for processing the pulse wave have been developed to obtain additional information related to determining rigidity indices [3, 4]. In these techniques, the analog pulse wave signal from the photodetector is processed using different analog-to-digital converter (ADC) models with a different number of bits and clock frequency. Studies have shown that obtaining new information from a pulse wave is already difficult after processing it using an ADC.

In the designs of sensors for pulse oximeters, CCD matrices with different bit depth and number of pixels (standard version 2080 by 64 pixels) with frame-by-frame transfer can be used to record the pulse wave signal. When an image of a pulse wave is formed on the monitor screen of the device and its subsequent processing, a line is cut out through the zone where the maximum signal is located. In this case, the signal-to-noise ratio decreases since when steps are formed in a line, all the noise is read from the CCD matrix (frame transfer), and the useful signal is only from a certain pixel. In addition, optical pulse wave sensors cannot use a CCD with a small value of electrons per pixel (pixel well depth) to ensure high sensitivity since cooling is difficult to implement. This also reduces the sensor's resolution, especially with weak pulse wave signals. We propose to use an array of charge-coupled devices with horizontal charge transfer to register laser radiation. This allows us to eliminate several previously noted disadvantages when using photodiodes and CCD matrices.

Materials and methods

Fig. 1 shows a block diagram of recording a pulse wave signal using CCD array.

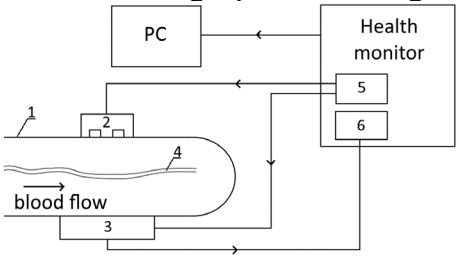


Fig. 1. Block diagram for recording a pulse wave signal: 1-finger; 2-device for placing two semiconductor lasers with λ_1= 660 nm and λ_2= 940 nm; 3-CCD array; 4-blood vessel; 5-multifunctional power supply; 6-microcontroller.

To process the received signals, we adapted our previously published technique [5]. It proposes using specially developed functions in areas of increasing and decreasing pulse wave, considering its shape and data about the person.

Results and Discussion

Fig. 2. shows, for an example, the results of processing pulse wave signal of a patient obtained by our sensor and previously used.

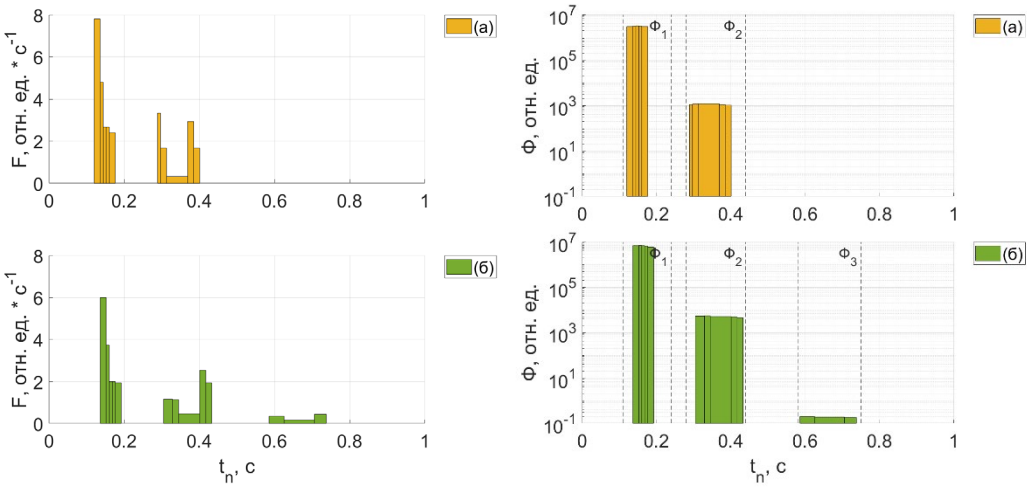


Fig. 2. Results of processing the maxima (left) and rising fronts (right) of one period of the pulse wave: graph (a) corresponds to its registration using a CCD matrix, graph (b) – CCD array.

It was found that in the pulse wave zone with a low signal-to-noise ratio in the laser absorption signal using new design of the sensor processing makes it possible to identify clear existence of the third maximum, which was not visible using previous ones. All such kind of differences were examined by doctors with other medical equipment.

Conclusion

The research showed that using a new design of an optical sensor makes it possible to generate a form of pulse wave, which contains more information about human health. The probable disorders that we established using new data based on abnormalities in the functioning of the cardiovascular system were confirmed when these people were examined using certified medical equipment.

REFERENCES

1. Nascimento L .M. S.d. et. al. Sensors and Systems for Physical Rehabilitation and Health Monitoring—A Review. Sensors. 2020, vol. 20. 4063

2. Kouz K. et. al. Pulse Wave Analysis to Estimate Cardiac Output. Anesthesiology. 2021, vol. 134. pp. 119–126.

3. Sequí-Domínguez I. et. al. Accuracy of Pulse Wave Velocity Predicting Cardiovascular and All-Cause Mortality. A Systematic Review and Meta-Analysis. J. Clin. Med. 2020, vol. 9. 2080.

4. Saugel B. et. al. Continuous noninvasive pulse wave analysis using finger cuff technologies for arterial blood pressure and cardiac output monitoring in perioperative and intensive care medicine: a systematic review and meta-analysis. British Journal of Anaesthesia. 2020, vol. 125. pp. 25–37.

5. Davydov R. et. al. New Methodology of Human Health Express Diagnostics Based on Pulse Wave Measurements and Occlusion Test. Journal of Personalized Medicine. 2023. vol. 13(3), 443.

Improving Compliance of Brain MRI Studies with the Atlas using a Modified TransMorph Neural Network

N. A. Nefediev[1]✉, N. E. Staroverov[2], R. V. Davydov [1]

[1] Alferov University, Saint Petersburg, Russia;

[2] Saint Petersburg Electrotechnical University "LETI", Saint Petersburg, Russia;

✉nikolay-nefedev@yandex.ru

Abstract. The work carried out a study on modifying the TransMorph architecture by integrating an input data preprocessing unit. The goal was to achieve better similarity scores between studies in the dataset and the reference atlas. The data was assessed based on the structure similarity metric. The results suggest that the use of a Sobel filter can lead to improvement.

Keywords: DIR, TransMorph, brain segmentation, MRI, neural network, AI in medicine.

Introduction

Deformable image registration (DIR) is an important task in the field of image processing. In general, DIR is a spatial correlation of objects in one image (moving) to another image (fixed or reference).

In medicine, deformations of CT and MRI studies often arise due to shifts in the patient's position relative to the positioning of the specialist or the urgency of the study when it is not possible to perform the correct positioning.

The main obstacle in the use of neural network algorithms for the analysis of deformed studies in medicine most often lies in the fact that training occurs on a set of studies with unclear semantics, and when processing the deformed study, various types of errors may occur.

To eliminate biases in the study, image registration algorithms are used. There are classical approaches, the bottleneck of which is the performance of the algorithms. An alternative is to use neural network architectures, which show an order of magnitude better performance. To improve MRI data, we used TransMorph neural network [1].

Materials and methods

When solving the DIR problem, algorithms solve a typical energy optimization problem between two images:

$$E(I_m, I_f, \phi) = E_{sim}(I_m \circ \phi, I_f) + \lambda R(\phi), \quad (1)$$

where I_m и I_f - shifted and fixed image, ϕ - deformation field, which distorts the shifted image (i.e. $I_m \circ \phi$), $R(\phi)$ ensures the smoothness of the deformation field, λ is the regularization hyperparameter that determines the tradeoff between image similarity and deformation field regularity.

This equation reduces to solving the optimization problem:

$$\phi = \arg\min_{\phi} E(I_m, I_f, \phi), \quad (2)$$

We used the TransMorph architecture, which is based on the idea of using Swin Transform as an encoder [2]. In Transmorph, the Swin Transform blocks have been configured, which adapts the self-attention mechanism for the DIR task. The modernization consists of expanding the Transmorph architecture using a data preprocessing unit. To do this, a convolutional block with kernels configured in accordance with the parameters of the Sobel filter was built into the network.

The DIR reference study was the brain atlas. The atlas also served to calculate the structural similarity index measure (SSIM) for the studies under consideration [3, 4]. SSIM is one of the methods for assessing the similarity of two images and displays the structural changes of one image relative to the reference:

$$SSIM(x, y) = \frac{(2\mu_x\mu_y + c_1)(2\sigma_{xy} + c_2)}{(\mu_x^2 + \mu_y^2 + c_1)(\sigma_x^2 + \sigma_y^2 + c_2)}, \quad (3)$$

where μ_x и μ_y are mean x and mean y respectively, σ_x^2 и σ_y^2 are variance x and variance y respectively, σ_{xy} is the covariance between x and y. $c_1 = (k_1 L)^2$, $c_2 = (k_2 L)^2$ - two variables, in which L is the dynamic range of the pixel-values (k_1=0.01, k_2=0.03 by default).

Results and Discussion

The impact of the original and modified versions of TransMorph was assessed on 20 randomly selected studies from the IXI dataset using the SSIM metric [5]. Results are showed in Fig. 1.

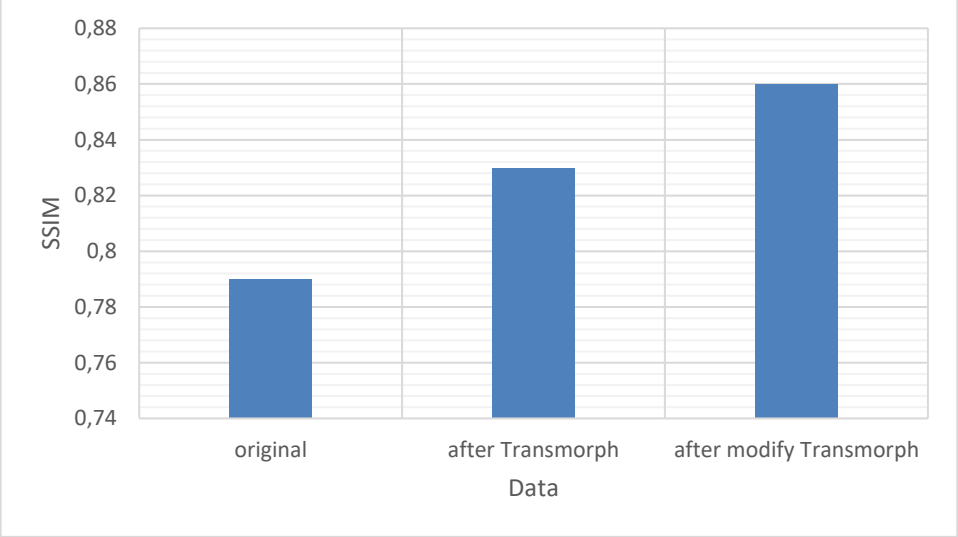


Fig 1. SSIM metric value on original data and data after applying TransMorph and modified TransMorph.

The research work carried out shows the prospects for using data preprocessing for DIR. The received positive results (and obtaining them on a more variable dataset) will allow use the processed data to train segmentation networks to help analyze MRI studies of the brain.

Conclusion

In the research a modified TransMorph architecture is proposed by integrating an input data preprocessing unit. Better similarity scores between studies in the dataset and the reference atlas are received. Received results could be used in improving training of neural networks used to analyze the results of MRI brain studies.

REFERENCES

1. Junyu Chen, Eric C. Frey, Yufan He, William P. Segars, Ye Li, Yong Du, TransMorph: Transformer for unsupervised medical image registration, Medical Image Analysis, Volume 82, 2022, 102615, ISSN 1361-8415, https://doi.org/10.1016/j.media.2022.102615.

2. Yucheng Tang, Dong Yang, Wenqi Li, Holger R. Roth, Bennett Landman, Daguang Xu, Vishwesh Nath, Ali Hatamizadeh. Self-Supervised Pre-Training of Swin Transformers for 3D Medical Image Analysis. Proceedings of the IEEE/CVF Conference on Computer Vision and Pattern Recognition (CVPR), 2022, pp. 20730-20740.

3. Junyu Chen, Eric C. Frey, Yufan He, William P. Segars, Ye Li, Yong Du, TransMorph: Transformer for unsupervised medical image registration, Medical Image Analysis, Volume 82, 2022, 102615, ISSN 1361-8415, https://doi.org/10.1016/j.media.2022.102615.

4. Chen J, Li Y, Du Y, Frey EC. Generating anthropomorphic phantoms using fully unsupervised deformable image registration with convolutional neural networks. Med Phys. 2020;47(12):6366-6380. https://doi.org/10.1002/mp.14545.

5. Brain Development. URL: https://brain-development.org/ixi-dataset/

IRON MEDIATED DNA-CATECHIN COMPLEXES

D. A. Nikitin ✉, **N. A. Kasyanenko**
Saint-Petersburg State University, Saint-Petersburg, Russia;
✉st075754@student.spbu.ru

Abstract. Naturally occurring polyphenols such as catechins exhibit great biological activity and can be used a component in cancer-treatment medications. For instance (+)-catechin can reduce proliferation rate of malignant cells which is further impeded once iron chloride (III) is introduced to the system. In this study we investigated whether DNA can form complexes with (+)-catechin in the presence of iron ions as to get closer to produce an efficient nontoxic multicomponent antitumor medication. The research was carried out with UV spectroscopy, dynamic light scattering, atomic force microscopy, low-gradient viscometry.

Keywords: DNA, catechin, trivalent iron, DNA complexes

Introduction

As of recent, interest has grown towards implementing plant-based compounds in pharmaceuticals. The natural origin of these compounds should result in reduced toxicity and higher biocompatibility of final drugs. Among other molecules, natural polyphenols, catechins specifically, might be considered the most promising [1]. Their exceptional biological activity manifests in their antifungal, antibacterial, antioxidant and antitumor properties [1, 2]. Furthermore, catechins biological activity can be enhanced in complexes with trivalent iron [3].

Considering DNA to be the main target of antitumor drugs, we set out to investigate the possibility of DNA forming complexes with (+)-catechin in the presence of trivalent iron ions.

Materials and Methods

Experimental methods: spectroscopy, dynamic light scattering, atomic force microscopy, low-gradient viscometry were used to detect changes in DNA's spectral or hydrodynamic properties which would correspond to complex formation in solution.

The research was carried out using calf thymus DNA, (+)-catechin and iron (III) chloride acquired from Sigma Aldrich. All the samples were prepared in 0,005 M NaCl solutions. Sodium ions act as counterions to DNA.

Results and Discussion

Both spectral and hydrodynamic properties of solutions of DNA in the presence of (+)-catechin remained unaltered compared to same of free DNA. The result is rather apparent, as both catechin and DNA possess negative charges in solutions, their interaction should be unlikely

Similarly, absorption spectra of catechin in the solutions with iron chloride do not differ from the absorption spectra of free catechin in solution without iron ions. Nonetheless, the data from dynamic light scattering revealed the presence of two discrete types of nanoparticles with hydrodynamic radii of (40±10) nm and (200±50) nm in these solutions. Atomic force microscopy confirmed these results.

The formation of DNA complexes with iron (III) is evident from the absorption spectra of DNA in solutions with and without iron chloride. Moreover, introducing iron ions to DNA solutions causes the shrinkage of macromolecule. The hydrodynamic radius of DNA and the specific viscosity of DNA solution decrease. DNA condensation was observed with an increase in iron ions concentration. This could be attributed to changes in the electrostatic interactions and decrease in polyelectrolyte swelling of the macromolecule.

DNA conformation in solutions containing three components (DNA, catechin and iron ions) depends slightly on the order of the addition of components to the stock solution. However, experimental obtained by various methods indicate the formation of DNA complexes with iron ions and catechin simultaneously.

Conclusion

The presence of iron (III) ions in DNA solution can mediate the formation of DNA -catechin complexes.

REFERENCES

1. **Cadoná, F. C., Dantas, R. F., de Mello, G. H., & Silva-Jr, F. P**. (2021). Natural products targeting into cancer hallmarks: An update on caffeine, theobromine, and (+)-catechin. Critical Reviews in Food Science and Nutrition, 1–20.

2. **Farhan, M.; Rizvi, A.; Ahmad, A.; Aatif, M.; Alam, M.W.; Hadi, S.M.** Structure of Some Green Tea Catechins and the Availability of Intracellular Copper Influence Their Ability to Cause Selective Oxidative DNA Damage in Malignant Cells. Biomedicines 2022, 10, 664.

3. **Manna, M. S., Saha, P., Ghoshal, A. K.** (2014). Iron complexation of pharmaceutical catechins through selective separation. RSC Advances, 4, 26247-26250.

Methodology of potentiometric microbiological testing as applied to the comparative evaluation of antibiotic properties of essential oils

V. V. Romanova [1], **A. Yu. Zaitseva** [1], **V. S. Sibirtsev** [1,2]✉

[1] Institute for Analytical Instrumentation of the Russian Academy of Sciences, Saint Petersburg, Russia;

[2] Sankt-Petersburg state chemical and pharmaceutical university, Saint Petersburg, Russia

✉vs1969r@mail.ru

Abstract. One of the important conditions for ensuring the proper level of safety and quality of life is timely and qualitative testing of pro- and antibiotic properties of both new and already authorized food, pharmaceutical and other products. This article describes a newly developed method of potentiometric microbiological testing, which provides for periodic instrumental recording of pH changes, as well as the potential difference between the chlorosilver reference electrode and indicator iron and copper electrodes "1st kind" , characteristic of the liquid nutrient medium incubated in the presence and absence of test samples (TS) and viable test microorganisms (TM), for which lactic acid bacteria are typical representatives of human and natural microbiota. The presented method of microbiological research is more express and informative, less labor- and material intensive, which makes it more accessible for wide application.

Keywords: microbiological testing, potentiometric biotesting, biological activity, plant extracts, essential oils.

Funding: The research was carried out within the framework of the State Assignment No. 075-00439-24-00, FFZM-2022-0010, state registration number 122032300337-4.

Introduction

Recently, the development of objective, rapid and widely applicable methods to quantify the pro- and antibiotic properties of numerous samples in various industries such as food, pharmaceutical and others has become increasingly urgent. Existing standard microbiological testing procedures involving visual assessment of overall microbial survival or the size of the zone of colony growth inhibition are time-consuming, material-intensive, and labor-intensive, providing somewhat subjective and static information about impaired microbial viability. Therefore, the use of various instrumental technologies, particularly optical and electrochemical techniques, appears promising for microbiological testing. In addition, there is a growing deficiency of biologically active substances (BAS) of natural origin in pharmaceutical, food and other products consumed by society. Plant extracts, particularly essential oils (EO), have been widely used as functional supplements due to their selective prebiotic, antimicrobial, normalizing, therapeutic, normalizing, antioxidant, flavor and other properties. The aim of this study is to develop a rapid and objective instrumental methodology to evaluate the pro- and antibiotic properties of various food products, ingredients and supplements, including the effects of different EO on human microbiota dynamics [1].

Materials and Methods

The objects of study in this work were EO obtained by such a large russian manufacturer as “Mirrolla” LLC, from such types of plant raw materials, which are quite widely used in food, pharmaceutical, cosmetic and other industries such as peel of orange (№ 1), tangerine (№ 2), bergamot (№ 3), grapefruit (№ 4), lemon (№ 5) and lime (№ 6); as well as leaves of bigardia (№ 7), flowers of bigardia (№ 8), leaves of tea tree (№ 9), seeds of star anise (№ 10) and seeds of common anise (№ 11). Based on the existing instrumental methods of bioanalysis [2-5], a methodology has been developed to assess the effect of various concentrations of these EO on antimicrobial activity. A liquid nutrient medium was prepared for each batch of EO and Lactobacillus acidophilus ATCC 4356 was inoculated. The pH was adjusted to 7.2 ± 0.2 and incubation at 37 °C was continued until the number of viable microorganisms reached

approximately 5 ×10^6 cells/ml (pH 6.5 ± 0.1). Then the test solution was adjusted to a pH of 8.0 ± 0.1, poured into measuring vessels and incubated at a temperature of 37 ° C, controlling the pH and redox potential using specially manufactured by the authors of this article.

Results and Discussion

The experimental data obtained by the method described above are presented in Table 1.

Table 1

General degrees of inhibition of the vital activity of *Lactobacillus acidophilus* at different durations of their incubation in the presence of different amounts of "essential oils" , determined by "standard visual" ($\varepsilon_{S,k}$, %) and potentiometric ($\varepsilon_{V,k}$, %) microbiological testing methods developed by us

Nm	C_{TS}	*k*	EO number										
			1	2	3	4	5	6	7	8	9	10	11
1	0.5	24	-22	-17	-15	-15	-27	-23	-20	-36	-25	-34	-21
2	1	2	-57	-77	-62	-71	-68	-68	-71	-96	-94	-85	-59
		4	-49	-66	-54	-49	-69	-62	-65	-89	-83	-85	-62
		6	-44	-47	-46	-49	-65	-59	-63	-82	-80	-78	-57
2	0.5	2*	-39	-47	-32	-32	-44	-49	-32	-81	-80	-63	-33
		4**	-34	-34	-28	-22	-41	-44	-30	-64	-60	-57	-34
		6***	-31	-25	-26	-21	-38	-38	-28	-50	-41	-49	-30
2	0.1	2	-12	-16	-16	-15	-18	-27	-21	-27	-26	-18	-18
		4	-14	-14	-14	-12	-15	-22	-20	-21	-20	-16	-16
		6	-11	-10	-11	-10	-11	-18	-18	-16	-14	-15	-11

Notations: For the method of determining $\varepsilon_{V,k}$, as well as the correspondence of EO numbers to specific types of plant raw materials used for their preparation, see the section "Materials and Methods". *Nm* correspond to the "standard visual" (1) and developed by us potentiometric (2) methods for determining ε. C_{TS} (vol. %) – initial EO concentration in the test medium with viable microorganisms; *k* (h) – duration of incubation of the test medium. The indices "*", "**" and "***" denote rows of ε_V values, with 85, 90 and 95 % confidence correlating with the ε_S values at the same C_{TS}. The relative error in determining ε for all values indicated in the table ranged from 50 to 70 % for ε_S and from 10 to 20 % for ε_V.

Conclusion

We are convinced that with the help of the potentiometric technique presented in this article it is possible to assess the influence of various chemical compounds, including BAS extracted from various vegetable raw materials. In addition, the technique presented here, compared to standard methods of microbiological testing, is significantly less material intensive and provides much more opportunities for automating the analysis process.

REFERENCES

1. **Sutherland J., Miles M., Hedderley D., Li J., Devoy S., Sutton K., Lauren D.**, Invitro effects of food extracts on selected probiotic and pathogenic bacteria, International Journal of Food Sciences and Nutrition. 60 (8) (2009) 717–727.

2. **Sibirtsev V.S., Glibin E.N., Ivanov S.D.,** Variation of spectral properties of actinocin derivatives due to equilibrium transformations, Russian Journal of Organic Chemistry. 36 (12) (2000) 1812–1818.

3. **Sibirtsev V.S.,** Fluorescent DNA probes: study of mechanisms of changes in spectral properties and features of practical application, Biochemistry (Moscow). 72 (8) (2007) 887–900.

4. **Sibirtsev V.S., Uspenskaya M.V., Garabadgiu A.V., Shvets V.I.**, An integrated method of instrumental microbiotesting of environmental safety of various products, wastes, and territories, Doklady Biological Sciences. 485 (6) (2019) 59–61.

5. **Sibirtsev V.S., Nechiporenko U.Yu.**, Method of electrochemical biotesting for comparative analysis of probiotic and antibiotic properties of various plant extracts, Fine Chemical Technologies (Tonkie Khimicheskie Tekhnologii). 15 (6) (2020) 34–43.

N-arylated DABCOnium salts for thiol and selenol sensing

B. Ranishenka [1]✉, Y. Lamekina[1], T. Seviarynchyk[1], D. Bugaenko[2]✉, A. Karchava[2], V. Shmanai [1]

[1] Institute of Physical Organic Chemistry, National Academy of Sciences of Belarus, Minsk, Belarus;

[2] M. V. Lomonosov Moscow State University, Moscow, Russia

✉ranishenka@gmail.com, bugad357@yandex.ru

Abstract. A new luminescent probe platform based on N-Arylated DABCOnium cation for organic thiol and selenol detection have been proposed. A coumarin based fluorescent probe was specially designed to check and assess capability and applicability of the approach for thiol and selenol analysis. The probe had good solubility in water low background luminescence and yielded product with high luminescent quantum yield (72%) which was near pH independent. The probe selectivity to a number of nucleophiles was demonstrated as well as its stability to such reducing agents as dithiotriethol (DTT) and tris(2-carboxyethyl)phosphine (TCEP). High reactivity toward thiophenols and selenophenols was shown. Kinetics of the reactions have been studied and corresponding protocols for quantitative analysis developed with calibrating curves building. Limit of detection (LOD) for thiocresol (22 nM) and phenyl selenide (6 nM) have been evaluated.

Keywords: thiols, thiophenols, selenols, diphenyl diselenide, fluorescent probe, coumarin.

Funding: This work has been supported by Russian Foundation for Basic Research (grant № 20-53-04030) and Belarusian Republican Foundation for Fundamental Research (grant № X21PM-107).

Introduction

Biogenic thiols are substantial part of living cells functioning [1]. Thiophenols have toxic effect on human body causing various injury [2]. Selenol containing species are playing significant role in living organisms. An importance of selenium for human health makes necessary to control it in food. Pharmacological and toxicological properties organoselenium compounds are under investigation [3]. The mentioned areas require thiol and selenol group analytics. Fluorescent probes are usefull analytical instrumentation for that. A plenty of new probes for aliphatic and aromatic thiols have been developed last decades [1,2]. All of them can be described by several chemical approaches. Most of the platforms used for thiols detection are not appropriate for selenols [4]. Thus, developing new working principles for thiol and selenol fluorescent probes design is desirable and it is more precious for selenol probes.

Results and Discussion

In our previous report [5], we observed N-Aryl DABCO salts react with thiols with DABCO cycle cleavage in comparably mild conditions. Thus, we have applied this principle to produce new fluorescent probe **1** (Figure 1). Evaluation of applicability of **1** for thiol sensing revealed some obstacles. The product of the reaction had strongly pH dependent fluorescence and was sufficiently quenched in the basic reaction conditions. We suppose photoinduced electron transfer (PET) mechanism takes place. The reaction rate of probe **1** was too slow for analytical application.

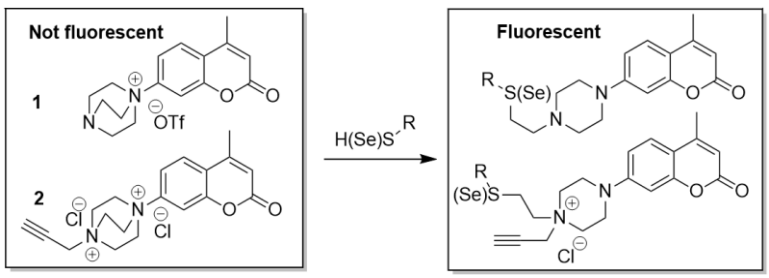


Fig. 1. The scheme of the probe **1** and **2** reaction with thiol and selenol nucleophiles

We have continued the probe design by improving reactivity of **1** by its quaternization with propargyl bromide (probe **2**). Nitrogen free electron pair blocking resulted in anticipated pH independent fluorescence for the reaction products. Besides, quaternary amine group in the products improves their solubility in water. Estimated fluorescent quantum yield of the thiocresol product in water was 73% (in contrast with 0.05% for **2**). The product had close fluorescence intensity in water, dimethyl sulfoxide (DMSO) and their mixtures. Finally, probe **2** had orders of magnitude higher reactivity comparing with **1** that permits its application for analytical purposes.

Our experiments demonstrated that probe **2** is not applicable for aliphatic thiol and selenol analysis because of unknown side reactions, which require investigation. Nevertheless, the probe is appropriate for aromatic thiols and selenols. It has shown good selectivity toward such strong nucleophiles as azide and cyanide anions as well as amines and phenol. It was moderately stable for DTT and TCEP reducing agents. This permitted its application for thiophenols and selenophenols quantitative detection. Figure 2 shows calibration curve for phenyl selenide detection with LOD measured 6 nM. Analogous thiocresol analysis (at pH 8.5) gives LOD 22 nM.

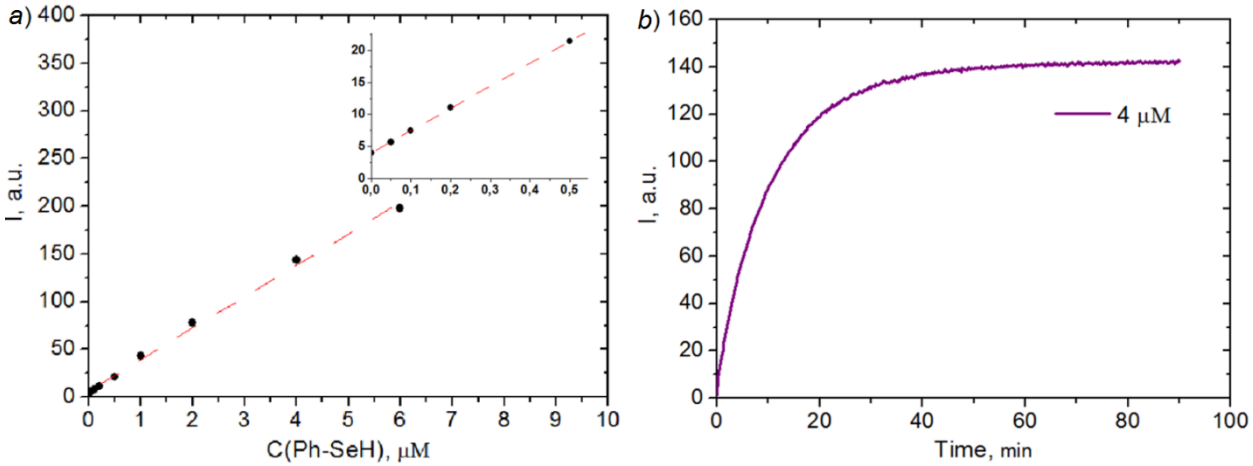


Fig. 2. (*a*) Calibration curve for selenophenol in the range 0-6 μM (60 μM of **2** at pH 7.0, 80% DMSO and 36 °C; selenophenol was generated from diphenyl diselenide by 1 mM TCEP; incubation time was 70 min). (*b*) Typical curve of luminescence enhancement in the used reaction conditions.

Conclusion

A new luminescent probe design for organic thiols and selenols have been proposed. Coumarine based probe have been applied to demonstrate workability of the principle for analytical application. The probe had high luminescent quantum yield, high selectivity and was more appropriate for aromatic thiols and selenols detection with good detection limits.

REFERENCES

1. **Wang S., Huang Y., Guan X.**, Fluorescent probes for live cell thiol detection, Molecules. 26 (12) (2021) 3575.

2. **Bugaenko D. I., Karchava A. V., Yunusova Z. A., Yurovskaya M. A.**, Fluorescent probes on the basis of coumarin derivatives for determining biogenic thiols and thiophenols, Chemistry of Heterocyclic Compounds. 55 (2019) 483-489.

3. **Rosa R. M., Roesler R., Braga A. L., Saffi J., Henriques J. A. P.**, Pharmacology and toxicology of diphenyl diselenide in several biological models, Brazilian Journal of Medical and Biological Research. 40 (2007) 1287-1304.

4. **Maeda H., Katayama K., Matsuno H., Uno T.**, 3′-(2, 4-Dinitrobenzenesulfonyl)-2′, 7′-dimethylfluorescein as a Fluorescent Probe for Selenols, Angewandte Chemie. 118(11) (2006) 1842-1845.

5. **Bugaenko D. I., Yurovskaya M. A., Karchava A. V.**, N-Arylation of DABCO with diaryliodonium salts: general synthesis of N-aryl-DABCO salts as precursors for 1, 4-disubstituted piperazines, Organic letters. 20(20) (2018) 6389-6393.

Laser welding of biological tissues using galvanoscanner and focused laser radiation transport

D. I. Ryabkin [1,2]✉, **V. V. Suchkova** [1,2], **A. Yu. Gerasimenko**[1,2]
[1] I.M. Sechenov First Moscow State Medical University, Moscow, Russia;
[2] National Research University of Electronic Technology MIET, Zelenograd, Moscow, Russia;
✉ ryabkindi@gmail.com

Abstract. Laser welding is a promising method of restoring the integrity of biologically active tissues. Compared with traditional methods, laser welds are non-toxic, leak-proof for liquids immediately after formation and form small scars. The main limitation of the existing methods of radiation transportation in the existing methods of laser welding of biological tissues is the impossibility of local heating of the seam formation area at a depth of more than 0.3 mm without significantly increasing the area of thermal necrosis of the biological tissue being joined. The paper proposes a new method for transporting laser radiation to the local area of laser weld formation. A synchronized lens and a gold-scan mirror are used to transport laser radiation. The radiation is transported through less optically dense biological tissues. Because focused radiation is used, the intensity reaches a maximum in the area of weld formation. A lower intensity of radiation when passing through biological tissues allows minimizing the area of thermal necrosis of the tissue. The simulation result showed the possibility of local heating of the area of formation of the laser weld, heating to the denaturation temperature of the solder 42-45 °C.

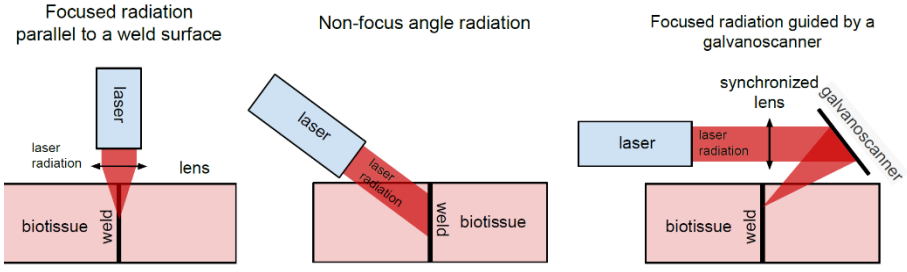
Keywords: mathematical modeling, laser soldering, tissue reconstruction
Funding: The work was supported by the Russian Science Foundation grant 22-75-00089, https://rscf.ru/project/22-75-00089/.

Introduction

Each surgical intervention, regardless of the degree of invasiveness, makes it necessary to restore the integrity of dissected biological tissues. Traditional methods of restoring the integrity of biological tissues have a number of disadvantages: lack of tightness for liquids immediately after formation, toxicity, and the formation of a large scar. Laser welding of biologically active tissues is devoid of these disadvantages. However, the method of laser welding of biological tissues does not allow the formation of deep joints. The research is aimed at overcoming this limitation.

Materials and Methods

The absorption of laser radiation in the model was calculated using Bouguer-Lambert-Bera law [1], the degree of formation of the laser weld and temperature necrosis of biological tissues using the Arrhenius equation [2, 3]. Heat transfer has been calculated using the heat transfer equation. Solders are used to increase the strength of the seams [4]. The main limitation in the formation of a deep weld is the intense absorption in the upper layers of the solder. An increase in the intensity of laser radiation leads to a more intense heating of the connected biological tissues, which leads to temperature necrosis. To date, two irradiation schemes are used for the area of laser weld formation (Fig. 1 a and b). When using both schemes, the transport of radiation deep into the seam will inevitably lead to an increase in the area of thermal necrosis of biological tissue.



a b c

Fig. 1. Способы транспортировки лазерного излучения до области формирования шва: focused radiation parallel to a weld surface (a), non-focus angle raiation (b), focused radiation guided by a galvanoscanner (c)

The paper simulates the use of an irradiation scheme for the formation of a laser weld using a galvanoscanner with a synchronized lens (Fig.1 c).

Results and Discussion

Fig. 2 shows the temperature distribution in the area of laser weld formation at a depth of l up to 1 mm. The peaks on the temperature graphs clearly indicate local heating of the weld formation area. The area of elevated temperature to the right of the peak illustrates the area of seam formation, which was heated earlier and did not have time to cool down. Increasing the pulse duty cycle will reduce the overall heating of both the seam formation area and the already formed seam.

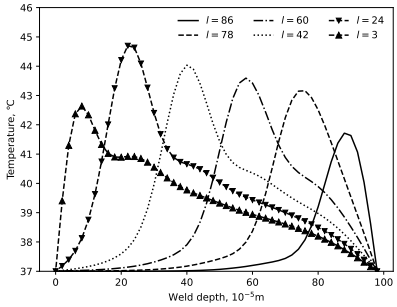


Fig. 2. The dependence of the temperature in the laser seam on the depth for different focusing depths *l*

Conclusion

In the work, the possibility of forming deep laser welds using a new method of transporting laser radiation is shown by mathematical modeling. The proposed method of transporting laser radiation will allow the welding of biological tissues up to several millimeters thick.

REFERENCES

[1] **Ryabkin D.,** Amendments of weld formation in human skin laser soldering. J. of Biophotonics, 16(8) (2023) e202300070.

[2] **Pearce J.A.,** Comparative analysis of mathematical models of cell death and thermal damage processes. Int. J. Hyperthermia, 29(4) (2013) 262-280.

[3] **Gosalia K., Weiland J., Humayun M.,** Thermal elevation in the human eye and head due to the operation of a retinal prosthesis, IEEE Trans. Biomed. Eng. 51(8) (2004) 1469–1477.

[4] **Gerasimenko A. Yu.,** Use of indocyanine green in nanocomposite solders to increase strength and homogeneity in laser welding of tendons. Biomedical Engineering, 50(1) (2017) 310-313.

Survival rate, viability and transfection of eukaryotic cells on GaP and GaAs nanowires.

Z. P. Sosnovitskaia[1], **S. V. Shmakov**[1✉], **E. A. Makhneva** [1], **V. M. Kondratev** [1,2], **A. D. Bolshakov**[1,2]

[1] Alferov University, Khlopina 8/3, 194021, St. Petersburg, Russia

[2] Moscow Center for Advanced Studies, Kulakova str. 20, Moscow 123592, Russia

✉*stas-svs@list.ru*

Abstract. The delivery of genetic material into eukaryotic cells is a significant challenge in life sciences. Many of the transfection methods used are highly toxic. This study aims to investigate the possibility of using mechanoporation, which is mechanical membrane poration using semiconductor nanowires (NWs, also known as whiskers), and to explore the correlation between the transfection conditions and the efficiency and toxicity of the method.

The survival of Hela and CT26 cells on NSCs was investigated based on the morphology and chemical composition of whiskers. We also examined the changes in the cytoskeleton of Hela cells and the cell cycle of Hela and CT26 cells cultured on whiskers. Additionally, we demonstrated the possibility of mechanoporation using HEK 293T.

This study demonstrates that cells can divide on a NWs, and their survival is dependent on the morphology of the crystals. No significant changes in the cell cycle were detected when cultured on whiskers. The degree of cytoskeleton disruption is directly related to the average length of the nanowires. On short crystals, the cytoskeleton is preserved. The example of plasmid encoding GFP and HEK 293T cells demonstrates the successful delivery of genetic material by mechanoporation.

Keywords: transfection, mechanoporation, nanowires

Funding: The work was supported by RSF (grant № 23-24-00288**)**

Introduction

Transfection - the delivery of nucleic acids into eukaryotic cells - is one of the most relevant tasks in modern life sciences. The creation of genetically modified cells allows solving a wide range of problems. This work demonstrates the feasibility of mechanoporation, a new physical method of cell transfection using semiconductor nanowires (NWs, also known as whiskers) - thin vertical needles - and the study of cell survival and viability on NWs as a function of morphology and chemical composition.

Materials and Methods

Viability studies were conducted using cervical cancer cell line Hela murine colon carcinoma cell line CT26 EGFP expressing the *EGFP* gene. The cells were cultured on the surface of GaP NWs with average lengths of 4, 8.5, and 32 μm, as well as GaAs with lengths of 2 and 24 μm. A control group was cultured on a bare Si surface. Living cells were evaluated using Hoechst 33342 dye and dead cells were recorded with propidium iodide staining, both through confocal microscopy. Confocal microscopy was used to visualize the actin cytoskeleton and endocytosis. Flow cytometry was employed to investigate the cell cycle of cells cultured on whiskers.

The possibility of transfection by NWs was demonstrated by adding a plasmid encoding GFP to the culture medium using HEK 293 T cells. The experiments used GaP whiskers with characteristic lengths of 2, 4 and 8.5 μm.

Results and discussion

The results of the study on the survival of cells cultured on NWs are presented in Figure 1. It was observed that the length of whiskers affects cell viability. The highest number of dead cells was recorded on GaP NWs with a average length of 32 μm and GaAs with an average length of 24 μm. The number of live cells compared to the control sharply decreases during the first day, and subsequently, the viability of cells on the crystals does not differ from the control. When studying the

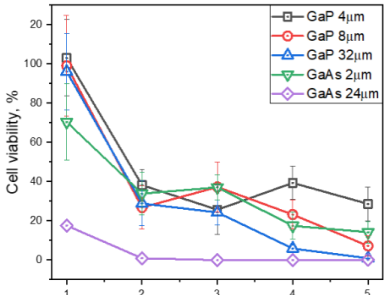


Fig.1. cells' viability on vertical NWs with varying geometry and composition.

actin cytoskeleton of cells cultured on nanowires, it has been observed that long crystals penetrate inside the cell and damage the cytoskeleton. However, on short whiskers, the cytoskeleton remains intact. The cell cycle of Hela cells remains almost unchanged when cultured on crystals, whereas CT26 shows a significant increase in the subG phase on GaAs 2 μm and GaP 8.5 μm. This increase may indicate the beginning of apoptosis, but the ratio between the other phases remains the same. The plasmid encoding GFP was added to the culture medium to perform transfection. Confocal microscopy revealed that cells expressed the GFP gene on the nanowires, but not on the bare Si substrate. Flow cytometry confirmed the transfection.

The cells were capable of degrading and endocytosing whiskers, which was confirmed by flow cytometry when cultured on NWs with fluorescent inserts.

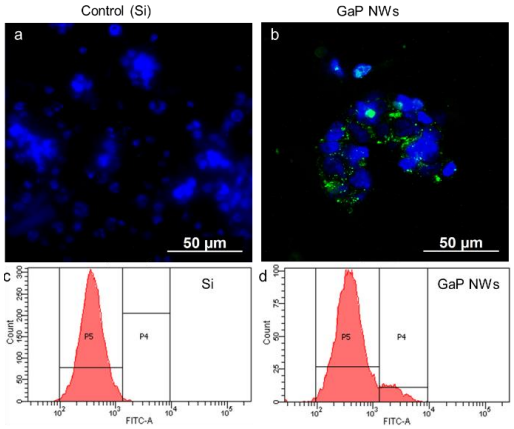


Fig.2. Transfection with the use of vertical NWs. Confocal fluorescence images of the HEK 293T: a) on bare Si substrate, b) on 2 μm long vertical GaAs NWs. Histograms of the cells' fluorescence in flow cytometry FITC channel, cells cultured on: c) Si substrate, d) on 2 μm long GaAs NWs.

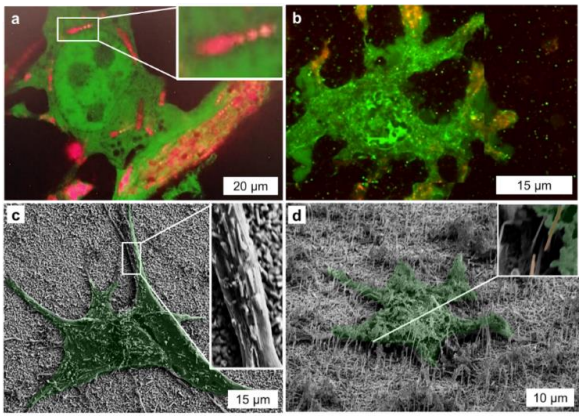


Fig.3**.** a) confocal fluorescence image of a cell with broken NWs infiltrated by the cell after 72 h of incubation b) fluorescence image of a cell with endocytosed NWs after 120h incubation; c) false color SEM image of a single cell on vertical NWs; d) inclined view false color SEM image of a cell.

Conclusion

The study compared the viability of CT26 cells on GaP, GaAs nanocrystals , and bare Si and obtained data on the dependence of cell survival on the average length of the nanocrystals. The results indicate that cell survival on short nanocrystals is higher than on long ones. The study demonstrates the relationship between the degree of cytoskeleton destruction and whisker morphology, and indicates that there were no significant changes in the cell cycle during culturing on nanocrystals. The experimental results show that the cell is capable of destroying and endocytizing whiskers.

REFERENCES

1. **Choi S, Kim Y, Lee JW, Park J, Prausnitz MR, Allen MG**, Intracellular protein delivery and gene transfection by electroporation using a microneedle electrode array. Small 2012;8:1081–91.
2. **Figueroa E, Bugga P, Asthana V, Chen AL, Stephen Yan J, Evans ER**, et al. A mechanistic investigation exploring the differential transfection efficiencies between the easy-to-transfect SK-BR3 and difficult-to-transfect CT26 cell lines. J Nanobiotechnology 2017;15:1–15.
3. **Fedorov V V, Bolshakov AD, Dvoretckaia LN, Sapunov GA, Kirilenko DA, Mozharov AM**, et al. Self-Catalyzed MBE-Grown GaP Nanowires on Si(111): V/III Ratio Effects on the Morphology and Crystal Phase Switching. Semiconductors 2018;52:2092–5. https://doi.org/10.1134/S106378261816008X.

Intravital microscopy: dorsal skinfold chamber model.

M. E. Stepanov [1✉], **A. A. Vlasov** [1], **P. A. Demina**[1,2,3], **R. A. Akasov**[1,2,3], **G. Babayeva**[4], **A. N. Generalova**[1,2,3], **E. V. Khaydukov** [1,2,3]

[1] Moscow State Pedagogical University, Moscow, Russia;

[2] FSRC «Crystallography and Photonics» RAS, Moscow, Russia

[3] Shemyakin-Ovchinnikov Institute of Bioorganic Chemistry RAS, Moscow, Russia

[4] Research Institute of Molecular and Cellular Medicine, RUDN University, Moscow, Russia

✉stepanov_me@mail.ru

Abstract. Intravital microscopy (IVM) is a great tool to investigate multicellular living organism in all of its natural complexity. It combines precision of light microscopy with real-time character of traditional magnetic resonance/computed tomography imaging. In this work we demonstrate effectiveness of self-engineered dorsal skinfold chamber IVM model on examples of brightfield and fluorescent microscopy to study vasculature as well as extravasation of small Cy-5 dye molecules.

Keywords: IVM, DSC, bioimaging, vasculature, extravasation, cyanine dyes, Cy-5.

Funding: The study was prepared as part of the work on the topic «Laser technologies for biomedical applications» (№ 122122600055-2) under the state order of the Ministry of Education of the Russian Federation.

Introduction

The intravital microscopy (IVM) is an innovative method “to see the unseen” as was elegantly put into words by the authors of [1]. As opposed to the traditional *in vitro* and *ex vivo* methods, IVM method is an *in vivo* one, meaning that it works on level of multicellular living organisms providing an opportunity to observe cells and tissues in their native environment conditions (including all the endogenous signaling pathways and complex interactions) in real time while staying at the cell-resolution level or even beyond [2]. Moreover, the observation process can be done in none- or minimal-invasive way to let the physiological/pathological processes under interest to develop naturally [3].

There are several different ways to provide *in vivo* observation in mouse models. Most general obstacle for their use is that live tissue is not opaque. To overcome this an intrinsic requirement for the tissue to be at least partially transparent to the light used to carry out the microscopy appears. Generally, there are some ways to avoid the issue, for example: 1) use light wavelengths from tissue transparency windows (red part of visible or near infrared) which are most suitable for low-background observation, 2) use thin tissue layers (light typically penetrates only ~10 μm of living tissue), 3) use some special illumination conditions (as in multiphoton IVM case [4]). Considering these requirements some standard models were created to ether look through thin (ear, transdermal) or transparent (eye, ocular) tissues, or through surgically implanted windows allowing long lasting observation. Among the last category one of the most convenient models is dorsal skinfold chamber (DSC) model [5], where observation is carried out through the window made in the skinfold on mouse back after partial resection of the skin layers.

DSC model allows to investigate a number of processes including metabolic changes, angiogenesis, properties of vessels and blood flow (vasodilatation under different factors, velocities of blood flow, extravasation), pharmacokinetics of drugs or carriers, immune system dynamics, cancer development details, microenvironment and complex interactions between the cells and so on [6].

In this work we implemented the DSC mice model to carry out IVM in brightfield and fluorescent regimes to study microparameters of native tissues: vasculature and fluorescent dye distribution.

Materials and Methods

The self-engineered polycarbonate DSC was surgically mounted on shaved mouse back in sterile conditions after subjecting mouse to anesthesia (20-40 mg/kg Xylazine intramuscularly and 5-10 mg/kg Zoletil intraperitoneally 10 minutes after). Skin in window area was partially resected

and then covered with glass. Several mice were surgically prepared in this way. Two days after operation mice were anesthised in the same way to conduct the IVM observations using the fluorescent microscope Motic AE31E. White Halogen illumination (Koehler setup) was used to perform brightfield studies; set of appropriate fluorescent filters was used to conduct the fluorescent illumination. Raptor Photonics Camera (digital FALCON EMCCD FA285-CL) was used as a detector. In each case the objectives were lifted using special spacers to compensate for the lifting of the DSC window above the height of microscope table. The Cy-5 amine dye injected intravenously was used to contrast the vasculature.

Results and Discussion

The DSC-based brightfield studies of mice vasculature has shown the effectiveness of method as well as the applicability the newly designed construction. Mice weren't showing any signs of stress related to the implanted dorsal chambers demonstrating the usual behavior (up to month) which we contribute to the lightness and compactness of the construction. Several experiments were carried out to study the overall contrasting capabilities of the method, which was shown to be varying depending on the anatomical features and individual operation details. In some of the cases non-transparent layers of the mouse subcutaneous tissues were clearly found to block the light. Even in these cases we managed to see through and study vasculature characteristics using Cy5-amine dye (excitation/emission at 646nm/662nm). Using the method, we managed to observe the blood flow clearly and studied the kinetics of extravasation of the dye to the surrounding tissues.

It is important to note some of the difficulties we encountered with while preparing the experiments. Surgical operation of the kind requires some expertise since it is possible otherwise to leave some none-transparent subcutaneous tissue behind, which will conceal the details by scattering light. The spacers used for objectives need to be carefully chosen to compensate for the overall height of mouse holding construction. The material for the DSC should preferentially be light-weighted (plastic) and biocompatible [7].

Conclusion

In present work DSC method based on self-engineered polycarbonate construction was implemented to perform IVM on mice. The vasculature and tissues were clearly seen both in brightfield and fluorescent regimes which allowed the investigation of vasculature characteristics and fluorescent dye Cy-5 amine extravasation dynamics.

REFERENCES

1. **Ishii M.** Intravital imaging technology reveals immune system dynamics in vivo // Allergol Int. – 2016. – T. 65, № 3. – C. 225-7.
2. **Jing Y., Zhang C., Yu B., Lin D., Qu J.** Super-Resolution Microscopy: Shedding New Light on In Vivo Imaging // Front Chem. – 2021. – T. 9. – C. 746900.
3. **Coste A., Oktay M. H., Condeelis J. S.,** Entenberg D. Intravital Imaging Techniques for Biomedical and Clinical Research // Cytometry A. – 2020. – T. 97, № 5. – C. 448-457.
4. **Liang Y., Walczak P.** Long term intravital single cell tracking under multiphoton microscopy // J Neurosci Methods. – 2021. – T. 349. – C. 109042.
5. **Laschke M. W., Menger M. D.** The dorsal skinfold chamber: A versatile tool for preclinical research in tissue engineering and regenerative medicine // Eur Cell Mater. – 2016. – T. 32. – C. 202-15.
6. **Giampetraglia M., Weigelin B.** Recent advances in intravital microscopy for preclinical research // Curr Opin Chem Biol. – 2021. – T. 63. – C. 200-208.
7. **Xie W., Lorenz M., Poosch F., Palme R., Zechner D., Vollmar B., Grambow E., Struder D.** 3D-printed lightweight dorsal skin fold chambers from PEEK reduce chamber-related animal distress // Sci Rep. – 2022. – T. 12, № 1. – C. 11599.

Modified natural polymers with bioactive additives for restoration of critical bone defect

M. Yu. Suchkov [1,2✉], **V.I. Kuzyaeva** [3], **I.S. Sergeev** [3,4], **G. Babaeva** [5], **P.A. Demina** [2,3,6], **A.V. Sochilina** [2,3,6], **R.A. Akasov** [2,3,7], **T.V. Egorova** [2], **E.V. Khaydukov** [2,3,6], **A.N. Generalova** [6]

[1]Pirogov Russian National Research Medical University, Moscow, Russia;
[2]Moscow State Pedagogical University, Moscow, Russia;
[3]National Research Centre "Kurchatov Institute", Moscow, Russia;
[4]Skolkovo Institute of Science and Technology, Moscow, Russia;
[5]Research Institute of Molecular and Cellular Medicine, RUDN University, Moscow, Russia;
[6]Shemyakin-Ovchinnikov Institute of Bioorganic Chemistry RAS, Moscow, Russia;
[7]Sechenov First Moscow State Medical University, Moscow, Russia

✉ max.suchkov3001@yandex.ru

Abstract. A critical bone defect is a defect that cannot self-repair and therefore requires a tissue engineering approach. Photocrosslinkable hydrogels based on natural polymers are promising biomaterials for the critical bone defect treatment, highly demanded in tissue engineering due to cell compatibility, possibility of 3D structure formation, high biocargo capacity and capability for customization. In this work, we demonstrate that photocrosslinkable materials based on gelatin and hyaluronic acid modified with glycidyl methacrylate are able to form crosslinked hydrogel *in situ* under short-term near-UV irradiation. The photocompositions containing bioactive factors (autograft and autologous cells) were studied *in vivo* using the model of the critical bone defect in the calvaria of mice. The designed hydrogel photocompositions can be injected into the bone defect and photocrosslinked under 365 nm irradiation leading to partial recovery of the critical bone defect within 45 days.

Keywords: critical bone defect, hydrogel scaffolds, biocompatible natural polymers, hyaluronic acid, gelatin, glycidyl methacrylate, *in situ* photocrosslinking.

Funding: The article was prepared as part of the work on the topic «Laser technologies for biomedical applications» (№ 122122600055-2) under the state order of the Ministry of Education of the Russian Federation. The work was financially supported by the Russian Science Foundation, grant 21-79-10384 (in vivo polymerization).

Introduction

A critical bone defect (CBD), which occurs as a result of trauma, surgery and oncology [1], is a defect that is not capable of self-regeneration [2], and it remains an unsolved issue today. Standard protocols based on bioceramics, metals, syngeneic and xenogeneic transplantation, and scaffolds 3D printed for the regeneration of CBD need optimization, as they have several disadvantages. It takes a long time to produce the scaffolds. The risks of complications are significant: development of autoimmune reaction, acute inflammation, scaffold rejection due to non-resorption. However, the use of bioactive scaffolds based on biocompatible natural polymers, such as hyaluronic acid and gelatin [3], is a promising solution. Although, in order to use them, modification with groups capable of covalent crosslinking [4] is necessary, since it will increase mechanical strength and inhibit enzymatic degradation of scaffolds. Conjugation with reagents containing double bonds, such as glycidyl methacrylate (GMA), allows the crosslinking of polymer derivatives not only with traditional radical initiators, but also with photoinitiators that activate the reaction under the light irradiation of a specific wavelength, which opens the possibility of *in situ* filling with liquid materials containing living cells [5] and bioactive additives, thus expanding the potential for future use of laser technologies.

Materials and Methods

The study involved performing surgery under general anesthesia to create an artificial CBD on the calvarium of Balb/c mice, approximately 5 mm in diameter. A liquid hydrogel based on

modified with glycidylmethacrylate hyaluronic acid (GMA-HA) and modified with glycidylmethacrylate gelatin (GMA-gelatin) containing the photoinitiator LAP (lithium phenyl-2,4,6-trimethylbenzoylphosphinate) at a concentration of 0.12%, was injected into the area where the surgery was performed on each animal. Next, the compositions were photocrosslinked using UV radiation at a wavelength of 365 nm. After this, a seam was created and treated with BF-6 glue. Within 3 days of the surgery, the animals received an antibiotic treatment with Amoxiclav at a volume of 100 µl.

Intravital observation of CBD regeneration was conducted using computed tomography on the IVIS Spectrum CT visual analysis platform on days 14, 28 and 45 after the surgery. The data were analyzed using the ImageJ program. Histological sections were prepared and stained with hematoxylin and eosin, following the standard procedure.

Results and Discussion

All mice were divided into two experimental groups of 15 and 12 mice, respectively. In group I photocompositions containing GMA-HA (20%) or GMA-gelatin (15%) in the presence of autologous bone tissue and without autograft were studied. By the end of the experiment on day 45 in group I, regeneration with a photocomposition based on GMA-gelatin in the presence of an autograft occurred most effectively compared to other compositions (the degree of defect coverage was approximately 95%). However, histological examination demonstrated that calcification of the hydrogel occurred without the formation of new osteoblasts, unlike GMA-HA (~ 64%).

In group II hydrogels based on GMA-HA (20%) and GMA-HA with an admixture of GMA-gelatin at a ratio of (19%: 1%) and (17%: 3%), respectively, were studied in the presence of mesenchymal stem cells (MSC), derived from the mice, or osteoblasts (Diff), differentiated from MSC *in vitro*. As a result, regeneration with photocompositions based on GMA-HA in the presence of a suspension of MSC and Diff cells occurred more efficiently (~ 40% and ~ 35%, respectively) compared to other compositions of the group II. Nevertheless, in all instances, regeneration was significantly inferior to results from group I (~ 64 %).

Conclusion

The use of photocompositions based on GMA-HA and GMA-gelatin show potential for effective restoration of CBD compared to operated controls. The best results in the restoration of the critical bone defect are achieved through the use of autologous bone tissue. Safety dose of 365 nm light radiation (100 mW/cm^2, 5 sec) and nontoxicity of hydrogel components, confirmed by histomorphological analysis, indicate new opportunities for *in situ* manufacturing of bone tissue equivalents and implantable devices directly *in vivo*.

REFERENCES

1. **Tan B, Tang Q, Zhong Y, Wei Y et al.**, Biomaterial-based strategies for maxillofacial tumour therapy and bone defect regeneration, Int J Oral Sci. 13 (1) (2021) 9.
2. **Schemitsch E.**, Size Matters: Defining Critical in Bone Defect Size, J of Orthopaedic Trauma. 31(10) (2017) 20-22.
3. **Collins M. N., Ren G., Young K. et al.**, Scaffold Fabrication Technologies and Structure/Function Properties in Bone Tissue Engineering, Adv. Funct. Mater. 31 (2021).
4. **Sochilina A. V. et al.**, Preparing Modified Hyaluronic Acid with Tunable Content of Vinyl Groups for Use in Fabrication of Scaffolds by Photoinduced Crosslinking, J of Bioorganic Chemistry. 47 (2021) 828-836.
5. **Chai S., Huang J., Mahmut A., Wang B. et al.**, Injectable Photo-Crosslinked Bioactive BMSCs-BMP2-GelMA Scaffolds for Bone Defect Repair, Front Bioeng Biotechnol. 10 (2022).

Investigation of solder based on nanoparticles with metallic properties for laser reconstruction of blood vessels

V. V. Suchkova [1]✉, **D. I. Ryabkin**[1,2], **P. A. Varlamova**[2], **A. Yu. Gerasimenko**[1,2]

[1] I.M. Sechenov First Moscow State Medical University, Moscow, Russia;

[2] National Research University of Electronic Technology MIET, Zelenograd, Moscow, Russia

✉suchkova_v_v@staff.sechenov.ru

Abstract. Laser blood vessel reconstruction is a modern, non-invasive method of blood vessel closure. Until now, most previous work has used protein and dye-based solders (laser absorbers) to form welds. However, the addition of nanoparticles to the solder, which have outstanding bactericidal properties and the ability to accelerate wound epithelialisation, has the potential to improve the efficiency of optical wound healing. The aim of the study was to experimentally investigate the physicochemical properties of dispersed solders including antibacterial nanoparticles of metals Ni, Al, Fe_3O_4 and carbon nanotubes with metallic properties, biopolymer - albumin, and dye localizing laser radiation in the area of wound dissection - indocyanine green, the formation of a biological tissue compound and the study of their mechanical properties. The selected nanoparticles have a high absorption coefficient of laser radiation, which provides high efficiency of laser energy utilization and allows recovery with minimal losses. The effectiveness of solders with different metal nanoparticles was experimentally tested in cattle vessels. Tissue reconstruction was performed by diode laser with a wavelength of 810 nm. The suture was formed within 1 minute. The laser exposure temperature was 55°C for each particular specimen. The results showed that the highest tensile strength was in the specimen with carbon nanotubes. The achieved strength with carbon nanotubes was 950 kPa.

Keywords: vessel reconstruction, nanoparticles, laser soldering

Funding: The work was supported by the Russian Science Foundation grant 22-75-00089, https://rscf.ru/project/22-75-00089/.

Introduction

Laser blood vessel reconstruction is a modern method of tissue healing, which is a non-invasive alternative to traditional methods. Laser tissue reconstruction is based on the reversible change in the molecular structure of tissues under the thermal action of laser radiation. To prevent thermal necrosis of tissues, solder is applied to the area of dissection, which is an aqueous dispersion of protein albumin and dye indocyanine green [1]. The addition of nanoparticles to the solder, which have outstanding bactericidal properties and the ability to accelerate wound epithelialization, can potentially increase the efficiency of the optical method of wound healing [2,3].

The aim of the study was to experimentally investigate the physicochemical properties of dispersed solders incorporating antibacterial metal nanoparticles Ni, Al, Fe_3O_4, and carbon nanotubes with metallic properties, to form vessel connection and investigate their mechanical properties. However, increasing the concentration of carbon nanotubes leads to a significant increase in the density and viscosity of the solder, making it less manageable and controllable.

Materials and Methods

Solder manufacturing. All solders were an aqueous dispersion of bovine serum albumin at a concentration of 25 wt.%, indocyanine green 0.1 wt.%, and the corresponding nanoparticles at concentrations ranging from 0.001 wt.% to 0.1 wt.%. A total of 28 different solders were prepared, varying in the type and concentration of nanoparticles. All solders were produced using the same technology. Metal nanoparticle powder was added to distilled water until the desired concentration was achieved. The resulting mixture was processed with a submersible ultrasonic homogenizer until the medium became homogeneous. Then, with continuous stirring, indocyanine green and bovine serum albumin were added to the dispersed medium. The resulting solder was treated in an ultrasonic bath until the protein was completely dissolved.

Solder research methods. The following were selected as the main characteristics of solders affecting the strength of the laser connection of vessels: optical characteristics (absorption and transmittance), solder viscosity, studies of agglomerate sizes using the method of dynamic light scattering, and solder density.

Ex vivo testing of solders. The efficacy of solders with different nanoparticles was tested experimentally on bovine vessels. Tissue reconstruction was performed using a diode laser with a wavelength of 810 nm. The suture was formed within 1 minute. The laser exposure temperature was 55°C for each specific sample [4,5].

Results and Discussion

Research results have demonstrated that carbon nanotube-based solder provides the highest strength of vessel connections. The tensile strength was 950±30 kPa. Solder based on carbon nanotubes has the highest absorption capacity, allows to localize the radiation as much as possible in the area of the joint formation and increases the strength of the formed joints by 10 times in comparison with solder without nanoparticles. The nanoparticles used in concentrations below 0.05% do not make a significant contribution to the viscosity and density of solders. However, increasing the concentration of carbon nanotubes leads to a significant increase in the density and viscosity of the solder, making it less manageable and controllable. The worst values were shown by aluminum-based nanoparticles with a particle size of 50 nm. During welding, the particles, due to their high thermal conductivity, quickly began to burn at the same soldering temperature as the other samples and led to thermal necrosis of the surrounding tissue. This is caused by the high tendency of aluminum nanoparticles to agglomerate. When radiation hits a large agglomerate, it leads to tissue overheating.

Conclusion

A new approach based on the high efficiency of laser energy and the excellent bactericidal properties of nanoparticles may lead to accelerated epithelialization of wounds and improved healing. The results of experiments on bovine aorta suggest that the use of solders with metal nanoparticles and carbon nanoparticles with metallic properties may be promising for the development of laser tissue reconstruction methods.

REFERENCES

1. **Gomes D.F., Galvana I, Ramos Loja M.A.**, Overview on the Evolution of Laser Welding of Vascular and Nervous Tissues, Applied sciences. 9 (2019) 9102157.

2. **Gerasimenko A. Y., Morozova E. A., Ryabkin, D. I.**, Reconstruction of soft biological tissues using laser soldering technology with temperature control and biopolymer nanocomposites**,** Bioengineering. 9(6)(2022) 238.

3**. Ratto F., Matteini P., Rossi F.**, Photothermal effects in connective tissues mediated by laser-activated gold nanorods, Nanomedicine: Nanotechnology, Biology and Medicine. 5(2) (2009)143-151.

4. **Ryabkin D.I., Suchkova V.V., Gerasimenko A.Yu.**, Modelling of laser welding of biological tissues using focused radiation, St. Petersburg State Polytechnical University Journal. Physics and Mathematics. 16 (3.2) (2023) 344–348.

5. **Li C., Wang K., Huang J**. Simulation of the effect of spot size on temperature field and weld forming in laser tissue welding, Optik. 155(2018) 315-323.

Fluorescent cell imaging with femtosecond laser pulses-produced protein nanoaggregates

A. A. Astafiev [1]✉, A. M. Shakhov [1], M. S. Syrchina [1], V. A. Nadtochenko [1]

[1]N.N. Semenov Federal Research Center of Chemical Physics,
Russian Academy of Sciences, Kosygina 4, Moscow, Russia

✉wrongclue@gmail.com

Abstract. Proteins can form aggregates with bright visible fluorescence in response to various physicochemical stimuli. Here we examined products formed by irradiation of aqueous solution of the bovine serum albumin with high intensity femtosecond laser pulses. Laser irradiation results produces nanoscale protein aggregates with broadband optical absorption and appreciable visible fluorescence. We demonstrate that these fluorescent aggregates are biocompatible and can be effectively employed for live cell imaging

Keywords: proteins, femtosecond laser pulses, nanomaterials, fluorescence, bioimaging.

Funding: This study was funded by Russian Science Foundation, grant number № 21-72-20169.

Introduction

Femtosecond laser synthesis of fluorescent nanoproducts from biomolecules is an intriguing phenomenon, which can be exploited in novel approaches to bioimaging [1-2]. Previously we demonstrated laser synthesis of fluorescent carbon dots (CDs) from essential amino acids [3]. As a next step, we study products, obtained from a model protein bovine serum albumin (BSA). It is known, that albumin can form aggregates, which unlike the monomer protein, emit bright visible fluorescence [4]. We examined, if the femtosecond laser irradiation can trigger similar aggregation of BSA and formation of fluorescent products and studied their optical properties. We probed biocompatibility of BSA products and their employment as fluorescent cell imaging agents.

Materials and Methods

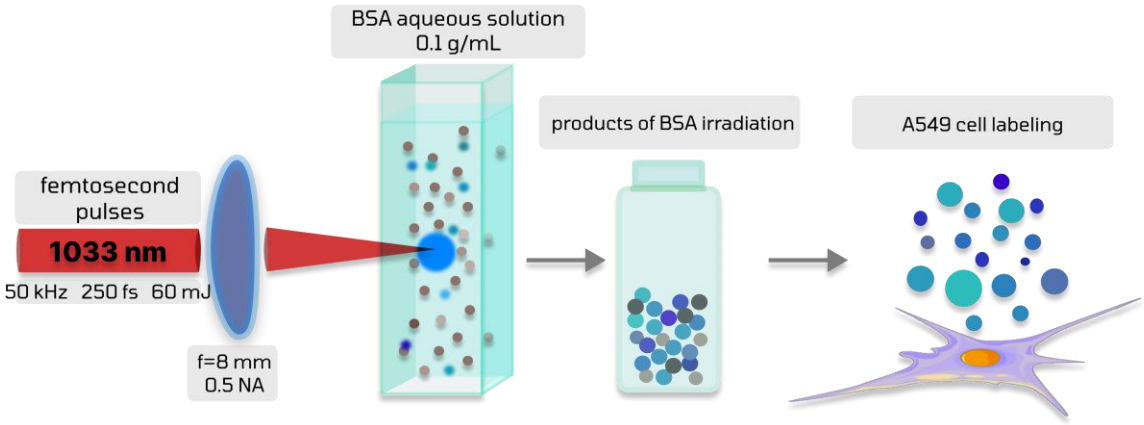


Fig.1 Experimental setup.

Synthesis and characterization of products. Aqueous solution of BSA (1 mL, 0.1 g/mL) in a glass vial was irradiated with trains of femtosecond laser pulses focused by a spherical lens (f=8 mm, 0.5NA). Central wavelength of laser pulses was 1033 nm, repetition rate - 50 kHz, duration - 250 fs, pulse energy - 60 μJ. Absorption of photoluminescence spectra of BSA in water were recorded with Shimadzu spectrophotometer (UV-3600) and spectrofluorometer (RF-5031 PC). Fluorescence quantum yield (356 nm excitation) was estimated with the slope method using ethanol solution of anthracene as a standard. Fluorescence decay and fluorescence anisotropy decay kinetics in aqueous solution were registered with pulsed laser excitation at 360 nm at 450 nm emission wavelength using time-correlated single-photon counting module (SPC-150N, Becker&Hickl GmbH). Protein aggregate size was analyzed with dynamic light scattering (DLS) technique using a Photocor Compact-Z setup.

Labeling of living A549 cells. Suspension of A549 cells (lung adenocarcinoma) were incubated at 37 °C in 5% CO_2 humidified atmosphere with CDs dissolved in medium in the ratios of 1:200, 1:40 and 1:8 for 12 hours. Fluorescent images and lambda scans of the cells after labeling were obtained using a laser scanning confocal microscope Zeiss LSM 980 (Carl Zeiss Microscopy, Jena, Germany), 20x Plan-Apochromat objective (NA = 0.8). One-photon excitation was performed with a 405 nm laser. Fluorescence was recorded at 420–750 nm range.

Results and Discussion

Laser irradiation resulted in yellowing of the BSA solution and emergence of broadband optical absorption in the near-Ultraviolet and visible range with large extinction values ~10^4 $M^{-1}cm^{-1}$ (Fig. 1). Irradiated BSA emitted visible fluorescence with emission maximum at 420 nm, excitation maximum at 334 nm and a quantum yield of 7.4%. Fluorescence spectra were excitation wavelength-dependent. DLS demonstrated formation of aggregates in the irradiated BSA solution with characteristic hydrodynamic radius of ~30 nm. Large fluorescence anisotropy decay time (34 ns) confirmed that fluorescence is attributed to BSA or its aggregates. Cell imaging revealed cellular uptake of fluorescent particles. Vesicles with bright blue fluorescence were observed within cytoplasm of individual cells. Lambda scanning showed specific areas of brightest fluorescence in blue spectral diapason, corresponding to the positions of vesicles in fluorescent image of cell. Also, gradually reducing ability of cells to attach substrate was noted and was proportional to concentration of CDs. Cells incubated in highest concentration of CDs was predominantly detached from substrate. We demonstrated applicability of femtosecond-laser produced protein aggregates for cell fluorescent imaging.

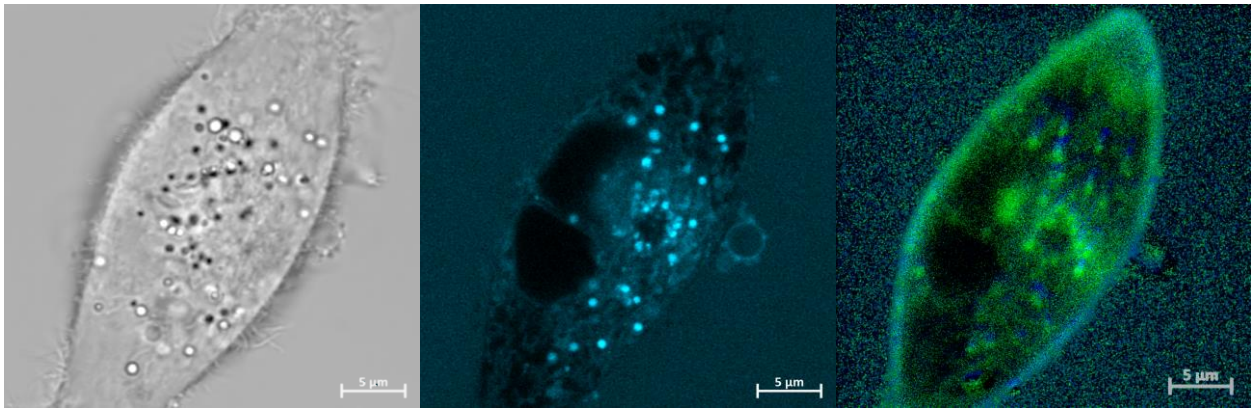


Fig.1. Confocal images of individual A549 cell, incubated with CDs at ratio of 1:40. Bright- field image of the cell *(a)*, confocal fluorescent image at 405 nm wavelength *(b)*, lambda stack and fluorescence distribution within the cell *(c)*.

REFERENCES

1. **Sun Q., Qin Z., Wu W., Lin Y., Chen C., He S., Li X., Wu Z., Luo Y., Qu J.,** In vivo imaging-guided microsurgery based on femtosecond laser produced new fluorescent compounds in biological tissues, Biomedical Optics Express. 9 (2018) 581-590.
2. **Astafiev A.A., Shakhov A.M., Osychenko A.A., Syrchina M. S., Karmenyan A.V., Tochilo U.A., Nadtochenko V.A.,** Probing intracellular dynamics using fluorescent carbon dots produced by femtosecond laser in situ, *ACS Omega*. *5* (21) (2020) 12527-12538.
3. **Astafiev A. A., Shakhov A. M., Gulin A. A., Vasin A. A., Gubina M. V., Syrchina M.S., Nadtochenko V. A**. Femtosecond laser synthesis and comparative analysis of fluorescent carbon dots from L-lysine aqueous solution, Journal of Physics: Conference Series. 2086 (2021) 012121
4. **Bhattacharya A., Bhowmik S., Singh A. K., Kodgire P., Das A. K., Mukherjee T. K.** Direct Evidence of Intrinsic Blue Fluorescence from Oligomeric Interfaces of Human Serum Albumin, A C SLangmuir. 33 (40) (2017) 10606-10615

Structure of bovine serum albumin in solution and films as revealed from vibrational spectroscopy

E. V. Fedotova ✉, **S. V. Paston**
Saint-Petersburg State University, Saint-Petersburg, Russia
✉st077318@student.spbu.ru

Abstract. This study explores the impact of salt concentration and the degree of hydration on the structure of bovine serum albumin (BSA) using vibrational spectroscopy methods, specifically Fourier transform infrared spectroscopy and Raman scattering. BSA, a key plasma protein, plays essential roles in binding and transporting various molecules in the bloodstream. The research focuses on understanding how do the interaction with ions and water molecules affect the secondary and tertiary structure of globular proteins, emphasizing the significance of environmental factors in protein conformation. The results indicate distinct responses in the vibrational spectra of BSA to salt concentration variations, with the Amide I band being particularly sensitive in different conditions. It is shown that BSA structure in dehydrated films containing NaCl is closer to native, hence ions prevent albumin from denaturation and β-aggregation.

Keywords: bovine serum albumin, protein film, Raman spectroscopy, FTIR spectroscopy.

Introduction

A wide variety of approaches based on vibrational spectroscopy have been used to study protein structure. The advantages of this method are a small amount of sample, the ability to study multicomponent systems and complex structures (such as cells, tissues, biological fluids), and the use of a substance in the liquid or solid phase. Methods for diagnosing various diseases are now being actively developed, based on measuring the vibrational spectra of blood, hair and other biological samples, followed by analysis of the structure of proteins [1]. Therefore, an important task is to study the influence of the degree of hydration and the ionic composition of the medium on the secondary and tertiary structure of globular proteins. In this work, the structure of bovine serum albumin (BSA) in solutions and films is studied by varying NaCl concentration using Fourier transform infrared spectroscopy and Raman scattering.

BSA, a prevalent plasma protein, is extensively utilized for studying various aspects of protein behavior, such as folding and aggregation, as well as for biotechnological purposes. BSA primarily functions in binding, transporting, and delivering a wide array of small molecules and metal ions in the bloodstream. Structurally, BSA consists of a single polypeptide chain organized into three domains (I, II, III), with a dominant α-helical secondary structure at room temperature.

Materials and Methods

BSA (DiaM, USA), NaCl reagent grade.

BSA dehydrated films were obtained from protein solutions dried by a nitrogen stream. Raman spectra were measured by Express Raman spectrometer SENTERRA (Bruker). The excitation source was a green and red laser (532, 785 nm), the spectral resolution was 3 cm^{-1}. The laser power on the sample was about 10 and 100 mW. The curve fitting analysis was implemented using the OPUS/IR v 5.0 program and Origin Pro.

IR spectra of albumin solutions and films were recorded on IR Fourier spectrometer Nicolet 8700 (Thermo Scientific), on ATR attachment, with a resolution of 2 cm^{-1}.

Results and Discussion

The protein IR spectra were measured in aqueous solutions with varying NaCl concentrations, as well as in films obtained by drying these solutions. In the vibrational spectra of proteins, the band of peptide group Amide I (about 1650 cm-1) is very sensitive to various forms of secondary structure [2]. The presence of salt causes a hypsochromic shift of this band, and in films under low humidity conditions this shift is more pronounced. Raman spectrum of a

protein along with the vibrational bands of peptide group contains strong signals from amino acids side chains, and it was found to be very sensitive to their conformations and surroundings.

Table 1

Bands assignments for Raman spectra of BSA

		Wavenumbers, cm^{-1}					
Film composition	water	507	557, 570	896, 937	960	1408	1448
	NaCl	503	563	896, 937	-	1404	1444
Band assignment		S-S bridges	S-S bridges	Cα-C, α-helix	Cα-C β-sheet	COO^-	CH_2/CH_3

Table 2

Protein structure markers from Raman spectra of BSA

Structure markers		$\frac{I_{1650}}{I_{1615}}$, $\frac{\%\alpha}{\%\beta}$	$\frac{I_{1365}}{I_{1330}}$, Trp	$\frac{I_{850}}{I_{828}}$, Tyr
Film composition	water	2.72	0.09	0.75
	NaCl	3.48	0.14	0.44

Several vibrational modes can be used to analyze BSA structure (Tables 1,2). One can see that in water media the content of β-sheets is larger then in the presence of NaCl. Analysis of the bands corresponding to vibrations of aromatic amino acids showed that in the films in the presence of salt they are in a less polar environment. Changes observed also in positions of S-S bridges, indicating aggregation process. We can conclude that BSA structure in dehydrated films containing NaCl is closer to native, i.e. ions prevent albumin from denaturation and β-aggregation.

Conclusion

In summary, the experimental study involving the measurement of protein spectra in different conditions highlights the intricate sensitivity of vibrational bands, particularly the Amide I band, to variations in salt concentration and humidity levels. The observed hypsochromic shift in the Amide I band in the presence of salt, especially accentuated in low-humidity film conditions, underscores the impact of environmental factors on protein structure. The investigation into aromatic amino acids vibrations further reveals the influence of salt on the protein environment, indicating a shift towards a less polar state. BSA structure in dehydrated films containing NaCl is closer to native. These findings shed light on the structural alterations of proteins in response to varying conditions and provide insights into the interplay between environmental factors and protein conformation.

Acknowledgments

The work was carried out using the equipment of the resource center of the Research Park of St. Petersburg State University "Center for Optical and Laser Materials Research".

REFERENCES

1. **Chernyshev D.A., Mikhailets E.S., Telnaya E.A.**, et. al, Analysis of infrared spectra of blood serum of patients with multiple myeloma, Journal of Physics: Conference Series, 2103 (2021) 012052, doi:10.1088/1742-6596/2103/1/012052.

2. **Barth. A**. Infrared spectroscopy of proteins. Biochimica et Biophysica Acta, 1767 (2007) p. 1073–1101.

Scattering of ultrashort laser pulses on pseudoknots RNA

A. A. Kharlamova [1]✉

[1] Department of Fundamental and Applied Physics, Northern Arctic Federal University named after M.V Lomonosov 1, Arkhangelsk 1, Russia;

✉ Kharlamova.anastasya2015@yandex.ru

Abstract. The paper theoretically models the scattering spectra of ultrashort laser pulses on an RNA pseudonode and considers the possibility of using the obtained data in genome analysis. Several configurations of pseudo-RNA nodes were selected as a sample for theoretical modeling of the interaction of a laser pulse with matter: a hairpin, a double loop, and a spiral junction. The study of such structures is interesting for the analysis of the DNA genome, as well as for the study of functions such as viral replication, RNA splicing and RNA editing. At the moment, the study of such structural features is difficult, existing methods cannot give an accurate result, especially on long sections of the molecule. In this paper, the interaction of an ultrashort laser pulse with a molecule of four variants is theoretically modeled, when the RNA does not have a pseudonode and when there are hairpins and loops in the structure. The results obtained show the expediency of using laser pulses as a method for determining such structures.

Keywords: ultrashort laser pulses, scattering spectrum, pseudoknots, DNA, RNA.

Funding: The research was supported by the state task of the Russian Federation No. FSRU-2024 -0005.

Introduction

Pseudoknotes of RNA are molecular structures whose main function is the regulation of gene expression and protein synthesis. The molecule is formed by folding onto itself and contains two rod-loop structures that are closed by pairing complementary nucleotides inside the RNA chain. Pseudonodes are interesting for their functions in various biological processes. They affect the stability of DNA, the efficiency of its translation in protein, and the processes of ribosome modification. That is why it is important to search for RNAs containing pseudoknotes in the components of the genome. The main way to predict pseudoknotes are statistical methods and standard methods of minimizing free energy. The main disadvantage of these methods is that such algorithms consider the interaction between closely spaced nucleotides, whereas the formation of a pseudoknotes occurs when nucleotides interact far from each other [1-3]. There are various ways to improve dynamic programming algorithms for finding pseudoknotes, but there is no basic method that could satisfy researchers yet. In this paper, we propose the use of X-ray diffraction analysis data for the study of pseudoknotes RNA [4, 5]. The scattering spectra from various DNA configurations with pseudoknotes in the structure are calculated. The obtained spectra show that the proposed approach can detect a node in a molecule and distinguish it from similar ones.



a) b)

Fig. 1. RNA models for theoretical modeling of the scattering spectrum (*a*) RNA without pseudoknotes (b) Pseudoknotes of the RNA hairpin

Materials and Methods

The article proposes to consider the RNA molecule as a polyatomic system on which an ultrashort laser pulse falls. The modeling of the scattering spectrum is based on the Dirac-Hartree-Fock-Slater model [6,7].

Results and Discussion

As a result of mathematical modeling of the interaction of an ultrashort laser pulse with various DNA configurations, radiation spectra were obtained, the analysis of which confirms the effectiveness of using laser pulses in studies of similar structures (Fig. 2).

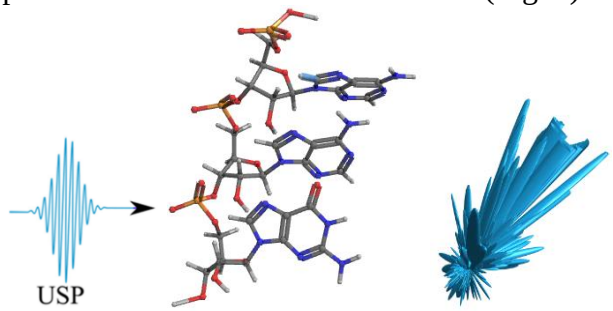


Fig. 2. The process of RNA interaction with an ultrashort pulse and obtaining a 3d spectrum

Conclusion

After analyzing the obtained spectra, we can conclude that the ultrashort pulse method is applicable for studies of changes in the structure of DNA and RNA within several atomic distances.

Acknowledgments

The author expresses gratitude to his supervisor Makarov Dmitry Nikolaevich for significant comments and important advice during the research and the design of this work.

REFERENCES

1. **Staple DW, Butcher S.E**., Pseudoknots: RNA Structures with Diverse Functions. PLoS Biology 3 (2005).

2. **Griffiths-Jones S.,** Annotating Noncoding RNA Genes. Annual Review of Genomics and Human Genetics 8, (2007) 279-298.

3. **Yuan, C., Sun, Y.,** Efficient known ncRNA search including pseudoknots. BMC Bioinformatics 14 (2013).

4. **Shigaev A. S., Ponomarev O. A., Lakhno V. D.,** Theoretical and experimental studies of open states of DNA, Mathematical Biology and Bioinformatics: Physics and Mathematics. 8 (2) (2013) 553-664.

5. **Suryanarayana C., Norton M.**, X-Ray Diffraction: Springer Science & Business Media 2013.

6. **Makarov D. N., Kharlamova A. A.,** Scattering of X-ray Ultrashort Pulses by Complex Polyatomic Structures: J. Mol. Sci 23 (1) (2022) 163.

7. **Makarov D. N., Kharlamova A. A.,** Peculiarities of Scattering of Ultrashort Laser Pulses on DNA and RNA Trinucleotides: J. Mol. Sci 23(23), (2022) 15417.

THE AUTHOR

ANASTASIIA KHARLAMOVA
Kharlamova.anastasya2015@yandex.ru
ORCID:-0000-0002-8192-615X

Pteridines Sensors Based on Amino Acids-Stabilized Gold Nanoclusters

N. V. Shekhovtsov [1✉], **T. S. Sych** [1], **A. A. Buglak** [1], **A. I. Kononov** [1]
[1] St Petersburg University, Saint-Petersburg, Russia
✉st054916@student.spbu.ru

Abstract. Pteridines are an important group of heterocyclic compounds found in human body and used in diagnostics of various disorders (e.g. oxidative stress, inflammation, cancer). In this study, a simple and selective approach is presented for determination of three pteridines: pterin, leucopterin and folic acid. As possible fluorescent sensors for these compounds, several gold nanoclusters were synthesized using various aromatic amino acids (L-Tryptophan, 3,4-Dihydroxy-L-phenylalanine, L-Tyrosine and L-Phenylalanine). It was found that their luminescence was quenched or enhanced on addition of pterin, leucopterin and folic acid depending on the analyte and the stabilizing matrix. I.e. the clusters acted as either 'turn-off' or 'turn-on' sensors. The wide ranges of linear dependence on concentration as well as obtained limit of detection values suggest that these amino acids-stabilized complexes can be considered potential cost-effective systems for pteridines detection in biological fluids.

Keywords: pterin, folic acid, luminescent cluster, metal nanosensors, amino acids.

Funding: This study was supported by the Russian Science Foundation grant number 20-73-10029.

Introduction

Pteridines are a group of organic compounds found in living organisms mostly as coenzymes. Various pteridines (e.g., pterin (Ptr) and folic acid (FA)) are significant biomarkers, and their concentration in biological fluids is used in diagnostics of inflammation, phenylketonuria, cancer, etc. [1]. The strategies of pteridines detection include various chromatography methods [2] and capillary electrophoresis [3], which are time-, labor-consuming and expensive. Hence, developing of new simple, cheap and fast techniques is in great demand.

Fluorescent gold nanoclusters (NCs) are promising biosensors due to their good biocompatibility and high chemical stability as well as low toxicity [4]. Among other biocompatible compounds that are used for metal cluster synthesis, aromatic amino acids (AAs, such as L-Tryptophan (Trp), 3,4-Dihydroxy-L-phenylalanine (DOPA), L-Tyrosine (Tyr) and L-Phenylalanine (Phe)) possess the advantages of low molecular weight and the ability to serve as reducing agents.

In our study, we synthesized new fluorescent amino acid-templated gold nanoclusters (AA-Au NCs) emitting in the violet-blue region of the visible spectrum. The clusters obtained were applied to the in vitro determination of Ptr, leucopterin (Lep) and FA.

Materials and Methods

In a typical synthesis procedure, a solution of AA (DOPA, Trp, Tyr or Phe) at a certain pH was mixed with chloroauric acid ($HAuCl_4$) and then incubated for 1 hour at 60 °C with constant stirring. The obtained AA-AuNCs emitted in the violet-green range upon excitation with UV light. All of them were tested for sensitivity to Ptr, Lep and FA. In each sensing test, the luminescence intensity of a cluster was measured in the absence and in the presence of various concentrations of the analyte. The observed changes (if any occurred) were then analyzed and the sensor characteristics were derived, including limit of detection (LOD) of the analyte.

Absorption spectra were obtained with a Specord 210 Plus double-beam spectrophotometer (Analytik Jena). Fluorescence emission and excitation spectra were recorded at room temperature using an RF-6000 spectrofluorophotometer (Shimadzu).

Results and Discussion

Figure 1 shows the absorption and luminescence emission spectra of Trp-stabilized NCs (Trp-AuNCs) (a), as well as the plot of its luminescence intensity *I* enhancement vs. FA

concentration *[FA]* (b). The good linear relation between normalized intensity I/I_0 and *[FA]* with R^2 = 0.99 and a strong slope resulted in a relatively low LOD value of 200 nM.

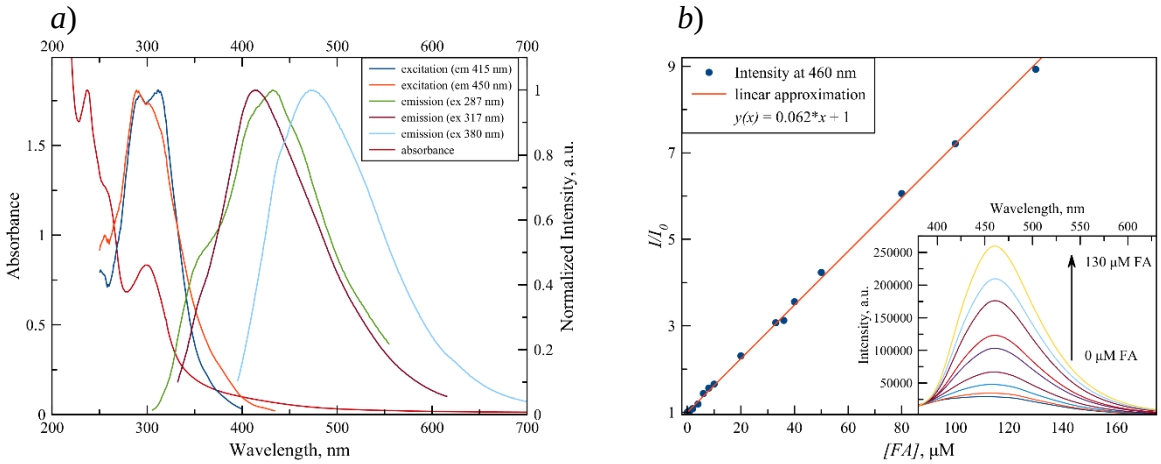


Fig. 1. Absorption, fluorescence excitation and emission spectra of Trp-Au NCs (*a*) and enhancement of Trp-Au NCs luminescence in the presence of FA (*b*).

LOD values obtained for other clusters and analytes are presented in Table 1. Phe-stabilized NCs (Phe-Au NCs) showed sensitivity towards all the three compounds (Ptr, Lep, FA) through luminescence quenching, although the strength of the quenching varied depending on the analyte. Interestingly, the luminescence of the other three AA-Au NCs complexes turned out to change only in the presence of one of the pteridines (depending on the stabilizing matrix), while not being sensitive to the other two. Given the fact that these three analytes have similar structural groups, the selective sensitivity of each of the clusters makes them promising cost-efficient sensors for analytical applications.

Table 1

Obtained LOD values

Cluster / Analyte	Phe-Au NCs	Tyr-Au NCs	DOPA-Au NCs	Trp-Au NCs
Folic Acid	6 μM (Q)	–	–	0.2 μM (E)
Pterin	11 μM (Q)	4.4 μM (E)	–	–
Leucopterin	9 μM (Q)	–	2.8 μM (Q)	–

Letters in brackets indicate the observed effect on increasing analyte concentration: *Q* for luminescence quenching and *E* for luminescence enhancement. Dash lines mean that the cluster was found to be insensitive to the analyte.

Conclusion

Using a set of aromatic amino acids (DOPA, Tyr, Phe and Trp), different types of gold luminescent nanoclusters have been synthesized. The clusters have been applied to sense pteridines, namely pterin, leucopterin and folic acid. The Phe-templated cluster was able to sense all the three compounds, while other NCs showed selective sensitivity to them. The AA-Au NC-based method of FA and Ptr detection presented in this study is potentially significant as a new cost-effective strategy of pteridine detection in biological fluids, namely blood serum and urine.

REFERENCES

1. **Lindsay A., Baxter-Parker G., Gieseg S. P.**, Pterins as Diagnostic Markers of Mechanical and Impact-Induced Trauma: A Systematic Review: 9, Journal of Clinical Medicine. 8 (9) (2019) 1383.

2. **Espinosa-Mansilla A., Durán-Merás I.**, Pteridine determination in human serum with special emphasis on HPLC methods with fluorimetric detection, Pteridines. 28 (2) (2017) 67–81.

3. **Krajíček J. et al.**, Capillary electrophoresis of pterin derivatives responsible for the warning coloration of Heteroptera, Journal of Chromatography A. 1336 (2014) 94–100.

4. **Chakraborty I., Pradeep T.**, Atomically Precise Clusters of Noble Metals: Emerging Link between Atoms and Nanoparticles, Chemical Reviews. 117 (12) (2017) 8208–8271.

Antibacterial properties of riboflavin under photodynamic exposure in a culture of fluorescent bacteria *E. Coli*.

P. P. Shram[1, 2]✉, R. A. Akasov[1], A. M. Kolchenko[1], T. V. Egorova[1].
[1]Moscow State Pedagogical University, Moscow, Russia;
[2]Pirogov Russian National Research Medical University, Moscow, Russia.
✉pp.shram@mpgu.su

Abstract. Healthcare-associated infections are an important problem in modern medicine. Due to the antibiotic resistance of nosocomial strains, new methods of treating infectious diseases are being actively sought, one of which is antibacterial photodynamic therapy. In this work, we showed that the endogenous photosensitizer riboflavin has antibacterial photodynamic activity. We evaluated half-maximal inhibition concentrations against fluorescent *E. Coli* bacteria using blue and near-ultraviolet light sources in different irradiation modes. The advantages of riboflavin for therapy are due to the low toxicity and water solubility of its derivatives, high photochemical yield, and the ability to work in visible light. Antibacterial photodynamic therapy using riboflavin as a photosensitizer can become an effective method for treating postoperative complications associated with wound infection by antibiotic-resistant microorganisms.

Keywords: Antimicrobial photodynamic therapy, photosensitizer, riboflavin, antibiotic resistance.

Funding: The article was prepared as part of the work on the topic «Laser technologies for biomedical applications» (№ 122122600055-2) under the state order of the Ministry of Education of the Russian Federation.

Introduction

Healthcare-associated infections pose a serious threat to patient health. In modern medicine, these infections are most often associated with invasive procedures and surgical interventions [1]. Antibacterial photodynamic therapy, which is based on the use of photosensitizers, may be a promising method for the treatment of postoperative infectious diseases. Flavins, which participate in the formation of reactive oxygen species in both type I and type II photochemical reactions, can be used as a photosensitizing agent [2, 3]. The effectiveness of riboflavin as a photosensitizer has been demonstrated in studies examining its antibacterial activity using ultraviolet light [4], in the sterilization of blood plasma [5], and in photoactivated collagen cross-linking to increase corneal stiffness [6].

Materials and Methods

To evaluate the antibacterial photodynamic activity of riboflavin, we used *E. Coli* bacteria strain BL21(DE3), transformed with plasmid DNA, which encodes the fluorescent protein mKate (excitation maximum 588 nm, emission maximum 633 nm). Bacteria were grown on LB agar and in the presence of flavin mononucleotide, a coenzyme form of riboflavin, of various concentrations were irradiated with a light source of 450 nm (blue) or 365 nm (UV) for 10 or 20 minutes with a radiation power density of 63.7 mW/cm^2, and then placed in a thermostat at a temperature 37 ºC for two days.

The results were recorded under an imaging system containing a radiation source with a wavelength of 530 nm and a camera with a filter that transmits light from the red range of the spectrum. The resulting photographs were processed in the ImageJ program by calculating the integral brightness of the image in the area of each well.

Results and Discussion

To analyze the effectiveness of the antibacterial photodynamic activity of riboflavin, the survival rate of E. coli was assessed; the survival rate of control wells (without flavin mononucleotide) was taken as 100%.

The IC_{50} (half-maximal inhibition concentrations) values (mg/ml) estimated in GraphPad Prism 8.0 based on the data obtained were 0.54±0.23 and 0.11±0.04 for 10 and 20 minutes at 365 nm irradiation, and ~1. 2 and 0.61±0.18 for 10 and 20 minutes at 450 nm irradiation, respectively. The IC_{50} in the 10-minute blue group was different from the 20-minute blue and 10-minute UV groups, $p<0.05$. The IC_{50} in the 20-minute UV group was different from the 10-minute UV and 20-minute blue groups, $p<0.05$.

Conclusion

Riboflavin exhibits antibacterial photodynamic activity when exposed to blue or UV light. Irradiation at a wavelength of 365 nm results in a stronger suppression of bacterial growth compared to 450 nm, which may be due to the inherent toxicity of UV radiation. Additionally, an increase in irradiation time leads to an increase in the antibacterial activity of FMN at both 450 nm and 365 nm, due to an increase in the total light dose.

Acknowledgments

Fluorescent *E.Coli* bacteria were kindly provided by Dr. D. Kostyushev (Sechenov University).

REFERENCES

1. **Sikora A, Zahra F.**, Nosocomial Infections. 2023 Apr 27. In: StatPearls [Internet]. Treasure Island (FL): StatPearls Publishing; 2023 Jan–. PMID: 32644738.

2. **Insińska-Rak M, Sikorski M, Wolnicka-Glubisz A.**, Riboflavin and Its Derivates as Potential Photosensitizers in the Photodynamic Treatment of Skin Cancers. Cells. 2023 Sep 19;12(18):2304. doi: 10.3390/cells12182304. PMID: 37759526; PMCID: PMC10528563.

3. **Abrahamse H, Hamblin MR**. New photosensitizers for photodynamic therapy. Biochem J. 2016 Feb 15;473(4):347-64. doi: 10.1042/BJ20150942. PMID: 26862179; PMCID: PMC4811612.

4. **Makdoumi K, Bäckman A, Mortensen J, Crafoord S**., Evaluation of antibacterial efficacy of photo-activated riboflavin using ultraviolet light (UVA). Graefes Arch Clin Exp Ophthalmol. 2010 Feb;248(2):207-12. doi: 10.1007/s00417-009-1231-2. Epub 2009 Nov 18. PMID: 19921518.

5. **Ettinger A, Miklauz MM, Bihm DJ, Maldonado-Codina G, Goodrich RP**. Preparation of cryoprecipitate from riboflavin and UV light-treated plasma. Transfus Apher Sci. 2012 Apr;46(2):153-8. doi: 10.1016/j.transci.2012.01.004. Epub 2012 Feb 17. PMID: 22342281.

6. **Chan TC, Lau TW, Lee JW, Wong IY, Jhanji V, Wong RL**. Corneal collagen cross-linking for infectious keratitis: an update of clinical studies. Acta Ophthalmol. 2015 Dec;93(8):689-96. doi: 10.1111/aos.12754. Epub 2015 May 19. PMID: 25990098.

A new technique for determining calibration coefficients in the esCCO method

E. V. Porfirieva ✉
Peter the Great Saint-Petersburg Polytechnic University, Saint Petersburg, Russia;
✉ porfirev-69@mail.ru

Abstract. The need to expand the use of the esCCO method for operational monitoring of human health in real time was justified. This is especially important when a doctor or medical professional has to make the necessary decisions in a very short period of time. To do this, he needs reliable data with the most detailed information about the patient's health status to determine the state of his health. The peculiarities of using the esCCO method for measuring cardiac output are noted. The main reason why inaccurate information can be obtained at the outlet when monitoring cardiac output has also been identified. A new technique has been proposed that reduces its significant impact on the result of measuring human cardiac output. Experimental data on the study of the dynamics of changes in cardiac output over time by the esCCO method using a new technique were presented and compared with previously obtained results.

Keywords: cardiovascular system, human health status, cardiac output.

Introduction

In the modern world, human health is influenced by many factors. Under the influence of these factors, changes occur in the body. People use funds to maintain activity and efficiency. This often has a negative effect on the body. The human cardiovascular system is particularly affected.

But it is difficult for many people to work effectively without biological additives and medicines. When using them, it is necessary to control changes in the body. Since any impact on the biological system leads to a reaction, this reaction must be monitored in real time, preferably non-contact. This is due to the fact that measurements must be repeated after a certain period of time. They should be easy to perform and not cause harm. Damage or side effects prevent frequent repetition of measurements to monitor the condition for short periods of time.

Currently, many non-invasive methods of monitoring the state of the cardiovascular system in express mode have been developed [1]. For this purpose, methods based on ECG, echocardiograms, daily monitoring and esCCO technology (assessment of continuous cardiac output) are widely used [2]. The search for new solutions is extremely relevant. An option may be to use ESCO technology, which has its own problems. Therefore, the purpose of our work is to develop a methodology to improve the efficiency and reliability of using esCCO technology to monitor changes in real time as a result of various factors.

Methods for measuring cardiac output

In medical institutions, cardiac output is obtained by invasive methods. These methods are very difficult to use, and it is also impossible to predict how a person will react to such an introduction into the body. Studies using these methods cannot be associated with the frequency required for monitoring, which can negatively affect the control of a person's condition. The esCCO method has a great advantage because the methods used are non-invasive. This allows you to perform measurements many times in a short period of time. There are several models of Nihon Kohden Visor monitors (BSM3532, BSM3733, etc.) that implement esCCO technology. In our work, the Nihon Kohden BSM-3562 bedside monitor is used for measurements (Fig. 1).



Fig. 1. Nihon Kohden BSM-3562 bedside monitor (with esCCO).

Features of the application of the esCCO method and the new methodology

A special feature of the esCCO method is that data from sensors is taken simultaneously [2, 3]. Sensors have different calibration functions. And with the help of these data, the cardiac output is calculated using the formula:

$$esCCO = k \cdot (\alpha \cdot PWTT + \beta) \cdot HR \quad (1)$$

where k is a calibration coefficient based on the biometric characteristics of the patient; α is constant that was determined experimentally during the development of the esCCO method; PWTT is pulse wave transit time; β is a variable derived from pulse pressure; HR is the heart rate.

Studies have shown that α is not a completely constant value. There may be several ways to calculate β. People are different, and there may be such coefficients. Based on the analysis of the results of the publication, we have compiled tables for the k coefficient (for men and women). We propose the following methodology. Within the framework of the systems included in the device, it is possible to set the coefficients k, α and δ for the patient in the diagnosis of the cardiovascular system. A standardized signal is formed for a group of people who do not have bad habits, chronic diseases and hereditary abnormalities and who are engaged in sports. Additionally, height and weight are measured. The cardiac output is then measured using the classic ESCO technology. The standardized signal is compared with the patient's parameters. Then, using the ratio (1) and a graphical comparison of the two graphs, the values of k, α and δ are set.

Experimental results and discussion

The changes in cardiac output are shown (Fig. 2) as an example of the developed technique.

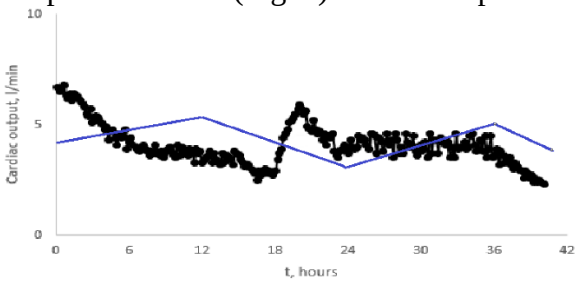


Fig. 2. The dependence of the change in cardiac output on time t (male: 45 years old, 72 kg, 175 cm).

Figure 2 shows the dynamics of changes in cardiac output in a black graph. The blue graph shows the standard cardiac output for this group. Cardiac emissions vary. There may be significant discrepancies with the real picture. Additional calibration of k, α and δ is required. Our method was tested using an invasive method. The error in measuring cardiac output using this method is less than 1%. The discrepancy between the coefficients k, α and δ ranged from 3 to 8%.

Conclusion

The results obtained show that the proposed method for determining the coefficients k, α and δ for calculating cardiac output is promising for use. The accuracy of the data obtained is significantly improved. It should be noted that it is necessary to continue research on the approbation of this technique on various groups of patients.

REFERENCES

1. **Bataille, B., Bertuit, M., Mora, M., Mazerolles, M., Cocquet, P., Masson, B., Moussot, P., Ginot, J., Silva, S., Larché J.** Comparison of esCCO and transthoracic echocardiography for non-invasive measurement of cardiac output intensive care, British Journal of Anaesthesia. 109(6) (2012) 879-88.

2. **Biais, M., Berthezène, R., Petit, L., Cottenceau, V., Sztark, F.** Ability of esCCO to track changes in cardiac output, British Journal of Anaesthesia. 115(3) (2015) 403-410.

3. **Mazing, M.S., Zaitceva, A.Y., Kislyakov, Y.Y., Avdyushenko, S.A.** Monitoring of oxygen supply of human tissues using a noninvasive optical system based on a multi-channel integrated spectrum analyzer. International Journal of Pharmaceutical Research. 12 (2020) 1974–1978.

Methodology of Mass Spectrometric Quality Control and Toxicosafety of Dairy Products

J.V. Liamina [2,3], O. A. Abdillaeva[1], Yu. A. Titov [2], A. Yu. Zaitseva[2], A. G. Kuzmin [2], V. S. Sibirtsev [1,2]✉

[1] Saint Petersburg State Chemical Pharmaceutical University, Saint Petersburg, Russia;
[2] Institute of Analytical Instrumentation, Saint Petersburg, Russia;
[3] Alferov University, Saint Petersburg, Russia
✉ vs1969r@mail.ru

Abstract. This study employed a compact gas mass spectrometer to evaluate "fresh" and "accelerated expired" yogurts from different manufacturers with various starters and additives. Principal component analysis was used. By analyzing 7 samples, differentiation based on freshness, microbial starters, raw materials, and additives was achieved. Identification of potentially toxic packaging materials was also possible. The combination of methods demonstrated the effectiveness of gas mass spectrometry for quality control, composition analysis, and toxicosafety assessment of dairy products and packaging materials[1-6].
Keywords: mass spectrometry, dairy products, packaging materials, quality control, toxicosafety, food additives

Introduction

Dairy products' quality and safety concerns due to functional food additives and potentially harmful substances necessitate enhanced tools for quality control and toxicity assessment in the dairy industry[1-5]. Mass spectrometry offers advantages such as speed, sensitivity, and selectivity for analyzing food products and packaging materials[6].

Materials and Methods

Seven commercially produced yogurt samples with various functional additives were selected. Vapors were collected and analyzed using the "MC7-200" gas quadrupole mass spectrometer with electron impact ionization. Accelerated expiration samples and packaging materials were also analyzed similarly. Principal component analysis and traditional methods were employed[7].

Results and Discussion

The method successfully differentiated samples based on freshness, microbial starters, dairy raw materials, and additives. Analysis revealed potentially toxic plastics used in the packaging of samples 3 and 6.

Conclusion

The approach demonstrated effectiveness for monitoring the composition and quality of dairy and other food products (including packaging materials), offering advantages such as efficiency, cost-effectiveness, accessibility, and minimal operator qualifications required.

Acknowledgments

This work was carried out at the IAI RAS within the framework of the state assignment of the Ministry of Science and Higher Education of the Russian Federation No. 075-01157-23-00

In conclusion, the results of our research on yogurt samples industrially produced by various manufacturers with different starters and materials used for packaging have demonstrated that our approach can serve as an effective method for monitoring the composition and quality of dairy and

other food products (including packaging materials). This method offers advantages such as high efficiency, cost-effectiveness, accessibility for widespread use, and minimal operator qualifications required.

REFERENCES

1. **Sibirtsev V. S., Naumov I. A., Kuprina E. E., Olekhnovich R. O.** Use of impedance biotesting to assess the actions of pharmaceutical compounds on the growth of microorganisms. Pharmaceutical Chemistry Journal. 50 (7) (2016) 481–485. http://doi.org/10.1007/s11094-016-1473-3
2. **Kokina M. S., Frioui M., Shamtsyan M., Sibirtsev V. S., Krasnikova L. V., Konusova V. G., Simbirtsev A. S.** Influence of pleurotus ostreatus beta-glucans on the growth and activity of certain lactic acid bacteria. Scientific Study and Research: Chemistry and Chemical Engineering, Biotechnology, Food Industry. 19 (4) (2018) 465–471. https://researchgate.net/publication/329935544

THE AUTHORS

LIAMINA Julia V.
e-mail: julia.liamina@gmail.com, tel.: 8-981-976-25-20
ORCID: 0009-0001-5367-1604

ABDILLAYEVA Oyshakhon A.
e-mail: ojshahon.abdillaeva@spcpu.ru, tel.: 8-960-264-57-17
ORCID: 0000-0001-9565-5832

TITOV Yuri A.
e-mail: jurtit34@rambler.ru tel.: 8-812-363-07-62
ORCID: 0000-0002-4205-9620
Scopus ID 6603964394
SPIN 2702-6572

ZAITSEVA Anna Y.
e-mail: anna@da-24.ru, tel.: 8-812-363-07-30
ORCID: 0000-0002-5299-2561
SPIN 5748-1072

KUZMIN Alexey G.
e-mail: agqz55@rambler.ru tel.: 8-812-363-07-62
ORCID: 0000-0003-4951-3301
SPIN: 3964-9998

SIBIRTSEV Vladimir S.
e-mail: vs1969r@mail.ru, tel.: 8-904-601-59-78
ORCID: 0000-0003-0829-5213
Scopus ID 6603964394
SPIN 1707-0169

Voltage controlled generator for multifunctional radar station

N. S. Afanasiev ✉
Peter the Great Saint-Petersburg Polytechnic University, Saint-Petersburg, Russia Federation;
✉afanasiev2.ns@spbstu.edu.ru

Abstract: Traditional frequency synthesizers (MF) struggle to provide the wide and stable reference signals (1-18 GHz) required by modern multifunctional radar stations. This bulkiness is due to the complexity of MF designs, which combine various electronic components. This article proposes a novel Voltage Controlled Generator (VCG) design specifically suited for such radars. The focus of the VCG is on compactness, temperature resistance, and achieving good stability with small tuning steps. This makes it ideal for antenna applications where high-precision frequency is less critical than stability. The design utilizes a semiconductor varicap to achieve these goals. The proposed circuit demonstrates excellent stability with a maximum frequency deviation of less than 2.2 MHz within 100 milliseconds. The author also explores the advantages of incorporating a buffer amplifier or frequency doubler within the VCG. These additions can improve resistance to external factors and potentially provide additional functionalities like isolated outputs. Overall, this VCG design offers a promising alternative to traditional MFs for multifunctional radar applications.

Keywords: Voltage controlled generators, broad-band amplifier, frequency doubler, varicap.

Introduction

The development of various directions in radiophysics and information transmission systems required the development of a source of reference signals with a stable frequency, which is rebuilt in a wide range [1]. A particularly wide range is required in multifunctional radar stations (radars) [2]. Due to the inability to build such a generator for any given frequency with high stability, frequency synthesizers (MF) are used – devices for converting the oscillation frequency from one value to another with a small tuning step and low errors. The schemes for constructing MF, depending on specific technical requirements, are different, but each of them uses a set of typical electronic components: frequency-controlled generators, frequency multipliers and dividers, mixers, frequency filters, elements of digital technology. The nomenclature of these electronic components is extremely diverse, so choosing them correctly is a difficult task. If it is necessary to adjust the frequency in the range from 1 to 18 GHz, the design of the MF becomes quite cumbersome, which creates difficulties with their placement on a mobile radar platform. In this situation, the most appropriate is the use of frequency-controlled voltage generators (VCG).

Materials and Methods

The main technical characteristics of the VCG can be divided into three groups: signal quality characteristics in a given frequency range, frequency control characteristics and sensitivity parameters to external influences. Based on the requirements for these characteristics, the design of the VCG is being developed.

In Fig. 1, I propose the following scheme based on a semiconductor varicap VD with negative resistance to ensure the compactness of the VCG and its resistance to temperature influences that occur at the antenna post. For the emitter of an antenna device, high frequency accuracy is not required, its stability and a small range change step are important when solving special tasks.

It should be noted that the use of varicap matrices makes it possible to adjust the microwave frequency in the range from 10 to 15 times, which is necessary for a multifunctional radar. The main characteristic, which need to control, a during the radiation frequency restructuring of a parabolic antenna in a radar is the frequency departure during its restructuring. Depending on the tasks being solved, different requirements are imposed on this time to compensate for this deviation.

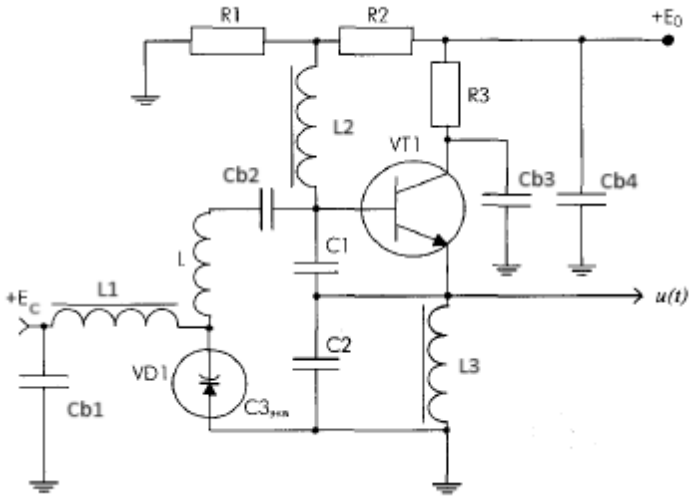


Fig. 1. An example of a VCG circuit diagram: VT1 is a transistor based on GaAs; Cb1 Cb2, Cb3, Cb4 – blocking capasitors; L1, L2 и L3 – blocking throttles; R1 и R2 - the circuit for the formation of the unlocking voltage of the transistor; R3 - transistor operating current limitation resistor VT1

Results and discussion

The characteristic of frequency tuning is shown in Fig. 2.

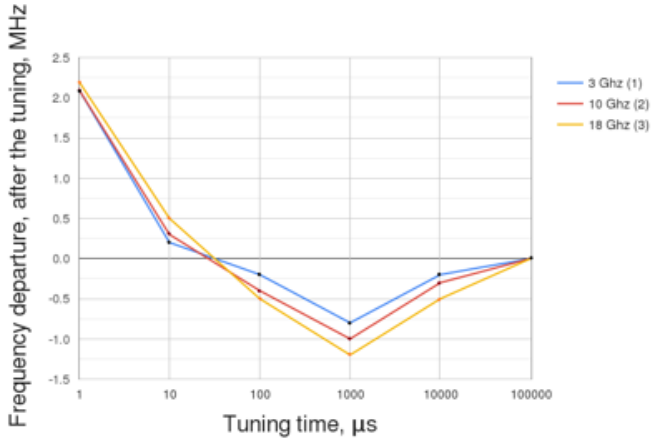


Fig. 2. Dependence of the care after the tuning frequency of the generator on time: 1 – 3 GHz; 2 – 10 GHz; 3 - 18 GHz.

The analysis of the data presented in Fig. 2 shows the reliable operation of the automatic frequency tuning circuit F. The maximum frequency F in the range of 100 ms is less than 2.2 MHz, which characterizes the good stability of the developed VCG.

Conclusion

According to the results of the research, it was found that VCG with a built-in buffer broadband amplifier or frequency doubler have a lower sensitivity to the phase of the reflection coefficient. The built-in buffer amplifier allows in some models to have two mutually isolated outputs for connecting the load.

REFERENCES

1. **Gelgor A. Pavlenko L., Fokin G., Popov E., Lavrukhin V.** LTE base stations localization, Lecture Notes in Computer Science (including subseries Lecture Notes in Artificial Intelligence and Lecture Notes in Bioinformatics). 8638 (2014) 191–204.

2. **Browne J.**, Waveform generator makes the jump to 25 GHz, Microwaves and RF 55(2) (2016) 66.

Tunnel effect investigation in GaN/Si heterostructure

D. A. Barykin [1,2]✉, **K. Yu. Shugurov** [1], **A. M. Mozharov** [1]
[1] Alferov University, Saint-Petersburg, Russia;
[2] Saint-Petersburg Politechnic University, Saint-Petersburg, Russia
✉ d.a.barykin02@mail.ru

Abstract. GaN nanowires are perspective elements for high performance electronic devices fabrication. In this work, theoretical investigation of tunnel effect in GaN nanowire/Si heterostructure is presented. Tunneling probability was calculated out according to Wentzel-Kramers-Brillouin approximation. Numerical model also included Shockley-Reed-Hall recombination mechanism and thermionic current in addition to the tunnel component. During simulation we obtained current-voltage characteristics for wide range of GaN doping levels and based on this data the cutoff frequencies of the diode structures were calculated as well.

Keywords: gallium nitride, nanowires, tunnel effect, silicon, Wentzel-Kramers-Brillouin approximation

Funding: This study was supported by the Russian Science Foundation grant No. 23-79-01279.

Introduction

Over the last 70 years, many semiconductor microwave devices have been developed, such as Schottky diodes, Gunn diodes, as well as tunnel and backwards diodes, which operation principle is based on the tunnel effect. These devices are widely used in circuits for detection, amplification and generation of high-frequency signals [1].

Nowadays, tunnel effect based diodes are mainly made of materials such as Ge, GaSb, GaAs and Si. However, narrow-gap semiconductors have low temperature stability due to their small bandgap. Although Si is economically and technologically feasible, its indirect band structure (same as Ge) limits the tunnel current, which significantly affects the performance of output device [2]. On the other hand, GaAs based diodes can provide higher peak-to-valley current ratio due to low tunneling effective mass, but at the same time GaAs has low thermal conductivity and difficult fabrication techniques. Therefore, it is reasonably to search for new material systems such as GaN nanowires (NWs), that have a number of features: high crystal quality due to mechanical stress relaxation, direct band structure, high thermal stability, high current densities commutation (up to 2 MA/cm^2 [3]), doping support up to 10^{20} cm^{-3} [4], ability to operate under unfavorable conditions and good heat dissipation due to high surface-to-volume ratio.

This work is devoted to the theoretical study of the tunnel effect in GaN NW/Si heterostructure.

Materials and Methods

In this work, the COMSOL Multiphysics software package implementing the finite element method was used to simulate the investigated effects. NWs as usual have diameters of about 100-200 nm, so taking into account structure with high doping levels (which is typical for devices with a tunnel effect) it can be assumed that junction thickness is significantly less than NW diameter. Therefore, we considered two-layer one-dimensional n-GaN/p-Si system. There were three points of silicon doping level: 1×10^{19}, 5×10^{19} and 1×10^{20} cm^{-3}, while the GaN doping level ranged from 5×10^{17} to 5×10^{19} cm^{-3}. Both tunneling and thermionic current components were calculated.

The quasi-classical Wentzel-Kramers-Brillouin approximation (WKB method) [5] was taken as the basis for the theoretical representation of band-to-band tunneling. It allows describing the tunneling of charge carriers with sufficient accuracy and taking into account both types of charge carriers. Shockley-Reed-Hall recombination mechanism was also taken into account in the calculation. Since the level of hole concentration in the GaN region is extremely

low, recombination was considered only in the silicon region. The lifetime of charge carriers in Silicon was equated to 10 μs.

Results and Discussion

Silicon doping concentrations were chosen according to the maximum solubility of boron, aluminum and gallium impurities [6]. The data obtained for different impurity concentrations showed no qualitative changes in the current-voltage (IV) characteristics with doping level increasing. IV curves analysis showed the best maximum peak current to be about 16.5 kA/cm^2 which is comparable to commercially produced tunnel diodes. The corresponding peak voltage point was 0.16 V. Since these types of diodes are known to operate under high switching rates we extracted from IV curves the minimum resistance values of negative differential resistance region. Together with zero-bias junction capacitance it is needed to calculate resistive cut-off frequency of the diode structures. In our case the highest frequency reached a value of 10 GHz.

Conclusion

In this work, the tunnel effect in GaN NW/Si heterostructure was theoretically investigated. Assuming the junction thickness is significantly less than NW diameter 1D system was considered including thermionic current component and Shockley-Reed-Hall recombination mechanism. IV characteristics for different GaN and Si doping levels were obtained. It was shown that the maximum peak current reaches 16.5 kA/cm^2 with the corresponding voltage of 0.16 V. It was also found that theoretical resistive cut-off frequency for such diode structures reaches 10 GHz.

REFERENCES

1. Clinton E. A., Vadiee E., Shen S. C., Mehta K., Yoder P. D., Doolittle W. A., Negative differential resistance in GaN homojunction tunnel diodes and low voltage loss tunnel contacts, Applied Physics Letters. 112 (25) (2018).

2. Tabe M., Tan H. N., Mizuno T., Muruganathan M., Anh L. T., Mizuta H., Nuryadi R., Moraru D, Atomistic nature in band-to-band tunneling in two-dimensional silicon pn tunnel diodes, Applied Physics Letters. 108(9) (2016) 093502.

3. Shugurov K, Mozharov A, Sapunov G, Fedorov V, Tchernycheva M, Mukhin I, Single GaN Nanowires for Extremely High Current Commutation, Physica Status Solidi (RRL) – Rapid Research Letters, 15(4) (2021) 2000590.

4. Fang Z., Robin E., Rozas-Jiménez E., Cros A., Donatini F., Mollard N., Pernot J., Daudin B., Si Donor Incorporation in GaN Nanowires, Nano Letters 15(10) (2015) 6794–801.

5. Yang K., East J. R., Haddad G. I., Numerical modeling of abrupt heterojunctions using a thermionic-field emission boundary condition, Solid-State Electronics 36(3) (1993) 321-330.

6. Antoniadis D. A., Diffusion in silicon, NATO ASI Series, Series E: Applied Sciences, (1983) 1–48.

A compact MEMS switch for advanced radar systems

I. A. Belozerov✉, **I. V. Uvarov**
Valiev Institute of Physics and Technology of Russian Academy of Sciences,
Yaroslavl Branch, Yaroslavl, Russia
✉igas2580@yandex.ru

Abstract. MEMS switches are of significant interest for advanced radioelectronic systems. High RF performance combined with small size and low power consumption make them especially attractive for use in phased array antennas, aviation and space equipment. This work presents a switch based on a tiny cantilever with a length of 50 μm. Its working characteristics are compared with the calculation results. The advantages of the switch in comparison with other products are demonstrated.

Keywords: MEMS switch, cantilever, pull-in voltage, contact resistance, contact force

Funding: This work is supported by the program no. FFNN-2022-0017 of the Ministry of Science and Higher Education of Russia for Valiev Institute of Physics and Technology of RAS and by the Foundation for Assistance to Small Innovative Enterprises, grant No. 7GUPKES18/91740, and is performed using the equipment of the Facilities Sharing Centre "Diagnostics of Micro- and Nanostructures".

Introduction

Switches fabricated using microelectromechanical systems (MEMS) technology are actively considered as a new element base for microwave devices [1]. Small size, low insertion loss, high isolation and low power consumption make them attractive for phased array antennas, aircraft and space radar systems. The MEMS switch contains a cantilever located above driving and signal electrodes. Applying voltage to the driving electrode creates an electrostatic force that bends the cantilever and brings it in contact with the signal electrode. This design is simple and reliable. Its compact size ensures high switching speed and resistivity to internal mechanical stress. This paper presents one of the smallest MEMS switches known to date. The pull-in voltage and contact resistance are measured and compared with the calculation results. The advantages of the switch in comparison with previously created devices are revealed.

Materials and Methods

The switch is schematically shown in Figure 1. The movable electrode is a 50 μm long aluminum cantilever, which has a width of 10 μm at the attachment sites and 40 μm at the free end. The driving electrode surrounds the signal one in order to increase the area of the electric field. The shape of the cantilever and electrodes was optimized during previous work and provides the highest contact force for a given length and width [2]. The cantilever has a thickness of 3.6 μm and is equipped with two contact bumps of 0.5 μm in height. The gap between the cantilever and the electrodes is 1 μm. According to finite element method (FEM) simulation, the switch has a pull-in voltage V_{PI} of 85 V. The natural frequency of the cantilever f_0 = 750 kHz allows one to estimate the actuation time as $t_{on} = 3.67*(V_{PI}/V_D)*(1/2\pi f_0)$ = 0.7 μs, where V_D = 90 V is the driving voltage. The switch is fabricated on a thermally oxidized silicon wafer by surface micromachining, as described previously [3]. The contacts are made of ruthenium.

Results and Discussion

The measured pull-in voltage is of 64 V, which is 25% lower than the calculated value. The reason for the discrepancy is the bending of the cantilever under the internal mechanical stress. Due to the short cantilever length, this bending results in a small change in the gap by 0.2 μm, which does not lead to the switch failure. The pull-in voltage decreases to 40 V after 10^5 cycles. The voltage drop is explained by the plastic deformation of the cantilever, leading to a reduction in the air gap. FEM simulation predicts the mechanical stress of 80 MPa in the

deformed cantilever. This value exceeds the yield strength of aluminum, which equals to 22 MPa.

The contact resistance during the long-term test is presented in Figure 2. The results are shown for the cantilever-based device (red curve) and the switch with an active opening mechanism (blue curve) developed by the authors previously [4]. The contact resistance of the cantilever-type switches is in the range of 10–15 Ohms during the first 11 thousand cycles. Then it increases to several tens or hundreds of Ohms due to the formation of friction polymers on the surface of ruthenium contacts [5]. However, the cantilever-based switch has 1-2 orders of magnitude lower resistance compared to the device equipped with torsion springs. The probable reason is the higher impact force of the cantilever that helps to break the contamination film on the contact surfaces.

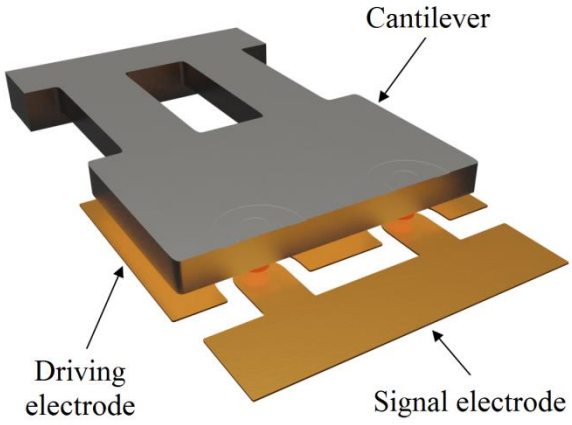


Fig. 1. Schematic illustration of the MEMS switch.

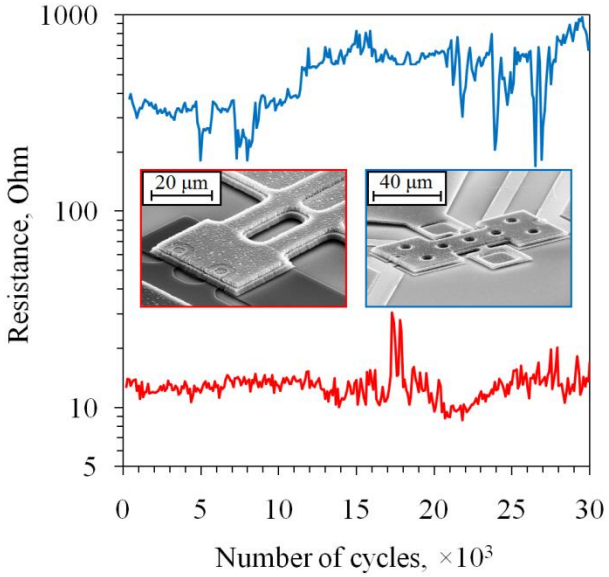


Fig. 2. Dependence of the contact resistance on the number of switching cycles for two types of switches.

REFERENCES

1. **Rebeiz G. M., Patel C. D., Han S. K., Ko C.-H., Ho K. M. J.**, The search for a reliable MEMS switch. IEEE Microw. Mag. 14 (2013) 57-67.

2. **Uvarov I. V., Belozerov I. A.**, Design Guideline for a Cantilever-Type MEMS Switch with High Contact Force, Micro. 4(1) (2023) 1-13.

3. **Belozerov I. A., Uvarov I. V.**, MEMS Switch Based on a Cantilever with Increased Contact Force, Russian Microelectronics. 52(6) (2023) 475-482.

4. **Uvarov I. V., Marukhin N. V.**, A seesaw-type MEMS switch with enhanced contact force: the first results, Journal of Physics: Conference Series. IOP Publishing. 2086(1) (2021) 012069.

5. **Czaplewski D.A., Nordquist C.D., Dyck C.W., Patrizi G.A., Kraus G.M., Cowan W.D.**, Lifetime limitations of ohmic, contacting RF MEMS switches with Au, Pt and Ir contact materials due to accumulation of ‘friction polymer’ on the contacts, J. Micromech. Microeng. 22(10) (2012) 105005.

Wireless power transfer in MRI with a detuned birdcage coil

Oleg I. Burmistrov [1]✉, **Nikita A. Olekhno**[1]
[1] ITMO University, Saint Petersburg, Russia
✉oleg.burmistrov@metalab.ifmo.ru

Abstract. In this work, we develop an application of a transmit birdcage coil for wireless power transfer during the receive phase within a magnetic resonance imaging (MRI) scanner. The study includes numerical simulations and an experimental verification of a numerical model with a clinical birdcage coil. We obtain numerically magnetic fields inside the magnetic resonance imaging scanner with a phantom, the specific absorption rate with a human voxel model, and the resulting voltage on receiving antennas. Therefore, we characterized possible distortions on MR images, demonstrated safety of the setup for a patient, and evaluated the RF-RF efficiency numerically, respectively. Finally, we propose devices placed in MRI bore which can provide a wireless power supply with the detuned birdcage coil and receive antennas system.

Keywords: MRI, magnetic resonance imaging, birdcage coil, WPT, wireless power transfer, resonators

Funding: This work was supported by the Russian Science Foundation (Project No. 21-79-30038).

Introduction

Magnetic resonance imaging (MRI) is an important method of medical diagnostics for the diseases including cancer and injuries. Near field antennas (called local coils) are used in MRI bore to enhance the functionalities of an MRI scanner and require a wire connection to the scanner during the scanning process. However, wire connection of local coils has many disadvantages, including patient discomfort, lowered speed of the patient positioning by medical stuff, periodic replacement required by connectors and wires, and wrong cable positioning a within MRI bore which can cause an additional heating of the patient [1]. The cable provides data transfer and power supply.

Wireless data transfer can solve this problems [2,3]. Power supply without any cables between local coil and MRI scanner able to realize by energy harvesting at the scanning (Larmor) frequency, and wireless power transfer at non-Larmor frequency [4]. The general problem of energy harvesting is low power (above 500 mW) [5, 6] which able to power supply limit types of receive local coils. However, for wireless power transfer needs an additional antenna [7 – 10] or time of power transfer is low [11] as time for nuclei excitation (an excitation phase) much less than time of receive signal from nuclei (a receive phase). As we demonstrate, the solution of this problems is wireless power transfer while a receive phase without an additional transmit antenna. We used Siemens Avanto Body Coil with modified detuning system as the transmit structure.

Materials and Methods

We apply CST Microwave Studio 2022 software package for numerical simulations. The numerical model includes a birdcage coil with modified detuning system, radio frequency (RF) screen, a receive system, and a phantom or the voxel model of human (Gustav model in CST Bio models library) with all electromagnetic parameters of tissues and organs. The birdcage coil numerical model based on Siemens Avanto Body Coil with two ports include matching circuit. Moreover, diodes for detuning system replacement to inductors in the birdcage coil. An open cylinder surface made by annealed copper is model of the RF screen. The receive system consist of two equal orthogonal loop coils with a port includes a matching circuit in each of them. The cylinder with diameter 300 mm, and length 500 mm made by salted water is model of phantom. Voltage on the dummy load, magnetic field within the birdcage coil simulated with frequency domain solver (modified finite element method), while time domain solver (modified finite difference time domain) was used to obtain the specific absorption rate (SAR) of the voxel human model.

Permittivity and conductivity of the Siemens Test Phantom liquid for 1.5 T MRI scanners measured by SPEAGs DAK 12 and Planar S5048 (vector network analyser). Also, Planar S5048 was used for measurements of scattering parameters of Siemens Avanto Body Coil.

Results and Discussion

For numerical simulations, we measured permittivity (80) and conductivity (1 Sm/m) of Siemens Test Phantom for 1.5 MRI scanners. Then, we verified our numerical model by compare the scattering parameters of the Siemens Avanto Body Coil and the model one. Then, we added a detuning system (inductors) to the model, and we calculated scattering parameters of the birdcage coil to obtain resonance frequency for fundamental mode. Finally, we obtain safety, RF-RF efficiency, distortion of MR-images by calculating specific absorption rate for the voxel human model, voltage on dummy load within receive coils, and magnetic field, respectively. Safety is limitation factor for input power to the birdcage coil as a human body heating while the scan. However, received power sufficient for power supply a lot of receiving local coil types, and medical sensors, while the scan is safety. Moreover, the magnetic field doesn't distort at Larmor frequency within the phantom hence MR-images won't change by the wireless power transfer system with detuned birdcage coil.

Conclusion

The birdcage coil with modified detuning system able to power supply a lot of local coil types wirelessly during the receive phase. The power transfer system is safe for a patient, and MR-images doesn't distort by the receive system.

REFERENCES

1. M. Dempsey, *et al.*, Thermal Injuries Associated with MRI, *Clin. Radiol.* **56**, 457 (2001)
2. J.Wei, *et al.*, A realization of digital wireless transmission for MRI signals based on 802.11b, *J. Magn. Reson.* **186**, 358 (2007)
3. K. Aggarwal, *et al.*, A millimeter-wave digital link for wireless MRI, *IEEE Trans. Med. Imaging* **36**, 574-583 (2017)
4. L. Nohava, *et al.*, Perspectives in wireless radio frequency coil development for magnetic resonance imaging, Front. Phys. **8**, 11 (2020)
5. P. Seregin, O. Burmistrov, *et al.*, Energy-Harvesting Coil for Circularly Polarized Fields in Magnetic Resonance Imaging, *Phys. Rev. Appl.* **17**, 044014 (2022)
6. A. Ganti, *et al.*, A novel energy harvesting circuit for RF surface coils in the MRI system, *IEEE Trans. Biomed. Circuits Syst.* **15**, 791 (2021)
7. K. Byron, *et al.*, An RF-gated wireless power transfer system for wireless MRI receive arrays, *Concepts Magn. Reson. Part B Magn. Reson. Eng.* **47B**, e21360 (2017)
8. K. Byron, *et al.*, An MRI compatible RF MEMs controlled wireless power transfer system, *IEEE Trans. Microw. Theory Tech.* **67**, 1717 (2019)
9. A. Ganti, *el al.*, Achieving electromagnetic compatibility of wireless power transfer antennas inside MRI system, *Wirel. Power Transf.* **6**, 138 (2019)
10. S. Ullah, *et al.*, Wireless, battery-free, and fully implantable micro-coil system for 7 T brain MRI, *IEEE Trans. Biomed. Circuits Syst.* **16**, 430 (2022)
11. O. Burmistrov, *et al.*, Wireless power transfer in magnetic resonance imaging at a higher-order mode of a birdcage coil, *Phys. Rev. Appl.* **21**, 014047 (2024)

Mobius strip inspired design of a multiband dipole-like circularly polarized antenna

V. D. Burtsev[1]✉, A.V. Nikulin[1], T.S. Vosheva[1], N.M. Nazarov[2], D. S. Filonov[1]
[1]Center for Photonics and 2D Materials, Moscow Institute of Physics and Technology, Dolgoprudny 141701, Russia,
[2]Bauman Moscow State Technical University,
✉burtsev.vd@phystech.edu

Abstract. This paper describes the design of a multi-band antenna with a dipole-like radiation pattern with circular polarization inspired by the Mobius strip. The paper presents the exact geometry of the emitter, as well as maps of the near and far electromagnetic fields. For each band under consideration (~11 GHz, ~22 GHz, ~33 GHz), the spectra of multipole field coefficients in the Fraunhofer zone are given, as well as a qualitative description of the physical processes taking place. The results obtained can be applied further in telecommunication technologies, for example, in the development of satellite multiple access systems with frequency division of channels.

Keywords: Mobius strip, antenna design, multipolar decomposition, satellite communications systems.

Funding: This research was supported by the Ministry of Science and Higher Education of the Russian Federation under the project no 075-11-2022-011 (numerical part) and the Russian Science Foundation under the project no 23-29-00152 (manufacturing and measurements part).

Introduction

One of the challenges of modern satellite systems is the creation of a so-called alarm button [1—4] — a transceiver device that could work from anywhere on the Earth's surface and communicate directly with satellites in Earth orbit, telling them the coordinates of the source. In addition, ground-based satellite antennas value the ability to emit on circular polarization [5—7], and the antennas of wearable devices often have a quasi-dipole radiation pattern [8], [9] that allows them to shine in all directions at once in one plane, so the stability of the channel can be independent of the rotation of the antenna. In this paper, we propose a promising antenna prototype for the designated tasks, providing predictable behavior of the radiation pattern at multiple frequencies. In its plane, the antenna emits isotropically with circular polarization.

Methods

The numerical modeling in all the frequency ranges was carried out using the finite element method-based solver in CST Studio Suite (Fig. 1 (a—c)). To explain the operating principle of the proposed antenna, the multipolar decomposition method was used [10]. With calculated maps of the far electric field in the frequency ranges under consideration, the amplitudes and phases of multipole coefficients up to the 20^{th} order in terms of the orbital number l were calculated. Then, those of the coefficients that make the most significant contribution to the energy spectrum of the antenna were taken into consideration.

Results and Discussion

The results obtained indicate constructive interference of magnetic and electric dipoles inside the proposed structure at each multiple frequency. These components are phase shifted, thereby achieving circular polarization. The antenna performed similarly at multiple frequencies: ~11 GHz (Fig. 1 (d—g)), ~22 GHz (Fig. 1 (h—l)), and ~33 GHz (will be included in full proceeding text), — providing omnidirectional radiation pattern in its plane.

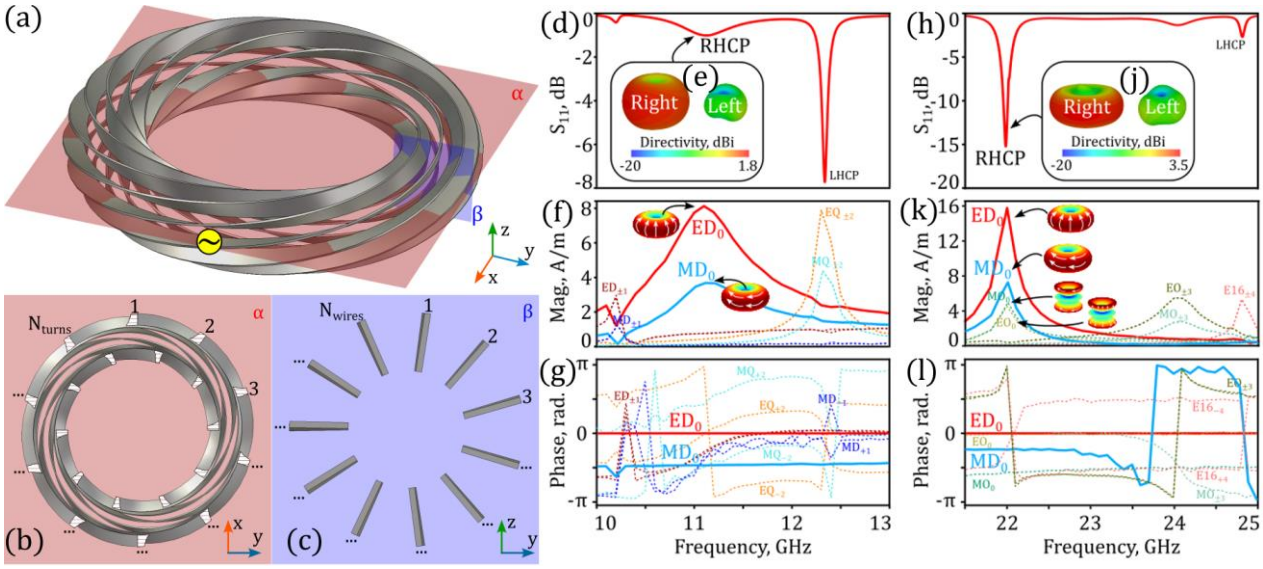


Fig. 1. Geometry: (a) general view, (b) face cross-section, (c) bundle cross-section; — and results at 10..13 GHz and 21.5..25 GHz: reflection coefficient (d) and (h), right hand polarized patterns (e) and (j), multipolar amplitudes (f) and (k), and phases (g) and (l).

REFERENCES

[1] ITU, *Handbook on Emergency Telecommunications*. 2005.

[2] A. Afolabi, O. Moses, M. Opeyemi, B.-O. Abraham, and A.-Z. Temidayo, "Design and Construction of A Panic Button Alarm System for Security Emergencies," *Int. J. Eng. Tech.*, vol. 4, no. 3, pp. 649–652, 2018, doi: 10.29126/23951303/IJET-V4I3P105.

[3] N. Majumdar, P. Bhargava, and R. K Shirin, "Emergency Panic Button using Microcontrollers," *Int. J. Comput. Appl.*, vol. 99, no. 9, pp. 1–3, 2014, doi: 10.5120/17398-7955.

[4] N. Karusala and N. Kumar, "Women's safety in public spaces: Examining the efficacy of panic buttons in New Delhi," *Conf. Hum. Factors Comput. Syst. - Proc.*, vol. 2017–May, pp. 3340–3351, 2017, doi: 10.1145/3025453.3025532.

[5] A. J. Fenn and L. W. Rispin, "A Terrestrial Air Link for Evaluating Dual-Polarization Techniques in Satellite Communications," vol. 9, no. 1, pp. 3–18, 1996.

[6] S. Gao, Q. Luo, and F. Zhu, *Circularly Polarized Antennas*. Wiley-IEEE Press, 2014. [Online]. Available: https://www.wiley.com/en-us/Circularly+Polarized+Antennas-p-9781118374412

[7] P. Naseri, S. A. Matos, J. R. Costa, C. A. Fernandes, and N. J. G. Fonseca, "Dual-Band Dual-Linear-to-Circular Polarization Converter in Transmission Mode Application to Band Satellite Communications," *IEEE Trans. Antennas Propag.*, vol. 66, no. 12, pp. 7128–7137, 2018, doi: 10.1109/TAP.2018.2874680.

[8] N. F. M. Aun, P. J. Soh, A. A. Al-Hadi, M. F. Jamlos, G. A. E. Vandenbosch, and D. S. Schreurs, "Revolutionizing Wearables for 5G: 5G Technologies: Recent Developments and Future Perspectives for Wearable Devices and Antennas," *IEEE Microw. Mag.*, vol. 18, no. 3, pp. 108–124, 2017, doi: 10.1109/MMM.2017.2664019.

[9] B. Wang and S. Yan, "Design of Smartwatch Integrated Antenna with Polarization Diversity," *IEEE Access*, vol. 8, pp. 123440–123448, 2020, doi: 10.1109/ACCESS.2020.3006076.

[10] V. D. Burtsev, T. S. Vosheva, S. Y. Prokhorov, A. A. Khudykin, and D. S. Filonov, "Broadband antenna array realization with printed meta-elements and its multipoles spectra," *Photonics Nanostructures - Fundam. Appl.*, vol. 58, 2024, doi: 10.1016/j.photonics.2023.101215.

Control of the functional characteristics of spin light-emitting diodes InGaAs/GaAs/Al2O3/CoPt

M. V. Ved,[1✉], **E. I. Malysheva**[1], **P. B. Demina**[1], **M. V. Dorokhin**[1], **A. V. Zdoroveishchev**[1]

[1] Research Institute for Physics and Technology of Nizhny Novgorod State University, Nizhny Novgorod, Russia

✉ved@nifti.unn.ru

Abstract. Spin light-emitting diodes based on InGaAs/GaAs heterostructures and a $CoPt_x$ alloy ferromagnetic contacts, where the composition varied within ($1 \leq x \leq 2.5$), were formed and studied. It was shown that varying the composition of the ferromagnetic contact provides control over the type of magnetic field dependence of the circular polarization degree of electroluminescence. It was shown that control is carried out by modulating the magnetic characteristics of the films when varying the composition. The obtained result shows the possibility of controlling the magnetization of the contacts of a spin light-emitting diode using a magnetic field, which seems useful from a practical point of view.

Keywords: magnetic thin films, spin injection, spin light-emitting diodes, III-V semiconductors

Funding: This study was supported by the Russian Science Foundation (project no. 21-79-20186).

Introduction

Spin light-emitting diodes (SLEDs) based on III-V semiconductor heterostructures with a ferromagnetic (FM) metal injector are one of the basic elements of spintronics. To date, SLED functions have been implemented at room temperature in a whole series of works. For further development associated with their integration into existing or new integrated optoelectronic circuits, it is necessary to control such important functional characteristics of SLED as residual polarization and switching magnetic field. Control of these characteristics can be achieved by modulating the properties of the ferromagnetic injector. In injectors based on $CoPt_x$ alloys, the composition x can vary within wide limits, and the above-mentioned parameters also vary.

Materials and Methods

The semiconductor part of LED, which is a heterostructure with an $In_{0.18}Ga_{0.82}As/GaAs$ quantum well, was grown by MOVPE on n-GaAs substrates, and then a thin 1 nm dielectric layer – Al_2O_3, and a metal film based on the $CoPt_x$ alloy were deposited on the surface of the structures using electron beam evaporation. Thus, a Schottky contact was formed based on the ferromagnetic metal/tunnel-thin dielectric/semiconductor system. Technologically, the $CoPt_x$ contact was a multilayer structure [Co(a)/Pt(b)]10, where a and b are the thicknesses of each layer in nm. The composition of the layer was specified by setting the technological values of the thickness x = b/a. Four samples were formed, with different compositions: sample 1 (a=2, b=5); sample 2 (a=3, b=5); sample 3 (a=4, b=5) and sample 4 (a=4, b=4). The composition was selected in accordance with previously obtained results, which showed the presence of perpendicular magnetic anisotropy in such films [1], which is a necessary condition for obtaining circularly polarized electroluminescence.

The work carried out measurements of the magnetic field dependences of the degree of circular polarization of electroluminescence, measurements of circular polarization during transmission and reflection of unpolarized light from a CoPt film (control structures formed on i-GaAs substrates were used for measurements).

Measurements of the magnetic field dependences of the polarization characteristics were carried out in the magnetic field range 0 – 2000 Oe at a temperature of 10 K. The degrees of circular polarization for all geometries were calculated using the formula:

$$P_{EL(T,R)} = \frac{I(\sigma^+) - I(\sigma^-)}{I(\sigma^+) + I(\sigma^-)} \cdot 100\%$$

where $P_{EL(T,\,R)}$ is the circular polarization degree of EL, transmitted or reflected radiation, $I(\sigma^+)$ and $I(\sigma^-)$ are the intensity of σ^+ and σ^- polarized radiation.

Results and Discussion

When diodes are introduced into a transverse magnetic field, the EL becomes partially circularly polarized. The dependences of the circular polarization degree on the magnetic field for the studied samples are shown in Fig. 1(a). All P_{EL} dependences describe a hysteresis loop that reaches saturation in fields up to 550–1300 Oe. The form of the $P_{EL}(H)$ dependences is determined by the magnetic field dependences of the magnetization of the studied $CoPt_x$ layers, which clearly demonstrates the similarity of the hysteresis loops of the circular EL polarization ($P_{EL}(H)$) and the polarization of light passing through the magnetic layer $P_T(H)$ (the $P_T(H)$ dependences are presented in the Fig. 1(b)). For both cases, the magnitude of the coercive field (H_c), as well as the saturation magnetic field (H_s), depends on the selected composition. The minimum values of H_c and H_s were obtained for the sample with the greatest thickness of the Co layer (a = 4), while varying the Pt content has a slight effect on these parameters. As the Co thickness decreases, the H_c and H_s values monotonically increase to values of 1300 Oe and 1700 Oe respectively.

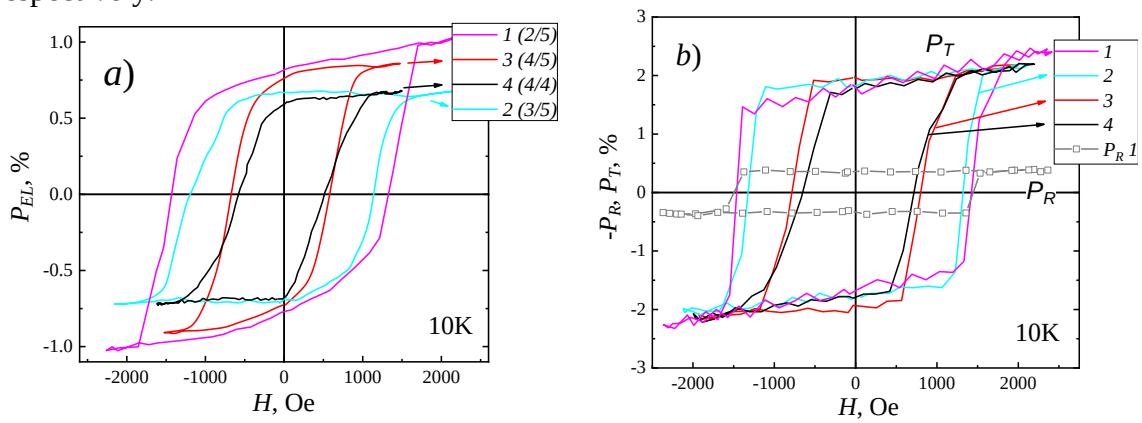


Fig. 1. (a) Magnetic field dependences of the circular polarization degree of EL, measured at a temperature of 10 K and a diode current of 10 mA (current density 50 mA/mm^2). The sample number for each curve is indicated on the graph (composition values are given in parentheses); (b) Magnetic field dependences of the circular polarization degree of transmission (P_T - lines) and reflection (P_R - points), measured at a temperature of 10 K. The sample number for each curve is indicated on the graph.

In Fig. 1(b), the dots show the magnetic field dependence $P_R(H)$ for sample 1. The $P_R(H)$ dependence is determined by the magnetization of the ferromagnetic contact, and the polarization value does not exceed 0.4%. Due to the geometry of the experiment, the polarization of the reflected light has the opposite sign and, therefore, reduces the P_{EL} value. It should be noted that samples with the highest P_{EL} values are characterized by the lowest P_R values, which indirectly confirms the influence of the reflected light on the measured value of the circular polarization degree.

Conclusion

Thus, the work demonstrated the possibility of controlling the parameters of the magnetic field dependence of the circular polarization degree of EL in spin LEDs with a $CoPt_x$ multilayer magnetic contact. Control of the coercive field and saturation magnetic field within the range of 500–1500 Oe is carried out by varying the thickness of the Co layer. The influence of the Pt thickness on the magnetic characteristics has not been established; however, the Pt thickness affects the maximum value of the circular polarization degree of EL. It is assumed that the mechanism that controls the parameters of the hysteresis loop is a change in the magnetic anisotropy constant; the mechanism responsible for the change in P_{EL} is spin precession in the built-in magnetic field of an inhomogeneous magnetic film.

REFERENCES

1. **M.V. Dorokhin, et.al.**, Manipulation of micromagnetic structure of thin Co/Pt multilayer films by precise variation of Co and Pt thicknesses, Journal of Alloys and Compounds. 926 (2022) 166956.

Manufacturing of C-Cu-C laser targets

L.E. Guss, V.N. Gornov, A.V. Savelyev, O.V. Titova
FSUE "RFNC-VNIITF named after Academician E.I. Zababakhin", Snezhinsk, Russia
E-mail: dep5@vniitf.ru (for Guss L.E.)

Annotation. In this work, the technology for manufacturing free-hanging targets for laser experiments was developed. The target consists of sequentially deposited C-Cu-C layers with thicknesses of 50; 50; 50 nm, respectively. The formation of thin films was carried out by magnetron sputtering. Studies were carried out on the chemical composition of the layers, surface topology and the content of diamond-like bonds in the carbon layers.

Keywords: magnetron sputtering, multilayer coatings, laser target, free-hanging film

Introduction

This paper presents a technology for manufacturing free-hanging multilayer targets for experiments on measuring the range of X-ray radiation in copper plasma [1, 2]. The target itself consists of two carbon disks, 5 mm in diameter, between which half a copper disk is located [3,4].

Materials and methods

To obtain a free-hanging film, a thin separating layer of table salt (~ 100 nm) is sprayed onto a substrate with a diameter of 25 mm and a thickness of 1 mm using resistive sputtering.

Next, to obtain a C-Cu-C film with a thickness of 50-50-50 nm, a magnetron sputtering installation was used. The vacuum was evacuated to $6.5 \cdot 10^{-5}$ mbar, the operating pressure was set to $3.0 \cdot 10^{-3}$ mbar, and argon was used as the working gas.

During the deposition process of the first layer of carbon, a mask with a diameter of 25 mm with 8 holes with a diameter of 5 mm was used. Nearby were aluminum foil 30 microns thick, used to examine the resulting coating on an electron microscope, and a test sample with a mask for measuring the layer thickness. After deposition, the foil and mask were removed. To deposit a layer of copper, another mask with a diameter of 25 mm, with 8 half-holes, was placed, and samples were installed nearby to study the composition and measure the thickness of the layer. The last layer of carbon was sprayed in the same way as the first.

After deposition, the substrate with the film was carefully immersed in distilled water so that after the salt dissolved, the film separated from the glass surface and floated to the surface of the water. The film floating on the surface of the water was caught using a mandrel, removed from the water, and dried.

Results and discussions

As a result of the work done, a free-hanging C-Cu-C film was obtained. The thickness of each coating layer was measured using an optical profilometer. Thickness of the bottom carbon layer d = 50 nm ± 10 nm, the copper layer d = 56 ± 5 nm and the top carbon layer d = 50 nm ± 10 nm.

To check the layers for the absence of impurities, **the method of X-ray spectral microanalysis** was used.

The chemical elemental composition of the carbon layer contains only lines belonging to aluminum, oxygen and carbon. Where oxygen and aluminum are found in aluminum foil.

The chemical elemental composition of the copper layer includes only copper. No other impurities were found.

Raman spectroscopy (RSS) using a Raman microscope was used to determine the number of diamond-like bonds [5, 6].

According to the data obtained, the content of diamond-like bonds for the studied film sample with a thickness of 50 nm was, on average, 55%.

Conclusion

The technology for manufacturing free-hanging C-Cu-C targets for laser experiments has been developed. The layer thicknesses are 50-56-50 nm, respectively. The coating was studied for the elemental composition and content of diamond-like bonds in the carbon layer. The elemental composition of each layer did not reveal the presence of impurities in the layers of carbon and copper. The content of diamond-like bonds in the carbon layer is 55%.

REFERENCES

1. A.V. Potapov, E.A. Loboda, V.Yu. Politov, etc. Plasma physics,33, №3 (2007). (in Russian)

2. V.Yu. Politov. Modeling of thermal wave propagation in a target under conditions of irradiation with high-intensity p-polarized laser radiation. Quantum electronics, 43(5) (2013) 443-457.(in Russian)

3. R.A. London, J.I. Castor. Design of short pulse laser driven opacity experiments. High Energy Density Physics, 9 (2013) 725-730.

4. S.J. Davidson, K.Nazir, S.J. Rose, R.Smith, G.J. Tallents. Short-pulse laser opacity measurements. Joutnal of Quantitative Spectroscopy & Radiative Transfer 65 (2000) 151-160.

5. Graselli G., Snavili M. et al. Applications of Raman spectroscopy in chemistry. Per. from English - M.: Mir, (1984) 216.

6. Uglov V.V., Kuleshov A.K. etc. Raman scattering of light in hydrogenated metal-carbon composite films. Journal of Applied Spectroscopy, 73(3), May-June (2006) 346.(in Russian)

Structure of a software -hardware complex for the study of ferroelectrics

N. S. Emelyanov✉, **A. E. Zhurina, E. A. Pecherskaya, A. E. Shepeleva**
Penza State University, Penza, Russia;
✉ emelianoff.nikita@gmail.com

Abstract. The work presents the structure of a software- hardware complex that allows you to determine the electrical parameters of ferroelectrics with high accuracy, and thanks to the software, process the obtained parameters and effectively study the electrophysical parameters of ferroelectric elements. The software -hardware complex consists of a measuring unit, a computer, and software. The software allows you to process the data obtained as a result of measurements, analyze them and provide the user with information about the results of measuring the electrical parameters of the samples under study. The uniqueness of the developed software-hardware complex lies in the modification of the traditional Sawyer-Tower circuit, which makes it possible to increase the efficiency of measurements and reduce methodological errors in measuring electrical parameters. When using the principle of information redundancy, the method of the modified Sawyer–Tower circuit helps to increase the accuracy of measurements by 4 times compared to measuring instruments implemented using other measurement methods.

Keywords: Ferroelectrics, electrophysical parameters, Sawyer–Tower circuit, software - hardware complex.

Introduction

Due to the unique ferroelectrics properties, they are actively used in nano- and microelectronics. Therefore, it is important to qualitatively study the electrophysical parameters of ferroelectrics and products based on them. A structure of a software-hardware complex for the study of ferroelectrics is proposed. The developed measuring complex demonstrates unique capabilities: firstly, it allows to obtain with great accuracy the electrical parameters of ferroelectrics and elements based on them, taking into account their shapes and sizes; secondly, it makes it possible to take into account the influence of temperature on the sample, thanks to the presence of a thermal chamber [1]. The software of the complex allows to process the data obtained as a result of measurements, analyze them and provide the user with information about the electrical parameters of the samples.

Materials and Methods

The work is based on improving electrical models of ferroelectric materials in order to reduce methodological errors in measuring electrical parameters, which are important to take into account when studying thin-film samples in which size effects may occur. In order to reduce the instrumental components of measurement errors, a modification of the Sawyer-Tower circuit and the creation of channels on its basis for measuring the electrophysical parameters of active dielectrics are proposed, which forms the basis of the created software- hardware complex [2].

Results and Discussion

The software- hardware complex consists of a computer and measuring unit. The structure of the software – hardware complex is shown in Figure 1.

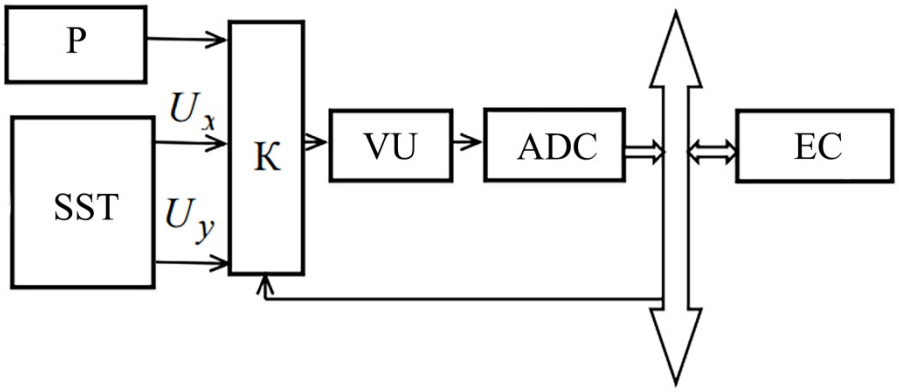


Fig. 1. cture of the measuring unit. P – converter of electrical resistance to voltage; SST – Sawyer-Tower circuit; K – commutator of measuring signals; VU – output amplifier; ADC – analog-to-digital converter.

The measuring unit contains a high-voltage amplifier that allows you to set the voltage amplitude on the sample to 250 V, the voltage frequency is set in the range from 10 to 2000 Hz. The test sample is connected to an improved Sawyer-Tower measuring circuit. Measuring signals proportional to the electric field strength and electrical displacement in the sample after a series of transformations are transmitted to the computer. The measuring unit is controlled and the measuring information is processed by a personal computer (PC), which is connected to the measuring unit using an interface module via a USB port. The software- hardware complex is designed to operate at ambient temperatures from +10 to +35 ºC and relative air humidity up to 80% at 25 ºC. The measuring unit is made in a plastic case in accordance with modern requirements for electrical safety and electromagnetic compatibility for measuring instruments used in testing laboratories.

Conclusion

The work presents the structure of a software- hardware complex that allows you to determine the electrical parameters of ferroelectrics with high accuracy, and thanks to the software, process the obtained parameters and effectively study the electrophysical parameters of ferroelectric elements. When using the principle of information redundancy, the method of the modified Sawyer–Tower circuit helps to increase the accuracy of measurements by 4 times compared to measuring instruments implemented using other measurement methods.

Acknowledgments

The work was supported by the grant of the Ministry of Science and Higher Education of the Russian Federation «Synthesis and research of promising nanomaterials, coatings and electronics devices» (FSGE-2024-0004).

REFERENCES

1. **Emelyanov N.S., Zhurina A.E., Pecherskaya E.A., Shepeleva J.V., Maksov A.A.,** A software-hardware complex for the study of electrophysical parameters of active dielectrics, St. Petersburg State Polytechnical University Journal. Physics and Mathematics. 16 (3.1) (2023) 341–345. DOI: https://doi.org/10.18721/JPM.163.162.

2. **Vakulenko A.F., Vakhrushev S.B., Filimonov A.V., Zhang N.**, An automatic system for measuring the ferroelectric hysteresis loops using the modified Sawyer – Tower circuit, St. Petersburg Polytechnical State University Journal. Physics and Mathematics. 12 (4) (2019) 89–96. DOI: 10.18721/JPM.12409.

A mmWave dielectric antenna with symmetric beam compatible with PCB machinery

M. Ershova[1✉], **A. Prikhodko**[1,2,4], **A. Shurakov**[1,2,3], **G. Gol'tsman**[1,2,4]
[1] Moscow Pedagogical State University, Moscow, Russia;
[2] HSE University, Moscow, Russia;
[3] National University of Science and Technology "MISIS", Moscow, Russia;
[4] Russian quantum center, Skolkovo, Moscow, Russia;
✉ mi_ershova@student.mpgu.edu

Abstract. The current decade is associated with the start of active deployment and use of fifth generation networks, while the ongoing developments in the sixth generation communication technologies should be finalized in the upcoming decade. It is forecasted that sufficiently directive wireless transceivers will become integral parts of the next generation wireless communication systems. In this study, we report on the development of a low-cost millimeter wave dielectric antenna with nearly symmetric beam. The antenna makes use of a dual-stage dielectric multimode interference power divider terminated by 16 dielectric tapers with flare angles of 6-12°. It is designed for operation at frequencies of 50-77 GHz. The design is developed for fabrication by the means of printed circuit board prototyping machinery from high-permittivity laminates and, therefore, is compatible with the Si platform for solid-state electronics and integrated photonics. The fabricated antenna samples exhibit half-power beamwidths of 13-14° with corresponding side lobe levels of approximately −10 dB, as measured at 52 GHz.

Keywords: millimeter wave, dielectric rod antenna, antenna array, high-permittivity laminate, direct machining.

Funding: This study was funded by the Russian Science Foundation grant number No. 21-72-10119, https://rscf.ru/project/21-72-10119/.

Introduction

Currently, science and technology are interested in the development of low-cost, efficient and compact modules capable of transmitting and receiving of millimeter wave (mmWave) signals. Wireless channels of the fifth and sixth generation (5/6G) communication networks require sufficiently directive transceivers as their crucial elements [1]. Moreover, novel mmWave antenna solutions are in demand by such applications as radar systems or atmospheric monitoring within the context of meteorological and climatological remote sensing [2, 3], etc.

In this study, we report on the development of a low-cost mmWave integrated dielectric rod antenna (DRA) array. Our design makes use of a dual-stage dielectric multimode interference power divider (MMIPD) [4] terminated by a 4×4-element planar array of dielectric tapers [5] with flare angles of 6-12°. Such a design can be easy tuned for efficient operation at any desired frequency within 50-77 GHz. It is developed for fabrication by the printed circuit board (PCB) prototyping machinery from high-permittivity laminates and, therefore, is naturally compatible with solid-state electronics and integrated photonics based on Si platform.

Results and Discussion

Figure 1 (a) provides a photograph of the fabricated DRA arrays with flare angles α of 6° and 12°. They are developed for operation at 52 GHz, and their MMIPDs are equipped with input taper interfaces for coupling with rectangular metallic waveguides of a constant waveform source and power detector during beam profile measurements. The developed structures are characterized by simplicity and cheapness of fabrication. The DRA array samples are fabricated by the means of direct machining from a high-permittivity PCB laminate (FSD1020T series). This material possesses relative permittivity of 10.2 and a loss tangent of 0.002 at 10 GHz according to the specifications provided by the manufacturer, and its dielectric properties at 130-160 GHz are briefly reported in [6]. Unwanted metallization is preliminary removed within 60 s etching in nitric acid. The first and the second stages of the samples' MMIPDs are attached through dielectric holders made from a low-permittivity material by a 3-dimensional (3d) printing.

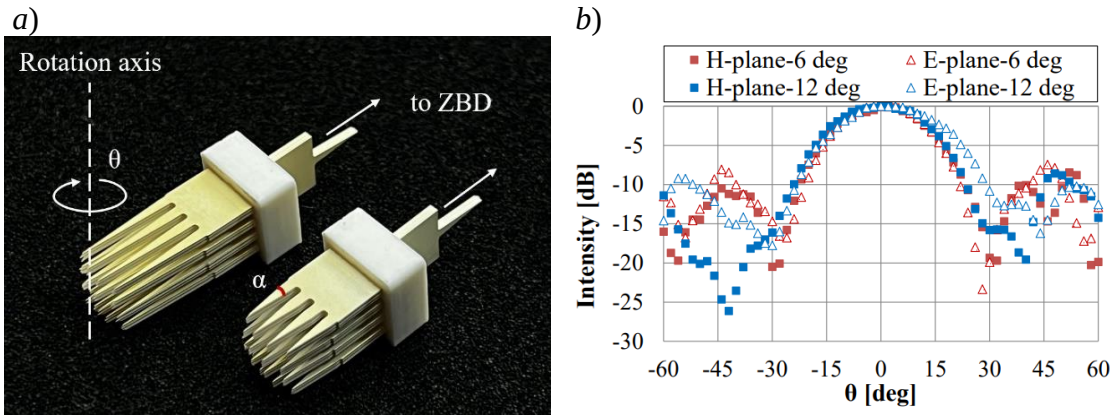


Fig. 1. (a) Photograph of the fabricated DRA arrays; (b) H- and E-plane beam profiles of the fabricated samples measured at 52 GHz.

The fabricated DRA array samples are further experimentally studied. Experimental setup for the far-field radiation pattern measurements mainly makes use of a 50-77 GHz backward-wave oscillator (BWO) and a zero-biased Schottky diode detector (ZBD). As shown in figure 1 (b), measured H- and E-plane beam profiles of the fabricated DRA arrays are nearly identical at operating frequency of 52 GHz. They are characterized by half-power beamwidths of 13-14° with corresponding side lobe levels of approximately −10 dB for both antenna samples. Thus, fabrication tolerance is quite low, and potential errors in fabrication of the most mechanically vulnerable elements, i.e., dielectric tapers, do not compromise performance of the integrated dielectric structure. Results of the simulations and detailed performance analysis of the developed antenna structures, including 3d radiation patterns, are to be presented at the conference site. Given that the proposed antenna design is naturally compatible with Si platform, it can be of use in solid-state electronics and integrated photonics of the mmWave band.

REFERENCES

1. **Boulogeorgos A., Alexiou A., Merkle T., Schubert C., Elschner R., Katsiotis A., Rodrigues F.**, Terahertz Technologies to Deliver Optical Network Quality of Experience in Wireless Systems Beyond 5G. IEEE Communications Magazine. 56(6) (2018) 144–151.

2. **Michler F., Scheiner B., Reissland T., Weigel R., Koelpin A.**, Micrometer Sensing With Microwaves: Precise Radar Systems for Innovative Measurement Applications. IEEE Journal of Microwaves, 1(1) (2021) 202–217.

3. **Westwater E., Crewell S., Matzler C.**, A review of surface-based microwave and millimeter-wave radiometric remote sensing of the troposphere, September 2004URSI Radio Science Bulletin. 310 (2004) 59-80.

4. **Soldano L., Pennings E.**, Optical multi-mode interference devices based on self-imaging: principles and applications. Journal of Lightwave Technology, 13(4) (1995), 615–627.

5. **Prikhodko A., Yaropolov T., Shurakov A., Gol'tsman G.**, Parametric model of a dielectric rod antenna array for terahertz applications, Proceedings of the 34th European Modeling & Simulation Symposium (EMSS 2022).

6. **Prikhodko A., Belikov I., Lvov A., Shurakov A., Gol'tsman G.**, Millimeter wave photonic crystal waveguides fabricated via direct machining, St. Petersburg Polytechnic University Journal. Physics and Mathematics. 15 (3.3) (2022).

System of the temperature controller for the rubidium frequency standard

E. V. Isupova [1]✉, **A. P. Valov** [2]

[1] Peter the Great Saint-Petersburg Polytechnic University, Saint Petersburg, Russia;

[2] The Bonch-Bruevich Saint Petersburg State University of Telecommunications, Saint Petersburg, Russia

✉ isupova.e24@mail.ru

Abstract. Temperature is a factor that degrades the frequency stability of the rubidium quantum frequency standard. Therefore, we face the following task: maintaining high long-term temperature stability, which depends on the stability of many circuit parameters. The article presents the developed thermoregulation scheme, which includes a Wheatstone bridge, which uses a thermistor, an instrumental amplifier with 3 operational amplifiers and a PID controller, which provides stable and accurate adjustment of the system, minimizing error and responding to changes in real time. A laboratory test of the developed scheme and the previous version was carried out. According to the results of the analysis, it is shown that the developed scheme has a lower imbalance of the bridge and a lower error signal.

Keywords: Thermoregulation, Wheatstone bridge, instrumental amplifier, PID-controller.

Introduction

A device that can produce a wide range of frequencies and compare the studied and generated frequencies is known as a standard. The rubidium quantum frequency standard contains a quantum discriminator that is designed to detect any deviation in the frequency of a probing signal from the transition frequency of an atom of rubidium-87 isotope and generate an error signal. In addition to the thermostatic base, the quantum discriminator also has thermoregulators for the spectral lamp, filter cell, and gas cell.

All thermal stabilization systems operate on the same principle: when the temperature of an object that needs to be thermoregulated deviates from a specific value, the amount of heat or cold applied to that object must be adjusted accordingly [1]. The setpoint of the thermostat can be affected by a variety of uncontrollable factors such as fluctuations in room temperature, drift in bias voltages and currents, drift in bridge resistances, thermal voltages between dissimilar metals, noise, and others. The goal of the thermostat is to keep the temperature of the temperature sensor within a given range with a certain level of accuracy.

When designing thermostatic systems, there are several challenges that need to be addressed, one of which is maintaining long-term stability. This depends on the stability of temperature sensor parameters, which can be ensured by using high-precision wire thermistors made from copper or platinum wire.

Materials and Methods

This paper presents a new approach to stabilize the temperature of a spectral lamp used in a quantum discriminator. The proposed system includes a direct heating thermistor with negative temperature coefficient of resistance (TCR) and a Wheatstone bridge to measure the temperature. Figure 1 shows the schematic diagram of the proposed system. The thermistor is used as a feedback element to adjust the voltage applied to the lamp, thus maintaining a stable temperature. This approach has the potential to improve the accuracy and reliability of the quantum discriminator by minimizing temperature fluctuations.

The error signal can be calculated using the following formula:

$$U_{bridge2} - U_{bridge1} = U_{in}\left(\frac{R_2}{R_2 + R_d} - \frac{R_6}{R_6 + R_4}\right), \quad (1)$$

The main sources of error in thermoregulators are the temperature coefficient of bridge resistance and the drift of input bias voltage in interface operational amplifiers. Figure 1 illustrates that an increase or decrease in R_6 has the opposite effect on $V_{bridge1}$ compared to an increase or decrease in R_4 [2]. This implies that if R_6 and R_4 have similar temperature coefficients, the

temperature effect on $V_{bridge1}$ can be minimized or even eliminated. However, this is not possible with R_2. Therefore, it is ideal for R_2 to have a very low temperature coefficient itself.

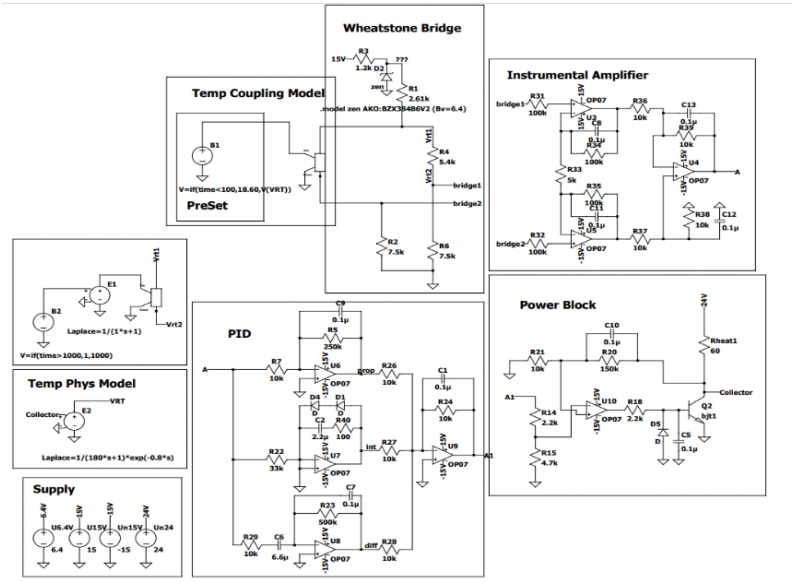


Fig. 1. Thermal stabilization scheme for the quantum frequency standard.

Results and Conclusion

Figure 2 illustrates the results of monitoring changes in the resistance of a thermal sensor within a thermal chamber over two cycles of the thermostat. The black curve represents a circuit with a differential amplifier and proportional amplifier, while the purple curve illustrates a circuit featuring an instrumental amplifier (IA) and PID controller. Every 4 hours, the air temperature within the chamber was altered.

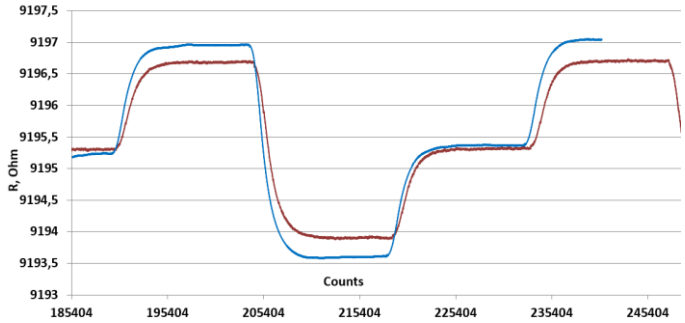


Fig. 2. Graph of the change in resistance of the temperature sensor in the thermal chamber. The blue line represents the current circuit, and the red line represents the improved circuit.

The change in resistance of the thermal sensor in the improved circuit is 20% lower than in the original design, indicating greater isolation of the bridge from the rest of the circuit, which was achieved through the use of the IA. This means that the signal is less unbalanced, and the error is reduced. The results obtained from temperature stabilization will improve the short- and long-term stability of the output frequency in the quantum frequency standard. This is particularly important because the frequency is more sensitive to changes in temperature in different parts of the device, especially in the optical component. In the future, this design will be tested in a thermal chamber as part of the QFS.

REFERENCES

1. **Ingberman M.I., Fromberg E.M., Graboy L.P.,** Thermostating in communication technology, Moscow, (1979).

2. **Madhavan Unni P. K., Gunasekaran M. K., Kumar A.,** ±30 μK temperature controller from 25 to 103° C: Study and analysis, Review of scientific instruments, 74 (1) (2003) 231-242.

New stripline linear sensor design for industrial applications

D. Yu. Klimenko ✉
Peter the Great Saint-Petersburg Polytechnic University, Saint-Petersburg, Russia Federation
✉dasha.klimenko.01@inbox.ru

Abstract: The development of our own production of linear sensors plays a key role in ensuring national security. This eliminates dependence on imports of similar components and ensures the reliable functioning of local systems. Basic linear sensors are highly reliable, easy to use and highly accurate. The developed linear sensor represents a significant achievement in the field of sensor technology. Its special strip line configuration allows for highly accurate and reliable measurements over a wide range of operating conditions. The control and information processing circuit designed for this sensor ensures efficient operation and optimal use of the acquired data. The first tests of the linear sensor confirmed its high quality and accuracy. The significant potential of a linear sensor on a domestic basis opens the way to its further improvement and use in various fields of industry. This product can meet national needs for high-tech components and help promote the domestic technology industry in the global market.

Keywords: Linear sensor, digital processing, signals, phase shift.

Introduction

Developing our own manufacturing base for linear sensors is an important aspect of national security. This allows us to free ourselves from dependence on the import of such components and guarantee the stable functioning of domestic systems. Nowadays, linear sensors are widely used in many sectors of the economy, from industry to consumer electronics. Basic linear sensors are reliable, simple and accurate [1]. Can be applied as motion control, valve position sensor, industrial potentiometer replacement, LVDT replacement, actuator position feedback, front panel precision controls. At the same time, domestic production can help reduce import costs and provide the ability to repair equipment [2]. This stimulates national research and development, helps create new jobs and improve the country's technological competitiveness. Localization of linear sensor production also provides more convenient technical support and service for domestic customers. Quick access to the components and services you need allows you to respond more quickly to market needs, improve service quality, and improve customer satisfaction.

Materials and Methods

The characteristics of linear sensors include: simple non-contact target, full absolute measurement, standard 4-layer PCB manufacturing process, temperature stability, high repeatability. Can be applied as motion control, valve position sensor, industrial potentiometer replacement, LVDT replacement, actuator position feedback, front panel precision controls.

In Fig. 1 shows the developed highly sensitive sensor 10 cm long, made in the form of strip lines of a special configuration. One of the main features of this development is the use of domestically produced components [2] to ensure high quality, reliability, improved stability characteristics and measurement accuracy.

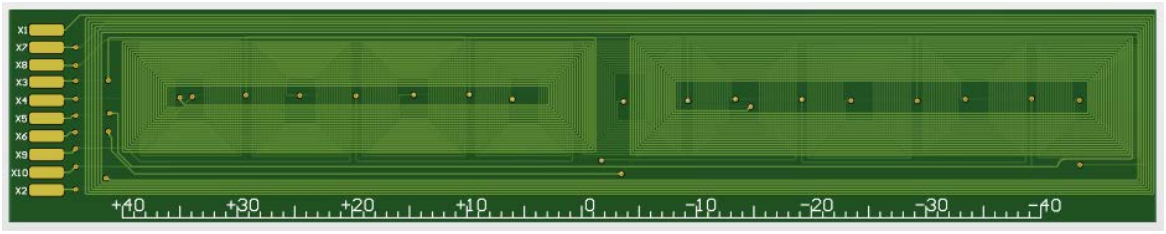


Fig. 1. Model of the sensitive element of the linear displacement sensor

To ensure the measurement mode, a control and information processing circuit was developed, which is shown in Fig. 2. This circuit uses a microcontroller from Milandr, which makes it possible to apply digital processing methods and obtain a minimum error [3].

Results and discussion

The secondary conversion block is shown in Fig. 2.

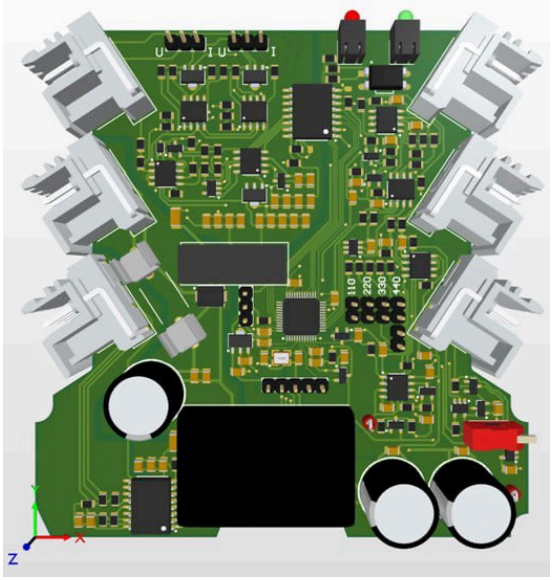


Fig. 2. Secondary conversion block

The first tests of the sensor showed that its error was only 1%. This result confirms the high quality of development and accuracy of measurements.

Conclusion

Thus, the development of linear sensors on a domestic basis helps to increase the competitiveness of various sectors of the economy in which they are used. The availability of reliable and innovative solutions improves productivity, efficiency and product quality, which in turn helps to expand exports and attract investment. Considering all these factors, the developed domestically based linear sensor has significant development potential to meet national needs for such key components and contribute to the development of the domestic technology industry.

REFERENCES

1. **Mingazova I.,** Linear displacement transducers, Young Scientists Forum. 7 (23) (2018) 633-638.
2. **Prokofiev G., Stakhin V., Obednin A.,** MODERN DOMESTIC SPECIALIZED CIRCUITS FOR POSITION SENSORS, Izvestiya SFedU. Engineering Sciences. 3 (164) (2015) 200-211.
3. **Horowitz P., and Hill W.,** The Art of Electronics, Second Edition, Cambridge University Press, Cambridge, UK, 1998.

Analysis of the trajectory of a symmetrical spinning top in the Earth's magnetic field

S. A. Klimova ✉
A. A. Goldberg

Peter the Great St.-Petersburg Polytechnic University
✉sonaklimova30@gmail.com

Abstract. The original canonical variables and integrals of motion are expressed. Using the generating function of the canonical transformation, a Hamiltonian is obtained whose generalized coordinates are cyclic frequencies. An explicit form of the dependence of the system energy on the moments of inertia in the action-angle variables for this model is found. A top charged uniformly throughout its entire volume in a magnetic field is associated with the Lagrange function through the Euler angles. A system configuration has been found in which the problem is solved analytically. An expression is obtained for the case of a non-stationary magnetic field. An analysis of solved cases is presented

Keywords charged symmetrical top, Larmor frequency, uniform magnetic field, Euler angles, nuclear magnetic resonance, nutation period, Larmor precession, non-stationary magnetic field.

Introduction

Solving a number of problems associated with launching various rockets from moving objects, lifting underwater vehicles, as well as using torque in work related to drilling, diamond processing and geological exploration of minerals, it is necessary to take into account a number of new circumstances that influence the trajectory of the top. One of them is the magnetic field of the Earth and various objects that can be placed nearby. The modern classical theory of describing the trajectory of a top has a number of shortcomings that do not allow taking into account some physical phenomena, including the magnetic field, which introduces an error when comparing theoretical models and experimental data and creates problems for practical use of calculations in various devices.

Therefore, we propose a new model for analyzing the trajectory of a spinning top in a Cartesian coordinate system and in a system of action-angle variables, the total energy of which is compared to the Lagrangian through Euler angles. In addition, during the calculations, a method is proposed for finding an explicit form of dependence of the total energy on the moments of inertia, as well as three equations describing the symmetry of the spinning top motion with respect to cyclic frequencies $(\omega_\varphi, \omega_\psi, \omega_\theta)$ expressed in terms of moments of inertia $(I_\varphi, I_\psi, I_\theta)$. When considering the motion of a spinning top in a magnetic field, integrals of motion are found, which allows us to say which quantities describing the system are preserved even under the influence of an external magnetic field. Of particular interest is the configuration of the system, in which it will be possible to express the solution analytically. A description of the motion of a spinning top in the case of an nonstationary external magnetic field is proposed using the methods of perturbation theory.

Materials and Methods

Our model, within the framework of classical theory, is described by three coordinates of the center of inertia of the top and Euler angles (φ, ψ, θ), which determine the orientation of the axes of the moving coordinate system relative to the stationary system. Fig. 1 shows the appearance of a spinning top with a coordinate system and a system of acting forces, moments and a magnetic field. The Lagrange function for describing mechanical motion is expressed in the following form [1]:

$$E = L = \frac{I_x}{2}\left(\dot{\varphi}^2 \sin^2\theta + \dot{\theta}^2\right) + \frac{I_z}{2}\left(\dot{\varphi}\cos\theta + \dot{\psi}\right)^2 - \frac{eH}{2Mc}\left(\left(I_x \sin^2\theta + I_z \cos^2\theta\right)\dot{\varphi} + I_z\dot{\psi}\cos\theta\right),$$

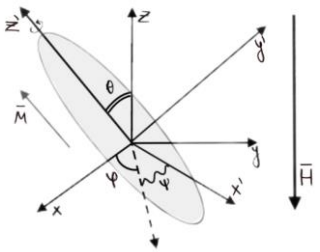


Fig. 1 Model of a spinning top with angles and direction of rotation with orientation of the magnetic field

where

$I = \begin{pmatrix} I_x & 0 & 0 \\ 0 & I_y & 0 \\ 0 & 0 & I_z \end{pmatrix}$ - the inertia tensor, for a symmetric spinning top, is fulfilled $I_y = I_z$

Further, when considering a spinning top in a uniform magnetic field $\bar{H} \| \bar{M}$, we use the expression [2], considering that the mutual position of individual moments in the magnetic field remains unchanged:

$$\frac{d\bar{M}}{dt} = \left[\bar{M} \times \gamma \bar{H}_0 \right]$$

Results and Discussion

As a result of the transformations, we obtain a system of equations:

$$\begin{cases} \dot{\varphi} = 2\left|\frac{eH}{2mc}\right| \sin^2\left(\frac{I_z}{2I_x}\dot{\psi}_н t\right) \\ \dot{\theta} = \left|\frac{eH}{2mc}\right| \sin\theta_н \sin^2\left(\frac{I_z}{I_x}\dot{\psi}_н t\right) \\ \dot{\psi} = \dot{\psi}_н \left(1 - \frac{|eH|}{mc\dot{\psi}_н} \cos\theta_н \sin^2\left(\frac{I_z}{2I_x}\dot{\psi}_н t\right)\right) \end{cases}$$

In an external magnetic field, passing into a rotating coordinate system, we obtain:

$$\bar{M} \times \gamma \left(\bar{H}_0 + \frac{\bar{\Omega}}{\gamma} \right), \ \bar{\Omega} = -\gamma \bar{H}_0 = \overline{\omega_L}, \ \bar{H}_{eff} = \bar{H}_0 + \frac{\bar{\omega}}{\gamma} + \bar{H}_{ext}$$

Conclusion

Considering that the relative position of individual moments in the magnetic field remains unchanged, $\bar{M}$ precesses relatively $\bar{H}_{eff}$, in the laboratory coordinate system $\bar{M}$ rotates relatively $\bar{H}_0$ with the Larmor frequency $\overline{\omega_L} = \frac{e\overline{H}}{2mc}$. By adding a field H_{ext}, a "reversal" of the magnetic moment will be observed. When considering an unsteady magnetic field, using the methods of perturbation theory, all forces and phenomena that can have a significant effect on the spinning top will be taken into account. In the future, when improving this model, taking into account the influence of the "neighboring" dipole, it will be possible to describe multiple nuclear resonance, spin wave propagation and other phenomena in magnonics.

REFERENCES

1. **Landau L. D., Liefshitz E. M.**, Theoretical physics, Vol. 1, Mechanics, Nauka, Moscow, 1976.
2. **Leshe A.** Nuclear induction. Veb Deustscher Verlag Der Wissenschaften, Berlin, 1963.

The role of ectons in the vacuum breakdown process

V. Y. Kozhevnikov [1✉], **A. V. Kozyrev** [1], **A. O. Kokovin** [1]
[1] Institute of High Current Electronics SB RAS, Tomsk, Russia;
✉Vasily.Y.Kozhevnikov@ieee.org

Abstract. This paper presents a valuable addition to the kinetic theory regarding vacuum breakdown formation in a planar vacuum gap, specifically focusing on the cathode plasma emission known as 'ectonic' (pulse-periodic/quasi-particle) nature. We investigate contributions of ectonic and continuous types of emission from the cathode in terms of their effects on the mechanism of anomalous ion acceleration and cathode plasma expansion during a short-term switching of the emission current corresponding to the death and birth of ectons.

Keywords: vacuum breakdown, Vlasov-Poisson equations, ectons.
Funding: The research was supported by RSF (project No. 23-29-00239).

Introduction

During the period of 2021-2023, in a series of theoretical papers by the employees of the Laboratory of Theoretical Physics of the Institute of High-Current Electronics SB RAS, a first self-consistent collisionless kinetic theory of cathode plasma expansion was formulated. It opened up a possibility to explain the physical nature of the plasma expansion phenomenon in vacuum discharge in details, as well as allowed to predict the average speed of a cathode plasma expansion in the vacuum diodes of various designs. It was shown that in a vacuum gap the key physical mechanism for the plasma expansion, regardless of the diode geometry and the connected electrical circuit, is the collisionless electrodynamic mechanism. It lies in the fact that the peripheral region of a dense cathode plasma in external electric field acquires an excess negative volume charge, leading to the appearance of a "virtual cathode" of amplitude $\Delta\varphi < 0$. The presence of this region ensures the influence of accelerating electrodynamic forces on ions near the emission center at the cathode, due to which the ions start to move towards the anode and acquire "anomalously" high values of kinetic energy $\varepsilon_i > qU_0$. The possibility of the so-called "deep potential well" near the cathode $|\Delta\varphi| > U_0$ existence has been also predicted by the proposed theory. This effect is entirely assured by the emission center parameters and does not depend on the voltage amplitude U_0 that is applied to the diode.

In this study, we expand our research experience to investigate the influence of the ectonic mechanism of cathode plasma emission on the phenomenon of anomalous ion acceleration, which results in the expansion of the cathode plasma. Building upon the kinetic theory established previously, we elucidate the mechanism of plasma emission from the cathode and present the results of numerical solutions of the kinetic equations for the model of a planar vacuum diode, considering the periodic variation in the emission current density. Our proposed approach enables a clear demonstration that the previously identified collisionless mechanism remains fundamentally significant even when the emission operates in a pulsed regime. Specifically, the death of one ecton is followed by the emergence of another, leading to the interception of the discharge current throughout the vacuum discharge.

REFERENCES

1. **Kozhevnikov V. Yu., Kozyrev A. V., Kokovin A. O., Semeniuk N. S.**, The kinetic simulation in vacuum electronics: uncovering the fundamental nature of non-Maxwellian distribution function effects., St. Petersburg State Polytechnical University Journal: Physics and Mathematics. 15 (3.3) (2022) 76–81.

2. **Kozyrev A., Kozhevnikov V., Semeniuk N. S., Kokovin A. O.**, Initial kinetics of electrons, ions and electric field in planar vacuum diode with plasma cathode., 32 (10) (2023) 105010.

Terahertz integrated H-plane bend: simulation and experimental investigation

A. K. Kozhukhovsky[1]✉, **S. S. Svyatodukh**[1, 2], **S. V. Seliverstov**[1] **and G. N. Goltsman**[2, 3]

[1] Physics Department, Moscow State Pedagogical University, Moscow, Russia

[2] National Research University Higher School of Economics, Moscow, Russia

[3] Russian Quantum Center, Moscow, Russia

✉ak_kozhukhovskii@student.mpgu.edu

Abstract. The usefulness of sub terahertz range is proved. Recently we have studied how to manufacture and use silicon waveguides and obtained insignificant signal loss. Final purpose is creating the integrated photonic circuit which needs not only straight parts which we have done already, but bend structures with minimal signal loss also. The insertion loss of the structure we made is -0.3 dB at frequency of 145.5 GHz. It is simulated and experimentally tested. Once again it proves us about possibility to create fully-fledged construction that has a lot of practical usage. It is a future of communication system, medicine and Artificial Intelligence development. In the end we will be able to make a physical structure which will be a hardware implementation of Artificial Neural Network with much lower energy consumption.

Keywords: terahertz photonics, waveguide, photonic integrated circuit, H-plane bend.

Funding: The study was supported by a grant from the Russian Science Foundation No. 2172-10119, https://rscf.ru/project/21-72-10119/.

Introduction

The interest of big data processing is actual in our world. To make a well-working device we study examples of using of THz range. We have to say that the basic problem of THz range is an absorption by water vapor contained in a surrounding air, but it has a lot of practical usage on short distances. The proofs of the usage of THz radiation were demonstrated as the future of fast internet [1], augment reality [2] and high resolution live-streaming [3]. But not only for internet sphere we are making a such device. Except for wireless communication, a short-range THz radar (distances of the order of several tens of meters) can operate with high resolution (for example with a large amount of fog in air) when classical systems as a lidar or optical stereo camera cannot operate. Such a system is also demonstrated previously. It can be used for delivery-robots and autopiloting of transport. All of this can serve as an example of perspective to use THz range. Our goal is to do the special device in the form of integral photonic circuit, to start to use all opportunities of THz range. To make such a device, we need not only straight parts, but bend also, without which we will not be able to make completed device.

Materials and Methods

In this paper we present the results of simulation and measuring of loss of a H-plane bend based on a THz waveguide made from a high resistivity silicon substrate. Along the waveguide we formed effective medium in such way that TE radiation mode could propagate inside of structure [4]. We used the finite element method in the simulation. The simulation frequency was variable from 126.5 GHz to 145.5 GHz. The parameters of the structure are the following: the length of tapers is 3500 μm, the width of the waveguide is 585 μm, the radius of perforations is 73 μm, the distance between centers of perforations is 165 μm, the radius of curvature is 4000 μm. A photo of the fabricated structure is shown in Fig.1(b). In the experiment the structure was placed in a plastic holder in a such a way the plastic didn't touch the effective media, it is the reason of the total width of the structure is more than the waveguide's width. As a detector we used the Schottky diode and as a radiation source a backward wave oscillator was used.

Results and Discussion

The simulation proved our expectations and showed a signal loss that is equal to -0.1dB. As we made a sweep through the frequency that is shown in Fig 1(a). On the plot we can see that loss of signal decreases by increasing of frequency. Also, on this plot we can see the "star" that shows experimental result for the S21 measurement of the H-plane bend at the frequency of 145.5 GHz. The results of the experiment and simulation approximately are the same. Real structure has a loss of signal of -0.3 dB.

a) *b)*

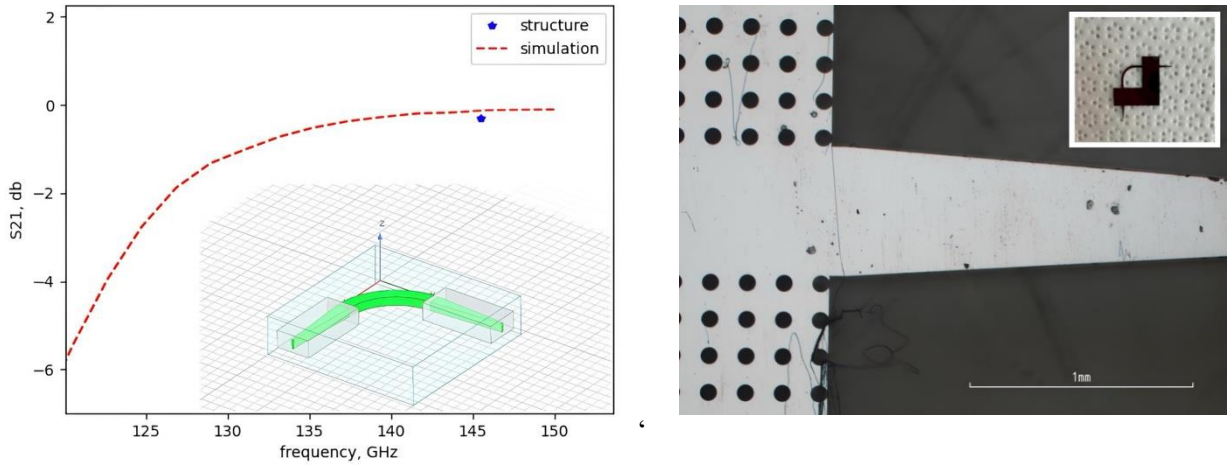


Fig 1. Dependence of the S21 parameter at different values of frequency(a) and manufactured structure photograph made by a microscope(b). The inset shows a photo of the fabricated structure.

According to the plot, we can say that the experimental data is in a good agreement with simulation results.

Conclusion

The H-plane bend structure is the next step to make the fully-fledged integrated photonic circuit that will let us use all opportunities of THz range. According to the investigations of our team and data we receive, it looks possible to make a full-fledged domestic work product created using domestic materials.

References

1. **N. Khalid, N. A. Abbasi, & O. B. Akan**, "Statistical characterization and analysis of low-THz communication channel for 5G internet of things," Nano Commun. Networks 22, 100258 (2019).

2. **C. Chaccour & W. Saad**, "On the ruin of age of information in augmented reality over wireless terahertz (THz) networks," in 2020 IEEE Global Communications Conference (GLOBECOM 2020) (IEEE, 2020), pp. 1–6.

3. **K. Nallappan, H. Guerboukha, C. Nerguizian, & M. Skorobogatiy**, "Live streaming of uncompressed HD and 4K videos using terahertz wireless links," IEEE Access 6, 58030–58042 (2018).

4. **Seliverstov Sergey, V., Svyatodukh Sergey, S., Prokhodtsov Aleksey, I., & Goltsman Grigory, N.** Optimization of a prism coupler for a THz photonic integrated metamaterial Si waveguide: simulation and experiment, St. Petersburg State Polytechnical University Journal. Physics and Mathematics. 16 (3.2) (2023) 406–410.

Field plates design optimization to increase breakdown voltage of GaN HEMT

E.A. Kozlovskaya [1]✉, **D.M. Kurbanbaeva** [1], **K.A. Tsarik** [1], **A.V. Lashkov** [1]
[1] National Research University of Electronic Technology, 124498 Moscow, Russia
✉ k89296190714@gmail.com

Abstract. This article presents the results of modeling the heterostructure of a normally-off n-channel transistor with various designs of field plates on electrodes. The use of field plates makes to possible to effectively control the distribution of the field in the channel and increases the breakdown voltage. The optimal design parameters of field plates to achieve maximum breakdown voltage were determined by study of the current-voltage characteristics, the distribution of the field in the channel and the concentration of the majority carriers in the channel. According to the simulation results, the use of two field plates at source and drain in the design increases the breakdown voltage by 25 %. Adding a field plate to the gate increases the breakdown voltage by 18 %. The triple lattice field plate gate design allows for improved electric field modulation and increased breakdown voltage by 30 % (relative to the original GaN HEMT without field plate).

Keywords: GaN, power transistor, field plate, breakdown voltage.

Funding: The work was supported by the Ministry of Education and Science in the framework of state task FSMR-2022-0004.

Introduction

A breakdown in HEMT (high electron mobility transistor) is a critical event, as it can lead to irreversible damage to the device [1]. Therefore, when designing such transistors, special attention is paid to their ability to withstand high voltages. Over the past two decades, in the course of research in the field of GaN HEMT, experts have proposed and implemented design solutions that allow an order of magnitude increase in breakdown voltage (BV). Currently, such methods of preventing breakdown are used as surface passivation by insulating layers, increasing the distance between gate and drain, increasing the thickness of the buffer layer, the application of buffer layers of complex composition (doped layers and superlattices), inclusion of field plates (FP) of various shapes and sizes into transistor design. Each of these methods has its advantages and disadvantages, and the choice of a particular method depends on the specific requirements of the application and the available resources. The use of FPs allows the electric field to be redistributed in the transistor channel between gate and drain. The shift of strong fields from critical areas to less significant areas of transistor leads to an increase in the BV [2, 3]. Preventing a sharp increase in the electric fields intensity under the edges of gate and drain electrodes reduces probability of occurrence of an avalanche breakdown. Due to the uniform distribution of the electric field, FP also helps to improve the thermal stability of transistor, preventing local overheating, and increase the reliability and durability of HEMT. In the work, the effect of different FP designs on the BV was investigated by computer simulation. The BV was estimated by current-voltage characteristic, including the distribution of the field and charge carriers in the channel to confirm the breakdown.

Materials and Methods

Modeling has been done with Sentaurus Technology Computer Aided Design (TCAD). Sentaurus TCAD contains several most closely to reality physical models that describe the physics of the device (spontaneous and piezoelectric polarization, drift-diffusion model, thermodynamic model).

The design of the HEMT heterostructure layers is shown in Fig.1 (*a*-*e*). The heterostructure consisted of a 2 mkm $Al_{0.05}Ga_{0.95}N$ buffer layer, a 300 nm GaN channel layer, a 15 nm $Al_{0.25}Ga_{0.75}N$ barrier layer, a 1 nm AlN spacer layer and a 100 nm Mg-doped p-type GaNcap-layer. The GaN HEMT without FPs (Fig.1 (*a*)) has a BV of about 300 V, which is not enough to application in the field of power electronics. According to the simulation results, the presence of a FP at the source (Fig.1 (*b*)) does not significantly affect the BV of the transistor. However, when using field plates

at the source and drain (L_S = L_D = 10 mkm, h_{SG} = 1 mkm, h_S = 1.5 mkm, h_D = 0.5 mkm) in the design, the BV increases by 25 % (Fig.1 (*c*)). Adding a FP to the gate (Fig.1 (*d*)) (L_g = 6 mkm and H_g = 0.005 mkm) increases BV by 18 %. The design of the gate FP in the form of a triple lattice (Fig. 1 (*e*)) makes it possible to improve the modulation of electric field and increase the BV by 30 % (relative to the initial GaN HEMT without FP). Lattice parameters: L_{g1} = 0.9 mkm, L_{gg1} = 0.3 mkm.

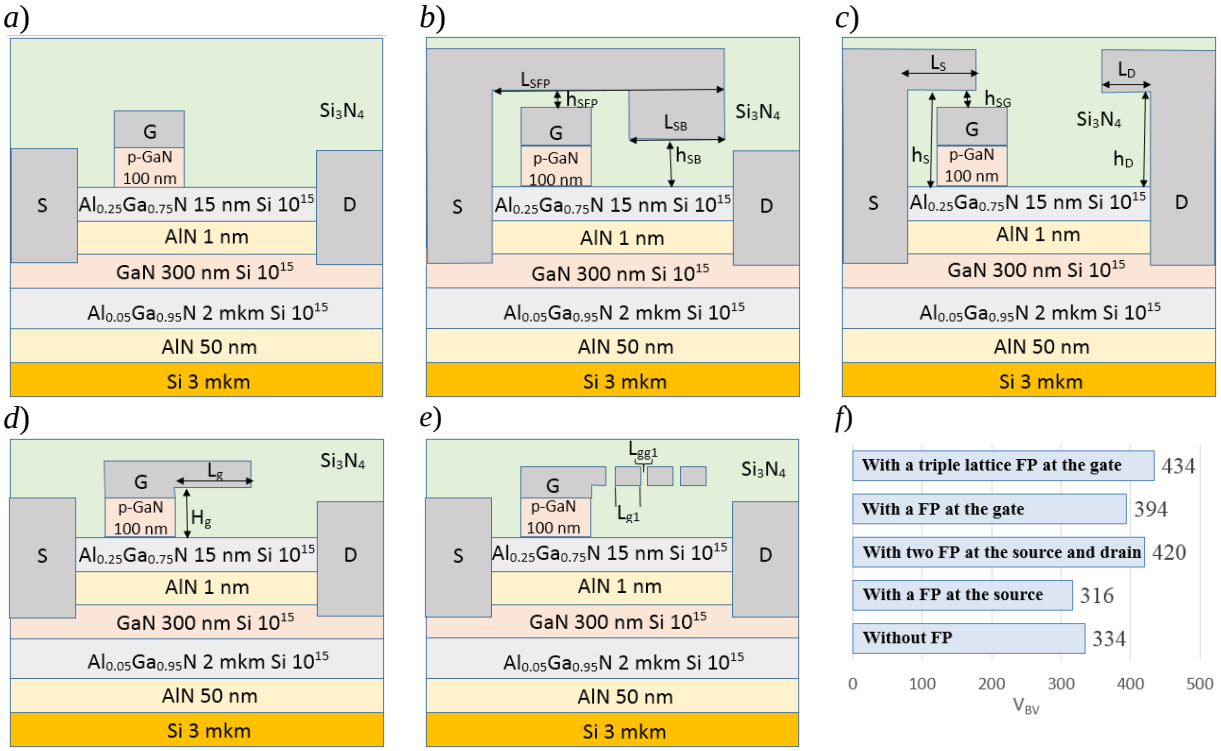


Fig. 1. Schematic cross-section GaN HEMT without FP (*a*), with a FP at the source (*b*), with two FP at the source and drain (*c*), with a FP at the gate (*d*), with a triple lattice FP at the gate (*e*). Comparison of the maximum breakdown voltages obtained as a result of modeling various FP designs (*f*)

Conclusion

The work demonstrated the simulation of normally-off n-channel p-GaN/$Al_{0.25}Ga_{0.75}N$/AlN/GaN/$Al_{0.05}Ga_{0.95}N$/AlN/Si HEMT by Sentaurus TCAD. Studying the influence of the FPs design on the BV made it possible to select the optimal parameters of FPs to achieve maximum BV of HEMT for the specified heterostructure. Comparison of the maximum BV for different FP designs showed the advantage of a transistor with a triple lattice FP at the gate over other transistors (Fig. 1 (*f*)).

REFERENCES

1. **J. Wuerfl, E. Bahat-Treidel, F. Brunner, E. Cho, O. Hilt, P. Ivo, A. Knauer, P. Kurpas, R. Lossy, M. Schulz, S. Singwald, M. Weyers, R. Zhytnytska**, Reliability issues of GaN based high voltage power devices, Microelectronics Reliability, Vol. 51(9-11), 2011, pp. 1710-1716.

2. **X. Xia, Z. Guo, H. Sun**, Study of Normally-Off AlGaN/GaN HEMT with Microfield Plate for Improvement of Breakdown Voltage, Micromachines, Vol. 12(11), 2021, 1318.

3. **P. Wang, C. Deng, H. Cheng, W. Cheng, F. Du, C. Tang, C. Geng, N. Tao, Q. Wang, H. Yu**, Simulation of High Breakdown Voltage, Improved Current Collapse Suppression, and Enhanced Frequency Response AlGaN/GaN HEMT Using a Double Floating Field Plate, Crystals, vol. 13(1), 2023, 110.

Combined resistive-capacitive MEMS switch for advanced communication systems

M. O. Morozov[1,2]✉, **I. V. Uvarov**[1]

[1]Valiev Institute of Physics and Technology of Russian Academy of Sciences, Yaroslavl Branch, Universitetskaya 21, 150007 Yaroslavl, Russia

[2] P.G. Demidov Yaroslavl State University, Sovetskaya 14, 150003 Yaroslavl, Russia

✉matvey19991@mail.ru

Abstract. The main characteristic of a MEMS switch is the ratio of capacitances in the open and closed states. For conventional switches, this ratio usually does not exceed ten and can be increased several times by using a floating potential electrode. In this work, the dependence of the capacitive characteristics, isolation and insertion loss of a switch with the «floating» electrode on the substrate properties is investigated.

Keywords: MEMS switch, floating potential, capacitance ratio, isolation, insertion loss, finite element method.

Funding: This work is supported by the program no. FFNN-2022-0017 of the Ministry of Science and Higher Education of Russia for Valiev Institute of Physics and Technology of RAS and by the Foundation for Assistance to Small Innovative Enterprises, grant No. 18GUES18/91354.

Introduction

MEMS switch is a compact electromechanical relay fabricated by microelectronic techniques. It provides low insertion loss and high isolation in combination with small size and low power consumption, which makes it promising for wireless communication systems, including 5G and 6G networks. The best candidates for advanced communication systems are capacitive MEMS switches, which are based on the change in capacitance between signal and grounded conductors of a transmission line. The most important characteristic of these switches is the capacitance ratio in the open and closed states C_{on}/C_{off}, which needs to be as high as possible [1]. However, conventional MEMS structures typically have the C_{on}/C_{off} below 10 [2,3] and do not provide the required switching effect. This work is devoted to the combined resistive-capacitive MEMS switch with enhanced capacitance ratio.

Materials and Methods

The proposed switch is schematically shown in Fig. 1 (*a*). The movable electrode is an aluminum beam with a length of 100 μm, which is fixed on torsion suspensions. Driving electrodes are placed under each arm of the beam, while a floating potential electrode is located on the dielectric coating of the transmission line. This electrode is made from ruthenium and has a lateral dimensions of 35x46 μm. When a voltage is applied to one of the driving electrodes, the beam comes in contact with the «floating» electrode. A shunt capacitor of 40 pF is formed between the ground and signal conductors and blocks the signal. When the voltage is removed, the capacitance of the beam-line system becomes small, so the signal passes through the transmission line with minimal loss. The switch design is thoroughly described in our previous work [4].

Results and Discussion

The switch is simulated by the finite element method (FEM). The chip model is shown in Fig. 1 (*b*). The dependence of capacitance characteristics on the silicon substrate resistivity ρ is shown in Fig. 1 (*c*). An increase in ρ reduces both C_{on} and C_{off} by reducing the parasitic capacitance. The capacitance ratio increases up to 7.4 for high-resistivity silicon substrate with ρ = 50 kΩ·cm. However, C_{on}/C_{off} remains low due to high C_{off} = 7.3 pF caused by a large parasitic capacitance of the chip. Dielectric substrates significantly increase C_{on}/C_{off} compared to Si substrates. Borosilicate glass Borofloat 33 ensures the highest C_{on}/C_{off} = 46.1, while sapphire

substrate provides the ratio of 27.7. Therefore, the proposed switch has several times higher C_{on}/C_{off} compared to conventional switches.

Isolation and insertion loss are calculated in the frequency range from 1 to 20 GHz. Substrates made from glass, sapphire and high-resistivity Si with ρ = 5 kΩ·cm are considered. For all the substrates, the isolation decreases with the frequency, as shown in Fig. 1 (*d*). Silicon and sapphire show similar isolation values across the entire range, while glass provides significantly better isolation from 3 to 16 GHz. As with isolation, silicon and sapphire demonstrate close results for insertion loss, which does not exceed 0.8 dB across the entire range. The glass substrate has strong loss oscillations as frequency increases, with large peak values reaching 1.6 dB. Acceptable S-parameters are more than 15 dB for isolation and less than 1dB for insertion loss. The switch fabricated on glass provides these characteristics within the frequency range of 1 to 12 GHz. The switches made on sapphire and silicon have the working range of 1–10 GHz and 1–9 GHz, respectively.

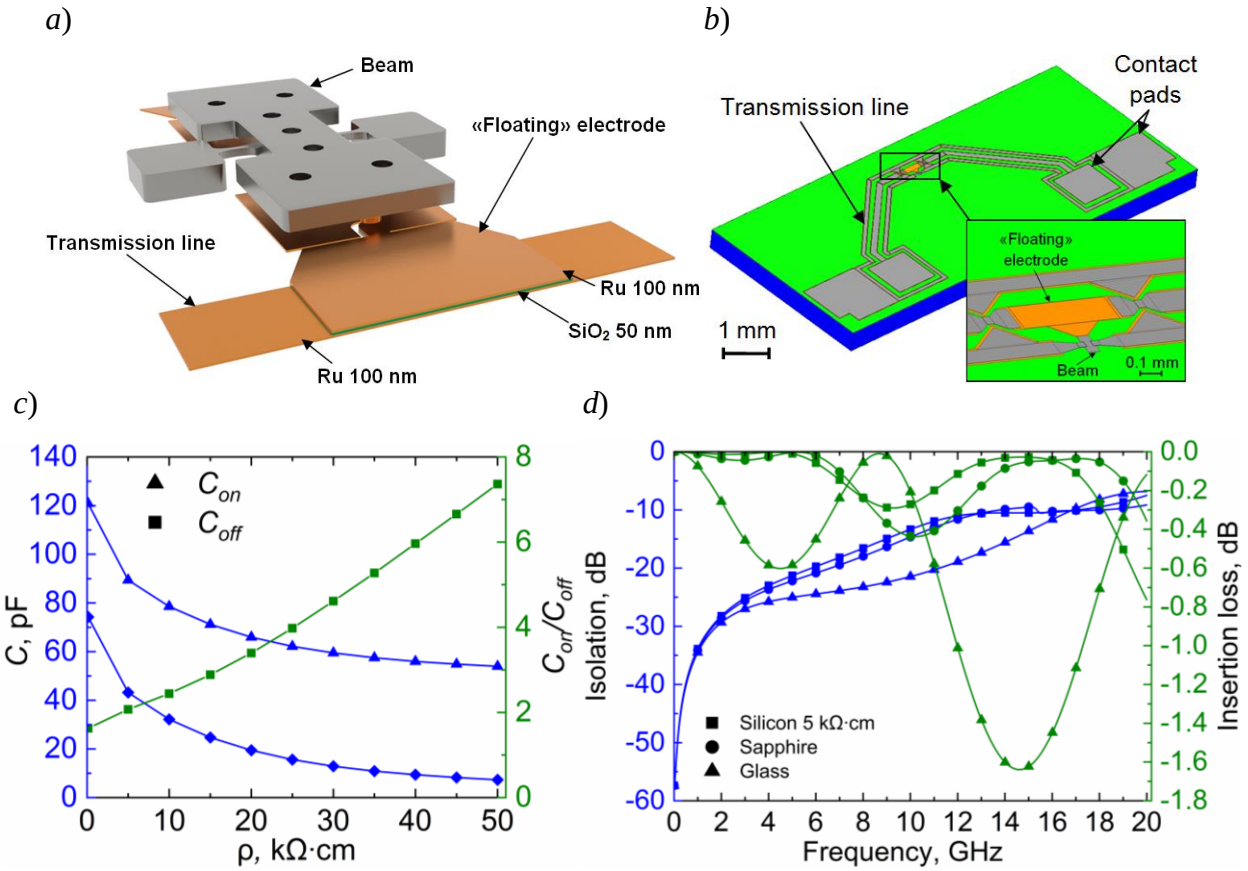


Fig. 1. Schematic illustration of the switch (*a*); Chip model (*b*); Dependence of the capacitive characteristics on the substrate resistivity (*c*); Dependence of isolation and insertion loss on the signal frequency (*d*)

REFERENCES

1. **Grichener A., Rebeiz G.M.,** High-reliability RF-MEMS switched capacitors with digital and analog tuning characteristics, IEEE Trans. Microw. Theory Techn. 58 (2010) 2692–2701.

2. **Yang H.-H., Zareie H., Rebeiz G.M.,** A high power stress-gradient resilient RF MEMS capacitive switch, J. Microelectromech. 24 (2015) 599–607.

3. **Zareie H., Rebeiz G. M.,** High-power RF MEMS switched capacitors using a thick metal process, IEEE transactions on microwave theory and techniques. 61(1) (2012) 455–463.

4. **Morozov M. O., Uvarov I. V.,** Performance Calculation for a MEMS Switch with a Floating Electrode, Russian Microelectronics. 52(6) 2023 493–503.

Development of a Ku-band phased array antenna for satellite communication

A. V. Nikulin[1, 2]✉, V. D. Burtsev[2], G. V. Antoshkin[2], S. Y. Prokhorov[3], T. S. Vosheva[2], N. M. Nazarov[1], A. N. Kosmynin[1], D. S. Filonov[1, 2]

[1]Telecom RnD Center, Moscow Institute of Physics and Technology, Moscow, Russia;
[2]Center for Photonics and 2D Materials Moscow Institute of Physics and Technology, Dolgoprudny, Russia;
[3]Department of Advanced Programs, The State Space Corporation "Roscosmos", Moscow, Russia.
✉nikulin.av@phystech.edu

Abstract. In this work, we develop a transmit (Tx)-only/receive (Rx)-only Ku-band phased array antenna for satellite communications. We used a patch antenna driven in a circular polarization for both transmit and receive sub-arrays. The array has been optimized using full-wave electromagnetic simulations in terms of adjacent element coupling, realized gain, and beam elevation. In the simulations, we achieved a realized gain of 32.2 dBi for the Rx subarray and 33.4 dBi for the Tx subarray obtained in a broad scanning angle range from -15° to +45°.

Keywords: phased array, Ku-band, electronic beam scanning, electromagnetic simulations.

Funding: This research was supported by the Ministry of Science and Higher Education of the Russian Federation, project number 075-11-2022-011.

Introduction

As satellite communication systems evolve, there is a steady need for antenna designs that can meet the requirements of modern data transmission [1], [2]. Phased array antennas are notable for their electronic beam steering capabilities, which can offer a degree of flexibility and compactness when compared to traditional mechanical steering methods [3], [4]. Our study discusses the development of phased array antennas suitable for the Ku-band. The work explores the optimization of antenna elements to achieve beam scanning and signal integrity improvements, which are important for maintaining communication in areas without traditional infrastructure, such as cellular networks.

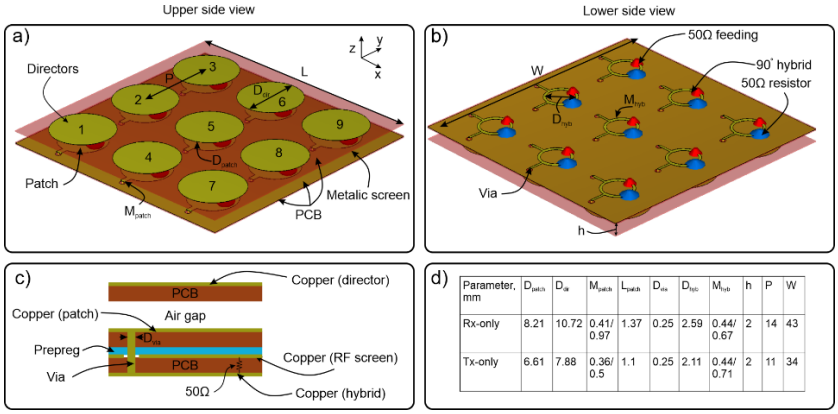
Materials and Methods

We performed electromagnetic simulations to develop a phased array antenna operating in the Ku-band. The focus was placed on patch antenna elements with a directors due to their acceptable frequency band-width and potential possibility of operation in a large array [6]. The initial optimization step was devoted to fine-tuning an individual antenna element within a compact 3 × 3 array configuration (**Figure 1**). The antenna was made of lossy copper, which was placed on a WL-CT338 substrate of 0.203 mm in thickness, whereas adjacent layers were connected by a WL-PP350 prepreg of 0.1 mm in thickness. The PCB stack is shown in **Figure 1 (c)**, and the geometrical parameters of the setup are shown in **Figure 1 (d)**. We considered two separate configurations corresponding to transmit (Tx)-only/receive (Rx)-only arrays. In these simulations, we could take into account inter-element interaction while avoiding overcomplication of the simulation setup. We conducted our simulations with the Time Domain Solver in the CST Studio Suite. As a next step, we used array-factor functionality to predict the performance of the full-size array (Rx: 40 ×24 elements and Tx: 52 ×24 elements). This full-size array has a total size of 561 mm × 337 mm, and 573 mm × 265 mm. In our simulations, we examined S-parameters, realized gain, and cross-polarization.

Results and Discussion

Simulation results are shown in **Table 1**. We obtained the high realized gain, which is under project framework requirements: 32.2 dBi for the Rx-only array and 33.4 dBi for the Tx-only

array. The side lobe levels were successfully kept below -12.3 dB, even at the extreme positions of the main lobes. The array demonstrated a high level of cross-polarization suppression, which is a critical parameter in reducing potential interference, with the Rx-only subarray showing -24.3 dB and the Tx-only subarray at -34 dB.



Parameter, mm	D_{patch}	D_{dir}	M_{patch}	L_{patch}	D_{via}	D_{hyb}	M_{hyb}	h	P	W
Rx-only	8.21	10.72	0.41/ 0.97	1.37	0.25	2.59	0.44/ 0.67	2	14	43
Tx-only	6.61	7.88	0.36/ 0.5	1.1	0.25	2.11	0.44/ 0.71	2	11	34

Fig. 1. Upper side view (a), the lower side view with feeding network (b), and a cross-sectional view of an individual element (c), geometrical parameters of the arrays (d)

Table 1. Performance Summary of the Proposed Antenna Array

Parameter	Receive	Transmit
Matching, dB	-30.7	-26.6
Worst coupling, dB	-17.2	-20.4
Gain (0), dBi	33.2	34.5
Gain (+45), dBi	32.2	33.4
Cross-polarization (0), dB	-24.3	-34
Side lobes (0), dB	-13.2	-13.2
Side lobes (+45), dB	-12.3	-12.3
Beam width ϕ=90 (0)	4	4.1
Beam width ϕ=90 (+45)	5.7	5.8

Conclusion

The simulations have shown that with scanning angles of -15° to +45°, the Rx-only and Tx-only provide realized gain above 32.2 dBi and 33.4 dBi, respectively. Side lobe levels remained under -12.3 dB, with notable cross-polarization performance. Future efforts will focus on developing a feeding system and connecting the array to beamformers.

REFERENCES

1. **Panagopoulos, A. D., Arapoglou, P.-D. M., and Cottis, P. G.,** 2004, Satellite communications at KU, KA, and V bands: Propagation impairments and mitigation techniques**,** IEEE Communications Surveys and Tutorials, Vol. 6(3), pp. 2–14.

2. **Roberto Vincenti Gatti, Luca Marcaccioli, Elisa Sbarra, and Roberto Sorrentino,** 2009, Flat Array Antennas for Ku-Band Mobile Satellite Terminals, International Journal of Antennas and Propagation, Vol. 2009.

3. **Chuan Liu, Shiwen Yang and Zaiping Nie,** 2013, Design of a parabolic reflector antenna with a compact splash-plate feed, Cross Strait QuadRegional Radio Science and Wireless Technology Conference, pp. 241– 244.

4. **Y.A. Litinskaya, A.M. Alexandrin, K.V. Lemberg, S.V. Polenga, Y.P. Salomatov,** 2013, Phased array antenna with combined electronical and mechanical beam steering for satellite networks, International Siberian Conference on Control and Communications (SIBCON).

5. **Gokhan Gultepe, Tumay Kanar, Samet Zihir, Gabriel M. Rebeiz,** 2013, A 1024-Element Ku-Band SATCOM Phased-Array Transmitter With 45-dBW Single-Polarization EIRP, IEEE Transactions on Microwave Theory and Techniques, Vol. 69(9), pp. 241–244

Research of thin Ti/Al films resistivity and transparency change after thermal treatment to determine the possibility of solid solution formation and decrease of the ohmic contacts formation temperature

K. G. Nikitin ✉, L. A. Barsukov, D. D. Tuzhilin, A. V. Romashkin
National Research University of Electronic Technology, Moscow, Russia
✉halkwww@mail.ru

Abstract. Decreasing the temperature of rapid thermal annealing (RTA) for ohmic contact formation is a relevant problem to solve. Annealing at 450 °C has led to a 1.7-fold increase in transparency and a 2-fold increase (up to 128 μΩ·cm) in resistance of Ti/Al thin films. The same annealing procedure for the Al layer without Ti, on the contrary, has resulted in films resistance decrease down to ~27 μΩ·cm and transparency increase by 1.3 times due to a decrease in the effective thickness of Al (due to partial oxidation). Changes in the transparency and conductivity of the Ti/Al layer structure can assumably be explained by the partial formation of a Ti/Al solid solution, which resistivity differs from Al in 2.2 times, and therefore, due to a decrease of the solid solution temperature formation, there is a hypothesis of possible RTA temperature reduction to form the low-resistance contacts to the GaN HEMT transistors.

Keywords: thin films, rapid thermal annealing, ohmic contacts, TiAl compounds, transparency, Raman spectroscopy.

Funding: This research was supported by the Ministry of Science and Higher Education of the Russian Federation in the framework of state task FSMR-2023-0002.

Introduction

Rapid thermal annealing (RTA) at ~850 °C is crucial for ohmic contact to HEMT transistors formation. However, RTA does affect heterostructure's electro-physical parameters, and it is an important problem to decrease RTA temperature [1]. It was proposed to reduce the temperature by using nanothin metal layers, due to its lower melting point compared with bulk ones, to form Ti/Al solid solution compound and activation of related processes, necessary for the formation of high temperature ohmic contacts.

Materials and Methods

Ti (2.3 nm)/Al (11.2 nm) layers on the SiO_2 (300 nm)/Si substrates were deposited using thermal evaporation (0.25 Å/s). Thermal treatment was performed in chamber at 20 °C/min in Ar atmosphere with flow rate ~ 1 l/min. Metal layers resistivity was measured using the 4-probe method. Obtained layers transparency before and after thermal treatment was investigated with Raman spectroscopy by comparing the intensities of Raman scattering signal from Si with and without metal layers on top. It was also observed that after a few days a TiO_2 layer (~4.5 nm) grows from the initial thin Ti layer (~2.5 nm) if there are no layers on top, and TiO_2 forms a slight antireflection coating effect for Si with native oxide (Fig.1a). Obtained Al, Ti/Al films thickness and roughness, as well as oxide growth were controlled with the atomic force microscopy (AFM).

Results and Discussion

It was investigated that even 450 °C annealing is enough to form Ti/Al compounds. Thermal treatment has led to the increase in the film's transparency from 14.1 to 23.5 % (in 1.7 times, Fig. 1b), as well as in its resistivity – from 64 μOhm · cm (2.4 times larger than reference for Al, which is typical for the nanoscale layer) up to 128 μOhm · cm (in 2 times). Overall layers thickness has increased from 29.5 nm to 31.8 nm (Al layer thickness decreased for 1.1 nm due to partial oxidation) after annealing. Same measurements were conducted for the Al without Ti layer: on the contrary, the resistivity decreased from 75 μOhm · cm to ~27 μOhm · cm (due to the clusters integration), whereas transparency increased from 18.9 to 23.2 % (only in 1.2 times, Fig.

1c), as the result of effective Al thickness decrease for 3.3 nm due to the partial oxidation (overall layer thickness increased from 36.4 to 42.9 nm), which align with the reference [2]. An increase of roughness for the Ti/Al, compared to Al was also observed (Fig. 1d).

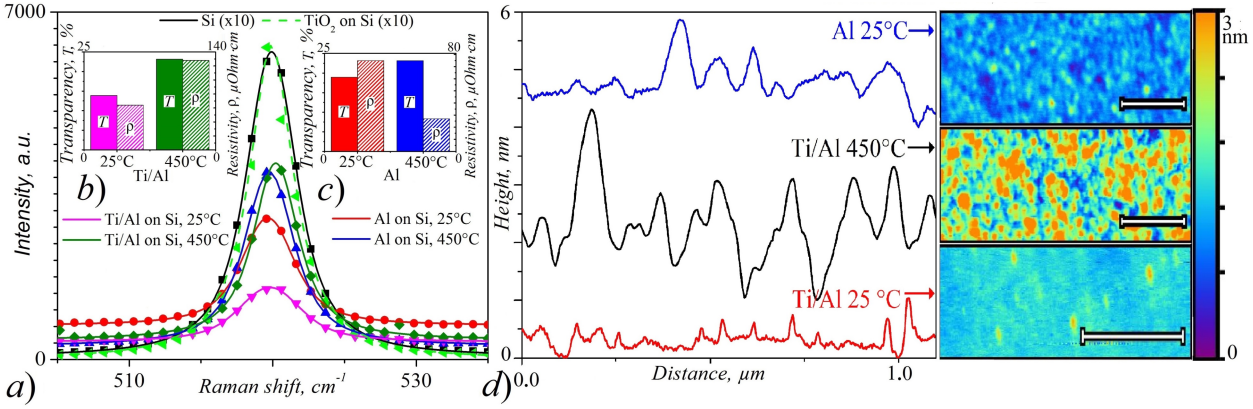


Fig. 1. Raman spectra of Si with Al and Ti/Al nanothin layers (*a*); transparency of Ti/Al layer (*b*), Al layer (*c*); AFM data, scale bar is 0.5μm (*d*).

Conclusion

Thus, considering layers uniformity maintenance with even the roughness increase, despite that XRD has shown no sight of solid solution crystallites of TiAl or $TiAl_3$ compounds, due to the opposite changes in the resistivity of Ti/Al and Al, whereas changes in transparency are similar for both, partial Ti/Al solid solution formation can be presumed (with resistivity exceeding the reference for Al in 2.2 times [3]). Therefore, considering that temperature of ohmic contacts formation during RTA is caused by the necessity of the Ti atoms redistribution, that is crucial in the reactions between N and Ti, Al, with formed at the same time Ti-Al compounds solid solutions (which occurs at >800 °C for the bulk layers [4]). However, Ti melting point can be significantly decreased by using the nanoscale structures [5], but the data obtained for the nanoscale structures used demonstrates the Ti-Al solid solutions formation at the remarkably lower temperatures, hence, as we assume, a significant decrease of the RTA temperature can be achieved while the ohmic contacts formation to the GaN HEMT transistors channel.

REFERENCES

1. **Zhang L. Q., Wu X. L., Miao W. Q., Wu Z. Y., Xing Q., Wang P. F.**, Process of Au-free source/drain ohmic contact to AlGaN/GaN HEMT, Crystals. 12 (6) (2022) 826.

2. **Hass G., Waylonis J. E.**, Optical constants and reflectance and transmittance of evaporated aluminum in the visible and ultraviolet, J. Opt. Soc. Am. 51 (7) (1961) 719-722.

3. **Wöltgens H. W., Friedrich I., Njoroge W. K., Theiß W., Wuttig M.,** Optical, electrical and structural properties of Al–Ti and Al–Cr thin films, Thin solid films. 388 (1-2) (2001) 237-244.

4. **Zhang F., Chen S. L., Chang Y. A., Kattner U. R.,** A thermodynamic description of the Ti-Al system, Intermetallics. 5 (6) (1997) 471-482.

5. **Wang B., Wang G., Chen X., Zhao J.,** Melting behavior of ultrathin titanium nanowires, Physical Review B. 67 (19) (2003) 193403.

Effect of the electrostatic focusing lens voltage on structures size in 3D printing by charged Au nanoparticles.

A. N. Patarashvili [1]✉, A. A. Efimov [1], M. S. Ivanov [1], M. R. Ghorbani Fard [1], D.M. Maslennikov [1], M.M. Zebreva [1], V. V. Ivanov [1]

[1] Moscow Institute of Physics and Technology, Dolgoprudny, Russia

✉patarashvili@phystech.edu

Abstract. The paper demonstrates a method for three-dimensional aerosol printing of charged nanoparticles using electrostatic focusing through a conductive matrix lens. The study showcases successful printing of narrow and highly conductive structures on a silicon substrate using 20-180 nm gold nanoparticles and alternating voltage on a stainless-steel mask. The results show that structures significantly smaller than the ma sk holes were achieved, and an experimental relationship between structure width and lens voltage was established.

Keywords: focusing nanoparticles, microstructure, inkjet printing, aerosol charging, additive manufacturing.

Funding: This research was funded by the Russian Science Foundation Grant No. 22-79-10127, https://rscf.ru/project/22-79-10127/.

Introduction

Creating narrow and conductive microstructures is a challenging yet promising field of study within printed electronics. These structures have potential applications as transparent electrode arrays, 3D interconnects, transparent heaters, optical metamaterials for light absorption or reflection, and photonic crystals. Various methods exist for focusing nanoparticles using physical forces like electrostatic [1,2], magnetic [3], or capillary [4]. This study outlines an experimental setup for generating conductive structures through electrostatic focusing and examines how the electric potential of a matrix lens impacts the size of the resulting structure.

Materials and Methods

The scheme of the experiment is shown in Figure 1. The distance from the copper plate to the substrate is 20 mm, and the thickness of the dielectric layer is 0.18 mm.

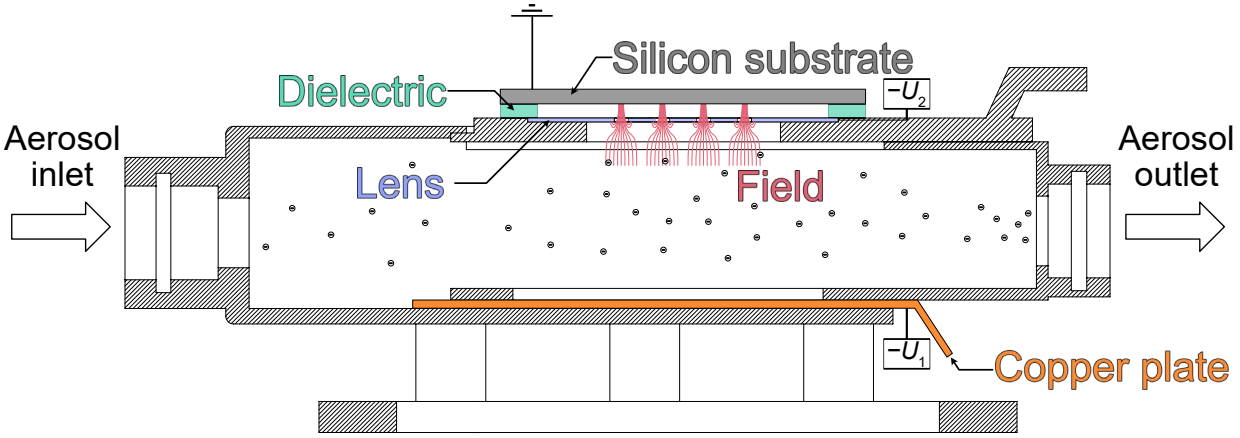


Fig. 1. The schematic of the experimental setup

The motion of charged nanoparticles during focusing is influenced by various forces, including the Brownian force ($\overline{F_B}$) caused by random collisions with gas molecules, the Coulomb force from interactions between particles and the substrate ($\overline{F_C}$), and the drag force ($\overline{F_{Drag}}$) (presented in equation (1)). These forces can be mathematically described using the Langevin equation, which helps understand how nanoparticles move and aggregate in a controlled manner during the focusing process.

$$m\frac{d\overline{V_p}}{dt} = \overline{F_B} + \overline{F_{Drag}} + \overline{F_C} \quad (1)$$

In equation (1), m represents the nanoparticle mass, and $\overline{V_p}$ represents the nanoparticle velocity. The study involves changing the voltage on an electrostatic matrix lens, which causes variations in the direction and strength of the electric field and Coulomb force.

Results and Discussion

The experiments demonstrate that the size of the printed structure can be controlled by adjusting the voltage on the mask. This relationship is visually represented in Figure 2 and quantitatively summarized in Table 1.

Table 1

The effect of lens voltage on the structure size.

Plate voltage U_1, V	Lens voltage U_2, V	Lens hole size d_L, µm	Structure size d_S, µm
-25	-5	280	100
	-10		82
	-15		70
	-20		61
	-25		52
	-30		37
	-33		24
	-35		18
	-37		14

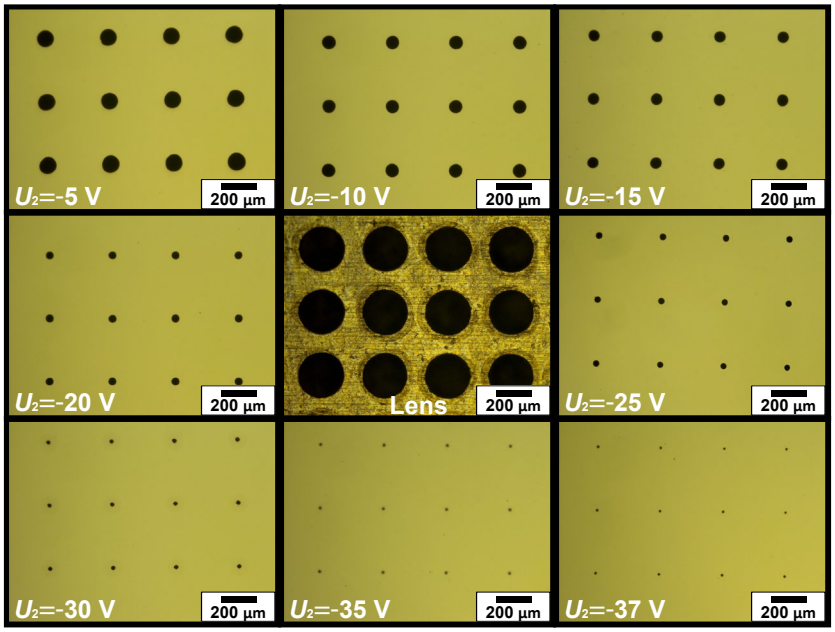


Fig. 1. Images of structures obtained at various lens voltage U_2 with an image of the lens (in the center).

Conclusion

The paper discusses a test chamber designed for printing charged nanoparticles, featuring an optimal geometry that enables control over the size of the d_S structure. By adjusting the voltage on the U_2 electrostatic lens from -5 V to -37 V and maintaining a lens hole size of d_L=280, the size of the structure can be varied from 100 µm to 14 µm.

Acknowledgments

This research was funded by the Russian Science Foundation grant No. 22-79-10127, https://rscf.ru/project/22-79-10127/.

REFERENCES

1. **Jung, W., Jung, YH., Pikhitsa, P.V. et al.**, Three-dimensional nanoprinting via charged aerosol jets, Nature. (592) (2021) 54–59.

2. **Liu S., Ai J., Zhang Y., and Feng J.**, Programmable and Parallel 3D Nanoprinting Using Configured Electric Fields, Advanced Functional Materials (2023) 2308734.

3. **Wolf H. and Birringer R.**, Pattern formation in an array of magnetic nanoscale rods mimics magnetic-dipole interaction-driven spinodal decomposition, Journal of Applied Physics. 98 (7) (2005) 74303.

4. **Lutfurakhmanov A., Loken G. K., Schulz D. L. and Akhatov I. S.**, Capillary-based Applied Physics Letters 97 (12) (2010) 124107.

A 100 MHz signal conversion device with low phase noise

A.A. Popov ✉, **D. D. Savin**
Peter the Great Saint-Petersburg Polytechnic University, Saint Petersburg, Russia;
✉alexander_popov_work@mail.com

Abstract. The object of research is phase noise in low–noise operational amplifiers. The aim of the work is to develop a signal conversion device with a frequency of 100 MHz with low phase noise. As a result of the development of the device, a selection of low-noise operational amplifiers corresponding to a given bandwidth and the required noise characteristics of the current and voltage at the input was made. As a result of calculations, low-noise operational amplifiers LMH6629SD, AD8099ARD and LMH6739MQ were selected. The simulation of the phase noise power specter density (PNPSD) was carried out based on the data presented in the terms of reference and in the documentation of the devices. Guided by the results obtained during the simulation, it was concluded that the LMH6629SD amplifier theoretically satisfies the conditions of the task. In both cases, the values obtained during the simulation coincided with the values of the PNPSD measured in practice. Based on the work done, it was concluded that it is possible to achieve the conditions set in the task if the LMH6629SD operational amplifier is used as an element base.

Keywords: Phase noise, Signal converter, VHF, Hydrogen standard, Low noise amplifier, Current noise, Voltage noise.

Introduction

Modern designs of highly stable microwave generators have several disadvantages, such as the relatively large size of the structure and the high cost. If a device, for example, in a quantum frequency reference, has more than one block requiring a high-frequency signal, the dimensions of this device will be large [1, 2]. This creates problems in use on satellites and mobile objects and leads to an increase in the cost of the design of the device in which the microwave generator is installed and the cost of its operation.

The solution to the above problem can be our converter (Fig. 1).

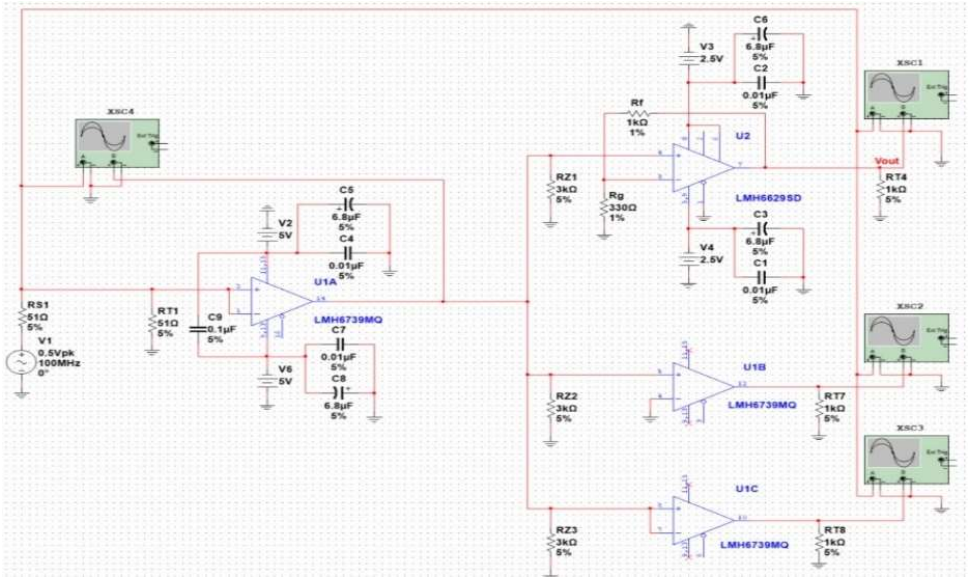


Fig. 1. Electric circuit of device in NI Multisim 14.3.

An increase in the number of coherent output signals may be required to provide reference signals to consumers who perform joint tasks. For example: in the case of location determination using GLONASS or GPS signals, by different receiving devices that receive coherent reference signals from a single source, in the case of calculating the value of the final time scale discrepancy

using the integrated use of equipment for receiving and transmitting signals of the HF, VHF and UHF ranges, the reference generator for which is one frequency standard.

Materials and Methods

A highly stable signal with a frequency of 100 MHz is supplied to the input of the converter, with specified values of the phase noise power specter density (PNPSD) at various settings, and three signals of a given amplitude with a low PNPSD.

We selected low-noise operational amplifiers (OA) as the element base of the device [1]. They have the values of input noise currents and voltages already specified in the documentation. This fact allows the theoretical calculation of the noise characteristics of the designed device.

Results and discussion

For the developed design of the frequency converter, an analysis of low-noise operational amplifiers was carried out to ensure the maximum signal-to-noise ratio of the output signal.

Table 1

PNSD of signal in case of connecting N9310A generator.

PNPSD, dB/Hz	Frequency tuning					
	1 Hz	10 Hz	100 Hz	1 kHz	10 kHz	100 kHz
N9310A	-49.36	-67.51	-79.02	-85.45	-86.57	-102.44
ОА 1432УД11У	-49.36	-67.51	-79.02	-85.45	-86.57	-102.44
ОА LMH6629 (model)	-49.36	-67.51	-79.02	-85.45	-86.57	-102.44
ОА LMH6629 (real)	-41.30	-55.55	-77.14	-84.91	-85.90	-99.79
ОА AD8099ARD (model)	-49.36	-67.51	-79.02	-85.45	-86.57	-102.44
ОА AD8099ARD (model)	-32.69	-51.88	-77.52	-88.20	-86.63	-107.89

Based on our research, it can be revealed that the LMH6629SD amplifier is the best for this circuit, since it has the lowest noise coefficient. However, switching on with a gain factor of 1 and 2 for this amplifier is abnormal and is accompanied by a deterioration in PNPSD. Therefore, to implement these coefficients, an LMH6739MQ amplifier was chosen, which is designed for gain coefficients 1 and 2. Also, as an alternative, a domestic op-amp 1432УД11У can be used, which has a wide bandwidth compared to the rest. A simulation of the circuit operation was performed in the NI Multisim and MATLAB programs, which confirmed the operability of the circuit and the adequacy of the proposed signal division technique.

Conclusion

The conducted research has shown that the developed converter can be manufactured using domestic components, which is extremely important. The use of such converters significantly reduces the size, cost of assembly and placement of equipment for mobile objects and artificial satellites and other devices that require coherent reference signals.

REFERENCES

1. **Boudot R., Rubiola E.** Phase Noise in RF and Microwave Amplifiers, IEEE Transactions on Ultrasonics, Ferroelectrics, and Frequency Control. 59(12) (2012). 2613–2624.

2. **Tomlin T.** Analysis and Modelling of Jitter and Phase Noise in Electronic Systems: Phase Noise in RF Amplifiers and Jitter in Timing Recovery Circuits, The University of Western Australia School of Electrical. Electronic, and Computer Engineering Crawley. 2004. 201 p.

Subterahertz circularly polarized 1k-pixel reflective surface for 6G applications

A. Razakova[1,3✉], **A. Prikhodko**[1,2,4], **A. Lvov**[1,2], **A. Shurakov**[1,2,3], **G. Gol'tsman**[1,2,4]

[1] Moscow Pedagogical State University, Moscow, Russia;
[2] HSE University, Moscow, Russia;
[3] National University of Science and Technology "MISIS", Moscow, Russia;
[4] Russian quantum center, Skolkovo, Moscow, Russia;
[✉]aa_razakova@student.mpgu.edu

Abstract. Wireless communication is a hot topic of research and development at this moment. The need for increase in data transfer rates and connection stability within vast digitalization of people interactions sets new tasks for scientific community. One of them is the utilization of higher operating frequencies of 140-150 GHz. This is an obvious way to obtain bigger channel capacity. However, for line-of-sight wireless channels, it may potentially lead to severe propagation losses, including absorption in water-containing atmospheric environments and scattering off static or dynamic objects. In this work, we report on the development of a technologically robust reflective surface that can be used in the sixth generation reflection-aided data links. The proposed reflective surface utilizes 36×36 spiral metallic elements implemented on top of a thin back-metalized quartz plate. The fabricated prototype, designed for 50º deflections from specular propagation paths at angles of incidence within ±75º, is successfully used for a non-distorting reflection of a 6º wide Gaussian beam at 145 GHz. It supports both linear and circular polarizations, and exhibits cross-polarization level of approximately −25 dB.

Keywords: subterahertz, reflectarray, wireless channel, 6G communication.

Funding: This study was funded by the Russian Science Foundation grant number 22-79-10279, https://rscf.ru/project/22-79-10279/.

Introduction

New solutions in wireless communication technologies are of great interest in modern scientific and industrial considerations. Development of novel applications and services imposes high data rate and stability requirements on wireless networks [1]. The migration of operating frequencies into the subterahertz (sub-THz) band, on the way of increasing baud rates, is accompanied by the appearance of new signal attenuation factors leading to ultra-directional data links in the sixth generation (6G) wireless networks. Thus, line-of-sight communication channels are potentially exposed to signal blockages and scattering off obstacles [2]. Reflection-aided data links with either static, semi-static or dynamically reconfigurable reflective surfaces [3] are among novel solutions to avoid this problem. In this work, we report on a static reflective surface (RS) that can be used for handling of a few degree wide Gaussian beams (GBs) during the first deployment stage of 6G wireless networks. It utilizes 36×36 spiral metallic elements [4] implemented on top of a thin back-metalized quartz wafer and is designed for non-specular channels operating at 140-150 GHz.

Results and Discussion

Here we present the results of development, fabrication and performance tests of the RS prototype. We rely on electromagnetic (EM) simulations in computer-aided system equipped with finite element method. The Floquet port analysis is used to acquire desired geometries of the RS spiral elements. Three values of the spiral arm length are chosen to provide a 120º phase shift between two adjacent RS columns upon reflection of a sub-THz wave. The resulting beam of the entire RS is constructed according to the multibeam interference theory by the array factor method [5]. The spiral elements are nearly halfwave-spaced which results in the deflection angle $\theta = 50º$, as shown in fig. 1(a). The figure also contains a 3-dimensional schematic of the central part of the developed RS with 9×9 spiral elements. Here $\mathbf{E_0}$ is the electric field strength vector, $\mathbf{k}$ is the wave

vector, and φ_1, φ_2, φ_3 are the phases of the reflection coefficients in the basic triplet of adjacent spiral elements used to pave the RS area ($\varphi_2-\varphi_1 = \varphi_3-\varphi_2 = \varphi_1-\varphi_3 = 120^o$).

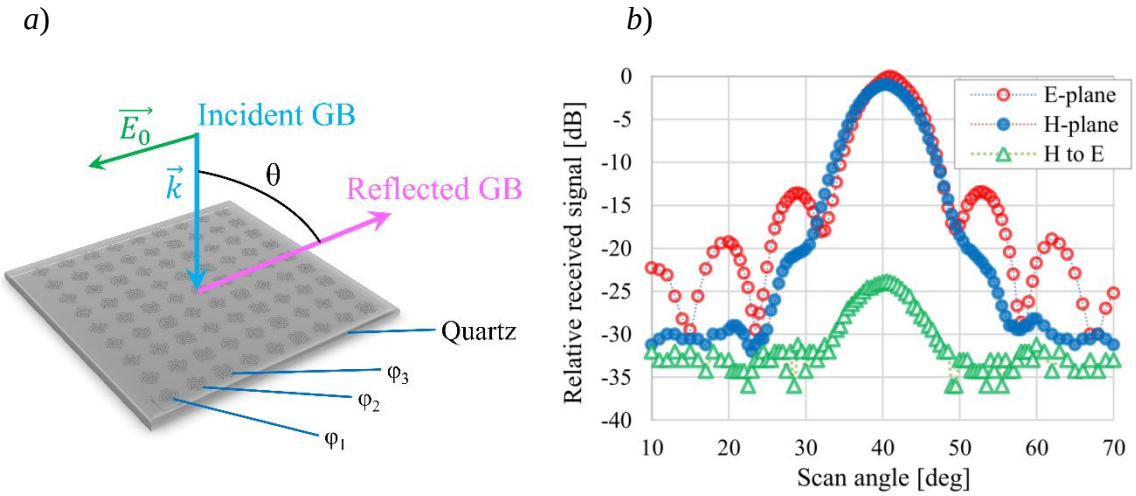


Figure 1. Schematic of the proposed reflective surface in action (a) and measured radiation pattern of the fabricated prototype (b).

The developed RS prototype is fabricated in a cleanroom process. It includes forming of a Ti/Au (5/400 nm) spiral array on a 140 μm thick quartz wafer. The back side metallization is implemented by attaching a 400 μm thick sapphire wafer entirely covered by Ti/Au (5/400 nm) sputtered thin film. Results of the RS prototype beam profile measurements in the setup reported by us elsewhere [6] are presented in fig. 1(b). The prototype is successfully used for a non-distorting reflection of a 6º wide Gaussian beam at 145 GHz. It supports both linear and circular polarizations, and exhibits cross-polarization level of approximately −25 dB. We think that our findings should be interesting to developers of the next generation wireless systems operated at 140-150 GHz.

REFERENCES

1. **Yeh C., Do Jo G., Ko Y. J., Chung H. K.**, Perspectives on 6G wireless communications, ICT Express. 9 (1) (2023) 82–91.

2. **Shurakov A., Moltchanov D., Prikhodko A., Khakimov A., Mokrov E., Begishev V., Belikov I., Koucheryavy Y., Goltsman. G.**, Empirical blockage characterization and detection in indoor sub-THz communications, Computer Communications. 201 (2023) 48–58.

3. **Shurakov, A., Prikhodko, A., Belikov, I., Razakova, A., Goltsman, G.**, Integrated Circuit of an Intelligent Reflecting Surface for sub-THz Wireless Communication, In 2023 IEEE 18th International Conference on Nano/Micro Engineered and Molecular Systems (NEMS). (2023) 183-187.

4. **Xue F., Wang H., Yi M., Liu G., Dong X.**, Design of a broadband single-layer linearly polarized reflectarray using four-arm spiral elements., IEEE Antennas and wireless propagation letters. 16 (2016) 696-699.

5. **Balanis, C. A.,** Antenna theory: analysis and design, John Wiley & Sons, Hoboken, New Jersey, 2016.

6. **Shurakov A., Rozhkova P., Khakimov A., Mokrov E., Prikhodko A., Begishev V., Koucheryavy Y., Komarov V., Goltsman G.**, Dynamic Blockage in Indoor Reflection-Aided Sub-Terahertz Wireless Communications, IEEE Access. 11 (2023) 134677-134689.

Polyethylene-on-quartz platform for subterahertz reconfigurable reflective surfaces

P. Rozhkova [1✉], **A. Prikhodko**[1,2,4], **A. Shurakov**[1,2,3], **G. Gol'tsman**[1,2,4]

[1] Moscow Pedagogical State University, Moscow, Russia;

[2] HSE University, Moscow, Russia;

[3] National University of Science and Technology "MISIS", Moscow, Russia;

[4] Russian quantum center, Skolkovo, Moscow, Russia;

✉ pv_rozhkova2@student.mpgu.edu

Abstract. Subterahertz frequency band is preallocated for the deployment of sixth generation wireless networks. Mastering of this band is challenging and requires development of appropriate hardware and software. The properties of components used should be authentically known for the purpose of accurate designing and prototyping. This research focuses on the radiophysical properties of a polyethylene-on-quartz sandwich as a potential dielectric platform for the implementation of reconfigurable reflective surfaces. The sandwich is exposed to spectral studies, statistical analysis of feasible fabrication tolerances and compatibility with cleanroom metal deposition and patterning processes. Its technological robustness is assessed upon prototyping of a 16-element planar reflectarray designed for operation in specular and non-specular reflection regimes at 155 GHz and 120 GHz, respectively. Using the measured value of quartz permittivity of a 3.55 and the loss tangent of a 0.001, we calculate the reflectarray reflection losses of approximately 1.5 dB. The calculations agree well with the results of its radiation pattern measurements conducted at 155 GHz. This hints that the developed passive platform is suitable for integration with A3B5 active layers with nonlinear elements ensuring fast beam steering in the subterahertz band.

Keywords: subterahertz, polyethylene-on-quartz, permittivity, reconfigurable reflective surface, reflection loss, 6G network.

Funding: This study was funded by the Russian Science Foundation grant number 22-79-10279, https://rscf.ru/project/22-79-10279/.

Introduction

Subterahertz (sub-THz) frequency band is preallocated for the deployment of wireless networks of the sixth generation (6G). Mastering of sub-THz carrier frequencies is challenging. Therefore, there appears a necessity to develop appropriate hardware and software. The properties of components used should be authentically known for the purpose of accurate design and implementation of 6G wireless modules and systems. This research is focused on the radiophysical properties of a metallization-equipped polyethylene-on-quartz platform potentially suitable for the implementation of reconfigurable reflective surfaces. A series of measurements of the reflection spectra of a 140 μm thick quartz substrate in both *s*- and *p*-polarizations is carried out at 130-160 GHz. The quartz substrate is exposed to V/Cu (5/200 nm) and Ti/Au (10/300 nm) deposition and patterning on the front and rear sides. Its front side is further coated by a 100 μm thick polyethylene layer, whose surface is exposed to V/Cu (5/400 nm) deposition and patterning at the later stage. The resulting structure has a nominal geometry identical to that reported by us earlier in [1], yet the actual linear and angular dimensions differ from their nominals due to fabrication errors. The unit cell model of the reflectarray [2] is accordingly adjusted, and its simulated performance is further experimentally justified.

Results and Discussion

In our spectral studies intended to distinguish exact relative permittivity of the chosen quartz substrate potentially ranging from 3.5 to 4.5 [3], the quartz material under the test (MUT) is represented by a two-inch diameter wafer. In order to evaluate the permittivity of the MUT, we assess the reflective properties of the material. The experimental setup along with the employed methods are described by us in details elsewhere [4]. The optical paths between 130-160 GHz transmitter and receiver with respect to MUT are identical and equal to Fraunhofer distance. We conduct measurements for the angles of incidence θ equal to 30, 45, 60 deg and

consistently acquire MUT's complex permittivity of 3.55 (1 + 0.001*i*) for both transverse electric (TE) and transverse magnetic (TM) waves. Using the characteristic matrix (CM) [5] based fitting of the experimental spectral data, we achieve measurement accuracy of approximately 10-20%. The CM fit-functions are compared with the predictions of Fresnel equations (FE). Results of our findings are summarized in Fig. 1(*a*).

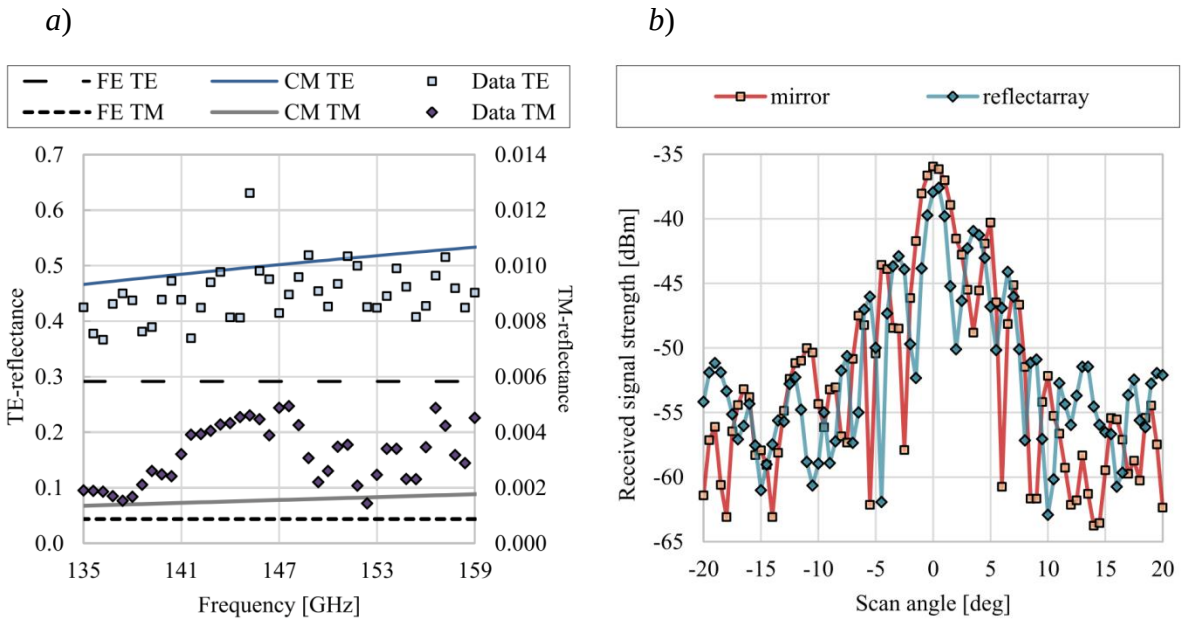


Fig. 1. – (a) Reflection spectra of the quartz substrate at θ = 60 deg close to Brewster's angle; (b) far-field radiation patterns of the fabricated reflectarray and the array-sized mirror measured at 155 GHz.

Once the dielectric and conducting properties as well as the actual geometry of the developed V/Cu / polyethylene / V/Cu / quartz / Ti/Au reflectarray structure are assessed, we measure its radiation pattern in the far-field and evaluate reflection losses at 155 GHz. Experiments reveal excessive losses of 1.5-2 dB as compared to those of the array-sized mirror measured in the same setup. This validates relevance of the reflectarray design in terms of radiophysics and hints its technological robustness in terms of fabrication tolerances and compatibility with cleanroom processes. Overall, we can conclude that the developed passive platform is suitable for integration with A3B5 active layers with nonlinear elements ensuring fast beam steering in the sub-THz band. This should be interesting to developers of reconfigurable reflective surfaces for reflection-aided 6G wireless channels.

REFERENCES

1. **Shurakov, A., Prikhodko, A., Belikov, I., Razakova, A., Goltsman, G.,** Integrated Circuit of an Intelligent Reflecting Surface for sub-THz Wireless Communication, In 2023 IEEE 18th International Conference on Nano/Micro Engineered and Molecular Systems (NEMS). (2023) 183-187.

2. **Prikhodko A., Yaropolov T., Shurakov A., Gol'tsman G.**, Unit cell model of a terahertz intelligent reflecting surface with Schottky microcontacts, In Proceedings of the 35th European Modeling & Simulation Symposium (EMSS) (2023) 019.

3. **Lamb W.**, Miscellaneous data on materials for millimetre and submillimetre optics, International Journal of Infrared and Millimeter Waves. 17 (12) (1996) 1997–2034.

4. **Shurakov A., Rozhkova P., Khakimov A., Mokrov E., Prikhodko A., Begishev V., Koucheryavy Y., Komarov V., Goltsman G.,** Dynamic Blockage in Indoor Reflection-Aided Sub-Terahertz Wireless Communications, IEEE Access. 11 (2023) 134677-134689.

5. **Born M., Wolf E.**, Principles of Optics, Cambridge University Press, 2019.

Surface roughness modeling for extremely high frequency applications

A. P. Sedov[1]✉, A. V. Nikulin[1], V. D. Burtsev[1], T. S Vosheva[1], D. S. Filonov[1]

[1]Center for Photonics and 2D Materials, MIPT, Dolgoprudny 141701, Russia;
✉sedov.ap@mipt.ru

Abstract. In this work, we show electromagnetic simulations of surface roughness in multiple conventional antennas applicable for 6G networks potentially operating in the W-band (75–110 GHz). Operations at such high frequencies require the accuracy of surface processing, where errors become to the order of the wavelength. We show simulations of surface roughness in four devices, such as a horn antenna, a patch antenna, a rectangular waveguide, and a microstrip transmission line.

Keywords: extremely high frequency, surface roughness, electromagnetic simulations.

Funding: The work has been supported by the Russian Science Foundation (Project 23-29-00152).

Introduction

One potential application that uses extremely high frequencies, such as W-band (75–110 GHz), is the 6G networks [1], [2]. Several antennas could be used at such a high frequency, among them a horn antenna and a patch antenna. In addition, one could use rectangular waveguides and microstrip lines. At such a high frequency, the manufacturing defect has an important role in antenna performance [3]. In this paper, we aim to study this role using electromagnetic simulations.

Materials and Methods

To simulate surface roughness, we perform numerical analysis using electromagnetic simulations in the CST Studio Suite. We separate all devices into two groups, such as additive devices and chemically etched devices, according to the manufacturing method (Figure 1). In the first group, we simulated a horn antenna and a rectangular waveguide with the WR-10 flange. In the second group, we simulate a patch antenna and a microstrip line.

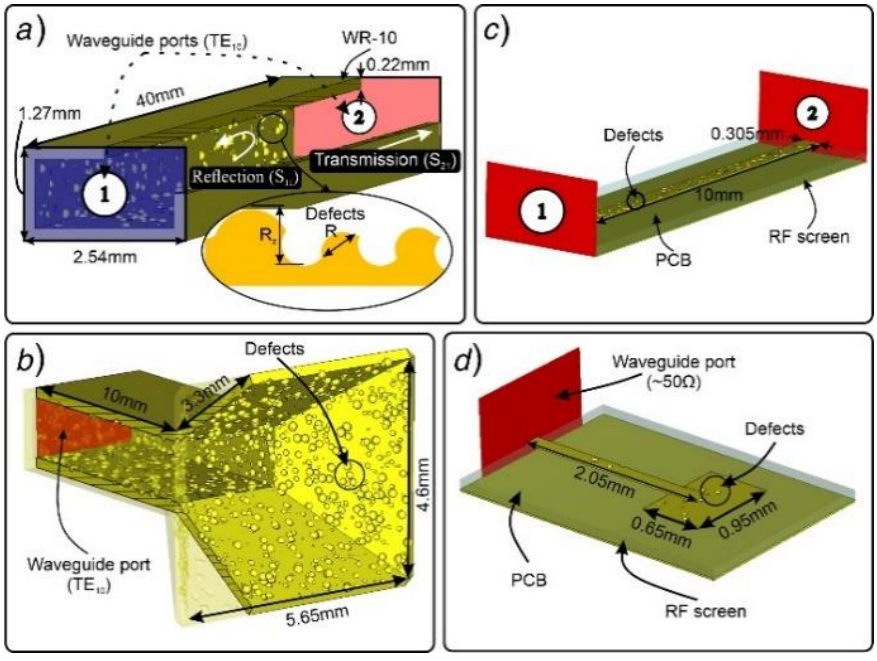


Fig. 1. Simulation setups and general view of the structures with defects: waveguide (a), horn antenna (b), microstrip (c), patch antenna (d).

In the first group, we modeled surface roughness as a set of bumps or hollows, whereas we modeled only hollows in the second group. These defects have a spherical shape with a radius of R. The simulated sets are shown in **Figure 1**. For the waveguide, we assessed transmission coefficient S_{21} (**Figure 2a, c**), whereas for the horn and patch antennas, we assessed reflection coefficient S_{11} (**Figure 2b, d**). We performed a statistical analysis with 75 random series of simulations, and then the S-parameters were evaluated as the worst value at a frequency point.

Results and Discussion

In the case of the waveguide, the worst value of the transmission coefficient decreases to -3.9 dB (Figure 2a), whereas the acceptable cases (R = 0.05 mm and R = 0.1 mm) show that S_{21} does not exceed -0.3 dB. For the horn antenna, we observe that for R = 0.1 mm, the worst S_{11} is nearly −10 dB (**Figure 2b**), which is considered acceptable. For the microstrip, we observe that for the R = 0.4 mm and 0.3 mm, the worst S_{11} is nearly -1.6dB (**Figure 2c**), which is close to the acceptable scenario. Finally, in the case of patch antennas, we can see that the worst reflections for R = 0.5 mm and 0.4 mm are approximately -15 dB (**Figure 2d**).

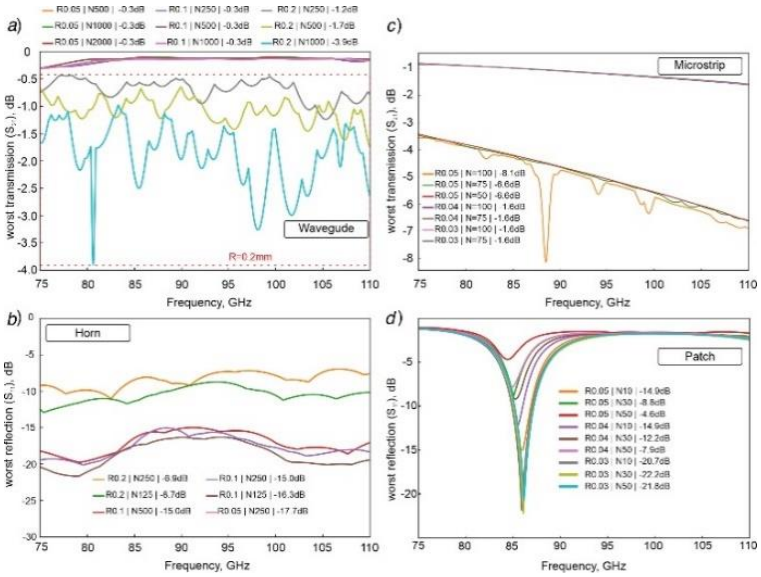


Fig. 2. Transmission coefficient of waveguide (a), worst reflection coefficient of the horn antenna (b), worst transmission coefficient of microstrip (c), worst reflection coefficient of the patch antenna (d).

Conclusion

We analyzed four structures: a waveguide, a horn, a microstrip, and a patch. We have shown that surface roughness R = 0.1 mm is acceptable for waveguide and horn, whereas in the case of microstrip and patch, one has to provide surface defects of 0.04 mm.

REFERENCES

[1] **T. S. Rappaport, Y. Xing, O. Kanhere, S. Ju, A. Madanayake, S. Mandal, A. Alkhateeb, and G. C. Trichopoulos**, "Wireless communications and applications above 100 GHz: Opportunities and challenges for 6g and beyond," *IEEE Access*, vol. 7, pp. 78729–78757, 2019.

[2] **M. Polese, V. Ariyarathna, P. Sen, J. V. Siles, F. Restuccia, T. Melodia, and J. M. Jornet**, "Dynamic spectrum sharing between active and passive users above 100 GHz," *Commun. Eng.*, vol. 1, no. 1, p. 6, 2022.

[3] **M. A. Al-Tarifi and D. S. Filipovic**, "On the design and fabrication of W-band stabilised-pattern dual-polarised horn antennas with DMLS and CNC," *IET Microwaves, Antennas Propag.*, vol. 11, no. 14, pp. 1930–1935, 2017.

Transmittance of TE and TM radiation modes in a dielectric THz integrated waveguide

S. V. Seliverstov [1✉], **S. S. Svyatodukh** [1,2], **A. K. Kozhukhovsky**[1], **and G. N. Goltsman** [2,3]

[1] Moscow State Pedagogical University, Moscow, Russian Federation;

[2] National Research University Higher School of Economics, Moscow Institute of Electronics and Mathematics, Moscow, Russian Federation;

[3] Russian Quantum Center, Moscow, Russian Federation

✉sv.seliverstov@mpgu.su

Abstract. The sub-terahertz range has attracted the attention of the scientific and technological community around the globe. The reason lies in the fact that this range is most suitable for the purpose of creating a new generation communication system with ultra-high speed of wireless data transfer. This task is inextricably linked with the creation of appropriate waveguide structures with low absorption. Traditional metal hollow waveguides are of little use for the compact design of such complex devices. In this paper, we report the results of modeling and measuring the transmittance of TE and TM radiation modes along an integrated terahertz all-dielectric waveguide. It is shown that in the waveguide structure under study, the transmittance coefficients differ slightly for both modes and does not exceed -0.5 dB at frequencies in the range from 126.5 to 145.5 GHz. The main losses in this case arise at the matching tapers. The obtained results confirm the competitive advantages of these waveguides as the basic elements of a future next-generation data transmission system.

Keywords: photonic integrated circuit, dielectric waveguide, microwave photonics.

Funding: The study was supported by a grant from the Russian Science Foundation No. 21-72-10119, https://rscf.ru/project/21-72-10119/.

Introduction

Recent progress in information technologies associated with the development of such areas as big data processing, neural networks, augmented reality and the Internet of things has led to the need for a sharp increase in the speed of wireless data transfer. An obvious direction in solving this problem is the transition to higher frequencies of the carrier signal. The number one candidate at the moment is the subterahertz range [1]. But to effectively master this range, it is necessary to create compact and inexpensive devices, the basic element of which is a waveguide. In this paper, we report on the simulation, successful fabrication and measurement of effective-medium [2] integrated silicon waveguides optimized for a radiation frequency of 0.15 THz and having low absorption in TE and TM operating modes. The obtained characteristics of the waveguides confirm the possibility of their use as basic elements of future next-generation communication systems with ultra-high data transfer rates.

Materials and Methods

It is well known that the electric and magnetic fields of a plane monochromatic wave propagating along a dielectric waveguide in the absence of free charge carriers obey the following governing wave equations:

$$\Delta\vec{E} + \frac{n^2\omega^2}{c^2}\vec{E} = 0, \qquad \Delta\vec{H} + \frac{n^2\omega^2}{c^2}\vec{H} = 0. \tag{1}$$

where ω is the circular radiation frequency, n is the refractive index of the medium, and c is the speed of light in vacuum.

The equations (1) make it possible to obtain the distribution of electric and magnetic fields using boundary conditions. However, an analytical solution is possible only in a limited number of simple cases. In practice, these equations have to be solved by numerical methods. This paper presents a numerical solution of the resulting equations using the finite element method for the case of a rectangular silicon effective-medium waveguide. The transmittance of the waveguide in

the case of excitation of TE and TM fundamental wave modes in it is also analyzed in detail. The excitation of the TE or TM mode in the model was specified by the orientation of the rectangular waveguide with respect to the dielectric (the long side of metal waveguide was perpendicular to the substrate in the case of excitation of the TM mode and parallel in the case of the TE mode).

A high-resistivity silicon substrate was chosen as the basis for the waveguides. The structure of the waveguide was specified by a square grid of through holes with a diameter of 73 μm and a period of 165 μm. The waveguides were matched to the source and detector using tapers. The experiment examined the transmittance spectrum of waveguides in the range 126.5-145.5 GHz. A tunable generator based on a backward wave oscillator was used as a radiation source, and a Schottky diode was used as a detector. Waveguide tapers were inserted into the center of hollow metal waveguides connected to the detector and source. For precise placement, special 3D printed plastic holders were used.

Results and Discussion

The resulting distribution of electric and magnetic field strength vectors for TE and TM polarizations is presented in Fig. 1. Both graphs were obtained under the condition that the same power was supplied to the input port of the waveguide structure. The simulation showed approximately the same value of the waveguide insertion loss for both radiation modes (about -0.5 dB at a radiation frequency of 145.5 GHz). These losses are mainly due to the influence of matching tapers [3]. The obtained result agrees well with the experimental data.

a) *b*)

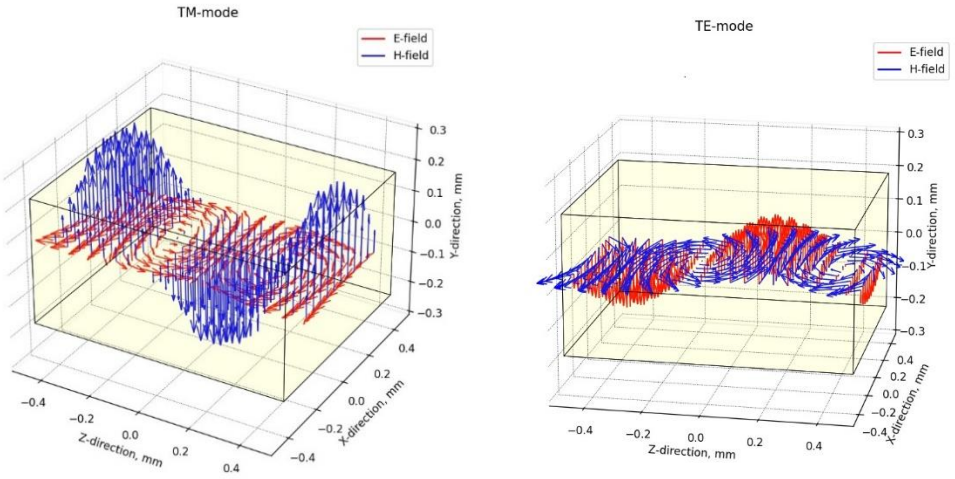


Fig. 1. Vector-field distribution of TM (*a*) and TE (*b*) radiation mode propagating along the waveguide.

Conclusion

The paper demonstrates a subterahertz integrated effective-medium waveguide in the TE and TM operation modes. The obtained characteristics confirm the possibility of its use in future next-generation communication systems with ultra-high data transfer rates.

REFERENCES

1. **Koenig, S., Lopez-Diaz, D., Antes, J., Boes, F., Henneberger, R., Leuther, A., Tessmann, A., Schmogrow, R., Hillerkuss, D., Palmer, R., Zwick, T., Koos, C., Freude, W., Ambacher, O., Leuthold, J., & Kallfass, I.** Wireless sub-THz communication system with high data rate, Nature photonics. 7 (12) (2013) 977-981.

2. **Gao, W., Yu, X., Fujita, M., Nagatsuma, T., Fumeaux, C., & Withayachumnankul, W.,** Effective-medium-cladded dielectric waveguides for terahertz waves. Optics express, 27(26), (2019), 38721-38734.

3. **Seliverstov Sergey, V., Svyatodukh Sergey, S., Prokhodtsov Aleksey, I., & Goltsman Grigory, N.** Optimization of a prism coupler for a THz photonic integrated metamaterial Si waveguide: simulation and experiment, St. Petersburg State Polytechnical University Journal. Physics and Mathematics. 16 (3.2) (2023) 406–410.

Research of the dependence of the clamping force of a silicon wafer by ESC on the holding time

V. S. Traktirshchikov [1,2✉], **M. E. Shiryaev** [2,3]
[1] JSC “SPE «ESTE», Zelenograd, Moscow, Russia;
[2] National Research University of Electronic Technology «MIET», Zelenograd, Moscow, Russia;
[3] LLC "Estika", Zelenograd, Moscow, Russia
✉traktirshikoff@yandex.ru

Abstract. The paper presents the results of a study of the dependence of the retention force of a silicon substrate generated by an electrostatic clamping of a technological desk on the retention time. Ways to improve the experimental stand for further research
on the issue of electrostatic clamping are also proposed.

Keywords: Electrostatic chuck, electrostatic fastening device, electrostatics, electrode, microelectronics.

Introduction

Currently, there are no manufacturers of desk of microelectronic equipment with an electrostatic chuck (ESC) in the Russian Federation. Studying the principles and operating conditions of the device will make it possible to form a theoretical and production base for the design and manufacture of ESCs, which will reduce the dependence of Russian manufacturers on foreign suppliers.

This article examines the study of the dependence of the holding force by electrostatic clamping of a silicon substrate on the holding time.

Materials and Methods

The principle of operation of the device and the technological conditions of the process entail appropriate requirements for the design and materials used and the high-voltage power source [1].

In general, the electrostatic chuck consists of the following elements:

- one or more high-voltage electrodes having common or different potentials;
- a surface dielectric layer insulating the electrodes from the wafer and the process table;
- a high voltage source that generates a potential of the required value on the electrodes.

The experiment stand includes a technological desk (Fig. 1, a) on which the ESC is placed and fixed. A wafer is placed on the surface of the ESC. The wafer is glued to a foil that allows transmitting the grounding potential with conductive glue. A fastener (Fig. 1, b) is glued to the foil. The fastener allows applying a uniform pull-off force. To determine the force generated by the ESC, readings are taken from the dynamometer at the moment of separation of the substrate from the ESC. The dynamometer is coupled to the mounting of the substrate and moves vertically upwards.

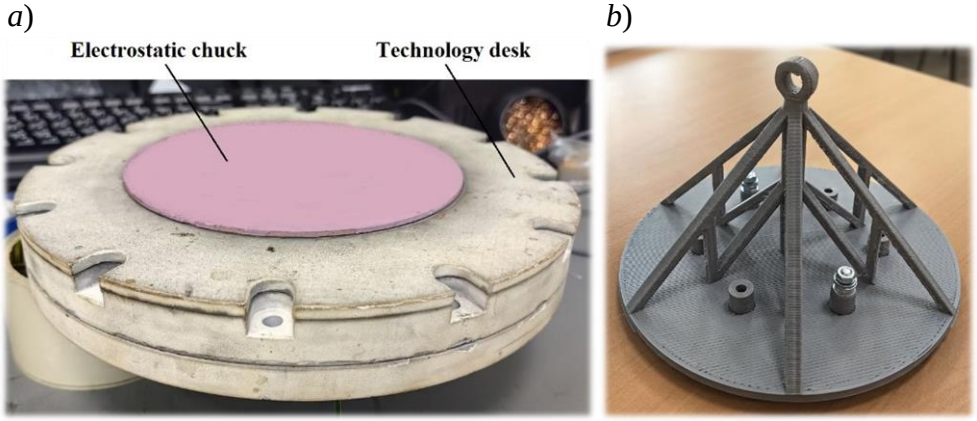


Fig. 1. Elements of the experimental stand: technology desk (*a*), fastener (*b*)

To determine the dependence of the force on the holding time, the clamping force was measured after a temporary pause. For each time delay value, 3 force measurements were performed. The average values of measurements are included in the results of the experiment.

Results and Discussion

Table 1 shows the measurement results. In Figure 1, you can see the results graphically.

Table 1

Dependence of the clamping force on the holding time

Time, s	3	5	10	15	20	25	30	35	45	60
Force, N	2.25	2.99	3.15	2.99	5.15	5.42	5.81	5.60	5.52	5.38

Notations: The amount of effort for each time value is the average of the three measurements.

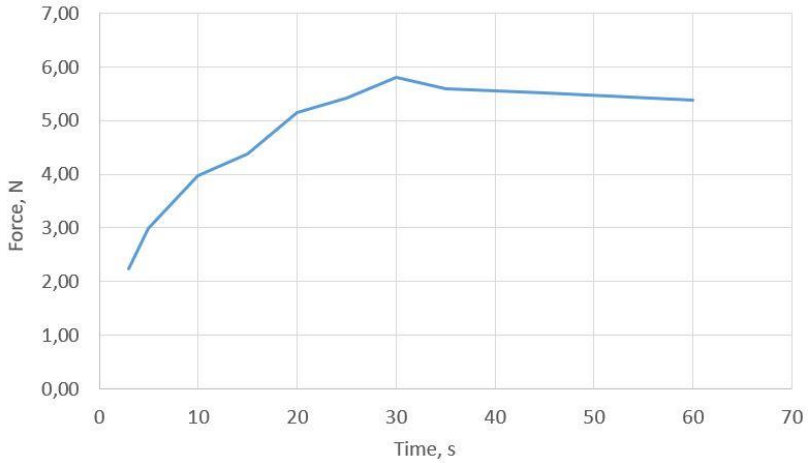


Fig. 2. Dependence of the clamping force on the holding time

The value of the substrate clamping force varies depending on the time the substrate is on the ESC. When examining designs and methods of electrostatic confinement, it is necessary to pause for correct measurement. During this pause, the electrostatic clamp must have time to reach the operating value of the clamping force. In this case, it is necessary to pause for at least 25 seconds [2].

Taking into account the fact that the average values of three measurements are taken to plot the graph, it should be noted that the measurement accuracy is insufficient. In further investigation of the clamp, the measurement accuracy should be improved. This can be done using a guide rail and an automated electric drive.

It is also noted that in the case when the power supply is disconnected from the high-voltage electrode, there is still a substrate retention force of 1 newton. Perhaps this is due to the fact that the experiment is carried out at atmospheric pressure, and when the plate is torn off, a holding vacuum is formed under its surface. The reason may be different, the issue is subject to study. Further research will make it possible to select the optimal materials and designs for the manufacture of an electrostatic chuck

Conclusion

The force with which the electrostatic clamp holds the silicon substrate varies depending on how long the substrate lies on the ESC before separation. For further ESC studies, temporary pauses of at least 25 seconds should be maintained on the described experimental stand before measuring the clamping force. It is necessary to provide an automated drive that will ensure the separation of the substrate with constant conditions, and a guide that will increase the accuracy of the substrate placement on the ESC [3, 4].

REFERENCES

1. **Sun Y., Cheng J., Lu Y., Hou Y., Ji L.**, Design space of electrostatic chuck in etching chamber. Journal of Semiconductors 36.8 (2015): 084004.

2. **Chen R., Huang Y., Tang Q.**, An analytical model for electrostatic adhesive dynamics on dielectric substrates. Journal of adhesion science and Technology 31.11 (2017): 1229-1250.

3. **Wang X., Cheng, J., Wang K., Yang Y., Sun Y., Cao M., Han C., Ji L.**, Modeling of electrostatic chuck and simulation of electrostatic force. Applied Mechanics and Materials 511 (2014): 588-594.

4. **Wang X., Cheng J., Wang K., Yang Y., Sun Y., Cao M., Ji L.**, Finite element analysis on factors influencing the clamping force in an electrostatic chuck. Journal of Semiconductors 35.9 (2014): 094011.

Increasing frequency stability of atomic frequency standards by organizing a group frequency standard

A V Shavshin[1],

[1] The Bonch-Bruevich Saint-Petersburg State University of Telecommunications, Saint Petersburg, 191186, Russia.

✉ shavshin2107@gmail.com

Abstract. The need to modernize atomic frequency standards in satellite and ground-based systems is substantiated to improve the accuracy and stability of the frequency of output signals. Within the framework of the article, a system of group frequency standard was developed, the modernization of the atomic frequency standards included in its composition was carried out, and an algorithm for identifying anomalies in the operation of the system was presented. The performance results improved the Allan deviation values, indicating that the stability of the output signal of the group frequency standard is improved, which is superior to that of the single frequency standard.

Keywords: Atomic frequency standard, group frequency standard, Allan deviation, error signal, automatic gain control.

Introduction

Optimizing the parameters of atomic frequency standards (AFS), as well as increasing their stability and accuracy through the implementation of a group frequency standard (GFS) with an integrated machine learning system, is an extremely important task at the moment. Rubidium and cesium frequency standards are the basis for synchronizing communication and telecommunications networks, and are also actively used in GLONASS navigation systems [1]. The transition to advanced technologies in the field of satellite navigation is necessary because the requirements for the output parameters of AFS are increasing every year, and classical methods for generating highly stable signals are becoming unsuitable for meeting them. The creation of a group frequency standard will improve the accuracy of measurements and the stability of the operation of the frequency generator in the event of a failure of one of the frequency sources. This will reduce the risk of error and ensure continuity of measurements. The technological solution in the form of a GFS with an integrated machine learning system has the potential for wide application, both in satellite telecommunications and navigation systems, and in ground-based telecommunications systems, aviation and other areas where frequency accuracy and stability are of paramount importance.

Group frequency standard and methods for its modernization

The proposed method for creating a GFS based on artificial intelligence will allow automatic adjustment of the output signal of the group frequency standard system using machine learning methods, bypassing the time delay that currently occurs when switching from a failed half-set of a quantum frequency standard to a spare one. The block diagram of the group standard is shown in Fig. 1.

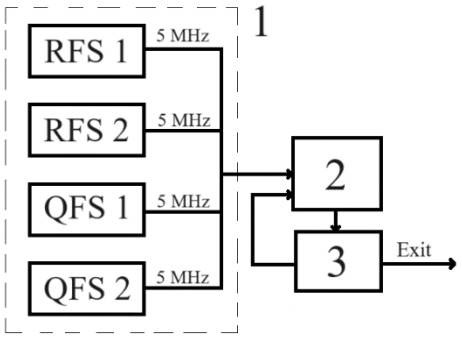


Fig. 1. Block diagram of a group frequency standard: 1 – group frequency standard, consisting of two rubidium and two cesium frequency standards, 2 – phase comparator and AI controller, 3 – quartz oscillator.

The creation of automatic gain control system of the output signal of the microwave path of the formation of frequency converters, in turn, will make it possible to modernize the rubidium and cesium frequency standards included in the group standard system, increasing the stability and accuracy of the frequency of their output signals. [2]. Also, the implementation of a group frequency standard system in satellite systems will allow the simultaneous use of the entire payload on board, without leaving it in reserve, but using it to improve the output parameters of the group frequency standard multiple times.

To implement the operation of the group frequency standard, an algorithm for identifying errors in individual frequency standards included in the system was also developed, which is shown in Fig. 2.

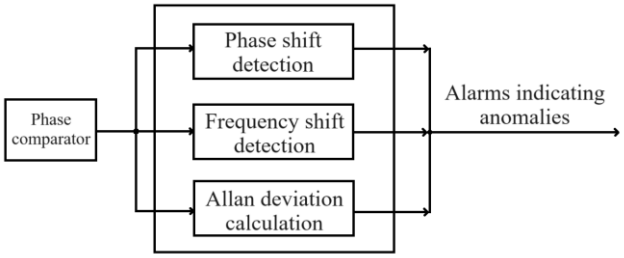


Fig. 2. Algorithm for the operation of a group frequency standard.

Results and Discussion

The results of modeling the operation of the group frequency standard circuit are presented in Fig. 3.

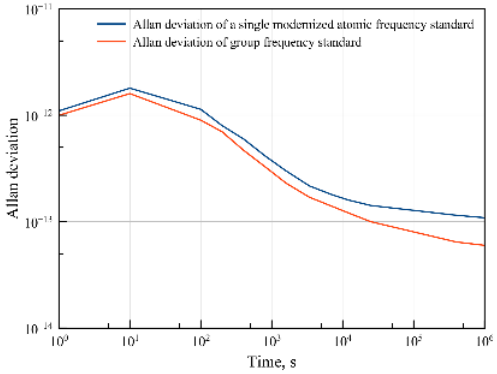


Fig. 3. Allan deviation for the case of operation of a single frequency standard, upgraded using automatic gain control (blue graph) and for the case of operation of a group frequency standard (red graph).

The operation of modernized atomic frequency standards as part of a group frequency standard made it possible to improve the Allan deviation of the output signal by 17%, which confirms the correct operation of the system.

Conclusion

The result of the work done was the creation of a group frequency standard, development of machine learning methods to adjust the operation of the frequency standard, as well as the introduction of automatic gain controls into frequency standard circuits.

Thanks to the actions described above, it was possible to improve the stability of the output signal, increasing the Allan deviation value by 17%.

REFERENCES

1. **Petrov A.A.** Improvement frequency stability of cesium atomic clock for satellite communication system, Lecture Notes in Computer Science. 9247 (2015) 739-744.

2. **Shavshin A.V.** Development of automatic gain control for atomic frequency standard on rubidium-87 atoms, St. Petersburg Polytechnic University Journal. Physics and Mathematics. 15(3.2) (2022) 364-369.

A fast and strong microactuator powered by explosion of a hydrogen-oxygen mixture

P. S. Shlepakov [1]✉, I**. V. Uvarov** [1], **V. B. Svetovoy** [2]

[1] Valiev Institute of Physics and Technology RAS, Yaroslavl Branch, Yaroslavl, Russia;

[2] A.N. Frumkin Institute of Physical Chemistry and Electrochemistry RAS, Moscow, Russia

✉p.shlepakov@bk.ru

Abstract. A fast electrochemical actuator operating in an explosive regime is demonstrated. In this regime, hydrogen and oxygen nanobubbles generated by water electrolysis merge into a microbubble, which explodes with a significant energy output. The explosions push the membrane up to 100 μm in 10 μs. The actuator can withstand more than 40 000 cycles without degrading. It has a volume of 3.1 nl and develops a force up to 0.5 N, which is significantly larger than the force produced by other actuators.

Keywords: electrochemical actuator, membrane, alternating polarity electrolysis, nanobubbles, microbubble, explosion.

Funding: This work is supported by Program № FFNN-2022-0017 of the Ministry of Science and Higher Education of Russia for Valiev Institute of Physics and Technology of RAS.

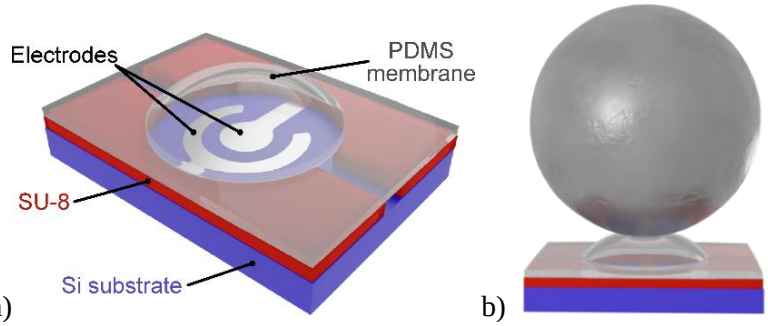
Introduction

Microfluidic systems open new possibilities in chemical analysis, cell research, rapid disease diagnosis and other fields of biology and medicine. Microfluidic chips can deliver drugs directly to target organs or tissues, reducing side effects and increasing treatment efficiency [1]. A drug delivery module contains a micropump that supplies a drug to a body from a built-in reservoir. A key element of the pump is an actuator that creates reciprocating motion of a membrane. The actuator must be compact, develop a large force, and be compatible with microtechnology. An electrochemical actuator meets these requirements. It has a chamber filled with an electrolyte. Gas bubbles produced by electrolysis push the membrane up and then recombine releasing the pressure.

The main drawback of electrochemical actuators is the long response time due to slow gas recombination. Recently, a novel actuator has been developed, which operates several orders of magnitude faster [2]. A micropump based on this actuator demonstrates ultra-precise dosage of 0.14 nl per cycle, but has a moderate pumping rate [3] that can be significantly increased by an explosive operating regime. Hydrogen and oxygen nanobubbles merge into a microbubble that explodes with significant energy release. In this work, the performance of this explosive actuator is demonstrated.

Materials and Methods

The actuator is schematically shown in fig. 1a. It is fabricated on an oxidized silicon substrate. Ruthenium electrodes are located in a cylindrical chamber with a diameter of 500 μm and a height of 16 μm made of SU-8 photoresist. The chamber is covered by a 30 μm thick polydimethylsiloxane membrane. One electrode is grounded, while a series of 500 kHz alternating polarity voltage pulses is applied to the second electrode. The amplitude of pulses exceeds a threshold voltage, at which the concentration of H_2 and O_2 nanobubbles reaches a critical level. The densely packed nanobubbles combine into a microbubble containing a stoichiometric mixture of gases and nanodroplets of electrolyte. The combustion reaction is ignited spontaneously and leads to an explosive expansion of the bubble, which is translated to fast and large membrane deflection.



a) b)

Fig. 1. Schematic image of the actuator (a) and a scheme of loading the membrane with a ball (b)

The expanding microbubble causes a decrease of the current flowing through the electrodes. The pulse generator detects the current drop and interrupts the series of pulses to prevent secondary parasitic explosions and gas accumulation in the chamber. The stroke of the membrane is measured by a camera mounted on an optical microscope. A force developed by the actuator is evaluated by loading the membrane with a metallic ball of 1 mm in diameter and 4.1 mg in mass, as shown in fig. 1b, and a metal plate with the size of 3.9×2.0×0.6 mm and mass of 35 mg.

Results and Discussion

The interruption of the process immediately after the main explosion reduces the amount of remaining bubbles and allows the actuator to operate cyclically at a frequency of up to 10 Hz. The actuator withstands more than 40 000 explosions without any signs of wear. Thus, the explosive operation demonstrates durability of the device. The average stroke is about 100 μm, which is an order of magnitude higher than the deflection in the non-explosive regime.

Photographs of the metal ball before and after the explosion are shown in fig. 2. The actuator throws the ball to a height of 29 mm. The ball receives an energy of 1.2 μJ and has an initial velocity of 0.75 m/s. According to the current waveforms, the membrane deflection reaches the maximum in 10 μs, so that the initial acceleration of the ball is 7700g. Thus, the actuator with a volume of 3.1 nl develops a force of about 0.31 N and moves a macroscopic object - 200 times larger in volume and 1 300 times heavier than itself. When the membrane is loaded with a metal plate, the actuator develops a force of 0.5 N that is orders of magnitude larger than develop devices of comparable size.

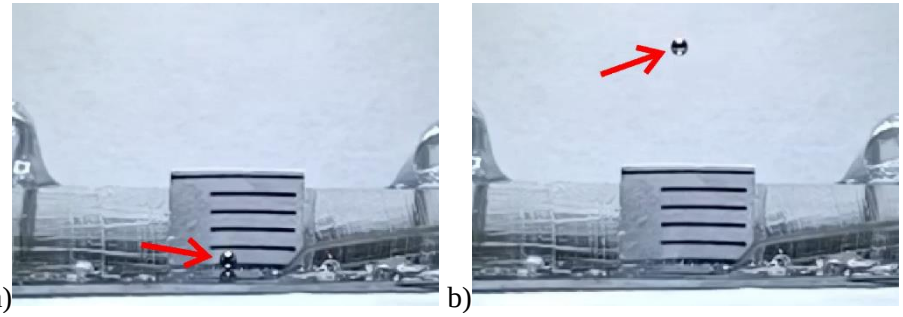

a) b)

Fig. 2. Photographs of the ball (indicated by the red arrow) laying on the membrane (a) and thrown by the explosion (b)

REFERENCES

1. **Pons-Faudoa, F. P., Ballerini, A., Sakamoto, J., Grattoni, A**. Advanced implantable drug delivery technologies: transforming the clinical landscape of therapeutics for chronic diseases, Biomedical microdevices. 21 (2019) 1-22.

2. **Uvarov, I. V., Lokhanin, M. V., Postnikov, A. V., Melenev, A. E., Svetovoy, V. B.** Electrochemical membrane microactuator with a millisecond response time, Sensors and Actuators B: Chemical. 260 (2018) 12-20.

3. **Uvarov, I. V., Shlepakov, P. S., Abramychev, A. M., Svetovoy, V. B**.). Fast Electrochemical Micropump for Portable Drug Delivery Module, Russian Microelectronics. 52 (3) (2023) 186-194.

Electroconductive properties of Pt/(100) β-Ga2O3 Schottky barrier diode based on Czochralski grown crystal

A. Almaev[1,2], Vladimir Nikolaev[3,4], Nikita Yakovlev[1]✉, Alexander Tsymbalov[1]

[1]Laboratory of Metal Oxide Semiconductors, Research and Development Center for Advanced Technologies in Microelectronics, National Research Tomsk State University, Tomsk 634050, Russia

[2]Fokon LLC, Kaluga 248035, Russia

[3]Laboratory of physics of profiled crystals, Ioffe Institute of the Russian Academy of Sciences, Saint Petersburg 194021, Russia

[4]Perfect Crystals LLC, Saint Petersburg 194223, Russia

✉nik_mr_x@mail.ru

Abstract. Pt/(100) β-Ga_2O_3 Schottky barrier diodes were fabricated using a plate cleaved from the crystal grown by Czochralski method. Their electroconductive characteristics were studied. The following values were obtained: the Schottky barrier height (1.69/1.62/1.74 eV), ideality coefficient (1.09/1.14), saturation current density (9.91×10^{-15} A/cm^2), diode series resistance (7.98 kOhm) and net donor concentration ($(1.8–2.4)\times10^{18}$ cm^{-3}). The diodes demonstrate a high rectification ratio of 10^{10} a.u. at an applied voltage of ±1 V and a relatively low experimental value of the leakage current density ~10^{-11} A/cm^2.

Keywords: β-Ga_2O_3; Schottky barrier diodes; power electronics.

Funding: The support the Decree of the Government of the Russian Federation No. 220 of 09 April 2010 (Agreement №. 075-15-2022-1132 of 01 July 2022).

Introduction

Monoclinic gallium oxide is characterized by a large bandgap energy Eg ~4.5–4.9 eV, high electric breakdown field Ebr ~8 MV/cm, and high theoretical Baliga's figure of merit (BFOM), which is 3444 [1,2], versus 340 and 870 for SiC and GaN, respectively. β-Ga_2O_3 is rapidly gaining popularity as a base material for power electronics elements, which are promising for improving electrical energy conversion systems for electric vehicles, air conditioning, and power distribution systems [3]. β-Ga_2O_3 bulk crystals are grown utilizing melt growth techniques such as Czochralski process (CZ), edge-defined film-fed growth (EFG), floating zone method (FZ) etc. Such substrates possess relatively low dislocation density ~10^3 cm^{-2} and high crystal perfection [1,2]. By now, Schottky barrier diodes (SBD) based on β-Ga2O3 with a breakdown voltage U_{br} = 2-4 kV are being successfully developed. Vertical and planar metal-oxide-semiconductor field-effect transistors (MOSFET)

Structures based on (100) β-Ga_2O_3 crystals still remain poorly studied, hence, there are rare examples of device development. The SBDs utilizing EFG grown (100) β-Ga_2O_3 substrates were studied in Ref. [4]. These diodes demonstrate attractive electrical characteristics: high rectification ratio of 10^{10} a.u., ideality factor of 1.1, high Schottky barrier height of 1.3–1.39 eV, high forward current density of 50–150 A/cm^2 at applied voltage of 2 V and low saturation current density of 2×10^{-16} A/cm^2.

In this work, we developed an SBD based on the Pt/(100) β-Ga_2O_3 interface and studied its electroconductive and photoelectric properties. The substrate crystal was grown by CZ method.

Materials and Methods

A bulk crystal of beta gallia in a form of a cylindrical boule was grown by CZ. The setup and the process parameters are described in detail in Refs. [5]. Then the crystal was cleaved into fragments presumably along the cleavage planes. Such unintentionally doped (UID) Ga_2O_3 substrates have ~600 μm thickness. These samples were considered for the investigation and further were used as a base material for the fabrication of vertical type SBD samples.

1 mm in diameter, 100 nm in thick Pt contacts were deposited on the β-Ga_2O_3 plate surface by DC magnetron sputtering through a shadow mask to make SBD anode. A continuous 100 nm

thick ohmic Ti contact was deposited on the back of the β-Ga_2O_3 wafer, the later's surface was treated with acetone, isopropyl alcohol and deionised water prior to metallization.

Results and Discussion

The obtained SBD β-Ga_2O_3 were studied using the thermionic emission model and Cheng's method. Figure 1 shows the J-U characteristic in linear and semilogarithmic coordinates (Figure 1 inset), which were studied using the thermionic emission model. Figure 2 shows the dependences of dU/dln(J) on J and H(J), obtained using the Cheng method from the analysis of the J-U characteristics.

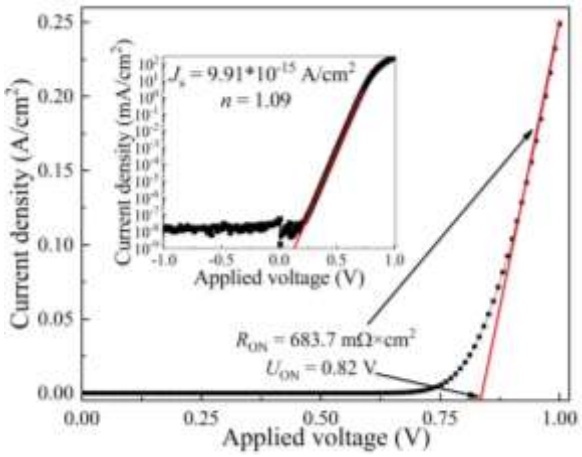


Fig. 5. Forward branch of *J-U* characteristic of the SBD based on Pt/β-Ga_2O_3. Insert shows the *J-U* characteristics in a semi-logarithmic scale.

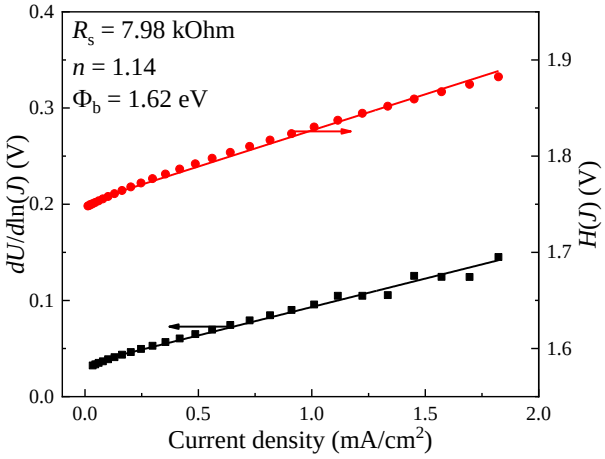


Fig. 6. Cheng's method plots of *dU*/*d*ln(*J*) vs *J* and *H*(*J*) vs *J* for the SBD based on Pt/β-Ga_2O_3.

As a result, the resulting DBS had the following characteristics: ON-resistance Ron = 683.7 mOhm× cm^2; ON-voltage U_{on} = 0.82 V; ideality coefficient n = 1.09; Schottky barrier heigh $\boldsymbol{\varphi}_b$ = 1.69 eV; saturation current density $J_s = 9.91\times 10^{-15}$ A/cm^2; rectification ratio of 10^{10} a.u. The results obtained by the Cheng method and using the thermionic emission model coincide.

REFERENCES

1. **Sheoran H., Kumar V., Singh R. A.**, A Comprehensive Review on Recent Developments in Ohmic and Schottky Contacts on Ga2O3 for Device Applications, ACS Appl. Electron. Mater. 4, 2589–2628 (2022) https://doi.org/10.1021/acsaelm.2c00101
2. **Fu B., Jia Z., Mu W., Yin Y., Zhang J., Tao X**, A review of β-Ga2O3 single crystal defects, their effects on device performance and their formation mechanism, J. Semicond. 40, 011804 (2019) doi: 10.1088/1674-4926/40/1/011804
3. **Onuma T., Saito S., Sasaki K., Masui T., Yamaguchi T., Honda T., Higashiwaki M.,** Valence band ordering in β-Ga2O3 studied by polarized transmittance and reflectance spectroscopy, Jpn. J. Appl. Phys. 54, 112601 (2015) DOI 10.7567/JJAP.54.112601
4. **He Q., Mu W., Dong H., Long S., Jia Z., Lv H., Liu Q., Tang M., Tao X., Liu M.**, Schottky barrier diode based on β-Ga2O3 (100) single crystal substrate and its temperature-dependent electrical characteristics, Appl. Phys. Lett. 110, 093503 (2017) https://doi.org/10.1063/1.4977766
5. **Butenko P.N., Boiko M.E., Guzilova L.I., Krymov V.M., Shapenkov S.V., Sharkov M.D., Verbitskii V.N., Zarichny A.A., Nikolaev V.I.,** Enhancing the perfection of bulk (1 0 0) β-Ga2O3 crystals grown by Czochralski method, Journal of Crystal Growth. 630, 127597 (2024) https://doi.org/10.1016/j.jcrysgro.2024.127597.

All-electronic memristor based on charge carrier confinement in bulk semiconductor of metal-semiconductor-metal structure

Abolfazl Mahmoodpoor[1], Alexandr Marunchenko[1] and Sergey Makarov[1,2,*]

1) ITMO University, School of Physics and Engineering, Kronverkskiy pr. 49, 197101, St. Petersburg, Russia

2) Qingdao Innovation and Development Center, Harbin Engineering University, Qingdao 266000, Shandong, China

* Email Address: s.makarov@metalab.ifmo.ru

Keywords: Semiconductor device simulation, Numerical modelling, All-electronic memoristor

Abstract:

Memristors have gained significant attention in recent years due to their potential applications in computing and memory technology by offering higher performance, lower power consumption, and increased storage capacity. In this paper, we present a new type of memristor by analyzing the dynamic behavior of charge carriers within a metal-semiconductor-metal structure. We show that an all-electronic memristor is achieved through the confinement of majority charge carriers within the bulk semiconductor by the favor of high barrier Schottky contacts. Our findings reveal a remarkable current offset between forward and backward scans, along with exceptional current pulse consistency with a tunable current level using pulse frequency. These characteristics greatly simplify the process of designing electrical circuits incorporating this memristor variant. Furthermore, our research paves the way for the development of crystalline semiconductor-based memristors. While various semiconductors with controllable doping densities can be considered as potential candidates for this type of memristor, our calculations using silicon demonstrate the integration of this semiconductor with current technology holds significant promise for two terminal memristors.

Radiation behaviour study of linear voltage regulator

S. B. Rybalka✉, **A. A. Demidov**, **E. A. Kulchenkov, K. S. Pilipenko**
Bryansk State Technical University, 50 let Oktyabrya blwd. 7, Bryansk, 2410035, Russia
✉sbrybalka@yandex.ru

Abstract. For positive low-dropout linear voltage regulator IS-LS1-3.3V it is established that output voltage and consumption current vary slightly in all total investigated ionizing dose interval and do not cause voltage regulator failure. Analytical dependencies of output voltage and consumption current on the total ionizing dose have been obtained.

Keywords: ionizing dose effects, voltage regulator, X-ray irradiation.

Funding: This study was supported by the Russian Ministry of Science and High Education (agreement with the Russian Ministry of Science and High Education of 9 February 2023 No. 075-11-2023-008).

Introduction

For development of industries such as cosmonautics, aircraft engineering, nuclear power, it is necessary to achieve reliable functioning of the electronic components such as voltage regulators that used under radiation conditions [1, 2]. Therefore, with taking into account, the main aim of this work is to study the radiation hardness to the effects of the total ionizing dose of the positive low-dropout linear voltage regulator IS-LS1-3.3V produced by JSC "GRUPPA KREMNY EL" (Bryansk) in framework of import substitution program, using the developed hardware and software complex based on the X-ray research complex.

Materials and Methods

As the object of research was the positive low-dropout linear voltage regulator prototype IS-LS1-3.3V (analogue of LT1963 (JSC "GRUPPA KREMNY EL" (Bryansk)) with output voltage of 3.3 V and made by epitaxial-planar bipolar technology. Studies of the IS-LS1-3.3V voltage regulator for hardness to ionizing radiation by the effects of total ionizing dose were carried out using the developed hardware and software equipment based on an X-ray research complex (XRRC-0401) with calibration at the "Gamma MRX MEPhI" isotope equipment [3].

Results and Discussion

During the radiation experimental study of IS-LS1-3.3V positive low-dropout (LDO) linear voltage regulator prototype the following operation mode was used for XRRC-0401: anode voltage of 70 kV, anode current of 150 μA. The distance from the window of the X-ray source equals of 40 mm and rate of radiation dose exposure equals of 35.3 un./s (un. – the units of the X-ray comparator DRI-0401). In Fig. 1*a* are shown experimental results for voltage regulator obtained during radiation experiment. As can be seen, the output voltage V_{OUT} slowly increase with increasing of total ionizing dose D. It is important to note that output voltage not reaches the lower and upper limit of voltage regulator operation mode (3.135-3.465 V). Thus, at value of total ionizing dose equals of 8×10^3 un. (that is equal of ~282 s (~4.7 minutes)) output voltage V_{OUT} equals of 3.29 V. Further, during increasing of radiation dose exposure the output voltage V_{OUT} increase nonlinearly and at final value of total ionizing dose equals of 1002×10^3 un. (~35430 s (~590.5 minutes)) the output voltage value is 3.33 V ($\Delta V_{OUT}\approx0.04$ V), i.e. in this case the voltage regulator scheme preserves a functional state without failure. As follows from Fig. 1*b* the consumption current I_{cc} varies slightly between 1.59 mA (622×10^3 un.) and 1.25 mA (707×10^3 un.) and reaches 1.246 mA at final value of total ionizing dose equals of 1002×10^3 un. (~35430 s (~590.5 minutes)). It should be noted that a similar results were detected in the similar type of positive LDO linear regulator designed specifically for space applications [4]. From a practical viewpoint, it is important to know for voltage regulator the analytical dependence on the radiation dose. On the basis of above experimental data, analytical dependence of the output voltage V_{OUT} and consumption current I_{cc} on the total ionizing dose D for voltage regulator were calculated.

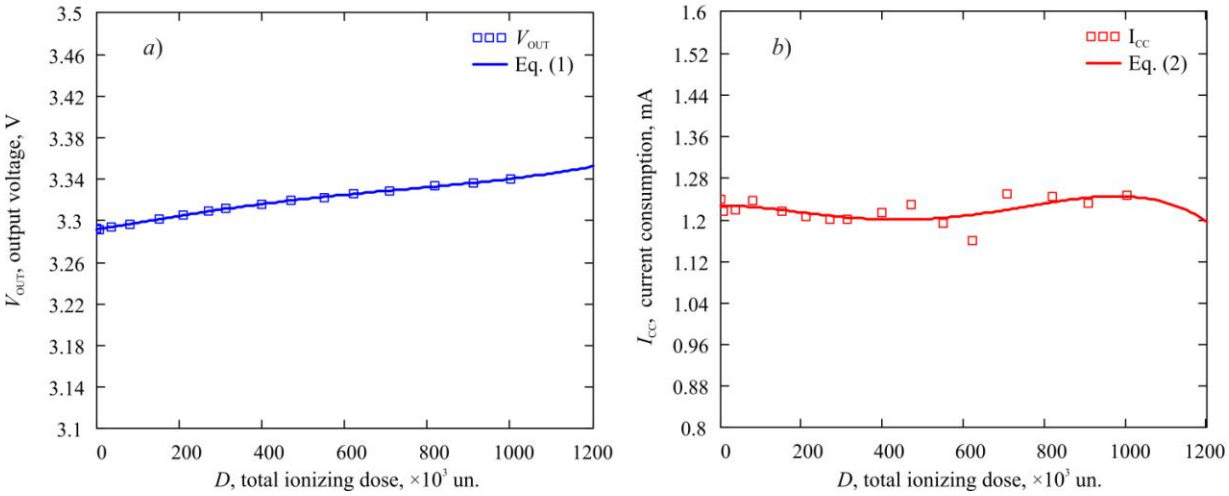


Fig. 1. The experimental (points) and theoretical (lines) data for output voltage dependence V_{OUT} (*a*) and consumption current I_{cc} (*b*) on total ionizing dose *D* for IS-LS1-3.3V voltage regulator.

The analytical dependence of the output voltage V_{OUT} and consumption current I_{cc} on the total ionizing dose *D* for voltage regulator (in active operating mode at input voltage of 24 V and load current of 5 mA) are following:

$$V_{OUT} = 3.204\times10^{-14}D^4 - 4.435\times10^{-11}D^3 - 9.187\times10^{-9}D^2 + 7.041\times10^{-5}D + 3.291, \quad (1)$$

$$I_{cc} = -6.276\times10^{-13}D^4 + 1.183\times10^{-9}D^3 - 5.368\times10^{-7}D^2 - 9.1\times10^{-7}D + 1.226, \quad (2)$$

where *D* – the total ionizing dose (10^3 un.), V_{OUT} – the output voltage (V), I_{cc} – the consumption current (mA).

Conclusion

The radiation hardness to the effects of the total ionizing dose of the positive low-dropout linear voltage regulator IS-LS1-3.3V produced in framework of import substitution program, has been studied using the developed hardware-software complex based on the X-ray research complex. It is established experimentally that output voltage varies slightly from 3.29 up to 3.33 V ($\Delta V_{OUT}\approx1.2\%$) in all total ionizing dose interval and preserves a functional state without failure. It is shown that the consumption current varies slightly between 1.59 mA and 1.25 mA. For voltage regulator have been calculated the analytical dependencies for the output voltage and consumption current on the total ionizing dose.

Acknowledgments

This work was carried out with financial support of the Russian Ministry of Science and High Education within the framework of complex project by creation of highly technological industry «Integrated microcircuits of analog signal converters in metal-polymeric package of various types: development and mastering of technology, replacement of imported analogs and organization of serial production» (agreement with the Russian Ministry of Science and High Education of 9 February 2023 No. 075-11-2023-008) at the organization of the leading performer of RDDTE (Research and Development Design and Technological Engineering) the Bryansk State Technical University.

REFERENCES

1. **Volovich G. I.,** Circuit Technique of Analog and Analog-digital Electronic Devices, DMK Press, Moscow, 2018.

2. **Kulchenkov E. A., Rybalka S. B., Demidov A. A.**, Study of Radiation Hardness of Linear Voltage Regulator, Advances in Applied Physics. 5(11) (2023) 445–454.

3. JSC "Specialized electronic systems" (SPELS). URL: http://www.spels.ru. Accessed Mar. 25, 2024.

4. Ultra Low Dropout Positive Fixed Linear Regulator IRUH33P253A1M. URL: https://www.irf.com/product-info/datasheets/data/iruh33p253a1m.pdf. Accessed Mar. 30, 2024.

Method for increasing of the voltage regulator radiation hardness

K. S. Pilipenko, E. A. Kulchenkov, S. B. Rybalka✉, A. A. Demidov
Bryansk State Technical University, 50 let Oktyabrya blwd. 7, Bryansk, 2410035, Russia
✉sbrybalka@yandex.ru

Abstract. For positive low-dropout linear voltage regulator the additional circuit elements have been developed in the output stage of the for positive linear voltage regulator, forming compensatory feedback and making it possible to increase voltage regulator radiation hardness.

Keywords: voltage regulator, ionizing dose effects, X-ray irradiation.

Funding: This study was supported by the Russian Ministry of Science and High Education (agreement with the Russian Ministry of Science and High Education of 9 February 2023 No. 075-11-2023-008).

Introduction

Today, the one of the main task is to increase the radiation hardness of electronic components to the effects of ionizing radiation [1, 2]. Therefore, the urgent question is to study a methods for increasing radiation hardness, especially, studying the response of individual elements of a linear voltage regulator IS-LS3-5V microcircuit, produced by JSC "GRUPPA KREMNY EL" (Bryansk) in framework of import substitution program, to total ionizing dose of ionizing radiation, using the developed hardware and software complex based on the X-ray research complex.

Materials and Methods

The positive low-dropout linear voltage regulator prototype IS-LS3-5V (analogue of LM2937 type) produced by JSC "GRUPPA KREMNY EL" (Bryansk) with output voltage of 5 V and made by epitaxial-planar bipolar technology. Investigation of the IS-LS3-5V voltage regulator for hardness to ionizing radiation by the effects of total ionizing dose were carried out using the developed hardware and software equipment based on an X-ray research complex (XRRC-0401) with calibration at the "Gamma MRX MEPhI" isotope equipment [3].

Results and Discussion

Additional circuit elements have been developed in the output stage of the linear voltage regulator, forming compensatory feedback, as a result of which the output voltage parameter of the voltage regulator remains within the limits established by the technical requirements at large values of the total ionizing dose [4]. This method can be implemented both at the stage of manufacturing a microcircuit chip, and as an external wiring diagram when using already produced serial products. Fig. 1*a* shows part of the electrical circuit of the IS-LS3-5V positive voltage regulator integrated microcircuit where the measurements were carried out.

In a known linear voltage regulator, the base of an additional n-p-n transistor is connected to the second inverted input of the operational amplifier, the collector of which is connected to the positive bus of the regulator, and the emitter is connected through the current generator to the negative bus of the regulator and a resistor is connected between the feedback pin and the second input of the operational amplifier, the value of which is determined by the formula:

$$R = \beta \Delta U_{\text{REF}} / I_{\text{G}}, \quad (1)$$

where β – the gain with the common emitter of the additional transistor after exposure to radiation; ΔU_{REF} – change in reference voltage from the nominal voltage after exposure to radiation; I_{G} – the magnitude of the generator current in the emitter circuit of the additional transistor. When exposed to radiation, the magnitude of the output voltage of the reference voltage source increases. An additional n-p-n transistor is a radiation dose sensor. The higher the radiation dose, the lower its gain in a common emitter circuit. At doses less than 200×10^3 un. (un. – the units of the X-ray comparator DRI-0401), the gain of the n-p-n transistor changes slightly. Since the emitter current of the additional n-p-n transistor is set by the current generator and remains stable, when exposed to ionizing radiation, the current in the base circuit increases,

the voltage drop across the resistor in the feedback circuit also increases, which leads to an increase in the potential at the inverted input of the operational amplifier. This causes the operational amplifier's output current to decrease, the output transistor to turn off, and the drain-to-source voltage drop to increase, thereby compensating for the drift of the output voltage due to the effect of ionizing radiation on the reference voltage source. In our case the calculated by equation (1) value of resistor *R* in the feedback circuit is 90 kΩ. In Fig. 1*b* presents the results of studies on the radiation hardness of voltage regulator without a compensation circuit (solid line) and using the method discussed above (dashed-line). As can be seen from Fig. 1*b*, the output voltage of the modified voltage regulator integrated circuit remains almost constant.

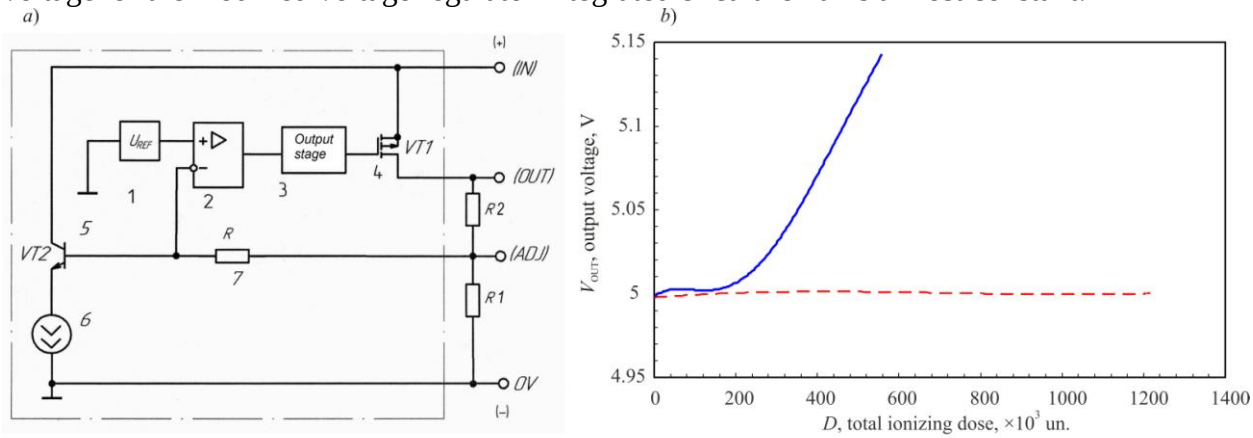


Fig. 1. (*a*) Diagram of positive voltage regulator IS-LS3-5V: 1 – reference voltage source at the bandgap width; 2 – operational amplifier; 3 – output stage; 4 – output transistor; 5 – additional n-p-n transistor; 6 – current generator; 7 – additional resistor; 0V – positive bus; ADJ – feedback pin for adjusting the stabilization voltage; OUT – output of the voltage regulator; IN – positive bus; R1 and R2 –the stabilization voltage settings divider; (*b*) The output voltage V_{OUT} dependence on total ionizing dose *D* for IS-LS3-5V voltage regulator: solid line – original voltage regulator integrated circuit, dashed-line – modified voltage regulator integrated circuit.

Conclusion

The method of radiation hardness increasing to the positive low-dropout linear voltage regulator prototype IS-LS3-5V (produced by JSC "GRUPPA KREMNY EL" (Bryansk)) with output voltage of 5 V has been developed. It is shown that additional circuit elements in the output stage of the linear voltage regulator form compensatory feedback and make it possible to increase its radiation hardness.

Acknowledgments

This work was carried out with financial support of the Russian Ministry of Science and High Education within the framework of complex project by creation of highly technological industry «Integrated microcircuits of analog signal converters in metal-polymeric package of various types: development and mastering of technology, replacement of imported analogs and organization of serial production» (agreement with the Russian Ministry of Science and High Education of 9 February 2023 No. 075-11-2023-008) at the organization of the leading performer of RDDTE (Research and Development Design and Technological Engineering) the Bryansk State Technical University.

REFERENCES

1. **Gaul S. J., Vonno N., Voldman S. H., Morris W. H.**, Integrated Circuit Design for Radiation Environments, Wiley & Sons, Chichester, 2020.

2. **Volovich G. I.,** Circuit Technique of Analog and Analog-digital Electronic Devices, DMK Press, Moscow, 2018.

3. JSC "Specialized electronic systems" (SPELS). URL: http://www.spels.ru. Accessed Mar. 30, 2024.

4. Patent RU 219091 U1, 2023. Authors: Derbunov I.V., Bryukhno N.A., Dantsev O.O., Kulchenkov E.A.

Technological aspects of island thin films usage in sensors for various purposes

S. V. Sidorova [1]✉, **S. V. Kiryanov** [1]
[1] Bauman Moscow State Technical University, Moscow, Russia
✉sidorova@bmstu.ru

Abstract. The paper presents the optimization of Co, Ni and Al island thin films formation modes by thermal evaporation in vacuum with tunnel current control. An analysis of scanning electron microscope images for island coatings of Co and Ni is provided. The influence of the island structure of the magnetoresistive sensor on sensitivity is established.

Keywords: Island film, island nanostructures, low-dimensional magnetism, spin-tunnel magnetoresistive sensor, gas-sensitive sensor.

Introduction

In recent years, considerable attention has been paid to the development of innovative sensor technologies due to their crucial role in various fields, ranging from industrial monitoring to biomedical diagnostics. Among these applications, magnetoresistive spin tunnel effect sensors and gas sensors have demonstrated significant potential due to their level of sensitivity and versatility. An opportunity to modernize the technology of creating such sensors is the use of insular thin films, which have unique properties that contribute to expanding their characteristics from miniaturization and speed to increasing operating cycles and increasing sensitivity.

By investigating the relationship between the morphology of insular thin films and the sensitivity of sensors, it is possible to improve the performance and reliability of devices. It should be noted that both hard and soft ferromagnets can be used for magnetic field sensors [1]. For gas-sensitive sensors, both noble metals (silver, platinum, gold) and metals that allow the production of fast oxides (aluminum, magnesium) should be used. It is also interesting to combine the indicated materials for both magnetic field sensors and a gas sensor.

The aim of this report is to study and establish the dependence of the morphology of insular thin films made of ferromagnets and other metals on the formation modes.

Materials and Methods

The application of insular thin films of metals was carried out using a laboratory stand created on the basis of an unit for the formation of thin-film coatings in vacuum, located at the MT11 Department of Bauman Moscow State Technical University. Dielectric substrates with copper contacts at the edges were prepared in advance for film deposition. To form the island layer, the method of thermal evaporation with a conical spiral made of refractory material was used. The power supply of the thermal evaporation module has been set to the current stabilization mode.

According to the results of the analysis, hard (Co) and soft (Ni) ferromagnets were selected to work out the modes of formation of the island layers of the magnetic field sensor. As a result of the same analysis, aluminum was selected to form a sensitive layer in the gas sensor.

Evaporation of the material was observed at different currents on the evaporator. Therefore, it was necessary to work out the formation modes for each material separately. Previously, copper contact pads were applied to all substrates, to which a Keithley 6485 picoammeter was connected to monitor the tunneling current (TT) right during the coating formation process. Thus, control took place at the control stand of the initial stages of growth of thin-film coatings [2, 3] directly in the process of their formation.

The modes were tested in several stages: determining the stages of formation, applying samples individually according to selected stages, controlling the geometry of structures, obtaining a series of samples with selected characteristics and checking the reproducibility of the experiment.

The geometry of the island structures was evaluated in the images after examination with a scanning electron microscope.

Results and Discussion

As a result of experimental studies, a series of dependencies of the tunnel current on the time of coating formation was obtained. The following parameters are recommended for the formation of Ni island coatings: current – 4.5...5.5A, time – 14...17 sec; for Co: current – 8...9.5A, time – 48...51 sec; for Al: current – 3.5...4.5A, time – 3...11 sec.

It should be noted that the sensitivity of sensors with island layers on average exceeds the sensitivity of samples with solid layers by 3 times [4].

Conclusion

The results of these experimental studies can open up new horizons in the market of magnetic sensors and gas-sensitive sensors [5]. In the future, it is planned to study the effect of the number of layers on the sensitivity of STMP samples [6], as well as the formation of a test sample of a gas medium sensor based on an island thin film.

REFERENCES

1. **Kiryanov S.V., Yurkin N.O., Kouptsov A.D., Sidorova S.V.**, Application of island thin films for microelectronics devices, 979-8-3503-9952-3/23/$31.00 ©2023 IEEE.

2. **Sidorova S.V.**, **Kiryanov S.V., Yurkin N.O., Zhuravleva V.S.**, **Gulyaeva P.S.** Investigation of the properties of metallic insular thin films for use in nanoelectronics products, XXIX scientific and technical conference with the participation of foreign specialists "Vacuum science and technology": Collection of works. – M.: Electro-vacuum technologies, 2022

3. **Sidorova S.V., Yurchenko P.I.,** Formation of insular nanostructures in vacuum, ENTI Science and Education, October 2011.

4. **Boltaev A.P., Pudonin F.A., Sherstnev I.A**. Features of magnetoresistance of multilayer systems of magnetic nanostructures in weak magnetic fields // FTT. 2011. Vol. 53, No. 5. p. 892.

5. **Janine Walker, Priyanka Karnati, Sheikh A. Akbar, Patricia A. Morris.** Selectivity mechanisms in resistive-type metal oxide heterostructural gas sensors. Sensors and Actuators B: Chemical 2022.

6. **Kiryanov S.V., Sidorova S.V.**, The introduction of an insular thin film into the stmp sensor NNB IX, St. Petersburg, May 13 – 15, 2021.

Technological aspects of increasing capacitor capacitance method

S. V. Sidorova [1,2✉], **I. E. Pimenov** [2], **A. D. Kouptsov** [1]
[1] Bauman Moscow State Technical University, Moscow, Russia;
[2] FSUE «NAMI» State Research Center of the Russian Federation, Moscow, Russia
✉sidorova@bmstu.ru

Abstract. The paper substantiates the relevance of introducing an island layer onto the capacitor plates to increase the capacity. The use of combined targets for the formation of an island layer of the required geometry is proposed. The results of testing the deposition rates of dielectric and conductive layers using magnetron sputtering are presented. The configurations and geometric parameters of the combined target are determined. Models of combined targets have been developed.

Keywords: capacitor, electric capacitance, magnetron sputtering, island thin films, deposition rate, aluminum oxide, copper.

Introduction

Modern trends are actualizing the task of increasing the specific capacitance of capacitors. An increase in capacity can be achieved by reducing the distance between the plates, increasing the effective area of the plates (for this, an island coating layer is formed on the surface of the electrode) and increasing the dielectric constant of the dialectic material. Island structures serve as potential wells for charges, which makes it possible to increase efficiency by reducing its own energy consumption. The formation of an island structure is one of the most complex technological processes, since it is necessary to stop the deposition process before individual clusters begin to form bridges and at the same time achieve their maximum size [1].

The goal of this paper is to develop a method for forming an island coating for the plates of a high-capacity capacitor.

Materials and Methods

The capacitor plates are made of conductive material with the lowest resistance. Copper, which has high conductivity, was selected for the capacitor plates. The material of the dielectric layer must have a high dielectric constant, which affects the capacitance of the capacitor, so aluminum oxide was chosen [2–4].

An option for forming a coating is the magnetron sputtering method. It is distinguished by high coverage uniformity and the ability to control the rate of coating growth. The difficulty in obtaining individual islands is the specificity of forming the coating using magnetron sputtering. To solve this problem, it is proposed to use a combined target that combines dielectric and conductor materials. When using such a target design, the dielectric material should prevent active coalescence from occurring [5–7].

The rate of formation of the conductive and dielectric layers was calculated by assessing their thicknesses. To do this, processes were carried out to deposit layers of aluminum oxide and copper, the thickness of the layers was measured and the deposition rates of the materials were calculated. The deposition rate method was used when measuring a witness sample. The interface between the substrate and the film was prepared to ensure the correctness of the measurements by installing the silicon substrate-template on the silicon substrate-base with polished surfaces facing each other. The formation of thin-film coatings was carried out on the basis of an unit located at the MT11 Department of Bauman Moscow State Technical University.

Scanning of the coating substrate interface was carried out using the probe method [8, 9]. The thickness was determined as the difference in scanning heights.

Results and Discussion

Models of combined targets with cylindrical, ring and segmented conductor inserts in a dielectric matrix have been developed. Segmental triangular inserts are made in the form of petals

covering the spray surface. The design is complicated by the fact that the petals are thin and require frequent replacement. The introduction of cylindrical inserts into the target is problematic due to the complexity of processing aluminum oxide and the possibility of cracking the target. It should be noted that soldering or adhesive jointing is unacceptable from the point of view of the purity of the technological process. The most appropriate option seems to be a combined target with a ring insert. However, it is necessary to calculate the geometry of the insert location in the target erosion zone.

Sputtering of the material of the island target should occur in such a way that the volume of the deposited material of the islands and the filling dielectric corresponds to their volumetric proportions in the structure of the island layer on the capacitor plates. The deposition rate of metals is higher, so for calculations and measurements it is enough to form samples with three iterations of process times - 30, 60 and 90 minutes.

For dielectric targets, the coefficient of material sputtering by argon ions is lower, therefore, the deposition rate is low. Therefore, the total deposition time to obtain a film thickness sufficient for measurement was increased.

The relative measurement error does not exceed 1.3% for Cu and 4.2% for Al_2O_3.

Conclusion

The studies carried out made it possible to work out the deposition rates of the dielectric and conductive layers. The calculations carried out taking into account deposition rates and the required topology of the capacitor plates made it possible to determine the geometry of the target. Models of combined targets have been developed.

Designs of combined targets made of aluminum oxide with copper inserts have been prepared for the formation of an island thin-film coating.

REFERENCES

1. RF Patent No. 2020123399, 07/15/2020. Island thin-film capacitor // Russian Patent No. 200183. 2020. Bulletin. No. 28 / Sidorova S.V., Andreasyan O.G.

2. **Komandin G. A.,** et al. Dielectric losses of thin-film SiO2 samples on Al in the THz-IR range. Solid State Physics 62.2 (2020): 223-228.

3. **Abyzov A. M.** Aluminum oxide and aluminum oxide ceramics (Review). Part 1. Properties of Al 2 O 3 and industrial production of dispersed Al2O3. New Refractories 1 (2019): 16-23.

4. **Kozyukhin S. A.,** et al. Dielectric properties of nanocrystalline tungsten oxide in the temperature range 223–293 K. Semiconductor Physics and Technology 52.7 (2018): 745-750.

5. **Monakhov, I. S., and M. G. Tyurganov.** Initial stages of growth of tungsten and copper films during magnetron sputtering. Moscow State Institute of Electronics and Mathematics: 1-5.

6. **Sidorova S.V.** Methods for the formation of thin films: the initial stage of formation // Handbook. Engineering magazine. M.: Mechanical Engineering, 2011, No. 9.

7. **Streletskiy, O. A.,** et al. Size control of silver nanoclusters during ion-assisted pulse-plasma deposition of carbon-silver composite thin films. Vacuum 175 (2020): 109286.

8. **Dedkova, A. A., V. Yu. Kireev, and M. A. Makhiboroda.** Possibilities and limitations of the contact profilometry method in determining the height difference for monitoring topological elements and layer thickness. Nanostructures. Mathematical Physics and Modeling 20.2 (2020): 23-40.

9. **Suabrey, G. Z.** Use of quartz vibrator for weighting thin films on a microbalance. Zeitschrift für Physik 155 (1959): 206-212.

Development of an excitation signal generation system for a rubidium frequency standard

A. P. Valov[1,2]✉, D. V. Zaletov[2], E. V. Isupova[3]

[1] The Bonch-Bruevich Saint Petersburg State University of Telecommunications, Saint Petersburg, Russia;

[2] AO "Obukhovskiy zavod", Saint Petersburg, Russia

[3] Peter the Great Saint-Petersburg Polytechnic University, Saint-Petersburg, Russia Federation;

✉tony.valov2015@yandex.ru

Abstract. In the digital age, information transmission systems, telecommunications and satellite navigation systems, as well as metrology services play an important role. However, the development of these technologies leads to the need to constantly improve the frequency standards used for signal synchronization.

To improve the stability of the signal produced by the frequency standard, a new system has been proposed for generating a microwave signal with a frequency that matches the frequency of the atomic transition of rubidium-87 atoms.

Keywords: Frequency standard, atomic clock, phase-locked loop, frequency synthesizer, stabilization.

Introduction

In today's world, accurate measurement of time and frequency is critical for conducting numerous experiments in various scientific fields, such as atomic physics, exploration of the earth's surface or outer space. Without highly stable frequency and time sources, normal operation of communication equipment and metrological services is impossible.

Quantum frequency standards (QFS) occupy a special place among devices for determining frequency and time. Their advantage lies in the use of laser radiation and optical elements to stabilize the frequency, thereby ensuring high stability of the systems. A slight frequency deviation can lead to significant errors, especially when transmitting large amounts of data.

On the one hand, expanding the range of tasks for which satellite navigation systems are used requires increasing the accuracy of determining the position of objects to 0.5 meters. On the other hand, the development of scientific and technological progress leads to changes in the composition of the electronic equipment used, which also requires constant modernization of the QFS.

The development and implementation of new QFS models are labor-intensive and costly processes, and often there is no opportunity and resources for their full implementation. Therefore, existing systems are most often upgraded to improve their characteristics, such as reducing size and weight, reducing energy consumption and increasing metrological accuracy. It is important to note that modernization can concern both the entire design of the QFS and its individual components or blocks [1-3]. One of the solution to modernize the QFS is to replace old excitation signal generation system that uses only frequency converter and frequency synthesizer by new system that uses PLL generator system and frequency synthesizer.

Materials and Methods

QFS on rubidium-87 atoms is based on a phenomenon known as optical pumping of atoms. Rubidium-87 is used in atomic clocks due to certain quantum properties that allow time to be accurately measured.

The operation of the rubidium frequency standard (RFS) is based on complex processes of interaction between light and rubidium-87 atoms. The key element of this system is a quartz oscillator, tuned to the frequency of the quantum transition of rubidium-87 atoms. The process of adjusting the frequency of a quartz oscillator to the quantum-frequency transition of rubidium-87 atoms is carried out using a microwave signal supplied from a frequency converter (FC) and an atomic discriminator (DA), which houses a multiplying microwave diode, to a vacuum cell filled with rubidium-87 atoms and buffer gas.

Having examined in detail the principle of microwave signal formation, we can highlight a number of disadvantages of this system. The main disadvantage is the lack of direct control of the frequency of the generated microwave signal, since the final stage of synthesis of the required frequency occurs inside the atomic discriminator. This complicates control and requires assessing frequency coincidence using indirect signs [4]. Another disadvantage is the difficulty of matching the signal mixture with the multiplying diode of the atomic discriminator.

Results and Discussion

The above disadvantages limit the possibilities for improving system performance. An analogue of a microwave signal generation system is considered to overcome these limitations.

The generation system being developed must synthesize an intermediate signal with a frequency of 100 MHz and a microwave signal with a frequency of 6.8347 GHz.

It is proposed to synthesize the required signal frequency using a multi-loop phase-locked loop (PLL) circuit , the main elements of which are a voltage-controlled oscillator (VCO), a phase detector (PD) and a low-pass filter (LPF).

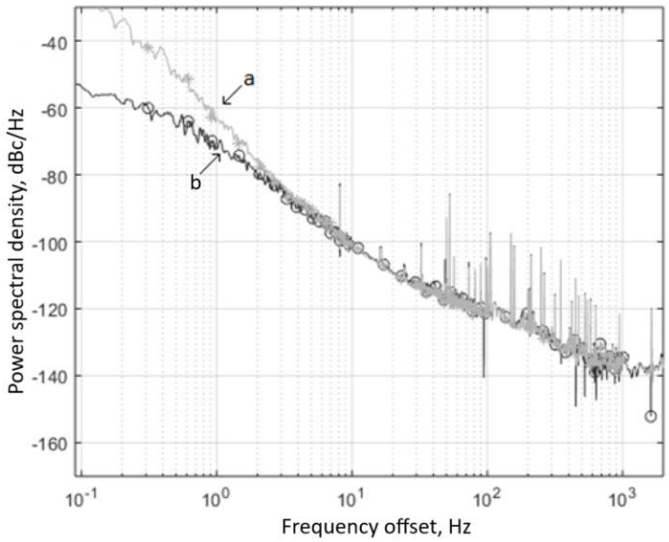


Fig. 1. Power spectral density of 100 MHz signal: a) signal without PLL system; б) signal with PLL system

A prototype PLL circuit for 100 MHz was developed and experimental studies were carried out on the output characteristics of the power spectral density of a 100 MHz signal with and without a PLL loop (Fig. 1)

Conclusion

An experimental study of the resulting circuit made it possible to verify the operability of the circuit for detuning frequencies less than 10 Hz. To improve the operation of the PLL loop for detuning more than 10 Hz, it is proposed to refine the low-pass filter and replace the voltage-controlled oscillator with a more stable oscillator and with lower phase noise characteristics.

REFERENCES

1. **Riehle F.,** Frequency standard. Basic and applications, WILEY-VCH Verlag CmbH Co. KGaA: New-York, 2008.

2. **Arinushkina, K., Grevsteva, A., Valov, A., Lukashev, N.** Development of the Controllable C-field Current Stabilizer for the Atomic Beam Tube of the Cesium Atom Clock. Springer Proceedings in Physics. 268 (2022) 589–596.

3**. A.P. Valov, R.A. Dmitriev, V.V. Davydov, A.V. Shavshin**, Investigation of a method for improving phase noisein the frequency standard generator block, St. Petersburg Polytechnic University Journal. Physics and Mathematics. 2023. Vol. 16. No. 3.2/

4. **A. A. Petrov, V. E. Shabanov, D. V. Zalyotov, A. L. Bulyanitsa, and D. V. Shapovalov**, “Modernization of the frequency synthesizer of cesium atomic clock,” IEEE International Conference on Electrical Engineering and Photonics, EExPolytech 2018, vol. 8564389 pp. 52-55, Saint-Petersburg, October 2018.

SUPERCONDUCTING SINGLE PHOTON DETECTOR WITH MULTIMODE FIBER COUPLING FOR PLIM\FLIM APPLICATIONS

V. Andreev[1,4,6]✉, P. Morozov[2,6], M. Yakovleva[5], A. Kostyukov[5], G. Goltsman[1,4]

[1] National Research University Higher School of Economics, 20,Myasnitskaya ulitsa, Moscow, 101000, Russia;

[2]LLC SCONTEL, 11kA,Derbenevskaya Naberezhnaya, Moscow, Russia;

[3]Privolzhskiy Research Medical University, 10\1,Sq. Minina and Pozharskogo, Nizhny Novgorod, 603005, Russia

[4]Moscow Pedagogical State University, 1\1,Malaya Pirogovskaya Street, Moscow,119991, Russia

[5]N.M. Emanuel Institute of Biochemical Physics RAS, 4,Kosygina Street, Moscow,119334, Russia

[6]LLC «SCONTEL»,11kA, Derbenevskaya Naberezhnaya,Moscow,115114, Russia

✉vsandreev@hse.ru

Abstract. In this paper we presents system for direct time-resolved measurement of luminescence coupled with multimode optical fiber large area superconducting single photon detector (SSPD) for visible and near-infrared range applications. SSPDs positively outperform other types of single-photon detectors and may be the best solution for many applications. But the sensitive area of which is rather small and well suited to be coupled to a single-mode optical fiber. Research shows that large area SSPD coupled with multimode fiber can be fabricated. This detectors was coupled with the phosphorescence\fluorescence lifetime imaging microscopy (PLIM\FLIM) system. This detectors works well in visible range and also could have high efficiency in near infrared range. This provides wide range of applications in luminescence measurement. For the test object we used lipofuscin granulas, as well researched object. As excitation laser we used Becker&Hickl BDL-473-SMC picosecond diode laser with wavelength of 473 nm.

Keywords: SNSPD, luminescence, imaging, microscopy, lifetime.

Funding: This study was funded by Russian Science Foundation grant number 23-72-00014.

Introduction

This paper presents system for direct time-resolved measurement of luminescence coupled with multimode optical fiber large area SSPD for visible and near-infrared range applications. Modern FLIM\PLIM research mostly provides data for visible wavelength range. There are growing request for system that can also work in near-infrared range. Superconducting single photon detectors (SSPDs) positively outperform other types of single-photon detectors and may be the best solution for many applications. But the sensitive area of which is rather small and well suited to be coupled to a single-mode optical fiber. Research shows that large area SSPD coupled with multimode fiber can be fabricated [1].

Materials and Methods

Therefore, we provide FLIM\PLIM system with large area SSPD coupled with multimode fiber. For FLIM\PLIM we use TCSPC Becker&Hickl [2] laser scanning system with confocal microscope Zeiss Axio Observer.A1 with optical scanning system. It is well suited for visible range applications and uses hybrid detector for photon counting for standard system.

Optical scanning system was modified by us to use multimode fiber for single photon counting for also visible and near infrared applications with low noise, therefore high signal to noise ratio measurements.

Results and Discussion

One of the promising applications of the FLIM method in medicine is the detection of fundus autofluorescence, the source of which is lipofuscin granules in retinal pigment epithelium cells.

We provide measurement of lipofuscin fluorescence lifetimes and intensity imaging and data in visible range. Excitation laser was Becker&Hickl BDL-473-SMC picosecond diode laser with wavelength of 473 nm wich is near with lipofuscin absorbance peak. At the fiber was put 500 lp filter to cut unwanted radiation to pass thru to the detector. The data obtained is shown at Figure 1, 512x512 pixels images each contained fluorescence decay data. The fit procedure was made with each pixel, the quality of the fit is described by X^2 with is close to 1 at all valuable points.

All data is consistent with the previously obtained data [3].

a) *b*)

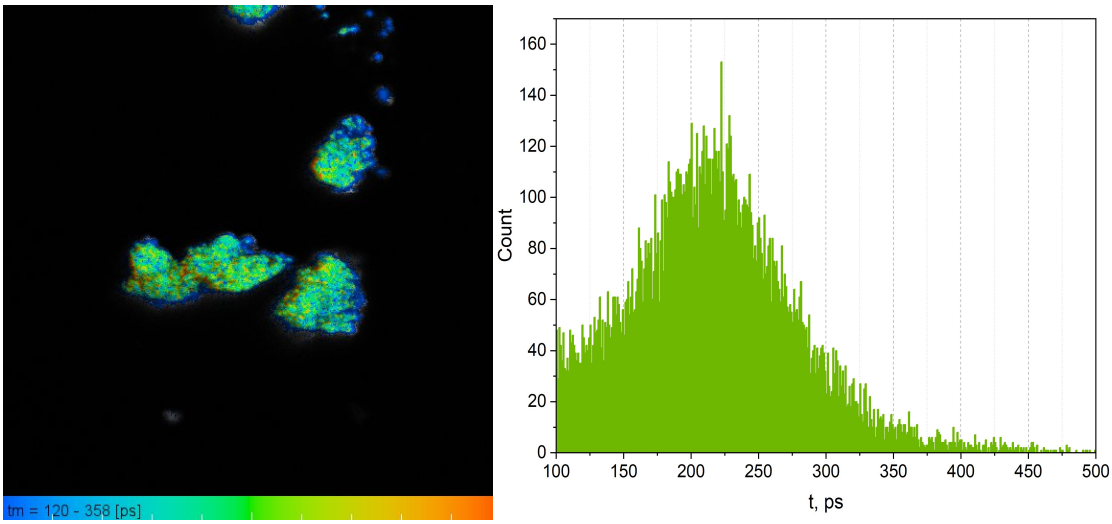


Fig. 1. Fluorescence lifetime of the lipofuscin, (*a*) FLIM image, (*b*) average lifetime histogram.

Conclusion

All data obtained is corresponding to the previously obtained data. The usage of SNSPD opens measurement in the near infra-red range. The properties of the SNSPD in NIR are well known to public. Potentially this approach could be used for detecting singlet oxygen luminescence, its luminescence photons at 1270 nm. [4] Also this is complicated by the very low quantum yield in different solutions.

REFERENCES

1. **Moshkova, M., Morozov, P., Divochiy, A., Vakhtomin, Y., & Smirnov, K.** (2019, December). Large active area superconducting single photon detector. In Journal of Physics: Conference Series (Vol. 1410, No. 1, p. 012139). IOP Publishing.

2. Becker&Hickl. URL: https://www.becker-hickl.com/

3. **Yakovleva, M. A., Radchenko, A. S., Feldman, T. B., Kostyukov, A. A., Arbukhanova, P. M., Borzenok, S. A., ... & Ostrovsky, M. A. (2020).** Fluorescence characteristics of lipofuscin fluorophores from human retinal pigment epithelium. Photochemical & Photobiological Sciences, 19, 920-930.

4. **Krasnovsky Jr, A. A.** (1998). Singlet molecular oxygen in photobiochemical systems: IR phosphorescence studies. Membrane & cell biology, 12(5), 665-690.

Millifluidic polyol synthesis of Ag nanowires and microplotter printing of transparent conductive films

P.V. Arsenov [1]✉, D.D. Kazarinova [1], I.S. Vlasov [1], M.A. Popov [1], I.A. Volkov [1]

[1] Moscow Institute of Physics and Technology (National Research University), 141701 Dolgoprudny, Moscow Region, Russia;

✉ arsenov@phystech.edu

Abstract. A millifluidic polyol process was used to produce silver nanowires (AgNWs) for their application in patterning of transparent conductive electrodes by microplotter printing. Obtained dependences of transmission spectra and sheet resistance are in good agreement with the theory. Transparent conductive electrodes with a high transparency of more than 80 % were obtained at a wavelength of 550 nm with a sheet resistance of 52-229 ohms/sq. So the method of synthesis of AgNWs and application of microplotter printing are suitable for creating transparent conductive electrodes in optoelectronic devices.

Keywords: polyol synthesis, silver nanowires, microplotter printing, transparent conductive electrodes.

Funding: This research was funded by the Russian Science Foundation grant No. 23-79-10081.

Introduction

Transparent conductive electrodes (TCE) are widely used in electronics, for example, as parts of touch screens, solar panel elements and optoelectronic devices. Films based on metal oxides, such as ITO, are most actively used. However, they cannot be used in the case of flexible or curved substrates due to the fragility and low resistance to bending. Their disadvantages also include a high refractive index and the high cost of large-area metal oxide films fabrication. For this reason, TCEs based on carbon nanotubes, graphene and metal nanowires become increasingly common. One of the key tasks is to obtain TCEs based on extended nanoobjects with a sheet resistance value of less than 100 Ohm/sq. with transparency of at least 80% at a wavelength of 550 nm [1-4]. Silver nanowires (AgNWs) are the most suitable in terms of optoelectronic characteristics [2,3]. This work is devoted to the study of TCEs based on AgNWs deposited by microplotter printing.

Materials and Methods

In this work AgNWs were synthesized by the polyol method. The schematic chart of the synthesis used is demonstrated at Figure 1.

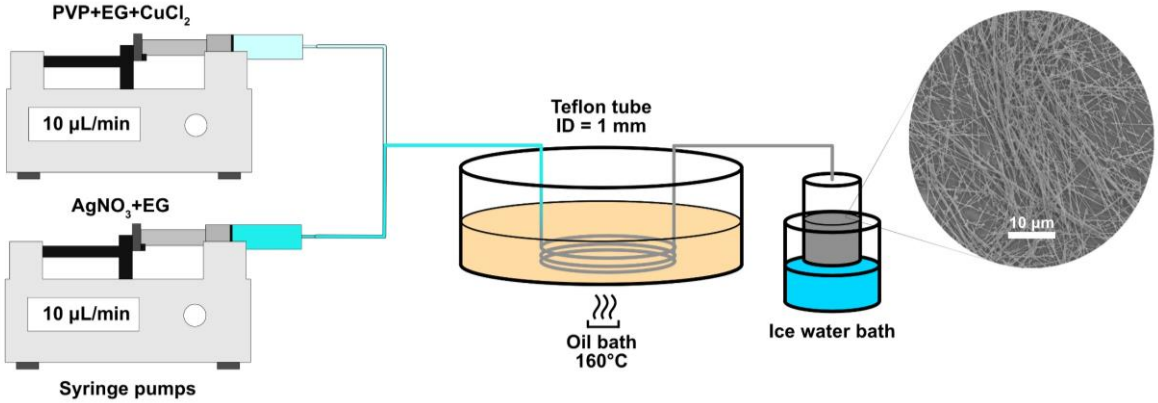


Fig. 1. Schematic illustration of AgNW process synthesis.

Reagent solutions of $CuCl_2$, polyvinylpyrrolidone (PVP), and $AgNO_3$ were prepared in ethylene glycol (EG). In synthesis, 40 µL of $CuCl_2$ was added to each PVP and $AgNO_3$ solution with concentrations in EG of 20 mg/ml and 10 mg/ml, respectively. Then, 5 mL $AgNO_3$ solution and 5 mL PVP solution were injected into oil bath using a syringe pumps through a 1.0 mm I.D

Teflon tube at 10 μL/min. The tube was coiled and place inside an oil bath at a temperature of 160°C. Time of the reaction was determined by the flows speed.

Ag nanowires based films were fabricated on quartz glass substrates with the use of SonoPlot GIX Microplotter II (SonoPlot, Middleton, USA). Ag NWs based inks were loaded into glass capillary with a tip inner diameter of about 340 μm, which was used for films deposition. Ag NWs based films with the size of 12x12 mm and various number of layers were printed by moving the dispenser at a speed of 10 mm/s. After printing, all the films were dried at a temperature of 100 °C for 1 hour in an air atmosphere.

Results and Discussion

The sheet resistance of films was measured using digital multimeter APPA 505 (MGL APPA Corporation, Taipei, Taiwan). The transmission specrta in the range of 400 – 2500 nm was measured using spectrophotometer Jasco V-770 (Jasco, Easton, USA). Figure 2 demonstrates transmission spectra of the films (Figure 2a) and fitted dependences of the film transmittance on the sheet resistance (Figure 2b).

a) *b*)

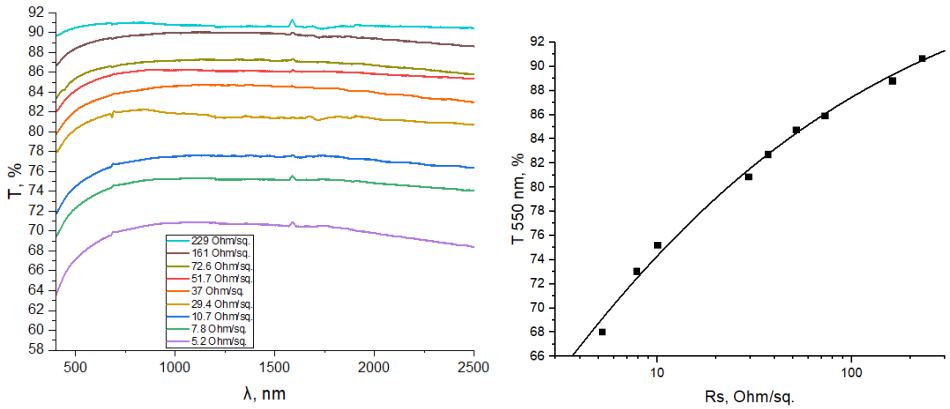


Fig. 2. (*a*) Transmission spectra of dried printed films based on synthesized Ag nanowires (*b*) Transmittance versus sheet resistance for printed films based on silver nanowires at a wavelength of 550 nm.

Conclusion

Obtained dependences are in good agreement with the theory known from the literature [5]. In addition, films with a high transparency of more than 80 % were obtained at a wavelength of 550 nm with a sheet resistance of 52-229 ohms/sq. These microplotter printed films are suitable for creating transparent conductive electrodes in optoelectronic devices.

Acknowledgments

This research was funded by the Russian Science Foundation grant No. 23-79-10081.

REFERENCES

1. **Scardaci V., Coull, R. Lyons, P. E. Rickard D., Coleman J. N.**, Spray deposition of highly transparent, low-resistance networks of silver nanowires over large areas, Small, 7(18) (2011), 2621–2628.

2. **Lee J. Y., Connor S. T., Cui Y., Peumans P.**, Solution-processed metal nanowire mesh transparent electrodes. Nano letters, 8(2) (2008), 689–692.

3. **Madaria A. R., Kumar A., Zhou C.**, Large scale, highly conductive and patterned transparent films of silver nanowires on arbitrary substrates and their application in touch screens. Nanotechnology, 22(24) (2011), 245201.

4. **Wu H., Hu L., Rowell M. W., Kong D., Cha J. J., McDonough J. R., Zhu J., Yang Y., McGehee M. D., Cui Y.**, Electrospun metal nanofiber webs as high-performance transparent electrode. Nano letters, 10(10) (2010), 4242–4248.

5. **De S., Coleman J. N.**, The effects of percolation in nanostructured transparent conductors. Mrs Bulletin, 36(10) (2011), 774-781.

Relative intensity noise of 89X nm-range single-mode vertical-cavity surface-emitting lasers

M. A. Bobrov[1]✉, **S. A. Blokhin**[1], **Ya. N. Kovach**[1], **A. A. Blokhin**[1], **N.A. Maleev**[1], **A. G. Kuzmenkov**[1], **A. S. Pazgalev**[1], **A. P. Vasil'ev**[2], **V. M. Ustinov**[2]

[1] Ioffe Institute, Saint Petersburg, Russia

[2] SHM R&E Center RAS, Saint Petersburg, Russia

✉bobrov.mikh@gmail.com

Abstract.

The relative intensity noise of single-mode polarization-stable vertical-cavity surface-emitting lasers emitting in the 89X nm range is studied. Different behavior of the relative intensity noise as a function of the laser current (output optical power) depended on the detection frequency.

Keywords: vertical-cavity surface-emitting laser, single-mode, relative intensity noise

Funding: Research was supported in part by the Ministry of Science and Higher Education of the Russian Federation (project reference number FFUG-2022-0011).

Introduction

The research into compact atomic sensors based on alkali atomic vapour has intensified for the last decade; in particular, a lot of attention has been given to quantum magnetometers with optical pumping and atomic clock working on coherent population trapping (CPT) [1]. Lasers used in such sensors must meet a number of requirements, and vertical-cavity surface-emitting lasers (VCSELs) with emission in the spectral range 79X nm (for Rb-based cells) and 89X nm (for Cs-based cells) [2] have proven to be the most suitable and promising for this purpose. Today, much effort is focused on providing single-mode lasing with stable polarization; however, the noise of lasers is also important. VCSEL output optical power fluctuation could lead to the light-shift (AC Stark-shift) of the alkali atomic energy levels and deterioration of the signal-to-noise ratio, which is the limiting factor for the long-term frequency stability of the atomic clock or the maximum variation sensitivity of the quantum magnetometers.

In this paper, the results of studying the relative intensity noise (RIN) for 89X nm-range intracavity-contacted VCSELs operating in single-mode regime with stable linear polarization are presented.

Materials and Methods

The VCSEL design is hybrid vertical microcavity formed by semiconductor and dielectric distributed Bragg reflectors (DBRs). The injection of the charge carriers into the active region based on InGaAs quantum wells was realized through the intracavity contacts and low-Q composite DBR. An AlAs/AlGaAs aperture layer was implemented to form a diamond-shaped current aperture using a water-vapour selective oxidation method.. A detailed description and the fabrication issue of the VCSELs are presented in [3].

Results and Discussion

All results were obtained at room temperature to avoid the negative influence of temperature fluctuations on the noise characteristics of the unpackaged lasers. The VCSELs with a 2 μm current aperture demonstrated lasing with a threshold current less than 0.5 mA and a differential efficiency greater than 0.6 W/A (Fig. 1., *a*). The laser self-heating effect appeared at operating currents more than 1.5 mA, which corresponds to an output optical power greater than 0.7 mW. The polarization study revealed that VCSEL emission is linearly polarized along the [110] crystallographic direction without the presence of any polarization hopping or switching in the whole range of operating currents, due to the asymmetric field of mechanical stresses formed near the active region by the diamond-shaped oxide aperture [4]. Measured orthogonal polarization suppression ratio (OPSR) exceeds 20 dB. The lasing spectra are dominated by the fundamental mode (single-mode lasing), and no evidence of spectral splitting between two orthogonally polarized modes is observed. The side-mode suppression ratio was more than 30 dB in the whole range of operating currents.

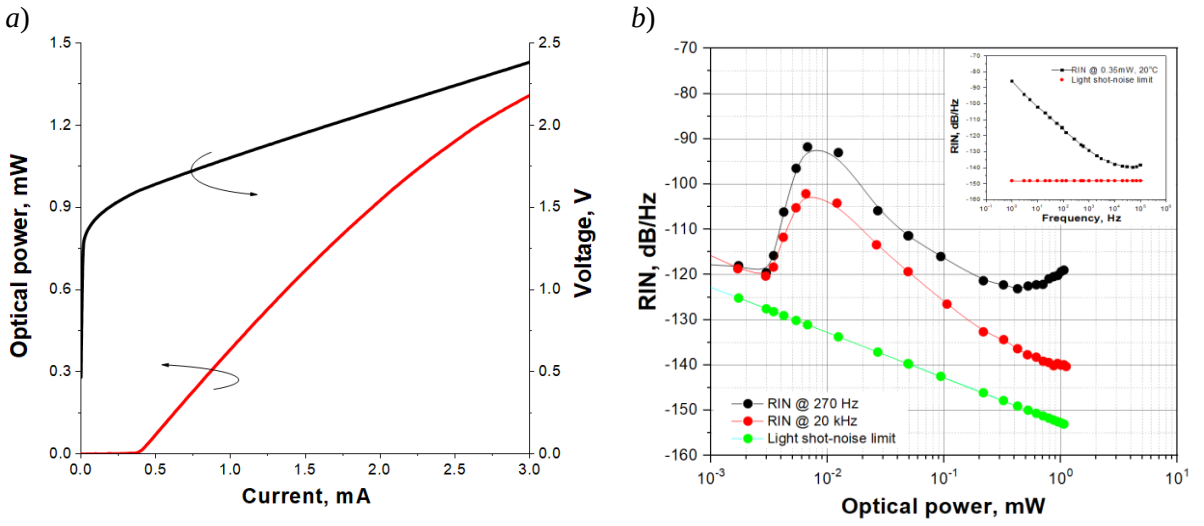


Fig. 1. Light-current-voltage characteristics (a) and RIN as a function of output optical power in free-running regime (b) for 89x nm-range VCSEL measured at 20°C.

Analysis of the frequency dependencies of the RIN showed that there is a characteristic behavior of 1/f noise at low frequencies with its transition to white noise at frequencies above 10 kHz (inset Fig. 1., *b*), which is similar to works [5-6]. However, the RIN dependance on the output optical power (operating current) additionally affected by the detection frequency. In the spontaneous emission mode, the increase of the output optical power leads to the sharp rise in the RIN (near the lasing threshold). Next, with the beginning of the lasing generation, the situation is opposite: at frequencies higher than 10 kHz, there is a pronounced inversely proportional noise reduction with saturation at -140 dB/Hz, whereas at lower frequencies, the U-shaped behavior is revealed. The observed U-shaped behavior could be connected with the laser polarization stability [7]. As a result, with the increase of output optical power, the RIN first decreases, as presented in the work [6], but with the output optical power more than 0.5 mW, the rise of the low-frequency RIN is observed.

Conclusion

In this work, we analyzed the RIN of 89X nm-range single-mode VCSELs. The low-frequency RIN has 1/f behavior up to 10 kHz, whereas white noise starts to prevail at higher frequency. In the range of 10-100 kHz at the output optical power of more than 0.1 mW, the RIN does not exceed -125 dB/Hz.

REFERENCES

1. J. Kitching, Chip-scale atomic devices, Applied Physics Reviews. 5(3) (2018) 031302.
2. Padullaparthi B.D., Tatum J.A., Iga K. VCSEL industry: communication and sensing.
3. Blokhin S.A. et al. Vertical-cavity surface-emitting lasers for compact atomic sensors // St. Petersburg Polytechnic University Journal. Physics and Mathematics. 16 (3.2) (2023) 16-22.
4. M.A. Bobrov et al. Polarization characteristics of 850-nm vertical-cavity surface-emitting lasers with intracavity contacts and a rhomboidal oxide current aperture // Semiconductors. 50 (10) (2016) 1390-1395.
5. Gruet F. et al. Metrological characterization of custom-designed 8946 nm VCSELs for miniature atomic clocks // Optics Express. 21 (5) (2013) 5781-5792.
6. Kroemer E. et al. Characterization of commercially available vertical-cavity surface-emitting lasers tuned on Cs D1 line at 8946 nm for miniature atomic clocks // Applied Optics. 55 (31) (2016) 8839-8847.
7. Zappe H.P. et al. High-spectral-purity VCSELs for spectroscopy and sensors // Proceedings of SPIE. 3945 (2000) 106-116.

Influence of optical feedback on a signal of a semiconductor laser

M. V. Boltanskii[1✉], **E. I. Maksimova**[1], **R. A. Shakhovoy**[1,2]
[1]QRate, Moscow, Russia
[2]Moscow Technical University of Communications and Informatics, Moscow, Russia
✉m.boltanskiy@goqrate.com

Abstract. Gain-switched semiconductor lasers can produce pulses with naturally randomized phase, which makes them a convenient light source for quantum key distribution and random number generation. Nevertheless, semiconductor lasers are vulnerable to external optical feedback, a phenomenon, characterized by injection of a certain part of laser radiation into the laser's diode cavity. Although optical feedback may be used to decrease relaxation oscillations and chirp, it may have negative effect on laser pulses. Here, we study the influence of optical feedback on the pulse shape of a gain-switched laser.

Keywords: Gain-switched laser, optical feedback, laser pulse interference.

Funding: Disclose all sources of funding of the study, providing project titles and/or grant numbers if available (e.g.: This study was funded by [name of funder] grant number [xxx]).

Introduction

External optical feedback is known to have positive effect on laser radiation. It can reduce frequency chirp [1] and suppress relaxation oscillations of laser pulses [2]. However, optical feedback often causes certain unwanted effects, e.g. chaos [3], and it has especially strong influence on lasers, operating in the continuous mode. To prevent unwanted feedback, laser modules are often equipped with an optical isolator. In this work, we studied the influence of optical feedback on gain-switched distributed feedback (DFB) laser in the absence of optical isolation.

Materials and Methods

The fiber-optic experimental scheme used to demonstrate the effect of optical feedback on a laser signal is shown in figure 1. It consisted of a 1550 nm DFB laser diode, a ring mirror (a looped beam splitter) and a Mach-Zehnder interferometer. The mirror was equipped with an optical variable delay line (VDL), and the interferometer was equipped with an optical isolator to eliminate unwanted reflections. We also used a polarization controller to compensate polarization distortions and a bandpass filter to cut a part of the laser spectrum associated with chirp.

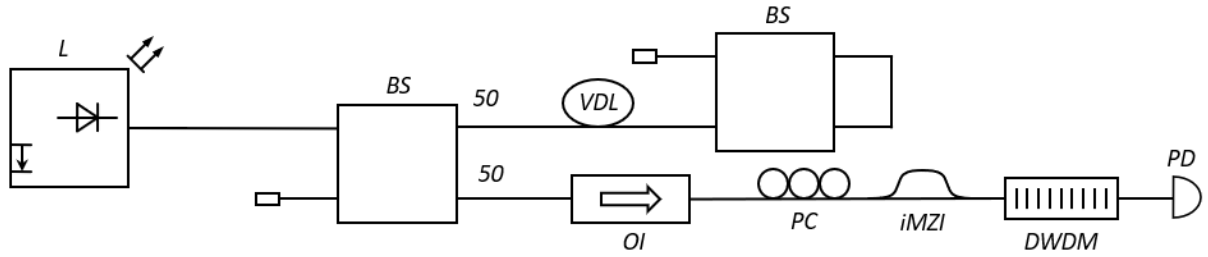


Fig. 1. The experimental scheme. L – laser module, BS – beam splitter, OI – optical isolator, VDL variable optical delay line, PC – polarization controller, iMZI – Mach-Zehnder interferometer, DWDM – bandpass filter, PD – photo detector.

Results and Discussion

Figure 2 shows the waveforms of laser pulses at different VDL parameters. Each picture is indicated with a delay value in picoseconds.

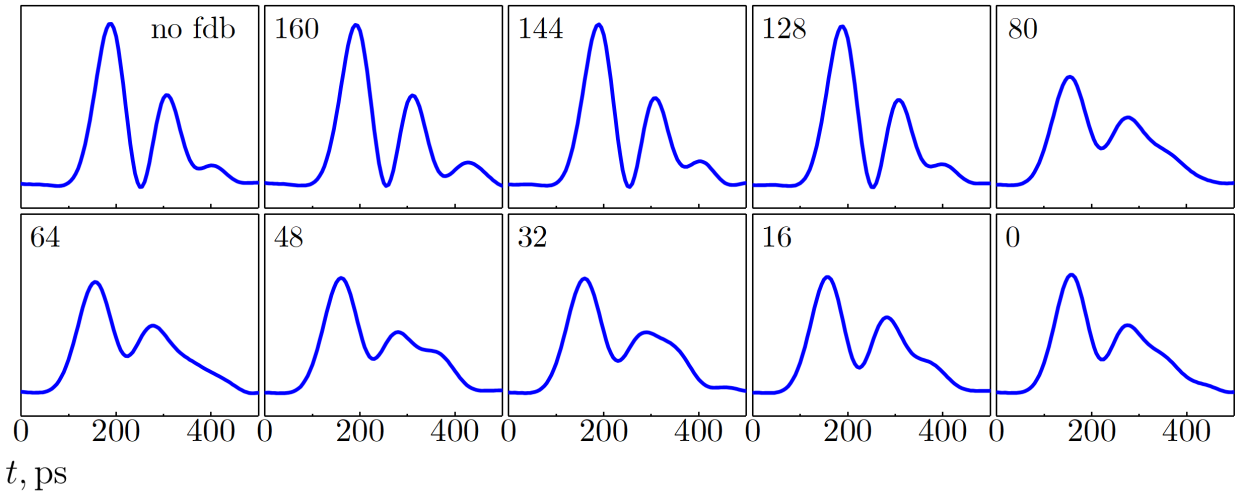


Fig. 2. Laser pulse shapes with different optical feedback parameters.

As delay line decreases, pulse oscillations are suppressed, which is associated with influence of optical feedback, which reaches its higher limits at (80-48 ps) delay line (DL) values. We have also conducted simulations of laser pulse generation, the results of which will be demonstrated at conference proceedings.

Conclusion

We performed an experiment to study the influence of optical feedback on a signal of a gain-switched laser. It was shown that laser radiation reflected into the diode cavity may significantly change the pulse waveform.

Acknowledgments

We appreciate Maxim Fadeev for the support in the experiment conduction.

REFERENCES

1. **Roy Lang & Kohroh Kobayashi,** Suppression of the Relaxation Oscillation in the Modulated Output of Semiconductor Lasers, IEEE Journal of quantum electronics, vol. QE-12, No. 3, 1976.
2. **Grillot, Frédéric & Provost, Jean-Guy & Kechaou, Kk & Thedrez, Bruno & Erasme**, Frequency Chirp Stabilization in Semiconductor Distributed Feedback Lasers with External Control. Proceedings of SPIE - The International Society for Optical Engineering. 8255. 3-. 10.1117/12.906470, 2012.
3. **B. Al Bayati, A. Ahmad & K. Al Naimee**, Influence of optical feedback strength and semiconductor laser coherence on chaos communications, J. Opt. Soc. Am. B 35, 918-925, 2018.

Gallium phosphide/black silicon heterojunction solar cells

E. A. Vyacheslavova ✉, **A. V. Uvarov**, **A. A. Maksimova**, **A. I. Baranov**, **A. S. Gudovskikh**
Saint Petersburg Academic University, St. Petersburg, Russia, 194021
✉cate.viacheslavova@yandex.ru

Abstract. A new type of heterojunction solar cell based on GaP/*b*-Si was proposed. The nanostructured surface of *b*-Si was obtained by cryogenic etching in an SF_6 and O_2 as process gases. The average height of the *b*-Si structures varies from 1.4 to 2.1 μm. The heterojunction was fabricated via low temperature method such as plasma-enhances atomic-layer deposition (PEALD). The thicknesses of the deposited GaP layer are fixed to be 30 nm. This thin GaP layer allowed achieving a *FF* of 54.5% without transparent conductive oxide and with a test grid. The use of GaP layer as an emitter a broadening of the *EQE* spectrum boundary in the short-wavelength region.

Keywords: black silicon, cryogenic etching, gallium phosphide, PEALD, heterojunction solar cell.

Funding: This study was supported by the Russian Science Foundation Grant No. 23-29-00735.

Introduction

The technology of a solar cell production based on the amorphous/crystalline (*a*-Si:H/*c*-Si) heterojunction is the main concept for a highly efficient silicon solar cell. However, these heterojunction devices are limited by non-ideal optical and electronic properties.

One of the effective methods of reducing optical reflectance in solar cells can be considered the use of a nanostructured black silicon (*b*-Si). The *b*-Si has excellent optical properties in both a wide wavelengths range and incidence angles [1]. Gallium phosphide (GaP) can be a promising candidate material for the emitter layer of heterojunction cell. GaP has an indirect bandgap energy (2.27 eV) and a low lattice mismatch with Si, that provides to low parasitic absorption [2, 3]. Due to these properties, a conception based on GaP/*b*-Si heterojunction are an extremely promising solution for photovoltaic application.

Experimental section

We used cryogenic etching (-150 °C) in an SF_6/O_2 gas mixture to obtain *b*-Si structures. Etching was carried out using p-type (1-20 Ω•cm) B-doped monocrystalline silicon (100). The samples were cleaned using the Shiraki technology after the etching [4]. To form GaP layers on the nanostructured *b*-Si surface, the PEALD method was used at a temperature of 380 °C [5]. The trimethylgallium (TMG) metallic compound and phosphine (PH_3) gas were used as sources of Ga and P atoms. The GaP layer was *n*-doped by silicon (SiH_4/H_2 gas mixture). An aluminum layer was deposited on the backside of the samples to obtain ohmic contact. Then, samples were annealed at various temperatures (600-700 °C) for 1 minute in an RTA. After that, a front contact in the form of a silver grid (1x1 cm) was formed.

The *b*-Si morphology was examined by SEM. The total reflectance spectra were detected using a spectrometer and an integrating sphere. The electrical performances of GaP/*b*-Si solar cells were characterized using illuminated current-voltage at AM1.5G. These measurements were carried out using an aperture (area = 16 mm^2).

Results and Discussion

The etched silicon wafers consist of high density of *b*-Si structures. The average height *b*-Si varies from 1.4 to 2.1 μm. According to the TEM the GaP leyer thickness was fixed to be 30 nm. The Raman spectra showed signals at 365 cm^{-1} and 402 cm^{-1} corresponding to the TO and LO optical modes of crystalline GaP. The elemental mapping analysis indicated the uniform distribution of components (Ga and P) over the entire *b*-Si surface.

Photovoltaic parameters such as V_{OC}, J_{SC}, *FF* and efficiency were calculated from illuminated *I–V* characteristics. The *J–V* curves of the solar cells based on *b*-Si are shown in Figure 1 (*a*). The GaP/*b*-Si heterojunction cell show a good performance achieving V_{OC} of 473 mV, J_{SC} of 34.7 mA/cm^2 and *FF* of 54.5% without transparent conductive oxide and with an Ag grid pitch of 2 mm. A power conversion efficiency of 9% was received.

Figure 1 (*b*) shows the total reflectance spectrum of GaP coated black silicon. It can be seen that sample has total reflectance below 5% up to 1050 nm. The external quantum efficiency (*EQE*) was measured and is demonstrated in Figure 1 (*b*). The maximum *EQE* value is 81.5%. We can observe in the short-wavelength region a significant advantage of the GaP over *a*-Si:H on the *EQE* (see our previously published article [6]).

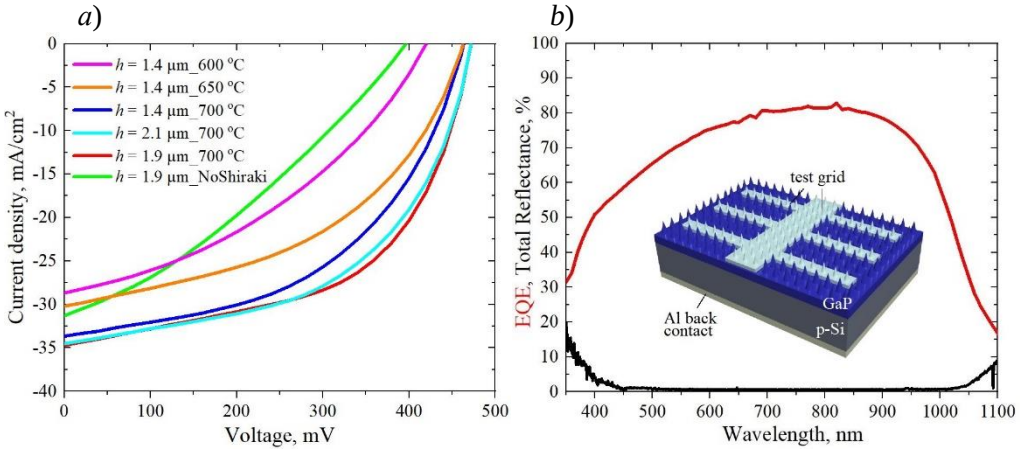


Fig. 1. *J–V* characteristics (*a*) and *EQE* spectrum (*b*) of the solar cells based on GaP/*b*-Si

Conclusion

We have successfully fabricated the GaP/*b*-Si heterojunction solar cells. The deposition of GaP layers on *b*-Si was carried out by the low temperature PEALD method. A solar cell efficiency of 9% was demonstrated. The *EQE* value is improving in the short-wavelength region through the lower light absorption of GaP layer.

Acknowledgments

This study was supported by the Russian Science Foundation Grant No. 23-29-00735.

REFERENCES

1. **Srivastava S.K., Kumar D., Singh P.K., et. al.**, Excellent antireflection properties of vertical silicon nanowire arrays Solar Energy Materials and Solar Cells, 94 (2010) 1506–1511.

2. **Li T., Mastro M., Dadgar A.**, III-V Compound Semiconductors: Integration with Silicon-Based Microelectronics (CRC Press) (2010) 603.

3. **R. Corkish.**, Some candidate materials for lattice-matched liquid-phase epitaxial growth on silicon, Sol. Cells 31 (1991) 537-548.

4. **Ishizaka A., Shiraki Y.**, Low Temperature Surface Cleaning of Silicon and Its Application to Silicon MBE, Electrochem. Soc. 133 (1986) 666.

5. **Uvarov A. V., Gudovskikh A. S., Baranov A. I., Vyacheslavova E. A., et. al.**, Conformal growth of GaP on high aspect ratio Si structured surface via plasma-enhanced atomic layer deposition, Surface and Coatings Technology 477 (2024) 130357.

6. **Vyacheslavova E.A., Uvarov A.V., Maksimova A.A., et. al.**, Heterojunction solar cells based on nanostructured black silicon, St. Petersburg Polytechnic University Journal. Physics and Mathematics 16 (3.1) (2023) 434-438.

Lateral mod modification of Fabry-Perot semiconductor laser by focused ion beam

I.N. Grigorenko [1,2✉], **G.V. Voznyuk** [1], **M.I. Mitrofanov** [1], **V.A. Kryuchkov** [1], **I.V. Shushkanov** [1], **A.A. Podoskin** [1], **S.I. Pavlov** [1], **A.F. Tsatsulnikov** [3], **V.P. Evtikhiev** [1]

[1] Ioffe Institute, St Petersburg, Russia;

[2] ITMO University, St Petersburg, Russia;

[3] Submicron Heterostructures for Microelectronics, Research & Engineering Center, RAS, St Petersburg, Russia;

✉ilyagrigorenko@mail.ru

Abstract. We demonstrate the possibility of lateral mode modification via irradiation the Fabry-Perot semiconductor laser front mirror by focused ion beam (FIB). It was found that local irradiation of the laser front mirror in the region of maximum intensity of lateral modes leads to suppression of their generation. The threshold current density and differential laser efficiency remain virtually unchanged after FIB treatment. The proposed approach makes it possible to form a particular lateral mode composition in ready-made laser diodes with ridge waveguide.

Keywords: focused ion beam, radiation defect, semiconductor laser, lateral mode

Introduction

Semiconductor injection lasers are widely used due to their reliability, compact size and high-energy efficiency. One of the main tasks facing developers of such lasers is increasing the emitted power. For injection lasers with ridge waveguide to increase the optical power a waveguide expansion in lateral direction is needed, however this leads to the appearance of new high-order modes. To suppress multimode lasing, many different designs have been developed - external resonators, output mirrors with a given reflection coefficient profile [1], diffraction gratings as part of the resonator [2], conical waveguides [3], introduction of additional internal losses via radiation defects in local area of the active region [4]. During ion-solid interaction a high-energy ion beams cause radiation defects formation [5]. The radiation defects act as centers of non-radiative recombination leads to quenching of luminescence. The propagation depth of radiation defects depends on the energy of the irradiating ions. It was shown in [6] that propagation depth of radiation defects in AlGaAs/GaAs double heterostructure after milling with 30 keV Ga+ ion beam is more than 900 nm.

Materials and Methods

Laser heterostructure with separate-confinement AlGaAs/GaAs with InGaAs quantum well active region was fabricated by MOCVD epitaxy and ridge waveguide semiconductor laser with 9 μm wide and 3 mm length cavity was manufacturing. An anti-reflection AlN layer with a thickness of 133 nm was deposited on the laser front mirror. The laser was mounted p-side down on copper heat sinks using indium solder. The laser generation wavelength is 1060 nm. Measurements of near-field patterns and light-current characteristics were carried out with pulsed laser power. The pulse duration was 100 μs and a frequency of 2.86 kHz. The near-field was recorded via an optical microscope with a magnification of ×96, and the optical power was recorded via a silicon photodetector.

Results and Discussion

Before FIB milling the laser, threshold current was 119 mA and the differential quantum efficiency was 61%. An inflection in the light-current characteristic (figure 1 (a)) was observed at 300 mA, which corresponded to appearance of additional maximum in the near-field (Figure 1 (b)). We produced local FIB milling in the area of the laser front mirror corresponding to this maximum. A rectangular area 1×0.5 μm^2 was milled by 30 keV Ga+ and 2 nA working current. The depth of the milled area studied by atomic force microscope (AFM) in semi-contact regime. AFM measurements showed that the depth of the milled region is 65 nm. Milling at such depth partially remove the AlN layer without touching the laser mirrors. In this way, radiation defects

will penetrate deep into the laser without breaking the protective function of the AlN layer. After milling the threshold current decreased to 112 mA and the differential quantum efficiency increased to 67%. There is no additional maximum observed in the near-field picture.

Thus, we have demonstrated a controllable change in the mode composition in the lateral direction of a semiconductor laser by FIB without significantly changing its characteristics.

a) *b*)

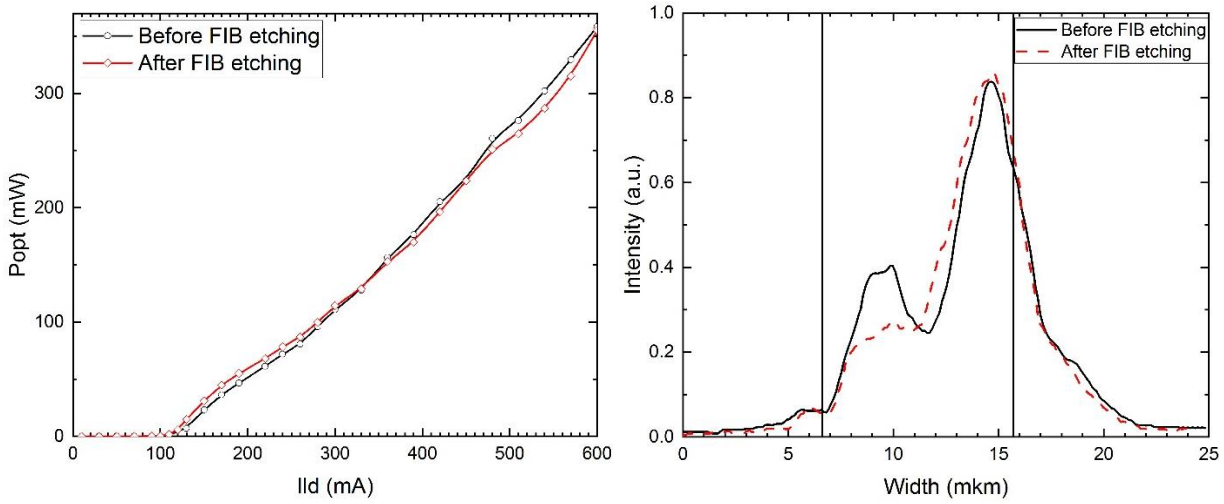


Fig. 1. Light-current characteristics before and after FIB etching (a), near field cross section before and after FIB etching at 500 mA current (b).

Conclusion

We demonstrated the possibility of a controllable change in the lateral mode composition by suppression of unwanted maximum in near-field emission of ridge waveguide injection laser by precise focused ion beam milling. Our research reveals new application of focused ion beam lithography for fine correction of optical characteristics of ready-made semiconductor lasers.

REFERENCES

1. **Payusov A., Serin A., Mukhin I., Shernyakov Y., Zadiranov Y., Maximov M., Gordeev N.**, Lateral mode control in edge emitting lasers with modified mirrors, IOP Conf. Series: Journal of Physics: Conf. Series 917 (2017) 052035.

2. **Ghafouri-Shiraz H.,** Distributed Feedback Laser Diodes and Optical Tunable Filters, John Wiley and Sons Ltd. ISBN 0-470-85618-1 (2003).

3. **Ben-Michael R., Koren U., Muller B.I., Young G., Chien M., Raybon G.**, InP-based multiple quantum well lasers with an integrated tapered beam expander waveguide, IEEE Photonics Technology Letters Vol. 6, (12), (1994), 1412 – 1414.

4. **Musil C.R., Patterson B.D., Auderset H.**, Modification of semiconductor laser diodes by focused ion beam milling, Nuclear Instruments and Methods in Physics Research B 127/ 128 (1997) 428-432.

5. **Volkert C.A., Minor A.M.**, Focused Ion Beam Microscopy and Micromachining, MRS Bulletin Vol. 32, (5), (2007), 389–399.

6. **Voznyuk G.V., Grigorenko I.N., Lila A.S., Mitrofanov M.I., Nikolaev D.N., Evtikhiev V.P.**, On the effect of etching with a focused Ga+ ion beam in the energy range 12−30 keV on the luminescent properties of the Al0.18Ga0.82As/GaAs/Al0.18Ga0.82As heterostructure, Semiconductors, Vol. 56, No. 12, (2022) 894-897.

Optimization of Mid-Infrared Quantum Cascade Detectors

A. S. Dashkov [1,2✉], **N. A. Kostromin** [1,2,3], **D. A. Barykin** [1,2,3], **L. I. Goray** [1,2,4,5]

[1] Alferov University, Saint-Petersburg, Russian Federation;

[2] ETU "LETI", Saint-Petersburg, Russian Federation;

[3] SPbPU, Saint-Petersburg, Russian Federation;

[4] Institute for Analytical Instrumentation, Saint-Petersburg, Russian Federation;

[5] University associated with IA EAEC, Saint-Petersburg, Russian Federation

✉dashkov.alexander.om@gmail.com

(Please provide an institutional email address if available)

Abstract. In this work, the optimization of the design of the quantum cascade detectors with a genetic algorithm is considered. The results obtained demonstrate strong dependence on the parameters of the optimization algorithm and significant modification of the initial design. The analysis of the obtained designs also shows that additional regularization techniques are required to achieve better output characteristics of the device.

Keywords: quantum cascade detector, numerical optimizaition, genetic algorithm, mid-infrared spectral range.

Funding: The research was supported by the Russian Science Foundation grant No. 23-29-00216, https://rscf.ru/project/23-29-00216/.

Introduction

Quantum cascade detectors (QCD) is unipolar devices, which have a variety of applications in physics, chemistry and medicine. Since the mid-infrared region is filled with the distinctive absorption lines of different molecules, the development and adaption of existing designs of MIR QCDs provide even greater benefit for future studies [1]. However, the problem of the creation and adjustment of new QCD designs remains to be important and relevant scientific task [2]. In this work, we present the techniques to create new more robust MIR QCD devices. These techniques include numerical optimization methods, including genetic algorithm. Another challenge in creating high-efficiency QCDs is the design of efficient waveguides. Due to the fact that in quantum wells only the polarization oriented parallel to the growth axis can be absorbed, such structures as transmission gratings [1], metamaterials can be used as waveguides [4].

Materials and Numerical Modelling Methods

The research is mainly focused on the QCD designs based on AlGaAs/GaAs heterostructures. During the simulation process the Schrodinger-Poisson system of equations is solved numerically using modified shooting and single band kp-methods and effective mass approximation and envelope functions approximations. The optimization process is performed with genetic algorithm, via python geneticalgorithm package [3].

For clear calculation of waveguides modes critically important knowing data about complex refractive index and extinction coefficients. In the MIR range of electromagnetic frequencies, the Drude-Lorentz model is used to describe the complex dielectric permittivity. To calculate spectra, the refractive index and extinction coefficient (absorption index) are calculated by solving the Fresnel equation. To obtain the transmission and reflection spectra of the entire structure, the transfer matrix method through the entire QCD structure is used.

Results and Discussion

The result of the optimization process shows that stated problem can be efficiently solved with a number of limitations and simplifications. The main limitation is that the loss function or the target function has to be manually constructed. In this work, we considered the combination of the weighted transition energy and weighted scattering time from the upper level. The other important limitation is a necessity of using a rather extensive search strategy in genetic algorithm

approach: increasing initial population size N and mutation probability p (Fig 1c). One can also conclude that as a result of the optimization process the optical transition scheme[5] is significantly altered, which without proper assessment may lead to the worsening of the sensitivity and operating speed of detector (Fig 1a and 1b).

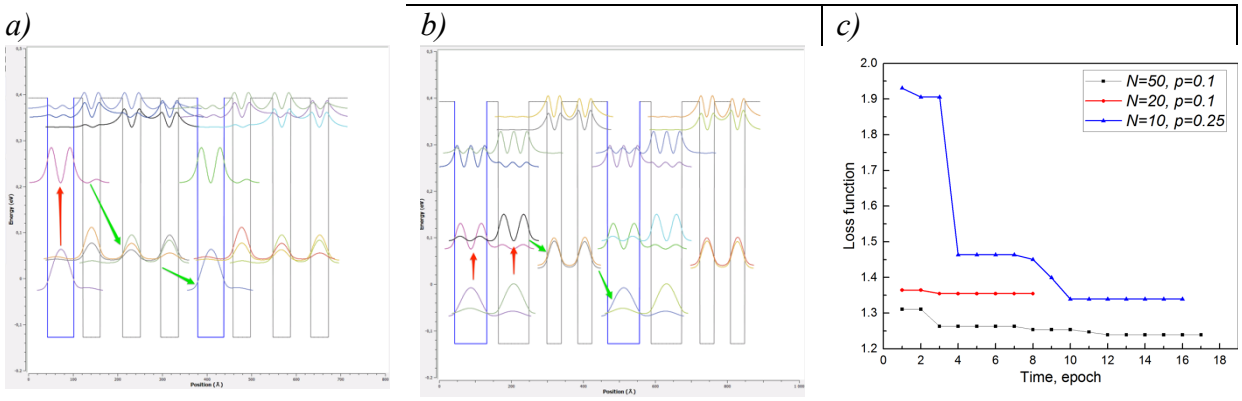


Fig 1. (a) The initial energy band diagram of QCD under study; (b) The energy band diagram of the optimized design (c) The evolution curve obtained during optimization via genetic algorithm.

Conclusion

The obtained results show the applicability of the numerical evolutionary algorithms for the creation of new constructions of quantum cascade detectors. However, these results also demonstrate the strong necessity of embedded regularization techniques for better results convergence and obtaining devices with advantageous output characteristics.

REFERENCES

1. **Delga A.,** Quantum cascade detectors: A review, Mid-infrared Optoelectronics. (2020) 337–377.

2. **Popp J., Haider M., Franckié M., Faist J., Jirauschek C.** Bayesian optimization of quantum cascade detectors, Optical and Quantum Electronics, 6 (53) (2021) 287.

3. Genetic Algorithm Package for Python. URL: https://github.com/rmsolgi/geneticalgorithm. Accessed Apr. 1, 2024.

4. Benz A., Krall M., Schwarz S., Dietze D., Detz H., Andrews A. M., Schrenk W., Strasser G. and Unterrainer K., Resonant metamaterial detectors based on THz quantum-cascade structures, Scientific Reports. (2014) 4269.

5. **Chen, Y., Zhu, Y., Guo, K., Zhai, S., Zhuo, N., Zhang, J., Liu, J.** Broadband quantum cascade detectors with a cutoff wavelength of 20 μm. Infrared Physics & Technology, 136 (2024) 105040.

Security of BB84-like protocol on coherent states with different intensities

E. A. Dedkov [1,2,3,4]✉, **R. A. Shakhovoy**[1,3]

[1] QRate, Novaya av. 100, Moscow, Russia;

[2] Russian Quantum Center, Bolshoy Boulevard 30, bld. 1, Skolkovo, Moscow 121205, Russia;

[3] NTI Center for Quantum Communications, National University of Science and Technology MISiS, Leninskiy prospect 4, Moscow 119049, Russia;

[4] Moscow Institute of Physics and Technology, 9 Institutskiy per., Dolgoprudniy 141701, Russia

✉dedkov.ea@phystech.edu

Abstract. There are a large variety of quantum key distribution (QKD) protocols, which can provide unconditional security. However, most of them require equal intensities of states emitted, which can be achieved only with some precision. Moreover, in some state preparation schemes, for example, in those based on optical injection, equal intensities can not be achieved without additional elements, which increase in cost and complexity of QKD setup. In this work we analyze the influence of different state intensities on achievable secret key rate in classical BB84 scheme.

Keywords: quantum key distribution, BB84, coherent pulses with random phases, decoy state.

Introduction

Discrete variable quantum key distribution (DV QKD) protocols allow two distant users, often referred to as Alice and Bob, distributing secret key. It is essential for such protocols to use single-photon states, however, one generally employs coherent states. Fortunately, with slight modification, DV QKD protocols based on attenuated laser pulses may be reduced to single-photon protocols. This reduction often relies on the implicit assumption, that the intensities of coherent states are the same for different bases and bit choices. In this work we perform a careful analysis of consequences, to which the violation of this assumption brings.

Materials and Methods

When establishing security proof for a QKD protocol based on the coherent states, the following framework is commonly used [1]. Alice prepares her coherent states on a Hilbert space of two photonic modes. Each state has some intensity $\mu_j = |\alpha_j|^2$, $j \in \{z0, z1, x0, x1\}$. It can be shown, that in case Alice each time produces α_j with random phase, the averaged states are Poisson mixture of n-photon states (here $j, \bar{j}$ denote some orthogonal Fock bases):

$$\rho_j = e^{-\mu_j} \sum_{n=0}^{\infty} \frac{\mu_j^n}{n!} |n\rangle_j \langle n| \otimes |0\rangle_{\bar{j}} \langle 0|.$$

The probability that Bob detects n-photon state of type j sent by Alice is called *yield*, and is denoted as Y_n^j, the fraction of n-photon states of type j, which produced the wrong click is called *error rate* and is denoted as e_n^j. It was shown in [1], that in case Alice may choose from a set of different intensities for each state type $\mu_j \in \{\mu_j^{(1)}, \mu_j^{(2)}, \ldots, \mu_j^{(m)}\}$ she can improve her protocol with the help of so-called decoy state technique, and estimate a good bounds on Y_1^j and e_1^j, which are the only quantities we need for key rate calculation.

If Alice is permitted to prepare each state type with only one intensity, i.e. the setup do not support decoy states, the estimation of single-photon yields and error rates are weaker, but still can be done if we replace all vacuum states to a single-photon ones, which, in fact, has no influence on security:

$$Y_1^j \geq Y_1^{j,L} = 1 - \frac{e^{\mu_j}}{1+\mu_j}\left(1 - Q_{\mu_j}\right),$$

$$e_1^j \leq e_1^{j,U} = \frac{E_{\mu_j} Q_{\mu_j}}{Y_1^{j,L} e^{-\mu_j}\left(1+\mu_j\right)}.$$

Usually, such estimations are done for different bases or for all sequence, i.e. the index j is omitted, which means that we implicitly assume $Y_n^i = Y_n^j$ with $i \neq j$. Note, however, that in case of different intensities we need to determine yields and error rates separately for each state type. Fortunately, this does not require revealing any additional information to Eve.

Another modification intensity difference introduce to the security proof is that the single-photon states carrying different bit value in each basis become distributed not equiprobably. If μ_{0z} and μ_{1z} are intensities of 0 and 1 bit in the Z-basis, and Alice prepares these states with conditional probabilities $p_{0|z}$ and $p_{1|z}$ respectively, then the actual probabilities of emitting single-photon state carrying each bit value will be

$$\tilde{p}_{0|z} = \frac{p_{0|z} e^{-\mu_{0z}} \mu_{0z}}{p_{0|z} e^{-\mu_{0z}} \mu_{0z} + p_{1|z} e^{-\mu_{1z}} \mu_{1z}},$$

$$\tilde{p}_{1|z} = \frac{p_{1|z} e^{-\mu_{1z}} \mu_{1z}}{p_{0|z} e^{-\mu_{0z}} \mu_{0z} + p_{1|z} e^{-\mu_{1z}} \mu_{1z}}.$$

In proofs based on quantum coin, like [2,3], one need to use these probabilities $\tilde{p}_{0|z}, \tilde{p}_{1|z}$ instead of $p_{0|z}$ and $p_{1|z}$. This introduce quantum coin imbalance Δ, which should be taken into account. Fortunately, we may eliminate it, if choose appropriate probability distribution for state preparation $p_{0|z}$ and $p_{1|z}$, namely if we want symmetric BB84 version and $\Delta=0$, we need to select $p_{0|z} = e^{-\mu_{1z}} \mu_{1z} / \left(e^{-\mu_{0z}} \mu_{0z} + e^{-\mu_{1z}} \mu_{1z}\right)$, $p_{1|z} = 1 - p_{0|z}$.

Results and Discussion

Using the security proof, presented here, we may characterize the influence of state intensities mismatch on the achievable secure key rate. We will stick to the case when the intensities of all states except the state $1x$ are equal: $\mu_{0z}=\mu_{1z}=\mu_{0x}=\xi^{-1}\mu_{1x}$. Fig. 1 represent the key rate per state sent dependent on transmission channel length for various scenarios (modelling parameters are listed in Table 1). It is worth noting that key rate for BB84 with same intensities almost follows the key rate with different intensities and balanced probabilities. Moreover, all of key rates for scenario without decoys are almost the same. This is the result of the usage of dark counts for key generation. Fig. 2 shows the dependence of the key rate for various fixed transmission probabilities on intensity mismatch parameter ξ.

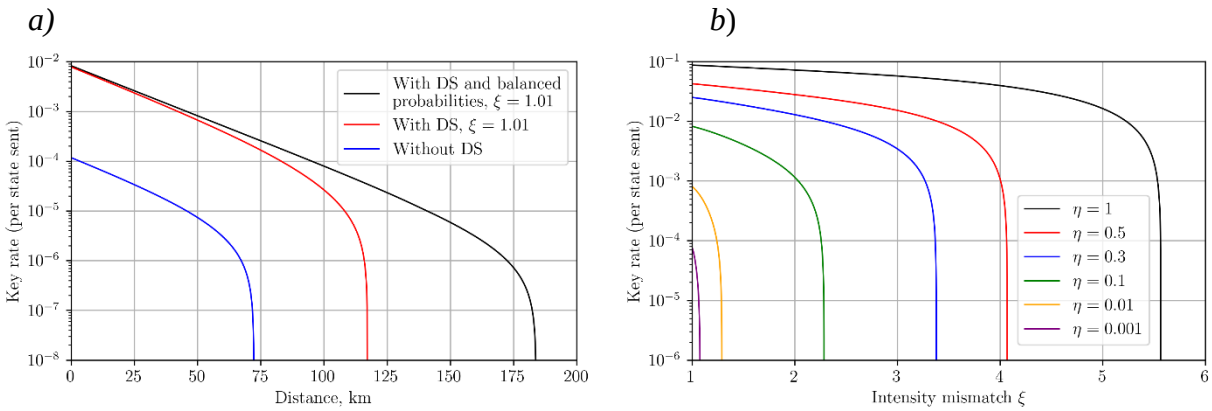


Fig 1. *a*) Plot of key rate per state sent vs channel length. *b*) Plot of key rate per state sent at different channel transmission parameters η (including detector efficiency and transparency) vs intensity mismatch parameter.

Fiber transparency	α=0.02 dB/km	Basic state intensity for decoy-state protocol	μ_{ds}=0.3
Detector efficiency	η=0.1	Basic state intensity for protocol without decoys	μ_{wods}=0.003
Dark count probability	$p_{dc}=10^{-6}$	Decoy state attenuation coefficient	λ_1=0.5, λ_2=0.1
Probability of wrong click	p_{err}=0.01	Error correction efficiency	f_{ec}=1.22

Table 1. Parameters for key rates estimation.

Conclusion

We have analyzed the modified version of BB84 protocol on coherent states with different intensities of signal pulses. Despite our analysis is largely simplified and there possibly can exist better key rate formulas, we have shown that it is possible to distribute secret key without any correction of intensity. Moreover, such a protocol can be brought back to ideal BB84 just with adjustment of bit values distribution, which may be done classically and requires no additional hardware changes.

REFERENCES

1. **Ma X., Qi B., Zhao Yi, Lo H.-K.**, Practical decoy state for quantum key distribution, Physical Review A. 72 (2005) 012326.

2. **Koashi M.**, Simple security proof of quantum key distribution based on complementarity, New Journal of Physics, 11 (2009) 045018.

3. **Gottesman D., Lo H.-K., Lütkenhaus N., Preskill J.**, Security of quantum key distribution with imperfect devices, Quantum Information & Computation. 4(5) (2004) 325-360.

Polarization extinction ratio conversion due to pointing system impact in satellite quantum key distribution

A. V. Duplinsky [1,3]✉, **A. V. Khmelev** [1,4,5], **R. M. Bakhshaliev** [1,3], **D. O. Sevryukov** [1,3], **K. A. Barbyshev** [1,2] **and V. L. Kurochkin** [1,2,5]

[1] QSpace Technologies, Moscow, Russia

[2] National University of Science and Technology MISiS, Moscow, Russia

[3] HSE University, Moscow, Russia

[4] Moscow Institute of Physics and Technology, Dolgoprudny, Russia

[5] Russian Quantum Center, Skolkovo, Russia

✉al.duplinsky@goqrate.com

Abstract. Quantum key distribution via satellites enables the technology to be applied at transcontinental sizes; nevertheless, in contrast to fiber systems, using a free-space optical communication channel presents certain extra technological obstacles. The contribution of the acquisition, pointing and tracking system's operation to the potential quantum bit error value is investigated in this research. The polarization extinction ratio measurements varying with the pointing mirror angular position are reported, based on these data, the upper limit of the quantum bit error is predicted for several types of satellite passages.

Keywords: quantum key distribution, polarimetry, extinction ratio, free-space optics.

Funding: This work was supported by the Ministry of Education and Science of the Russian Federation in the framework of the Program of Strategic Academic Leadership “Priority 2030” (Strategic Project “Quantum Internet”).

Introduction

Satellite quantum key distribution (QKD) channel requires acquisition, pointing and tracking system (APT) on both sides of the channel, most often it is a closed feedback loop consisting of a controlled fast mirror and a camera [1]. However, mirror angular inclinations during system operation cause polarization extinction ratio (PER) conversion, which negatively affecting the quantum bit error (QBER). In 2023, the Vector [2] payload was developed and successfully launched into orbit to demonstrate classical satellite laser communication, also to test technical solutions and service systems for the future satellite payload to perform QKD, including APT.

Methods and Results

To assess the expected APT impact, Vector payload optical prototype was used. Its APT active element is performed by an aluminum-coated MEMS mirror with 5 mm aperture diameter. The prototype’s optical signal was measured using a polarimeter for ± 2° both axis deflection angles with a step of 1°). Thus, the entire working area of the MEMS mirror was scanned and PER for these points were measured. The scanning results are presented in Fig. 1.

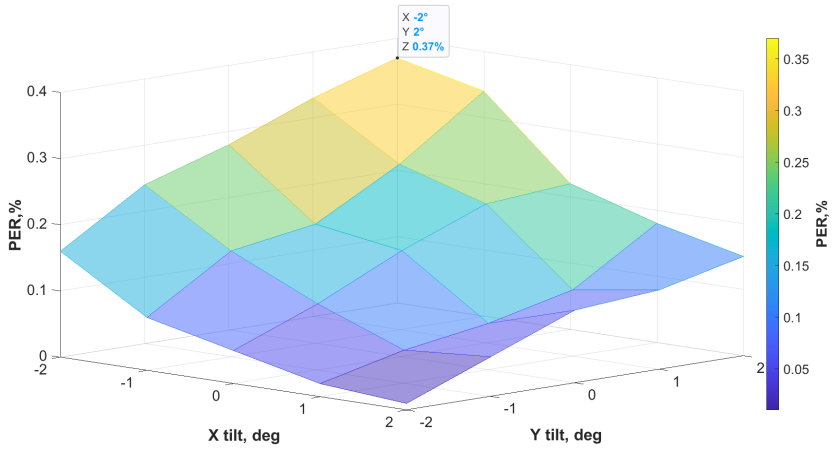


Fig. 1. Scaning results graph for different MEMS angles.

The lowest PER point angular coordinates are (-0.4°; 0.4°), and its value is 0.37 %. Using this PER as the upper bound of the transmitter error, we may estimate the potential QBER maximum value.

$$e_{\text{det}}^{\text{U}} = e_{\text{det}}^{\text{Rx}} + e^{\text{Tx,U}}, \tag{1}$$

where e^{Rx}_{det} is the intrinsic error of the receiver when the input beam is perfectly polarized, $e^{Tx,U}$ is the upper bound of the transmitter error.

Utilizing the previously published model [3], let's estimate the upper maximum of the predicted QBER during a quantum key distribution session for a prospective satellite using a similar APT optical architecture.

$$\text{QBER}(t) = \frac{e_0 Y_0 + e_{\text{det}}^{\text{U}}\left(1 - e^{-\mu\eta(t)}\right)}{Y_0 + 1 - e^{-\mu\eta(t)}}, \tag{2}$$

where μ is the intensity of signal states, e_0 is the error rate of the background, Y_0 is the background signal, η(t) is the link efficiency, e^{U}_{det} is the upper bound of an intrinsic error caused by measurement fidelity.

The predicted QBER function for 2 sessions with different satellite passage maximum elevation angles θ_{El}^{max} = 32.5° and θ_{El}^{max} = 90°, using μ = 0.8, e_0 = 0.5, $Y_0 = 5 \cdot 10^{-6}$ clicks are presented in Fig. 2. The elevation angle reaches its maximum during the passage at 0 (s) - point, which also happens to be the instant with the lowest QBER value. The largest QBER occurs at the edges, when the angle between satellite and the ground station is at its minimum and the distance is at its maximum.

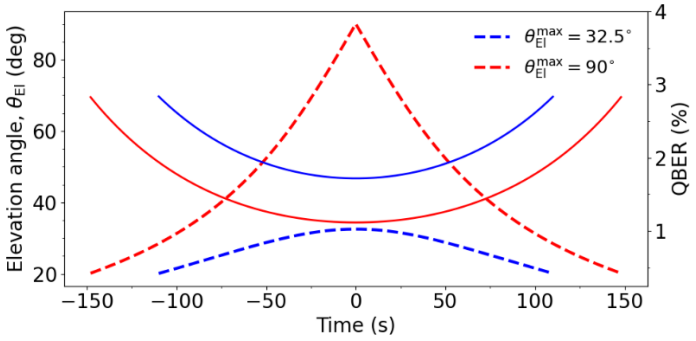


Fig. 2. QBER modeling results for two different passages.

Figure 2 shows that, during these QKD sessions, the QBER value remains under 3%; for any higher PER values, these lines will pass below.

Conclusion

Polarization extinction ratio scanning and quantum bit error rate modeling show the possibility of using such an APT technical solution in the payload design for satellite quantum key distribution realization.

REFERENCES

1. **Liao, S. K., Cai, W. Q., Liu, W. Y., Zhang, L., Li, Y., Ren, J. G., ... & Pan, J. W.,** Satellite-to-ground quantum key distribution, Nature. 549(7670) (2017) 43-47.

2. **Miller, A. V., Pismeniuk, L. V., ... & Bakhshaliev, R. M.,** Vector—towards quantum key distribution with small satellites. EPJ Quantum Technology. 10(1) (2023) 52.

3. **Khmelev, A. V., Ivchenko, E. I., ... & Kurochkin, Y. V.,** Semi-Empirical Satellite-to-ground quantum key distribution model for realistic receivers. Entropy. 25(4) (2023) 670.

Photovoltaic potential in the Subarctic region

Deng Yuanbiao[1, 2]✉, and V. V. Davydov[1, 3]

[1] Peter the Great Saint-Petersburg Polytechnic University, Saint Petersburg, Russia,

[2] Jiangsu Normal University, Xuzhou, China,

[3] The Bonch-Bruevich Saint Petersburg State University of Telecommunications, Saint Petersburg, Russia.

✉ dyuanbiao@gmail.com

Abstract. With the world's policy support for solar energy and other renewable energy sources, solar photovoltaic technology has seen rapid development.However, from Saint Petersburg's perspective, generating solar Photovoltaic (PV) energy in a Subarctic setting is hindered by several challenges, which diminish the enthusiasm for its adoption. Our work demonstrates that St. Petersburg is capable of generating more solar photovoltaic energy in summer than Central Europe, East Asia, and Southeast Asia. This finding could enhance our understanding of the seasonal and annual potential of solar PV energy in Subarctic region.

Keywords: Solar energy,climatic,Subarctic,photovoltaic potential.

Introduction

Solar energy, recognized as a clean and efficient source of energy, has witnessed significant growth globally over the past few decades. Much of the current research on the reliability of PV modules focuses on subtropical and temperate regions, characterized by short winter periods and high solar activity, whereas limited research has been undertaken in the Arctic and Subarctic regions. Factors such as uneven daylight duration and snow pack periods of more than three months, which are predefined characteristics of the Arctic and Subarctic regions, tend to reduce the solar PV potential of the region [1].

This study analyses the climate of the Subarctic region, utilizing St. Petersburg as an example. It also compares this region with others to demonstrate the potential for photovoltaic development in the Subarctic region .

Materials and Methods

St. Petersburg is located at 59°north latitude and 30°east longitude,South of the Arctic circle, stationed in the transitional zone between the Arctic and the Subarctic region.

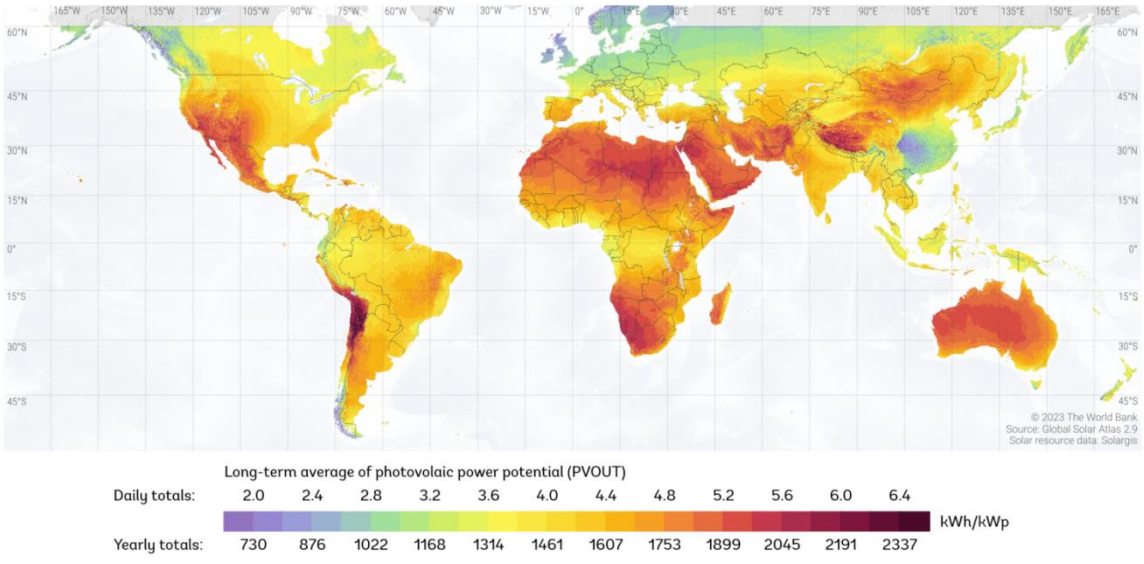


Fig. 1. Global photovoltaic power potential

Figure 1 presents a study on PV power potential as published by the World Bank [2]. The figure indicates that the solar potential of the Nordic and western Russian regions is comparable to that of Central Europe and marginally exceeds that of the Sichuan Basin region in China.

Investigations into the photovoltaic potential of the Subarctic region must consider the seasonal variations in solar radiation within this area. Summers in St. Petersburg, Moscow, and the Nordic region feature favourable temperatures, largely cloudless skies, and long hours of dayligh. In contrast,winter is marked by long periods of snow and abundant of clouds.

Results and Discussion

PVsyst is a widely used simulation software commonly used to evaluate solar PV yield and facilitate system optimization.To give a more visual representation of St Petersburg's photovoltaic potential in the summer, we compared it to nine cities: Hong Kong, Mumbai, Tokyo, Singapore, London, Miami, Bangkok, Seoul and Wuhan.The solar panels used for the simulation in the study were LG 450 N2W-E6 and the tilt angles were all set to the optimum tilt angle, considering only 3% soiling degradation.Figure 2 presents the simulation results, indicating that St. Petersburg has a higher PV potential in June, July and August than the other nine cities.

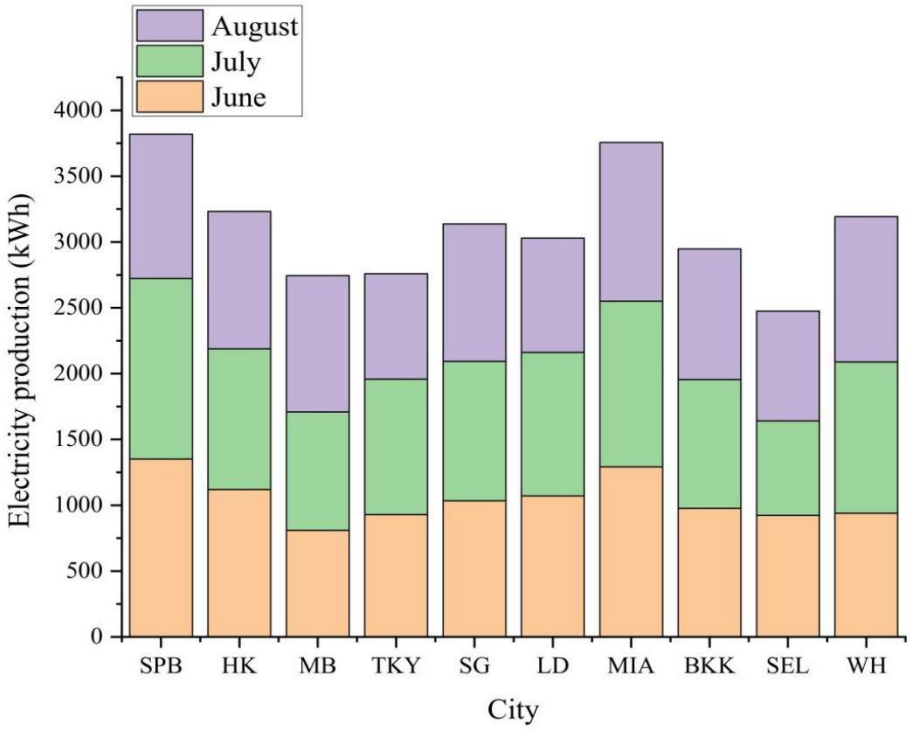


Fig. 2. Comparison of summer PV production in the cities considered in the study

Conclusion

With increasing emphasis on solar PV development globally, the Subarctic region has great potential for solar PV development. Considering the unique climate of the Subarctic region, generating more solar PV in the summer , and mitigating the negative impacts of winter weather extremes constitute the primary factors necessary for the development of solar energy in the region.

REFERENCES

1. **Vinay S., Antonio C., Eva P.,**Experiences from seasonal Arctic solar photovoltaics (PV) generation- An empirical data analysis from a research infrastructure in Northern Finland, Renewable Energy,Vol. 217,(2023)119162.

2. 2020 The World Bank, Source: Global Solar Atlas 2.0, Solar resource data: Solargis.

Heterostructure design features for 975 nm high-power laser diodes

E.V. Ershov [1]✉, A.V. Fomin [1], M.V. Lupachev [1], O.A. Rogachkov [1], A.A. Naidin [1]
[1] FSUE «RFNC – VNIITF named after Academ. E.I. Zababakhin, Snezhinsk, Russia
✉e-mail: Dep5@vniitf.ru

Abstract: The heterostructure design has been optimized to achieve high radiation output power and high conversion efficiency of 970-980 nm laser diodes. The influence of active layer geometry and waveguide layer doping on the output electrical and optical LD chip parameters has been studied. As a result of the optimization, operating LD output of 11.6 W has been achieved at a current of 12 A with the maximum conversion efficiency of 63 %.

Keywords: laser diode, laser cavity, heterostructure, quantum well.

Introduction

Laser diodes (LDs) based on InGaAs/AlGaAs/GaAs with radiation wavelength λ_{rad} = 975 nm are widely used for fiber laser pumping. Specific requirements to heterostructures (HS) design are imposed by high optical output and operation modes of such lasers. The ways to improve LD output are intensively investigated by domestic and foreign scientific communities [1-2] while heterostructure design is constantly refined. Thus, output power is increased by 1) optimizing quantum well (QW) parameters, and 2) doping profile of HS waveguide layers. Therefore, the research aimed at optimizing HS design with an extended waveguide is of high interest since it allows achieving high optical output and high conversion efficiency of 975 nm LD chips.

Materials and Methods

For the research, the InGaAs/GaAs/AlGaAs HS were grown by MOCVD. The HS design for samples 1-8 is presented in Table 1.

Table 1. Design and composition of HS layers

Layer	Composition
n-substrate	GaAs(001)
buffer	GaAs:Si
n-cladding	$Al_{1,75\cdot x}Ga_{(1,75\cdot x)-1}As$:Si
waveguide	$Al_xGa_{1-x}As$
active region	$In_yGa_{1-y}As$/(Al)GaAs
waveguide	$Al_xGa_{1-x}As$
p-cladding	$Al_{1,75\cdot x}Ga_{(1,75\cdot x)-1}As$:Zn
contact p-layer	GaAs:Zn

The samples 1-8 were used to manufacture LDs with a cavity length of 4 mm and an emitting stripe width of 100 μm using the developed planar technology. The LD chips end facets were anti-reflective and reflective coated. The LD chips were soldered p-side down on a heat-conducting submount with vacuum Au-Sn eutectic solder coating. Light-current and voltage-current LD chips were characterized using equipment for electrical and optical measurements in CW laser generation mode at the currents from 0 to 12 A.

Results and Discussion

At the first stage of the work, the effect of QW thickness, *d*, and QW number on the LD chip output power, P_{max}, was investigated. The dependencies of P_{max} on QW thickness and QW number are shown in Figure 1.

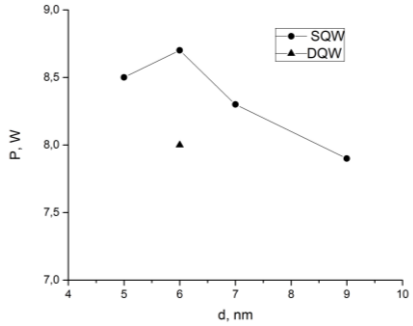
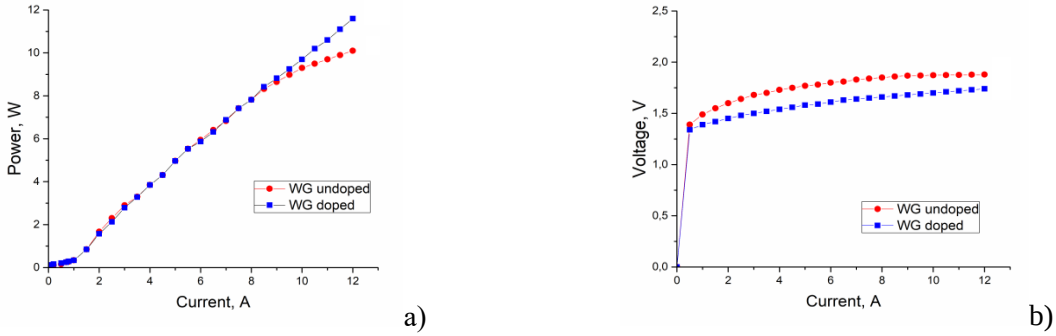


Figure 1. LD chip output power, P_{max}, vs. QW thickness, d, and QW number at a pumping current of 10 A

Figure 1 shows that P_{max} = 8.7 W was reached for the LD chips with QW thickness of 6.0 nm. P_{max} decreases with varying the QW thickness, also it decreases from 8.6 W down to 8.0 W with double quantum well as the active region (AR). This is due to the increase in the threshold current density, J_{th}, from 125 A/cm^2 up to 180 A/cm^2.

At the second stage, the effect of QW energy depth on the LD output characteristics was studied. For this, HS samples with varying Al molar fraction in $Al_xGa_{1-x}As$ barrier layers from 0% up to 20% were grown. According to the light-current measurements (Figure 2), P_{max} of 10.1W was achieved with the molar fraction Al = 10% at pump current 12 A with bias U=1.88V.

Additionally, the effect of HS waveguide layer doping on the LD light-current and voltage-current characteristics was investigated. For this, HS samples with $Al_{0.1}Ga_{0.9}As$ barrier layers was manufactured where waveguide layers adjacent to n-cladding and p-cladding were doped with Si and Zn, respectively. The waveguide region adjacent to the quantum well remained undoped to keep the optical loss below 1 cm^{-1}.



a) b)

Figure 2. Light-current and voltage-current LD chip characteristics manufactured from HS with doped and undoped waveguide layers

The light-current characteristics (Figure 2a) measured for the LD chips manufactured from doped-waveguide HS show the increase in P_{max} up to 11.6 W at operating current 12 A. No saturation of light-current characteristics within the operating current range from 1 A to 12 A was observed. The voltage-current characteristics (Figure 2b) shows the decrease in operating voltage U from 1.88 V down to 1.74 V at 12 A for doped-waveguide chips. The LD chip efficiency was 56 % at operating pump current of 12 A. The maximum conversion efficiency of 63 % was achieved at 5 A.

Conclusion

The optimized HS design allowed for LD output power of 11.6 W at 12 A with the maximum conversion efficiency of 63 %.

References

1. I.A. Danilov, A.V. Ivanov, V.P. Konyaev, Yu.V. Kurnyavko et al. Semiconductor lasers with improved emitting characteristics. *Quantum Electronics*, 52, No. 12, 2022, pp. 1079-1087 (in Russian).

2. Wang X., Crump P., Wenzel H., Liero A., Hoffmann T. et. al. *IEEE J. Quantum Electron.*, 46 (5), 658 (2010).

3D laser cleaning as a novel approach to artworks conservation

D. V. Zhurba [1,2], **V. A. Parfenov** [1✉]
[1] Saint-Petersburg State Electrotechnical University «LETI», Saint-Petersburg, Russian Federation;
[2] ITMO University, Saint-Petersburg, Russian Federation
✉ vaparfenov@etu.ru @mail.com

Abstract. Until recently, restoration cleaning has been carried out primarily manually. Manual laser cleaning is a time-consuming process that requires highly skilled restorers. The introduction of automation, which increases the quality and speed of laser cleaning, will significantly expand its application range and reduce the complexity of restoration work.In this article, we present the results of our experimental work on automated 3D laser cleaning. The proposed approach allows for precise cleaning of objects of complex geometric shape under the control of a CNC machine. To remove dirt from the surface of such objects, we have developed an original approach based on a combination of three-dimensional scanning of the object and obtaining a point cloud of the surface to be cleaned, creating a control program for surface cleaning on a CNC machine. The demonstration of the automated cleaning process took place on corroded steel samples of complex geometric shape. A fiber ytterbium pulsed laser with an average power of 100 W with a wavelength of 1.06 microns and a pulse duration of 100 ns was used for cleaning.

Keywords: laser cleaning, fiber nanosecond laser, restoration of metal objects, CNC, 3D scanner

Funding: The research was supported by the Federal Academic Leadership Program Priority 2030 (manufacturing and measuring).

Introduction

Today, lasers are considered an innovative tool in conservation, promising selective and delicate cleaning applications. Among the most promising tasks of laser cleaning is the removal of dirt and other contaminants from the surface of sculptures and other Cultural Heritage [1-4]. Although laser treatment is frequently used in artworks conservation there remains much room for further research concerned with development of novel methodologies and new approaches. Until recently, restoration cleaning was carried out mainly manually. Manual laser cleaning is a time-consuming process that requires a highly qualified restorer, which limits its mass use. In this article, we will present the results of experimental work on automated 3D laser cleaning. The proposed approach allows for precise cleaning of objects of complex geometric shape under the control of a CNC machine. To remove dirt from the surface of such objects, we have developed an original approach based on a combination of three-dimensional scanning of the object and obtaining a point cloud of the surface to be cleaned, creating a control program for surface cleaning on a CNC machine.

Materials and Methods

Shining 3D EinScan HX was used to scan the surface of the object being cleaned and create a cloud of surface points. This scanner provides fast 3D scanning by combining LED light and laser scanning mode. Next, a control program in G-code for CNC was created using the CAM system. Cleaning was carried out on an automated laser cleaning machine, including an ALONP-100IM device (manufactured by NPP VOLO LLC, Russia, St. Petersburg) with a pulsed fiber laser (wavelength 1.06 microns, pulse duration about 100 ns, average power 100 Watts).

Results and Discussion

The experiments were carried out on steel parts that had undergone years of atmospheric corrosion, and there were also layers of old paint and bitumen on their surfaces. Figure 1, a

shows a fragment of the preparation of the control program. The trajectory of the laser treatment exactly corresponds to the profile of the treated surface. After preparing the control program, the part was positioned on the machine table and the cleaning program was started (Figure 1, b).

a) *b*) *c*)

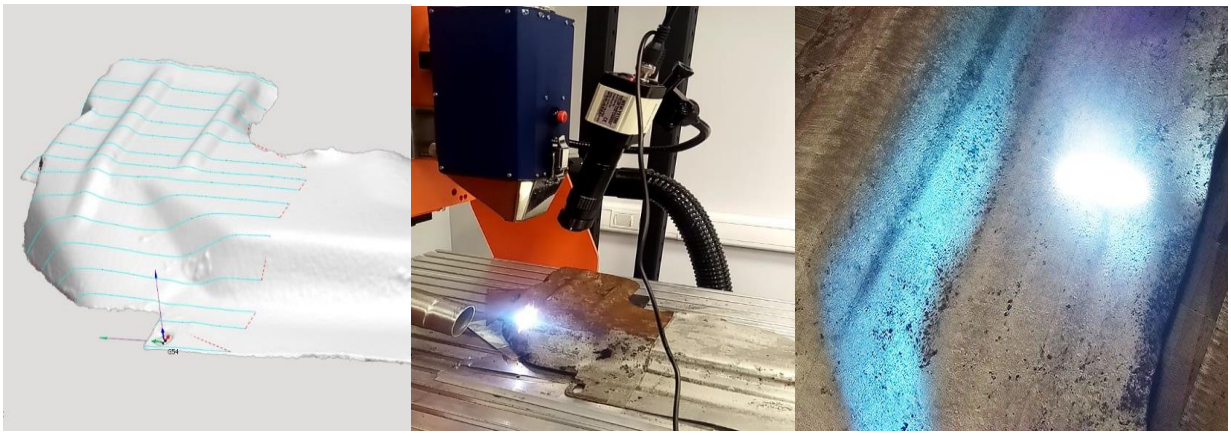


Fig. 1. The laser cleaning process. Preparation of the control program (a), the restoration object is positioned on the machine table, the cleaning program is started (b), visual control of the degree of laser cleaning (c).

The processing quality was monitored visually during the program operation (Figure 1,c). The number of repetitions of the program and the laser operation parameters were adjusted to obtain the required cleaning quality.

Conclusion

The results of our experiments showed that automated laser cleaning has several advantages over manual laser cleaning. First, the cleaning performance of the automated system is 1.5-2 times higher than that of the manual system, as the optimal scanning trajectory is chosen and the working distance between the laser and the surface to be cleaned is accurately maintained. This results in a higher quality of cleaning and a better surface appearance. Second, since laser cleaning can be done 24/7 without interruption, it is easier for the restorer to work. They only need to monitor the quality of the process and ensure there are no errors. Third, automated laser cleaning is perfect for cleaning unique objects as well as objects that are monotonous or identical objects. This reduces the cost of restorations.

In the future, it is important for us to pay attention to automating the process of controlling the degree of purification and adjusting the control program during cleaning. This will allow us to further increase productivity and the quality of our processing.

REFERENCES

1. **Cooper M.**, Laser Cleaning in Conservation: An Introduction, Butterworth-Heinemann, Oxford. 1998.

2. **Siano S., Salimbeni R., Pini R., Giusti A., Matteini M.**, Laser cleaning methodology for the preservation of the Porta del Paradiso by Lorenzo Ghiberti, Journal of Cultural Heritage. 4 (2003) 140–146.

3. **Siano S., Giamello M., Bartoli L., Mencaglia A., Parfenov V., Salimbeni R.**, Laser cleaning of stone by different laser pulse duration and wavelength, Laser Physics 2008. 18 (1) 1–10.

4. **Dobrusina S. A., Parfenov V. A., Podgornaya N. I., Samsygina N. D., Titov S. V., Petrov A. A., and Aseev V. A.**, Laser removal of foxing from the pages of books and paper documents, J. Opt. Technol. 90 (2023) 617–625.

Conference materials
UDC 628.9
DOI: https://doi.org/10.18721/JPM.

Competing processes affecting the properties of nitride MQWs of LEDs

A. E. Ivanov [1✉], A. **E. Chernyakov** [1], **N.A. Talnishnich** [1], **E.I Shabunina**[2], **N. M. Shmidt** [2]
[1] SHM R&E Center, RAS, St. Petersburg 194021, Russia
[2] Ioffe institute PAS St. Petersburg, 194021, Russia
✉ a-e-ivano-v@yandex.ru

Abstract. Using the simplest control method of level disorder (LD) of random solid solution alloy fluctuation (RAF) in MQWs of nitride LEDs, emitting from 270 to 540 nm, allowed us to identify two competing processes affecting the properties of nitride. Both develop under the injection current in MQWs located at depletion layer of p-n junction. One of the processes leads to a narrowing and the other to a broadening of full wide at have maximum (FWHM) of the electroluminescence spectra (EL) of nitride LEDs under injection current. It was found that the FWHM narrowing is caused by the rearrangement of position of the main components of a nitride alloy under current to a more equilibrium state. This process promotes efficient radiative recombination (RR) at a fixed wavelength. The FWHM broadening is caused by the process of nonequilibrium filling of spatial RAF. The range of currents at which the participation of this competing process begins, leading to a decrease in RR efficiency, has been clarified. It has been shown experimentally that higher the LD, affecting the properties of the nitride alloy in MQWs and the greater the carrier loss, resulting in the EQE reduction at the maximum.

Keywords: MQW LEDs, alloy disorder level, width of the spectrum, LEDs efficiency.

Introduction

It is mention in the latest review [1] that insufficiently studied features of nitride-based alloy prevent the realization of their potential in the creation of emitting devices with high external quantum efficiency (EQE) in the spectral range from ultraviolet to blue. In particular, such phenomena as a FWHM narrowing, as well as a FWHM broadening of EL spectra in QWs of LEDs under the injection current can decrease EQE values [2,3]. However, the processes causing these phenomena in QWs located in depletion layer (DL) of p-n junction have been However, the processes causing these phenomena in QWs located in depletion layer (DL) of p-n junction have still relatively little-understood problem [3]. Despite the fact, that the EQE maximum of LEDs is achieved in DL of p-n junction. The present study was aimed at revealing reasons for these phenomena.

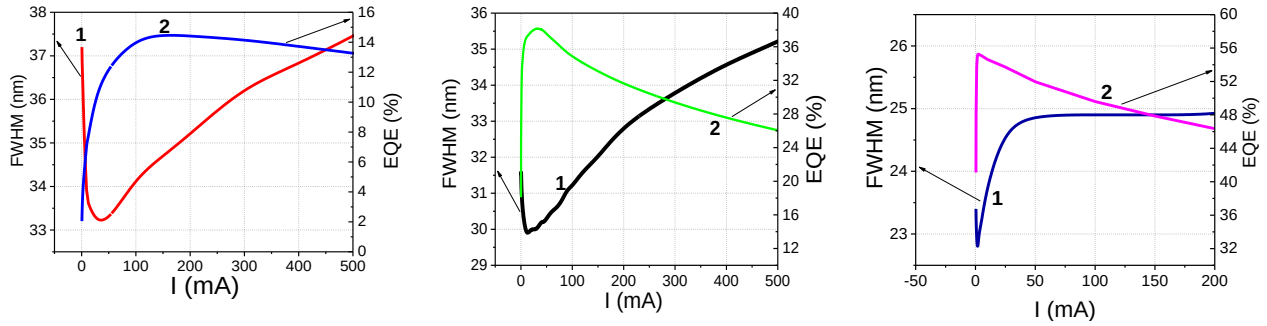
Materials and Methods

The commercial LEDs emitting from 270 to 540 nm with EQE ranging from 4% to 70% were studied. We carried out a joint analysis of changes in FWHM values and the dependence of EQE on the injection current of these LEDs, as well as the distribution of the emission wavelength over the area of green LEDs. EL spectra and FWHM were controlled by Optronic Laboratories OL770-LED system with an OL ISA-670 integrating sphere.

Results and Discussion

Figure 1 shows the experimental dependencies of FWHM and EQE values on the injection current using the example of green and blue LEDs with different alloy LD. Alloy LD of LEDs correlates with the value Δ, which is the difference between the values of the threshold voltage (u_{th}) determined from the direct branch of the I-V characteristics and the voltage corresponding to the wavelength of the study LEDs at the maximum (u_0), $\Delta = u_{th}-u_0$ [4]. The Δ values, correlated with LD, are given in the captions to Fig.1. According [2], the higher the value of Δ, the higher the alloy LD in QWs of LEDs. High LD of random alloy fluctuation of LEDs is

confirmed in the map of the distribution of peak wavelength over the area of green LEDs. It demonstrates the presence of local regions with weak radiative recombination in the wavelength range 400-600 nm. The FWHM narrowing due to an increase in current, and followed by FWHM broadening with a further increase in current for all LEDs at Figure 1.



a) b) c)

Fig. 1. The dependences FWHM (1) and EQE (2) versus injection current of LEDs with different LD: a – green 0.72 V, b – green 0.46 V and c – 0.13 V.

At the same time, the greatest narrowing of 3.8 nm is observed when the injection current increase to 40 mA on LEDs with a maximal LD Figure 1a (curve 1). The narrowing effect decreases with a decrease in LD Figure 1b,c(curves 1)., and is realized at significantly lower injection currents, up to 1 mA for LEDs with minimal LD Figure 1c(curve 1) and accompanied by an increase in EQE at a fixed wavelength in the same current range Figure 1c (curve 2). We assume that this effect is caused by the rearrengement of coordinate position of the main components of a nitride alloy located in regions with disrupted alloy stoichiometry , to a more equilibrium state. Such a process is possible in nitrides due to the transfer of additional energy to these components during capture and recombination of injected charge carriers. The FWHM broadening is caused by the process of nonequilibrium filling of spatial random alloy fluctuation with injected charge carriers and is accompanied by radiative recombination (RR) in a certain wavelength range . The range of currents at which the participation of this competing process begins , leading to a decrease in RR efficiency Figure 1 curves 2. It is shown from Figure 1. , that the higher the alloy LD, the greater the carrier loss due to competing process, resulting in the EQE reduction at the maximum.

Conclusion

The competing processes has been clarified which affecting the properties of nitride MQWs of LEDs. It depends on the disorder level of the solid solution (alloy LD). The higher the disorder of the solid solution and the change in its properties under the influence of current, the stronger the EQE reduction at maximum of radiative recombination. As a result of the near-field study, regions with emission wavelengths different from the peak were discovered, which contribute to the width of the spectrum. Although our analysis has been for InGaN LEDs, it applies equally well to AlGaN quantum-well LEDs, which also have alloy disorder.

REFERENCES

1. **C. Weisbuch, S. Nakamura, Y-R Wu, J.S. Speck** Nanophotonics 10(1) 3-21 (2021). https://doi.org/10.1515/nanoph-2020-0590
2. **E. Shabunina, A. Chernyakov, A. Ivanov, et. al.** *J Appl Spectrosc* **90**, 24–28 (2023). https://doi.org/10.1007/s10812-023-01497-8
3. **N. Pant, X. Li, E. DeJong, D. Feezell, R. Armitage, E. Kioupakis** AIP Advances 12(12):125020 (2022) DOI: 10.1063/5.0134995
4. **Y. Robin, M. Pristovsek, H. Amano, F. Oehler, R. A. Oliver, C. J. Humphreys**, J. Appl. Phys. 124, 183102 (2018).

Development of Semitransparent Perovskite Solar Cells with double electron transport layer and modified top electrode

V. S. Ivanov [1✉], **D. Sapori** [1]

[1] School of Physics and Engineering, ITMO University, Kronverksky Pr. 49, bldg. A, St. Petersburg, 197101, Russia

✉vladimir.ivanov@metalab.ifmo.ru

Abstract. In this work we report on semitransparent perovskite solar cell fabrication using double electron transport layer and double top electrode. Such devices may be used in tandem solar cells, and one of the main problem is to make transparent top electrode, since it is usually made of metal. The combination of ITO/Ag is used in which silver is deposited to improve conductivity. ZnO nanoparticles are incorporated in device as second electron transport layer to protect all below layers from ITO sputtering damage, it was deposited via spin-coating process. The best semitransparent perovskite solar cell made with these modifications showed 11.5% efficiency with high V_{oc} value of 1.1 V.

Keywords: Perovskite solar cells, photovoltaics, semitransparent electrode, double electron transport layer.

Introduction

Nowadays perovskite solar cells (PSCs) are the most promising photovoltaic devices. The first working cell was produced in 2009 [1], and in only fifteen years the power conversion efficiency has reached the value of more than 26.1% [2]. Such fast development is due to excellent physical properties of perovskite material, especially bandgap tunability in the whole visible range plus UV and IR part of spectrum [3].

There is a theoretical efficiency limit of one-junction solar cell named Shockley-Queisser limit [4]. Tandem systems with two or more active materials should be produced to overcome 30% efficiency value. Theoretical calculations showed that the most common perovskite material $CH_3NH_3PbI_3$ ($MAPbI_3$) with bandgap of 1.55 eV may be combined with Si or CIGS, and such tandem can obtain ~40% efficiency [5].

Perovskite material has greater bandgap than Si or CIGS, therefore PSC should be semitransparent to pass the light to the bottom cell. The main problem here is top electrode which is made of metal. Indium tin oxide (ITO) is the most popular transparent electrode, which is used as bottom electrode in PSCs. Usually, it is deposited via magnetron sputtering of high energy ions under high (> 200°C) temperature, and in case of perovskite devices such conditions may damage all organic layers. Therefore, there are two main problems which should be solved to have semitransparent perovskite solar cell with ITO as top electrode: the problem of perovskite degradation under high temperature, and the problem of sputtering damage to organic transport layers.

Materials and Methods

Perovskite solar cells in this work had the following p-i-n structure: ITO/Poly[bis(4-phenyl)(2,4,6-trimethylphenyl)amine (PTAA)/perovskite/3'H-cyclopropa[1,9][5,6]fullerene-C60-Ih-3′-butanoic acid 3′-phenyl methyl ester (PCBM60)/ZnO NPs/ITO/Ag. Classical $MAPbI_3$ was used as perovskite, all layers except ITO and Ag were deposited via spin-coating process. Top ITO film was sputtered, and Ag was thermally evaporated. JV curves were measured to characterize the devices. In case of ITO films transparency spectrum, resistivity and thickness were measured while optimization work.

Results and Discussion

Inorganic ZnO nanoparticles were deposited onto the PCBM to protect it from sputtering damage, such combination works as double electron transport layer (ETL), enhancing transport

properties of the device. In the most cases such protective layers are deposited by ALD technique, which is expensive and problematic for mass production. In this work nanoparticles were spun from the liquid – this technology is much cheaper, faster, and easier. The first step of the work was to optimize the ZnO incorporation process. Device with PCBM/BCP double ETL was used as reference having the best efficiency of 16.9%. After the optimization, device with ZnO showed high PCE value of 17.2%, which can be used as base device for next ITO deposition.

Since protective double ETL of good quality was achieved, work on ITO sputtering under room temperature has begun. First main goal was to achieve ITO film under room temperature with low resistivity and high transparency. With O_2 flux equal to 5 sccm, resistivity was 109 Ohm/sq, almost transparent yellowish films were obtained. In such conditions the first semitransparent devices were made, and PCE of only 6.2% was obtained. Spatial silver frame was used to improve the conductivity leaving ITO window as a pixel. However, fill factor (FF) of the device was too law – only 35%, while V_{oc} had good value of 1.1 V. Then it was found that changing O_2 flux value may affect the resistivity of the film, 11 sccm led to only 38 Ohm/sq, T spectrum showed also better transparency. In such conditions champion semitransparent device with PCE of 11.6% was achieved with high FF value of 62%.

Conclusion

In this work semitransparent perovskite solar cells with double ETL and electrode were fabricated. High V_{oc} value of 1.1 V and FF of 62% led to PCE of 11.6%. Protective inorganic ZnO nanoparticles were spun onto PCBM to avoid high energy ion damage while sputtering process. Changing gas flux under room temperature conditions led to low resistance and high transparency of ITO films. Further optimization of ITO sputtering process should be done to improve J_{sc} of the semitransparent device, and after tandem solar cells of Si/perovskite or CIGS/perovskite may be produced.

REFERENCES

1. **Kojima A., Teshima K., Shirai Y., Miyasaka T.** Organometal halide perovskites as visible-light sensitizers for photovoltaic cells. Journal of the American chemical society 2009, 131, 6050-6051.

2. **Szabo G., Park N-G., Angelis F., Kamat P.** Are Perovskite Solar Cells Reaching the Efficiency and Voltage Limits?. ACS Energy Lett. – 2023. – 8, 9, 3829-3831.

3. **Unger E. L., Kegelmann L., Suchan K., Sorell D., Korte L.**, **Albrecht S.** Roadmap and roadblocks for the band gap tunability of metal halide perovskites. Journal of Materials Chemistry A. – 2017. – 5, 11401-11409.

4. **Shockley W., Queisser H. J.** Detailed Balance Limit of Efficiency of *p-n* Junction Solar Cells. J. Appl. Phys. – 1961. – 32, 510-519.

5. PVEducation. URL: https://www.pveducation.org/pvcdrom/tandem-cells. Accessed March 25, 2024.

Fast axis collimation lens misalignment influence on the fiber coupling efficiency of high-power laser diode module

A.N. Ignatev✉, A.V. Fomin
FSUE "FRNC-VNIITF named after Academ. E.I. Zababakhin", Snezhinsk, Russia
dep5@vniitf.ru

Abstract. The paper analyzes the effect of the displacement of short-focus acylindrical lenses for fast axis collimation on the change in the efficiency of laser radiation coupling into an optical silica fiber in a module based on high-power single laser diodes. The results of optical simulation and experimental data are compared, and the direction of displacement, which is the most critical from the point of view of ensuring maximum efficiency of the optical system, is determined.

Keywords: laser module, coupling efficiency, FAC lens alignment.

Introduction

The search for various solutions to transform the radiation of single laser diodes (LDs) and implement efficient coupling of laser radiation into optical fibers remains a pertinent challenge in the development of fiber coupled laser diode modules (LMs). One of the key factors influencing the effectiveness of the LM optical system is the precision and stability of optical element positioning during assembly [1-3]. This study explores the most critical displacement directions of lenses for collimating the radiation of fast axes (FAC lenses) in LMs with spatially combined radiation from seven single LDs of the 975 nm spectral range (Fig. 1a), followed by coupling into silica optical fiber with a core diameter of 105 μm and a numerical aperture of 0.15 [4]

Materials and Methods

FAC lenses with a focal length of 0.3 mm were used for collimating the fast axis radiation of LDs with a divergence of 29° (at the 95% level) in LMs. During lens alignment, the lens was moved in three linear and three angular directions (Fig. 1b). To assess changes in the efficiency of laser radiation coupling into the fiber, directions of the X, Z axes, and angular rotation around the Z axis (Rz) were selected as the most sensitive to positioning errors.

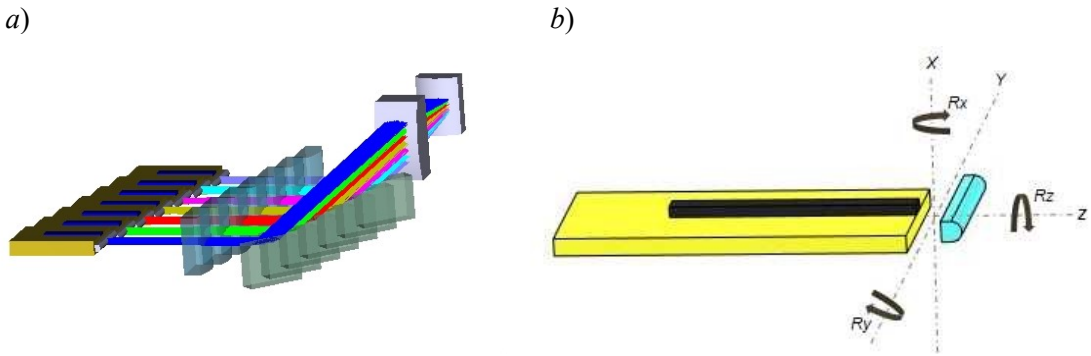


Fig. 1. Optical scheme of the LM (*a*) and directions of FAC lens displacement during alignment (*b*).

Changes in coupling efficiency resulting from optical modeling software of the optical scheme were calculated as the ratio of the radiation power registered by the detector located at the output of the optical fiber to the initial power of the LD. For experimental evaluation, one of the LD FAC lenses was removed in the LM, after which alignment of a new FAC lens was performed using micrometric adjustments. The optimal position of the new FAC lens was determined by the maximum value of the LM radiation power detected at the output of the optical fiber. This position of the FAC lens was perceived as the zero point.

Results and Discussion

Fig. 2 shows the dependences of the coupling efficiency, simulated using software modeling and based on experimental data. As seen from the figure, the results of optical simulation are in high agreement with experimentally obtained data. However, the sensitivity of the optical scheme significantly varies depending on the selected direction of FAC lens displacement. For instance, when the lens is shifted along the X axis by ± 1 μm, the coupling efficiency decreases by 50%, whereas a similar displacement along the Z axis (away from the LD) results in an efficiency drop of no more than 5%. For angular displacement of the lens in the Rz direction, the power decrease does not exceed 15% when rotated by ± 1°.

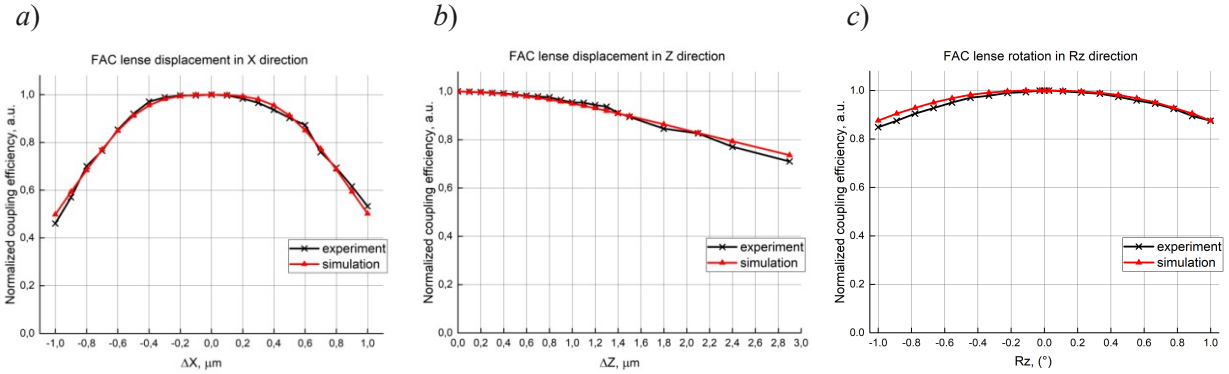


Fig. 2. Relation between coupling efficiency and FAC-lense misalignment in X axis direction (*a*), Z axis direction (b) and rotation in Rz direction (c*в*)

Conclusion

This study evaluated the impact of FAC lens positioning errors on the efficiency of laser radiation coupling into LM fibers. The results allow us to determine of the most sensitive displacement directions of other optical elements, which must be taken into account in the LM assembly technology. The obtained dependencies can serve as an important tool for assessing the causes of LM performance degradation during operation. Furthermore, in the development of optical systems, additional attention may be given not only to ensuring maximum efficiency of laser radiation coupling but also to the stability of the optical system against optical element displacements.

REFERENCES

[1] **Yixiong Yan, Yu Zheng, Ji'an Duan, Zhenli Huang**, Influence of positioning errors of the laser collimator on the beam shape and coupling efficiency, Optical Fiber Technology (58) (2020) 102301.

[2] **Yu Junhong, Guo Linhui, Wu Hualing, Meng Huicheng, Tan Hao, Gao Songxin, Wu Deyong**, Analysis influence of fiber alignment error on laser–diode fiber coupling efficiency, Optik - International Journal for Light and Electron Optics 127 (2016) 3276–3280.

[3] **Lvlin Qiao, Dejian Zhou, Lei Xiao**, Beam collimation and focusing and error analysis of LD and fiber coupling system based on ZEMAX, In: AIP Conference Proceedings 1890 (2017) 040045.

[4] **Fomin A. V., Usmanov S. R., Ignatev A. N., Kadigrob E. V.,** Fiber coupled laser module with brightness exceeding 10 MW/cm2·sr, Technical Physics. 4 (92) (2022) 616–619.

Modeling the broadband measuring source using the optical fiber nonlinear properties

A. I. Isupov [1]✉, **M.A.Orlov** [1], **E. I. Andreeva** [1]

[1] St. Petersburg State University of Telecommunications. prof. M.A. Bonch-Bruevich, St. Petersburg, Russia;

✉me022@mail.ru

Abstract. Modeling of the broadband measuring laser source for testing spectral-selective components of fiber-optic communication systems with wavelength division multiplexing has been carried out. It is shown that, due to the use of nonlinear effects in an optical fiber, it is possible to achieve a multiple broadening of the laser source spectrum. The results of the experimental investigation are presented.

Keywords: fiber-optic communication system, Wavelength Division Multiplexing, optical fiber, nonlinear effects.

Introduction

The development of fiber-optic communication systems with wavelength division multiplexing has led to the development and implementation of a wide class of passive spectral-selective devices for such systems [1-3]. The production and introduction of spectrally selective devices is associated with the need to accurately measure their performance in each spectral range with the required accuracy. Measurement sources such as ASE are traditionally used to measure the spectral bandwidth of spectrally selective passive elements of fiber-optics communication system. They provide a wide spectral band at a relatively high power of optical radiation. Broadband sources, complete with spectrally selective meters, such as an optical spectrum analyzer (OSA), allow you to visualize the results of measuring the bandwidth of the device under test. Narrow-band lasers, complete with broadband measuring power (OPM, Optical Power Meter) are used for accurate measurements of device operating parameters. In this case, the optical power meter must have either a smooth spectral sensitivity characteristic, or the possibility of considering its non-uniformity using calibration coefficients in each spectral range. However, such sources can be used in the third transparency window of quartz-quartz optical fibers (near the wavelength of 1550 nm). If the spectral-selective elements are designed to operate in a different spectral range, it is necessary to provide for their testing by other measuring devices.

The aim of this work is to study the possibility of creating a broadband measuring source using a semiconductor laser and the nonlinear properties of an optical fiber.

Computer simulation

The computer simulation of the effect of nonlinear broadening of the laser spectrum in the optical fiber was made with considering optical power losses and group velocity dispersion. The optical simulation block diagram (Fig. 1) contains of the picosecond pulses source (1), optical preamplifier (booster) (2), standard single mode optical fiber (SSMF) or dispersion shifted fiber (DSF) (3), demultiplexer (4) (with Δf = 100 GHz, for example) and optical spectrum analyzer (5).

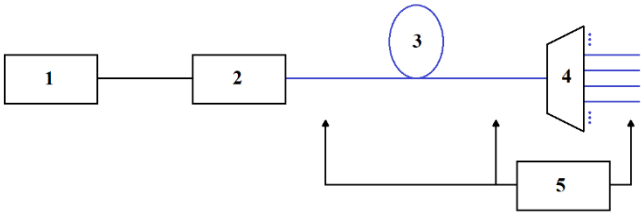


Fig. 1. The optical block diagram of the computer simulation: 1 – laser, 2 – optical amplifier, 3 – optical fiber, 4 – demultiplexer, 5 – optical spectrum analyzer

Picosecond pulses from the laser (1) after amplification (2) are fed to the input of the SSMF or DSF (3). The input power P_o of the optical pulses was selected to be sufficient for the formation of a high-order soliton. Such pulse undergoes self-compression with a significant broadening of

the spectrum. The spatial dynamics of the spectrum broadening as it propagates along the optical fiber is shown in figure 2. Envelope of the optical pulse remained the same.

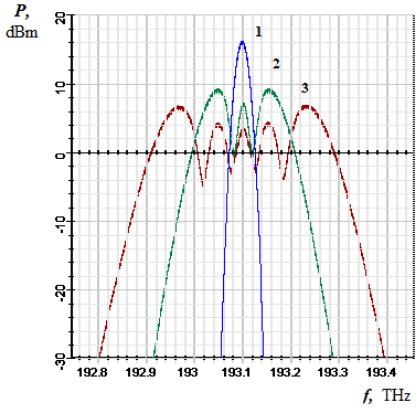


Fig. 2. The pulse spectrum at the entrance to the optical fiber (1) and after passing 1.2 (2) and 2 km (3)

Experimental Results and Discussion

The experimental setup included the laser source, the narrow-band filter, Er-amplifier, the standard optical fiber and the optical spectrum analyzer. Operating wavelength of the laser λ=1546.12 nm (39th DWDM channel). Fiber optic parameters: dispersion D=16.67 ps/nm/km (β_2=-20 ps^2/km), Kerr nonlinearity coefficient γ=1.2 W^{-1}km^{-1} loss 0.2 dB/km. The Previal erbium amplifier provided 24 dBm of optical power in the optical fiber.

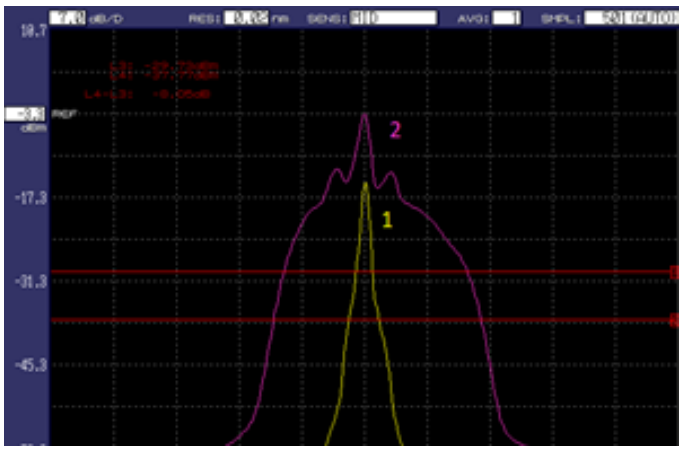


Fig. 3. Spectrum Optical signal spectrum at the output of the optical fiber without an amplifier (1) and with an amplifier (2)

Studies have shown that to achieve greater spectral width at the output of the optical fiber, it is necessary to use a laser with a narrow spectrum to input radiation. Notch filters can be used to improve efficiency.

Conclusion

Thus, the possibility of broadening the spectrum of an optical signal in the optical fiber using standard components has been demonstrated. To enhance the effect, the optical fiber with shifted (reduced) dispersion can be used.

REFERENCES

1. **Agrawal G.** Nonlinear Fiber Optics, 6th Edition, Elsevier, 2019**.**

2. **A. Isupov, D. Andreev, E. Andreeva.** The broadband light source modeling using the optical fiber nonlinearity, Proc. of ITNT-2023, vol, p.10922, Samara, 2023.

3. **Agrawal G**. Fiber-Optics Communication Systems, 5th Edition - New York, 2021.

Suppressed phase segregation in $CsPbBr_2I$ based PeLEC

R. Kenesbay [1]✉, **A. S. Toikka** [1,2], **M. Baeva** [1], **D.M. Mitin** [1]
[1] St. Petersburg Academic University, St. Petersburg, Russian Federation
[2] ITMO University, St. Petersburg, Russian Federation
✉ ramazan.kenesbay.1999@gmail.com

Abstract. In this paper we describe a method to reduce phase segregation in halide perovskite light-emitting electrochemical cell (PeLEC) based on $CsPbBr_2I$ by doping by Mn and passivation by polyvinylidene fluoride (PVDF). For more efficient carrier injection poly(3,4-ethylenedioxythiophene) polystyrene sulfonate (PEDOT : PSS) as hole transport layer (HTL) and 2,2',2"-(1,3,5-Benzinetriyl)-tris(1-phenyl-1-H-benzimidazole) (TPBi) as electron transport layer (ETL) were deposited. Measurement of photoluminescence (PL) and electroluminescence (EL) showed single peaks which correspond to suppressed phase segregation. Peak position of EL for fabricated device is ~670 nm. Current-voltage and luminance-voltage characterization showed that the knee voltage is at ~ 4.5V and the maximal luminance is 45 cd/m^2. Proposed composition of light emitting perovskite layer opens opportunities of creating phase stable and efficient red light emitting device and perovskite RGB devices. These advancements allow to reach a perovskite phase-stable device.

Keywords: perovskite, PeLEC, phase segregation, mixed anion.
Funding: The research was supported by grant from the Russian Science Foundation № 22-79-10286.

Introduction

Lead halide perovskites (LHP) are semiconductor materials used as an active layer in light-emitting devices and solar cells. The advantages of LHP are the simplicity of synthesis, and the devices based on this material have high external quantum efficiency [1]. By varying the halogen anion in the material chemical composition ($CsPbBr_3$, $CsPbBr_2I$, $CsPbBrI_2$, etc.) it is possible to tune the bandgap, and, consequently, control the spectrum of perovskite radiation. However, perovskites with a mixed halogen composition (for example, $CsPb(Br_xI_{(1-x)})_3$ have a lower photoluminescence quantum yield and quantum efficiency compared to perovskites with single of halogen, which is due to the occurrence of phase segregation, that is, the formation of regions with an increased content of bromine or iodine ($CsPbBr_3$ and $CsPbI_3$). Phase segregation leads to trap states density increase and changes the band gap width limiting the structure's external quantum efficiency [2]. There are various methods to prevent the phase segregation, such as: doping (for example with Mn), controlling the size and shape of grains, and thin film surface modification [3,4]. In this work we present phase-stable red PeLEC with mixed-halide perovskite material.

Materials and Methods

PeLEC consist of indium tin oxide (ITO) (as a front electrode), PEDOT : PSS (as a HTL), perovskite-polymer layer, TPBi (as a ETL), Al metallization (as a rear electrode), and LiF (as buffer layer for creating a physical border between layers). **Figure 1a** shows the principal scheme of device structure. Doped by Mn $CsPbBr_2I$-polyethylene oxide-PVDF-lithium bis(trifluoromethanesulfonyl)imide layer was formed inside the inert N_2 atmosphere inside the glove box system by drop casting and spin-coating perovskite-polymer solution. PVDF passivate defects and fill pinholes in the film increasing the continuity of the film. PEDOT:PSS was deposited by spin-coating method on atmosphere. TPPBi, LiF and Al were deposited by thermal evaporation method inside glove box system. To characterize optical properties of samples photoluminescence spectra were measured. Also, to determine the electro-optical properties, current density-Voltage (J-V) and luminance-voltage (L-V) curves were obtained.

Results and Discussion

For optical characterization of perovskite-polymer film PL spectra were measured, see **Figure 1b**. The result of phase segregation in a pure $CsPbBr_2I$ produces two peaks in the spectrum for Br-rich areas (~600 nm) and I-rich areas (~667 nm) (**Figure 1b**, blue curve) We can note that the PL spectrum of our sample (**Figure 1b**, black curve) has one peak at 633.5 nm with FWHM 44.0 nm. The EL spectra (**Figure 1b**, red curve) has also one peak with position 667.1 with FWHM 66.6 nm. This is the evidence that photoinduced and electric field induced phase segregation was suppressed, due to the partial replacement of the Pb by Mn in the perovskite crystal structure, which keeps halide ions (Br- and I-) in their "designated" lattice sites. The peak position shift between EL and PL may be explained by existence of the charge carriers trap states inside of the materials bandgap through which radiative recombination goes (this effect is not observed at high-enough incident optical power during PL measurements) [4]. From current density-voltage and luminance-voltage curves (**Figure 1c**) we can see that the device's knee-point voltage is ~ 4.5 V and maximal luminance ~ 45 cd/m^2 at ~5V. The PeLEC starts emitting light after ~ 3.7 V,which corresponds well with the mixed anion halide perovskite bandgap energy. The diode form of J-V curve is a sign of an optimized device structure.

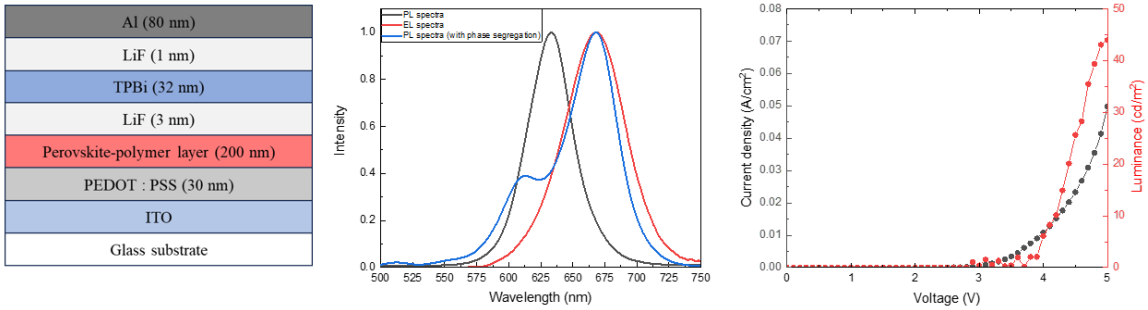


Fig. 1. (a) PeLEC device structure, (b) PL, EL and PL (with phase segregation) spectra,, (c) Current density-voltage and luminance-voltage characteristics

Conclusion

Addition Mn and PVDF allows to obtain phase-stable PeLEC. That perovskite-polymer layer has resistance to photo and electric field induced phase segregation.

Acknowledgments

The research was supported by grant from the Russian Science Foundation № 22-79-10286.

REFERENCES

1. **Guo Z., Jena A. K., Kim G. M., Miyasaka T.,** The high open-circuit voltage of perovskite solar cells: a review, Energy & Environmental Science, (3171-3222) (2022) 15–8.

2. **Zhang H., Jin Z.,** Suppressed light-induced phase transition of CsPbBr2I: Strategies, progress and applications in the photovoltaic field, Journal of Semiconductors, (071901) (2021) 42–7.

3. **Zheng L., Hurst T., Li Z.,** Manganese Doped Perovskite CsPb0. 9Mn0. 1Br2I Solar Cells with Enhanced Stability and Reduced Toxicity, Georgia Journal of Science, (1-16) (2022) 80–2.

4. **Yin X., Guo Y., Liu J., Que W., Ma F., Xu K.,** Photoinduced phase segregation leading to evident open-circuit voltage loss in efficient inorganic CsPbIBr2 solar cells, The Journal of Physical Chemistry Letters, (7035-7041) (2020) 11–17.

Numerical optimization of semiconductor waveguide structures

N. A. Kostromin [1,2,3]✉, **A. S. Dashkov** [1,3], **D. A. Barykin** [1,2,3]
[1] Alferov University, Saint-Petersburg, Russian Federation
[2] Saint-Petersburg Politechnic University, Saint-Petersburg, Russian Federation
[3] Saint-Petersburg Electrotechnical University, Saint-Petersburg, Russian Federation
✉ d.a.barykin02@mail.ru

Abstract. Research on radiation sources in the IR and THz ranges operating at room temperature is still highly attractive to this day. Waveguides play a critical role in these structures and their improvement is also required. This paper studies the optimization of waveguides based on GaAs material with different doping levels of layers to reduce absorption losses and increase the optical confinement factor. The optimization is carried out in three steps: selection of optimization parameters, determination of initial values of parameters and Bayesian optimization. The thickness and doping level of heavily doped layers are chosen as optimization parameters. The results show the Bayesian algorithm converges to the desired values rather quickly. It was found that the dependence of the waveguide output characteristics on concentration is weaker than on layer thickness. An increase in layer thickness leads to an increase in losses. Weak asymmetry in the structure can lead to a slight improvement in the confinement factor value.

Keywords: QCL, waveguide, gallium arsenide, optimization, Bayesian

Funding: The research was supported by the Russian Science Foundation grant No. 23-29-00216, https://rscf.ru/project/23-29-00216/.

Introduction

Infrared (IR) and terahertz radiation sources at room temperature have recently attracted considerable interest. The study of such devices began in the early 1970s [1], but the first active quantum-cascade lasers emitting light from interband electronic transitions were created in the 1990s [2]. Waveguides play a critical role in these structures, coupling radiation in the active area and providing optical feedback with minimal absorption losses. Optimizing such waveguides is a intensive task. Elaborate experimental research often requires regular fabrication of new structures, which is expensive. Another potential solution to this problem is to develop a model that can simulate the waveguide output from available experimental data and optimize designed structures. Such an approach would eliminate the need for time-consuming modelling and high cost experimental studies.

Materials and Methods

In this paper, a GaAs-based waveguide with different doping levels of the layers is considered [3]. The structure of the waveguide is described in Table 1.

Table 1

Waveguide structure

Material	Parameters	
	Width, μm	Doping, cm^{-3}
GaAs	1.0	6×10^{18}
GaAs	3.5	4×10^{16}
Active Region	1.63	
GaAs	3.5	4×10^{16}
GaAs	1.0	6×10^{18}
GaAs Substrate		3×10^{18}

The main aim is to find a waveguide configuration in which the absorption loss is minimal and the optical wave confinement factor Γ in the structure is maximized. Optimization of the waveguide structure is carried out in three stages: selection of optimization parameters, which significantly influence on the values of output characteristics; their initialization and the

application of the Bayesian optimization [4]. The thickness and doping level of the heavily doped layers adjacent to the active region were chosen as optimization parameters. Optical confinement and loss factor values were calculated for a range of doped layer widths from 1 μm to 10 μm, and for concentrations from 10^{15} cm^{-3} to 10^{17} cm^{-3} [5]. Due to the results obtained, Bayesian optimization was performed in a similar range for layer thicknesses only.

Results and Discussion

In the process of loss and confinement factor modeling, it was found that the dependence of the waveguide output characteristics on concentrations is much weaker than the dependence on layer thicknesses. Further optimization was carried out for thickness ranges only. It was concluded from the data that the mode confinement factor decreases with increasing layer thickness. When a weak asymmetry in the structure appears (the thickness of GaAs layer located closer to the substrate is larger), there is a noticeable improvement in the values of Γ. As the thickness of the layers increases, the losses expectably increase as well. In this case, the asymmetry of the structure did not play a major role. The optimization was performed based on 10 initial points and 10 iterations in sequence. In the case of confinement factor optimization, the algorithm arrived at the best value in 7 steps. In the case of loss optimization, the path took 2 steps. In both cases, the algorithm came to the desired extremum rather quickly.

a) *b*)

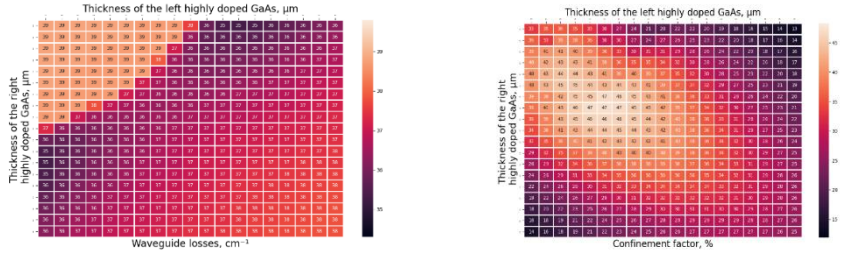


Fig. 2. Heatmaps of waveguide and losses mode confinement factor as a function of adjacent layer thickness.

Conclusion

In this paper, ways to improve the structure of GaAs-based waveguide with different doping levels and thicknesses of layers using the Bayesian optimization are investigated. The dependences of the confinement factor and losses on the thickness of highly doped layers are obtained. It is shown that the algorithm used is able to obtain the best values for the minimum number of iterations.

Acknowledgments

The research was supported by the Russian Science Foundation grant No. 23-29-00216, https://rscf.ru/project/23-29-00216/.

REFERENCES

1. Kazarinov R. F., Suris R. A. On the possibility of amplifying electromagnetic waves in a semiconductor with superlattices, Physics and Technology of Semiconductors. - 5 (4) (1971), 797–801.

2. Faist J., Capasso F., Sivco D.L., Sirtori C., Hutchinson A. L., Cho A. Y., Quantum Cascade Laser, Physical Review B, 50 (12) (1994), 8663–8667.

3. Sirtori, C., Kruck, P., Barbieri, S., Page, H., Nagle, J., Beck, M., Faist, J., Oesterle, U., Low-loss Al-free waveguides for unipolar semiconductor lasers, Applied Physics Letters, 75(25) (1999), 3911-3913

4. Franckié, M., Faist, J., Bayesian Optimization of Terahertz Quantum Cascade Lasers. Physical Review Applied, 13(3) (2020).

5. Williams B. S., Terahertz quantum cascade lasers: in partial fulfillment of the requirements for the degree of Doctor of Philosophy

Quantum state preparation with optical injection: Issue of intersymbol interference

I. Kudryashov[1,2], R. Shakhovoy[1,3]
[1]QRate, Moscow, Russia
[2]Moscow Institute of Physics and Technology, Dolgoprudny, Russia
[3]Moscow Technical University of Communications and Informatics, Moscow, Russia
✉i.kudryashov@goqrate.com

Abstract. Intersymbol interference may significantly affect the security of quantum key distribution. In this paper, we study this problem in the context of quantum state preparation with pulsed optical injection.

Keywords: Optical injection, intersymbol interference, semiconductor lasers.

Introduction

There are various methods for preparing quantum states for quantum key distribution (QKD). A technique based on pulsed optical injection [1-3] is becoming more widespread as it allows suppressing relaxation oscillations, reducing chirp and improving pulse interference. Here we address the problem of intersymbol interference in case of quantum state preparation with optical injection.

Materials and Methods

A system of master and slave distributed feedback lasers connected via optical circulator was used in this research. Both lasers were working in a gain-switching mode on different wavelengths: 1549.3 nm and 1550.6 nm. A WDM filter centered at 1549.32 nm was placed at the output of an optical circulator. The filter blocked slave laser emission and passed master laser emission. Under master laser radiation, slave laser pulses changed their form and frequency due to the frequency locking effect. In the absence of master laser emission, slave laser pulses were blocked. Slave laser pulses under frequency locking effect passed through the WDM filter before entering the integral Mach Zehnder interferometer, where the quantum states were decoded.

The slave laser emitted short pulses at frequency of 1.25 GHz and the master laser emitted 2 types of signals: short pulses, comparable in width to the slave laser pulses and pulses 2 times wider. Quantum states were created using short master laser pulses for time-bin encoding and long master laser pulses for encoding via phase difference.

Results and Discussion

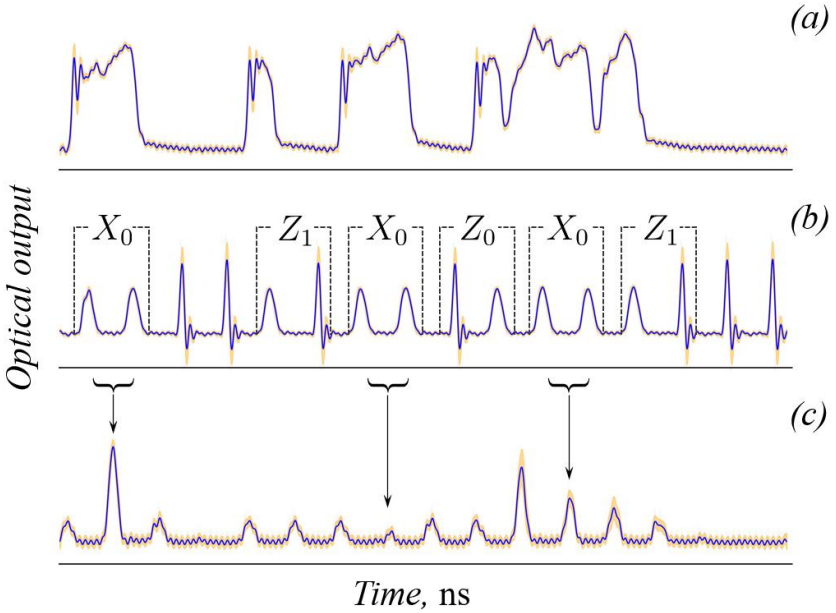


Fig. 1. Pulses coming from the master laser (a), pulses that are coming out of the optical circulator (b), the result of the interference (c).

The intersymbol interference is a distortion of a signal in which one state/symbol interferes with a subsequent one. The example of intersymbol interference can be seen on the Fig.1(c). Master laser pulses are displayed on the Fig.1(a). During the encoding process, the last master laser pulse of the previous quantum state (Z_0) affected the next coming pulse that belonged to the following quantum state (X_0), thus disturbing the interference of pulses inside one quantum state. This caused certain issues during decoding process on the Fig.1 (c). The interference from second and third X_0 states in the sequence is different from the constructive interference of the first X_0 state.

Conclusion

We demonstrated the case of intersymbol interference that occurs during optical-injection-based encoding. One of the possible solutions to minimize this effect is to decrease the pulse repetition rate for the master laser.

REFERENCES

1. **Z. L. Yuan, B. Frohlich, M. Lucamarini, G. L. Roberts, J. F. Dynes, and A. J. Shields**, Directly phase-modulated light source, Phys. Rev. X 6, 031044 (2016).

2. **R. Shakhovoy, M. Puplauskis, V. Sharoglazova, V. Duplinskiy, Alexanderand Zavodilenko, A. Losev, and Y. Kurochkin**, Direct phase modulation via optical injection: theoretical study, Optics Express 29, 9574 (2021).

3. **T. K. Paraiso, I. De Marco, T. Roger, D. G. Marangon, J. F. Dynes, M. Lucamarini, Z. Yuan, and A. J. Shields**, A modulator-free quantum key distribution transmitter chip, npj Quantum Information 5, 42 (2019).

Investigation of microfluidic topology formation with the use of IR pulse laser

V. V. Lavrinenko [1]✉, **A. V. Vasilyeva** [1], **V. A. Parfenov** [1]

[1] Saint-Petersburg State Electrotechnical University «LETI», Saint-Petersburg, Russia;

✉lavrinenko_valerav@inbox.ru

Abstract. The work considers the possibility of creating microfluidic topology elements on a stainless-steel plate using laser processing. The results of multi-stage exposure of an IR laser radiation to a metal surface in order to create microchannel parts (grooves) with a semicircular profile, as well as through holes that form part of typical microfluidic topologies, are presented. The features of laser radiation affection on metal plate are described in this work.

Keywords: Microfluidics, microfluidic topology, laser processing, laser perforation.

Introduction

Lab-on-a-chip systems are currently one of the fastest growing fields in applied photonics and, in particular, biophotonics. Technologies based on microfluidic systems are very diverse. In particular, they are used by biochemists and medical scientists to analyze biological and chemical liquids, to create new drugs, to manipulate different groups of cells, and even to simulate the work of human and animal organs [1-3]. The main requirements for such systems are high energy and economic efficiency, low weight, compactness, high sensitivity and high operating speed [4].

In a separate group of chips, one can select microfluidic devices for monitoring and analyzing microfluidic fluids. They can be made from a wide range of materials such as transparent silicone elastomer, photoresist, glass, silicon and various metals. Depending on the material used microfluidic drawing can be created using soft lithography, casting, hot stamping, mechanical milling, 3D printing and laser micro-processing [5].

The creation of a microfluidic pattern using laser microprocessing has a number of features and advantages compared to other methods, for example, environmental friendliness, lack of mechanical contact with materials and adaptability to production needs, and the use of metal as a material for the workpiece reduces the cost of manufacturing these products, which makes them more accessible to a wide range of research and applications.

Materials and Methods

The research was carried out on a 2 mm thick stainless steel metal plate, which was exposed to a precision laser mark system “MiniMarker2” (Laser Center LLC, Russia), based on a fiber ytterbium laser. The topology elements were designed using specialized software MaxiGraf (Laser Centre LLC) supplied with a laser marker. The laser treatment was performed in several stages, during which processing parameters such as pulse duration, pulse repetition rate, scanning speed of the laser beam and the plane of focus changed.

The transverse dimensions of grooves were measured using an optical microscope NVMicro (NORGAU, Russia). The width of the grooves was measured in three places: in the center and additionally one dimension at the edges of the structure. If an element of the topology had a “threshold”, then it was measured in a similar way. This allowed us to find an error in measuring the width of microchannels, which turned out to be about 1%.

The depth of the grooves was measured using a high-precision manual 3D measuring machine Sinowon iTouch, which is manufactured by the Malaysian company MSP METROLOGY. To obtain an accurate depth value, the surface focusing method was used. The change in focal length when the scan line hit the topology was the value of the groove depth. 5 measurements were made on each groove, after which the average depth value was calculated along the entire length of the groove. The measurement error was about 1%.

Results and Discussion

During multi-stage exposure to a steel plate with a fiber ytterbium laser with a wavelength of 1064 nm and a pulse duration of tens to hundreds of nanoseconds, it was possible to identify

the processing modes of the workpiece to create experimental grooves representing elements of a microfluidic system (Fig. 1 a, b). As a result of microscopic studies, it was revealed that in some cases, when parameters such as the average power of the laser installation and the pulse duration changed, a multistage groove profile was formed.

The peculiarity of such grooves (Fig. 1, a) was the presence of a “threshold” with a width of about 400 microns at the upper plane of the plate processing. The grooves of another type (Fig. 1. b) did not have this element, and the profile geometry was visually smoother, close to semicircular.

Also, during the work, it was found the formation of an oxide film at the bottom of the structures (Fig. 1. a). The film can potentially have a positive effect in reducing the roughness of the channel walls by filling the irregularities with an oxide layer.

By selecting the modes of laser exposure, it was possible to drill a through hole in a metal plate, the taper of which is about 0.05, which is an important practical result.

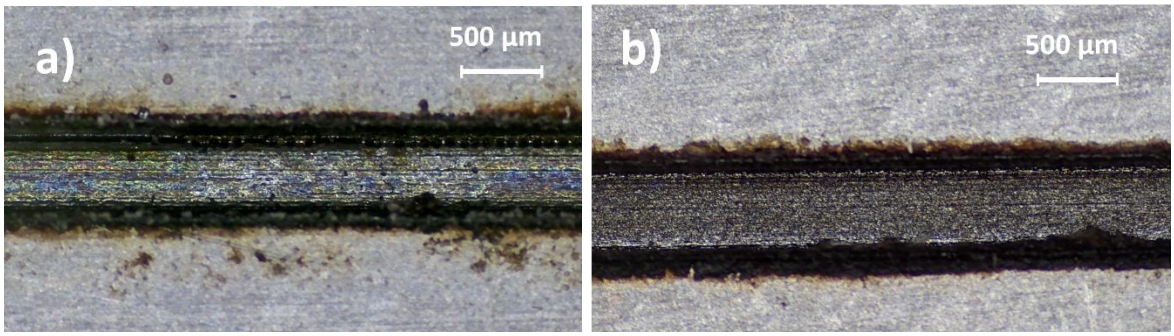


Fig. 1. Photos of grooves with a stepped profile (a) and with a semicircular profile (b)

Conclusion

Using laser treatment with IR radiation, it was possible to obtain grooves on the surface of stainless steel with a profile close to a semicircular up to 500 microns depth. The presence of oxide films potentially reduces surface roughness by smoothing out micro-roughness. This phenomenon will be further investigated using a probe scanning microscope and a microprofilometer, which will allow us better understanding about the oxide film affection to the surface roughness of the grooves.

Multi-stage laser processing made it possible to obtain through-holes with a diameter of up to 600 microns in a 2 mm thick steel plate. During the work, the geometric dimensions of the holes were monitored and their taper was calculated, which amounted to a value of about 0.05, which meets the requirements for the input channels of the microfluidic chip.

REFERENCES

1. **Halimova A.A., Kovalenko A.V., Paramonov G.V.** "Organs-on-a-chip": assessment of prospects for use in the pharmaceutical industry, Medical & pharmaceutical journal “Pulse". Vol. 24 (5) (2022) pp. 81-87.

2. Organs-on-a-chip: A new paradigm for toxicological assessment and preclinical drug development / **D. Bovard, A. Iskandar, K. Luettich** et al. // Toxicology Research and Application. Vol. 1 (2017) pp. 1-16.

3. Microfluidic Organ-on-a-Chip Technology for Advancement of Drug Development and Toxicology / **J. D. Caplin, N. G. Granados, M. R. James** et al. // Advanced Healthcare Materials. Vol. 4 (10) (2015) pp. 1426-1450.

4. Multichannel sensor system for simultaneous polling of several refractometric sensors based on a photonic integrated circuit / **A.G. Zakoyan, G.S. Voronkov, Ya.V. Aleksakina** et al. // Special issue "Photon-express-science". 6 (2023) pp. 135-136.

5. **K. L. Wlodarczyk, D. P. Hand, M. M. Maroto-Valer**. Maskless, rapid manufacturing of glass microfuidic devices using a picosecond pulsed laser, Scientific Reports. 9 (2019) pp. 1-13.

Research and development of terahertz photodetectors based on graphene integrated on a dielectric waveguide

A. N. Lyubchak[1,2,3,✉], **K. V. Shein**[1,2], **P. I. Bondareva**[1,2], **I. A. Gayduchenko**[1], **G. N. Goltsman**[1,2,3]

[1]National Research University Higher School of Economics, Moscow, 101000, Russia;
[2]Moscow Pedagogical State University, Moscow, 119435, Russia;
[3]LCC Scontel, Moscow, 115114, Russia;
*anlyubchak@miem.hse.ru

Abstract.

Terahertz (THz) integrated circuits is a promissing platform to create low cost and efficient components for high-speed sixth-generation (6G) communication networks. One of the key components for this application is detectors and mixers intagrated on THz wavegide. Graphene, due to its unique and tunable properties such as zero band gap, high charge mobility and low electronic heat capacity, has already demonstrated promise in free space THz detector, mixers and modulators development. Moreover, graphene photodetectors integrated on the waveguide have already been demonstrated in visible and near infrared regions. In this work we present simulation results of a graphene-based photodetector integrated on silicon THz waveguide and technological rout to fabricate such type of detector.

Keywords: terahertz, dielectric waveguide, photonic-integrated circuit.

Funding: The research was supported by RSF (project No. 23-72-00014).

Introduction

Graphene is a two-dimensional material that has attracted widespread attention due to its unique properties. It is characterised by a wide light absorption spectrum [1], high light response speed and the ability to change conductivity [2,3], which makes it ideal for use in photonic and optoelectronic devices, including ultrafast graphene photodetectors [4,5].

The development of 6G mobile networks involves the use of the terahertz spectrum band, which plays a key role in enabling data transmission at high speeds of up to a terabit per second over significant distances over wireless networks [6].

Previously, photonic crystal waveguides of the millimeter range were manufactured, created by mechanical processing of laminate printed circuit boards with high dielectric permeability. Waveguides are characterized by a low power attenuation coefficient at a frequency of 145 GHz [7]. At the moment, a bolometric mixer with hot electrons compatible with the technology of integrated silicon photonic crystals operating at 2.7 THz is already being manufactured [8]. The ideas of these two works formed the basis of our work. In this paper, we present a graphene-based photodetector integrated on silicon waveguides. Fabrication of the photonic crystal from silicon enables the use of CMOS.

Results and Discussion

This section presents simulation results of integrated silicon platform operating at 150 GHz. The waveguide structure includes quarter-wave vacuum inserts on the sides, terminating with radiation boundaries. Two wave ports (ports 1 and 2) are used to excite the front and back ends of the waveguide. A tapered slotted line with a graphene sheet between them is modelled with a gold sheet and a lumped port in the centre (port 3). Figure 1*a* shows the electromagnetic model of a 150 GHz silicon waveguide has the following dimensions: taper expansion angle $\alpha = 10^{\circ}$, waveguide width W_{wg} = 585 μm, height L_{wg} = 400 μm, hole period a = 528 μm, hole diameter d = 316 μm. The loss in the modelled structure was 0.18 dB. Figure 1*b* shows the electromagnetic model of a silicon ribbon waveguide integrated with a tapered slot line of length L_{tsl} = 1287 μm, angle $\theta = 165^{\circ}$. Reflection and transmission coefficients with values $S33$=-10 dB and $S31$=$S32$=-4 dB are observed.

a) *b*)

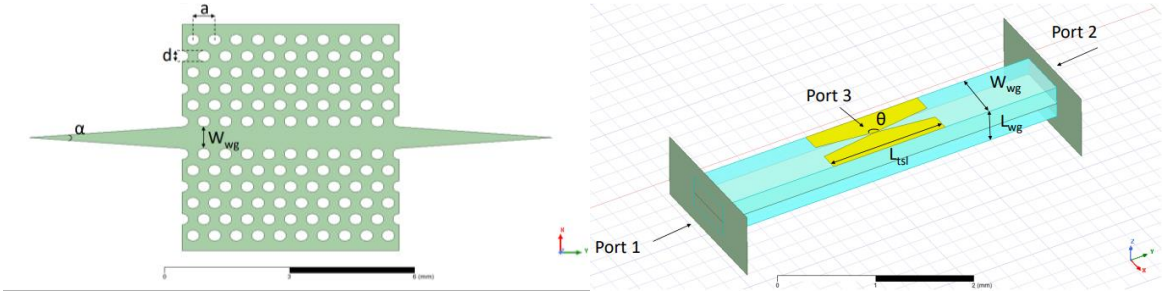


Fig. 1. The electromagnetic model of a 150 GHz silicon waveguide (*a*) and the electromagnetic model of a silicon ribbon waveguide integrated with a tapered slot line (*b*)

Conclusion

A model of graphene-based photodetector integrated on silicon photonic crystal waveguide has been demonstrated. The design has been evaluated by electromagnetic modelling, resulting in an input loss of 0.18 dB. Reflection and transmission coefficients are observed for a graphene photodetector structure with values of *S*33=-10 dB and *S*31=*S*32=-4 dB.

Acknowledgments

The research was supported by RSF (project No. 23-72-00014).

REFERENCES

1. **Xia, F.N.; Wang, H.; Xiao, D.; Dubey, M.; Ramasubramaniam, A**., Two-dimensional material nanophotonics. Nat. Photonics, 8 (2014), 899–907.

2. **Xia, F.N.; Mueller, T.; Lin, Y.M.; Valdes-Garcia, A.; Avouris, P.**, Ultrafast graphene photodetector. Nat. Nanotechnol. 4 (2009), 839–843.

3. **Novoselov, K.S.; Geim, A.K.; Morozov, S.V.; Jiang, D.; Zhang, Y.; Dubonos, S.V.; Grigorieva, I.V.; Firsov, A.A.**, Electric field effect in atomically thin carbon films. Science, 306 (2004), 666–669.

4. **Mueller, T.; Xia, F.N.; Avouris, P.**, Graphene photodetectors for high-speed optical communications.Nat. Photonics 4 (2010), 297–301.

5. **Urich, A.; Unterrainer, K.; Mueller, T.**, Intrinsic response time of graphene photodetectors. Nano Lett. 11 (2011), 2804–2808

6. **Yang, Y., Yamagami, Y., Yu, X., Pitchappa, P., Webber, J., Zhang, B., Singh, R**., Terahertz topological photonics for on-chip communication, Nature Photonics, 14(7) (2020), 446-451.

7. **Prikhodko A. N., Belikov I. I., Lvov A. V., Shurakov A. S., Goltsman G. N**., Millimeter wave photonic crystal waveguides fabricated via direct machining. St. Petersburg State Polytechnical University Journal. Physics and Mathematics, 15 (3.3) (2022) 345–349.

8. **Shurakov, A. S., Belikov I. I., Prikhodko A. N., Ershova, M., Goltsman G. N.**, Superconducting Electronic–Photonic Platform for HEB-Based Terahertz Spectrometers. Applied Sciences, 13(10) (2023), 5892.

Antisolvent modification by carbon nanodots to enhance the performance of $FACsPbI_3$ solar cells

I. V. Margaryan [1,2]✉, E.D. Ogorodnikov[1], L.N. Borodina[1], A.A. Vedernikova[1], E.V. Ushakova[1], A.P. Litvin[3]

[1] ITMO University, Saint-Petersburg, Russia;
[2] Jilin University, Changchun, China;
[3] Harbin engineering university, Qingdao, China
✉igormargaryan@niuitmo.ru

Abstract. Perovskite solar cells (PSCs) draw much attention due to their tremendous progress in power conversion efficiency (PCE) during the last decade. Low-cost and easy-to-fabricate production process makes them promising for next generation photovoltaics. However, perovskites still suffer from high defect density hindering the further improvement of PSCs performance. Antisolvent modification by various additives is emerging approach for passivation of perovskite surface defects. Herin, we demonstrate chlorobenzene (CB) antisolvent engineering by nitrogen-rich amphiphilic carbon nanodots (CNDs). The interaction between functional groups of CNDs and perovskite layer results in improved morphology, defect passivation leading to significant increase of short-circuit current (J_{sc}), fill factor (FF), PCE and stability of PSCs devices.

Keywords: Perovskites, solar cells, carbon nanoparticles, antisolvent.

Funding: The authors thank the Priority 2030 Federal Academic Leadership Program for support of this work.

Introduction

Antisolvent treatment is widely used technique in perovskite solar cell's fabrication process. It facilitates perovskite precursor solution evaporation, promotes heterogenous nucleation and provides uniform polycrystallinity of perovskite layer. However, antisolvent application does not relieve perovskite from the numerous defects such as uncoordinated Pb^{2+} and I^- dangling bonds. These defect states significantly contribute in current loss and perovskite layer deterioration forming deep trap states hindering the current flow and facilitating the ion migration [1]. Therefore, the passivation of surface trap states and grain boundaries is required to address the issue of PSCs performance further improvement. Antisolvent engineering is a relatively new passivation strategy that suggests the introduction of passivators in perovskite layer through antisolvent solution. Upon the application of modified antisolvent the additives are supposed to be distributed on the surface of perovskite layer leading to passivation of the most trap-rich area of perovskite layer. Hence, we studied the passivation of $FACsPbI_3$ layer by CNDs, which are famous for their ability to make bonds through functional groups on their surface [2].

Materials and Methods

SnO2 precursor was spun on ITO substrate at 2000 rpm for 5 s and at 4000 rpm for 30 s followed by annealing at 180 °C for an hour to form ETL and treated with ultraviolet ozone for 20 min before deposition of the next layer. 36 μL of $Cs_{0.1}FA_{0.9}PbI_3$ perovskite precursor was spun at 1000 rpm for 10 s and 5000 rpm for 30 s. 100 μL of pure CB antisolvent or treated with 0.03- 0.15 mg/ml of CD was dripped onto the spinning substrate at the 25th second from the beginning. Thereafter, the perovskite films were annealed at 150 °C for 10 min. Once the samples cooled to room temperature 25 μL of Spiro-OMeTAD precursor was spin-coated at 5000 rpm for 30 s to form a hole-transporting layer. Finally, 80 nm thick Ag electrodes were deposited by thermal evaporation.

Results and Discussion

Resulting device is schematically illustrated in Figure 1a. Obtained PCE upon different CDN concentration shows that at concentration of 0.08 mg/ml PCE reaches its highest value (Figure 1b). Therefore, the determination of appropriate additive concentration is crucial during the perovskite passivation. Whereas open circuit voltage (V_{OC}) values do not show any increase

(Figure 1b), J_{SC} exhibit significantly higher current density at concentration of 0.08 mg/ml (Figure 1c). Figure 1e also shows significant improvement of FF upon CDN antisolvent treatment, which can be also observed in Figure 1f. Increase of J_{SC} and FF may be caused by both morphological improvement and surface trap passivation.

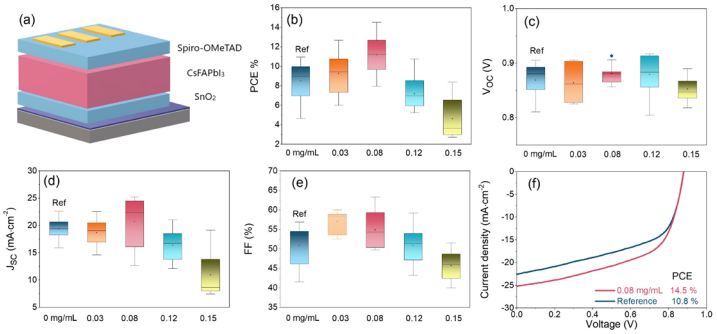


Fig. 1. Schematic architecture of fabricated PSCs (*a*). PCE (*b*), Voc (*c*), Jsc (*d*), and FF (*e*) for the devices fabricated with different amount of CD in the antisolvent. J-V curves (*f*).

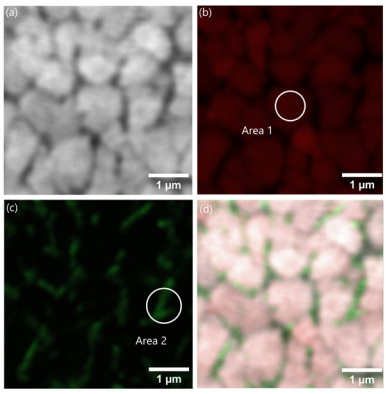


Fig. 2. CLSM analysis of a perovskite film fabricated with 0.08 mg/mL CDs in the antisolvent. Optical image of a polycrystalline film obtained in a reflection mode (*a*), PL images taken in 650−720 (*b*) and 450−570 nm spectral ranges (*c*), superimposed image (*d*).

In the CLSM images of perovskite film treated by modified antisolvent (Figure 2a-d) the red and green emissions are attributed to perovskite and CNDs photoluminescence, respectively. That indicates the presence of CNDs on the surface of perovskite film. Moreover, it can be clearly seen that CNDs are distributed mainly at perovskite grain boundaries implying efficient CNDs-perovskite bonds formation and defect passivation. We speculate that this interaction is the main reason of J_{SC} and FF improvement and overall CNDs-treated PSCs photovoltaic parameters enhancement.

Conclusion

In summary, we demonstrated that nitrogen-rich amphiphilic CNDs as antisolvent modifiers significantly improve the performance of PSCs mainly due to interaction between functional groups of CNDs and dangling bonds on the surface of perovskite layer. This approach may contribute in elucidation of additive engineering during PSCs fabrication.

Acknowledgments

The authors express their gratitude to the ITMO University Core Facility Center "Nanotechnologies".

REFERENCES

1. **X. Sun, D. Li, L. Zhao, Y. Zhang, Q. Hu, T.P. Russell, F. Liu, J. Wei, H. Li,** (111)-Dominated Perovskite Films by Antisolvent Engineering, Advanced Materials 35 (2023) 2301115.

2. **J. Liu, R. Li, B. Yang,** Carbon Dots: A New Type of Carbon-Based Nanomaterial with Wide Applications, ACS Central Science 6 (2020) 2179–2195.

A study of laser cleaning of paper with fat-containing contaminations

A. D. Neelova ✉, **T.K. Lepekhina, D.V. Zhurba, V.A. Parfenov**
Saint-Petersburg State Electrotechnical University «LETI», Saint-Petersburg, Russia;
✉angelina.neelova@gmail.com

Abstract. This paper is devoted to investigation of laser cleaning of paper with fat-containing contaminations. In recent years, laser technologies have been widely used in the preservation of Cultural Heritage (CH). One of the main fields of laser application in this area is the cleaning of CH objects from natural and anthropogenic contaminations. It is known that there exist two main approaches to the laser cleaning, e.g. dry cleaning and wet cleaning. We will present experimental results of wet laser cleaning with the Ytterbium fibre laser (wavelength of 1064 nm) of fat-containing contaminations from model samples and fragments of a real historical artefact such as XIXth century book.

Introduction

Studies conducted in the last decade have brought significant evidence that laser cleaning has a real potential for application in conservation of paper [1-3]. Laser irradiation could be used for treating various deteriorations such as dust, soot, fungi, foxings, etc.

Paper contaminations with fat-containing substances are highly widespread in conservation practice. There could be found vegetable fat or animal fat, or a combination of both. For example, one of the most common contaminations is “finger grip”, a trace of human skin oils. The removal of such contaminations by traditional conservation methods which imply using organic solvents that could be dangerous for the conservators is a laborious process. Thus, developing of a novel approach to the described problem is an actual scientific task.

The authors of this work have already reported about laser cleaning of different kinds of paper using Ytterbium fibre laser [3-5]. Earlier authors presumed that laser cleaning is suitable only for surface paper contaminations. However it could be different in case of laser cleaning with the use of auxiliary liquid (for example distilled water), so called wet cleaning. The technology of wet laser cleaning is well-known in the field of cleaning stone and metal [6].

Experiment

During the experiment model paper samples as well as fragments of a real historical artefact were cleaned with laser irradiation and later studied. To imitate fat contamination copy paper samples were soaked in olive and castor oils and then put into thermal cabinet with the temperature of 102-104 °C for 12 days. Latter was performed to simulate the process of paper ageing. Fragments of a real artefact, a book of religious content published in the XIXth century, were laser treated as well. Given fragments were contaminated with lamp oil and wax. In the process of wet laser cleaning 5% aqueous solution of sodium hydrogen carbonate ($NaHCO_3$) served as an auxiliary liquid, which is widely used in conservation practice for removing fat contaminations from paper. It is known that sodium hydrogen carbonate decomposes under the temperature higher than 60 °C into sodium carbonate, water and carbon dioxide. By using thermal processes that occur during laser ablation we can achieve such chemical reaction to “whip out” fat molecules from paper fibres.

Results and Discussion

Preliminary study of reflectance of model paper samples contaminated with oils gave us an information that dry laser cleaning could not give positive results due to the fact that on the working wavelength of laser (1064 nm) the paper reflects nearly 90% of the irradiation. The fact was proved empirically.

In case of wet laser cleaning it was shown that use of laser irradiation with following parameters: wavelength of 1064 nm, pulse duration of 100 ns, peak power density varies from $1.6 \cdot 10^5$ W/cm^2 to $3.2 \cdot 10^5$ W/cm^2, the pulse repetition frequency of 20 kHz makes possible an effective removal of fat-containing contaminants. Wet laser cleaning performed on the model paper samples as well as on the fragments of the historical book was a success. Treated areas were considerably lighten in colour. It was noticed that wax contamination was removed as well. The results are shown in Figure 1.

a) b)

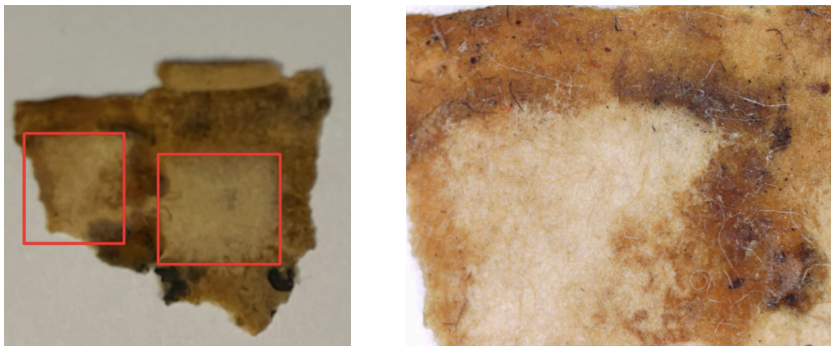


Fig.1. Fragment of artefact book after laser cleaning (a). Cleaned areas are marked in red. Images by optical microscope of laser treated area (b).

Images obtained by the means of scanning electron microscopy proved that the laser irradiation caused no visible damage to the paper fibres. Fourier Transform Infrared (FTIR) spectra were obtained to prove the efficacy of laser treatment.

Conclusion

Removing fat-containing contaminations from paper showed the advantage of wet laser cleaning of paper in relation to the given task. Paper samples as well as fragments of an artefact were successfully cleaned from lamp oil and wax during the experiment. Investigation of laser treatment results by means of optical microscopy and scanning electron microscopy showed no damage to the paper after laser treatment. FTIR spectroscopy proved the efficacy of laser treatment. Nevertheless further investigations of the laser irradiation influence on paper and its chemical and mechanical as well as other properties are needed.

REFERENCES

1. **Kautek W.** Chapter 2.4 of Handbook on the use of lasers in conservation and conservation science. Brussels, COST Office, 2008.
2. **Mokrushin Yu. M., Parfenov V. A.** // Journal of Optical Technology, 2008, V. 75, P. 476-477.
3. **Parfenov V., Galushkin A., Tkachenko T., Aseev V.** // Quantum Beam Science, 2022, V. 6, No. 3, P. 23.
4. **Neelova A. D., Vasilieva A. V., Rongonen S. L., Vasiliev O. S., Safronov D.V., Parfenov V. A.** // Proceedings of the IEEE Conference of Russian Young Researchers in Electrical and Electronic Engineering (EIConRus). 2022, P. 1134-1137.
5. **Neelova A. D., Shepilova E. M., Nosova E. I., Rongonen S. L., Parfenov V. A.**// St. Petersburg Polytechnic University Journal. Physics and Mathematics. 2023.V. 69. №. 3.2. P. 114-119.
6. **Parfenov V. A.** // Proceedings of Saint-Petersburg Electrotechnical University, 2017, №10. P. 62–74.

Nano-sized red LEDs based on GaPNAs nanowires synthesized on silicon substrates

K. N. Novikova [1✉], **A. S. Goltaev** [1], **A. A. Maksimova** [1,2], **A. K. Kaveev** [3], **V. V. Fedorov** [1,4], **A. M. Mozharov** [1,4]

[1] Alferov University, Saint Petersburg, Russia;

[2] Saint Petersburg Electrotechnical University "LETI", Saint Petersburg, Russia

[3] Ioffe Institute, Saint Petersburg, Russia;

[4] St. Petersburg State Polytechnic University, Saint Petersburg, Russia

✉novikova_k@spbau.com

Abstract. In this work, we present a method for the synthesis of radial pin p-GaP/GaPNAs/n-GaP heterostructures on a silicon substrate using molecular beam epitaxy. Nano-sized red light-emitting diode structure was created and its optical properties were studied.

Keywords: Red LEDs, GaPNAs, GaP, molecular beam epitaxy, «core-shell».

Funding: The study was funded by the St. Petersburg Science Foundation grant (23-RB-02-08).

Introduction

One of the promising directions in the development of modern electronics is the creation of integrated optoelectronic circuits, where, for example, waveguide optical connections or light-emitting elements can act as optical elements. A perspective material for creating such devices is gallium phosphide. This semiconductor material has a wide bandgap of 2.27 eV with indirect zone structure and a relatively high refractive index beside other visible transparent material. The initially indirect gap material GaP becomes direct gap with the addition of nitrogen and arsenic, which makes it possible to create optoelectronic devices based on it, for example, red light-emitting diodes. Thus, in [1], a method for creating a light-emitting heterostructure based on planar GaPNAs layers is presented, but planar layers may contain the parasitic influence of defects in the crystal structure. [2] Relaxing elastic stresses on the nanowires (NWs) side make possible to synthetize high crystalline quality NWs arrays even on mismatched substrates, such as Si [3], which can reduce the cost of production.

Materials and Methods

In this work, we proposed the creation of light-emitting structures based on GaPNAs nanocrystals. Also, we presented the synthesis by molecular beam epitaxy of ordered radial p-i-n core-shell heterostructures p-GaP/GaPNAs/n-GaP on a silicon substrate. The resulting homogeneous arrays of NWs were studied by scanning and transmission electron microscopy. To study the electrical properties of the resulting structures, contact mesas were formed from ITO to NW arrays. The fabrication of an ohmic contact to the Si growth plate was carried out using aluminum deposition. SU-8 photocurable resin was applied between the bottom and top contacts to provide electrical insulation. (Fig.1)

a) *b)*

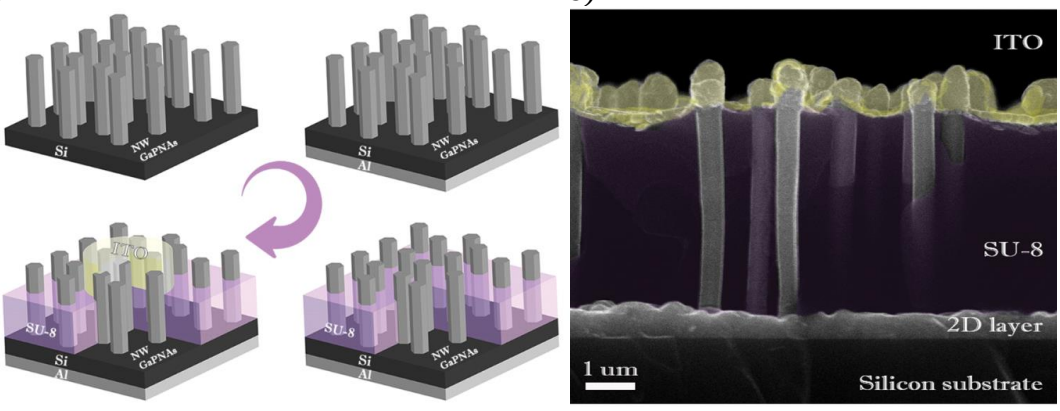


Fig. 1. Scheme of creating a light-emitting structure (a) and SEM-image of the resulting structure (b).

Results and Discussion

The measured current-voltage characteristics of the synthesized structure showed a diode dependence, and the glow of individual NWs was observed. (Fig.2)

a) *b)*

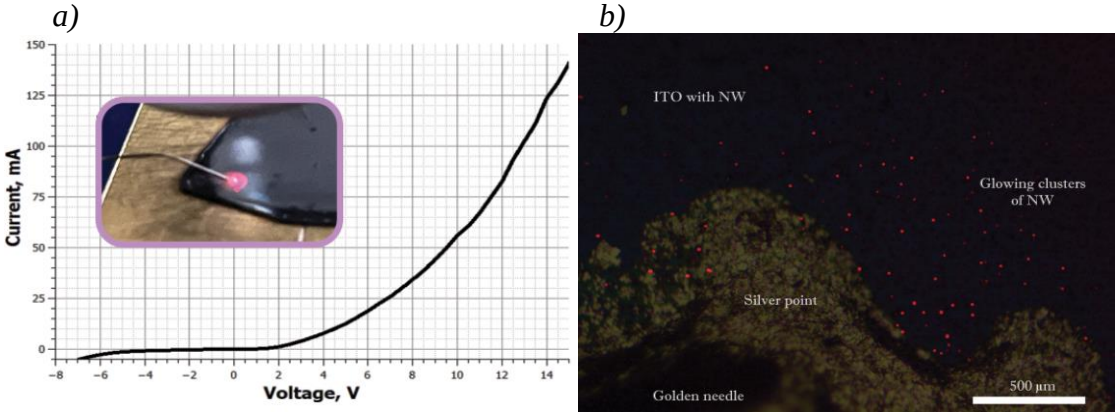


Fig. 2. Current-voltage characteristic of the LED, in the inset is an image of a luminous structure at the probe station (a) and optical image of the measured structure (b).

The resulting electroluminescence and photoluminescence spectra showed a peak with a maximum at a wavelength of about 700 nm. (Fig.3) The asymmetrical shape of the electroluminescence peak may indicate the presence of built-in nitrogen levels in the GaP bandgap.

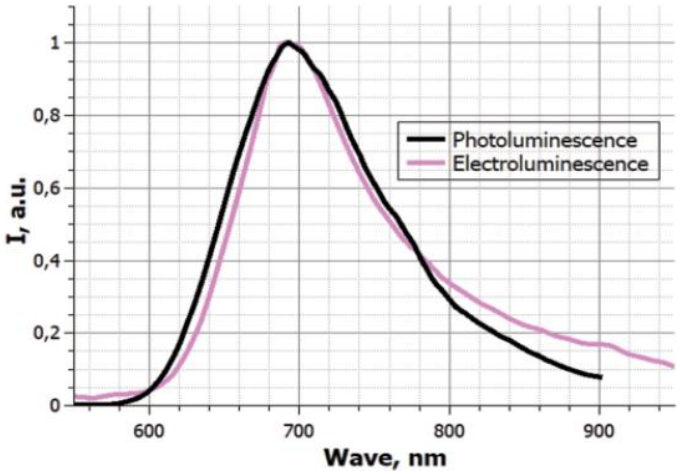


Fig. 3. Spectra of photoluminescence and electroluminescence

Conclusion

This work for the first time demonstrates the synthesis of radial NWs with a GaPNAs insert, which, due to their geometry, can be used as flexible LEDs, RGB displays or bright screens. Nano-sized red LEDs based on GaPNAs nanowires was created and its optical properties were studied.

Acknowledgments

The study was funded by the St. Petersburg Science Foundation grant (23-RB-02-08).

REFERENCES

1. **Fedorov V. V.** et al. Dual-functional light-emitting and photo-detecting GaAsPN heterostructures on silicon // Mater Sci Semicond Process. 2023. Vol. 168. P. 107867.

2. **Schöne J.** et al. Defect Formation and Strain Relaxation in graded GaPAs/GaAs, GaNAs/GaAs and GaInNAs/Ge Buffer Systems for high-efficiency Solar Cells // J Phys Conf Ser. 2013. Vol. 471. P. 012008

3. **Fedina S. V.** et al. Processes of formation of epitaxial arrays of self-catalytic GaP nanowires on Si (111) // J Phys Conf Ser. 2021. Vol. 2103, № 1. P. 012127.

Studying the color characteristics of painting materials using spectrophotometry

O. A. Pironin [1✉], **L. A. Smirnova** [2], **V. A. Parfenov**[1]
[1] Saint Petersburg Electrotechnical University "LETI" Saint Petersburg, Russia
[2] Academy of Fine Arts, Saint Petersburg, Russia
✉oapironin@stud.etu.ru

Abstract. This study presents a comparative analysis of the color characteristics of three industrially produced monopigment inks: Ochre Gold (yellow iron oxide), Sienna Natural (yellow iron oxide), and Sienna Natural (natural earth). The study was carried out using the non-destructive analytical method of spectrophotometry, usually used for studies of works of painting in combination with the methods of X-ray fluorescence spectrometry, as well as Raman and FTIR spectroscopy. The reliability of the study information was ensured by the necessary number of measurements of several samples of each paint, also two ways of analyzing the data were used. The first method is a comparison of a complete series of measurement values in the form of spectral curves of the visible part of the spectrum. The results are clearly presented in the form of charts that allow a quick evaluation of the data ratio of the three different colors. The second method is to automatically search for a reference (standard). A special function of the spectrophotometer is used - making comparisons with reference samples of the measured sample. The analysis established similarities and differences in the color characteristics of yellow iron oxide and natural earth pigments. The analysis of the obtained data, allowed us to draw conclusions about the importance of the information indicated by the manufacturer of paints on the packaging. The results obtained have practical relevance for artists in the choice of colors, to achieve a stable result. The prospect of further application of spectrophotometry for analyzing the properties of art materials is noted.

Keywords: Spectrophotometry, color perception, painting research, paints
Funding: No external funding was obtained for this study.

Introduction

The choice of artistic means is a key aspect of the process of creating a work of art that determines the final result. Often artists do not have exhaustive competence in the field of paint production, they rely on the main information of the manufacturer's labels - the name of the paint describing the color. Additional information on composition and properties is often overlooked. Nevertheless, a legitimate question arises: how important is information about the composition of paints and does it contribute to making the best decision when choosing a paint?

A deeper understanding of the optical properties of modern paints at the disposal of artists can be helped by the application of specialized analytical research methods [1, 2]. One of them is the spectrophotometric method, which allows accurate comparative evaluation of color characteristics and identification of pigment by them [3, 4].

The object of the study was monopigment inks. According to the manufacturer's information, two of them with the names "Ochre Gold" and "Sienna Natural" contain the same pigment - yellow iron oxide. The third paint with the name "Siena Natural" contains a pigment, natural earth. The spectrophotometer became our faithful assistant in comparing the color characteristics of the color of these inks.

Materials and Methods

In the framework of this study, a Spectroguide 45/0 gloss spectrophotometer manufactured by BYK - Gardner Gmbh (Germany) was used to test modern art materials. This device is designed to adapt to the peculiarities of the human eye [5].

During the experimental part of the study were analyzed color characteristics of the samples of the studied paints, prepared taking into account the requirements of GOST in the study of paint

coatings. These samples are specially prepared substrates on the surface of which a paint layer has been applied [6]. Water-based paints (acrylic and tempera based on polyvinyl acetate dispersion) produced by "Nevskaya Palitra" company were chosen for the study. The product line of this manufacturer includes several series of paints, including the ones under study: "Ladoga" - paints for beginners, and "Master-class" - professional paints of high quality. The study focused on examining the color characteristics of the color samples obtained. It was necessary to understand how different pigments in the composition of paints with the same name affect their color and the perception of this color by the human eye.

Results and Discussion

Two methods of comparing paints were used: 1) "Sienna Natural", containing the pigment yellow iron oxide; 2) "Ochre Gold", pigment - yellow iron oxide; 3) "Sienna Natural", pigment - natural earth. The first method was to compare the dependence of reflectance characteristics on wavelength. The spectrophotometer's "Auto Search Standard" function was used in the second method to examine the colorful samples. The analysis established differences in the color characteristics of the pigments yellow iron oxide and natural earth. The data were correlated with the results of measurements of samples of monopigment paint "Siena" produced on the basis of pigment - yellow iron oxide, which is not traditional for paint of this color. The fixed differences are due to the peculiarities of the production process, the quality of the raw materials and the composition of the paints. The results of the analysis are clearly presented in the comparison charts.

Conclusion

Our analysis allowed us to draw an important conclusion about the differences between inexpensive and professional paints. Which emphasizes the value of the information printed on the colorful tubes in "small print", the importance of its interpretation and the need for a conscious approach to the choice of paints by artists.

The findings have significant practical value for artists seeking predictable and stable results in their creative endeavors. Understanding the color characteristics of different paints and the influence of pigment type on the final result allows artists to make more informed decisions when choosing materials and achieve the desired effects in their works.

The obtained data emphasize the prospect of further study of optical properties of art materials and works of art using spectrophotonometry methods.

REFERENCES

1. Trachtenberg A, Malka O, Kootery KP, Beglaryan S, Malferrari D, Galletti P, et al. Colorimetric analysis of painting materials using polymer-supported polydiacetylene films, New J Chem. 40 (11) (2016) 9054–9059.

2. Marchiafava V, Bartolozzi G, Cucci C, De Vita M, Picollo M. Colour measurements for monitoring the conservation of contemporary artworks, Journal of the International Colour Association. 13 (2014) 36–42.

3. Maines C, Johnston-Feller R. Color Science in the Examination of Museum Objects, Journal of the American Institute for Conservation. 41 (2) (2002) 194 p.

4. Jabr Y. J., Smirnova L. A., Parfenov V. A. Study of color characteristics of pigments and paints by spectrophotometer, St. Petersburg State Polytechnical University Journal: Physics and Mathematics. 16 (3.2) (2023) 171–176

5. International Commission on Illumination. A method for assessing the quality of daylight simulators for colorimetry /International Commission on Illumination, CIE. Vienna: CIE Central Bureau. (1999) 36 p. (Technical Report / CIE).

6. JSC Quality Control [Internet]. [cited 2024 Mar 30]. Quality control of paint and varnish materials and coatings. Available from: https://qualicont.ru/doc/byk-coatings.pdf

Development of an experimental device for measuring the internal stresses of single crystal diamond plates

I. O. Podoylov[1]✉, **A. A. Kharlamova** [1]

[1] Department of Fundamental and Applied Physics, Northern Arctic Federal University named after M.V Lomonosov 1, Arkhangelsk 1, Russia;

✉ i.podojlov@narfu.ru

Abstract. The paper presents a stand for measuring the internal stresses of monocrystalline diamond plates. The device is necessary to assess the quality of single crystal diamond plates as promising materials for quantum sensing. The use of diamond plates in engineering and instrumentation is limited by their quality. The device under development is used to assess the quality of the diamond plate according to the internal voltage indicator. The resulting device is an optical microscope with a modified polarizer system based on the phenomenon of double refraction and capable of detecting changes in the anisotropy coefficient of the sample under study. Also, software was developed for the stand that allows analyzing the received data. The result of the work of the stand is a map of the internal stress distributions in the test sample. The stand was tested on monocrystalline diamond plates with various anisotropy indicators. The results showed the effectiveness of the developed device, which recorded the internal stresses in the plates in all areas of graphitization, in places of cracks, etc.

Keywords: anisotropy, polarizers, internal stresses, diamonds, optical microscope.

Funding: The research was carried out with the support of the state assignment of the Russian Federation No. FSRU-2024 -0005 and the Russian Science Foundation, project No. 23-12-20014.

Introduction

Today, the possibility of using synthetic diamond plates in the technological field is of increasing interest. The high sensitivity of diamond plates to magnetic fields opens up the possibility of their use as high-precision contactless electric current sensors in a wide range of measurements. Careful quality control is required to produce high-tech devices using diamond plates. The most important parameter for evaluating the quality of the plate is the presence of internal stresses. In the process of growing diamond plates and processing them, internal stresses may occur, which can lead to problems during their operation [1-5]. In addition, this leads to a change in optical parameters, which leads to a decrease in the sensitivity of such elements. In this regard, it became necessary to develop a device for detecting internal stresses (Fig.1).



Fig. 1. The device and its optical scheme

Materials and Methods

The principle of operation of the developed stand is based on the phenomenon of double refraction. Diamond plates have the optical property of anisotropy, i.e. the refractive index of such a material depends on the direction of light propagation. In this paper, a device is presented that registers the change in anisotropy. The developed stand is based on the Levenhuk MD 30 T optical

microscope, modified by a rotating linear and circular polarizer system. Additionally, an electronic 2D positioning system was developed that allows moving the slide table with the sample under study.

Results and Discussion

As a result, a stand has been developed that allows recording internal stresses in diamond plates. The device gives an estimate of the magnitude of the anisotropy, and shows the value of the difference in the refractive index of ordinary and extraordinary rays. The result of the stand is a snapshot of internal stresses in a color code, each color of which corresponds to a certain indicator of anisotropy (Fig. 2).

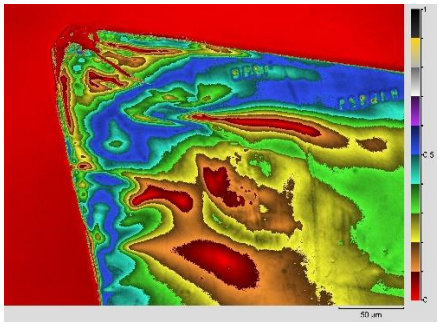


Fig. 2. Internal stress distribution map of the diamond plate

Conclusion

As a result, a stand was developed that allows to record internal stresses in diamond plates. The stand has been successfully tested on monocrystalline diamond plates and has shown its effectiveness.

Acknowledgments

The authors express their gratitude to AGD DIAMONDS for the resources provided during the development of the stand.

REFERENCES

1. **Glazer A. M., Lewis J. G., Kaminsky. W.,** An Automatic Optical Imaging System for Birefringent Media: Mathematical, Physical and Engineering Sciences 452 (1996) 2751-2765.

2. **Howell. D.,** Strain-induced birefringence in natural diamond: a review: European Journal of Mineralogy 24, (2012) 575–585.

3. **Howell. D., I. G. Wood I. G.,** Quantifying strain birefringence halos around inclusions in diamond, Contributions to Mineralogy and Petrology 162, (2013) 1113-1113.

4. **Bulanova G.P., Griffin W.L., Ryan C.G.,** Nucleation environment of diamonds from Yakutian kimberlites: Mineral. Mag. 62, (1998) 409–419.

5. **Howell D., Woods I.G., Nestola F., Nimis P., Nasdala L.,** Inclusions under remnant pressure in diamond: A multi-technique approach, Eur. J. Mineral., 24, (2012) 563–573.

Experimental study of the broadband optical source with hybrid amplification

A. I. Pozdniakov [1]✉, **E. I. Andreeva** [1]

[1] St. Petersburg State University of Telecommunications. prof. M.A. Bonch-Bruevich, St. Petersburg, Russia;

✉me022@mail.ru

Abstract. The possibility of jointly using erbium-doped and distributed Raman amplifiers to obtain a broadband optical radiation source has been demonstrated experimentally. Components typical for WDM-systems were used. The possibility of significant broadening of the spectrum in an optical fiber due to its nonlinear properties is demonstrated.

Keywords: fiber-optic communication system, Raman amplifier, erbium amplifier, optical fiber, nonlinear effects.

Introduction

Changing the spectrum of an optical signal transmitted along a fiber light guide is of ever-increasing interest for creating systems for generating ultrashort high-power optical pulses and creating broadband radiation sources, including supercontinuum sources [1-3]. The use of standard WDM components to produce broadband powerful radiation sources is of particular interest.

An experimental study of the possibility of creating the broadband optical source showed the feasibility of hybrid (local + distributed) signal amplification in optical fiber.

The aim of this work is to study the possibility of creating a broadband measuring source using a semiconductor laser and the nonlinear properties of an optical fiber.

Experimental Results and Discussion

The block diagram of the experimental setup is shown in Fig. 1. The optical signal from the narrow-band laser (1) enters the input of the erbium-doped fiber amplifier (EDFA) (2). Amplification occurs practically without changing the spectral characteristics. In the optical fiber (4) pumped simultaneously with the signal from 4 lasers in such a way that the frequency range and possible polarization mismatch are completely covered. As a result, the optical signal is further amplified, and its spectrum is broadened. The optical spectrum was monitored by the optical spectrum analyzer (OSA) (5).

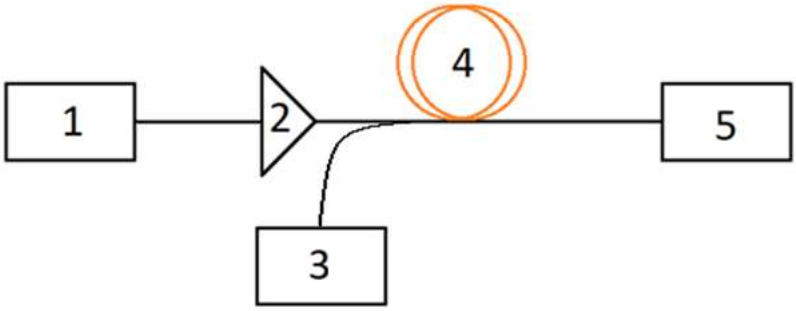


Fig. 1. Block diagram of the experimental study: 1 – optical pulse laser source, 2 — EDFA, 3 – Raman amplifier, 4 – optical fiber, 5 – OSA.

The results of measuring the signal spectrum at the input to fiber optic line 1, using only erbium amplifier 2 and with additional Raman amplification 3 are shown in Fig. 2.

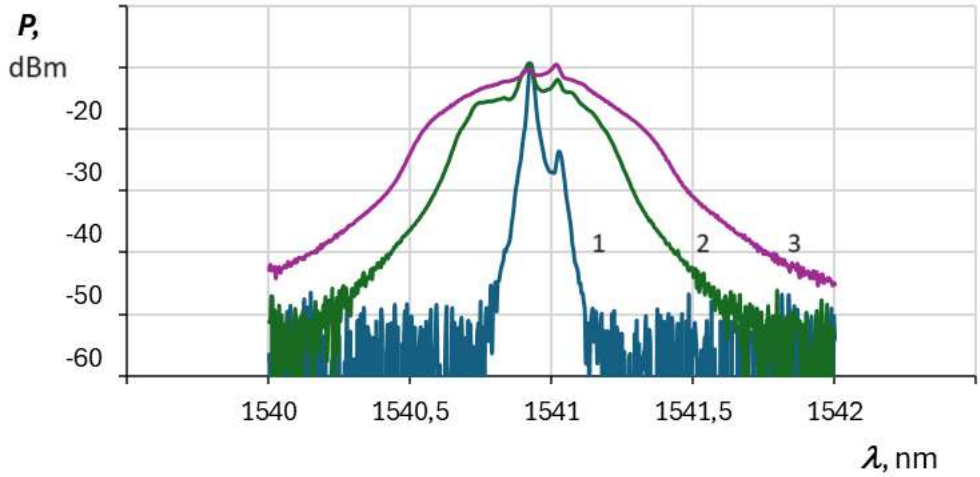


Fig. 2. The optical signal spectrum at the input to the optical fiber (1), at the output of the optical fiber using only erbium amplifier (2) and with additional Raman amplification (3).

To enhance this effect, additional pump lasers and/or a dispersion-shifted fiber can be used.

Conclusion

Thus, the possibility of broadening the spectrum of an optical signal in the optical fiber using standard components has been demonstrated. To enhance the effect, the optical fiber with shifted (reduced) dispersion can be used.

REFERENCES

1. **Agrawal G.** Nonlinear Fiber Optics, 6th Edition, Elsevier, 2019**.**

2. **A. Isupov, D. Andreev, E. Andreeva.** The broadband light source modeling using the optical fiber nonlinearity, Proc. of ITNT-2023, vol, p.10922, Samara, 2023.

3. **Agrawal G**. Fiber-Optics Communication Systems, 5th Edition - New York, 2021.

EXPERIMENTAL STUDY OF THE USE OF OPTICAL CABLES WITH DIFFERENT TYPES OF FIBERS IN MONITORING SYSTEMS

V. E. Pylaev [1]✉, **E. I. Andreeva** [1]

[1] St. Petersburg State University of Telecommunications prof. M.A. Bonch-Bruevich, St. Petersburg, Russia

✉e-mail: me022@mail.ru

Abstract. The comparative study of the sensitivity to local vibration of the single-fiber optical cable with the standard singlemode optical fiber (SSMF) and the optical fiber with reduced bending losses (BLIF) was carried out. The measurement was carried out for a single vibration action – the fall of a kettlebell, and the harmonic acoustic signals. During the experimental study, the advantage of the used optical cable with BLIF was revealed.

Keywords: fiber-optic reflectometers, optical fiber, SSMF, BLIF, Rayleigh scattering, DAS, fiber-optic acoustic distributed sensor.

Introduction

The distributed fiber-optic physical field sensors occupy a special place among sensor systems and represent a wide class of devices for a wide range of applications. The advantages of fiber-optic sensors over electrical ones are the possibility of a completely passive design, variety of shapes, immunity to electromagnetic interference and aggressive environments [1-3], small size and weight. As a result, they can be used in explosive atmospheres, flammable mixtures and strong electromagnetic fields [1-3]. Such fiber systems consist of a sensitive element - a conventional optical fiber - and a unit for generating an optical probing signal and analyzing the signal backscattered in the fiber. The operating principle is based on the time domain reflectometry technique (Optical Time Domain Reflectometer, OTDR). Local measurement of physical parameters using such sensors makes it possible to monitor in real time.

The purpose of this work is to study the influence of the choice of the optical fiber as part of a distributed sensor system on its parameters and the possibility of increasing spatial resolution when testing an object with a coherent reflectometer due to the optimal choice of optical fiber.

Experimental study

At the test site, a trench was dug in the ground 120 cm deep, 30...40 cm wide, 30 m long. An optical cable was laid into the trench every 30 cm in height, starting from the bottom of the trench and covered with soil. After compacting the optical cable with soil, a period of 2 ... 3 weeks was maintained in the trench to stabilize the system parameters. The schematic block diagram of the measuring stand is shown in Fig. 1.

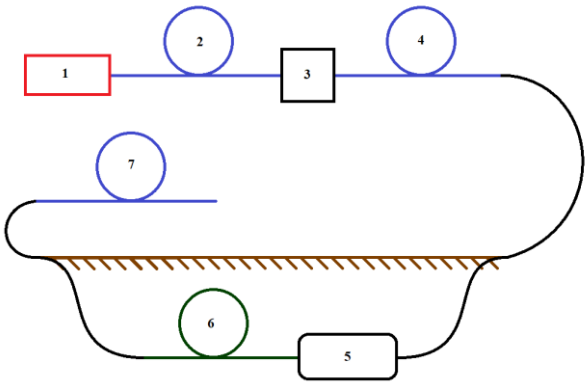


Fig. 1. Structural block diagram of the measuring stand: 1 – coherent optical reflectometer, 2 – optical fiber, 3 – optical 19” cross-panel, 4 – multi-fiber optical cable, 5 – optical coupling for splicing a multi-fiber fiber-optic cable with test samples of optical cables in the trench, 6 – optical cable (segment) under test, 7 – optical fiber.

The tested optical cable 6, using an optical coupling 5, was commutated with a multi-fiber trunk cable 4, connected through a normalizing coil 3 to the coherent reflectometer Danube 1. An effect is made next to the cable: turning on sound at various frequencies from a reference frequency generator. To create a vibration-acoustic effect, an acoustic system was used, to which a harmonic signal was supplied. Signal frequencies varied from 5 Hz to 200 Hz.

Results and Discussion

The tested optical cable samples differed in the type of optical fiber. In the first case, a standard optical fiber (SSMF, Standard Singlemode Fiber) was used, in the second case, the fiber with reduced bending losses (BLIF, bending-loss insensitive single-mode optical fiber) was used (Fig. 2). Fiber parameters: dispersion D=16.67 ps/nm/km (β_2 = 20 ps^2/km), loss 0.2 dB/km at operating wavelength λ=1550 nm.

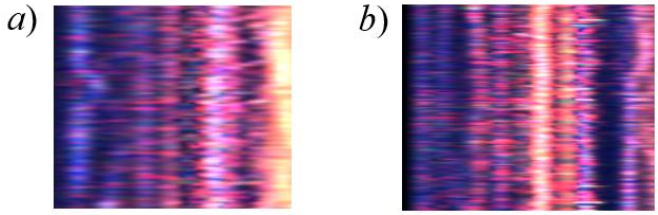


Fig. 2. “Waterfall” for recording vibration effects with an optical cable with SSMF (a) and with BLIF (b)

Table presents the results of measuring the response for the case of a weight (inert projectile) 10 kg weight falling at a distance 10 m from the optical cable route.

Table 1

Energy of the reflectometer signal – response to vibration impact

Optical Fiber	Depth *l*, cm		
	l_1 =60 cm	l_2 = 90 cm	l_3 = 120 cm
SSMF	4,9	1,8	1,0
BLIF	5,1	3,94	3,0

The table shows that for a dumbbell weighing 10 kilograms, the signal energy is greater, therefore the effect is better discernible if the optical fiber with reduced bending losses is used as a sensor element.

The maximum permissible detection range is also longer for an optical cable with the optical fiber with reduced bending loss.

Conclusion

The comparative study of the sensitivity to point vibration effects of a single-fiber optical cable with the standard optical fiber and the optical fiber with reduced bending losses was carried out. The measurements were carried out for a single vibration impact - dropping a weight, and harmonic acoustic impact. An experimental study revealed the advantage of using an optical cable with the optical fiber with reduced bending losses.

REFERENCES

1. **Nikitin S., Fomiryakov E., Kharasov D., Nanii O., Treshchikov V.**, Characterization of ultra-narrow linewidth lasers for phase-sensitive coherent reflectometry using eom facilitated heterodyning. Journal of Lightwave Technology. 2019. Vol. 38. No. 6. PP. 1446−1453.

2. **Cunzheng Fan, Hao Li, Keqing Zhang, Huanhuan Liu**, 300 km ultralong fiber optic DAS system based on optimally designed bidirectional EDFA relays. Photonics Research, vol. 11, no. 6, p. 968-977, 2023.

3. **Andreev D., Andreeva E., Podnikolenko A**. Finding the Route of Laying the Optical Cable Using the Coherent Reflectometer. 2022 International Conference Laser Optics (ICLO), 2022, pp. 1-1.

Calibration of the parameters of the polarization controller for polarization control algorithms

N. V. Rudavin[1,3,5] ✉, P. A. Kupriyanov[1,2,3], V. F. Mayboroda[1,3], V. Y. Iashchuk[1], R. A. Shakhovoy[1,2,3,4]

[1]QRate, Novaya av. 100, Moscow, Russia;
[2]Moscow Institute of Physics and Technology, 9 Institutskiy per., Dolgoprudny, Moscow Region, 141701, Russian Federation;
[3]NTI Center for Quantum Communications, National University of Science and Technology MISiS, Leninsky prospekt 4, Moscow 119049, Russia;
[4]Russian Quantum Center, Bolshoy Boulevard 30, bld. 1, Skolkovo, Moscow 121205, Russia;
[5]HSE University, 20 Myasnitskaya ulitsa, Moscow 101000, Russia
✉rudavinnv@yandex.com

Abstract. In various applications of optical communication, such as coherent communication or quantum key distribution (QKD), a polarization controller on the receiver's side is typically used to control the polarization of light in an optical fiber. For the effective operation of some polarization control algorithms, it is necessary to know the half-wave voltage and the bias voltage of the polarization controller. In this paper, we propose simple and robust methods to calibrate these parameters in QRate commercial QKD system.

Keywords: polarization control algorithm, quantum key distribution.

Introduction

In commercial implementations of QKD systems, polarization encoding is often used [1]. One of the challenges associated with this approach is the time-varying distortion of polarization states in the quantum channel. This distortion is caused by random birefringence in a standard single-mode fiber, which can occur due to temperature fluctuations or mechanical deformations. These distortions can lead to an increased the quantum bit error rate (QBER) in QKD systems, which reduces the rate of secret key generation. To compensate the impact of polarization states distortion, electronic polarization controllers (EPC) based on fiber-squeezers are often used. Accordingly, for optimal compensation of polarization distortion using these controllers, various algorithms, that utilize the QBER as a minimization function, are being developed.

Polarization control algorithms can be divided into two main groups: those that use information about the internal structure of the controller and those that do not. Some polarization control algorithms, such as those based on the gradient descent method [2], do not use this information. More advanced algorithms, however, take advantage of knowledge of the parameters that define the polarization controller, allowing for rotations at strictly defined angles, depending on previously measured QBER values, thus achieving faster convergence of the algorithm [3].

Materials and Methods

EPCs, which are used in commercial QKD implementations, consist of three or four piezoelectric squeezers which compress the optical fiber at different angles relative to its core. By adjusting the compression ratio of each element by changing the voltage applied to it, it is possible to change the polarization state of the transmitted quantum state in an arbitrary way, thereby compensating for random changes in polarization in the optical fiber ahead of the EPC. To be able to perform a given polarization state transformation, it is necessary to know the half-wave voltages V_π of the actuators. To determine it on the selected actuator, we increased the voltage on it until the SOP vector draws a complete circle on the Poincare sphere. A voltage equal to half of the measured voltage corresponds to the V_π of the actuator. The voltage corresponding to the rotation at an arbitrary angle can be calculated by the formula:

$$V_\alpha = \frac{\alpha}{\pi} V_\pi \tag{1}$$

Due to features of the technical process, EPC actuators can exert pressure on the fiber even when no voltage is applied to it, causing polarization conversion. If EPC with three actuators is used, its side actuators rotate around the X axis, the central actuator rotates the polarization around the Y axis. If a zero voltage on the central one is shifted, then the axes of rotation of the side actuators will not coincide. Since in some polarization control algorithms the relative orientation of the axes is significant, it is necessary to shift the reference scale on the voltage V_{bias} corresponding to the identity transformation. To select the value V_{bias} we first increased the voltage on the first actuator by drawing a full circle on the Poincare sphere, and then increased the voltage on the third actuator to obtain a second circle. By adjusting the voltage on the central actuator, we can ensure that the circles coincide. Then the equality for the rotation matrices will be satisfied:

$$R_X(V_\alpha)R_Y(V_{bias})R_X(V_\beta) = R_X(V_{\alpha+\beta}) \quad (2)$$

Results and Discussion

In our experiment we used polarization control algorithm, that makes an estimation of the partial derivatives of QBER for each of the three orthogonal axes. Based on the results of these measurements, the axis and the angle of rotation are selected on the EPC. The procedure is iteratively repeated until the minimum QBER value is reached. We launched the algorithm with well-chosen V_π and V_{bias}, and also with $V_\pi' = 1.15 \times V_\pi$ and $V_{bias}' = 1.15 \times V_{bias}$. You can see (Fig 1), that mismatching in the parameters' values leads to decrease in the convergence rate.

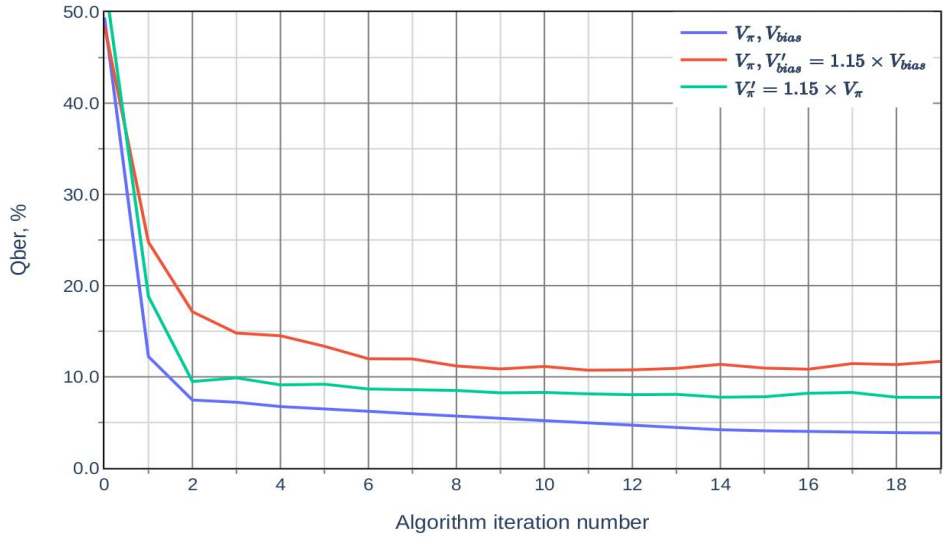


Fig. 1. Dependence of the convergence rate of the algorithm on the accuracy of parameters adjustment

Conclusion

In this work, we proposed calibration methods of the parameters of polarization controller: half-wave voltages and bias voltage of the central actuator. We also conducted experiment showing that the accuracy of the selection of these parameters strongly affects the convergence rate of the polarization control algorithm.

REFERENCES

1. **Gisin, N., Ribordy, G., Tittel, W., & Zbinden, H.**, Quantum cryptography. Reviews of modern physics, 74.1 (2002): 145.

2. **Mekhtiev, E. E., Gerasin, I. S., Rudavin, N. V., Duplinsky, A. V., & Kurochkin, Y. V.** Polarization control algorithm for QKD systems. In Journal of Physics: Conference Series (Vol. 2086, No. 1, p. 012092)

3. **Chen, H., An, X. B., Wu, J., Yin, Z. Q., Wang, S., Chen, W., & Han, Z. F.**, Hong–Ou–Mandel interference with two independent weak coherent states. Chinese Physics B 25.2 (2016): 020305.

Study of the Influence of the Surface Density of In(Ga)As/GaAs Quantum Dots on the Microdisk Laser Characteristics

A. S. Ryupina [1]✉, N. A. Fominykh [1], I. S. Makhov [1], K. A. Ivanov [1], Yu. A. Guseva [2], M.M. Kulagina [2], S. A. Mintairov [2], N. A. Kalyuzhnyy [2], V. V. Andryushkin [3], A. G. Gladyshev [3], D. S. Papylev [3], L. Ya. Karachinsky [3], N. V. Kryzhanovskaya [1]

[1] HSE University, St. Petersburg, Russia

[2] Ioffe Institute, St. Petersburg, Russia

[3] ITMO University, St. Petersburg, Russia

✉ ryupina27@gmail.com

Abstract. Heterostructures with quantum dots of different compositions: InAs/GaAs and $In_{0.4}Ga_{0.6}As$/GaAs were investigated. The 10 times higher surface density of quantum dots corresponds to the $In_{0.4}Ga_{0.6}As$/GaAs. The lower threshold current density and higher output power were observed for microlasers with active region based on quantum dots with higher surface density.

Keywords: microdisk lasers, quantum dots, photoluminescence, surface density.

Funding: This work was supported by the by a grant from the Russian Science Foundation № 22-72-10002, https://rscf.ru/project/22-72-10002/. Development of the structures with InGaPAs quantum dots was supported by the Ministry of Science and Higher Education of the Russian Federation, research project no. 2019-1442 (project reference number FSER-2020-0013). The photoluminescence studies were supported by the Basic Research Program of the National Research University Higher School of Economics.

Introduction

Semiconductor microdisk (MD) lasers can be used as compact radiation sources on microchips due to their high quality factor and small footprint [1]. The active region of MD lasers can be based on quantum dots (QDs) in order to provide low threshold current and high characteristic temperature [2]. The surface density of QDs strongly affects microlaser characteristics [3]. In this work the influence of the surface density of III-V QDs on the threshold current density and output power of MD lasers were studied.

Materials and Methods

All studied structures were fabricated on GaAs substrates by molecular beam epitaxy (MBE) or by metalorganic chemical vapour deposition (MOCVD). For photoluminescence (PL) studies following structures emitting in the same spectral range (~1.1 μm) were grown. The heterostructure PL1 had an active region based on one layer of Stranski-Krastanow InAs/GaAs QDs and the heterostructure PL2 had one layer of $In_{0.4}Ga_{0.6}As$/GaAs QDs. More detailed description of structures PL1 and PL2 may be found in the paper [4] and in the paper [5], respectively. For MD lasers p-i-n heterostructures with multilayer active region similar to PL1 and PL2 structures were synthesized. MD lasers with 32 μm diameter were formed by photolithography and plasma-chemical etching [5].

The PL spectra of heterostructures PL1 and PL2 were obtained in temperature range 4K – 300K. PL was excited by the 527 nm Nd:YLF laser (cw, excitation power was varied from 0.198 mW to 10 mW). The laser beam was reflected by the narrow-band reflection filter and directed to the Mitutoyo M Plan Apo NIR HR 10x objective focusing the laser light on the sample. The same objective collected the sample's PL emission that passed through the narrow-band filter to the monochromator entrance slits and then to the InGaAs detector. Electroluminescence (EL) setup consisted of Keithley 2400 Series SourceMeter® power supply, Mitutoyo M Plan Apo NIR HR 50x objective and a Yokogawa AQ6370C optical spectrum analyser. All the EL studies of the MD lasers were performed in a continuous wave regime at room temperature.

Results and Discussion

The surface density of QDs in PL1 and PL2 structures was obtained from the transmission electron microscopy data (table 1). Different approached to QDs synthesis results in surface density of QDs in order of magnitude higher for PL 2 structure than that for PL1 structure. Studies of the PL spectra at different excitation densities and in temperature range 4-300 K revealed numerous effects associated with saturation of the states in QDs due to limited number of QDs in the layer. For example, the PL study showed that at low excitation power for both heterostructures QD peaks were the dominant lines in the spectra. For the heterostructure 1 increase of the pumping power up to 6 mW results in the appearance of the excited states, wetting layer and GaAs – associated PL lines. However, for heterostructure 2 with higher surface density of QDs such effect is not so pronounced in the studied range of pumping power. Next, we studied lasing characteristics of the MD lasers. The EL studies show that output power was app. 10 times higher for the MD laser formed from the high-density $In_{0.4}Ga_{0.6}As/GaAs$ QDs (table 1) compare to its low-density counterpart. The threshold current density was also found to be lower in the case of heterostructure 1 (table 1).

Table 1. The parameters of the studied samples.

Active region	Surface density, cm^{-2}	Laser emission wavelength, nm	Threshold current density, kA/cm^2	Output power of MD laser, mW
InAs/GaAs QDs	$3 - 5 \cdot 10^{10}$ [6]	1104	0.87	$7.98 \cdot 10^{-4}$
$In_{0.4}Ga_{0.6}As/GaAs$ QDs	10^{11} [5]	1090	1.63	$65.6 \cdot 10^{-4}$

Conclusion

The heterostructures with InAs/GaAs and $In_{0.4}Ga_{0.6}As/GaAs$ QDs of different density were investigated. The results of this work show that microlaser characteristics such as threshold current density and output power can be tuned by changing the surface density of QDs.

Acknowledgments

The work was carried out on the equipment of the unique scientific facility No. 2087168 “Complex Optoelectronic Stand.”

REFERENCES

1. **Zhukov A. E., Kryzhanovskayaa N. V., Moiseev E. I., Kulagina M. M., Mintairov S. A., Kalyuzhnyy N. A., Nadtochiy A. M., & Maximov M. V.**Ultimate Lasing Temperature of Microdisk Lasers. *Semiconductors*, 2020, Vol. 54, No. 6, pp. 677–681.
2. **Shchekin O.B., Ahn J. & Deppe D.G**. High temperature performance of self-organised quantum dot laser with stacked p-doped active region. *Electronics Letters*, 2002, Vol. 38, Is. 14. DOI: 10.1049/el:20020509
3. **Zhukov A.E., Maksimov M.V. & Kovsh A.R.** Device characteristics of long-wavelength lasers based on self-organized quantum dots. *Semiconductors*, 2012, Vol. 46, No. 10, p. 1225-125. DOI:10.1134/S1063782612100223
4. **Balakirev S., Kirichenko D., Chernenko N., Shandyba N., Komarov S., Dragunova A., Kryzhanovskaya N., Zhukov A., Solodovnik M.** Influence of the Arsenic Pressure during Rapid Overgrowth of InAs/GaAs Quantum Dots on Their Photoluminescence Properties. *Crystals*, 2023, T. 13, №. 9, c. 1358.
5. **Maximov M.V., Nadtochiy A.M., Mintairov S.A., Kalyuzhnyy N.A., Kryzhanovskaya N.V., Moiseev E.I., Gordeev N. Yu., Shernyakov Yu. M., Payusov A.S., Zubov F. I., Rouvimov S. S., Zhukov A.E.** Light emitting devices based on quantum well-dots. *Applied Sciences*, 2020, T. 10, №. 3, c. 1038.
6. **Zhukov A.E.** Lasers and microresonators based on quantum dots. POLYTECH-PRESS, 2019, St. Petersburg.

Development of a device for automated measurement photovoltaic characteristics of solar cells

A. V. Saenko, **G. E. Bilyk**, **V. V. Zheits**
Institute of Nanotechnologies, Electronics, and Equipment Engineering,
Southern Federal University, Taganrog, Russia
✉avsaenko@sfedu.ru

Abstract. The paper proposes a capacitive method and develops a device for automated measurement of the photoelectric characteristics of solar cells. The method is to use a capacitor capacitance as a variable load. The main advantage of this method is the speed of constructing the current-voltage characteristic of the solar cell, which eliminates drifts and increases the accuracy of the measured electrical parameters by reducing negative external influences over time, in particular heating of the solar cell and instability of the lighting source. The studies have shown that the error in measuring the photovoltaic parameters of solar cells compared to the values stated in the specification is about 2 %.

Keywords: solar cell, capacitive method, current-voltage characteristic, photoelectric parameters.

Funding: The study was supported by the grant of Russian Science Foundation № 23-29-00827, https://rscf.ru/project/23-29-00827/ at the Southern Federal University.

Introduction

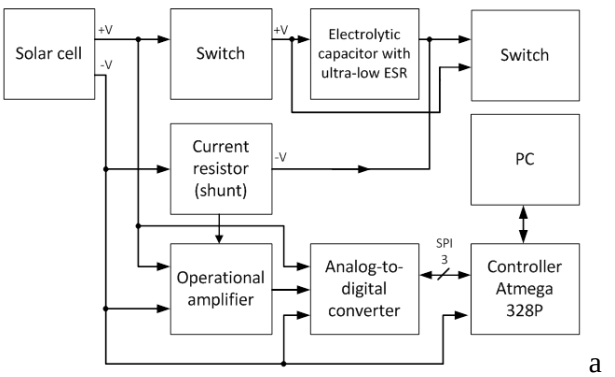
Currently, increasing the efficiency of solar energy conversion and reducing the cost of solar cell manufacturing are the main goals of solar energy. In this regard, control and optimization of photovoltaic parameters in the production of solar cells is essential, which requires the development of promising devices for measuring their photoelectric characteristics and determining parameters [1].

The classic method of measuring the current-voltage characteristic of a solar cell is to connect a variable resistive load to it, which can be a rheostat or a resistance store [1, 2]. A current resistor (shunt) with a known resistance is connected in series with the variable load, which makes it possible to determine the current generated by the solar cell depending on the resistance of the variable load or lighting intensity. Typically, laboratory voltmeters are used as measuring instruments, one of which monitors the voltage drop across the solar cell, and the second monitors the voltage drop across the current resistor. The disadvantage of this method is the long time it takes to measure the current-voltage characteristic, during which the solar cell is illuminated for a long time, which leads to its heating and negatively affects the accuracy of the obtained electrical parameters.

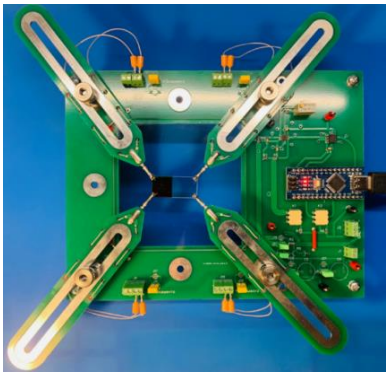
Methods and Discussion

The paper proposes a capacitive method, which consists of using a capacitor capacitance as a variable load. Based on it, a device has been developed for automated measurement of the photoelectric characteristics of solar cells. When the capacitor is in a discharged state and is switched to the solar cell, the maximum current consumption by the capacitor occurs, the value of which corresponds to the short circuit current of the solar cell. As the capacitor charges and reaches its maximum capacity, the solar cell goes into idle mode. A PVG612A high-speed solid-state relay was selected as the switch, and an AD8626 two-channel operational amplifier was used as the amplifier. To digitize electrical parameters, an analog-to-digital converter AD7680 is used. To illuminate the solar cell, a stand based on a halogen lamp with a 150 W reflector was used, the emission spectrum of which is as close as possible to the AM1.5 solar spectrum. Light intensity was determined using a MAX44009 light sensor. This method allows you to obtain the resolution of the measured current-voltage characteristic of tens of thousands of points (measurements) and is limited only by the capabilities of the measuring device or the analog-to-digital converter used.

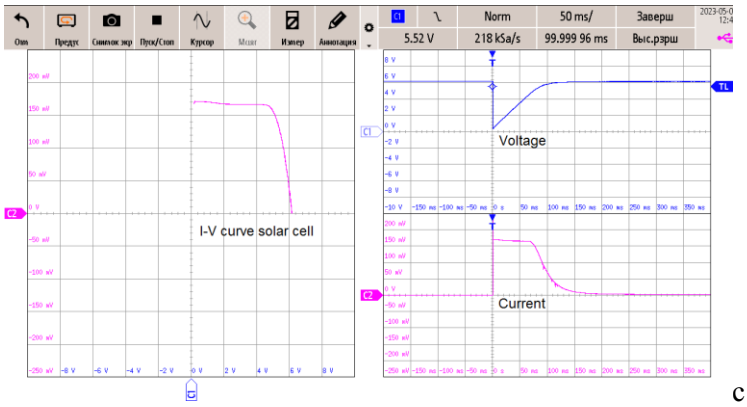
The block diagram and appearance of the developed device based on the capacitive method is shown in Fig. 1 (a, b). To evaluate the accuracy of measuring current-voltage characteristics using the developed device, a test solar cell (area 5 cm^2) with a specified maximum power of 0.775 W (nominal voltage 5 V and current 155 mA) was used. The results of measuring the current-voltage characteristic are presented in Fig. 1 (c), where the maximum power was 0.788 W at a nominal voltage of 4.98 V and a current of 158.31 mA. Thus, the error in measuring the maximum power was about 2 %, which is a good result and may be associated with a non-optimal choice of lighting source parameters.



a



b



c

Fig. 1. Block diagram (a), appearance (b) of the developed device and measured current-voltage characteristic (c) of the solar cell

Conclusion

The paper proposes a capacitive method, on the basis of which a device has been developed for automated measurement of the photoelectric characteristics of solar cells. The studies have shown that the measurement error of photoelectric parameters compared to the values stated in the specification is about 2 %. The proposed method may be of particular interest in the development and manufacture of solar cells in order to find optimal photovoltaic parameters, when it is necessary to measure the current-voltage characteristics of a large number of solar cells.

Acknowledgments

The study was supported by the grant of Russian Science Foundation № 23-29-00827, https://rscf.ru/project/23-29-00827/ at the Southern Federal University.

REFERENCES

1. **Mustafa Q. Ali, Monaf S. Tapou, Hayder A. Dhahad**. Fully Automated Measurement Setup for Photovoltaic Panel Performance Evaluation and Testing under LabVIEW Platform // Journal of Advanced Research in Fluid Mechanics and Thermal Sciences, 77, (2021), 132-150.

2. **Saenko A.V., Bilyk G.E., Malyukov S.P.** Research of the photoelectric parameters of ZnO/Cu_2O heterojunction solar cells // St. Petersburg State Polytechnical University Journal: Physics and Mathematics, 16, 1, (2023), 221-226.

InGaAs metamorphic diode for 1550 nm wavelength grown on GaAs substrate by MOCVD

I.V. Samartsev ✉, N.V. Baidus, D.M. Balyasnikov, A.V. Kruglov, S.Yu. Zubkov

Research Institute of Physics and Technology, Nizhny Novgorod State University, Nizhniy Novgorod 603022, Russia

✉ samartsev@nifti.unn.ru

Abstract. The results of studies aimed for creation of photodiodes formed on GaAs substrates for 1550 nm region wavelength are shown. The epitaxial growth technique of InGaAs photodiode structures based on InAlGaAs metamorphic buffer layer by metalorganic chemical vapor deposition (MOCVD) has been developed. The dark current density at room temperature was 3×10^{-4} A/cm^2 with a reverse bias of -2 V and photosensitivity at wavelength of 1550 nm was 0.6 A/W.

Keywords: MOCVD, nanomaterials, A3B5 semiconductors, infrared photodiodes.

Funding: Federal academic leadership program «Priority 2030» of Ministry of Science and Higher Education of the Russian Federation.

Introduction

Photodiodes operating in the short infrared range (up to 3 μm) grown on GaAs substrates are interest as a replacement for devices currently used for this range grown on InP substrates. One of the directions of creating such photodiodes is the use of metamorphic buffers (MB) [1, 2]. The practical implementation of metamorphic heterostructures on GaAs, the characteristics which would not be low to those of heterostructures on InP, is hindered by incomplete suppression of the intergrowth of dislocations into active layers of the structure and the appearance of surface micro relief. Thus, it is current task to search for and optimize the MB design in order to improve the crystal quality of the obtained heterostructures. In this paper, we present the results of the study of photosensitive heterostructures and photodiodes based on them, obtained by MOCVD on GaAs (100) substrates using MB.

Experimental samples

The investigated heterostructures were produces by the MOCVD using an AIX 200RF setup on GaAs (001) substrate misoriented towards [1 1 0] by 2°. The first, 0.2 μm thick n-GaAs buffer layer was grown. Next, parabolic-graded $In_xAl_{0.08}Ga_{1-0.08-x}As$ MB with a total thickness of 1.5 μm, n- and p-layers of InAlGaAs, and an i-layer of InGaAs with a relative In content of 50% and a thickness of 1 μm were grown. The sources of Ga, In and Al were trimethylgallium (TMG), trimethylindium (TMI) and trimethylaluminum (TMA), and the source of As was arsine. The growth temperature and speed were 570 ºC and 0.5 nm/sec. The thickness of layers was calculated based on the growth rate and time. The concentrations of group III elements were determined using photoluminescence and x-ray diffraction methods. Photodiodes with a mesa 1.4 mm size were fabricated based on the grown heterostructure. The design of photodiodes is shown in Figure 1.

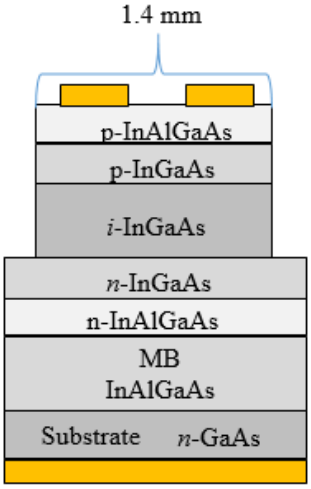


Figure 1. The design of the photosensitive structure.

Results and Discussion

The surface roughness was studied using atomic force microscopy. The root mean square deviation (RMS) was 23 nm. The dislocation density can be estimated from the density of etching pits, which was calculated using optical microscopy and amounted to 10^6 cm^{-2}.

Figure 2 shows a typical spectrum of photocurrent measured at room temperature.

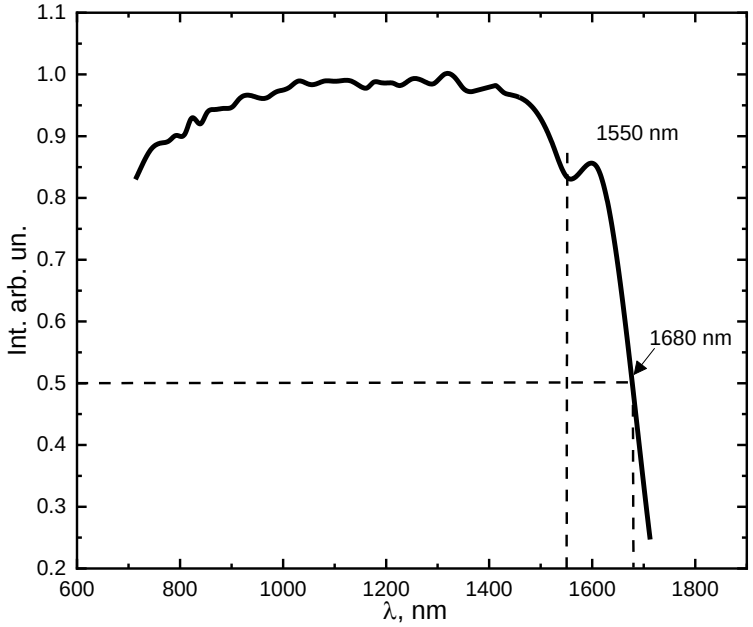


Figure 2. Photocurrent spectrum of photodiodes at room temperature.

The photodiodes had a photosensitivity up to 1680 nm at the 50% level of the maximum. Wavelength 1550 nm is located at 83% of maximum intensity. This indicates that these photodiodes are promising for applications in the telecommunications. For photodiodes with a mesa structure with 1.4 mm diameter dark current was 5×10^{-6} A at room temperature and reverse bias of -2 V, which corresponds to a current density of 3×10^{-4} A/cm^2. Photosensitivity measured using a laser with continuous radiation at a wavelength of 1550 nm with radiation output through an optical fiber was 0.6 A/W. It is a good enough value, because the photosensitivity value at a given wavelength of commercial photodiodes grown on matched InP substrates is about 1.1 A/W.

Conclusion

Metamorphic InGaAs/AlInGaAs/GaAs photodiodes grown on a GaAs substrate demonstrated good photosensitivity and low dark current density at a reverse bias of -2 V. Thus, the technology for producing photodiodes at a wavelength of 1550 nm on GaAs substrates using metamorphic buffer layers is promising. Further research will be aimed at increasing photosensitivity to 1 A/W and developing a photodiode design operating at high frequency.

REFERENCES

1. **K. Swaminathan, L.-M. Yang, T. J. Grassman, et. al.,** Opt. Express. 19 (2011) 7280-7288.

2. **P. Jurczak, K.A. Sablon, M. Gutiérrez, et. al.**, Infrared Physics & Technology, 81 (2017) 320-324.

GaN based ultraviolet narrowband photodetectors

O. A. Sinitskaya [1✉], **K. Yu. Shubina** [1], **D. V. Mokhov** [1], **A. I. Baranov** [1], **A. M. Mizerov** [1], **E. V. Nikitina** [1,2]

[1] Alferov University, St. Petersburg, Russia;

[2] Ioffe Institute, St. Petersburg, Russia

✉olesia-sova@mail.com

Abstract. In this work ultraviolet metal-semiconductor-metal photodetectors with semitransparent Ni/Au interdigitated electrodes based on GaN/*i*-GaN/c-Al_2O_3 heterostructure were fabricated. The current-voltage and spectral characteristics of the formed photodetectors were studied. It was found that the devices have a maximum responsivity at a wavelength of 364 nm with full width at half maximum of 11 nm, thus the presented PDs are narrowband.

Keywords: GaN, ultraviolet photodetector, narrowband photodetector, metal-semiconductor-metal.

Funding: The work was supported by the Ministry of Education and Science (grant №FSRM-2023-0006).

Introduction

At present, ultraviolet (UV) photodetectors (PD) play a critical role in numerous technological applications, ranging from environmental monitoring and control of ultraviolet emitters to various alarm systems [1]. In recent years, there has been a growing demand for high-performance UV PDs with enhanced sensitivity, speed, reliability and high selective spectral responsivity. The latter characteristic is especially important for PDs used in optical communication and biophotonics applications [2].

The quest for efficient and reliable narrowband PDs has prompted significant research efforts aimed at exploring new materials and device architectures. In this context, GaN epitaxial layers have emerged as promising candidates owing to their unique properties, including a wide bandgap (3.4 eV), high electron mobility and excellent thermal and chemical stability [3].

Currently, there are various types of PDs designs. However, among them, the most attractive are the metal-semiconductor-metal (MSM) PDs, the advantages of which are fast operating speed, high sensitivity and simplicity of fabrication [1]. In this article narrowband UV MSM PDs fabricated on the GaN epitaxial layers are presented.

Materials and Methods

GaN epitaxial layers were grown by plasma-assisted molecular beam epitaxy (PA MBE) using Veeco GEN 200 industrial type MBE setup on *i*-GaN/c-Al_2O_3 templates pre-grown by metalorganic chemical vapour deposition. The surface morphology of the synthesized samples was examined using a scanning electron microscope (SEM). The conductivity type, concentration and mobility of charge carriers in the GaN epitaxial layers were assessed using Hall effect measurements based on the Van der Pauw four-point probe method.

Subsequently, MSM PDs with semitransparent Ni/Au interdigitated electrodes were fabricated using standard laser lithography technique, e-beam and thermal vacuum evaporation. Current-voltage (I-V) and spectral characteristics of the formed PDs were obtained.

Results and Discussion

SEM images (see figure 1, a, b) show that the resulting layers have a rough surface morphology. As a result of Hall measurements, it was discovered that GaN epitaxial layers have *n*-type conductivity, which is typical for III-N materials [4], with a carrier concentration of $n \sim 1.1\times10^{18}$ cm^{-3} and mobility of $\mu \sim 95$ $cm^2/(V\times s)$. A photomicrograph of the formed PDs with semitransparent Ni/Au interdigitated electrodes is presented in Fig. 1, c.

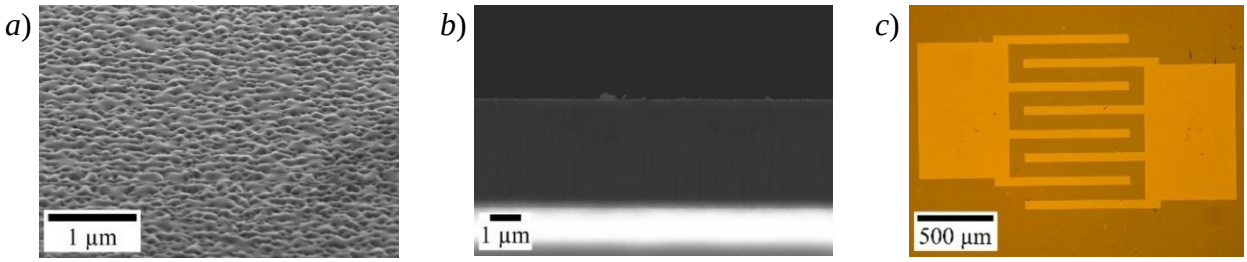


Fig. 1. SEM images of the GaN/*i*-GaN/c-Al_2O_3 epitaxial structure: isometry (a) and cross-section (b), photomicrograph of metal electrodes (c)

The I-V characteristics of the UV PDs were measured both in the dark and under 365 nm UV LED illumination. It was noted that exposure to UV radiation resulted in an increase in current. However, it is evident from Fig. 2, a, that the PDs exhibit a very high dark current (6 mA at a bias of 1 V), which may be attributed to the elevated defect density in the epitaxial GaN layers.

The spectral response of the device over the wavelength range of 300–450 nm at 0.025 V bias is presented in Fig. 2, b. It can also be seen that the presented PDs have a narrowband detection configuration with a maximum at 364 nm and full width at half maximum (FWHM) of 11 nm. The observed characteristic could be linked to surface charges trapped at surface states or transitions associated with defect levels in GaN [5], but this requires further study.

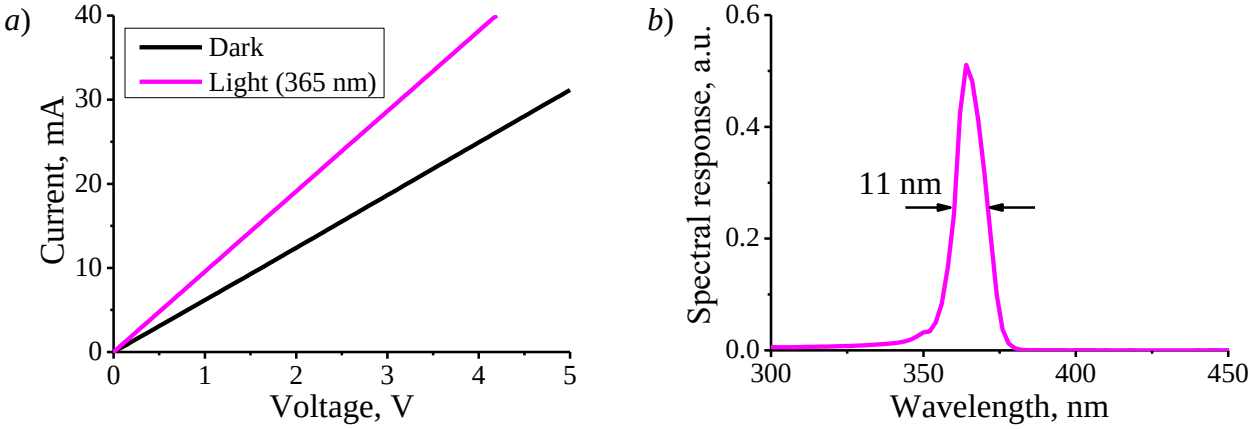


Fig. 2. I–V (a) and spectral response (b) of the formed PDs

Conclusion

In this report, UV narrowband PDs based on the GaN/*i*-GaN/c-Al_2O_3 heterostructure were demonstrated. It was found that the fabricated devices have a maximum responsivity at a wavelength of 364 nm and FWHM of 11 nm. Thus, PDs based on such GaN heterostructures, due to their high spectral selectivity, can be promising for use in communication systems and biophotonics.

REFERENCES

1 **Munoz E., Monroy E., Pau J. L., Calle F., Omnes F., Gibart P.**, III nitrides and UV detection, Journal of Physics: Condensed Matter. 13 (32) (2001) 7115.

2. **Wilson G. A., DeFreez R. K.**, Improving diode-laser-induced fluorescence detection of airborne biological particles by exciting multiple biofluorophores, Chemical and Biological Sensing V. – SPIE. 5416 (2004) 157-167.

3. **Bi W., Kuo H.-C., Ku P.-C., Shen B.**, Handbook of GaN semiconductor materials and devices, Boca Raton: Taylor & Francis, CRC Press, Abingdon, 2017.

4. **Monish M., Mohan S., Sutar D. S., Major S. S.**, Gallium nitride films of high n-type conductivity grown by reactive sputtering, Semiconductor Science and Technology. 35 (4) (2020) 045011.

5. **Chatterjee A., Khamari S. K., Kumar R., Porwal S., Bose A., Raghavendra S., Dixit V. K., Sharma T. K.**, Ultranarrow Band UV Detection in GaN with Simple Device Architecture, physica status solidi (RRL)–Rapid Research Letters. (2022) 2200322.

Identification of unreadable marginalia by means of hyperspectral imaging: case study of the Ostrog Bible from the Library of the Academy of Sciences and the Russian National Library

P.S. Baranov [1]✉, V.A. Parfenov [1], S.L. Rongonen [2], N.M. Sokolov [1]

[1] St.Petersburg Electrotechnical University, Saint-Petersburg, Russian Federation

[2] Russian Academy of Science Archive, St-Petersburg branch, Saint-Petersburg, Russian Federation

Abstract. Case study of visualization of unreadable marginals (fading of ink, spreading of ink, crossed out ink, scraping of ink, gluing with restoration materials) of the Ostrog Bibles using hyperspectral imaging were made. Unreadable by different reasons marginalia needs different approaches while using hyperspectral camera. And the level of "readable" is anyway different.

Keywords: hyperspectral imaging, unreadable marginalia, Ostrog bible, manuscript

INTRODUCTION

The Ostrog Bible, the first printed Bible in the Church Slavonic language, common to the ancestors of modern Russians, Belarusians and Ukrainians. Despite it have been well studied, there are many unread marginalia on copies. The choice of a hyperspectral camera for the experiment on reading marginalia was due to a complex of reasons.

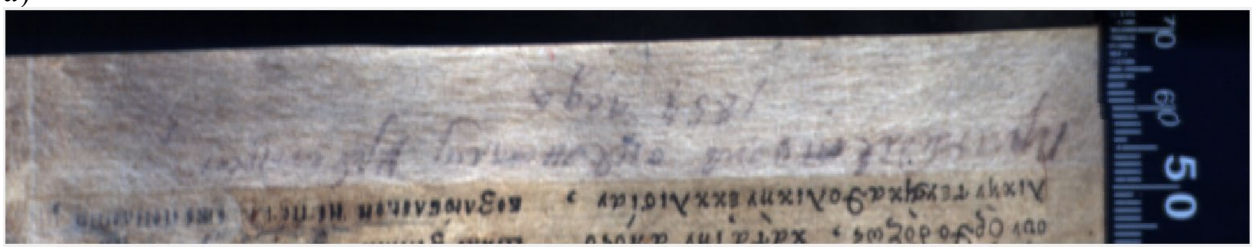
MATERIALS AND METHODS

The material associated with the object of a rich history of existence, allowed us to obtain a sufficient number of diverse contexts (ink fading, ink spreading, ink strikethrough, ink scraping, gluing with restoration materials). Have these contexts been registered by a hyperspectral camera in the IR and UV bandwidths of the spectrum with further processing using the original software.

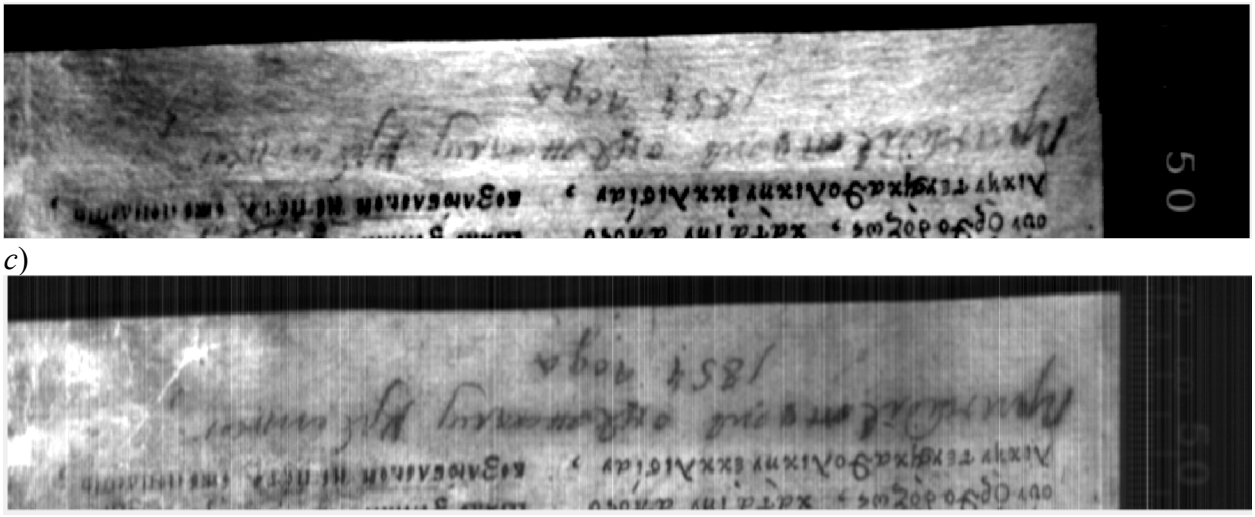
RESULTS AND DISCUSSION

The study of pieces of art using a hyperspectral camera has already been carried out with positive results [1–4]. The aim of our work was the attempt to find a way using advanced opto-electronic techniques to read invisible marginalia. In our experiments we used NIR hyperspectral camera operating in the range 400 – 1100 nm and original self-developed software. Using this approach, we were able to visualize the number of poorly readable marginalia. The case of gluing handwritten marginalia with restoration paper also gives good reading results, with both spectra working, IR and UV.

a)



b)



c)

Fig. 1. Marginalia covered with restoration paper. Original(*a*) and shooting in IR(*b*) and UV spectrum(*c)*

The best results were shown on contexts whose "invisibility" was caused by ink fading. The UV spectrum shows an excellent result, while the IR spectrum does not give any result in this case.

CONCLUSION

Various reasons for extinction or "invisibility" of handwritten marginalia can be read using hyperspectral imaging. The choice of a successful shooting criterion depends on the characteristics of the "damage" of the marginalia, as well as on the material with which the inscription was made. Let us mention that in some contexts, hyperspectral imaging has revealed traces of bio damage on paper.

ACKNOWLEDGMENTS

We sincerely thank the staff of the manuscript departments of the Library of the Academy of Sciences and the Russian State Library for providing this. we have the opportunity, time and premises to conduct the experiment.

REFERENCES

1. Cotte P. Dupraz D. Spectral imaging of Leonardo Da Vinci's Mona Lisa: An authentic smile at 1523dpi with additional infrared data," IS&T Archiving 06 (2006).

2. **Elias M., Cotte P.** Multispectral camera and radiative transfer equation used to depict Leonardo's sfumato in Mona Lisa," Applied Optics 47 (June 2008).

3. Pouli P, Zafiropulos V., Balas C., Doganis Yi. Laser cleaning of inorganic encrustation on excavated objects: evaluation of the cleaning result by means of multi-spectral imaging. Amerimni Galanos Journal of Cultural Heritage 4 (2003) 338s–342s

4.Viguerie L. de, Rochut S., Alfeld M., Walter P., Astier S., Gontero V., Boulc'h F. XRF and reflectance hyperspectral imaging on a 15th century illuminated manuscript: combining imaging and quantitative analysis to understand the artist's technique, Heritage Science 6 (1) (2018) 11.

THE AUTHORS

BARANOV Pavel
ORCID: 0000-0002-8102-3858
tv.lab@yandex.ru
PARFENOV Vadim
vadim_parfenov@mail.ru

ORCID: 0000-0002-2048-4677
RONGONEN Sofia
sofiagonobobleva@mail.ru
ORCID: 0000-0002-9050-3239
SOKOLOV Nikita
nmsokolov@etu.ru
ORCID

Luminescence enhancement in inelastic tunnelling of electrons by changing the geometry of the tunnelling contact

N. A. Solomonov [1,2✉], **D. V. Lebedev** [1,3], **K. N. Novikova** [1,2], **S. V. Fedina** [1,2], **N. V. Vaulin** [1], **L. N. Dvoretskaya** [1], **A. V. Arhipov** [2], **A. O. Golubok** [3], **I. S. Mukhin** [1,2]

[1] Alferov University, Saint Petersburg, Russia;

[2] Peter the Great St.Petersburg Polytechnic University, Saint Petersburg, Russia;

[3]Institute for Analytical Instrumentation of the Russian Academy of Sciences, Saint Petersburg, Russia;

✉solomonov.nik@gmail.com

Abstract: We have experimentally investigated the light emission resulting from inelastic electron tunneling in the transition with hemispherical gold nanoantennas (d=400 nm, h=300 nm) created by direct fs-laser ablation and a tungsten scanning microscope probe. We found two characteristic modes of luminescence: standard - increased signal is observed in the region of nanoantennas at tunneling currents below 2.25 nA and inverted-anomalous, where the gold surface is mainly luminescent, while dark spots are observed on the antennas on the contrary. In the inverted-anomalous mode we observe record signal values of $4 \cdot 10^4$ photons per second. We attribute the anomalous effect to the realization of a conditionality for resonant tunneling of electrons with excitation of optical states.

Keywords: golden nanoantenna, femtosecond laser printing, nanoscale on-chip light sourse, luminescence from tunnel junction, inelastic tunneling of electrons, resonant electron tunneling, scanning tunneling microscope.

Funding: The work was supported by the Russian Science Foundation (grant № 21-79-10346).

Introduction

One of the main challenges on the way to the design and successful realization of full-fledged optoelectronic integrated chips is the development of a nanoscale on-chip photon source whose emission can be excited and controlled by electrical signals and which is compatible with current semiconductor technologies.

A promising option for the realization of a nanoscale light source that meets all of the above requirements is the use of tunneling contact between two metal surfaces distant from each other by a subnanometer distance (metal-insulator-metal (MIM)). In the process of inelastic tunneling through the MIM, part of the electron energy can be used up to create a photon, but the probability of such a process is extremely small $\sim 10^{-5}$-10^{-6}, which does not allow the use of simple planar MIM photon sources in practice. However, as shown in our previous work [1], by modifying one of the electrodes of a MIM structure using point femtosecond laser ablation and creating gold hollow nanoantennas on its surface, the external quantum efficiency (EQE – photon ratio per number of tunneled electrons) for the regions above the nanoantennas can be increased by an order of magnitude compared to the planar surface, but the EQE still remains at uncompetitively low values. The aim of this work is to further improve the EQE in a MIM structure with gold nanoantennas by optimizing the geometrical and energetic parameters of the tunnel gap and investigating the photon emission phenomena resulting from inelastic tunneling.

Materials and Methods

The initial sample is a 50 nm gold film deposited on an optically smooth glass substrate by electron beam evaporation without additional adhesive layers. Rows of nanoantennas with a period from 1 to 1.5 μm and a diameter of 400 nm were printed on the gold film by femtosecond laser ablation [2]. The nanocontact with the sample is formed using a tungsten etched probe in an ultrahigh vacuum tunneling microscope (Omicron UHV VT AFM/STM) and can be precisely modified during measurements. Spatial maps of tunnel contact luminescence (STM-L) were recorded using an external data acquisition system based on a single-photon counter with a spectral

range of 400-900 nm, and the counter readings were synchronized with the STM microscope [3]. The optimum tunnel contact parameters were searched for at a fixed bias voltage of 2.7 V (one of the characteristic luminescence peaks of the structures on tunnel VACs) and tunnel currents in the range of 100-5000 pA by repeatedly recording STM-L distributions. In Figure 1, two STM-L images were selected from a series of experimental data, showing two characteristic results of the search for optimal parameters, the standard luminescence mode - Fig. 1 (a, b, c), the anomalous mode - Fig. 1 (d, e, f)

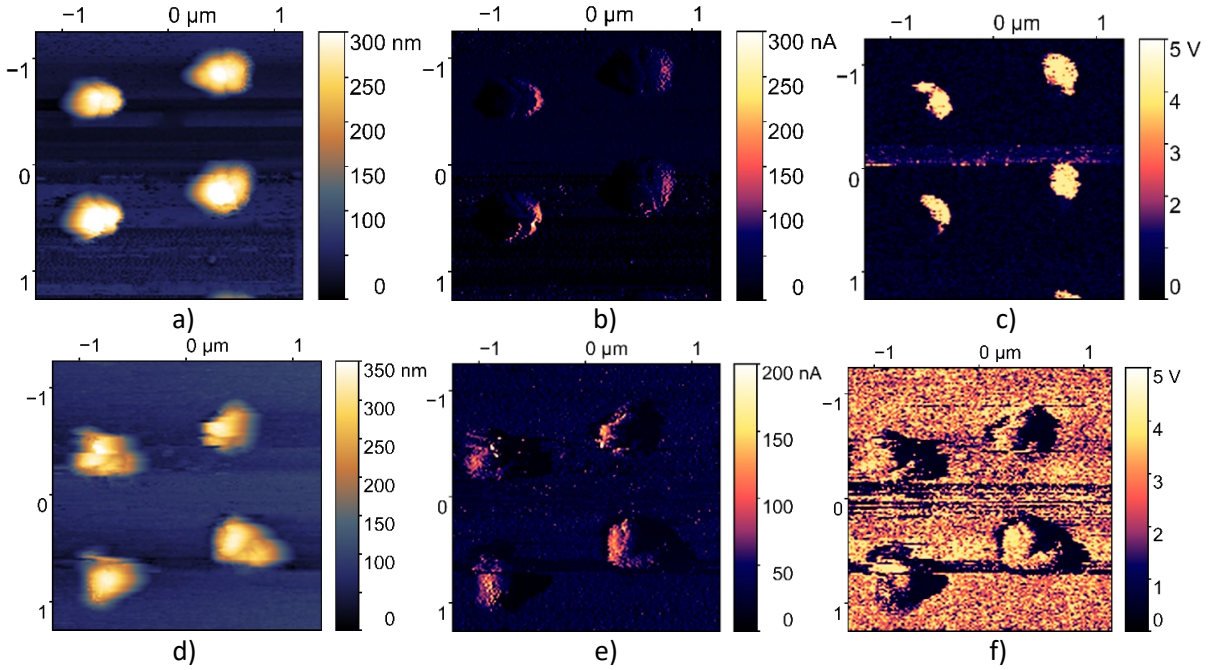


Fig.1 Synchronized recording of topography and tunnel luminescence (STM-L technique): a, d) - STM topography of nanoantennas, b), e) - map of tunnel currents, c), f) - map of tunnel luminescence (STM-L).

Results and Discussion

In the whole investigated range of tunnel contact parameters, two modes can be distinguished: the first, the mode of standard luminescence, consists in a smooth increase of the signal on the STM-L map when the tunnel current is increased to ~2.25 nA (increasing current = probe coming closer to the surface). Further increase of the current leads to a sharp change of the picture to an anomalous one, the luminescence signal sharply increases over the whole surface area on the STM-L map by about 5 times in amplitude from $5 \cdot 10^3$ photons per second to more than $4 \cdot 10^4$ photons per second, while above the nanoantenna zone, on the contrary, an area of weak luminescence is observed. When the currents are reduced back to 2nA or when 3nA is exceeded, the glow mode is switched back to normal.

Conclusion

The fact of such a sharp change in the luminescence pattern and increase in the luminescence intensity, respectively, EQE, may indicate the manifestation of resonant tunneling of electrons with excitation of optical states or the manifestation of other effects. Electron tunneling processes occurring in the anomalous luminescence regime require further deeper investigations.

REFERENCES

1. **Lebedev D. V., et al.,** Indirect Detection of the Light Emission in the Local Tunnel Junction." physica status solidi (RRL)–Rapid Research Letters 14.3 (2020): 1900607.

2. **Pavlov, D. V., et al.,** Laser-induced surface relief nanocrowns as a manifestation of nanoscale Rayleigh-Plateau hydrodynamic instability, Applied Surface Science. 511 (2020): 145463.

3. **Lebedev D. V., Solomonov N. A.**, Femtosecond Laser-Printed Gold Nanoantennas for Electrically Driven and Bias-Tuned Nanoscale Light Sources Operating in Visible and Infrared Spectral Ranges, The Journal of Physical Chemistry Letters 14.22 (2023): 5134-5140.

COMBINING COMPRESSED SAMPLING AND NEURAL NETWORKS FOR SINGLE-PIXEL IMAGING

D. V. Sych [1], **A. A. Reutov** [1], **D. V. Babukhin** [1]

[1] P.N. Lebedev Physical Institute, Russian Academy of Sciences, Moscow, Russia;
denis.sych@gmail.com

Abstract. Single-pixel approach provides novel capabilities for imaging beyond the conventional multi-pixel cameras. An important feature of single-pixel imaging is the need for computational methods that convert the raw measurement data into the image. There are several modern methods for image computation, including compressed sampling and neural networks. In this work we compare their abilities and show how to combine them in order to improve the result of computation.

Keywords: Single pixel imaging, compressed sampling, neural networks.

Funding: This study was funded by RSF grant number 23-22-00381.

Introduction

Single-pixel imaging (SPI) is an alternative method to obtain an image without a multi-pixel sensor [1]. In SPI the object of interest is illuminated by a sequence of spatially-structured light patterns, and a single-pixel detector measures the total amount of reflected (or transmitted) light. The image can be computed from the measurement data and information about the spatial structure of light patterns. The problem that we consider in this work is how we can perform and optimise this computation based on novel algorithmic methods of compressed sampling and neural networks. In particular, we investigate what results can be achieved by each of these methods separately, and what benefits can we obtain from the joint use of these methods.

Materials and Methods

There are several methods to compute the image of an object in SPI. First of all, let's consider the model of SPI data acquisition. The desired NxN image can be represented by a one-dimensional column I, where N^2 elements are real values (intensity of each pixel). Similarly, a light pattern with resolution NxN can be represented as a one-dimensional raw of N^2 elements. For simplicity, we consider binary light patterns, i.e. each element is either 0 or 1. A sequence of M light patterns is represented by a MxN^2 matrix P. Then the sequence of single-pixel signals S can be modelled as

$$S=P*I.$$

To reconstruct the image I, we can perform matrix P inversion, and the result is $I=P^{-1}*S$. However, there are several problems related to this approach. First, the number of patterns M should be equal to the total number of pixels N^2. This limits the minimum data acquisition time, and, taking into account realistic pattern demonstration rates, it limits the objects to almost stationary. Second, for a sufficiently high resolution, the matrix inversion is computationally complex. Despite the result can be algorithmically defined, the realistic time needed for this computation makes it impractical. A possible solution is to use matrices P for which the result is known analytically. Patterns based on Hadamard matrices allow for the fast matrix inversion, since the inversion is related to the matrix transposition. The use of Hadamard matrices allow for a high resolution, although it is limited to a power of 2 (e,g. 32x32, 64x64, 128x128, *etc*).

The second method of SPI image computation — compressed sampling — is based on numerical optimisation. The idea is to make use of realistic image sparsity and employ less light patterns than the number of pixels: $M<N^2$. In a sense, this is similar to image compression

methods, e.g. JPEG. But, in contrast to image compression which deals with the complete image beforehand, compressed sampling optimises data acquisition itself and performs compression already at the measurement process. It has been shown, that linear programming based on L1 metric minimisation is suitable for this task [1]. The implementation problems of this method include pattern optimisation, i.e. what patterns should be used to get more informative data, and the computational algorithm itself.

A third group of methods for SPI includes neural networks [2,3]. There are several architectures that can be used for this task, and the applicability of neural networks to SPI covers several image processing tasks. For example, we show how convolutional neural networks (CNN) can be used for image classification without an unnecessary intermediate step of image reconstruction. We also employ convolutional auto encoder (CAE) and generative adversarial networks (GAN) to acquire an image of the target object. Finally, CAE can be used for pattern optimisation.

Results and Discussion

Our results concern all three groups of the above-mentioned methods for SPI.

First, we show optimised systems of light patterns based on modification of Hadamard matrices. The standard way is to use pairs of color-conjugated patterns and measure the differential signal from them. In our approach, we use only one light pattern at a time, which halves the total number of light patterns, while obtains the same final image.

We also show another optimisation of light patterns, which is performed for the case of some *a priori* information about the image. For example, we have considered images of hand-written digits from the MNIST dataset, and show what set of light patterns can be used in this case. We found that the total number of patterns can be reduced by an order of magnitude.

Next, we show how three different SPI methods (matrix inversion, compressed sampling, and neural networks) work on the same data, and compare their performance. We also take into account the influence of realistic detection noise and technical inaccuracies on the image reconstruction. This is realised by computer simulation of an SPI system.

Further on, we show how to perform high-resolution image reconstruction based on block-structured patterns of rectangular shape. Traditional SPI methods deal with low-resolution images that rarely exceed 128x128 pixel resolution. In our approach we show the possibility of image reconstruction that exceeds a megapixel resolution for the realistic computational time.

Conclusion

In this work, we show applicability of several image sampling, image processing, and image reconstruction methods for SPI. We found that the choice of an SPI algorithm depends on a particular task, experimental equipment, and presence of *a priori* information. The matrix inversion based on modified Hadamard matrices is the most robust method, while compressed sampling and neural networks can greatly reduce the data acquisition time in some cases.

REFERENCES

1. **M. F. Duarte, M. A. Davenport, D. Takhar, J. N. Laska, T. Sun, K. F. Kelly, R. G. Baraniuk**, Single-Pixel Imaging via Compressive Sampling, IEEE Signal Processing Magazine 25, 83 (2008)

2. **C. F. Higham, R. Murray-Smith, M. J. Padgett, M. P. Edgar**, Deep learning for real-time single-pixel video, Scientific Reports 8, 2369 (2018)

3. **Z, Zhang, X. Li, S. Zheng, M. Yao, G. Zheng, and J, Zhong**. Image-free classification of fast-moving objects using “learned” structured illumination and single-pixel detection. Optics Express, 28, 13269 (2020)

Surfaces modifications in functional layers for Liquid Crystal devices

A. S. Toikka [1,2,3]✉, **N. V. Kamanina** [1,2,3]

[1] Lab for Photophysics of Nanostructured Materials and Devices, Joint Stock Company Scientific and Production Corporation S.I. Vavilov State Optical Institute, St. Petersburg, Russia;

[2] St. Petersburg Electrotechnical University, St. Petersburg, Russia

[3] Petersburg Nuclear Physics Institute, Gatchina, Russia

✉astoikka.nano@mail.com

Abstract.

It is known that the nanostructuration process has been occupying one of the main priority places among other aspects of science, technology and technology development for the last 10 years. In the current research the influence of the single-walled carbon nanotubes (CNTs) on the alignment properties of the indium-tin oxides (ITO) was considered. The formation of the composite thin films based on ITO with CNTs was provided by the laser-oriented deposition with the CO_2 laser. The average electrical strength during the deposition of CNTs varied in the range of 100-600 V/cm. Structures compared via surface free energy (SFE) with the Owens-Wendt method. According to comparison, deposited CNTs provide the reduce of the polar component of SFE caused by the surface passivation and to rise of the dispersive component of SFE caused by an impact of the Van der Waals forces. Thus, the transparent contacts based on ITO with CNTs could be considered as the tunable alignment layers of the nematic liquid crystal devices, so, the architecture of the related devices could be simplified.

Keywords: liquid crystals, alignment, indium tin oxides, carbon nanotubes, laser-oriented deposition.

Funding: The research was carried out at the expense of a grant from the Russian Science Foundation No. 24-23-00021.

Introduction

Nematic liquid crystals (NLC) – is an anisotropic media with the electrically tunable birefringence. Based on this aspect, the various electro-optical devices, such as: modulators, phase retarders, deflectors, lenses and switchers - could be realized on the NLC structure. The one of the key characteristic of the NLC-based devices is the distribution of the liquid crystal dipoles versus the space and time. According to the Oseen-Frank theory [1] the orientation (bulk part) of NLC depends on the viscous-elastic forces and external field. According to Ericksen theory and Rapini-Papoular potential [2] the pre-tilt orientation (surface part) of NLC depends on the relationship between the polar and dispersive components of the surface free energy of the alignment layer and surface free tension of the liquid crystal mesophase. In the current paper, the surface free energy comparison of various modification of the alignment layers based on the indium tin oxides (ITO) was considered.

Materials and Methods

In this work, it was proposed to use the transparent contacts based on the thin films of the indium tin oxides (ITO) as the conductive and orienting layers. To achieve this, the single-walled carbon nanotubes (CNTs) were deposited onto the ITO surface via the laser-oriented deposition method with varying electric field strength in the range of 100-600 V/cm. The source of the ITO contained 10 wt.% of the tin oxide and particle size was in the range of 3-12 mm (Cerac Inc.). Single-walled carbon nanotubes had chirality <7,6> with average diameter 0.83 nm (Aldrich Co., No. 704121). For the surface diagnostic, the wetting angle measurement and the Owens-Wendt method for the calculation of the surface free energy were used [3]. Distilled water and isopropyl alcohol were used as the testing liquids.

Results and Discussion

In case for the deposition of CNTs on the ITO surface, the surface free energy changes dramatically and depends on the average electric field during the deposition as shown in Table 1.

Table 1

Surface free energy of ITO modifications and orientation of 5CB liquid crystals

Surface	Surface free energy, mJ/m^2		5CB contact angle, ° (initial/saturation)
	Polar	Dispersive	
ITO	8.2	22.2	39.5/38.4
ITO +CNTs (100 V/cm)	0.8	29.2	52.1/52.8
ITO+CNTs (200 V/cm)	1.3	25.0	60.1/59.0
ITO+CNTs (600 V/cm)	1.8	31.4	58.5/58.4

Based on the comparison of the polar components, it should be mentioned, that CNTs leads to the passivation of the ITO surface. The rise of the dispersive component after the CNTs deposition is a marker of an increase of the Van der Waals interactions between the modified surface and material of the liquids.

Conclusion

The tuning of the polar and dispersive components of the surface free energy of the ITO modifications leads to possibility to implement them as the universal layers in the construction of the liquid crystal devices. The type of the alignment depends on the NLC-material. In case for the standard 5CB liquid crystals, CNTs provides the change of the alignment in the direction from the planar to homeotropic. Thus, the orientation of NLC and related parameters of the NLC-based devices could be controlled via the deposition mode of CNTs. This process can extend the area of the LC devices use with good advantage.

REFERENCES

1. **Frank F.C.**, Liquid crystals: On theory of liquid crystals, Discuss. Faraday Soc. 25 (1958) 19–28.

2. **Rapini A., Papoular M.**, Distorsion d'une lamelle nematique sous cham magnetique conditions d'ancrage aux parois, J. Phys. Colloques, 30 (3) (1969) 54-56.

3. **Owens D.K., Wendt R.C.**, Estimation of the surface free energy of polymers, J. Apply. Polym. Sci. 13 (8) (1969) 1741-1747.

Red light emitting diode based on $CsPbBr_2I$ perovskite

A.S. Toikka [1,2]✉, **R. Kenesbay** [1], **M. Baeva** [1], **D.M. Mitin** [1]
[1] Alferov University, St. Petersburg, Russia;
[2] ITMO University, St. Petersburg, Russia
✉astoikka@yandex.ru

Abstract. In this research, the performance of the $CsPbBr_2I$-based light-emitting diode was demonstrated. PEDOT:PSS and TPBi were used as hole and electron transport layers respectively. Indium tin oxide thin films and Al performed the function of bottom (transparent) and top contacts respectively. The threshold voltage was 3.0 ±0.1 V. Maximum electroluminance peak was in range 680-682 nm with full-width at half maximum of 65-70 nm. The electroluminance spectra of light-emitting diode demonstrated the absence of phase segregation versus time.

Keywords: halide-lead perovskites, mixed anion, light emitting diode.
Funding: research was supported by RSF grant № 22-79-10286.

Introduction

Halide perovskites – are semiconductor materials with ABX_3 structure, where A and B are mono- and divalent cations respectively, and X – is a halide anion. The optical properties, including absorption, refraction, pholomuninance and electroluminance spectra of inorganic perovskites could be tuned via the exchange of $B=Pb^{2+}$,$Sn^{2+}$and $X=I^-$,Br^-,Cl^- ions. Thus, this phenomenon is relevant for optoelectronic applications – solar cells, photodetectors, light-emitting devices, etc. In the context of ABX_3-based light emitting structures, the problem of red-region electroluminance exists. It is caused by the need to use perovskites with mixed anions – $(Br_xI_{1-x})_3$, because $ABBr_3$ and ABI_3 structures correspond to green and infrared spectral regions respectively. The one of dramatic problems for compositions with mixed anion – is a phase segregation with the local changes of stoichiometry and the related degradation of perovskite structure with the formation of non-radiative defects states and the decrease of conversion efficiency. So, the application of nanocrystals [1], quasi-2D [2], multi quantum wells [3] of perovskites could be considered as a technical decision for light emitting diodes (LED) in the red spectral range. However, the direction with thin-film-based red LED has room for improvement. In case for thin films, the main focus is on finding the compromise between the morphology (crystal size, quantity of micro and macro defect), roughness and optical performance via the preparation of perovskite-based solution, the operation regime of spin-coating and the further thermal treatment. In the current research, the performance of LED based on $CsPbBr_2I$ thin film and related regime for materials preparation were demonstrated.

Materials and Methods

The architecture of LED contained indium tin oxide (ITO), PEDOT:PSS, perovskite, LiF, TPBi, LiF/Al layers. ITO was used as the bottom electrode (Fig. 1).

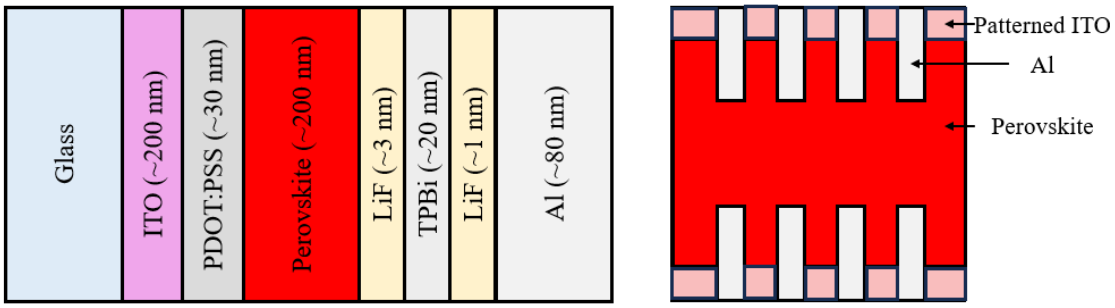


Fig. 1. The architecture of $CsPbBr_2I$-based LED: functional layers and bottom-view

In preparation for spin-coating of hole transport layer based on PEDOT:PSS at 3000 rotates per minute (rpm), the surface of ITO was treated in an oxygen plasma atmosphere with partial pressure 0.30±0.05 mbar and generator power 10 W for 2 minutes. For the preparation of the $CsPbBr_2I$ solution, CsI and $PbBr_2$ precursors with dimethyl sulfoxide (DMSO) solvent were used. The preparation and spin-coating of perovskite solution were in the M-Braun glove box in an N_2

atmosphere. Perovskite solution deposited via spin-coating with 1000 rpm for 1 minute. Nucleation and annealing temperatures of perovskite-based films were 60°C and 70°C respectively. Lithium fluoride performed the functions of buffer layers (physical barrier from deposited particles of TPBi and Al respectively), TPBi – had functions of the electron transport layer, LiF/Al corresponded to a top contact. All layers except PEDOT:PSS and perovskites were deposited via the thermal evaporation method inside vacuum evaporation chamber in the M-Braun glove box. The measurement/characterization of electroluminescence (EL) of perovskite-based LED (PeLED) structures was performed by conjugated CAS 120 spectroradiometer and Keithley 2401 DC power source.

Results and Discussion

The threshold voltage of the developed PeLED structure is 5.4 ±0.1 V (Fig. 2a). For comparison, the band gap of $CsPbBr_2I$ is approximately 2.1 eV.

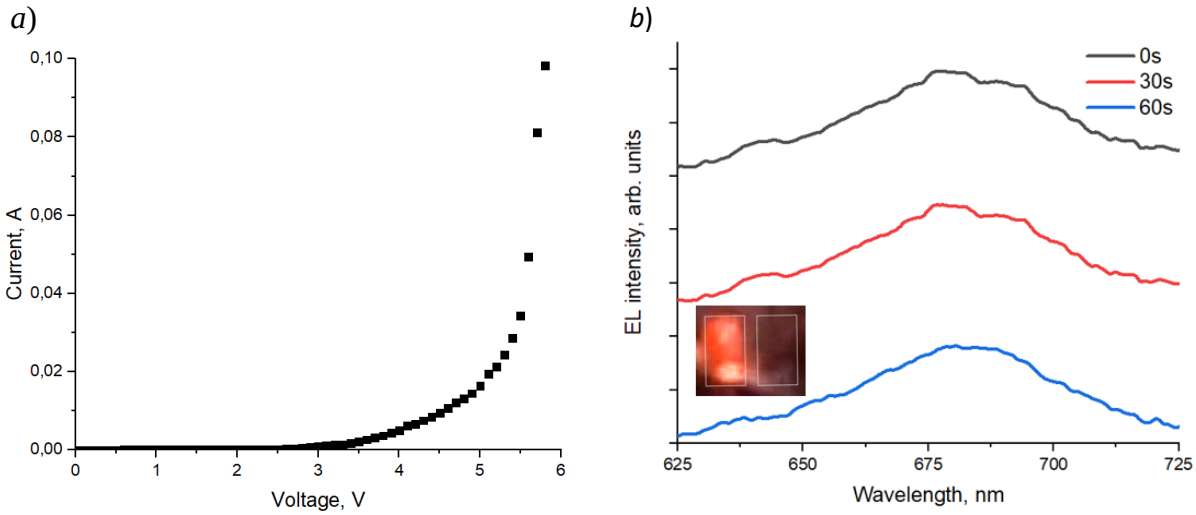


Fig. 2. Performance of $CsPbBr_2I$-based pixel of PeLED with 5 mm × 2 mm size: IV-curve (*a*) and EL spectra (*b*)

According to Fig.2b, the deep-red EL was observed. The inset of Figure 2b shows EL of operating pixel. The central wavelength of the EL peak was in range 680-682 nm (≈1.82 eV) and full-width at half maximum (FWHM) was 65-70 nm. It should be mentioned, that position of EL spectra doesn't change versus time, so the phase segregation to Br- and I-reached phases doesn't emerge. The difference between energy of the corresponding EL peak (1.82 eV) and the band gap of $CsPbBr_2I$ (2.1 eV) caused by non-radiative states inside the band gap and the further radiative recombination to valence band. Also due to this aspect, the relatively high FWHM was observed.

Conclusion

The nucleation temperature 60˚C and annealing temperature 70˚C of $CsPbBr_2I$-based structures provide the stable position of EL peak versus time. The application of PEDOT:PSS and TPBi as hole and electron transport layers respectively in the case of $CsPbBr_2I$ contributes to the realization of red PeLED with a relatively small threshold voltage (5.4 ±0.1 V).

REFERENCES

1. **Li H., Lin H., Ouyang D., et. al.**, Efficient and Stable Red Perovskite Light-Emitting Diodes with Operational Stability >300 h.v., Advanced Materials. 33 (2008820) (2021) 1-9.

2. **Tian Y., Zhou C., Worku M., et. al.**, Highly efficient spectrally stable red perovskite light-emitting diodes, Advanced Materials. 30 (1707093) (2018) 1-7.

3. **Zhang S., Yi C., Wang N., et. al.**, Efficient Red Perovskite Light-Emitting Diodes Based on Solution-Processed Multiple Quantum Wells, Advanced Materials. 29 (1606600) (2017) 1-6.

Stability of photovoltaic performance of solar cells sensitized with dye based on thieno[3,2-b]indole / 2,2'-bithiophene

N.M. Tolkach [1]✉, A.S. Steparuk [2], E.V. Tekshina [3], N.S. Demina [2], D.A. Krupanova [1], P.I. Lazarenko [1], S.A. Kozyukhin [3]

[1] National Research University of Electronic Technology, Zelenograd, Moscow, Russia;
[2] Ural Federal University of the first President of Russia B. N. Yeltsin, Yekaterinburg, Russia;
[3] Kurnakov Institute of General and Inorganic Chemistry of the RAS, Moscow, Russia
✉ n.m.tolkach@gmail.com

Abstract. In order to improve stability, environmental friendliness and reduce the cost of manufacturing dye-sensitive solar cells (DSSC), research was conducted into the stability of output photovoltaic characteristics under different climatic operating conditions (temperature, light intensity and humidity) for a new organic π-conjugated dye with a D-π-A structure based on thieno[3,2-b]indole/2,2'-bitiophene. It was found that changes in temperature lead to reversible changes in efficiency parameters. This indicates a sufficient stability of DSSC components and IS-BTh-1 dye.

Keywords: dye-sensitized solar cells, photovoltaic devices, climatic conditions, metal-free organic dyes, donor-π-linker-acceptor structure, quantum yields.

Funding: This work was supported by the Russian Foundation for Basic Research, project # 22-73-00291.

Introduction

Dye-sensitized solar cells (DSSC) were invented by Gretzel and O'Regan in 1991 as a low-cost alternative to traditional solar cells [1]. These devices convert solar energy directly into electricity, making them an attractive option for large-scale solar power production. The DSSC consists of three main components: 1) a photoanode – a glass substrate coated with several layers of materials, including FTO (fluorine-doped tin oxide) and nanocrystalline TiO_2, which functions as a wide-band semiconductor that absorbs light; 2) light-absorbing dyes – these dyes are adsorbed onto the surface of TiO_2 and help it absorb light; 3) an electrolyte – this component transports electrons between the photoanode and the rest of the solar panel, allowing for the conversion of solar energy into electrical energy; 4) a sensitizing dye – a glass substrate coated with Pt/FTO that acts as an electron collector.

The sensitizing dye plays a dual role in the process - it separates the electrical charges and transfers the excited photoelectrons into the conduction band of TiO_2. Currently, there are two main types of sensitizing dyes: metal-containing complexes such as ruthenium complexes that have good photosensitizing properties - high quantum yields and good efficiencies. In addition, there are eco-friendly and inexpensive metal-free organic dyes that have a common donor-π-linker-acceptor (D-π-A) structure.

At the same time, one of the most significant qualities of any solar panel is its stability in terms of photovoltaic performance over time under varying climatic conditions, such as temperature, light, and humidity. This is especially true for architecturally integrated solar systems that use DSSC, whose use has been particularly promising.

Therefore, the research and development of second-generation dyes with the aim of improving stability, reducing environmental impact, and lowering the cost of manufacturing DSSC is a relevant area, and we have carried out this work to investigate it.

Materials and Methods

To change the temperature, humidity, and illumination, a REOCAM TCH-150 climate chamber and a 50-watt halogen lamp were used. The lamp provided an illumination of one thousand watts per square meter, with a beam diameter of one centimeter. An AKIP-1124 direct

current voltage source and AKIP V7-78/1 voltmeter were also used to study the photovoltaic characteristics.

Results and Discussion

In our previous research [4], we developed and synthesized a novel metal-free organic π-conjugated dye named IS-BTh-1. This dye has a D-π-A structure based on thieno[3,2-b]indole and 2,2′-biothiophene.

We evaluated the stability of solar cells (SC) based on IS-BTH-1 for temperature ranges from −20 °C to 55 °C and humidity levels ranging from 10 % to 85 %, under cyclic exposure conditions. During one cycle, lasting 240 minutes, the temperature and humidity varied. Illumination changes in correspondence with two cycles of temperature and humidity variations occurred at the beginning of each cycle, when the halogen lamp is turned on and off.

During initial tests, the SC based on the IS-BTH-1 dye demonstrated the following characteristics: efficiency coefficient – 4.41%, open circuit voltage (Uoc) – 0.64 V, short-circuit current density (Jsc) – 11.61 mA/cm², filling factor (FF) – 0.59.

The efficiency of the SC varied when exposed to different temperatures. The maximum efficiency was observed at − 5 °C. This is a result of the balance between the changes in Uoc and Jsc. An increase in temperature leads to a decrease in Uoc, which is associated with an increase in the rate of charge carrier recombination on the photoanode.

During the study of the influence of temperature in the range of -20°C to 55°C during the day (6 cycles) on the voltage characteristics of the DSSC, it was found that temperature changes lead to reversible changes in the efficiency parameters, including Uoc and Jsc as well as FF, indicating the sufficient stability of the DSSC components and the dye IS-BTh-1.

The impact of humidity on the DSSC parameters has not been established, indicating a high level of tightness in the design of the device. As a result of a study on the long-term cyclic effects, an assessment of the stability of the IS-based DSSC using the IS-BTH-1 method took place. The estimated time for degradation to reach an 80% level was 192 hours (48 cycles), and the estimated time for parameters to reach 50% was 264 hours (66 cycles).

Conclusion

This result is likely due to the decomposition of the DSSC structure and the depletion of the electrolyte solution. Therefore, the IS-BTh-1 dye demonstrated fairly good stability, making it an interesting material for future research.

Acknowledgments

This work was supported by the Russian Foundation for Basic Research, project # 22-73-00291.

REFERENCES

1. **Dragonetti C., Colombo A.** Recent Advances in Dye-Sensitized Solar Cells. Molecules, 26(9), (2021), 2461–2463.

2. **Steparuk A.S., Irgashev R.A., Zhilina E.F., Emets V.V., Grinberg V.A., Krivogina E.V., Belova E.V., Lazarenko P.I., Rusinov G.L., Kozyukhin S.A.** Performance evaluation of dye-sensitized solar cells (DSSCs) based on metal-free thieno[3,2-b]indole dyes. Journal of Materials Science: Materials in Electronics, 33(9), (2022), 6307–6317.

3. **Steparuk A.S., Irgashev R.A., Zhilina E.F., Emets V.V, Grinberg V.A., Tekshina E.V., Belova E.V., Lazarenko P.I., Tolkach N.M., Rusinov G.L., Kozyukhin S.A.** New thieno[3,2-b]indole conjugates with 5-(methylene)rhodanine-3-acetic acid in dye-sensitized solar cells. Mendeleev Communications, 32(4), (2022), 523–526.

4. **Steparuk A.S., Irgashev R.A., Zhilina E.F., Emets V.V, Grinberg V.A., Tekshina E.V, Belova E.V, Tolkach N.M., Lazarenko P.I., Rusinov G.L., Kozyukhin S.A.** Thieno[3,2-b]indole / 2,2′-bithiophene-based D-π-A dyes for dye sensitized solar cells. Dyes and Pigments, 222, (2024), 111917.

Threshold current of separate spectral components of the emission spectrum of InGaN LEDs

I. V. Frolov [1,2]✉, **O. A. Radaev** [1], **V. A. Sergeev** [1]
[1] Ulyanovsk Branch of Kotel'nikov Institute of Radio-Engineering and Electronics of Russian Academy of Sciences, Ulyanovsk, Russia;
[2] Ulyanovsk State Technical University, Ulyanovsk, Russia
✉ilya-frolov88@mail.ru

Abstract. The results of measurements of the threshold current of ultraviolet, blue and green InGaN LEDs on different spectral components of the full emission spectrum are presented. It is shown that the threshold current of long-wave components of the spectrum is greater than the threshold current of short-wave components, and for green LEDs this difference is more significant than for ultraviolet and blue LEDs.

Keywords: LED, InGaN/GaN heterostructure, emission spectrum, threshold current, measurement.

Funding: The work was carried out within the framework of the state task of Kotelnikov Institute of Radioengineering and Electronics of Russian Academy of Sciences.

Introduction

Light-emitting InGaN/GaN heterostructures with multiple quantum wells are characterized by a nonuniform distribution of indium in the InGaN quantum well [1] and a significantly nonuniform distribution of defects over the volume of the active region of the heterostructure [2]. The development of methods and means for assessing the inhomogeneity of indium distribution for the purpose of diagnostic quality control of InGaN/GaN heterostructures is an urgent task. In [3] it is shown that the *P-I* characteristics measured in the range of extreme currents are sensitive to defects in the heterostructure. The threshold current of a light-emitting heterostructure, defined as the minimum current at which radiation occurs, is an informative parameter characterizing its quality [4]. The paper presents the results of measurements of the threshold current on different spectral components of the emission spectrum.

Objects of research and methods

Commercial LEDs based on $In_xGa_{1-x}N$/GaN heterostructure ultraviolet (UV) (λ_{max} = 363 nm, x = 0.02), blue (λ_{max} = 465 nm, x = 0.19) and green (λ_{max} = 525 nm, x = 0.38) glow.

Emission spectra of LEDs at several values of low currents (100–1000 nA for blue and green LEDs and 25–70 μA for UV LEDs) were measured with an Ocean Optics USB 2000 spectrometer having a resolution of 1.5 nm and saved into text files. The exposure time of the optical signal during measurements was set in the range of 100 ms is 5 s. From the complete emission spectra, components in different parts of the spectrum in 5 nm increments were programmatically isolated and the *P-I* characteristic was constructed. To determine the threshold current I_{th}, the measured *P-I* characteristic was approximated by a function of the form

$$P(I_i) = \frac{m}{2}\left(\sqrt{1+2q(I_i - I_0)} - 1\right)^2, i = 1,2,3 \quad (1)$$

obtained in [5] on the basis of the ABC model of charge carrier recombination in a heterostructure in the range of low currents at which the effect of Auger recombination can be neglected, and whose parameters m and q are related to the recombination parameters of the light-emitting structure.

Results and Discussion

The results of measuring the threshold currents of separate spectral components of the investigated LEDs are shown in Fig. 1. For all LEDs studied, the threshold current of long-wavelength components of the spectrum is greater than the threshold current of short-wavelength components: for ultraviolet by 5%, for blue by 8%, for green by 42%.

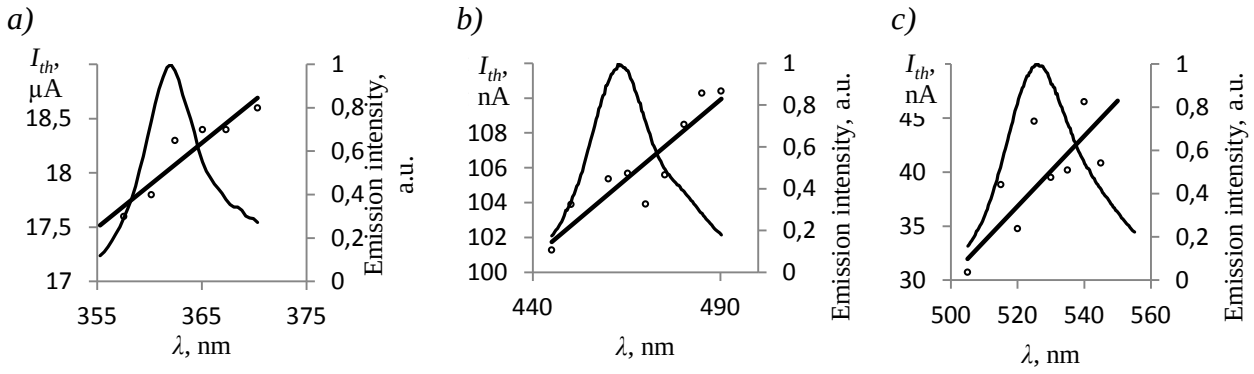


Fig. 1. Results of measurements of the threshold current of violet (a), blue (b) and green (c) LEDs in different parts of the emission spectrum

According to the model presented in [6], an LED can be represented by a set of parallel-connected microdiodes that have the same parameters of wide-gap n-GaN and p-GaN emitters, but differ from each other in the indium content in quantum wells. Radiative recombination first occurs in regions with lower indium concentrations, forming the short-wavelength wing of the emission spectrum. As the current increases, radiation appears in regions with higher indium concentrations (long-wavelength wing of the spectrum). The greater the inhomogeneity of the indium concentration in the quantum well, the greater the relative difference in the Ith values in the long- and short-wavelength components of the spectrum.

Conclusion

The results obtained can be used to develop a technique for indirectly assessing the degree of uniformity of indium distribution in InGan/GaN light-emitting heterostructures.

REFERENCES

1. **Baek S.-H., Lee H.-J., Lee S.-N.** High-performance flat-type InGaN-based light-emitting diodes with local breakdown conductive channel, Scientific Reports. 9 (2019) 13654.

2. **Peng Z., Lu Y., Gao Y., Chen G., Zheng J., Guo Z., Lin Y., Chen Z.** Effect of Carrier Localization and Shockley-Read-Hall Recombination on the Spatial Distribution of Electroluminescence in InGaN LEDs, IEEE Photonics Journal. 10 (2018) 8201908.

3. **De Santi C., Buffolo M., Renso N., Neviani A., Meneghesso G., Zanoni E., Meneghini M.** Evidence for defect-assisted tunneling and recombination at extremely low current in InGaN/GaN-based LEDs, Applied Physics Express. 12 (5) (2019) 052007.

4. **Sergeev V. A., Frolov I. V., Radaev O. A.** The Relationship between the Defectness of Emitting Nanoheterostructures of Green InGaN/GaN LEDs and Their Threshold Current Values, Technical Physics Letters. 43 (2) (2017) 224–226.

5. **Sergeev V. A., Radaev O. A., Frolov I. V.** LED Internal Quantum Efficiency Meter, Instruments and Experimental Techniques. 66 (6) (2023) 987–994.

6. **Nikiforov S.G.** Development of measuring instruments and methods for monitoring the parameters of semiconductor emitters based on III-V compounds used in highly reliable devices: dis. ...Dr. Tech. Sciences: 05.11.13. – Accredited center for certification testing of lighting devices and radiation sources, ARHILIGHT LLC. – M., 2015. – 386 p. (In Russian).

Influence of the Substrate Type on the Photoelectric Characteristics of Ga_2O_3/GaAs Structures

V. M. Kalygina [1]✉, A. V. Tsymbalov [1]

[1] National Research Tomsk State University, Tomsk, Russia;

✉vmkalygina@mail.ru

Abstract. The work considers the influence of three types of substrates: *n*-GaAs:Te, GaAs:Cr and *p*-GaAs:Zn on the electrical and photoelecric characteristics of Ga_2O_3/GaAs structures. Gallium oxide thin films were produced by radio frequency magnetron sputtering of Ga_2O_3 target onto different types of gallium arsenide substrates. The structures shows sensitivity to deep ultraviolet radiation and demonstrate a photovoltaic effect. The samples based on metal/Ga_2O_3/*n*-GaAs exhibit a fast response time of 350 ms and a recovery time of 100 ms.

Keywords: Gallium oxide, RFMS, heterostructure, UV.

Funding: This work was supported by a grant under the Decree of the Government of the Russian Federation No. 220 of 9 April 2010 (Agreement No. 075-15-2022-1132 of 1 July 2022).

Introduction

Gallium oxide is a native oxide on the surface of GaN, GaAs, and other compounds containing gallium atoms [1]. The properties of the films and the characteristics of the metal/Ga_2O_3 interface and the semiconductor/Ga_2O_3 heterojunction depend both on the preparation method, the thickness of the deposited layers [2], the pressure of the gas mixture during the fabrication process and on subsequent technological processes [3]. Devices in the shortwave range, according to the specifications, operate in the mode of continuous action ultraviolet (UV) radiation, including short-range secure communication systems, UV astronomy, monitoring of ozone holes. Therefore, it is of interest to study the behavior of detectors under continuous exposure to UV radiation. One of the promising areas for the development of shortwave radiation detectors are devices capable of operating in an autonomous mode (self-powered) [4]. Self-powered photodetectors have a simple design and can be integrated with the technology of fabricating metal-insulator-semiconductor (MIS) structures [5].

Materials and Methods

Epitaxial GaAs layers doped with Te, Zn, and Cr at concentrations of 9.5×10^{14} cm^{-3}, 9×10^{15} cm^{-3}, and 1×10^{17} cm^{-3}, respectively, were used as a substrate. Thin films of gallium oxide 120–150 nm thick were obtained by radio frequency magnetron sputtering of a Ga_2O_3 target in an Ar/O_2 gas mixture on GaAs substrates with (100) orientation. A barrier Pt-contact was deposited onto the surface of the gallium oxide film. The source of UV radiation was a VL-6.C Kr-F lamp with a 254 nm filter.

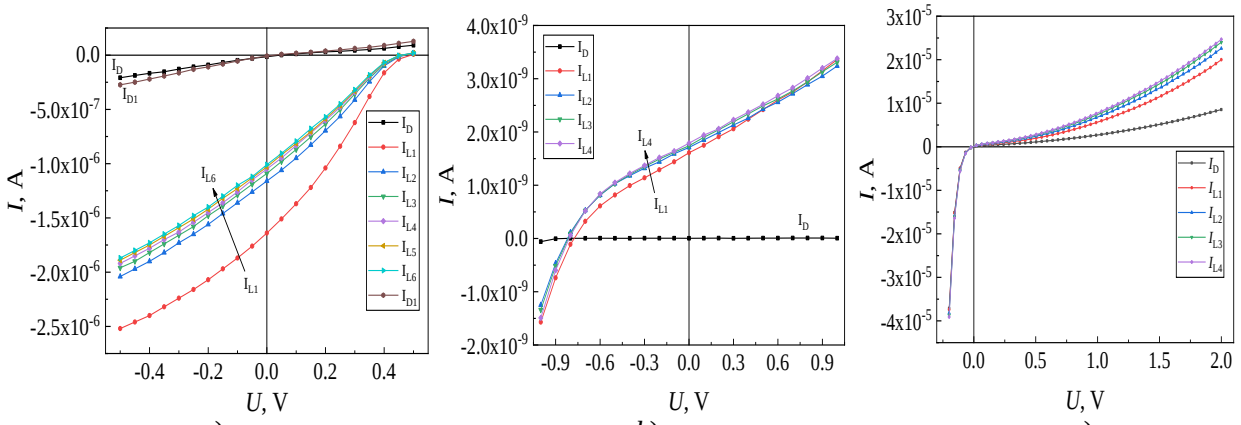
Results and Discussion

The dark current-voltage characteristic is non-linear and the rectification ratio at voltages of ± 4 V is 10^3 (Fig. 1*a*). Exposure to ultraviolet radiation leads to an increase in the reverse current, and the forward current changes slightly. The effect of radiation with a wavelength of 254 nm is most noticeable at low voltages on the sample, near U ≈ 0 V. The structures exhibit the photovoltaic effect and can function without an external power source, a characteristic typical of self-powered photodiodes. The open circuit voltage (U_{oc}) measures 0.4 V, and the short circuit current (I_{sc}) measures 1.4 μA.

The dark current-voltage characteristics of the Ga_2O_3/GaAs:Cr samples are symmetrical relative to the voltage polarity (Fig. 1*b*). The current increases under UV exposure with λ = 254 nm regardless of the voltage polarity on gate. The structures exhibit a photovoltaic effect, but the open-circuit voltage is observed at negative potentials and is 0.8 V. The short circuit current is 2-5×10^{-9} A, indicating that the substrate has *p*-type semiconductor properties.

Structures based on Ga_2O_3/GaAs:Zn have high dark current values: 8.5 μA at 2 V (Fig. 1*c*). Exposure to ultraviolet radiation leads to an increase in current to 25.7 μA.

Table 1 shows response time τ_r and recovery time τ_d of the Ga_2O_3/GaAs structures. The structures exhibit high-speed performance and can be used as UV detectors.



a) *b*) *c*)

Fig. 1. *I-V* characteristics of structures based on *n*-GaAs:Te (*a*), GaAs:Cr (*b*) and *p*-GaAs:Zn (*c*) measured in dark conditions and under UV exposure with λ = 254nm. I_D—initial dark current, I_{D1}—dark current measured immediately after UV exposure, I_{L1}–I_{L6} currents measured during exposure to radiation.

Title 1. Comparison of the characteristics of the considered structures.

Structure	τ_r, ms	τ_d, ms	U_{oc}, V	I_{sc}, nA	Photovoltaic effect
Ga_2O_3/*n*-GaAs:Te	350	100	0.4	1400	+
Ga_2O_3/GaAs:Cr	500	100	0.8	2	+
Ga_2O_3/*p*-GaAs:Zn	250	150	–	–	–

Conclusion

Samples based on Ga_2O_3/*n*-GaAs are metal/insulator/semiconductor structures with a space charge region width of 123 ± 5 nm. The GaAs:Cr substrate exhibits the properties of an *p*-type semiconductor in combination with a Ga_2O_3 film.

The studied structures are sensitive to the deep UV irradiation. Samples of Ga_2O_3/*n*-GaAs and Ga_2O_3/GaAs:Cr exhibit the properties of photodiodes capable of operating in self-powered mode. The response time τ_r and recovery τ_d, do not exceed 500 ms for all types of structures. In conclusion, it can be noted that the considered structures can be used as UV radiation detectors.

REFERENCES

1. **Alhalaili B., Mao H,. Dryden D.V., Cansizoglu H., Bunk R.J., Vidu R., Woodall J., Islam M.S.**, Influence of Silver as a Catalyst on the Growth of β-Ga_2O_3 Nanowires on GaAs, Materials (Basel). 13(23) (2020) 5377.

2. **Wang X., Chen Z., Guo D., Zhang X., Wu Z., Li P., Tang W.**, Optimizing the performance of a β-Ga_2O_3 solar-blind UV photodetector by compromising between photoabsorption and electric field distribution, Optical Materials Express. 8(9) (2018) 2918-2927.

3. **Калыгина В.М., Киселева О.С., Копьев В.В., Кушнарев Б.О., Олейник В.Л., Петрова Ю.С., Цымбалов А.В.**, Влияние термического отжига на свойства гетероструктур Ga_2O_3/GaAs:Cr, Журнал технической физики. 11(93) (2023) 1631–1636.

4. **Kaur D., Kumar M.**, A Strategic Review on Gallium Oxide Based Deep-Ultraviolet Photodetectors: Recent Progress and Future Prospects, Adv. Optical Mater. 9 (2021) 2002160.

5. **Peng B., Yuan L., Zhang H., Cheng H., Zhang S., Zhang Y., Zhang Y., Jia R.**, Fast-response self-powered solar-blind photodetector based on Pt/Ga_2O_3 Schottky barrier diodes, Optik. 245 (2021) 167715.

Mg_2Si contact layer for narrowband Si detector with 1045 nm peak photoresponse

I. M. Chernev [1]✉, E. Y. Subbotin [1], A. S. Gouralnik [1], K. N. Galkin[1], D. L. Goroshko[1], O. A. Goroshko[1], O. V. Kropachev[1], A. V. Gerasimenko [2], S. A. Kitan[1], O. E. Lisenkov[1,3] N. G. Galkin [1]

[1] Institute of Automation and Control Processes FEB RAS, Vladivostok, Russia;
[2] Institute of Chemistry FEB RAS, Vladivostok, Russia;
[3] Institute of High Technologies and Advanced Materials, FEFU, Vladivostok, Russia

✉ chernev@iacp.dvo.ru, igor_chernev7@mail.ru

Abstract. Mg_2Si film ~600 nm was synthesized by pulsed reactive deposition Mg on Si(111) at 340 °C in UHV. Structural investigations by XRD demonstrates high pronounced direction of epitaxial growth Mg_2Si (111) || Si(111). The photoresponse of structure AuSb/Si/Mg_2Si/AuSb illuminated from the backside of Si substrate represents the bell-shaped curve with the peak at 1045 nm and intensity 1.1 mA/W and FWHM ~102 nm under the 2.6 V bias.

Keywords: magnesium silicide, silicon, films, epitaxy, reactive epitaxy, pulsed deposition, crystal structure, microscopy, photoresponse.

Funding: The research was carried out within the state assignment of IACP FEB RAS (Theme FWFW-2021-0002).

Introduction

The narrowband detectors of SWIR range (1000-1100 nm) are highly interested for the applications in many fields such as medical imaging, health monitoring, optical communication system as well as sorting/identifying systems [1,2]. The increasing interest for this optical range is due to its high penetration ability in biological tissues and atmosphere (cloud, fog, smog) as well as its low scatter losses. The narrowband detectors which can work in this enough short optical range demonstrate high selectivity for eliminating of background noises as well.

Recently it was demonstrated that metal silicides (Yb, Y, Ca, Ba, Sr, Fe) can be applied as contact layers to n-Si [3-4]. This approach allows to minimize the barriers at the interface "silicide/Si" due to the Fermi level pinning. Lower contact barriers lead to more effective transport of photogenerated carriers from Si to external circuits. Thereby the silicides can be used as electron selective contact layers for doping free silicon solar cells and other Si based photosensitive devices. Mg_2Si in this respect looks enough perspective candidate as electron selective contact owing to its low work function value 3.6-4 eV [5] in comparison with 4.51 eV for silicon.

In this work we demonstrate a ~ 600 nm thick Mg_2Si film prepared on Si (111) by ultra-fast Mg deposition ($\approx 10^4$ nm/s) at the substrate temperature 340°C. Its crystal structure and spectral photoresponse are presented.

Results and Discussion

Mg_2Si film was prepared on unintentionally doped n-type Si(111)-1000 Ω×cm substrate by ultra-fast deposition of high purity Mg at $T_{sub} \approx 340$°C. This growth technique allows to synthesize highly-oriented Mg_2Si film on Si(111) substrate [6] with Mg_2Si [111] || Si[111].

Fig. 1(a) demonstrates the XRD data and it could be clearly seen that only the peaks of the Mg_2Si planes (111), (222) and (333), as well as Si peaks (111) and (222) are presented.

The film thickness of ~600 nm was estimated with the Beer-Lambert law from absorption intensity on IR active phonon mode of Mg_2Si at 270 cm^{-1}.

The structure AuSb/Si/Mg_2Si/AuSb was tested as photodetector with illumination from the backside of the Si substrate (see Fig. 1(b)). The spectral photoresponse is bell-shaped curve with the peak at 1045 nm and FWHM ~102 nm and 1.1 mA/W intensity under the 2.6 V bias.

Visible light strongly absorbs when propagating through enough thick Si wafer (~500 μm) therefore the backside illumination of the structure AuSb/Si/Mg_2Si/AuSb allows to minimize the visible part of photoresponse and make it equal zero at applying 2.6 V bias.

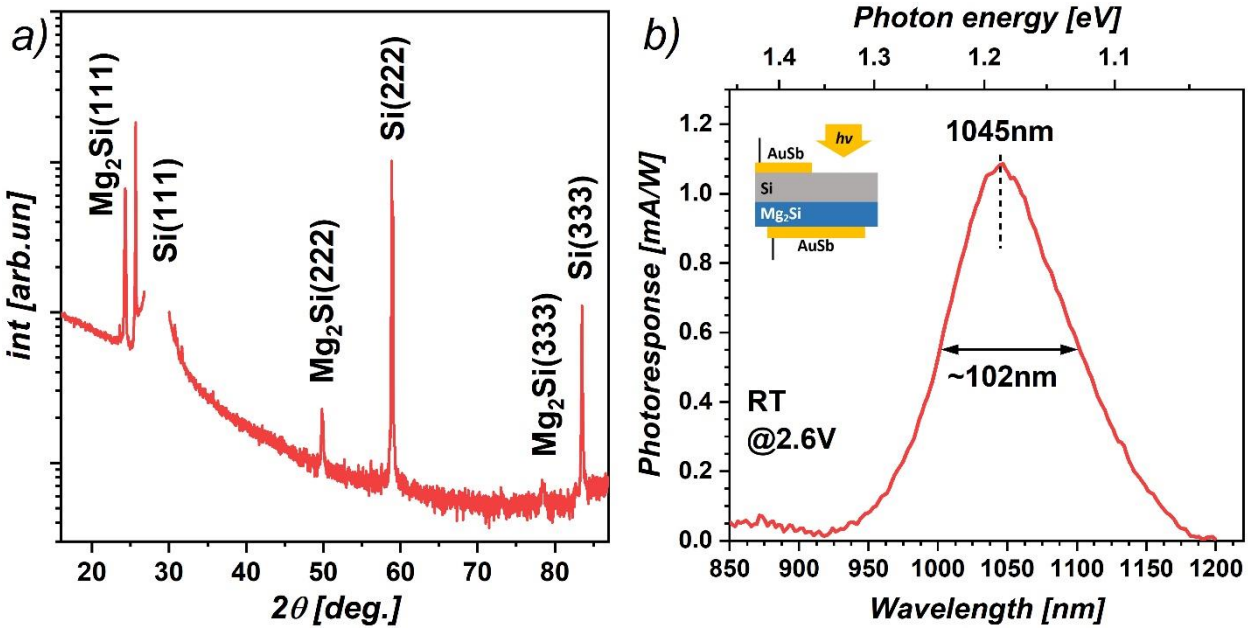


Fig. 1. (a) - XRD patterns of Mg_2Si film, (b) - photoresponse spectra for the AuSb/Si/Mg_2Si/AuSb structure at 2.6 V bias.

Conclusion

Highly-oriented ~600 nm thick Mg_2Si film was formed by pulsed Mg deposition onto Si at 340°C. Photoresponse measurements of structure AuSb/Si/Mg_2Si/AuSb illuminated from the backside of the Si substrate showed the narrowband photoresponse with the peak at 1045 nm and FWHM ~102 nm and 1.1 mA/W intensity under the 2.6 V bias.

REFERENCES

1. **Rathnamalala C. S. L., Hernandez S., Lucero M. Y., Swartchick C. B., Kalam Shaik A., Hammer N. I., East A. K., Gwaltney S. R., Chan J., Scott C. N.,** Xanthene-based nitric oxide-responsive nanosensor for photoacoustic imaging in the SWIR window, Angew.Chem. 135 (2023) e202214855.

2. **Z. Wu, Y. Zhai, H. Kim, J. D. Azoulay, and T. N. Ng,** Emerging design and characterization guidelines for polymer-based infrared photodetectors, AccountsChem.Res. 51(12) (2018) 3144–3153.

3. **Lin L., Guo Y., Robertson J.,** Metal silicide Schottky barriers on Si and Ge show weaker Fermi level pinning, Appl Phys Lett. 101(5) (2012) 052110.

4. **Cho J., Sivaramakrishnan Radhakrishnan H., Recaman Payo M., Debucquoy M., Van Der Heide A., Gordon I., Szlufcik J., Poortmans J.** Low Work Function Ytterbium Silicide Contact for Doping-Free Silicon Solar Cells, ACS Appl Energy Mater. 3(4) (2020) 3826-3834.

5. **El-Amir A.A.M., Ohsawa T., Nabatame T., Ohi A., Wada Y., Nakamura M., Fu X., Shimamura K., Ohashi N.,** Ecofriendly Mg_2Si-based photodiode for short-wavelength IR sensing, Mater Sci Semicond Process. 91 (2019) 222-229.

6. **Chernev I. M., Subbotin E. Yu., Kozlov A. G., Gerasimenko A. V., Ustinov A. Yu., Galkin N. G., Poliakov M. V., Volkova L. S., Dudin A. A., Gouralnik A. S.,** Thick p-type Mg_2Si film on Si: Growth, structure and transport properties, J. Alloys and Compounds. 964 (2023) 171301.

Development of a space debris recognition system based on artificial intelligence

A V Shavshin[1], D A Boldarev[2], R A Dmitriev[1], D Y Klimenko[2] and A A Hudina[2]

[1] The Bonch-Bruevich Saint-Petersburg State University of Telecommunications, Saint Petersburg, 191186, Russia.

[2] Peter the Great Saint-Petersburg Polytechnic University, Saint Petersburg, 195251, Russia.

✉ shavshin2107@gmail.com

Abstract. The need to create a system based on artificial intelligence for a spacecraft for collecting space debris is substantiated. The system automatically makes a decision regarding whether an object overboard is space debris with a magnetic component in its composition and determines whether the dimensions of the object are suitable for its placement and storage inside the spacecraft. Special software and a digital version of the system have been created to test functional units. The validity of the work carried out was confirmed, and the initial database for the classification of space debris was collected.

Keywords: Artificial intelligence, laser ranging, recognition system, computer vision, space debris, orbital satellite, optical signal.

Introduction

Every year the amount of space debris in Earth's orbit increases, which is why this problem becomes one of the most dangerous for operating satellites, spacecraft and astronauts [1]. The creation of a space debris recognition system based on artificial intelligence, using information obtained using the reflected optical signal of laser radiation, will allow special satellites that collect space debris to detect debris flying by, eliminating the risk of its collision with operating vehicles.

Space debris recognition system using laser ranging based on artificial intelligence

The radiation system (1) consists of an optical signal source and two radio signal sources. An optical laser is used to implement the laser ranging method, in which a beam of light is directed into the working sector to detect space objects (2). After an object appears in the working sector, the optical signal reflected from it goes to an optical sensor (3), capable of transforming the optical signal into an electrical one. The reflected optical signal carries information about the size, shape and trajectory of the object under study. The resulting electrical signal is sent to an analog-to-digital converter (ADC) (4) to convert it into digital format. Then the digital version of the signal goes through a preprocessing stage to obtain information about the size, shape and trajectory of the object under study, after which it is sent to the input of the microcontroller (5), which is the main element of the artificial intelligence system. Using machine learning algorithms, the neural network classifies the objects under study based on the database and the input data of the reflected optical signal. Next, a radio signal is sent to objects classified by the neural network as "presumably metals" to obtain accurate information about the composition of the objects. The reflected radio signal goes through the same cycle to perform object classification.

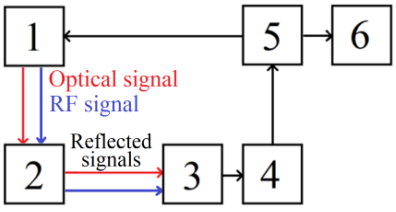


Fig. 1. Block diagram of the space debris recognition system: 1 – radiation system, 2 – subsequent object, 3 – optical sensor for receiving the reflected signals, 4 – analog-to-digital converter, 5 – microcontroller, 6 – user software interface.

The first step to creating a physical prototype of the system is to implement a digital version of the system, shown in Fig. 2.

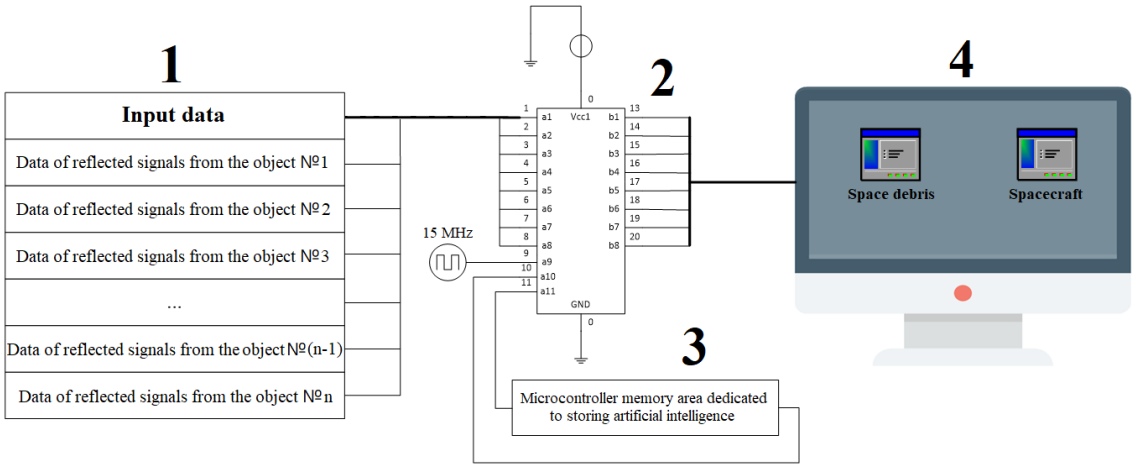
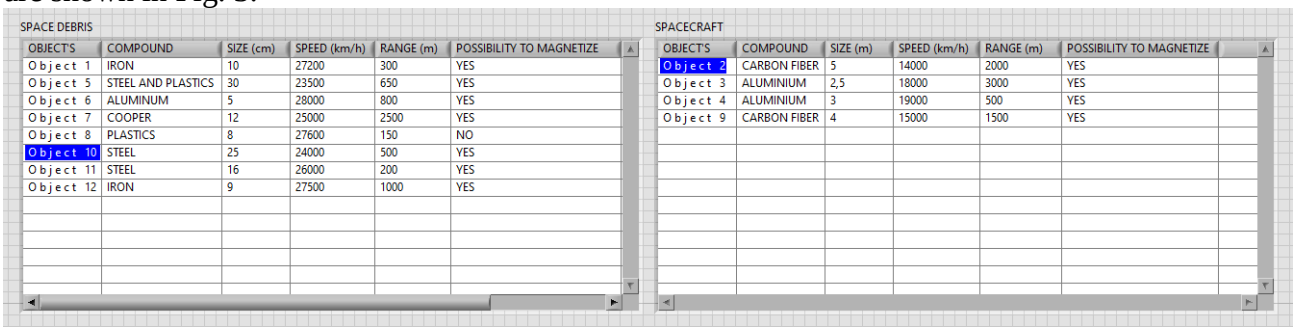


Fig. 2. Block diagram of the digital version of the space debris recognition system: 1 – database of optical signals reflected from various objects, 2 – microcontroller, 3 – memory area allocated for storing the neural network, 4 – software user interface for displaying output data.

In order to test artificial intelligence algorithms and all functional units of the microcontroller software (2), its input receives signals from a pre-prepared database of optical signals reflected from various objects (1), information for which was collected through laboratory research and information from open sources. Next, using machine learning algorithms [2], an artificial intelligence model (3) is trained on the basis of known signals, so that the neural network can then independently classify new objects that were not in the original sample.

Results and Discussion

The output data and the optical signal classification process reflected in the user interface are shown in Fig. 3.



SPACE DEBRIS

OBJECTS	COMPOUND	SIZE (cm)	SPEED (km/h)	RANGE (m)	POSSIBILITY TO MAGNETIZE
Object 1	IRON	10	27200	300	YES
Object 5	STEEL AND PLASTICS	30	23500	650	YES
Object 6	ALUMINUM	5	28000	800	YES
Object 7	COOPER	12	25000	2500	YES
Object 8	PLASTICS	8	27600	150	NO
Object 10	STEEL	25	24000	500	YES
Object 11	STEEL	16	26000	200	YES
Object 12	IRON	9	27500	1000	YES

SPACECRAFT

OBJECTS	COMPOUND	SIZE (m)	SPEED (km/h)	RANGE (m)	POSSIBILITY TO MAGNETIZE
Object 2	CARBON FIBER	5	14000	2000	YES
Object 3	ALUMINIUM	2,5	18000	3000	YES
Object 4	ALUMINIUM	3	19000	500	YES
Object 9	CARBON FIBER	4	15000	1500	YES

Fig. 3. Input data of the digital version of the space debris recognition system and a classified set of reflected optical signals.

The results obtained show the correct operation of artificial intelligence, which classifies objects based on the input data of the reflected optic and radio signals.

Conclusion

The results of research and work done show that a space debris recognition system based on artificial intelligence has the potential to successfully detect and classify space debris. Artificial intelligence algorithms implemented in the system make it possible to effectively process and analyze large volumes of data on space debris.

REFERENCES

1. **Kessler D., Powell J.** Space Anxienty: The Threat from Space Debris. Springer. New York. (2009) 296.

2. **Goodfellow I., Bengio Y., Courville A.** Deeo Learning. MIT Press. Canada. (2016) 652.

Influence of light incidence angle on silicon solar cells performance with different texturing

E.Y. Yarchuk [1✉], **E. A. Vyacheslavova** [2], **A. O. Monastyrenko** [2], **A. S. Gudovskikh** [1,2]
[1] Saint Petersburg Electrotechnical University, St Petersburg, Russia
[2] Saint Petersburg Alferov University, St Petersburg, Russia
✉ernst_yarchuk@mail.ru

Abstract. The influence of the angle of incidence of the light flux on the photovoltaic characteristics of two types *a*-Si:H/c-Si heterojunction solar cells is investigated: KOH textured with a pyramidal surface, and black silicon with a nanostructured surface. Current-voltage characteristics and power depending on the angle of incidence of the solar flux – from 14 mW/cm^2 to 3 mW/cm^2 for *a*-Si:H/c-Si and from 9 mW/cm^2 to 2 mW/cm^2 for black silicon in the angle range 0-75° were obtained. Solar cell based on black silicon retains its characteristics 6% better as the angle of incidence of light increases to 75°.

Keywords: black silicon, amorphous silicon, heterojunction solar cell, current-voltage characteristic, angle of incidence.

Funding: The research was supported by the Russian Science Foundation Grant No. 23-29-00735, https://rscf.ru/project/23-29-00735/.

Introduction

One of the solutions to the issue of electricity availability is solar energy, which is actively developing now. It is estimated that the increase in electricity generation in this area will reach 260 GW by 2026 [1]. Understanding the dependence of the current-voltage characteristics (CVC) of a solar cell (SC) at different angles of its inclination relative to the incident light flux allows us to take conclusions about changes of electricity generation during daylight hours and evaluate its efficiency. Silicon solar cells dominate among photovoltaic cells, as they are relatively cheap, accessible and durable.

The most promising concept of SC is heterojunction *a*-Si:H/c-Si (HJT) technology [2] with anti-reflection coatings and a pyramidal textured surface to reduce optical losses [3, 4]. Also promising is black silicon (*b*-Si), which has minimal reflection in a wide range of waves [5] and retains these properties at high angles of light incidence on it.

In this article the influence of the angle of incidence of the light flux on the silicon solar cells on their current-voltage characteristics is considered.

Materials and Methods

Figure 1 shows two types of heterojunction (HJT) silicon *a*-Si:H/c-Si solar cells with an area of 1 cm^2 taken for the research: HJT based on black silicon (*b*-Si) with a nanotextured surface (Fig. 1*a*) and HJT with conventional pyramidal structure (*pyr*-Si) (Fig. 1*b*).

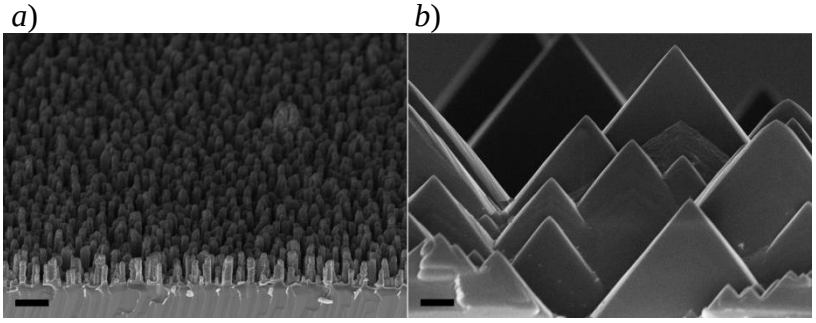


Fig. 1. SEM-images of the samples: *b*-Si (*a*), *pyr*-Si (*b*). The bare scale is 1000 nm

To study the angular dependences of the CVC, a rotary sample holder was made, which makes it possible to measure the CVC under a sunlight simulator over an effective range of angles without any shading.

Results and Discussion

The dependences of the CVC for these samples at angles of light incidence on them from 0° to 75°, the short circuit current and their power characteristics are shown in Figure 2.

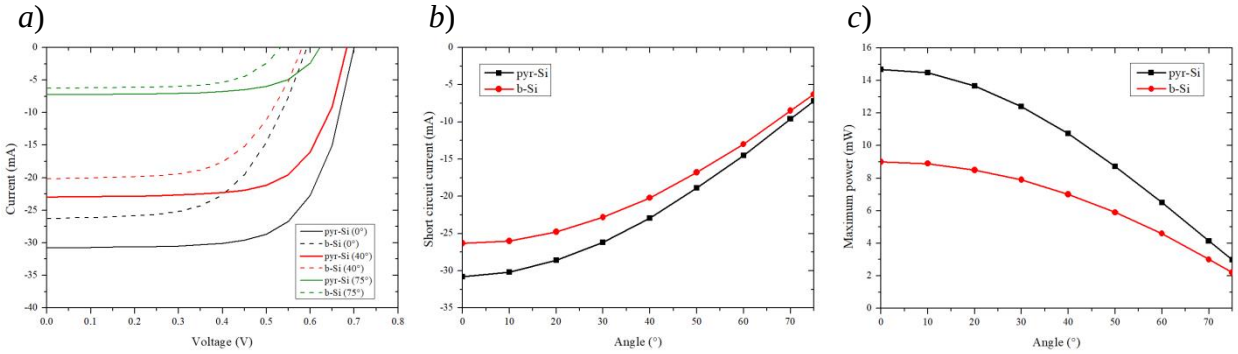


Fig. 2. Current-voltage characteristics for samples *pyr*-Si (solid lines) and *b*-Si (dashed lines) for angles of 0° (black lines), 40° (red) and 75° (green) (*a*), angular dependences of short circuit current (b) and maximum power (*c*) for samples *pyr*-Si (black lines) and *b*-Si (red)

The maximum power is observed at light incidence angles of 0-20° and decreases with increasing angle. The *a*-Si:H/c-Si demonstrates better characteristics (from 14.4 mW/cm^2 to 3 mW/cm^2, weakening – 79.2 %), but at the same time characteristics more strongly decrease with increasing light incidence angle than the *b*-Si sample, which at more modest absolute values (from 9 mW/cm^2 to 2.3 mW/cm^2, weakening – 74.5 %, 6 % better), remains more stable at large angles, which explained by the structure of its surface.

Conclusion

In this article, the influence of the angle of incidence of the light flux on the current-voltage characteristics of heterostructure solar cells with different surfaces was studied. As the angle of incidence of light increases, the characteristics of solar cells deteriorate, which is associated with reflection losses, but the nature of these changes is different. Thus, the *b*-Si shows more stability, while *pyr*-Si significantly loses its effective power with increasing angle. This shows the potential of black silicon research, and the need to improve black silicon production technologies.

Acknowledgments

The research was supported by the Russian Science Foundation Grant No. 23-29-00735, https://rscf.ru/project/23-29-00735/.

REFERENCES

1. A report by the International Energy Agency. Renewable electricity – Renewables 2021 – Analysis and key findings.

2. **Taguchi M., Yano A., Tohoda S., Matsuyama K., Nakamura Yu., Nishiwaki T., Kazunori F., Maruyama E.**, 24.7 % Record efficiency HIT solar cell on thin silicon wafer, IEEE J. of Photovoltaics. 4 (1) (2014) 96–99.

3. **Chuchvaga N. A., Kislyakova N. M., Tokmoldin N. S. Rakymetov B. A., Serikkanov A. S.**, Problems arising from using KOH-IPA etchant to texture silicon wafers, Technical Physics. 65 (10) (2020) 1685–1689.

4. **Atobaev O. K., Terukov E. I., Shelopin G. G., Kabulov R. R.**, Wet Chemical Treatment of Monocrytalline Silicon Wafer Surfaces, Applied Solar Energy. 57 (2021) 363–369.

5. **Liu X., Coxon P. R., Peters M., Hoex B., Cole J. M., Fray D. J.**, Black silicon: fabrication methods, properties and solar energy applications, Energy & Environmental Science. 7 (10) **(**2014) 3223–3263.

Ground receiving station with superconducting single photon detector in the laser communication system with the satellite «Impulse-1»

V.E. Merzlinkin [1,2✉], **D.O. Sevryukov** [1,3], **S.D. Levashov**[1,3], **V.L. Kurochkin**[1,2,4]
[1] QSpace Technologies, Moscow, Russia
[2] National University of Science and Technology MISIS, Moscow, Russia
[3] HSE University, Moscow, Russia
[4] Russian Quantum Center, Moscow, Russia
✉v.merzlinkin@goqrate.com

Abstract. Laser communication via satellite represents a promising avenue for data transmission in geographically isolated regions devoid of advanced infrastructure. This method is characterized by its high transmission speeds and low power requirements, presenting significant advantages. However, it is imperative that the optical channel exhibits greater transparency for light transmission, resulting in a severely restricted application of this technique for information transmission during adverse weather conditions or over extended distances. To mitigate these limitations, the employment of superconductive single-photon detectors as receivers has been proposed. This study demonstrates the successful deployment of laser communication using superconducting detectors aboard the compact spacecraft "Impulse-1" operated by QSpace. The results obtained demonstrate the possibility of the using superconducting detector with pulses in multiphoton mode.

Keywords: Laser communication, satellite, SSPD, PPM

Introduction

Laser communication between a low Earth orbit satellite and a ground station is one of the branches of the development of information transmission methods [1]. It has advantages in the speed and low power consumption, but certain fundamental limitations do not allow it to become a universal way of transmitting information to remote places. The utilization of superconducting detectors with a minimal dead time, high quantum efficiency, and a low frequency of dark count enables the transmission of a signal attenuated by atmospheric absorption and scattering as well as weather conditions [2-5].

Since the electrical response from the detector has a small jitter and leading edges, pulse-position modulation (PPM) is the most effective method for working with superconducting detectors [6]. The time position of a pulse within a period is used to encode about several bits of information.

We conducted a simulation of the laser communication channel considering the technical characteristics of the small spacecraft “Impulse-1”. We obtained a result from recording the reading of the detector pulses at a frequency of 25 MHz repetition (50 MBps).

Materials and Methods

The small spacecraft Impulse 1 of QSpace is a CubeSat, it has on board a laser terminal for classical communication transmitting a signal at a wavelength of 850 nm. The power of the laser signal is 20 mW, the maximum signal transmission frequency is 25 MHz with a pulse length of 5 ns, with these characteristics it is possible to implement the 2-PPM communication protocol, in it the amplitude and duration of the pulse remains unchanged, the information is encoded by the position of the pulse. Encoding scheme 2-PPM in a period: the first four 5 ns ($t_{\{00,01,10,11\}}$) are the time slots encoding the sequence of bits and next 20 ns t_{empty} is the relaxation time of the laser related to the characteristics of the terminal.

The superconducting detector used had a quantum efficiency of 60% and dark counts of 100 clicks per second at the current of 13.8 μA (80% of $I_{critical}$). The dead time of the detector is 10 ns.

The number of photons in the beam was described by the Poisson distribution. It is possible to introduce the probability of pulse detection by a superconducting detector of single photons as:

$$p_{pulse} = \sum_{n} \frac{<n>^{n} e^{-<n>}}{n!} \left(1 - \left(1 - Q_{efficiency}\right)^{n}\right) \quad (1)$$

where n is number of photons in the pulse, $<n>$ is the average value of photons number, $Q_{efficiency}$ is the quantum efficiency of SSPD.

Results and Discussion

The probability of receiving pulses from a laser source on a superconducting single photon detector is shown in Fig. 1. The probability of detecting a pulse is greater than 90% with an optical power exceeding four photons per pulse (*20 pW*). It is also evident that the data is close to the theoretical probability of reading the pulse. The noise in the remaining slots of the period is not exceeding 30 %.

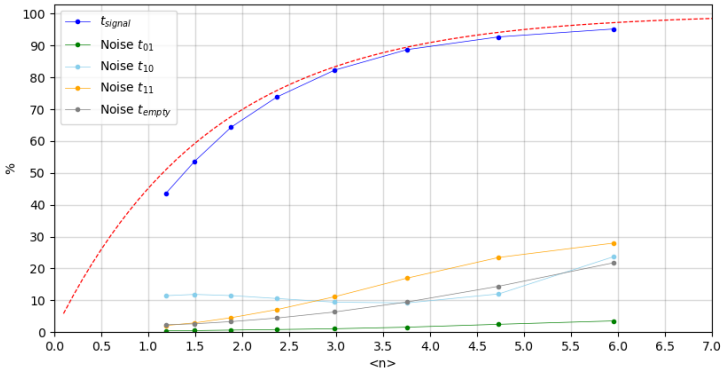


Fig. 1. Graphs of the total probability of receiving pulses (blue), theoretical probability (red) and probability of noise click in the remaining slots of 2-PPM coding

Conclusion

We have demonstrated that laser communication with the “Impulse-1” satellite is possible with a receiving part which is containing a superconducting detector of single photons. This increases the operating range of optical power, and it is possible to receive signal with a probability more than 90% by using 2-PPM coding and optical power more than *20 pW*. The quantity of noises did not exceed 30%.

REFERENCES

1. **Kaushal, H., & Kaddoum, G.,** Optical communication in space: Challenges and mitigation techniques. IEEE communications surveys & tutorials, 19(1), 57-96.

2. **Hao, H., Zhao, Q. Y., Huang, Y. H., Deng, J., Yang, F., Ru, S. Y., ... & Wu, P. H.,** A compact multi-pixel superconducting nanowire single-photon detector array supporting gigabit space-to-ground communications. Light: Science & Applications, 13(1), 25.

3. **Willis, M. M., Kerman, A. J., Grein, M. E., Kansky, J., Romkey, B. R., Dauler, E. A., ... & Boroson, D. M.,** Performance of a multimode photon-counting optical receiver for the NASA lunar laser communications demonstration. In International Conference on Space Optical Systems and Applications (ICSOS).

4. **Grein, M. E., Kerman, A. J., Dauler, E. A., Willis, M. M., Romkey, B., Molnar, R. J., ... & Boroson, D. M.,** An optical receiver for the lunar laser communication demonstration based on photon-counting superconducting nanowires. In Advanced Photon Counting Techniques IX (Vol. 9492, pp. 11-16). SPIE.

5. **Dauler, E. A., Robinson, B. S., Kerman, A. J., Anant, V., Barron, R. J., Berggren, K. K., ... & Yang, J. K.**, 1.25-Gbit/s photon-counting optical communications using a two-element superconducting nanowire single photon detector. In Advanced photon counting techniques (Vol. 6372, pp. 286-293). SPIE.

6. **Elganimi, T. Y.**, Performance comparison between OOK, PPM and PAM modulation schemes for free space optical (FSO) communication systems: Analytical study. International Journal of Computer Applications, 79(11).

LASER LOCATOR FOR UNDERWATER OBJECT DETECTION

D. A. Mys✉
Peter the Great Saint-Petersburg Polytechnic University, Saint-Petersburg, Russia Federation;
✉dima.mys@mail.ru.ru

Abstract: The developed laser locator is intended for use in monitoring underwater objects and structures during inspection technical work, as well as in monitoring the condition of the underwater part of offshore platforms, pipelines, cables and other underwater objects. A new object visualization system using a reflected laser radiation signal in various planes is proposed in the locator design. This allows you to define the contour of an object and identify it.

Keywords: underwater location, laser radiation, reflection, absorption, image, radiation power, aquatic environment, the object under study.

Introduction

Range and resolution are key characteristics of all underwater and aerial optical systems. In conventional underwater surveillance systems built according to the classical scheme (with floodlight), the achieved observation range does not exceed 0.7–0.8 Zb – transparency of water along the Secchi disk, up to 50 m. Presumably, the range of visibility can be increased by 2-3 times compared to systems using conventional lighting devices.

The main reason for the relatively short observation range of conventional underwater systems is the high absorption and scattering of light in the water. The scattering of light in water creates so-called "backscattering interferences", which significantly reduce the contrast of the image. The high level of light absorption by water requires the use of powerful lighting devices and highly sensitive photodetectors. Lasers are used as lighting devices, which make it possible to create powerful narrowly directed beams of light. To reduce the loss of light in water caused by its absorption, objects are illuminated in the blue-green spectral region of 520-540 nm, where light absorption by water is minimal.

To combat backscattering interference, two main methods are used – the isolation of a useful signal and backscattering interference in time (time selection) and in space (spatial selection). These methods are also used in other laser location systems.

The coordinates of the observed objects relative to the underwater vehicle are measured in such a system using the same laser measuring system. When it is running in rangefinder mode. The spatial resolution of the system in this range mode is determined by the duration of the light pulse and the shutter speed of the photodetector.

Despite the apparent simplicity of the description of the technology, its practical implementation is due to the solution of a number of very complex technical and technological problems.

Materials and Methods

A laser stray beam was aimed at the pool wall. The object of the study was pool tiles and seams, between tiles, as well as the transition from one material (tile of one color (black) - tile of another color (white)).

Images were recorded on a black-and-white CCD matrix based on the registration of reflected laser radiation from the pool wall. These images are shown in Figures 3.

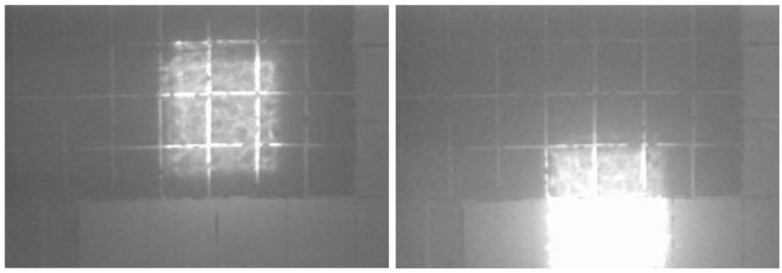


Figure 3 – (Left)The result of shooting when the scattered beam is directed to the center of perspective (at right angles to the pool wall) of the object under study.

(Right)The result of shooting when the scattered beam is directed towards the lower perspective boundary (at an angle to the pool wall) of the object under study.

The primary image processing of the pool wall (a line cutout from the image) was performed and an oscillogram of the intensity distribution (laser radiation amplitude) in the horizontal plane was obtained.

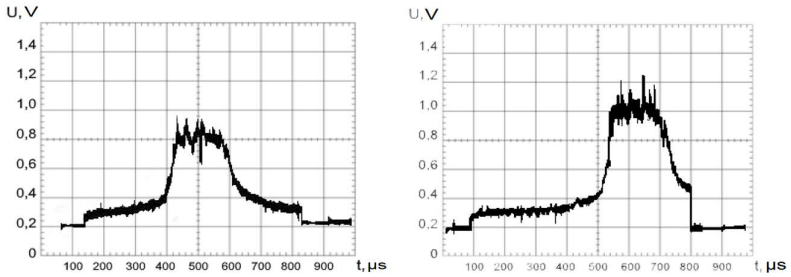


Figure 5-(Left)Waveform when the scattered beam is directed to the center of perspective (at right angles to the pool wall) of the object under study.

(Right)Waveform with the direction of the scattered beam to the lower boundary of the perspective (at an angle to the pool wall) of the object under study.

Conclusion

As a result of the experiment, photographs were obtained showing the contours of the pool tiles and the illumination of the camera when the direction of laser radiation is shifted.

The analysis of the obtained results shows that the developed design of the laser locator allows you to get an image of an object under water. The image quality allows you to distinguish contours on the surface of an object and identify them. It has also been experimentally proved that in a laser locator it is necessary to ensure a change in the power of laser radiation by at least an order of magnitude for its effective operation without illumination in images from the object under study.

REFERENCES

1. **D. Nikolaev, V. Chetiy, and V. Dudkin**, “Determining the location of an object during environmental monitoring in conditions of limited possibilities for the use of satellite positioning,” IOP Conference Series: Earth and Environmental Science, vol. 578(1), pp. 012052. November 2020.
2. **A. Moroz, A. Cheremisin, V. Meshalkin, and N. Semenova**, “On the possibility of growing vegetables and fruits on the lunar base,” IOP Conference Series: Earth and Environmental Science, vol. 578(1), pp. 012006, November 2020.

The quest for direct band beta iron disilicide: collaboration of theoretical and experimental approaches

S.A. Balagan [1]✉, A. V. Shevlyagin [1]

[1] Institute of Automation and Control Processes, FEB RAS, Vladivostok, Russia;

✉balagan@iacp.dvo.ru

Abstract. In the presented work, a theoretical study of the effect of β-$FeSi_2$ lattice deformation on the type and magnitude of the first transition in the electronic band structure was carried out. Images of nanocrystallites obtained using high-resolution transmission electron microscopy were used as a source of deformation data. All in all 137 variants of β-$FeSi_2$ lattice deformation were considered in the work. Six types of first transitions different from the first transition in unstrained β-$FeSi_2$ were discovered. The values of the first transitions from 0.02 to 0.64 eV (direct) and from 0.01 to 1.12 eV (indirect) were obtained.

Keywords: silicon, beta Fe disilicide, *ab initio* calculation

Funding: The research was carried out within the state assignment of IACP FEB RAS (Theme FWFW-2022-0003).

Introduction

In accordance with modern investigations β-$FeSi_2$ can be applied in light emitting, light absorbing and thermoelectric devices [1-4]. In all of these cases, it is significant to understand electron band structure nature of the material. Previous studies have shown that β-$FeSi_2$ light emitting ability depends on change of the fundamental transition as a consequence of lattice deformation. Lattice parameter variation is especially pronounced, when nanocrystallites (NCs) are embedded under different conditions. Within this investigation a wide range of high-resolution transmission electron microscopy (HRTEM) data was analyzed to extract information about β-$FeSi_2$ lattice deformation embedded into Si under different conditions. Based on the data obtained, *ab initio* calculations were carried out and the results will be discussed below.

Calculation details

The density-functional theory calculations were performed with the package VASP. The plane-wave basis with the ultra-soft Vanderbilt pseudopotential and the generalized gradient approximation (GGA) to the exchange-correlation functional were used. Non-spherical contributions from the gradient corrections were included. Monkhorst-Pack k-points grid of 8×8×8 and cut-off energy of 350 eV were used. The indirect fundamental energy gap was found of 0.60 eV (GGA theoretical value is of 0.62 eV [5] and experimental one is of 0.839 eV [6]).

Results and Discussion

To check how β-$FeSi_2$ band structure changes with a particular deformation HRTEM data were collected from literature and our previous experiments: 137 NCs were analyzed within this work to determine lattice deformation and then electron band structure was calculated for each strained cell. 113 of them had indirect band gap and 24 ones had direct band gap. Structures with direct band gap are in deformations range of Δa from +0.6 to +7.3%, Δb from -8.1 to +6.2%, Δc from -4.1 to +1.8%. Structures with indirect band gap are in deformations range of Δa from -9.7 to +10.4%, Δb from -6.0 to +7.3%, Δc from -7.7 to +5.3%. Positive Δ value corresponds to tension and negative one corresponds to compression. Thus β-$FeSi_2$ has narrow range of a and c lattice constants deformation, which allow existence of band structure with the first transition of direct type. On the other hand β-$FeSi_2$ shows flexible band structure depending on deformation allowing to obtain band gap in range from 0.02 to 0.64 eV (direct type) and in range from 0.01 to 1.12 eV (indirect type), that is opportunity to create light emitting and receiving devices of different frequency ranges using different creation conditions, but same material.

The other side of β-$FeSi_2$ band structure flexibility is location of the first transitions in reciprocal space. Fig. 1 shows obtained band structures with examples of fundamentally different first transitions: 2 direct ($\Gamma\rightarrow\Gamma$, $Y\rightarrow Y$) and 4 indirect ones ($Y\rightarrow\Gamma$, $\Lambda^*\rightarrow\Gamma$, $\Lambda^*\rightarrow Y$, $\Lambda^*\rightarrow T$).

Unstrained bulk β-$FeSi_2$ has Y→Λ* first transition. On the one hand direct-indirect type change is a reason why light radiation can be observed from some NCs, but not from others of similar size, on the other hand different direct transition positions in reciprocal space explain different experimentally observed luminescence spectra: band walleyes located in various points have various charge carrier effective mass, oscillator strength and energy with regard to Fermi level.

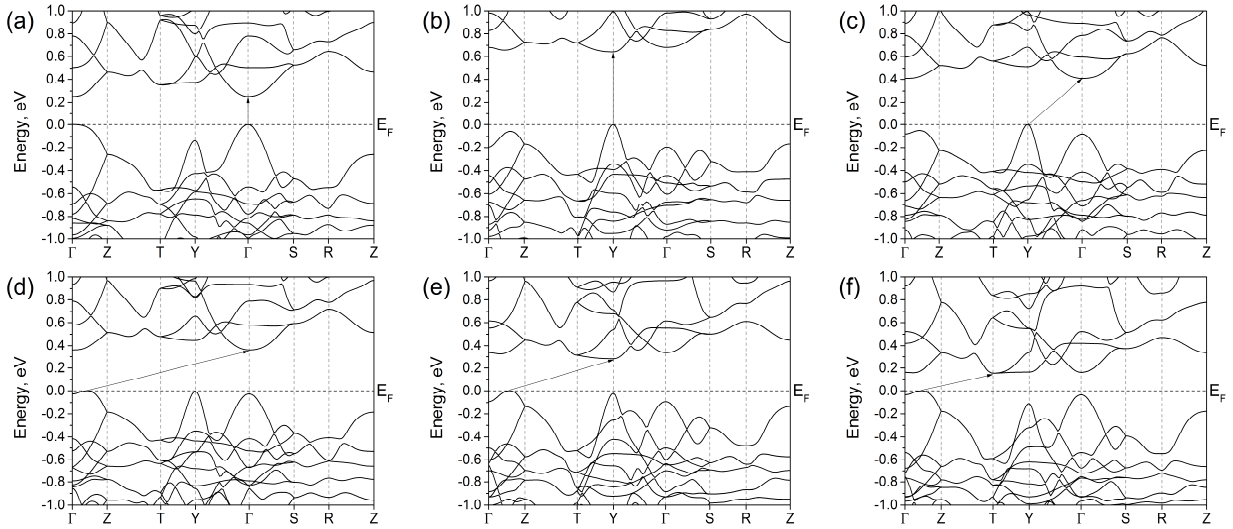


Fig. 1. β-$FeSi_2$ electron band stricture depending on the deformation (Δa, Δb and Δc are specified for each plot): +4.6%, -4.8%, +0.1% (*a*), +0.6%, -1.3%, -4.0% (*b*), +2.9%, -1.2%, +3.2% (*c*), +4.5%, -1.3%, +1.9% (*d*), +6.6%, -0.5%, -3.2% (*e*), +8.4%, -1.7%, -2.0% (*f*). The Fermi level is taken as the zero-energy point. Arrows show the first transition.

Conclusion

It was demonstrated that the first transition of direct type exists in narrow deformation range of 7.9%, 14.3% and 5.9% for a, b and c lattice constants, respectively. Whereas indirect one exists in wide range of 20.1%, 13.3% and 13.0% for a, b and c lattice constants, respectively. Six first transition types differed from fully relaxed bulk β-$FeSi_2$ were observed: 2 direct (Γ→Γ, Y→Y) and 4 indirect ones (Y→Γ, Λ*→Γ, Λ*→Y, Λ*→T).

Acknowledgments

All quantum mechanics calculations were distributed between computing facilities of IACP FEB RAS Shared Resource Center ‘Far Easten Computing Resource’ (https://cc.dvo.ru) and HPC cluster ‘Academician V.M. Matrosov’ (Irkutsk Supercomputer Center of SB RAS, https://hpc.icc.ru/).

REFERENCES

1. **Qiu P. et al.,** Exceptionally heavy doping boosts the performance of iron silicide for refractory thermoelectrics, Advanced Energy Materials 12 (18) (2022) 2200247.

2. **Akiyama K. et al.,** MOCVD growth of β-$FeSi_2$ film on modified Si surface by silver and enhancement of luminescence, 506 (2019) 131-134.

3. **Shevlyagin A. V. et al.,** A room-temperature-operated Si LED with β-$FeSi_2$ nanocrystals in the active layer: μW emission power at 1.5 μm, Journal of Applied Physics (121) (2017) 11.

4. **Balagan S. A. et al.,** Theoretical approach to embed nanocrystallites into a bulk crystalline matrix and the embedding influence on the electronic band structure and optical properties of the resulting heterostructures, Journal of Physics: Condensed Matter 30 (24) (2018) C. 245301.

5. **Moroni E. G. et al.,** Cohesive, structural, and electronic properties of Fe-Si compounds, Physical Review B. 59 (20) (1999) 12860.

6. **Maeda Y.,** Luminescence properties of β-$FeSi_2$ and its application to photonics, Applied surface science 254 (19) (2008) 6242-6247.

Effect of diameter on lattice thermal conductivity of α-$FeSi_2$ and ε-FeSi nanowires

S.A. Balagan [1]✉, N. G. Galkin [1]

[1] Institute of Automation and Control Processes, FEB RAS, Vladivostok, Russia;

✉balagan@iacp.dvo.ru

Abstract. In this study the effect of α-$FeSi_2$ and ε-FeSi nanowires diameter on the lattice thermal conductivity was considered. *Ab initio* modeling was performed in the temperature range of 100-700 ˚K and nanowires diameter range of 6-48 nm. Results showed that at minimal considered diameter nanowires have 1.4-4.5 times lower lattice thermal conductivity than bulk material depending on temperature and nanowire elongate direction.

Keywords: silicon, Fe silicides, nanowires, *ab initio* calculation, thermal conductivity

Funding: This study was supported by the Russian Science Foundation, grant No. 22-12-00036.

Introduction

The current technology evolution has resulted in high energy consumption. While it's necessary to increase energy efficiency, it's also important to look for new sources of energy [1]. Using heat released by burning fuel or electrical devices with thermoelectric converters is one method of increasing energy efficiency. Another possible application of thermoelectrics is generating electricity for spacecraft [2]. The Seebeck coefficient, electrical conductivity, and thermal conductivity all affect a material's thermoelectric efficiency. In turn, thermal conductivity also encompasses phonon and electron thermal conductivity. The investigation of the lattice thermal conductivity of ε-FeSi and α-$FeSi_2$ is the main emphasis of this work.

Calculation details

The density-functional theory calculations were performed with the package VASP. Generalized gradient approximation (GGA) to the exchange-correlation functional was used. Non-spherical contributions from the gradient corrections were included. Γ-centered k-points and q-points grids were used and the cut-off energy was of 300 eV. Relaxation was performed with respect to the atoms' positions, volume, and the shape of the cell. For structure relaxation k-points grids were of 24×24×12 and 12×12×12 for α-$FeSi_2$ and ε-FeSi, respectively. Forces constants calculations were performed with the k-point grid of 3×3×3 for both materials and supercells were of 4×4×2 and 2×2×2 unit cells for α-$FeSi_2$ and ε-FeSi, respectively. The phonon properties were calculated within the harmonic approximation using Phonopy package. The elements of dynamical matrix were determined by employing density-functional-perturbation theory. Lattice thermal conductivity was calculated by means of Boltzmann transport equation solving implemented in ShengBTE package. Q-points grid was of 32×32×32 for both materials.

Results and Discussion

Calculation showed that obtained phonon bands structures are in good agreement with that of in Refs. [3-4]. The results show that α-$FeSi_2$ has less acoustic phonon frequency value compared to ε-FeSi, which is one of the factors for lower lattice thermal conductivity, since usually the main contribution to lattice thermal conductivity comes from acoustic phonons.

Lattice thermal conductivity calculation show that on the one hand α-$FeSi_2$ and ε-FeSi have commensurable phonons group velocity and on the other hand α-$FeSi_2$ has an order of magnitude higher scattering rate, thereby one has an order of magnitude lower phonons mean free path. As well this is an important factor reducing lattice thermal conductivity. Approximately 80% of the contribution to lattice thermal conductivity comes from acoustic phonons in both materials, which as well means lower thermal conductivity value of α-$FeSi_2$ compared to ε-FeSi.

Obtained lattice thermal conductivity values are shown in Fig. 1. Bulk materials values are in agreement with results in Refs. [5-6]. Depending on temperature and heat spread direction bulk α-$FeSi_2$ has 2 – 4 times lower lattice thermal conductivity compared to that of ε-FeSi.

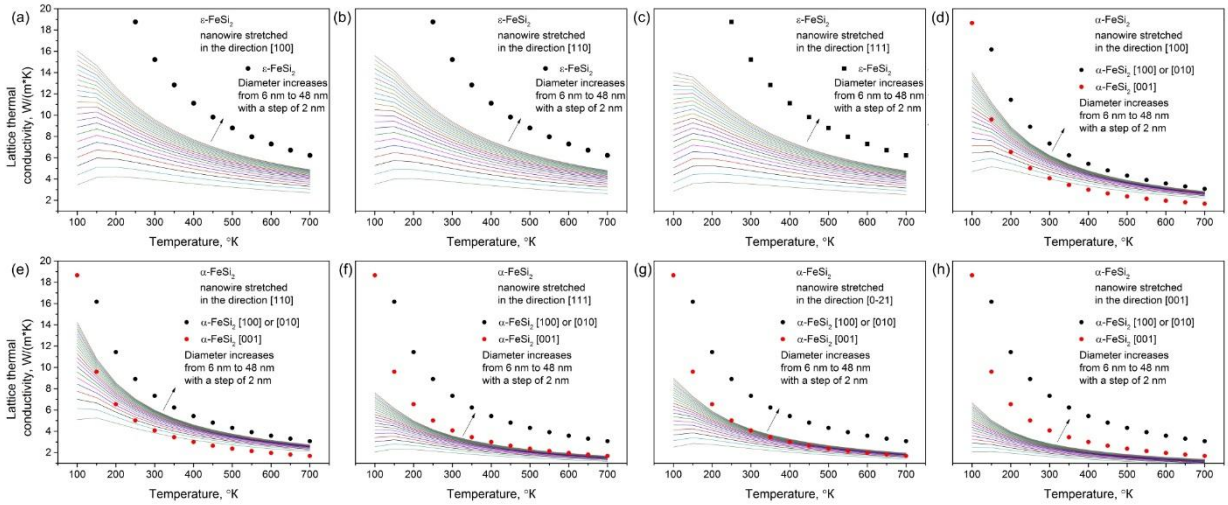


Fig. 1. ε-FeSi nanowires lattice thermal conductivity in directions: [100] (*a*), [110] (*b*), [111] (*c*) and that of α-$FeSi_2$: [100] (*d*), [110] (*e*), [111] (*f*), [0$\bar{2}$1] (*g*), [001] (*h*). Black and red dots are bulk crystal data.

Lattice thermal conductivity calculation of α-$FeSi_2$ nanowires showed significant dependence on the direction in which the nanowire is elongated: 2 – 2.5 times. The same calculations performed for ε-FeSi showed weak dependence of 1.02 – 1.20 times. Results of the calculation were applied in Ref. [7].

Conclusion

α-$FeSi_2$ and ε-FeSi nanowires diameter effect on the lattice thermal conductivity was considered. Calculations showed strong dependence of α-$FeSi_2$ nanowires lattice thermal conductivity on the direction in which nanowire is elongated and weak one for ε-FeSi nanowires.

Acknowledgments

Boltzmann transport equation solving and quantum mechanics calculations were performed with the use of the computing facilities of IACP FEB RAS Shared Resource Center ‘Far Easten Computing Resource’ (https://cc.dvo.ru) and HPC cluster ‘Academician V.M. Matrosov’ (Irkutsk Supercomputer Center of SB RAS, https://hpc.icc.ru/) , respectively.

REFERENCES

1. **Hasan M. N. et al.,** Inorganic thermoelectric materials: A review //International Journal of Energy Research 44 (8) (2020) 6170-6222.

2. **Candolfi C. et al.,** Thermoelectric materials for space applications, CEAS Space Journal 13 (2021) 325-340.

3. **Khan N. et al.,** Combined inelastic neutron scattering and ab initio lattice dynamics study of FeSi, Physical Review B. 105 (13) (2022) 134304.

4. **Kalt J. et al.,** Lattice dynamics and polarization-dependent phonon damping in α-phase $FeSi_2$ nanostructures //Physical Review B. 101 (16) (2020) 165406.

5. **Waldecker G., Meinhold H., Birkholz U.,** Thermal conductivity of semiconducting and metallic $FeSi_2$, Physica Status Solidi (a) 15 (1) (1973) 143-149.

6. **Stern R. et al.,** Influence of point defects on the thermal conductivity in FeSi, Physical Review B. 97 (19) (2018) 195201.

7. **Argunov Efim V. et al.,** Ultrathin Cr and Fe monosilicides on Si (111) substrate: formation, optical and thermoelectrical properties, St. Petersburg Polytechnic University Journal. Physics and Mathematics 68 (3.1) (2023) 84-89.

Influence of the doping level in the absorption layer of InGaAs/InP 2.5 um photodetectors on their electrical properties

O. V. Barantsev[1]✉, E. I. Vasilkova[1], E. V. Pirogov[1], K. Yu. Shubina[1], K. O. Voropaev[2], A. A. Vasil'ev[2], L. Ya. Karachinsky[1], I. I. Novikov[1] , M. S. Sobolev[1]

[1]Alferov University, Saint-Petersburg, Russia

[2] JSC "OKB-Planeta", Velikiy Novgorod, Russia

✉ ovbarantsev@gmail.com

Abstract. $In_{0.83}Ga_{0.17}As$/InP PIN-photodiode heterostructures with different doping levels have been grown by molecular beam epitaxy. Metamorphic buffer layers were applied to prevent misfit dislocations nucleation in active layers. Electrochemical capacitance-voltage and current-voltage curves of fabricated photodetectors have been studied. The impact of various dark current mechanisms has been estimated after the investigation of current-voltage curves obtained at different temperatures.

Keywords: Metamorphic buffer layers, infrared photodetectors, molecular beam epitaxy.

Funding: The study was funded by the Ministry of Science and Higher Education of the Russian Federation (grant №FSRM-2023-0006).

Introduction

InGaAs/InAlAs/InP photodetectors operating in the spectral range of 2.2–2.6 um have a wide range of applications. They can be used in infrared spectroscopy devices, gas analysers, and night vision sensors [1]. However, to achieve high performance in this spectral range, $In_{0.83}Ga_{0.17}As$ absorption layer must be used. Since the absorption layer and InP substrate have a mismatch of 2.1% in the lattice constant, metamorphic buffer layers (MBLs) need to be used.

The properties of optoelectronic devices are closely connected with the density of misfit dislocations. In photodiodes, such defects can lead to dark current increasing. Dark current is a noise, which prevents photodetectors from functioning at low luminous intensities [2]. MBLs can effectively suppress generation of misfit dislocations in the absorption layer, but it is necessary to find optimal design and growth parameters to achieve the best device characteristics. In the present work, influence of the doping level in the absorption layer has been investigated.

Materials and Methods

PIN-photodiode heterostructures were manufactured by molecular beam epitaxy using a semi-industrial Riber49 setup. N^+-type "epi-ready" InP (100) wafers were used to grow two structures with different doping levels and superlattice inserts in the absorption layer, called S-1 and S-2.

At the beginning of growth, a thin 100 nm lattice-matched $In_{0.52}Ga_{0.48}As$ layer was grown. Next, n^+-InAlAs metamorphic buffer layers were formed by gradually increasing In mole fraction at growth temperatures of 500-510°. MBLs contained three InAlAs/InAs superlattice inserts. Structure S-1 was made with an inverse step in MBLs: In mole fraction was increased up to 86%. S-2 was manufactured without an inverse step, but $In_{0.83}Ga_{0.17}As/In_{0.83}Al_{0.17}As$ digital superlattice inserts before and after the absorption layer were formed. MBLs growth was followed by thermocycling process of peak temperature rise up to 630° and slow cooling to 50°. After MBLs, 1.5 um $In_{0.83}Ga_{0.17}As$ active layer was grown. The absorption layer was slightly n-doped using Si. The doping concentration of the active layer in S-2 was 4 times higher than in S-1. At the end, 0.6 um p^+-type contact layers doped with Be were formed on the top of the heterostructure.

Photosensitive areas and contacts were fabricated using a standard photolithography procedure. A schematic structure of produced PIN-photidiodes is presented in Fig. 1.

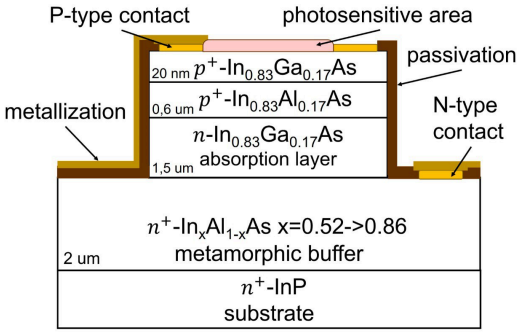


Fig. 1. Schematic structure of the PIN-photodiode.

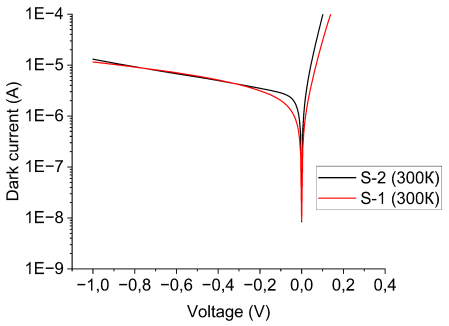


Fig. 2. I-V curves of structures at 300K.

ECV profiles were measured by Electrochemical capacitance voltage profiler ECV Pro (Nanometrics, USA). The I-V curves at different temperatures were obtained using The Keithley 2400 measuring setup.

Results and Discussion

ECV measurements helped to calculate carrier concentrations in the active layer of two samples. In S-1 its value is $2 \cdot 10^{16}$ cm^{-3}, and in S-2 it is $8 \cdot 10^{16}$ cm^{-3}, which is 4 times higher, as expected. In p^+-type and n^+-type contact layers, carrier concentrations are $2 \cdot 10^{18}$ cm^{-3}, showing that PIN structures were successfully manufactured.

I-V curves of structures at room temperature of 300K are shown in Fig. 2. They are highly asymmetrical, showing a diode-like behaviour. At reverse bias voltages less than 0.2 V, dark currents values of samples are different: in S-2 the dark current is higher by almost an order of magnitude. However, at higher bias voltages, the dark currents of structures are nearly identical, reaching the value of $\sim 1.2 \cdot 10^{-5}$ A at a bias voltage of -1 V. This probably indicates that high doping of active layers leads to an increase in diffusion dark currents. But, as it is still necessary to slightly dope active layers, doping concentration should be $\sim (1 - 2) \cdot 10^{16}$ cm^{-3}.

Current-voltage curves, obtained at different temperatures, show that diffusion and generation-recombination dark currents are dominating at high temperatures 200-300 K. At lower temperatures surface leakage and tunnelling mechanisms prevail. Dark current values decrease with temperature, showing the largest drop by more than two orders of magnitude at reverse bias voltages less than 0.4 V. It presumably indicates the high influence of diffusion dark current mechanism.

Conclusion

$In_{0.83}Ga_{0.17}As$/InP PIN-photodiode heterostructures with different doping levels and superlattice inserts have been researched. It was discovered, that doping concentrations of active layers should be $\sim (1 - 2) \cdot 10^{16}$ cm^{-3} for achieving better performance. The value of the dark current was determined to be $\sim 1.2 \cdot 10^{-5}$ A at a bias voltage of -1 V at room temperature. The influence of different dark current mechanisms was determined based on dark current values temperature dependence.

REFERENCES

1. **I. D. Burlakov, L. Y. Grinchenko, A. I. Dirochka, N. B. Zaletaev**, Short wavelength infrared InGaAs detectors, Advances in Applied Physics (Uspekhi Prikladnoi Fiziki) 2(2), 2014.

2. **Li Ping, Li Tao, Deng Shuangyan, Li Xue, Shao Xiumei, Tang Hengjing, Gong Haimei**, Dark current analysis of mesa type In0.83Ga0.17As p-i-n photodiodes with different annealing treatment, Infrared and Laser Engineering Vol.45 No.5, 2016.

Formation of nanocones on the surface of $Pb_{0.4}Sn_{0.6}Te$ films during ion-plasma treatment with argon ions with an energy of 140 eV

Y. D. Belov[1]✉, S. P. Zimin[1,2], I. I. Amirov[1], L. A. Mazaletskiy[1,2]

[1]Yaroslavl Branch of the Valiev Institute of Physics and Technology, Russian Academy of Sciences, Yaroslavl, Russia

[2]P.G. Demidov Yaroslavl State University, Yaroslavl, Russia

✉yadbelov@gmail.com

Abstract. The article examines the modification of the surface of $Pb_{0.4}Sn_{0.6}Te$ epitaxial films during ion-plasma treatment in argon plasma. Lead-tin telluride films with a thickness of 2 μm were grown on (111) BaF_2 substrates by molecular beam epitaxy. Ion-plasma treatment RF high-density low-pressure inductively coupled argon plasma were carried out discharge at an ion energy of 140 eV. The duration of the process was 60 and 120 s. The parameters of an ensemble of nanocones are studied, and the evolution of the cone heights, their lateral dimensions, and surface density with varying processing time is described.

Keywords: argon plasma, lead-tin telluride, nanostructuring

Funding: This study was funded by ministry of Science and Higher Education of Russia for Valiev Institute of Physics and Technology number FFNN-2022-0017of RAS.

Introduction

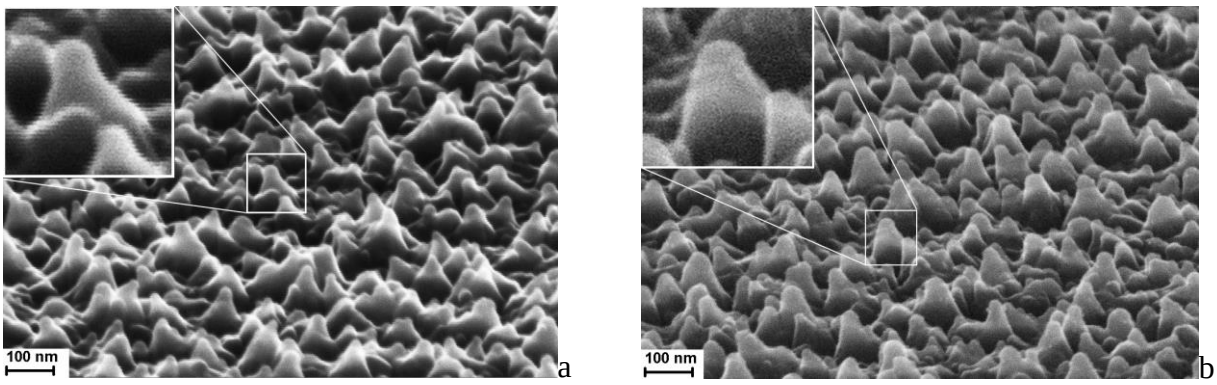
Currently, among the methods for modifying the surface of IV-VI semiconductors, ion-plasma processing methods stand out favorably, which make it possible to control the architecture and parameters of the created micro- and nanostructures in a wide range by varying the ion energy and duration of treatment [1]. The purpose of this work was to study nanostructures that appear on the surface of $Pb_{0.4}Sn_{0.6}Te$ epitaxial films during ion-plasma treatment with an argon ion energy of 140 eV, intermediate between previous experiments of 25 [3] and 200 [4] eV.

Materials and Methods

$Pb_{0.4}Sn_{0.6}Te$ films were grown by molecular beam epitaxy using a Riber 32 P setup (INPE, Brazil) on (111) BaF_2 substrates by the authors of [2]. Ion-plasma processing of the samples was carried out in a dense argon plasma reactor of a high-frequency induction discharge (13.56 MHz, 800 W) [1]. The treatment was carried out at ion energies of 140 eV, the treatment duration was 60 and 120 s. Surface morphology studies were carried out by scanning electron microscopy (SEM) using a Zeiss Supra-40 microscope.

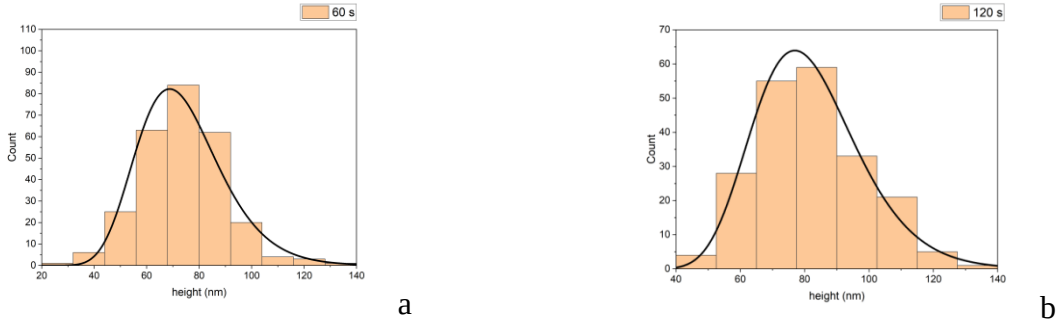
Results and Discussion

The initial samples had a smooth surface with the presence of dislocation pits. During plasma treatment of $Pb_{0.4}Sn_{0.6}Te$ films, the formation of ensembles of cone-shaped structures shown in Fig. 1 was observed. After treatment for 60 s, the cones had a height of 70 nm and had a metal quasi-spherical cap [4]. The formation of such nanocones was not observed under similar processing conditions for $Pb_{1-x}Sn_xTe$ films with compositions close to lead telluride or tin telluride. When the processing time was increased to 120 s, the height of the structures increased to 80 nm. In this case, the lateral dimensions of the bases of the nanocones were 60 nm for 60 s and 65 nm for 120 s. The surface density of the structures after 60 s of treatment was $\sim 1*10^{10}$ cm^{-2}; with increasing treatment time to 120 s, the density decreased to $\sim 7*10^{9}$ cm^{-2}. Based on the graphs (Fig. 2), it was determined that the amount of material on the surface increased by 10%.



a b

Fig. 1 Modification of the surface of the $Pb_{0.4}Sn_{0.6}Te$ film after treatment in argon plasma with an ion energy of 140 eV for 60 (a) and 120 (b) s. View at an angle of 70º.



a b

Fig. 2 Histograms of the distribution of heights of cone-shaped structures after treatment for 60 (a) and 120 (b) s.

Conclusion

During plasma treatment of $Pb_{0.4}Sn_{0.6}Te$ films, the growth of nanocones occurs according to the "vapor-liquid-solid" mechanism with a parallel process of ion sputtering and begins at shorter treatment times (60 s). It is shown that changing the geometric parameters of nanocones for treatment times of 60 and 120 s for x = 0.6 is a slow process, which is an unexpected effect. A detailed discussion of the results is provided.

Acknowledgments

SEM investigations were carried out at the Facilities Sharing Centre "Diagnostics of Micro- and Nanostructures" with the support of the Ministry of Science and Higher Education of Russian Federation. Authors are grateful to E. Abramof, P. H. O. Rappl (Brasil) for the provided samples.

REFERENCES

1. **Zimin S. P., Gorlachev E. S., Amirov I. I.,** Inductively Coupled Plasma Sputtering: Structure of IV-VI Semiconductors. In Encyclopedia of Plasma Technology 1st ed. J L Shohet, (2017) 679-691.

2. **Rappl P. H. O., Closs H., Ferreira S. O., Abramof E., Boschetti C., Motisuke P., Ueta A. Y., Bandeira I. N.,** Molecular beam epitaxial growth of high quality $Pb_{1-x}Sn_xTe$ layers with $0 \leqslant x \leqslant 1$, Journal of Crystal Growth, 191(3) (1998) 466-471.

3. **Zimin S. P., Amirov I. I., Naumov V. V., Belov Y. D., Abramof E., Rappl P. H. O.,** Surface modification of lead–tin telluride films with low-energy argon ions, J. Surf. Invest.: X-Ray Synchrotron Neutron Tech, 10 (1) (2022) 66-74.

4. **Zimin S. P., Gorlachev E. S., Amirov I. I., Naumov V. V., Juskenas R., Skapas M., Abramof E., Rappl P. H. O.,** Plasma-assisted surface nanostructuring of epitaxial $Pb_{1-x}Sn_xTe$ ($0 \leq x \leq 1$) films, Semiconductor Science and Technology, 34 (9) (2019) 095001.

Non-resonant vibrational scanning probe microscopy techniques for studying nanomaterials

A. A. Bobkov [1,2]✉, **I. A. Novikov** [1,2]

[1] Saint Petersburg Electrotechnical University "LETI", Saint-Petersburg, Russia;

[2] "Active Photonics" BV, Saint-Petersburg, Russia

✉ a.bobkov@ntmdt-russia.com

Abstract. Since its introduction, the atomic force microscope (AFM) has become an important research phenomenon in surface physics. There is a great demand for a wide range of AFM instruments using the method of studying the effective local properties of a sample surface at a nanometer spatial level, including such mechanical properties of the surface: Young's modulus, rigidity, adhesion.

Keywords: AFM, SPM, jumping microscopy, sol-gel

Introduction

Classical measurement techniques in AFM are divided into two groups: static and dynamic [1]. In the first case, the analysis of materials is carried out by tracking the deviation of the elastic console of the probe sensor (cantilever) from its initial position, and in the second - by changing the amplitude and phase of forced oscillations of the probe as a result of interaction with the sample. Excitation of oscillations in dynamic modes is carried out at the natural frequencies of the cantilever, which amount to hundreds of kHz and depend on the design of the probe.

In addition to traditional research methods consisting of mapping the surface of a sample, it is also possible to carry out local measurements of the mechanical and electrical properties of an object by taking "approach-retraction curves" - the dependence of the bending of the elastic console on the distance z above the sample. This method of measuring surface properties is called scanning hopping microscopy (SJM) or in the devices of "NT MDT" BV HybriD mode (HD).

The essence of HD mode is to sequentially measure the dependence of the force of pressing the probe to the surface of the sample on the distance between the probe and the sample F(z) at each point of the scanning area. Thus, moving from pixel to pixel it is possible to obtain the distribution of a large number of structure parameters over the surface within one scan. This scanning mode is considered more gentle both in relation to the samples and in relation to the probe due to the absence of lateral interaction forces, leading to twisting of the probe and subsequently to its breakage.

Materials and Methods

Let us consider the capabilities of SPM using the example of studying the sol-gel system of zinc oxide and silicon dioxide (Fig. 1). Nanostructured zinc oxide and its composites are a promising material that is used in various devices (semiconductor devices, flexible screens, LEDs, etc.) and various fields (solar energy, photocatalysis, sensors, medicine) [2].

AFM studies were carried out using an NTEGRA Prima scanning probe microscope manufactured by "NT MDT" BV.

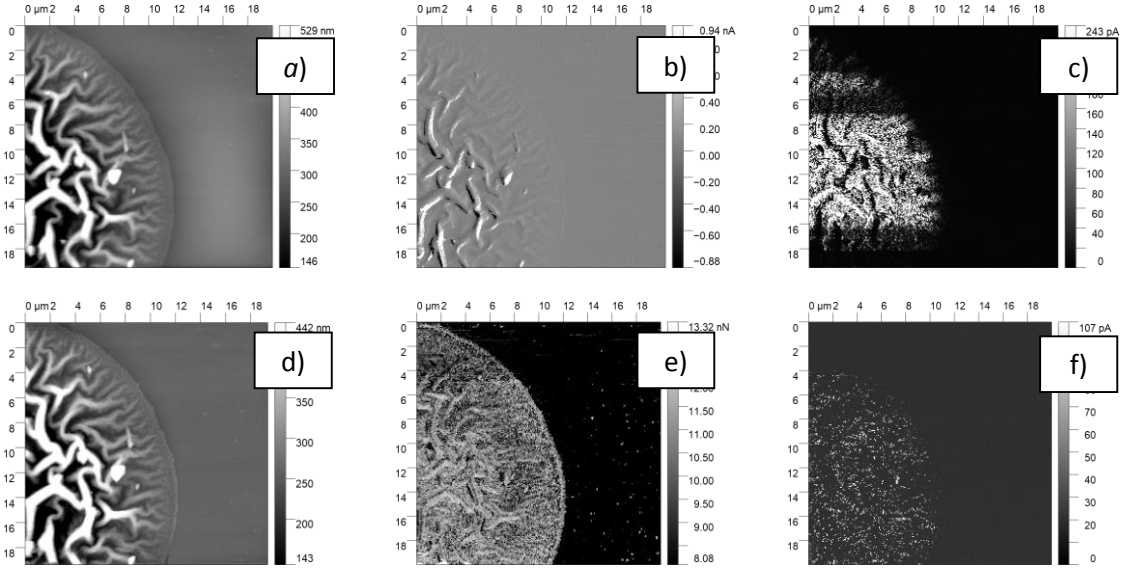


Fig. 1. AFM images of the sol-gel system ZnO-SiO2 on a Si substrate, obtained in contact (a-c) and SPM (d-f) modes

Results and Discussion

In Fig. 1 shows the results of scanning the same area, first in contact mode using the technique of measuring spreading resistance, and then in HD mode. As you can see, HD is not inferior to classical measurement methods in terms of the quality of the resulting surface topography image, as can be seen from a comparison of the images in Fig. 1, a) and fig. 1, d). Image in Fig. 1, b) represents the arithmetic mean value of the forces of lateral twisting of the cantilever (LF signal) in the forward and reverse passes, displaying a map of the distribution of friction forces over the surface. Current distribution map in Fig. 1, c) quite clearly demonstrates the differences in the electrically conductive properties of the substrate and the sol-gel system deposited on it. Adhesion forces in Fig. 1, e) demonstrate differences in the amount of adhesion between the probe and the sample during the scanning process, making it possible to qualitatively distinguish lyophilic and lyophobic areas of the surface. The current map (Fig. 1, f)), obtained in the HD mode, more accurately measures conductivity channels due to the absence of lateral twisting of the cantilever during scanning, which is inherent in traditional methods for studying spreading resistance, which reduces the contact area between the probe and the surface sample.

Conclusion

This work demonstrated new opportunities for a comprehensive study of nanostructured materials within the framework of scanning probe microscopy. Jumping microscopy in combination with existing operating modes of atomic force microscopes will undoubtedly make it possible to carry out micro- and nanoscopy of the properties of materials in a qualitatively new way [3].

REFERENCES

1. Atomic force microscopy for the study of nanostructured materials and instrumental structures: textbook. allowance / **V.A. Moshnikov, Yu.M. Spivak, P.A. Alekseev, N.V. Permyakov**. – St. Petersburg: Publishing house of St. Petersburg Electrotechnical University “LETI”, 2014. – 144 p.

2. Nanostructured oxide materials in modern micro-, nano- and optoelectronics / **O. A. Aleksandrova, at all.**. // edited by V. A. Moshnikova, O. A. Aleksandrovoy. St. Petersburg: Publishing house of St. Petersburg Electrotechnical University "LETI", 2017. 266 p.

3. **Novikov I.A., Teslenko E.G.** Trends in the development of atomic force microscopy for use in the field of nanotechnology // Science of the present and future. – 2023. – T. 1. – P. 240-243.

Optically active nanocomposites based on CsPbBr3 nanocrystals and chiral carbon dots

A.A. Vedernikova [1]✉, A.A. Efimova [1], H. Huang [2], E.V. Ushakova [1,3]

[1] ITMO University, Saint Petersburg, Russia;

[2] Soochow University, Suzhou, China;

[3] City University of Hong Kong, Hong Kong SAR, China

✉aavedernikova@itmo.ru

Abstract. Chiral nanomaterials are one of the rapidly expanding fields of nanoscience. Here, organic-inorganic nanocomposites, where chirality of $CsPbBr_3$ nanocrystals (NCs) was triggered by chiral carbon dots (C-dots), were developed. NCs were synthesized by ligand-assisted coprecipitation at room temperature, where chiral C-dots were used as one of precursors. Nanocomposites have circular dichroism signal with dissymmetry factor up to $1 \cdot 10^{-3}$ in the region of electron transitions of NCs, which can be preserved up to a month.

Keywords: chirality, carbon dots, perovskites

Funding: This work was supported by Priority 2030 Federal Academic Leadership Program and conducted within the RPMA grant of School of Physics and Engineering of ITMO University.

Introduction

Chirality is one of the most unique phenomena in nature and can be employed in the fields of bioapplications, chemistry, optical and electrical devices. Perovskite nanocrystals (NCs) have outstanding electrical properties and chiral NCs have emerged as promising materials for spintronics [1]. Spintronics devises could manipulate of the charge of current carriers and their spin which promise to process exponentially more information than traditional electronics [2].

Composites of perovskites with different type of nanomaterials have potential in developing new material with novel properties. In this work, organic carbon dots (C-dots) induce chirality and the inorganic NCs are responsible for optical excitation without exposure to external magnetic fields, which could be a solution to the problem of high cost and difficulties in manufacturing spintronics devices.

Materials and Methods

C-dots synthesis. Chiral C-dots were obtained by solvent free heating of precursors. Common organic precursors for perovskites - formamidinium bromide and chiral (R)-methylbenzylamine were transferred into closed stainless-steel autoclave in inert atmosphere in glovebox. After that, it was heated in an oven at 180 °C for 4 hours. Resulting stock solution cooled to room temperature naturally. Obtained C-dots were dissolved in isopropyl alcohol and this solution was further purified from unreacted molecular by cellulose dialysis tubes with a molecular weight of 500 Da for ~ 24 hours against alcohol.

NCs synthesis. The colloidal $CsPbBr_3$ NCs were synthesized following the procedure reported previously [3]. For chiral NC sample, the 150 μL (0.6 mg) of chiral C-dots were added in cooled solution of $PbBr_2$ precursor and was ultrasonicated for 15 min and then heated to 90 °C again. And then the synthesis procedure followed the reported one [3].

Characterization. The absorption spectra were detected under the illumination of the light source (Oceaninsight, DH-2000-BAL), the photoluminescence (PL) spectra were detected under 365 nm excitation (Oceaninsight, L365A), and all the data were recorded by a fluorescence spectrophotometer (Oceaninsight, QEPRO). Circular dichroism spectra were measured on a spectrometer J-815 (JASCO).

Results and Discussion

As a result of the synthesis process, the N,O-doped C-dots were formed. The optical properties of C-dots are shown in Figure 1. Obtained C-dots have absorption band at 320 nm and PL band at 443 nm while excited at 365 nm. Circular dichroism (CD) spectrum (Figure 1b) demonstrates three bands at 260, 288 and 318 nm. The negative extremum is attributed to signal from (R)-methylbenzylamine. Both positive extrema can be attributed to aggregates of chiral molecules. The dissymmetry factor (g-factor) for 318 nm peak is estimated as $3.5 \cdot 10^{-4}$.

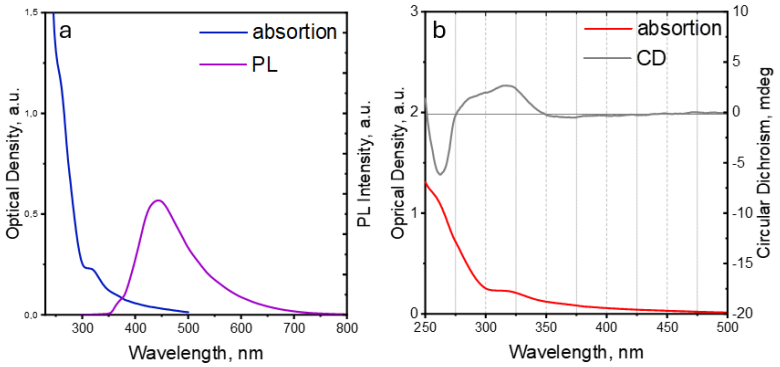


Fig.1. Absorption and PL spectra (a), CD and absorption spectra (b) of C-dots. Designation of the curves is shown in the legend for each figure.

The addition of chiral C-dots during the perovskite NCs synthesis leads to an appearance of new absorption band at 435 nm (Figure 2a) and to PL band blue shift (Figure 2b). The CD spectrum (Figure 2b) demonstrate two negative extrema in region of electron transitions of NCs. The g-factor of 460 nm peak is estimated as $1 \cdot 10^{-3}$. Obtained nanocomposites can preserve the CD signal up to month but with noticeable decrease in signal intensity.

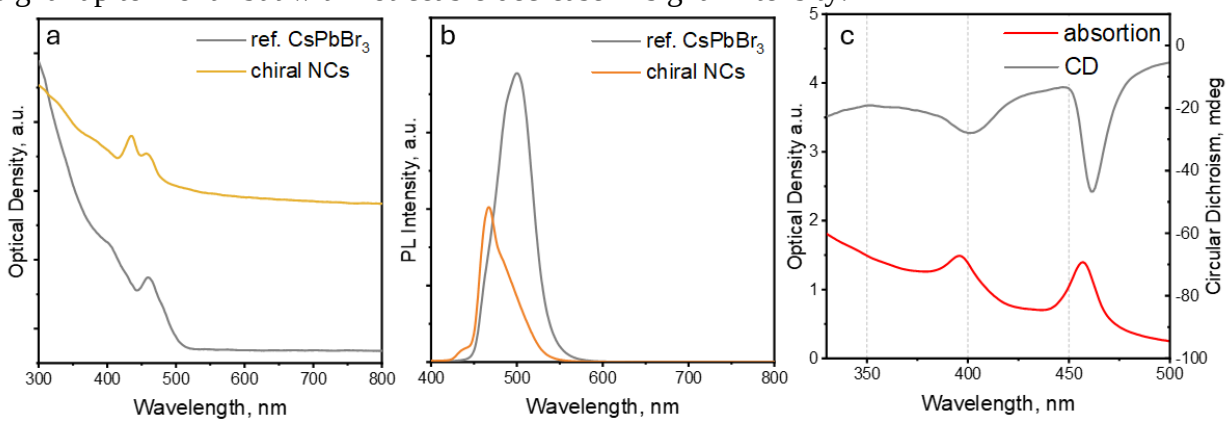


Fig. 2. Absorption (a), PL (b) spectra of referent $CsPbBr_3$ and chiral NCs, CD spectrum (c) of chiral NCs. Designation of the curves is shown in the legend for each figure.

Conclusion

In conclusion, the synthesis protocol of chiral nanocomposites based on perovskite NCs with chemical formula $CsPbBr_3$ and chiral C-dots was developed. The obtained NCs have CD signal in the region of 350-500 nm with g-factor of $1 \cdot 10^{-3}$.

Acknowledgments

The authors express their gratitude to the School of Optoelectronic Science and Engineering and Collaborative Innovation Center of Suzhou Nano Science and Technology, Soochow University, China.

REFERENCES

1. **Long G., Sabatini R., Saidaminov M. I., Lakhwani G., Rasmita A., Liu X., Sargent E. H. and Gao W.** Chiral-perovskite optoelectronics, Nature Reviews Materials. 5 (2020) 423–39.

2. **Hirohata A., Yamada K., Nakatani Y., Prejbeanu I., Diény B., Pirro P. and Hillebrands B.** Review on spintronics: Principles and device applications. Journal of Magnetism and Magnetic Materials 509 (2020) 166711.

3. **Zhang Y., Sun R., Ou X., Fu K., Chen Q., Ding Y., Xu L., Liu L., Han Y., Malko A. V.** Metal Halide Perovskite Nanosheet for X-ray High-Resolution Scintillation Imaging Screens. ACS Nano 13 (2019) 2520–5

Study of evolution of SiC/Si hybrid structures by RHEED and Owens-Wendt methods

M.G. Vorobev[1]✉, A.S. Toikka[2], S.A. Kukushkin[1]
[1] Institute for Problems in Mechanical Engineering of the RAS, St. Petersburg, Russia;
[2] Vavilov State Optical Institute, St. Petersburg, Russia;
✉vmg@ipme.ru

Abstract. To study the evolution of the crystal structure of SiC/Si substrates, a number of samples with growth times of 1, 3, 5, 10, 20, 30 and 40 minutes were grown by the method of coordinated substitution of atoms. These samples were investigated by reflection high-energy electron diffraction (RHEED) and measurement of the contact angle by the sessile drop method. The evolution of the surface reconstruction of epitaxial silicon carbide has been analyzed. It is shown how the free surface energy varies with time and the relationship between the surface reconstruction and time is shown.

Keywords: silicon carbide, semiconductors, RHEED, OWRK method.

Funding: This research was supported by a state order to the Institute for Problems in Mechanical Engineering of the Russian Academy of Sciences, project No. FFNF-2021-0001, theme №121112500383-9.

Introduction

The method of coordinated substitution of atoms is a technique for producing epitaxial silicon carbide on silicon.[1] Silicon carbide can be used as a substrate for the growth of AIIIBV semiconductor structures, which can be used in sensors or high-electron-mobility transistors HEMT.[2] However, for high-quality epitaxy of semiconductors on crystalline structures, it is necessary to know the properties of the substrate surface. In [3,4], studies on the evolution of SiC/Si crystal structure by various methods including Raman spectroscopy, ellipsometry and others are presented. For this study, we used reflection high-energy electron diffraction methods and the method of measurement of the contact angle by the sessile drop method, which has not been used before.

Materials and Methods

Silicon carbide films were produced on n- and p- Si wafers for 1, 3, 5, 10, 20, 30 and 40 minutes. The silicon wafers were subjected to a pre-growth treatment, during which possible contamination by organic impurities, foreign microparticles, metal ions and anions were removed from their surface. The growth temperature was 1270 °C, growth was carried out in CO atmosphere with gas flow Q(CO) =12 ml/min. The gas pressure in the reactor was 270 Pa.

The microstructures were analyzed using two methods. Reflection high-energy electron diffraction was taken on an electronograph EMR-100 at an electron energy of 50 keV. Determination of surface properties by wetting method was carried out on an OCA 15EC. The liquids used were distilled water and toluene as polar and nonpolar systems.

Results and Discussion

Analysis of wetting angles showed that the SiC film has a free surface energy of about 40 mJ/m^2, with values ranging from 35 mJ/m^2 to 56 mJ/m^2 Analysis of RHEED images showed that silicon carbide obtained at growth times of 1, 5, 10, 30 and 40 minutes has a reconstruction of (3x3), while samples grown at 3 and 20 minutes have a reconstruction of (2x2). In the early stages of growth, the surface energy of the films on substrates of both conductivity types changes little, but the differences are more significant with increasing growth. Since the growth took place in CO atmosphere, without the addition of silane SiH4, the pores under the silicon carbide film play a major role in the surface formation.

At early stages of growth, when the surface is not formed and the pores are small, the difference in surface energy is insignificant. However, at further growth (more than 20 minutes),

there is a growth of pores and increase in their number due to which there are strong surface stresses, and the reconstruction of the surface has less influence on the value of surface energy. It is also observed that there is a difference in the conductivity of the substrates, the free surface energy of n-type substrates is higher than that of p-type substrates.

Conclusion

In this work, the time dependences of the free surface energy of SiC/Si hybrid structures grown by the method of coordinated substitution of atoms have been investigated. It is shown that at small growth times the surface reconstruction has a decisive role in the surface energy value. However, when the growth time increases, the influence of the reconstruction is not paramount.

Acknowledgments

This research was supported by a state order to the Institute for Problems in Mechanical Engineering of the Russian Academy of Sciences, project No. FFNF-2021-0001, theme № 121112500383-9. Authors would like to thank V.V. Antipov for RHEED measurements and A.S. Grashchenko for samples growth.

References

1. **S.A. Kukushkin, A.V. Osipov**. Epitaxial Silicon Carbide on Silicon. Method of Coordinated Substitution of Atoms (A Review), Russian Journal of General Chemistry. 92 (2022) 584-610.

2. **S.A. Kukushkin, L.K. Markov, A.S. Pavlyuchenko, I.P. Smirnova, A.V. Osipov, A.S. Grashchenko, A.E. Nikolaev, A.V. Sakharov, A.F. Tsatsulnikov, G.V. Sviatets**. SiC/Si Hybrid Substrate Synthesized by the Method of Coordinated Substitution of Atoms: A New Type of Substrate for LEDs, Coatings. 13(7) (2023) 1-17.

3. **Y.A. Eremeev, M.G. Vorobev, A.S. Grashchenko, A.V. Semencha, A.V. Osipov, S.A. Kukushkin**. Change of the elastic strain in SiC films growing on Si substrates by the method of consistent atomic substitution, Physics of the Solid State. 65(1) (2023) 68-72.

4. **I.A. Eremeev, M.G. Vorobev, A.S. Grashchenko, E.V. Pirogov, V.D. Andreeva, A.V. Osipov, S.A. Kukushkin**. Evolution of the crystal microstructure of hybrid SiC/Si substrates grown by the method of atomic substitution, St. Petersburg Polytechnic University Journal. Physics and Mathematics. 16(1.1) (2023) 113-118.

Investigation of properties of periodic multilayer BP/Si nanoheterostructures grown by PECVD.

G. E. Vtorygin [1], A. I. Baranov [1✉], A. V. Uvarov [1], A. A. Maksimova [1,2], E.A. Vyacheslavova [1], A. S. Gudovskikh [1,2]

[1] Alferov University, St Petersburg, Russia;

[2] St Petersburg Electrotechnical University "LETI", St Petersburg, Russia;

✉baranov_art@spbau.ru

Abstract. Periodic BP/Si multilayer structure was grown on n-Si wafers by PECVD mode at low temperature with diborane. SEM image confirmed good quality of layer alternation with the same thickness for BP and Si respectively. Different capacitance measurements allowed to detect point defects and interface states in BP/Si heterostructure.

Keywords: heterojunction, boron phosphide, superlattice, DLTS.

Funding: The reported study was supported by the Russian Science Foundation under the grant number 21-79-10413, https://rscf.ru/project/21-79-10413/.

Introduction

Nowadays, there is an active search for new semiconductor materials to replace amorphous silicon as an emitter in solar cells on monocrystalline silicon substrates. In [1], it was theoretically shown that boron phosphide (BP) is one of the most promising binary compounds for creating a p-type emitter for n-Si substrates, since it is indirect gap and has a large difference between the energy of indirect (2 eV) and direct transition (4 eV), which leads to a large conduction band gap at the p-BP/n-Si heterojunction, creating a selective contact for holes. Recently, we grew BP layers using plasma-chemical deposition at low temperatures and studied their electrical properties, where they showed significant incorporation of carbon due to the use of trimethylboron, which, among other things, led to pinning of the Fermi level at the BP/n-Si heterointerface [2] . For this reason, in subsequent experiments we began to use diborane [3], which made it possible to achieve an optical band gap of 1.9 eV of BP layer. Furthermore, using of periodic nanoheterostructures GaP/Si grown by PE-ALD allowed to decrease optical bandgap energy [4] and defined conduction band offset of 0.39 eV by DLTS and admittance spectroscopy [5]. Therefore, in this work, we will study properties of multilayer periodic BP/Si nanoheterostructures grown by PECVD mode on silicon wafer with diborane.

Materials and Methods

BP and Si layers were grown in a standard Oxford PlasmaLab 100 PECVD (13.56 MHz) plasma chemical deposition in continuous PECVD mode on n-type double-sided polished c-Si (1×10^{15} cm^{-3}). Multilayer sample consists of 7 quantum wells of silicon between 8 barriers of BP. Suggested thicknesses of BP and Si layers were 20 nm and 10 nm respectively. Schottky barriers to superlattice BP/Si were formed by vacuum evaporation of gold in BOC Edwards Auto500 setup, and ohmic contact was formed from the bottom side of silicon wafer. Admittance spectroscopy and capacitance-voltage measurements were performed using a precision E4980A Keysight (former Agilent) LCR-meter. Measurements of capacitance DLTS were performed using an automated installation based on a Boonton-7200B capacitance bridge in the temperature range of 40-400 K in helium cryostate Janis CCS-400H/204.

Results and Discussion

SEM image of multilayer periodic BP/Si nanoheterostructures grown by PECVD is shown in Figure 1. Obviously, we obtained perfect periodic structure with the same thickness for all BP and Si layers respectively. Further, capacitance measurements were performed, and DLTS spectra for different conditions are shown on Figure 2. In result, different two series peak were detected for both cases. We suggest that some of responses are associated with point defects in

BP and interface states in BP/Si heterointerfaces. More detailed analysis of such performance will be presented in conference: admittance spectroscopy and DLTS in another conditions will be done to define nature of responses.

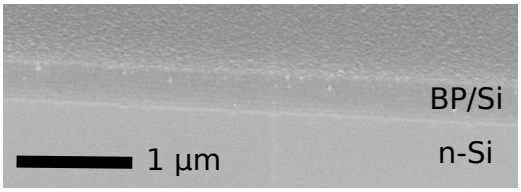


Fig. 1. SEM image of multilayer periodic BP/Si nanoheterostructures grown by PECVD.

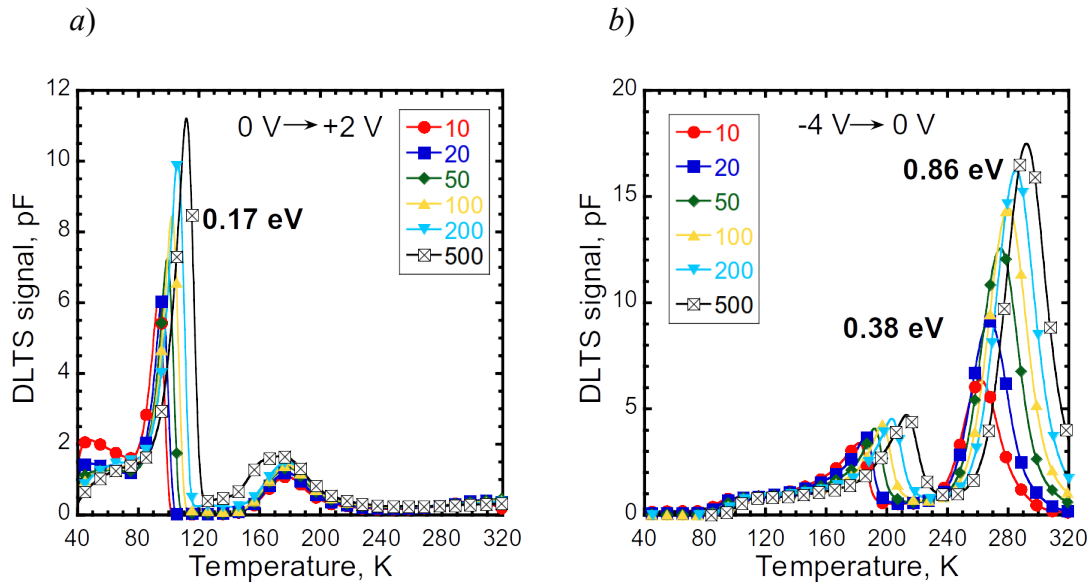


Fig. 2. DLTS spectra for V_{init}=0 V, V_{pulse}=+2V (a) and V_{init}= -4 V, V_{pulse}= 4 V (b) for different emission rates.

Conclusion

Periodic BP/Si multilayer structure was grown on n-Si wafers by PECVD mode at low temperature with diborane. SEM image confirmed good quality of layer alternation with the same thickness for BP and Si respectively. Different capacitance measurements allowed to detect point defects and interface states in BP/Si heterostructure.

REFERENCES

1. **Varley J.B., Miglio A., Ha V., van Setten M.J., Rignanese G., Hautier G.**, High-Throughput Design of Non-oxide p-Type Transparent Conducting Materials: Data Mining, Search Strategy, and Identification of Boron Phosphide, Chem. Mater. 29(6) (2017) 2568–2573.
2. **Maksimova A.A., Uvarov A.V., Baranov A.I., Gudovskikh A.S., Kudryashov D.A., Vyacheslavova E.A., Morozov I.A., LeGall S.S., Kleider J.P.,** Investigation of Plasma Deposited Boron Phosphide and Its Contact to Silicon, ACS Appl. Energy Mater. 5(5) (2022) 5367-5373.
3. **Maksimova A.A., Uvarov A.V., Pozdeev V.A., Kirilenko D.A., Baranov A.I., Vyacheslavova E.A., Gudovskikh A.S.,** Boron phosphide grown by PECVD and its optical properties, St. Petersburg State Polytechnical University Journal: Physics and Mathematics. 16(3.2) (2023) 273–277.
4. **Uvarov A. V., Gudovskikh A.S., Baranov A.I., Maksimova A.A., Maksimova A.A., Kudryashov D.A., Vyacheslavova E.A, Yakovlev G.E., Zubkov V.I.,** Plasma-Deposited Multilayer GaP/Si p-i-n Structure for Tandem Silicon-Based Solar Cells, ACS

Appl. Energy Mater. 5(5) (2022) 5374–5380.
5. **Gudovskikh A.S., Baranov A.I., Uvarov A.V., Kudryashov D.A., Kleider J.P.,** Space charge capacitance study of GaP/Si multilayer structures grown by plasma deposition, J. Phys. D. Appl. Phys. 55(13) (2022) 135103.

MBE Growth of InGaN Nanowires: Influence of the III/V Flux Ratio on the Structural and Optical Properties

V. O. Gridchin [1,2]✉, S. D. Komarov[3], I. P. Soshnikov[1,2,4], R. R. Reznik[2], G. E. Cirlin [1-3]

[1] Alferov University, Saint Petersburg, Russia;

[2] St Petersburg University, Saint Petersburg, Russia;

[3] IAI RAS, Saint Petersburg, Russia;

[4] HSE University, Saint Petersburg, Russia;

[5] Ioffe Institute, Saint Petersburg, Russia

✉gridchinvo@gmail.com

Abstract. The direct integration of epitaxial III-N heterostructures on Si substrates is a promising platform for the development of optoelectronic devices. In this work we investigate the influence of the III/V flux ratio on the structural and optical characteristics of core-shell InGaN nanowires grown by plasma-assisted molecular-beam epitaxy. It is found that the formation of InGaN nanowires with a core–shell structure occurs when the III/V flux ratio (taking into account the In-incorporation coefficient) is about 0.9–1.2. The samples exhibit photoluminescence at room temperature with a maximum in the accordance with chemical composition. The results obtained may be of interest for studying the growth processes of InGaN nanowires and creating RGB light-emitting devices based on them.

Keywords: Nanowires, molecular beam epitaxy, InGaN, GaN, optical properties, morphological properties

Funding: The work was carried out with financial support under the Russian Science Foundation (project no. 23-79-00012).

Introduction

InGaN-based ternary compounds are of significant interest for the creation of light-emitting devices operating in the spectral range of emission from near ultraviolet (UV) to near infrared (IR) due to their direct band gap structure with an energy varying from ~0.7 to 3.4 eV [1]. However, their active use is hampered by the difficulty of obtaining high quality thin layers since for the InN–GaN pair the lattice mismatch in the wurtzite structure is about 11 % [2]. For this reason and due to the polarization properties of wurtzite structures, the efficiency of commercial InGaN LEDs decreases sharply with increasing In content in the InGaN active region. [3]. One of the promising ways to improve the quality of grown structures and obtain highly efficient LEDs based on InGaN ternary compounds may be the synthesis of nanowires (NWs).

In this work, for the first time, study of the effect of the III/V flux ratio on the formation and properties of InGaN nanowires is presented.

Materials and Methods

InGaN nanowires were grown on boron-doped silicon substrates with (111) crystallographic orientation on a Riber Compact 12 setup. Before loading into the growth chamber, the substrates were treated in a solution of hydrofluoric acid and deionized water in a ratio of 1:3 to remove silicon oxide from the surface. Then the substrates were loaded into the growth chamber, heated to 950°C, and annealed for 20 min. After that, the temperature was lowered to 650°C. After stabilization of the substrate temperature, a nitrogen-plasma source was initiated at a power of 450 W and a nitrogen flux of N2 corresponding to a pressure of 1.4 × 10–5 Torr. Then the shutters of the In and Ga sources were opened simultaneously, and the growth of InGaN continued for 21 h 25 min. A series of experiments was carried out, in which the fluxes F_{In} and F_{Ga} were equal to each other, the nitrogen flux was constant, but the total value $F_{III} = F_{In} + F_{Ga}$ was varied. Flux measurements were carried out using a Bayard–Alpert gauge directly at the growth surface of the substrate.

The morphological properties of the samples were studied by scanning electron microscopy (SEM) using a Supra 25 Zeiss device. Studies of the photoluminescence were carried out at the Unique Scientific Installation “Complex optoelectronic stand of the National Research University,

Higher School of Economics, St. Petersburg" using photoluminescence (PL) spectroscopy at room temperature with a He–Cd laser (radiation wavelength of 325 nm) and a pump power of 6.5 mW. The signal was detected using a Sol instruments MS5204i monochromator and a silicon photodetector

Results and Discussion

At relatively low total fluxes F_{III}, InGaN nanocrystals with a height of 1.2 μm are formed on the Si(111) surface. Moreover, the diameter of the nanocrystals at the vertices sharply narrows to 10–50 nm. In the nanocrystals of this type, a sharp narrowing in their diameter indicates the formation of several InGaN phases with different In contents [4]. When F_{III} is increased to 2×10^{-7} Torr, spatially separated InGaN nanowires with a height of ~2 μm and a diameter of ~100 nm are formed (Fig. 1b). This growth mode was studied in detail in [5]. Nanowires of this type have a spontaneously formed core–shell structure and contain In in the cores in an amount of ~40–45 %. At total F_{III} fluxes equal to 2.5 and 3×10^{-7} Torr, similar nanowires are formed, but of higher height and diameter than the previous one. A further increase in metal fluxes F_{III} up to 5×10^{-7} Torr (Fig. 1c) leads to the Me-rich growth conditions and formation of a merged nanocolumnar layer with a height of 2.7 μm. The diameter of the nanocolumns reaches 600 nm.

The results of energy-dispersive X-ray spectroscopy in SEM equipment were compared with measured photoluminescence spectra at room temperature. Using modified Vegard's law and taking into account In desorption from the growth surface we estimated the In composition in grown samples.

Conclusion

Thus, to form InGaN nanowires with a spontaneous core– shell structure, it is necessary to maintain neither too high nor too low the ratio of III/V fluxes taking into account In desorption. The results obtained may be of interest for studying the growth processes of InGaN nanowires using plasma-assisted molecular-beam epitaxy and creating light-emitting systems based on one group of materials using RGB technology.

REFERENCES

1. **H. Morkoç**, Handbook of Nitride Semiconductors and Devices, Materials Properties, Physics and Growth (John Wiley & Sons, 2009), 1331.

2. **Ho I., Stringfellow G.,** Solid Phase Immiscibility in GaInN, Applied Physics Letters. 69 (18) (1996) 2701–2703.

3. **Usman M., Munsif M., Mushtaq U., Anwar A. R., Muhammad N.** Green gap in GaN-based light-emitting diodes: in perspective, Critical Reviews in Solid State and Materials Sciences, 46(5), (2021) 450-467.

4. **T. Shugabaev, V. O. Gridchin, S. D. Komarov, D. A. Kirilenko, N. V. Kryzhanovskaya, K. P. Kotlyar, R. R. Reznik, Y. I. Girshova, V. V. Nikolaev, M. A. Kaliteevski, and G. E. Cirlin**, Photoluminescence redistribution of InGaN nanowires induced by plasmonic silver nanoparticles, Nanomaterials. 13 (6), (2023) 1069.

5. **I. P. Soshnikov, K. P. Koltyar, R. R. Reznik, V. O. Gridchin, V. V. Lendyashova, A. V. Vershinin, V. V. Lysak, D. A. Kirilenko, N. A. Bert, and G. E. Cirlin**, Specific Features of Structural Stresses in InGaN/GaN Nanowires, Semiconductors. 55 (10), (2021) 795.

The method of obtaining Ni and Co nanowires in porous anodic alumina matrices

E. A. Grushevski[1], ✉, N. G. Savinski[1], O. S. Trushin[1]

[1]Federal State Budgetary Institution of Science K. A. Valiev Institute of Physics and Technology of the Russian Academy of Sciences Yaroslavl Branch, Yaroslavl, Russia;

✉yaregor@mail.ru

Abstract. This paper focuses on the investigation of producing Ni and Co nanowire arrays synthesized using Al_2O_3 porous template. Porous alumina samples were obtained by double electrochemical anodizing of the prepared foil in 0.5 M oxalic acid, at a voltage of 60 V and a temperature of 25 °C. The pore diameter distribution maximums are about 85 nm. Nanowires were electrodeposited in a 3-electrode electrochemical cell into prepared matrices in a potentio/galvanostatic mode. Studies of the surface of porous membranes and the geometry of nanowires were carried out using scanning electron microscope.

Keywords: anodization, aluminum oxide matrices, nanowires, electrochemical deposition.

Funding: The work was carried out within the framework of the State program № FFNN-2022-0018 of the Ministry of Science and Higher Education of Russia on the equipment of the center for the collective use of scientific equipment "Diagnostics of micro- and nanostructures".

Introduction

One of the best and most extensive methods for ensuring repeatability and high quality of the resulting nanostructures is the use of porous anodic aluminium oxide (PAAO) templates [1-3], in particular arrays for the growth of controlled, self-organizing, as well as highly ordered structures, including nanorods, nanowires, nanotubes, nanocomposite materials with strict adherence to product dimensions at a packing density of 10^9-10^{11} units/cm^2. Much attention has been drawn to the study of magnetic nanomaterials and nanostructures with strong shape anisotropy, promising for use in nanosensors, spintronic devices and high-density magnetic recording. It is known that one of the most common method obtaining such nanowires (NW) is a template synthesis – filling required material in narrow channels in porous matrices. The unique properties of porous anodic aluminum oxide (PAAO) membranes make this material potentially the best template for electrochemical deposition of Ni nanowires. [4-5]

Materials and Methods

To produce porous matrices of aluminum oxide, we used 2×2 cm Al (99, 9% purity) plates with a 1 mm thickness. To obtain a smooth surface, the samples were electropolished, resulting in a mirror-like surface. Anodizing was carried out using 0.5 M oxalic acid with the temperature about 25 °C in a potentiostatic mode at 60 V. The duration of the first anodization was t = 60 minutes, after which the oxide layer was removed in CrO_3 (1.8%) + H_3PO_4 (6%) at T = 80 °C for 10 minutes. Second anodization for all samples was carried out for 1 hour. Then the voltage was lowered to 5 V at a speed of 60 mV/s to thin the barrier layer. In this work, aluminum was not removed, and the barrier layer was destroyed when the polarity was reversed at the beginning of the deposition process. [3] Ni nanowires were electrodeposited in a 3-electrode electrochemical cell using $NiCl_2$*$6H_2O$+H_3BO_3+H_2O solution into prepared matrices in a galvanostatic mode at a current density of 75 mA/cm2 for 10 minutes. Co nanowires were electrodeposited in a 3-electrode electrochemical cell using $CoSO_4 \cdot 7H_2O$+ $CoCl_2 \cdot 6H_2O$+H_3BO_3+H_2O solution into prepared matrices in a potentiostatic mode at a voltage of 850 mV for 10 minutes.

Results and discussion

Figure 1a shows an SEM image of the PAAO template before deposition. The SEM image of PAAO was further analyzed using ImageJ software, and pore diameter (Dp) = 85 ± 2.2 nm, pore distance (Dc) = 116 ± 5 nm and pore length (Lp) = 50 ± 1.5 microns were determined.

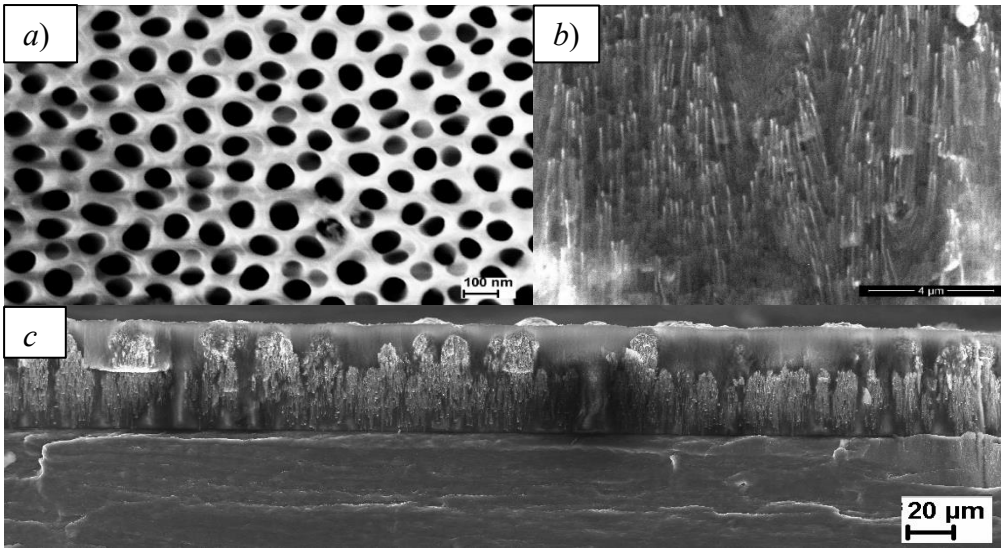


Fig. 1. (*a*) SEM image of the PAAO template before deposition (*b*) Co nanowires in porous alumina (*c*) Ni nanowires in porous alumina

Figures 1b and 1c show obtained Co and Ni nanowires, respectively. As can be seen from Figure 1c, some nanowires grew to the surface of the matrix. This is probably due to the imperfection of the structure of the porous matrix, including double and dead-end pores. In the pores, the nickel nanowires are separated from each other by the matrix, but when they come to the surface, as a result of their growth characteristics, they begin to form “caps”, which subsequently merge with each other into large agglomerations of nickel.

Conclusions

Porous templates were obtained by double electrochemical anodizing in 0.5 M oxalic acid at a temperature of 25 °C in a potentiostatic mode at 60 V. A technological scheme for obtaining Ni and Co nanowires with 250 aspect ratio in porous anodic alumina matrices has been developed and were investigated by scanning electron microscopy.

Acknowledgments

The work was carried out within the framework of the State program № FFNN-2022-0018 of the Ministry of Science and Higher Education of Russia on the equipment of the center for the collective use of scientific equipment "Diagnostics of micro- and nanostructures".

References

1. **Masuda H., Yamada H., Satoh M.**, Highly-ordered nanochannel-array architecture in anodic alumina, Appl. Phys. Lett. 71 (1997) p. 2770.
2. **Muratova E. N.**, Artificially and naturally ordered micro- and nanoscale capillary membranes based on anodic aluminum oxide: Ph.D. Thesis, St. Petersburg: ETU “LETI” (2014) 232 p.
3. **Vorobeva A. I., Utkina E. A., Komar O. M.**, Homogeneous deposition of nickel in the pore of ordered thin aluminum oxide, Russian Microelectronics. 42 (2013) 79-88.
4. **Safeer A., Ahmad N., Khan S., Azam L., Bashir D.**, Magnetization behavior of electrochemically synthesized Co2MnSn full Heusler alloy nanowire arrays, J. Appl. Phys. 125 (2019) Art. No. 034302.
5. **Varvaro,G., Casoli,F.**,Ultrahigh–density magnetic recording storage materials and media designs, Stanford: Pan Stanford Publishing (2016) 509 p.

Surface and electrical properties of La-SnO_2 thin films

G. V. Tolstyak[1], A.P. Starnikova[2]✉, I.A.Gulyaeva[2], E. M. Bayan[1], V. V. Petrov[2]

[1]Department of Chemistry, Southern Federal University, Rostov-on-Don, 344090, Russia;

[2]Institute of Nanotechnologies, Electronics, and Equipment Engineering, Southern Federal University, Taganrog, 347922, Russia

✉iten@sfedu.ru

Abstract. The surface and electrical properties of La-SnO_2 thin films (1, 3, 5, 10 % La^{3+}) were studied. The temperature dependence of the film resistance and the activation energy of conductivity depend nonlinearly on an increase in the La^{3+} content in the films. With an increase in the La^{3+} content in films in the temperature range of 300–400 K, the activation energy of conductivity initially drops by half, and in the temperature range of 400–570 K it doubles.

Keywords: tin oxide, lanthanum, thin films, electrophysical properties.

Funding: This study was financially supported by the Russian Science Foundation, Project No. 24-29-00203, https://rscf.ru/en/project/24-29-00203/.

Introduction

Materials based on tin dioxide are currently being actively studied around the world. The main reason is the unique properties of this material. Among them, good semiconductor properties are distinguished: tin dioxide has high electrical conductivity, due to which it is used in gas sensors. To improve the properties of this compound, various transition metals are used, including lanthanum compounds [1].

Materials and Methods

$SnCl_4 \cdot 5H_2O$ and $La_2(CO_3)_3$ were used as starting materials. The synthesis was carried out in several stages. The first stage was to obtain an intermediate product - a mixture of organic salts of lanthanum and tin. The lanthanum additive content was 1, 3, 5 and 10 mol. %. The second stage included the preparation and cleaning of polycor substrates for film application. The third stage is the production of films by pyrolysis for 2 hours at 600 °C. The synthesis method is described in detail in [2]. The formed films were studied by X-ray phase analysis, atomic force microscopy (AFM) and Kelvin probe force microscopy. Also, using an automated stand [2], the dependences of the surface resistance of films on temperature were studied.

Results and discussion

According to X-ray phase analysis, it was found that the films were formed in the crystalline structure of cassiterite. Using the Scherrer formula, the average sizes of crystallites forming films were estimated; they are 16-26 nm and depend on the content of the La^{3+}.

Next, after deposition of V-Ni contacts onto the formed films, the dependence of their resistance (R) on temperature was studied (Fig. 1). From the figure you can see that the dependence of resistance on temperature for a material containing 1 mol. % is almost linear, but at higher concentrations of La^{3+} the dependence becomes nonlinear. The film resistance behaves in the opposite way in two temperature ranges. In the temperature range from 300 K to 430-450 K, the film containing 10% La has the lowest resistance, and the film containing 3% La has the highest resistance. In the high temperature range the situation is reversed. The film containing 3% La has the lowest resistance, and the film containing 10% La has the highest resistance. The activation energy of electrical conductivity (Ea) was calculated in two temperature ranges of 300–400 K and 400–570 K using the Arrhenius equation [3]. For samples containing 1, 3, 5 and 10 % La^{3+}, Ea values in the temperature range 300–430 K were 0.14, 0.09, 0.07 and 0.07 eV, respectively, and in the temperature range 430–570 K Ea were 0.44, 0.87, 0.84 and 0.98 eV, respectively.

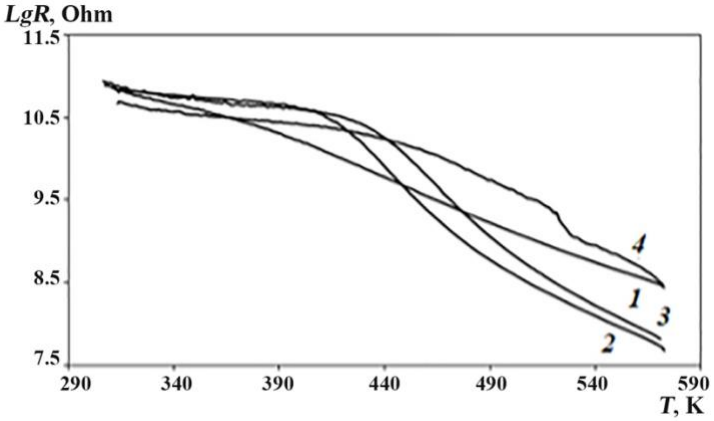


Fig. 1. Temperature dependence of the resistance of materials obtained by solid-phase pyrolysis with a content of La^{3+} 1 (1), 3 (2), 5 (3), 10 (4) %.

It has been established that in the temperature range of 300–430 K, with an increase in the La^{3+} content in the films, the temperature dependence of the electrical conductivity decreases. This may be due to the binding of oxygen vacancies by La^{3+} ions. At temperatures above 430 K, for the film with La:Sn=1:99 the activation energy is 0.44 eV, which is close to the energy level corresponding to oxygen vacancies in the SnO_2 band gap. However, for films with 3, 5 and 10 mol. % La^{3+}, the activation energy is almost twice as high. This may be due, on the one hand, to the appearance of deep levels in the band gap of SnO_2 associated with the ionization of adsorbed oxygen, and, on the other hand, to the incorporation of La ions into the SnO_2 crystal lattice.

Studies of surface morphology using AFM showed that 3% La-SnO_2 films have a roughness with a maximum height difference (Sy) of up to 150 nm. This is 1.2–3 times higher than that of films containing 1% La^{3+} and 5% La^{3+}. For a film containing 10% La^{3+} content, the roughness reaches 124 nm. The value of the surface potential (Vb), measured by the KPSM method, correlates with fluctuations in the Sy values. The 3%La-SnO_2 film also has a maximum Vb value of 57 mV. At the same time, the Vb values for films containing 1% La^{3+} and 5% La^{3+} are 2-4 times lower. For a film containing 10% La^{3+}, the value of the surface charge also increases and amounts to 43.7 mV.

Conclusion

Thin nanocrystalline films of SnO_2 with lanthanum contents of 1, 3, 5 and 10 mol. % La^{3+} were obtained. It has been shown that an increase in the La^{3+} content in films leads to an uneven change in the electrical resistance of the films in the range from 300 to 570 K. Films containing 3% La^{3+} and 10% La^{3+} have the most different values of electrical resistance, developed morphology and surface potential.

REFERENCES

1. **Tammanoon N., Wisitsoraat A., Phokharatkul D., Tuantranont A., Phanichphant S., Yordsri V., Liewhiran C.** Highly sensitive acetone sensors based on flame-spray-made La_2O_3-doped SnO_2 nanoparticulate thick films, Sensors and Actuators B: Chemical. 262 245-262 (2018).

2. **Petrov, V. V., Ivanishcheva A.P., Volkova, M. G., Storozhenko, V. Y., Gulyaeva, I. A., Starnikova, A. P., Pankov I.V., Volochaev V.A., Khubezhov S.A., Bayan E.M..** High gas sensitivity to nitrogen dioxide of nanocomposite ZnO-SnO_2 films activated by a surface electric field, Nanomaterials. 12(1) 2025 (2022).

3. **Gulyaeva I.A., Ivanisheva A.P., Volkova M.G., Storozhenko, V.Yu., Khubezhov S.A., Bayan E.M., Petrov V.V.**, Investigation of electrophysical, photo- and gas-sensitive properties of ZnO–SnO_2 sol–gel films J. Adv. Dielect. 14, 1 (2024) 2245002.

Ab initio study of In adsorption on $Al_xGa_{1-x}As$ substrates during first stages of droplet epitaxy

D. D. Dukhan✉, S. V. Balakirev, M. S. Solodovnik
Laboratory of Epitaxial Technologies, Southern Federal University, Taganrog 347922, Russia
✉duhan@sfedu.ru

Abstract. In this work we study In adsorption on $Al_xGa_{1-x}As$ substrates during first stages of droplet epitaxy with goal of explaining anomalous behavior observed in previous experiments where increase in content of chemically active Al in $Al_xGa_{1-x}As$ substrates has led to increase in surface mobility of In adatoms affecting final distribution of InAs quantum dots. DFT simulations showed that when In adatoms are interacting with As-terminated substrates directly there is no deviation from normal behavior, but when In is bonding with fully formed In wetting layer results are in agreement with those observed in our experiments - increase in Al led to decrease in adsorption energy which means that surface mobility of adatoms has increased. We hypothesize that this droplet epitaxy specific effect is caused by lack of As stabilizing layer, allowing formation of In dimer rows and direct interaction of adatoms with them.

Keywords: density functional theory, III-V, indium, surface mobility, quantum dots, droplet epitaxy, molecular beam epitaxy

Funding: This work was supported by the Russian Science Foundation Grant No. 22-79-10251 and by the Ministry of Science and Higher Education of the Russian Federation Grant No. FENW-2022-0034 at the Southern Federal University.

Introduction

Use of InAs/AlGaAs quantum dots for single-photon emission requires low density (< 10^8 cm^{-2}), high uniformity and reproducibility of size, shape and distribution of quantum dots (QD). Droplet epitaxy (DE) growth method allows for fine control over all these parameters but shows some unpredictable behavior concerning Al's chemical activity. When growing QDs on surfaces of Al containing substrates it is expected that high chemical activity of Al would inhibit adsorbates mobility by giving opportunity for adsorbates to form stronger bonds with surface. This effect results in almost linear increase in QD density with increase in Al content in substrates when grown in Stranski-Krastanov mode [1]. But in droplet epitaxy effect is opposite – as shown in our previous work [2] increase in Al content leads to decrease in droplet density meaning that adatom mobility increased (Fig. 1). To see if this effect can be derived from first principles calculations we modeled GaAs, $Al_{0.5}Ga_{0.5}As$ and AlAs at 0.25 ML and 1.25 ML coverage representative of first stages of droplet epitaxy and calculated resulting adsorption energies, which describe strength of bonding between substrate and adatoms moving over it.

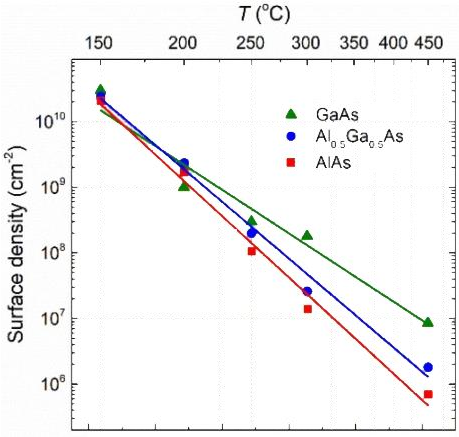


Fig. 1. Surface density of nanostructures after deposition of 3 ML of In on the GaAs, $Al_{0.5}Ga_{0.5}As$ and AlAs surfaces at different temperatures.

Methods

Ab initio calculations of slab models were conducted using density functional theory (DFT). It was applied by using the Vienna ab initio simulation package with the projector augmented wave potential construction. For approximating the exchange-correlation functional we used Perdew's generalized-gradient-approximation (PBE). DFT+U method based on Dudarev's approach was used to properly describe interactions of p-band electrons. Simulation of parameters affected by random distribution of atoms in $Al_{0.5}Ga_{0.5}As$ alloy was achieved by use of special quasirandom structures. Adsorption energy was obtained using formula (1)

$$Eads_{0.25ML(1.25ML)} = E_{A3B5(+InML)+In} - E_{A3B5(+InML)} - E_{In} \quad (1)$$

where $E_{A3B5(+InML)+In}$ is total free energy of GaAs (covered by 1 ML of In) with In atom on top, $E_{A3B5(+InML)}$ is energy of GaAs (covered by 1 ML of In) and E_{In} – energy of indium atom in vacuum. The more negative value of *Eads* means stronger bond between adsorbate and surface, which suppresses adatom mobility leading to higher density of nanostructures.

Results and discussion

Table 1 shows highest adsorption energy found after placing In adatom at adsorption points forming uniform 5x5 grid over substrate surface for all coverages and substrates. $Eads_{0.25ML}$ at low coverage of 0.25 ML, where In atoms directly interact with As-terminated substrates, shown no deviation from expected results – substrates with higher Al content shown higher *Eads*. But calculation of $Eads_{1.25ML}$ has shown that when In interacts with reconstructed surface of completed In wetting layer (relaxation step during calculation of $E_{A3B5+InML}$ resulted in In adatoms forming dimer rows), behavior changes to one seen in our droplet epitaxy experiments, where increase in content of chemically active Al led to lower adsorption energy and consequently higher surface mobility. This shows that observations made in our experiments are in agreement with theory and can be explained by nature of droplet epitaxy during which wetting In layer forms in absence of stabilizing As flux.

Table 1

Adsorption energies of In adatom on In wetting layer covering $Al_xGa_{1-x}As$ substrates

	Eads (eV)		
	GaAs	$Al_{0.5}Ga_{0.5}As$	AlAs
0.25 ML coverage	-3.453	-3.701	-3.823
1.25 ML coverage. Adatoms forming dimer rows	-4.289	-4.096	-3.989

This means that change in dependance of adatom mobility on Al content can be explained by absence of stabilizing As layer, which normally prevents In from forming dimer rows and doesn't allow for direct bonding of adatom In to complete In layer. These differences of droplet epitaxy from Stranski-Krastanov growth can be responsible for studied effect, which makes them a subject of closer study by us in the future.

REFERENCES

1. **Andrews A. M. et al.** Independent control of InAs quantum dot density and size on Al x Ga 1–x As surfaces. Journal of Materials Science: Materials in Electronics 19 (2008) 714-719.

2. **Balakirev S. V. et al.** Anomalous behavior of In adatoms during droplet epitaxy on the AlGaAs surfaces. Nanotechnology 31.48 (2020) 485604.

Combined approach of patterning on SiO_2/Si substrate using ion beam and chemical wet etching

M M Eremenko [1]✉, J Y Jityaeva [2], N A Shandyba [1], N E Chernenko [1], S V Balakirev [1], M S Solodovnik [1]

[1] Laboratory of Epitaxial Technologies, Southern Federal University, Taganrog 347922, Russia;
[2] Laboratory of Functional Nanomaterials Technology, Southern Federal University, Taganrog 347922, Russia

✉eryomenko@sfedu.ru

Abstract. In this work, we studied the influence of combined processing of SiO_2/Si substrates using focused ion beams (FIB) and wet chemical etching on the possibility of forming pyramidal cavities and their geometric parameters. It has been shown that etching FIB-modified samples only in KOH leads to the formation of pyramidal cavities covered with a shell, possibly made of porous silicon layer. We have shown that the use of an isotropic etchant before anisotropic etching allows to remove a porous silicon layer. An increase in the implantation dose led not only to an increase in the depth of the cavities, but also to an increase in the undercut of the oxide layer.

Keywords: wet chemical etching, silicon, monolithic integration, focused ion beam, nanopatterning.

Funding: This work was funded by the Ministry of Science and Higher Education of the Russian Federation; project No. FENW-2022-0001 and No FENW-2022-0034.

Introduction

Patterning semiconductor Si substrates using various lithography methods is currently one of the promising approaches in monolithic integration of GaAs on Si, in particular using selective area growth techniques [1]. However, submicron lithographic surface patterning processes are labor-intensive and very expensive. On the other hand, the surface modification with focused ion beams (FIB) makes it possible to simplify the procedure for forming a submicron-sized pattern on the surface, and also eliminate the step of using photoresist. Early studies of clear Si surface modification using the FIB method with subsequent GaAs growth showed (despite high spatial selectivity) polycrystalline growth within modified area with cavities [2]. Therefore, in this work, we propose to use a combination of FIB surface modification and wet chemical etching for nanopatterning of SiO_2/Si substrate that can act as a template for subsequent direct epitaxial growth of GaAs.

Materials and Methods

At the first stage, Si(001) samples with a 200 nm thick SiO_2 layer were etched by the Ga^+ FIB. FIB-modification was carried out by processing of substrate square areas with sizes varying from 0.1×0.1 to 1×1 μm. The accelerating voltage was 30 kV, and the ion beam passes were varied in the range from 1 to 1000. Next, the part of samples were placed in isotropic silicon etchant HNO_3:H_2O:NH_4F. And then all samples were etched in 30% KOH to form a pyramidal cavities. The obtained samples were examined by scanning electron microscopy (SEM).

Results and Discussion

The results of sample treatment in 30% KOH after FIB processing are shown on Figure 1a. It was shown that during etching a porous film formed on the surface of the modified area. Moreover, etching of the sample led to the formation of a pyramidal cavity under the film. We suppose that this film is a layer of silicon with gallium ions implanted during FIB treatment which is etched much more slowly than crystalline silicon. Therefore, for subsequent epitaxial growth it is necessary to remove this film.

The nature and type of etching changes when an isotropic silicon etchant is used at the first stage of chemical treatment of the sample (Figure 1b-d). According to the results obtained, it is clear that pyramidal cavities without any film were formed in the FIB modified areas. Apparently, an isotropic silicon etchant also removes damaged silicon layers.

The geometric characteristics of the resulting cavities also depend on the FIB processing modes. Increasing the number of ion beam passes during FIB treatment increases the depth of the modified area, which in turn increases the amount of undercut after etching in KOH (Figures 1b, d). It is worth noting that the use of FIB modes with a number of passes below 150 resulted in the absence of Si substrate wet etching due to the remaining unetched oxide layer (Figure 1c). As can be seen from the obtained results, the SiO_2 film remains hanging over the edges of the etched area in each of the obtained results with pyramidal cavities (Figure 1a, b, d). In the future, we plan to determine the optimal parameters of FIB and wet chemical etching to ensure the absence of undercut.

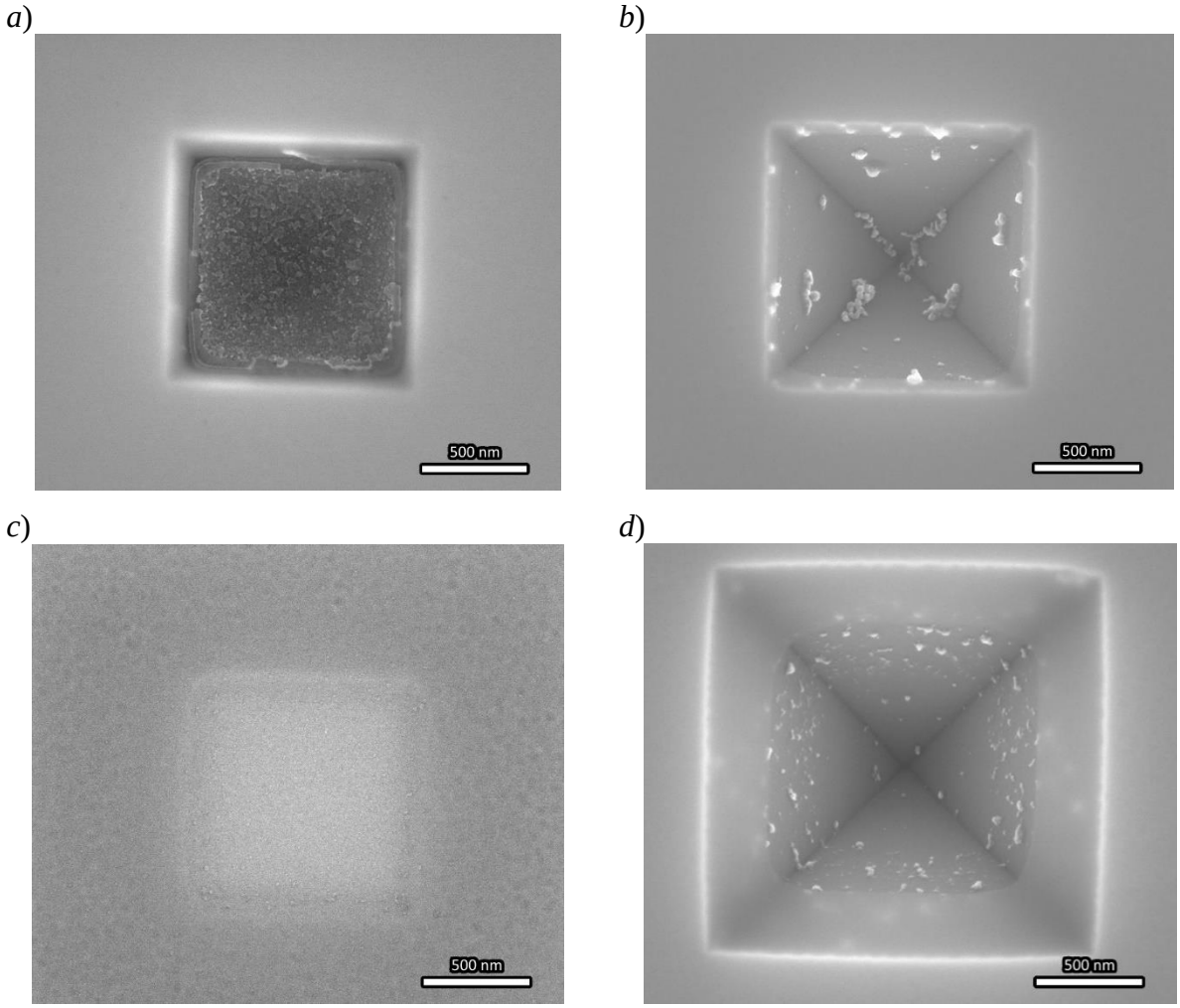


Fig. 1. SEM-images of FIB-modified SiO_2/Si areas (*a*) after etching in 30% KOH, (*b-d*) after etching in an isotropic silicon etchant and 30% KOH. FIB beam passes: (*a, b*) 250, (c) 50, (*d*) 1000.

Conclusion

In conclusion, we have proposed a new approach to forming a submicron template on SiO_2/Si substrates for monolithic integration of GaAs on Si. It is expected that this approach will increase the selectivity of growth processes and will also make it possible to obtain nanostructures with high crystalline perfection due to the possibility of localizing defects on the faces of etched cavities.

REFERENCES

1. **Park J.-S., Tang M., Chen S., Liu H.**, Heteroepitaxial Growth of III-V Semiconductors on Silicon, Crystals. 10 (2020) 1163.

2. **Eremenko M. M., Shandyba N. A., Chernenko N. E., Balakirev S. V., Solodovnik M. S., Ageev O. A.**, Investigation of GaAs MBE growth on FIB-modified Si(100), Proceedings of SPIE. 12157 (2022).

Technique for characterizing a nanocapillary probe: aperture and mechanical stability measuring

M. V. Zhukov [1]✉, **S. Yu. Lukashenko**[1], **I. D. Sapozhnikov**[1], **M. L. Felshtyn**[1], **O. M. Gorbenko**[1], **A. O. Golubok**[1]

[1] Institute for Analytical Instrumentation of RAS, Saint Petersburg, Russia

✉cloudjyk@yandex.ru

Abstract. The report presents a technique for assessing the aperture and mechanical stability of a nanopipette using AFM with piezo tube self-sensing sensor. The pipette aperture was imaged by AFM in the "hopping" semi-contact mode using a test array of periodic needles while the nanopipette was attached to the sensor as a probe. Nanopippete resonance oscillation amplitude was measured using approach curve. The force acting on the pipette at the moment of impact on the surface was estimated taking into account the amplitude, resonant frequency and effective mass of "nanopipette – piezo tube" oscillator.

Keywords: nanopipette, mechanical stability, atomic force microscopy, scanning ion-conductance microscopy, piezoresonant sensors

Introduction

With the development of biology and medicine more attention going on to the study of biological objects in the native state with ultra-high nanoscale resolution. Among the promising approaches for studying biological objects can be marked pipette-based methods, such as scanning ion-conductance microscopy, patch-clamp and nano-injection pipettes [1]. Obviously, the quality and resolution of these methods are determined by the shape and size of nanopipettes (NPs), that is why characterization of NPs is now so important. In addition, the mechanical stability of the NPs is an important parameter, since these methods essay mechanical lateral and axial loads.

Among the methods for inspection NPs are optical and scanning or transmission electron microscopy (SEM, TEM) [2]. However, the optical methods are limited by the diffraction limit, then SEM and TEM are limited by the NP material (dielectric), the presence of charging, melting and carbon contamination under the electron beam, as well as the complexity of sample preparation when using TEM.

It would be possible to use atomic force microscopy (AFM) for characterization of NPs, but there is a difficulty of targeting the top of an NP with a size of less than one micron. This difficulty is solved automatically with the help of an inverted version of AFM, when a probe located on a cantilever is examined using an array of identical needles located on the surface of a sample. However, when using a standard AFM cantilever, it is impossible to attach NP with large mass to it. To solve this problem, we propose the design of a piezo tube sensor [3], which will make possible to attach the NP on the self-sensing sensor. In addition, using AFM and optical microscope it is possible to measure the amplitude, resonant frequency and effective mass of "nanopipette – piezo tube" oscillator and estimate the impact force and mechanical stability of the NP.

Thus, the aim of the work is to develop a technique for studying the aperture and mechanical stability of nanocapillaries using piezo tube self-sensing sensors in AFM.

Materials and Methods

In order to study the NP aperture a lattice of periodic needles TGT01 [4] was used, since the radius of the needles ~10 nm is smaller or comparable to the dimensions of the capillary NP aperture. The amplitude of resonance NP oscillations is measured from approach curve in the "hopping" semi-contact mode. Capillaries made of borosilicate glass with an internal diameter of about 0.69 mm were used as blanks for the NP. To form NP capillaries, micropipette puller was used. Piezo tube as sensor were used for the NP probes (Fig. 1a).

Results and Discussion

Fig. 1a presents a general view of the NP mounted on a piezoresonant sensor in the SEM. The resonant frequency of the piezotube without NP and with NP was about 9.15 kHz and 6.63 kHz, the Q-factor was about 18.5 and 22.1, respectively. The signal from the piezoresonant sensor is directly proportional to the vibration amplitude. The force setpoint in the semi-contact AFM mode is set by amplitude suppression value in percentage, which occurs when a force interaction between the probe and the sample is established. The interaction force was estimated from the acceleration value of the probe, taking into account the 10% suppression of oscillations amplitude at the moment of contact and effective mass of the piezotube - glass NP oscillatory system. The optimal forces for scanning were no more than 15-20% of amplitude suppression for sustaining mechanical stability of NP (break area when begin loss of interaction at Fig.1b).

When using the standard semi-contact AFM method, disruptions were noticed in the region of the vertices without a clear boundary of the NP aperture. Presumably, this is due to the needle tip stuck in the NP or multiple contacts with the walls of the NP. To increase the reliability of the data, a «hopping» scanning technology was developed and applied, which lies on retracting and approaching a probe in each point of the scanning area (Fig. 1c). The number of pixels varying from 80x80 to 120x120 to maximize scanning rate and reduce thermal drift. The use of the «hopping» technique makes it possible to estimate the geometry and size of the NP aperture.

a) *b)* *c)*

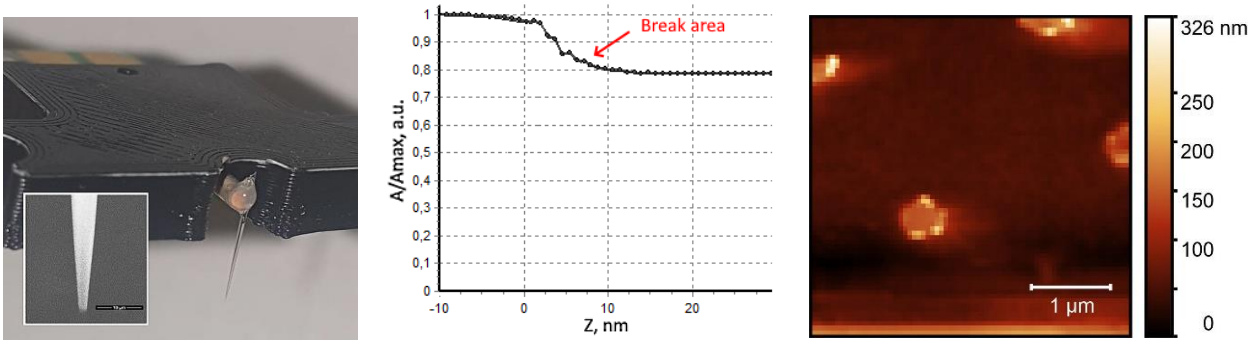


Fig. 1. Optical image of the sensor piezotube with NP probe (a), inset presents apex region of the NP in SEM (scale bar 10 µm). Approach curve (b) and image of arrays of the needles (TGT01 lattice) scanned by NP probe by means of «hopping» semi-contact AFM mode (c).

Conclusion

The piezo tube self-sensing sensor allowed to fixate large glass NP at its end, determine its resonant frequency, mass and forces arising in the semi-contact AFM when scanning an array of periodic needles. Using the «hopping» technique in AFM make it possible to accurately measure the geometry and dimensions of the NP aperture, whereas the standard semi-contact mode cause image artifacts. Optimal scanning modes and forces have been selected, at which the geometry of the NP is preserved. Thus, a technique for measuring mechanical stability and NPs apertures is proposed.

REFERENCES

1. **Maalouf M. M., Jain M., Actis P., Pourmand N.,** Single-cell manipulation using nano pipettes, Nanotechnology, 2, (2012), 384-387.

2. **Perry D., Momotenko D., Lazenby R. A., Kang M., Unwin P. R.,** Characterization of nanopipettes, Analytical chemistry, 88(10), (2016), 5523-5530.

3. **Gorbenko O. M., Zhukov M. V., Lukashenko S. Y., Pichahchi S. V., Sapozhnikov I. D., Felshtyn M. L., Golubok, A. O.,** On the Spatial Resolution of a Piezoresonance Probe Sensor with a Tungsten Needle, Journal of Surface Investigation: X-ray, Synchrotron and Neutron Techniques, 17(3), (2023), 578-584.

4. **Neto C., Craig V. S.,** Colloid probe characterization: radius and roughness determination, Langmuir, 17(7), (2001), 2097-2099.

Study of the electrophysical properties of $BaTiO_3$ films formed in the process of micro-arc oxidation

A. E. Zhurina[1]✉, **N. S. Emelyanov**[1], **E. A. Pecherskaya**[1], **P. E. Golubkov**[1], **G. V. Kozlov**[1]
[1] Penza State University
✉gelya.zhurina@mail.ru

Abstract. In order to increase the technology reproducibility for producing thin ferroelectric films, the electrical properties of $BaTiO_3$ films formed in the process of micro-arc oxidation were studied. After processing the Ti plate, a $BaTiO_3$ coating is obtained in cross section, representing a microstructure near the substrate, in the form of a dense and continuous nanograins structure, which has ferroelectric properties. Barium titanate films produced by micro-arc oxidation on titanium substrates have better corrosion protection than native oxide and anodized material. To be able to effectively control parameters during the ferroelectric structures synthesis, it is proposed to manufacture the structure using an intelligent automated system for the controlled synthesis of micro-arc coatings. To study the electrophysical parameters of the resulting sample, it is proposed to use a software and hardware complex developed by the authors for the study of active dielectrics, which allows to study various structures based on active dielectrics, taking into account heterogeneous parameters that influence the measured physical quantities.

Keywords: Micro-arc oxidation, ferroelectrics, $BaTiO_3$ films, electrophysical parameters.

Funding: The work was supported by the grant of the Ministry of Science and Higher Education of the Russian Federation № 1022041100284-5-2.3.1 «Fundamentals of the digital twin of the technological process of forming oxide coatings with specified properties by microarc oxidation».

Introduction

Thanks to the development of technologies that make it possible to synthesize nanostructures from ferroelectrics, new opportunities to increase the electronic devices efficiency are opening up. The development of various methods for creating structures contributes to obtaining the specified parameters. One of these methods is the method of depositing BaCO3 and $BaTiO_3$ layers on titanium using plasma electrolytic oxidation [1, 2]. It is a little-used and little-studied method for the ferroelectric structures synthesis, and therefore is of great scientific interest.

Materials and Methods

This work purpose is to study the relationships between the electrophysical properties of structures created by this method in order to synthesize ferroelectric structures with the required properties. To do this, it is proposed to produce a structure using an intelligent automated system for the controlled synthesis of oxide coatings using the micro-arc oxidation (MAO) method [3]. The measuring unit of the automated system is a set of measuring channels that make it possible to measure the technological parameters of the MAO process and the thickness of the growing MAO coating in real time.

The $BaTiO_3$ coating was prepared on Ti wafers using micro-arc oxidation in an alkaline electrolyte. After processing the wafer, a $BaTiO_3$ coating is obtained in cross section, representing a microstructure near the Ti substrate, in the form of a dense and continuous nanograins structure, which has ferroelectric properties.

To obtain ferroelectric ceramic coatings, rectangular titanium samples measuring 20 mm x 15 mm, which were pre-cleaned with acetone and deionized water were used.

Micro-arc oxidation was carried out in an acetate-alkaline electrolyte (0.5 M $Ba(CH_3COO)_2$ and 2 M NaOH) at a current density of 0.5 A/dm^2 at a sinusoidal current with a frequency of 50 Hz with a ratio of anodic and cathodic currents equal to 1. Electrolyte preparation was carried out by constantly mixing the components when heated to 60°C for 1

hour. Before oxidation, the electrodes of the galvanic cell (titanium anode and stainless steel cathode) were immersed in the electrolyte for 30 minutes to stabilize.

Results and Discussion

Studies of the electrophysicall properties of crystals are based on precision measurements of the temperature spectra of thermally stimulated depolarization currents and take into account the frequency-temperature spectra of the dielectric loss tangent tgδ(ω,T) [4]. Therefore, instruments for measuring impedance (including capacitance, resistance) of linear dielectrics cannot be used in relation to the study of small-sized active dielectrics. It is proposed to use the software and hardware complex developed by the authors [5] for the study of active dielectrics, which allows to study various structures based on active dielectrics, taking into account heterogeneous parameters that influence the measured physical quantities, including the temperature influence.

Thanks to the automated system developed by the authors, it is possible to examine the resulting $BaTiO_3$ sample and obtain such important parameters as experimental dependences of the polarization and dielectric loss tangent of the sample on the electric field strength at different temperatures. The shape of ferroelectric hysteresis loops can be influenced by many factors (sample thickness, material composition, heat treatment, presence of charged defects, temperature, etc.). The study of their influence on the material properties was carried out based on an analysis of the shape and characteristics of the P-E hysteresis loops. The main measuring instrument of the installation's measuring unit [5] is a capacitance and dielectric loss tangent (tgδ) meter, which is based on the Sawyer-Tower circuit.

Conclusion

This unique measuring instrument makes it possible to study various structures based on active dielectrics, taking into account heterogeneous parameters that influence the measured physical quantities. Thanks to the automated system developed by the authors, it is possible to study the synthesized $BaTiO_3$ sample and obtain such important parameters as the experimental dependence of polarization and the dielectric loss tangent of the sample on the electric field strength at different temperatures.

REFERENCES

1. **Hsiao-Chien Wu, Jiechao Jiang, Efstathios I. Meletis**, Microstructure of $BaCO_3$ and BaTiO3 coatings produced on titanium by plasma electrolytic oxidation. Applied Surface Science (2019) 0169-4332.

2. **Chu-Tsun Wu, Fu-Hsing Lu**, Corrosion resistance of BaTiO3 films prepared by plasma electrolyticoxidation, Surface and Coatings Technology (166) (2002) 31–36.

3. **Pecherskaya E., Golubkov P., Karpanin O., Kozlov G., Anatoliy V.,** Intellectual system of controlled synthesis of oxide coatings. Measuring. Monitoring. Management. Control № 2 (28) (2019) 99-107.

4. **Kalytka, V.; Mekhtiyev, A.; Neshina, Y.; Alkina, A.; Aimagambetova, R.; Mukhambetov, G.; Bashirov, A.; Afanasyev, D.; Bilichenko, A.; Zhumagulova, D.;** et al. Physical and Mathematical Models of Quantum Dielectric Relaxation in Electrical and Optoelectric Elements Based on Hydrogen-Bonded Crystals. Crystals, 13, (2023) 1353. https://doi.org/10.3390/cryst13091353

5. **Emelyanov N.S., Zhurina A.E., Pecherskaya E.A., Shepeleva J.V., Maksov A.A.,** A software-hardware complex for the study of electrophysical parameters of active dielectrics, St. Petersburg State Polytechnical University Journal. Physics and Mathematics. 16 (3.1) (2023) 341–345. DOI: https://doi.org/10.18721/JPM.163.162.

INFLUENCE OF ISOVALENT BISMUTH ON THE PROPERTIES OF GALLIUM ARSENIDE

D.A. Zdoroveyshchev[1]✉, **O.V. Vikhrova**[1], **Yu.A. Danilov**[1], **Yu.A. Dudin**[1], **V.P. Lesnikov**[1]
A.V. Zdoroveyshchev[1], **A.E. Parafin**[2], **M.N. Drozdov**[2]
[1]Lobachevsky State University of Nizhny Novgorod, Nizhny Novgorod, Russia
[2] Institute for Physics of Microstructures of the Russian Academy of Sciences, Nizhny Novgorod, Russia
✉danielzdoroveishev@yandex.ru

Abstract. The work shows the possibility of doping gallium arsenide with bismuth during ion implantation and a diluted magnetic semiconductor GaMnAs during pulsed laser deposition in a vacuum. It was investigated the influence of thermal and laser annealing on the properties of these structures. Studies of the galvano-magnetic properties of GaMnAs:Bi in comparison with GaMnAs, as well as studies of the optical properties of GaAs:Bi are presented.

Keywords: Gallium arsenide, ion implantation, pulsed laser deposition, bismuth doping.

Funding: This work was supported by the Priority 2030 Strategic Academic Leadership Program of the Ministry of Science and Higher Education of the Russian Federation.

Introduction

Currently, a search is underway for ways to modify the properties of gallium arsenide, which could expand the range of its applications in the field of nanoelectronics. One such method may be doping with impurities isovalent to arsenic, for example, bismuth. The introduction of bismuth into GaAs leads to a significant change in its properties. Thus, it is reported that the band gap decreases with the introduction of small concentrations of bismuth [1]. It is also known about the influence of Bi on the properties of the dilute magnetic semiconductor GaMnAs, one of the promising materials for semiconductor spintronics [2].

Materials and Methods

In this work, two methods of doping gallium arsenide with bismuth were used: introducing Bi atoms into a layer grown by pulsed laser deposition (PLD) by joint sputtering of GaAs targets and metallic Bi; and implantation of bismuth ions (Raduga-3M accelerator with an accelerating voltage of 30 or 80 kV). Also, the GaMnAs and GaMnAs:Bi structures were obtained using the PLD method by joint sputtering of targets made of GaAs, metallic Mn and Bi under the same conditions for their subsequent comparison. The Mn content was about 14 at.%, the bismuth content was about 7 at.%. The thickness of the resulting layers is about 50 nm. Then the structures were subjected to pulsed laser annealing (PLA) with a KrF excimer laser with a variable pulse energy density. The structures obtained by ion implantation were subjected to two types of annealing: rapid thermal annealing (RTA) in argon at 800 °C for 10 s, and PLA with different energy densities per pulse.

On structures obtained by ion implantation, reflection and transmission spectra were studied in the wavelength range from 0.18 to 1.8 μm, and the depth distribution of impurities was studied using the secondary ion mass spectrometry method. The magnetic field dependences of the Hall resistance and magnetoresistance for the structures obtained by the PLD method were studied in the temperature range 7 - 300 K.

Results and Discussion

Analyzing the results of measuring the transmittance spectra for a GaAs:Bi structure obtained by ion implantation and subjected to PLA and RTA, we can say that the intrinsic absorption edge has shifted to the region of longer waves compared to the original single-crystal GaAs substrate. Estimating the band gap of the resulting layer from the transmission spectra, we obtain a value of $E_g \approx 1.398$ eV at room temperature, which is less than the value of 1.42 eV for GaAs. Comparing the values with the data [1], we can conclude that the effective bismuth concentration affecting the absorption edge is about 1 at. %.

This value is consistent with the experimental bismuth distribution profiles obtained by the SIMS method. On the depth distribution profiles of bismuth, in all cases a maximum is observed

at a depth of about 5 nm. This maximum does not agree with the theoretical calculation using the TRIM program when taking into account the surface sputtering coefficient. Its presence may be due to the characteristics of the pulsed ion source used, namely: heating of the target and subsequent segregation of bismuth to the surface. In this case, the contribution to the optical absorption is apparently made by a deeper layer with a «tail» of the Bi distribution. The surface maximum may correspond to bismuth clusters or to an oxide.

Fig. 1 shows the magnetic field dependences of the magnetoresistance at T = 7 K for GaMnAs and GaMnAs:Bi structures obtained by the PLD method with post-growth PLA. These dependences represent hysteretic negative magnetoresistance, which indicates the presence of ferromagnetism in the layers under study.

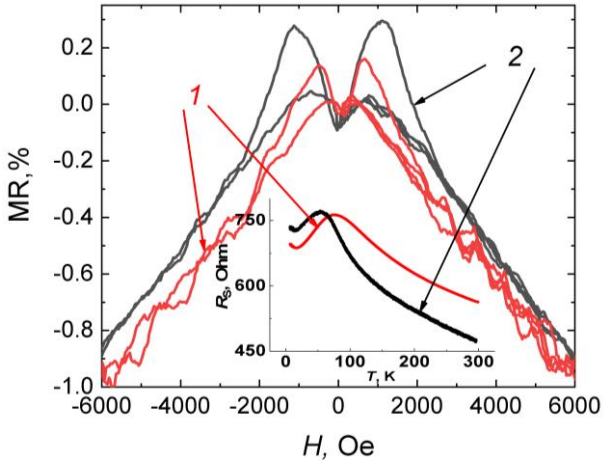


Fig. 1. Magnetic field dependences of magnetoresistance at T = 7 K of GaMnAs (*1*) and GaMnAs:Bi (*2*) structures subjected to PLA with 400 mJ/cm^2. The inset shows the temperature dependences of the layer resistance for these structures.

The inset in the figure shows the temperature dependences of the layer resistance for these structures, which at temperatures of 300 – 100 K are semiconductor in nature, and at low temperatures they have maxima which can be interpreted as the Curie temperature of these compounds. According to these graphs, the Curie temperature for GaMnAs:Bi is $T_C \approx 54$ K, and for a similar structure without bismuth $T_C \approx 75$ K. It can be concluded that the Curie temperature decreases with the introduction of bismuth. In this case, an increase in magnetoresistance and coercive field occurs, which is evident from the magnetic field dependences of the position and amplitude of the maxima. This behavior is consistent with literature data [2].

Conclusion

The work experimentally demonstrated the possibility of doping with bismuth both GaAs in the process of ion implantation and the GaMnAs compound in the process of pulsed laser deposition. The GaMnAs:Bi compound subjected to post-growth pulsed laser annealing has a semiconductor dependence of resistance on measurement temperature and is a ferromagnet with a Curie temperature of about 54 K, demonstrating negative hysteretic magnetoresistance. When compared with a similar GaMnAs layer without bismuth, it was revealed that the introduction of bismuth leads to a decrease in the Curie temperature, an increase in the coercive field and magnetoresistance. During the study of the optical properties of samples synthesized by ion implantation, it was shown that bismuth reduces the band gap.

REFERENCES

1. **Mohmad A.R., Bastiman F., Hunter C.J., Richards R.D., Sweeney S.J., Ng J.S., David J.P.R., Majlis B.Y.**, Localization effects and band gap of GaAsBi alloys, Phys. Stat. Solidi B. 251 (2014) 1276.

2. **Andrearczyk T., Levchenko K., Sadowski J., Domagala J.Z., Kaleta A., Dłuzewski P., Wróbel J., Figielski T., Wosinski T.**, Structural Quality and Magnetotransport Properties of Epitaxial Layers of the (Ga,Mn)(Bi,As) Dilute Magnetic Semiconductor, Materials. 13 (2020) 5507.

MODEL OF THE RELATIONSHIP BETWEEN THE PARAMETERS OF SMART GLASSES BASED ON FUNDAMENTAL PHYSICAL AND CHEMICAL LAWS

E. A. Pecherskaya ✉, **T. O. Zinchenko**, **O. V. Karpanin**, **G. V. Kozlov**, **P.E. Golubkov**, **J.V. Shepeleva**

Department of Information and measuring technology and metrology, Penza State University, Penza 440026, Russia;

✉pea1@list.ru

Abstract. Promising materials for producing transparent conductive oxides and electrochromic coatings included in the structure of electrochromic glasses are considered. Based on fundamental physical and chemical laws, models for coloring the material of an electrochromic panel and a model for the relationship between the parameters of smart glasses have been developed. Tungsten oxide, which has a visible light transmittance range from 0.1 to 0.8, was chosen as the electrochromic material. The simulation was carried out in two states: bleached and colored, with daylight illumination at a level of 500 lux over the panel area, and at a distance equal to two-thirds to the light source. The upper illumination limit in the model corresponds to the illumination value that causes the panel to switch between colorless and colored states. Potassium hexacyanoferrate acts as an anode. The process and reaction of coloring tungsten oxide is considered. The material coloring occurs due to light photons, which cause the transfer of electrons between the ion and the iron. Optical density, relaxation time, absorption coefficient and contrast ratio are also considered.

Keywords: Electrochromic panel, coloring, tungsten oxide, illumination, optical density.

Funding: The work was supported by the Russian Science Foundation (RSF grant 23-29-00343).

Introduction

Based on the relationship between electrophysical and optical properties, a model that describes the effect of illumination on the transmission and coloring process of an electrochromic coating has been developed.

Materials and Methods

The simulation was performed using tungsten oxide electrochromic panels, which have visible light transmittance ranges from 0.1 to 0.8. Simulation of optical properties was carried out in 2 states: bleached and colored, with daylight illumination at a level of 500 lux over the panel area, and at a distance equal to two-thirds to the light source. The upper illumination limit in the model corresponds to the illumination value that causes the panel to switch between colorless and colored states.

Results and Discussion

Simulation of material coloring and optical properties of an electrochromic panel.

The most common electrochromic material is tungsten oxide [1, 2]. The coloring process when applying electric current is associated with the properties of tungsten oxide and the following chemical reaction:

$$[WO_3 + yG^+ + ye^-]_{coloring} \leftrightarrow [G_yWO_3]_{blue}, \quad (1)$$

where G+ is lithium, potassium, sodium ions, e is an electron, y is the stoichiometric coefficient.

The electron enters the tungsten oxide structure and the tungsten charge decreases by 1:

$$W^{+6} + e^- = W^{+5}\ . \quad (2)$$

Photons of light hitting the tungsten oxide coating provide energy sufficient for intervalent transfer:

$$W^{+5} + W^{+6} + h\nu \rightarrow W^{+6} + W^{+5}. \quad (3)$$

$KFe[Fe(CN)_6]$ acts as the anode of the electrochromic coating.

Coloring reaction:

$$KFe[Fe(CN)_6]_{coloring} \leftrightarrow [Fe^{+3} + [Fe(CN)_6]^{-3} + K^+ + e^-]_{blue} \quad (4)$$

Thanks to light photons ,electrons transfer between iron ions, which causes coloring of the material.

Conclusion

A model of the relationship between the electrophysical, optical, and morphological parameters of smart glasses based on fundamental physical and chemical laws and a model of the relationship between the functional thin-film layers of electrochromic panels have been developed.

REFERENCES

1. **Mikkel Juelsholt, Olivia Aalling-Frederiksen, Troels Lindahl Christiansen, Emil T. S. Kjær, Niels Lefeld, Andrea Kirsch, Kirsten M. O. Jensen,** Influence of precursor structure on the formation of tungsten oxide polymorphs, Materials Chemistry. 62(37):14949-14958.

2. **Shrisha S Raj, Naga Srinivas G and Sridhar S,** Tungsten Oxide-based Materials: Synthesis, Properties, and Applications, Volume 8 Issue 4. 000274.

Nanoparticles based on organic donor-acceptor compounds for biomedicine

Yu.A. Isaeva [1]✉, A.N. Efremov [1,2], I.V. Dyadishchev [2], D.O. Balakirev [1], R.A. Akasov [3], Yu.N. Luponosov [1]

[1] Enikolopov Institute of Synthetic Polymer Materials, Russia, Moscow;

[2] Lomonosov Moscow State University, Russia, Moscow;

[3] I.M. Sechenov First Moscow State Medical University of the Ministry of Health of the Russian Federation, Russia, Moscow

✉yu.isaeva@ispm.ru

Abstract. This work presents the synthesis of organic donor-acceptor (D-A) molecules based on triphenylamine (TPA) with various donor and acceptor moieties. The relationship between their molecular structure and properties was investigated to optimize their effectiveness in phototherapy and improve the specificity of their effects on cancer cells. Additionally, aqueous dispersions of nanoparticles 50–300 nm in size based on these compounds were prepared and studied with and without amphiphilic polymer matrices. The study demonstrated the potential of the acquired materials for cancer photodynamic therapy due to their high toxicity towards cancer cells (IC50<0.02 mmol and PI>50), generation of reactive oxygen species (ROS), effective light absorption, and photoluminescence in the red spectral range.

Keywords: donor-acceptor small molecules, photodynamic therapy, nanophotosensitizer

Funding: The work was carried out with financial support from the Ministry of Science and Higher Education of the Russian Federation (FFSM-2021-0005) and was prepared as part of the work on the topic «Laser technologies for biomedical applications» (№ 122122600055-2) under the state order of the Ministry of Education of the Russian Federation.

Introduction

Phototherapy, which includes photodynamic and photothermal therapy, is a promising cancer treatment due to its simplicity, high efficacy, and minimal drug resistance. A significant advancement in this field is phototheranostics, which combines diagnostics and therapy through light excitation. However, current materials have drawbacks, including low efficiency and complex synthesis, as well as insufficient specificity in delivering therapeutic agents to tumour sites. The aim of our study was to create photosensitizers using modern approaches. We utilized donor-acceptor organic compounds, which are known in organic electronics and photonics and are gaining interest in biomedical technologies due to their ability to interact with tumors with low toxicity and high biocompatibility. Our synthesis focused on organic D-A molecules with triphenylamine as an electron-donating fragment and various electron-withdrawing groups. We also prepared and analysed aqueous dispersions of nanoparticles based on these molecules, known for their ability to target tumour cells. Incorporating polymer nanocarriers with organic photosensitizers enhances stability and biocompatibility, promising improved properties and effective delivery to tumor sites for clinical use.

Materials and Methods

Organic dyes were synthesized using a range of organic synthesis reactions, such as bromination reactions, cross-coupling conditions, and the Knoevenagel reaction. The resulting molecules were purified using standard organic chemistry methods, including vacuum distillation, column chromatography, and recrystallization. The compounds' purity and structure were confirmed using modern physicochemical methods. Optical absorption spectroscopy and cyclic voltammetry were used to determine the compounds' optical properties and band gap values. Nanoparticles were obtained using a nanoprecipitation method, which relies on a rapid change in solvent polarity. The cytotoxicity of the resulting nanoparticles was assessed in vitro using the standard MTT test on cancer cell cultures SKBR3 (human breast cancer cell line) and MCF7 (estrogen-dependent breast cancer cells). Photodynamic activity was studied using green light with a wavelength of 530 nm.

Results and Discussion

A series of D-A molecules based on TPA were synthesized in this work (Fig. 1a). The relationship between the molecular structure and properties of these compounds was studied to optimize their effectiveness in phototherapy and influence selectivity and specificity towards cancer cells. The study investigated the influence of structure on the optical and electrochemical properties, phase behavior, and thermal stability of resulting compounds. Nanoparticle dispersions were obtained from synthesized organic photosensitizers and in combination with amphiphilic polymer matrices. The study also investigated the effect of polymer encapsulation on the size, stability, and cytotoxicity of the resulting nanoparticle dispersions. Among the synthesized substances, TTInd showed the most promise with a half-maximal inhibitory concentration (IC50) of 0.02 mmol and a phototoxicity index (PI) of 50 (Fig. 1b). When encapsulated in polyethylene glycol–polylactic acid (PEG–PLA) block copolymer, its IC50 values were <0.02 mmol and PI >50. Fluorescence images were obtained using a Leica TCS SPE confocal laser scanning microscope and ROS generation in cells was investigated with the fluorescent compound dichlorodihydrofluorescein diacetate (DCFDA).

a) *b*)

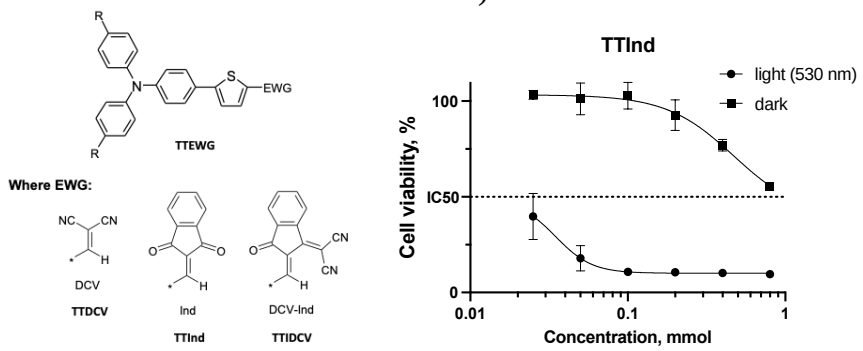


Fig. 1. Chemical structures of D-A molecules *(a)*, viability of SKBR3 cells after addition of different concentrations of NPs in the absence or presence of laser irradiation (530 nm) *(b)*.

Conclusion

Thus, various organic D-A molecules were synthesized, and nanoparticles based on them were obtained with or without polymer encapsulation. The properties of these nanoparticles were studied to optimize their effectiveness in phototherapy and enhance their specificity in targeting cancer cells. Encapsulation in an amphiphilic polymer improved photodynamic properties in some cases. The study showed promising properties for photodynamic theranostics, with effective light absorption and high toxicity towards cancer cells.

Acknowledgments

The biological experiments were caried out as part of the work on the topic «Laser technologies for biomedical applications» (№ 122122600055-2) under the state order of the Ministry of Education of the Russian Federation.

REFERENCES

1. **Paek S., Qin P., Lee Y., Cho K.-T., Gao P., Grancini G**., **Oveisi E., Gratia P., Rakstys K., Al-Muhtaseb S., Ludwig C., Ko J., Nazeeruddin M. K.,** Dopant-Free Hole-Transporting Materials for Stable and Efficient Perovskite Solar Cells, Adv. Mater. 29 (2017) 1606555.

2. **Justin Thomas K. R., Lin J., Velusamy M., Tao Y.-T., Chuen C.-H.**, Color Tuning in Benzo[1,2,5]thiadiazole-Based Small Molecules by Amino Conjugation/Deconjugation: Bright Red-Light-Emitting Diodes, Adv. Funct. Mater. 14 (2004) 83–90

3. **Lu B., Huang Y., Zhang Z., Quan H., Yao Y.,** Organic conjugated small molecules with donor–acceptor structures: design and application in the phototherapy of tumors, Materials Chemistry Frontiers. 6 (20) (2022) 2968-2993.

The influence of chiral ligands on the optical properties of $AgBiS_2$ nanocrystals

S. P. Karamysheva [1✉], **E. V. Ushakova** [1,2], **S. A. Cherevkov** [1]
[1] ITMO University, Saint-Petersburg, Russia;
[2] City University of Hong Kong, Hong Kong SAR, China
✉spkaramysheva@itmo.ru

Abstract. Currently, semiconductor nanocrystals are considered as a promising material for use in many fields, especially for the fabrication of photodetectors, solar cells, and displays. Among them, there is a special subclass of biocompatible and eco-friendly ones – nanocrystals of a ternary composition based on silver, indium or bismuth, and sulfur. The optical and electrical properties of such structures are considered special, which is why they have found wide application in many fields. It can be controlled by changing their shape, size, and making surface modifications. Thus, in this work, a synthesis method of nanostructures of ternary compounds based on silver, bismuth, and sulfur with chiral molecules was developed, and the influence of chiral molecules on their spectral characteristics was studied. A study of the electronic structure of the synthesized nanocrystal-chiral ligand systems using circular dichroism and magnetic circular dichroism spectroscopy together with their morphological properties was provided. The developed nanomaterial is promising for use as an active material in chiral photodetectors.

Keywords: nanocrystals, ternary compounds, chirality, circular dichroism, magnetic circular dichroism, atomic force microscopy

Funding: This study was funded by the Federal Academic Leadership Program "Priority 2030".

Introduction

Nowadays, semiconductor nanocrystals (NCs) are considered as a material for various current tasks in photovoltaics, sensorics, and other industries due to their unique optical and electrical properties. To expand their applications in biomedicine and in connection with concern for the environment, classical NCs based on mercury, cadmium, and tellurium are gradually being replaced by NCs of ternary compounds of the composition I-V-VI_2 and I-III-VI_2. Such nanomaterials have properties that can be controlled by changing their shape [1] and composition [2], their synthesis route, or surface functionalization [3]. Thus, in this work the $AgBiS_2$ NCs synthesis method was developed, and the influence of chiral ligands (CLs) on the $AgBiS_2$ NCs spectral characteristics was examined.

Materials and Methods

The synthesis of $AgBiS_2$ NCs was based on the method reported in [4] with some modifications using several types of CLs: L-Cysteine (L-Cys), L-Phenylglycine (L-PhG), L-Tryptophane (L-Try), and L-Glutathione (L-Glu). Reference samples that did not contain CLs were also prepared by this method. Instead of CLs, thioglycolic acid (TGA) was used in the synthesis.

The morphology of the obtained NCs was studied by atomic force microscopy (AFM) using a Solver PRO-M atomic force microscope with a Smena measuring module (NT-MDT, Russia). The absorption properties of the obtained samples were studied using a UV-3600 spectrophotometer (Shimadzu, Japan). The circular dichroism (CD) and magnetic circular dichroism (MCD) spectra were recorded on a JASCO J-1500 spectrometer.

Results and Discussion

A protocol for the synthesis of $AgBiS_2$ NCs-CLs nanostructures was developed and presented in Figure 1. Four L-CLs types were used here (see Materials and Methods).

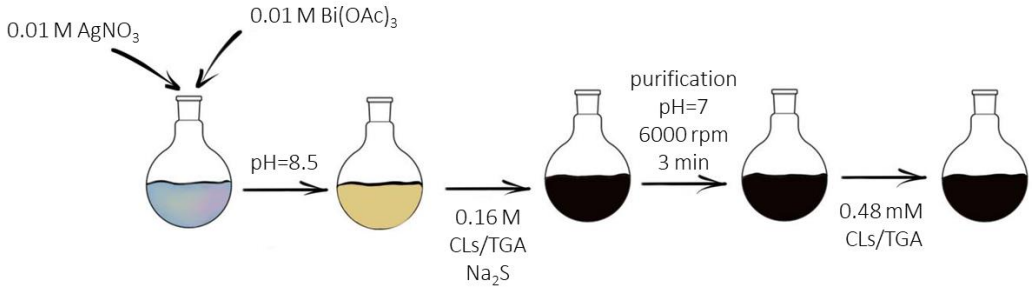


Fig. 1. Scheme of syntheses of $AgBiS_2$ NCs-CLs nanostructures

These performed reactions showed that the presence of an SH-group in the chiral molecule is necessary for the formation of NCs, otherwise aggregation of nanoparticles occurs at the stage of adding CLs with the formation of large flakes. That is why, as a result of the reaction with L-Try and L-PhG, the previously described effect occurred. Analysis of NCs using AFM showed that their average size does not exceed 25±1 nm. CD and MCD spectra of NCs with L-Cys or L-Glu did not coincide with the reference spectra of free L-Cys and L-Glu molecules. In the case of a NCs with L-Cys, when a magnetic field is applied, the absorption spectrum at the first optical transition (~325 nm) does not change, but at the second transition (~250 nm), the optical density is decreased twice while CD and MCD spectra coincide. For NCs with L-Glu, the magnetic field influences the optical density at first and second optical transitions similarly as for the NCs with L-Cys. At the same time, Zeeman splitting obviously occurs and the spectrum changes sign depending on the sign of the magnetic field. The first derivatives of the absorption spectra are different from both CD and MCD spectra for both NCs samples.

Conclusion

In this study, $AgBiS_2$ NCs with two types of chiral molecules (L-Cys and L-Glu) were synthesized. The study of the electronic structure of NCs using the of CD and MCD spectroscopy made it possible to study the nature of the broadband absorption of such nanostructures in more detail, as well as to consider in detail the influence of chiral ligands on the excitonic transitions of $AgBiS_2$ NCs. Taking into account high optical density in a wide spectral range, developed NCs are promising for the fabrication of photodetectors.

Acknowledgments

The authors express their gratitude to the ITMO University Core Facility Center “Nanotechnologies”. The authors thank the Federal Academic Leadership Program “Priority 2030” for financial support.

REFERENCES

1. Dai H. et al. A paper-based photoelectrochemical aptsensor using near-infrared light-responsive $AgBiS_2$ nanoflowers as probes for the detection of Staphylococcus aureus in pork // Talanta. Elsevier B.V. – 2024. – Vol. 266.
2. Martín-Rodríguez R., Geitenbeek R., Meijerink A. Incorporation and luminescence of Yb3+ in CdSe nanocrystals // J Am Chem Soc. – 2013. – Vol. 135. – № 37. – P. 13668–13671.
3. Kuznetsova V. et al. Ligand-induced chirality and optical activity in semiconductor nanocrystals: Theory and applications // Nanophotonics. De Gruyter Open Ltd. – 2020. – Vol. 10. – № 2. – P. 797–824.
4. Branzi L. et al. Chiral non-stoichiometric ternary silver indium sulfide quantum dots: investigation on the chirality transfer by cysteine // Nanoscale. Royal Society of Chemistry. – 2022. – Vol. 14. – № 33. – P. 12174–12182.

Laser-stimulated tin-induced crystallization of silicon on flexible nonwoven substrates

A. A. Serdobintsev[1], **A. M. Kartashova**[1], **L. D. Volkovoynova**[1]
[1]Saratov State University, Saratov, Russian Federation
✉nasty280801@gmail.com

Abstract. The work is devoted to the formation of polycrystalline silicon coatings on a non-woven fibrous polymer material using a metal layer for absorption of laser radiation. The results of experimental studies confirming the presence of crystallized silicon structures on nonwoven polymer substrates are presented.

Keywords: nanofibrous nonwoven material, magnetron sputtering, laser-stimulated silicon crystallization, metal-induced silicon crystallization.

Funding: This study was funded by the Russian Science Foundation (project № 23-22-00047, https://rscf.ru/project/23-22-00047/).

Introduction

Silicon is an affordable and well-studied material used in many fields of science and technology, for example, in micro- and nanoelectronics or solar energy harvesting. Devices using its polycrystalline form are among the most promising. An example is solar panels made of polycrystalline silicon. Recent research shows that polycrystalline silicon combines advantages such as efficiency close to that of crystalline silicon and a relatively low cost of production [1]. Silicon films can be crystallized in various ways, but most of them are realized at sufficiently high temperatures. Metal-induced [2] or laser-stimulated [3] crystallization methods are used to lower the crystallization temperature. However, both of these methods reduce the crystallization temperature of silicon insufficiently for use bendable polymers as substrates. Combining the two approaches mentioned above allows minimizing the thermal effect on the substrate and opens up the possibility of using a larger range of materials [4]. Electrospinned nonwoven substrates are a unique basis for the production of nanostructures, since the diameter of their fibers initially lies in the range of hundreds of nm's.

Materials and Methods

Initially, nonwoven nanofiber substrates made of polyacrylonitrile (PAN) were obtained by electrospinning. Then silicon and tin coatings were sequentially deposited by magnetron sputtering. Four samples were obtained, differing in the time of metal deposition (30-120 s), while the time of silicon deposition remained unchanged (300 s). On the obtained samples, 2x2 mm^2 squares were annealed with a pulsed laser with a wavelength of 1064 nm. The power of the laser radiation and the pulse duration were equal to 0.2 W and 4 ns, respectively, and the frequency and speed varied.

Crystallization was verified using Raman spectroscopy. A laser with a wavelength of 532 nm was used. The signal accumulation time was 10 seconds at each point at a radiation power of 0.0125 mW, the laser spot size was 1.3 microns. The spectra were recorded at 16 points in increments of 15 microns.

Results and Discussion

Three of the four samples showed the presence of crystalline Si phase, but even the peak of amorphous silicon is missing in the spectra taken from the sample with the thinnest tin layer (Fig. 1*A*). This indicates that not only the metal, but also the semiconductor was ablated during the laser treatment. As for the rest of the samples, the most homogeneous crystallization, which is little dependent on variation in the parameters of laser annealing, was shown by a sample whose metal layer was deposited for 60 seconds. Typical spectra of crystallized points are shown in Figures 1*B*-1*D*. Figure 1*B* corresponds to a sample whose metal layer was deposited for 60 seconds, Figure 1*C* – 90 seconds, and Figure 1*D* – 120 seconds. Graphs 1*B*-1*D* show that there is a clearly distinguishable peak in the spectrum, close to the peak of monocrystalline silicon (520

cm^{-1}), however, its intensity decreases, and the full width on half maximum (FWHM) increases with increasing thickness of the metal layer.

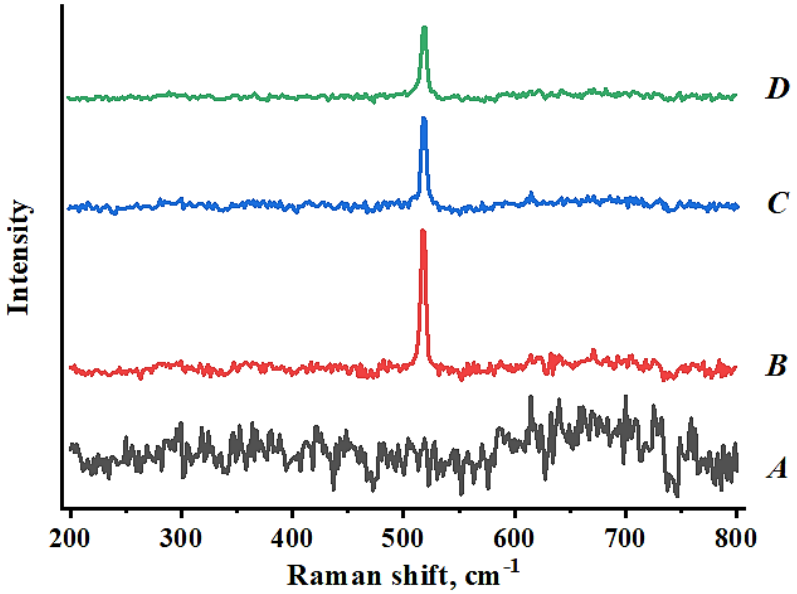


Fig. 1. Typical Raman spectra of samples with different tin deposition times

Conclusion

Within the framework of this work, crystallized silicon structures on nonwoven polymer substrates were obtained by laser-stimulated metal-induced crystallization. The thickness of the tin layer, which allows for homogeneous crystallization in a wide range of laser processing modes, was experimentally revealed. While thicker layers of tin showed less predictable behavior, the thinner layer of metal led to almost complete ablation of both layers of the sample.

Acknowledgments

This study was funded by the Russian Science Foundation (project № 23-22-00047, https://rscf.ru/project/23-22-00047/).

REFERENCES

1 **B. M. Abdurakhmanova, M. M. Adilov**, Characteristics of Solar Cells Based on Polycrystalline Silicon, Doklady Physics. 67 (11) (2022) 439-441.

2 **D. Van Gestel et al.**, Metal induced crystallization of amorphous silicon for photovoltaic solar cells, Physics Procedia. 11 (2011) 196–199.

3 **Kirill Bronnikov, Alexander Dostovalov, Artem Cherepakhin, Eugeny Mitsai, Alexander Nepomniaschiy, Sergei A. Kulinich, and Alexey Zhizhchenko, and Aleksandr Kuchmizhak**, Large-Scale and Localized Laser Crystallization of Optically Thick Amorphous Silicon Films by Near-IR Femtosecond Pulses, Materials. 13 (2020) 5296.

4 **A.A. Serdobintsev, A.M. Kartashova, P.A. Demina, L.D. Volkovoynova, I.O. Kozhevnikov**, Formation of crystalline silicon structures on nanofiber nonwovens using laser-stimulated metal-induced crystallization, Physics of the Solid State. 65 (12) (2023) 2132-2134.

DEPOAITION OF COPPER AND GOLD ONTO POROUS SILICON

K.B. Kim [1]✉, S.I. Niftaliev [1], S.S. Chernenko[1], D.S. Zolotukhin[2], A.S. Lenshin [1, 2]

[1] Voronezh State University of Engineering Technology, Voronezh, Russia;

[2] Voronezh State University, Voronezh, Russia

✉ kmkseniya@yandex.ru

Abstract. The use of porous silicon for design of sensing probes and sensors is of a great capability in the field of the control for the environment, medicine, industry and some other areas. Unique properties of this material make it on of the most challenging materials for the development of high-performance and sensitive probes for the analysis. Porous silicon was obtained by electrochemical anodization of single-crystalline silicon KEF (100). Applying vacuum-thermal deposition technique gold and copper were deposited onto the surface of porous silicon. Analysis of the surface of the original porous silicon as well as that one with the deposited gold and copper was performed by X-ray photoelectron spectroscopy technique (XPS). Results of XPS analysis demonstrated the presence of metallic gold on the surface of porous silicon without the inclusions of admixtures and oxides. In the case of porous silicon samples with the deposited copper the presence of copper oxides was observed along with pure metal of Cu. Results of the present study show an important contribution in the development of the modern technologies concerned with the formation of functional materials with the novel properties.

Keywords: porous silicon, gold, copper, X-ray photoelectron spectroscopy

Funding: The study was carried out with the financial support of the Russian Foundation for Basic Research within the framework of scientific project No. 22-73-0154.

Introduction

Porous silicon has certain unique properties due to its microporous structure making it a prospective one for the fabrication of gas sensors and various chemical substances. Functionalization of its surface with metals such as copper and gold is of a key role in the improvement of its properties and performance for the detection of minimal concentrations of the analyzed substances. Design of sensors based on porous silicon with the point metal coatings makes it possible to considerably increase their sensitivity and ability to respond on the chanhes of the environment.

Materials and methods

Within the frames of the study the layers of copper (porSi-Cu) and gold (porSi-Au) were deposited on the substrates of porous silicon (KEF 100) [1] by vacuum-thermal deposition. Using X-ray photoelectron spectroscopy (XPS) analysis of the surface and composition of the samples including original substrate and the obtained nanocomposites with gold and copper according to the technique presented in [2].

Results and Discussion

Survey spectra of porSi-Au samples demonstrated the presence of metallic gold that did not include admixtures and oxides. Metallic copper and copper oxides were detected in the samples of porSi-Cu.

Conclusion

The obtained experimental data show a potential of vacuum-thermal technique for synthesis of nanocomposites based on porous silicon, including copper and gold.

REFERENCES

1. Kashkarov V.M., Lenshin A.S., Popov A.E., Agapov B.L., Turishchev S.Yu. Composition and structure of nanoporous silicon layers with galvanically deposited Fe and Co., Bulletin of the Russian Academy of Sciences: Physics 72 (4) (2008) 453-458.

2. Lenshin A. S., Kashkarov V. M., Domashevskaya E. P., Bel'tyukov A. N., Gil'mutdinov F. Z. Investigations of the composition of macro-, micro- and nanoporous silicon surface by ultrasoft X-ray spectroscopy and X-ray photoelectron spectroscopy, Applied Surface Science. 359 (2015) 550–559.

Formation of transparent memristor structures based on ZnO using RF magnetron sputtering

A. V. Saenko, **K. A. Kozyumenko**, **N.V. Polupanov, V.A. Smirnov**
Institute of Nanotechnologies, Electronics, and Equipment Engineering,
Southern Federal University, Taganrog, Russia
✉koziumenko@sfedu.ru

Abstract. Transparent memristor structures based on ZnO were formed by radio-frequency (RF) magnetron sputtering in an argon atmosphere at room temperature on glass substrates, and their resistive switching was studied for use in artificial vision systems. Analysis of the measured current-voltage characteristic showed that the change in resistance from the HRS state to the LRS state occurs at 2.0 ± 0.1 V, and from LRS to HRS at -2.0 ± 0.1 V, while the switching current is 4 mA. HRS is shown to be 2.3 ± 0.3 kΩ and LRS is shown to be 1.3 ± 0.3 kΩ.

Keywords: zinc oxide, RF magnetron sputtering, memristor structure, current-voltage characteristic.

Funding: The reported study was funded by the Russian Federation Government (Agreement № 075-15-2022-1123) (in part of memristor structures resistive switching investigation). The fabrication of metal oxide thin films by magnetron sputtering were supported by a grant from the Russian Science Foundation № 23-29-00827, https://rscf.ru/project/23-29-00827/, at Southern Federal University.

Introduction

Memristors are one of the most promising new generation non-volatile storage devices due to their unique structure and outstanding performance characteristics. The development of transparent memristors opens up great opportunities for their use in optoelectronic neuromorphic systems, artificial intelligence and computer vision systems. For the development of artificial vision, the optically transparent memristor and its synaptic behavior are very important, since it directly responds to optical input, and also has memory and real-time processing of sensory data and visual information. Some metal oxides, such as ZnO, TiO_2, etc., have been widely studied for creating memristor-based synapses by achieving stable switching behavior [1–2].

Zinc oxide (ZnO) is one of the most promising semiconductor nanomaterials, which has a unique combination of optical and electrophysical properties, and also exhibits biosynaptic characteristics necessary for the creation of transparent memristor structures.However, the synaptic response of transparent memristor structures based on ZnO thin films has not yet been sufficiently studied for use in neuromorphic systems, transparent and flexible electronics.

Materials and Methods

This work is devoted to the formation of transparent ZnO-based memristor structures using high-frequency (RF) magnetron sputtering in an argon atmosphere at room temperature on glass substrates and the study of their resistive switching for use in artificial vision systems that are capable of detecting, processing and storing visual information in real time. time.

Transparent memristor structures based on ZnO (Figure 1, a) were formed by magnetron sputtering using a VSE-PVD-DESK-PRO installation (AcademVac, Russia). Thin films of nanocrystalline ZnO were deposited on glass substrates with a transparent conductive ITO layer at room temperature by RF magnetron sputtering of a 99.99% pure ZnO ceramic target in a pure argon (Ar) atmosphere. The spray power was 75 W, and the operating pressure was $5 \cdot 10^{-3}$ mbar. ITO films with a thickness of 200 nm (bottom electrode) were deposited on glass substrates by magnetron sputtering in a pulsed mode with a frequency of 100 kHz at room temperature in an Ar atmosphere. The spray power was 200 W, and the operating pressure was $2 \cdot 10^{-3}$ mbar. The surface morphology of ZnO films was studied using a Nova Nanolab 600 scanning electron microscope (FEI Company, the Netherlands) and an atomic force microscope (AFM) in semi-contact mode at

the NTEGRA nanolaboratory (NT-MDT, Russia). The thickness of the ZnO films was measured using an Alpha-Step D-100 profilometer (KLA-Tencor, USA) and was about 80-90 nm.

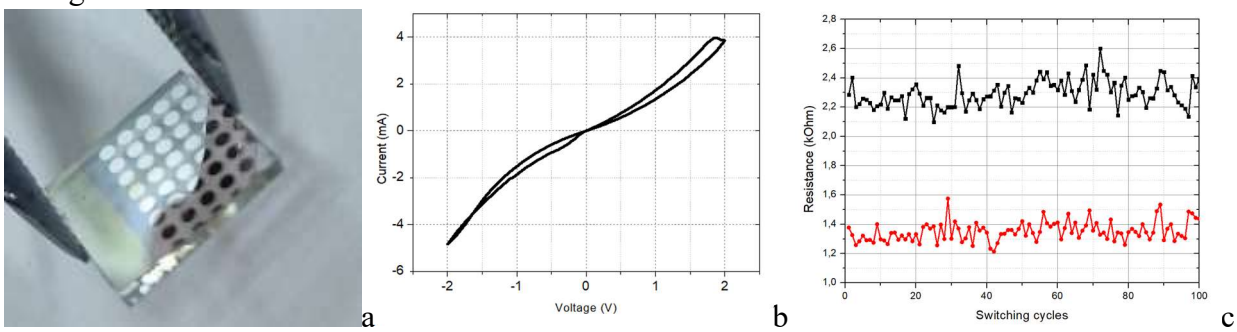
A top silver (Ag) electrode with a thickness of 100 nm and a diameter of 550 μm was deposited on the surface of the ZnO film by MF magnetron sputtering at room temperature in an Ar atmosphere using a metal mask. The spray power was 150 W, and the operating pressure was $2 \cdot 10^{-3}$ mbar. Measurements of the current-voltage characteristics of memristor structures were carried out at room temperature in air using a Keithley 4200-SCS semiconductor parameter measurement system (Keithley, USA) and an EM-6070A submicron sensing setup with tungsten probes. Voltage was applied to the top Ag electrode and the bottom ITO electrode was grounded.

Results and Discussion

Analysis of SEM images of the resulting ZnO films showed that the surface morphology is homogeneous (without cracks and pores) with an average grain size of 20-30 nm, and on the cross-section a columnar structure characteristic of ZnO is visible with a direction perpendicular to the plane of the substrate.

Analysis of AFM images of the resulting films showed that ZnO films on glass substrates, obtained at room temperature in an argon atmosphere, have a nanocrystalline structure. In this case, ZnO films have a relatively smooth surface (3 × 3 μm) with an average roughness value of 5.9 ± 0.2 nm.

Analysis of the obtained results of measuring current-voltage characteristics (Fig. 1, b) and studying resistive switching (Fig. 1, c) of glass/ITO/ZnO/Ag memristor structures showed that the change in resistance from the HRS state to the LRS state occurs at 2.0 ± 0.1 V, and from LRS to HRS at -2.0 ± 0.1 V, with a switching current of the order of 4 mA. It is shown that HRS is 2.3 ± 0.3 kOhm, and LRS is 1.3 ± 0.3 kOhm, the state resistance ratio is HRS/LRS = 1.77 at a reading voltage of 1 mV.



a b c

Rice. 1. Study of the layout of a ZnO-based memristor: a) layout; b) current-voltage characteristic; c) resistive switching.

Conclusion

Thus, the possibility of forming a memristor with a glass/ITO/ZnO/Ag structure using RF magnetron sputtering in an argon atmosphere at room temperature has been demonstrated. The results obtained can be used in the manufacture of memristor structures on glass and flexible substrates for use in artificial vision systems that are capable of detecting, processing and storing visual information.

REFERENCES

1. **P. Praveen, T. Priya Rose, K.J. Saji.** Top electrode dependent resistive switching in M/ZnO/ITO memristors, M = Al, ITO, Cu, and Au // Microelectron-ics Journal, 2022, 121, 105388.

2. **Tiedong Cheng, Jingjing Rao, Xingui Tang, Lirong Yang, Nan Liu.** Analog Memristive Characteristics and Conditioned Reflex Study Based on Au/ZnO/ITO Devices // Electronics, 2018, 7, 141.

Stokes and Anti-Stokes Luminescent Rare-Earth-Doped Tantalum Oxide Nanoparticles

E.D. Koshevaya [1,2✉], **E.F. Krivoshapkina** [3], **P.V. Krivoshapkin** [3]

[1] State Research Center-Burnasyan Federal Medical Biophysical Center of Federal Medical Biological Agency, Moscow, Russia;

[2] Institute of Chemistry, Komi Science Centre of the Ural Branch of the Russian Academy of Sciences, Syktyvkar, Russia;

[3] ITMO University, Saint-Petersburg, Russia

✉katiakosh@gmail.com

Abstract. Doping of oxide nano- and microparticles with rare earth elements (REEs) is used to fine-tune their structural, optical, and electrochemical properties. On the way to establish the structure−property relationship, we dope tantalum oxide (Ta_2O_5) particles with REEs to study their effect on the oxide structure and luminescence. Two synthesis approaches (sol−gel (SG) and solvothermal (ST)) were used to obtain powders with different textures. Experimental and theoretical studies of amorphous and crystallized tantalum oxide NPs by means of X-ray powder diffraction, Rietveld analysis, EXAFS/XANES spectroscopy, and density functional theory calculations were performed. All samples (doped and undoped) crystallized in orthorhombic phase with no admixtures. It was demonstrated that Ta_2O_5 is a promising wide-spectrum luminescent material: by combining REEs, both Stokes and anti-Stokes luminescence in the visible region were obtained. By means of optical absorption spectroscopy, it was shown that the prepared samples could be classified as wide band gap semiconductors.

Keywords: luminescent nanoparticles, solvothermal synthesis, sol-gel synthesis, tantalum oxide, wide band gap semiconductors

Introduction

Luminescent nano- and microparticles have emerged as a new type of light emitters with great potential for use in biological imaging, super-resolution nanoscopy, information security lasing, luminescent thermometers, solar cells, and so on [1]. Among them, oxide phosphors doped with REEs are inexpensive and ecofriendly materials, which could generate different emission colors in a wide range of visible and IR spectra. Tantalum oxide, known for its high biocompatibility, transparency to light, and low photon energy (100−450 cm^{-1}), represents an ideal host matrix for luminescent materials. Therefore, we synthesized undoped, Eu-doped, and Er,Yb-codoped Ta_2O_5 NPs to find out if the synthesis conditions and the texture of the material affect the structure and dopant incorporation, as well as optical properties.

Materials and Methods

For ST synthesis, 0.130 mL of tantalum (V) ethoxide was added in a dropwise manner to 12.5 mL of isopropyl alcohol under an inert atmosphere. Then, a 20 mL Teflon cup filled with the obtained mixture was transferred to a steel autoclave and carefully sealed. The autoclave was heated in a furnace to 200 °C for 12 h.

For SG synthesis, Tantalum (V) ethoxide (0.155 mL) was added in a dropwise manner to isopropyl alcohol (4.66 mL) under an inert atmosphere (argon). Then, 37% hydrochloric acid (0.165 mL) was gradually added. The reaction mixture was kept at ambient temperature for 24 h. The resulting sol was poured into a polypropylene mold with a removable bottom, closed with a parafilm, and kept for 24 h until the gel was formed. After that, the gel, preliminarily immersed into fresh isopropyl alcohol, was put into an autoclave for supercritical CO_2 drying.

In the case of doped samples, erbium, ytterbium, or europium acetate hydrate were previously dissolved in isopropyl alcohol at 75 °C. The mass of each dopant precursor was calculated and weighed to achieve the desired dopant concentration (Eu, 0.5−3 mol % and Er/Yb, 0.5/ 0.5−1.5/1.5 mol % with respect to tantalum).

The structure of tantalum oxide NPs was investigated by means of XRD, TEM, X-ray absorption near-edge spectroscopy (XANES), and extended X-ray absorption fine structure

spectroscopy (EXAFS). Rietveld analysis was used for the refinement of crystal structures. The band gap values of the undoped and doped Ta_2O_5 NPs were determined by optical absorption spectra measurements and density functional theory (DFT) calculations. Luminescence properties of doped NPs were studied under UV and NIR excitation.

Results and Discussion

In this work, two synthesis methods were used for NP preparation: SG and ST approaches. Both these are soft-chemistry liquid techniques that allow the use of similar precursors and dispersion mediums. The reaction products in both cases were fine white powders. The TEM and XRD studies showed that the as-prepared (noncalcined) NPs were amorphous. According to TEM images, particles have size of 20 and 30 nm for SG and ST, respectively. Crystallized samples were obtained after heat treatment at 800 °C for 1 h. It was shown that NPs crystallize in the orthorhombic phase regardless of the synthesis method and dopant incorporation. Peak shifting may indicate that the crystallographic positions of Ta^{5+} ions have been successfully occupied by REE ions in the host lattice

By means of XANES and EXAFS spectroscopy analyses, it was shown that Eu, Er, and Yb ions are incorporated into the oxide matrix as trivalent ions. A comparison of amorphous and crystalline samples showed that the oxygen environment of metallic elements in amorphous samples is usually more ordered than that in crystalline ones.

The Stokes luminescence properties of Eu-doped samples were studied under UV excitation. It showed intense red luminescence due to Eu^{3+} electronic transitions. The obtained spectra confirmed the crystalline nature and orthorhombic structure of SG and ST samples. It was demonstrated that the synthesis method influences the structure: the asymmetry ratios R_{21} indicate that a more symmetric Eu^{+3} environment is formed during the SG synthesis of NPs. The anti-Stokes luminescent (upconversion) Ta_2O_5:Er/Yb NPs were excited by a NIR laser. The upconversion spectra of Ta_2O_5:Er/Yb NPs contain radiative transitions of Er^{3+} ions with an intense green signal. It was shown that the synthesis method had no effect on the luminescence properties of the samples. The positions and intensity ratios of the lines in the spectra of SG and ST particles coincide. Luminescence proceeds according to a two-photon mechanism: to generate one quantum of upconversion luminescence, two quanta of exciting photons are required. All samples can be characterized as wideband gap semiconductors, with the band gap of 3.6−4.2 eV. The values calculated by the DFT method are close to the experimental ones. It was shown that REE doping narrows the band gap of Ta_2O_5.

Conclusion

The obtained data provide new information regarding the influence of dopants and temperature on the tantalum oxide NP structure and optical properties. It is shown that at a low dopant concentration (0.5 mol %), the structure and electronic properties of NPs do not change radically, but such samples acquire high luminescence properties. This information is helpful for the design of Ta_2O_5-based materials with desired properties, such as for developing highly efficient upconversion materials, X-ray-excited optical luminescence imaging materials, and high-performance photocatalysts.

Acknowledgments

Investigations were partially carried out using the equipment of the "Khimiya" Common Use Centre (Institute of Chemistry, FRC Komi SC UB RAS).

REFERENCES

1. Koshevaya E.D., Khramov E.V., Svetogorov R.D., Krasnov A.G., Martakov I.S., Shishkin I.I., Krivoshapkina E.F., Krivoshapkin P.V. Stokes and Anti-Stokes Luminescent Rare-Earth-Doped Tantalum Oxide Nanoparticles, Inorganic Chemistry. 62 (26) (2023) 10369–10381.

1x2 and 2x1 superstructures changes during the growth of Ge on Si(100)

O. I. Kukenov ✉, **V. V. Dirko, K. A. Lozovoy, A. P. Kokhanenko, X. A. Maier**
National Research Tomsk State University, Tomsk, Russia
✉okukenov@mail.ru

Abstract. The paper presents the results of studies of superstructural changes in the surface during the epitaxial synthesis of Ge on Si(100). The surface analysis was carried out by reflection high-energy electron diffraction in two directions of substrate orientation: [110] and [100].

Keywords: molecular beam epitaxy, reflection high-energy electron diffraction, step-flow growth, homoepitaxy.

Funding: Work with the financial support of the Russian Science Foundation grant No. 23-62-10021.

Introduction

Semiconductor nanostructures, due to the effect of size quantization, open up new opportunities for creating elements of photonics and electronics [1]. To create high-quality nanostructures, appropriate growth conditions and methods for controlling growth processes are required. The implementation of the reflection high-energy electron diffraction (RHEED) method in a molecular beam epitaxy (MBE) system allows for analysis of the surface during the growth process [2]. The synthesis of Ge on Si(100) is accompanied by the transition of the 2x1 and 1x2 superstructures to 2xN [3]. Moreover, the mechanism of monolayer formation strongly depends on the temperature of the substrate, as it is determined, among other things, by the kinetic energy of atoms. The goal of the work is to determine the dependence of the formation of 2D Ge monolayers on Si(100) on temperature in a wide range.

Materials and Methods

The experiments were carried out on the Katun-100 MBE installation while analyzing growth processes using the RHEED method. The essence of the method is that a stream of high-energy electrons is directed at a small grazing angle to the surface under study. When reflected from it, due to the correspondence of the electron wavelength with the crystal lattice parameter, diffraction patterns appear on the luminescent screen. Ge synthesis occurred after standard pre-epitaxial preparation of Si wafers and deposition of a 50 nm buffer layer. The studies used Si(100) substrates with misorientation angles less than 0.1°.

Results and Discussion

The Si(100) surface with a small misorientation angle (<2°) has a structure of alternating terraces of two types, on which a 2x1 or 1x2 superstructure is located [4]. Dimer rows consisting of 2x1 and 1x2 dimers are located along the entire length or width of the terrace, depending on its type. When Ge is deposited onto such a surface using the MBE method, newly formed dimer rows with length N appear, which are separated by dimer vacancies. The growth of two-dimensional Ge layers continues until approximately 4 ML, after which it turns into 3D growth, at which hut-clusters begin to form [5]. Studies of the Si(100) surface during the synthesis of Ge were carried out by the RHEED method in the direction of incidence of the electron beam [110] and [100] at temperatures in the range from 200 to 800 °C. The results of the analysis of diffraction patterns in the [100] direction showed that during the synthesis of Ge on Si(100), as well as during the synthesis of Si on Si(100), a temperature range of 500–600 °C is observed, at which a transition occurs from the growth mechanism due to the formation 2D islands to the step-flow mechanism of terrace growth [6]. The work also carried out studies of the emergence of the 2xN superstructure using diffraction patterns in the [110] direction at temperatures in the range from 200 to 800 °C.

Conclusion

As a result of the experiments, the dependence of the ratio of the intensity of the reflection from the 2x1 to 1x2 superstructure during the deposition of Ge on Si(100) on temperature (200–800 °C) when the electron beam was incident in the [100] direction was obtained. It has been shown that there is a maximum in the intensity of reflections from the 2x1 and 1x2 superstructures in the temperature range of 500–600 °C, which we associate with the transition from the growth mechanism due to the formation of 2D islands to the step-flow growth mechanism of terraces. When analyzing the Ge/Si(100) surface in the direction of the electron beam [110], the dependence of the time of formation of the 2xN superstructure on temperature in the range of 200–800 °C was obtained.

REFERENCES

1. **Lozovoy K. A., Douhan R. M. H., Dirko V. V., Deeb H., Khomyakova K.I., Kukenov O. I., Sokolov A. S., Akimenko N. Yu., Kokhanenko A. P.** Silicon-Based Avalanche Photodiodes: Advancements and Applications in Medical Imaging, Nanomaterials. 13(23) 2023 3078-1 – 3078-24.

2. **Hafez M. A., Zayed M. K., Elsayed-Ali H. E.**, Review: Geometric interpretation of reflection and transmission RHEED patterns, Micron, Rep. 159 (2022) 103286.

3. **Voigtlander B.**, Fundamental processes in Si/Si and Ge/Si epitaxy studied by scanning tunneling microscopy during growth, Surf. Sci. Rep. 43 (2001) 127 – 254.

4. **Sakamoto K., Sakamoto T., Miki K., Nagao S.** Observation of Si(001) vicinal surfaces on rheed, journal of the electrochemical society. 136(9) (1989) 2705 – 2710.

5. **Dirko V. V., Lozovoy K. A., Kokhanenko A. P., Voitsekhovskii A. V.**, High-resolution RHEED analysis of dynamics of low-temperature superstructure transitions in Ge/Si(001) epitaxial system, Nanotechnology, 33(11) (2022) 115603-1 – 115603-8.

6. **Kukenov O.I., Sokolov A.S., Dirko V.V., Lozovoy K. A., Kokhanenko A. P.** Analysis of the temperature dependence of homoepitaxial growth of Si on Si by reflection high-energy electron diffraction, St. Petersburg State Polytechnical University Journal. Physics and Mathematics. 16 (3.1) (2023) 112–116.

Droplet microfluidic synthesis of HKUST-1 metal-organic frameworks

A.O. Kuleshova[✉], **I.G. Koryakina, A.V. Lyubimova, M.V. Zyuzin, V.A. Milichko**
Department of Physics and Engineering, ITMO University, St. Petersburg, Russia
[✉] alina.kuleshova@metalab.ifmo.ru

Abstract. Metal-organic frameworks, as a class of organic-inorganic hybrid materials with a crystalline structure, have lots of different applications, for example, gas absorption and storage, catalysis, optical sensing and data storage. The properties of these materials are defined by synthesis conditions. Droplet microfluidics method allows precise control of the synthesis process (reaction time, droplet volume, temperature), which would affect structural properties of obtained crystals. In this work, droplet microfluidics synthesis of HKUST-1 MOFs was conducted. This method reduces the synthesis time down to 7 minutes and enables control of the parameters of materials. It was demonstrated that varying the parameters of synthesis, such as droplet volume and synthesis temperature, enables the production of frameworks with particular properties.

Keywords: metal-organic frameworks, droplet microfluidics, synthesis.

Funding: This work was supported by the Russian Science Foundation (project no. project 21-72-30018)

Introduction

Metal-organic frameworks (MOFs) are a class of crystalline porous materials, which have a number of outstanding qualities, such as large surface area and high porosity [1]. These materials are most often used for gas storage [2] or as catalysts [3]. However, MOFs could also be used as optical sensors [4] or, for example, for data storage [5]. Memristors based on metal-organic frameworks could be considered an attractive substitute for traditional memory devices, taking into account their design simplicity and low energy consumption [6]. To expand the opportunities of application of these materials, there needs to be a universal synthesis method with the possibility to control the parameters of the obtained product.

The use of droplet microfluidics enables precise control of the synthesis process, as well as reduction of synthesis time in comparison with conventional chemical synthesis methods. This opens up new opportunities for accelerating the synthesis process and optimising the production of memory elements based on MOFs. In particular, droplet microfluidics creates discrete droplets of dispersed phase containing MOF precursors within the channel of a microfluidic chip (MFC). These droplets could be considered as microreactors with a certain volume of precursors, which could be controlled.

Materials and Methods

In this work, HKUST-1 ($C_{18}H_6Cu_3O_{12}$) MOFs were synthesised using droplet microfluidics. The synthesis is conducted in a microfluidic chip (MFC) with a flow focusing geometry, which was fabricated using selective laser etching. Precursors were supplied to the MFC using syringe pumps (Harvard Apparatus, USA). Fluorinated oil FC-40 was used as the continuous phase. The dispersed phase was copper nitrate ($Cu(NO_3)_2$) and trimesic acid (H_3BTC), dissolved in dimethylformamide at concentrations $C_1 = 0.167$ mmol/ml and $C_2 = 0.113$ mmol/ml respectively. The synthesis temperature was varied using a heating substrate. The substrate temperature was controlled via the applied voltage. The synthesis was carried out at the following temperatures: 22°C, 50°C, 80°C and 110°C. To change the volume of microreactors, the continuous phase flow rate was varied. The structures were synthesised at a continuous phase flow rate of 10 and 300 μL/min. The resulting MOF structures were analysed by SEM and pXRD. The microfluidic synthesis MOFs were then used for rapid fabrication of a ReRAM device, then from these devices I-V characteristics were obtained.

Results and Discussion

HKUST-1 MOFs were synthesised at synthesis temperatures of 22°C, 50°C, 80°C and 110°C and continuous phase flow rates of 10 and 300 μL/min. With a continuous phase flow rate increase from 10 to 300 μL/min, diameter of microreactors decreased from 404 to 35 μm. Increase in temperature also influenced the volume of microreactors: diameter increased from 35 to 201 μm. MOFs synthesised at different temperatures were characterised by SEM and pXRD. It was discovered that particle size increased from 275 to 450 nm with the rise in synthesis temperature. Data from pXRD analysis showed that the major reflexes of the samples synthesised at different temperatures are all in accordance with the reference data. However, there is a difference in intensities of reflexes of microfluidic MOF samples obtained at different temperatures. From the width of the reflexes crystallite size and lattice strain were calculated. ReRAM devices with HKUST-1 synthesised using droplet microfluidics and HKUST-1 synthesised with the microwave-assisted method were created. I-V characteristics of these devices were measured. It was discovered that due to increased amounts of defects in microfluidic MOFs devices with these crystals had a maximum on/off ratio 1.5 times higher compared to HKUST-1 MOFs obtained via the microwave method.

Conclusion

In this work, HKUST-1 MOFs were synthesised with flow rate and temperature variation. It was discovered with SEM and pXRD analysis that these parameters influenced the crystal size, the crystallite size and lattice stress. The properties of ReRAM devices with microfluidic MOFs were measured and compared with MOFs synthesised via microwave synthesis.

Acknowledgments

This work was supported by the Russian Science Foundation (project no. project 21-72-30018)

REFERENCES

1. **Furukawa H, Ko N, Go YB, Aratani N, Choi SB, Choi E, Yazaydin AÖ, Snurr RQ, O'Keeffe M, Kim J, Yaghi OM.** Ultrahigh porosity in metal-organic frameworks. Science. 2010 Jul 23;329(5990):424-8.
2. **Li H, Li L, Lin RB, Zhou W, Zhang Z, Xiang S, Chen B.** Porous metal-organic frameworks for gas storage and separation: Status and challenges. EnergyChem. 2019 Jul 1;1(1):100006.
3. **Wang Q, Astruc D.** State of the art and prospects in metal–organic framework (MOF)-based and MOF-derived nanocatalysis. Chemical reviews. 2019 Jun 27;120(2):1438-511.
4. **Bachinin S, Marunchenko A, Zhestkij N, Gunina E, Milichko VA**. Metal-organic framework single crystal infrared photodetector. Photonics and Nanostructures-Fundamentals and Applications. 2023 Jul 1;55:101145.
5. **Wang Z, Nminibapiel D, Shrestha P, Liu J, Guo W, Weidler PG, Baumgart H, Wöll C, Redel E.** Resistive switching nanodevices based on metal–organic frameworks. ChemNanoMat. 2016 Jan;2(1):67-73.
6. **Shu F, Chen X, Yu Z, Gao P, Liu G.** Metal–Organic Frameworks–Based Memristors: Materials, Devices, and Applications. Molecules. 2022 Dec 14;27(24):8888.

Influence of annealing conditions on the characteristics of nanoholes formed by focused ion beams on the GaAs(111) surface

E. A. Lakhina✉, N. E. Chernenko, N. A. Shandyba, D. V. Kirichenko, S. V. Balakirev, M. S. Solodovnik

Laboratory of Epitaxial Technologies, Southern Federal University, Taganrog 347922, Russia

✉lakhina@sfedu.ru

Abstract. In this paper, we study the effect of annealing of GaAs(111) substrates under various conditions on the morphological characteristics of nanoholes formed by focused ion beams. In the absence of annealing and when annealing in the absence of the arsenic flux, the depth and lateral size of nanoholes increase with the number of ion beam passes. In the case of annealing of the substrates in the arsenic flux, the dependences of the hole depth and lateral size on the number of beam passes is non-monotonic, which is attributed to the competition of the processes of surface etching by gallium droplets during thermal oxide removal and droplet crystallization in the arsenic flux. We demonstrate technological conditions enabling formation of highly symmetric nanoholes in the form of triangular pyramids.

Keywords: focused ion beams, annealing, local droplet etching, GaAs(111).

Funding: This study was funded by the Russian Science Foundation Grant No. 23-79-10313, https://rscf.ru/project/23-79-10313/, at the Southern Federal University.

Introduction

Emitters of single and entangled photons have recently attracted increased interest due to the possibility of their use in quantum information devices. A good candidate for these emitters is an epitaxially grown InAs quantum dot (QD) formed at a specified site of the GaAs surface. QDs with C_{3v} symmetry are particularly important and can be grown on surfaces with (111) orientation [1]. Because of their symmetry, such QDs demonstrate vanishing fine structure splitting, which favors a high degree of entanglement of photon pairs [2]. Despite the increased interest in this topic, the results of studies on the formation of nanoholes on the GaAs(111) surface – QD nucleation centers – by focused ion beams (FIB) followed by annealing in a molecular beam epitaxy (MBE) chamber to restore the disturbed crystalline regions have not been presented so far.

In this paper, the influence of FIB and MBE technological conditions on the characteristics of nanoholes formed on the GaAs(111) surface are investigated and formation of nanoholes with high C_{3v} symmetry is achieved.

Materials and Methods

FIB modification was carried out with a Ga^+ ion source at an accelerating voltage of 5 kV and an impact time of 5 ms. A number of ion beam passes (N) varied from 1 to 60. Then FIB-modified substrates were transferred to an MBE chamber for the annealing in the ultra-high vacuum ($1 \cdot 10^{-7}$ Pa) or in the arsenic atmosphere ($4 \cdot 10^{-5}$ Pa).

Results and Discussion

Atomic force microscopy (AFM) images of nanoholes formed by FIB without subsequent annealing demonstrate that FIB impact leads to the formation of a shallow hole surrounded by a halo of redeposited substrate material (Figure 1*a*,*c*,*d*). Annealing of the FIB-modified substrate results in the local droplet etching (LDE) of the (111) surface by Ga droplets and the formation of holes with a shape of close-to-regular triangular pyramids (Figure 1*b*,*e*,*f*). The presence of the As atmosphere during annealing leads to a drastic increase in the size of holes obtained after 1 FIB pass (Figures 1*b*, 2). While both a depth (Figure 2*a*) and a lateral size (Figure 2*b*) of holes increases almost monotonically with the number of FIB passes for substrates before annealing and with annealing in the As-free atmosphere, the presence of arsenic leads to rises and dips in the dependences of hole size on the number of FIB passes. This behavior can be explained by the competition of the processes of surface etching by gallium droplets and droplet crystallization in the arsenic flux.

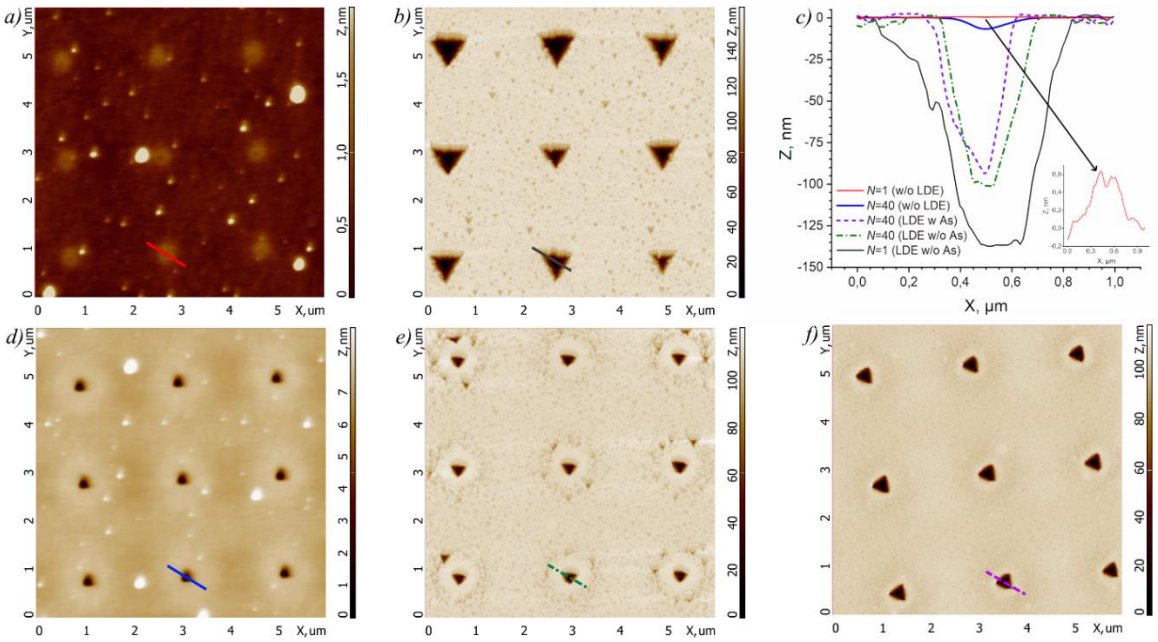


Fig. 1. AFM images of hole arrays formed by FIB: *a*) without LDE, *N*=1; *b*) with As, *N*=1; *c*) AFM cross-sections; *d*) without LDE, *N*=40; *e*) with As, *N*=40; *f*) without As, *N*=40.

A comparative analysis of AFM images of unmodified areas of the surface annealed with and without As flux showed that the average size of nanoholes in the first case is approximately twice larger than in the second case. This difference is probably attributed to the thermodynamics of interaction of gallium and arsenic oxides with the GaAs surface and As flux. However, it is important to note that the direct thermal decomposition of the substrate can also depend on the As flux.

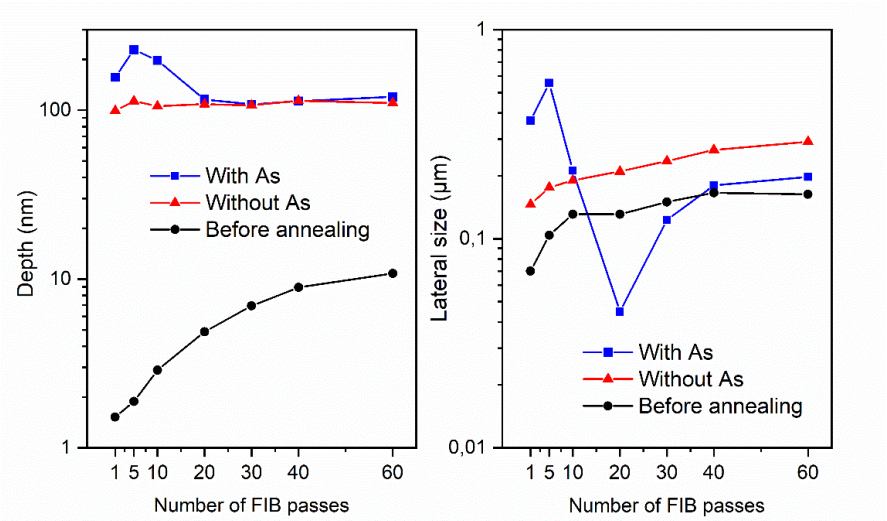


Fig. 2. Dependences of the depth (*a*) and the lateral size (*b*) of holes formed by FIB with and without subsequent annealing in the As or As-free atmosphere.

Conclusion

Thus, the arsenic flux has a significant effect on the transformation of nanoholes formed by the FIB method, leading to an increase in their size at a small number of FIB passes and to a its decrease at a large number of FIB passes. Highly symmetrical nanoholes in the form of triangular pyramids were obtained after arsenic-supplied annealing of the GaAs(111) substrate with arrays of FIB impact points formed at $N = 60$.

REFERENCES

1. **Mano T., Ohtake A., Kuroda T.**, Phys. Status Solidi A. (2023) 2300767.
2. **Tuktamyshev A., Fedorov A., Bietti S. et al.**, Appl. Phys. Lett. 13 (2021) 118.

Thin-film zinc oxide as a sensitive element of a conductometric NO_2 sensor

E. M. Lebedeva [1✉], **G. R. Nizameeva** [1,2], **V. V. Kuznetsova** [1,3], **I. R. Nizameev** [1,3]

[1] Arbuzov Institute of Organic and Physical Chemistry, FRC Kazan Scientific Center of RAS, Kazan, Russia;

[2] Kazan National Research Technological University, Kazan, Russia;

[3] Kazan National Research Technical University Named after A.N. Tupolev-KAI, Kazan, Russia

✉e-mail: elgina.lebed@mail.ru

Abstract. In this work, thin-film zinc oxide is considered as a sensitive element of a conductometric NO_2 sensor. Zinc oxide was synthesized by the sol-gel method and deposited on a glass substrate. The surface morphology of the resulting film was studied by atomic force microscopy. The dependence of the resistance of ZnO films on the number of layers deposited on the substrate was also studied. The sensory properties of ZnO were studied in a NO_2 environment with a concentration of 50 ppm at room temperature.

Keywords: gas sensor, zinc oxide film, nitrogen dioxide, sensor response

Funding: The reported study was funded by the government assignment for FRC Kazan Scientific Center of RAS.

Introduction

Air pollution is the most pressing environmental problem of our time. Air mainly consists of nitrogen, oxygen, carbon dioxide, and argon. However, the composition of the air we consume has changed in proportion to the level of human industrialization. A huge amount of toxic particles and vapors have entered the atmosphere, such as CO, H_2S, NH_3, NO, NO_2, etc. [1,2]. Among them, nitrogen dioxide NO_2 is one of the most toxic air pollutants. Various types of sensors are used to detect and monitor NO_2 levels. Among such devices, conductometric sensors based on semiconductor metal oxides are distinguished by such advantages as high sensitivity to low gas concentrations, ease of manufacture, and low cost. Zinc oxide (ZnO) is an essential n-type semiconductor metal oxide material with low toxicity and chemical stability to oxidizing and reducing gases, which allows it to be used in many devices, such as transparent electrodes, supercapacitors, and gas sensors. In this work, we propose to use thin-film ZnO as a sensitive element of a conductometric NO_2 sensor.

Materials and Methods

Zinc oxide was synthesized by a simple and inexpensive sol-gel method and deposited as a thin film on the surface of a glass substrate with gold electrodes. A centrifugation method was used to obtain a uniform and homogeneous ZnO layer. The ZnO film deposited on the glass surface was exposed to UV radiation with a wavelength of 395 nm for 30 s to improve the conductivity. The resistance of the ZnO film depending on the number of layers deposited on the glass was studied using the standard method. The morphology of the ZnO film on the surface of a glass substrate was studied by atomic force microscopy (AFM) in semi-contact mode. The sensor properties of a sensing element based on ZnO films were studied in a specially designed gas sensor test station. The test station allows the creation of a model gas environment with a known concentration of components. The resistance of the sensing element was measured in air, as well as in a model gas mixture containing 50 ppm NO_2 to determine the sensitivity of ZnO to nitrogen dioxide. The sensory response was calculated as the ratio of these two resistances. The measurements were carried out at room temperature.

Results and Discussion

Figure 1a shows an AFM image of the surface morphology of the ZnO film. As you can see, the film has a grainy texture. Grain sizes range from 40 to 80 nm. Measurements established that

the conductivity of the zinc oxide film depends on the number of layers deposited on the glass substrate (Fig. 1b) and appears only after the application of the second layer. Increasing the number of layers leads to a decrease in resistance. The optimal number of layers is 10. A further increase in the number of layers no longer leads to a change in resistance.

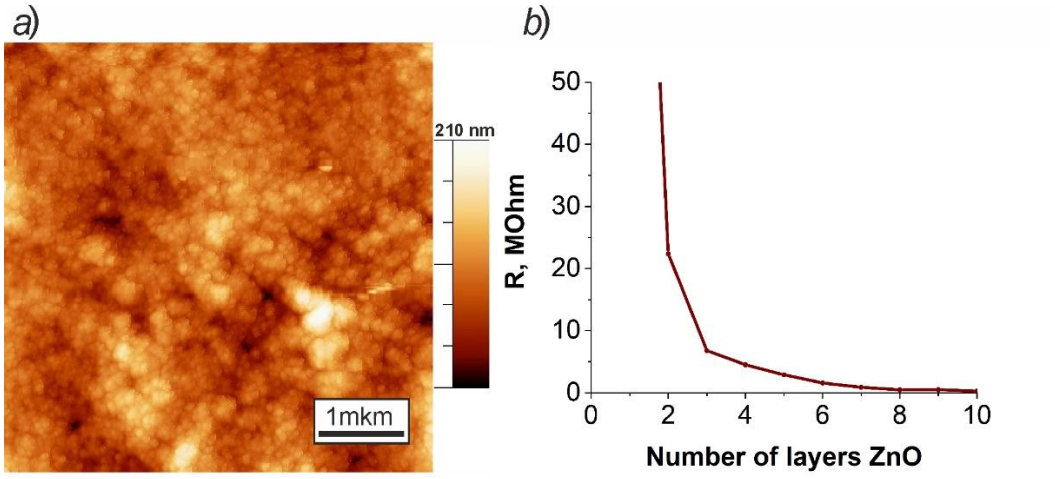


Fig. 1. Morphology of the ZnO film surface (*a*) and dependence of the resistance R on the number of ZnO layers on the glass surface (*b*)

Sensory studies carried out in a special test station showed that after exposure to NO_2, the resistance of ZnO films increases compared to the initial resistance value in air. Based on the change in resistance, the sensory response of the sensitive element was calculated. The calculated value of the response is equal to 39%.

Conclusion

As a result of the work, it was established that films synthesized by the sol-gel method and deposited on the surface of a glass substrate have a granular structure with a grain size from 40 to 80 nm. It has been shown that the resistance of ZnO films depends on the number of layers deposited on the glass and the minimum resistance value is achieved when the number of layers is 10. Sensory studies have shown that the resulting ZnO film is highly sensitive to nitrogen dioxide with a response of 39%.

REFERENCES

1. **Muhammad A., Nazar A. S., Arshad S. B., Mohammad A. M.,** Effects of Mg doping on optical and CO gas sensing properties of sensitive ZnO nanobelts, Cryst. Eng. Comm. 16 (2014) 6080.

2. **Hyung-Sik W., Chang-Hoon K., Il-Doo K., Jong-Heun L.,** Selective, sensitive, and reversible detection of H_2S using Mo-doped ZnO nanowire network sensors, J. Mater. Chem. A 2 (2014) 6412.

MBE Growth and Optical Properties of InAs QD Heterostructures on Si

V. V. Lendyashova [1-3]✉, I. V. Ilkiv[1,2], V. G. Talalaev[4], T. M. Shugabaev[1,2], B. R. Borodin[3], R. R. Reznik[1,2,5], G. E. Cirlin [1-3,5]

[1] St. Petersburg State University, St. Petersburg, Russia;
[2] Alferov University, St. Petersburg, Russia;
[3] Ioffe Institute, St. Petersburg, Russia;
[4] Martin Luther University Halle-Wittenberg, Halle, Germany
[5] IAP RAS, St. Petersburg, Russia
✉erilerican@gmail.com

Abstract. This paper presents the results of studies on the growth of thin GaAs layers on silicon substrates by molecular beam epitaxy. It has been demonstrated that the formation of an epitaxial GaAs layer without the formation of antiphase domains on Si(100) substrates no more than 4° offcut towards the [110] direction can be achieved by using thin Si buffer layers and their subsequent high-temperature annealing. It has been shown that hybrid GaAs/Si substrates obtained by the proposed technology can be used to grow heterostructures with active layers based on InAs/InGaAs quantum dot-well structures. These structures exhibit strong photoluminescence signal at room temperature in the 1.2-μm region.

Keywords: Molecular beam epitaxy, silicon, gallium arsenide, indium arsenide, indium gallium arsenide, submicron layers, quantum dots, heterostructures, telecommunications

Funding: The samples were grown under the financial support of Russian Science Foundation grant № 23-79-01117.

Introduction

The integration of III-V semiconductor heterostructures on silicon is a significant interest to creating new telecommunication devices based on them [1]. One of the promising approaches is monolithic integration by direct synthesis of III-V heterostructures on silicon substrates using submicron buffer layers. Also, using arrays of self-organizing III-V quantum dots (QD) as the active region may lead to more intense emission compared to heterostructures based on quantum wells (QW). This work is about processes of submicron GaAs layers formation by molecular beam epitaxy (MBE) method on silicon substrates with the subsequent creation on their basis of InAs QD heterostructures.

Materials and Methods

The structures were synthesized using a Riber Compact 21 EB200 MBE setup. Si(100) wafers with a misorientation of 4° were used as substrates. Studies of the morphological features of the synthesized samples were carried out using atomic force microscopy and scanning electron microscopy (SEM). For this purpose, an Ntegra Aura atomic force microscope (AFM) was used, operating in semi-contact mode using silicon probes (HANC, TipsNano) with a tip radius of curvature <10 nm. Optical properties were measured using photoluminescence (PL) at room temperature. Pumping was carried out by a green laser with a wavelength of 527 nm, operating on second harmonic generation. PL spectra were recorded using an InGaAs photodetector. The width of the entrance and exit slits of the monochromator was 1500 μm with a grating of 400 (1200).

Results and Discussion

Firstly, the substrates were chemically treated with followed thermal annealing in a growth chamber and a 50 nm thick Si buffer layer was grown. After this, the substrate temperature was lowered to 350°C and a 150 nm thick seed GaAs layer was formed. Then a GaAs layer (200 nm) containing an elastically stressed $In_{0.1}Ga_{0.9}As$ layer was grown at 450°C. At the final stage, a 0.5 μm thick GaAs layer was grown at 550°C, after which cyclic thermal annealing of the entire structure was carried out. The morphology of the synthesized heterostructures was studied by

atomic force microscopy (AFM). InAs quantum dots-quantum wells heterostructures were grown on the obtained GaAs buffer layers and their emissive properties were assessed.

For this purpose, sequential growth of a 150 nm GaAs layer, a 150 nm $Al_{0.3}Ga_{0.7}As$ layer and a 100 nm GaAs layer was performed at a temperature of 550°C. Then, at a temperature of 480°C, self-organizing growth of InAs QD with a thickness of 2.5 monolayers and a 5 nm $In_{0.1}Ga_{0.9}As$ quantum well covering them was carried out. After this, the substrate temperature was increased to 590°C and a 100 nm GaAs layer. Finally, a double coating layer including 100 nm $Al_{0.3}Ga_{0.7}As$ and 10 nm GaAs was formed at a temperature of 550°C. Upon completion of growth, the sample was cooled to room temperature and unloaded from the MBE setup to study its optical properties.

PL spectra of a heterostructure were obtained at room temperature. The maximum photoluminescence intensity is located around 1196 nm, and the full width at half maximum is about 81 meV. The relatively wide spectrum may be associated with a close to bimodal size distribution of quantum dots [2, 3]. The optical properties of InAs QD in GaAs on a silicon substrate were compared with a similar light-emitting InAs/GaAs heterostructure on a GaAs substrate. As a result, it was found that the intensity of the photoluminescence signal (at the maximum point) from InAs/InGaAs QD/QW in GaAs on a silicon substrate, in comparison with a similar heterostructure on a GaAs substrate, is about 55%.

Conclusion

As a result of the work performed, it was found that the use of Si buffer layers can significantly improve the crystalline quality of subsequently formed GaAs buffer layers. Based on the submicron GaAs buffer layers light-emitting structures with sufficiently high optical quality were obtained. The photoluminescence in the region of 1.2 μm at room temperature were demonstrated. Thus, the obtained heterostructures are high interest for the creation of telecommunication devices on silicon.

REFERENCES

1. **Chen X. et al.,** The emergence of silicon photonics as a flexible technology platform. Proceedings of the IEEE. 106(12) (2018) 2101-2116.

2. **Ilkiv I.V., Lendyashova V.V., Talalaev V.G., Borodin B.R., Mokhov D.V., Reznik R.R., Cirlin G.E.,** MBE growth and optical properties of InAs quantum dots in Si. 2022 International Conference Laser Optics (ICLO). IEEE. (2022), 1-1.

3. **Lendyashova V.V., Ilkiv I.V., Borodin B.R., Ubyivovk E.V., Reznik R.R., Talalaev V.G., Cirlin G.E.,** SUBMONOLAYER INAS QUANTUM DOTS IN SILICON GROWN BY MOLECULAR BEAM EPITAXY. St. Petersburg Polytechnic University Journal: Physics and Mathematics. 15(S3.2) (2022), 25-79.

Influence of in-situ plasma treatment during PE-ALD of GaN on growth rate and morphology

A.A. Maksimova [1,2]✉, **A. V. Uvarov**[2], **E. A. Vyacheslavova** [2], **A. I. Baranov**[2], **A. S. Gudovskikh** [1,2]

[1] Saint Petersburg Alferov University, St Petersburg,

[2] Russia Saint Petersburg Electrotechnical University, St Petersburg, Russia

✉deer.blackgreen@yandex.ru

Abstract. Different approaches for PE-ALD realisation including continuous hydrogen plasma mode, use of plasma at nitrogen step only as well as argon plasma surface activation were explored. The structural and optical properties of GaN layers grown on Si and sapphire substrates at different conditions were studied

Keywords: gallium nitride, plasma treatment, atomic layer deposition.

Funding: The research was supported by the Russian Science Foundation Grant No. 24-29-00735, https://rscf.ru/project/24-19-00150/.

Introduction

GaP based diluted nitride is a perspective material for III-V/Si solar cells []. However, a low temperature mass production technology is more preferable for its successful photovoltaic application. To avoid the problem of nitrogen incorporation control sub-monolayer digital alloy (SDA) approach to PE-ALD process was successfully applied to improve control of nitrogen incorporation into GaPN [2]. Using a combination of a sequence of layers in the form of short-period superlattices (digital alloys) GaN/GaP allowed one to precise control of the band gap with compensation of elastic stresses arising from the difference in the lattice constant. However, the growth rate and morphology of the GaN layers should be precisely controlled during the growth of the short-period superlattices. Recently, the use of in-situ annealing in argon plasma was shown to improve the crystalline quality to the epitaxial level of AlN [3] and GaP [4] layers obtained by PE-ALD. Here we explore the influence on the growth rate and morphology GaN layers using PE-ALD at temperatures below 400 °C using in-situ annealing in hydrogen and argon plasma.

Materials and Methods

Plasma deposition of GaN layers was carried out at 350°C using Oxford Plasma Lab 100 PECVD setup with capacitive coupled RF (13.56 MHz) plasma. Trimethylgallium (TMG) 8% diluted in hydrogen (H_2) was entered into the chamber because H_2 was used as a gas carrier. To realize the PE-ALD process the Ga monolayer was followed by N_2 plasma treatment leading to formation of GaN sub-monolayer. The schematic presentation of the PE-ALD process without and with Ar in-situ plasma treatment (Fig. 1a,b). Continuous hydrogen plasma mode with pulsed power increase was also explored.

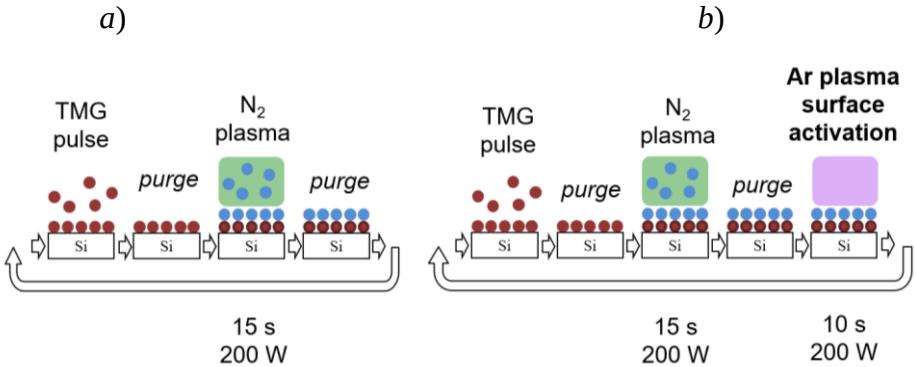


Fig. 1. PE-ALD realization of the GaN growth (*a*) with Ar in-situ plasma treatment (*b*)

Results and Discussion

The atomic force microscopy (AFM) images of the 40 nm thick GaN samples are presented in Figure 2. The growth rate and surface roughness strongly dependence on plasma treatment. Growth per cycle (GPC) and RMS are equal to 0.095 nm/cycle and 0.49 nm, respectively, for PE-ALD without plasma, while Ar in-situ plasma treatment leads to GPC increase to 0.185 nm/cycle and RMS decrese to 0.38 nm. Such behaviour is acosiated with local surface heating, which leads to enhancment of Ga precursor mobiliy. Continuous hydrogen plasma treatment leads to GPC rise to about 0.2 nm/cycle, while the surface roughness increases (Fig. 2c) with RMS of 1.19 nm. The parasitic deposition during hydrogen plasma treatment is supposed to acure in this case.

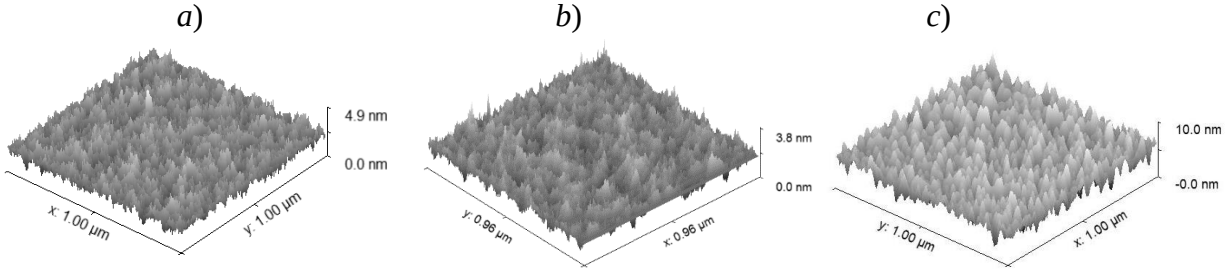


Fig. 2. AFM images of 40 nm thick GaN on Si grown by PE-ALD without (*a*) and with Ar plasma treatment (b), with continuous hydrogen plasma mode (*c*)

Conclusion

In conclusion, the way to improve the surface roughness as well as increase growth rate by using in-situ Ar plasma treatment during PE-ALD of GaN was demonstrated. On contrary, usage of hydrogen plasma during the process leads to drastic increase of surface roughness due to parasitic plasma deposition.

Acknowledgments

The research was supported by the Russian Science Foundation Grant No. 24-29-00735, https://rscf.ru/project/24-19-00150/.

REFERENCES

1. **Geisz, J.F.; Olson, J.M.; Friedman, D.J.; Jones, K.M.; Reedy, R.C.; Romero, M.J.** Lattice-Matched GaNPAs-on Silicon Tandem Solar Cells , in Proceedings of the 31th IEEE Photovoltaic Specialists Conference, 2005, 695.

2. **Gudovskikh, A. S.; Kudryashov, D.A.; Baranov, A.I.; Uvarov, A.V.; Morozov, I.A.; Monastyrenko, A.O.; Maksimova, A.A.; Nashchekin, A.V.; Vyacheslavova, E.A.; Nevedomskiy, V.N.** Low-Temperature Plasma Deposition of III-V Compounds on Silicon for Multijunction Solar Cells,ACS Applied Energy Materials, 5, 5, 5356-5366, 2022,

3. **H.-Y. Shih, W.-H. Lee, W.-C. Kao, Y.-C. Chuang, R.-M. Lin, H.-C. Lin, M. Shiojiri, M.-J. Chen,** Sci. Rep. 2017, 7, 39717.

4. **Uvarov, A.V.; Gudovskikh, A.S.; Nevedomskiy, V.N.; Baranov, A.I.; Kudryashov, D.A.; Morozov, I.A.; Kleider, J.-P.** Low temperature epitaxial growth of GaP on Si by atomic-layer deposition with plasma activation J. Phys. D: Appl. Phys. 2020, 53 345105.

Modified highly fluorescent carbon dots for immunochemical application

P. D. Nasirov✉, Ye. D. Gribova, S. A. Novikova, P. P. Gladyshev
Dubna State University, Dubna, Russia
✉e-mail: chembioslne@gmail.com

Abstract. The present study proposed a two-step approach to synthesise highly fluorescent carbon dots (CDs) with specified surface functionality for application in advanced immunoassay. The main disadvantage of CDs such as low fluorescence quantum yield was reduced due to the use of combination of citric acid (CA) and tris-(hydroxymethyl) aminomethane (THA) as precursors. In this study, the obtained carbon dots were modified with maleic anhydride to obtain a COOH-functionalised surface for immunochemical application.

Key words: carbon dots, immunoassay, fluorescence, nanomaterials.

Introduction

Citric acid (CA) is one of the most abundant precursors for the carbon dot's (CD) synthesis. Nevertheless, in a number of studies [1-3] it was proved that when attempting to synthesise CA-derived carbon dots, the obtained materials could be characterised as agglomerates of small-molecule fluorophores rather than as fluorescent carbon nanoparticles. A solution to this issue can be found by supplementing the composition of reagents for CD's synthesis with various amine-containing additives. In this study, tris-(hydroxymethyl) aminomethane (THA) was proposed as a suitable additive for the synthesis of highly fluorescent CA-based CDs for use in immunoassay.

Materials and Methods

The samples of CD's were prepared from CA and THA by solvothermal method. In the first step, the CA and THA were dissolved in deionised water and heated in a hydrothermal reactor at 200°C for 10 min. In the next step, CDs and equivalent amount of maleic anhydride were dissolved in acetonitrile, acidified with orthophosphoric acid and heated to 80°C. After 6 hours, sodium hydroxide was slowly added to the reaction mixture up to alkaline pH. The precipitate was filtered off, washed with diethyl ether and dried in air.

Results and Discussion

The optical properties of the synthesised CDs were evaluated by UV/Vis spectroscopy and fluorimetry (Fig. 1).

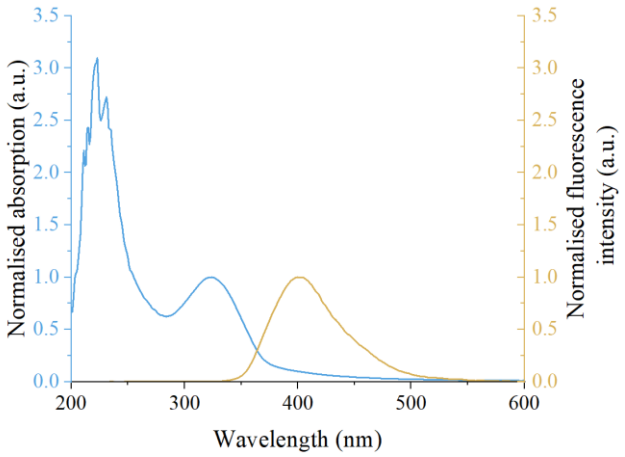


Fig. 1. Absorption and fluorescence spectra of (CA, THA)-derived CDs

The UV spectrum of the obtained sample has two absorption bands: near 220 nm and 330 nm. The absence of dependence of the fluorescence maximum on the excitation wavelength is characteristic of this CD's sample. This suggests the presence in the particles' electronic structure of a single emissive state corresponding to absorption at a wavelength of 330 nm (Fig. 2). The fluorescence quantum yield was 65.77%, which is excellent compared to the average value of this value for CDs of 2-20%.

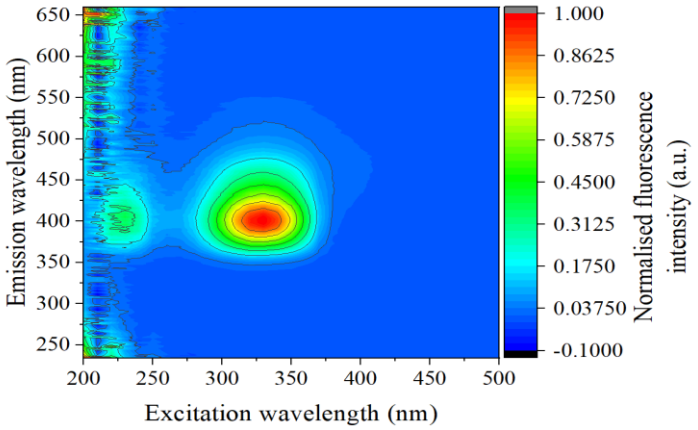


Fig. 2. Diagram of dependence of CD's fluorescence intensity on excitation wavelength

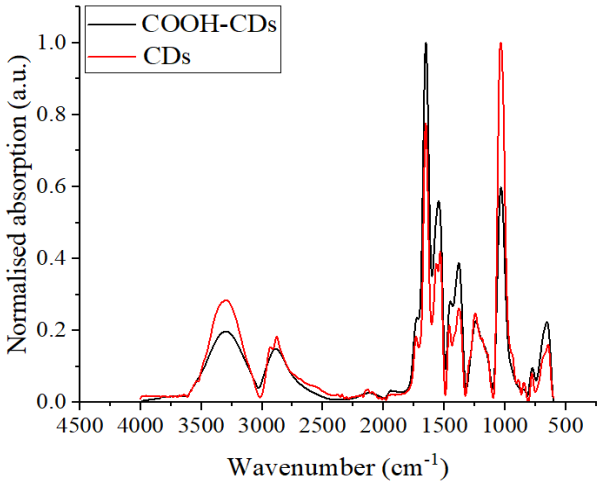


Fig. 3. IR spectra of modified and non-modified (CA, THA)-derived CD's

CA and THA-derived CD's IR spectra analysis shows the presence of intense absorption bands (1030 cm^{-1} and 3290 cm^{-1}) corresponding to vibrations of the O-H bond. (Figure 3). To obtain COOH-functionalised CDs, a technique for covalent attachment of maleic anhydride to hydroxyl groups on the CD's surface was proposed. The IR spectrum of the resulting CD's sample shows an increase in the intensity of the 1690 cm^{-1} band corresponding to the vibrations of the carbonyl C=O bond (Fig. 3).

Conclusion

The result of this work is a two-step synthesis of CDs with outstanding optical characteristics and COOH-functionalised surface. The obtained results allow us to conclude that there is a high potential for the application of these particles in immunochemical assay.

Acknowledgments

The research is supported by the Innovation Promotion Fund under contract No. 18848GU/2023 dated 28.09.2023.

REFERENCES

1. Song R. W. et al. Supramolecular Aggregation of Carbon Nanodots //Nano Letters. – 2023. – Vol 23, №. 24 – P. 11669-11677.
2. Zhu S. et al. Beyond bottom-up carbon nanodots: Citric-acid derived organic molecules //Nano Today. – 2016. – Vol. 11, №. 2 – P. 128-132.
3. Liu X. et al. Structure and photoluminescence evolution of nanodots during pyrolysis of citric acid: from molecular nanoclusters to carbogenic nanoparticles //Journal of Materials Chemistry C. – 2017. – Vol. 5, №. 39 – P. 10302-10312.

Registration of the sensor response based on a network of oriented nickel oxide fibers to nitrogen dioxide using impedance spectroscopy

G. R. Nizameeva [1✉,2], **E. M. Lebedeva** [1], **V.V. Kuznetsova** [1], **I. R. Nizameev** [1, 3]

[1] Arbuzov Institute of Organic and Physical Chemistry, FRC Kazan Scientific Center of RAS, Kazan, Russia;

[2] Kazan National Research Technological University, Kazan, Russia;

[3] Kazan National Research Technical University Named after A.N. Tupolev-KAI, Kazan, Russia

✉e-mail: guliya.riv@gmail.com

Abstract. The effect of different concentrations of nitrogen dioxide on the sensory response of a sensing element based on a grid of oriented nickel oxide fibers was investigated in the work. The impedance spectroscopy technique was used to measure the change in resistance of the sensing element in the presence of a target gas. The sensory response values calculated from the impedance curves showed the high sensitivity of the oriented nickel oxide fibers mesh to nitrogen dioxide.

Keywords: gas sensor, oriented nickel oxide fibers, impedance spectroscopy, sensor response

Funding: The reported study was funded by the government assignment for FRC Kazan Scientific Center of RAS.

Introduction

Semiconductor metal oxides are widely used to create energy conversion devices, energy storage, electrocatalysis, photocatalysis, etc. [1] They are of particular interest in the field of environmental monitoring since they have high sensitivity to toxic gases and a short response time [2]. This allows the use of semiconducting metal oxides to create gas analyzer active elements that can measure concentrations of gaseous pollutants down to ppb levels. The ability to obtain metal oxides using simple and inexpensive methods is another advantage of their use in gas analyzers. The operation of metal oxide gas analyzers is based on the adsorption of molecules of the target gas on the surface of the sensitive element (metal oxides) which leads to a change in the conductivity of the sensitive element. This suggests that electronic interactions occur between the molecules of the adsorbed target gas and the sensitive material. This work examines the effect of different concentrations of nitrogen dioxide in a model gas mixture on the electrical properties of a sensing element based on a network of oriented nickel oxide fibers.

Materials and Methods

The network of oriented nickel oxide fibers that acts as the sensing element is formed from nickel fibers. Nickel fibers were synthesized in a simple and inexpensive way - by chemical deposition of metal from the liquid phase and deposited in the form of an oriented grid on the surface of a glass substrate with conductive electrodes. The electrodes are designed to measure the resistance of the sensing element in an air atmosphere and the presence of NO_2. Next, the fibers were coated with a thin film of nickel and then oxidized. To determine the sensory response and the effect of different concentrations of nitrogen dioxide on the sensory response of the sensing element, impedance spectroscopy was used. The impedance curves of the sensing element were recorded in the frequency range from 1 Hz to 500 kHz in a model gas mixture containing NO_2 (from 5 *ppm* to 50 *ppm*).

Results and Discussion

The impedance curves of a sensing element based on a nickel oxide oriented network were measured at various nitrogen dioxide concentrations. The curves were analyzed by constructing Nyquist and Bode curves and the equivalent circuit corresponding to these curves. From the

obtained curves, the complex resistances of the sensing element in an air atmosphere and the presence of NO_2 were determined. The obtained data made it possible to calculate the sensory response of the sensitive element to nitrogen dioxide at its various concentrations in the model gas mixture. The sensory response was calculated as the ratio of the complex resistance of the sensing element in the air to its resistance in the NO_2 environment. The results are presented in Table 1.

Table 1

The sensor response to NO_2

NO_2 concentration in the model gas mixture, *ppm*	The sensor response S, %
5	0,8
10	2
20	6,6
25	12,7
30	17
40	21,6
50	26

The results show that as the concentration of nitrogen dioxide in the model gas mixture increases, the sensory response also increases. As expected, the best response of the sensitive material is observed at a NO_2 concentration of *50 ppm* and is 26%. The dependence of the sensory response on the amount of NO_2 suggests that electronic interactions occur between the sensitive layer and nitrogen dioxide molecules adsorbed on its surface, which leads to a change in the electrical resistance of the sensing element based on a grid of oriented nickel oxide fibers.

Conclusion

A sensitive element based on an oriented nickel oxide network was developed to detect nitrogen dioxide molecules. The sensory response of the developed sensing element to the target gas was calculated using the impedance spectra recorded at various concentrations of nitrogen dioxide in the model gas mixture.

REFERENCES

1. **Alexandria R. C. B, Amanda L. C, Andricus R. B., Byron H. F.,** Electrochemical impedance spectroscopy of metal oxide electrodes for energy applications, ACS Applied Energy Materials. 3 (1) (2020) 66-98.

2. **Isaac N. A., Pikaar I., Biskos G.,** Metal oxide semiconducting nanomaterials for air quality gas sensors: operating principles, performance, and synthesis techniques**,** Microchimica Acta. 189 (5) (2022) 196.

Investigation of the effect of functional sublayers on the characteristics of deposited diamond-like carbon coatings

B.A. Parshin [1]✉, **M.O. Makeev** [1], **P.A. Mikhalev** [1]

[1] Bauman Moscow State Technical University, Moscow, Russia;

✉parshbgal@bmstu.ru

Abstract. The influence of functional sublayers on the structural and optical characteristics, as well as the surface state of deposited diamond-like carbon coatings was studied using Raman spectroscopy, spectrophotometry and atomic force microscopy.

Keywords: diamond-like carbon, functional sublayers, sp^2-hybridization, sp^3-hybridization, roughness

Funding: the research was carried out within the state assignment of the Ministry of Science and Higher Education of the Russian Federation (theme No. FSFN-2024-0016)

Introduction

The application of thin-film coatings as functional layers opens up the possibility of obtaining the necessary surface properties of products. Among the various types of such coatings, particular attention is paid to diamond-like carbon coatings (DLC). In general, the structure of a diamond-like coating can contain different concentration ratios of sp^3, sp^2, sp^1 carbon configurations [1]. Currently, there are a number of methods for the preparation and deposition of diamond-like carbon coatings, listed and described in detail in the review [2]. One of the problems in obtaining DLC coatings that limits their areas of application is their high internal stresses, which can reach 10 GPa. When the critical value of internal stresses is exceeded, the DLC coating falls off. Traditional approaches to reducing internal stresses are to increase the growth temperature and reduce the energies of expansion particles. However, these methods inevitably lead to a decrease in the yield of the diamond phase. In this regard, the use of intermediate functional sublayers plays an important role in ensuring the strength characteristics and durability of applied coatings.

Materials and Methods

DLC coatings were deposited by pulsed laser deposition (PLD) on a NanoFab-100 in a vacuum chamber at a pressure of ~10^{-6} mbar. To sputter the target material, high-purity pyrolytic graphite (99.99%), an excimer KrF laser with a wavelength of 248 nm and a pulse duration of about 30 ns at a frequency of 10 Hz was used.

To determine the structure of the diamond-like carbon coatings, the method of Raman spectroscopy in the visible range was used, which makes it possible to determine the ratio of sp^3, sp^2 carbon hybridizations. The optical characteristics of the resulting samples were monitored by visible spectrophotometry. Atomic force microscopy methods were used to study the surface condition of the resulting coatings.

Results and Discussion

The results of studies using atomic force microscopy of DLC coatings show noticeable differences in the state of the surface of samples with and without functional sublayers. As can be seen in fig. 1a, the surface of the sample deposited on an aluminum mirror contains a large number of defects, which is associated with high internal stresses that arise in the coating due to significant differences in the temperature expansion coefficients of the substrate and coating, which lead to cracking of the coating. The DLC sample deposited on the Ti-sublayer has a roughness of less than 5 nm, as shown in fig. 1b.

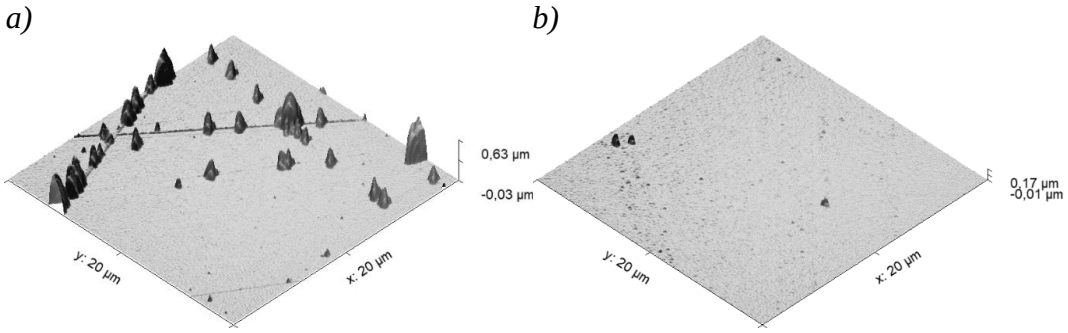


Fig. 1. AFM surface images of (*a*) DLC coating on Al surface and (*b*) DLC coating on Ti-sublayer

A study of the optical properties of the samples shows that the use of functional sublayers reduces the reflectance. As was shown earlier, samples with applied sublayers have low roughness. Thus, the change in the optical properties of the samples occurs due to the fact that the reflective properties of the mirror surface in the optical range of the spectrum are largely determined by the refractive and absorption indices of the functional sublayers and the absorbing properties of the DLC coating, rather than by the substrate material.

Examination of samples using Raman spectroscopy shows the presence of a carbon phase in the range from 1000 to 1800 cm-1 [3, 4]. In all spectra, a slight asymmetry was observed in the G-peak region, so the Breit-Wigner-Fano and Lorentz functions were used to describe the G- and D-peaks, respectively. Samples with applied sublayers showed a high content of sp^3 phase, which corresponds to ta-C diamond-like carbon.

Conclusion

The results of the study show that samples of DLC coatings with a deposited functional Ti-sublayer have a high ratio of sp^3 and sp^2 carbon phases and correspond to the ta-C type, which is characterized by high hardness. Also, examination of the surface of these coatings did not reveal any significant defects, which indicates a decrease in internal stresses. Thus, the use of functional sublayers makes it possible to obtain coatings with a high content of the sp^3 phase, which have high strength characteristics, combined with high surface quality.

REFERENCES

1. **Robertson J.,** Diamond-like amorphous carbon, Mat. Sci. Eng. R. 37 (2002) 129-281.

2. **Hainsworth S.V.,** Diamond-like carbon coatings for tribology: production techniques, characterization methods and applications, Int. Mat. Reviews. 52 (2007) 153-174.

3. **Ferrari A.C. and Robertson J.,** Interpretation of Raman spectra of disordered and amorphous carbon, Physical review B. 61 (2000).

4. **Ferrari A.C. and Robertson J.,** Raman spectroscopy of amorphous, nanostructured, diamond-like carbon, and nanodiamond, Phil. Trans. R. Soc. A. 362 (2004) 2477–2512.

Quantum efficiency of water photocatalytic decomposition by Ag-Ag_2S nanostructures

V. V. Pesnyakov [1]✉, A. I. Sidorov [1], N. V. Nikonorov [1]
[1] ITMO University, Saint-Petersburg, Russia
✉ vvpesnyakov@itmo.ru

Abstract. In this paper quantum efficiency of Ag-Ag_2S nanostructures is studied. Results reveal the increase in quantum efficiency of studied structures by two times in comparison with the Cu substrate. At the same time Ag_2S structures does not exhibit any increase of quantum efficiency after applying 3 V to the structure.

Keywords: photocatalysis, silver nanostructures, semiconductor nanoparticles

Introduction

Photocatalysis is an effective method for converting solar energy, offering an approach to solving energy and environmental problems. Under the influence of sunlight, a multi-stage reaction occurs to produce gaseous forms of oxygen and hydrogen, which can additionally be used in industry or as fuel. There are many catalytic materials that are known today [1]. In this paper Ag and Ag_2S nanostructures' photocatalytic quantum efficiency was studied.

Materials and Methods

In this research nanoporous silver layers were synthesized by a substitution reaction on cuprum substrates from an aqueous solution of copper sulfate (3,75 g/l) and consist of micro- and nanodendrites. To study photoelectrochemical catalysis, samples were placed in an aqueous solution of $NaNO_3$ and irradiated with a fiber source of UV-visible radiation with a voltage of 0.5 - 5 V applied to the photocatalytic cell through a 1 kOhm ballast resistor. Quantum efficiency was determined by the formula [2]: $\eta = N_e/N_{ph}$, where $N_e = I_{ph}\hbar\omega$, $N_{ph} = P_{Abs}e$, N_e – number of photoelectrons, N_{ph} – number of absorbed photons, I_{ph} – photocurrent, P_{Abs} – absorbed radiation power, ω – radiation frequency.

Results and Discussion

Quantum efficiency dependency of the applied voltage is presented in figure 1. Even pure cuprum substrate exhibit quantum efficiency 0,04% at the applied 5V to the photocatalytic sell. However, Ag_2S structures do not show higher quantum efficiency then the pure Ag up until 3V and equal to the Ag at 4-5V.

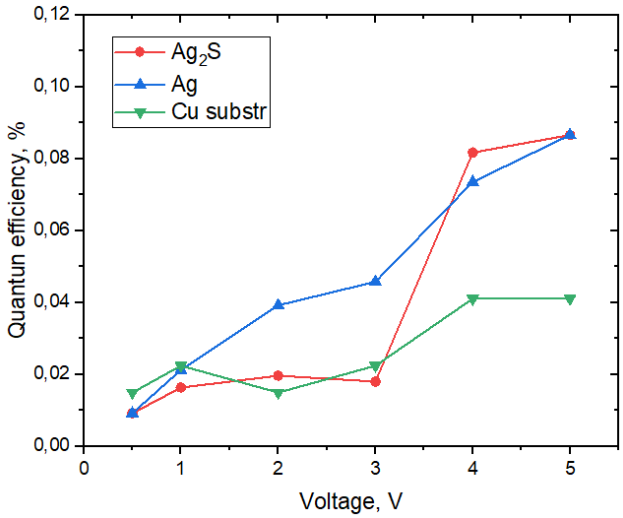


Fig. 1. Quantum efficiency of the studied structures to the applied voltage

Conclusion

Photocatalytic quantum efficiency of Ag and Ag_2S nanostructures were studied. Ag nanoporous layer exhibit twice higher quantum efficiency then the pure cupper substrate when 5V is applied to the sell. However, Ag_2S structures do not show much higher quantum efficiency then the pure Ag.

The research was supported by the Russian Science Foundation grant No. 20-19-00559.

REFERENCES

1. **Takanabe, Kazuhiro.** Photocatalytic water splitting: quantitative approaches toward photocatalyst by design., Acs Catalysis 7.11 (2017): 8006-8022.

2. **Jiao, Yang, et al.** Synthesis of three-dimensional honeycomb-like Au nanoporous films by laser induced modification and its application for surface enhanced Raman spectroscopy. Optical Materials Express 7.5 (2017): 1557-1564.

Study of the effect of surfactants on surface tension of PEDOT:PSS aqueous solution

V. A. Pozdeev [1,2] ✉, A. V. Uvarov [1], A.S. Gudovskikh [1,2], A. O. Monastyrenko [1]

[1] St. Petersburg Alferov Academic University, St. Petersburg, Russia;

[2] St. Petersburg Electrotechnical University "LETI", St. Petersburg, Russia

✉pozdeev99va@gmail.com

Abstract. In this paper we investigate a technique to determine the minimum surface tension and minimal surfactant concentration (Triton X-100) in a poly(3,4-ethylenedioxythiophene):polystyrenesulfonate (PEDOT:PSS) aqueous solution to achieve full wetting of surfaces with silicon and fused silica.

Keywords: PEDOT:PSS, poly(3,4-ethylenedioxythiophene) polystyrene sulfonate, conductive polymer, surfactants, Triton X-100.

Funding: This work was supported by the Russian Science Foundation under grant number (№23-22-00367) https://rscf.ru/project/23-22-00367/.

Introduction

One of the drawbacks of applying PEDOT:PSS coatings from an aqueous solution is that water exhibits relatively high surface tension, leading to poor wettability on different substrates. Polymer solutions have slightly lower surface tension [1], but it is insufficient for complete wetting of silicon and fused silica substrates. Surfactants are traditionally used for effectively reducing surface tension. However, the high content of surfactants has a negative impact on the electrophysical properties of PEDOT:PSS [2].

To determine the surface tension of a liquid at which complete wetting of a specific substrate occurs (critical surface tension), one can use the Zisman plots at zero contact angle [3].Through the dependence of surface tension on surfactant concentration in the PEDOT:PSS solution, one can determine the required surfactant concentration to achieve the desired surface tension value of the solution and attain complete wetting of the substrate. This will help avoid excessive addition of surfactants to the solution, and significantly reduce material consumption when determining the appropriate concentration.

Materials and Methods

Contact angles were determined using a photographic method based on the width and height of the drop on the half-width. When using drops ranging from 1 μL to 3 μL, the influence of gravity on the drop shape can be neglected, allowing us to consider the drop as a segment of a sphere [4]. When determining the values of contact angles, the consideration of evaporation, drop spreading, and absorption of water vapor from the environment was achieved by extrapolating the kinetic curve onto the time axis. The obtained contact angle value can be considered to correspond to the equilibrium contact angle [4].

The measurements were taken at a fixed humidity and close to room temperature. Humidity control was maintained using a saturated solution of an inorganic salt, as detailed in the method presented in this paper[5].

To determine the surface tension, two test substrates made of different materials were utilized. Water and dimethyl sulfoxide were employed to assess the surface energy of the substrates. Aqueous solutions with varying concentrations of surfactants were utilized to study Zisman plots. The dependance between the surface tension of the PEDOT:PSS solution and the concentration of the surfactant contained within it was obtained through a similar procedure. Triton X-100 was used as the surfactant.

Results and Discussion

The surface tension, particularly its polar and dispersive components, was determined using formulas derived from the Owens-Wendt method [6]. The surface energy values and their dispersive and polar components for the substrates were also determined under the same conditions using formulas derived from the same method.

As a result, Zisman plots were obtained along with the critical surface tension values for silicon and fused silica. The dependence of the surface tension of the PEDOT:PSS solution on the concentration of Triton X-100 was determined.

Conclusion

This study demonstrated a methodology to determine the minimum required concentration of surfactants in an aqueous polymer solution for its subsequent application to a substrate surface. The critical surface tension for silicon and fused silica was determined, and numerical values of the minimum required concentration of Triton X-100 in the PEDOT:PSS solution for complete wetting were obtained. The results of this study can be used in the production of electronic devices based on organic semiconductor material PEDOT:PSS.

REFERENCES

1. Holmberg, K.; Jönsson, B.; Kronberg, B.; Lindman, B., Surfactants and Polymers in Aqueous Solution. 2nd ed.; Wiley: Chichester, U.K., 2003.

2. Pozdeev V., Uvarov A., Gudovskikh A., Maksimova A., Vyacheslavova E., Study of the effect of solvents and surfactants on electrical properties of PEDOT:PSS films, St. Petersburg State Polytechnical University Journal. Physics and Mathematics. (2023).

3. Zisman W. A., Relation of the Equilibrium Contact Angle to Liquid and Solid Constitution, Advances in Chemistry. (1964) 1–51

4. Lyakhovich A. M., Shakov A. A., Lyalina N. V. Effect of ambient humidity to wetting angles of various hydrophilic surfaces, Protection of Metals and Physical Chemistry of Surfaces. 46 (5) (2010) 534–539.

5. Young J. F., Humidity control in the laboratory using salt solutions—a review, Journal of Applied Chemistry. 17(9) (1967) 241–245.

6. Owens, D. K., & Wendt, R. C., Estimation of the surface free energy of polymers, Journal of Applied Polymer Science. 13(8) (1969) 1741–1747.

Structural engineering of bactericidal Mn-doped ZnO-ZrO_2 nanocomposites as effective photogenerators of reactive oxygen species

K. A. Portnova [1]✉, **A. A. Shelemanov** [1], **S. K. Evstropiev** [1]
[1] ITMO university, Saint-Petersburg, Russia;
✉ksiu.san@gmail.com

Abstract. In the article, ZnO-ZrO_2 nanocomposites doped with Mn obtained by the polymer-salt method were studied. The crystal structures and morphology of the composites were studied using X-ray diffraction and SEM analysis. Photoluminescence spectra and the dependence of photogeneration of singlet oxygen on the power density of exciting blue light were obtained. A study was conducted on the antibacterial activity of composites.

Keywords: ceramics, nanocomposites, photocatalysis, crystal.
Funding: This work was funded by Russian Science Foundation (No. 20-19-00559).

Introduction

Bactericidal metal oxide materials are the object of intensive investigations [1]. Numerous oxide semiconductor materials are effective photocatalysts, demonstrate the antibacterial activity and have excellent thermal stability and chemical durability. Composites based on ZnO demonstrate high antibacterial activity [1–3]. Modification of ZnO-based materials by other oxides provides the significant enhancement of their bactericidal characteristics. These additions decrease the size of ZnO crystals, increase their specific surface areas and modify the crystal and electronic structures and morphology of ZnO materials. In [4] Mn additions are used for the modification of ZnO and ZrO_2. Polymer-salt synthesis is facile and effective method used for the preparation of different ZnO-based nanomaterials [2]. It allows to obtain composites with a large specific surface area. The aim of this work is the design of the chemical synthesis of effective bactericidal Mn-containing ZnO-ZrO_2 nanocomposites obtained by the polymer-salt method. Used approach of nanocomposites development included the study and design of their morphology and the crystal structure for the enhancement of luminescent properties, the ability to ROS photogeneration, and the improvement of bactericidal properties.

Materials and Methods

Polymer-salt technique was used for the preparation of powder samples. The crystal structure of prepared powders was investigated by XRD method using device Rigaku Ultima IV. The diffraction patterns were scanned from 20^o to 100^o ($2\boldsymbol{\theta}$). Based on the obtained XRD data, we estimated the crystal sizes using the Scherrer formula (1):

$$d = \frac{K \times \lambda}{\beta \times cos\theta}, \quad (1)$$

where d is the average crystal size; K is the dimensionless particle shape; λ is the X-ray wavelength; β - is the width of the reflection at half height; θ is the diffraction angle.

The morphology and chemical composition of prepared samples were studied by SEM and energy-dispersive analysis using the electronic microscope TESCAN VEGA3 equipped by the setup for energy-dispersive analysis Advanced Aztec Energy. Photoluminescence spectra in near IR spectral region were measured upon excitation by the radiation of LEDs with emission bands maximums at 370 nm and 405 nm using a spectrometer SDH-IV. The luminescence spectra in UV and visible spectral ranges were measured using the spectrofluorometer Perkin Elmer LS50B. The method described in [3] was used for the estimation of bactericidal properties of prepared coatings. The Gram-positive bacteria *Staphylococcus aureus ATCC 209P* and Gram-negative bacteria *Escherichia coli ATCC 25922* were applied as test bacteria. Bactericidal activity was estimated by the measurement of the size of an inhibited area, which is formed on surface containing bacteria.

Results and Discussion

The obtained XRD data indicate the formation of hexagonal ZnO crystals as main crystal phase in the obtained powders. The embedding of Mn ions deforms the crystal cells of ZnO crystals that can promote the structural defects formation in them. The average ZnO crystals size calculated using Scherer's formula is 9 nm in all samples. As a result of the SEM analysis, images of composite ZnZrMn1 at different magnification values were obtained. Photos show that the composite contains a big porous aggregates having size tens microns. The increase of visible light intensity enhances singlet oxygen generation (Fig. 1a). The observed dependence of the luminescence band (λ = 1270 nm) intensity I_{SO} from the intensity of excited visible irradiation (λ_{ex} = 405 nm) I_{ex} is not linear.

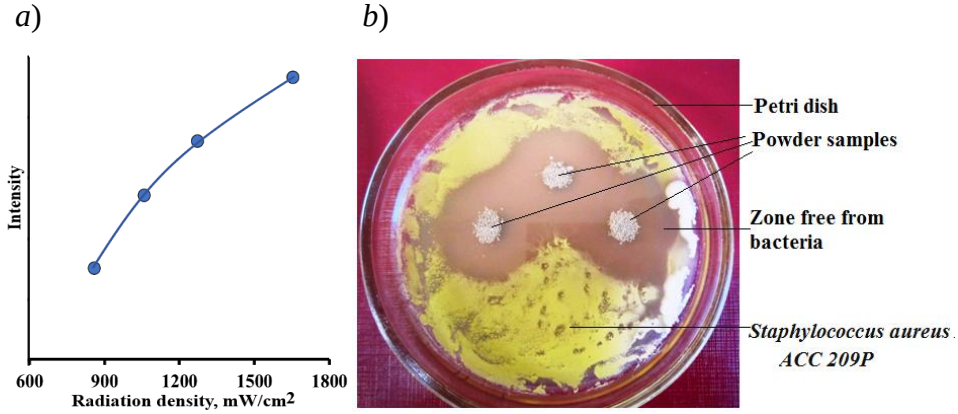


Fig. 1. Dependence of the luminescence intensity from the excited radiation density (a). Photo demonstrating the formation of zones free from bacteria *Staphylococcus aureus ACC 209P* (b).

The measurements of photoluminescence spectra showed the presence of numerous different intrinsic defects in the structures of ZnO and ZrO_2 crystals. Figure 1b shows the photo indicating the formation of zones free from bacteria *Staphylococcus aureus ACC 209P*. The results of antibacterial tests show that ZnO-ZrO_2 materials demonstrate higher antibacterial activity against bacteria *Staphylococcus aureus ACC 209P* than powders prepared earlier [2].

Conclusion

Mn-doped ZnO-ZrO_2 composites having high antibacterial properties were synthesized non-isothermal polymer-salt method. The crystal structures and morphologies of materials were studied by XRD and SEM analysis. The embedding of Mn ions into the structure of ZnO expanses and deforms its crystal cells. The measurements of photoluminescence spectra showed the presence of many different intrinsic defects in the structures of ZnO and ZrO_2 crystals. It was found that obtained composites demonstrate the strong ability to generate singlet oxygen under visible ($\lambda_{ex.}$=405 nm) irradiation. The dependence of the concentration of photogenerated singlet oxygen from the intensity of excited light is non-linear. Mn-doped ZnO-ZrO_2 composites demonstrate the high antibacterial activity against gram-positive bacteria *Staphylococcus aureus ACC 209 P*. Bactericidal activity of prepared composite against gram-negative bacteria *Escherichia coli ATCC 25922* is low.

REFERENCES

1. **Li Y**. et al. Mechanism of photogenerated reactive oxygen species and correlation with the antibacterial properties of engineered metal-oxide nanoparticles // ACS nano. American Chemical Society, 2012. Vol. 6, № 6. P. 5164–5173.
2. **Evstropiev S**. et al. Bactericidal properties of ZnO-SnO_2 nanocomposites prepared by polymer-salt method // Materials Science and Engineering: B. 2021. Vol. 264. P. 114877.
3. **Huang Z**. et al. Toxicological Effect of ZnO Nanoparticles Based on Bacteria // Langmuir : the ACS journal of surfaces and colloids. 2008. Vol. 24. P. 4140–4144.
4. **Armah E**. et al. Solubility of Mn in ZnO Crystallites Synthesized Using Solid State Techniques // Advanced Nano Research. 2020. Vol. 3. P. 28–39.

Investigation of the luminescent properties of glasses activated by $CsPbBr_3$ perovskite nanocrystals and europium ions

A. D. Ratova ✉, **A. N. Babkina**
ITMO University, St. Petersburg, Russia;
✉ratova.anastasia@mail.ru

Abstract. A series of borogermanate glasses with $CsPbBr_3$ perovskite nanocrystals with the addition of Eu^{3+} ions is synthesized. With a change in the concentration of Eu^{3+} ions, a change in the luminescent properties of glasses in the visible range is observed.

Keywords: Perovskite nanocrystals, borogermanate glasses, trivalent europium
Funding: No funding

Introduction

Optical materials based on perovskite lead halide cesium nanocrystals are promising due to their unique optical, optoelectronic and photoelectric properties [1]. Due to the large absorption coefficient, high carrier mobility and emission efficiency, enabling perovskite to become ideal materials for combining with silicon photodetectors [2]. In addition, it has been widely used in initial solar cells, high-energy ray detection, light-emitting diode, lasers, and other fields in the span of an only few years. The rare-earth Eu^{3+} ion-doped $CsPbX_3$ nanocrystals can achieve a higher photoluminescent quantum yield due to the energy transfer from excitons to Eu3+ ions, thus improving the response of photodetectors. Herein, a series of borogermanate glasses co-doped with CsPbBr3 perovskite nanocrystals and Eu^{3+} ions was synthesized and its luminescent properties ratio were studied under condition of different Eu2O3 concentration

Materials and Methods

The initial glass matrix had the following composition: 6.67 ZnO-5.81 Na_2O-31.3 B_2O_3-50.53 GeO_2 mol. %. For subsequent nucleation of nanocrystals, Cs_2CO_3, KBr, PbO were also introduced in the glass composition. The perovskite nanocrystals were nucleated in a borogermanate network via spontaneous volume crystallization during glass annealing and additional heat treatment at temperatures above glass transition temperature (470°C). The synthesis was carried out in air atmosphere at a temperature of 950°C using quartz ceramics crucibles. A series under study contained glasses with different Eu_2O_3 concentration: 0.25, 0.5 and 1 mol.% (samples #1, #2, #3 correspondingly).

The glass optical density spectra were measured by a Lambda 650 spectrophotometer (Perkin Elmer) in the spectral range of 200–900 nm with a step of 1 nm at room temperature. For the luminescence and excitation spectra recording, the LS-55 spectrofluorimeter (Perkin Elmer) was used. source and remote-controlled monochromator.

Results and Discussion

Figure 1a shows the luminescence spectra of samples #1,2,3, in the range of 375-600 nm under the excitation of 365-397 nm. According to the graphs it can be seen that for the glass with the lowest concentration of Eu_2O_3 narrow band with the maximum at 535 nm, corresponding to $CsPbBr_3$ perovskite nanocrystals, was observed. Luminescence spectra of sample #2 possessed two bands at 450 and 500 nm. Decay time measurements showed that green band demonstrated lifetime of tens of nanoseconds wherein blue band had lifetime of approximately hundreds of nanoseconds. Luminescence spectra of the glass with the biggest Eu_2O_3 concentration showed mostly Eu^{3+} bands. Figure 1b shows the luminescence spectra for the same samples # 1,2,3, in the range of 500-775 nm with a delay of 0.01 s. In this case, the spectra look almost the same, have three pronounced peaks at long wavelengths of 591 nm, 613 nm, 700 nm. Due to the shorter lifetimes of blue and green luminescence associated with perovskite crystals and clusters, when recording luminescence spectra with a delay of 0.1 ms from the exciting pulse, only luminescence

bands of europium ions are visible in the spectra. of the spectra are different, have a different number of peaks.

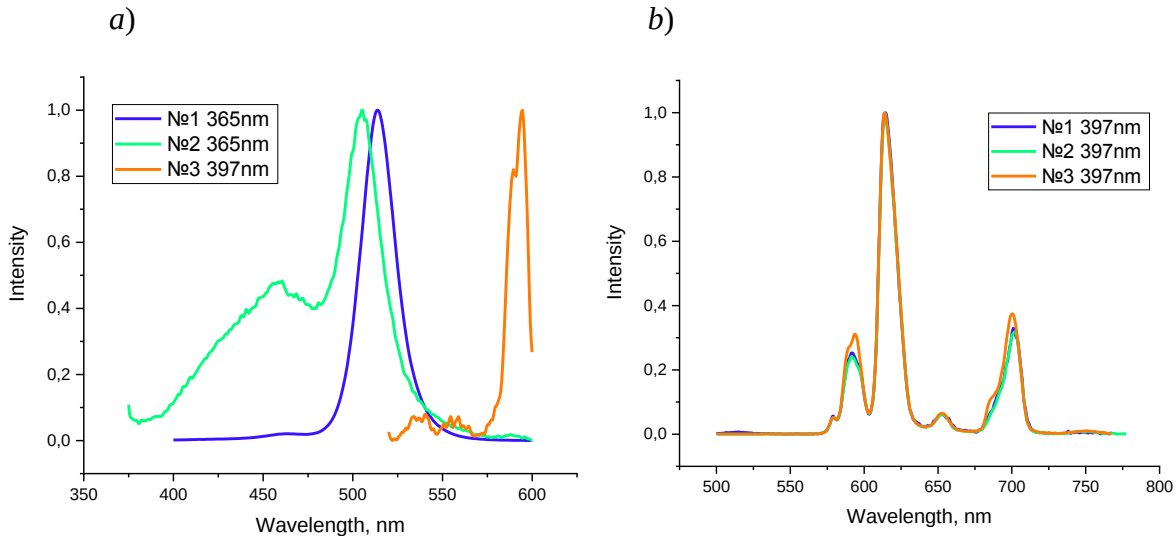


Fig. 1. Graphs of luminescence spectra of three samples under study without delay (a) and with delay 0.1ms (b) (excitation wavelength varied from 365 up to 397 nm)

Conclusion

As a result of the work, borogermanate glasses with $CsPbBr_3$ perovskite nanocrystals and different concentrations of Eu_2O_3 were synthesized. It was shown that at low concentrations, Eu^{3+} ions played the role of crystallization centers for the nucleation of perovskite nanocrystals. At a high concentration of Eu^{3+} ions, perovskite crystals nucleated only during additional heat treatment. An intermediate concentration of Eu^{3+} ions led to the formation of $CsPbBr_3$ perovskite nanocrystals in the glass matrix, as well as probably clusters for perovskite crystals.

REFERENCES

1. **Airton Germano Bispo-Jr, Amanda Justino de Morais, Claudia Manuela Santos Calado, Italo Odone Mazali, Fernando Aparecido Sigoli.** "Lanthanide-doped luminescent perovskites: A review of synthesis,." Journal of Luminescence (2022).

2. **Jing Ding, Shouying Mu , Weidong Xiang , Nan Ding , Wen Xu, Xiaojuan Liang.** " Eu^{3+} doped $CsPbCl_2Br_1$ nanocrystals glass for enhanced the ultraviolet." Journal of Luminescence (2023).

Formation of silver nanoparticles in glass by vacuum thermal poling

I. V. Reshetov [1,2]✉, **E. S. Babich** [1,2]
[1] Alferov University, St. Petersburg, Russia;
[2] Peter the Great St. Petersburg Polytechnic University, St. Petersburg, Russia
✉reshetov_iv@spbstu.ru

Abstract. It is shown that the vacuum poling of soda-lime silicate glass followed by silver-for-sodium ion exchange results in the formation of silver nanoparticles (NPs) in subcathode region of the glass. The latter was confirmed by the presence of silver NPs' localized surface plasmon resonance peak in optical absorption spectra of the samples. The NPs were formed in the subsurface region of the glass, for this spectral peal did not disappear after mechanical cleaning of the glass surface. The possibility of forming a 2D-structured pattern from silver NPs, repeating the relief of cathode electrode used for poling, has also been demonstrated.

Keywords: soda-lime glass, thermal poling, silver nanoparticles.

Funding: This study has been supported by the Ministry of Science and Education of Russian Federation, project FSRM-2023-0009

Introduction

Thermal poling of glasses consists in the application of a DC voltage to a heated glass plate. This process leads to compositional [1] and structural [2,3] changes in the subanode layer of a glass and, accordingly, alternates physical properties of such layer. In particular, when poled soda-lime glass in air, electric current through the sample occurs due to the influx of atmospheric positive hydrogen/hydronium ions (H_3O^+) [4]. This results in displacement of alkaline ions and formation of alkaline-depleted and hydronium-enriched layer in subanode region of the glass which significantly slows down or even prevents ionic exchange [5]. This allows creating 2D-structured pattern from silver NPs in subanode layer of the glass by poling silver-for-sodium exchanged glass with structured (relief) anode electrode and subsequent thermal treatment in reducing atmosphere. However, recent studies have also shown that the thermal poling of silver-for-sodium exchanged glasses being performed in air leads to the growth of silver dendrites in the subcathode layer of the glasses without the use of reducing atmosphere [6]. This allows us to conclude that poling itself creates reducing centers. Indeed, when poled soda-lime glass in vacuum, we recorded an electric current through the glass, despite the absence of penetration of positive species into it, the current being only several times less compared to the case of air-poling. We hypothesized that this current could arise partly as a result of the structural changes of the glass, and partly as a result of the drift of negative species (for example, electrons). Since negatively charged entities in glasses can act as reducing centers for silver ions, we tested their presence in the subcathode layer of soda-lime glass poled in vacuum by performing silver-for sodium ion exchange. This work is devoted to a description of corresponding experiments and demonstration of the possibility to form 2D-structured patterns from silver NPs by combination of vacuum thermal poling and silver-for-sodium ion exchange without using additional thermal treatment.

Experimental and results

In the experiments we used slides of soda-lime glass, which composition in wt.% is: 72.2% SiO_2, 14.3% Na_2O, 6.4% CaO, 4.3% MgO, 1.2% K_2O, 1.2% Al_2O_3 and 0.4% other oxides. 1 mm thick glass slides were thermally poled in a vacuum chamber at about 2×10^{-5} mmHg pressure at 300 °C under 800 V DC voltage. The experimental setup is shown in the inset in figure 1. After poling, we performed silver-for-sodium ion exchange by immersion the samples for 20 min in $Ag_{0.05}Na_{0.95}NO_3$ (in wt.%) melt heated to 325 ºC.

We measured optical absorption of the samples with UV-VIS spectrometer Specord 50. The corresponding spectrum is shown in figure 1. The presence of localized surface plasmon

peak at ~410 nm (marked with the arrow) confirmed the formation of silver NPs in poled glasses after the ion exchange. Mechanical removal of subanode layer of the glass and cleaning of the cathode surface of slide did not remove this peak, which indicated that the NPs are in the subcathode region of the glass. This allowed us to assume that poling with structured cathode electrode would result in formation of 2D patterns from silver NPs.

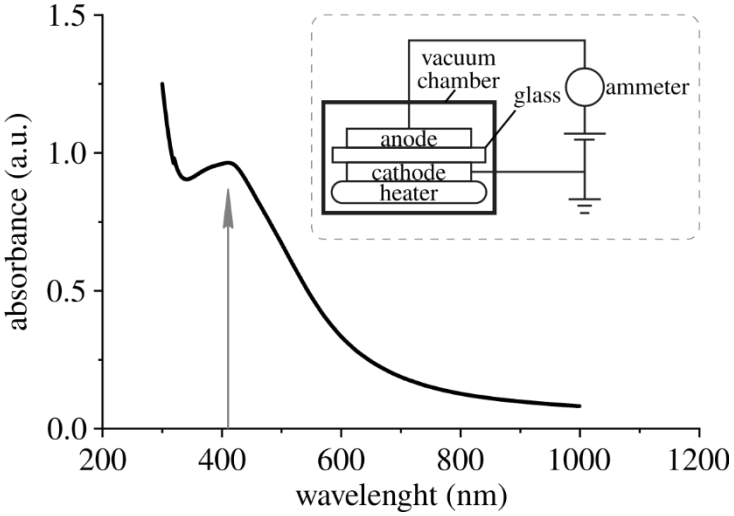


Fig. 1. Optical absorption spectrum of soda-lime glass after vacuum thermal poling and silver-for-sodium ion exchange. The inset schematically shows the setup used for poling

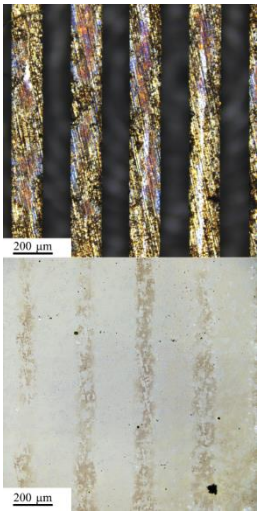


Fig. 2. Photos of the cathode electrode (top) and its replica formed by silver NPs in the subcathode layer of a sample (bottom)

The result of poling experiment with a bronze grid pressed to the glass slide used as cathode electrode is shown in figure 2. One can see that the dark strips, which corresponds to the glass with silver NPs, replicates the structure of the cathode electrode.

Finally, the results of performed studies allows concluding that the technique described presents a novel approach to create 2D-structured glass metal composites without using thermal treatment in reducing atmosphere.

REFERENCES

1. **Lepienski C. M., Giacometti J. A., Ferreira G. L., Freire Jr F. L., Achete C. A.**, Electric field disctribution and near-surface modifications in soda-lime glass submitted to a dc potential, Journal of Non-Crystalline Solids. 159 (3) (1993) 204–212.

2. **An H., Fleming S.,** Second-order optical nonlinearity and accompanying near-surface structural modifications in thermally poled soda-lime silicate glasses, JOSA B. 23 (11) (2006) 2303–2309.

3. **Ziemath E. C., Araujo V. D., Escanhoela C. A.,** Compositional and structural changes at the anodic surface of thermally poled soda-lime float glass, Journal of Applied Physics. 104 (5) (2008).

4. **Doremus R. H.,** Mechanism of electrical polarization of silica glass, Applied Physics Letters. 87 (23) (2005) 1-2.

5. **Babich E., Reduto I., Redkov A., Reshetov I., Zhurikhina V, Lipovskii A.,** Thermal poling of glasses to fabricate masks for ion exchange, Journal of Physics: Conference Series. 1695 (1) (2020) 012107.

6. **Brunkov P. N., Lipovskii A. A., Melehin V. G., Red'kov A. V., Statsenko V. V.,** Formation of silver fractal structures in ion-exchange under poling, Technical Physics. 60 (2015) 270-274.

Study of the fluorescent properties of boron nitride quantum dots depending on functionalizing ligands

E. A. Sidorov ✉, **E. D. Gribova**, **G. A. Bondarenko**, **P. P. Gladyshev**
Dubna State University, Dubna, Russia
✉ siea.18@uni-dubna.ru

Abstract. Boron nitride quantum dots (BNQDs) are promising agents for the creation of drugs for boron neutron capture therapy. However, studies of the dependence of optical properties on the conditions of their synthesis are at an early stage. In this work, a study was carried out of the effect of BNQD functionalization with urea, thiourea, L-cysteine, and phenylenediamine on their fluorescent properties. It is shown that when N-methyl-2-pyrrolidone is used as a solvent for the synthesis of boron nitride quantum dots by exfoliation of bulk boron nitride powder followed by solvothermal treatment with the addition of various amino-containing ligands, it is possible to tune the fluorescence of boron nitride quantum dots in the range from 404 to 545 nm.

Keywords: Quantum dots, boron nitride, photoluminescence

Introduction

Over the past few years, BNQDs have attracted increasing attention due to their unique combination of properties found in QDs: chemical stability, biocompatibility, low cytotoxicity, and tunable optical properties. BNQDs are promising candidates for boron neutron capture therapy due to their high boron content and the possibility of simultaneous fluorescent visualization of therapeutic agent delivery. The optical properties of BNQDs are determined by the synergistic effect of their size, number of layers, the presence of various edge and plane defects, and the nature of edge functional groups [1]. The dependence of the optical properties of BNQDs on their synthesis parameters has not yet been fully investigated. For biomedical applications of the fluorescent properties of BNQDs, it is necessary that the fluorescence band be in the near-infrared region of the spectrum. However, currently, most BNQD samples described in the literature are characterized by blue and green fluorescence. This necessitates the determination of the synthesis conditions that affect the position of the fluorescence band. This work is devoted to the study of the dependence of the fluorescent properties of BNQDs on functionalization with nitrogen-containing ligands.

Materials and Methods

Hexagonal boron nitride (technical grade, LenReaktiv, Russia); ethanol (≥99.5%, J.T. Baker, USA); N-methyl-2-pyrrolidone, NMP (reagent grade, LenReaktiv, Russia); urea (analytical grade, LenReaktiv, Russia); thiourea (≥99.0%, Sigma-Aldrich, USA), L-cysteine (≥98%, Sigma-Aldrich, USA); p-Phenylenediamine (98%, CDH, India); o-Phenylenediamine (99.5%, Sigma-Aldrich, USA); syringe filters (0.22 μm pore size, Millipore, USA); CM2203 spectrofluorometer (Solar, Belarus); Eppendorf 5425 microcentrifuge (Eppendorf, Germany); CAUX-120 analytical balance (CAS, South Korea).

Results and Discussion

By functionalizing BNQDs with various ligands, it is possible to fine-tune their band structure. In this work, BNQDs were synthesized "top-down" by ultrasonic treatment of bulk boron nitride powder in N-methyl-2-pyrrolidone (NMP) and subsequent solvothermal treatment at 200 °C. Urea, thiourea, L-cysteine, o-phenylenediamine (o-PDA), and p-phenylenediamine (p-PDA) were used as amino ligands. The optical properties of the BNQDs were investigated using electronic and fluorescence spectroscopy. The fluorescence properties of BNQDs were studied at different excitation wavelengths (280–460 nm) with a 20 nm step. The color map in the excitation–emission coordinates is presented as a figure, where the fluorescence wavelength is plotted on the abscissa axis and the excitation wavelength is plotted on the ordinate axis.

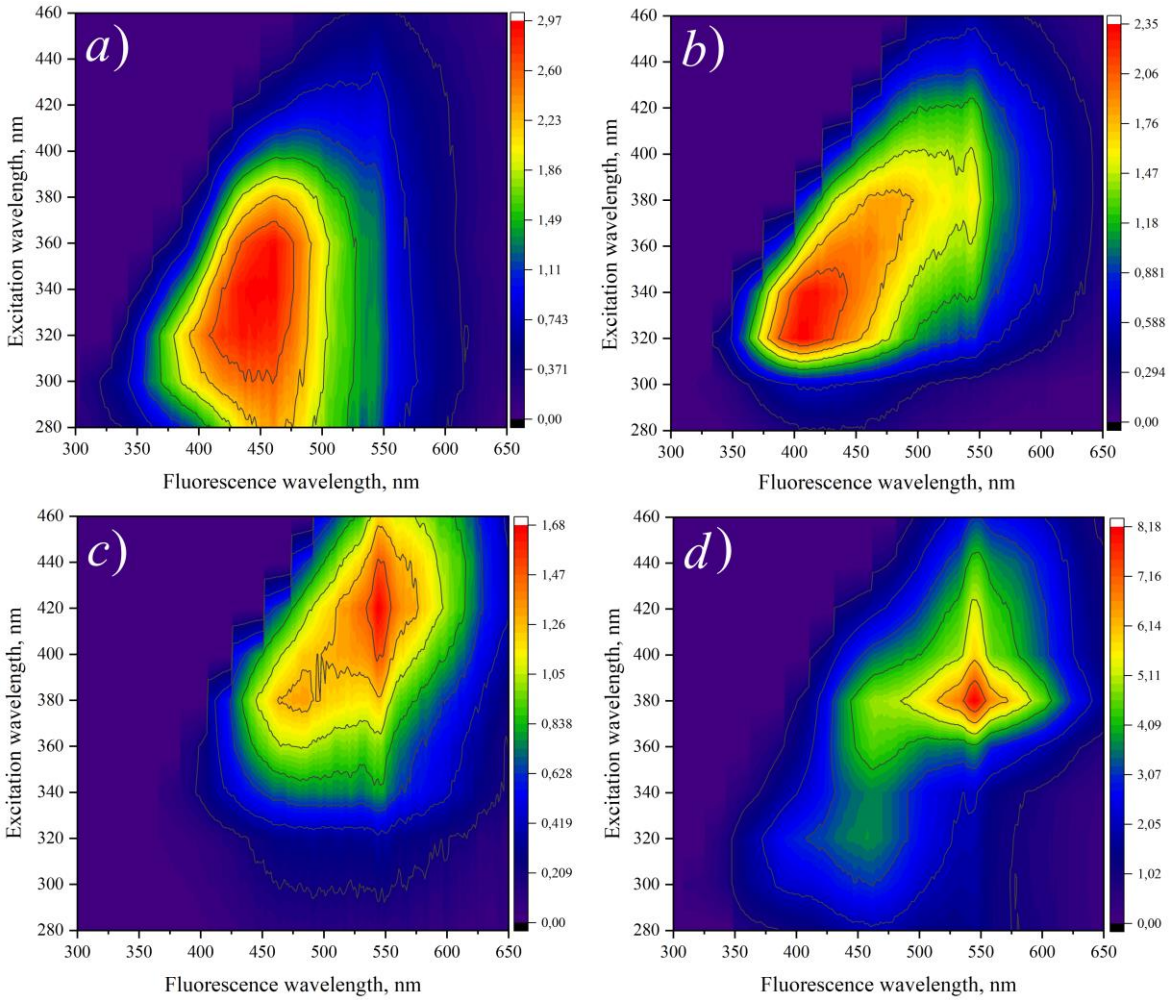


Fig. 1. Color map of the dependence of BNQD fluorescence on excitation wavelength: a) NMP, b) NMP/Urea, c) NMP/Thiourea, d) NMP/o-PDA

Analyzing the obtained spectra, we can conclude that the addition of nitrogen-containing compounds to the reaction mixture shifts the maximum of the fluorescence peak to the red region of the spectrum (in the case of functionalization with thiourea, o-PDA, and p-PDA) and to the blue region of the spectrum in the case of functionalization with urea. The dependences obtained are most likely related to the influence of nitrogen-containing ligands on the electronic configurations, density of states, orbital localization, and bandgap of BNQDs [2].

Conclusion

By functionalizing BNQDs with various nitrogen-containing ligands, it is possible to tune the optical properties of BNQDs. However, the fluorescent properties of the obtained BNQDs do not currently allow them to be used for in vivo fluorescent visualization of cancer cells. However, they can be used to create agents for boron neutron capture therapy in combination with carbon dots. In addition, it is possible to use BNQDs as fluorescent markers of cancer cells in vitro. For the further development of this area, it is necessary to shift the maximum of the fluorescence band to the near-infrared region.

REFERENCES

1. **Rawat J., Sajwan, D., Garimella S. V., Sharma H., Dwivedi, C.**, Boron Nitride quantum dots: A rising star in sensing applications, Nano Trends. 2 (2023) 100008.

2. **Cui P., Wu Q., Zhiwei, L.**, Exploring the dual capabilities of BNQDs: a comprehensive study on enhancing photoelectric performance and photoluminescence via ligand functionalization, J Mol Model. 30 (1) (2023) 6.

Gas sensing properties of TiO_2-SnO_2 nanocrystalline thin films for NO_2 sensing

A.P. Starnikova[1]✉, M.G. Volkova[1,2], E. M. Bayan[2], V. V. Petrov[1]

[1]Institute of Nanotechnologies, Electronics, and Equipment Engineering, Southern Federal University, Taganrog, 347922, Russia;

[2] Department of Chemistry, Southern Federal University, Rostov-on-Don, Russia

✉starnikova@sfedu.ru

Abstract. TiO_2-SnO_2 nanocrystalline thin films containing 1, 5 or 50 mol.% TiO_2 were synthesized by low-temperature oxidative solid-phase pyrolysis. Gas sensing properties were measured by exposure of 50 ppm nitrogen dioxide at an operating temperature 250 °C. It was shown that the maximum response (245) is characteristic of a material containing 1 mol. % TiO_2. The same material remains sensitive to gas even at 50 °C.

Keywords: Thin films, nanomaterials, gas-sensitive properties, tin dioxide, titanium dioxide.

Funding: This study was funded by the Russian Science Foundation grant number 24-29-00203, https://rscf.ru/en/project/24-29-00203/.

Introduction

Tin dioxide is one of the most popular wide-gap n-type oxide semiconductors today. The combination of relative cheapness, chemical stability and safety allows ony to use this material in various devices, including gas-sensitive sensors. The creation of composite nanomaterials based on SnO_2 with other oxides with a similar type of conductivity leads to an improvement in the gas response of sensors and a reduction in the response/recovery time due to a combination of defects in the structure. Titanium dioxide is one of the most promising oxides for improving gas-sensitive properties [1]. For example, for a two-layer TiO_2/SnO_2 material, a response of 7.54 to 50 ppm ethanol at an operating temperature of 260 °C was shown, and the response/recovery time was 33/298 s [2]. The authors have shown that an increase in the number of layers leads to a decrease in the positive effect of heterojunctions and oxygen adsorption and, as a consequence, to a deterioration in the gas-sensitive properties of the composite.

The authors found that amorphous SnO_2 films exhibit a response of 500 to exposure of 20 ppm NO_2 at an operating temperature of 210 °C [3]. The deposition of TiO_2 on these films leads to an increase in the response by more than three times (1650), which may be due to the transition of electrons from TiO_2 to SnO_2 due to the formation of an n-n heterojunction.

The aim of this work was to study the gas-sensitive properties of nanosized thin film TiO_2-SnO_2 materials synthesized by oxidative solid-phase pyrolysis.

Materials and Methods

The TiO_2-SnO_2 nanocrystalline thin films were synthesized by low-temperature pyrolysis according to a previously described procedure [4]. The amount of titanium dioxide introduced was 1, 5 and 50 mol. %: materials $1TiO_2$-$99SnO_2$, $5TiO_2$-$95SnO_2$ and $50TiO_2$-$50SnO_2$, respectively.

The gas-sensitive characteristics of TiO_2-SnO_2 films to exposure of nitrogen dioxide (NO_2), as well as zinc oxide nanostructures, were studied using an installation for studying the electrical properties of gas sensors [5] using a dynamic installation "Microgas-F".

Results and Discussion

According to X-ray diffraction analysis, all materials have a cassiterite structure, as expected for materials based on tin dioxide. The smallest particle size was observed for the $50TiO_2$-$50SnO_2$ material, which may be due to the highest concentration of defects due to the introduction of a large amount of titanium dioxide.

Figure 1 shows the responses of $1TiO_2$-$99SnO_2$, $5TiO_2$-$95SnO_2$ and $50TiO_2$-$50SnO_2$ films formed by oxidative pyrolysis technology at a temperature of 250 °C to 50 ppm of NO_2.

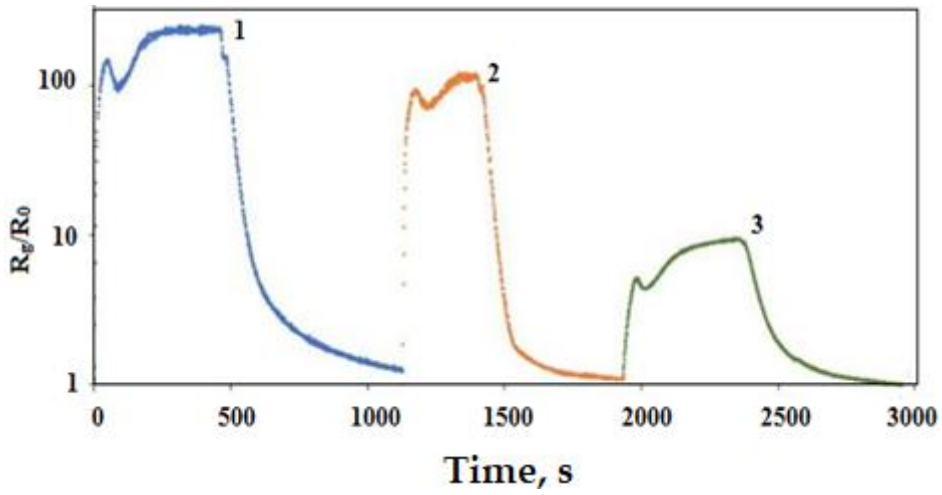


Fig.1. Responses of film samples $1TiO_2$-$99SnO_2$ (1), $5TiO_2$-$95SnO_2$ (2) и $50TiO_2$-$50SnO_2$ (3).

A study of the gas response (S) dependence of nanocrystalline TiO_2-SnO_2 thin films at an operating temperature of 250 °C showed that the maximum value is observed for the material with a minimum content of titanium dioxide (1 mol. %) and is equal to 245. For the material $5TiO_2$-$95SnO_2$ the value of S is almost two times less (107) for the same gas concentration. Studies have also shown that a sensor based on $1TiO_2$-$99SnO_2$ film is sensitive to 5 ppm NO_2 at 50 °C (S = 2), while sensors based on $5TiO_2$-$95SnO_2$ and $50TiO_2$-$50SnO_2$ films ceased to show sensitivity below 150 and 250 °C, respectively. Low operating temperatures of gas sensors are essential for stable operation of gas sensors.

Conclusion

A study of the gas-sensitive properties of nanocrystalline TiO_2-SnO_2 thin films showed that all films have response to 50 ppm NO_2, and with increasing TiO_2 concentration in the film, the gas-sensitive properties deteriorate. The highest gas response at low operating temperatures is shown for the $1TiO_2$-$99SnO_2$ material, which allows us to recommend small amounts of titanium dioxide as an additive to improve the film materials properties based on tin dioxide.

REFERENCES

1. **Kumar V., Gautam Y. K., Gautam D., Kumar A., Adalati R., Singh B. P.,** Highly sensitive and selective hydrogen gas sensor with humidity tolerance using Pd-capped SnO_2 thin films of various thicknesses, Fuels. 4(3) (2023) 279-294.

2. **Tian X., Hu Z., Wang T., Wang H., Zhang Q., Wei X.,** Influence of multi-layer TiO_2/SnO_2 heterojunctions on fast and sensitive ethanol detection, Vacuum. 207 (2023) 111620.

3. **Nowak P., Maziarz W., Rydosz A., Kowalski K., Ziąbka M., Zakrzewska K.** SnO_2/TiO_2 thin film n-n heterostructures of improved sensitivity to NO_2, Sensors. 20(23) (2020) 6830.

4. **Gulyaeva I. A., Ivanishcheva A. P., Volkova M. G., Bayan E. M.**, Surface and electrophysical properties study of thin TiO_2-SnO_2 nanocomposite films, St. Petersburg State Polytechnical University Journal: Physics and Mathematics. 15(S3.3) (2022) 265-270.

5. **Gulyaeva I.A., Ivanisheva A.P., Volkova M.G., Storozhenko, V.Yu., Khubezhov S.A., Bayan E.M., Petrov V.V.**, Investigation of electrophysical, photo- and gas-sensitive properties of ZnO–SnO_2 sol–gel films, Journal of Advanced Dielectrics. 14, 1 (2024) 2245002.

Study of the electrical properties of ZnO nanorods under the influence of controlled intensity UV radiation

A. P. Starnikova[1]✉, **K.V. Kolomytsev**[1], **V. V. Petrov** [1]

[1] Institute of Nanotechnologies, Electronics, and Equipment Engineering, Southern Federal University, Taganrog, Russia

✉a.starnikova@mail.ru

Abstract. Arrays of zinc oxide (ZnO) nanorods were synthesized on quartz substrates by a hydrothermal method. The nanorods were grown in a predominantly vertical orientation and had a length of 500–800 nm and an average cross-sectional size of 40–80 nm. Tin nanoclusters with average sizes of 30 ± 5 nm and 15 ± 3 nm were formed on top of ZnO nanorods. Annealing was carried out at 300 °C for 2 h to form ZnO/SnO_2 nanorod arrays. To fabricate resistive sensor elements, V/Ni contact metallization was applied on top of the samples. A study of the electrical characteristics of ZnO/SnO_2 nanorod arrays showed that exposure to UV radiation of different intensities leads to a change in the electrical resistance of the sensor structure and affects the settling time of the readings of the obtained samples.

Keywords: ZnO, nanorods, electrophysical properties, ultraviolet irradiation.

Funding: This study was supported by the Russian Science Foundation under grant [No. 23-29-00742, [https://rscf.ru/en/project/23-29-00742/] at the Southern Federal University.

Introduction

Zinc oxide (ZnO) is a promising metal oxide that is widely used as a sensing layer in chemiresistive sensors [1]. One of the ways to increase the selectivity of semiconductor oxides is to modify their surface with nanoparticles of metal oxides, for example SnO_2. It is known that when gas-sensitive materials are exposed to UV radiation, the greater the radiation intensity, the higher the response obtained [2]. Studies of the electrical characteristics of ZnO/SnO_2 nanorod arrays when exposed to UV radiation with controlled intensity in the range from 55 to 133 μW/cm^2 have not yet been carried out. These studies are the purpose of this work.

Materials and Methods

Arrays of ZnO nanorods with vertical orientation were synthesized by hydrothermal method on quartz substrates. The nanorods had a length of 500–800 nm and an average cross-sectional size of 40–80 nm. Tin nanoclusters with average sizes of 30 ± 5 nm (ZnO/SnO_2(1) sample) and 15 ± 3 nm (ZnO/SnO_2(2) sample) were formed on top of ZnO nanorods using vacuum thermal evaporation. For the final formation and stabilization of the electrical characteristics of ZnO/SnO_2 nanostructures, annealing was carried out at a temperature of 300°C for 2 hours [3]. Next, to produce sensor elements, V/Ni contact metallization with a metal layer thickness of 0.2 μm was formed on top of the nanorods using thermal vacuum evaporation.

Results and Discussion

Studies of the electrical properties of the obtained samples were carried out using a hardware-software measuring complex, which makes it possible to measure the electrical characteristics of sensor structures, including when exposed to UV radiation [4]. Previously, we estimated the photoconductivity relaxation time constant (τ) when exposed to UV radiation with a wavelength of 400 nm and a radiation intensity of 133 μW/cm^2 [3]. The time constants had similar values for the ZnO/SnO_2(1) and ZnO/SnO_2(2) samples and ranged from 8 to 12 s. Large values of τ correspond to large values of Ea and φb. This indicates the influence of the activation energy of conductivity and the potential barrier of the ZnO nanostructure on the mechanism of current transfer. The results also indicate that after turning on the UV radiation, it is necessary to wait more than 3 minutes for the resistance of the gas sensor to stabilize.

In this work, additional studies were carried out in which the samples were irradiated with UV radiation from a LED with a wavelength of 400 nm with an adjustable radiation intensity from

55 to 133 μW/cm^2. Figure 1 shows the dependences of the resistance (R) of the samples under study on the time of exposure to UV radiation of different intensities.

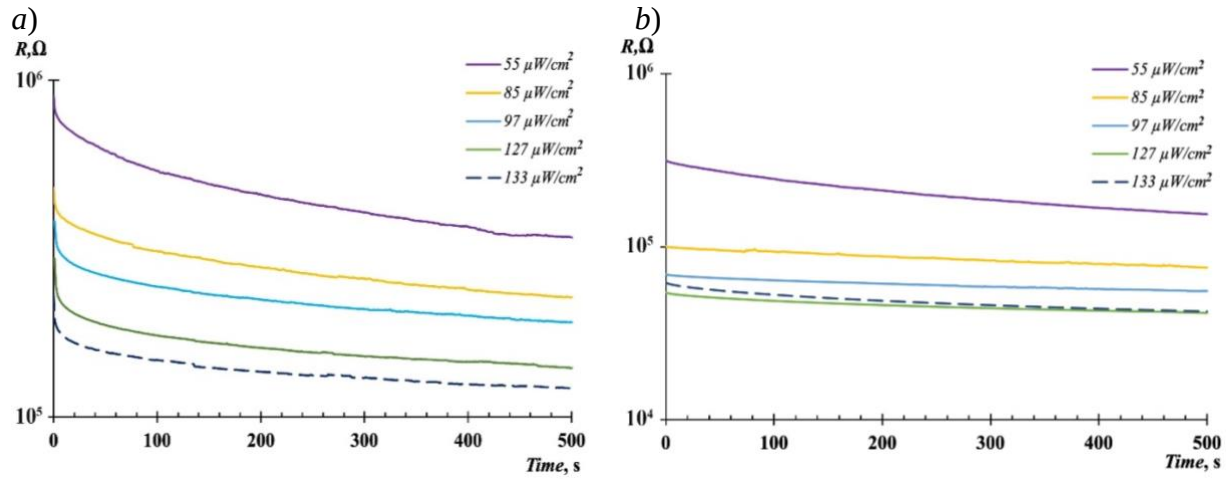


Fig. 1. Dependence of the resistance of samples ZnO/SnO_2(1) (a) and ZnO/SnO_2(2) (b) on the time of exposure to UV radiation with adjustable intensity from 55 to 133 μW/cm^2

Research has shown that when samples are exposed to UV radiation, their resistance drops due to the generation of photoexcited charge carriers. This leads to an activated state of the surface due to a sharp increase in the concentration of free electrons. The photoresponse time was assessed based on the time it took to reach 90% of the maximum signal value. The photoresponse time for the ZnO/SnO_2(1) sample when exposed to UV radiation with intensities ranging from 55, 85, 97, 127 and 133 μW/cm^2 was 390, 325, 290, 333 and 321 s, respectively, and for the ZnO/SnO_2(2) was 394, 446, 430, 359 and 388 s, respectively. Thus, the establishment of equilibrium between the generation of charge carriers by UV radiation and their recombination occurs faster in a sample with large tin nanoclusters.

Conclusion

The work shows that an increase in the intensity of UV radiation from 55 to 133 μW/cm^2 causes a decrease in the resistance of the samples under study. In addition, the ZnO/SnO_2(1) sample with an average tin nanocluster size of 30 ± 5 nm has a shorter photoresponse time.

Acknowledgments

Electrophysics measurements were conducted using equipment from the Research Center for Microsystem Engineering and Multisensory Monitoring Systems, Southern Federal University (SFedU).

REFERENCES

1. **Que M., Lin C., Sun J., Chen L., Sun X., Sun Y.** Progress in ZnO nanosensors. Sensors (2021) 21(16) 5502.

2. **Chinh Nguyen Duc, Hien Truong Thi, Do Van Lam, Hieu Nguyen Minh, Quang Nguyen Duc, Lee Seung-Mo, Kim Chunjoong, Kim Dojin.** Adsorption/desorption kinetics of nitric oxide on zinc oxide nano film sensor enhanced by light irradiation and gold-nanoparticles decoration. Sens. Actuators B Chem. (2019) 281, 262–272.

3. **Ivanisheva A.P., Sysoev V.V., Abdullin Kh.A., Nesterenko A.V., Khubezhov S.A., Petrov V.V.**, The Application of Combined Visible and Ultraviolet Irradiation to Improve the Functional Characteristics of Gas Sensors Based on ZnO/SnO_2 and ZnO/Au Nanorods. Chemosensory 11(3) (2023) 200.

4**. Gulyaeva I.A., Ivanisheva A.P., Volkova M.G., Storozhenko, V.Yu., Khubezhov S.A., Bayan E.M., Petrov V.V.**, Investigation of electrophysical, photo- and gas-sensitive properties of $ZnO–SnO_2$ sol–gel films J. Adv. Dielect. 14, 1 (2024) 2245002.

The effect of the rate of temperature change on the thermomigration of liquid inclusions in silicon

B. M. Seredin[1], **V. P. Popov**[1], **A. V. Malibashev**[1], **A. D. Stepchenko**[1]✉

[1] Platov South-Russian State Polytechnic University (NPI), Novocherkassk, Russia;

✉Stepchenko.A.D@yandex.ru

Abstract. The influence of the rate of temperature change of the composition on the consistency of the processes of dissolution, crystallization and atomic transfer in a liquid inclusion and at its boundaries, characteristic of stationary conditions of thermomigration, is theoretically estimated. Using the example of the silicon-aluminum system, the influence of a stepwise and smooth monotonic temperature change on the processes determining thermal migration and the velocity of movement of the liquid inclusion is established. A critical rate of temperature change has been found, above which thermomigration becomes impossible.

Keywords: thermomigration, silicon, crystallization, dissolution.

Funding: The work was carried out with the support of the Ministry of Education and Science of the Russian Federation within the framework of the state assignment to the M.I. Platov South Russian State Polytechnic University (NPI) under the FENN-2023-0005 program.

Introduction

Thermomigration (TM) of liquid inclusions (zones) under the influence of a temperature gradient is used in physico-chemical studies and for the formation of electrically heterogeneous structures in the volume of a silicon wafer [1]. The TM process is carried out at a sufficiently high temperature, significantly exceeding the temperature of formation of the zone. The heating or cooling time of the composition is commensurate with the time of the stationary migration mode. At the same time, the temperature change causes supersaturation (or undersaturation) of the melt solution and is an additional driving force, the effect of which on TM has not been previously studied. The rate of temperature change can affect the self-consistent processes of dissolution, crystallization and atomic transfer in the zone, which determine the velocity and shape of the liquid zone. The aim of the work is to theoretically assess this effect using the example of the silicon-aluminum system.

Results and discussion

In stationary conditions, with constant heater power, the temperature in the zone increases as a result of its migration at a constant rate υ in the direction of the temperature gradient G. The temperature change in the composition while maintaining the temperature gradient can also be caused by controlling the heater power, which leads to a violation of the consistency of these three processes in the zone necessary for TM. This is due to the fact that the temperature change occurs faster than the diffusion determination of the concentration of components in the zone. The estimation of the recovery time τ of the concentration profile with an abrupt (stepwise) temperature change was performed using computer simulation of the process. The value τ did not depend on the temperature jump and increased sharply with an increase in the thickness of the zone ℓ in the direction of movement and with a decrease in temperature T, relative to which the temperature jump was made. For typical parameters ℓ, equal to 0.05 and 0.1 mm, and temperatures T, equal to 1423 and 1373 K, the value τ was 0.25 and 1 s, respectively. During this time, the zone stops, and then continues to migrate at a constant rate corresponding to the new temperature value.

A change in the temperature of the composition affects the atomic-kinetic processes of dissolution or crystallization at the boundaries of the zone. An increase in temperature slows down or blocks crystallization at the "cold" boundary of the zone and promotes dissolution at the "hot" boundary, while a decrease in temperature hinders or blocks dissolution at the "hot" boundary and promotes crystallization at the "cold" boundary.

We find the critical rate of a smooth monotonous temperature change a_{cr} in the composition, based on the equality of the thicknesses of the layers grown due to thermomigration h_G, and h_T cooling (or heating) of the zone in a short period of time Δt: $h_G = \upsilon\, \Delta t$ and $h_T = \Delta C\, \ell$ Here ΔC is the change in the concentration of silicon in the zone when the temperature changes by ΔT during Δt: $\Delta C = \frac{dC}{dT}\Delta T$, where dC/dT is the cotangent of the angle of inclination of the liquidus line on the phase diagram of the system state, $\Delta T = a_{cr}\, \Delta t$. The change in the volume of silicon during the phase transition is neglected. Equating h_G and h_T, we obtain the formula for the critical rate of temperature change: $a_{cr} = \upsilon \Big/ \left(\frac{dC}{dT}\Delta T \right)$. The numerical value of a_{cr} for typical process conditions was ~ 1 K/s. If the actual rate of temperature change ($a > a_{cr}$), then the movement of the zone is impossible due to the blocking of one of the two processes at the boundaries of the zone, depending on the heating or cooling of the composition. At $a < a_{cr}$, the velocity of movement of the zone can both decrease and increase. The decrease of υ corresponds to the same difficulty of crystallization and dissolution processes. Dissolution is more difficult for the Si-Al system [1], which leads to deformation (compression) of the local zone in the direction of movement. Taking into account the additional driving force and adjusting the heating rate during the TM process, it is possible to weaken the restrictions at the dissolution boundary, while maintaining an acceptable crystallization rate. In this case, an increase in velocity and a decrease in the degree of deformation of the zone are achievable.

Conclusion

Thus, a stepwise change in the temperature of the composition suspends the movement of the zone for a short time, and with a smooth monotonous change in temperature, the velocity of movement of the zone can both decrease and increase at heating (or cooling) rates lower than the found critical value. When the temperature change rates exceed the critical one, the movement of the zone becomes impossible. In the region of velocities lower than the critical one, temperature changes can control the deformation of the local zone during its migration.

REFERENCES

1. **Lozovskij V. N., Lunin L. S., Popov V. P.** Zonnaya perekristallizaciya gradientom temperatury poluprovodnikovyh materialov / Moskva : Metallurgiya, 1987.

The features of Mg_2Si growth by ultra-fast reactive epitaxy on porous Si(100) surface

Subbotin E. Yu.[1], Kozlov A. G.[2], Goroshko D. L.[1], Chernev I. M.[1], Khoroshilov D. A.[1], Zhizhchenko A. Yu.[1], Goroshko O. A.[1], Gouralnik A.S.[1], Galkin N. G.[1]

[1] Institute of Automation and Control Processes, FEB RAS, Vladivostok, Russia;

[2] Far Eastern Federal University, Vladivostok, Russia.

✉subbotineu@iacp.dvo.ru, jons712@mail.ru

Abstract. In the paper growth features of magnesium silicide (Mg_2Si) on porous silicon substrate were considered. The silicon substrate was treated by the well-known metal-assisted chemical etching (MACE). At the work optimal regimes of applying the lithography patterns, depositing catalytic metal (Ti/Au) and etching were selected. Applying patterns were carried out by high-resolution electron lithography. The growth of Mg_2Si film was conducted by ultrafast reactive epitaxy at 340 °C with following annealing in Ar atmosphere at 500 °C. As the result, the ~370 nm Mg_2Si film was synthesized on porous substrate. It was revealed that porosity of silicon substrate allows to "tune" volume ratio of 3D-defects in the Mg_2Si film.

Keywords: silicon, magnesium silicide, epitaxy, MACE, lithography, μTEG, SEM, FIR.

Fundings: This study was supported by the Russian Science Foundation, grant No. 23-72-01128.

Introduction

Recently, the research and development of micro-thermoelectric converters (μTEC) are the key focus for many scientists [1]. The important feature of such converters is high density (10^6 cm^{-2}) of micrometer size thermocouple that allows to generate a sufficient voltage at a low temperature gradient with a quick responsible.

The anisotropic MACE combined with the high-resolution lithography able to produce the ordered high-density array of semiconductor structures with a desired lateral size and an aspect ratio [2]. The Mg_2Si was chosen due to its thermoelectric parameters [3], state of development, biological and environment compatibility of Mg and Si and relatively low cost of components. Also, by the reactive epitaxy on a chemically modified silicon surface a high-density array of nano- and microwires/-walls for the μTEC with vertically aligned thermocouples [1] and nano-/microroad for planar type ones [4] are produces. Firstly, the feature of the growth silicide on the chemical etched silicon surface should be considered. One of is the key artifacts such etching is high surface porosity that can effects on the diffusion and the intermixing processes.

Result and discussion

The applying the micrometer size mask with controllable parameters for the followed etching was carried out by the high-resolution electron lithography. As a catalytic metal was chosen Au 30 nm with 2 nm Ti as the adhesive layer. Etching was conducted in solution HF (4.6M), H_20_2 (0.44M) and deionized water. The result of such MACEing of the substrate is presented on Fig. 1a. For creating the high surface concentration porosity the p^+-Si(100) was chosen. The growth of Mg_2Si was carried out by ultrafast reactive epitaxy at 340 °C in ultra-high vacuum conditions [5] with following annealing in Ar atmosphere at 500 °C.

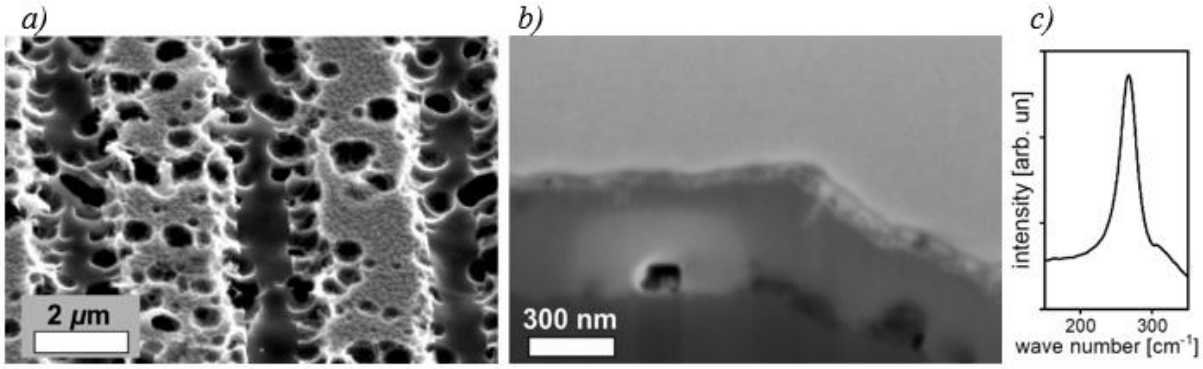


Figure 1. Scanning electron microscopy image of: a) the Si surface after etching, b) cross section the Mg_2Si film synthesized on the surface. C) Fourier-spectra with Mg_2Si peak at 267.1 cm^{-1}.

The 370 nm Mg_2Si film is presented on Fig. 1b. The peak at 267.1 cm^{-1} on Fourier-spectra indicate on successful siliciding (Fig. 1c). Some number of initial pores and inclusions are observed on the cross section (Fig. 1b). Important to note, the variating of the film thickness and the etching regime "tunes" the volume ratio of 3D-defects (e.g. pores) that is non-trivial task for a defect engineering in μTECs.

Conclusion

In the work the growth Mg_2Si film on porous silicon substrate was presented. The synthesis is carried out in ultra-high vacuum conditions at 340 °C by ultrafast reactive epitaxy, thickness of the film ~370 nm. Such porous morphology leads to the appearance 3D-defects on the film/substrate interface and provides additional opportunities for a defect engineering and thermoelectric properties optimizations.

Acknowledgement

The work was supported by the Russian Science Foundation, grant No. 23-72-01128.

REFERENCES

1. **Zhang Q., Deng K., Wilkens L., Reith H., Nielsch K.** Micro-thermoelectric devices //Nature Electronic 5 (6) (2022) 333–347.

2. **Shi, Z., Jefimovs, K., Stampanoni, M., Romano, L.** High aspect ratio arrays of Si nano-pillars using displacement Talbot lithography and gas-MacEtch //Material Science in Semiconductor Processing 157 (2023) 107311.

3. **Ning H., Mastrorillo G.D., Grasso S., Du B., Mori T., Hu C., Xu Y., Simpson K., Maizza G., Reece M.J.** Enhanced thermoelectric performance of porous magnesium tin silicide prepared using pressure-less spark plasma sintering //Journal of Material Chemistry A. 3 (33) (2015) 17426–17432.

4. **Ohkubo I., Murata M., Lima M., Sakurai T., Sugai Y., Ohi A., Aizawa T., Mori T.** Miniaturized in-plane π-type thermoelectric device composed of a II–IV semiconductor thin film prepared by microfabrication //Material Today Energy 28 (2022) 101075.

5. **Chernev, I. M., Subbotin, E. Y., Kozlov, A. G., Gerasimenko, A. V., Ustinov, A. Y., Galkin, N. G., Poliakov M. V., Volkova L. S., Dudin A. A., Gouralnik, A. S.** // Thick p-type Mg2Si film on Si: Growth, structure and transport properties. Journal of Alloys and Compounds 964 (2023) 171301.

Creation of portable sensors based on quantum dots of different composition for determination of heavy metal ions

N. N. Troshkina ✉, E. A. Alekseeva, S. A. Novikova, E.D. Gribova
Dubna State University, Dubna, Russia
✉tnn.18@uni-dubna.ru

Abstract. To realize fast detection of metal ions in real time, within the framework of the work, capillary and paper sensors based on quantum dots synthesized in aqueous medium, composition CdTe/CdS/ZnS with different organic ligands on the surface were created. The study of stabilizing coatings of quantum dots for the identification of certain heavy metal ions as well as the requirements for them has been carried out. The analysis of physicochemical properties of quantum dots showed selectivity of the selected stabilizers to some metal ions, due to which it was possible to create simple and selective sensors.

Keywords: quantum dots, nanoparticles, metal ions, multiplexed determination, fluorometry, fluorescence quenching.

Introduction

Heavy metal pollution is a serious threat to the ecological environment and human health. Thus, it is necessary to achieve a fast, selective, sensitive, and portable instrument for the detection of heavy metal ions. To overcome the disadvantages of conventional methods such as labor intensive, low sensitivity, high cost and difficult to operate, quantum dot (QD) based nanomaterials are used in the sensors, which significantly improve the sensor performance. Due to their excellent physicochemical properties, high specific surface area, high adsorption and reactivity, nanomaterials can act as probes or provide enhanced sensitivity.

For QDs, which are used to create sensors for metal ions, there are many requirements for their shape, size, emission color, and position of the absorption band. The main criteria are the hydrophilicity of the nanoparticle surface for the determination of substances in an aquatic environment. There are two most common approaches to the synthesis of QDs: organometallic colloidal synthesis and aqueous colloidal synthesis. It is worth noting that QDs synthesized by aqueous colloidal synthesis have hydrophilic properties, making them suitable for use in many fields of application. In addition, the advantages of this method include relatively low synthesis temperatures, environmental friendliness, and cost-effectiveness of synthesis [1].

In sensors, signal detection is based on recording a change in one of the physical properties (optical, thermal, mechanical, magnetic, electrical) of the sensitive material caused by interaction with the analyte. Changing the optical properties of QDs, such as emission color, intensity, polarization, or emission kinetics, can be used as a principle in an optical sensing system. In addition, the resulting changes can be recorded directly by the human senses or indirectly through signal conversion, amplification, and visualization. All these factors determine the design of sensors and the mechanism of their action when detecting various substances [2].

To achieve sensor specificity, it is first necessary to modify the QD surface [3]. Ligands attached to the surface determine the possibility of conjugation of QDs with biological molecules (bioconjugation) or interaction with other analyzed particles [4]. There are various ways to achieve QD-based probe selectivity. Detection of ions using photoluminescent changes in QDs involves the use of several ligands such as derivatives of thioalkyl, mercaptoacetic or dihydrolipoic acids [5].

Results and Discussion

As part of the work, QDs were obtained in an aqueous medium of the composition CdTe/CdS/ZnS with various organic ligands on the surface, such as mercaptopropionic acid, thioglycolic acid, L-cysteine, glutathione. A study of stabilizing QD coatings was carried out to identify certain heavy metal ions, as well as requirements for them, and, based on the results, selective stabilizers for metals were identified, such as: Hg^{2+}, Cd^{2+}, Cu^{2+}, Ag^{+}, which can be used

to modify various QDs and create a universal sensor for determination of several metal ions simultaneously.

To realize rapid real-time detection of metal ions, capillary and paper sensors based on synthesized QDs with various stabilizers were developed, and after room temperature drying, calcination, and processing, the sensors achieved good response time and detection accuracy.

The detection of metal ion concentration of 1×10^{-5} M can be realized in 5-6 s. Moreover, the cost of the sensor is low, and the detection method is very simple. The sensor requires only 3 μL of solution for analysis, which not only saves the test solution, but also greatly improves the limits of the detection environment.

Conclusion

The results of the study revealed the influence of metal ions on the properties of QDs of different composition synthesised by aqueous colloidal method. In this connection portable sensors based on QDs were developed for determination of such heavy metals as: Hg^{2+}, Cd^{2+}, Cu^{2+}, Ag^{+}.

REFERENCES

1. **Novikova, S. A., Gribova, E. D., Andreev, E. V., Gladyshev, P. P., Kalganova, N. V., & Ibrahim, M. A.** (2019). Colloidal Synthesis and Characterization of Hydrophilic CdTe Quantum Dots for Medical Diagnostics. *Egyptian Journal of Chemistry*, *62*(The First International Conference on Molecular Modeling and Spectroscopy 19-22 February, 2019), 77-88.

2. **Lesiak, A., Drzozga, K., Cabaj, J., Bański, M., Malecha, K., & Podhorodecki, A.** (2019). Optical sensors based on II-VI quantum dots. *Nanomaterials*, *9*(2), 192.

3. **Gidwani, B., Sahu, V., Shukla, S. S., Pandey, R., Joshi, V., Jain, V. K., & Vyas, A.** (2021). Quantum dots: Prospectives, toxicity, advances and applications. *Journal of Drug Delivery Science and Technology*, *61*, 102308.

4. **Ramírez-Herrera, D. E., Reyes-Cruzaley, A. P., Dominguez, G., Paraguay-Delgado, F., Tirado-Guízar, A., & Pina-Luis, G.** (2019). CdTe quantum dots modified with cysteamine: a new efficient nanosensor for the determination of folic acid. *Sensors*, *19*(20), 4548.

5. **Yin, H., Truskewycz, A., & Cole, I. S.** (2020). Quantum dot (QD)-based probes for multiplexed determination of heavy metal ions. *Microchimica Acta*, *187*, 1-25.

Obtaining chiral metasurfaces from SiO_2 target by oblique angle deposition

I. S. Fattakhov✉, **O. S. Trushin, A.A.Popov, L.A. Mazaletsky**
Valiev Institute of Physics and Technology of Russian Academy of Sciences,
Yaroslavl Branch, Yaroslavl, Russia
✉33ychenikan@mail.ru

Abstract. Thin film growth by oblique angle deposition on Si and glass substrate from SiO_2 target is experimentally studied. Formation of regular arrays of vertical SiO_2 nanocolumns has been observed at incidence angles more than 80 degrees with rotation of substrate.Such films might be perspective material for applications as optical filter and circular polarizers.

Keywords: chiral metasurfaces, circular dichroism, oblique angle deposition

Funding: This work was carried out on the equipment of the centre for collective use of scientific equipment "Diagnostics of micro- and nanostructures" within the framework of the State assignment of the P.I. K.A. Valiev RAS Ministry of Education and Science of the Russian Federation on topic No. FFNN-2022-0018 "Fundamental and applied research in the field of creating promising instrument nanostructures for storing information on new physical principles."

Introduction

Oblique angle deposition allows controlled nanostructuring the surface [1, 2]. By setting certain parameters of the deposition during experiment, it is possible to obtain a metasurface consisting of nanocolumns or nanospirals. Controlling the direction of rotation, the spirals can be left- or righttwisted [3]. This causes the chiral properties when interacting with incident light.

Materials and Methods

Experiments on the deposition of thin films on an inclined substrate were carried out on an Oratoria-9 electron beam evaporation unit. The deposition conditions were as follows: base vacuum 4 10^{-6}Torr, electron beam – 4 kV, current 0.5 A. For SiO_2targetsubstrate was a single-crystal silicon wafer without oxide. During deposition substrate inclination angle was fixed at 75°. The rotation speed of substrate for SiO_2 target was 0.2 – 0.3 rpm. The growth rate of the film was equal to 1 nm/s.The surface morphology of deposited films was investigated by scanning electron microscopy (SEM) (Supra 40).

Results and Discussion

Cross-section of the film deposited at incidence angle 75º and rotation rate of 0.3 rpm is shown at Figure 1. To confirm the growth mechanisms of angle deposition [4] second sample was deposited without rotation and its cross section is shown at Figure 2. The spiral step is changing during experiment. This is related to different evaporation rates of the source at different point of the electron beam. To prevent this periodic electron beam oscillation was added to ensure uniform evaporation. Result cross-section of the deposited this way thin film is shown at Figure 3. Cross-section of sample without rotation is shown at Figure 4.

In summary, the results of experimental studies of the growth of thin films by oblique angle deposition with rotation of substrate were obtained to SiO_2 sources. Studies of optical properties of the films are currently in progress. Optical properties of these films allow to design optical filters and circular polarizers.

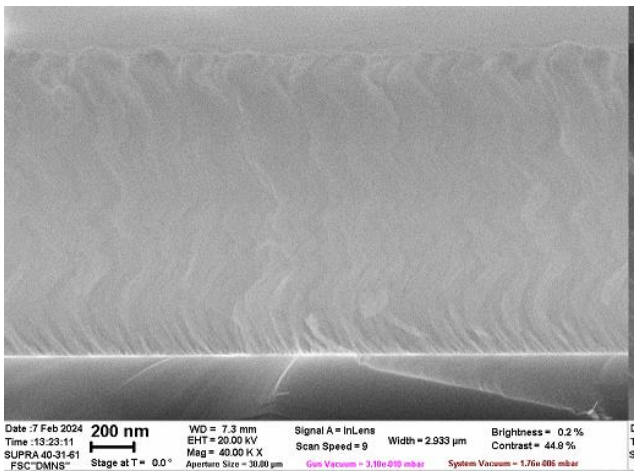


Fig. 1. Cross-section of the sample with rotation 0.3 rpm.

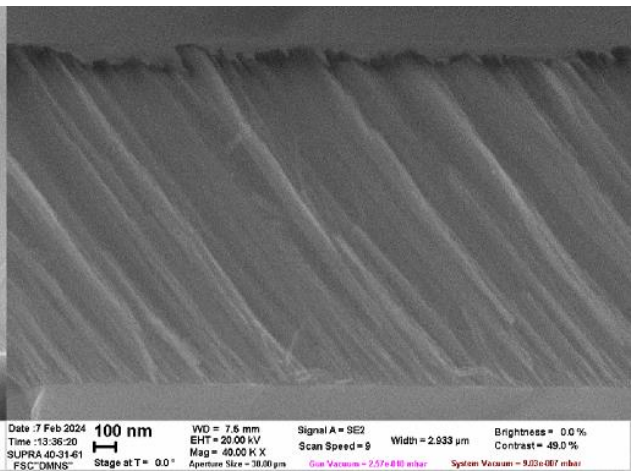


Fig. 2. Cross-section of the sample without rotation.

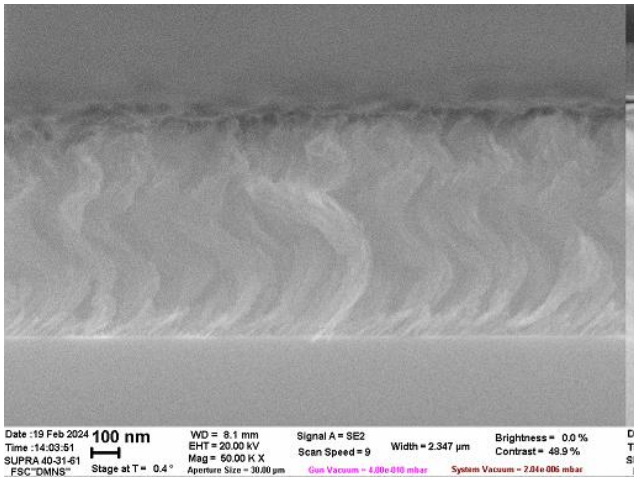


Fig. 3. Cross-section of rotating sample with beam oscillation.

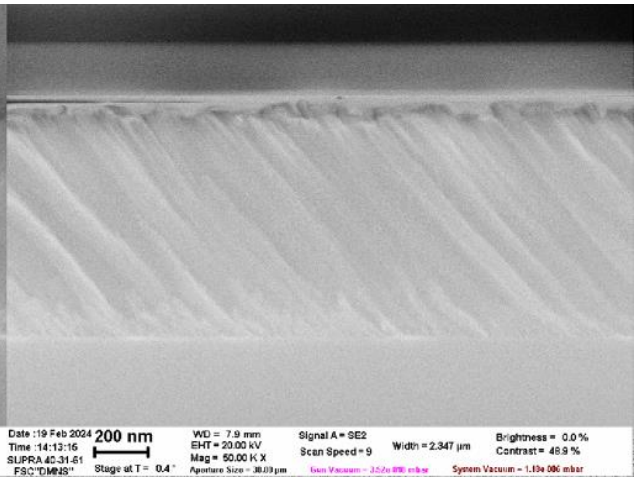


Fig. 4. Cross-section of static sample with beam oscillation.

REFERENCES

1.**Barranco A., Borras A., Gonzalez-Elipe A., Palmero A.,** Perspectives on oblique angle deposition of thin films: From fundamentals to devices, Progress in Materials science, 76, (2016), 59-153.

2. **Hawkeye M., Taschuk M., Brett M.,** Glancing Angle Deposition of Thin Films, UK: John Wiley & Sons Ltd, 2014, 1-299.

3. **Trushin O.S., Fattakhov I.S., Popov A.A., Mazaletsky L.A., Lomov A.A., Zakharov D.M., Gaidukasov R.A., Miakonkikh A.V., Shendrikova L.A.,** Tailoring magnetic anisotropy and optical characteristics of nanostructural Co Films by oblique angle deposition, Physics of the Solid State, 2023, 6, 953.

4.**Fattakhov I.S., Trushin O.S., Popov A.A., Mazaletsky L.A.,** The growth of nanostructured cobalt thin film at oblique angle deposition,St. Petersburg State Polytechnical University Journal. Physics and Mathematics, 2022, 15(3.3), 97-100.

5. **Liu F., Umlor M. T., Shen L., Weston J., Eads W., Barnard J., Mankey G.J.,** The growth of nanoscale structured iron films by glancing angle deposition, Journal of Applied Physics, 1999, 85, 5486.

E-beam resist AR-N 7520 in the formation of the photonic structures

K. A. Fetisenkova[1,2]✉, A.E. Melnikov [2], A.V. Miakonkikh[2], A.E. Rogozhin[2], A.A. Tatarintsev[2]

[1]Moscow Institute of Physics and Technology, Moscow, Russia;
[2] Valiev Institute of Physics and Technology of RAS, Moscow, Russia
✉fetisenkova.ka@phystech.edu

Abstract. The study of plasma resistance of the AR-N 7520 was carried out. The selectivity of the reactive ion etching (RIE) of silicon through the mask of negative electron resist AR-N7520 also was investigated. The dependence for selectivity was obtained at different fractions of SF_6 in the feeding gas and at the different values of bias voltage. A high etching selectivity of 8 ± 1.8 was obtained for the etching process. The dependence of the resist line height on the exposure dose is presented. The optimal value for the line exposure dose was found to be 8200 pC/cm.

Keywords: electron-beam lithography; etching kinetic; novolak; reactive-ion etching, waveguide

Funding: This study was supported by Program no. FFNN-2022-0021 of the Ministry of Science and Higher Education of Russia for Valiev Institute of Physics and Technology of RAS.

Introduction

The study of the e-beam resist properties, optimization of the electron beam lithography (EBL) parameters, and the etching process are important for nanoelectronics and photonics because the resolution of EBL is defined by the properties of e-beam resist and by processes during development and exposure [1-3].

The negative e-beam resist AR-N 7520 belongs to the novolaks and has high contrast and high plasma etching resistance [4, 5]. The study of EBL and RIE processes with AR-N 7520 will enable a technology for forming silicon waveguides and other photonic nanostructures with lower sidewall roughness and different aspect ratios.

Materials and Methods

A p-type silicon (100) wafers were pretreated in n-methylpyrrolidone and acetone. To promote adhesion, the silicon wafer was held in hexamethyldisilazane (HMDS) vapor at 85 °C for 10 minutes. The AR-N7520 with a concentration of 7.3% (PGMEA, 1-methoxy-2-propanol acetate) was spin-coated onto the surface using an SM-180 centrifuge (SAWATEC AG, Switzerland) at a centrifuge speed of 3000 rpm. The thickness of the resist layer was measured using a spectral ellipsometer M-2000X (J.A. Woollam Co., Inc., USA) and amounted to 100 ± 1nm. The exposure was carried out on a Raith-150 e-beam lithograph (Raith, Inc., USA) with the e-beam energy of 30 keV, the beam current was 150 pA. The pattern of lines of 1 mm in length was formed. The line exposure dose ranged from 4000 to 16000 pC/cm with a step of 200 pC/cm. Development was performed in 25% tetramethylammonium hydroxide (TMAH) solution for 50 s at 21°C.

RIE was performed on a Dual PlasmaLab 100 (Oxford Instruments Plasma Technology, UK) using an inductively coupled plasma (ICP) of the SF_6/C_4F_8 feeding gas. The wafers were segmented to obtain a set of samples with identical patterns of lines (60 lines per sample). Variation of the SF_6 fraction in feeding gas in the range of 15% – 25% was investigated at 125 V DC bias. The effect of DC bias voltage on the etching process was studied in the range of 80 V – 150 V at a constant fraction of SF_6 in feeding gas 22%. The etching process time was 30 s.

Images of the pattern of lines after etching and the thickness of the AR-N 7520 resist before and after the etching process, and the depth of silicon etching were obtained using a scanning electron microscope (SEM) Ultra 55 (Carl Zeiss AG, Germany).

The selectivity of the silicon RIE through the AR-N7520 mask was calculated as the ratio of the Si etching depth to the decrease in the height resist line during the etching process:

$$S = \frac{d_{Si}}{d_o - d} \quad (1)$$

where d_{Si} is the depth of silicon etching, d_0 is the height of the resist line before etching and d is the height of the resist line after etching. The etching rate was calculated as the ratio of the etching depth to the etching time for each line.

Results and Discussion

To optimize the silicon RIE through the AR-N 7520 mask influence of the SF_6 fraction in the feeding gas (15%, 18%, and 25%) was studied. Figure 1 shows the dependence of the silicon etching rate, resist etching rate, and selectivity for the RIE at different SF_6 fractions in the feeding gas and constant bias voltage of 125 V.

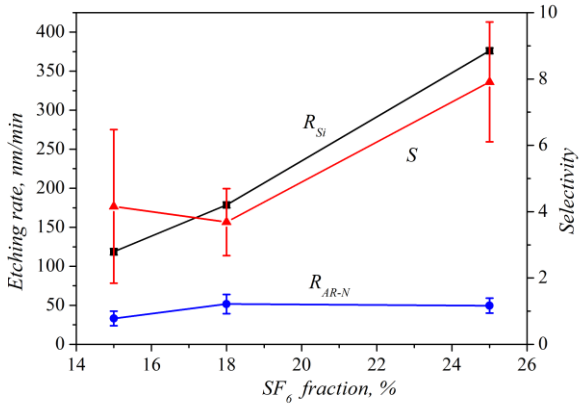


Fig. 1. Dependence of silicon etching rate (R_{Si}), etching rate of AR-N 7520 resist (R_{AR-N}), and selectivity (S) on the SF_6 fraction in the feeding gas

The resist etching rate remains almost constant with an increasing fraction of SF_6 in the feeding gas, and the etching selectivity of silicon to the AR-N 7520 increases.

Conclusion

The process with a fraction of SF_6 in the feeding gas equal to 25% and a bias voltage of 125 V provides an etching selectivity of 8.0 ± 1.8. Selectivity does not depend on the exposure dose, at dose values over 4000 pC/cm.

Acknowledgments

The investigation was supported by Program no. FFNN-2022-0021 of the Ministry of Science and Higher Education of Russia for Valiev Institute of Physics and Technology of RAS.

REFERENCES

1. **Gao J., Zhang S., Cui X., Cong X., Guo X., Hu R., Wang S., Chen J., Li Y., Yang G.** Effective Optimization Strategy for Electron Beam Lithography of Molecular Glass Negative Photoresist, Advanced Materials Interfaces. 10(20) (2023) 2300194.

2. **Nedeljkovic M., Khokhar A. Z., Hu Y., Chen X., Penades J. S., Stankovic S., Chong H. M. H., Thomson D. J., Gardes F. Y., Reed G. T., Mashanovich G. Z.** Silicon photonic devices and platforms for the mid-infrared, Optical Materials Express. 3(9) (2013) 1205–1214.

3. **Gangnaik A. S., Georgiev Y. M., Holmes J. D.** New generation electron beam resists: a review, Chemistry of Materials. 29(5) (2017) 1898–1917.

4. **Grigorescu A. E., Hagen C. W.** Resists for sub-20-nm electron beam lithography with a focus on HSQ: state of the art, Nanotechnology. 20(29) (2009) 292001.

5. **Borzenko T., Fries P., Schmidt G., Molenkamp L. W., Schirmer M.** A process for the fabrication of large areas of high resolution, high aspect ratio silicon structures using a negative tone Novolak based e-beam resist, Microelectronic engineering. 86(4-6) (2009) 726–729.

Hierarchical self-assembly of SiO_2-SnO_2 nano- and microstructures in combined sol-gel systems

I. A. Filippov[1], **N.D. Yakushova**[1], **A. A. Karmanov**[1✉], **I. A. Gubich**[2], **I.A. Pronin**[1]

[1]Penza State University, Penza, Russia;

[2]NIIFI, Penza, Russia

✉starosta07km1@mail.com

Abstract. Using the IR spectroscopy method, studies were carried out on the processes of hierarchical self-assembly of SiO_2-SnO_2 nano- and microstructures in combined sol-gel systems obtained by mixing film-forming sols with different maturation times, which meets the goals and objectives of nanostructural engineering. Characteristic absorption peaks were identified that correspond to the process of hydrolytic polycondensation and carry information about the process of self-assembly in the analyzed systems.

Keywords: nanostructure engineering, hierarchical self-assembly, sol-gel technology, spectroscopic investigation.

Funding: The study was supported by a grant from the Russian Science Foundation № 23-79-01280, https://rscf.ru/project/23-79-01280/

Introduction

In recent years, wide-bandgap semiconductor metal oxides such as ZnO, SnO_2, TiO_2, In_2O_3, etc. have attracted increasing interest. First of all, this is due to the wide scope of their practical application, including, among other things, solving gas sensory problems [1]. At the same time, it is becoming increasingly important to develop new methods and approaches to nanostructure engineering that make it possible to control the properties of these materials both through macro-level influences and by controlling the process of their synthesis at the earliest stages. For example, it is known that varying the maturation time of a film-forming sol leads to a new type of micro- and nanostructure of the metal oxide material [2]

Materials and Methods

Combined sol-gel SiO_2-SnO_2 systems were prepared within the framework of nanostructure engineering methods and approaches, which were first proposed to control the process of hierarchical self-assembly of zinc oxide nano- and microstructures [3]. The main idea is to mix film-forming sols with different maturation times in a given volume ratio (1:1, 2:1, 1:2). As part of this study, an analysis of a two-component SiO_2-SnO_2 system with a mass fraction of tin dioxide of 80 wt% was carried out.

The qualitative composition of film-forming sols, as well as the processes of hierarchical self-assembly, were studied by IR spectroscopy on an IR-Fourier spectrometer FSM 1201 (Infraspek LLC, Russia) within the framework of the method of multiple attenuation of total internal reflection using a MVTIR36 ZnSe cell.

Results and Discussion

Figure 1 shows the IR spectra of combined sol-gel systems SiO_2-SnO_2 with a maturation time of 1 hour (sample no. 1) and 24 hours (sample no. 5), respectively, as well as IR spectra of sols obtained by mixing samples no. 1 and no. 5 in a volume ratio of 2:1 (sample no. 2), 1:1 (sample no. 3) and 1:2 (sample no. 4), respectively. Analysis of the presented IR spectra shows that mixing film-forming sols with different maturation times does not lead to the emergence of new characteristic vibrational modes. This allows us to conclude that new chemical bonds are not formed, and there is no noticeable change in the qualitative composition of combined sol-gel systems when mixing sols with different maturation times.

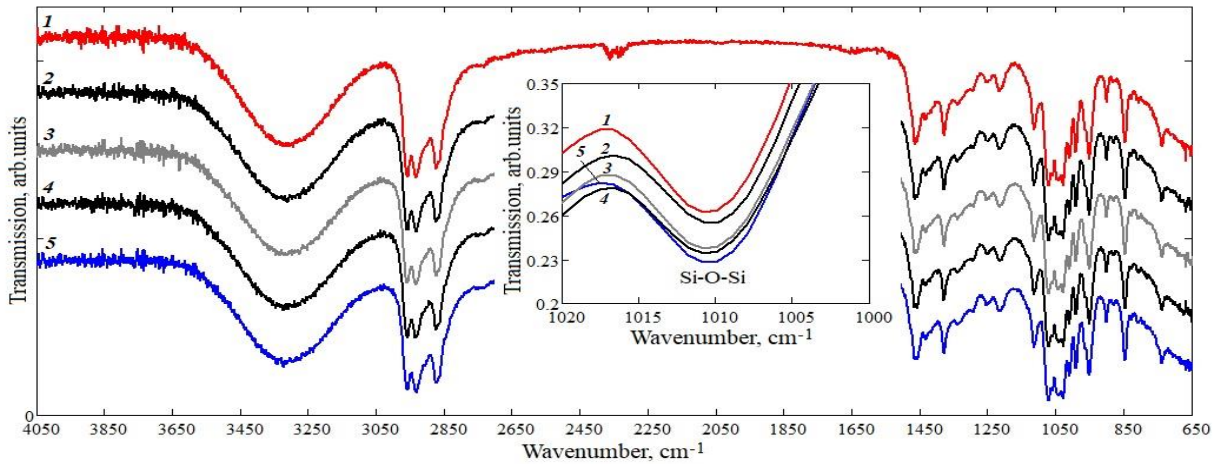


Fig. 1.

IR transmission spectra of combined sol-gel systems with different maturation times: 1 – 1 hour, 2 – 1 hour + 24 hours in a volume ratio of 2:1, 3 – 1 hour + 24 hours in a volume ratio of 1:1, 4 – 1 hour+24 hours in a volumetric ratio of 1:2, 5 – 24 hours

To analyze self-assembly processes occurring in the considered combined sol-gel systems, the most informative is the absorption peak with a maximum of 1010 cm-1 (inset in Fig. 1), which corresponds to the results of previous studies [4]. This vibrational mode corresponds to symmetrical stretching vibrations of Si-O-Si and a decrease in transmission with increasing maturation time of film-forming sols corresponds to the process of hydrolytic polycondensation, the consequence of which is the hierarchical self-assembly of nano- and microstructures of SiO_2-SnO_2, which have a fractal nature [5].

Conclusion

Thus, this study shows that infrared spectroscopy is a promising method for studying the hierarchical self-assembly of SiO_2-SnO_2 nano- and microstructures in combined sol-gel systems. It has been established that the mixing of sols with different maturation times affects the intensity of the characteristic peaks and absorption bands corresponding to the process of hydrolytic polycondensation.

REFERENCES

1. **Ben Arbia M., Helal H., Comini E**. Recent Advances in Low-Dimensional Metal Oxides via Sol-Gel Method for Gas Detection, Nanomaterials. 4(14) (2024) 359.

2. **Xiong L., Li J., Ye F., Wang H., Guo Y., Ming X., Chen Q., Zhang S., Xie R., Chen Z., Lv Y., Hu G., He Y., Fang G.** Bifunctional SnO_2 colloid offers no annealing time effect compact layer and mesoporous scaffold for efficient perovskite solar cells, Advanced Functional Materials 36 (31) (2024) 2103949.

3. **Karmanov A. A., Sukhov I. V., Yakushova N. D., Igoshina S. E., Pronin I. A.** Hierarchical Self-Assembly of Nano- and Microstructures of Zinc Oxide in Combined Sol-Gel Systems, Nano- i mikrosistemnaya tekhnika. 2 (26) (2024) 96-103.

4. **Pronin I. A., Averin I. A., Yakushova N. D., Karmanov A.A., Moshnikov V.A., Ham M.-H., Cho B.K., Korotcenkov G.** Structural features of silica coating obtained from sol cooled to the temperature of liquid nitrogen, Arabian Journal for Science and Engineering. 10 (42) (2017) 4299-4305.

5. **Hasmy A., Primera J., Woignier T.** Cluster–cluster aggregation with mobile impurities, Journal of Sol-Gel Science and Technology. 1 (90) (2019) 87-94.

CoSi ultrathin films on Si(111) substrate: comparison of the stage's formation in ultra-high vacuum and during annealing in argon

D. L. Goroshko, K. N. Galkin, I. M. Chernev✉, A. M. Maslov, O. V. Kropachev, E. Yu. Subbotin, O. A. Goroshko, N. G. Galkin

Institute of Automation and Control Processes FEB RAS, Vladivostok, Russia;

✉ igor_chernev7@mail.ru

Abstract. This study identified the optimal conditions for the formation of ultrathin films of cobalt monosilicide (CoSi) on a silicon substrate during the annealing process (T = 400-500 °C) of chromium layers, both in ultra-high vacuum conditions and in an argon environment during isochronous annealing.

Keywords: cobalt layer, cobalt monosilicide, films, isochronous annealing, ultra-high vacuum, argon environment, electronic structure, phonon structure, optical properties.

Funding: This study was funded by the grant from the Russian Science Foundation (RSF) No. 22-12-00036, https://rscf.ru/project/22-12-00036.

Introduction

The study of monosilicides of transition metals such as Cr, Mn, Fe and Co with a cubic structure B20 with space group $P2_13$ and breaking the symmetry of spatial inversion becomes an urgent task [1]. Moreover, cobalt monosilicide (CoSi) belongs to a topological Weyl semimetal [2], which has interesting electrical and thermoelectric properties [3]. However, studies were mainly carried out on single crystals and bulk polycrystals of CoSi. At the same time, the question of the formation of thin (25 - 700) nm CoSi films remains poorly studied [4,5].

Materials and methods

Experiments on the deposition of ultra-thin cobalt layers were carried out in a Varian ultra-high vacuum unit with a base vacuum of $2x10^{-10}$ Torr, equipped with an Auger electron spectroscopy (AES) and characteristic electron energy loss spectroscopy (EELS) analyzer. Cobalt layers 4 – 7.7 nm thick were deposited at room temperature onto an atomically clean Si(111)7x7 surface obtained after high-temperature annealing at T=1150 ^oC. On a number of samples, solid-phase annealing was carried out at temperatures of 400-500 °C, as well as isochronous annealing at temperatures of 275-700 °C in increments of 25 °C with recording of AES and EELS spectra. Individual Co films were unloaded without annealing and then annealed in a temperature range (30-550°C, increment 25°C) with argon purging and simultaneous recording of Raman spectra to monitor the onset of CoSi formation. Reflection and transmission spectra were recorded on spectrophotometer VERTEX v80 (BRUKER).

Results and Discussion

Analysis of the AES and EELS spectra showed that the formation of CoSi begins at a temperature of 325 ^oC, which is confirmed by a decrease in the concentration of cobalt and an increase in the concentration of silicon, and stoichiometric CoSi is formed at temperatures of 400-600 ^oC (Fig. 1a). This is confirmed by the data of the EELS spectra (Fig. 1b), when surface (13.3 eV) and volume (20.2-20.5 eV) plasmons corresponding to CoSi are formed in the

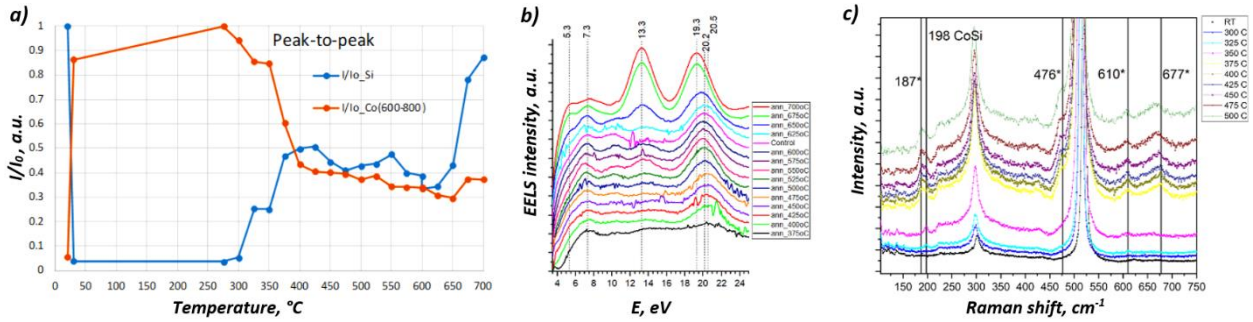


Fig. 1. Dependence of Co and Si concentrations on annealing temperature (a). Changes in the EELS spectra with increasing annealing temperature (b). Raman spectra at different annealing temperatures of the Co film d_{Co}=7.7 nm at λ_{laser} = 675 nm. Peaks marked with asterisk are related to Co_3O_4 oxide (c).

temperature range 400-600 ºC. The transition from CoSi to $CoSi_2$ is observed at temperatures above 675 °C, which corresponds to a shift of the bulk plasmon to the position of 19.3 eV, corresponding to $CoSi_2$ (Fig. 1b)). Registration of Raman spectra during annealing in an argon environment confirmed the limit of the formation temperature (325 °C) and the increase in the intensity of the Raman peak at 198 cm^{-1}, corresponding to CoSi, with increasing annealing temperature to 550 °C (Fig. 1c). The formation of cobalt oxide during annealing in an argon environment was also discovered due to the decomposition of $Co(OH)_2$ formed on the Co layer after the film was unloaded in air, which correlates with the data of [6], which considered stepwise annealing of thick Co films in air. FIR spectra also confirmed CoSi formation with phonon peaks 302.6 $см^{-1}$ and 418.8 $см^{-1}$, which amplitudes increase with CoSi thickness.

Conclusion

The temperature range (400–600 °C) for the formation of ultrathin CoSi films on a Si(111) substrate upon annealing of Co layers with a thickness of 4.0–7.8 nm has been determined. It has been shown that UHV annealing and annealing in an argon environment led to similar results, which is confirmed by AES – EELS spectra and Raman spectroscopy data. The influence of a $Co(OH)_2$ layer adsorbed on Co in air on silicide formation has been established.

REFERENCES

1. **Dutta P.** and **Pandey S.K.,** Investigating the electronic structure of MSi (M = Cr, Mn, Fe &Co) and calculating U_{eff} & J by using cDFT, Computational Condensed Matter 16 (2018) e0035(1-7).

2. **Pshenay-Severin D.A., Ivanov Y.V., Burkov A.A., Burkov A.T.**, Band structure and unconventional electronic topology of CoSi, Journal of Physics: Condensed Matter 30 (2018) 135501.

3. **Pshenay-Severin D.A., Ivanov Yu.V., Burkov A.T., Novikov S.V., Zaitsev V.K.** and Reith **H.,** Electronic Structure and Thermoelectric Properties of Transition Metal Monosilicides, Journal of Electronic Materials 47 (2018) 3277–3281.

4. **Normuradov M.T., Bekpulatov I.R., Imanova G.T., Igamov B.D.**, Structures for constructing devices from formed Mn_4Si_7 and CoSi films, Advanced Physical Research 4 (2022) 142-154.

5. **Li Z., Yuan Y., Hübner R., Rebohle L., Zhou Y., Helm M., Nielsch K., Prucnal S., and Zhou S.**, B20 Weyl Semimetal CoSi Film Fabricated by Flash-Lamp Annealing, ACS Applied Materials & Interfaces 15 (2023) 30517-30523.

6. **Liu F.M., Ye J.H., Ren B., Yang Z.L., Liao Y.Y., See A., Chan L., Tian Z.Q.**, Raman spectroscopic studies of the formation processes of cobalt silicide thin films, Thin Solid Films 471 (2005) 257 – 263.

Quantum dots formation by InGaAs decomposition onto a patterned GaAs surface

N. E. Chernenko [1]✉, I. S. Makhov [2], I. A. Melnichenko [2], K. D. Yakunina [1], S. V. Balakirev [1], N. V. Kryzhanovskaya [2], M. S. Solodovnik [1]

[1] Laboratory of Epitaxial Technologies, Southern Federal University, Taganrog, Russia

[2] International Laboratory of Quantum Optoelectronics, HSE University, St. Petersburg, Russia

✉nchernenko@sfedu.ru

Abstract. In this work, we present the results of experimental studies of the formation processes and optical properties of ordered arrays of InGaAs nanostructures obtained by layer of quantum well material deposition onto nanopatterned GaAs surface. For GaAs nanopatterning we used a combination of focused ion beam treatment and local droplet etching techniques allowing to create arrays of holes with different morphology. Using room-temperature photoluminescence (PL) mapping we have shown that quantum well material localizes inside the created holes but position of corresponding PL peak (960 – 970 nm) is independent of morphology and is determined only by the chemical composition of the deposited material. Based on low-temperature (5 K) PL measurements we conclude that inside the holes quantum well decomposes due to the difference in a mobility of Ga and In adatoms during its material deposition with formation a "quantum well + quantum dot" system. While the quantum well peak locates approximately at 920 nm, the quantum dot lines lie in the wavelength range of 930 – 950 nm.

Keywords: quantum dots, A3B5, decomposition, structuring, molecular beam epitaxy, nanostructures, nanopatterning

Funding: This work was supported by the Russian Science Foundation Grant No. 22-79-10251 and by the Ministry of Science and Higher Education of the Russian Federation Grant No. FENW-2022-0034 at the Southern Federal University.

Introduction

Great interest in quantum dots (QD) is due not only to their unique properties, but also to the need to create highly efficient compact (micro- and nano-sized) light sources including non-classical sources of single and entangled photons based on them. Since the properties of QDs largely depend on their structural characteristics, the requirements for the accuracy of their control increase as the size of devices based on them decreases. And despite the long history of studying QDs, the development of effective methods for controlling their properties, including the position of individual structures in an array, remains an urgent task. One of the most promising methods of QD control is the preliminary structuring of the surface by creating holes (or recesses) of various geometries, which are the preferred sites for the nucleation and growth of self-organized nanostructures. This paper presents the results of studies on the possibility of forming QDs by deposition of quantum well (QW) material onto a structured surface.

Materials and Methods

Preliminary nanopatterning of GaAs surface was carried out on GaAs/AlGaAs heterostructure using a focused ion beam (FIB). As a result, square arrays of holes with different geometric characteristics were formed. The ion beam accelerating voltage was 5 kV, and the distance L between the holes in the array was 0.5 and 1 μm. The number of ion beam passes N varied from 1 to 60. Then pre-growth treatment was carried out using the original local droplet etching technique [1], because of which pyramidal-shaped holes with lateral sizes varied from 98 to 292 nm were formed at the points of beam exposure. Then a 10 nm thick InGaAs layer with an indium content of 17% was deposited onto the structured surface. This layer was placed in the center of the optical cavity formed by the AlGaAs/GaAs/AlGaAs heterostructure. After formation sample were studied by photoluminescence spectroscopy at 5 and 300 K.

Results and Discussion

The results of experimental studies showed that when 10 nm InGaAs is deposited onto a structured surface, the material is localized in the region of the holes (Fig. 1*a*). PL signal distribution maps (300 K) show the dependence of the PL signal intensity in the wavelength range 900 – 1050 nm on the initial morphology specified by the parameters of nanopatterning. PL measurements at different points of the signal maximum showed that the position of the long-wavelength peak corresponding to InGaAs is unchanged for all points and locates in the region of 960 – 970 nm, regardless of the initial morphology. Such wavelength corresponds to the emission of InGaAs/GaAs QWs with the same composition on non-patterned surfaces.

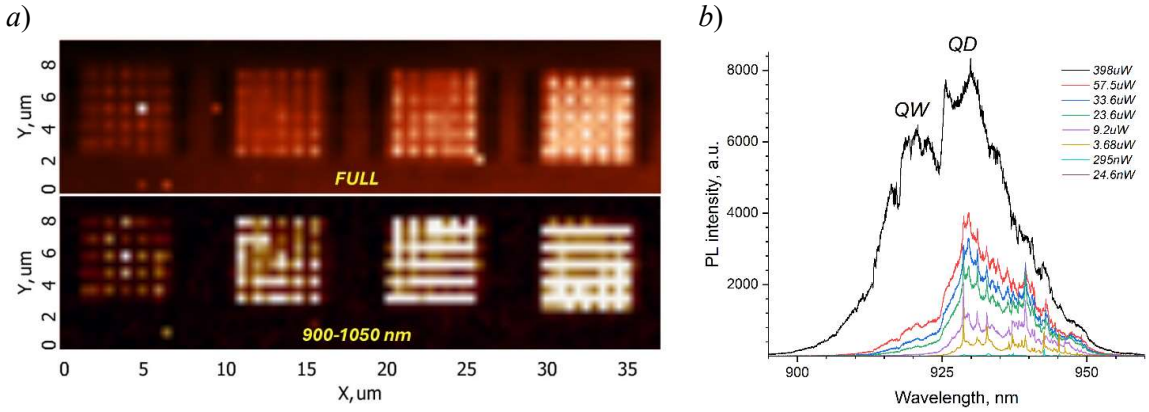


Fig. 1. PL spectra in patterned areas: a) PL intensity distribution map at 300 K for arrays with L = 1.0 μm and N varied from 20 (left array) to 60 (right array) passes (upper panel – full spectra; lower panel – spectra in the wavelength range 900 – 1050 nm); b) spectra at different excitation powers for an array with L = 0.5 μm and N = 40 passes.

Analysis of the PL spectra at 5 K (Fig. 1*b*) showed that localized nanostructures emit in the wavelength range 900 – 950 nm. At low temperature as the excitation power decreases, the peak splits into short- (900 – 930 nm) and long-wavelength (930 – 950 nm) components. We associate this with the formation of two types of structures inside every hole and the corresponding redistribution of contributions between them when the morphological parameters change. In Fig. 1*b* as the pump power decreases, the maximum intensity shifts to the long-wavelength region due to the rapid decay of the short-wavelength shoulder. At the same time, the spectrum is discretized, and the lines of individual QDs are isolated. Based on this we conclude that inside the holes QW decomposes due to the difference in a mobility of Ga and In adatoms during its material deposition with formation a "quantum well + quantum dot" system.

Conclusion

Thus, we have demonstrated for the first time the possibility of forming ordered arrays of QDs emitting in the wavelength range 930 – 950 nm by depositing an InGaAs QW layer onto nanopatterned GaAs surface. We have shown that inside pyramidal-shape holes InGaAs decomposes due to the difference in a mobility of Ga and In adatoms resulting in the formation a "quantum well + quantum dot" system.

REFERENCES

1. **Chernenko N.E., Kirichenko D.V., Shandyba N.A., Balakirev S.V., Eremenko M.M., Solodovnik M.S.**, Experimental study of nanoholes formation using local droplet etching of FIB-modified GaAs (001) surface, St. Petersburg State Polytechnical University Journal: Physics and Mathematics. 15 (3.3) (2022) 48 – 53.

Control of properties and geometric characteristics of selectively formed GaAs nanowires within the FIB treatment area on Si(111)

N. A. Shandyba [1]✉, M. M. Eremenko [1], V. A. Sharov [2,3], S. V. Balakirev [1], M. S. Solodovnik [1]

[1] Laboratory of Epitaxial Technologies, Southern Federal University, Taganrog 347922, Russia

[2] Alferov University, Saint Petersburg 194021, Russia

[3] Ioffe Institute, Saint Petersburg 194021, Russia

✉shandyba@sfedu.ru

Abstract. This paper presents the results of experimental studies on the selective formation of GaAs nanowire arrays on the Si(111) substrate surface and the control of their properties. It has been shown that pre-treatment of the Si(111) surface with a native oxide layer by a focused Ga-ion beam with further low-temperature annealing and high-temperature growth allows the formation of selective GaAs nanowire arrays with a different set of parameters that can be controlled by changing the ion dose in the range of 0.052 – 52 pC/μm^2. We also demonstrated the possibility of obtaining arrays with a yield of vertically oriented nanowires at the level of 100% and very high density (up to 8 μm^{-2}). At the same time outside the modified areas, the formation of nanowires was almost completely suppressed. Moreover, based on Raman spectroscopy study we have found that our approach allows to obtain nanowire arrays with clear zinc-blende crystal phase in wide range of nanowire sizes.

Keywords: nanowires, gallium arsenide, focused ion beam, molecular beam epitaxy, A3B5.

Funding: This work was funded by the Ministry of Science and Higher Education of the Russian Federation; the state task in the field of scientific activity No. FENW-2022-0034.

Introduction

Currently, A3B5 nanowires (NW) are of great interest as key elements for creating promising photonic and nanoelectronic devices. The availability of technology capable of precisely controlling the NW position and their various properties and geometric parameters is required for the creation of various devices. To date, one such technology is focused ion beam (FIB) treatment of the substrate surface prior to NW growth. However, this method is still poorly understood and requires additional research. In this paper, we study the selective growth of GaAs NW arrays within the FIB treatment area on the Si(111) surface with a native oxide layer and the dose effect on their properties and geometric characteristics.

Materials and Methods

Experimental studies were carried out on Si(111) p-type epi-ready substrate with a native oxide layer. The ions were implanted into the substrate at an accelerating voltage of 30 kV according to a template consisting of several 5×5 μm areas in which the dose ranged from 0.052 – 52 pC/μm^2. Then annealing was performed at a temperature of 600°C for 1 hour. After that, the NW growth was carried out with substrate temperature of 750°C with a nominal deposition rate of 0.25 ML/s for 48 minutes by the MBE method. The sample was analyzed by SEM and Raman spectroscopy methods.

Results and Discussion

SEM images analysis of the surface after NW growth shows that GaAs NW arrays selectively form within areas treated with an ion beam (Fig. 1a). At the same time, their growth is practically suppressed outside the modification area and only the formation of low-density GaAs crystallites is observed. It is also seen that changing the dose allows to control key NW characteristics, such as: density, length, diameter and yield of vertical NWs. The character of the dose effect on the NW parameters is presented through the dependences plotted based on SEM images statistical processing.

The analysis of the obtained dependences shows that the curves change character from the FIB dose is rather complex and nonlinear. So, selective formation of an NW array with almost

100 % verticality value is observed at the beginning of the ion dose range (0.052 pC/μm^2 – Fig.1a, b). This is an unexpected result considering that the growth occurs on the substrate surface with a native oxide layer. The value of the NW density in this case is ~ 5 μm^{-2}. Then, as the ion dose increases, the NW density slightly increases (up to ~ 7 μm^{-2}) and the values of the NW verticality, length and diameter begin to decrease. However, the verticality also remains in the region of high values (about 80 %). A further rise in the dose leads to a sharp decrease and stabilization of all key NW characteristics values in the region of minimum values in the dose range of 1.56 – 26 pC/μm^2. This is due to the formation of polycrystalline GaAs base which changes the conditions and mechanism of NW growth on the surface within the treatment area. Meanwhile, also interestingly, this stabilization stops at a subsequent increase in ion dose (52 pC/μm^2) which leads to a sharp increase in all NW characteristics. Mechanisms underlying the FIB dose effect on the NW parameters is reflected in [1].

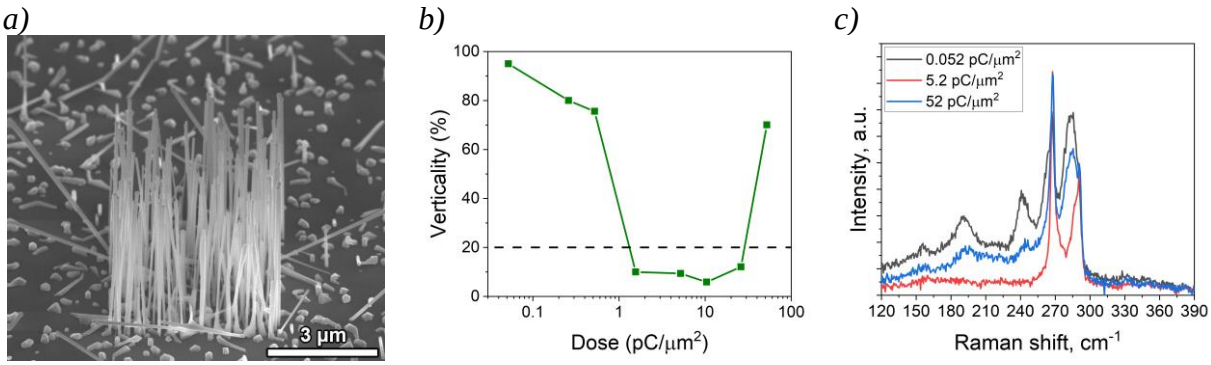


Fig. 1. Tilted SEM image of modified area after GaAs nanowire growth for ion dose of 0.052 pC/μm^2 (a). Dependence of the NW verticality on Ga ion dose (b). Dash line correspond to values for unmodified area. The Raman spectrum is obtained from NW arrays formed within areas treated with different doses (c).

It is important to note that such growth selectivity is achieved by using a combination of low-temperature annealing and high-temperature growth. This reduces the number of pores formed on the substrate surface in the native oxide layer outside the modification area during the annealing stage. Simultaneously, this temperature facilitates their formation within the ion beam treatment area through the chemical interaction of embedded Ga ions diffusing to the substrate surface with oxide atoms [1]. The high growth temperature reduces the probability of nucleation outside the modification area while increasing it within the FIB treatment area due to the abundance of nanopores and active diffusion of Ga atoms over the Si surface. According to the results of Raman spectroscopy, in the NW arrays predominantly observed TO, LO and SO phonon modes responsible for the zinc-blende GaAs crystal lattice (Fig. 1c). The absence of the wurtzite phase (E_2 mode) of the hexagonal lattice in the spectra indicates that the NW growth occurred within the FIB treatment area in a single sphalerite phase over the entire ion dose range.

Conclusion

Thus, it was shown that a certain combination of growth process parameters and pre-treatment of the Si(111) substrate surface with a native oxide layer by Ga-ion beam enables the selective formation of GaAs NW arrays with a clear zinc-blende crystal phase. Herewith, the geometric characteristics of NWs can be controlled by adjusting the ion dose which in a defined range allows to maintain the verticality values in the interval of 80 – 100 %.

REFERENCES

1. **Shandyba N., Balakirev S., Sharov V., Chernenko N., Kirichenko D., Solodovnik M.**, Modulation of GaAs nanowire growth by pre-treatment of Si substrate using a Ga focused ion beam, Nanotechnology. 34 (46) (2023) p.465603.

Study of the sodium iodide influence on the selectivity of thin-film gas-sensitive structures

A.E. Shepeleva [1]✉, M.D. Novichkov [1], S.A. Gurin [1], A.A. Ryzhov [1], E.A. Pecherskaya [2]

[1] Joint-stock company "Scientific Research Institute of Electronic-Mechanical Devices", 440060, Penza, Karakozova 44, Russia

[2] Federal State Budgetary Educational Institution "Penza State University", Penza, Russia

✉anastasiya.shepeleva.01@mail.ru

Abstract. The result of the sodium iodide dopant influence on the selectivity of thin-film gas-sensitive structures is presented. Zinc oxide nanorods were synthesized by hydrothermal method. The resulting structure was studied for gas sensitivity to vapors of detected gases and has high performance in the presence of an alloying additive.

Keywords: gas sensitive layer, dopant, response time, recovery time

Introduction

The centers of adsorption, desorption and catalysis (surface OH groups) that occur on the sensitive material surface have a strong influence on such parameters as the sensitivity and speed of the sensor. In this regard, solving the problems of managing surface functional groups and increasing hydrophilicity is necessary for gas sensors. These problems are solved by adding dopants [1].

Experimental technique

To assess the effect of doping on the functional properties of the surface and the adsorption of hydroxyl groups, the gas-sensitive characteristics of zinc oxide nanorods with the addition of a dopant, iodine, were analyzed.

Synthesis by the hydrothermal method was carried out in a thermostat at a temperature of 85 °C for 1 hour. Solution100 mM HMTA and 100 mM Zn(NO3)2·2H2O sodium iodide is in an amount of 10 mM. The resulting samples were immersed in distilled water to remove residual impurities from the surface. Next there was annealing at a temperature of 350 °C [2].

Results and Discussion

Nanorods were studied in vapors of acetone and isopropyl alcohol in one case, when they were grown under standard conditions [3], and in another, when a dopant of sodium iodide was added (Fig. 1).

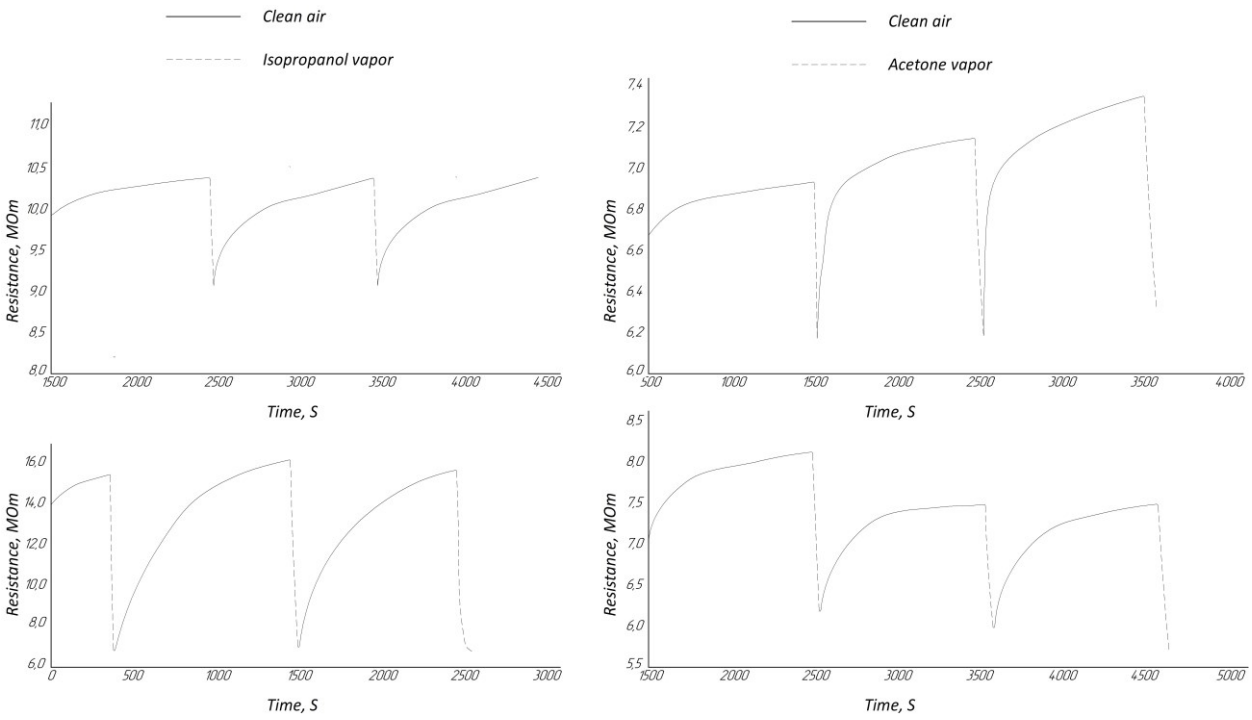


Figure 1. Dependence of response on time without dopant and with its addition to vapors of different gases

In the absence of sodium iodide, when gas is supplied, the resistance drops. In this case, the response time in acetone vapor is about 13 seconds, the recovery time is 655 seconds. In isopropanol vapor - about 45 seconds and 680 seconds, respectively.

In the case of doping, the response time of the resulting structure when exposed to acetone is about 18 seconds, the recovery time is 580 seconds. For isopropanol - about 25 seconds and 640 seconds, respectively.

The calculated sensitivity to the detected gases in the absence of a dopant is 13% for acetone and 10% for isopropanol. In this case, the sensitivity of the structure with the dopant (S) was 16% for acetone and 54% for isopropanol.

Conclusion

The gas-sensitive layer, which contains the dopant sodium iodide, is more sensitive to vapors of detected gases. The improvement in response time and recovery time demonstrates their dependence on the number of functional surface groups. Additional functional groups, influencing adsorption and desorption, improve these indicators.

REFERENCES

1. The multisensor array based on grown-on-chip zinc oxide nanorod network for selective discrimination of alcohol vapors at sub-ppm range / **A. Bobkov, V. Moshnikov, A. Varezhnikov [et al.]** // Sensors. – 2019. – Vol. 19, No. 19. – P. 4265. – DOI 10.3390/s19194265.

2. **I. A. Averin,** Control of parameters of resistive structures by annealing / **I. A. Averin, R. M. Pecherskaya** // Proceedings of the international symposium "Reliability and Quality". – 2008. – T. 2. – P. 144-145.

3. Synthesis of zinc oxide nanorods and nanoparticles by chemical route and their comparative study as ethanol sensors / **Singh R. C., Singh O., Singh M. P., Chandic P. S.** //Sensors and Actuators B: Chemical. – 2008. – T. 135. – №. 1. – C. 352-357.

Chemical composition and electrical properties of SiFe-based systems

A. S. Shkapina [1]✉, **R. N. Kriukov** [1], **Yu. A. Dudin**[1], **M. V. Dorokhin**[1], **S. Yu. Zubkov**[1], **A. V. Zdoroveyschev**[1]

[1] Lobachevsky State University of Nizhny Novgorod, Nizhny Novgorod, Russia;
✉alenashkapina@yandex.com

Abstract. This work shows the possibility of making new thermoelectrical system based on SiFe in ion implantation process. These structures were subjected to high-temperature annealing of various durations. Further, we used the X-ray photoelectron spectroscopy to construct the spectra of the distribution of chemical elements and the bonds between them along the depth of the sample depending on the annealing time. Thereby, increasing annealing time leads to the destruction of Si-Fe bonds. This fact can cause the decreasing of efficiency. According to the dependence of thermal conductivity on the annealing duration, there is a tendency towards its decrease.

Keywords: ion implantation, X-ray photoelectron spectroscopy, thermoelectricity, efficiency, thermal conductivity.

Funding: This work was supported by the Priority 2030 Strategic Academic Leadership Program of the Ministry of Science and Higher Education of the Russian Federation.

Introduction

One of the areas of modern research is the development of thermoelectric generators. However, they have a significant drawback - low efficiency. Therefore, scientists are looking for ways to increase the efficiency of these systems. One possible solution is to use multiple phases in a system. Transition metal silicides are suitable materials for this purpose [1]. There are works that prove the effect of non-stoichiometry on output characteristics, so the issue of composition and its influence on efficiency is important. One of the methods that can help solve the diagnostic problem is X-ray photoelectron spectroscopy (XPS). In combination with ion profiling by depth, XPS allows us to obtain information about the distribution of elements in a thin film or layered structure. Ion implantation is one of the most promising method for synthesis of thermoelectric. During this process, the initial structure is destroyed. Therefore, further annealing is an integral part of working with samples obtained by ion implantation. As previously stated, the resulting structure can be a thermoelectric. To confirm this information, measurements of thermoelectric parameters are required. In our case, thermal conductivity acts as such a parameter. By changing the thermal conductivity, we can assume the behavior of the efficiency of the structure.

Materials and Methods

Iron ions were implanted in Si-substrate at the «Raduga-3M» accelerator. The ion dose was 5×10^{16} cm^{-2} and accelerating voltage was 80 kV. There is no mass analyzer in the «Raduga-3M» system, which makes it difficult to analyze the structures obtained, as ions with different charges are present in the ion beam.

After ion implantation the sample was divided into six parts; five of them was subjected to high-temperature annealing of various duration (15 - 900 s). The entire process is conducted in an argon atmosphere to avoid the presence of oxides in the material. Also the argon presence allows rapid cooling. The annealing temperature was 1000 °C.

Subsequently, XPS spectra were obtained for all samples on Omicron Multiprobe complex. Al K_α radiation with an energy of 1486.7 eV was used to excite photoemission (PE). Diameter of the analysis area was 3 mm. Layer profiling over the sample depth was carried out by etching with Ar^+ ions. Ion beam has 20 mm diameter, 1 keV energy, homogeneous radial distribution of the ion current density and 45° angle of inclination. The analysis of the peak shift within this method allows one to draw the conclusions on the chemical bonds and phase composition of the films.

Atomic concentration in the layers was determined by the method of relative sensitivity factors [2]. Photoelectron lines (PE lines) Si 2*p*, Fe 2*p*, O 1*s* и C 1*s* were analyzed. Structure of PE lines due to chemical shifts was investigated using the mathematical software CasaXPS [3].

In addition to these methods, the 3-ω method was also used to measure the thermal conductivity of the structure[4].

Results and Discussion

An increase in annealing duration results in iron diffusing deep into the sample (Fig. 1a). Additionally, XPS profiles enable us to estimate integral concentration, which is different for each sample and may indicate an inhomogeneous distribution of iron ions during ion implantation in the beam.

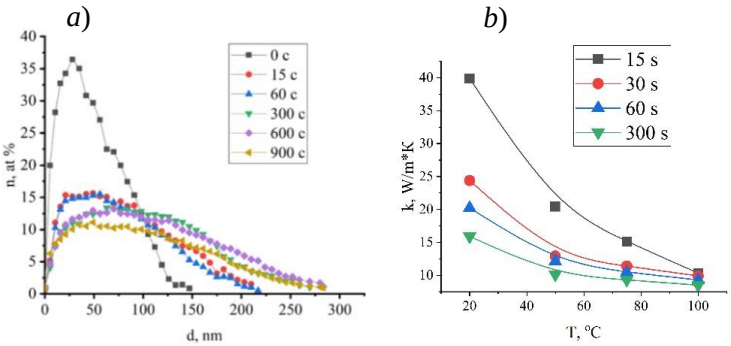


Fig.1. (*a*)iron distribution profiles for different annealing durations, (*b*) temperature dependence of thermal conductivity of ion-synthesized $FeSi_x$ structures for different annealing times

As for the chemical bonds between Si and Fe, with an increase in annealing time. This may be due to the reconstruction of the silicon matrix since annealing was carried out at a temperature of 1000oC. Thus, in order to maximize the yield of a material with a high concentration of Fe-Si bonds, it is necessary to optimize the time of thermal annealing. Based on the data obtained, the optimal value is 60 seconds. Alternatively, we can abandon high-temperature annealing and use pulsed lasers.

As the annealing time increases, the thermal conductivity decreases (Fig.1b). This can be a significant contributor to improving the quality of the final structure. A significant reduction in thermal conductivity can be attributed to the formation of metal–silicide complexes. These complexes, in turn, block phonon modes [5]. This prevents the propagation of heat through the structure via lattice vibrations.

Conclusion

In this work, the use of iron silicide-based thermoelectrics as a new source of energy was shown. It was possible to observe the diffusion of iron deep into the sample with an increase in annealing time. Annealing also affects the number of silicon-iron bonds formed; namely, they collapse during prolonged annealing. Thus, in order to obtain structures with optimal parameters, it is necessary to select an optimal annealing time, or abandon high-temperature annealing and use pulsed laser annealing. It was also possible to achieve a decrease in the thermal conductivity of the structure by increasing the duration of its annealing process. This fact may become significant when calculating the efficiency of the structure; namely, it is possible to increase the efficiency of thermoelectric conversion.

REFERENCES

1. **Jian Yu, Jing Kuang**, **Jiaxin Long**, **Xiaoli Ke**, **Xingkai Duan**, **Zhiyuan Liu** Effects of nonstoichiometry on thermoelectric properties of CoSi based materials / Journal of Materials Science: Materials in Electronics 2020, V. 31, pp. 2139-2144

2.**Briggs, D.; Seah, M. P.** Practical surface analysis by auger and X-ray photoelectron spectroscopy, 3rd ed.; John Wiley and Sons: New York, USA, 1985.

3. www.casaxps.com.

4. **David de Koninck** Thermal Conductivity Measurements Using the 3-Omega Technique: Application to Power Harvesting Microsystems / David de Koninck. // Department of Mechanical Engineering McGill University Montréal, Canada. – 2008. – 106 c.

5. **Rowe D.M.** Thermoelectrics Handbook. Macro to Nano. – New York: CRC Press, 2006. – 1008 p.

Study of GaPN(As) layers grown by molecular beam epitaxy on silicon substrates

E. V. Nikitina [1,2], **K. Yu. Shubina** [1✉], **M. S. Sobolev** [1], **E. V. Pirogov** [1]

[1] Alferov University, Saint Petersburg, Russia;

[2] Ioffe Institute, Saint Petersburg, Russia

✉kshubina@spbau.ru

Abstract. In this work bulk layers of GaPN(As) solid solutions grown by molecular beam epitaxy on gallium phosphide and silicon substrates are studied. The morphology, structural and optical properties of diluted nitride epilayers synthesized on GaP and Si are compared. The possibility of obtaining GaPN(As) epitaxial layers of optical quality on lattice-mismatched silicon substrates is demonstrated.

Keywords: dilute nitride semiconductors, molecular beam epitaxy, silicon, GaP

Funding: This study was funded by RSCF (grant number 23-79-00032).

Introduction

Solid solutions of materials containing a small mole fraction of nitrogen, the so-called dilute nitrides, are difficult to theoretically describe and experimentally grow, but are of great interest for many optoelectronic applications. It is known, that the addition of nitrogen to GaP makes this ternary solution GaPN direct gap and, with a nitrogen mole fraction of about three percent, makes it lattice matched with silicon [1]. Moreover, by varying the composition of a quaternary solution of GaPNAs, it is possible to obtain a semiconductor material with the bandgap range from 1.5 to 2.0 eV which is also lattice-matched with silicon [2, 3]. Thus, dilute nitride semiconductor compounds have a potentially wide application range, especially for integration with silicon in optoelectronic integrated circuits, and also as top cascades in multijunction solar cells on silicon substrates [4, 5].

Materials and Methods

In this study, heterostructures with bulk GaPN and GaPNAs layers were were grown by plasma assisted molecular beam epitaxy on gallium phosphide substrates with a (100) orientation and on silicon substrates with a (100) orientation misoriented in the [110] direction by 4 and 6°.

The composition of ternary and quaternary solid solutions was determined by X-ray diffraction analysis using a high-resolution X-ray diffractometer DRON-8, the anode material was copper with radiation type Kα1 (λ = 1.5405 Å). The morphology of the resulting heterostructures was characterized using a Supra 25 Zeiss scanning electron microscope with a surface resolution of 5 nm. The optical properties of the resulting heterostructures were studied by photoluminescence (PL) spectroscopy in the range from 550 nm to 800 nm.

Results and Discussion

The photoluminescence spectra of the samples are presented in Figure 1. First, it is clearly seen that the synthesized dilute nitride materials GaPN and GaPNAs are direct gap semiconductors. The peak PL intensity of the GaPN layers grown on GaP and silicon substrates are comparable. It means that GaPN layer grown on Si substrate has good crystalline quality. A slight shift of the peak position from sample to sample can be noted. It depends on the substrate used for epitaxial growth and consequently the solid solution composition and mole fraction of nitrogen used for lattice matching.

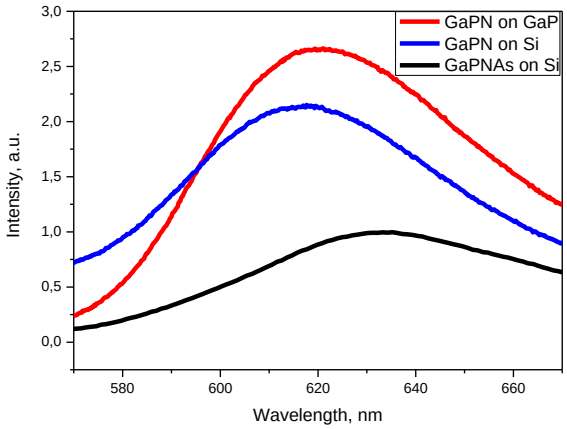


Figure 1. PL spectra of the obtained samples.

Conclusion

In this work GaPN and GaPNAs epitaxial layers were synthesized on GaP(100) and misoriented Si(100) substrates. The morphology, structural and optical properties of the obtained samples were studied. The possibility of epitaxial growth of the optical quality dilute nitride layers lattice-matched with Si(100) is shown.

REFERENCES

1. **Furukawa Y., Yonezu H., Morisaki Y., Moon S.-Y., Ishiji S., and Wakahara A.**, Monolithic implementation of elemental devices for optoelectronic integrated circuit in lattice-matched Si/III–V–N alloy layers, Japanese Journal of Applied Physics. 45 (2006) L920–L922.

2. **Geisz J. F. and Friedman D. J.**, III–N–V semiconductors for solar photovoltaic applications, Semiconductor Science and Technology.17 (2002) 769–777.

3. **Kudrawiec R.**, Parameterization of the band gap energy for GaNxAs1-x-zPz alloys, Journal of Applied Physics. 101 (11) (2007) 116101.

4**. Sukrittanon S., Liu R., Ro Y. G., Pan J. L., Jungjohann K. L., Tu C. W., Dayeh S. A.**, Enhanced conversion efficiency in wide-bandgap GaNP solar cells, Applied Physics Letters. 107 (2015) 153901-1–5.

5**. Zhang X., Liu L., Chi F., Wang K., Lin K. and Wang Y.**, Theoretical investigation of lattice-matched III-N-V/Si double-junction solar cells, Journal of Physics D: Applied Physics. 55 (2022) 475104.

Influence of the wet-chemical treatment on the optical properties of core-shell InGaN nanowires

T. Shugabaev[1,2]✉, V.O. Gridchin[1-3], A.S. Kulagina[1,2], I.S. Machov[4], A.M. Nadtochiy[4], A. I. Khrebtov[1,2], V. V. Lendyashova[1,2], N. V. Kryzhanovskaya[4], G. E. Cirlin[1-3]

[1] Alferov University, St. Petersburg, Russia;
[2] St. Petersburg State University, St. Petersburg, Russia;
[3] Institute for Analytical Instrumentation RAS, St. Petersburg, Russia
[4] HSE University, St. Petersburg, Russia;
✉talgashugabaev@mail.ru

Abstract. We study the impact of the shell in spontaneously formed InGaN nanowires on their optical properties. It is shown that removing the shell from the initial nanowires induces the photoluminescence enhancement and narrows their spectrum emission. Fitting of experimental dependencies of integrated PL intensity on excitation power by using ABC-model allowed us estimate relative contribution of different recombination processes. It has been established that radiative recombination dominates in the initial and no-shell nanowires.

Keywords: core-shell InGaN nanowires, etching of nanowires, photoluminescence enhancement, power dependent photoluminescence spectra , ABC-model

Funding: The samples growth and optical properties studies were done under the financial support of Russian Science Foundation grant № 23-79-00012.

Introduction

InGaN nanowires (NWs) are prospective candidates for fabrication ultra-high resolution micro- and nano- light-emitting devices over a wide range of wavelengths. InGaN NWs can be grown on lattice-mismatched substrates without forming structural defects, in particular on cheap and available Si substrates [1]. The synthesis of ternary InGaN compounds in the morphology of nanowires allows to obtain nanostructures with any emission wavelength in the visible range due to all possible variations in the In content [2]. Moreover, orange and red-emitting InGaN nanocolumns with a high density of localized states due to large In fluctuation was shown to potential achieve high luminescence efficiency. [3].

Recently, it was shown that InGaN NWs grown by plasma-assisted molecular beam epitaxy spontaneously formed with the core-shell structure [1]. Where the core contains 35-40 % In ($In_{0.35-0.40}Ga_{0.65-0.60}N$), and the shell is almost pure GaN with 0-4 % In content. In this work, for the first time, we study the influence of the shell of the NWs on their photoluminescence (PL) properties. We determine the contribution of different recombination processes based on dependencies of integrated PL intensity on excitation power.

Materials and Methods

The InGaN NWs were grown directly on p-type Si(111) substrates using Riber Compact 12 molecular beam epitaxy setup, equipped with Ga, In effusion cells, and a nitrogen plasma source. Prior to growth, the substrates were heated up to a temperature of 920 °C and annealed for 20 min to remove the native oxide. The residual pressure in the chamber was $7 \cdot 10^{-8}$ Torr. Then, the substrate temperature was decreased and a plasma source was turned on. After reaching the temperature of 655 °C, gallium and indium shutters were opened simultaneously. The growth time of InGaN NWs was 20 hours.

We subjected the initial NW arrays to chemical treatment. Wet chemical etching was carried out in the solution KOH:H_2O (1:5) at a temperature of 75°C for 50 seconds to remove the GaN shell.

The morphology of the samples was studied by scanning electron microscopy (SEM Supra 25 Zeiss). Room temperature PL of the samples was excited by a continuous wave He-Cd laser with 325 nm wavelength. The laser spot diameter on the sample was about 1 μm. A silicon CCD

matrix was used as a detector. Time-resolved measurements of PL were carried out using optical gating by the upconversion method. The sample was pumped and optically gated using a Coherent Mira 900 D Ti:sapphire laser in the femtosecond mode with a 120 fs laser pulse duration and 76 MHz repetition rate.

Results and Discussion

It has been revealed enhancement of integral PL intensity's NWs with an etched shell relative to the initial NWs over the entire excitation power range. Define enhancement factor of PL intensity (EF) as:

$$EF = \frac{I_{etch.PL}}{I_{init.PL}} \qquad (1)$$

where $I_{init.PL}$ – integrated PL intensity of initial InGaN NWs, $I_{etch.PL}$ – integrated PL intensity of etched InGaN NWs. In this case, the EF varies and reaches a maximum value of 3 at an excitation power density of $6.4 \cdot 10^3$ W/cm^2. With a further increase in power, a decrease in the EF is observed, which we attribute to the photodegradation of the etched NWs. To determine the reasons for the increase in PL intensity, we used time-resolved PL spectroscopy. The results of measuring the PL kinetics at cryogenic and room temperatures showed an increase in the PL lifetime upon removal of the shell in the initial NWs. However, a detailed analysis of the time characteristics and possible mechanisms of PL enhancement will be discussed by us in further investigation.

Moreover, we note that the position of the PL bands of the samples saved with increasing laser power, which can confirm the direct-gap nature of the emission of these structures and, probably, the low number of defects. The values of the half-width at half-maximum for all samples didn't change regardless of the magnitude of the applied power, which is an advantage of these NWs as the active material of light-emitting devices.

In order to evaluate the luminescent properties of InGaN NWs with and without a shell, we analyzed the recombination processes in them using the ABC-model. It was done by fitting logarithm of excitation level as a function of logarithm of square root of integrated PL [4]. Experimental dependencies are well fitted with consideration of all three main mechanisms of recombination (Shockley-Read-Hall, radiative and Auger recombination). In both the case of NWs with a shell and in the case of NWs without a shell, radiative recombination predominates in the experimental range of pump power density.

Conclusion

This study should be useful for understanding the influence of shell on the luminescent properties of InGaN NWs. Analysis of the experimental dependence of integrated PL intensity on excitation power by the ABC model showed that etching the shell doesn't reduce the contribution of radiative recombination to InGaN NWs. Moreover, PL intensity enhancement was observed in the case of etched NWs. The results obtained can be useful for creating efficient LEDs based on molecular beam epitaxy growth InGaN NWs.

REFERENCES

1. Gridchin, V. O., et al. Multi-colour light emission from InGaN nanowires monolithically grown on Si substrate by MBE. Nanotechnology 32(33) (2021) 335604.

2. Roche, Elissa, et al. "Circumventing the miscibility gap in InGaN nanowires emitting from blue to red." Nanotechnology 29(46) (2018): 465602.

3. Shimosako, N., et al. "Carrier density dependence of localized carrier recombination dynamics in orange-emitting InGaN/GaN nanocolumns." Journal of Applied Physics 128(13) (2020).

4. Nadtochiy, A. M., et al. "InGaAs/GaAs hybrid quantum well-dot nanostructures: Impact of substrate orientation and recombination mechanisms." Journal of Physics: Conference Series. 917(3) (2017)

Evaluation of c-Si/CsPbBr3solar cells: afors-het thickness simulation and analysis of optoelectrical properties

Boudjemila Linda[1, 2], V. V. Davydov[1]
[1]Peter the Great Saint-Petersburg Polytechnic University, Saint Petersburg, Russia
[2] University Of Science And Technology Houari Boumediene, Algiers, Algeria
lariessai21@gmail.com

Abstract. The following work presents the study of the optoelectrical properties of the thin layer of CsPbBr3 nanoparticles by a numerical simulation using the afors-het program. The variation in thickness causes the internal dynamics of the electrical charge to change, as well as the optical properties. A potential in optoelectronic properties is considered.

Keywords: solar cell, photoelectric converters, nanoparticles, numerical simulation, optoelectrical properties.

Introduction

Currently, photovoltaic solar occupies the greatest interest among other types of renewable energy. Thanks to the abundance of materials on the earth's layer such as silicon and the infinite solar deposit on a human scale. In this work, a modeling of the optimal performance of a solar cell based on halide perovskite nanoparticles (ABX3). This heterojunction was carried out in order to improve the efficiency of solar cells by benefiting from existing techniques in the industrial field such as PECVD and the simplicity of the manufacturing process of perovskite materials without forgetting the low cost of manufacturing. The mobility of the charges of this heterostructure was previously studied by experimentation in a laboratory presented in the previous work. The objective of this work is to model the optoelectronic parameters and the effect of thicknesses, temperature on the electrical characteristics of a Perovskite-based solar cell with a view to optimizing by simulation using the Afors-Het software. To simulate the physical characteristics (short-circuit current density, open circuit voltage Voc, Form factor FF, Conversion efficiency of the solar cell studied (μ).

Materials and Methods

The optimization of the cell studied is done by simulation. Optimization by simulation follows a mathematical model of the real system, it has the advantage of being easy, inexpensive and we can predict the optimal parameters which contribute to the manufacture of a cell with the best performance. AFORS-HET (Automat FOR Simulation of Heterostructures) is a program that was developed at Helmholtz-Zentrum Berlin für Materialien und Energie. Afors-Het is a digital simulation program for different types of third generation solar cells, i.e. homojunction or heterojunction solar cells. Using this program, we can carry out a complete optoelectronic study and analyze the results by varying some parameter such as thickness, chemical concentrations. We can obtain the output I–V curves, quantum efficiency, photo and electro luminescence and many other parameters can be calculated [1]

Results and discussion

In the solar cell studied, the active perovskite layer is sandwiched between the heterojunction cell located at the bottom and an HTM (Hole Transport Material) layer, thus creating a p-i-n configuration Fig.1. The transport layer must have high electron mobility and higher bandgap [2]. The success of perovskite as a solar absorber, incoming light can be absorbed by the perovskite within a thin layer of about 2 μm, depends largely on the long diffusion length of the charges and the high mobilities of the carriers in the medium. The operating principle of the perovskite-based solar cell is based on the absorption of photons by the active perovskite layer. The perovskite

absorber has a low exciton binding energy which indicates the generation of free charge carriers upon photon absorption and occurs within pico seconds. These generated free charge carriers are then transported to the Interface Contacts. During the transfer process, the desired process takes place in three steps: — Photo-excitation in the perovskite absorber. — Electron transfer in ETL. — Transfer of holes in HTL (or equivalent transfer of electrons from HTL to perovskite)

However, a large number of undesirable processes can occur. These processes consist of: — A recombination of photo-generated species. — A back charge transfer at the interfaces of HTL and TiO2 with perovskite. — Direct contact between HTL and TiO2.

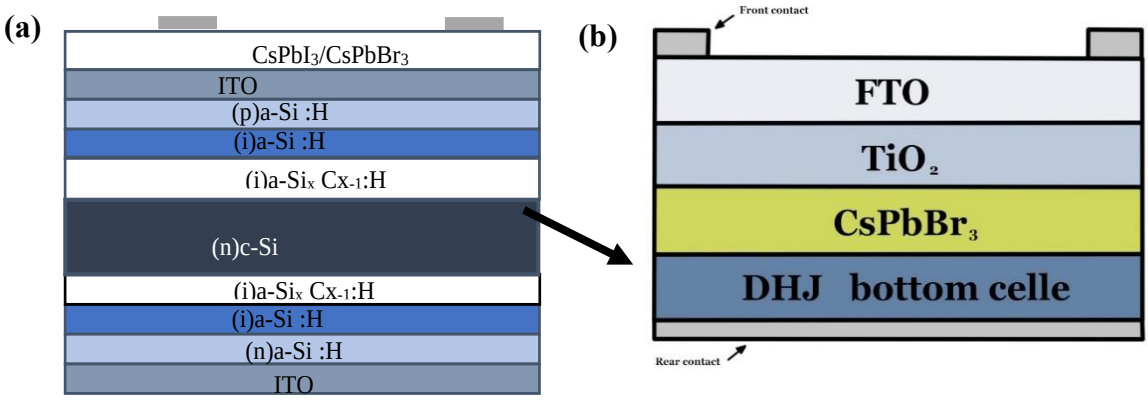


Fig.1. Structures of c-Si solar cells analyzed in this study: with (a) a doubled a-Si:H/c-Si heterojunction solar used as a bottom cell in this study [3] (b) flat c-Si hetero-junction solar cells.

By increasing the thickness, we have a reduction to 0. The effect of the thickness of the absorbent layer on the performance and form factor is very important because by increasing the thickness from 0.1 µm up to 0.5 µm, we notice a very interesting increase in efficiency until saturation, then it begins to decrease. The form factor decreases linearly with increasing thickness. By increasing the band gap energy from 1.4eV to 1.9eV (or the concentration of the absorbing layer), we will have a loss in current density of 8 (mA/cm2) and an increase of 0.47V at the output voltage.

Conclusion

Optimal performance of the mixed perovskite-based solar cell is envisaged to be determined by simulations using Afors-het software. Variation in the thickness of the perovskite layer controls the quality of the solar cell by modifying the diffusion length and their mobilities. Simulation results predict higher optimal conversion efficiency than c-Si monojunction solar cells.

REFERENCES

1. **Lee T. D. et al.** A review of thin film solar cell technologies and challenges Renew, Sustain. Energy Rev.36 (2017) 786-794.

2. **Chakrabarti T., Saha M., Khanda A., Sarkar S. K.** Modeling of lead-free ch 3 nh 3 sni 3-based perovskite solar cell using zno as etl. In Advances in Communication, Devices and Networking, Proceedings of ICCDN 2017, Springer, 2018, 125–131.

3. **Boudjemila L., Davydov V. V., Aleshin A. N., Malyshkin V. M., Terukov E. I.** Electrical characteristics of CsPbI3 and CsPbBr3 lead halide pervoskvite nanocrystal films deposited on Si-c solar cells for high-efficiency photovoltaics, St. Petersburg State Polytechnical University Journal. Physics and Mathematics. 15 (3.2) (2022) 91–96.

Эластичный электрод на основе текстурированных одностенных углеродных нанотрубок для гибкой электроники

Кочетков Ф. М.[1], Колесина Д.Е.[1,2] Кочетков Ф. М.[1], Воробьёв А. А.[1], Новикова К.Н.[1], Голтаев А.С.[1], Неплох В.В.[1], Мухин И. С.[1,2]

1. СПбАУ РАН им. Ж. И. Алфёрова, 194021, ул. Хлопина, 8, к. 3, Санкт-Петербург.

2. СПбПУ им. Петра Великого, 195251, ул. Политехническая, дом 29, Санкт-Петербург.

УДК: 538. 911

Одним из современных направлений исследований в области физики полупроводников является разработка и исследование органических светодиодов на основе нитевидных нанокристаллов (ННК) А3Б5. ННК могут быть инкапсулированы в полимерную матрицу полидиметилсилоксана (ПДМС) и электрически соединены с прозрачными растяжимыми электродами, так как мембраны способны к растяжению. В качестве растяжимого электрода наиболее эффективными являются тонкие слои одностенных углеродных нанотрубок (ОУНТ), нанесенные на пленки из ПДМС. ОУНТ сохраняют высокие эксплуатационные характеристики при упругой деформации, а также обладают стабильным электрическим контактом к ННК. Для сохранения электропроводности и оптической прозрачности при растяжении наносится рисунок методом оптической литографии [1].

В работе рассматривается технология изготовления растяжимого электрода на основе ПДМС/ОУНТ. Электроды были созданы методом оптической литографии на ОУНТ с использованием жертвенного слоя полиметилглутаримида (ПМГИ), который был отделен от стекла растворением в диметилсульфоксиде. Формирование рисунка осуществлялось травлением в плазме O_2. Для создания растяжимого устройства массив GaP ННК был инкапсулирован в ПДМС методом гравитационной накрутки и отделен от ростовой подложки. С устройством проведены тесты на растяжение и измерены вольтамперные характеристики.

Работа выполнена при поддержке РНФ №23-79-01151.

Список используемых источников

1. Mukhangali S. et al. Elastic single-walled carbon nanotubes pixel matrix electrodes for flexible optoelectronics //Applied Physics Letters. – 2022. – Т. 121. – №. 24.

Rapidly varying and static pressure sensor

D.V. Agafonov [1]✉, S.A. Gurin [1], M.D. Novichkov [1], A.E. Shepeleva[1], A.A. Ryzhov[1], D.V. Deryabin[1]

[1] Penza Scientific Research Institute of Electronic and Mechanical Devices (NIIEMP), Penza, Russia

✉dmitryagafonov@list.ru

Abstract. The development of a design and technological solution for the sensitive element of a static and rapidly varying pressure sensor based on the integration of strain gauge and piezoelectric films of nanometer size, which made it possible to create a multifunctional sensitive element with small pressure deviations from actual values is presented.

Keywords: sensitive element, pressure, pressure sensor, strain gauge, piezoelectric thin films.

Introduction

The current stage of information and measurement systems development for the management and control of special equipment is characterized by increasing requirements for stability, reliability and speed in such areas as the automobile industry, oil production and nuclear energy [1-3]. The most important parameter for measurement and monitoring is pressure, with which you can prevent the possibility of emergency situations and at the same time save human lives [4]. In this regard, the number of pressure sensors inevitably increases.

Experimental technique

The pressure sensor (figure 1) is based on a round silicon membrane with a rigid center. The substrate surface is oxidized until an oxide with a thickness providing reliable electrical insulation. Four X20N75Yu nichrome strain gauges to it, made on the basis of thin-film heterostructures with a low temperature coefficient of resistance (no more than 5 ppm) due to a combination of nanometer-thick layers with different mechanical and electrical characteristics are applied. Film piezoelectric transducers of the bending type are characterized by a combination of high sensitivity characteristic for bulk ceramic piezoelements, and high quality factor provided by the nano-sized thickness of the piezofilm [5].

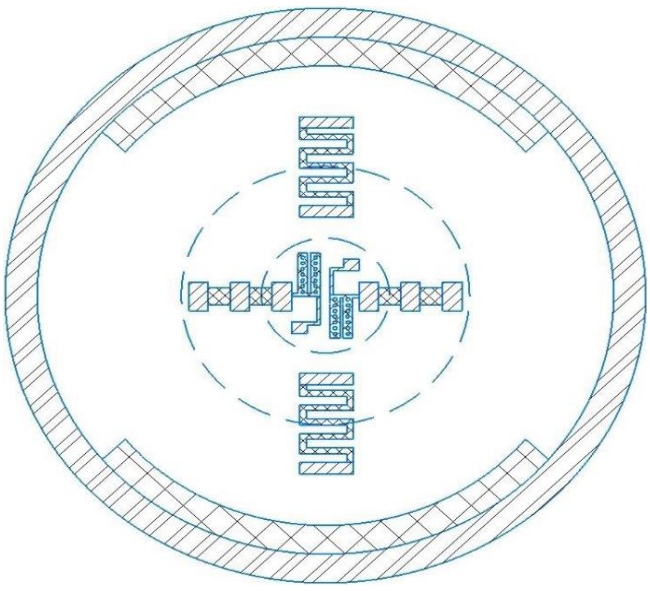


Figure 1. Топология чувствительного элемента

Results and Discussion

The technical characteristics of the developed pressure sensor and currently manufactured analogues are shown in Table 1.

Table 1 – Technical characteristics of the developed sensor

Pressure sensor	Measuring range, MPa		Basic measurement error, %	Temperature of the measured medium, °C
	dynamic	static		
Developed pressure sensor	0,05…25	2,8…63	±1	-60…+250
DPS	0,12...5,6	22,4...125	8	-30...+200
Vt 309	0,25...5,6	11...90	10	-196...+200

The presented sensor with the above characteristics is simple in design, reliable in operation, has a long service life, small size and fast response.

Conclusion

The design of the pressure sensor have been determined for the production of highly sensitive and thermally stable strain gauges from the X20N75Yu alloy and piezoelectric transducers from ZnO deposited on an elastic silicon membrane using magnetron sputtering, which make it possible to obtain the specified properties of thin films and enhanced heat removal at increased electrical loads.

REFERENCES

1. **Belozubov E.M., Vasil'ev V.A., and Gromkov N.V.** Problems and Basic Research Directions in the Field of Thin-film Nano- and Microelectromechanical Systems of Pressure Sensors // Automation and Remote Control – USA, Pleiades Publishing, Ltd., 2011, Vol. 72, No. 11, p. 345 – 352.

2. **D V Ryabov, E A Pecherskaya, J V Shepeleva and R M Pecherskaya** 2014 Automated method of measuring the temperature dependences of the dielectric parameters of ferroelectrics with second kind phase transition J. Phys.: Conf. Ser. 541 012012.

3. **C W Khor, C Leung and O Le Neel** 2012 Reliability analysis of CrSi Thin Film Resistors Proc. 19th IEEE International Symposium on the Physical and Failure Analysis of Integrated Circuits pp. 1–4.

4. **Zelentsov Y A and Zelentsov V Y** 2007 An investigation of the relation between the temperature dependences of the initial unbalance and the output signal of resistance strain sensor bridge circuits Measurement Techniques 50(1) 66-8.

5. **Fimin A V, Gurin S A, Pecherskaya E A, Golubkov P E, Kozlov G V and Kraynova K Y** 2019 Sensitive elements of microelectronic sensors of fast variable and static pressure Journal of Physics: Conference Series 1410(1) 156697.

Thermal entanglement in three-qubit Tavis-Cummings model with many-photon transitions

A. R. Bagrov [1]✉, **E. K. Bashkirov** [1]

[1] Samara National Research University, Samara, Russia

✉alexander.bagrov00@mail.ru

Abstract. In this paper, we consider the model consisting of an isolated qubit and two qubits trapped in a lossless resonator and interacting with resonator thermal field via many-photon transitions. We obtain the exact solution of the model under consideration. On its basis we calculate the negativity as a measure of pair qubits entanglement. It is shown that, for many-photons processes entanglement is stronger than for that in the linear one-photon processes and can suppress the sudden death of qubit-qubit entanglement.

Keywords: qubits, thermal field, entanglement, many-photon transitions, sudden death of entanglement.

Introduction

The quantum entanglement is now seen as a necessary resource to help with information processing tasks. Two-qubit and multi-qubit entangled states enable for quantum computation and other operations. At present there are a number of theoretical and experimental works devoted to investigation of the properties of entangled states. But the quantitative entanglement criteria are currently only defined for two-qubit states. For many-qubit system, the situation is more involved as there exist several inequivalent classes of entanglement. For the simplest case of three-qubit system, all pure and mixed states are classified into three types. They are separable, biseparable and genuine entangled GHZ and W states [1]. The genuine entangled GHZ and W states are not equivalent under the stochastic local operations and classical communication (SLOCC). The quantum information processing require maximally entangled states. However, through interaction with environment the decoherence usually occurs. Kim and co-author showed that a chaotic field of the resonator can entangle two atoms [2]. Later a number of authors investigated the entanglement induced by a thermal cavity in two-qubit (see Refs in [3]) and three-qubit systems [4]. In [5] the authors considering the dynamics of two-atom two-photon Jaynes-Cummings model (JCM) showed that the entanglement induced by nonlinear interaction is larger than that induced by linear one-photon interaction. This result motivated us to focus our attention on studying the thermal three-atom JCM with multi-photon transitions.

Model and its solution

We consider a system consisting of three identical qubits A, B and C. Two qubits B and C resonantly interact with the quantized electromagnetic field of the resonator. The qubit A can move freely outside the resonator. The Hamiltonian of the interaction of such a system in the dipole approximation and the rotating wave approximation can be written as

$$H = \sum_{l=1}^{3} \hbar\gamma(\sigma_l^+ c^m + \sigma_l^- c^{+m}), \tag{1}$$

where $\sigma_l^+ = |e\rangle_{ll}\langle g|$ and $\sigma_l^- = |g\rangle_{ll}\langle e|$ are the transition operators between the excited $|e\rangle_l$ and the ground $|g\rangle_l$ states in the l-th qubit ($l = 1,2,3$), c^+ and c are the creation and the annihilation operators of the photons, γ is the qubit-photon coupling. The initial qubits state is assumed to be biseparable such as $|\Psi_1(0)\rangle_{ABC} = \cos\alpha\,|e,g,g\rangle + \sin\alpha\,|g,e,g\rangle$ or $|\Psi_2(0)\rangle_{ABC} = \cos\alpha\,|e,g,e\rangle + \sin\alpha\,|g,e,e\rangle$. The initial cavity field state is assumed to be thermal $\rho_F(0) = \sum_k w_k\,|k\rangle\langle k|$, where $w_k = \bar{k}^k / \left(1+\bar{k}\right)^{k+1}$ and $\bar{k}$ is the mean thermal photon number $\bar{k} = \left(\exp\left[\hbar\omega / k_B T\right] - 1\right)^{-1}$, k_B is the Boltzmann constant and T is the resonator temperature.

We derived the exact solution of the quantum Liouville equation for whole density matrix $\rho(t)$. By averaging over the field and third qubit variables, we found the reduced qubit-qubit density matrix and calculated negativity for the pairs of qubits.

Results and Discussion

In Fig 1 we plot the time-dependence of negativities ε_{12} and ε_{23} for initial qubits state $|\Psi_1(0)\rangle_{ABC}$ with $\alpha = \pi/4$ and different values of photon multiple. One can see from Fig. 1 that the entanglement sudden death (ESD) effect takes place for small values of photon multiple m and disappears for large values of the mentioned parameters. One can also see that the entanglement from one pair of atoms transfers to other pairs of atoms in the evolution process. The results of numerical calculations of pairwise negativities for another state $|\Psi_2(0)\rangle_{ABC}$ showed that the time behavior of ε_{12} and ε_{13} is similar to that for state $|\Psi_1(0)\rangle_{ABC}$. But thermal field does not induce entanglement of atom 2 and 3 for all values of model parameters.

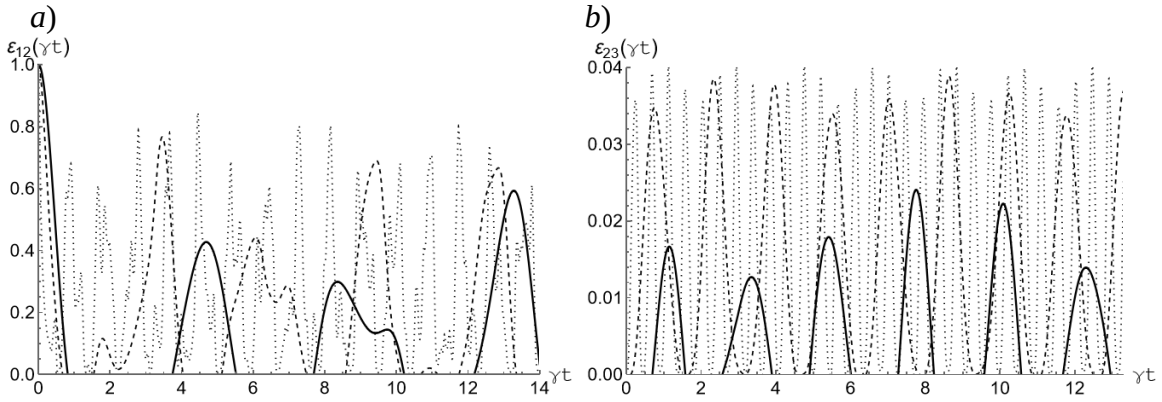


Fig. 1. The negativity criterion ε_{12} (a) and ε_{23} (b) vs scaled time γt for initial qubits state $\cos\alpha\,|e,g,g\rangle + \sin\alpha\,|g,e,g\rangle$. The photon multiple $m=1$ (solid), $m=2$ (dashed), $m=4$ (dotted). The mean photon number $\bar{k}=1$ (a) and $\bar{k}=0.1$ (b).

Conclusion

In this paper, we studied the dynamics of a system of three identical qubits, one of which is in a isolated state, and the other two are trapped in an ideal resonator and interact resonantly with the mode of the electromagnetic field of this resonator through multiphoton transitions. The biseparable states of qubits and thermal state of field were in the focus of our attention. To investigate the entanglement of the pair of qubits we calculated the negativity. For biseparable states ESD effect takes place for small values of multiples and disappears for large values of mentioned parameter. The transition of entanglement from one pair of atoms to other pairs of atoms in the evolution are also observed.

REFERENCES

1. **Dur W., Cirac J. I.,** Classification of multiqubit mixed states: Separability and distillability properties, Phys. Rev. A. 61 (2000) 0423149(1-11).

2. **Kim M. S, Lee J., Ahn D., Knight P. L.,** Entanglement induced by a single-mode heat environment**,** Phys. Rev. A. 65 (2002) 040101(R) (1-4).

3. **Bashkirov E. K.,** Thermal entanglement in Tavis-Cummings models with Kerr media, SPIE Proc. 12193 (2022) 121930Q(1-8).

4. **Cai J.-F., Liu H.-P.,** Entanglement in Three-Atom Tavis Cummings Model Induced by a Thermal Field, Commun. Ther. Phys. 43 (2005) 427-431.

5. **Zhou L., Song H. S.,** Entanglement induced by a single-mode thermal field and criteria for entanglement, J. Opt. B. 4 (2002) 425-429.

Optimization of superconducting adiabatic neural network implementing boolean function

M. V. Bastrakova [1]✉, **D. S. Pashin** [1], **A. E. Schegolev** [1,2], **N. V. Klenov**[3], I. **I. Soloviev**[2]
[1] Lobachevsky State University of Nizhny Novgorod, Nizhny Novgorod, Russia;
[2] Skobeltsyn Institute of Nuclear Physics, Lomonosov Moscow State University, Moscow, Russia
[3] Faculty of Physics, Lomonosov Moscow State University, Moscow, Russia
✉bastrakova@phys.unn.ru

Abstract. In this article, we consider designs of simple analog artificial neural networks based on adiabatic Josephson cells with a sigmoid activation function. A new approach based on the gradient descent method is developed to adjust the circuit parameters, allowing efficient signal transmission between the network layers. The proposed solution is demonstrated on the example of the system implementing XOR and OR logical operations.

Keywords: hardware implementation of neural networks; superconducting quantum interferometer; quantum parametron; optimisation procedure; nonlinear dynamics.

Funding: This study was funded by rant of the Russian Science Foundation grant number 22-72-10075.

Introduction

A distinctive feature of the current era of information technology evolution is the development and implementation of artificial intelligence (AI). The most popular and promising hardware implementations are the so-called neuromorphic chips or neuromorphic processors. There are a number of technology platforms that ensure the implementation of technologies at the hardware level, promising advances in operational and/or energy-efficient characteristics. Photonic-superconducting interfaces and other hybrid optical-superconducting neural networks are an important part in the development of this field of applied science. These systems use light pulses to transmit signals, and superconducting circuits based on quantum interferometers to process and store information.

Previously, we presented the concept of an adiabatic interferometer-based superconducting neuron (*S*-neurons) [1, 2] with ultra-low energy dissipation per operation (in the zJ range). The development of an adiabatic perceptron requires the realization of a large number of connections between neurons via superconducting synapses [3]. Combining these elements into an analog network implies the generally difficult task of studying the complex nonlinear dynamics of the system. In this article we propose a solution to this problem and demonstrate the results on the example of a three-neuron network simulation an XOR and OR logic gate.

Methods

The classical logic element XOR (logical inequality operator) has two inputs and one output, and in cases where the input signals do not match, the output should be “1”, in all other cases – “0”. The basic superconducting neural network demonstrated in this paper and performing the role of the above-mentioned logic element will consist of three S-neurons (two input and one output), see Fig. 1 (a).

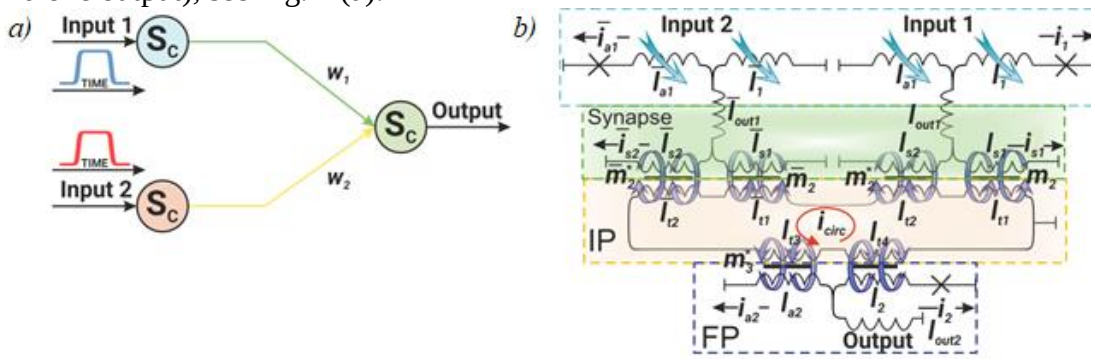


Fig. 1. *(a)* Schematic representation of the 3-neural network XOR and (b) its superconducting implementation.

Signals of different levels will be sent to the input of the neural network, in the form of smoothed trapezoids (see Fig. 1 (a)), corresponding to the logical “0” and “1”, respectively. The optimization task is reduced to finding such system parameters at which the output layer neuron will fire in accordance with the truth table for the XOR logic element. The scheme in Fig. 1 is described by a system of 5 Kirchhoff equations at nodal points and 7 phase balance equations. Solving the optimization problem based on gradient descent methods for this system of equations allows you to set up a neural network to work as the simplest boolean operations XOR and OR.

Results and Discussion

For the developed neural network configuration, it will be important to choose the values of the weighting coefficients: for XOR they must be antisymmetric, and for OR they must be symmetric. In case of deviation from this principle, a result will be obtained at the network output that does not match the truth table for these elements. In Fig. 2 schematically shows the truth tables for the resulting neural networks. The case of no signal at the input of both input neurons is not shown: if there is no signal at both inputs of the circuit, then there is no signal at the output (“0” + ”0” = ”0”).

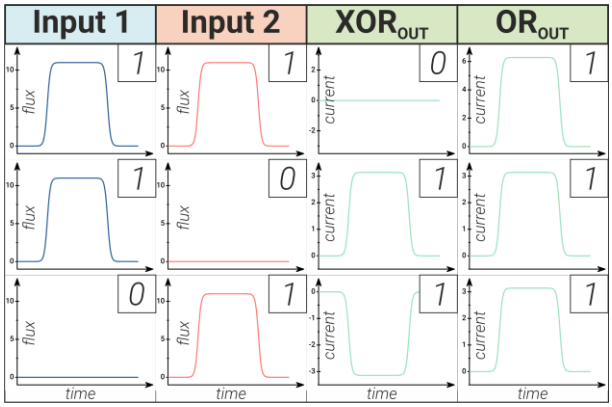


Fig. 2. Demonstration of the implementation of a neural network with XOR and OR logic.

Regarding the analog logic element OR, it is worth noting one point: in the case of classical digital OR, if two “1” signals are applied to the input, then the output will also generate a “1” signal with the same level as the input (features of digital circuits). In our case, if two “1” signals are applied to the input, then an analog signal will be generated at the output, the level of which is twice as high as in both cases (“1” + “0” or “0” + “1”).

Conclusion

In this paper, we proposed and calculated the original configuration of a simple artificial neural network based on superconducting adiabatic cells with Josephson junctions with a sigmoidal activation function. Optimized parameters of the circuit operation for performing the simplest boolean operations are found.

REFERENCES

1. **Bastrakova M., Gorchavkina A., Schegolev A., Klenov N., Soloviev I., Satanin A., Tereshonok M.** Dynamic processes in a superconducting adiabatic neuron with non-shunted Josephson contacts, Symmetry 13 (2021) 1735.

2. **Bastrakova M. V., Pashin D. S., Rybin D. A., Schegolev A. E., Klenov N. V., Soloviev I. I., Gorchavkina A. A., Satanin A. M.** A superconducting adiabatic neuron in a quantum regime, Beilstein Journal of Nanotechnology 13 (2022) 653.

3. **Schegolev A., Klenov N., Soloviev I., Tereshonok M.** Learning cell for superconducting neural networks, Superconductor Science and Technology 34 (2020) 015006.

Percolation dynamics in the memristive system Ag nanoparticles - HfO_x

Yu. O. Vasilevskaya [1,2]✉, **A. I. Savitskiy** [1], **K. I. Litvinova**[1], **R. T. Sibatov**[1,2]
[1] Scientific-Manufacturing Complex «Technological Centre», Zelenograd, Russia
[2] Institute of Integrated Electronics, National Research University of Electronic Technology (MIET), Zelenograd, Russia

✉fedorovauo@mail.ru

Abstract. Research in the field of neuromorphic computing allows us to hope for the creation of more productive and energy-efficient computing systems, as well as the development of new machine learning algorithms based on simulating the principles of brain functioning. This work examines percolation memristive systems of silver nanoparticles in a dielectric matrix of hafnium oxide. The conductivity of the nanoparticle system is ensured by the formation of atomic filament threads between the adjacent nanoparticles with the formation of at least one conductive cluster between the electrodes. The systems exhibit hysteresis on the I-V curves, which manifests itself when a sawtooth change in the electric current being applied. The results may be useful for understanding and controlling memristive behavior in nanoparticle systems that can be used in neuromorphic computing.

Keywords: percolation network, metal nanoparticles, resistive switching, filament, neuromorphic computing.

Funding: The work was supported by the Ministry of Science and Higher Education of the Russian Federation (project FNRM-2022-0008).

Introduction

The exponential growth of electronics and computing capabilities, as well as advances in CMOS technology, have opened up opportunities for the implementation of machine learning and artificial intelligence algorithms. Memristive devices and memristive architectures are considered as promising alternative solutions in next-generation computing technologies [1]. Memristive devices have demonstrated capabilities for data storage, digital and logic applications, and neuromorphic data processing by emulating neural and synaptic dynamics for brain-like computing, and options for hardware implementation of artificial neural networks [2].

In this work we present a study of the percolation memristive ensembles of nanoparticles. These systems comprise metallic nanoparticles (or, e.g., nanowires) arranged between metal electrodes. When a voltage is applied, a conductive cluster forms, bridging the gap between the electrodes, transitioning system from an insulating to conducting state. Conductivity is achieved through atomic pathways connecting nanoparticles. These percolation networks with plasticity look like a promising alternative compared to the crossbar systems [3]. They are well suited for use in reservoir computing, which requires complex systems with short-term memory and space-time correlations. Moreover the manufacturing technology is less complex and needs no high-precision and expensive lithography processes.

Materials and Methods

To investigate electrical properties, planar structures of thermally oxidized silicon substrates (100 nm thick layer of SiO_2) were used. These structures featured two opposing gold electrodes arranged in an interdigital pattern, with pins measuring 12 μm in length and 10 μm in width, separated by a 2 μm gap (figure 1). Within this gap, an array of silver nanoparticles was positioned using the vacuum thermal evaporation method. The size and density of these particles were finely tuned by controlling the amount of material evaporated (Ag ~ 4.7 mg). Metal deposition onto the sample surface was achieved through a metal mask with a strategically placed opening in the interelectrode gap area, partially covering the electrodes. The distance between the evaporator and the deposition surface was maintained at 20 cm. After Ag deposition, only a few samples were subjected to further vacuum annealing (230°C) to reveal the

effect of annealing on memristive properties. Samples with a thin layer of HfO_x (layer thickness 15 nm) were synthesized using the atomic layer deposition method.

Results and Discussion

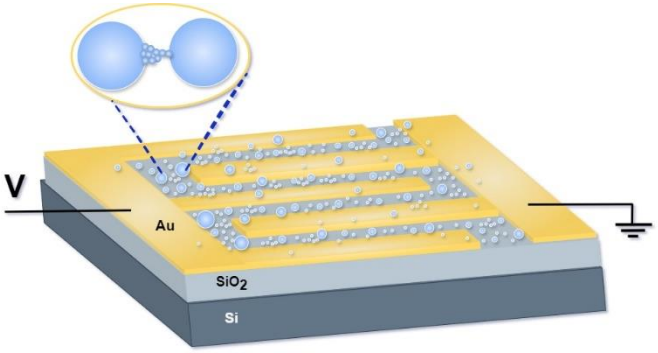


Fig. 1. Schematic illustration of a typical experimental sample structure

After the application of constant voltage, systems passed from a capacitive to a memristive state. Figure 2 presents the obtained dependences for percolating nanoparticle systems. However, the graphs do not cross zero, which indicates the presence of its own “nanobattery”.

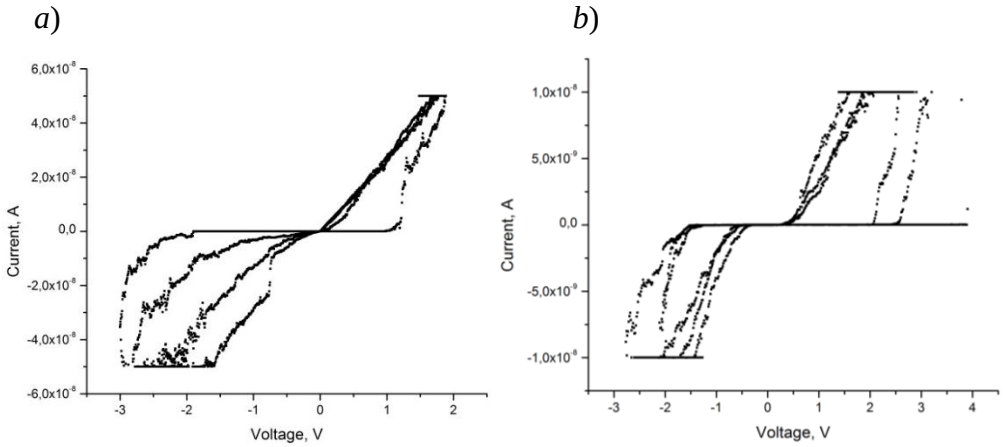


Fig. 2. Voltammograms of the structure with (a) Ag nanoparticles and (b) Ag nanoparticles coated with hafnium oxide; graphs include three cycles

Conclusion

The work achieved electrical characteristics for ensembles of silver nanoparticles with and without coating them with a dielectric layer of hafnium oxide. Hafnium oxide showed no negative effect on the memristive behavior of the nanoparticle ensemble and was used to isolate the structure from environmental influences. The results could hold significant implications for comprehending and controlling memristive behavior potentially leading to advancements in neuromorphic computing applications.

REFERENCES

1. **Mikhaylov, A. N., Gryaznov, E. G., Koryazhkina, M. N., Bordanov, I. A., Shchanikov, S. A., Telminov, O. A., Kazantsev, V. B.**, Neuromorphic computing based on CMOS-integrated memristive arrays: current state and perspectives, Supercomputing Frontiers and Innovations. 10 (2) (2023) 77-103.

2. **Milano G., et al.**, Quantum conductance in memristive devices: fundamentals, developments, and applications, Advanced Materials. 34 (32) (2022) 2201248.

3. **Zhang G., et al.**, Functional Materials for Memristor-Based Reservoir Computing: Dynamics and Applications, Advanced Functional Materials. 33 (42) (2023) 2302929.

GREEN SYNTHESIS OF TITANIUM NANOPARTICLES SUITABLE FOR CREATING TRANSPARENT ELECTRODES

A. A. Vodyashkin [1]✉

[1] Bauman Moscow State Technical University, Moscow, Russia;

✉av.andrey2013@yandex.ru

Abstract. This work presents a green method for producing titanium dioxide nanoparticles. The resulting nanoparticles were characterized using DLS, XRD, FTIR, and SEM. The resulting nanoparticles consisted of an anatase phase with small admixtures of brookite and an amorphous phase, which is associated with organic substances from the extract. Titanium nanoparticles showed high colloidal stability induced using rosehip extract. The developed particles have a high potential for use as one of the components for creating transparent electrodes.

Keywords: nanoparticles, TiO2, transparent electrodes, dynamic light scattering, green synthesis

Funding: the research was carried out within the state assignment of the Ministry of Science and Higher Education of the Russian Federation (theme No. FSFN-2024-0016)

Introduction

Nanoparticles of various materials are becoming increasingly important in various areas of human activity [1]. TiO2 nanoparticles are one of the most promising materials that cover the widest fields from photocatalysis to biomedicine. It is especially worth noting that highly porous and structured coatings of TiO2 nanoparticles can be used as transparent electrodes on various materials. To increase the specific surface area during the synthesis of nanoparticles, various coating agents can be used [2].

Green methods are promising ways to obtain titanium nanoparticles. Such methods provide high stability, as well as a developed surface due to the use of biologically active substances that act as coating agents [3]. It is important to note that such methods are easily scalable and environmentally friendly technologies that can be used in a wide variety of fields, including the creation of transparent electrodes.

Materials and Methods

Particle synthesis: Rose hip plant extract was obtained by sonicating rose hips for 20 min at 40 °C, after which the solution was filtered twice. Titanium nanoparticles were obtained by the sol-gel method in which a volume of 100 ml of acidified water (pH 4) was heated to 75 °C and a solution consisting of 8.5 ml of titanium isopropoxide, 6.5 ml of 2-propanol and 10 ml of rose hip extract was introduced. After incubation for 90 min. heating was stopped, and stirring was continued for another 72 h. The resulting particles were dried on a rotary evaporator and dispersed for further experiments.

Dynamic light scattering, scanning electron microscopy, X-ray diffraction analysis, IR spectroscopy, UV-visible spectroscopy, and electrophoretic light scattering were used to analyze the particles.

Results and Discussion

Titanium dioxide nanoparticles obtained using plant materials had an average size of 21 nm according to DLS data. It is worth noting that the particles maintained their size over 3 months, which was confirmed using DLS and visible spectroscopy. High stability can be ensured due to the biologically active substances included in the extract. Figure 1 shows a diffraction pattern of titanium dioxide nanoparticles. As can be seen in Fig. 1, the presence of a crystalline phase of Anatase (data no. 21-1272 IDD PDF-2) in the form of nanoparticles (broad peaks) and an X-ray amorphous, possibly organic phase, which is associated with the use of the extract, is noticeable. In addition, the sample contains the Brookite phase (data no. 15-875 IDD PDF-2) - a characteristic small peak in the region $2\theta \sim 30{,}7^{o}$.

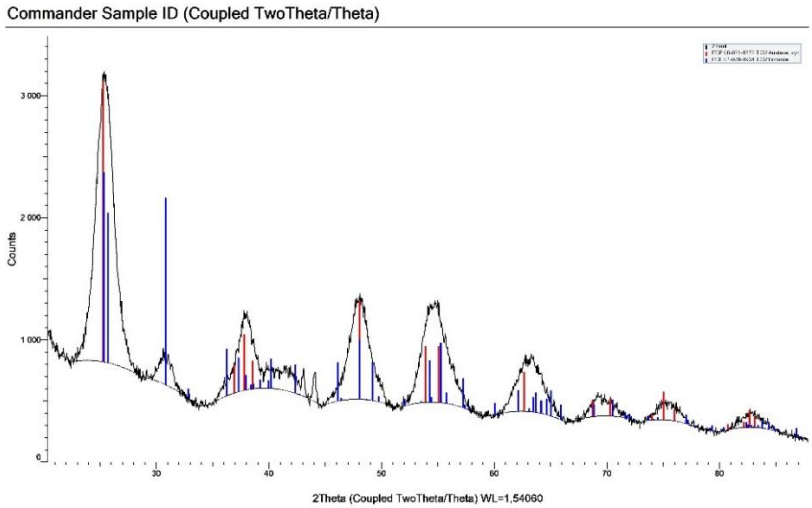


Fig. 1. X-ray diffraction pattern TiO2

Figure 2 shows the FTIR spectrum of the resulting nanoparticles. The band at 1628 cm^{-1} corresponds to asymmetric C=O stretching of carboxyl groups. The strong absorption band at 1384 cm^{-1} correspond to C–O stretching from alcohol, carboxylic acid, ester and ether.

The results of FTIR spectrometry confirm that the synthesized nanoparticles are stabilized by biologically active components of rosehip fruit extract, including organic acids, flavonoids, tocopherols and ascorbic acid.

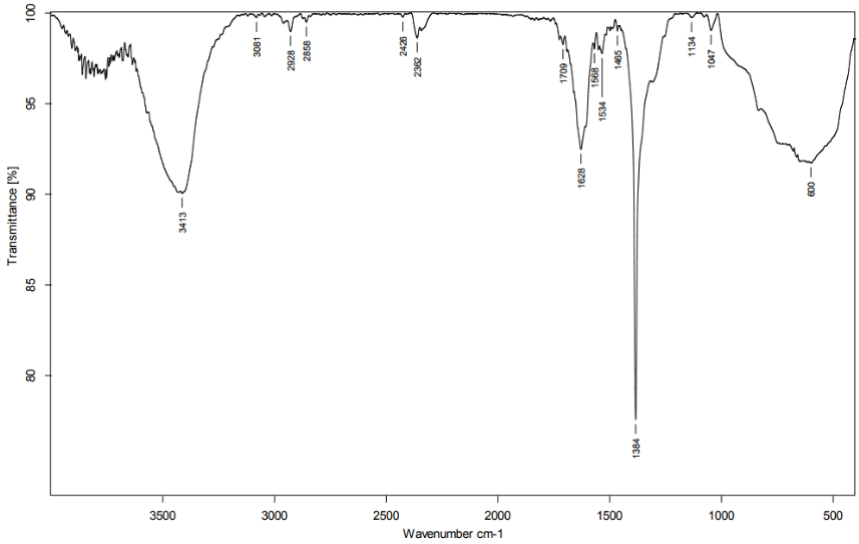


Fig. 2. FTIR spectra of TiO2 nanoparticles

Conclusion

This research shows how to make titanium dioxide nanoparticles using XRD and DLS. Due to the use of plant extract during synthesis, nanoparticles have a high colloidal stability and a developed surface. The properties obtained provide a high potential for the applicability of the developed nanoparticles in the creation of transparent electrodes.

REFERENCES

1. **Mitchell, Michael J., et al.** "Engineering precision nanoparticles for drug delivery." *Nature reviews drug discovery* 20.2 (2021): 101-124.

2. **Verma, Vishal, et al.** "A review on green synthesis of TiO2 NPs: photocatalysis and antimicrobial applications." *Polymers* 14.7 (2022): 1444.

3. **Zhang, Shan-Ting, et al**. "Tuning the properties of F: SnO 2 (FTO) nanocomposites with S: TiO 2 nanoparticles–promising hazy transparent electrodes for photovoltaics applications." *Journal of Materials Chemistry C* 5.1 (2017): 91-102.

Digital signal processing in the process of measuring parameters of magnetic materials

A. V. Volik ✉, E. A. Pecherskaya, Yu. A. Varenik
Penza State University, Penza, Russia;
✉ minor401@gmail.com

Abstract. The principles of digital signal processing in the form of electrical voltage, which contain the information necessary for indirect measurement of magnetic induction, magnetic field strength, magnetic permeability and other parameters of magnetic materials are outlined. The structure of the processor module is presented, which implements the technique for measuring the parameters of magnetic materials and monitors the serviceability of the measuring installation. An interface has been developed that allows remote control of an information-measuring system for measuring the parameters of magnetic materials.

Keywords: magnetic materials, digital processing, magnetic induction, coercive force, measurement, processor module.

Introduction

Modern electronics is developing towards the widespread use of digital signal processing, which is performed in various ways and methods: using general-purpose microcontrollers, programmable logic integrated circuits (FPGAs), digital controllers (DSP) [1].

Digital signal processing methods are the most effective, as they provide more stable temperature and time parameters and allow changing the coefficients of transfer functions. Digital signal processing methods have less impact on the signal output parameters. This is due to the absence of parasitic parameters inherent in passive components, such as capacitors and resistors, which are one of the components of analog integrator circuits.

Integrating circuits are used in various functional units: voltage-frequency converters, frequency-voltage converters, analog-to-digital converters, control units in automatic control systems, pulse generators, active analog filters [2]. As the device operates, it is necessary to change its parameters in the integrating circuit, namely the time constant, that is, to rebuild it. In turn, it is accompanied by transition processes that influence the result of integration.

The developed automated information-measuring system (IMS) for studying the parameters of magnetic materials is based on indirect measurements of magnetic induction and coercive force by integrating the secondary winding voltage and magnetizing current, respectively [3].

During the development process, it is possible to expand the functionality of the installation due to the modularity of the design. The main functional blocks of the measuring installation are: a standby power supply (provides power to the auxiliary units of the installation - a board with a microprocessor, operational amplifiers in the measuring channel, a board with a hardware integration module), a switching power supply (generates voltages for the magnetizing winding of the test sample), a processor module, integration module (performs numerical integration in hardware - is under development).

The processor module is based on an STM32F429 microcontroller. Figure 1 shows the block diagram of the processor module.

The processor module includes: SPI modules for interaction with the TFT display, UART and Ethernet for user interaction, built-in memory controller for data exchange with an external SDRAM chip, an analog-to-digital converter (ADC) using 4 channels, and a digital-to-analog converter (DAC) to set a code proportional to the magnetizing current value. Service and user information is stored in an external EEPROM memory chip. Channel 1 of the ADC is used to diagnose the power supply. Channel 2 receives readings from the current sensor of the current shaper, which sets the magnetic field strength. In channel 3, the EMF proportional to the magnetic induction is measured.

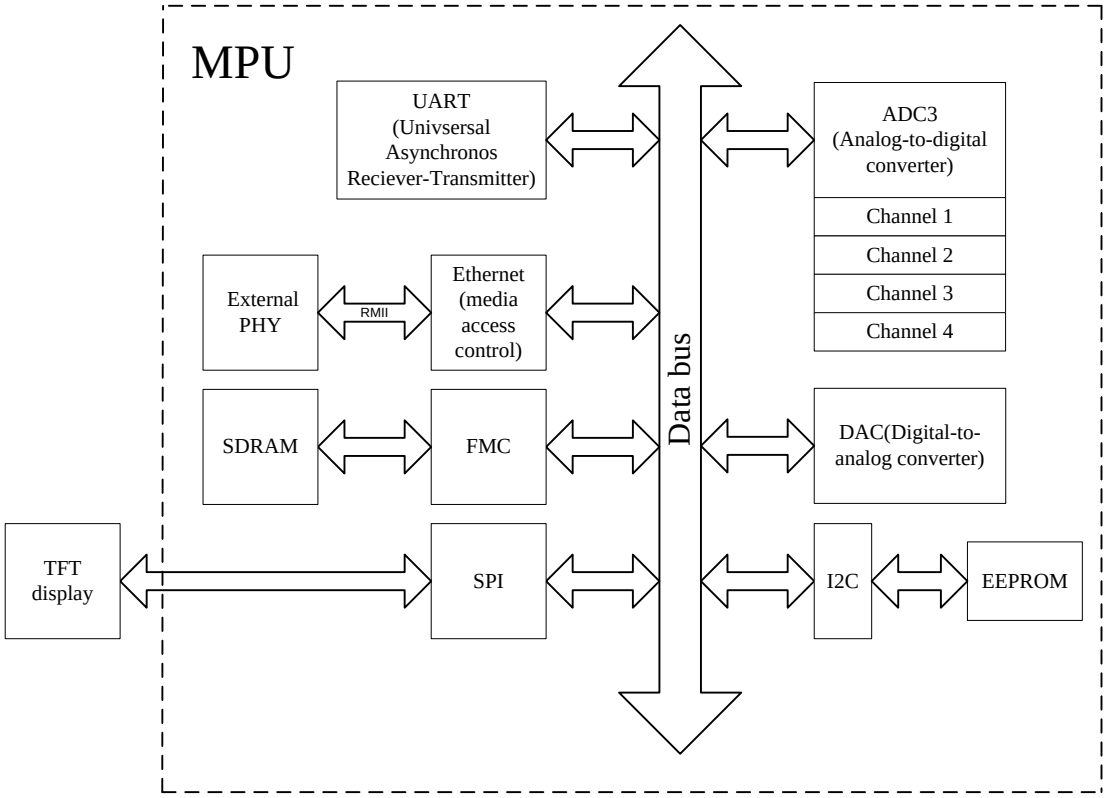


Figure 1. Structure of the processor module

The use of two interfaces allows to expand the functionality of the installation. Using the RS232 interface, you can configure installation parameters (setting Ethernet network parameters). Thanks to a special client application, measurement results are displayed on the monitor. The disadvantage of this approach is the dependence on the target platform on which the client application must be deployed. The Web Interface does not have this drawback, access to which is provided by the Ethernet interface. For its work, the current version of the web browser must be installed on the client computer. Based on the use of Web Interface, remote work with the measuring installation, which is advisable to use both for educational purposes when performing remote laboratory work, and in scientific research of magnetic materials and structures based on them is organized.

Acknowledgments

The work was supported by the grant of the Ministry of Science and Higher Education of the Russian Federation «Synthesis and research of promising nanomaterials, coatings and electronics devices» (FSGE-2024-0004).

REFERENCES

1. **Varfolomeev V.I., Zhenishek E.Yu, Lupin A.V., Minaev V., Sakharov N.V., Babaritskiy P.A.** Temperature control system for the electromagnetic system of the Globus-M2 tokamak, Technical Physics Letters. 48. 33. (2022) 10.21883/TPL.2022.08.55057.19264.

2. **Pecherskaya E.A., Artamonov D.V., Kondrashin V.I., Golubkov P.E., Karpanin O.V., Zinchenko T.O.** Software - Hardware Complex for Measurement and Control of Ferroelectrics Parameters, IOP Conference Series: Materials Science and Engineering, 225 (1) (2017) 012254.

3. **Volik, A.V., Pecherskaya, E.A., Varenik, Y.A., Zinchenko, T.O., Artamonov, D.V., Timohina, O.A.** Metrological aspects of an automated method for measuring electrophysical parameters of soft magnetic materials Journal of Physics: Conference Series, 2086 (1), 012072, (2021) DOI: 10.1088/1742-6596/2086/1/012072

Modeling of the scanning track formation in the selective laser melting process of 316L steel

A.A. Gajna[1], A.A. Mozhaiko[2]

[1]Peter the Great Saint Petersburg Polytechnic University, Saint Petersburg, Russia

[2]SIC "Kurchatov Institute" - Central Research Institute of KM "Prometheus", St. Petersburg, Russia

✉ ganja.aa@edu.spbstu.ru

Abstract. Selective laser melting (SLM) is a perspective method characterized by the application of metallic powder materials and the heating to melting temperature by a laser beam in such a way that the layer of metallic powder is fully molten throughout. The study focuses on the single laser track formation and the effects of laser radiation parameters on the melt pool size. The research aims to investigate the effects of three factors: laser power, scanning speed, and laser focal spot diameter, on the melt pool dimensions in a sample. A computational model constructed in COMSOL Multiphysics finite element software is used to predict the properties of the sample and determine optimal processing parameters. Results show that the melt width and depth depend on above laser parameters. Modeled results are verified by comparison with experimental samples. This research contributes to our understanding of SLM processes and provides valuable insights into optimizing processing parameters for achieving desired sample properties.

Keywords: selective laser melting, heat transfer modeling, finite element method, austenitic steel, melting pool

Introduction

One of the most advanced manufacturing processes in additive technologies is selective laser melting [1], which consists in sequential layer-by-layer melting of powder material under the influence of laser radiation. In this paper, we study the process of forming a single scan track during selective laser melting of austenitic 316L steel [2]. The dependences of the melt pool size on laser radiation parameters, such as power, scanning speed, and laser beam diameter, are determined.

Materials and Methods

Computer modeling is used to study the formation of a melt pool in the process of selective laser melting and allows predict the properties of the irradiated sample based on the calculation results. It can help determine the optimal mode for constructing a sample with the required properties. The COMSOL Multiphysics finite element package [3] was chosen as the main tool for calculating the selective laser melting process. Different modes were considered with a changing laser radiation power in the range from 100 W to 800 W, scanning speed from 100 mm/s to 800 mm/s, and focal spot diameter from 50 microns to 200 microns.

Results and Discussion

As a result of this work, we obtained dependences of melt pool width and depth on the parameters of laser radiation of numerical simulation. Results of modeling were compared with experimental samples (Fig. 1).

a) BE1 b) BE2 c) BE4,5

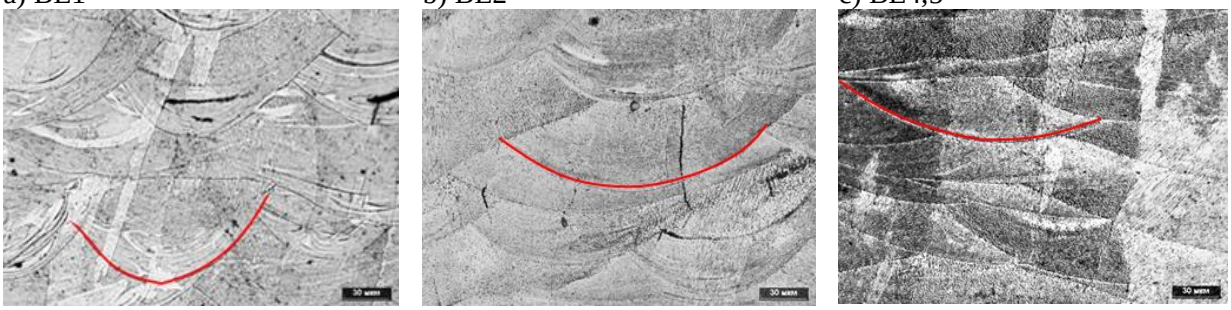


Fig. 1. The effect of the laser focal spot diameter on the melt pool geometry. Beam Expander: (a)

As the laser power increases, melt pool width and depth increases. The dependences of the laser focal spot diameter on melt pool width and depth do not change monotonously (Fig. 2). Also, as the scanning speed increases, all melt pool dimensions decrease (Fig. 3).

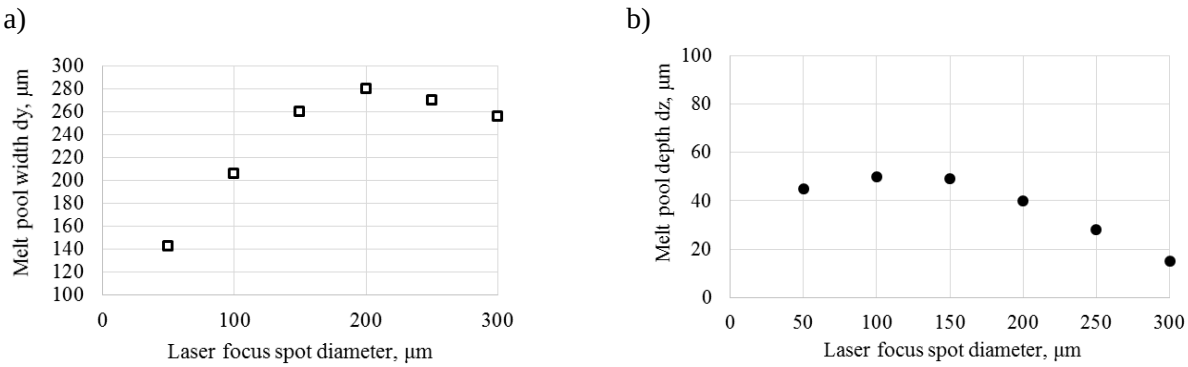


Fig.2. Dependence of laser focus spot diameter on the melt pool width (a) and depth (b) in simulation model

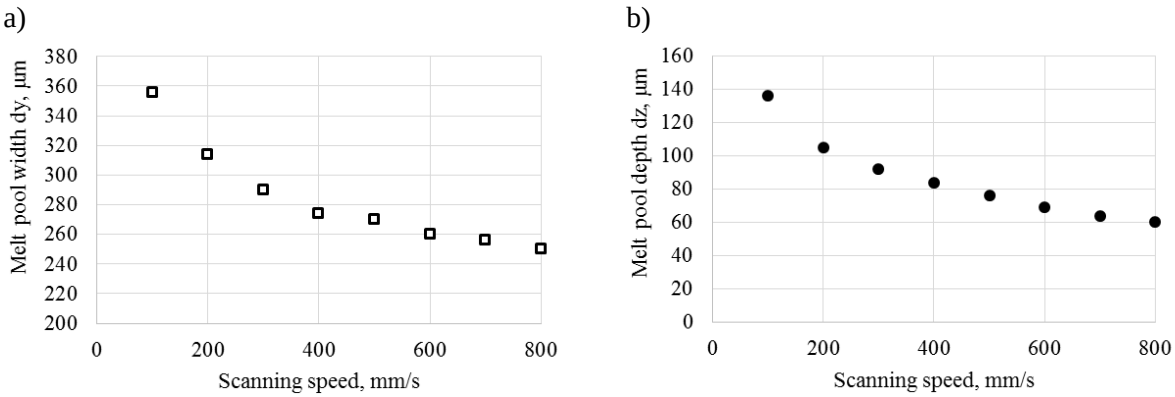


Fig.3. Dependence of laser scanning speed on the melt pool width (a) and depth (b) in simulation model

Conclusion

Experimental and numerical studies of the scanning track formation in the selective laser melting process for 316L steel were carried out. The surface modification in terms of melt pool dimensions were performed by controlling laser power, scanning speed and laser focal spot diameter. The following conclusions are made based on the research:

1. From simulation results, it was concluded that melt pool sizes were increased by increasing laser power.

2. It was established that melt pool sizes were decreased by increasing scanning speed.

3. In the experiment, it was revealed that with an increase in laser focal spot diameter melt pool depth decreased and width increased. This corresponds to the small values of the diameter in simulation. Further, it can be seen from simulation results that with an increase spot diameter melt pool width, as well as the depth, begins to decrease.

REFERENCES

1. **Yap C. Y. et al**. Review of selective laser melting: Materials and applications, Applied physics reviews. 2(4) (2015) 234-239.

2. **Kuznetsov P. A. et al.** Structure and mechanical properties of 316L austenitic steel obtained by selective laser alloying, Deformation and destruction of materials. 4 (2016) 9-13.

3. COMSOL: Multiphysics Software for Optimizing Designs

DETERMINATION OF THE EQUIVALENT ELECTRIC CIRCUIT PARAMETERS OF A GALVANIC CELL IN THE MICRO-ARC OXIDATION PROCESS

E. A. Pecherskaya ✉, P. E. Golubkov, D.V. Yakushov, A.E. Shepeleva, G.V. Kozlov
Penza State University, Penza, Russia;
✉pea1@list.ru, iit@pnzgu.ru

Abstract. The analysis and identification of the electrochemical equivalent circuits parameters of a galvanic cell in the micro-arc oxidation process were conducted in this work. It is shown that to simulate a galvanic cell it is advisable to use an equivalent circuit consisting of two parallel links (active resistance and a constant phase element) with a resistor connected in series. It was revealed that the parameter *C* of the equivalent circuit correlates with the coating thickness.

Keywords: Micro-arc oxidation, electrochemical impedance spectroscopy, equivalent electric circuit, parametric identification.

Funding: The work was supported by the grant of the Ministry of Science and Higher Education of the Russian Federation "Fundamentals of the digital twin of the technological process of forming oxide coatings with specified properties by microarc oxidation" (№ 123091800009-1.)

Introduction

One of the most important tasks when developing digital twins is the choice of a mathematical model that adequately describes the object of study. For the micro-arc oxidation (MAO) process, the object of study is a galvanic cell, which is a "metal-oxide-electrolyte" system from a chemical point of view. Currently, such systems are modeled using electrical equivalent circuits. Thus, in [1], to simulate a galvanic cell, an equivalent circuit containing classical active and reactive elements (resistance and capacitance) is used. This substitution circuit does not take into account some features of the research object, as a result of which the model has limited accuracy. As a rule, electrical equivalent circuits for modeling electrochemical systems contain idealized elements characterizing physical and chemical processes in the "metal-oxide-electrolyte" system (Warburg impedance *W*, constant phase element *CPE*, etc.) [2 – 4], while the structure of the electrical equivalent circuit may be different. However, this approach is currently used mainly to study the corrosion resistance of finished samples of micro-arc oxide coatings, and not the process of their formation. Thus, refining the mathematical model of the process of micro-arc oxide coatings formation taking into account electrochemical impedances is an urgent scientific task.

Materials and Methods

Samples of micro-arc oxide coatings were obtained by processing 10 billets of aluminum alloy AD31 measuring 20x15x2 mm. Micro-arc oxidation was carried out using a symmetrical sinusoidal current in the anode-cathode mode at a current density of 11 A/dm^2. Electrolyte composition: 9 g/l Na_2SiO_3, 2 g/l NaOH. The oxidation time was 10, 30, 60, 90, 120, 180, 240, 300, 600, 900 s. For each sample, before processing and at the indicated times, the real and imaginary part, modulus and argument of the impedance were measured in the frequency range from 20 Hz to 2 MHz using a Keysight E4980A LCR meter, as well as forming curves and oscillograms of the current and voltage of the galvanic cell with using the micro-arc oxidation installation software. Based on the results of the study, the impedance frequency characteristics were plotted for each sample. For modeling, three electrical equivalent circuits of the galvanic cell were used: 1) a parallel *R-CPE* link with a series resistor; 2) two parallel links with a series resistor; 3) ladder circuit. The parameters of equivalent circuit elements *C* and *n* were determined in MATLAB using the parametric identification method. The model error was calculated from the deviation of the calculated frequency characteristics of the galvanic cell impedance from the

experimental ones. The coatings thickness was determined using a point autofocus probe surface texture measuring instrument Mitaka PF-60.

Results and Discussion

In the course of studying the frequency characteristics of the galvanic cell impedance (Fig. 1) for the obtained samples with MAO coating, the dependences of the parameters of the equivalent circuits of the galvanic cell on the oxidation time were obtained. It was revealed that the equivalent circuit consisting of two parallel *R-CPE* links with a series resistor has the smallest adequacy error. A parameter *C* correlation of the equivalent circuit and the coating thickness was found.

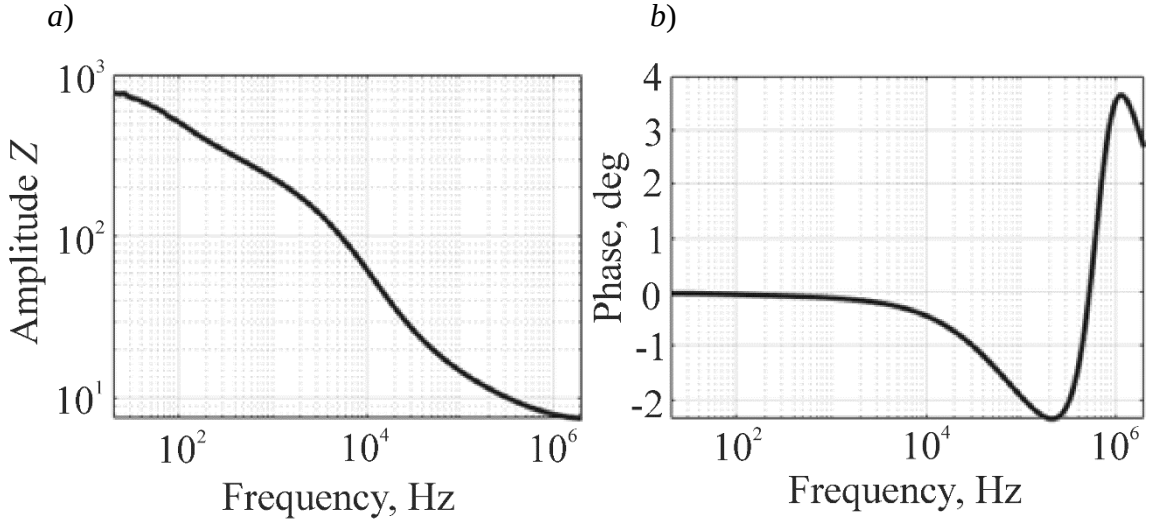


Fig. 1. Amplitude-frequency (a) and phase-frequency (b) characteristics of the galvanic cell impedance

Conclusion

The obtained results were used to improve the mathematical models underlying the digital twin of the micro-arc oxidation process.

REFERENCES

1. **Semenov A., Pecherskaya E., Golubkov P., Gurin S., Artamonov D., Shepeleva Y.**, Parametric identification of the mathematical model of the micro-arc oxidation process, Heliyon. 9 (2023) e19995.

2. **Kaseem M., Zehra T., Dikici B, Dafali A., Yang H. W., Ko Y. G.**, Improving the electrochemical stability of AZ31 Mg alloy in a 3.5wt.% NaCl solution via the surface functionalization of plasma electrolytic oxidation coating, Journal of Magnesium and Alloys. 10 (2022) 1311–1325.

3. **AlMashhadani H. A., Khadom A. A., Khadhim M. M.**, Effect of Polyeugenol coating on surface treatment of grade 23 titanium alloy by micro arc technique for dental application, Results in Chemistry. 4 (2022) 100555.

4. **Hafili F., Chaharmahali R., Babaei K., Fattah-Alhosseini A.**, Duty cycle influence on the corrosion behavior of coatings created by plasma electrolytic oxidation on AZ31B magnesium alloy in simulated body fluid, Corrosion Communications. 3 (2021) 62–70.

Formation of mesoporous silica coating on cores with different surface properties

D. A. Eurov [1]✉, **E. Yu. Stovpiaga** [1], **D. A. Kurdyukov** [1]
[1] Ioffe Institute, 194021 St. Petersburg, Russia
✉edan@mail.ru
(post@mail.ioffe.ru)

Abstract. An approach has been developed for the synthesis of mesoporous silica shell on the surface of various spherical composite particles with different zeta potential. It is demonstrated that the surface charge of the core particles influences the porous structure of the obtained shell.

Keywords: Spherical particles, core-shell nanostructures, silica shell, zeta potential, pores.
Funding: This work was funded by the Russian Science Foundation, project no. 23-79-00018.

Introduction

Nanotechnology has been a wide and growing field of research since the end of the last century. It deals with materials of various types at nanoscale level, where they demonstrate novel properties compared to their bulk counterparts. The synthesis, characterization, and applications of nanoparticles are among the most important sections of the wide range of nanotechnology areas [1]. To expand the functionality of this kind of materials researchers create not only simple nanoparticles, which are made from single substance, but also composite ones often possessing the so-called core-shell structure. The purpose of the coating can be varied, such as surface modification, increasing the functionality, stability, reduction in consumption of precious materials, and so on [1]. Core/shell nanoparticles are gradually attracting more and more attention, since they exhibit distinctive properties of the different materials applied together, which is especially important to meet the diverse application requirements. They are widely used in, for example, catalysis [2], electronics [3], biomedicine [4]. For biomedical purposes silica shell is highly sought after, since silica is biocompatible (approved by FDA and EFSA), possess tunable surface functionalization, high adsorption capacity, and allows protecting healthy tissues from interaction with toxic drugs.

Results and Discussion

Here, we develop a new method for covering of various spherical particles possessing different surface charge with a mesoporous silica ($mSiO_2$) shell. We used the following particles as the cores: 1 – non-porous spherical silica particles synthesized by the Stöber method [5], 2 – mesoporous spherical silica particles filled with silicon $mSiO_2/Si$ [6], 3 – mesoporous spherical silica particles filled with magnetite $mSiO_2/Fe_3O_4$ [7], and 4 – mesoporous spherical silica particles filled with gadolinium oxide $mSiO_2/Gd_2O_3$ [8]. The results of the zeta potential measurements show (Fig. 1a) that all the particles possess different surface charge almost in the whole range of pH values under study.

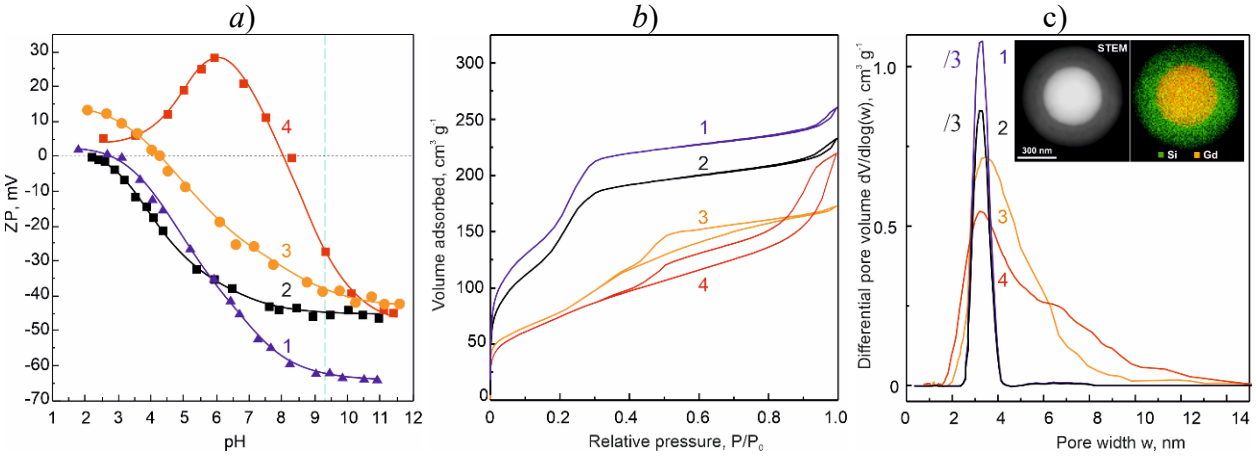


Fig. 1. Zeta potentials of non-porous silica (*1*), $mSiO_2/Si$ (*2*), $mSiO_2/Fe_3O_4$ (*3*) and $mSiO_2/Gd_2O_3$ (*4*) particles (*a*); N_2 adsorption and desorption isotherms measured at 77 K (*b*) and NLDFT pore size distributions (*c*) for the same particles covered with a mesoporous silica shell. Inset: STEM image and EDX maps for $mSiO_2/Gd_2O_3$ particles coated with $mSiO_2$ shell.

A mesoporous silica shell is synthesized via basic hydrolysis of tetraethoxysilane (TEOS) in a water-ammonia-ethanol mixture containing organic pore-forming agent – cetyltrimethylammonium bromide (CTAB). The core particles added to the reaction mixture act as nucleation centers. The formation of mesoporous silica proceeds by an aggregative mechanism, when CTAB forms cylindrical micelles, which are covered, as a result of TEOS hydrolysis with a layer of amorphous SiO_2. Then, the SiO_2/CTAB clusters coagulate with the formation of the shell on the surface of core particles. Pores remain in place of CTAB after its removal by thermal annealing. The pH of the reaction mixture was adjusted to ~9.3 (marked by a blue dashed line in Fig. 1a). At this value all the particles possess negative surface charge over -30 mV, which indicates their aggregative stability. This determines the fact that they do not coagulate and present in the solution as individual particles, which ensures the coating of each particle with a silica layer of the same thickness without their coalescence.

Fig. 1b show the isotherms for the particles after coating with shell. It can be seen, that for the non-porous SiO_2 and $mSiO_2$/Si particles possessing the highest in absolute value zeta potential the largest amount of the adsorbate is observed after the coating. The specific surface area (SSA) values calculated by the Brunauer-Emmett-Teller (BET) method for these particles are 580 and 530 $m^2\ g^{-1}$ respectively. The corresponding pore volumes are 0.41 and 0.37 $cm^3\ g^{-1}$. The pore size distribution (Fig. 1c) indicates the presence of one pronounced peak at 3.1 nm, which corresponds to the size of CTAB micelles. When the surface charge of core particles decreases in absolute value (in the case of $mSiO_2/Fe_3O_4$ and $mSiO_2/Gd_2O_3$ particles) isotherms of the particles after coating are lower indicating the lower BET SSA. Indeed, the corresponding values are 320 and 270 $m^2\ g^{-1}$. This may be due to that CTAB molecules in the vicinity of surface with lower charge form the so-called platelet micelles, rather than cylindrical produced in the case of SiO_2 and $mSiO_2$/Si particles possessing higher negative surface charge, which leads to the formation of larger pores with lower SSA. This is confirmed by the pore size distributions (Fig. 1c), which is substantially wider in this case. Note, the pronounced peak at 3.1 nm remains. Probably, larger pores are formed closer to the cores in the place of platelet CTAB micelles. Then, after a certain thickness the subsequent growth of the shell continues via coagulation of SiO_2/CTAB clusters consisting of cylindrical CTAB micelles. The obtained values of pore volume for $mSiO_2/Fe_3O_4$–shell and $mSiO_2/Gd_2O_3$–shell are 0.37 and 0.33 $cm^3\ g^{-1}$ respectively. The thickness of shell regardless of the core particles can be controlled from tens of nanometers to several hundreds by varying the concentrations of the reagents.

Conclusion

An approach for the covering of various spherical particles having different surface charge with mesoporous silica shell possessing high SSA and pore volume is proposed. The synthesis of shell is carried out via basic hydrolysis of organosilane in a water-ammonia-ethanol mixture containing pore-forming agent. The synthetic conditions are selected in such a way that the cores are present in a form of aggregatively stable particles ensuring the formation of uniform layer of the same thickness on each particle. It is found that the lower the zeta potential of core is the wider the pore size distribution of the resulted shell is observed, however with the presence of a characteristic peak at 3.1 nm. The developed technique is a promising tool for the obtaining core-shell particles for biomedical applications that allows protecting the core and expanding the functionality of the particles.

Acknowledgments

The authors thank D.A. Kirilenko for TEM and EDX measurements.

REFERENCES

1. **Chaudhuri R G** et al., 2012 *Chem. Rev.* **112** 2373.
2. **Gawande M B** et al., 2015 *Chem. Soc. Rev.* **44** 7540.
3. **Pajor-Świerzy A** et al., 2022 *Adv. Colloid Interface Sci*. **299** 102578.
4. **Chatterjee K.** et al., 2014 *Adv. Colloid Interface Sci.* **209** 8.
5. **Stöber W** et al., 1968 *J. Colloid Interface Sci.* **26** 62.
6. **Kurdyukov D A** et al., 2019 *Microporous Mesoporous Mater*. **281** 1.
7. **Stovpiaga E Yu** et al., 2017 *Phys. Solid State*. **59** 1623.
8. **Eurov D A** et al., 2015 *J. Nanopart. Res*. **17** 82.

Silicon/graphite nanocomposite for lithium-ion battery anode

Sh. Sh. Isokjanov✉, **V. V. Krivetskiy**, **E. V. Mazin**
Moscow Institute of Physics and Technology, Moscow, 117303, Russia
✉Isakjanov2997@gmail.com

Abstract. One of the most promising areas of battery improvement is the use of silicon in anodes. It has emerged as a promising candidate for next-generation lithium-ion batteries (LIBs) due to its tenfold higher capacity compared to traditional graphite anodes (4200 mAh·g^{-1} vs. 372 mAh·g^{-1}). However, the practical application of silicon in LIBs is hindered by several challenges, including rapid capacity fading, unstable cycling behavior, and significant volume expansion during lithium insertion/extraction.

This work presents a novel approach for fabricating high-performance LIBs with silicon-based anodes and metallic lithium counter electrodes in a compact "Cell-coin 2032" form factor. The silicon-containing anode material was synthesized via the thermal decomposition of SiH4 in a gas phase followed by deposition onto a carbon matrix. A doctor blade technique was employed to deposit the composite onto a copper foil current collector. Laser engraving was utilized to define the electrode topology. The developed technology enables the production of compact, planar LIBs suitable for a wide range of electronics applications.

Keywords: Lithium-ion batteries, silicon-carbon anodes, composite electrodes, laser engraving, doctor blade technique, coin-type cells, solid electrolyte interphase (SEI).

Introduction

The ever-increasing demand for high-performance energy storage solutions necessitates the development of next-generation LIBs with improved energy density [1]. While graphite has served as the dominant anode material in commercial LIBs, its limited theoretical capacity (372 mAh·g^{-1}) restricts further advancements. Silicon, with a tenfold higher theoretical capacity (4200 mAh·g^{-1}), emerges as a promising alternative. However, the significant volume change experienced by Si during lithium insertion (~300%) leads to mechanical stress, pulverization of the electrode, and a rapid decrease in capacity [2]. This article will delve into recent progress in overcoming these challenges and realizing the potential of Si-based anodes for LIBs.

Materials and Methods

A silicon-carbon composite material (Si/C) was synthesized via high-temperature thermal decomposition of SiH_4 gas under high pressure, followed by the growth of nano-sized amorphous silicon on the graphene planes of highly exfoliated graphite. The graphite, in turn, was obtained from intercalated compounds of fluorinated graphite $C_nF{\cdot}yXF_m$, where X is a halogen (Cl, Br, I). Next, the Si/C composite was dispersed using a high-pressure homogenizer to obtain a homogeneous suspension (figure 1). The resulting composite served as the primary anode material for lithium-ion batteries.

The functional layer consisted of the Si/C composite, Super C65, and carboxymethylcellulose (CMC) for one electrode and metallic lithium for the other.

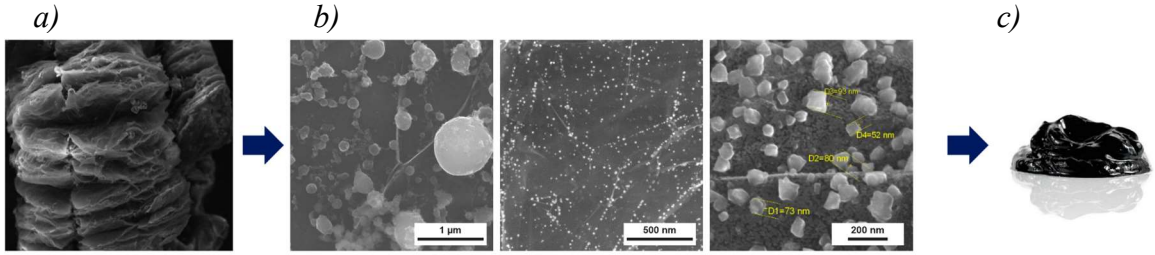


Fig. 1. Graphene planes of highly stratified graphite *(a)*, SEM images of Si/C composite material *(b)* and the resulting homogeneous suspension based on Si/C *(c)*

A water-based suspension-paste was prepared from the aforementioned materials and deposited onto copper foils using the doctor blade technique. The prepared samples were dried in a vacuum oven. Laser engraving was employed to define the electrode topology, ensuring precision and reproducibility during electrode fabrication.

The "Cell-coin 2032" coin-type batteries were assembled in a glovebox. A standard commercial 1M $LiPF_6$ solution in EC – MEC 1:3 + 1% VC mixture was used as the electrolyte. The assembly followed standard battery assembly procedures, including stacking the components and hermetically sealing them inside the casing to ensure electrical insulation and structural integrity.

Results and Discussion

Three samples were fabricated and investigated following the described methodology. The battery capacity measurements were performed using a Neware battery analyzer with its proprietary software "BTS Client 8.0.0.512". Cyclic voltammetry was conducted within the potential range of 0.01 V - 1.5 V at a current rate of 0.05C for 5 cycles. To visualize the cycling behavior of the samples, graphs were constructed (Figure 2).

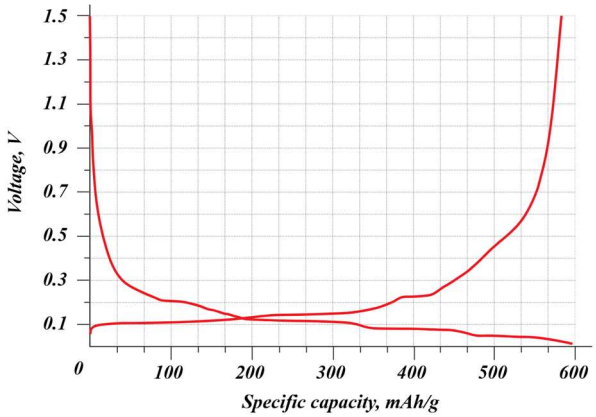


Fig. 2. Cyclic scanning of tablet-type battery samples at 0.05C

The experimental specific capacity of the batteries ranged from 589 to 609 mAh/g, which exceeds the theoretical capacity of 450 mAh/g and is almost twice the capacity of commercial coin cell counterparts with a graphite-based anode.

The obtained results demonstrate the potential of Si/C composites as a promising anode material for lithium-ion batteries.

Conclusion

The successful fabrication of silicon-based composite anodes using this method represents a significant step towards high-performance LIBs with extended cycle life and improved energy density. Further research will focus on optimizing fabrication, investigating different electrolytes, and evaluating long-term performance.

Si/C composite anodes hold great promise for revolutionizing lithium-ion battery technology and paving the way for next-generation high-energy portable and stationary energy storage devices. Overcoming challenges such as scalability, cost-effectiveness, and material properties will be key to realizing this potential.

REFERENCES

1. **Kiehbadroudinezhad M., Merabet A., Hosseinzadeh-Bandbafha H.,** Review of Latest Advances and Prospects of Energy Storage Systems: Considering Economic, Reliability, Sizing, and Environmental Impacts Approach. Clean Technologies. 4 (2022) 477–501.

2. **Hu M., Wu H., Zhang G.,** High-performance silicon/graphite anode prepared by CVD using SiCl4 as precursor for Li-ion batteries, Chemical Physics Letters, Vol. 833 (2023) 140917.

Investigation of electrical characteristics of semiconductor film structures obtained on a flexible substrate

A. V. Kozlowski [1]✉, **L. D. Volkovoynova** [1], **A. A. Serdobintsev** [1]
[1] Saratov State University, Saratov, Russian Federation;
✉kozlowsky@bk.ru

Abstract. In the frame of this work the current-voltage characteristics of thin films of polycrystalline silicon on a flexible polymer substrate were studied, measured when the film was bent in both tension and compression modes. The samples were fabricated by laser-stimulated metal-induced crystallization of amorphous Si films, deposited by magnetron sputtering on a flexible polyimide film. It has been established that the resistance of a polycrystalline Si film depends on the degree and type of deformation. The change in electrical resistance can be associated with an increase and decrease in the intergranular distance when the film is stretched and compressed, respectively. The resulting films are promising for the fabrication of semiconductor strain sensors and active elements of flexible electronics.

Keywords: crystallization of amorphous silicon, metal-induced crystallization, laser-stimulated crystallization, infrared laser radiation, flexible electronics.

Funding: This study was funded by the Russian Science Foundation (project No. 23-22-00047, https://rscf.ru/project/23-22-00047/).

Introduction

Over the past decades, flexible electronics have undergone significant development due to its wide range of applications in various fields, including telecommunication systems, medicine, sensors, wearable devices, etc. [1]. An important problem in flexible electronics is the deposition of polycrystalline semiconductor thin films on flexible polymer substrates, which have a melting temperature lower than the crystallization temperature of semiconductor materials. In [2] reports a new method for the crystallization of thin silicon films, combining the advantages of laser and metal-induced crystallization technologies, which makes it possible to fabricate a polycrystalline silicon film on a flexible polyimide substrate. However, the stability of the electrical characteristics of polycrystalline films synthesized by this method on a polyimide film during its deformation has not previously been studied.

Therefore, the purpose of this work is to study the current-voltage characteristics (I-V curves) of thin films of polycrystalline silicon obtained by laser-stimulated metal-induced crystallization, measured when the film is bent in both tension and compression modes.

Materials and Methods

Amorphous silicon and metal films were deposited onto the surface of 0.5 mm thick polyimide substrates using a Nexdep vacuum magnetron deposition system (Angstrom Engineering Inc., Canada). During the deposition process, both films were applied sequentially, without intermediate devacuum of the chamber. The power of the silicon magnetron source during the deposition process stabilized at the level of 500 W, the metal one - at the level of 300 W. The thickness was controlled using a quartz sensor and was 1 μm for silicon and 40 nm for metal (Sn or Al). The resulting structures were processed on a MiniMarker-2 machine (Laser Center, Russia), equipped with a pulsed fiber laser with a wavelength of 1064 nm. Laser processing was carried out at a laser power of 0.2 W, a pulse repetition rate of 100 kHz and a laser beam speed of 1500 mm/s, the duration of the pulse was 100 ns. Thus, the metal film served simultaneously as a laser radiation absorption layer and a crystallization inductor. The formation of a crystalline silicon phase was confirmed by Raman spectroscopy on a Renishaw inVia spectrometer (UK).

To realize the bending of the resulting films at a given angle, both in the stretching and compression modes, 3D printed equipment was manufactured that made it possible to secure two clamps. In this case, one clamp was stationary, and the second could be moved around the circle (Fig. 1).

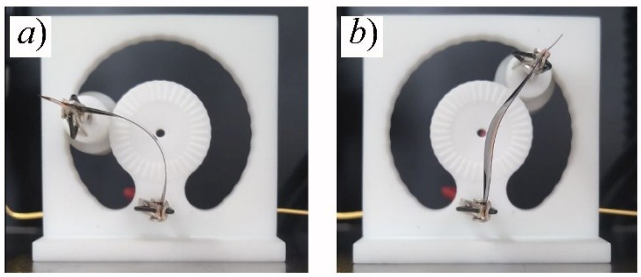


Fig. 1. Implementation of tension (*a*) and compression *(b*) modes of a polycrystalline silicon film on a flexible substrate when it is bent at a given angle

Current-voltage characteristics (I-V curves) were measured using a probe station and an Agilent B1500a semiconductor device analyzer.

Results and Discussion

The I-V curves of amorphous silicon films are linear, while those of polycrystalline silicon films are nonlinear. When the film is bent in tension mode, its conductivity decreases, and when it is bent in compression mode, it increases. Moreover, the resistance of amorphous silicon films changes non-monotonically with increasing bending angle. Figure 2 shows the effect of Si film bending on its resistance after laser-stimulated metal-induced crystallization.

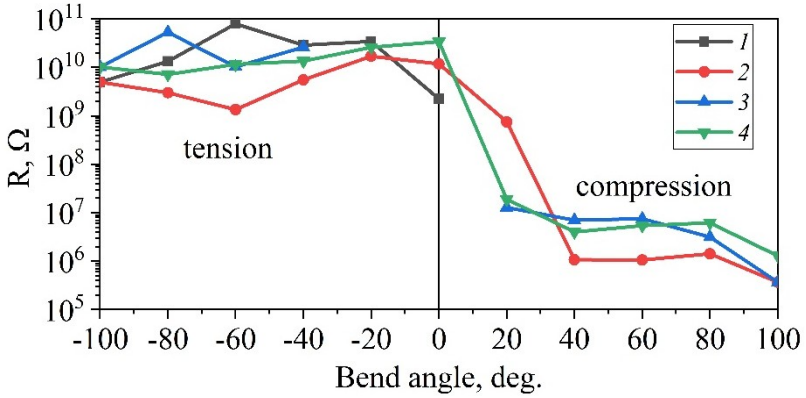


Fig. 2. Effect of Si film bending on its resistance when going through 4 cycles of tension and compression

When the film is stretched, its resistance is on average 1.57×10^{10} Ω, and when compressed it is 5.26×10^{8} Ω. Such changes may be associated with an increase and decrease in the intergranular distance when the film is stretched and compressed, respectively.

Conclusion

Thus, thin films of polycrystalline silicon were obtained on a flexible substrate. It was found that the film resistance depends on the degree and type of deformation, therefore these films are promising for the fabrication of semiconductor strain sensors and active elements of flexible electronics.

Acknowledgments

This study was funded by the Russian Science Foundation (project No. 23-22-00047, https://rscf.ru/project/23-22-00047/).

REFERENCES

1. **Gao W., Ota H., Kiriya D., Takei K., Javey A.** Flexible electronics toward wearable sensing, Accounts of Chemical Research. 52 (3) (2019) 523–533.

2. **Serdobintsev A.A.**, **Luzanov V.A.**, **Kozhevnikov I.O.**, **Ryabukho P.V.**, **Mitin D.M.**, **Bratashov D.N.**, **Starodubov A.V.**, **Pavlov A.M.** Thin amorphous silicon films crystallization upon flexible substrates, J. Phys. Conf. Ser. 1400 (2019) 055034.

Towards Nanowire-Based Multi-Environment Alkali and Acid Sensing

V.M. Kondratev [1,2✉], **A.D. Bolshakov** [1,2,3]
[1] Alferov University, Saint Petersburg, Russia;
[2] Moscow Institute of Physics and Technology, Dolgoprudny, Russia
[3] Yerevan State University, Yerevan, Armenia;
✉kvm_96@mail.ru

Abstract. The purpose of this study is to use silicon nanowires to selectively detect ammonia (NH_3) and hydrochloric acid (HCl) in vapor and liquid form using electrical impedance spectroscopy (EIS). The highly sensitive silicon sensors developed in this work can be used to indirectly and directly analyze the composition of liquid solutions containing NH_3 and HCl.

Keywords: nanowires, selective adsorption sensor, electrical impedance spectroscopy, spectroscopy data analysis, nanotechnology.

Funding: The Ministry of Science and Higher Education of the Russian Federation (Grant FSRM-2023-0009; agreement 075-03-2023-106, project FSMG-2021-0005).

Introduction

The effects of analyte adsorption by nanostructures on their electronic characteristics have been widely employed in various sensor applications based on optical, resistive, capacitive, current-voltage characteristics analysis [1-5]. Historically, polycrystalline metal oxide films such as SnO_2 were one of the first materials used for the gas detection fabricated in different geometries [4]. Electronic characteristics of such sensors are mainly governed by the depletion in the vicinity of a reactive surface during the adsorption processes. The key disadvantages of these sensors are poor performance in a humid environment and low selectivity [5].

Here we fabricate Si NW based sensors and thoroughly examine their electronic properties with an aid of EIS upon exposure to NH_3 and HCl vapors.

Materials and Methods

We achieved these results by using Si nanowires obtained through cryogenic plasma etching, which have a high aspect ratio and provide a large surface area for enhanced sensitivity. These nanowires were placed on a contact platform, and EIS was used to detect the analytes. The study also introduces three types of sensors based on Si nanowires: untreated Si nanowires, Si nanowires treated with hydrofluoric acid (HF), and Si nanowires decorated with silver nanoparticles (Ag NPs). These sensors were developed as part of an optimization effort to improve the performance of the sensor [6-7].

Results and Discussion

This study proposes a novel approach for interpreting EIS spectra. Instead of solely analyzing impedance or frequency, the suggested approach involves considering the response in a frequency-resistance F(R) space. This innovative analysis method provides a new perspective for understanding and interpreting the behavior and characteristics of the sensor's response. By visualizing the response in the F(R) space, it becomes possible to identify patterns and correlations that may be overlooked with traditional analysis methods.

The best sensitivity results were obtained with untreated Si nanowires, which provided a detection limit of 4 $\mu mol \cdot L^{-1}$ and resistive sensitivities of 0.8% per $\mu mol \cdot L^{-1}$ for HCl and 4 $\mu mol \cdot L^{-1}$, −0.2% per $\mu mol \cdot L^{-1}$ for NH_3, respectively. Treatment with HF stimulated surface oxidation and increased the density of adsorption sites, making it promising for detecting analyte concentrations up to 1000 $\mu mol \cdot L^{-1}$ [6-7].

Conclusion

The findings of this study are particularly interesting from the perspective of developing sensors for biological markers of health based on silicon for personalized human medicine. These sensors could enable real-time measurements and the direct and indirect detection of acids and alkalis at room temperature within the range of «biological» concentrations from 62.5 to 1000.0 $\mu mol \cdot L^{-1}$.

Acknowledgments

A.D.B. thanks Ministry of Science and Higher Education of the Russian Federation (agreement 075-03-2023-106, project FSMG-2021-0005) for support of the experiments.

V.M.K. thanks Ministry of Science and Higher Education of the Russian Federation (Grant FSRM-2023-0009) for support of analysis of the experimental data.

REFERENCES

1. **Kondratev V. M., et al.**, Gallium phosphide nanowires for “biological concentrations” ammonia detection, 2022 J. Phys.: Conf. Ser. 2172 012006.

2. **Nalimova S. S., Kondratev V. M.**, Study of Surface Acid-Base Properties Of Gas-Sensitive Metal Oxides, 2020 IEEE Conference of Russian Young Researchers in Electrical and Electronic Engineering (EIConRus), 2020, 987-990.

3. **Kadinskaya S. A., Kondratev V. M., Kindyushov I. K., Kuznetsov A., Punegova K. N.**, Hydrothermal ZnO-based Nanostructures: Geometry Control and Narrow Band UV Emission, 2022 Conference of Russian Young Researchers in Electrical and Electronic Engineering (ElConRus), 2022, 958-961.

4. **Seiyama T., Kato A., Fujiishi K., Nagatani M.**, Analytical Chemistry 1962 34 (11), 1502-1503.

5. **Kondratev V. M., Kuznetsov A., Gridchin V. O., Fedina S. V., Aubekerov K.**, III–V Nanowires for Biological Ammonia Concentrations Detection, 2022 Conference of Russian Young Researchers in Electrical and Electronic Engineering (ElConRus), 2022, 970-974.

6. **Kondratev V. M. et al**., “Silicon Nanowire-Based Room-Temperature Multi-environment Ammonia Detection,” ACS Appl Nano Mater, vol. 5, no. 7, pp. 9940–9949, Jul. 2022.

7. **Kondratev V. M. et al**., “Si Nanowire-Based Schottky Sensors for Selective Sensing of NH3 and HCl via Impedance Spectroscopy,” ACS Appl Nano Mater, vol. 6, no. 13, pp. 11513–11523, 2023.

Development of solid-state composite cathode material for solid-state lithium-ion batteries based on lithium ferrophosphate LiFePO4.

A. A. Lagutkina✉, **V. A. Vizgalov**
Moscow Institute of Physics and Technology, Moscow, 117303, Russia

✉lagutkina.aa@phystech.edu

Abstract. In the past few decades all-solid-state lithium-ion batteries have become a promising frontier due to their increased safety, higher energy density and unique mechanical properties. One of the main issues in this field is establishing steady transport of lithium ions across the electrode–electrolyte interface, which requires modifications of the electrode structure.

In this research we investigated mechanical properties, capacity and coulomb efficiency of a composite cathode based on solid polymer electrolyte as a binder, lithium ferrophosphate as active material and carbon black as electron conductor. Composite cathode was prepared with the help of ball-milling to reduce the particle size and increase the homogeneity of the material, which resulted in mechanically stable flexible crack-free electrodes after coating, drying and calendaring. Achieved specific capacity of the electrodes corresponds to theoretical values, shows long-term sustainability in systems with liquid electrolyte and is applicable to solid-state systems.

Keywords: All-solid-state lithium-ion battery, composite electrodes, lithium ferrophosphate electrodes, solid electrolye, polymer electrolyte.

Introduction

Compared to the commonly used lithium-ion batteries with liquid electrolyte, all-solid-state lithium-ion batteries offer a number of significant advantages: increased safety due to the elimination of flammable organic liquid electrolyte materials, retarding dendritic growth, allowing to use metal lithium as anode, increased mechanical stability and extended voltage range. Stable contact between the solid electrolyte and the electrodes can be achieved, for example, by using composite electrode materials that help blur the interphase boundary, reduce its resistance and increase the maximum battery current. The "pores" of such electrodes are filled with solid polymer electrolyte at the stage of manufacturing the electrodes themselves, before assembling the cell [1]. Polymer electrolyte used instead of traditional binder ensures both mechanical integrity and ionic conductivity throughout the entire volume of the electrode. The uniform distribution of particles of the active material, carbon and electrolyte in the electrode material results in high and uniform ionic and electronic conductivity throughout the volume of the electrode, close contact of the particles with each other and with the current collector and decreasing resistance of the "electrode-electrolyte" interface. A schematic representation of a battery with a composite electrode is shown at figure 1.

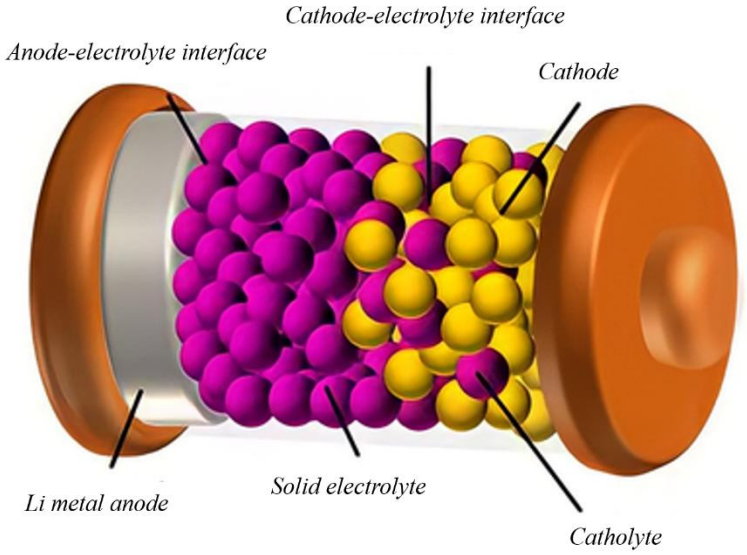


Fig 1. Schematic of interfaces in solid-state batteries

Materials and Methods

Several modifications of composite positive electrodes based on lithium ferrophosphate were investigated. A mixture based on lithium bis(trifluoromethanesulfonyl)imide (LiTFSI) and polyethylene oxide (PEO) with the addition of polyvinylidene fluoride (PVDF) for mechanical stability was used as a solid polymer electrolyte in the electrode. The mass ratio was calculated from the optimal molar ratio EO:Li = 8:1 (1 Li^+ ion per 8 ethylene oxide segments) that showed the highest ionic conductivity and transference number under standard operating conditions [2]. Polymer electrolyte was mixed with the help of magnetic stirrer in argon atmosphere. The optimal cathode slurry contained 35% of electrolyte binder, 5% of carbon black Super P, 60% of active material $LiFePO_4$ and was ball-mixed for 2 hours at room temperature, coated on aluminum foil with the doctor blade, dried at 60℃ for 24 hours and subjected to calendaring process. Laser engraving was utilized to define the electrode topology. Standard coin-cell batteries with commercial liquid electrolyte were assembled to test the conductivity and capacity of the electrode material.

Results and Discussion

By varying the composition and manufacturing conditions, high adhesion of the material to the aluminum current collector, specific capacity and ionic conductivity were achieved. The manufactured electrodes were examined in semi-cells with lithium metal anode and liquid electrolyte. Capacity measurements were performed with the help of Neware Battery Testing System. During the first five cycles the average specific capacity reached a value of 168 mAh/g at 0.05C and exceeded theoretical value of 165 mAh/g, Coulomb efficiency reached 99,7%.

Conclusion

Investigated polymer-based lithium ferrophosphate cathode material shows promising mechanical characteristics and specific capacity. It is applicable for batteries with PEO-based solid electrolytes – popular subject of scientific research in the field of all-solid-state batteries. Further research on materials is vital for development of safe, sustainable and mobile energy sources.

REFERENCES

1.**Al-Salih H. [et. al.].** Composite Cathodes for Solid-¬State Lithium Batteries: “Catholytes” the Underrated Giants, Advanced Energy and Sustainability Research. (3) (2022)

2. **E. E. Ushakova [et. al.].** Free-standing Li+ -conductive films based on PEO– PVDF blends, Royal Society of Chemistry Advances (10) (2020)

Methods and instruments for measuring surface morphology and mechanical parameters of oxide coatings

A.A. Maksov[1]✉, S.A. Gurin[1], P.E. Golubkov[1], E.A. Pecherskaya[1], Yu.V. Shepeleva[1]
Penza State University, Penza, Russia
✉maksov.01@mail.ru

Abstract. Studies of the topology of coating surfaces, obtained by micro-arc oxidation, have been carried out. The dependence of coatings properties (roughness, porosity, electrical strength) on current and time processing was revealed. The obtained results can be used in the development of digital twin of the micro-arc oxidation process.

Keywords: micro-arc oxidation, digital twin, surface morphology, roughness, electrical strength, porosity.

Funding: The work was supported by the grant of the Ministry of Science and Higher Education of the Russian Federation "Fundamentals of the digital twin of the technological process of forming oxide coatings with specified properties by microarc oxidation" (№ 123091800009-1).

Introduction

Currently, there is a large number of studies aimed a studying the influence of heterogeneous factors of the MAO process on the properties of the formed coatings, including mechanical ones. For example, in [1] it is shown that porosity and coating roughness increases with increasing number of plasma discharges at low current densities. In [2], using electron microscopy, it was revealed that the porosity of coatings decreases with treatment time, but at the same time increases roughness. Adding TiO_2 nanoparticles to the electrolyte is also achieved by the increase porosity, thickness and surface roughness coating [3]. In [4] it is shown that that adding glycerol to the electrolyte leads to an increase in the number of pores and reducing their size, which reduces surface roughness. These studies are not unified, since they were carried out on different technological equipment under different processing modes and do not allow compare the results of experiments with each other, which limits their use as training data for the digital twin of the micro-arc process oxidation [5].

Materials and methods

To study surface morphology and mechanical parameters of micro-arc oxide coatings, 16 samples, presented in the form plates measuring 20x15x3 mm (surface area 0.05971 dm^2) and whose surface was previously brought to a roughness Ra in the range from 0.1 to 0.2 μm were selected. At the first stage, the samples were milled on a universal machine; at the second stage were polished on a manual grinding – polishing machine MP-100S MTDI (Korea) by sequentially sorting sandpapers with grades from P240 to P2000 (ISO6344 marking) and final polishing with a feta cloth using paste GOI. The treated samples were placed in a galvanic bath with electrolyte, containing 0.5 g/l NaOH and 80 g/l Na_2SiO_3. Coatings were obtained using a micro-arc oxidation (MAO) installation on a sinusoidal current. Current density was 15 A/dm^2 and 21 A/dm^2, anode and anode-cathode current modes were used in for 120 s, 240 s, 480 s, 960 s, respectively. Then the surface topography of selected samples research was carried out using a scanning electron microscope VEGA 3, and the roughness of the coatings – with a laser 3D contourograph and profilometer Mitaka FS150.

Results and discussion

Figure 1 shows the morphology of the oxide coating, obtained as a result of processing for 960 s at a current density of 15 A/dm^2 in anode mode, as an example.

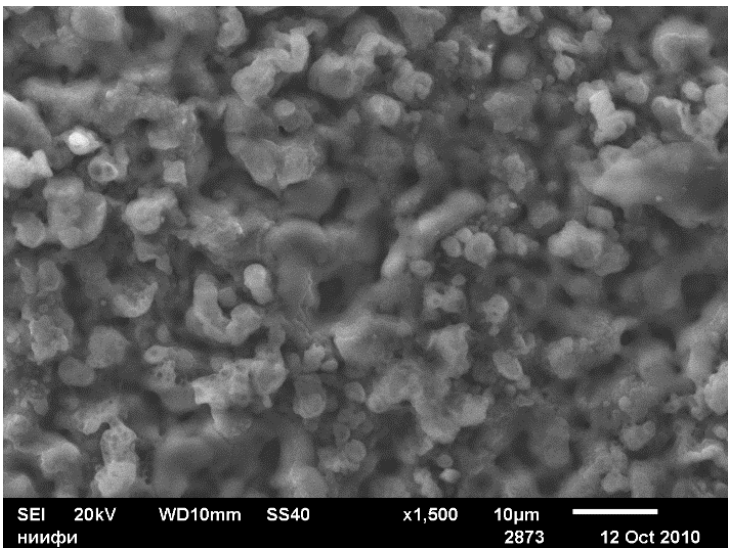


Fig. 1 – Surface morphology of the oxide coating obtained as a result of processing for 960 s at a current density of 15 A/dm^2 in anode mode

It is shown that obtained coatings using the proposed technological modes, can be considered multilayer, with basic adhesive coating, intermediate porous and highly porous layer with developed surface.

The results of the above data analysis show that with increasing time of the MAO process in the anode and anode-cathode modes surface roughness increases, according to the arithmetic mean of absolute values of profile deviations within the base length Ra.

The process is characterized by high reproducibility and is also traceable dependence of coating properties (roughness, porosity, electrical strength) on current strength.

Conclusion

The research results allow the use of the plasma growth model of oxide coatings as the basis for the development of a digital process twin of microarc oxidation. The obtained empirical results are appropriate use as training data for intelligent algorithms as a part of digital twin.

REFERENCES

1. **Mortazavi G., Jiang J., Meletis E.I.**, Investigation of the plasma electrolytic oxidation mechanism of titanium, Applied Surface Science. 488 (2019) 370-382.

2. **Moga S.G., Negrea D.A., Ducu C.M., Malinovschi V., Schiopu A.G., Coaca E., Patrascu I.**, The Influence of Processing Time on Morphology, Structure and Functional Properties of PEO Coatings on AZ63 Magnesium Alloy, Appl. Sci. 12 (2022) 12848.

3. **Mozafarnia H., Fattah-Alhosseini A., Chaharmahali R., Nouri M., Keshavarz M.K., Kaseem M.**, Corrosion, Wear, and Antibacterial Behaviors of Hydroxyapatite/MgO Composite PEO Coatings on AZ31 Mg Alloy by Incorporation of TiO_2 Nanoparticles, Coatings. 12 (2022) 1967.

4. **Jangde A., Kumar S., Blawert C.**, Evolution of PEO coatings on AM50 magnesium alloy using phosphate-based electrolyte with and without glycerol and its electrochemical characterization, Journal of Magnesium and Alloys. 8 (2020) 692-715.

5. **Golubkov P.E., Pecherskaya E.A., Gurin S.A., Alexandrov V.S., Artamonov D.V., Maxsov A.A.** Influence of process parameters on the properties of microarc oxide coatings, St. Petersburg State Polytechnical University Journal. Physics and Mathematics. 16. № S3.1. (2023) 368-373.

Study of thermal and electrical conductivity properties of grain boundaries in metals and semiconductors with bcc and fcc crystal lattices

E. V. Morozova[1]✉, **D. A. Timkaeva**[1]
Ulyanovsk State University, Ulyanovsk, Russia
✉kat-valezhanina@yandex.ru

Abstract. This study employs first-principles calculation methods to investigate the thermoelectric properties of high-angle grain boundaries in metals (iron, titanium, copper, and nickel) and semiconductors (silicon carbide, boron nitride) with symmetric tilt boundaries of two types of crystal lattice: body-centered cubic and face-centered cubic. Grain boundaries play a significant role in carrier and phonon transport in materials. Altering geometric parameters is one of the simplest ways to control thermoelectric characteristics. By varying the grain rotation axis, rotation angle, and grain self-orientation, we derived the dependence of the electrical and thermal conductivity of studied materials on the geometry of the modeled device at room temperature. The results presented in this work may provide insights into the influence of such type of surface defect on the heat and electrical conductivity of the investigated materials.

Keywords: grain boundary, electrical conductivity, thermal conductivity.

Funding: The reported study was supported by the Russian Science Foundation under the grant number 22-11-00036.

Introduction

The grain boundary (GB) is a two-dimensional (surface) defect in the atomic structure, separating two differently oriented grains (crystallites). Typically, it is a disordered multi-atom system with a wide variety of forms. GBs play a significant role in carrier and phonon transport in materials [1,2]. Various studies indicate that GBs are an active element of the material's defect structure, affecting properties such as plasticity, diffusion, fracture, and deformation at elevated temperatures, among others. GBs are described by several geometric parameters, including the grain rotation axis, their rotation angle, and the intrinsic orientation of the boundary in space. Boundaries with neighboring grains misoriented by less than 10 degrees are classified as low-angle, while those with greater misorientation are classified as high-angle GBs. The bonding at GBs differs from that in a regular crystalline lattice. Due to the formation of a specific structure at the grain contact region different from the perfect crystal structure, the properties of boundaries can differ from those of the bulk material [3].

The present study investigates the influence of a surface defect such as GB on the thermoelectric properties of grains of transition metals (iron, copper, titanium, nickel) and semiconductors (silicon carbide, boron nitride) with face-centered cubic and body-centered cubic lattices.

Materials and Methods

The calculations were carried out within the framework of the Slater-Koster method using the DFTB formalism for electronic properties and molecular dynamics for thermal characteristics. The system, simulating the device, was divided into three regions: the left and right semi-infinite electrode regions and the central part. Transport coefficients were calculated using the non-equilibrium Green's function (NEGF) method, density functional theory (DFT), and non-equilibrium molecular dynamics. The studied parameters were computed using the following relationships:

$$G_{\mathrm{e}} = \left.\frac{dI}{dV_{\mathrm{bias}}}\right|_{dT=0}, S = -\left.\frac{dV_{\mathrm{bias}}}{dT}\right|_{I=0}, \lambda_{\mathrm{e}} = \left.\frac{dI_Q}{dT}\right|_{I=0}, \Pi = \left.\frac{I_Q}{I}\right|_{dT=0} = SV_{\mathrm{bias}}. \quad (1)$$

Here, S is the Seebeck coefficient, G_{e} is electrical conductivity, T is absolute temperature, λ is thermal conductivity, which is equal to the sum of electronic λ_{e} and phonon λ_{ph} thermal conductivity.

Results and Discussion

In our work, to obtain the dependences of electrical and thermal conductivity, we changed such geometric parameters of symmetrical grain boundaries as the rotation axis of the grains, the rotation angle, and the proper orientation of the grain boundary in space. Examples of the calculation results are presented in Figures 1 and 2.

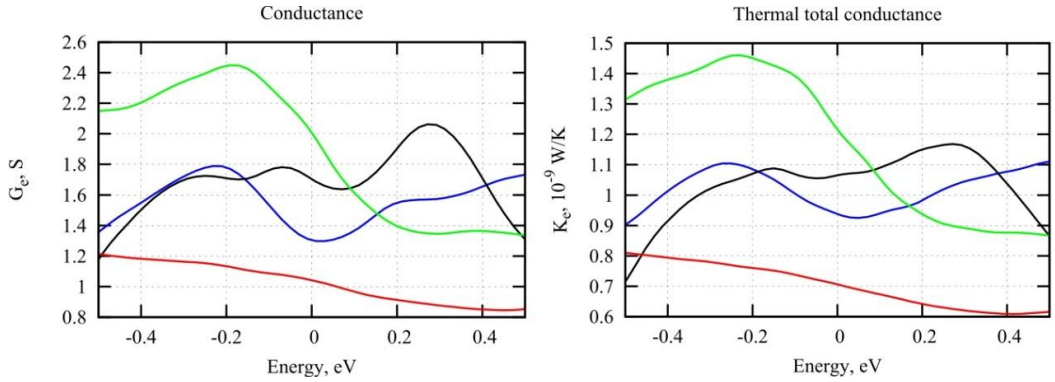


Fig. 1. Electrical conductivity (a) and thermal conductivity (b) coefficients for symmetric grain boundaries in metals with a [111] rotation axis: Fe – blue curve, Ti – black curve, Cu – red curve, Ni – green curve.

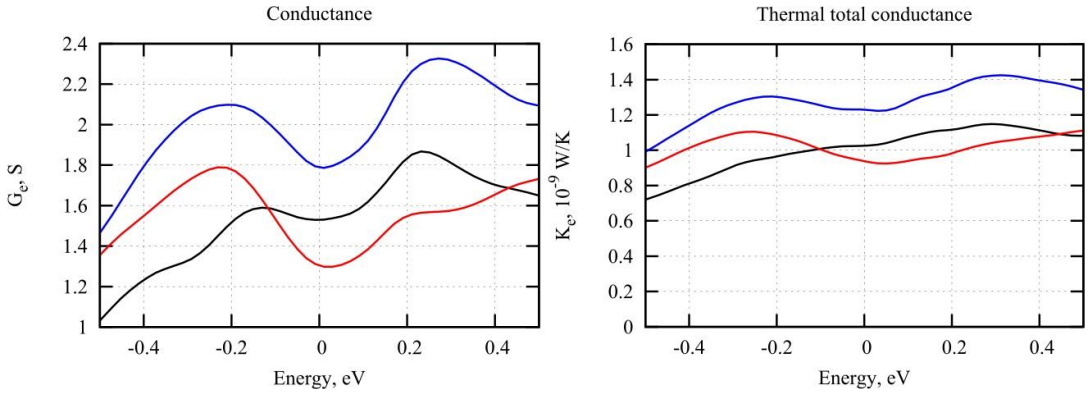


Fig. 2. Electrical conductivity (a) and thermal conductivity (b) coefficients for the symmetric grain boundary of iron with rotation axes [001] (blue curve), [011] (red curve), and [111] (black curve) are provided.

Conclusion

Based on the obtained results, it can be concluded that devices with symmetric tilt grain boundaries in metals exhibit a good electrical conductivity, with relatively low thermal conductivity coefficients (less than 2 nW/K). The grain rotation axis and the misorientation angle influence the device conductivity parameters to varying degrees for each material. For instance, metals with a face-centered cubic lattice will exhibit the highest electrical conductivity coefficient with grain rotation axes [001] and [011]. Thermoelectric efficiency parameters of semiconductors exhibit a pronounced dependence on the variation of the rotation axis. This indicates the importance of the grain orientation in determining the thermoelectric performance of the material.

REFERENCES

1. **Gottstein G.** 2004. Physical Foundations of Materials Science. Springer-Verlag Berlin Heidelberg: 510 p.
2. **Singh R., Schneibel J.H., Divinski S., Wilde G.** Grain boundary diffusion of Fe in ultrafinegrained nanocluster-strengthened ferritic steel. Acta Materialia. 2011. Vol. 59. pp. 1346–1353.
3. **Wachowicz E., Kiejna A.** Effect of impurities on grain boundary cohesion in bcc iron. Computational Materials Science. 2008. Vol. 43. pp. 736–743.

Research of thin Ti/Al films resistivity and transparency change after thermal treatment to determine the possibility of solid solution formation and decrease of the ohmic contacts formation temperature

K. G. Nikitin ✉, L. A. Barsukov, D. D. Tuzhilin, A. V. Romashkin
National Research University of Electronic Technology, Moscow, Russia
✉halkwww@mail.ru

Abstract. Decreasing the temperature of rapid thermal annealing (RTA) for ohmic contact formation is a relevant problem to solve. Annealing at 450 °C has led to a 1.7-fold increase in transparency and a 2-fold increase (up to 128 μΩ·cm) in resistance of Ti/Al thin films. The same annealing procedure for the Al layer without Ti, on the contrary, has resulted in films resistance decrease down to ~27 μΩ·cm and transparency increase by 1.3 times due to a decrease in the effective thickness of Al (due to partial oxidation). Changes in the transparency and conductivity of the Ti/Al layer structure can assumably be explained by the partial formation of a Ti/Al solid solution, which resistivity differs from Al in 2.2 times, and therefore, due to a decrease of the solid solution temperature formation, there is a hypothesis of possible RTA temperature reduction to form the low-resistance contacts to the GaN HEMT transistors.

Keywords: thin films, rapid thermal annealing, ohmic contacts, TiAl compounds, transparency, Raman spectroscopy.

Funding: This research was supported by the Ministry of Science and Higher Education of the Russian Federation in the framework of state task FSMR-2023-0002.

Introduction

Rapid thermal annealing (RTA) at ~850 °C is crucial for ohmic contact to HEMT transistors formation. However, RTA does affect heterostructure's electro-physical parameters, and it is an important problem to decrease RTA temperature [1]. It was proposed to reduce the temperature by using nanothin metal layers, due to its lower melting point compared with bulk ones, to form Ti/Al solid solution compound and activation of related processes, necessary for the formation of high temperature ohmic contacts.

Materials and Methods

Ti (2.3 nm)/Al (11.2 nm) layers on the SiO_2 (300 nm)/Si substrates were deposited using thermal evaporation (0.25 Å/s). Thermal treatment was performed in chamber at 20 °C/min in Ar atmosphere with flow rate ~ 1 l/min. Metal layers resistivity was measured using the 4-probe method. Obtained layers transparency before and after thermal treatment was investigated with Raman spectroscopy by comparing the intensities of Raman scattering signal from Si with and without metal layers on top. It was also observed that after a few days a TiO_2 layer (~4.5 nm) grows from the initial thin Ti layer (~2.5 nm) if there are no layers on top, and TiO_2 forms a slight antireflection coating effect for Si with native oxide (Fig.1a). Obtained Al, Ti/Al films thickness and roughness, as well as oxide growth were controlled with the atomic force microscopy (AFM).

Results and Discussion

It was investigated that even 450 °C annealing is enough to form Ti/Al compounds. Thermal treatment has led to the increase in the film's transparency from 14.1 to 23.5 % (in 1.7 times, Fig. 1b), as well as in its resistivity – from 64 μOhm · cm (2.4 times larger than reference for Al, which is typical for the nanoscale layer) up to 128 μOhm · cm (in 2 times). Overall layers thickness has increased from 29.5 nm to 31.8 nm (Al layer thickness decreased for 1.1 nm due to partial oxidation) after annealing. Same measurements were conducted for the Al without Ti layer: on the contrary, the resistivity decreased from 75 μOhm · cm to ~27 μOhm · cm (due to the clusters integration), whereas transparency increased from 18.9 to 23.2 % (only in 1.2 times, Fig.

1c), as the result of effective Al thickness decrease for 3.3 nm due to the partial oxidation (overall layer thickness increased from 36.4 to 42.9 nm), which align with the reference [2]. An increase of roughness for the Ti/Al, compared to Al was also observed (Fig. 1d).

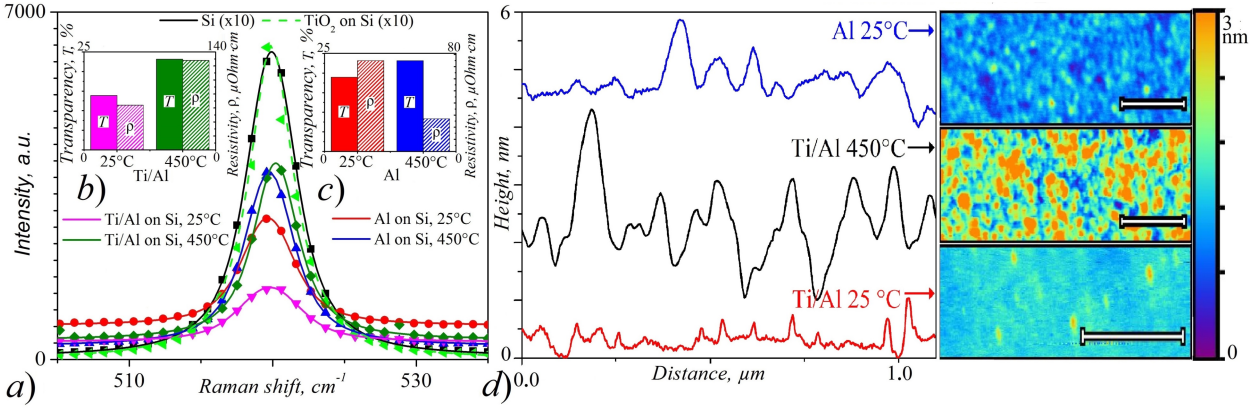


Fig. 1. Raman spectra of Si with Al and Ti/Al nanothin layers (*a*); transparency of Ti/Al layer (*b*), Al layer (*c*); AFM data, scale bar is 0.5μm (*d*).

Conclusion

Thus, considering layers uniformity maintenance with even the roughness increase, despite that XRD has shown no sight of solid solution crystallites of TiAl or $TiAl_3$ compounds, due to the opposite changes in the resistivity of Ti/Al and Al, whereas changes in transparency are similar for both, partial Ti/Al solid solution formation can be presumed (with resistivity exceeding the reference for Al in 2.2 times [3]). Therefore, considering that temperature of ohmic contacts formation during RTA is caused by the necessity of the Ti atoms redistribution, that is crucial in the reactions between N and Ti, Al, with formed at the same time Ti-Al compounds solid solutions (which occurs at >800 °C for the bulk layers [4]). However, Ti melting point can be significantly decreased by using the nanoscale structures [5], but the data obtained for the nanoscale structures used demonstrates the Ti-Al solid solutions formation at the remarkably lower temperatures, hence, as we assume, a significant decrease of the RTA temperature can be achieved while the ohmic contacts formation to the GaN HEMT transistors channel.

REFERENCES

1. **Zhang L. Q., Wu X. L., Miao W. Q., Wu Z. Y., Xing Q., Wang P. F.**, Process of Au-free source/drain ohmic contact to AlGaN/GaN HEMT, Crystals. 12 (6) (2022) 826.

2. **Hass G., Waylonis J. E.**, Optical constants and reflectance and transmittance of evaporated aluminum in the visible and ultraviolet, J. Opt. Soc. Am. 51 (7) (1961) 719-722.

3. **Wöltgens H. W., Friedrich I., Njoroge W. K., Theiß W., Wuttig M.,** Optical, electrical and structural properties of Al–Ti and Al–Cr thin films, Thin solid films. 388 (1-2) (2001) 237-244.

4. **Zhang F., Chen S. L., Chang Y. A., Kattner U. R.,** A thermodynamic description of the Ti-Al system, Intermetallics. 5 (6) (1997) 471-482.

5. **Wang B., Wang G., Chen X., Zhao J.,** Melting behavior of ultrathin titanium nanowires, Physical Review B. 67 (19) (2003) 193403.

Pressure and temperature sensing via ZnO-PDMS based membrane for wearable electronic applications

A. V. Nikolaeva [1✉], **V. M. Kondratev** [1,2], **S. A. Kadinskaya**[1,2], **D. E. Kolesina**[1,3], **F. I. Zubov**[1], **Simchuk O. I.**[1], **F. M. Kochetkov**[1], **L. N. Dvoretckaia**[1], **V. V. Lendyashova**[1], **A. O. Monastyrenko**[1], **A. D. Bolshakov** [1, 2, 4]

[1] Alferov University, Saint Petersburg, Russia;

[2] Moscow Institute of Physics and Technology, Moscow, Russia

[3] Peter the Great St. Petersburg Polytechnic University, Russia

[4] Laboratory of Advanced Functional Materials, Yerevan State University, Yerevan 0025, Armenia

✉nikalex2000@bk.ru

Abstract. In this work, we have grown vertically oriented ZnO microstructures via low-temperature hydrothermal method using microsphere photolithography and followed by etching to prepare the growth substrate and establish ZnO nucleation areas. The synthesized structures were rod-shaped ZnO microcrystals with a height of 5 μm and a diameter of about 400 nm. Such structures were encapsulated in poly(dimethylsiloxane) (PDMS) for ZnO-PDMS membrane formation. Based on this membrane, flexible and solid pressure sensors were fabricated. All sensors have been studied using electrical impedance spectroscopy in terms of the change in resistance and electrical capacitance when pressure is applied. A correlation between the electrical characteristics of such sensors and an applied mechanical pressure was demonstrated. One of such sensors shows the possibility of synchronous measurement of pressure and temperatures in the range of 25°C - 100°C was demonstrated. Fabricated sensors can find their application in the field of personalized healthcare and for the advancement of electronic skin (E-skin).

Keywords: ZnO, PDMS, sensor.

Funding: The Ministry of Science and Higher Education of the Russian Federation (Grant FSRM-2023-0009; agreement 075-03-2023-106, project FSMG-2021-0005; Grant FSRM 2023-0007, 075-03-2023-088; project FSRM-2023-0010; state order no. 0791-2023-0004; Grant 23-72-01133; Grant FSRM-2023-0010).

Introduction

The miniaturization of microelectronics-based sensors has played an influential role in the development of flexible wearable devices that can be repeatedly bent and subjected to mechanical deformation without degradation of functionality [1] and even with the ability to self-heal [2]. In addition, flexible sensors can find their application in personalized healthcare for measuring pressure, heart rate, and temperature, as well as for detecting biometric data, and creating human-machine interfaces.

An array of ZnO microcrystals encapsulated in a PDMS polymer matrix is a material that has both piezoelectric and semiconductor properties, as well as flexibility and resistance to deformation. The advantages of such a sensor also include the simplicity and low cost of synthesizing ZnO by hydrothermal method, which makes it easy to scale up the production technology of such a device.

This work is devoted to the synthesis of ZnO microstructures by low-temperature hydrothermal method using microsphere photolithography, fabrication and study of biocompatible, potentially flexible, wearable, miniature mechanical pressure sensors with the possibility of parallel temperature measurement.

Materials and Methods

The ZnO growth substrates were pre-processed using a photolithography technique [3] with quartz spheres, 1.5 μm in diameter, on a silicon (Si) substrate in a 30 nm thick silicon oxide (SiO_2) layer followed by etching in KOH to obtain an ordered array of 400 nm diameter holes. The ZnO microwires (MWs) were synthesized via low-temperature hydrothermal method which involves

the oriented growth of zinc oxide microstructures in an aqueous solution of growth precursors. Zinc oxide crystals were encapsulated in PDMS by g-coating method. The ZnO-PDMS membrane was separated from the substrate to fabricate a flexible pressure sensor with carbon nanotubes (CNT) as electrodes. The flexible sensor was studied in the pressure range 80 - 300 kPa.

For measuring pressures in the order of MPa and temperature sensing in the range of 25°C - 100°C, a solid sensor based on the ZnO-PDMS membrane was fabricated using Al_2O_3 ceramic substrates with counter-pinned gold contacts. All sensors were studied by electrical impedance spectroscopy technique using impedance meter Z500P (Elins Ltd., Russia) in the frequency range 500 Hz - 500 kHz with amplitude 100 mV and bias voltage 2 V.

Results and Discussion

Flexible and solid sensors based on the ZnO-PDMS membrane showed an increase in electrical capacitance (C) and a decrease in resistance (R) with increasing pressure. The increase in the electrical capacity of the sensors (C) can be explained in terms of the piezoelectric effect that occurs in an array of ZnO microcrystals under mechanical deformation. The decrease in sensor resistance (R) is associated with the establishment of contact between the top electrode and the tops of the microcrystals when pressure is applied.

The solid sensor showed a decrease in the real (Z') and an increase in the imaginary (Z''') part of the impedance by 5% and 10%, respectively, compared to the initial values when the temperature was changed by 75°C. The decrease in the real part of impedance (Z'), which is associated with resistance (R), with increasing temperature can be attributed to the semiconducting properties of ZnO.

Conclusion

Thus, a protocol for creating a flexible sensor for low-pressure measurements and a protocol for creating a solid sensor for high-pressure measurements was established. In addition, the possibility of synchronous measurement of pressure and temperature was demonstrated on the example of one of the sensors.

Acknowledgments

A.D.B. thanks Ministry of Science and Higher Education of the Russian Federation (agreement 075-03-2023-106, project FSMG-2021-0005) for support of the experiments.

V.M.K. and A.V.N. thanks Ministry of Science and Higher Education of the Russian Federation (Grant FSRM-2023-0009) for support of analysis of the experimental data.

F.M.K and D.E.K thanks the Ministry of Science and Higher Education of the Russian Federation (Grant FSRM 2023-0007, 075-03-2023-088) for support of the samples encapsulation.

V.V.L. thanks Ministry of Science and Higher Education of the Russian Federation as part of state order no. 0791-2023-0004 for support of the substrate preparation.

L.N.D thanks Russian Science Foundation (Grant 23-72-01133) for financial support of the lithography.

F.I.Z. and S.O.I. acknowledges financial support of the Ministry of Science and Higher Education of the Russian Federation under project FSRM-2023-0010. for support of the solid samples fabrication.

REFERENCES

1. **Sekitani T., Zschieschang U., Klauk H., Someya T.,** Flexible organic transistors and circuits with extreme bending stability, Nat Mater 9 (2010) 1015–1022. https://doi.org/10.1038/nmat2896.

2. **Yang M., Cheng Y., Yue Y., Chen Y, Gao H., Li L., Cai B., Liu W., Wang Z., Guo H., Liu N., Gao Y.,** High-Performance Flexible Pressure Sensor with a Self-Healing Function for Tactile Feedback, Advanced Science 9 (2022). https://doi.org/10.1002/advs.202200507.

3. **Dvoretckaia L.N., Mozharov A.M., Gavrilov M.S., Fedorov V.V.,** Microspherical lithography for selective epitaxy, in: 2022 International Conference Laser Optics (ICLO), IEEE, 2022: pp. 1–1. https://doi.org/10.1109/ICLO54117.2022.9840191.

Nanostructured bimetallic PtNi catalyst for electrochemical systems with solid polymer electrolyte

M.D. Novichkov [1]✉, S.A. Gurin [1], A.E. Shepeleva[1], E.A. Pecherskaya [1]
[1] Federal State Budgetary Educational Institution "Penza State University", Penza, Russia
✉novichkov1998maks@gmail.com

Abstract. A method for forming a nanostructured bimetallic PtNi catalyst on the surface of a solid polymer electrolyte is presented. Nickel particles, on which the bulk of the platinum catalyst is grown by chemical deposition, are obtained by magnetron sputtering. The resulting system has high catalytic activity and temporary stability.

Keywords: bimetallic catalyst, solid polymer electrolyte, catalytic layer, magnetron sputtering, chemical deposition.

Funding: Funding:The work was supported by the grant of the Ministry of Science and Higher Education of the Russian Federation «Synthesis and research of promising nanomaterials, coatings and electronics devices» (№ 124041700069-0).

Introduction

Modern hydrogen-oxygen fuel cells typically consist of two electrodes, an anode and a cathode, separated by a polymer electrolytic membrane (PEM) [1]. The PEM use in its original form in fuel cells shows low productivity, which requires the introduction of a catalyst into the reaction area [2]. The most active in the hydrogen oxidation are catalysts based on highly dispersed platinum clusters, the properties and structure of which significantly determine the degree of the electrolytic process intensification [3,4].

Experimental technique

The PtNi bimetallic catalysts synthesis was carried out in two stages. At the first stage, adsorption centers were obtained on the surface of a solid polymer electrolyte (Nafion) using magnetron sputtering of a nickel target. Next, by chemical precipitation from a solution of H_2PtCl_6 - 2 g/l, N_2H_4 - 1.0 g/l, NH_4OH (conc.) - 200 ml/l, the main catalyst volume was formed to form a shell-core structure of platinum on nickel on the PEM surface. Based on the membrane with the resulting catalyst, a membrane-electrode unit (MEU) with an electrode area of 7 cm^2 was manufactured for testing as a part of a water electrolyzer and a fuel cell.

Results and Discussion

The study of the current-voltage characteristics of the obtained MEUs was carried out in comparison with MEUs based on a membrane with a catalyst synthesized only by a chemical method (Fig. 2).

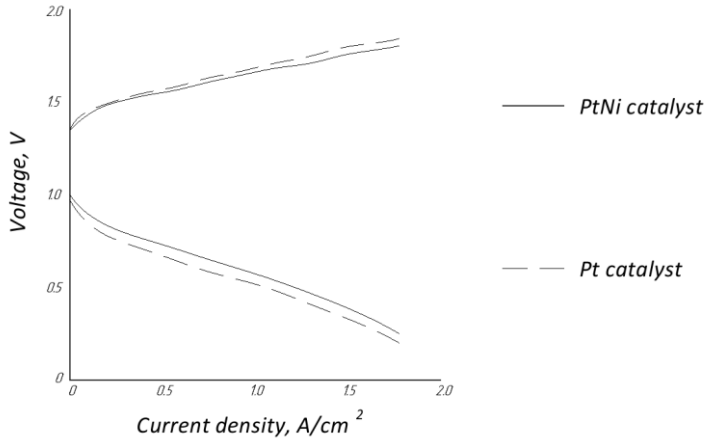


Figure 1. Current-voltage characteristics of the MEU

The characteristics of bimetallic catalysts are higher, which is explained by electronic effects (lowering the energy of vacant d orbitals). Thus, the water electrolysis voltage is 0.03 V less at a current density of 1 A/cm2, while the fuel cell voltage at the same current density is 0.05 V higher than the value for a MEU with a catalyst obtained by a chemical method.

It is also worth noting that the high energy of deposited particles during magnetron sputtering (10-20 eV) leads to energetic activation of the condensation process of particles on the substrate and, as a consequence, high coupling between the catalyst and the substrate [5], thereby having a positive effect on the MEU characteristics stability.

Conclusion

The use of a combination of magnetron sputtering and chemical deposition to form nickel and platinum layers, respectively, makes it possible to obtain bimetallic catalysts on the surface of solid polymer electrolytes characterized by high functional characteristics and their stability.

REFERENCES

1. **A.B. Yaroslavtsev, Y.A Dobrovolsky, N.S Shaglaeva, L.A. Frolova, E.V.Gerasimova, E.A.Sanginov**., Advances in Chemistry. 2012. V. 81. No. 3. Pp. 191-220.

2. **Grigoriev S.A., Fedotov A.A., Murzin, V. Yu., Khramov E.V.,** Study of nanostructured electrocatalysts synthesized by magnetron-ion sputtering of platinum on a metallized nanocarbon carrier. Electrochemistry. Publishing House of the Russian Academy of Sciences. 2015. V.51, No. 9, P. 915-929.

3. **Hodnik M., Zorko M., Bele M., Hocevar S., Gaberscek M.,** Identical location scanning electron microscopy: a case study of electrochemical degradation of PtNi nanoparticles using a new nondestructive method, J. Phys. Chem. C. – 2012. – V. 116. – № 40. – P. 21326–21333.

4. **Rabis A., Rodriguez P., Schmidt T.J.,** Electrocatalysis for Polymer Electrolyte Fuel Cells: Recent Achievements and Future Challenges. ACS Catalysis. 2012. V.2, P.864–890. 10.1021/cs3000864.

5. **Fateev V.N., Alekseeva O.K., Porembskii V.I., Mikhalev A.I., Nikitin S.M.,** Corrosion-resistant electrodes/current collectors for anodes of electrolysis cells with solid polymer electrolyte. International Scientific Journal "Alternative Energy and Ecology" (ISJAEE). 2017;(25-27):88-99.

The mechanism of filtering of nanoscale aerosols with renewable electret filters

Pershin N.A.[1], Sudin V.V.[2], Pershin A.N.[3], Ivanov V.V..[1]

[1]Moscow Institute of Physics and Technology (MIPT), 141701, Moscow Region, Dolgoprudny, Institutsky Lane, 9.

[2] A.A. Baikov Institute of Metallurgy and Materials Science, Russian Academy of Sciences, 119334, Moscow, Leninsky Prospect, 49

[3]OOO "ITI", 129110, Moscow, Banny str, 2, Building 1

e-mail: pershin.na@phystech.edu, vsudiyn@imet.ac.ru

Abstract: The mechanism of operation of renewable electret filters in capturing nanoscale aerosols of conducting material has been investigated. Nanoparticles of nickel oxide II (NiO) with sizes ranging from 50-100 nm were used as the test aerosol. It has been shown that the aerosol charged in a corona discharge is effectively captured by the investigated filter. The filtration efficiency depends on the total electric charge accumulated by the filter. Increasing the conductivity of the filter through the deposition of conducting particles leads to charge dissipation, a decrease in the overall electric charge of the filter, and a reduction in filtration efficiency.

Keywords: nanoparticles, aerosols, electret filter, clean rooms

Funding: Research agreement No. 2021-09 dated September 20, 2021 between LLC "ITI" and MIPT

Introduction

Air pollution with nanoscale aerosols has significantly increased in recent decades. It is known that such aerosols have a substantial negative impact on human health. In addition, high requirements for the content of nanoscale aerosols in the air of clean rooms are set by GOST R ISO 14644-1-2017. One of the promising methods for air purification from aerosols is the use of renewable electret filters, in which the filtering material accumulates charge from aerosol particles acquiring it in a corona discharge. This method is successfully used in supply and exhaust ventilation systems for medical institutions. However, the filtration mechanism is not fully understood, and it remains unclear which filter parameters most affect filtration efficiency. The aim of this study was to investigate the mechanism of operation of renewable electret filters and to study the evolution of their parameters as they become contaminated with conductive materials.

The cylindrical renewable electret filters investigated in this study were made of polypropylene using a melt blowing method and applying it to a rotating spindle. The filters had a thickness of 15 mm, a length of 440 mm, and an inner diameter of 130 mm. To ensure charge dissipation and prevent the possibility of electrical breakdown inside the filter, a steel wire was placed.

Materials and Methods

To carry out experiments measuring filtration efficiency, we assembled a test stand, the schematic of which is shown in Fig. 1.

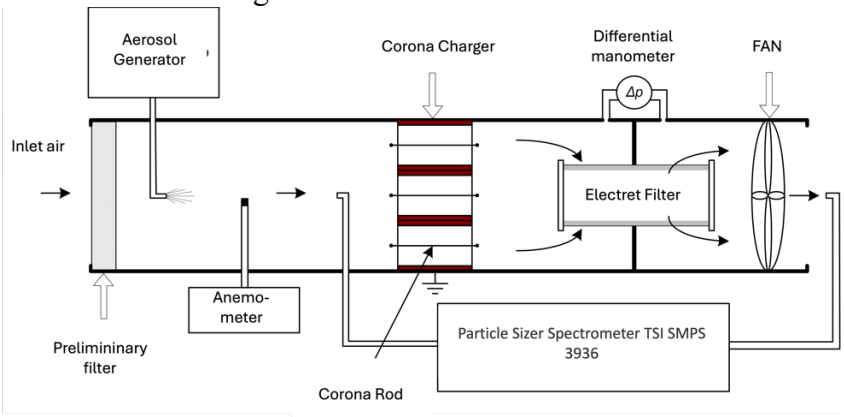


Fig 1 - Diagram of the setup for measuring filter efficiency.

Aerosol generation was carried out in a pulsed-periodic gas discharge on a nickel electrode in an air flow [4]. The concentration measurement was performed using a nanoparticle aerosol spectrometer with a TSI SMPS 3936 differential mobility analyzer. The aerodynamic parameters of the system were measured using a Testo 417 anemometer and Testo 517 differential pressure meter. A picoampere meter KEITHLEY 617 Programmable Electrometer was used to measure the current passing through the filter grounding wire. The total charge of the filter was measured by placing it in a Faraday cylindrical cell and measuring the potential difference between the cell electrode and the grounded electrode using an electrostatic kilovoltmeter C96. The structure of the deposited aerosol on the fiber surface was investigated using a FEI Quanta 200 scanning electron microscope.

Results and discussion

The size of the particles in the initial aerosol ranged from 20 to 220 nm, with the peak distribution varying from 56 to 100 nm. Diagrams of the aerosol particle size distribution are shown in Figure 2.

Measurement of aerosol concentration before and after the filter showed that the total particle penetration at a linear air flow velocity on the filter surface of 0.28 m/s (flow rate of 215 m3/h) was 0.23%. The efficiency of aerosol filtration is weakly dependent on size in the range of 60 to 220 nm and decreases for particles smaller than 50 nm.

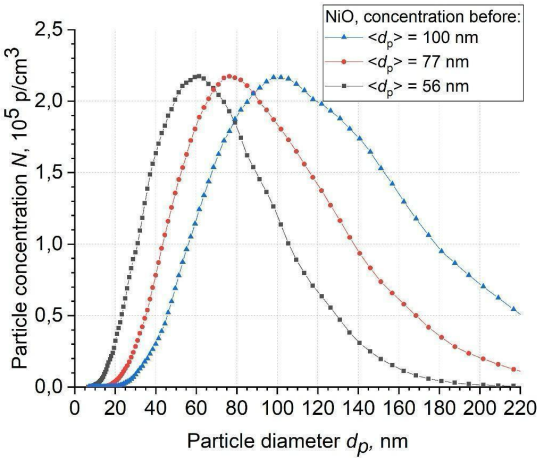
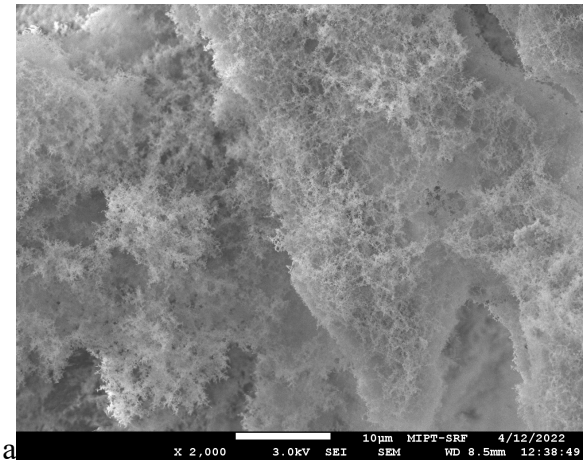


Fig. 2 - Distribution of aerosol particle sizes delivered to the filter

Particles of the aerosol deposited on the surface of fibers form dendritic structures. Their formation may be related to the uneven distribution of charge. A possible formation mechanism is associated with the increased attraction force of uncharged particles to a charged surface with a small radius of curvature. The view of the formed structures is shown in Figure 3. The deposition of aerosol on the filter surface is uneven. More particles are deposited near the grounding wire coils than between the coils, which can be observed by the change in color of the filter.

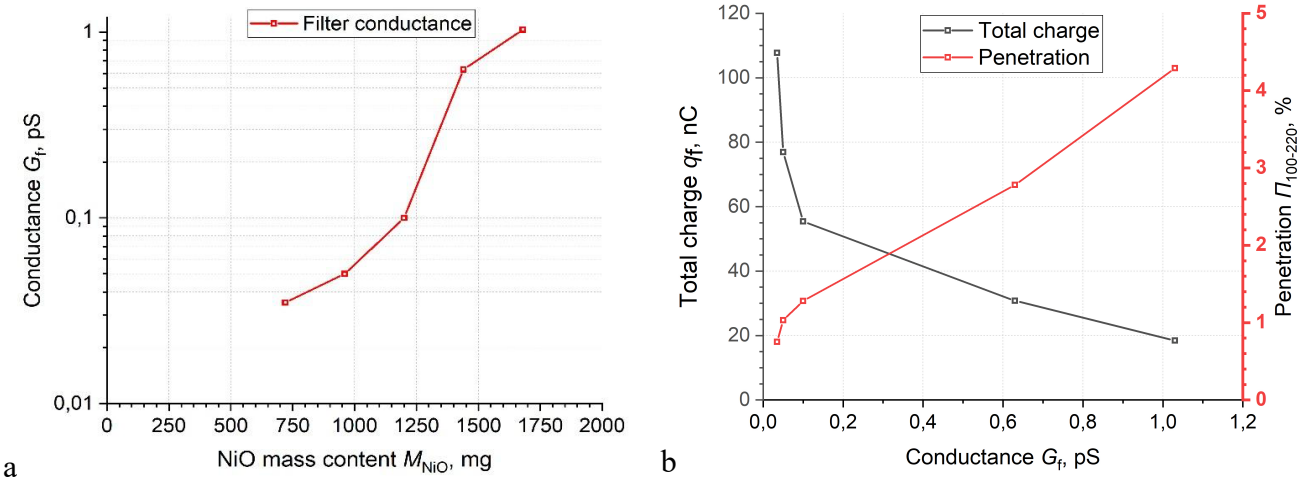


a

Figure 3 - Structure of aerosol particles deposited on the surface of filter fibers

Measurement of the current flowing between the wire inside the filter and the grounded electrode showed that when capturing larger aerosol particles, the current increases. This indicates that larger particles carry a greater charge, which is consistent with the results of other studies [5]. Increasing the concentration of aerosol particles while maintaining the size distribution leads to a proportional increase in the grounding current of the filter. Measurement of the total charge of the filter showed that it also linearly increases.

As the amount of aerosol deposited on the filter increases, the conductivity of the filter increases. At the same time, there is a decrease in the total charge of the filter and a decrease in the efficiency of aerosol filtration.



a b

Figure 4 - Dependence of filter conductivity on the amount of deposited nickel oxide (a), dependence of total charge and grounding current on filter conductivity (b)

Conclusions

1) Reusable electret filters effectively remove nanoscale aerosols from the air stream with uniform efficiency in the range of 60 - 220 nm.

2) The filter charge is determined by the balance between the total charge of the captured aerosol and the filter grounding current.

3) Filtration efficiency depends on the total filter charge and decreases with its reduction.

4) Deposition of conducting aerosols increases filter conductivity and reduces total charge and filtration efficiency.

References

1. **Jeevanandam J., Barhoum A., Chan Y. S., Dufresn, A., Danquah M. K.** (2018). Review on nanoparticles and nanostructured materials: history, sources, toxicity and regulations. Beilstein J. Nanotechnol. 9, 1050–1074. doi: 10.3762/bjnano.9.98
2. **Slezakova K., Morai, S., Carmo Pereira M.** Atmospheric nanoparticles and their impacts on public health. *Current topics in public health*. 2013 IntechOpen.
3. **Sokan-Adeaga A. A. et al.** Secondary inorganic aerosols: impacts on the global climate system and human health //Biodiversity Int J. – 2019. – Т. 3. – №. 6. – С. 249-59.
4. **Ivanov V.V., Efimov A.A., Mylnikov D.A., Lizunova A.A**. Synthesis of nanoparticles in pulsed-periodic gas discharge and their potential applications // Journal of Physical Chemistry. *2018. Vol. 92. No. 3. P. 494-500.*
5. **Yu Y. et al**. Effect of Oily Aerosol Charge Characteristics on the Filtration Efficiency of an Electrostatically Enhanced Fibrous Filter System //Separations. 2022. V. 9. №. 10. P. 320.

Study of the effect of surfactants on surface tension of PEDOT:PSS aqueous solution

V. A. Pozdeev [1,2] ✉, A. V. Uvarov [1], A.S. Gudovskikh [1,2], A. O. Monastyrenko [1]

[1] St. Petersburg Alferov Academic University, St. Petersburg, Russia;

[2] St. Petersburg Electrotechnical University "LETI", St. Petersburg, Russia

✉pozdeev99va@gmail.com

Abstract. In this paper we investigate a technique to determine the minimum surface tension and minimal surfactant concentration (Triton X-100) in a poly(3,4-ethylenedioxythiophene):polystyrenesulfonate (PEDOT:PSS) aqueous solution to achieve full wetting of surfaces with silicon and fused silica.

Keywords: PEDOT:PSS, poly(3,4-ethylenedioxythiophene) polystyrene sulfonate, conductive polymer, surfactants, Triton X-100.

Funding: This work was supported by the Russian Science Foundation under grant number (№23-22-00367) https://rscf.ru/project/23-22-00367/.

Introduction

One of the drawbacks of applying PEDOT:PSS coatings from an aqueous solution is that water exhibits relatively high surface tension, leading to poor wettability on different substrates. Polymer solutions have slightly lower surface tension [1], but it is insufficient for complete wetting of silicon and fused silica substrates. Surfactants are traditionally used for effectively reducing surface tension. However, the high content of surfactants has a negative impact on the electrophysical properties of PEDOT:PSS [2].

To determine the surface tension of a liquid at which complete wetting of a specific substrate occurs (critical surface tension), one can use the Zisman plots at zero contact angle [3].Through the dependence of surface tension on surfactant concentration in the PEDOT:PSS solution, one can determine the required surfactant concentration to achieve the desired surface tension value of the solution and attain complete wetting of the substrate. This will help avoid excessive addition of surfactants to the solution, and significantly reduce material consumption when determining the appropriate concentration.

Materials and Methods

Contact angles were determined using a photographic method based on the width and height of the drop on the half-width. When using drops ranging from 1 μL to 3 μL, the influence of gravity on the drop shape can be neglected, allowing us to consider the drop as a segment of a sphere [4]. When determining the values of contact angles, the consideration of evaporation, drop spreading, and absorption of water vapor from the environment was achieved by extrapolating the kinetic curve onto the time axis. The obtained contact angle value can be considered to correspond to the equilibrium contact angle [4].

The measurements were taken at a fixed humidity and close to room temperature. Humidity control was maintained using a saturated solution of an inorganic salt, as detailed in the method presented in this paper[5].

To determine the surface tension, two test substrates made of different materials were utilized. Water and dimethyl sulfoxide were employed to assess the surface energy of the substrates. Aqueous solutions with varying concentrations of surfactants were utilized to study Zisman plots. The dependance between the surface tension of the PEDOT:PSS solution and the concentration of the surfactant contained within it was obtained through a similar procedure. Triton X-100 was used as the surfactant.

Results and Discussion

The surface tension, particularly its polar and dispersive components, was determined using formulas derived from the Owens-Wendt method [6]. The surface energy values and their dispersive and polar components for the substrates were also determined under the same conditions using formulas derived from the same method.

As a result, Zisman plots were obtained along with the critical surface tension values for silicon and fused silica. The dependence of the surface tension of the PEDOT:PSS solution on the concentration of Triton X-100 was determined.

Conclusion

This study demonstrated a methodology to determine the minimum required concentration of surfactants in an aqueous polymer solution for its subsequent application to a substrate surface. The critical surface tension for silicon and fused silica was determined, and numerical values of the minimum required concentration of Triton X-100 in the PEDOT:PSS solution for complete wetting were obtained. The results of this study can be used in the production of electronic devices based on organic semiconductor material PEDOT:PSS.

REFERENCES

1. Holmberg, K.; Jönsson, B.; Kronberg, B.; Lindman, B., Surfactants and Polymers in Aqueous Solution. 2nd ed.; Wiley: Chichester, U.K., 2003.

2. Pozdeev V., Uvarov A., Gudovskikh A., Maksimova A., Vyacheslavova E., Study of the effect of solvents and surfactants on electrical properties of PEDOT:PSS films, St. Petersburg State Polytechnical University Journal. Physics and Mathematics. (2023).

3. Zisman W. A., Relation of the Equilibrium Contact Angle to Liquid and Solid Constitution, Advances in Chemistry. (1964) 1–51

4. Lyakhovich A. M., Shakov A. A., Lyalina N. V. Effect of ambient humidity to wetting angles of various hydrophilic surfaces, Protection of Metals and Physical Chemistry of Surfaces. 46 (5) (2010) 534–539.

5. Young J. F., Humidity control in the laboratory using salt solutions—a review, Journal of Applied Chemistry. 17(9) (1967) 241–245.

6. Owens, D. K., & Wendt, R. C., Estimation of the surface free energy of polymers, Journal of Applied Polymer Science. 13(8) (1969) 1741–1747.

Study of the influence of ambient temperature on the magnitude of the piezoelectric strain coefficient of nitrogen-doped carbon nanotubes for the creation of nanopiezotronics devices

M.V. Il`ina, O.I. Soboleva, M.R. Polyvianova✉, D.N. Khomlenko, O.I. Il`in
Institute of Nanotechnologies, Electronics and Equipment Engineering, Southern Federal University, Taganrog 347922, Russia
✉polyvianova@sfedu.ru

Abstract. The paper establishes the patterns of the influence temperature on the piezoelectric strain coefficient and the magnitude of the current generated by nitrogen-doped carbon nanotubes (N-CNTs) during their deformation. It is shown that the value of the piezoelectric strain coefficient N-CNTs with an increase in temperature from 25 to 85 ° C varies non–linearly from 7 to 71 pm/V, while in the temperature range of 25-75 ° C, stable current generation of 11 ± 4 nA is observed.

Keywords: carbon nanotubes, nanopiezotronics, piezoelectric response, piezoelectric force microscopy, atomic force microscopy.

Funding: This research was supported by the Ministry of Science and Higher education of the Russian Federation in the framework of the state task in the field of scientific activity, grant number FENW-2022-0001.

Introduction

Recent achievements in the field of nanotechnology, microelectronics and microelectromechanics have made it possible to create a wide variety of wearable and personalized electronics devices [1]. However, there are a number of problems related to the energy efficiency of such devices, their miniaturization, increased autonomy and safety [2]. Potentially, the solution to this problem is associated with the development and application of converters of mechanical vibrations into electrical energy – nanogenerators [3].

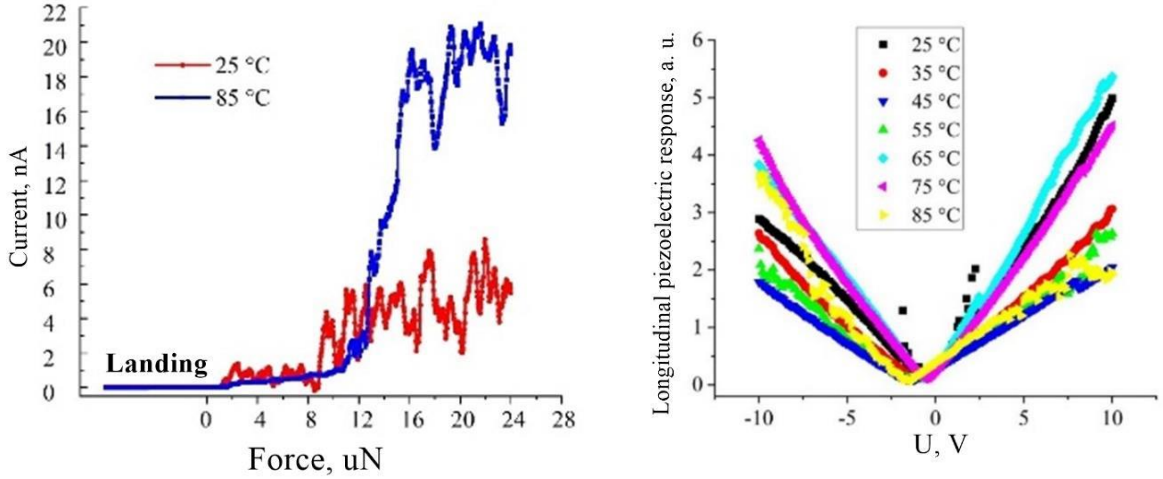
In this paper, the influence of ambient temperature on the piezoelectric properties of nitrogen-doped carbon nanotubes was studied to create devices that convert mechanical vibrations into electrical energy.

Materials and Methods

The experimental sample was an array of vertically aligned carbon nanotubes grown by plasma enhanced chemical vapor deposition in flows of process gases acetylene (C_2H_2. 35 cm^3/min) and ammonia (NH_3, 280 cm^3/min). The geometric parameters of the CNT array were estimated based on statistical image processing by scanning electron microscopy (SEM). Studies of the piezoelectric properties of vertically aligned N-CNTs were carried out by the method of piezoelectric force microscopy (PFM) atomic force microscopy (AFM)

Results and Discussion

The results of experimental studies of the effect of temperature on the value of the generated N-CNT current showed (Fig. 1, a) that at a temperature from 35 to 75 ° C, the value of the generated N-CNT current varies insignificantly and is 11 ± 4 nA. At a room temperature of 25 ° C, the current value is 7 ± 3 nA, and at a temperature of 85 ° C, an increase in the value of the generated current is observed to 21 ± 10 nA (Fig. 1, a). This dependence is probably due to the presence of an adsorption layer on the surface of N-CNT, which begins to desorb with an increase in temperature from 85 ° C and above. As a result, an increase in the piezoelectric response of the N-CNTs is observed (fig. 1, b).



a) b)

Fig. 1. The results of experimental studies of the influence of ambient temperature on the magnitude of the current generated by the N-CNT from the pressure force of the AFM probe (a) and the magnitude of the longitudinal piezoelectric response (b).

At the same time, the value of the piezoelectric strain coefficient N-CNT varied non-linearly with increasing temperature from 7 to 71 pm/V. The maximum value of d33 was observed at a temperature of 75 °C, the minimum value at 85 °C.

This pattern is associated with the thermal decomposition of intermediate amide fragments and pyridone, which can transform into pyridine and pyrrole type nitrogen, thereby increasing the value of the piezoelectric strain coefficient in the temperature range 65-75 ° C. A rapid decrease in the piezoelectric strain coefficient of N-CNT at 85 °C is probably observed due to the negative temperature coefficient of expansion of carbon nanotubes.

Conclusion

The paper establishes the regularities of the influence of the temperature value on the piezoelectric strain coefficient and the amount of current generated by N-CNTs during their deformation. It is shown that the value of the piezoelectric strain coefficient N-CNT with an increase in temperature from 25 to 85 °C varies non–linearly from 7 to 71 pm/V, while stable current generation of 11 ± 4 nA is observed in the temperature range of 25-75 ° C.

The results obtained can be used in the development of mechanical energy converters, the creation of highly sensitive microphones, strain sensors, as well as nanogenerators to ensure autonomous operation of wearable and implantable electronics.

REFERENCES

1. **Paradiso J.A., Starner T.** Energy Scavenging for Mobile and Wireless Electronics // IEEE Pervasive Comput. 2005. Vol. 4, № 1. P. 18–27.

2. J**hu C.-Y., Wang Y.-W., Shu C.-M., Chang J.-C., Wu H.-C.** Thermal explosion hazards on 18650 lithium ion batteries with a VSP2 adiabatic calorimeter // J. Hazard. Mater. 2011.

3. **Kwon J., Sharma B.K., Ahn J.-H.** Graphene Based Nanogenerator for Energy Harvesting // Jpn. J. Appl. Phys. 2013. Vol. 52, № 6S. P. 06GA02.

Change in the carbon nanotube thin layer refractive index after water and ammonia molecules adsorption

A. V. Romashkin [1✉], **R. Yu. Rozanov** [2], **A. V. Lashkov** [1], **A. E. Mitrofanova** [2], **D. D. Levin** [2], **A. S. Vishnevskiy** [3], **V. V. Svetikov** [2]

[1] National Research University of Electronic Technology, Moscow, Russia;
[2] JSC "Zelenograd Nanotechnology Center", Moscow, Russia;
[3] MIREA – Russian Technological University, Moscow, Russia
[✉] romaleval@gmail.com

Abstract. Spray-deposited carboxylated carbon nanotube (CNT) layers were characterized using AFM, Raman scattering and spectroscopic ellipsometry. The layers thickness, diameters and band gap of CNTs, as well as the changes in the CNT layer refractive index for 1450 nm and 1950 nm after H_2O and NH_3 adsorption were analyzed. Obtained refractive index changes and simulated results of necessary length of modified interferometer arm for π phase shift allow us to propose the use of such CNT layers to produce integrated interferometric sensors and solve gas recognition tasks.

Keywords: carbon nanotube, ellipsometry, integrated optics, interferometer, sensor.

Funding: This research was supported by the Ministry of Science and Higher Education of the Russian Federation in the framework of state tasks FSMR-2023-0002 (spray deposition, post-processing, AFM, Raman study, CNT layers ellipsometry data analysis) and partially FSFZ-2023-0005 (RTU MIREA: CNT layer ellipsometry in N_2 with H_2O, 2-propanol vapors).

Introduction

Recently, instead of using a complex system with various wavelengths to detect gases based on their absorption peaks, multisensor interferometric systems for gas recognition have been demonstrated. To achieve their high sensitivity it is important to develop thin modifying layers, that significantly alter their own refractive index (n) upon analyte adsorption [1,2]. It is also relevant for interferometric biosensors [3]. Modified nanocarbon materials are promising for these tasks.

Results and Discussion

We studied 3, 30, 60 nm (according to AFM (NT-MDT, Russia) data, Fig. 1a) layers of carboxylated carbon nanotubes (CNTs, P3-SWNT, Carbon Solutions, USA) with a diameter of 1.3–1.6 nm, according to Raman RBM-band (532 nm laser, Nano Scan Technology, Russia), spray deposited from a dispersion [4] onto a Si substrate with native oxide, followed by the residual solvent removal. Spectroscopic ellipsometry (SENTECH Instruments, Germany) was performed at angles of incidence: 75° (Fig. 1b-d), 70°, 65° at λ: 371–2300 nm for the layer after exposure in a chamber with H_2O (~12500 ppm: humidity change from 30 % to ~75 %) or NH_3 (~2000 ppm) and after 25 min of desorption under normal conditions at the same sample area, but different for each analyte. The values of n and carrier concentration (p) in the layer were estimated from the found Drude-Lorentz model parameters, obtained by fitting the spectroscopic ellipsometry experimental data [5]. Due to the layer thickness non-uniformity (~10 %) but using the same thickness in the model for each analyte, estimates of the n are slightly different (Fig. 1b). When exposed to H_2O, n increased from 2.516 to 2.518 at 1450 nm and from 2.659 to 2.668 at 1950 nm (corresponding to the CNT band gap values, E_{g_CNT}~0.64 eV, marked by vertical dashed lines in Fig.1b), p dropped from $1.76 \cdot 10^{19}$ to $1.70 \cdot 10^{19}$ cm^{-3} (~3.5 %, corresponds to the resistive response [4]). When exposed to NH_3, n dropped from 2.382 to 2.379 at 1450 nm, but increased from 2.585 to 2.565 at 1950 nm, p dropped from $2.06 \cdot 10^{19}$ to $2.02 \cdot 10^{19}$ cm^{-3} (~2 %).

Taking into account the differences in the concentrations of H_2O and NH_3, the measurement results indicate a change in the electronic structure of CNTs during adsorption, and are not associated with filling the pores of the layer. This is further supported by the nature of the n response changes, when the carrier gas changes. H_2O adsorption led to an increase in the n at

air conditions (Fig.1b), but decrease in the *n* when the carrier gas was dry N_2 (and the same behavior for 2-propanol: *n* also decrease with dry N_2). This effect is presumably related to a charge carriers type change: from holes in air conditions to electrons in dry N_2 [6].

According to the results of numerical modeling (Beam Propagation Method, BPM, in RSoft CAD Layout software), the required π phase shift is achieved in the Si_3N_4 waveguide Mach-Zehnder interferometer structure with a modified by CNT arm length: ~5800 μm for λ=1450 nm and ~1800 μm for λ=1950 nm, according to the ellipsometric data of CNT layer *n* changes for H_2O; ~3400 μm for λ=1450 nm and ~800 μm for λ=1950 nm, according to the CNT layer *n* changes for NH_3. Losses in the area with the CNT layer do not exceed 5 %.

Therefore, it is possible to use similar CNT layers to modify the surface of waveguides in integrated interferometric sensors, providing high sensitivity and selectivity.

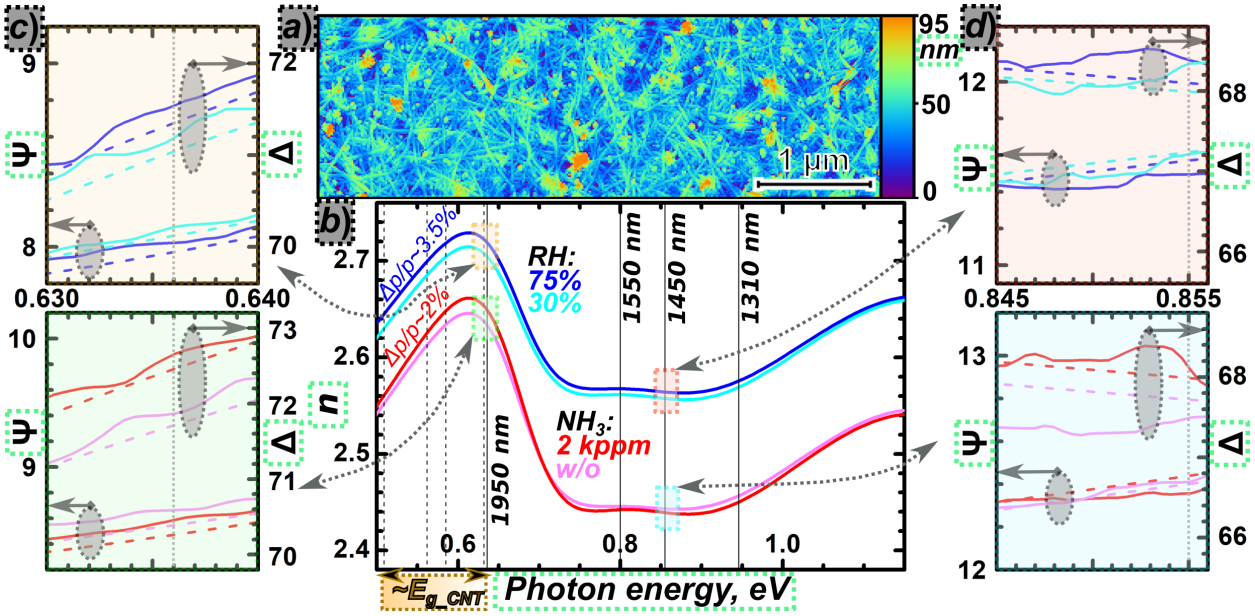


Fig. 1. AFM of the CNT layer (*a*). Refractive index with and without H_2O and NH_3 in air (*b*), experimental (solid) and calculated (dashed) Ψ and Δ ellipsometry data for 1950 nm (*c*), 1450 nm (*d*).

REFERENCES

1. **Laplatine L., Fournier M., Gaignebet N., Hou Y., Mathey R., Herrier C., Liu J., Descloux D., Gautheron B., Livache T.,** Silicon photonic olfactory sensor based on an array of 64 biofunctionalized Mach-Zehnder interferometers, Optics Express. 30 (19) (2022) 33955.

2. **Huang G., Li Y., Chen C., Yue Z., Zhai W., Li M., Yang B.,** Hydrogen sulfide gas sensor based on titanium dioxide/amino-functionalized graphene quantum dots coated photonic crystal fiber, Journal of Physics D: Applied Physics. 53 (32) (2020) 325102.

3. **Nekrasov N., Yakunina N., Pushkarev A. V., Orlov A. V., Gadjanski I., Pesquera A., Centeno A., Zurutuza A., Nikitin P. I., Bobrinetskiy I.,** Spectral-phase interferometry detection of ochratoxin a via aptamer-functionalized graphene coated glass. Nanomaterials. 11 (1) (2021) 226.

4. **Romashkin A. V., Lashkov A. V., Sysoev V. V., Struchkov N. S., Alexandrov E. V., Levin D. D.,** Energy-Efficient Chemiresistive Sensor Array Based on SWCNT Networks, WO_3 Nanochannels and SWCNT-Pt Heterojunctions for NH_3 Detection against the Background Humidity, Chemosensors, 10 (11) (2022) 476.

5. **Barnes T. M., Van de Lagemaat J., Levi D., Rumbles G., Coutts T. J., Weeks C. L., Britz D. A., Levitsky I., Peltola J., Glatkowski P.,** Optical characterization of highly conductive single-wall carbon-nanotube transparent electrodes, Physical Review B. 75 (23) (2007) 235410.

6. **Avouris P., Martel R., Derycke V., Appenzeller J.,** Carbon nanotube transistors and logic circuits, Physica B: Condensed Matter. 323 (1-4) (2002) 6-14.

Study of the influence of ambient humidity on the magnitude of the piezoelectric strain coefficient of nitrogen-doped carbon nanotubes for the creation of strain sensors

O.I. Soboleva✉, M.V. Il`ina, M.R. Polyvianova, A.A. Chefranov, O.I. Il`in
Institute of Nanotechnologies, Electronics and Equipment Engineering, Southern Federal University, Taganrog 347922, Russia
✉osotova@sfedu.ru

Abstract. The paper establishes the patterns of the influence of ambient humidity and temperature on the piezoelectric strain coefficient and the magnitude of the current generated by nitrogen-doped carbon nanotubes (N-CNTs) during their deformation .It is shown that at humidity up to 60%, stable current generation is observed during the deformation of N-CNTs, at higher humidity, the instability of measurements increases and the spread of the generated current increases significantly, which is associated with a decrease in the of the piezoelectric strain coefficient of N-CNTs.

Keywords: carbon nanotubes, nanopiezotronics, piezoelectric response, piezoelectric force microscopy, atomic force microscopy.

Funding: This research was supported by the Ministry of Science and Higher education of the Russian Federation in the framework of the state task in the field of scientific activity, grant number FENW-2022-0001.

Introduction

Currently, implantable electronics is an actively developing field of science. Mainly, various types of materials with a piezoelectric effect are used to transmit "tactile" sensations, effectively converting mechanical action into an electrical signal [1]. At the same time, the efficiency of energy conversion in such sensors is determined mainly by two factors: the electromechanical properties of the piezoelectric material and the design of the sensor itself. In addition, such designs can be used to create highly sensitive strain sensors or microphones [2,3]. Nitrogen-doped vertically aligned carbon nanotubes (N-CNTs) with anomalous piezoelectric properties can be one of the promising functional materials with a high piezoelectric strain coefficient and mechanical durability [4].

In this paper, the influence of ambient humidity on the piezoelectric properties of nitrogen-doped carbon nanotubes for the creation of strain sensors is investigated.

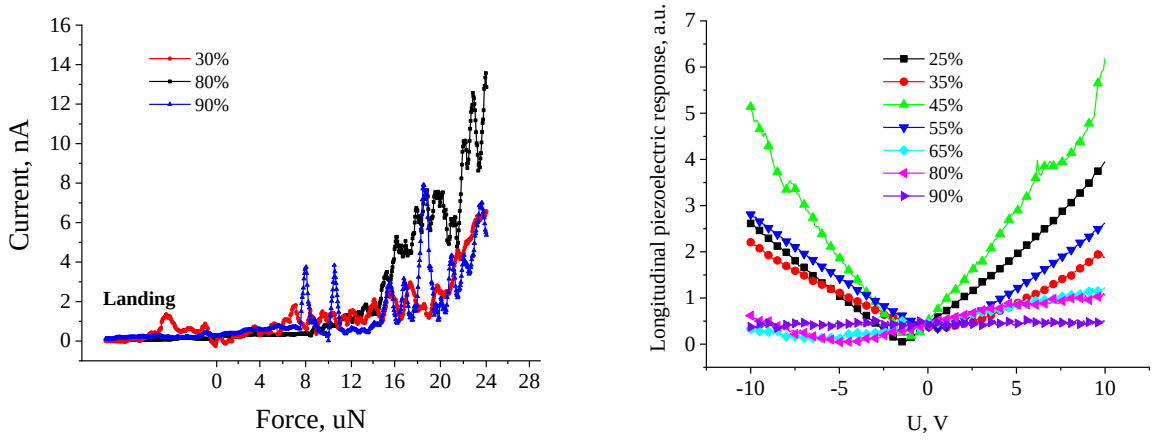
Materials and Methods

The experimental sample was an array of vertically oriented carbon nanotubes grown by plasma chemical deposition from the gas phase in streams of process gases acetylene and ammonia. Studies of the piezoelectric properties of vertically aligned N-CNTs were carried out by the method of piezoelectric force microscopy (PFM) atomic force microscopy (AFM). The geometric parameters of the CNT array were studied using a scanning electron microscope (SEM).

Results and Discussion

The results of experimental studies have shown that with an increase in humidity from 30 to 60%, the value of the current, generated by N-CNT, changes insignificantly and amounts to 7 ± 4 nA. With a further increase in humidity to 80%, the value of the generated current increases to 12 ± 4 nA, and at 90% it decreases again to 5 ± 3 nA (Fig. 1, a). This dependence is probably associated with a change in the magnitude of the piezoelectric response of the N-CNT (Fig. 1, b).

Thus, at a humidity of 30-55%, the value of the piezoelectric strain coefficient N–CNT was 33 ± 14 pm/ V, and then, with an increase in humidity to 90%, it decreased to 0.5 pm / V. This pattern is probably due to the formation of an adsorption layer of water on the surface of the N-CNT, which leads to a decrease in the magnitude of its polarization.



a) b)

Fig. 1. The results of experimental studies of the influence of ambient humidity on the magnitude of the current generated by the N-CNT from the pressure force of the AFM probe (a) and the magnitude of the longitudinal piezoelectric response (b).

Thus, it is established from Figure 1 that at humidity above 60%, unstable current generation with a high range of values is observed during the deformation of N-CNTs, as well as a significant decrease in the piezoelectric properties of N-CNTs

Conclusion

The paper establishes the regularities of the influence of the temperature value on the piezoelectric strain coefficient and the amount of current generated by N-CNTs during their deformation. It is shown that at humidity up to 60%, stable current generation is observed during the deformation of N-CNTs, at higher humidity, the instability of measurements increases and a significant increase in the spread of the generated current, which is associated with a decrease in the piezoelectric strain coefficient of N-CNTs.

The results obtained during the research can be used in the development of mechanical energy converters: strain sensors or highly sensitive microphones.

REFERENCES

1. Sawane M., Prasad M. MEMS piezoelectric sensor for self-powered devices: A review // Mater. Sci. Semicond. Process. Elsevier Ltd, 2023. Vol. 158, № December 2022. P. 107324.
2. Kwon S. ryung et al. A new type of microphone using flexoelectric barium strontium titnate / ed. Ecke W. et al. 2014. P. 90620Y.
3. Ju M. et al. Piezoelectric Materials and Sensors for Structural Health Monitoring: Fundamental Aspects, Current Status, and Future Perspectives // Sensors. 2023. Vol. 23, № 1.
4. Il'ina M. V. et al. Anomalous piezoelectricity and conductivity in aligned carbon nanotubes // J. Mater. Chem. C. 2021. Vol. 9, № 18. P. 6014–6021.

Transport properties of quasi-fractal in-plane heterostructures of graphene and hexagonal boron nitride

D. A. Timkaeva[1,2]✉, **R. T. Sibatov**[1,2]
[1]Ulyanovsk State University, Ulyanovsk, Russia;
[2] Scientific-Manufacturing Complex ‘‘Technological Centre’’, Moscow, Russia
✉dianatimkaeva@mail.ru

Abstract. The electron and phonon transport in quasi-fractal heterostructures graphene/hexagonal boron nitride (hBN) is investigated using first-principles computational methods. The quasi-fractal monolayers under study contain h-BN sections of different sizes in a single triangular block. Graphene and hexagonal boron nitride (h-BN) have similar crystal structures, the difference in permanent lattices is only 2%. Graphene is a semiconductor with a zero band gap and is characterized by very high carrier mobility at room temperature, whereas an atomically thin layer of hexagonal boron nitride h-BN is a dielectric with a wide band gap of 5.9 eV. The paper presents the dependences of electronic and phonon characteristics on the iteration number g. As the generation of the quasi-fractal increases, the electrical conductivity and thermal conductivity of the electrons decrease. As a result, the thermoelectric figure of merit decreases with increasing g. The optical absorption index increases with increasing iteration number g.

Keywords: fractal, graphene, boron nitride, Sierpinski triangle, density functional theory
Funding: The work is supported by Russian Science Foundation (proj. 22-11-00036).

Introduction

The characteristics of an electronic quantum system greatly depend on its dimensionality. The synthesis of artificial molecular systems with quasi-fractal geometry, as discussed in recent studies [1, 2], presents exciting opportunities for investigating the electronic properties of fractal atomic systems experimentally. In [2], a molecular quasi-fractal Sierpinski triangle was successfully created through the self-assembly of organic molecules on a surface. This unique structure features pairs of varying sizes within a single triangular unit and is predicted by the authors [2] to exhibit distinct optical, magnetic, and mechanical properties.

In our work, a number of quasi-fractal monolayers based on planar heterostructures of graphene and hexagonal boron nitride (h-BN) have been studied using first-principles computational methods.

Materials and Methods

To calculate the transfer of electrons and phonons, we will use the method of nonequilibrium Green functions (NEGF), in combination with DFT (LCAO). Optimization took place using the PseudoDojo pseudopotential [3] with a linear combination of atomic orbitals (LCAO) of the basis sets and the exchange correlation potential described by the generalized gradient approximation (GGA) with the Purdew–Burke–Ernzerhof functional (PBE) [4].

To study the absorption and optical conductivity spectra, the dielectric susceptibility $\chi(\omega)$ is calculated within the framework of the Kubo-Greenwood formalism implemented in the QuantumATK package [1]:

$$\chi_{ij}(\omega) = -\frac{e^2\hbar^2}{m^2 \in_0 A\omega^2} \sum_{nm} \frac{f(E_m) - f(E_n)}{E_{nm} - \hbar\omega - i\Gamma} \pi^i_{nm} \pi^j_{mn} \quad (1)$$

where A is the effective area, f is the Fermi–Dirac function, $\Gamma = 0.1$ eV is the broadening, π^i_{nm} is the matrix of dipole transitions between states n and m.

Results and Discussion

We have considered various stable configurations of quasi-fractal graphene/h-BN monolayers. The difference between the variants lies in the arrangement (sequence) of nitrogen, boron and carbon atoms. The resulting heterostructures contain h-BN sections of different sizes in a single triangular block. Figure 1 shows the band diagrams of quasi-fractal graphene/h-BN heterostructures for three generations of the iteration procedure.

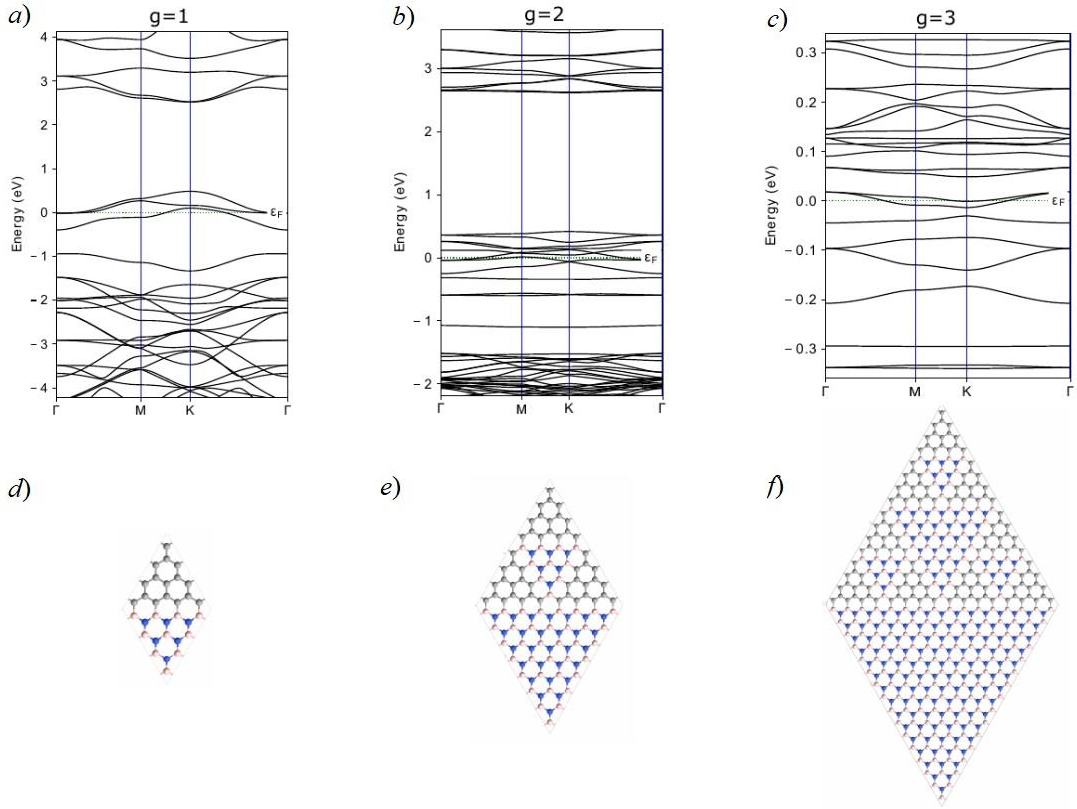


Fig. 1. Band structures of quasi-fractal in-plane heterostructures of graphene and hexagonal boron nitride of generations g=1,2 and 3.

The conductivity, thermal conductivity and thermoelectric characteristics of devices based on the quasi-fractal heterostructure of graphene and hexagonal boron nitride of three generations are calculated. These results are discussed in the report and extended version of this paper.

Conclusion

By constructing the transmission eigenstates, it is demonstrated that the electronic transport paths are concentrated in graphene blocks. As the generation of the quasi-fractal increases, the electrical conductivity and thermal conductivity of the electrons decrease, and the optical absorption index is growing. As a result, the thermoelectric figure of merit decreases with increasing g.

REFERENCES

1. **Kempkes S. N., Slot M. R., Freeney S. E., Zevenhuizen S. J., Vanmaekelbergh D., Swart I., Smith C. M.,** Design and characterization of electrons in a fractal geometry, Nature physics. 15(2) (2019) 127-131.

2. **Qi Q., Li C., Liu X., Jiang S., Xu Z., Lee R., Zhu M., Xu B., Tian W.,** Solid-state photoinduced luminescence switch for advanced anticounterfeiting and super-resolution imaging applications, Journal of the American Chemical Society. 139(45) (2017) 16036-16039.

3. **Van Setten M. J., Giantomassi M., Bousquet E., Verstraete M. J., Hamann D. R., Gonze X., Rignanese G. M.,** The PseudoDojo: Training and grading a 85 element optimized norm-conserving pseudopotential table, Computer Physics Communications. 226 (2018) 39-54.

4. **Perdew J. P., Burke K., Ernzerhof M.,** Generalized gradient approximation made simple, Physical review letters. 77(18) (1996) 3865.

Evolution of crystalline phases of P(VDF-TeFE) films filled with nanographite in various aprotic solvents

A. P. Khramov [1✉], **N. G. Savinski**[1], **E. A.Grushevski**[1]

✉[1]Valiev Institute of Physics and Technology of the Russian Academy of Sciences Yaroslavl Branch, Yaroslavl, Russia

✉artem.khramov.99.99@mail.ru

Abstract. The work under discussion describes the preparation and study of polyvinylidene fluoride (PVDF) films filled with chemically exfoliated nanographite and crystallized by drying from various solvents. The content of α, β and γ phases was estimated via X-ray diffractometry, Fourier transform infrared spectroscopy (FTIR) and Raman spectroscopy. It was found that films made from a solution of dimethyl sulfoxide (DMSO) have a higher content of the polar β-phase. Films filled with nanographite showed a slightly increased degree of crystallinity and β-phase content.

Keywords: tetrafluoroethylene P(VDF-TeFE), dimethyl sulfoxide (DMSO), N-Methyl-2-pyrrolidone (NMP), dimethylformamide (DMF), beta phase, FTIR, XRD, nanographite.

Funding: The work was carried out within the framework of the State program № FFNN-2022-0018 of the Ministry of Science and Higher Education for Russia Yaroslavl branch of Valiev Institute of Physics and Technology of RAS.

Introduction

The most promising in terms of the type of energy conversion are electroactive actuators, devices that convert electrical energy into mechanical energy. Due to their convenience and practicality of their electrical stimulation, they are increasingly being used in biological systems due to their promising properties[1].

Currently, considerable attention in actuating materials is paid to polyvinylidene fluoride (PVDF) and various composites based on it due to the characteristics of the material that distinguishes it from other ferroelectrics. For example, the presence of a negative piezoelectric coefficient d_{33} in polarized PVDF, which causes compression of the material in the direction of the applied electric field [2]. PVDF can mainly be found in three crystalline phases: α, β and γ, among which the last two are polar. Among the polar phases, the β phase is the most polar and, accordingly, have the strongest effect on the piezoelectric properties of PVDF [3].

The purpose of this work is to assess the change in the content of the β phase of fluoroplast-42 filled with nanographite using different solvents at different drying temperatures.

Materials and Methods

Electrochemically exfoliated nanographite was made in a two-electrode cell in an aqueous solution of 0.6M ammonium peroxide sulfate electrolyte using Graphite foil "Grapflex" RF. More details can found in our previous proceedings [4]. After that, 0.25g of the resulting powder was dispersed in bipolar aprotic solvent NMP or DMSO, or DMF 95g each. The solutions were mechanically dispersed and treated ultrasonically within 8 hours.

Fluoroplast-42 mark B (GOST 25428-82) which is a semicrystalline copolymer of polyvinylidene fluoride and tetrafluoroethylene P(VDF-TeFE), herein after referred to as F-42, was added in nanographite solutions at quantity of 4.75g so the resulting solutions can be defined as 5% mass solutions with a mass content of nanographite in relation to F-42 5% as well. The solutions were alternately stirred at 70 °C and treated on a mechanical disperser within 1.5 hours.

The resulting solutions were poured into Petri dishes and dried at temperatures 60, 90 and 150 °C respectively. The resulting films were studied via Raman spectroscopy with an EnSpectr R532 spectrometer, Fourier transform infrared spectroscopy with a FT-IR Perkin-Elmer -TWO spectrometer, and X-ray powder diffraction analysis with a DRON 3M diffractometer, scanning electron microscopy with a Supra-40 electron microscope, according to a method detailed in [5].

Results and Discussion

Fig. 1(a) shows a comparison of diffractograms of samples from DMSO and DMF at 90 °C. Diffraction peaks at 20.0°, 20.3° and 20.6° correspond to (110), (110/101) and (110/200) reflections of monoclinic α, monoclinic γ and orthorhombic β phases of F-42. The displacement about Δ(2θ)=0.12 of the peak 20.0-20.6 of the DMSO sample to the larger 2θ side indicates an increased content of polar phases. The diffractograms of NMP and DMF practically do not differ from each other. Hence, it can be concluded that DMSO is the best aprotic solvent among those proposed for the creation of high-polar F-42 films. Fig. 1(b) shows a comparison of the corresponding samples on the FTIR spectra. Peaks at 771 cm^{-1}, 840 cm^{-1}, 1234 cm^{-1} and 1275 cm^{-1} attribute to α-phase CF_2 bending, β or γ-phase CH_2 rocking, γ and β both CF out-of-plane deformation respectively. By the relative increase in the peak of the β phase, and the practically unchanged peaks of the α and γ phases, it can be concluded that DMSO among the polar phases mainly increases the content of the β phase.

The diffractograms of all samples at 150 °C are the same, which indicates the absence of solvent influence at a such high temperature, that is also confirmed by a comparison between DMSO samples at 90 °C and 150 °C, respectively. FTIR DMF spectra at 90°C between filled nanographite and unfilled samples show a slight increase in the β phase and crystallinity of the material.

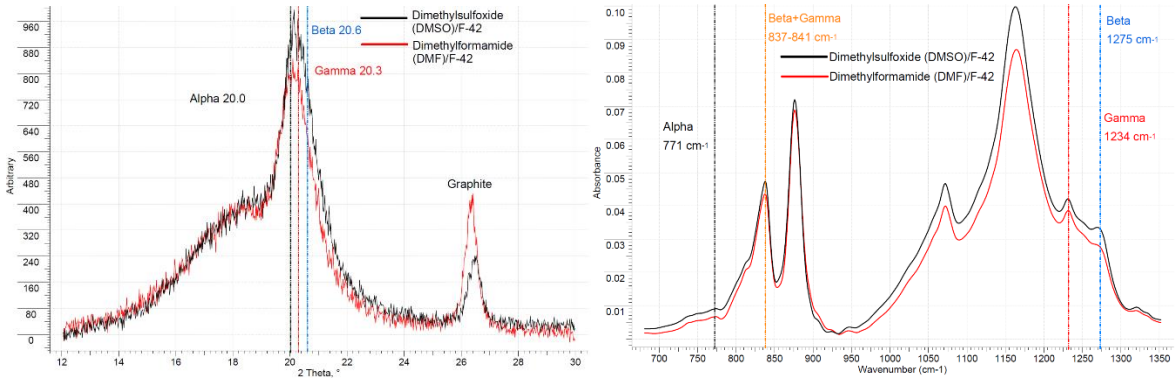


Fig. 1. Diffractograms of DMSO(DMF)/F-42-nanographite samples (*a*) and respective FTIR spectra at drying temperature 90°C(*b*). Blue, red and black dashed lines corresponds to respective β, γ and α phases. Orange dashed line indicate summarized peak of all three phases.

Conclusion

From XRD and FTIR readings, it can be concluded that content of most polar β-phase in F-42 films can be enhanced by filling with nanographite and drying in DMSO as best aprotic solvent among others at certain temperatures. There is a presence of DMSO solvent influence at a 90 °C and its absence at 150 °C.

REFERENCES

1. **Maksimkin A. V.** et al**.** Electroactive polymer-based composites for artificial muscle-like actuators: A review //Nanomaterials. – 2022. – T. 12. – №. 13. – P. 21.

2. **Bystrova A.V.** et al. Computer molecular modeling of piezoelectric properties of ferroelectric composites based on polyvinylidene fluoride with graphene and graphene oxide //Mathematical biology and bioinformatics. - 2017. – vol. 12. – No. 2. – P. 466-486.

3. **Li X.** et al. Preparation of PVDF flexible piezoelectric film with high β-phase content by matching solvent dipole moment and crystallization temperature //Journal of Materials Science: Materials in Electronics. – 2019. – T. 30. – P. 20174-20180.

4. **Grushevski E.** et al. The scalable production of high-quality nanographite by organic radical-assisted electrochemical exfoliation //Journal of Physics: Conference Series. – IOP Publishing, 2021. – T. 2086. – №. 1. – C. 012014.

5. **Cai X.** et al. A critical analysis of the α, β and γ phases in poly (vinylidene fluoride) using FTIR //RSC advances. – 2017. – T. 7. – №. 25. – P. 15382-15389.

Supramolecular ordering of thin glycerohydrogel plates of chitosan L- and D-aspartate

O. S. Ushakova [1], **T. N. Lugovitskaya** [2], **A. B. Shipovskaya** [1]✉

[1] Saratov State University, Saratov, Russian Federation;

[2] Ural Federal State University, Yekaterinburg, Russian Federation

✉Shipovskayaab@yandex.ru

Abstract. The supramolecular ordering of thin glycerohydrogel plates of chitosan L- and D-aspartate was studied using small-angle X-ray scattering. At the nanolevel of the supramolecular organization of the objects under study, two forms of bulk scattering domains were identified, namely: nanospheres and nanorods. The discovered nano-sized structures were visualized using transmission electron microscopy.

Keywords: chitosan, L- and D-aspartic acid, glycerohydrogels, small-angle X-ray scattering, microscopy.

Funding: This research was funded by a grant from the Russian Science Foundation No. 24-16-00172, https://rscf.ru/project/22-23-00320/.

Introduction

Nanostructured hydrogel composites based on chitosan (CS), a biodegradable polymer of natural origin, are promising for the design of novel materials for biodegradable electronics and sensors, including low-cost disposable products [1, 2]. The efficiency of such nanocomposites exceeds that of transparent thermoplastic synthetic polymers filled with inorganic nanoparticles.

In this work, solutions of CS in L-(D-)aspartic acid (AspA) were used to prepare nanostructured hydrogels. In the CS + L-AspA + H_2O system, the effect of counterionic condensation with phase segregation of the salt form of the polymeric substance at the nanoparticle level was discovered [3], which predetermines the possibility of a one-stage formation of a chitosan-containing hydrogel with nanosized CS · AspA aggregates included therein. To make a gel structure in the form of shape-stable thin-film plates, we used the approach tested for CS L- and D-ascorbates [4]. It consists in the formation of a system of interpenetrating spatial networks of organic and inorganic nature in a polymeric sample. The organic network is represented by a physical gel of CS and an inert structure former, whose −OH groups act as a template for the synthesis of an inorganic chemical network of silicon polyolate (~−Si−O−Si−~). Since a glycerol solution of silicon tetraglycerolate ($Si(OGly)_4$ · GlyOH) is the precursor of the inorganic phase, the sol–gel synthesis is accompanied by the formation of polymeric glycerohydrogels.

Materials and Methods

The starting reagents were CS with a viscosity-average molecular mass $\bar{M}_\eta$ = 200 kDa, a degree of deacetylation 82 mol %, and a moisture content of $W = 8 \pm 1$ wt% (Bioprogress Ltd., Russian Federation); glucomannan with $\bar{M}_\eta$ = 1100 kDa (Uspekh LLC, RF); L-AspA (JSC Bioamid, RF); D-AspA (Vekton Corp., RF; $Si(OGly)_4$ · 3 GlyOH (58.7 wt %, Ural Branch of Russian Academy of Sciences, Institute of Organic Synthesis named after I.Ya. Postovsky, RF); distilled water (Milli-Q, pH = 6.0).

To obtain glycerohydrogel plates, aqueous solutions of CS·L-AspA or CS·D-AspA, an aqueous glucomannan solution and a glycerol $Si(OGly)_4$ solution were mixed in a mass ratio of components 1 : 1 : 0.5 and thoroughly homogenized with a glass rod for 1–2 min. The finished mixture composition was transferred onto a horizontal glass substrate at a rate of 0.4 mL/cm^2 and kept at room atmosphere for ~72 h until gelation was completed.

Small-angle X-ray scattering (SAXS) measurements were carried out on a D8 Discover small-angle diffractometer (Bruker) with CuK_α radiation and a LynxEye solid-state position-sensitive detector in 0D mode, the slit width in front of the detector was 0.2 mm. The scattering intensity I_q was recorded in the range of the modulus of the scattering wave vector q = 0.2−7.1 Å^{-2}. The structural parameter n, which characterizes the morphology of scattering inhomogeneities, was determined from the tangent of the slope of the rectilinear sections of the scattering curve

($\ln I_q$; q), the average radius of gyration R_n of scattering inhomogeneities (in our case, having the physical meaning of the average linear size of scattering domains) was from the dependence in Guinier coordinates ($\ln I_q$; q^2).

Transmission electron microscopy (TEM) images were obtained on a Jeol JEM 2100 transmission electron microscope at an accelerating voltage of 200 kV. Sample preparation: 5 μl of the test object was placed onto a copper grid coated with a carbon film (10–100 nm), dried for 15 min in air, then 10 min in the airlock vacuum chamber of the microscope.

Results and Discussion

The SAXS curves of glycerohydrogel CS·L-AspA and CS·D-AspA plates in standard coordinates $I = f(\Theta)$ are almost identical and differ only in the intensity value at small scattering angles. The highest values of I are realized for the CS·L-AspA-based sample. Plotting the curves $I = f(\Theta)$ in double logarithmic coordinates $\ln I_q = f(\ln q)$ reveals two straight sections corresponding to different values of the scattering vector modulus. The first one, at which the fastest decrease in intensity I(q) is observed, corresponds to the range of scattering coordinates $q < 0.15$ Å^{-2}, the second one does to the range of the modulus of the scattering vector $q \sim 0.25$–0.45 Å^{-2}. The power-law decay index n at small q values for the CS·L-AspA and CS·D-AspA samples is 1.3 and 1.2, respectively, which indicates the presence of scattering volumetric domains in the form of hollow spheres in the spatial network of the hydrogel. In the range of higher q values, the slope of the SAXS curve decreases down to n = 0.5 and 0.3, which corresponds to the rod-shaped shape of the scattering inhomogeneities. Differences are noted in the quantitative indicators of the average radius of gyration of phase inhomogeneities in the supramolecular structure of our hydrogel plates. E.g., for the CS·L-AspA and CS·D-AspA glycerohydrogel the range of R_n values was 10–50 Å and 15–30 Å, respecvtively. Therefore, the CS·D-AspA sample is characterized by a smaller average size of scattering aggregates and a narrower range of variations in their valuesм. The shape of the scattering domains predicted by SAXS was visualized using TEM.

Conclusion

Structural diagnostics of the supramolecular ordering of the polymeric substance of thin glycerohydrogel CS·L-(D-)AspA plates in the nanometer range was carried out using SAXS and TEM. It has been established that the supramolecular structure of the “soft condensed” phase of the polymeric substance in the glycerohydrogel composition is represented by two types of scattering inhomogeneities, namely, hollow spheres and rod-shaped particles. The resulting nanocomposite shape-stable glycerohydrogels seem promising for solving applied problems of biodegradable electronics and sensorics.

REFERENCES

1. **Peng X., Dong K., Wu Z., Wang J., Wang Z. L.,** A review on emerging biodegradable polymers for environmentally benign transient electronic skins, Journal of Materials Science. 56 (30) (2021) 16765–16789.

2. **Dhayal V., Hashmi S. Z., Kumar U., Choudhary B. L., Kuznetsov A. E., Dalela S., Kumar S., Kaya S., Dolia S. N., Alvi P. A.,** Spectroscopic studies, molecular structure optimization and investigation of structural and electrical properties of novel and biodegradable chitosan-GO polymer nanocomposites, Journal of Materials Science. 55 (3) (2020) 14829–14847.

3. **Lugovitskaya T. N., Shipovskaya A. B., Shmakov S. L., Shipenok X. M.,** Formation, structure, properties of chitosan aspartate and metastable state of its solutions for obtaining nanoparticles, Carbohydrate Polymers. 277 (2022) 118773.

4. **Shipovskaya A. B., Gegel N. O., Babicheva T. S.,** Comparative analysis of nanosized structures in thin hydrogel plates of chitosan L- and D-ascorbate–hydrochloride, St. Petersburg State Polytechnical University Journal: Physics and Mathematics. 15 (3.3) (2022) 111–117.

RESISTIVE MICROELECTROMECHANICAL GAS SENSOR FOR DETECTION OF LOW CONCENTRATIONS OF HYDROGEN SULFIDE

I. Lazdin[1] , A. Kondrateva[2], I Komarevtsev[1,2], Y Enns[1,2], A Kazakin[1], M.Mishin[2], P. Karaseov [1]

[1]Peter the Great Saint-Petersburg Polytechnic University, St. Petersburg, Russia

[2]Alferov University, St. Petersburg, Russia

✉ lazdin.ia@edu.spbstu.ru

Abstract. In this contribution the manufacturing route to make a microelectromechanical (MEMS) resistive gas sensor for low analytic concentrations detection is proposes. Main technological and operating characteristics of the device are demonstrated. MEMS chip is created on a 50 μm thick silicon membrane. Nickel comb microheater electrodes of 100 μm and spaced 300 μm were used. 100 nm thick nickel oxide (NiO) gas-sensitive layer was deposited on top of the microheater. The operating temperature of the sensitive layer in measurement mode was varied from 130 to 205 °C. Results show sensitivity to presence of H_2S in a gas mixture with concentrations from 1 to 100 ppm as the conductivity change. The effective operating temperature of the heating elements was determined.

Keywords : microelectromechanical systems, gas sensor, nickel oxide, hydrogen sulfide

Funding : Work at Alferov University was supported by Ministry of Science and Higher Education of Russian Federation under the state assignment FSRM-2023-0009.

Introduction

Microelectromechanical systems are used in a variety of applications from gyroscopes and accelerometers to air pollution detection systems [1,2]. Of particular interest are MEMS gas sensors based on sensitive elements made of thin films of metal oxides. For such sensors, an urgent problem is the effectiveness of various sensitive layers for different gases. The search for designs that can increase the device energy efficiency while maintaining the sensitivity parameter of the sensor is of paramount importance.

Obviously, n-type semiconductor thin film acts as the active layer. This is caused by high mobility of charge carriers in this type of semiconductor, which provides high response rate of a device. At the same time, p-type semiconductors are promising for reducing gases such as hydrogen sulfide due to the acceptor-based interaction mechanism. The difficulty of detecting hydrogen sulfide with resistive gas sensors is due to the aggressiveness of the environment being studied. An inexpensive and chemically stable p -type semiconductor material is nickel oxide (NiO). The confirmed possibility of modifying the roughness of NiO films helps to increase the sensitivity of the active layer [3].

Thus, the goal of this work is to create a resistive microelectromechanical gas sensor with a thin-film sensing element made of nickel oxide. The possibility to detect H_2S content in a mixture of gases at concentrations from 1 to 100 ppm is considered.

Materials and Methods

The sensitive element is made of 0.4 mm thick monocrystalline silicon wafer and has lateral dimensions of 10 x 10 mm. The developed technological route is carried out using standard methods like photolithography and magnetron sputtering. Heater and two nickel comb electrodes, separated by an insulating dielectric, was deposited onto the chip using magnetron sputtering. The heater is made of nickel and has the form of a meander, the tracks of which pass between the teeth of the comb electrodes and is also covered with a protective dielectric on top, in contrast to the teeth of the electrodes. [4] The sensitive layer (NiO) is located on the membrane on top of all elements and is in electrical contact only with the teeth of the comb electrodes protruding as a resistance meter. The central part on the back side of the silicon chip is etched to make 50 μm thick

membrane, which reduces power consumption and increases performance. Additional annealing of the deposited NiO at 300-400 ^{0}C was performed in air ambient to increase its conductivity.

Results and Discussion

Measurements of the main electrical parameters of laboratory prototypes of the MEMS sensor, such as the resistance of the heater and gas-sensitive layer at various temperatures, were carried out.

The results show that the gas sensor based on nickel oxide manufactured using the proposed MEMS technology makes it possible to detect hydrogen sulfide in the range from 10 to 100 ppm (Fig. 1).

In this case, the operating power of the sensor ranges from 0.5 to 1.5 W. Moreover, a built-in micro-heater provides a heating function to improve measurement sensitivity. However, a systematic study requires taking into account the selectivity of the sensor in the case where gases other than hydrogen sulfide are also present in the air.

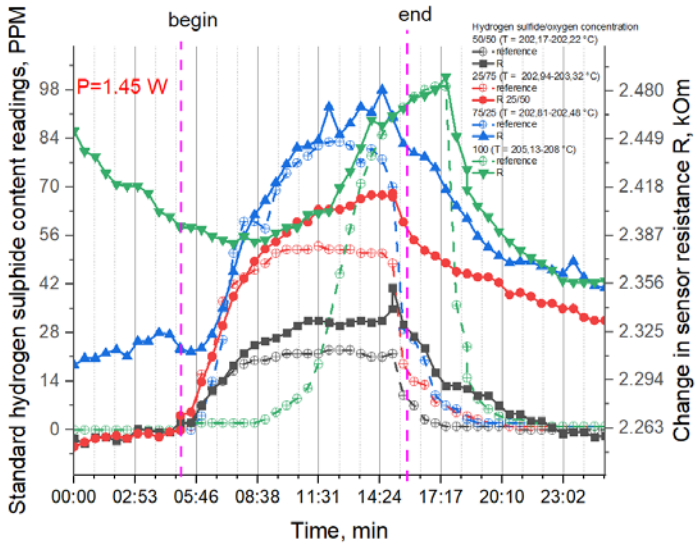


Fig. 1. Dependence of the influence of hydrogen sulfide on the resistance of the sensor in comparison with a reference sensor at various gas supply ratios

Conclusion

In this work, a technology to produce MEMSgas sensors was proposed. The hydrogen sulfide sensor with a sensitive layer of nickel oxide (NiO) were made using aforesited technology. A NiO sensitive layer deposited on the Si membrane showed sensitivity to hydrogen sulfide from 10 to 100 ppm, for annealed films at temperatures from 300 to 400 ^{0}C, the optimal operating temperature was 205 ^{0} C. This MEMS sensor is a resistive type with a self-heating thin NiO film is suitable for energy-efficient gas sensing applications.

REFERENCES

1. Dong, W. Gao, Q. Zhou, Y. Zheng, and Z. You, *Anal Chim Acta* , vol. 671, no. 1–2, pp. 85–91, Jun. 2010

2. S. Zampolli , *Sens Actuators B Chem* , vol. 101, no. 1–2, pp. 39–46, Jun. 2004,

3. H. Chen, H. Ma, Y. Zhu, M. Zhao, Z. Chen, and L. Zhang *Appl Surf Sci* , vol. 609, Jan. 2023

4. C. Y. Lee, P. R. Hsieh, C. H. Lin, P. C. Chou, L. M. Fu, and C. M. Chiang *Microsystem Technologies* , Sep. 2006, pp. 893–898. 349

Hybrid model of photolithography physicochemical processes for estimation of optical losses in waveguides

A. A. Sharapov [1,2]✉, **M. V. Litavrin** [1], **E. L. Kharchenko** [1], **A. A. Krylov** [1,2], **E. S. Gornev** [1]
[1] JSC "MERI", Zelenograd, Russia;
[2] MIPT (NRU), Dolgoprudny, Russia
✉andrey.sharapov@phystech.edu

Abstract. The study introduces a hybrid model of chemically amplified photoresists that bridges the gap between compact and comprehensive models, incorporating stochastic factor of resist contrast value. Comparative analysis with experimental results and the prediction of resist profiles and line-edge roughness are presented, as well as estimation of optical losses in waveguides caused by this roughness. This indicates the model's practical applicability and potential benefits for rapid recalibration under varying process conditions.

Keywords: line-edge roughness, chemically amplified photoresist, resist profile, optical losses.

Funding: This study was funded by the Russian Science Foundation, Grant # 24-91-18002.

Introduction

The push for technology nodes beyond 180-90 nm in integrated microelectronics technology, particularly in lithography, is driving the development of advanced photoresists. The work on creating new materials consists, among other things, in selecting the most successful composition of chemical substances that make up the photoresist. Each new resist composition must be tested directly on manufacturing equipment. Therefore, increasing the number of iterative optimizations of the composition leads to an increase in the number of experiments on production equipment, which in turn increases equipment downtime. Thus, the task of accurate modeling of the transfer of the pattern from the photomask to the photoresist layer on the wafer is highly relevant.

There can be two types of models for solving this problem – full and compact. Compact models demonstrate high performance; hence they are used for modeling the entire chip [1-2]. However, a key drawback of such models is their lack of universality: because the model is simplified, it cannot accurately describe a wide range of process parameters, and therefore its coefficients are calibrated specifically for a particular process. These coefficients also lack a clear physical meaning, so even a minor change in the process necessitates a recalibration of the model. Because of this, such models cannot be used for process development.

This paper presents results of the construction of a photoresist model that occupies an intermediate position between compact and full models.

Materials and Methods

The calculation of the 3-dimensional aerial image is performed using Calibre computational lithography software and interpolation technique which is proven to be applicable for the cases when the back anti-reflective coating prevents the formation of standing waves within the photoresist layer. The diffusion of photoacid and bases during the post-exposure bake is described by the Fick's law, and a simplified development model is based on lumped parameter model described in [3].

In the previously presented model, the stochastic contribution to the shape of the sidewalls was accounted for by considering the effect of photon shot noise and by constructing an imitational model of the photoresist polymer base as densely packed spheres [4]. In this work, the authors propose introducing stochastic variability in the contrast value, corresponding to variations in the polymer chain length within the composition of the photoresist.

Measurement of critical dimensions is performed by using CD-SEM. Line-edge roughness is calculated using the software developed by the authors [5]. Optical losses caused by scattering on the unevenness of the sidewalls with a specified amplitude, on the linear section of the photonic integrated circuit, are calculated using Lumerical FDTD.

Results and Discussion

Based on the presented model, the profile in the resist (Figure 1) and the roughness of the line edge are predicted. Suggested two-step parameters optimization approach provided better agreement with experimental results for developed and measured photoresist mask than in the previous work by the authors [6].

The results of measuring optical losses on a linear segment correspond to the modeled level of losses, caused by scattering on the roughness of the side surfaces, corresponding to the measured amplitude of edge roughness from SEM images.

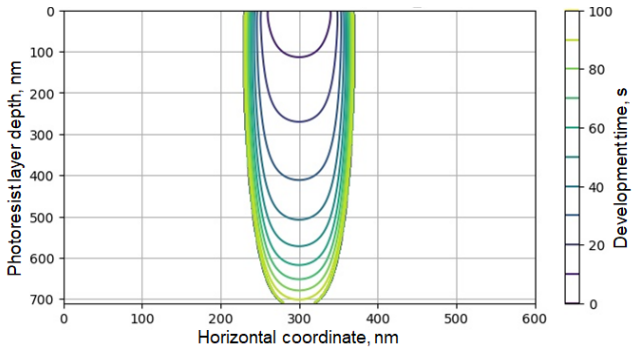


Fig. 1. Resist profile modeling

Conclusion

The research introduces a novel method for estimating the level of optical losses in linear waveguide structures, which are caused by the roughness of lateral surfaces. This method could be pivotal for assessing and optimizing future technological processes, ensuring enhanced performance and reliability of microelectronic devices.

Acknowledgments

The authors would like to express their gratitude to V.V. Kovalyuk from MISIS for providing experimental data of signal measurements on array of Mach-Zender interferometers for verification of modeling results.

REFERENCES

1. N.N. Balan et al., "The Use of Neural Network Algorithms in Computational Lithography Tasks," Nanoindustry, No. S96-2, 2020, pp. 543-548.

2. E.L. Kharchenko, E.V. Sokolova, E.S. Gornev, "Development and Application of Compact Models for Photoresist Masks," Nanoindustry, 16, S9 (119), 2023, pp. 508-511.

3. J. Byers, M. Smith, C. Mack, "Lumped Parameter Model for Chemically Amplified Resists," Proc. SPIE, 5377, Optical Microlithography XVII, 2004.

4. E.S. Shamin. et al. “Sidewall roughness model for optical losses calculation in photonic integrated circuits,” St. Petersburg State Polytechnical University Journal. Physics and Mathematics, 15 (3.3), 2022, pp. 70–75

5. A.A. Sharapov, G.V. Baranov, "Comparative Analysis of Techniques for Assessing the Quantitative Characteristics of Roughness of Nanoscale Structures," Proceedings of the Moscow Institute of Physics and Technology, vol. 10, No. 2(38), 2018, pp. 72-79.

6. M.V. Litavrin et al., "Extraction of Empirical Constants of Exposure and Post-Exposure Baking for Chemically Amplified Photoresists," Nanoindustry, 2024.

Chemical activity of dispersed particles of potassium compounds in the flame of a pyrotechnic composition

S. I. Ksenofontov[1], A. N. Lepaev [2]✉, O. V. Vasilyeva[3]

[1] Chuvash State Pedagogical University named after I. Ya. Yakovleva, Cheboksary, Russia;
[2] Cheboksary Institute (branch) of Moscow Polytechnic University, Cheboksary, Russia;
[3] Chuvash State University named after I. N. Ulyanova, Cheboksary, Russia
✉ it@polytech21.ru

Abstract. The structure of dispersed particles in a flame of a pyrotechnic composition has been studied. The possibility of obtaining dispersed particles of the target product with reduced corrosion ability has been demonstrated. A mechanism for the interaction of reacting dispersed particles with a potassium iodide crystal is proposed.

Keywords: flame, dispersed particle, potassium oxide, potassium iodide.

Pyrotechnic aerosol-forming compositions are effective fire extinguishing agents. A decrease in the concentration of active flame particles as a result of their recombination on the surface of dispersed particles leads to the cessation of combustion.

Many formulations include inorganic oxidizing agents such as potassium nitrate, flammable binders (phenol-formaldehyde resins), and dicyandiamide. Potassium oxide is a chemically aggressive product that causes corrosion of metal products. Satisfactory results were obtained with formulations containing potassium nitrate, sorbitol and ammonium iodide. The corrosive activity of the target product is significantly reduced when potassium oxide is combined with iodine.

Samples of dispersed particles were obtained by passing a glass plate through a flame. Microphotographs of sampler areas were obtained using a scanning electron microscope, and the elemental composition of dispersed particles was studied. Aerosol particles consisting of irregularly shaped hydrocarbon fuel residues (1), potassium carbonate (2), potassium iodide (3) are formed in the flame. The sampler area is dotted with submicron-sized particles in the central zone of the flame (Fig. 1*a*). The potassium iodide particle is presented in the form of a cube-shaped particle with an edge of 22 microns. A particle of unburned hydrocarbon fuel is located on one of the edges of the cube. The initial particles of the composition components have an average size of 70 microns.

а) *б*)

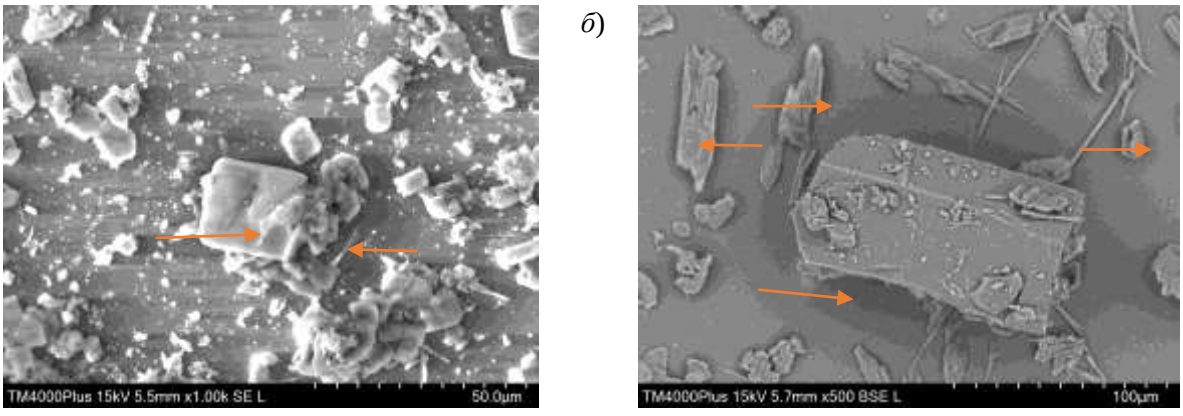


Fig. 1. Sampler sections are obtained by SEM

Particles that were detected in the peripheral zone of the flame are presented in Fig. 1*b*. A large prism-shaped particle of potassium iodide is located in the center of the picture. There are no other dispersed particles around it on the surface of the sampler. Many particles, both submicron in size and particles in the form of plates and elongated rods, settled on the outer surface of the prism. All this suggests that the surface of the potassium iodide particle serves as a

«third particle» for the recombination of both active flame particles - ions and electrons, and dispersed reacting particles.

It is also characteristic that «foreign» settled particles do not create defects and do not penetrate into the crystal structure. The probability of the introduction of «foreign» particles is not small, since the melting point of potassium iodide is 954 K, and the flame temperature, measured by the photopyrometric method, is 1380 K [1].

The observed potassium carbonate particles have an irregular shape. The crystallization process apparently occurs by a surface mechanism from the liquid phase [2]. According to the literature, potassium carbonate has a monoclinic modification at temperatures below 693 K. The crystal is a hexagonal modification with increasing temperature [3]. Mechanical destruction of the crystalline shell of a particle as a result of a collision with the body of the sampler leads to the appearance of whisker-like crystals. The dimensions of the whiskers are one micron in diameter and up to 25 microns in length.

Conclusion

1. Replacing potassium oxide particles with potassium iodide particles through a chemical combustion reaction reduces the corrosivity of the target product.

2. A physical mechanism for the interaction of reacting dispersed particles with a potassium iodide crystal has been discovered.

REFERENCES

1. **Porfiryev A. M., Ksenofontov S. I.** Program for determining the temperature field of flames «Flame – temperature». URL: http://ofernio.ru/portal/newspaper/ofernio/2010/8.doc.

2. **Ksenofontov S. I., Tashkova K.Yu., Lepaev A. N., Vasilyeva O. V., Kokshina A. V., Kazakov V. A., Razina A. G., Smirnov A. V., Abrukov V. S., Anufrieva D. A.** Morphology and elemental composition of whiskers of potassium carbonate in a pyrotechnic flame, St. Petersburg State Polytechnical University Journal: Physics and Mathematics. 3 (16) (2023) 304–309.

3. **Grigorieva I. S., Meilikhova E. Z.,** Physical quantities. Directory, Energoatomizdat, Moscow, 1991.

Research the effect of internal mechanical stresses in a multilayer structure on displacement for various designs of MEMS membranes

S. V. Malokhatko[1]✉, E .Yu. Gusev[1], L. Jiang[2], O. A. Ageev[1,3]

[1] Institute of Nanotechnology, Electronics and Electronic Equipment Engineering, Southern Federal University, Taganrog, Russia;

[2] Laser Institute, Qilu University of Technology (Shandong Academy of Sciences), Jinan, China;

[3] Research and Education Center "Nanotechnologies", Southern Federal University, Taganrog, Russia

✉malohatko@sfedu.ru

Abstract. The paper presents the results of modeling the structures of multilayer membranes of three types: round, square and square with transverse and angular beams. The displacement values for each type of multilayer membranes are obtained according to the effect of inner mechanical stresses in each layer. The influence of technological conditions of film formation in multilayer membranes on their stress-strain state of ultrasonic sensors has been studied.

Keywords: microelectromechanical sensors, multilayer membrane, mechanical stress.

Introduction

Microelectromechanical devices cover more and more fields of application [1]. Such devices include ultrasonic microelectromechanical sensors that can be used for industrial and medical purposes. The output characteristics of such devices depend on a sensing element consisting of a multilayer membrane-type structure. By changing the membrane design, certain functional parameters of the sensor can be improved. However, at the stage of multilayer structure fabrication, under the influence of various factors, internal mechanical stresses arise in the layers, which lead to displacement of structures without external influence [2]. The displacement of the structure leads to a decrease in sensitivity. Thus, an actual task is to study the effect of internal mechanical stresses on the displacement of a multilayer membrane, depending on its design.

Modeling and results

In this paper the effect of internal mechanical stresses on the displacement of a multilayer membrane depending on the design is researched. Modeling in the Comsol Multiphysics environment was carried out for three types of membranes: round (diameter of 500 μm), square (side length of 500 μm) and square with transverse and angular beams (length of 50 μm, width of 25 μm). The multilayer structure included the following layers $Si/SiO_2/Mo/ZnO$ (50/2/0.1/0.1 μm). The inner mechanical stresses that were taken into account during the simulation ranged from -80 to -500 MPa [3], from -1.5 to +1.5 GPa [4] and from -0.7 to +0.7 GPa [5] for SiO_2, Mo and Zn films, respectively. Figure 1 shows the displacement of a square membrane with transverse and angular beams under the action of internal compressive stresses of -100 MPa in the layer SiO_2. Depending on the internal mechanical stresses in the multilayer structure, displacement values are obtained for each type of membrane, which are presented in Table 1.

The results obtained can be used to optimize the designs and fabrication processes of multilayer structures used in acoustic sensors, micro mirrors and resonators.

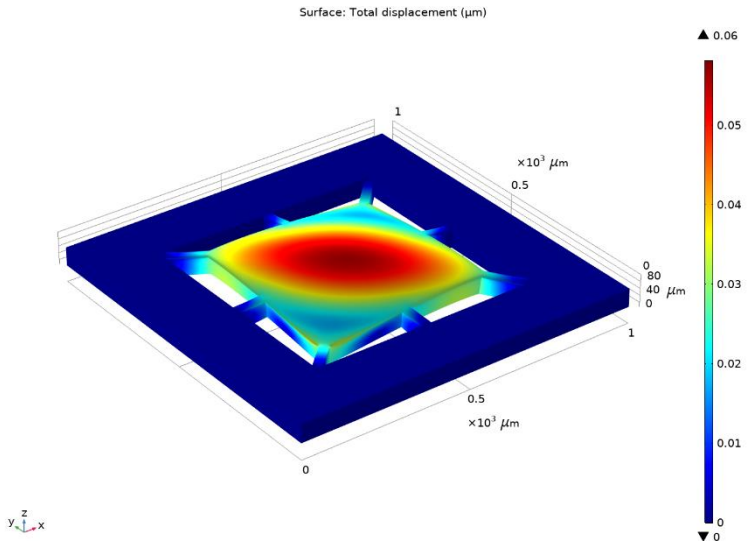


Fig. 1. Displacement of the membrane with transverse and angular beam c under the action of internal compressive stresses of -100 MPa in a SiO_2 film

Table 1

Displacement values of the multilayer membrane, nm

The shape of the membrane	Layer		
	SiO_2	Mo	ZnO
	From -80 to -500 MPa	From -1.5 to +1.5 GPa	From -0.7 to +0.7 GPa
Round	From 2.95×10^{-14} to 2.72×10^{-13} (↑)	From 4.35×10^{-13} (↑) to 5.23×10^{-13} (↓)	From 2.64×10^{-13} (↑) to 2.63×10^{-13} (↓)
Square	From 7.83×10^{-13} to 5.09×10^{-13} (↑)	From 6.23×10^{-13} (↑) to 6.23×10^{-13} (↓)	From 2.44×10^{-13} (↑) to 2.43×10^{-13} (↓)
Square with transverse and angular beam	From 20 to 570 (↑)	From 90 (↑) to 90 (↓)	From 40 (↑) to 40 (↓)

Acknowledgments

The work was done on the infrastructure of the Research and Education Centre «Nanotechnologies» of Southern Federal University and Laser Institute, Qilu University of Technology (Shandong Academy of Sciences).

REFERENCES

1. **Ageev O. A., Konoplev B. G.,** Nanotechnology in microelectronics, Nauka, Moscow, 2019.

2. Abadias G., Chason E., Keckes J., Sebastiani M., Thompson G., Barthel E., Doll G., Murray C., Stoessel C., Martinu L., Review Article: Stress in thin films and coatings: Current status, challenges, and prospects, Journal of Vacuum Science and Technology A: Vacuum, Surfaces, and Films. 36 (2) (2018) 020801.

3. Dostanko. A. P., The integrated technologies functional micro-and nanostructures, Bestprint, Minsk, 2013.

4. Shen Y.G., Effect of deposition conditions on mechanical stresses and microstructure of sputter-deposited molybdenum and reactively sputter-deposited molybdenum nitride films, Materials Science and Engineering. 359 (1-2) (2003) 158–167.

5. Conchon F., Renault P.O., Goudeau P., Bourhis E. Le, Sondergard E., Barthel E., Grachev S., Gouardes E., Rondeau V., Gy R., Lazzari R., Jupille J., Brun N., Residual stresses in sputtered ZnO films on (100) Si substrates by XRD, Materials Research Society Symposium Proceedings. 1201 (2009) 1201-H05-03.